Lecture Notes in Civil Engineering

Thomas Kang *Editor*

Proceedings of 5th International Conference on Civil Engineering and Architecture

Proceedings of ICCEA 2022

Springer

Lecture Notes in Civil Engineering

Volume 369

Lecture Notes in Civil Engineering (LNCE) publishes the latest developments in Civil Engineering—quickly, informally and in top quality. Though original research reported in proceedings and post-proceedings represents the core of LNCE, edited volumes of exceptionally high quality and interest may also be considered for publication. Volumes published in LNCE embrace all aspects and subfields of, as well as new challenges in, Civil Engineering. Topics in the series include:

- Construction and Structural Mechanics
- Building Materials
- Concrete, Steel and Timber Structures
- Geotechnical Engineering
- Earthquake Engineering
- Coastal Engineering
- Ocean and Offshore Engineering; Ships and Floating Structures
- Hydraulics, Hydrology and Water Resources Engineering
- Environmental Engineering and Sustainability
- Structural Health and Monitoring
- Surveying and Geographical Information Systems
- Indoor Environments
- Transportation and Traffic
- Risk Analysis
- Safety and Security

To submit a proposal or request further information, please contact the appropriate Springer Editor:

– Pierpaolo Riva at pierpaolo.riva@springer.com (Europe and Americas);
– Swati Meherishi at swati.meherishi@springer.com (Asia—except China, Australia, and New Zealand);
– Wayne Hu at wayne.hu@springer.com (China).

All books in the series now indexed by Scopus and EI Compendex database!

Thomas Kang
Editor

Proceedings of 5th International Conference on Civil Engineering and Architecture

Proceedings of ICCEA 2022

Springer

Editor
Thomas Kang
Department of Architecture
and Architectural Engineering
Seoul National University
Seoul, Korea (Republic of)

ISSN 2366-2557 ISSN 2366-2565 (electronic)
Lecture Notes in Civil Engineering
ISBN 978-981-99-4048-6 ISBN 978-981-99-4049-3 (eBook)
https://doi.org/10.1007/978-981-99-4049-3

Conference Committees

Conference General Chair

Thomas Kang, Seoul National University, South Korea

Conference Co-chair

Le Trung Thanh, Vietnam Institute for Building Materials, Vietnam

Conference Program Chair

Youngjin Lee, Boston Architectural College, USA
Xiangguo Wu, Harbin Institute of Technology, China

Technical Program Committees

Reazul Ahsan, The University of Utah Asia Campus, South Korea
Mohammad Arif Kamal, Aligarh Muslim University, India
Wong Wah Sang, University of Hong Kong, Hong Kong
Dat Doan, Auckland University of Technology, New Zealand
Allan Alzona, National University-Manila, Philippines
Mayas Ahmad Taha, Al Yamamah University, South Africa
Roshina Babu, The University of Utah Asia Campus, South Korea
Shavkat Buriboev, Samarkand State Architectural and Civil Engineering Institute (SSCI), Uzbekistan
Wonseok Chae, University of Wuppertal, Germany

Krisada Chaiyasarn, Thammasat University, Thailand
Miktha Farid Alkadri, University of Indonesia, Indonesia
Orlean G dela Cruz, Polytechnic University of the Philippines, Philippines
Jawdat Goussous, The University of Jordan, Jordan
Gregor Grunwald, Jade University of Applied Sciences, Germany
Emina Hadzalic, University of Sarajevo, Bosnia and Herzegovina
Hazrina Haja Bava Mohidin, University of Malaya, Malaysia
Pawinee Iamtrakul, Thammasat University, Thailand
Seong-Cheol Lee, Kyungpook National University, South Korea
Ha Minh Tuan, HUTECH University, Vietnam
Le-Minh Ngo, Ton Duc Thang University, Vietnam
Hyeon-Jong Hwang, Konkuk University, South Korea
Chavanont Khosakitchalert, Chulalongkorn University, Thailand
Tamara Kelly, Abu Dhabi University, UAE
Chompoonut Kongphunphin, Thammasat University, Thailand
Dante L. Silva, Mapua University, Philippines
Chayut Ngamkhanong, Chulalongkorn University, Thailand
Bakhriev Nuritdin, Samarkand State Architectural and Civil Engineering Institute (SSCI), Uzbekistan
Vachara Peansupap, Chulalongkorn University, Thailand
Shaoyun Pu, Southeast University, China
Lapyote Prasittisopin, Chulalongkorn University, Thailand
Rajesh Rai, Indian Institute of Technology (Banaras Hindu University), India
Porntip Ruengtam, Mahasarakham University, Thailand
V. V. N. Prabhakara Rao, VR Siddhartha Engineering College, India
Christiono Utomo, Institut Teknologi Sepuluh Nopember, Indonesia
Marcelo Villacis Ormaza, Universidad Tecnológica Indoamerica, Ecuador
Manat Srivanit, Thammasat University, Thailand
Varodom Suksawasdi, Faculty of Architecture and Planning, Thammasat University, Thailand
Cao Sunliang, Hong Kong Polytechnic University, Hong Kong
Sharifah S S Mahdzar, Universiti Teknologi Malaysia, Malaysia
Taki Eddine Seghier, UCSI University, Malaysia
Manny Anthony Taguba, National University-Manila, Philippines
Doris Toe Hooi Chyee, Universiti Teknologi Malaysia, Malaysia
Gokhan Tunc, Atilim University, Turkey
Wardah Fatimah Mohammad Yusoff, National University of Malaysia, Malaysia
Yaik Wah Lim, Universiti Teknologi Malaysia, Malaysia
Danai Wantanakorn, Rajamangala University of Technology Tawan-ok, Thailand
Haryati Yaacob, Universiti Teknologi Malaysia, Malaysia
Yanto Yanto, Jenderal Soedirman University, Indonesia
Mazlina Zaira Mohammad, Universiti Teknologi MARA, Malaysia
Khan Zaib Jadoon, International Islamic University Islamabad, Pakistan
Ting Zhang, Politecnico di Torino, Italy
Yuan Zhu, Southeast University, China

Preface

The 5th International Conference on Civil Engineering and Architecture (ICCEA 2022) was held in Hanoi, Vietnam, from December 16 to 18, 2022. The Technical Program Committee put together an excellent program, which includes the presentations from Keynote Speakers—Prof. Le Trung Thanh (Vietnam Institute for Building Materials, Vietnam), Prof. Masahiro Inoue (Keio University, Japan), Mr. Doan Thanh Ha (H&P Architects | HPA, Vietnam), and myself. The program included more than 70 papers that were accepted for presentations and publications in the ICCEA 2022 conference proceedings.

ICCEA offered a great opportunity for discussions of methods, technologies, systems, and practices in different areas of civil engineering and architecture among people from various places around the world. The conference enabled participants to exchange ideas with other researchers and build connections upon which international collaborations can stand firm and thrive, and aim at solving civil engineering and architecture problems, at present and in the future.

The proceedings of ICCEA 2022 cover a range of topics, including, but not limited to advanced building materials and the properties, concrete engineering and technology, architectural design and theory, structural health monitoring and construction surveying, urban planning and space design, BIM technology, bridge engineering and technology, historic building conservation, transportation engineering and management, structural design and structural mechanics, etc.

Efforts taken by peer reviewers contributed to improving the quality of papers provided constructive critical comments; improvements and corrections to the authors are gratefully appreciated. We are very grateful to the international/national advisory committee, session chairs, and administrative assistants who selflessly contributed to the success of this conference. Also, we are thankful to all the authors who submitted papers, because of which the conference became a story of success. It was the quality of their presentation and passion to communicate with the other participants that made this conference a grand success.

As you read these proceedings, please plan to submit a proposal to the ICCEA 2023 conference, which is scheduled for December 16–18, 2023, in Bali, Indonesia. We are looking forward to seeing you at ICCEA 2023!

Dr. Thomas Kang
Conference General Chair
ICCEA 2022
Professor
Seoul National University
Seoul, South Korea

Contents

Advanced Building Materials and the Properties

Composite Wave Sheets from Basalt Fiber for Pitched Roofing

N. F. Bakhriev and N. R. Qurolova

Abstract This article describes scientific research on the creation of highly efficient asbestos-free composite sheet roofing materials based on basalt fibers using nanotechnology and innovative developments, based on local conditions. Since in modern conditions the problems of environmentally friendly and durable materials are acute, and the authors propose an innovative method of replacing asbestos and chrysotile fibers in the production of waved roofing sheets. New ideas and results of experimental developments, technological regulations, and practical experiments in this direction are proposed. The Mega Invest Industrial joint venture is a high-tech basalt fiber producer in Central Asia and the second largest producer in the CIS, which produces a wide range of ultra-strong basalt fibers. The authors made an attempt to realize the idea of using local basalt fiber for the production of waving roofing sheets.

Keywords Strategy · Concept · Modernization · Nanotechnology · Innovation · Investment · Basalt · Basalt fiber · Waved sheet roof · Stone clinker · Active mineral elements · Improved structure · Kinetics · Surface viscosity · Transformations

1 Introduction

At the present stage, the construction and technical re-equipment of vital infrastructures, the construction and reconstruction of the appearance of each district, city, and, in general, the country as a whole have reached a new level. Naturally, the need for modern residential buildings and social facilities in our country is growing, and the most modern "smart city buildings" are being built. Accordingly, scientific developments on the creation of innovative, high-quality, environmentally friendly, and

N. F. Bakhriev (✉) · N. R. Qurolova
Department of Construction Materials, Samarkand State Architectural and Civil Engineering Institute (SSACEI), Samarkand, Uzbekistan
e-mail: bakhriyev.nf@mail.ru

T. Kang (ed.), *Proceedings of 5th International Conference on Civil Engineering and Architecture*, Lecture Notes in Civil Engineering 369,
https://doi.org/10.1007/978-981-99-4049-3_1

inexpensive building materials from local raw materials used in this area are relevant [1, 2].

The land of Uzbekistan is rich in natural resources necessary for the production of high-quality building materials. In the foothills of Kurama, Turkestan, and Tomdi in Uzbekistan, there are huge reserves of volcanic rock—basalt, a unique natural material necessary for the production of various building materials [3, 4].

A roof is the upper part of a building that protects it from snow, rain, solar radiation, and other adverse influences. Roofs must withstand the effects of constant and temporary loads, wind, snow pressure, solar canvas of high radiation, and exposure to an aggressive environment; especially they must be waterproof, moisture resistant, and resistant to chemical corrosion from constant wind and solar radiation [3, 4].

In our country, various roofing materials are used to cover the roofs of buildings and structures, such as metal profiles, ceramic tiles, metal tiles, asbestos-cement sheets, and others. These types of materials are mainly imported from the Russian Federation and neighboring countries. At the same time, asbestos raw materials required for the production of asbestos-cement sheet coverings in the country are also imported [5–7].

Due to its geographical position, Uzbekistan is a region with a dry and hot climate during the summer. According to the recommendations of the World Health Organization (WHO), in these climatic conditions, residential buildings and social facilities built from asbestos or asbestos-cement sheet coverings are considered extremely hazardous to public health [8, 9].

In particular, in the summer heat of +40 … 45 °C, asbestos-cement sheet roofing at high temperatures emits carcinogenic substances, and therefore, in today's modern construction, there are a number of restrictions on the production and use of asbestos raw materials. The demand for roofing materials is increasing, and the production of safe, efficient, roofing sheets leads to high costs. As a result, the demand for inexpensive, environmentally friendly, convenient, and safe modern roofing materials in production is growing [8, 9].

Our scientific research and analysis of the available data show that this area is rich in extremely relevant and innovative ideas. This article presents the subject of scientific research—the production of basalt fiber composite roofing materials—aimed at solving problems in the construction system of the republic in terms of efficiency and significance. In our study, the main goal was to develop sheet composite materials, with dispersed basalt fiber, thereby improving the operational and functional properties of roofing.

2 Proposed Methodology, Experiments, and Results

Expected research results and their significance:

- scientific and theoretical substantiation of the idea of obtaining composite sheet materials with a dispersed bond from basalt fiber.

- study of the reinforcing properties of basalt fiber.
- scientific substantiation of obtaining sheet materials, resistant to dry and hot conditions of Central Asia.
- obtaining basalt fiber and cement-based mixtures using the cavitations' method for preparing mixtures in order to ensure uniform distribution of basalt fiber inclusions and scientific substantiation of this hypothesis.
- studying methodological, technological, functional issues, mathematical modeling of optimal compositions for forming corrugated sheet materials;
- According to this goal, the research has the following tasks:
- -creation of dispersed reinforced composite materials based on basalt fibers and the radical development of this industry.
- as a result of studying the properties, physicochemical structure of basalt fibers, the idea of creating a sheet material based on them was put forward.
- the establishment of innovative traditions for the production of building composite materials from basalt fiber in modern construction is expected.
- theoretical substantiation and practical actions of the composition of composite structural sheet materials based on basalt fibers.

3 Materials, Experiments, and Control Methods

Basalt mineral of dark gray color, with a specific gravity of 2.5–3.0 g / cm^3. It consists mainly of plagioclase (labradorite), as well as pyroxene, olivine and magnetite, titanite, apatite, etc. Also, in terms of chemical composition, it is close to gabbroid, its analogue in the deeper layers of the earth's crust. Volcanic glass fills the gaps of granular crystals. Fully crystallized basalts are called dolerites. Its iron and magnesium-rich type, which forms on the ocean floor, is called oceanite, and the type that solidifies as a result of tectonic faults flowing onto land is called plat basalt. Basalt occupies a very large area on the ocean floor and on land. Basaltic lava also flows from modern volcanoes. Depending on the mineral composition, there are leucite basalt, nepheline basalt, magnetite basalt, calibrated basalt, apatite basalt, etc. [3–7].

Today China, Russia, and Ukraine, developed countries with significant basalt reserves, are leaders in the processing of basalt minerals and the production of various goods and construction products.

By melting the basalt mineral at high temperatures and spraying it onto roving frames, it can be converted to a fibrous fluffy state. Fabrics based on it can be used to replace asbestos fibers, some types of fiberglass, carbon fiber, and other mineral fibers in many industries.

Basalt fiber has a high modulus of elasticity and tensile strength. In recent decades, the latest technological solutions have been developed to reduce the cost of basalt fiber production; therefore, basalt fiber is now a more serious competitor to steel fibers. In this case, the size of the fiber (fiber length) added to the dry mix, the amount of added fiber (wt %), the type of material used as filler plays an important role. In particular, the research used basalt fiber, developed by the joint venture MEGA

Table 1 Chemical composition and physical structure of basalt fibers

S/n	Manufacturer country	Composition (minerals)								
		SiO_2	TiO_2	Al_2O_3	Fe_2O_3	FeO	MgO	CaO	Na_2O	K_2O
1	China	48.03	2.85	12.59	3.88	8.15	5.47	10.5	2.32	2.68
2	Uzbekistan	48.2	0.60	11.8	4.12	6.20	9.15	13.3	1.45	2.25
3	Basalt of the "Osmansoy" deposit	51.09	0.78	18.93	11.70	3.38	8.04	1.90	0.10	1.90

Fig. 1 **a** Basalt fiber, **b** basalt wool

INVEST INDUSTRIAL, which is the only producer of basalt fiber in Central Asia and the second largest in the CIS. Investments in the basalt plant amounted to $ 54 million, 80% of the basalt fiber produced at the enterprise goes to the production of accessories, and the remaining 20% goes to the manufacture of other products required for construction [3–7].

Basalt fiber will be produced from basalt roving by cutting to specific dimensions. Basalt roving brand BR 17–2400 MII63; fiber thickness 17 microns in diameter; the brand of the lubricant used for gluing the fibers, MII63; the average modulus of elasticity is 80 GPa [6, 7].

The high strength of basalt fibers, their frost resistance, resistance to aggressive environments, resistance to mold and microorganisms, and alkaline harmful environments expand the scope of its application. After all, the needle-like structure forms a solid frame. Basalt fibers make up one hundredth of the diameter of a thin fibrous tube. The fiber has a diameter of 10–21 μ and a length of 0.5–5 cm.

The thermal conductivity of basalt fibers is zero. Another key feature is its high temperature resistance. It does not dissolve in water; it is an environmentally friendly material that is resistant to chemically inert alkaline influences.

There are several types of basalt fiber. The study uses high-strength basalt fiber from the mining industry developed by the joint venture "MEGA INVEST INDUSTRIAL", composition 3. The chemical composition and physical structure of basalt fiber is given in Table 1 (see Fig. 1).

Basalt benefits:

- Environmentally friendly material with a natural formula of basalt stone;
- Free of carcinogenic and toxic-toxicological substances;
- Resistance to mold and microorganisms.

Absolute incombustibility at high temperatures, resistance to high temperatures of continuous use—700 °C, short-term use—up to 900 °C;

- Service life of more than 50 years due to the natural formula;
- High chemical resistance to alkaline and acidic environments;
- Basalt composites can replace steel and fiberglass reinforced plastic [5, 6, 10].

4 Proposed Methodology

In accordance with the task, a series of experiments was carried out to optimize the compositions of basalt-cement mixtures with nanofillers. The composition of the mixture was selected using a dry method, i.e., all constituent components of fiber, cement, and nanofillers were dried to a moisture content of no more than 1 wt. %. The calculated amount of basalt fiber was fluffed on the runners to the required dispersion. The finished fluffy mixture of basalt was used to prepare an aqueous solution on the next mixer 6 in Fig. 2. The scheme of technological production of roofing sheets by the method of a liquid dispersed mixture is shown in Fig. 2.

In order to determine the optimal number of constituent components and sign-changing technological parameters, a series of experiments was performed according to a linear three-factor mathematical plan [11, 12]. Flexural strength, concentrated load strength, and toughness of corrugated sheet were taken as response functions. Mechanical strength indicators were determined according to [13], on the basis of

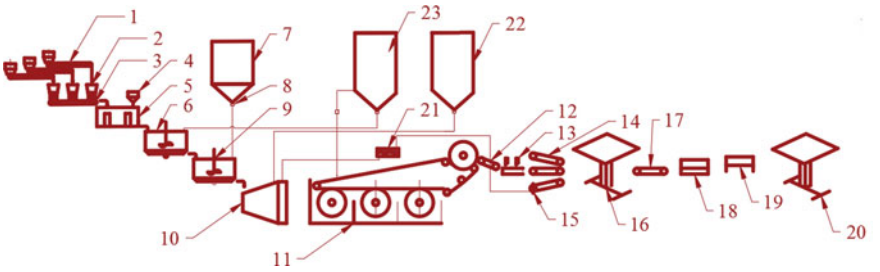

Fig. 2 Manufacturing technology of roofing sheets by the method of liquid dispersed cement-basalt mixture: 1, 3, 12, 15, 17—conveyor belts; 2, 4, 8—dispensers; 5—mixer with a runner; 6—water dryer for wet processing of fiber; 7—water tank (bunker); 9—turbo cavitations' mixer; 10—mixer for reprocessing of cut pieces; 11—machine for forming a flat strip with a roller drum; 13—scissors; 14—wave-forming vacuum press; 16—portable cart; 18—primary processing chamber; 19—finishing chamber; 20—carts; 21—cut mixer; 22, 23—silos mixers for storage of liquid slurry

Table 2 Intervals and levels of variation of factors

Factors to be verified		Variation level			Variation interval
Наименование	Cod	−1	0	+1	
Basalt fiber length, mm	X_1	5	10	15	5
The amount of cement in suspension, cement/water ratio, C/W	X_2	0.30	0.33	0.36	0.03
Basalt fiber content in suspension, %	X_3	10	12	14	2

an accredited laboratory No. 5, at the regional testing center of the Samarkand State Architectural and Civil engineering Institute (Sam SACEI).

Controlled factors include:

- length of basalt fiber (5…1 0…15 mm);
- the amount of cement in the suspension, the ratio of cemenwater, (0.3 … 0.33 … 0.36);
- content of basalt fiber in suspension (10 … 12 … 14%).

The values of the intervals of variation of the input parameters are given in Table 2.

To describe the correlation dependence of the parameters for optimizing the strength of sheet material for three-point bending and the kinetics of the increase in impact toughness from the pendulum load, depending on the selected experimental factors X_1, X_2, X_3, it seems sufficient to limit ourselves to analyzing the response surface of the linear equation.

Based on the conditions given in Table 2, drew up a plan of the experiment, according to which the constituent components were selected in the intended intervals of variation. The compositions of the liquid dispersed mixture, from which the basalt-cement sheet-like tape was formed, were selected strictly according to the experiment plan matrix. In the future, corrugated roofing sheets were cut from this canvas. Production-experimental samples were determined by mechanical strength indicators according to GOST [13].

The plan of the experiment to select the optimal composition of the suspension for the molding mass and the results of mechanical tests are shown in Table 3.

5 Analysis of Experiments and Research Results

Data processing and drawing up a regression equation based on the calculated correlation coefficients are shown in Table 4.

In accordance with the performed analysis of the results of the full-factorial experiment and taking into account the significance of the correlation coefficients, a regression equation was drawn up, which characterizes the flexural strength of waved roofing sheets (1).

Table 3 Experiment plan

S/n	Variable factors			Names of variable factors and their meanings			Mechanical strength indicators according to GOST							
	X_1	X_2	X_3	Basalt fiber length, mm	The amount of cement in suspension, C/W	Basalt fiber content in suspension, %	Bending strength, MPa			Average value, MPa	Impact strength, kDjs/m^2			Average value, kDjs/m^2
1	2	3	4	5	6	7	8	9	10	11	12	13	14	15
1	−1	−1	−1	15	0.36	14	13.2	13.6	13.6	**13.5**	1.6	1.6	1.4	**1.5**
2	1	−1	−1	5	0.36	14	11.8	12.7	12.9	**12.5**	1.7	1.7	1.9	**1.8**
3	−1	1	−1	15	0.30	14	12.9	12.5	13.2	**12.9**	1.8	2.2	2.0	**2.0**
4	1	1	−1	5	0.30	14	13.7	13.6	14.5	**13.9**	2.4	2.5	2.5	**2.5**
5	−1	−1	1	15	0.36	10	15.0	16.3	15.6	**15.6**	1.4	1.4	1.3	**1.4**
6	1	−1	1	5	0.36	10	18.6	17.9	19.3	**18.6**	1.8	1.7	1.9	**1.8**
7	−1	1	1	15	0.30	10	26.3	25.6	27.0	**26.3**	1.6	1.6	1.7	**1.6**
8	1	1	1	5	0.30	10	31.0	29.4	31.6	**30.6**	1.5	1.7	1.6	**1.6**
9	0	0	0	12.5	0.33	12	24.8	27.1	23.9	**25.3**	2.3	2.7	1.9	**2.3**
10	0	0	0	12.5	0.33	12	25.8	27.1	27.7	**26.9**	1.9	2.0	1.9	**1.9**

Table 4 Calculation of coefficients of the regression equation

Variable factors			Average value of bending strength, Y_i (MPa)	Correlation level						
X_1	X_2	X_3		X_1*Yi	X_2*Y_i	X_3*Y_i	X_1* $X_{2*}Y_i$	X_1*$X3$*Y_i	X_2*$X3$*Y_i	X_1*X_2*X_3*Y_i
−1	−1	−1	**13.5**	−13.5	−13.5	−13.5	13.5	13.5	13.5	−13.5
1	−1	−1	**12.5**	12.5	−12.5	−12.5	−12.5	−12.5	12.5	12.5
−1	1	−1	**12.9**	−12.9	12.9	−12.9	−12.9	12.9	−12.9	12.9
1	1	−1	**13.9**	13.9	13.9	−13.9	13.9	−13.9	−13.9	−13.9
−1	−1	1	**15.6**	−15.6	−15.6	15.6	15.6	−15.6	−15.6	15.6
1	−1	1	**18.6**	18.6	−18.6	18.6	−18.6	18.6	−18.6	−18.6
−1	1	1	**26.3**	−26.3	26.3	26.3	−26.3	−26.3	26.3	−26.3
1	1	1	**30.6**	30.6	30.6	30.6	30.6	30.6	30.6	30.6
Correlation coefficients			**$b_0 = 19.6$**	**$b_1 = 0.92$**	**$b_2 = 2.95$**	**$b_3 = 4.8$**	**$b_{12} = 0.43$**	**$b_{13} = 0.91$**	**$b_{23} = 2.73$**	**$b_{123} = 0.08$**
Significance of the coefficient			**19.6 > 0.67**	**0.92 > 0.67**	**2.95 > 0.67**	**4.8 > 0.67**	**0.43 < 0.67**	**0.91 > 0.67**	**2.73 > 0.67**	**0.08 < 0.67**

$$Y = 19.6 + 0.92X_1 + 2.95X_2 + 4.8X_3 + 0.91X_1X_3 + 2.73X_2X_3 \quad (1)$$

Here X_1 and X_2 are the values of the factors; $b_0 = 19.6$ is a free term equal to the response of the system at the initial stage of the experiment at $X_1 = X_2 = 1$; $b_1 = 0.92$; $b_2 = 2.95$; $b_3 = 4.8$—regression coefficients showing the degree of influence of the relevant factors on the output of the process; $b_{12} = 0.91$ is a coefficient indicating the presence of the effect of interaction between two factors (pair interaction). To unify the program of the experiment, we introduce a special sliding coordinate system, the origin of which coincides with the zero level of factors. Let us choose the scales of the variables in such a way that the intervals of variation of the factors are equal to one. Then, the initial factor level will correspond to 0, and the upper and lower levels of the factor, obtained by adding and subtracting the zero level and the step, will be equal to +1 and −1 [11].

Continuing the processing of the data obtained by the method of a full-factor experiment, based on the values of the impact strength from the pendulum load, taking into account the significance of the correlation coefficients, we compiled a regression equation that characterizes the impact strength of basalt-cement roofing sheets under a pendulum load shown in Table 5.

In accordance with the performed analysis of the results of the full-factorial experiment and taking into account the significance of the correlation coefficients, a regression equation was drawn up, which characterizes the flexural strength of waved roofing sheets (2) (Figs. 3 and 4).

$$Y = 1.8 + 0.1X_1 + 0.2X_2 - 0.2X_3 - 0.1X_1X_2X_3 \quad (2)$$

6 Discussions

As a result of processing the experimental data, a regression equation was obtained that adequately describes the kinetics of the adhesion strength of the mortar mixture depending on the content of the constituent components (3, 4).

$$Y = 19.6 + 0.92X_1 + 2.95X_2 + 4.8X_3 + 0.91X_1X_3 + 2.73X_2X_3 \quad (3)$$

$$Y = 1.8 + 0.1X_1 + 0.2X_2 - 0.2X_3 - 0.1X_1X_2X_3 \quad (4)$$

As a result of mathematical processing of the obtained data [11, 12], as well as analysis of isoperimetric diagrams, it was found that the factor X_1 (length of basalt fiber, mm) has the most significant effect on the bending strength of the proposed waved sheet (slate), since it has the greatest correlation coefficient. The degree of influence of the variable factors considered in these series of experiments and the optimality criteria are in the following sequence (5).

Table 5 Calculation of coefficients of the regression equation

Variable factors			Average value of bending strength, Y_i (MPa)	Correlation level						
X_1	X_2	X_3		$X_1{*}Y_i$	$X_2{*}Y_i$	$X_3{*}Y_i$	$X_1{*}X_{2*}Y_i$	$X_1{*}X_3{*}Y_i$	$X_2{*}X_3{*}Y_i$	$X_1{*}X_2{*}X_3{*}Y_i$
−1	−1	−1	**1.5**	−1.5	−1.5	−1.5	1.5	1.5	1.5	−1.5
1	−1	−1	**1.8**	1.8	−1.8	−1.8	−1.8	−1.8	1.8	1.8
−1	1	−1	**2.0**	−2.0	2.0	−2.0	−2.0	2.0	−2.0	2.0
1	1	−1	**2.5**	2.5	2.5	−2.5	2.5	−2.5	−2.5	−2.5
−1	−1	1	**1.4**	−1.4	−1.4	1.4	1.4	−1.4	−1.4	1.4
1	−1	1	**1.8**	1.8	−1.8	1.8	−1.8	1.8	−1.8	−1.8
−1	1	1	**1.6**	−1.6	1.6	1.6	−1.6	−1.6	1.6	−1.6
1	1	1	**1.6**	1.6	1.6	1.6	1.6	1.6	1.6	1.6
Correlation Coefficients			$\mathbf{b_0 = 1.8}$	$\mathbf{b_1 = 0.1}$	$\mathbf{b_2 = 0.2}$	$\mathbf{b_3 = -0.2}$	$\mathbf{b_{12} = 0.03}$	$\mathbf{b_{13} = 0.04}$	$\mathbf{b_{23} = -0.1}$	$\mathbf{b_{123} = -0.1}$
Significance of the coefficient			**1.8 > 0.09**	**0.1 > 0.09**	**0.2 > 0.09**	**0.2 > 0.09**	**0.03 < 0.09**	**0.04 > 0.0.09**	**−0.1 > 0.09**	**−0.1 < 0.09**

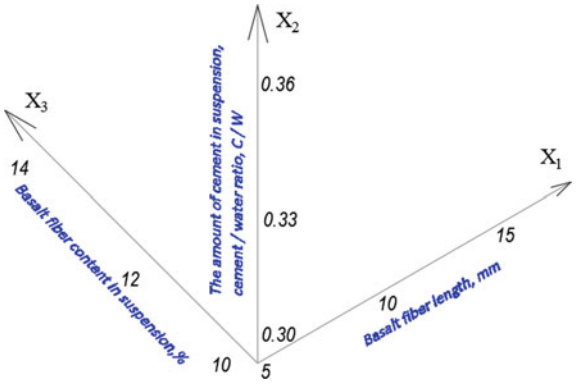

Fig. 3 Names of variable factors and their meanings: X_1—length of basalt fiber, mm; X_2—amount of cement in suspension, cement/water ratio; X_3 is the content of basalt fiber in the cement fiber suspension, wt %

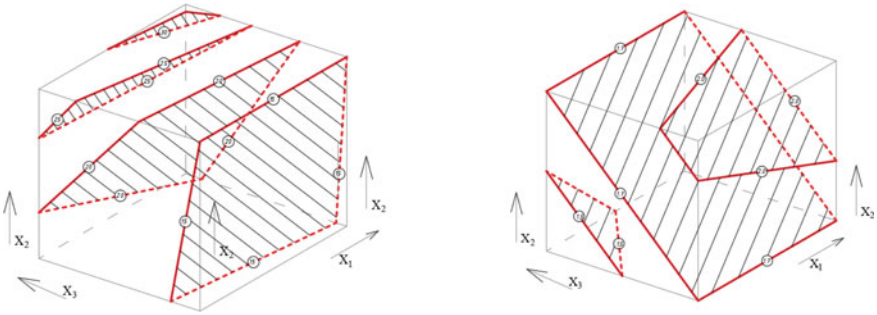

Fig. 4 Isoperimetric diagrams constructed according to the regression equation: **a**—responses of the bending strength of sheet material, MPa; **b**—responses of material stability to impact strength, kJ/m^2

$$X_1 > X_3 > X_2 \tag{5}$$

Also, the analyses found that the factor X_3 [the content of basalt fiber in the cement fiber suspension, (wt %)] has the most significant effect on the impact strength of the sheet.

7 Conclusion

Based on the planning of the experiment and mathematical processing of the results, a regression equation was obtained that reflects the dependence of the bending strength of the roofing sheet on the length of the fibers and their share in the volume of the water–cement suspension.

Isometric diagrams have been constructed that allow you to select the optimal composition of the water–cement suspension within the required limits, taking into account technological and raw materials factors.

As a result of a series of experiments, the optimal composition was obtained, at which the bending strength of the cement-basalt corrugated sheet reaches its maximum value, that is, 30.6 MPa.

8 Production

On the basis of the obtained laboratory, experimental–experimental conclusions, we have carried out pilot-experimental studies on the development of technology for the production of basalt-cement corrugated sheets in the conditions of the existing production line of chrysotile corrugated sheets of the Istiqlol Shulasi production company in the Samarkand region.

Portland cement M400 "HUAXIN CEMENT" of the Djizak region GOST 10178-85, Chrysotile asbestos GOST 12871-93 grades A 4-20, A 5-50 produced by "Kazakhstan" and basalt fiber of fiber JV LLC "MEGA INVEST INDUSTRIAL" Djizak region were used as starting materials, Farish district, Basalt quarry "Osmansoy", site "Osmonsoy-1" (0.5 cm fiber—30 kg; 1 cm fiber—50 kg; 1.5 cm fiber—20 kg).

The technology for the production of corrugated roofing sheets is made on the production base of corrugated roofing sheets of the "Istiqlol Shulasi" company in the Samarkand region, according to the technological scheme of Fig. 5.

For the purpose of practical comparison of physical and mechanical properties, batches of finished products were made in the form of corrugated chrysotile sheets and from basalt fibers, according to the following compositions shown in Table 6 (Fig. 6).

The results of experimental studies carried out in the production conditions of the "Istiklol Shulasy" company showed that it is possible to produce basalt-cement corrugated sheets on the current production line of chrysotile cement corrugated sheets, while it is possible to replace the asbestos fiber content partially or completely and obtain high-quality roofing sheets. Tests of finished roofing corrugated boards were carried out in the "Regional Testing Center—Laboratory No. 5", in accordance with GOST [13–15]. The test results and the conclusion of laboratory measurements of physical and mechanical parameters far exceed the traditional indicators of asbestos-cement roofing sheets.

Fig. 5 Basalt-cement corrugated roofing sheets manufacturing process

Table 6 Comparative analysis of physical and mechanical properties and methods of manufacturing chrysotile and basalt fiber sheets

S/n	The name of the components in the composition, kg						Ultimate bending strength, MPa	Density, kg/m^3	Impact strength, kJ/m^2
	Asbestos fiber	Basalt fiber			Portland cement, M400	Water, l			
		5 mm	10 mm	15 mm					
1	60	–	–	–	480	1500	15.2	1650	1.45
2	57	3	–	–			16	1600	1.5
3	56	4	–	–			17.5	1600	1.5
4	54	–	6	–			22.5	1580	1.77
5	54	–	–	6			24.0	1550	1.86
6	–	20	20	20			40.0	1450	2.20

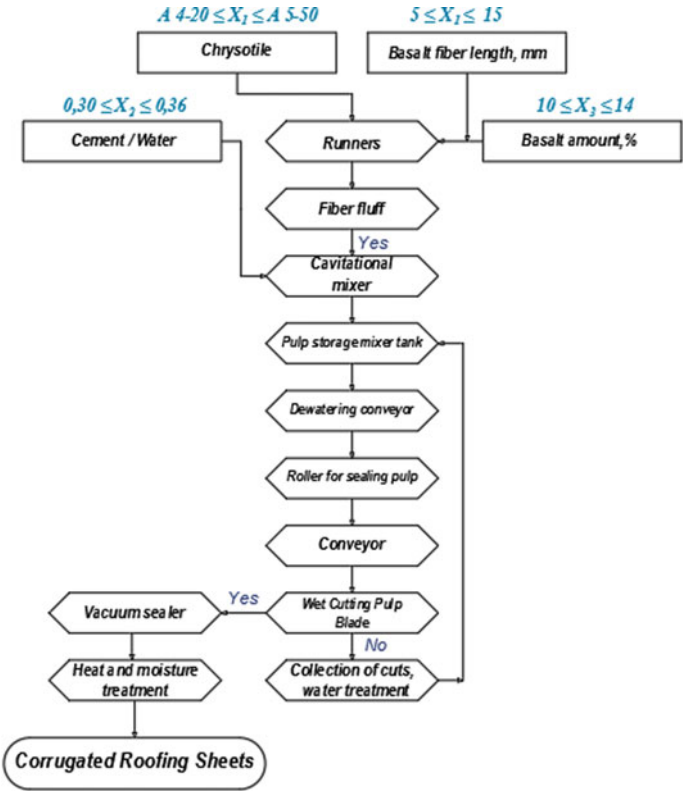

Fig. 6 Technological scheme for the production of corrugated roofing sheets

References

1. Resolution of the President of the Republic of Uzbekistan dated May 23, 2019 No PR-4335 "On additional measures for the accelerated development of the construction materials industry"
2. Tang C, Jiang H, Zhang X, Li G, Cui J (2018). Corrosion behavior and mechanism of basalt fibers in sodium hydroxide solution. Materials 11:1381. https://www.mdpi.com/1996-1944/11/8/1381/htm
3. Shevchenko VP (2013) Natural raw materials of the republic of Uzbekistan for superfine basalt fiber, (2):6–8. https://doi.org/10.17073/1683-4518-2013-2-6-8
4. Makhmudova, VSh (2008) Development of technology for obtaining low-temperature cement with the use of basalt fibers of Uzbekistan. Candidate of Technical Sciences thesis, Tashkent. http://basalt.world/ru/uzbekistan-narashhivaet-obyomy-proizvodstva-bazaltovogo-volokna/
5. Turukmane RN, Gulhane SS, Daberao AM (2019) Basalt-technical fiber for civil applications. SVKM'S NMIM'S, Maharashtra/India. https://www.textiletechnology.net/fibers/trendreports/Man-Made-Fiber-Year-Book-2018-October-2018-Basalt--technical-fiber-for-civil-applications-12475
6. Baxriyev NF, Qurolova NR (2020) Bazalt tolali composition tomyopqich varaqi qoplamalar va ularning xususiyatlari. In: Problems of architecture and construction. Int Sci J included in the register of the Higher Attestation Commission of the Republic of Uzbekistan (certificate No. 00757. 2000.31.01). #4, Samarkand, pp 83…87 (special issue)

7. Bakhriev NF, Qurolova NR (2020) Asbestos-free basalt roofing sheets based on basalt fiber, Collection of scientific papers. In: AI-International book edition of the countries of the commonwealth of independent states, "Young Scientist-2020", Nur-Sultan, Kazakhstan, 28 Sept 2020, vol IV, 60–65 pp
8. National-chemicals_Content_WHO_RUS_WEB4.pdf. https://www.euro.who.int/data/assets/pdf_file/0009/373689/National-chemicals_Content_WHO_RUS_WEB4.pdf
9. All types of asbestos can cause cancer. https://news.un.org/ru/story/2010/08/1168091
10. Chakartnarodom P, Prakaypan W, Ineure P et al (2020) Properties and performance of the basalt-fiber reinforced texture roof tiles. Case Stud Constr Mater 13:e00444
11. Kizatova M, Sultanova MZ et al (2022) Mathematical planning of a multi-factor experiment and optimization of the feed extrusion process. https://doi.org/10.1088/1757-899X/994/1/012022
12. Zhegera KV, Petuhova NA, Samigullina EA (2022) Proceedings of the 7th …, mathematical planning of the experiment in product design. Springer. https://doi.org/10.1007/978-3-030-85233-7_84
13. GOST 30340-2012 (2013) Corrugated chrysotile cement sheets. Specifications, Standartinform, Moscow
14. GOST 12871-2013 (2015) Chrysotil. General specifications. Standartinform, Moscow
15. GOST 31108-2020 (2021) Common cements. Specifications. Standartinform
16. Morozov NN, Bakunov VS et al (2001) Materials based on basalts from the European north of Russia. Glass Ceram 58:100–104
17. Sharma P (2016) An introduction to basalt rock fiber and comparative analysis of engineering properties of BRF and other natural composites. https://www.researchgate.net/publication/291516479
18. Nurafshon | European Smart Specialization Strategy Platform. https://demo.btgromania.ro/
19. Different Types of Roof, Roof trusses and their components. https://engineeringbasic.com/
20. Asbestos Roof Tiles Guide | Homebuilding. https://www.homebuilding.co.uk

3D Cement Printing: DFMA Guideline of Patterned Load-Bearing Walls for Small Residential Units

Wannapol Sadakorn, Santirak Prasertsuk, and Lapyote Prasittisopin

Abstract Cement-based materials are widely used materials in today's construction industry because of its durability and strength. However, there were practical challenges of using them as construction materials such as errors by craftsmen, construction time, and many wastes from construction process. The latest technology is becoming an important key in the construction industry in a near future is 3D printing technology with cement-based materials that can eliminate the practical challenges in terms of the operational cost and the construction time during construction process. This research aims to study the Design for Manufacture and Assembly (DFMA) process of 3D printing technology with cement-based system. The study program includes testing the strength performance of the load-bearing walls with geometric patterns. The results of the research were the DFMA guidelines to minimize the practical challenges and operational costs of construction. The knowledge of applying 3D printing technology using cement-based system was established for developing the DFMA guidelines for small residential houses.

Keywords Cement · 3D printing technology · Small residential · Load-bearing wall · Design for manufacture and assembly

1 Introduction

In the future, 3D printing technology using cement-based materials or additive manufacturing in construction will play a significant role in both the architectural and construction industries. This will aid the construction process in mitigating the practical challenges of building cost and practical challenges such as time and labor skills [1–6]. Currently, the 3D printing technology incorporating concrete materials

W. Sadakorn · L. Prasittisopin (✉)
Faculty of Architecture, Chulalongkorn University, Bangkok, Thailand
e-mail: lapyote.p@chula.ac.th

S. Prasertsuk
Faculty of Architecture and Planning, Thammasat University, Pathum Thani, Thailand

T. Kang (ed.), *Proceedings of 5th International Conference on Civil Engineering and Architecture*, Lecture Notes in Civil Engineering 369,
https://doi.org/10.1007/978-981-99-4049-3_2

has widely embraced several technologies in a variety of aspects, such as material and performance development [7–9], structural design [10–13], and construction and fabrication technique [14–16] have been widely implemented.

This research has experimented with their applications in architecture through the process of designing and constructing a small residence by focusing on the following research objectives:

1. Study the DFMA of load-bearing walls by using geometric patterns as element basis.
2. Analyze a structural capacity behavior of load-bearing walls and small residential.
3. Propose guidelines for DFMA of small residential with 3D printing technology with cement-based system including the installation and assembly.

The results of this research are the DFMA guideline proposal for a small residential house. The outcome of the study provides knowledge of 3D printing technology with cement-based material for better design and construction of residential units.

2 Research Methodology

The research work was divided into two major parts. The first part covered the study of relevant theories as well as the experimental geometrically patterned bearing wall to determine which model performed the maximum load. Next is to bring the load-bearing wall that has been tested. The final step was a summary of DFMA guidelines, including installation and assembly. The methodology of the study is outlined in Fig. 1.

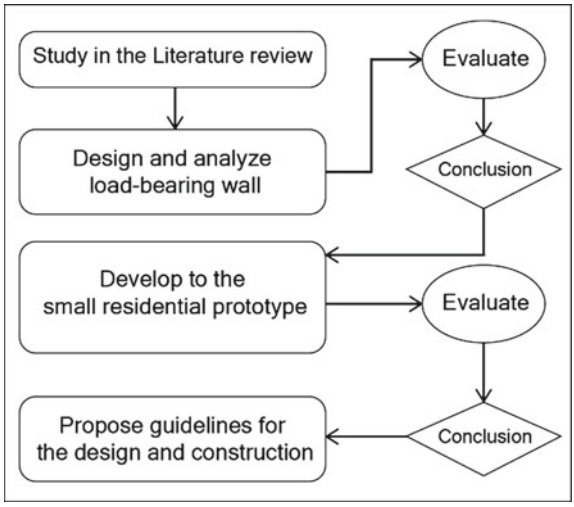

Fig. 1 Research process diagram

3 Design and Analysis of Load-Bearing Walls by Using Geometric Patterns as Element-Based

3.1 Calculation of the Optimal Ratio for the Wall Shape Design

In Figs. 2 and 3, 20 patterns of wall infill were studied. Then, each wall pattern was calculated the load capacity by the ANSYS engineering program. The optimum fill ratio in the load-bearing behavior was calculated and applied to load-bearing wall pat- tern design.

In Table 1, it can be concluded that when the ratio of the wall infill is greater, the maximum stress or strength increases. The strength begins to increase when the fill ratio is 3rd upwards, and the strength begins to exceed the need for structure and construction cost from the 6th ratio upwards. Therefore, an optimal ratio of strength is determined. Weight and construction cost is the 5th ratio to be used as the basis for shape design for load-bearing walls in the next step.

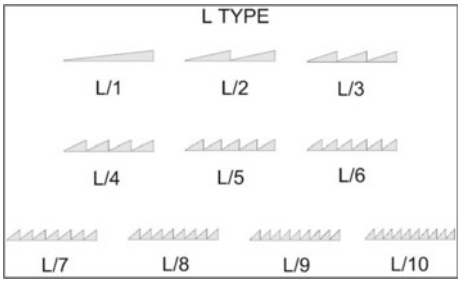

Fig. 2 Top of all ten L-shaped wall complement ratios

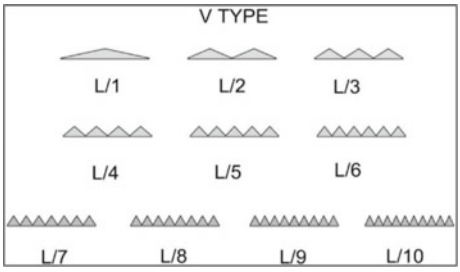

Fig. 3 Top of all ten V-shaped wall complement ratios

Table 1 Maximum stress values of different wall types from the least to greatest

Wall type	Total deformation (m)	Maximum stress (Pa)
V type 09	1.32E−06	63,008.00
V type 10	1.32E−06	63,521.00
L type 10	1.33E−06	66,279.00
V type 06	1.32E−06	67,827.00
V type 05	1.32E−06	68,409.00
L type 04	1.33E−06	78,096.00

3.2 A Pattern of the Load-Bearing Wall with Geometric Element

After obtaining ratios of five walls infill from a 1-m square wall, this ratio was used in the gridline design for the design of load-bearing wall shapes by the factors used in the design of the reference lines. There are three factors in total during designing including:

1. The basic form is from the triangle shape.
2. The limitation on the angle of inclination is not lower than 60 degrees.
3. The limitation of the protrusion angle is not less than 65 degrees.

In Fig. 4, the model can be used to design the load-bearing walls in total of 5 main types and 18 patterns. Later are to bring all the walls into the ANSYS engineering calculation program to study the load-bearing behavior and select the walls that are best suited (Fig. 5) [17].

3.3 Evaluation and Selection of Bearing Walls with Geometric Elements

The calculation of the load-bearing wall behavior was simulated the vertical force on the wall in the form of pressure of 40,000 Pa (Pascal), which is compared with the cross-sectional area of the wall having a size of 1200 sq. cm. (1.00 × 0.12 m). Compared to the vertical force on the wall, it is equal to 480 kg and distributedly applied in every main type and pattern. Therefore, the obtained behavior values can be identified and summarized in Table 2.

The structural calculation of load-bearing wall behavior by ANSYS program is given in Table 2. Results indicate that most of the load-bearing walls with double-sided pat- terns have better load-transfer behaviors than the single-sided patterns, and the maxi- mum compressive stress of the double-sided patterned wall is generally less than the single-sided patterned wall. In terms of the materials cost used in construction, the weight of the double-sided patterned wall is less than that of the single-sided patterned wall. When selecting the load-bearing walls with the most suitable properties according to construction principles, it is necessary to consider

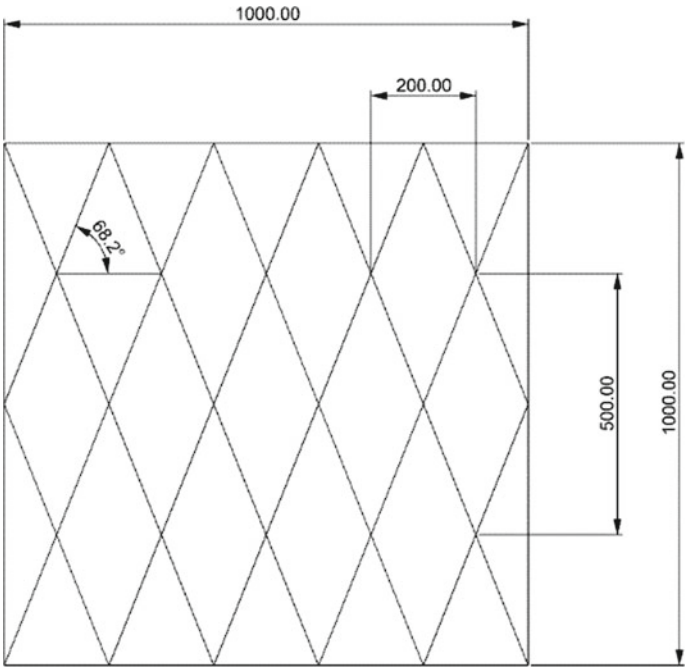

Fig. 4 Gridline for load-bearing wall shapes design

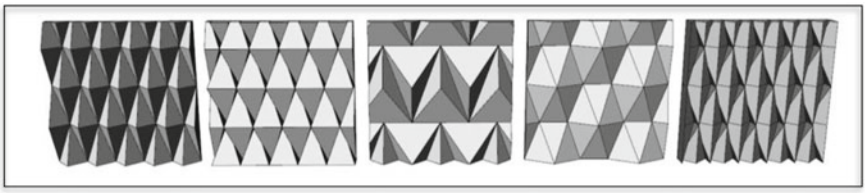

Fig. 5 Five types of load-bearing wall models through the Rhinoceros 5 program, arranged from left to right

Table 2 Six maximum stress values from total of 18 load-bearing walls

Wall type	Total deformation (m)	Maximum stress (Pa)
P01 type 02	1.39E−06	8.10E+04
P05 type 02	2.03E−06	1.18E+05
P01 type 04	1.61E−06	1.27E+05
P02 type 03	1.51E−05	1.77E+05
P01 type 03	4.15E−06	1.94E+05
P05 type 01	2.23E−05	2.03E+05

Fig. 6 P01 type 02 wall when finished construction

the strength and unit cost values as well as the unit weight of that wall. But in this case, the wall with the most suitable strength and stress behavior, in respective with the maximum stress value. The suitable wall considered as a prototype is the wall in the P01 Type 02 pattern (Fig. 6) [17].

4 Proposed Guidelines for the DFMA of Small Residential Houses

The next phase is the selection of the most appropriate wall for producing a small house design for DFMA assembly and installation guidelines.

4.1 Load-Bearing Wall Joint Design

For the joint design for load-bearing walls (Fig. 7), a prefabrication study has been conducted [18–22]. Therefore, the proposed concept of employing steel plate in dry manufacturing techniques for precast wall elements is implemented in this study. Figure 8 depicts the joint connection of the precast wall piece utilizing the steel plate and two bolts. The designated locations of the bolts are in the middle parts of the wall panels. In brief, results reveal that the proposed DFMA solution of 3D printing wall panel applied the basic fabrication is widely available in the market.

The dimension of the proposed joint between each wall panel is illustrated in Fig. 9. The joints are located at both ends of the load-bearing wall with protruding fins used to assemble between two pieces of the wall together. It is necessary to design the part, used for transportation of lift-up, an open hole that can be filled with the cement and embedded in the lifting point. The design is a dry joint process instead of the wet process. Due to reducing the installation time when it arrives construction site, the horizontal wall joints are used as steel plates, with the size of

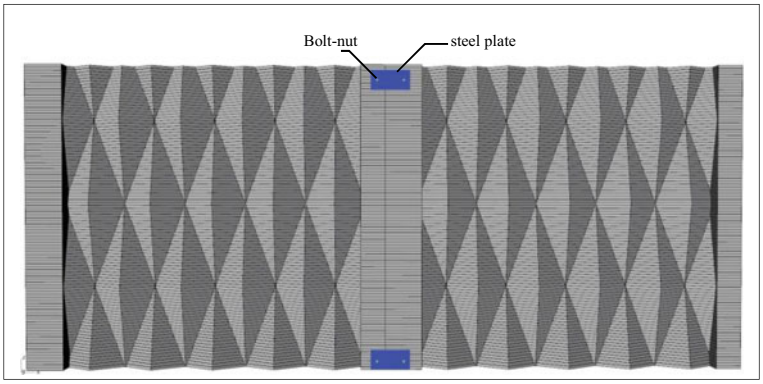

Fig. 7 Components of dry wall joints, type 2 in Rhinoceros 5 program

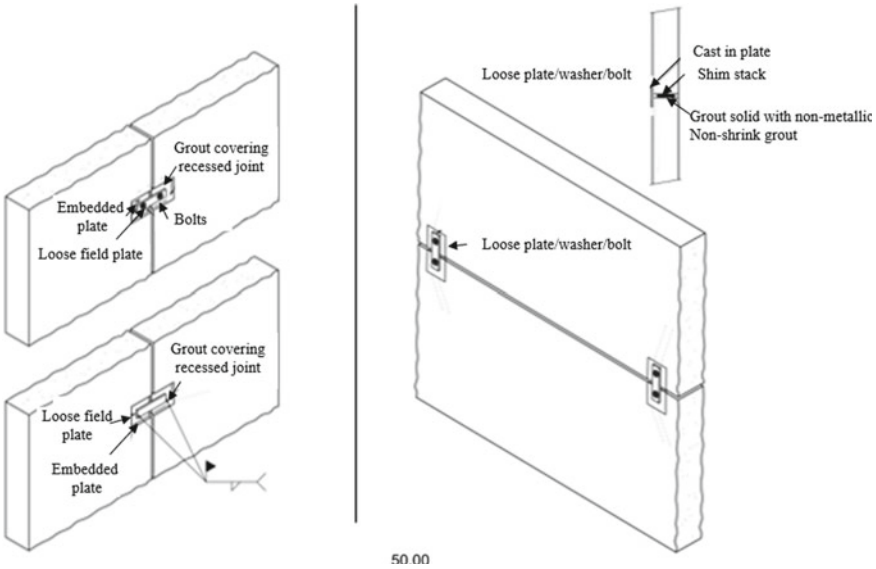

Fig. 8 Joint of the precast panel using dry method [10]

6.5 × 12.5 cm and the thickness of 4 mm, with holes for tightening nuts. The area where the joints are installed is designed to have a concave section inward. When the joints are installed, the jointing area can be cement plastered over to cover the joints.

As assembling each component for small resident unit, the details the component is illustrated in Fig. 10. For the housing components, the systems are discussed as follows:

1. The structural part consists of foundation, beam, and floor;

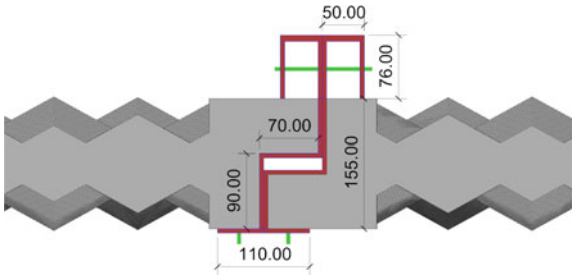

Fig. 9 Proposed joints dimension

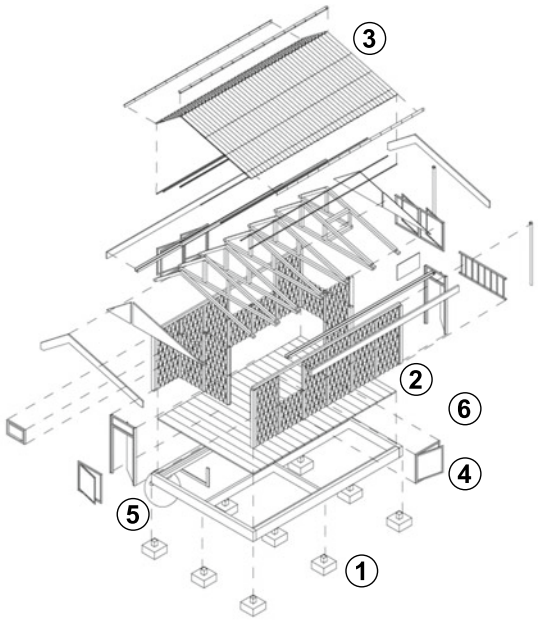

Fig. 10 Details of components for fabricating a 3D printing small residential unit

2. The wall part consists of wall, joint, and railing;
3. The roof part consists of roof frame, roof material, rain gutter, and water pipe;
4. The opening part consists of door and window;
5. The sanitary part consists of water pipe, water tanks, and sanitary ware;
6. The electronic part consists of consumer unit, lightbulb, switch, power socket, and electric wire.

5 Conclusions

The study of 3D printing technology with cement-based materials in residential architecture could be concluded as follows:

- Patterns of the 3D printing wall highly affected on its strength.
- The joint design using dry wall joint was a suitable way for assembling the wall panels.
- The fabrication of the 3D printing residential unit.

This research delivers the DFMA knowledge and guideline for designing and constructing the patterned 3D printing wall such that the 3D printing technology with cement-based materials can be efficiently used through architectural design.

References

1. Tuvayanond W, Prasittisopin L (2023) Design for manufacture and assembly of digital fabrication and additive manufacturing in construction: a review. Buildings 13(2):429
2. Prasittisopin L, Sakdanaraseth T, Horayangkura V (2021) Design and construction method of a 3D concrete printing self-supporting curvilinear pavilion. J Archit Eng 27(3):05021006
3. Ali MH, Issayev G, Shehab E, Sarfraz S (2022) A critical review of 3D printing and digital manufacturing in construction engineering. Rapid Prototyp J
4. Weng Y, Li M, Ruan S, Wong TN, Tan MJ, Yeong KLO, Qian S (2020) Comparative economic, environmental and productivity assessment of a concrete bathroom unit fabricated through 3D printing and a precast approach. J Clean Prod 261:121245
5. Prasittisopin L, Pongpaisanseree K, Jiramarootapong P, Snguanyat C (2020) Thermal and sound insulation of large-scale 3D extrusion printing wall panel. In: RILEM international conference on concrete and digital fabrication. Springer, Cham, pp 1174–1182
6. de Brito J, Kurda R (2021) The past and future of sustainable concrete: a critical review and new strategies on cement-based materials. J Clean Prod 281:123558
7. Long WJ, Tao JL, Lin C, Gu YC, Mei L, Duan HB, Xing F (2019) Rheology and buildability of sustainable cement-based composites containing micro-crystalline cellulose for 3D-printing. J Clean Prod 239:118054
8. Dorn T, Hirsch T, Stephan D (2019) Study on the influence of accelerators on the hydration of Portland cement and their applicability in 3D printing. In: Rheology and processing of construction materials. Springer, Cham, pp 382–390
9. Prasittisopin L, Termkhajornkit P, Kim YH (2022) Review of concrete with expanded polystyrene (EPS): performance and environmental aspects. J Clean Prod 132919
10. Zhang Y, Zhang Y, Yang L, Liu G, Chen Y, Yu S, Du H (2021) Hardened properties and durability of large-scale 3D printed cement-based materials. Mater Struct 54(1):1–14
11. Perrot A, Jacquet Y, Rangeard D, Courteille E, Sonebi M (2020) Nailing of layers: a promising way to reinforce concrete 3D printing structures. Materials 13(7):1518
12. Daungwilailuk T, Pheinsusom P, Pansuk W (2021) Uniaxial load testing of large-scale 3D-printed concrete wall and finite-element model analysis. Constr Build Mater 275:122039
13. Xiao J, Liu H, Ding T (2021) Finite element analysis on the anisotropic behavior of 3D printed concrete under compression and flexure. Addit Manuf 39:101712
14. Holt C, Edwards L, Keyte L, Moghaddam F, Townsend B (2019) Construction 3D printing. In: 3D concrete printing technology. Butterworth-Heinemann, pp. 349–370
15. El-Sayegh S, Romdhane L, Manjikian S (2020) A critical review of 3D printing in construction: benefits, challenges, and risks. Arch Civ Mech Eng 20(2):1–25
16. Xiao J, Ji G, Zhang Y, Ma G, Mechtcherine V, Pan J, Wang L, Ding T, Duan Z, Du S (2021) Large-scale 3D printing concrete technology: current status and future opportunities. Cement Concr Compos 122:104115
17. Jiramarootapong P, Prasittisopin L, Snguanyat C, Tanapornraweekit G, Tangtermsirikul S (2020) Load carrying capacity and failure mode of 3D printing mortar wall panel under axial

compression loading. In: RILEM international conference on concrete and digital fabrication. Springer, Cham, pp 646–657
18. Ma G, Ruhan A, Xie P, Pan Z, Wang L, Hower JC (2022) 3D-printable aerogel-incorporated concrete: Anisotropy influence on physical, mechanical, and thermal insulation properties. Constr Build Mater 323:126551
19. Prasittisopin L, Jiramarootapong P, Pongpaisanseree K, Snguanyat C (2019) Lean manufacturing and thermal enhancement of single-layer wall with an additive manufacturing (AM) structure. ZKG Int 4:64–74
20. Sun J, Xiao J, Li Z, Feng X (2021) Experimental study on the thermal performance of a 3D printed concrete prototype building. Energy Build 241:110965
21. Singhal S, Chourasia A, Chellappa S, Parashar J (2019) Precast reinforced concrete shear walls: state of the art review. Struct Concr 20(3):886–898
22. National Precast Concrete Association, Wall Panel Technical Drawings. https://precast.org/precast-products/wall-panel-technical-drawings/. Retrieved on 8 Dec 12 2000

An Investigation into the Compaction of Sandstone Aggregates Stabilised with Cement and Fly Ash

Nurul Amalina Ashikin Binti Ali, Eng Hie Tan, Soon Jiann Tan, El-Said Mamdouh Mahmoud Zahran, and Nurul Hasan

Abstract This paper experimentally investigated the compaction properties of sandstone aggregate stabilised with a mixture of Portland composite cement and Class F fly ash. This paper determined the influence of fly ash contents on the maximum dry densities, optimum moisture contents and air void contents of the stabilised sandstone using the 2.5 kg rammer compaction method. Fly ash contents of 0, 10, 20, 30 and 40% by mass of aggregate were added to sandstone aggregate samples with a constant cement content of 5% by mass of aggregate. The investigation showed that at 5% cement without fly ash, the maximum dry density peaked, while the optimum moisture content was the lowest among all investigated fly ash contents. It also showed that for every increment of 10% fly ash with a constant 5% cement content, the maximum dry density decreased linearly, and the optimum moisture content increased exponentially. From 10 to 30% fly ash content, the air void content

N. A. A. B. Ali (✉) · E. H. Tan
Civil Engineering Programme Area, Faculty of Engineering, Universiti Teknologi Brunei (UTB), Gadong BE1410, Bandar Seri Begawan, Brunei Darussalam
e-mail: naa.amalina.ali@gmail.com

E. H. Tan
e-mail: angelteh86@gmail.com

S. J. Tan
Centre for Transport Research, Universiti Teknologi Brunei (UTB), Gadong BE1410, Bandar Seri Begawan, Brunei Darussalam
e-mail: soonjiann.tan@utb.edu.bn

E.-S. M. M. Zahran
Department of Civil Engineering, Faculty of Science and Engineering, University of Nottingham Ningbo China, Ningbo 315100, China
e-mail: Elsaid.Zahran@nottingham.edu.cn

N. Hasan
Department of Petroleum and Chemical Engineering, Faculty of Engineering, Universiti Teknologi Brunei (UTB), Gadong BE1410, Bandar Seri Begawan, Brunei Darussalam
e-mail: nurul.hasan@utb.edu.bn

T. Kang (ed.), *Proceedings of 5th International Conference on Civil Engineering and Architecture*, Lecture Notes in Civil Engineering 369,
https://doi.org/10.1007/978-981-99-4049-3_3

increased and subsequently decreased from 30 to 40% fly ash content. The investigation concluded that fly ash is an effective stabiliser when cement-to-fly ash ratios are between 1:2 and 1:4 and should not exceed 1:6.

Keywords Compaction properties · Sandstone aggregate · Portland composite cement · Class F fly ash · Sub-base construction

1 Introduction

The roadbase and sub-base layers are typically built with unbound materials [1]. The densification process involves rearranging soil particles into a more tightly packed configuration that results in increased dry density (DD) and decreased air void content (AVC) in their compacted state. The maximum packing density has a significant effect on the stability of the structure [2]. The highest level of stability is achieved when the materials are compacted to their maximum dry densities (MDD) at the optimal moisture contents (OMC). When all grain sizes are present and distributed uniformly throughout the material (i.e. well-graded), soil interlocking and particle contact will be improved during compaction, resulting in a tightly packed structure [3]. The compaction properties of coarse-grained soils are governed by their gradations [4]. Compaction helps to increase density and stiffness and reduce permeability. Insufficient compaction can lead to settlement, whereas inadequate stiffness can lead to distress [5].

However, when marginal aggregate, such as sandstone, is compacted, the aggregate may be broken down, increasing smaller fragmented aggregate particles. Loads are then transferred to these loose, fragmented aggregate particles, which dominate the aggregate mixture, resulting in reduced stiffness, stability and durability of the roadbase and sub-base layers. Therefore, to use marginal sandstone aggregate as a sub-base material, one option is to chemically stabilise the unbound (loose) aggregate particles to form a bound mass. Chemical stabilisation is achieved by mixing traditional and/or non-traditional chemical stabilisers with soil particles to form stronger composite materials [6]. The selection of type and dosage is a function of soil classification, degree of improvement desired, cost and availability [6, 7]. Examples of traditional chemical stabilisers are cement, lime, fly ash (FA) and bitumen, and examples of non-traditional chemical stabilisers are ionic, enzyme, lignosulfonate, petroleum emulsion, polymer and tree resin [6, 8]. Blends of traditional chemical stabilisers such as cement-FA (CFA), lime-FA (LFA) and cement-lime-FA (CLFA) and blends of traditional-non-traditional chemical stabilisers such as cement-polymer are common in chemical (soil) stabilisation.

FA, also known as pulverised FA (PFA), is the by-product or waste product generated during the combustion process of coal. FA constituted between 70 and 90% of the ash type [9]. The utilisation, rather than disposal, of FA has been found to result in several environmental, technical and economic merits. Therefore, apart from concrete construction, FA is also widely used in the fields of soil improvement and pavement

stabilisation. From an economic point of view, using FA in construction projects presents an appealing alternative to disposal. FA can be used with other construction materials to increase the bearing capacity of the soil [10]. This is because when FA is used as mineral filler, it improves soil stability by changing the soil-FA particle size distribution or gradation [9] as FA could act as non-plastic fine silt [11]. As a result, FA presents comparable mechanical properties with those of silt [12]. FA gained popularity as an alternative for soil and pavement base stabilisation due to its ability to enhance the ride quality and serviceability of the road [13], as well as notable improvements in strength and durability [14].

Several soil types are classified using the Unified Soil Classification System (USCS) to well-graded sands, gravelly sands, little or no fines (SW), poorly-graded sands, gravelly sands, little or no fines (SP), SP-clayey sands, sand-clay mixtures (SC), SW-SC, SW-silty sands and sand-silt mixtures (SM), well-graded gravels, gravel-sand mixtures, little or no fines (GW), poorly-graded gravels, gravel-sand mixtures, little or no fines (GP), GP-clayey gravels, gravel-sand-clay mixtures (GC), GW-GC, GP-silty gravels, gravel-sand-silt mixtures (GM), GW-GM, GC-GM and SC-SM can be stabilised with FA [11].

Since FA is a pozzolan that contains siliceous and aluminous compositions as major constituents, it can form cementitious compounds when mixed with water and high-calcium compounds [9]. For instance, when FA is mixed with cement and water, it produces a strong cementitious binder. The two known classes of FA are Class C and Class F, and they are distinguished by the amount of calcium oxide (CaO) and the total amount of silicon oxide (SiO_2), aluminium oxide (Al_2O_3) and iron oxide (Fe_2O_3) found in them. Class C FA has CaO content greater than 10%, whereas Class F FA has CaO content less than 10%. Class C FA has $SiO_2 + Al_2O_3 + Fe_2O_3 \leq 70\%$, normally 50–70%, whereas Class F FA has $SiO_2 + Al_2O_3 + Fe_2O_3 \geq 70\%$. Since the CaO content is less than 10%, Class F FA is devoid of the self-cementing property; thus, it is the least used FA [15]. Class F FA requires high-calcium compounds such as cement and lime to act as activators but not Class C FA as it has self-cementing properties. With CFA blend, in principle, an increase in cement content (constant FA content) gives an increase in strength [7], whereas, with an increase in FA content (constant cement content), the strength may increase then decrease, giving a peak or optimal FA content as presented by Ref. [16]. The ratio CaO-to-SiO_2 is an important indicator of pozzolanic activity [17]. That ratio is very low for a Class F FA.

The most common cement-to-FA ratios (by replacement) used as soil stabilisers are 1:1 and 1:4 [9]. The addition of FA results in decreased MDD due to FA's lower specific gravity and increased OMC due to FA's higher specific surface [9]. When FA is used in excessive (very low cement-to-FA ratio), it can cause detrimental effects such as extremely slow strength gain and exceptionally lower strengths (compressive, tensile, shear and bending). Replacement of (Portland) cement with FA effectively dilutes the cement, resulting in a longer hydration period for the hydration products to make interconnections [18]. Excessive use of FA instead of cement reduces the amount of calcium ions (Ca^{2+}) in the cementitious system. Therefore, when cement is partly replaced with FA, the ultimate strengths rarely reach those of untreated samples unless the amount replaced is very low (about 15%) [18].

While past investigations had shown the success of Class F FA on subgrade stabilisation, for instance, stabilising expansive clays as cited by Ref. [19], there remains limited information about the use of Class F FA for stabilising sub-bases and roadbases of road pavements [15]. It has also been identified that the use of a mixture of Portland composite cement (PCC) and Class F FA as an aggregate stabiliser for sub-base construction using sandstone aggregate has not previously been reported. This paper aims to present the quantitative results of the compaction properties of sandstone aggregate treated with PCC and Class F FA. The focus is on the influence of Class F FA on PCC-stabilised sandstone aggregate and to examine the suitability and optimisation of Class F FA content as a suitable mineral filler. The results from this laboratory investigation will then be used to design future laboratory tests—unconfined compression test (UCT), indirect tensile test (ITT) and California bearing ratio (CBR) test. This study is a part of an ongoing research effort aimed at developing more sustainable and economical, as well as mechanically durable, roads.

2 Compaction Methodology

The 2.5 kg rammer compaction method outlined in BS1377-4: 1990 Clause 3.3 [20] was used to determine the dry densities and moisture contents of soils with particles up to medium gravel size. No more than 30% of soils (by mass) should be retained on the 20 mm and 37.5 mm BS sieve (coarse gravels) [20]. Reference [21] recommended that the ratio of the compaction mould to the largest nominal particle size should not be less than 5 or 6. In this investigation, the ratio is 5.5 (105 mm: 19 mm). The focus was on normal traffic loading, and hence, a 2.5 kg rammer compaction, equivalent to standard Proctor, was used.

The procedure to obtain the MDD and OMC for the samples is as illustrated in Fig. 1. The aggregate, cement and FA are mixed first before water is gradually introduced. The mixture is then compacted and extruded. Small samples from the top, centre and bottom are collected for oven-drying. The calculation, plotting and expression of results are as outlined in BS1377-4: 1990 Clause 3.3.5 [20].

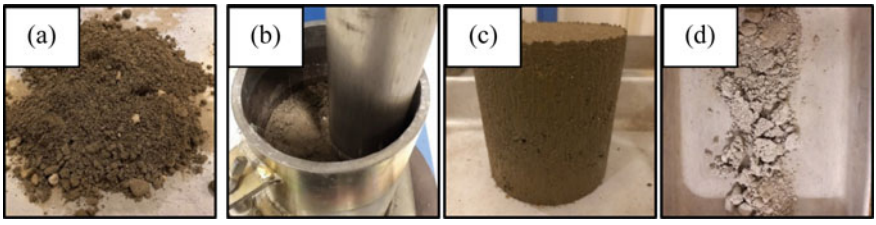

Fig. 1 Procedure to obtain maximum dry density and optimum moisture content: **a** mixing, **b** compaction, **c** extrusion and **d** sample after over-drying

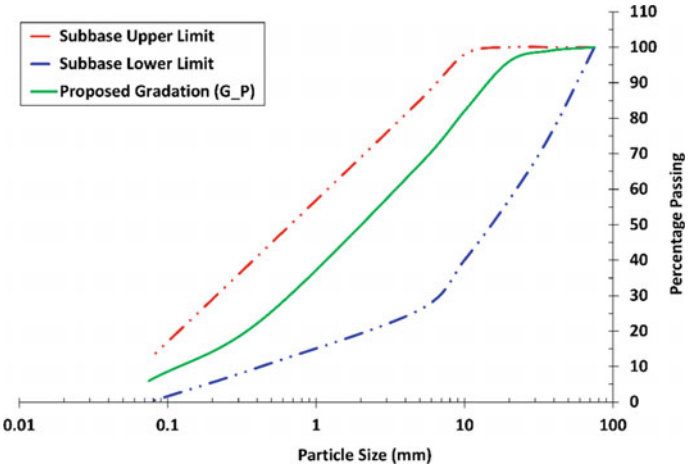

Fig. 2 Proposed gradation for sandstone aggregate mixture and the limits of gradation for sub-base [22] and sample of sandstone aggregate mixture

Table 1 Mechanical properties of sandstone aggregate mixture [22]

Mechanical properties	%	Limit (%)
Los Angeles abrasion value (LAAV)	35	≤35
Aggregate crushing value (ACV)	20	≤25
Aggregate impact value (AIV)	29	–

3 Materials

3.1 Aggregate

The aggregate used in this investigation was crushed sandstone sourced from a local quarry in the Temburong district of Brunei Darussalam. The specific gravity (S.G.) was between 2.3 and 2.5 [2]. This aggregate type is mainly used for sub-base construction in the country. The proposed particle size distribution for the aggregate samples is as shown in Fig. 2. The mechanical properties of the aggregate mixture are as shown in Table 1.

3.2 Portland Composite Cement

The PCC used in this investigation was Portland-FA blend CEM II/A-V (52,5N), according to BS EN 197-1: 2000 [23], and it has no ASTM equivalent. It contains between 6 and 20% of FA by mass of PCC. The S.G. was between 3.05 and 3.10. The

difference between CEM I, an equivalent to ASTM Type I ordinary Portland cement (OPC) and CEM II/A-V, is the clinker replacement by FA between 6 and 20%. Cement content between 3 and 5% by mass of soil is sufficient to bound the soil particles to produce hydraulically bound soil [24, 25]. Cement content less than 3% would provide insufficient tensile strength to the stabilised soil and is essentially unbound [24]. Cement content greater than 6% would begin to cause shrinkage cracking [26]. According to Ref. [27], a 5% or less cement by mass can be used effectively for soil stabilisation of a well-graded soil mixture of stone fragments or gravel, coarse sand and fine sand either with or without small amount of slightly plastic silt- and clay-size soil particles. The proposed PCC content for use in this investigation is at the upper limit of 5% cement content by mass of aggregate mixture.

3.3 Class F Fly Ash

The mineral filler used in this investigation was a Class F FA. It was supplied from a local coal power generation plant. According to the supplier, the bulk density and S.G. were 556 kg/m^3 and 2.26, respectively. The FA contents with a constant 5% PCC used in this investigation were 10%, 20%, 30% and 40% by mass of aggregate mixture. Therefore, the ratios of PCC-to-FA are 1:2, 1:4, 1:6 and 1:8.

4 Results and Discussion

Figure 3 illustrates the relationship between DD, moisture content (MC) and AVC lines for the compacted soil samples.

Since the S.G. of cement was greater than the aggregate, the MDD increased slightly from 0C0F to 5C0F. The OMC decreased from 0C0F to 5C0F, as some water would have been lost to the cementitious hydration reaction. The excess heat generated by the cement during the activation process could explain the decrease in the OMC [28].

Figure 4 illustrates the percentage changes in the OMC and MDD for the cement-FA-stabilised samples with respect to the untreated sample (i.e. 0C0F). It shows that the OMC increased exponentially with increasing FA content. It also shows that the MDD decreased linearly with increasing FA content. The lower S.G. of FA, as expected, reduce the MDD by replacing and occupying the space (void) that could be occupied by larger and denser aggregate particles [29]. The higher specific surface area of the FA particles could have resulted in an increase in OMC [30, 31].

Figure 5 shows the percentage changes in AVC for the cement-FA-stabilised samples with respect to the untreated sample (i.e. 0C0F). It shows that the AVC increased from 10% FA to 30% FA and decreased from 30% FA to 40% FA. The increase in AVC is the result of the increased in FA (silt-sized) content. Higher AVC content in compacted aggregate tends to reduce the strengths. The reduction in AVC

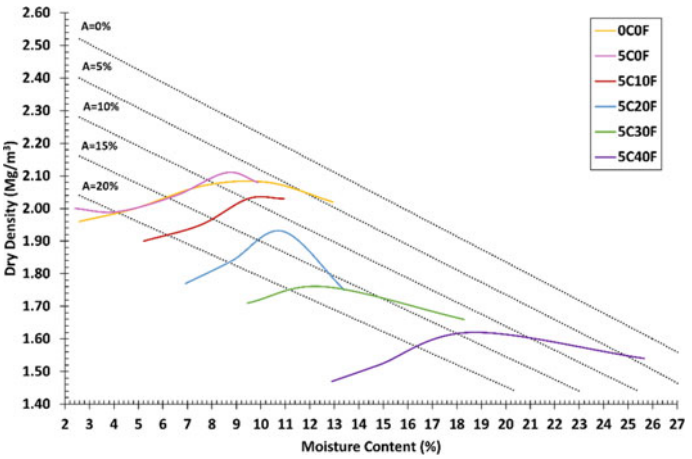

Fig. 3 Relationship between dry density, moisture content and air void content for the compacted soil samples treated with cement and fly ash

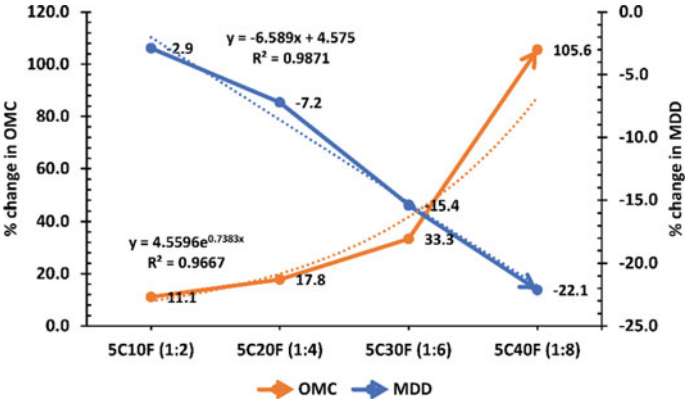

Fig. 4 % changes in optimum moisture contents and maximum dry densities of cement-fly ash-treated samples with respect to untreated sample (0C0F)

from 30% FA to 40% FA indicated that FA has become a more effective mineral filler. The drop in AVC (at 5C30F) is supported by the recommendation of Ref. [12]. Samples with lower MDD and higher OMC have greater porosity [1] and in this case, AVC.

At 5C30F, Fig. 4 show that the OMC and MDD lines intersect each other, and they coincide with the peak of % changes in AVC as shown in Fig. 5. This is a preliminary indication that the FA content should not be more than 30%, i.e. optimum C:F ratios are between 1:2 and 1:4, and maximum C:F ratio is 1:6. Reference [12] stated that the typical range for C:F ratio is from 1:3 to 1:4. Investigation by Ref. [28] showed that when C:F ratio increased from 3:5 to 3:15, the MDD decreased, and OMC

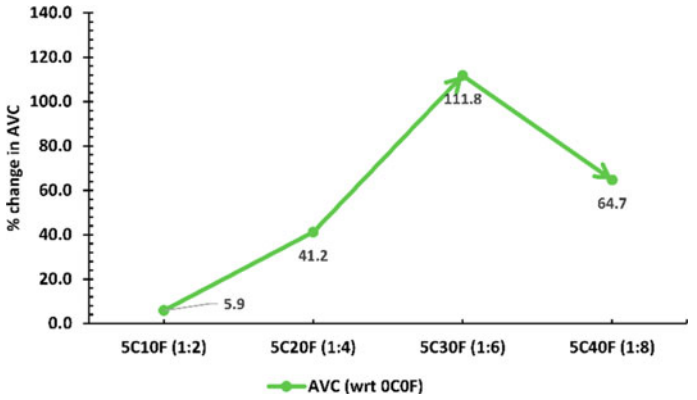

Fig. 5 % changes in air void contents of cement-fly ash-treated samples with respect to untreated sample (5C0F) and cement-treated sample (5C0F)

increased; the MDD was highest and OMC lowest when C:F ratio is 3:5 (1:1.67 ≈ 1:2). Investigation by Ref. [16], on the other hand, showed that when C:F ratio increased from 1:1 to 1:2, the MDD decreased, and OMC increased, whereas when C:F ratio increased from 1:2 to 1:4, the MDD increased, and OMC decreased; the MDD was highest and OMC lowest when C:F ratio is 1:4.

Any differences in the trends between this investigation and those of past relevant investigations can be attributed to the differences in aggregate-cement-FA mixtures such as the particle size distributions, aggregate types, cement types and contents and aggregate:cement:FA ratios. However, two consistent observations made in this investigation and those in the past investigations are that the amount of FA does not exceed 30% for sandy and gravelly soil stabilisation, and for silty and clayey soil stabilisation, the FA content can exceed 30%.

5 Conclusions and Recommendations

The influence of Class F FA on the compaction properties of PCC-stabilised sandstone aggregate mixtures was evaluated using the 2.5 kg rammer compaction method. In this investigation, a constant 5% PCC content was added to the sub-base aggregates with 0, 10, 20, 30 and 40% FA content by mass of aggregate. Based on the results, the following conclusions can be drawn as follows:

- Adding only cement (i.e. 5C0F), the MDD and OMC of the cement-stabilised sample increased and decreased, respectively, when compared to the untreated sample (i.e. 0C0F) as shown in Fig. 3.
- For every 10% of FA added to 5% cement, the MDD decreased linearly, and the OMC increased exponentially as shown in Fig. 4.

- AVC increased from 10% FA content to 30% FA content and then decreased from 30% FA content to 40% FA content as shown in Fig. 5. The decrease in AVC implies that the FA becomes a more effective mineral filler to the aggregate-cement-FA mixture.
- The points of intersection for OMC and MDD lines as shown in Fig. 4 and the peak of % changes in AVC as shown in Fig. 5 indicate that the optimum C:F ratios for the sandstone aggregate of gradation as shown in Fig. 2 are between 1:2 and 1:4, while the maximum C:F ratio is 1:6.

The compaction properties determined in this investigation cannot be used to directly interpret the strengths of sandstone aggregate treated with PCC and Class F FA. Further strength-based laboratory tests such as the following have been designed based on the current findings and will be conducted:

- UCT to determine uniaxial or unconfined compressive strength (UCS),
- ITT to determine indirect tensile strength (ITS) and
- CBR test to determine indirect shear strength in term of CBR value.

The results from the strength-based tests conducted under varying curing conditions (e.g. air-dry, moist-dry, wet, unsoaked and soaked) and periods (e.g. 7, 14, 28, 56 and 90 days) will provide better quantitative interpretation on the effects of Class F FA on PCC-stabilised sandstone aggregate mixtures and to support their application in road sub-base construction.

Acknowledgements The authors are grateful to Universiti Teknologi Brunei for their funding support (UTB/GSR/1/2021(4)) and SWEE Sdn. Bhd. for their material support.

References

1. Xiao Y, Tutumluer E, Qian Y, Siekmeier JA (2012) Gradation effects influencing mechanical properties of aggregate base–granular subbase materials in Minnesota. J Transp Res Board 2267(1):14–26
2. Karim RHA (2015) Foamed bitumen stabilised sandstone aggregates. Doctor of Philosophy, University of Nottingham
3. Goodary R, Lecomte-Nana GL, Petit C, Smith DS (2012) Investigation of the strength development in cement-stabilised soils of volcanic origin. Constr Build Mater 28(1):592–598
4. Verma G, Kumar B (2019) Prediction of compaction parameters for fine-grained and coarse-grained soils: a review. Int J Geotech Eng
5. Fragaszy RJ (1991) Compaction control of granular soils. Washington State Department of Transportation, Washington, USA
6. Kestler MA (2009) Stabilization selection guide for aggregate- and native-surface low volume roads. US Department of Agriculture, US
7. Sear LKA (2001) Use of fly ash for road construction, runways and similar projects. In: Properties and use of coal fly ash. Thomas Telford Publishing, UK
8. Tingle JS, Santoni RL (2003) Stabilization of clay soils with nontraditional additives. J Transp Res Board 1819:72–84
9. Kar KK (2022) Handbook of fly ash. Elsevier, US

10. White DJ, Harrington D, Thomas Z (2005) Fly ash soil stabilization for non-uniform subgrade soils, volume I: engineering properties and construction guidelines. Center for Transportation Research and Education, USA
11. Firoozi AA, Guney Olgun C, Firoozi AA, Baghini MS (2017) Fundamentals of soil stabilization. Int J Geo-Eng 8(1)
12. American Coal Ash Association (2003) Fly ash facts for highway engineers. Federal Highway Administration, US
13. Hatipoglu B, Edil TB, Benson CH (2008) Evaluation of base prepared from road surface gravel stabilized with fly ash. In: GeoCongress
14. Little D, Males EH, Prusinski JR, Steward B (2000) Cementitious stabilization. Transportation Research Board, USA
15. Arora S, Aydilek AH (2005) Class F fly-ash-amened soils as highway base materials. J Mater Civ Eng 17(6):640–649
16. Sani A, Muhammad NZ, Mehan A, Joel M (2018) Optimization of fly ash dosage for the stabilization of gravel soil using cement for use as flexible pavement material. Adv Sci Lett 24(6):3914–3917
17. Terpáková E, Števulová N (2020) Trends in the use of cement bypass dusts for their application in construction. Key Eng Mater 838:39–45
18. Poole TS (1995) Use of large quantities of fly ash in concrete. U.S. Army Corps of Engineers, USA
19. Brooks RM (2009) Soil stabilization with flyash and rice husk ash. Int J Res Rev Appl Sci 1(3):209–217
20. British Standards Institutions: BS 1377-4: 1990 (1990) Methods of test for soils for civil engineering purposes—part 4: compaction-related tests. British Standards Institutions, UK
21. Donaghe RT, Torrey VH (1994) A compaction test method for soil-rock mixture in which equipment size effect are minimized. Geotech Test J 17:363–370
22. Construction Planning and Research Unit (1998) GS 1: General specifications for flexible pavement. Construction Planning and Research Unit, Brunei Darussalam
23. British Standards Institutions: BS EN 197-1: 2000 (2000) Cement—part 1: composition, specifications and conformity criteria for common cements. British Standards Institutions, UK
24. Lay MG (2009) Stabilisation. In: Handbook of road technology, 4th edn. Spon Press, UK
25. Lay MG (2009) Handbook of road technology, 4th edn. Spon Press, UK
26. Gafar HSH, Qing WD (2003) Review of chemical stabilisation technologies and applications for public roads in Brunei Darussalam. J Road Eng Assoc Asia Australia 10(1):42–53
27. Portland Cement Association (1992) Soil-cement laboratory handbook. Portland Cement Association, Illinois, USA
28. Mahvash S, Lopez-Querol S, Bahadori-Jahromi A (2017) Effect of class F fly ash on fine sand compaction through soil stabilization. Heliyon 3(3):e00274
29. Dong W, Tawk M, Indraratna B, Heitor A, Rujikiatkamjorn C (2019) A mixture of coal wash and fly ash as a pavement substructure material. Transp Geotech 21
30. Zorluer I, Demirbas A (2013) Use of marble dust and fly ash in stabilization of base material. Sci Eng Compos Mater 20(1)
31. Tan EH, Zahran EMM (2019) A laboratory investigation of the compaction properties of road sub-base stabilised with cement and latex copolymer. In: IOP conference series: materials science and engineering. IOP Publishing Miri, Malaysia

Porous Asphalt Pavement Binder Performance and Standards under High Temperature and Heavy Load Conditions

Jialong Li, Yifei Wu, Hua Qiu, Changhong Wang, and Mingzhi Sun

Abstract Because of its porous, noise-reduction, and anti-skid qualities, porous asphalt pavement has attracted a lot of interest from the transportation industry recently. However, the porous asphalt pavement is prone to rutting deformation due to high temperature and heavy vehicles. To address this issue, we use high-viscosity binder to improve pavement performance and propose a technical standard for asphalt binder for porous asphalt pavement. The study about the performance of asphalt binder and the impact on the road performance of porous asphalt pavement under high temperature and heavy vehicles is currently being conducted. The research results can provide support for the application and popularization of porous asphalt pavement.

Keywords Porous pavement · Road performance · Binder · Technical standard

1 Introduction

The porous asphalt mixture has a skeleton void structure with high porosity. In actuality, heat, light, and water are more likely to age it. In order to enhance the durability and mechanical performance of the mixture, it is necessary to use a high-viscosity asphalt binder, and the asphalt binder should have certain anti-aging and anti-stripping ability.

The important role of asphalt binder in porous asphalt pavement has attracted extensive attention. Motamed [1] found that the response of asphalt binder had a

J. Li · Y. Wu · H. Qiu
Chongqing Fengjian Expressway Co., Ltd, Chongqing 404600, China

C. Wang
Chongqing Jiaotong University, Chongqing 400074, China

M. Sun (✉)
Research Institute of Highway Ministry of Transport, Beijing 100088, China
e-mail: mz.sun@rioh.cn

T. Kang (ed.), *Proceedings of 5th International Conference on Civil Engineering and Architecture*, Lecture Notes in Civil Engineering 369,
https://doi.org/10.1007/978-981-99-4049-3_4

significant impact on the road performance of porous asphalt mixtures under vehicle load conditions. Karki [2] found that the kind of asphalt binder had influenced the bonding effect of the porous asphalt pavement mixture through a whole life-cycle analysis of pavements. Tang [3] developed a high-viscosity modified admixture for the promotion of porous asphalt pavement binder and carried out factory production and application. Tan [4] proposed a high-viscosity binder material for porous asphalt pavement schemes that are compatible with the environment and vehicle roads, modified asphalt with polymer, and validated its mechanical index and road performance. Li [5] found that SBS modified asphalt +8% HVA has better performance by comparing the modifying effects of base asphalt and SBS modified asphalt with HVA.

In summary, scholars have studied the correlation between asphalt binder and porous mixture performance. Existing research has found that the adoption of high-viscosity asphalt binder has a considerable impact on the performance of porous asphalt pavement, and the modification technology of porous asphalt binder has achieved mature research results [6, 7]. However, porous asphalt binder adapted to high temperature and heavy vehicle loads is facing challenges, and it is worthwhile devoting much effort to this. Based on this situation, this paper plans to study the asphalt binder on porous asphalt pavement so as to provide technical support for the road performance and service life of porous asphalt pavement.

2 The Analysis of the Rutting Resistance of Porous Asphalt Mixture

2.1 Relation Between Asphalt Performance and the Durability of Porous Pavement

The climate conditions, load conditions, and test methods adopted by each standard are different, so the technical standard cannot be directly used. For reasons of performance and durability, it is necessary to develop technical specifications and binder standards for porous asphalt pavement that are compatible with the environment and vehicle load conditions.

A 3 km test section of porous asphalt pavement was constructed in China, in which SBS modified binder and high-viscosity modified binder were tested for performance comparison. The design void of SBS modified porous asphalt pavement is 17%, and that of high-viscosity modified asphalt porous pavement is 20%. According to the later research, it was found that the SBS modified porous asphalt pavement has a certain degree of early damage after less than 2 years of use (see Fig. 1), mainly as potholes and ruts. However, the test section with high-viscosity modified asphalt is basically disease-free.

In this work, we proved that the porous asphalt pavement had the possibility of serious water damage with SBS modified asphalt as the binder. When the porosity of

Fig.1 Porous asphalt pavement with SBS modified asphalt

the SBS modified asphalt mixture is large, it is necessary to conduct a comprehensive performance test. High-viscosity modified asphalt can significantly improve the water resistance, rutting resistance, dispersion damage resistance, and durability of porous asphalt mixtures. It is more suitable for porous asphalt pavement under high temperatures and heavy vehicle loads.

2.2 Effect of Asphalt Viscosity on Durability of Porous Asphalt Pavement

The viscosity of the asphalt must be improved in order to improve to durability of the asphalt mixture under high temperatures and heavy load traffic. This section studies the relationship between asphalt viscosity and the durability of porous asphalt mixtures through tests. The basalt aggregate was used in the test, and the asphalt material was SBS modified asphalt. The aggregate ratio is 1#: 2#: mechanism sand: mineral powder = 50:31:13:6, and the oil stone ratio is 4.6%. The viscosity of the asphalt is achieved by adjusting the dosage of high-viscosity additives. The main index of the porous asphalt mixture is tested by selecting four dosage levels of 0, 5, 10, and 15%. The test results are summarized in Table 1.

Table 1 Viscosity and performance of asphalt mixtures with different dosages of additives

The amount (%)	Technical index						
	Asphalt		Asphalt mixtures				
	Dynamic viscosity (Pa s)	Softening point (°C)	Void ratio (%)	Leakage loss (%)	Scattering loss (%)	Marshall (kN)	Dynamic stability (times/mm)
0	249.4	47.6	19.6	0.76	35.5	4.54	553
5	600.4	52.3	21.2	0.84	25.2	5.01	2091
10	21,915.3	88.6	20.2	0.44	15.5	5.72	9309
15	174,978.7	92.5	19.4	0.29	13.1	7.42	12,202

According to the test data, with the increase in dynamic viscosity of the modified asphalt, the wrapping property of asphalt becomes larger, and its anti-leakage loss ability is enhanced. After 10% dosage (dynamic viscosity above 20,000 Pa s), the asphalt film gets thicker with the leakage loss of mixture greatly reduced. The scattering loss decreases with the increase of dynamic viscosity. When the content of modified asphalt increases from 0 to 15%, the scattering loss decreases from 35.5 to 13.1%, which shows that high-viscosity asphalt has an obvious contribution to the anti-dispersion performance of porous asphalt mixtures. One of the most common diseases of porous asphalt pavement is the problem of loosening and scattering, which can be effectively solved by increasing the viscosity of the asphalt.

3 An Examination of the Rutting Resistance of a Porous Asphalt Mixture Under High Temperature and Heavy Traffic Conditions

The rutting damage of porous asphalt pavement is caused by high temperatures and heavy vehicle load conditions. Tests are designed from the above two aspects to study the dynamic stability of porous asphalt mixtures.

In the test to study the effect of temperature on the rutting resistance of porous asphalt pavement, the rutting test load was 0.7 MPa according to the standard method, and the test temperature was set to 55, 60, 65, 70 and 75 °C in order to test the dynamic stability index of rutting of porous asphalt mixture and analyze the effect of temperature change on the rutting resistance of porous asphalt mixture. In the test of the effect of load on the rutting resistance performance of porous asphalt pavement, according to the standard rutting test methods of operation specification, the test temperature is 60 °C, and the load pressure is set to 0.5, 0.6, 0.7, 0.8, and 0.9 MPa, in order to test the dynamic stability index of the porous asphalt mixture and analyze the rutting resistance of the porous asphalt mixture under different loads. The test results are shown in Fig. 2.

We found that the dynamic stability index of rutting tests decreases with the increase of load, and there is a mutation at around 0.6 MPa. This indicates that the high temperature stability of porous asphalt mixture deteriorates under heavy load traffic. Although high-viscosity asphalt will weaken the influence, the dynamic stability of the asphalt mixture can still arrive at 4371 times/mm at 0.9 MPa load. The dynamic stability of the rutting test decreases with temperature increasing. It is more sensitive to the change of temperature, and the effect of temperature on high temperature stability is significantly greater than that of load. Therefore, porous asphalt pavement should be given more attention to rutting damage caused by high temperatures.

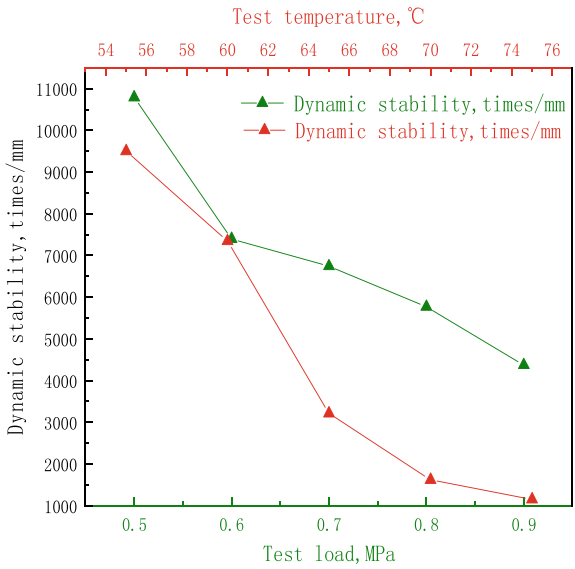

Fig. 2 Dynamic stability of porous asphalt mixtures in rutting tests under different temperatures and vehicle conditions

4 Porous Asphalt Binder Standard Under High Temperature and Heavy Load Conditions

High-viscosity asphalt binder has a good effect on the performance of porous pavement materials [8]. As can be seen from the above test, the increase in asphalt viscosity can change the sharp decline in rutting resistance of porous asphalt pavement, which is caused by high temperatures and heavy load traffic. The standards for the standardized design and construction of porous asphalt mixtures, the asphalt binder standards can provide a reference for this. Therefore, this section will study the binder standard of asphalt binder in the different conditions of high temperature and heavy load traffic.

According to the technical requirements for the dynamic stability of porous asphalt mixture in the rutting test, it must not be less than 3000 times/mm, but the rutting resistance performance in practical engineering often has a certain safety capacity, and the dynamic stability is mostly 4000–6000 times/mm. The load of China's rutting test is 0.7 MPa, which is consistent with the standard wheel load of pavement designed. However, China's roads often have heavy vehicle loads or even serious overload conditions [9]. The tire grounding pressure can arrive at 0.83 MPa when the overload is 50%, and 0.91 MPa when the overload is 100%, and 0.99 MPa when the overload is 200%. According to this condition (without considering the effect of high temperature), the standard of binder that must be reached for the calculation of high-viscosity asphalt must be seen in Table 2. In this table, the calculation takes into account the situation that the load is light when the car is main traffic.

Table 2 PAC asphalt binder standard at 60 °C under different pavement design loads

Design required dynamic stability (times/mm)	Actual wheel loads are considered in pavement design				
	0.6 MPa	0.7 MPa	0.8 MPa	0.9 MPa	1.0 MPa
4000	20,436	26,801	35,148	46,096	60,453
5000	31,012	40,671	53,339	69,953	91,740
6000	43,605	57,186	74,998	98,357	128,992

Unit Pa s

Table 3 Viscosity standard for PAC asphalt at 60 °C under different pavement temperature

Design required dynamic stability (times/mm)	Rutting test temperature (reflective of summer road temperatures in the zone)				
	55 °C	60 °C	62.5 °C	65 °C	67.5 °C
4000	6575	26,801	54,112	109,252	220,582
5000	9977	40,671	82,116	165,794	334,742
6000	14,029	57,186	115,460	233,116	470,666

Unit Pas

According to the new 'Technical Specification for Asphalt Pavement Construction', China's climate zone is divided into three summer extreme hot zones: the summer hot zone and the summer cold zone [10]. The average daily maximum temperature in the hottest month varies greatly across provinces. Correspondingly, the temperature of asphalt pavements in summer is certainly different. According to the requirements of high temperature stability of porous asphalt pavement, the dynamic viscosity of asphalt under different pavement temperatures should be calculated, and the results are shown in Table 3.

If porous asphalt pavements are built on heavy-load traffic roads in hot climate zones, the asphalt viscosity standard can be seen in Table 4.

Which needs special attention is that the temperature conditions of porous asphalt pavement in summer correspond to the temperature of rutting tests, when Tables 3 and 4 are adopted. That is, the summer temperature in different zones should be consistent with the amount of dynamic stability required by the design.

Table 4 Asphalt binder viscosity standard at 60°C considering both high temperature and heavy load

Design considerations loads	Design required dynamic stability (times/mm)	Rutting test temperature (reflective of summer road temperatures in the zones)				
		55 °C	60 °C	62.5 °C	65 °C	67.5 °C
$p = 0.7$ MPa	4000	6575	26,801	54,112	109,252	220,582
	5000	9977	40,671	82,116	165,794	334,742
	6000	14,029	57,186	115,460	233,116	470,666
$p = 0.8$ MPa	4000	8622	35,148	70,965	143,280	289,286
	5000	13,085	53,339	107,693	217,434	439,003
	6000	18,398	74,998	151,422	305,724	617,262
$p = 0.9$ MPa	4000	11,308	46,096	93,069	187,907	379,388
	5000	17,160	69,953	141,236	285,157	575,737
	6000	24,128	98,357	198,585	400,947	809,518
$p = 1.0$ MPa	4000	14,830	60,453	122,056	246,434	497,555
	5000	22,505	91,740	185,226	373,974	755,060
	6000	31,643	128,992	260,437	525,828	1,061,656

5 Conclusion

The rutting of porous asphalt pavement is prone to occur under high temperatures and heavy load traffic, thereby affecting the pavement flatness. The use of high-viscosity binder has a significant influence on the road performance of porous asphalt pavement. In this paper, the effect of binder on the road performance of porous asphalt pavement is studied through tests under high temperature and load vehicle conditions. The main conclusions are as follows:

(1) High-viscosity modified asphalt binder can significantly improve the durability of porous asphalt mixtures by increasing their resistance to water damage, rutting, and fly-away damage.
(2) Tests have shown that the influence of temperature on high temperature stability is significantly greater than the effect of loading. Therefore, it should be more concerned about rutting damage caused by high temperatures.
(3) To serve as a reference for the promotion of porous asphalt pavements and the development of asphalt viscosity standard for porous asphalt binder that is suitable for high temperature and heavy load conditions.

According to the study about the influence of binder on the performance of porous asphalt, this paper puts forward the technical standard of asphalt binder for porous pavement under high temperature and heavy load, which provides technical support for the application of high-viscosity binder. Due to the limited time and conditions, this paper only conducts a macro-quantitative study on the performance index of

mixture and binder and further will analyze the influence of asphalt on mixture from the microperspective.

References

1. Motamed A, Bhasin A, Liechti KM (2012) Interaction nonlinearity in asphalt binders. Mech Time-Depend Mater 16(2):145–167
2. Karki P, Mraiza Z, Karnei E (2022) Performance-graded asphalt binder selection catalog for asphalt overlays. Constr Build Mater 319:126012
3. Tang GQ (2015) Research on the key technology of double-layer porous asphalt pavement. Southeast University
4. Tan RM (2011). Application of high-viscosity modifiers in OGFC asphalt mixture. Chang'an University
5. Li FY (2017) Study on water stability of porous asphalt mixtures. Chongqing Jiaotong University
6. Hu J, Ma T, Zhu Y (2021) High-viscosity modified asphalt mixtures for double-layer porous asphalt pavement: design optimization and evaluation metrics. Constr Build Mater 271:121893
7. Azahar NM, Hassan NA, Jaya RP (2019) Properties of cup lump rubber modified asphalt binder. Road Mater Pavement Des 5:1–21
8. Zhu ZY, Zhou OQ, Zhou X (2021) An experimental study on the influence of different high-viscosity asphalts on the performance of noise-reducing porous pavement materials was conducted. Traffic Technol 6:1–4
9. Sun J, Yang CF, Du YM (2009) Discussion on vehicle load of heavy load highway bridge design based on traffic survey. J Hebei Univ Technol 38(1):1–5
10. Ministry of Communications Institute of Highway Science (2004) Technical specification for construction of highway asphalt pavement. People's Traffic Press

High-Temperature Behaviour of Concrete with Polypropylene Fibres

N. Kabashi, E. Krasniq, M. Muhaxheri, F. Salihu, and B. Gashi

Abstract In common conditions, concrete is subjected to a range no more severe than it will be imposed by environmental conditions. The critical cases in this paper are analysed during the exposure to higher temperatures in specific conditions, such as fire building, industrial applications, and metallurgy. Concrete thermal properties are more complex than for most materials because of the composition of different constituents and different behaviour of those materials. The behaviour is oriented in physical and mechanical properties, which are changeable in the function of temperatures. The main parameters targeted in this paper are compressive strength, and a decrease in the function of temperature to orientation at the critical point of the collapse. The microscopic analyses towards the presence of changeable structure of the concrete and loss of mass are also conducted. For different temperature cases, it is crucial to analyse the various parameters using the concrete samples already prepared with a determined mix design. Improvement is tentatively analysed using the fibres in the mix design. In the scope of output results, different codes are considered with reference to experimental results.

Keywords High temperature of concrete · Fibers · Compressive strength · Color

1 Introduction

Concrete is the most widely used construction material in the world; due to its durability, strength, resistance to fire, and less maintenance. Concrete, in the structure, must meet the requirements to fire safety based on EN 1992 [1], ACI 2014 [2], and other similar codes. The effect of normal temperatures is not an indicator of changing the mechanical properties such as strength and elastic modulus. At high temperatures, various physical, chemical, and mechanical changes will be detected, leading to the deterioration of concrete. At a temperature of 100 °C, the free water

N. Kabashi (✉) · E. Krasniq · M. Muhaxheri · F. Salihu · B. Gashi
University of Prishtina, Str.Bregu I Diellit P.N., Pristina, Kosovo
e-mail: naser.kabashi@uni-pr.edu

T. Kang (ed.), *Proceedings of 5th International Conference on Civil Engineering and Architecture*, Lecture Notes in Civil Engineering 369,
https://doi.org/10.1007/978-981-99-4049-3_5

starts evaporating rapidly. At a temperature of 150 °C, the dehydration of ettringite will start, followed by the decomposition of gypsum. When the temperatures reach 300 °C, the chemical-bound water starts to evaporate, resulting in a decrease in the compressive strength. Decomposition of portlandite starts in intervals from 400 to 550 °C. The second phase of C-S-H decomposes at temperatures between 600 and 800 °C, forming β-C2S [3]. At a temperature of 900^0C, the C-S-H breaks down completely. Based on that, the critical temperature of concrete is 400–900 °C, and in this range, the concrete losses mass and strength [4, 5].

2 Experimental Program

2.1 Materials and Methods

The concrete made with Portland cement is subjected to heat, and several transformations and reactions occur, even if there is only a moderate increase in temperature [6]. As aggregate, such constituent materials with 65–75% of concrete volume and the behaviour of concrete under high temperature are strongly influenced by aggregate type and properties (VI). The properties of concrete at elevated temperatures can be defined from several viewpoints (heating process, applications of load, and control parameters) [7].

The approved mix design for the testing procedure with properties of cement and such constituent materials is presented in Table 1.

In the scope of trying to improve the concrete's behaviour, this paper uses fibres with the parameters presented in Table 2.

Table 1 Chemical composition of cement according to the EN 197-1

Chemical oxides of cement (%)	Cement CEM II 42.5 (%)
SiO_2	18.01
Fe_2O_3	2.69
Al_2O_3	4.58
MgO	1.80
CaO	61.23
SO_3	2.67

Table 2 Properties of polypropylene fibres

Properties of fibres	Specifications
Length of fibres	12 mm
Diameter of fibres	18 μ
Density	0.91 gr/cm^3
Module of elasticity	6000–9000 N/mm^2
Melting point	160 °C

Table 3 Concrete mixture proportions and fibre content

Mixture	Cement (kg)	Water (lit)	Fraction I (kg)	Fraction II (kg)	Fraction III (kg)	Polypropylene fibres (kg/m^3)
Mix I	4.2	2.6	12.24	2.52	3.24	0
Mix II	4.2	2.6	12.24	2.52	3.24	0.5
Mix III	4.2	2.6	12.24	2.52	3.24	1
Mix IV	4.2	2.6	12.24	2.52	3.24	2

2.2 Mix Design of Concrete

The concrete mix design is prepared using the lime aggregate in three fractions: fraction I (0–4) mm, fraction II (4–8) mm, and fraction III (8–16) mm with fine aggregate/coarse aggregate of 64:32 ratio. The methodology consisted of the determined concrete class with various fibre content, which were exposed at high temperatures. All the specimens were prepared from the same batch of mixed concrete, with the only changes being the percentage of fibres as presented in Table 3. For each mixture, the 12 samples with dimensions 70 × 70 × 70 mm are prepared, imposed by the dimensions of the furnace door.

2.3 Setup-Process of Applying the Temperature

The samples prepared according to the approval mix design are cured in laboratory conditions (temperature 20 ± 2 °C) and humidity RH = (95–100)% for 28 days. After the drying process over the period of 12 h, the applied temperature increased 20 °C/min until the target temperature, according to the Eurocode (EC) and presented in Fig. 1 [8, 9].

The furnace for applying the high temperate in concrete samples is presented in Fig. 2. The heating rate curves of the furnance used are shown in Fig. 1, where the function is composed regarding to targeted temperature.

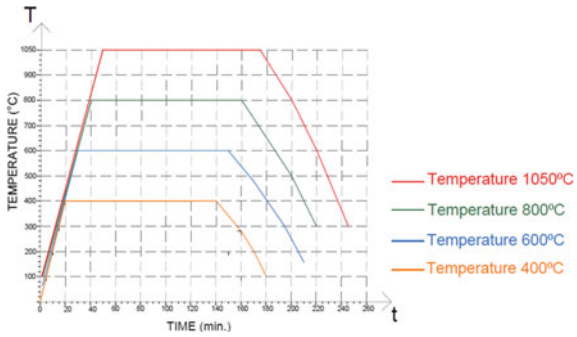

Fig. 1 Applied temperature in function of time

Fig. 2 Concrete samples under high temperature

3 Results and Discussion

3.1 Effect of High Temperature on the Loss of Mass of the Concrete Structure

Regarding the high temperature, the degradation process is oriented towards analysing the loss of mass and compressive strength of concrete. Mass loss determination is based on the mass before the high temperature is applied and in different stages of temperatures. The effect of fibres is not affected in these parameters, presented in Fig. 3.

Loss of mass is the result of changeable structures of concrete and type of aggregate [10]. Fibre content does not have a great impact when analysing the loss of concrete mass. There is a minor reduction factor for concrete samples subjected to 800 °C with a differentiation range up to 2.2%.

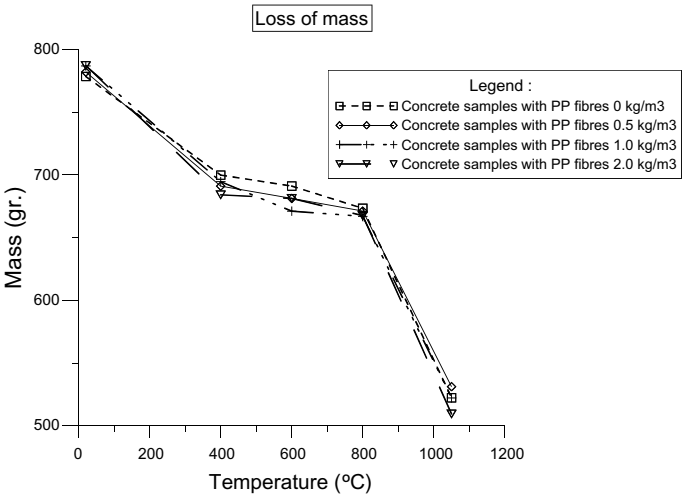

Fig. 3 Loss of mass in different stages of temperature

3.2 Degradation of the Structure of Concrete and Change in Colour of Concrete

Subjecting the samples to high temperatures is followed by the presence of cracking on the surface and the colour change, as presented in Fig. 4 [11].

Evaluations of the structure degradation of concrete are followed using microscopy analyses for different temperatures and presented in Fig. 5.

Increasing the temperature to 600 °C results in small cracks and voids in structures without fibres and no cracks in structures with fibres, as presented in Fig. 5b.

The temperature of 800 °C resulted in cracks and voids in both structures with and without fibres, as presented in Fig. 5c.

Increasing the temperature at 1050 °C results in cracks in the structure and an immense scale of voids in the structure in both mixed designs, which leads to the disintegration of the structure, presented in Fig. 5d.

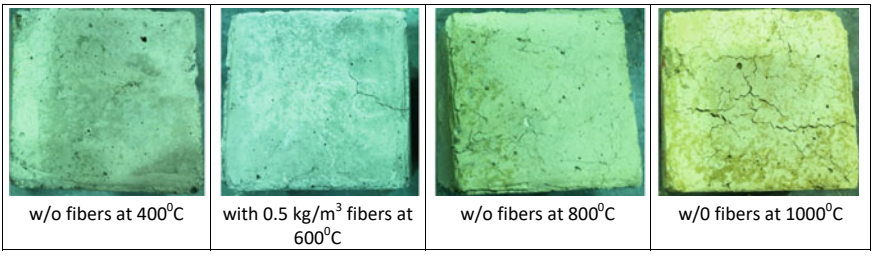

Fig. 4 Change the colour of concrete under high temperatures and the presence of cracks

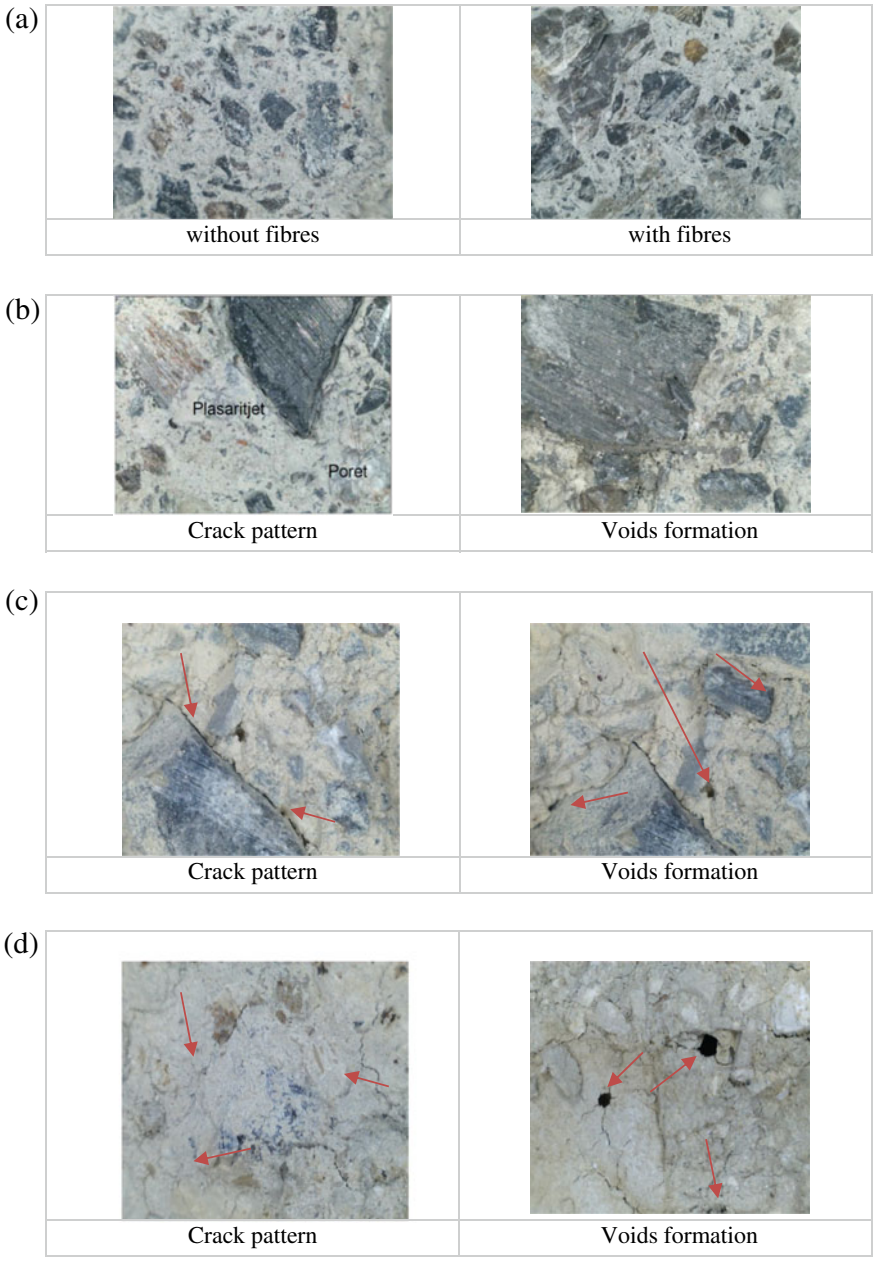

Fig. 5 **a** Microscopy evaluation on temperature 400 °C not detected the cracks in structure without and with fibres. **b** Microscopy evaluations on temperature 600 °C. **c** Microscopy evaluations on temperature 800 °C. **d** Microscopy evaluations on temperature 1050 °C

Table 4 Effect of high temperature on compressive strength

Mix	f_{ck} 20 °C MPa	Compressive strength and reduction (f_{ck}')						
		400 °C		600 °C		800 °C		1050 °C
		(Mpa)	%	(Mpa)	%	(Mpa)	%	(Mpa)
I-Etalon	27.6	20.59	25.6	12.22	55.8	5.3	94.7	Disintegrated
II PF 0.5 kg/m^3	29.2	22.12	24.2	12.22	58.2	7.52	74.2	Disintegrated
III PF 1.0 kg/m^3	31.0	21.87	29.5	10.53	66.0	6.49	79.1	Disintegrated
IV-PF 2.0 kg/m^3	30.5	25.37	16.9	14.61	52.1	6.41	79.0	Disintegrated

3.3 Compressive Strength of Concrete Samples Under High Temperatures

Changes in mechanical properties, that occur during applications at elevated temperatures, result in decreased compressive strength, resulting in the degradation of the concrete structure. In general, the high temperature is one of the effects which lead to the degradation of structure but always in a time process. The most common way to study the influence of elevated temperature on the properties of concrete is to expose the material to high temperature, cool it down to room temperature, and carry out testing, for instance, compressive strength. This method gives concrete "post-fire" or "post-exposure to high temperatures" properties [12–14].

Evaluations of the compressive strength under elevated temperatures, in this research paper, are presented in Table 4.

The effect of elevated temperature in concrete, based on the case study, is presented in Fig. 6. The effect of the percentage of polypropylene fibres in an amount of 2 kg/m^3 is very active up to the temperature of 400 °C. After that, the decrease is rapid when compared to plain concrete [9].

In the scope of analysing for behaviour, the elevated temperatures with the ASCE model and EC decrease are more severe because the aggregate is not similar, but in comparison with EC code, the behaviour is closely or more effective with 2 kg/m^3 of PP fibres [15].

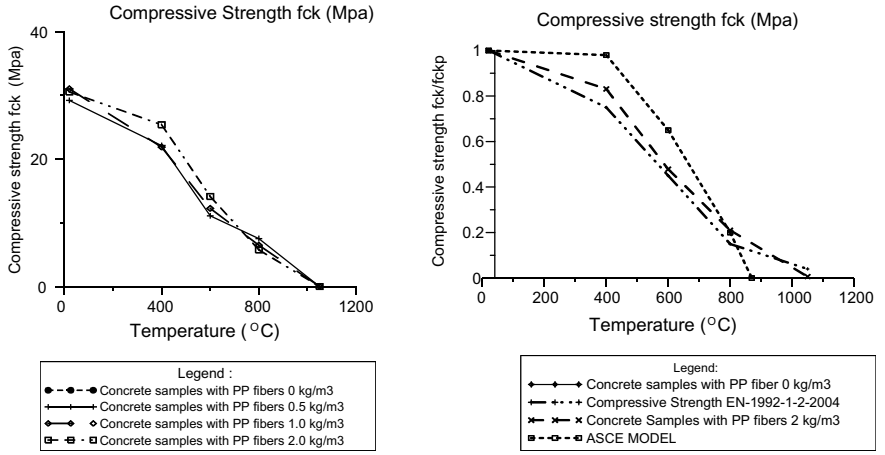

Fig. 6 Behaviour of the concrete—case study under elevated temperature and comparison between experimental case study, EC and ASCE model

4 Conclusion

This paper has presented an overview of the temperature effect on concrete experimented in samples prepared, maintained, and tested according to the standards, comparing the two study cases: plain concrete and concrete with polypropylene fibres.

- The mechanical properties of concrete exposed to elevated temperature are changeable, and the effect in concrete material is directly related to elements of the structure under fire or other high-temperature parameters.
- The mechanical properties under elevated temperatures change the microstructure and macrostructure under the microscope analysis.
- Polypropylene fibres have no effect after high-temperature exposure and significantly decrease the compressive strength with the presence of voids and cracks in concrete structures, as presented in microstructure analyses.
- ASCE material property models give better prediction when compared to EC and experimental models in the scope of properties of aggregate.

References

1. EN 1992-1-1 (1992) Eurocode 2—Design of concrete structures, Part 1–6: general rules and rules for buildings, European Prestandard, European Committee for Standardization
2. ACI manual of concrete practice (2014). American Concrete Institute, Farmington Hills, MI
3. Kalifa P, Chéné G, Gallé C (2001) High-temperature behaviour of HPC with polypropylene fibres. Cem Concr Res 31(10):1487–1499

4. Čítek D, Rydval M, Fořt J, Pokorný P, Pavlík Z, Kolísko J (2017) Residual material properties of high strength fibre reinforced concrete exposed to elevated temperatures. Solid State Phenom 259:85–89
5. Won D, Park W, Jang I, Han S, Han T (2014) Fire resistance performance of steel composite hollow RC column with inner tube under ISO 834 standard fire. Struct Concr 15(4):543–555
6. Snelson D, Wild S, O'Farrell M (2008) Heat of hydration of Portland Cement–Metakaolin–Fly ash (PC–MK–PFA) blends. Cem Concr Res 38(6):832–840
7. Tufail M, Shahzada K, Gencturk B, Wei J (2016) Effect of elevated temperature on mechanical properties of limestone, quartzite and granite concrete. Int J Concr Struct Mater 11(1):17–28
8. Liang X, Wu C, Yang Y, Li Z (2019) Experimental study on ultra-high performance concrete with high fire resistance under simultaneous effect of elevated temperature and impact loading. Cement Concr Compos 98:29–38
9. Khoury G, Majorana C, Pesavento F, Schrefler B (2002) Modelling of heated concrete. Mag Concr Res 54(2):77–101
10. Hager I (2013) Behaviour of cement concrete at high temperature. Bull Polish Acad Sci Tech Sci 61(1):145–154
11. Lee J, Choi K, Hong K (2009) Color and material property changes in concrete exposed to high temperatures. J Asian Arch Build Eng 8(1):175–782
12. Ahmed W, Lim C, Akbar A (2022) Influence of elevated temperatures on the mechanical performance of sustainable-fiber-reinforced recycled aggregate concrete: a review. Buildings 12(4):487
13. Jameran A, Ibrahim I, Yazan S, Rahim S (2015) Mechanical properties of steel-polypropylene fibre reinforced concrete under elevated temperature. Procedia Eng 125:818–824
14. Elshoura A, Okeil A (2022) Study of statistical uncertainties for temperature gradients in concrete bridges. ASCE-ASME J Risk Uncertainty Eng Syst Part A Civ Eng 8(1)
15. Cement and Concrete Research (1976) In: ASCE engineering mechanics specialty conference Waterloo, Ontario, 26–28 May 1976. 6(2):335–336

Composition Design and Performance of High Viscosity Micro-surface Pavement Material with Snow Melt Function

Mingyu Zhao, Yao Shi, Zhiqiang Li, Ruiwei Fang, and Qingjun Ding

Abstract The snow or ice that forms on pavement surfaces in cold weather results in severe traffic accidents and economic losses. Micro-surface material is a cost-effective preventive maintenance technology for road surface, which can guarantee the skid resistance and traffic capacity of the roads. Firstly, the composition design of high viscosity snow melting micro-surface was studied, and the change law of salt precipitation under different dosage was analyzed by conductivity test, combined with 1 h wet wheel abrasion test and load wheel sticky sand test to determine the best dosing of snow melting agent. Secondly, cohesive force test was designed to make up for the defect that the aggregate coating test could not be quantitatively analyzed. From the perspective of conventional road performance and snow melting performance, the feature of the three micro-surface material is analyzed. Finally, the performance of the paved test road is tested through the physical engineering. The results show that when the content of snow melting agent is 10%, the high viscosity snow melting micro-surface has the advantages of high adhesion strength with aggregate after demulsification, fast molding speed and high strength of mixture; the high viscosity snow melting micro-surface has good road performance and snow melting and deicing effect.

Keywords Road engineering · Micro surface · Snow melting · Emulsified asphalt · Conductivity · Pavement performance

M. Zhao (✉) · Y. Shi · Z. Li
School of Materials Science and Engineering, Shenyang Jianzhu University, Shenyang, China
e-mail: zmyzhaomingyu@sjzu.edu.cn

Z. Li
e-mail: lzq_221@stu.sjzu.edu.cn

R. Fang
Wuhan Municipal Construction Group Co., Ltd, Wuhan, China

Q. Ding
State Key Laboratory of Silicate Materials for Architectures, Wuhan University of Technology, Wuhan, China
e-mail: dingqj@whut.edu.cn

T. Kang (ed.), *Proceedings of 5th International Conference on Civil Engineering and Architecture*, Lecture Notes in Civil Engineering 369,
https://doi.org/10.1007/978-981-99-4049-3_6

1 Introduction

China's highway infrastructure construction has developed rapidly in recent years, and the amount of new highway construction is huge [1]. With the extension of the use period, many highways built in the early years entered the road repair and maintenance period. At the same time, with the frequent occurrence of dense traffic, heavy traffic and overloading, many new highways have early diseases in advance shortly after they are put into use. Under the multiple repeated effects of traffic load and natural factors [2], not only the function and service life of pavement are reduced, but also many potential safety hazards are generated. Therefore, there is an urgent need for new technologies for preventive maintenance of pavements [3].

Snow or ice on roads is one of the major safety hazards of winter driving, which not only affects daily transportation efficiency, but also has an impact on road performance [4]. At present, snow or ice melting technology is divided into "active" and "passive" Compared with the "passive" road snow deicing methods, the storage asphalt pavement, one of the "active" road snow deicing methods, has been concerned widely because of its own snow or ice melting function. However, with the increase of service time, the durability of the snow or ice melting function of salt storage asphalt pavement has been a hot issue [5]. Some studies have shown that compared with the life of asphalt pavement of 10–15 years [6], the maintenance time of snow melting and ice suppression function is still difficult to achieve the effect of snow melting to match the life of the pavement. Therefore, the development of long-lasting snow melting technology is of great significance [7].

Based on this, this paper prepared a functional preventive maintenance material with snow melting effect by compounding snow melting components in the preventive maintenance material [8]. High viscosity emulsified asphalt with excellent performance is used, and the salt compounds are mixed into the aggregate to prepare high viscosity snow melting micro-surface [9] and analyze the snow melting effect, road performance and engineering practical effect of high viscosity snow melting micro-surface, aiming to promote the development of pavement preventive maintenance technology [10].

2 Experiments

2.1 Raw Materials

Emulsified Asphalt. This paper uses high viscosity emulsified asphalt, SBS modified emulsified asphalt, SBR modified emulsified asphalt to prepare snow melting preventive maintenance materials, and specific asphalt performance indicators are as follows (Table 1).

Aggregate. Micro-surface mixture should have good anti-wear performance. Therefore, hard, rough, wear-resistant, pure aggregates such as basalt and pyrochlore

Table 1 Performance indicators of different types of asphalt

Test project		Unit	High viscosity emulsification Asphalt	SBS modified emulsified asphalt	SBR modified emulsification asphalt
Evaporation residue content		%	62.8	61.5	62.6
Standard viscosity C23,3		s	34	26	24
Nature of evaporation residues	60 °C power viscosity	Pa-s	90,352	3489	198
	Softening point	°C	89.5	75.5	55.8
	Ductility (5 °C)	cm	39.3	30.6	31.3

Table 2 Sieving results of aggregates

Size	0.075	0.15	0.3	0.6	1.18	2.36	4.75	9.5
0–3 mm	2.5	6.9	16.4	30.1	43.7	65.1	96.8	100
3–5 mm	1.2	3.0	4.2	5.5	7.6	14.2	89.9	100
5–10 mm	2.3	2.4	2.5	2.6	2.7	3.6	12.8	100

are supposed to choose. In this paper, three grades of basalt aggregates of 0–3 mm, 3–5 mm, and 5–10 mm from a stone factory in Hubei Jingshan are selected. The crushing value is 14.8%, Los Angeles abrasion value is 18.2%, water absorption rate is 0.46%, and screening results are shown in Table 2.

Filler. To improve the grading and road performance, mineral powder and cement were selected as fillers for the micro-surface materials in this paper, where mineral powder was provided by Hubei Jingshan Stone Factory with an apparent density of 2.672 kg/m3, 0.075 mm sieve passage rate of 2.5%, and cement was Huaxin ordinary silicate cement PO42.5.

Snow melting agent. After dissolving the salted compounds into the porous material and then modifying the organic hydrophobic material with several steps, we finally obtained an environmentally friendly salt-release material with certain slow-release property.

2.2 Test Methods

In this paper, the mixing test, cohesion test, wet wheel abrasion test, loaded wheel sticky sand test, wheel rutting deformation test method refer to Technical Guide to Micro Surface Treatment and Diluted Slurry Sealer. Horizontal shear resistance

test, vertical pullout test, low-temperature crack resistance test methods refer to test procedure for asphalt and asphalt mixture for highway engineering (JTG E20-2011).

In the conductivity value test, the specimen is placed into a container with a sealed lid, 1000 ml of deionized water is poured into the container to ensure that the specimen is completely submerged in the deionized water, and the conductivity is measured every 24 h.

3 The Composition Design of High Viscosity Snow Melting Micro-surface

3.1 Mineral Grading Design

The thickness of the micro-surface is about 1 cm, and the maximum nominal diameter of the aggregate in this paper is 9.5 mm. MS-3 type grading is used, and the synthetic grading curve is shown in Fig. 1. The aggregate and mineral powder from Hubei Jingshan Stone Factory is used to mix the mineral aggregate according to the grading requirements to synthesize the grading.

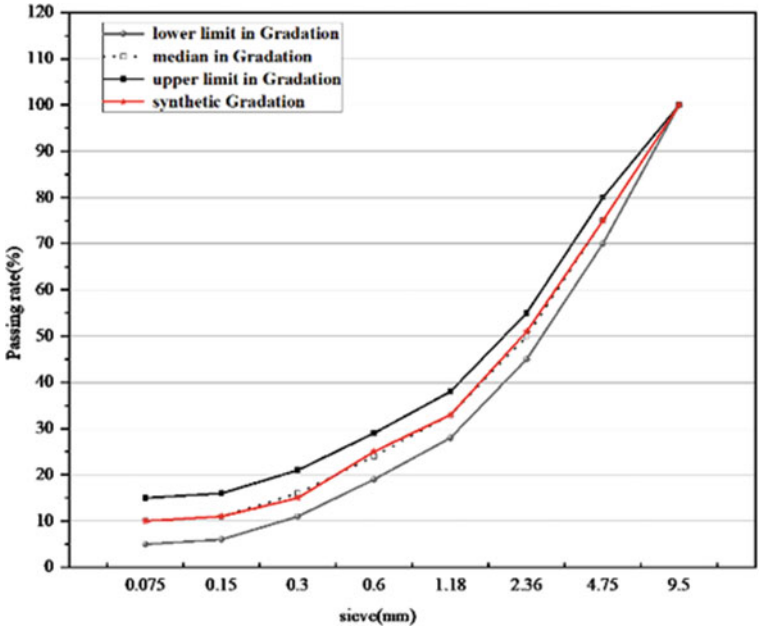

Fig. 1 Synthetic gradation of mineral materials

Table 3 Mixing with different water consumption

Water consumption/g	Mixable time/s	Mixing state
6	20	Mixing does not open
7	90	Thicker
8	120	Thicker
9	160	Uniformity
10	210	Uniform, thinner

3.2 Determination of Optimal Water Consumption

According to the mixing experiment to determine the best water consumption, it is preliminarily proposed to take 100 g of synthetic mineral aggregate, 11 g of high viscosity emulsified asphalt and 1 g of cement and observe the mixing state under different water consumption. The experimental results are shown in Table 3.

As can be seen from Table 3, with the increase of water consumption, the consistency of the mixture gradually decreases. The mixable time increases. However, if the mixture is too thin, it will affect the subsequent paving and forming of the mixture, delay the demulsification time and thus fail to meet the requirements of rapid opening of traffic. According to the experimental results, the best water consumption in this case is 9 g, that is, 9% of external mixing.

3.3 Determination of Cement Content

The amount of cement added to the mixture at the micro-surface is generally 0–3%, which mainly regulates the demulsification time and improves the molding strength. The excessive amount of cement will affect the mixing state and the low-temperature performance of the mixture. After determining the water addition as 9%, observe the influence of different cement content on mixing time and mixture forming strength. The results are shown in Fig. 2.

As can be seen from Fig. 2, with the increase of cement content, the mixing time decreases, which can speed up the demulsification time and accelerate the molding but the cement content is too high, the mixing state is not good, and the mixing time is too short. When the cement dosing is 1.5%, the mixing time and 30 min cohesion meet the requirements. Therefore, the cement content is set at 1.5%.

3.4 Determination of Optimal Oil-To-Stone Ratio

In micro-surface mixture, a suitable amount of asphalt is required. Too little will result in insufficient anti-wear capacity, and too much will result in oil flooding. In

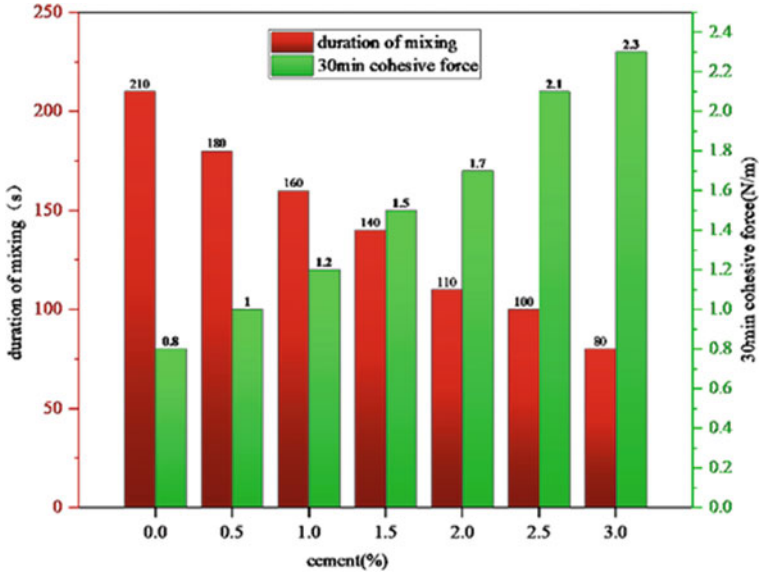

Fig. 2 Mixing with different cement dosage

the laboratory, the upper and lower limits of asphalt dosage are determined by the 1-h wet wheel wear value and the sand sticking value of loaded wheel under different asphalt-aggregate ratio. In China, the wear value of 1-h wet wheel is required to be not less than 540 g/m^2, and the sand sticking value of load wheel is not more than 450 g/ m^2. The experimental results under different oil-to-stone ratio are shown in Fig. 3.

From Fig. 3, it can be obtained that the oil-to-stone ratio between 6.4 and 7.5 meets the specification requirements, and the optimal oil-to-stone ratio is 6.7%. According to the calculation of 62% solid content of high viscous asphalt, the content of high viscous asphalt is 10.8% of synthetic aggregate. The same mineral aggregate composite gradation and the same design method are used to determine the mix proportion of SBS micro-surfacing and SBR micro-surfacing.

3.5 Determination of Snow Melt Content

Conductivity value test. Based on the conductivity value test of salt solution, the salting out law of high viscosity emulsified asphalt mixture with different amounts of snow melting agent is studied. Under the set test conditions, the content of fixed high viscous emulsified asphalt is 10.8%, the laboratory uses DSC-11A conductivity meter to test changes of snow melting and deicing asphalt mixture with the content of snow melting agent of 2, 6, 10, 14, and 18%, which is converted into salting out

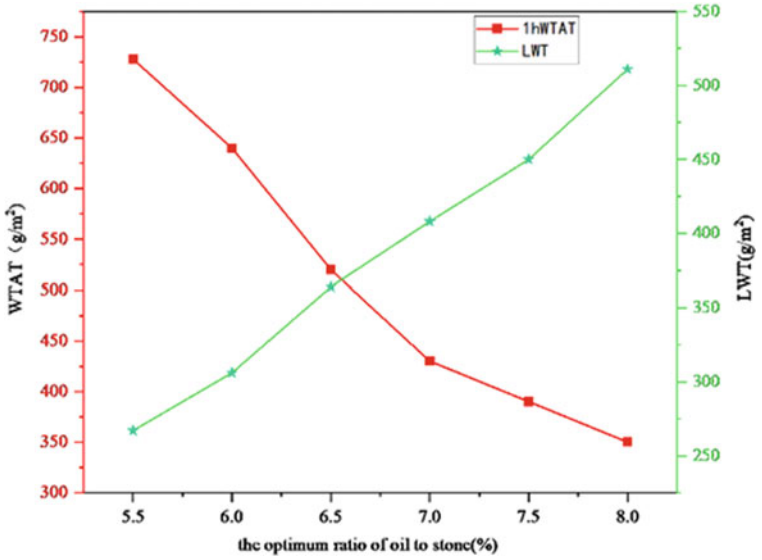

Fig. 3 Optimal oil-to-stone ratio

amount, and studies the influence of the content of snow melting agent on the snow melting and deicing effect of snow melting and deicing high viscosity emulsified asphalt mixture. The test results are shown in Fig. 4.

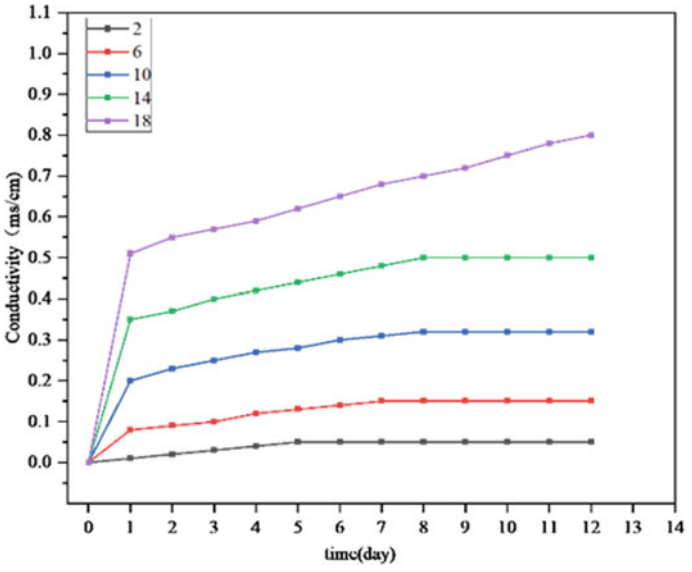

Fig. 4 Electrical conductivity of mixes at different blending rates

Table 4 Content of each component at the high viscosity micro-surface

Grouping	Synthetic minerals	Emulsified asphalt	Water	Cement	Snow melt
Mass ratio %	100	10.8	9	1.5	10

From Fig. 4 can be found that the amount of snow melting agent essentially determines the total amount of salt. Theoretically, the higher the amount of snow melting agent, the more salt can be released, and the better the effect of snow melting and deicing. However, too much snow melting agent will reduce the road performance. Therefore, the content of snow melting agent should comprehensively consider the snow melting and deicing effect and road performance, so that the micro-surface has a certain snow melting and deicing function and meets the requirements of actual road performance.

The best snow melt content. The test specimens were prepared with the ratio of 10.8% high viscosity emulsified asphalt, ordinary stone, 9% additional water and 1.5% cement, and different amounts of snow melting agent (2, 6, 10, 14, and 18%) were added to conduct 1 h wet wheel abrasion test and load wheel sticky sand test respectively.

As can be seen from Fig. 4, with the increase of snow melt content, the 1 h wet wheel wear value of the mixture increases; the amount of adhering sand of the mixture decreases. Therefore, considering the effect of snow melting and deicing and its road performance, the content of snow melting agent is determined to be 10% (Table 4).

4 Comparison of the Performance of the Three Micro-surface

4.1 Aggregate Wrapping Property

In road engineering, the adhesion grade between aggregate and asphalt is tested by the wrapping test of aggregate. Only when asphalt and aggregate in the mixture have good adhesion can the pavement performance of the mixture be guaranteed, and the effect of pavement maintenance be brought into play. As a surface maintenance material, if the adhesion of the aggregate is not up to standard, it is easy to produce loose, spalling, and other diseases under high-temperature or rainstorm environment and heavy traffic. Using the water immersion method for reference, this paper directly immerses the dried and cooled aggregate into emulsified asphalt at room temperature, takes it out and stands for 4 h until the emulsified asphalt is demulsified and fully formed, immerses it in 80 °C water temperature for 30 min, and then puts it into cold water to observe the peeling of its asphalt film. The results of the adhesion experiments of three kinds of emulsified asphalt are shown in Table 5.

Table 5 Experimental results of aggregate wrapping property of three emulsified asphalt groups

Experiment number	Spalling/%	Wrap rate/%	Adhesion grade
High viscosity	0	100	5
SBS	5	95	5
SBR	5	95	5

From Table 5, the adhesion grade of three emulsified asphalt is up to grade 5. Compared with SBS latex-modified emulsified asphalt SBR latex-modified emulsified asphalt, high viscous emulsified asphalt has higher coating rate and better adhesion with aggregate. Because the observation method used in the adhesion test of asphalt and mineral aggregate has certain errors, which cannot be quantitatively analyzed, it is necessary to continue to explore the adhesion between emulsified asphalt and aggregate.

4.2 Mixture Forming Strength

The cohesion experiment can not only judge the length of demulsification time of the mixture, but also detect the molding strength of the mixture, which reflects its adhesion performance from the side, making up for the defect that the aggregate wrapping test cannot be analyzed quantitatively, thus improving the accuracy of the test results. The cohesion at different times at different micro-surfaces is shown in Fig. 5.

From the trend diagram in Fig. 5, we can get that the adhesion strength of all three types of micro-surface increases with the extension of time. At 20 min, the early strength of high viscosity micro-surface has reached the required value of 30 min of specification ($\geq$1.2 N-m), and 30 min has almost reached the requirement of 1 h of specification ($\geq$2.0 N-m), which indicates that the high viscosity micro-surfacing has high adhesion strength to the aggregate after demulsification, fast forming speed and high strength. It plays a decisive role in the rapid opening of traffic in the later stage. The molding strength of SBS latex-modified micro-surface is better, and SBR latex-modified micro-surface is second.

4.3 Conventional Road Performance

The results of 1 h and 6d wet wheel wear values and rutting deformation test (width deformation rate) were measured for the three micro-surface mixtures under the same conditions to evaluate their wear resistance, water resistance and rutting resistance, respectively. The specific results of the experiments are shown in Table 6.

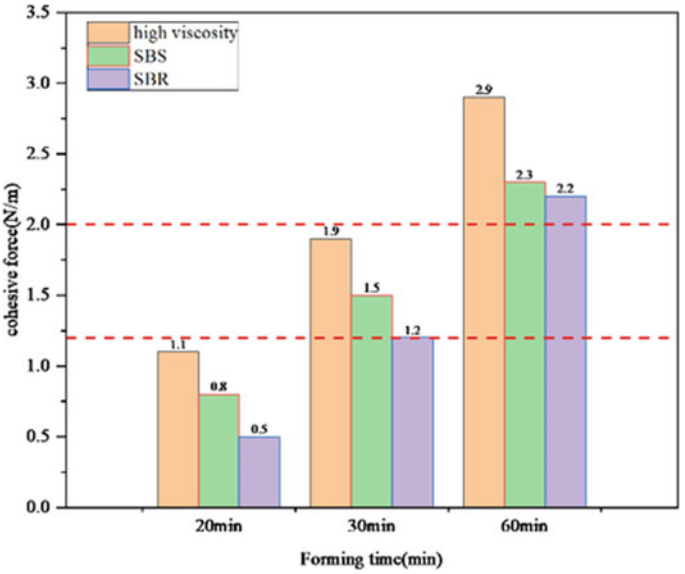

Fig. 5 Trend of cohesion at different micro-surface types at different times

Table 6 Experimental results of conventional road performance at different micro-meters

Mix type	Wet wheel wear value/g/m^2		Wheel rutting deformation rate/%
	1d	6d	
High viscosity	365	605	1.9
SBS	383	702	2.7
SBR	445	785	3.6

As can be seen from the data in Table 6, under the same conditions, the abrasion value and rutting deformation rate of high viscosity micro-surface are lower than the other two groups, indicating better wear resistance, water damage resistance and deformation resistance, and the performance of SBS micro-surface is better than that of SBR micro-surface. This is because the high viscous emulsified asphalt has strong adhesion to the mineral aggregate, which improves the water spalling resistance and wear resistance of the mixture. In addition, the stable three-dimensional network structure of high viscous asphalt strongly restrains the flow of asphalt molecules and reduces water damage. From Figs. 6 and 7, it can be visually found that the high viscosity micro-surface is more wear-resistant and has better deformation resistance than the SBR micro-surface.

Fig. 6 Abrasion diagram at high viscosity micro-surface (left) and SBR micro-surface (right)

Fig. 7 Rotation map of high viscosity micro-surface (bottom) and SBR micro-surface (top)

4.4 Interlaminar Shear Resistance

Anti-wear performance is not only reflected in the wear of tires and micro-surface pavement, when the shear resistance of micro-surface and the original pavement is insufficient, and the adhesion between layers is not enough, under the action of vehicle load, but the anti-wear performance of surface layer will also be greatly reduced, and there will continue to appear nudging, hugging, rutting and other diseases. In this paper, the interlaminar shear resistance performance is analyzed by direct shear apparatus and pull-out test at 25 °C. The three micro-surfaces were paved and formed in the same section and tested after they were fully cured, and the test results are shown in Fig. 8.

From Fig. 8, it can be seen that due to the high viscous emulsified asphalt with its super high dynamic viscosity, the bonding performance and shear resistance of the

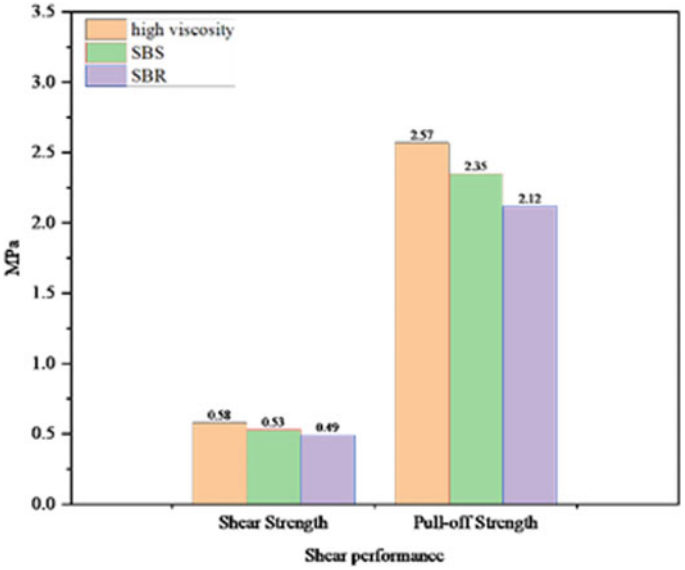

Fig. 8 Comparison of the shear resistance at different micro-surfaces

high viscous micro-surface mixture with the original pavement are better than the other two groups of micro-surface, which is consistent with the results of cohesion test. The high viscosity micro-surface effectively improves the defect of insufficient interlayer adhesion existing in the micro-surface at present.

4.5 Low-Temperature Crack Resistance

The low-temperature crack resistance of the three micro-surfaces is evaluated by referring to the Marshall specimen formed by hot mix to test the splitting strength at −5 °C, the three specimens formed by mortar test to test the bending resistance at −5 °C and the specific results are shown in Table 7.

Table 7 Test results of crack resistance of different modified emulsified asphalt micro-surface mixtures

Mix type	Cleavage strength/MPa	Flexural strength/MPa
High viscosity	1.61	1.73
SBS	1.59	1.66
SBR	1.26	1.18

Table 8 Test results of snow and ice melting performance of different modified emulsified asphalt micro-surface mixtures

Mix type	Whether white precipitate appears
Highly viscous	Yes
SBS	None
SBR	None

From Table 7, it can be seen that the splitting strength and flexural strength of the high viscosity micro-surface are significantly greater than those of the SBR micro-surface and are also better than those of the SBS micro-surface, indicating that the bond between the high viscosity emulsified asphalt and the aggregates is stronger, the cohesion of the micro-surface mixture is greater, and the low-temperature cracking resistance is better. When SBR is used as asphalt modifier, the modified asphalt has better low-temperature ductility. SBS modified asphalt has good high- and low-temperature performance because SBS has both rubber and resin properties. In this paper, high viscosity asphalt modifier is a high dose of SBS with the synergistic effect of compatibilizer and stabilizer, and its comprehensive performance is excellent. Combined with the splitting and folding test results, it can be concluded that the low-temperature crack resistance at the high viscosity micro-surface is better.

4.6 Snow Melting and Ice Suppression Performance

Silver nitrate method uses dilute nitrate solution to detect chloride ions, which is the most common direct detection method of salt storage asphalt mixture on site. The method is simple and convenient. It can be used not only for laboratory testing, but also for testing the effect of newly paved or existing salt storage pavement. Silver nitrate method is used to test the specimen of wheel rutting deformation test. The specific results are shown in Table 8.

From Table 8, it can be obtained that white precipitation appeared in the mix specimens at the high viscous snow melting micro-surface, and the chloride ion content decreased with the increase of the number of rutting meter crushing, which indicates that the wheel crushing action accelerated the salt release of the mixture at the high viscous snow melting micro-surface.

5 Engineering Applications

A section near the Lingshan mixing station in Jiangxia District, Wuhan, with heavy traffic and a certain slope, led to cracks and rutting of the pavement in the downhill section under the action of traffic load. For the rehabilitation program of this road section, the expert group decided to use high viscous micro-surface at this subject as the maintenance material, and a 2 km trial section was paved in this road in early

Fig. 9 Site construction drawing

September 2019. To strengthen the bond between the high viscous micro-surface and the original pavement and enhance the ability to resist slip deformation, the viscous layer oil also adopts high viscous emulsified asphalt with a sprinkling volume of 0.25 kg/m^2. According to the engineering experience and specifications, the micro-surface will be accepted in sections after it has been completely cured and stabilized. The photos of the construction site are shown in Fig. 9.

6 Conclusion

The best asphalt-aggregate ratio of high viscosity snow melting micro-surface is 6.7%. Taking the solid content of high viscosity emulsified asphalt as 62% and the content of snow melting agent as 10%, the best mix ratio is synthetic aggregate: cement: water: high viscosity emulsified asphalt = 100:1.5:9:10.8.

When the high viscosity snow melting micro-surface is treated for 20 min, the early strength has reached the standard value of 30 min ($\geq$1.2 N-m), and 30 min has almost reached the standard value of 1 h ($\geq$2.0 N-m), indicating that the high viscosity snow melting micro-surface has good adhesion with aggregate after demulsification, fast molding speed and high mixture strength.

The wear resistance, water damage resistance, rutting resistance, shear resistance and low-temperature crack resistance of the high viscosity snow melting micro-surface are better than those of the ordinary micro-surface which can make up for the defects of the current micro-surface, such as poor high-temperature performance and weak adhesion.

After passing the handover evaluation and acceptance, the engineering test section with high viscosity snow melting micro-surfacing is found to have excellent anti-sliding performance, almost impervious to water, and can effectively reduce road

noise, which has good economic and social benefits, and has far-reaching significance for the promotion of road preventive maintenance projects.

References

1. Liu Z, Chen S, He R et al (2015) Investigation on the properties of asphalt mixtures containing antifreeze fillers. J Mater Civ Eng 27(6):04014180
2. Hujran O (2018). Using computer simulation in the analysis of energy saving in green building; a case study. Int J Smart Grid Clean Energy (1)
3. Shan L, Li Z, Tian D et al (2021) Effect of anti-icing additives on the stability of emulsified asphalt binders. Constr Build Mater 275:121951
4. Coenen AR, Kutay ME, Sefidmazgi NR et al (2012) Aggregate structure haracterization of asphalt mixtures using two-dimensional image analysis. Road Mater Pavement Des 13(3):433–454
5. Hossain SMK, Fu L, Hosseini F et al (2016) Optimum winter road maintenance: effect of pavement types on snow melting performance of road salts. Can J Civ Eng 43(9):802–811
6. Liu K, Huang S, Jin C et al (2017) Prediction models of the thermal field on ice-snow melting pavement with electric heating pipes. Appl Therm Eng 120:269–276
7. Skelton EH, Terry L, Amirkhanian A (2022) Novel SHRP method showed alternative deicers outperform NaCl brine for certain winter roadway maintenance applications. J Environ Manage 320:115879
8. Meng Y, Xu R, Guo H et al (2021) Influences of sodium salt erosion on the self-healing ability and fatigue life of bitumen. Constr Build Mater 286
9. Wang Z, Zhang T, Shao M et al (2017) Investigation on snow-melting performance of asphalt mixtures incorporating with salt-storage aggregates. Constr Build Mater 142:187–198
10. Sajid HU, Jalal A, Kiran R et al (2022) A survey on the effects of deicing materials on properties of cement-based materials. Constr Build Mater 319:126062

Potassium Chloride Performance as Expansion Inhibitor Agent in Clayey Soils with Mineralogical Content of Montmorillonite

Juan Diego Torres, Angel Watanabe, Carlos Fernández, and Gary Durán

Abstract Expansive soils are a type of problematic soil that, due to its physicochemical characteristics, tends to undergo volumetric changes in its internal molecular structure when experiencing alterations in its moisture content. The relevance of his study lies in the numerous structural damages registered worldwide as a result of this phenomenon. Although there are agents for its stabilization, the current environmental trend leads to the search for alternative sustainable materials that guarantee favorable results in inhibiting its expansive character. In this sense, this research aims to evaluate the contribution of potassium chloride in the expansive parameters of a soil sample with mineralogical content of montmorillonite extracted from the locality of Talara, Peru. For this purpose, free swell tests and swelling pressure tests were performed on samples with dosages of 0, 2, 4, 6, and 8% potassium chloride by weight, obtaining as main result a significant reduction in the expansion potential.

Keywords Expansive soils · Clay · Montmorillonite · Potassium chloride · Swelling test

J. D. Torres (✉) · A. Watanabe · C. Fernández · G. Durán
Department of Civil Engineering, Peruvian University of Applied Sciences, Lima, Peru
e-mail: u201611128@upc.edu.pe

A. Watanabe
e-mail: u201616165@upc.edu.pe

C. Fernández
e-mail: carlos.fernandez@upc.edu.pe

G. Durán
e-mail: gary.duran@upc.edu.pe

T. Kang (ed.), *Proceedings of 5th International Conference on Civil Engineering and Architecture*, Lecture Notes in Civil Engineering 369,
https://doi.org/10.1007/978-981-99-4049-3_7

1 Introduction

Expansive soils have been a major challenge in geotechnical engineering since their causal attribution of numerous pathologies in structures in the late 1930s. Among the most frequent affectations that arise from the utilization of this soil type as foundation material for predominantly lightweight structures are the following: cracking of structural elements, cracking of walls and foundations, unevenness of floors, damage to buried facilities, slope instability, and bulging of embankments, among others. In the United States, annual damage losses attributable to this phenomenon exceed nine billion dollars; while, in countries such as China and the United Kingdom, this figure amounts to one billion and 0.5 billion dollars, respectively [1].

At the microscopic scale, its expansiveness is subject to the intervention of various factors such as its colloidal content, mineralogical composition, and type of exchangeable ions. However, the main cause of the degree of expansion lies in the type of clay minerals immersed in the microstructure of the particles [2]. Precisely, one of the minerals most likely to be affected by the effects of hydration is montmorillonite, a phyllosilicate mineral belonging to the group of smectics, which is structurally configured by a central layer of octahedrally ordered alumina interspersed by two tetrahedral eccentric layers of silica [3].

The electronegative charge of the basal surface of the montmorillonite sheets is produced by a deficiency of positive charge as a result of isomorphic substitutions as is the case of the replacement of a silicon atom (Si^{4+}) by a trivalent cation (Al^{3+} or Fe^{3+}) in tetrahedral positions or a trivalent cation (Al^{3+} or Fe^{3+}) by a divalent (Mg, Fe^{2+}) or a divalent cation (Mg^{2+}) by a monovalent (Li) cation in octahedral positions. Moreover, this type of substitutions can be added other mechanisms due to structural imperfections due to the existence of vacancy in the octahedral positions or the dehydroxylation of groups $(OH)^{-}$ [4, 5].

The excess negative charge is compensated by the attraction of alkaline and/or alkaline earth cations such as Na^{+}, K^{+}, Mg^{2+}, and Ca^{2+}, which, due to their adsorption energy with water molecules, facilitate the hydration of this type of minerals due to the formation of a diffuse double layer [6]. Additionally, its susceptibility is influenced by the relatively weak Van der Waals forces that link these TOT structural units with others, allowing their separation by action of the entry of water molecules more easily [7, 8].

The interest in this type of soils with a highly expansive tendency has led several authors to focus efforts on investigating the mechanism of action that occurs in the soil mass when they are subjected to cycles of wetting and drying. As a result, at present, different soil stabilization techniques are available, classified into two groups: mechanical and chemical. Within the group of mechanical stabilization, various methods can be employed, including compaction, soil replacement or mixing, pre-wetting, and reinforcement with geosynthetics. On the other hand, soil stabilization by chemical methods uses some traditional additives that are commonly used for the treatment of expansive soils such as cement, lime, and fly ash; as well as others not so common like polymers and bioenzymes [9].

While it is true, it has been scientifically proven that chemical stabilization is more efficient than physical stabilization, the application of cementitious materials such as Portland cement and lime have an impact on the environment, since their production processes generate a high level of pollution due to the energy consumption that this implies and the substantial emission of carbon dioxide gases (CO_2) [10, 11]. In addition, stabilization with these additives can change the pH of the soil, compromising the quality of soil and groundwater [12]. Given this scenario, it is essential to find an additive that mitigates the expansive effects of the soil in terms of study while contributing to the sustainable development of the planet.

In this context, the ongoing research aims to quantitatively evaluate the performance of potassium chloride as an inhibitor of expansion in a sample of clay soil with mineralogical content of montmorillonite, by determining the percentage of maximum reduction that provides the optimal content of the additive supplied.

2 Research Proposal

The choice of stabilization technique was based on a comparative experimental study conducted by Soltani et al. (2017), in which the capacity to reduce the expansion potential of some representative agents for different soil stabilization techniques was compared [13]. On the one hand, hydrated lime and Portland Type I cement were used for stabilization by chemical methods; while, on the other, ionic polymers and artificial fibers based on polypropylene to represent mechanical methods. From the results of the tests carried out, it was concluded that in all the proposed scenarios there was a considerable reduction in swelling in relation to the ground under natural conditions. However, agents such as cement and lime showed greater efficiency by presenting maximum reduction percentages of 79.5% and 72.5%, respectively.

With the defined technique, a research process was started with the aim of understanding the expansive character of clay minerals. In this sense, it was corroborated that several investigations have been carried out that have had as main objective to establish the influence of certain parameters in the triggering of this phenomenon. In this regard, Yi et al. (2018) investigated the adsorption energy that exists between the interlaminar surface of montmorillonite, interchangeable cations, and polar water molecules using molecular dynamics simulations. The results obtained showed that water molecules exhibit a higher degree of affinity with interchangeable cations than with the negatively charged surface of montmorillonite [14]. In this way, it was concluded that the hydrophilic nature of these clay minerals is induced by the effect of the electrostatic interaction of attraction between water molecules and cations.

Similar results were obtained by Peng et al. (2019) when investigating the driving force of montmorillonite swelling, since they determined that the adsorption energy of water molecules is much higher with the cations of the intermediate layer. Moreover, another contribution of this research is the inclusion of the concept of cation exchange capacity [15]. According to the authors, hydration ability is directly related to adsorption energy. In this regard, he points out that cations of Mg^{2+} have a higher

adsorption energy with water molecules than cations such as Ca^{2+}, Na^{+}, and K^{+} that respects the order Mg > Ca > Na > K; that is, monovalent potassium cations have a lower hydration capacity, so it constitutes the main component for the designation of the proposal of this research.

3 Experimental Methodology

3.1 Materials

Expansive Soil. For this research, a soil sample from Urb. Los Vencedores located in Talara, Peru was used. Its selection was based on a previous analysis of the places where soils with a high content of montmorillonite are found from a geotechnical zoning map of that city, which mentions that shale bases emerge in the study area at shallow depths. For this, a trial pit was made with a depth of 1.50 m where a sample of unaltered soil of cubic shape with edges of 0.30 m was extracted and sealed to preserve its structure and initial humidity.

Potassium Chloride. Potassium chloride is a haloid salt formed by colorless, non-hygroscopic crystals, which can be obtained by saltwater desalination, crystallization from a solution, among others. For this research, potassium chloride (KCl) was obtained with USP, FCC grade certification from the company BETHLABS S.R.L. The dosages arranged for the purposes of this investigation will be 2, 4, 6, and 8% by weight of soil mass.

3.2 Methods

Three main phases were defined in which, through laboratory tests, the behavior of potassium chloride as an inhibitor of the expansion of soils rich in montmorillonite was validated.

First, the X-ray diffraction (XRD) test was performed, for this purpose the Bruker D4 ENDEAVOR diffractometer was used with excitation conditions of 40 kV and 40 mA, which allowed to identify and quantify the mineral phases that contained the analyzed sample. This sample was previously subjected to a suspension in distilled water, filtered under vacuum, to observe the main peaks present in the sample in a clearer way. Next, the sample was saturated with ethylene glycol vapor for a moderate time (12 h) to cause displacement of the main peaks at smaller angles.

Subsequently, the physical characterization tests fundamental for the identification and classification of soils were carried out, complying with the guidelines indicated in the regulations. Among the most representative, we have the granulometric analysis by sieving and sedimentation (ASTM D 422), moisture content (ASTM D 2216), Atterberg limits (ASTM D 4318) and specific gravity of solids (ASTM D 854).

Finally, tests were carried out that directly determined the degree of expansion of the analyzed samples by calculating the percentage of one-dimensional swelling and the swelling pressure (ASTM D 4546). In order to evaluate the contribution of the additive**,** these tests were carried out separately for soil samples without any intervention and for samples with a content, as a percentage of the total weight of the sample, of 2, 4, 6, and 8% potassium chloride.

4 Results and Discussion

4.1 Mineralogical Analysis

Figure 1 shows the X-ray diffraction pattern of the soil sample tested with diffraction peaks that obey a crystalline phase mainly quartz. However, in terms of clay minerals alone, montmorillonite has the most intense peak, generated by an increase in its interplanar distance after saturation with steam with ethylene glycol for 12 continuous hours (see Fig. 2). This evaluation has also allowed the identification of other laminar minerals such as illite and, to a lesser extent, kaolinite.

The above can be seen quantitatively in Table 1. In it, the predominance of quartz is highlighted with a content of 32% of the total sample. In addition, the presence of some clay minerals with an expansive tendency such as montmorillonite and illite with values of 28% and 17%, respectively, is evident. While it is true, illite does not have the same physicochemical properties as montmorillonite, it has a limited expansion capacity, so it also contributes to expansive behavior.

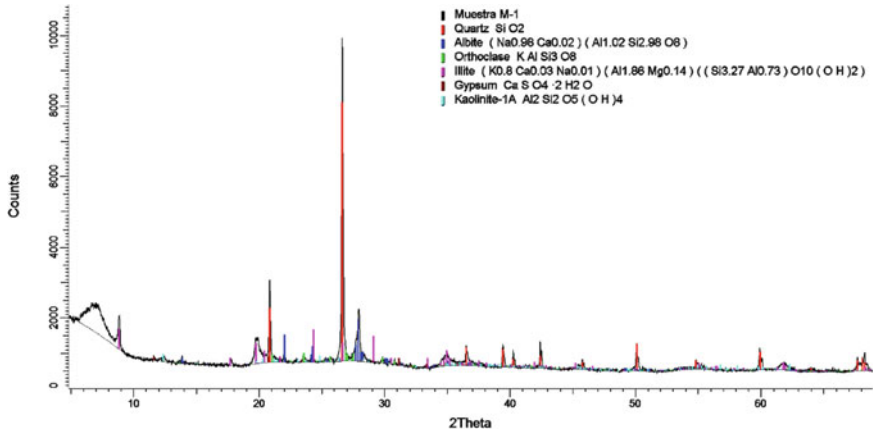

Fig. 1 X-ray diffraction patterns under powder diffraction analysis for the identification of the global mineralogy of the sample tested

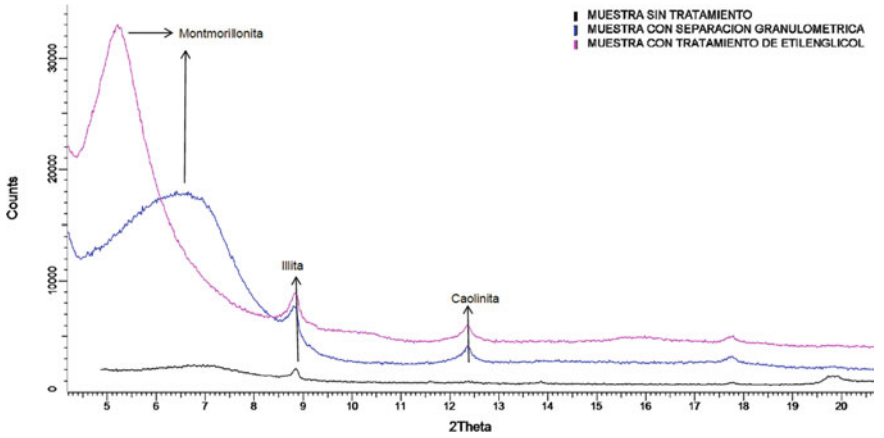

Fig. 2 X-ray diffraction patterns under selective treatments of particle size separation and ethylene glycol treatment

Table 1 Mineralogical composition of the sample by X-ray diffraction assay

Mineral	Chemical formula	Result
Quartz	SiO_2	32%
Montmorillonite	(Na, Ca)0, 3(Al, Mg)2$Si_4O_{10}(OH)_2 \cdot n(H_2O)$	28%
Illite	(K, H_3O) (Al, Mg, Fe)2(Si, Al)4O10[$(OH)_2(H_2O)$]	17%
Plagioclase	(Na, Ca) $(Al, Si)_4O_8$	15%
Kaolinite	$Al_2Si_2O_5(OH)_4$	4%
Feldspar	$KAlSi_3O_8$	2%
Gypsum	$CaSO_4 \cdot 2(H_2O)$	<L. D.

In this aspect, a total content of 45% of clay mineral positions to the sample analyzed as a soil with a high tendency to undergo contraction expansion processes and suppose the requirement of treatment for its stabilization.

4.2 Classification and Index Property Tests

According to the particle size tests carried out, the soil is mostly made up of fine fraction, whose value amounts to 95.4%. Of this content, 39.1% corresponds to silts, while 56.3% to clays (see Table 2).

The results of the Atterberg limits test indicate that the liquid limit and the plastic limit of the sample tested were 64% and 26%, respectively; while the plasticity index was calculated at 38%. According to Chen (1975), the values obtained show a very

Table 2 Results of sample characterization tests

Tests	Description	Result
Granulometry	Sand	4.6%
	Silt	39.1%
	Clay	56.3%
Atterberg limits	Liquid limit (LL)	64
	Plastic limit (LP)	26
	Plasticity index (PI)	38
Moisture content		10%
Specific gravity		2.599

high degree of expansion of the sample with liquid limits greater than 60% and plastic indices above 35% [16].

According to the Unified Soil Classification System (USCS), soil is classified as a high plasticity inorganic clay (CH) while the classification of soil according to the AASHTO method catalogs it with the denomination A-7-6 (20).

On the other hand, the sample presents a relatively low initial moisture content of 10.0%, taking into account that soils with humidity ranging from 15% are more likely to experience considerable volume changes due to the absorption of moisture content of approximately 35%.

4.3 One-Dimensional Swelling Tests

Free Swell Tests. In Fig. 3, a considerable increase can be seen in the first 85 min of testing for the untested sample, followed by a slight increase in its expansion until reaching a maximum one-dimensional swelling of 10.54%. In this sense, the time–expansion curves obtained for samples with different dosage of potassium chloride exhibit a marked reduction in expansion compared to the time–expansion curve of the standard sample.

Regarding the percentage of free expansion, in Table 3, the following results are presented for the different types of samples. In this regard, the sample of natural soil exhibits a free expansion of 9.27%. Based on the results obtained, researchers such as Seed, Woodward, and Lundgren (1962) classify this type of soil with a high degree of expansion as it is within the range of 5% and 25% [17]. For his part, Chen (1975) coincides with the previous premise by being between 3 and 10% [16].

For soil samples with 2%, 4%, 6% and 8% potassium chloride by weight, there are values of 1.24%, 1.09%, 0.74%, and 1.13%, respectively. These results can be seen graphically in Fig. 4, where the inhibitory nature of the different concentrations of potassium chloride can be seen more clearly.

In this scenario, the addition of 8% potassium chloride showed a slight deviation in the inhibitory character of the expansion, which implies a propensity to swelling

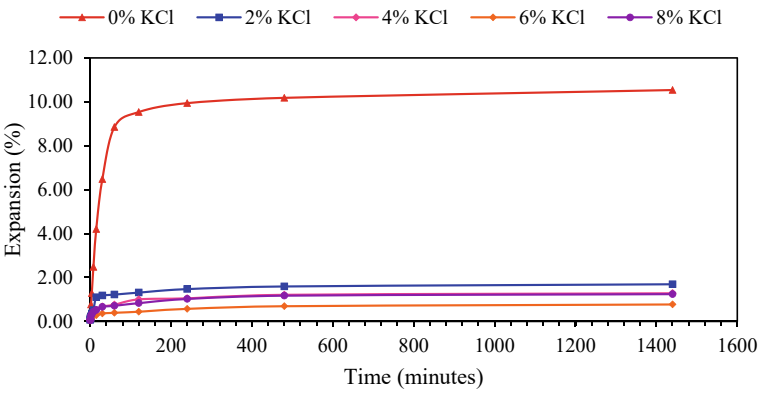

Fig. 3 Time–expansion curve for unprepared sample and prepared samples with concentrations de 2, 4, 6, and 8% potassium chloride by weight

Table 3 Free expansion and expansion time for different additive concentrations

Type of sample	Primary expansion time (min)	Secondary expansion time (min)	Free expansion (%)
Sample + 0% KCl	0.10–85	>85	9.27
Sample + 2% KCl	0.10–30	>30	1.24
Sample + 4% KCl	0.10–285	>285	1.09
Sample + 6% KCl	0.10–640	>640	0.74
Sample + 8% KCl	0.10–640	>640	1.13

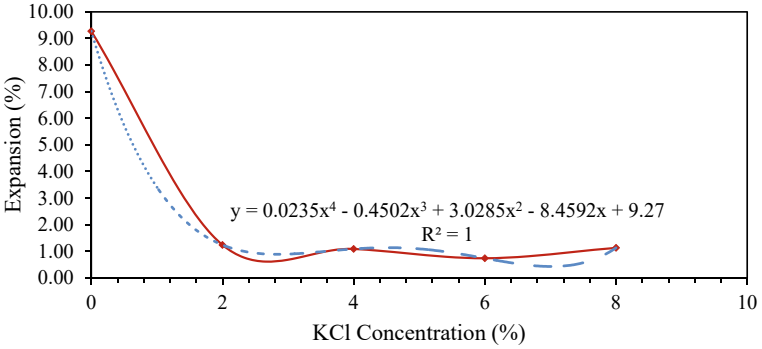

Fig. 4 Percentage of free expansion according to the concentration of potassium chloride by weight

for samples in which a higher concentration of potassium chloride is available. This tendency is due to an excess of monovalent potassium cations that, given their electrical charge, generate repulsive forces that lead to an increase in the interplanar distance.

Table 4 Swelling pressure for different additive concentrations

Type of sample	Swelling pressure (kg/cm^2)
Sample + 0% KCl	0.143
Sample + 2% KCl	0.140
Sample + 6% KCl	0.021
Sample + 8% KCl	0.018

Swelling Pressure Tests. The results of the controlled expansion tests, given in Table 4, show a decrease in swelling pressure as the dosage of potassium chloride increases. Moreover, this reduction is most noticeable from a concentration of 6% potassium chloride by weight.

5 Conclusions

This research has presented an analysis of the influence of potassium chloride on expansive parameters such as one-dimensional expansion and swelling pressure of a clay soil with a moderate content of the mineral montmorillonite. In this regard, based on the experimental results obtained, the main conclusions are the following:

- The one-dimensional swelling of the soil samples experienced a considerable decrease with the addition of potassium chloride, according to the indicated dosages, with percentages ranging between 86.62% and 92.02%.
- On the other hand, although to a lesser degree, the additive showed its effectiveness in reducing the swelling pressure with percentage points ranging between 85.31% and 87.41% for concentrations of 6% and 8%, respectively.
- The optimal concentration that guarantees a significant reduction of the expansive parameters is 6% potassium chloride by weight.

References

1. Jalal F, Xu Y, Jamhiri B, Memon SA (2020) On the recent trends in expansive soil stabilization using calcium-based stabilizer materials (CSMs): a comprehensive review. In: Advances in materials science and engineering
2. Barman D, Dash SK (2022) Stabilization of expansive soils using chemical additives: a review. J Rock Mech Geotechn Eng 14(4):1319–1342
3. Pan B, Yin X, Iglauer (2020) A review on clay wettability: From experimental investigations to molecular dynamics simulations. Adv Colloid Interface Sci 285:102266
4. Choo KY, Bai K (2016) The effect of the mineralogical composition of various bentonites on CEC values determined by three different analytical methods. Appl Clay Sci 126:153–159
5. Khalifa AZ, Cizer O, Pontikes Y, Heath A, Patureau P, Bernal SA, Marsh A (2020) Advances in alkali-activation of clay minerals. Cem Concr Res 132:106050

6. Han Z, Yang H, Bu M, He M. (2022) A molecular dynamics study on the structural and mechanical properties of pyrophyllite and M-Montmorillonites (M = Na, K, Ca, and Ba). Chem Phys Lett 803:139848
7. Zhang S, Wu Z, Chen J, Xu R, Wang M, Ni W (2022) Study on the hydration reaction of typical clay minerals under alkali and sulfate compound activation. Gels 8(9):564
8. Zamin B, Nasir H, Mehmood K, Iqbal Q, Farooq A, Tufail M (2021) An experimental study on the geotechnical, mineralogical, and swelling behavior of KPK expansive soils. In: Advances in civil engineering
9. Fondjo AA, Theron E, Ray R (2021) Stabilization of expansive soils using mechanical and chemical methods: a comprehensive review. Civ Eng Arch 9(5):1295–1308
10. Amakye SY, Abbey S (2021) Understanding the performance of expansive subgrade materials treated with non-traditional stabilisers: a review. Cleaner Eng Technol 4:100159
11. Han S, Wang B, Gutierrez M, Shan Y, Zhang Y (2021) Laboratory study on improvement of expansive soil by chemically induced calcium carbonate precipitation. Materials 14(12):3372
12. Noorzad R, Tanegonbadi B (2020) Volume change behavior of stabilized expansive clay with lignosulfonate. Sci Iranica 27(4):1762–1775
13. Soltani A, Taheri A, Khatibi M, Estabragh A (2017) Swelling potential of a stabilized expansive soil: a comparative experimental study. Geotech Geol Eng 35(4):1717–1744
14. Yi H, Jia F, Zhao Y, Wang W, Song S, Li H, Liu C (2018) Surface wettability of montmorillonite (0 0 1) surface as affected by surface charge and exchangeable cations: a molecular dynamic study. Appl Surf Sci 459:148–154
15. Peng J, Yi H, Song S, Zhan W, Zhao Y (2019) Driving force for the swelling of montmorillonite as affected by surface charge and exchangeable cations: a molecular dynamic study. Results Phys 12:113–117
16. Chen F (1975) Foundations on expansive soils. Elsevier Scientific Publishing Company
17. Seed H, Woodward R, Lundgren R (1962) Prediction of swelling potential for compacted clays. J Soil Mech Found Div 88:107–131

Comparison of Embodied Carbon on Residential Building Components Between House and Apartment Using BIM

Thanasak Phittayakorn, Chavanont Khosakitchalert, and Lapyote Prasitisopin

Abstract Climate change is currently an urgent issue globally. It is known that building sector generates a large amount of greenhouse gas emissions. Many scientists believe that embodied carbon from components in buildings influenced the embodied carbon of the whole building sector. This research study aims to use the life cycle assessment (LCA) as a tool for evaluating embodied carbon in building components, and BIM to generate the building material data. The building materials of two different building types including house and apartments are compared. The LCA of buildings is a complex task because of the complexity during the life cycle inventory and life cycle impact assessment phase for the quantity take-off materials stage. Therefore, an integration of LCA and BIM can help reduce the time consuming from evaluating embodied carbon during design. Results indicate that the conventional (CON) system is higher embodied carbon value than the precast (PCS) system. Additionally, the component of CON system generated embodied carbon the most is column and beam structure while, for the PCS system, the interior and exterior wall structure exhibits the highest value. The results offer information on embodied carbon value for designers concerning with design and building construction in the early stage.

Keywords Embodied carbon · Building component · Building material · Life cycle assessment · BIM

1 Introduction

Climate change is one of the most serious issues that we are facing nowadays. This issue negatively affects the environment and living creatures globally. Since, the energy and natural resources are much consumed for building construction projects,

T. Phittayakorn (✉) · C. Khosakitchalert · L. Prasitisopin
Faculty of Architecture, Chulalongkorn University, Pathumwan, Bangkok, Thailand
e-mail: 6471004925@student.chula.ac.th

T. Kang (ed.), *Proceedings of 5th International Conference on Civil Engineering and Architecture*, Lecture Notes in Civil Engineering 369,
https://doi.org/10.1007/978-981-99-4049-3_8

the building activity is one of main activities accounted for carbon emission through the atmosphere. The IPCC and Architecture, 2030 [1, 2] mentioned that the carbon emissions of the building sector generated greenhouse gas emission of up to 40% for the total greenhouse gas emission worldwide. To reduce carbon emission, many governments consent to international policies for mitigation of climate change such as zero-carbon emission building (ZEB) policy [3]. The international policies are important procedures to decrease carbon emissions from building construction. Although existing buildings are now much investigating to improve energy efficiency during operation, the reduction of embodied carbon requires a practice to achieve zero-carbon emissions through designing the building, selecting construction methods, and using low carbon materials [4, 5].

Life cycle assessment (LCA) is a typical tool to quantify carbon emission in various industries. The LCA concept entails the whole life cycle stages of building from the raw material extraction stage, manufacturing of building components, operational use, and transportation to the end-of-life or demolish stage [6, 7]. However, the LCA of buildings is a complex task because it consumes a great quantity of inputted information and processing time during the quantity take-off materials stage in life cycle inventory and life cycle impact assessment phases [8]. For these reasons, performing the LCA is not practical for defining environmental impact when material quantities of the buildings are not accurate.

The residential building for a low-income sector is generally built by the precast (PCS) method. While the conventional (CON) system is not a requirement for the massive demand at present, there are disadvantages such as an increase in time, wastage of materials, and the greater requirement of labor at the site [9]. Sherfudeen et al. [10] expected that 1.6 billion people are facing inadequate housing by 2025, and many developing countries require huge housing demand of more than 60 million housing units. Thus, residential building has continuously influenced the environmental impact of the building sector. The embodied carbon of building components and construction systems should be analyzed before building any construction [11].

To analyze the embodied carbon of the buildings, this study proposes the research program quantify the embodied carbon of building material and components using BIM because these are the main details of the whole building for building design in the early stage. Besides, the results of embodied carbon of different building materials and components are then compared. Designers can better elaborate the embodied carbon during the early design stage such as selecting the construction process, material, structure, and building system. This research can offer design guidelines for using BIM to evaluate the building of environmental perspective.

2 Method

The research method in this study consists of five steps entailing: (1) creating a model in the Revit program, (2) taking off quantities of materials from each component, (3) inputting the LCA database to MS Excel, (4) calculating the number of embodied carbons, and (5) interpreting the environmental impact in each building component.

2.1 Create BIM Models in Autodesk Revit

First, the BIM process was performed by Autodesk Revit 2022 throughout the study. The BIM software has a building material database in the library. The building material database is associated with the building's geometry, allowing it to extract from each building component. Each component contains surface area, volume, and material information. Therefore, the building model was created for two building types (two-floor house and two-floor apartment) because these buildings were single and multi-family residential designs to determine the area for reducing embodied carbon. This study would provide the better understanding of the existing level of embodied carbon and explore strategies to reduce the total carbon of residential buildings. The two-floor house and two-floor apartment models are shown in Figs. 1 and 2.

Fig. 1 Two-floor house with total service area of 46.42 m^2

Fig. 2 Two-floor apartment with total service area of 2226.10 m^2

2.2 Take-Off Material Quantities in Each Component

After creating the models of two different buildings, the BIM software was then used to extract the area or volume of each building component. Note that windows and doors were excluded since they are not the main structural components. The areas or volumes are immediately converted into BoQ.

Table 1 shows the notations of the relevant parameters conducted in this study. The parameters assessed include construction system, building components, and building material. The construction systems determined entail CON and PCS methods. The next column is the building components consisting of ten building components (i.e., exterior wall (EX), interior wall (INT), floor (FLR), column (COL), beam (BEM), footing (FOT), footing column (FCL), roof (RF), super-structure (STR), and sub-structure (SUB)). For the last column (building material), seven parameters assessed entail brick (BRI), autoclaved aerated concrete (AAC), cement board (CEB), gypsum (GYP), in situ concrete I, rebar (REB), and cold-rolled steel (CS).

Table 2 shows the summary of the quantities of the material take-off for each individual component of building material. The data were extracted from BIM material quantity take-off. The apartment designed has 24 rooms for each floor, and the house has three rooms for each floor. Then, these material take-off databases were transferred to the MS Excel software for quantifying the embodied carbon.

Table 1 Notation of relevant parameters

Construction system	Building component	Building material
Conventional (CON)	Exterior wall (EX)	Brick (BRI)
Precast (PCS)	Interior wall (INT)	Autoclaved aerated concrete (AAC)
	Floor (FLR)	Cement board (CEB)
	Column (COL)	Gypsum board (GYP)
	Beam (BEM) Footing (FOT)	In situ concrete (CON) Rebar (REB)
	Footing column (FCL)	Cold-rolled steel (CS)
	Roof (RF)	
	Super-structure (STR)	
	Sub-structure (SUB)	

Table 2 Summary of quantity of the material take-off for individual components of building structure

Building component	Building material	Unit	Quantity of material take-off	
			Two-floor house	Two-floor apartment
INT	BRI, AAC, GYP, PCS	m^2	20.2	3548.9
EX	BRI, AAC, CEB, PCS	m^2	88.4	623.7
FLR	C, PCS	m^2	46.4	2626.1
	REB	kg	366.8	1396.4
BEM	C, PCS	m^3	1.0	43.8
	REB	kg	333.7	2746.4
COL	C	m^3	40.6	162.1
	REB	kg	539.2	9734.1
FOT	C	m^3	3.6	40.5
	REB	kg	294.5	294.5
FCL	C	m^3	0.3	14.4
	REB	kg	124.4	124.4
RF	CS	kg	810.5	24,326.4

2.3 Input Database and Calculate Embodied Carbon

This study uses the LCA database from the inventory of carbon and energy (ICE). The database was summarized and given in Table 3. The ICE provides the generic embodied carbon data for widely adopted conventional building materials for product/manufacturing stage. It is reported that this stage entails the raw material extraction, transport, and manufacturing phase. The quantities of each material are multiplied with the LCA factors from the ICE database.

2.4 Calculating Embodied Carbon

The embodied carbon is normally calculated by multiplying the BoQ with the respective life cycle inventory data. In the presented approach, the mass of each material (M_j) is multiplied by the specific impact factor of the material (IF $= _{E,j}$) [12]. To define the whole building, each component of building was multiplied with the volume or area of a specific material. Next, the embodied carbon impact (I_E) of all components was calculated to maintain the I_E of the completed whole building (as given in Eq. (1))

$$I_E = \sum_j \left(M_j \times \mathrm{IF}_{E,j}\right) \tag{1}$$

Table 3 Databases used in embodied carbon

Building component	Building material	Unit	Embodied carbon (kg CO_2 eq/ unit)
EX + INT	BRI	m^2	40.5
	AAC	m^2	20.0
	CEB	m^2	0.4
	GYP	m^2	0.1
	PCS	m^2	37.15
	Plastering layer (EX + INT)	m^2	0.2
	Paint layer for EX	m^2	0.9
	Paint layer for INT	m^2	2.9
FLR	C	m^2	24.88
	PCS	m^2	55.9
	REB	kg	2.0
BEM	C	m^3	248.8
	REB	kg	2.0
COL	C	cu. m	248.8
	REB	kg	2.0
FOT	C	m^3	327.4
	REB	kg	2.0
FCL	C	m^3	327.4
	REB	kg	2.0
RF	CS	kg	2.7

where I_E is the embodied carbon impact; M_j is the amount of specific material; and $IF_{E,j}$ is the impact factor.

2.5 Interpretation

After completing the calculation in MS Excel, the results were visualized. The building construction systems mainly entails two systems (CON and PCS). Each system having different EX, INT, STR, SUB, and RF as notated in Table 4. The total of eight systems of the CON1 to CON4 and the PCS 1 to PCS4 were evaluated the effects of building components.

Table 4 Notation of building construction systems

Notation	Construction system	EX	INT	FLR	STR	SUB	RF
CON1	CON	BRI	BRI	C	C	C	CS
CON2		BRI	AAC		REB	REB	
CON3		AAC	AAC				
CON4		CEB	GYB				
PCS1	PCS	PCS	PCS	PCS	PCS	C	CS
PCS2		PCS	BRI		REB	REB	
PCS3		PCS	AAC				
PCS4		PCS	GYB				

3 Result

The results and analyses of embodied carbon for different building component and types calculated using LCA and BIM are shown in Figs. 3, 4 and 5. The plots indicate that the embodied carbon, the average value, and the percentage in different five components consisting of INT + EX, FLR, COL + BEM (STR), FOT + FCL (SUB), and CS (RF).

3.1 Embodied Carbon of Two-Floor House and Apartment

The influences of different building materials of two-floor house and two-floor apartment on embodied carbon are shown in Fig. 3a, b. Results indicate that for the CON systems, the CON1 system consumes embodied carbon larger than the CON2, CON3, and CON4 systems, respectively. The CON1 system exhibited the largest embodied carbon among the CON systems, whereas the CON4 system exhibited the smallest value. Meaningly, for the CON1 system generates more embodied carbon to the atmosphere. Furthermore, for the PCS1 to PCS4 systems, the embodied carbon of the PCS2 system is higher than those of the PCS1, PCS2, and PCS4 systems, respectively. The PCS2 system exhibited the highest embodied carbon among the PCS system, while the PCS4 exhibited the lowest embodied carbon. It is seen that most cases of PCS systems produce less embodied carbon than the CON systems by about 10%.

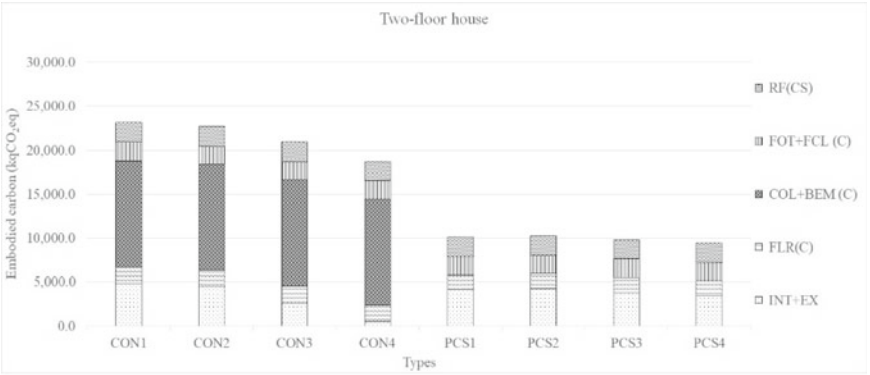

(a) Embodied carbon of different building materials of two-floor house

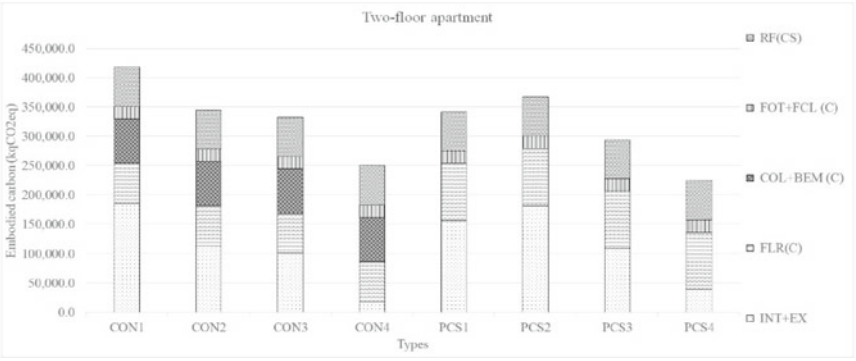

(b) Embodied carbon of different building materials of two-floor apartment

Fig. 3 Embodied carbon of different building material in build type: **a** two-floor house, **b** two-floor apartment

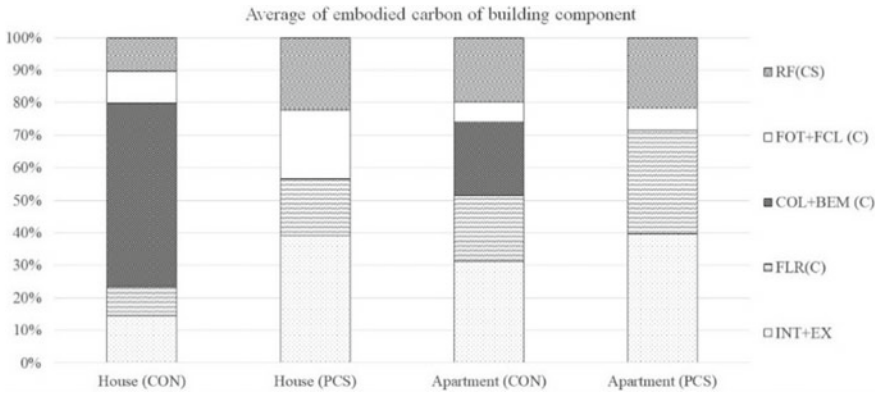

Fig. 4 Average embodied carbon per usable area of house and apartment for the CON and PCS systems

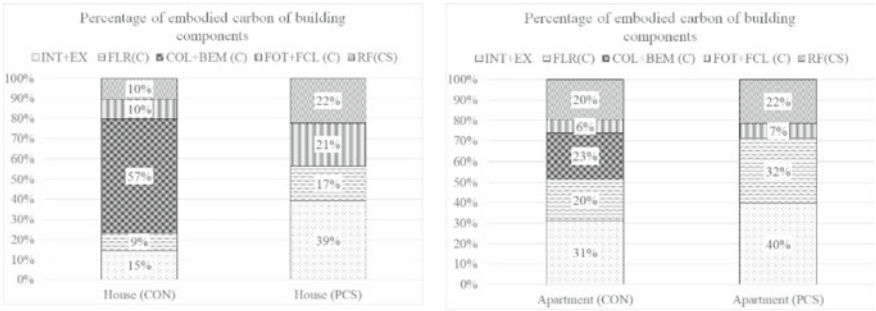

a) House b) Apartment

Fig. 5 Percentage of embodied carbon of the two-floor house and two-floor apartment for: **a** CON system, **b** PCS system

3.2 Average Embodied Carbon of Building Component and Type

Figure 4 exhibits the plot of the average values of embodied carbon in different building components and types. Results indicate that for the average embodied carbon of CON systems for two-floor house, the COL + BEM component is larger than the INT + EX, RF, FOT + FCL, and FLR components, respectively. The COL + BIM component exhibited the largest embodied carbon of CON system, whereas the FLR component exhibited the smallest value. Meaningly, for the building component of CON systems for house, the COL + BEM component can generate higher embodied carbon to the atmosphere. Furthermore, for the PCS system, the average embodied carbon of the INT + EX component exhibited higher than those of the FLR, RF, and FOT + FCL components, respectively. The INT + EX component is the main component generating the highest embodied carbon for two-floor house built by PCS method.

Nevertheless, for the CON system of two-floor apartment, the embodied carbon of the COL + BEM component is larger than the INT + EX, FLR, RF, and FOT + FCL components, respectively. The COL + BEM component exhibited the greatest embodied carbon among the CON systems for two-floor apartment. On the other hand, the FOT + FCL component exhibited the smallest embodied carbon value. Besides, for the PCS system of two-floor apartment, the INT + EX component has the embodied carbon more than the ones of the FLR, RF, and FOT + FCL components, respectively. The COL + BEM component exhibited the largest embodied carbon value among the CON system for two-floor apartment, whereas the FOT + FCL component exhibited the smallest value.

3.3 *Analysis of Percentage Component of House and Apartment with Different Building Materials*

In this section, the analysis of the percentage of embodied carbon of building components with the house and apartment building was determined. Figure 5a, b show the influences of the percentages of building components with the CON and the PCS systems, respectively. In Fig. 5a, results for the two-floor house of the CON system indicate that the component that generates the highest embodied carbon is the COL + BEM component. In contrast, the results for the PCS system indicate that the INT + EX component is the highest embodied carbon. When comparing the component generating the embodied carbon for the system, the results indicate that the percentage of the COL + BEM component for the two-floor house is 12% higher than the INT + EX component for the PCS system. Furthermore, the results in Fig. 5b exhibited that for the two-floor apartment, the highest embodied carbon values are the INT + EX component for both systems. Comparing the highest embodied carbon values shows that the percentage of the INT + EX component for the CON system is less than 9% compared to the PCS system.

4 Conclusion

This study determined the embodied carbon of building components between the two-floor house and apartment component using integrating LCA and BIM. Results can be concluded that the amount of embodied carbon of the CON system was higher than the PCS system. Moreover, the COL + BEM component of the CON systems showed the highest proportion in embodied carbon, while the FLR component showed the lowest proportion. In contrast, for the PCS system, the INT + EX component was the largest proportion, whereas the FOT + FCL components showed the smallest. Finally, when comparing the highest embodied carbon of components for construction systems, the COL + BEM component of the two-floor house was greater than the INT + EX component for the PCS system. However, the INT + EX component of the two-floor apartment for the CON system was lower than the two-floor apartment in the PCS system.

When designing the buildings, the outcomes from this study offer awareness about the embodied carbon of COL + BEM component for CON system and the INT + EX component for the PCS systems. Different construction methods and components for building types are likely to affect the embodied carbon significantly. The ongoing works are determining the cost and energy aspects from different buildings.

References

1. Grubert E, Stokes-Draut J (2020) Mitigation life cycle assessment: best practices from LCA of energy and water infrastructure that incurs impacts to mitigate harm. Energies (Basel) 13:992
2. Lewis E, Chamel O, Mohsenin M, Ots E, White ET (2018) Architecture 2030. In: Sustainaspeak, pp 24–26
3. Ohene E, Chan APC, Darko A (2022) Energy & buildings review of global research advances towards net-zero emissions buildings. Energy Build 266:112142
4. Victoria M, Perera S, Davies A (2015) Developing an early design stage embodied carbon prediction model: a case study, pp 267–276. https://rgu-repository.worktribe.com/output/246993/developing-an-early-design-stage-embodied-carbon-prediction-model-a-case-study. Accessed 5 Dec 2021
5. Miller D, Doh JH, Mulvey M (2015) Concrete slab comparison and embodied energy optimization for alternate design and construction techniques. Constr Build Mater 80:329–338
6. ISO (2006) Environmental management—life cycle assessment principles and framework (ISO 14040:2006). https://www.iso.org/standard/37456.html. Accessed 15 Feb 2022
7. Sereewatthanawut I, Prasittisopin L (2020) Environmental evaluation of pavement system incorporating recycled concrete aggregate. Int J Pavement Res Technol 13:455–465
8. Lasvaux S, Gantner J, Schiopu N, Nibel S, Bazzana M, Bosdevigie B, Sibiude G (2013)Towards a new generation of building LCA tools adapted to the building design process and to the user needs? In: Sustainable building, pp 406–417
9. Nanyam VN, Basu R, Sawhney A, Vikram H, Lodha G (2017) Implementation of precast technology in India-opportunities and challenges. In: Procedia engineering. Elsevier Ltd, pp 144–151
10. Sherfudeen AP, Kumar N, Raghavan N, Pillai RG, Kalidindi SN (2016) Promoting precast concrete for affordable housing—An overview on promotional policies worldwide and challenges and possibilities in India. Indian Concr J 90:13–24
11. Hollberg A, Ruth J (2016) LCA in architectural design—a parametric approach. Int J Life Cycle Assess 21:943–960
12. Díaz J, Antön LA (2014) Sustainable construction approach through integration of LCA and BIM tools. In: Computing in civil and building engineering—Proceedings of the 2014 international conference on computing in civil and building engineering, pp 283–290

The Use of Waste Concrete as a Filter for Separating Water-In-Oil Emulsions

Bao Wang, Shaotong Feng, Zhaoxin Li, Lei Chen, and Caihua Wang

Abstract The damage of construction waste on the environment and the resource utilization of the waste have become urgent problems to be solved. Traditional disposal techniques have a number of limitations, and hence, a need for efficient technique remains a worldwide challenge. Herein, based on the incredible attraction between concrete materials and water, we present the application of concrete waste particles layer for efficient separation of water-in-oil emulsions. In this study, surfactant stabilized water-in-oil emulsions have been successfully filtered by using only concrete waste particles as a filter. The results reveal that this technique efficiently implements the separation of water-in-oil emulsion, due to the great adsorption capability of concrete waste with water even concrete waste was in the state of oil wetted. Furthermore, the filtration process does not produce any harmful products. Overall, the application of absorbent concrete waste proposed in this study could be considered as a promising candidate for recycling of concrete waste and separating water-in-oil emulsions.

Keywords Concrete waste · Water-in-oil emulsion · De-emulsification · Particle filter · Wettability

B. Wang · S. Feng · C. Wang (✉)
School of Mechanical Science and Engineering, Northeast Petroleum University, Daqing, China
e-mail: wch.dqsy@163.com

B. Wang
e-mail: wb09@tsinghua.org.cn

S. Feng
e-mail: fengshaotong0513@163.com

Z. Li · L. Chen (✉)
State Key Laboratory of Tribology, Tsinghua University, Beijing, China
e-mail: leichen16@mail.tsinghua.edu.cn

Z. Li
e-mail: lizhaoxi16@mails.tsinghua.edu.cn

T. Kang (ed.), *Proceedings of 5th International Conference on Civil Engineering and Architecture*, Lecture Notes in Civil Engineering 369,
https://doi.org/10.1007/978-981-99-4049-3_9

1 Introduction

With the pace of urban construction, the increasing construction debris not only pollute the environment but also waste resources. Most of solid waste was generated in the building industry [1]. The cement performance and durability of concrete have a close relationship with the useful life of the building to some degree [2]. When the building achieves the required design working life, adequate measures should be taken to protect each structural element against the relevant environmental action [3–5]. Generally, the design life of general buildings in China is 50–100 years, they should be scrapped and rebuilt when reach retirement life [6]. Whether repairs or rebuilds, significant amounts of solid waste at the end of the process are often a tricky problem [7, 8]. Previously, due to lack of proper regulations on the disposal of solid wastes, rampant disposal was common [9, 10]. With the reinforcement of environmental awareness, the damage of construction waste on the environment and the resource utilization of the waste have become an urgent problem to be solved [11]. At present, land filling is one of the most economical and efficient ways to treat municipal construction waste [12]. However, limited landfill space and the goal of achieving a circular economy dictate the search for efficient usage of construction waste. Therefore, the comprehensive utilization has already drawn much attention [13]. Recycling of wasted building materials has practical application value in waste disposal, which means activities undertaken to extract substances from solid waste for use as raw materials or others [14]. Recycling raw materials from the ceramic industry or cement industry can provide long-term benefits for resource optimization [15, 16]. Most of the construction waste for solid wastes, general is in construction process or old buildings maintenance, dismantling produces. These construction waste might be of value as potential reusable building materials due to their chemical and mineralogical composition [17, 18]. It is feasible to substitute the coarse aggregate concrete by waste concrete aggregate. Therefore, the study on construction waste for reclaimed concrete prepared with waste concrete broken instead of rough aggregate is carried out [19].

Furthermore, the construction waste has been tried to be used in other ways. Previous studies have shown that superhydrophobic-oleophilic quartz sand filter has a good demulsification effect [20]. In addition to the surface modified quartz sand particles, the salt particle filter with super hydrophilicity under oil also has good demulsification effect [21]. Considering the similar major ingredient of the concrete waste and SiO_2, maybe it can achieve separating water-in-oil emulsions. Recent studies have shown that after immersing the metal wire mesh in cement, the wettability of the metal wire mesh surface can be changed to separate oil and water [22]. Both of the recycling of concrete waste and separation of oil–water were of great significance in the field of environmental protection [23]. Due to the rapid development of chemical and petroleum industries, a large number of oil–water mixtures are directly discharged into soil, rivers and oceans as wastes every day, causing environmental pollution and threatening human beings and marine life [24, 25]. Oil–water separation is the subject of theoretical and practical research around the world

because of the frequency with which oil spills occur and the increasing amounts of oily industrial wastewater that are produced [26, 27]. Therefore, it is imperative to achieve efficient, fast and low-cost separation of water-in-oil mixture.

In this research, recycled concrete waste were proposed to efficiently separate oil-in-water emulsion, which were considered together as two crunches in the field of environmental protection, wasted building materials and wasted water-in-oil emulsions.

2 Experimental Materials

In this study, all required materials were of commercial standard and utilized without any further purification. The surfactant Span 80 were purchased from Meryer (Shanghai) Chemical Technology Co., Ltd., and utilized in the original form to produce surfactant stabilized water-in-oil emulsion. The n-decane, petroleum ether, n-tetradecane and dimethicone were used as oil compounds in this study and were purchased from Meryer (Shanghai) Chemical Technology Co., Ltd. All the aqueous solutions produced in this study were made with deionized water.

2.1 Preparation of Water-In-Oil Filtration Concreted Waste Bed

The concrete waste was utilized to produce a water-in-oil filtration bed that acts as an adsorbent. As a common building material, concrete is a mixture of sand and cement. The cement was purchased from Qinhuangdao Asano Cement Co. LTD, with the type of P.O42.5(R), and apparent density of 3030 $kg{\cdot}m^{-3}$. The sand is natural river sand from Qinhuangdao Funding, with a maximum particle size 5 mm, and an apparent density of 2580 $kg{\cdot}m^{-3}$. Additionally, limestone rubble with a particle size ranging from 5 to 15 mm, and an apparent density of 2730 $kg{\cdot}m^{-3}$ was used as framework material. The concrete was made by mixing aforementioned three materials and water, with the mass ratio of cement: sand: water: framework material was 1.56: 4.02: 1: 6.56. The fully cured concrete block was tested for strength and brittleness, and thus the tested concrete waste was obtained. The concrete waste is crushed by a pulverizer and then screened by a metal screen to obtain filter materials of different particle sizes. The recycled concrete particles were screened by 80, 160 and 300 mesh sieves to obtain different sizes materials.

2.2 Water-In-Oil Emulsions Separation Experiment

The separation performance of the as-prepared concrete waste absorbent filtration bed is analyzed by using surfactant-stabilized water-in-oil emulsions. To prepare a water-in-oil emulsion, 1 g of ultrapure water was added to 99 g of n-decane, and then, 50 μl of Span 80 was added to the solution. The prepared solution was ultrasonically stirred for 30 min to form a surfactant-stabilized water-in-oil emulsion.

The schematic diagram of the experimental device for the water-in-oil emulsion separation experiment is shown in Fig. 1. A glass micro-sand core filter was used as the experimental device. Place the glass filter cup containing the concrete waste filter material on the open end of the conical receiving bottle, connect it with a single joint, and fix it with a ball mill clamp. A vacuum pump is connected to the conical receiving flask to generate negative pressure to achieve suction filtration of the water-in-oil emulsion. Pour the emulsion into the open end of the glass filter cup and collect the filtrate at the bottom of the conical receiving flask. The concrete waste filter materials of different thicknesses were prepared and placed in the glass filter cup to observe the influence of the thickness of the filter materials.

Basically, the water-in-oil emulsions separation experiment conducted with two physical conditions. In one case, the filtration process has been analyzed with the absence of negative pressure or under the effect of gravity. In the other case, a negative pressure is introduced into the experimental equipment to realize suction filtration. The suction filtration is realized by connecting the conical receiving bottle with a vacuum pump to produces a negative pressure of 0.06 MPa. When the conical

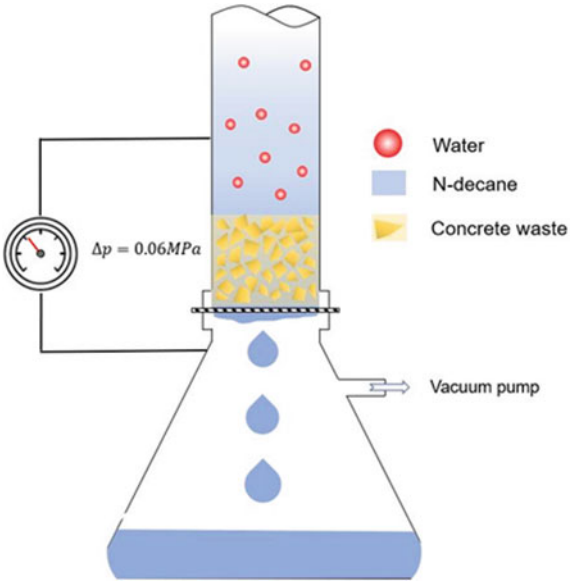

Fig. 1 A figure caption is always placed below the illustration. Short captions are centered, while long ones are justified. The macro button chooses the correct format automatically

receiving bottle is not connected with a vacuum pump, the emulsion can only be filtered under the sole effect of gravity.

2.3 Characterization

The surface morphology of concrete waste after crushing was observed by field emission scanning electron microscope (Sigma 300, Carl Zeiss AG, Germany). The contact angle of liquid was measured by contact angle meter (JC2000DSM, Beijing Zhongyi Kexin Technology Corp. LTD., China) with 2 μl water droplets at room temperature. The amount of water collected by the concrete waste filter bed is measured by a high-speed camera system (AcuEye, RockeTech Technology Corp. Ltd., China). The size of water droplets in oil-in-water emulsion was measured by optical microscope (DM2700M, Leica Microsystems Corp. LTD., Germany), and the surface state of oil-immersed sand was observed when it fell into water. In addition, the moisture in the filtrate was measured by Karl Fischer micromoisture meter (TP553, Time Power Measure and Control Equipment Corp. LTD., China).

3 Results and Discussion

The SEM images of filter bed, which is obtained by crushing concrete waste, is shown in Fig. 2. The shape of the crushed concrete waste is irregular small particles with a wide particle size distribution range, the average particle size of concrete waste is from 50 to 300 μm. In order to analyze the mechanism and characteristics of the size effect, metal sieves with different apertures were used to screen concrete particles with different sizes as experimental samples. The average particle size of concrete particles before screening is 300 μm, as shown in Fig. 2a, the average particle size of large particles in the experimental sample is 50 μm, and the diameter of small particles can reach several microns, as shown in Fig. 2b.

The wettability analysis of the concrete waste filtration bed was conducted by putting 2.2 g of concrete waste with 5 mm height inside a rectangular glass box that is settled ultrasonically. The experiment was conducted in environments of air, oil and water. The wettability of water on the concrete waste surface in air environment is present in Fig. 3a, which shows that water droplet is adsorbed quickly and effectively by the concrete waste layer. Meanwhile, the wettability of oil on the concrete waste in environments of air and water is also realized and presented in Fig. 3b, c. The results show that the oil droplet can spread over the concrete waste layer surface in air but it maintained a high contact angle in water environment because wet concrete waste repels the droplet and no adsorption is observed. In Fig. 3d, water droplet is adsorbed quickly and effectively by the concrete waste layer in oil environment. These results give an insight into how the concrete waste bed can be effectively used as an adsorbent for water-in-oil emulsions. These time-lapse images further confirm

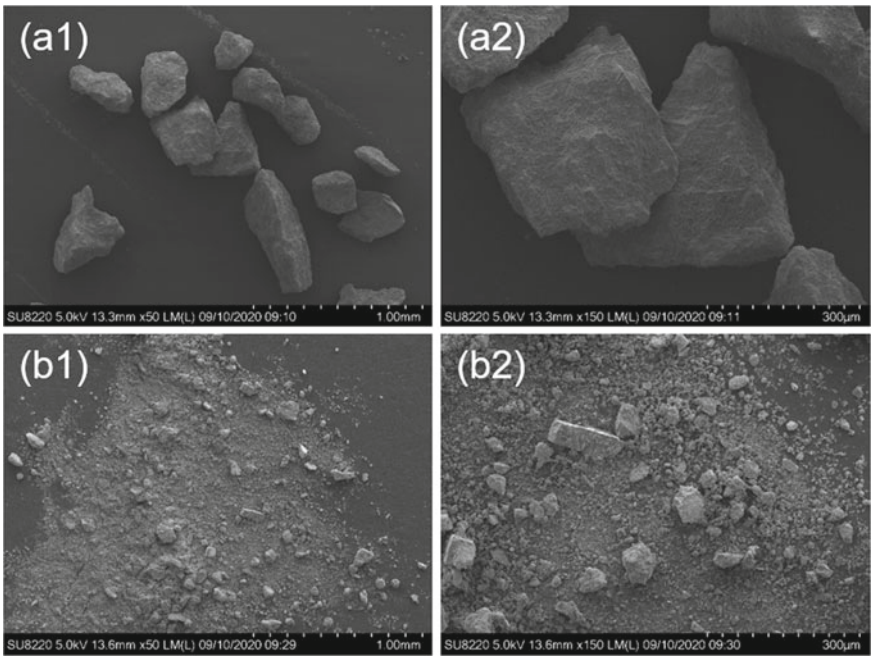

Fig. 2 SEM image of wasted building material (concrete waste). The crushed concrete waste was screened to obtain **a** samples with an average particle size of 300 μm, and **b** samples with an average particle size of 50 μm or less

that concrete waste has a high adsorption capacity of water–in-oil environment that indicates the suitability of the proposed method for water-in-oil filtration application.

The microscope and optical images of emulsions before and after filtration were captured by using an inverted microscope, as shown in Fig. 4. It can be seen clearly that all the water-in-oil emulsions are visually turbid. The microscopic images shown in Fig. 4a reveals that surfactant-stabilized emulsions contain micron-sized emulsified droplets, which demonstrate that the surfactant could further enhance the emulsification of water-in-oil. In addition, all collected filtrate samples were visually transparent and microscopic images revealed that filtrate oil is water-free. The results indicate that the efficient separation of surfactant-stabilized water-in-oil emulsions is realized by the proposed method.

In order to analyze the effectivity of the as-prepared water-in-oil filtration system, the experiment is conducted in two distinct conditions, the results are shown in Fig. 5. The water-in-oil emulsion filtration process is realized with the presence of negative pressure and the experiment is repeated with the absence of the negative pressure (under gravity). The results show that after filtration, the water content are around 60 ppm for both of these two filtration mode, and the calculated the separation efficiency is around 99.4%. Furthermore, the flux calculation for both methods is calculated and plotted in Fig. 5c. The thickness of the concrete waste filtration

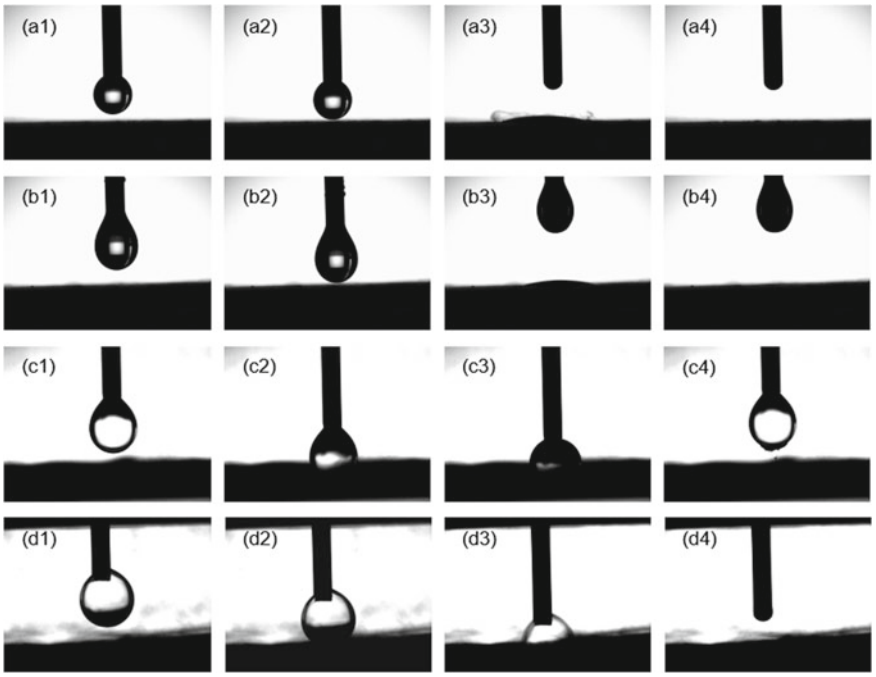

Fig. 3 The wettability analysis of the wasted building material (concrete waste): **a**, **b** water and oil droplets in air, **c** oil droplets in water, and **d** water droplets in oil

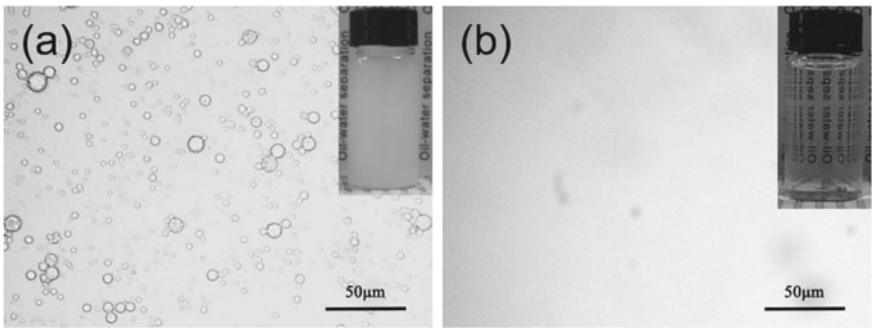

Fig. 4 The microscopic and optical images of surfactant-stabilized water-in-oil emulsions: **a** before separation, and **b** filtered under 0.06 MPa negative pressure condition

bed used in this case was equal to 10 mm. In the case of suction filtration, when the treatment capacity was less than 16 ml, the change in flux was significant. However, when the flow is further increased, the flux remained the same until the total treatment capacity reached 18 ml. Moreover, the flux of gravity-driven filtration process remained constant throughout the filtration process from 0 to 18 ml. Therefore, it

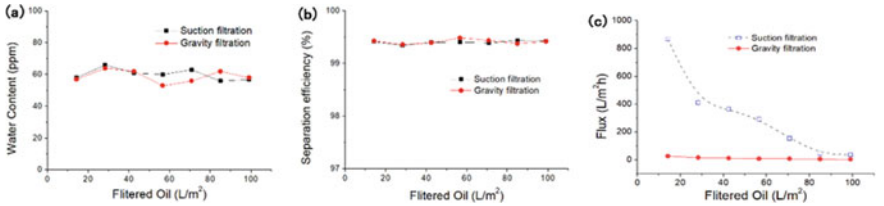

Fig. 5 Comparison between suction filtration and filtration by gravity. **a** Water content after filtration, **b** Separation efficiency after filtration, and **c** flux the separation of water-in-oil emulsions under 10 mm thickness of the concrete waste bed

can be concluded that when concrete waste particles are used as fillers for oil–water separation and filtration, they can achieve high-efficiency due to the adsorption of emulsified water droplets. Moreover, it is observed that the top layer of concrete crystal particles preferentially achieve adsorption.

The experimental results shown in Fig. 6a show that the thickness of concrete waste sand layer has a significant effect on the initial filtration flow rate, up to 1400 L/m^2h, but does not change the total amount of effective filtration emulsion at a single time. This may be because the thickness of the sand layer will affect the initial infiltration rate of the emulsion, but with the increase of filtration volume, the increasing resistance will become the key to affect the flow rate. Therefore, different sand layer thickness will not significantly change the total amount of filtered emulsion. On the other hand, as shown in Fig. 6b, c, the demulsification efficiency increases with the increase of the thickness of the sand layer. When the thickness of the sand layer reaches 20 mm, the demulsification efficiency can reach up to 99.5%, and the corresponding filtered liquid water content is about 50 ppm. In contrast, when the thickness of the sand layer is less than 5 mm, the filtration effect may be unstable, but the lowest filtration efficiency in the experiment is still more than 97%. As shown in Fig. 6d, the concrete waste layer could separate surfactant-stabilized water-in-oil emulsions with separation efficiency up to 99.7% and water content infiltrates less than 80 ppm. Besides, the filtration flux for surfactant-stabilized water-in-decane, water-in-N-tetradecane, and water-in-petroleum ether emulsions are different, which indicated the concrete waste sand layer possess a superior separation ability for various water-in-oil emulsions. The different filtration flux for different emulsions is attributed to their different viscosity.

The recycling stability of the concrete waste filter was evaluated and the results are shown in Fig. 7. Surfactant-stabilized water-in-diesel and concrete waste filters with a height of 20 mm were used for recycling tests. After each separation test, the concrete waste filter was ultrasonically cleaned with ethanol and dried at 100 °C and directly used for the next cycle. As shown in Fig. 7, the filtration flux of concrete waste filter maintained higher than 800 $L{\cdot}m^{-2}{\cdot}h^{-1}$ even after four times of usage, which indicated that the concrete waste filter exhibits outstanding recycling stability. the concrete waste filer maintained separation efficiency higher than 99.3% and water content in the collected diesel less than 100 ppm after four times of separation tests.

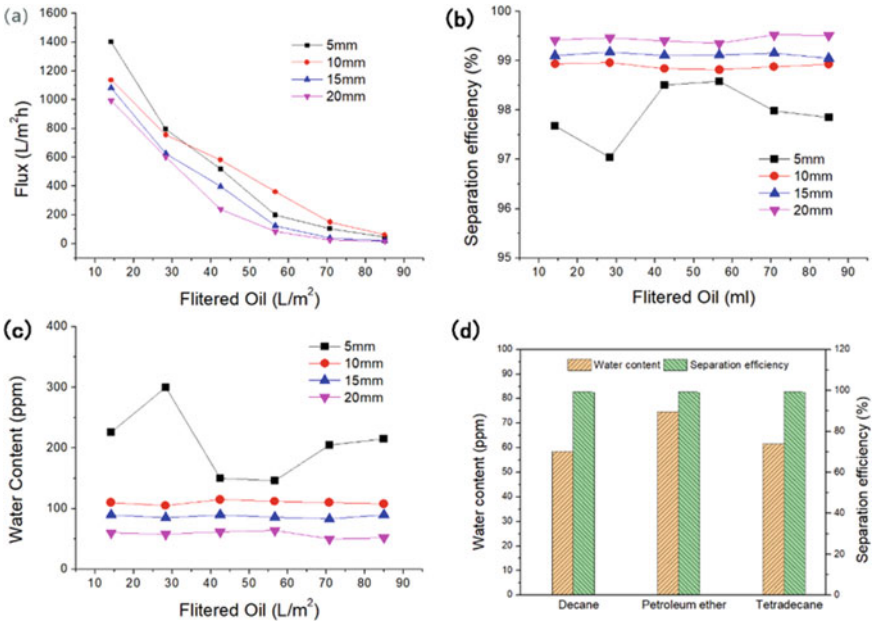

Fig. 6 The influence of particle filter thickness on **a** filtration flow rate, **b** separation efficiency, and **c** water content. **d** The influence of different types of oil emulsions on the demulsification of waste concrete sand layer

Additionally, for common materials, for example metal or wood, when the surface was wetted by oil (or water), the adsorbed oil (or water) was hard to erase in the absence of external forces. Nevertheless, as a special wetting material, the nature sand has a better affinity for water, even the oil wetted sand enters into water, the oil film adsorbed to the surface was replaced by water. SiO_2 is the major ingredient of sand in concrete waste, which has hydrophilic and oil-repellent properties and is used for adsorbing water droplets in oil. Because of the resemble component, the concrete waste has similar characteristics with sand, as shown in Fig. 8, there were only scattered water droplet on the sand surface after the oil wetted sand drop into water. This material covered completely with n-decane or dimethicone drop into water, the vast majority of surface was rapidly displaced by water. While the water immersed ordinary material could sustain the stable oil film. Based on this hydrophilicity, this material was proposed to adsorb water droplet in water-in-oil emulsion.

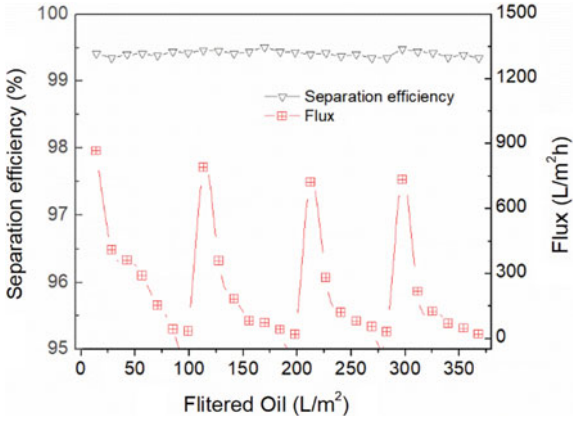

Fig. 7 Relationship between the Flux and separation efficiency in the filtrate and number of cycles

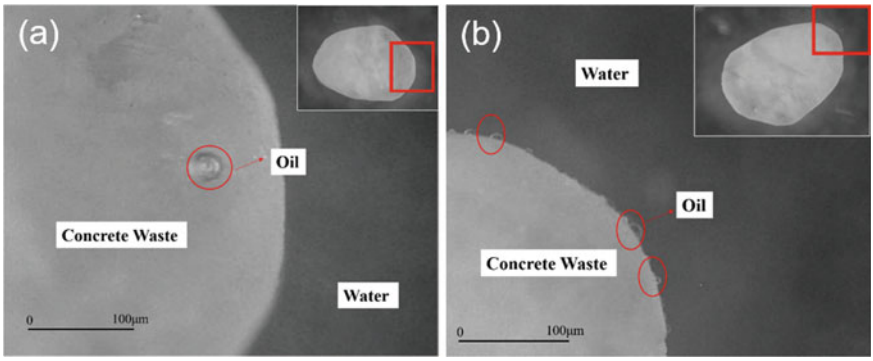

Fig. 8 Surface state when the oil-wetted sand drop in water. The type of oil used for wetting **a** n-decane, and **b** dimethicone

4 Conclusion

In this study, a specific concrete waste particle filtration scheme to achieve oil–water separation was proposed. After the concrete waste crushed into small particles, it is observed that it has the characteristics of hydrophilicity in oil, which can realize the effective demulsification of the water-in-oil emulsion, and the demulsification efficiency can reach up to 99.4%. After a cycle of filtration, the concrete waste sand is washed and dried to restore the demulsification efficiency.

The results show that the filtration flux decreases with the increase of the thickness of the filter layer. The filtration efficiency increases as the thickness of the filter layer increases, and is also affected by the type of oil in the emulsion. The particle size of concrete waste sand has an effect on the initial flow rate of filtration, but has no significant effect on the total amount of filtration. In order to reduce the environmental pollution caused by building waste, we would need a mechanism to

properly handle the concrete waste. The related approaches take additional resources and may not be suitable for energy and greenhouse reductions. Here, the grinding concrete waste was considered as a filtering material, which realizes utilization of trash. The concrete waste layer proposed by this study is a processing candidate for separating water-in-oil emulsion in a practical industry.

Acknowledgements This work was financially supported by the National Key R&D Program (Grant no. 2019YFC1907602), and the Northeast Petroleum University Youth Science Foundation of China (Grant No. 15071120619), and Tribology Science Fund of State Key Laboratory of Tribology (No. SKLTKF19B05).

Data Availability Statement
Some or all data, models, or code that support the findings of this study are available from the corresponding author upon reasonable request.

References

1. Guo Z, Tu A, Chen C (2018) Mechanical properties, durability, and life-cycle assessment of concrete building blocks incorporating recycled concrete aggregates. J Clean Prod 199:136–149
2. Bhushan B (2007) Nanotribology and nanomechanics of MEMS/NEMS and BioMEMS/BioNEMS materials and devices. Microelectron Eng 84:387–412
3. Volchatova IV, Statsenko YY (2019) The possibility of secondary use of building materials in the framework of the residential buildings renovation program. IOP Conf Ser Earth Environ Sci 229:012026
4. Cao Z, Liu G, Duan H (2019) Unravelling the mystery of Chinese building lifetime: a calibration and verification based on dynamic material flow analysis. Appl Energy 238:442–452
5. Ali TH, Akhund MA, Memon NA (2019) Application of artificial intelligence in construction waste management. In: 2019 8th International conference on industrial technology and management (ICITM), pp 50–55
6. Formoso Carlos T, Soibelman L, De Cesare C (2002) Material waste in building industry: main causes and prevention. J Constr Eng Manag 128:316–325
7. Silva RV, De Brito J, Dhir RK (2014) Properties and composition of recycled aggregates from construction and demolition waste suitable for concrete production. Constr Build Mater 65:201–217
8. Xu Y, Chen W, Jin R (2018) Experimental investigation of photocatalytic effects of concrete in air purification adopting entire concrete waste reuse model. J Hazard Mater 353:421–430
9. Seror N, Portnov BA (2018) Identifying areas under potential risk of illegal construction and demolition waste dumping using GIS tools. Waste Manage 75:22–29
10. Vishwakarma V, Ramachandran D (2018) Green concrete mix using solid waste and nanoparticles as alternatives—a review. Constr Build Mater 162:96–103
11. Nachalida Y, Beverley C, Kirstin R (2018) Solid waste management solutions for a rapidly urbanizing area in Thailand: recommendations based on stakeholder input. Int J Environ Res Public Health 15:1302
12. Hussain A, Malik MY, Khan M, Salahuddin T (2019) Application of generalized Fourier heat conduction law on MHD viscoinelastic fluid flow over stretching surface. Int J Numer Meth Heat Fluid Flow 30(6):3481–3496
13. Bizcocho N, Llatas C (2019) Inclusion of prevention scenarios in LCA of construction waste management. Int J Life Cycle Assess 24:468–484

14. Arslan O, Aytac Z, Uyar T (2016) Superhydrophobic, hybrid, electrospun cellulose acetate nanofibrous mats for oil/water separation by tailored surface modification. ACS Appl Mater Interfaces 8:19747–19754
15. Cascone S, Sciuto G (2018) Recovery and reuse of abandoned buildings for student housing: a case study in Catania, Italy. Front Architectural Res 7:510–520
16. Yoobanpot N, Jamsawang P, Simarat P (2020) Sustainable reuse of dredged sediments as pavement materials by cement and fly ash stabilization. J Soils Sediments 20:3807–3823
17. Gebremariam AT, Maio FD, Vahidi A, Rem P (2020) Innovative technologies for recycling end-of-Life concrete waste in the built environment. Resour Conserv Recycl 163:104911
18. Kazmi SMS, Munir MJ, Wu YF (2021) Application of waste tire rubber and recycled aggregates in concrete products: a new compression casting approach. Resour Conserv Recycl 167:105353
19. Kosajan V, Wen ZG, Zheng KF, Fei F, Wang ZJ, Tian HK (2021) Municipal solid waste (MSW) co-processing in cement kiln to relieve China's Msw treatment capacity pressure. Resour Conserv Recycl 167:105384
20. Liu P, Niu L, Tao X (2018) Preparation of superhydrophobic-oleophilic quartz sand filter and its application in oil-water separation. Appl Surf Sci 447:656–663
21. Wang B, Mahmood A, Chen L (2020) Under-oil superhydrophilic salt particle filter for the efficient separation of water-in-oil emulsions. Chem Commun 56:11585–11588
22. Gou X, Zhang Y, Long L (2020) Superhydrophilic and underwater superoleophobic cement-coated mesh for oil/water separation by gravity. Colloids Surf, A 605:125338
23. Wang J, Wang H, Geng G (2018) Highly efficient oil-in-water emulsion and oil layer/water mixture separation based on durably superhydrophobic sponge prepared via a facile route. Mar Pollut Bull 127:108–116
24. Liu X, Feng S, Wang C, Yan D, Chen L, Wang B (2022) Wettability improvement in oil-water separation by nano-pillar ZnO texturing. Nanomaterials 12(5):740
25. Alabresm A, Chen YP, Decho AW, Lead J (2018) A novel method for the synergistic remediation of oil-water mixtures using nanoparticles and oil-degrading bacteria. Sci Total Environ 630:1292–1297
26. Sun F, Huang SY, Ren H-T (2020) Core-sheath structured TiO_2@PVDF/PAN electrospun membranes for photocatalysis and oil-water separation. Polym Compos 41:1013–1023
27. Chen C, Weng D, Mahmood A (2019) Separation mechanism and construction of surfaces with special wettability for oil/water separation. ACS Appl Mater Interfaces 11:11006–11027

Concrete Engineering and Technology

Study on Simulation Test of Mass Machine-Made Sand Concrete Pouring

Lianjie Jin, Yonghong Shao, Jianying Wang, Heng Zhang, Zhishun Cheng, and Lin Li

Abstract The mass concrete structure is relatively thick, and the concrete pouring volume is large. During the pouring process, the cement will produce large hydration heat when it is hydrated and hardened, causing a large temperature difference between the inside and outside of the structure, leading to structural cracking, which seriously affects the late strength, working performance and service life of the concrete structure. In this paper, the temperature field during the pouring process of machine-made sand concrete is numerically simulated, and the variation law of the temperature field with different pouring processes is analyzed. The following conclusions are drawn: (1) Under the secondary pouring condition, the maximum temperature of the first pouring is in the concrete stratum and presents the law of temperature decreasing from the bottom layer core to the surrounding, and the maximum temperature reaches 60°; At the beginning of the second layer of concrete pouring, the maximum temperature is 48° at the bottom of the whole. With the overall temperature rising, the maximum temperature at the middle of the second layer reaches 72°. (2) For mass concrete poured in one time as a whole, in the early stage of concrete pouring, the temperature gradually rises from the casting temperature to the maximum temperature, and the temperature distribution is like an open cover pool. As time goes on, the maximum temperature range gradually shrinks to the center, and the maximum temperature increases first and then decreases with time. The maximum temperature of one-time overall pouring reaches 72°.

Keywords Numerical simulation · Machine made sand concrete · Heat of hydration · Temperature field · Mass pouring

L. Jin · Y. Shao (✉) · J. Wang · H. Zhang · Z. Cheng · L. Li
China Railway ERJU 4th Engineering Co., Ltd., Chengdu 610306, China
e-mail: 36119600@qq.com

T. Kang (ed.), *Proceedings of 5th International Conference on Civil Engineering and Architecture*, Lecture Notes in Civil Engineering 369,
https://doi.org/10.1007/978-981-99-4049-3_10

1 Introduction

Concrete is a quasi brittle material with low tensile strength in the field of civil engineering and construction. When the raw materials, mix proportion, construction technology and curing conditions are not controlled properly, it is easy to crack [1]. Many scholars have carried out a lot of research on the cracking mechanism and prevention technology of railway tunnel concrete. Xu [2] analyzed the cracking characteristics of tunnel lining through field investigation and similar model tests. Xie [3] analyzed the causes of circumferential cracks in tunnel lining and put forward prevention suggestions. Wang [4] analyzed the causes of temperature cracks in lining concrete of 696 railway tunnels and put forward prevention measures. However, the long-term large-scale infrastructure construction makes the river sand resources in China increasingly scarce. In order to implement the concept of green development, machine-made sand concrete has been popularized and applied in tunnel engineering in recent years. Scholars have achieved certain results in the research of raw material control, concrete mechanical properties, shrinkage and creep properties and mix proportion design of machine-made sand concrete [5]. Machine made sand has the characteristics of rough surface, clear edges and corners, high content of stone powder, and "large at both ends and small in the middle", which cannot be ignored in concrete performance [6–8]. Shanmuga-vadivu [9] studied the tensile strength, elastic modulus and mortar shrinkage of concrete with machine-made sand as fine aggregate. Van Deke [10] compared and analyzed the influence of stone powder content on the working performance, compressive strength, chloride ion permeability and shrinkage performance of machine-made sand concrete; Li [11] compared and studied the influence of different stone powder content on the shrinkage and strength of machine-made sand concrete. In terms of the performance research of high-strength machine-made sand concrete, Sun [12] used tailings and machine-made sand to prepare high-strength concrete, and discussed its mechanical properties and durability; Li [13] studied the mechanical properties and static elastic modulus of river sand concrete and medium high strength machine-made sand concrete through large plate cracking test. Although the proportion and materials of machine-made sand have a significant impact on its performance, the impact of temperature control measures on the cracks and durability of machine-made sand concrete in the actual pouring process can not be ignored. In view of this, this chapter, relying on the Jinyong railway project, studies the distribution law of temperature field during the pouring process of large volume machine-made sand concrete and analyzes the law of temperature change, so as to provide reference for the pouring process and quality control of machine-made sand concrete in practical projects.

2 Numerical Model of Concrete Heat Conduction

2.1 Basic Principles of Heat Transfer

During the construction of mass concrete, due to the hydration heat effect of concrete, the temperature difference between the inner surface and the outer surface of the bearing platform is too large, and the resulting temperature stress will cause temperature cracks in the mass concrete structure, which seriously affects the safety, reliability and durability of the structure. Under the action of hydration heat, construction environment and thermal insulation measures, the internal temperature field of mass concrete is very complex, which is also the main reason why the internal surface temperature difference, maximum adiabatic temperature rise and surface temperature of mass concrete structure are difficult to control.

According to Fourier's law, for one-dimensional heat conduction problem, the expression of thermal conductivity is shown in Eqs. 1 and 2. The values of thermal conductivity are different for different substances. Even for the same substance, the values of thermal conductivity are different under different conditions such as temperature, humidity, density and pressure. The research of concrete temperature field is to reveal the transfer process of temperature in the structure by understanding the thermal properties of concrete.

$$\lambda = c_v \cdot \alpha \tag{1}$$

$$\lambda = \frac{Q}{\frac{\Delta\theta}{\Delta h}\Delta FT} \tag{2}$$

where λ is coefficient of heat conductivity, W/(m·degree); α is thermal conductivity, m^2/h; c_v is Volume Heat, kJ/(m^3·degree); Q is quantity of heat, kJ; $\Delta\theta/\Delta h$ is temperature gradient, K/m; ΔF is the measure of area, m^2; T is time, h.

2.2 Heat Conduction Equation

For complex heat conduction problems, differential equations need to be established according to the law of conservation of energy. Suppose an isotropic micro cell, as shown in Fig. 1, with side lengths DX, Dy and DX respectively, and at unit time d τ. The sum of the net heat introduced into the micro unit and its own heat is equal to the internal energy of the micro unit. In combination with Fourier's law, its differential equation expression is shown in Eq. 3.

$$\rho c\frac{\partial t}{\partial \tau} = \frac{\partial}{\partial x}\left(\lambda\frac{\partial t}{\partial x}\right) + \frac{\partial}{\partial y}\left(\lambda\frac{\partial t}{\partial y}\right) + \frac{\partial}{\partial z}\left(\lambda\frac{\partial t}{\partial z}\right) + q_v \tag{3}$$

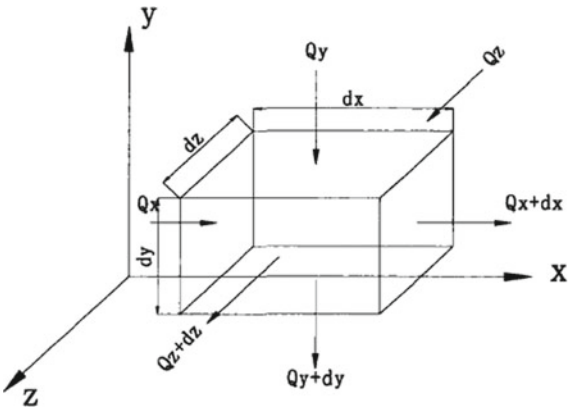

Fig. 1 Schematic diagram of heat conduction

where ρ is material density, kg/m^3; c is specific heat capacity, kJ/(kg·degree); $\partial t/\partial \tau$ is rate of temperature change with time, degree/h; q_v is internal heat source intensity, W/m^3.

For concrete, due to the hydration heat of cement, its adiabatic temperature rise rate can be calculated by Eq. 4.

$$\frac{\partial \theta}{\partial \tau}=\frac{Q}{c\rho}=\frac{Mq_c}{c\rho} \tag{4}$$

where θ is adiabatic temperature rise, degree; M is cement content, kg/m^3; Q is heat flow, W; q_c is heat released by hydration heat of cement in unit quantity and unit time, kJ/(kg·h^3).

The differential equation of concrete heat conduction is shown in Eq. 5.

$$\frac{\partial T}{\partial \tau}=a\left(\frac{\partial^2 t}{\partial x^2}+\frac{\partial^2 t}{\partial y^2}+\frac{\partial^2 t}{\partial z^2}\right)+\frac{\partial \theta}{\partial \tau} \tag{5}$$

2.3 Boundary Condition

Assuming that the temperature field of the concrete structure is a known function t_0 (x, y, z) in the spatial coordinate system at the initial moment when $t = 0$, the three-dimensional temperature field expression of the concrete structure is shown in Eq. 6.

$$t(x, y, z, 0) = t_0(x, y, z)=C \tag{6}$$

It is generally considered that the temperature distribution at the initial time of the concrete structure is a constant C, so for the mass concrete structure, its boundary conditions can be roughly divided into four types.

a. Surface temperature of concrete structure (t is time) τ, the known functions of are:

$$t(\tau) = f(\tau) \tag{7}$$

When the concrete is immersed in water, the surface temperature of the concrete is equal to the known water temperature.

b. Surface heat flow of concrete structure $\lambda \times \partial t/\partial n$ is time τ, the known functions of are:

$$-\lambda \frac{\partial t}{\partial n} = f(\tau) \tag{8}$$

where n is external normal direction of concrete surface.

c. Heat flow through concrete and structural surface $\lambda \times \partial t/\partial n$ is proportional to the difference between its surface temperature t and air temperature t_a, that is:

$$-\lambda \frac{\partial t}{\partial n} = \beta(t - t_a) \tag{9}$$

where β is surface heat release coefficient, kJ/(m^2·h·degree). When β is infinite, the surface temperature and the air temperature are approximately equal, and the boundary conditions of the concrete structure are the same as those of the first type. When β is 0, the surface of the concrete structure can be seen as not transferring heat. At this time, the structure is in an adiabatic state.

d. Interface continuity conditions, that is, when pouring in layers, the interface contact conditions between the concrete structure and the foundation soil and between the concrete structures are good, and the temperature is continuous. In the construction of mass concrete structures, the influence of foundation soil on the temperature and heat dissipation of structures should be considered, and the contact surface between the two is a continuous interface. If the hydration heat caused by one-time pouring of concrete is too large to be conducive to control or the amount of concrete pouring is large, layered pouring is usually used for construction, and the contact interface between layers also belongs to this continuous condition. The side and top surfaces of concrete structures need to be determined according to the situation. When the top surface is watered for curing, its boundary conditions are considered as the first case; When the concrete is not watered for curing, it will be in direct contact with the air, and then heat

convection will occur. At this time, it belongs to the third boundary condition, which is the same as the side condition; When thermal insulation measures are used for concrete, the influence of thermal insulation measures on heat release coefficient should also be considered.

3 Influence Factors of Concrete Temperature Field

3.1 Principle of Hydration Heat of Cement

The hydration heat of cement is a very important factor in temperature stress analysis of concrete structures. In the calculation and analysis of concrete temperature field, the hydration heat W can usually be calculated by direct method and indirect method. Among them, the direct method is to measure the adiabatic temperature rise of the concrete sample to be tested through the thermal test, while the indirect method is to calculate the adiabatic temperature rise by measuring the hydration heat of cement W in the absence of experimental conditions. Among them, the hydration heat w of cement can be calculated in three ways: exponential, hyperbolic and double exponential. The calculation formula is shown in Eqs. 10–12.

$$W(t) = W_0\left(1 - \mathrm{e}^{-mt}\right) \tag{10}$$

$$W(t) = \frac{W_0 t}{(n + t)} \tag{11}$$

$$W(t) = W_0\left(1 - \mathrm{e}^{-at^b}\right) \tag{12}$$

where t is age of the concrete, day; $W(t)$ is cement hydration heat corresponding to age t, kJ/kg; W_0 is maximum hydration heat of cement, that is, the corresponding cement hydration heat from time t to ∞, kJ/kg; m, n, a, b are constant. Among them, parameters a and b can be taken according to Table 1 according to different cement varieties. n is the age when the hydration heat of cement reaches half, and the value of m is related to the variety, pouring temperature and specific surface area of cement. According to different experimental conditions, the values are shown in Table 2.

Table 1 Summary of basic physical indexes of test soil samples

Cement type	W_0 (kJ/kg)	a	b
Ordinary portland cement 425#	330	0.69	0.56
Ordinary portland cement 525#	350	0.36	0.74
Ordinary Portland Dam Cement 525#	270	0.79	0.70
Slag silicate dam cement 425#	285	0.29	0.76

Table 2 Value table of m

Pouring temperature (degree)	5	10	15	20	25	30
M (1/d)	0.295	0.318	0.340	0.362	0.384	0.404

3.2 Adiabatic Temperature Rise

In the actual project, after the concrete is poured, the heat is released inside the structure due to the hydration reaction of cement and other materials, so that the temperature climbs rapidly, and the maximum temperature rise is the adiabatic temperature rise of the concrete θ. The magnitude of adiabatic temperature rise has an important influence on whether the maximum temperature can be reached inside the concrete and the temperature difference between the inside and the outside. The temperature rise will bring about the change of stress field and affect the size of temperature stress. When the structure volume is very large, the heat generated due to temperature rise cannot be quickly dissipated, which leads to cracks in the concrete structure. It can be seen that the adiabatic temperature rise of concrete is one of the important parameters in the analysis of concrete temperature field. The calculation formula is as follows:

$$\theta(t) = \frac{MQ_{\mathrm{co}}\left(1 - \mathrm{e}^{-mt}\right)}{c\rho} \tag{13}$$

where c is specific heat, J/(kg·°C); Q_{co} is hydration heat of cementitious material, kJ/kg; M is cement content, m^3.

When a single admixture is used, the value of k can be taken according to the value shown in Table 3. When two kinds of admixtures are used, the adjustment coefficient of hydration heat of different admixtures can be calculated according to Eq. 14.

$$k = k_1 + k_2 - 1 \tag{14}$$

where k_1 is adjustment coefficient of hydration heat when using fly ash as admixture; k_2 is adjustment coefficient of hydration heat when slag powder is used as admixture.

The adiabatic temperature rise of concrete is calculated as shown in Eq. 15.

Table 3 Values of hydration heat adjustment coefficient of admixtures under different dosage conditions

	0	10%		20%	30%	40%
Fly ash k_1	1	0.96		0.95	0.93	0.82
Slag powder k_2	1	1		0.93	0.92	0.84

$$\theta(t) = \frac{W(t)(M + kF)}{c\rho} \tag{15}$$

where k is reduction factor, it is 0.25 when using fly ash; F is amount of mixed materials, m^3.

3.3 Influence Factors of Concrete Temperature Field

After many years of engineering practice, it is found that the factors that affect the temperature field of concrete mainly include the type of cement, the amount of cement used, the molding temperature, the ambient temperature, the geometric dimensions of the structure, and the thermal conductivity of the concrete.

a. **Cement Type and Dosage**

The main reason for concrete temperature rise is the result of cement hydration heat. The heat generated by different types of cement hydration heat is significantly different, and the amount of cement per unit volume also has a great impact on the total heat of hydration.

b. **Molding Temperature**

The temperature of entering the formwork is the temperature when entering the formwork during concrete pouring, namely the initial temperature. As the temperature rise of concrete depends on the effect of cement hydration heat, if the ambient temperature is higher than the concrete temperature when entering the mold, the probability of temperature cracks in the concrete structure will be greatly reduced. Therefore, in actual construction, some cooling measures are usually taken to reduce the pouring temperature of concrete in advance, or sand and gravel are stacked in a cool place.

c. **Ambient Temperature**

When concrete construction is carried out in different regions and seasons, because the ambient temperature is always changing, the influence on the temperature difference inside and outside the concrete structure is very significant. When the ambient temperature is too low, the temperature gradient between the concrete surface and the interior of the structure will increase, the heat dissipation capacity of the surface will increase, and the internal and external temperature differences will increase, leading to the generation of temperature cracks. Therefore, in actual projects, hot water mixing is usually used to increase the temperature of the mixture, or the aggregate is heated in advance to increase its temperature.

d. **Geometric Dimensions**

The thickness of the concrete structure has a certain influence on the heat dissipation. Generally, the thicker the size, the smaller the influence of external factors on the

interior, and the harder it is for the concrete to dissipate heat. Therefore, in the actual project, it is necessary to control the thickness of concrete pouring in layers, so as to facilitate the internal heat dissipation, which will further shorten the time for the temperature to reach a stable state. If necessary, phased pouring can also be considered.

e. **Coefficient of Heat Conductivity**

According to the above principle, the thermal conductivity is an important indicator of the ability of a structure to transfer heat. The larger the thermal conductivity coefficient, the more heat exchange of the concrete structure per unit time, and the smaller the peak temperature inside the structure, thus reducing the internal and external temperature difference of the concrete structure. In addition, the thermal conductivity also affects the time when the peak temperature occurs. The greater the thermal conductivity, the earlier the peak temperature occurs.

4 Case Analysis

4.1 Project Overview

Some structures of Jinyong railway tunnel under construction are constructed with machine-made sand concrete. According to the parameters required by the finite element model of mass concrete temperature field, the concrete thermal parameters, ambient temperature, molding temperature and concrete surface insulation measures are set. Hexahedral grid elements are used to divide the structure into 37,500 elements. Among them, the thickness of the back sealing concrete layer is established according to the actual situation, and the influence of the back sealing concrete layer on the thermal conductivity of the concrete at the bottom of the structure is considered. The finite-element model is shown in Fig. 2.

The model mainly analyzes the following two working conditions:

Working condition 1 (two times of pouring, 2.5 m per layer): the casting temperature of concrete structure is 15 °C, the ambient temperature is 8 ± 5 °C, and the thermal insulation temperature rise of concrete is 44.8 °C.

Fig. 2 Finite-element model

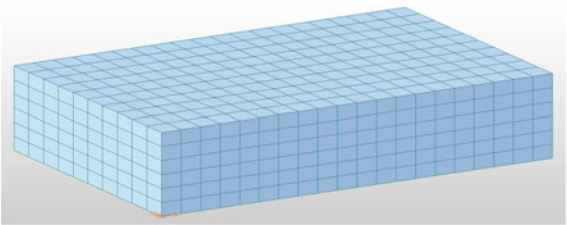

Working condition 2 (one-time pouring): the casting temperature of concrete structure is 15 °C, the ambient temperature is 8 ± 5 °C, and the thermal insulation temperature rise of concrete is 44.8 °C.

4.2 Analysis of Simulation Results

4.2.1 Numerical Simulation Results of Working Condition 1

According to the conditions described in working condition 1, the temperature field of mass concrete structure in the two pouring processes is simulated. A quarter of the models are selected to simulate the maximum temperature of the first pouring, the initial temperature of the second pouring and the time history curve temperature. The simulation results are shown in Figs. 3, 4, 5, 6 and 7.

In order to clearly reflect the temperature distribution law of hydration heat in the process of mass concrete pouring, after the completion of the second layer of concrete pouring, the temperature distribution law of a quarter of the model is selected for

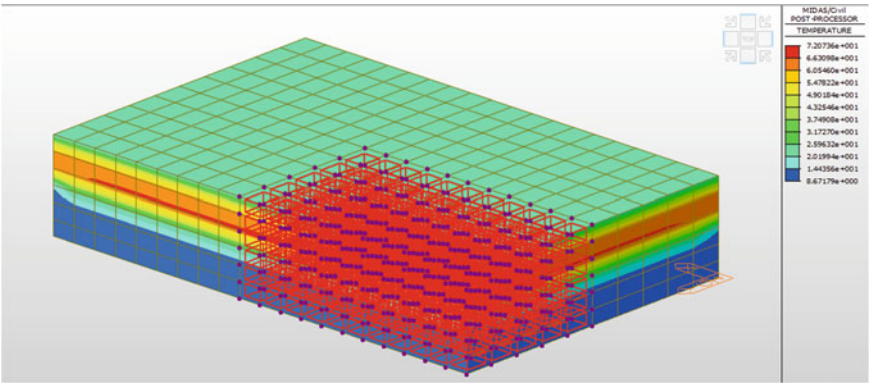

Fig. 3 Quarter structure model (Working condition 1)

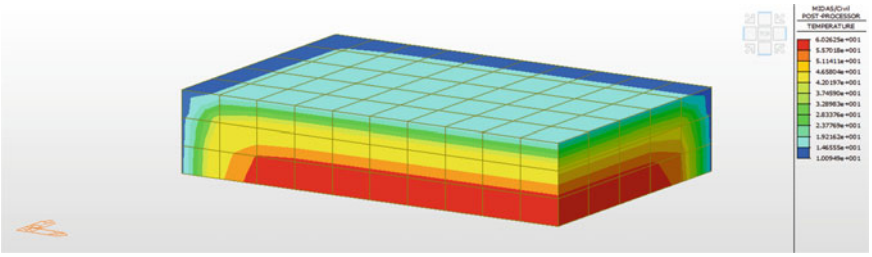

Fig. 4 Cloud chart of maximum temperature distribution of the first concrete pouring

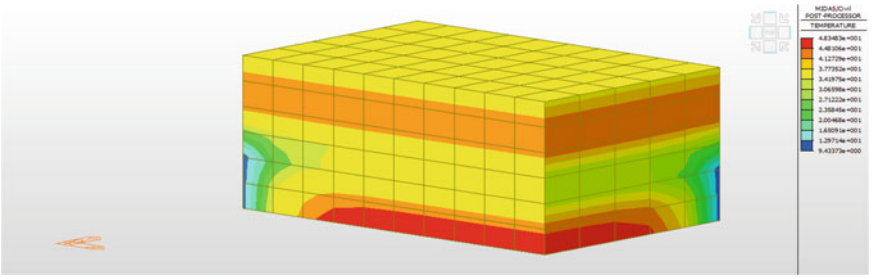

Fig. 5 Initial temperature distribution of second pouring concrete (Working condition 1)

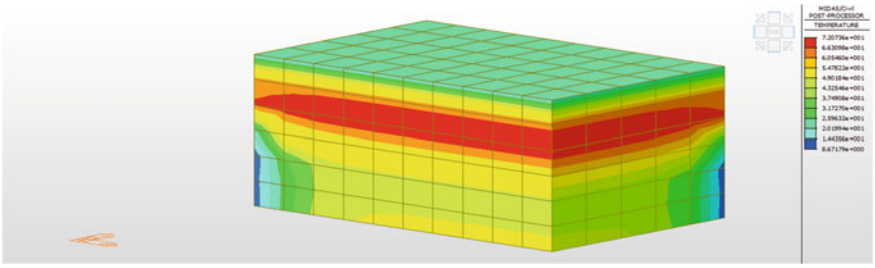

Fig. 6 Maximum temperature distribution (Working condition 1)

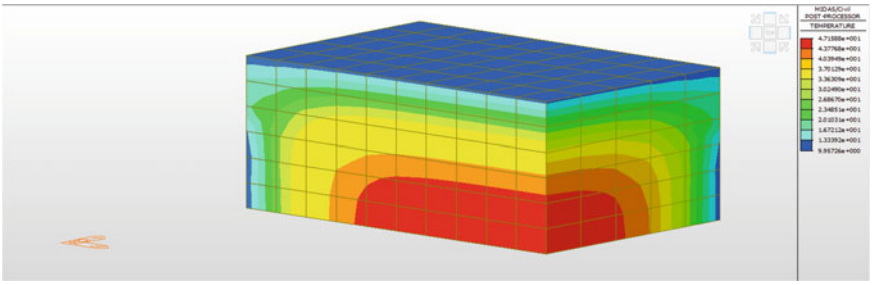

Fig. 7 Time history curve temperature distribution (Working condition 1)

analysis in three stages, namely, the concrete hydration heat reaches the maximum in the early stage of the concrete just entering the mold and the later stage of the completion of the pouring. It can be seen from the cloud diagram of temperature distribution of the first pouring in Fig. 4 that the maximum temperature of the first pouring is in the concrete stratum and the temperature decreases from the bottom core to the surrounding, and the maximum temperature reaches 60 °C; It can be seen from Figs. 3, 4, 5, 6 and 7 that the temperature in the middle of the second layer of concrete is relatively high at the initial stage of the second layer of concrete pouring, and the highest temperature is the lowest position of the whole, which is

48 °C; With the passage of time, the hydration of concrete releases heat, and the overall temperature rises. The highest temperature is concentrated in the middle of the second layer, and the maximum temperature reaches 72 °C and spreads from the middle to the surrounding; at the end of the second-layer pouring, with the diffusion of temperature, the highest temperature is concentrated at the bottom of the whole, which is 47 °C.

4.2.2 Numerical Simulation Results of Working Condition 2

According to the conditions described in Working Condition 2, the temperature field of mass concrete in two pouring processes is simulated. A quarter of the models are selected to simulate the initial temperature and time history curve temperature. The simulation results are shown in Figs. 8, 9, 10 and 11.

According to the cloud diagram of temperature distribution from Figs. 9, 10 and 11, at the initial stage of concrete pouring, with the continuous reaction of hydration heat, most of the concrete gradually rises from the molding temperature to the maximum temperature. During this process, the temperature distribution is in

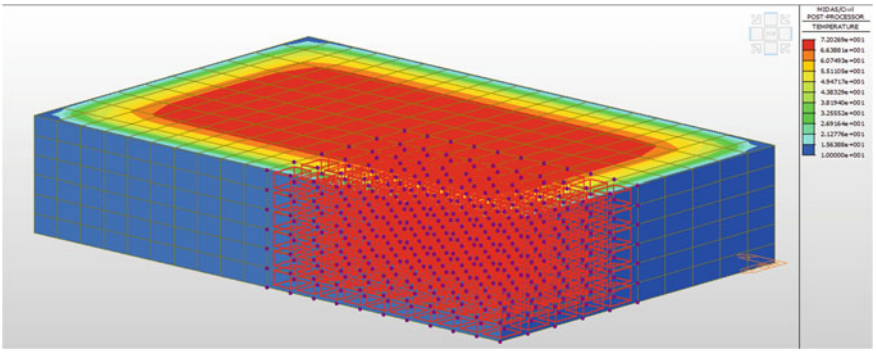

Fig. 8 Quarter structure model (Working condition 2)

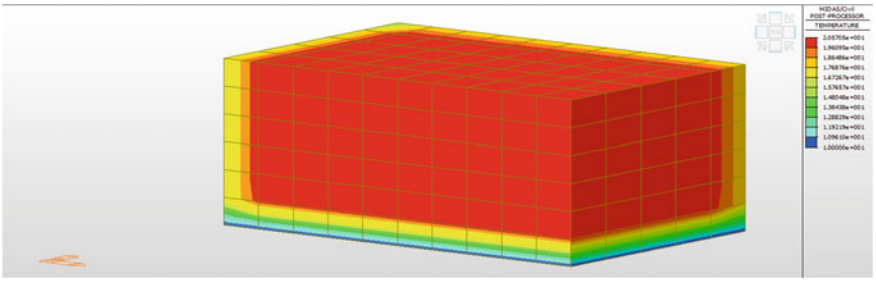

Fig. 9 Initial temperature distribution of second pouring concrete (Working condition 2)

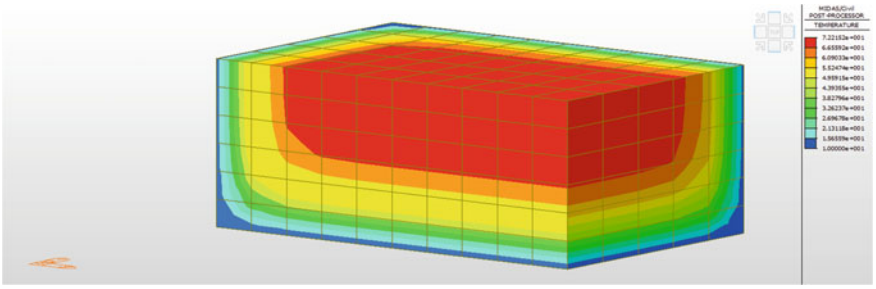

Fig. 10 Maximum temperature distribution (Working condition 2)

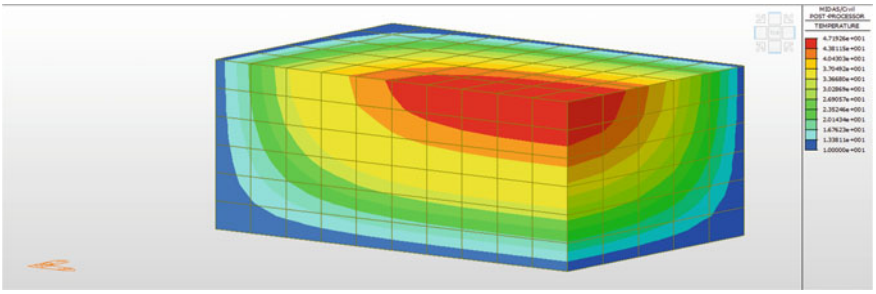

Fig. 11 Time history curve temperature distribution (Working condition 2)

the shape of an open pool, and gradually decreases from the central temperature to the surrounding. The central maximum temperature reaches 72°, gradually decreases from the time of maximum temperature with the passage of time, and the maximum temperature range gradually shrinks toward the center. Finally, the temperature is stable.

5 Conclusions

Through the simulation of the temperature field of mass concrete of large-span bridge cushion cap, it is concluded that under the secondary pouring condition, the maximum temperature of the first pouring is in the concrete stratum and presents the law of temperature decreasing from the bottom core to the surrounding, and the maximum temperature reaches 60°; At the initial stage of the second layer of concrete pouring, the highest temperature is 48° at the bottom of the whole. With the passage of time, the hydration of the concrete releases heat, and the overall temperature rises. The highest temperature is concentrated in the middle of the second layer, and the maximum temperature reaches 72° with the diffusion of temperature, the highest temperature is concentrated at the bottom of the whole, which is 47°.

For the mass concrete poured once as a whole, no matter how many layers of cooling water pipes are, the temperature change law is basically the same, and the additional layer of cooling pipe accelerates the speed of temperature drop in actual construction. At the initial stage of concrete pouring, the temperature gradually rises to the maximum temperature from the casting temperature. During this process, the temperature distribution is like an open cover pool. As time goes on, the maximum temperature range gradually shrinks to the center. The maximum temperature increases first and then decreases with time. The maximum temperature of one-time overall pouring reaches 72°.

References

1. Chen Z, Cui J, Zhu J et al (2006) Analysis and control of cracking in reinforced concrete. Eng Mech 23(Suppl 1):86−107
2. Xu GW, He C, Chen ZQ et al (2020) Mechanical behavior of secondary tunnel lining with longitudinal crack. Eng Fail Anal 113:104543
3. Xie L, Yang Q (2020) Cause analysis and prevention suggestions of circumferential cracks in tunnel lining. Highway 65(5):347–352
4. Wang J, Huang F, Li H et al (2020) Cause analysis and prevention measures of temperature cracks in railway tunnel lining concrete. Railw Eng 60(9):73−77
5. T/CECS G: K50-30-2018, Technical specification for highway manufactured sand high performance concrete
6. Li FL, Zeng Y, Li CY (2011) Evaluation of relations among basic mechanical properties of concrete with machine made sand. In: Advanced materials research 418−420:441−444. Transportation Technology Publications Ltd.
7. Yang R, Yu R, Shui ZH et al (2019) The physical and chemical impact of manufactured sand as a partial replacement material in ultra-high performance concrete (UHPC). Cement Concr Compos 99:203–213
8. Meng Y, Xie J, Shen W et al (2019) Study on the adaptability of manufactured sand in concrete. Concrete 5:58–61
9. Shanmugavadivu PM, Malathy R (2012) Effect of physical properties of manufactured sand as fine aggregate in elastic and shrinkage properties of concrete and mortar. Adv Mater Res 463(464):221–225
10. Fan D, Ma Q, Zhou Z et al (2016) Influence of stone dust on properties of concrete with manufactured sand. Bull Chin Ceram Soc 35(3):913–917
11. Li Z, Zhang A (2015) Positive and negative effects of machine-made sand on shrinkage and strength of concrete. Highway 60(5):181−183
12. Sun J, Wu D, Cao L et al (2019) Study on the performance of the mixed sand high strength concrete. Concrete 2019(9):146−149
13. Li Y, Ruan X (2013) Experimental study on crack resistance of machine-made sand concrete. J China Foreign Highw 33(5):248–251

Basic Research for Improving the Initial Strength of LPC-FA Concrete with C-S-H Accelerating Admixture

Kazuhito Niwase and Tasuku Akasaka

Abstract In concrete engineering in Japan, the rapid deterioration of structures in recent years and the increase in carbon dioxide emissions during cement manufacturing have become problems. In order to solve this problem of aging, it is necessary to use materials with excellent long-term durability. In addition, the amount of cement used needs to be reviewed to solve environmental problems. As a countermeasure for these, research is underway on concrete using low-heat Portland cement and fly ash. However, this concrete is difficult to consume due to its low initial strength, and it is rarely used in Japan. In this study, to improve this low initial strength, we examined the mix proportion of concrete to which an accelerating admixture is added. Also, to compare the prepared concrete with the conventional one, a test was conducted to see the compressive strength. There are four types of test performed. As a result, the concrete we have planned has shown the best results in all tests. In this study, it was found that adding an accelerating admixture to low-heat Portland cement is effective. The use of concrete in this research for future Japanese structures will lead to the solution of environmental and social problems.

Keywords LPC-FA concrete · Superplasticizer · Accelerating admixture · Mix proportion · Compressive strength

1 Introduction

Currently, the amount of carbon dioxide emitted by the cement industry worldwide is estimated to be about 1.6 billion tons, which is about 6% of the anthropogenic emissions (27.1 billion tons) [1, 2]. A large amount of carbon dioxide is emitted

K. Niwase (✉) · T. Akasaka
National Institute of Technology Hachinohe College, Hachinohe, Aomori, Japan
e-mail: niwase-z@hachinohe.kosen-ac.jp

T. Akasaka
e-mail: r03az03@hachinohe.kosen-ac.jp

T. Kang (ed.), *Proceedings of 5th International Conference on Civil Engineering and Architecture*, Lecture Notes in Civil Engineering 369,
https://doi.org/10.1007/978-981-99-4049-3_11

because limestone is calcined in the process of producing clinker, which is an intermediate product of cement. On the other hand, if cement demand continues to grow, especially in emerging and developing countries, cement production is expected to exceed 5 billion tons by 2050, from the current 2.3 billion tons, which is proportional to cement demand [1]. It is said that carbon dioxide emissions will also increase. If we cannot control the demand for cement by ourselves, we must significantly reduce the emission intensity in order to survive in a low-carbon society where the world as a whole is halved. However, innovative technologies that halve the basic unit have not yet been proposed in the cement industry. In order to reduce CO_2 emissions, it is necessary to implement carbon neutral and carbon negative such as reduction of cement usage fee, extension of concrete life, and CO_2 sequestration by concrete. Here, we focused on concrete with the aim of reducing the amount of cement used and extending the life of concrete, although a large amount of energy is used for cement production, 60% of CO_2 emissions are due to the decomposition of limestone, which is the raw material. Even if cement is made only from renewable energy, CO_2 can be reduced by only 40% [2]. Therefore, it is necessary to pay attention to the cement itself and the substitute for limestone, which is the raw material. In addition, by creating a highly durable structure that can be used for a longer period of time, it will lead to a reduction in the amount of cement used in the long term. Therefore, the design of concrete using Low-heat Portland cement, which is expected to develop long-term strength, fly ash, which is an industrial by-product, and fine limestone powder, (LPC-FA concrete) is underway. However, it is difficult to use it for general construction because the initial strength is low.

In this study, we conducted basic research for the purpose of improving the initial strength of LPC-FA concrete and evaluating its performance. The concrete designed in this study will have high long-term durability, which will reduce the maintenance of structures. It can be predicted that the concrete we are studying will be a countermeasure against the decrease and aging of civil engineers in Japan.

2 Outline of Experience

2.1 Materials and Mix Proportion

Design policy Currently, technological development of chemical admixtures is progressing, and products that can be expected to improve quality like never before are available. Therefore, in this study, the latest superplasticizer; SP and accelerating admixture; AC were used in combination to improve the initial strength of LPC-FA concrete. In addition, in order to improve the initial strength of this formulation and to confirm the degree of effect of cement and SP and AC, mix proportions in which ordinary Portland cement was mixed instead of low-heat Portland cement was added to the experimental case.

Materials As the binder, low-heat Portland cement and fly ash were added with and superplasticizer limestone fine powder in consideration of self-filling so that the quality of the specimen would not differ due to factors during driving. AC was adopted to see the improvement in initial strength. Also, in order to eliminate the influence caused by the aggregate as much as possible, the materials other than the binder were unified with the materials based on chemically stable limestone. Table 1 shows an outline of the materials used.

Mix Proportion Mix Proportions was created with reference to previous studies [3, 4]. Table 2 shows the concrete composition of the study. The composition is OPC-SP with only superplasticizer added to OPC, OPC-SP-AC with superplasticizer and accelerating admixture added to OPC, and LPC with only superplasticizer added to LPC. There are four types of LPC-SP-AC, which are SP and LPC with superplasticizer and accelerating admixture added. The common conditions were $W/B = 30\%$ and FA substitution rate 30%. SP and AC were added at $C \times 3\%$, and LS was set at 40% with respect to the fine aggregate.

Table 1 Outline of the materials

Material name	Code	Note
Ordinary portland cement	OPC	Density = 3.24 g/cm^3 specific surface area = 3730cm^2/g
Low-heat portland cement	LPC	Density = 3.24 g/cm^3 specific surface area = 3730cm^2/g
Fly ash	FA	Density = 2.17 g/cm^3, JIS II type specific surface area = 3610 cm^2/g
Limestone fine powder	LS	Density = 2.70 g/cm^3 specific surface area = 5250 cm^2/g
Sand: lime crushed sand	S	Density = 2.66 g/cm^3
Gravel: lime crushed stone	G	Density = 2.69 g/cm^3
Superplasticizer	SP	Carboxyl group-containing polyether compound
Accelerating admixture	AC	C-S-H, I type

Table 2 Mix proportion

Code	Unit amount [kg/m^3]							
	W	C	FA	LS	S	G	SP	AC
OPC-SP-AC	120	325	139	185	918	751	9.7	9.7
OPC-SP	129	325	139	185	918	751	9.7	-
LPC-SP-AC	120	325	139	185	920	753	9.8	9.8
LPC-SP	130	325	139	185	920	753	9.8	-

W: water, C: cement, FA: fly ash, LS: limestone fine powder, S: sand, G: gravel, SP: superplasticizer, AC: Accelerating admixture

2.2 Experimental Method

Specimens. The concrete was mixed in a mixing amount of about 20–50 L per batch and the mixing time for 180 s by a twin screw forced mixer. Each mix proportion was placing concrete in a batch of φ100 × 200 mm.

Assessment of liquidity. Slump flow test was performed to evaluate the fluidity. The slump flow test was carried out in accordance with the concrete slump flow test method (JIS A 1150) [5]. Assuming the construction on site, the test was conducted with mortar and concrete 5 min to 0, 30, 60, 90 and 120 min after kneading.

Evaluation of strength. Compressive strength test was performed to evaluate the strength. The compressive strength test was carried out in accordance with the compressive strength test method for concrete (JIS A 1108) [6] was underwater curing, and the ages were 3, 7, 28 and 91 days. The curing method for the mortar specimen φ5 × 10 cm was underwater curing, and the ages were 3, 7, 28 and 91 days.

Evaluation of mass transfer resistance. Electrophoresis test was performed in accordance with "Effective Diffusivity Factor Test Method for Chloride Ions in Concrete by Electrophoresis (Draft) (JSCE-G 571-2013)" [7]. When a constant DC voltage is applied to both sides of the concrete specimen in contact with the solution containing chloride ions, the chloride ions on the cathode side, which have a negative charge, pass through the pores of the concrete and electrophorese to the anode side. When the rate of increase in chloride ion concentration on the anode side reaches a certain level, the chloride ions in the pores are considered to be in a steady state, and the moving flux at this time is measured. The moving flux in the steady state reflects the pore structure of concrete and the ease of movement of ions in the pore solution, and the effective diffusion coefficient is applied by applying the electrochemical law (Nernst-Planck's formula). Can be calculated.

Evaluation of complex deterioration. The scaling test is a test for evaluating the resistance to scaling, which is the main deterioration of frost damage, and in this study, it is based on the RILEM-CDF method (Capillary Suction od De-icing Chemicals and Freeze–Thaw-Test). gone. This is also called the capillary permeation method, and it is supposed to be scaled in a chloride environment by absorbing water in advance with an aqueous solution of NaCl. In addition, tests can be performed with various specimen dimensions, and laboratory equipment can be arranged relatively easily.

3 Experimental Results and Consideration

Slump Flow Test. Figure 1 shows the results of the slump flow. The slump flow value 5 min after kneading and standing still is 48.0 cm for OPC-SP, 60.8 cm for OPC-SP-AC, 48.8 cm for LPC-SP, 47.5 cm for LPC-SP-AC, and OPC-SP. -Only AC exceeded 60 cm. The slump flow values 2 h after kneading are 47.5 cm for OPC-SP, 46.8 cm for OPC-SP-AC, 49.8 cm for LPC-SP, and 45.5 cm for LPC-SP-AC, which are the same for all mix proportions. It became a value of about. Although the loss of slump flow due to the passage of time of OPC-SP-AC became large, a sufficient slump flow value for medium-fluidity concrete was obtained for all mix proportions including OPC-SP-AC until 2 h after kneading. I was able to. Comparing LPC-SP-AC and LPC-SP, the slump flow values from immediately after kneading to 2 h after kneading were about the same. In addition, there was no significant difference in viscosity. From this, LPC-FA concrete, PAE high-performance AE water reducing agent and C-S-H hardening accelerator have good compatibility in fluidity, and AC should be added in the mix proportion of LPC as in this study. It is considered that the influence of the above on the liquidity is small. As for the properties related to pumpability, thixotropy was shown in which the viscosity decreased when the shear stress continued and increased when the shear stress continued.

Compressive Strength Test. Figure 2 shows the results of the compressive strength test. The compressive strength at 3 days of age is 50.9 N/mm^2 for OPC-SP-AC, 47.0 N/mm^2 for OPC-SP, 18.1 N/mm^2 for LPC-SP, and 28.8 N/mm^2 for LPC-SP-AC. OPC-SP-AC, OPC-SP and LPC-SP-AC have an initial strength (20N / mm^2 or more) higher than that of general concrete at the time of strength of 3 days, and sufficient strength can be obtained. It is considered that the reason why the initial strength was high despite the use of FA was that the W / B was 30% and the water-cement ratio was very small, resulting in fewer voids. The strength of LPC-SP-AC to which AC was added at 3 days of age was about 1.6 times that of LPC-SP, and it was confirmed that the addition of AC was effective in improving the initial strength.

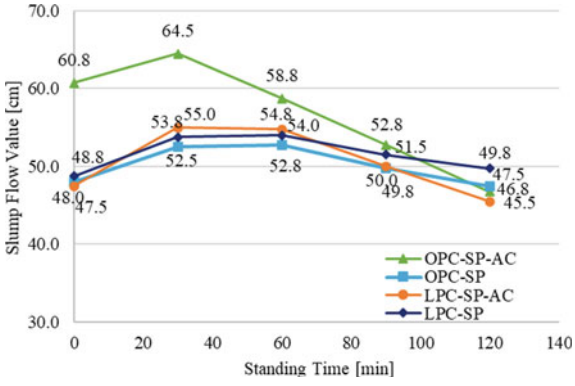

Fig. 1 Slump flow

Here, AC is a curing accelerator whose main component is nanoparticles of calcium silicate hydrate (hereinafter, C-S-H), and the seed crystals of C-S-H are introduced into the liquid phase to generate C-S-H from cement. LPC-SP-AC was about half the value at the time of strength at 3 days of age compared to the 2 mix proportions of OPC. However, the amount of increase in strength from 3 to 7 days of age and the amount of increase in strength from 7 to 28 days of material age are about twice the amount of increase in 2 mix proportion of OPC, and the strength of 28 days of material age has the highest compressive strength among the three mix proportions. This is thought to be due to the characteristic that the strength of LPC increases over a long period of time. The strength of LPC-SP-AC at 91 days was about 111 N/mm^2, and the strength at 365 days was about 116 N/mm^2, which were very large values. However, the increase in compressive strength from 91 to 365 days was 5 N/mm^2, which was a significant decrease compared to the previous increase. The intensity of OPC-SP-AC at 365 days was about 112 N/mm^2, and the intensity of OPC-SP-AC and LPC-SP-AC at 365 days did not make a big difference.

Electrophoresis test. In this test, the effective diffusion coefficient of chloride ions was on the order of 1.0×10^{-13} m^2/s in all mix proportions, which was a very small value. Since the value of the effective diffusion coefficient is very small, it is considered that this mix proportion has excellent mass transfer resistance and high resistance to salt damage that causes early deterioration of concrete structures. In addition, it was confirmed that the effective diffusion coefficient of this mix proportion was very small at the age of 28 days. It is considered that this is because the W / B of this mix proportion is as small as 30%, the voids are reduced, and an extremely dense cement matrix is formed (Fig. 3).

Scaling. Figure 4 shows the scaling amount obtained by the RILEM-CDF method at 365 days of age of OPC-SP, OPC-SP-AC and LPC-SP-AC. The scaling amount obtained in this experiment was a very small value for all mix proportions. It is considered that the reason why the scaling amount was very small is that the concrete of this composition confirmed by the compression test had high strength.

The scaling amount of LPC-SP-AC was about 0.004 g/cm^2 or less in each cycle of freezing and thawing for 300 cycles, which was an extremely small value. From this,

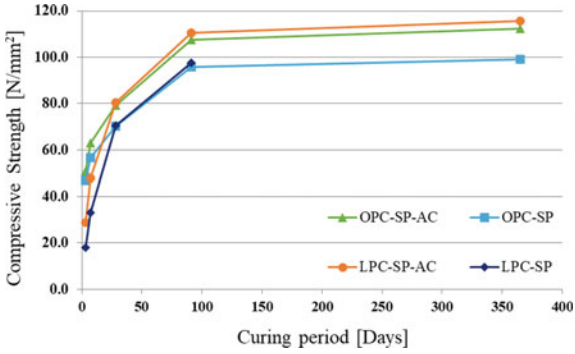

Fig. 2 Compressive strength

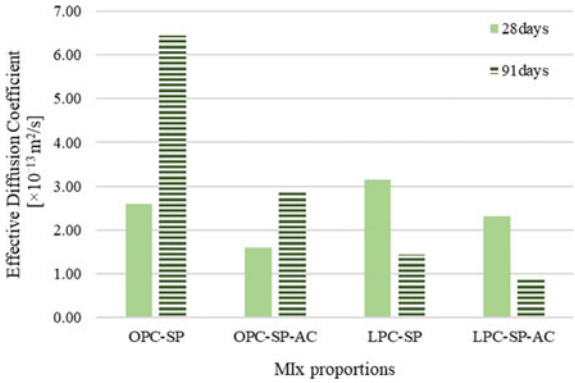

Fig. 3 Effective diffusion coefficient

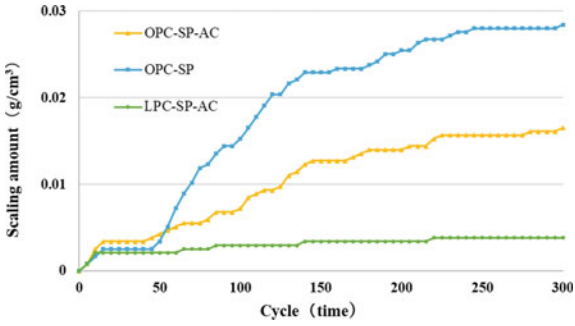

Fig. 4 Scaling amount

it was confirmed that excellent frost damage resistance can be expected. The scaling amount of LPC-SP-AC was smaller than that of the two OPC mix proportions.

In OPC-SP, a sharp increase in the amount of scaling was observed around 50 cycles. On the other hand, OPC-SP-AC did not show a sharp increase in the amount of scaling at a certain number of cycles. In addition, the result was that OPC-SP-AC had a smaller amount of scaling than OPC-SP throughout the 300 cycles. From this, it is considered that the addition of AC is effective in terms of frost damage resistance. By comparing LPC-SP and LPC-SP-AC, which are planned to be implemented in the future, it is necessary to confirm whether the addition of AC is effective for frost damage resistance even in LPC-FA concrete.

4 Summary

The following findings were clarified from this study.

(1) By using AC and SP together, sufficient fluidity could be obtained as medium-fluidity concrete in LPC-FA concrete.

(2) In this study, high viscosity was shown in all mix proportions. In addition, since thixotropy was also confirmed, it is necessary to confirm the pumpability in consideration of workability when adapting.
(3) It was confirmed that the initial strength of LPC-FA concrete was significantly improved by adding AC.
(4) It is considered that the reason why high initial strength could be obtained despite the use of fly ash is that this mix proportion has a low water cement ratio and a dense cement matrix is formed.
(5) OPC-SP-AC had the highest compressive strength at 3 days of age, but the increase in strength of LPC-SP-AC after 3 days of age was larger than that of OPC, and it was long-term. It was confirmed that LPC-SP-AC has high strength.
(6) Since the strength of high-strength concrete is affected by the crushing strength of coarse aggregate and the adhesion to mortar, it will be necessary to study aggregate in the future.
(7) The mortar and concrete used in this study show high mass transfer resistance and can be expected to have excellent salt damage resistance.
(8) It is expected that the concrete of this composition will have higher compressive strength and excellent mass transfer resistance due to the pozzolan reaction by fly ash.
(9) The scaling amount obtained by the freeze–thaw test was extremely small for all mix proportions. Among them, the scaling amount of LPC-SP-AC was particularly small.

5 Future Tasks

We will examine the chemical basis for the factors of high compressive strength, excellent mass transfer resistance, and frost damage resistance obtained by using AC.

Plan and carry out various tests using exposed specimens of LPC-FA concrete: Slump flow test, compressive strength test, electrophoresis test, scaling test.

We will study the optimization of the chemical admixture addition rate in consideration of economic efficiency.

References

1. Technology Roadmap—Low-Carbon Transition in the Cement Industry. https://www.iea.org/reports/technology-roadmap-low-carbon-transition-in-the-cement-industry, last accessed 2022/04/29
2. Kurokawa D, Hirano Y, Hirano H, Mori T, Sakai E (2021) Quality design of cement contributing low carbon and resource circulation society. Taiheiyo Cem Kenk Hoko 181:3–11
3. Kudo T, Niwase K (2020) Improvement of initial strength of LPC-FA concreter by using C-S-H type accelerator. In: 10th International Conference on Geotechnique, Construction Materials and Environment, pp 394–399. Melbourne, Australia

4. Suto S, Niwase K (2019) Study on improvement of early strength of highly durable concrete by combined use of chemical admixtures. In: The 3rd International Conference on Structural and Civil Engineering (ICSCE), pp 25–27
5. Japanese Industrial Standard, JIS A 1150 Concrete Slump Flow Test Method (2007)
6. Japanese Industrial Standard, JIS A 1150 Compressive Strength Test Method for Concrete (2018)
7. JSCE Standard, Electrophoresis Effective Diffusivity Factor Test of Chloride Ions in Concrete Test Method (Draft), JSCE-G 571-2003 (2003)

Effect of Water Sprinkling Curing of Mortar with Different Binder Materials and Different Pre-curing Times

Yuta Ito, Nana Katsuoka, Tsubasa Sato, and Shigeyuki Date

Abstract Precast concrete is often manufactured using steam curing, but it has been found that the performance of precast concrete after steam curing is lower than that of concrete cured in the atmosphere. In contrast, water sprinkling curing is being studied because it is relatively easy to wet the surfaces of concrete members without the need for a curing tank, and it is effective for increasing the compressive strength of some concrete. Previous studies have shown that the higher the maximum temperature during steam curing, the easier it is to obtain the strength-enhancing effect of water sprinkling curing. However, the effect of different binding materials and pre-curing times on water sprinkling curing has not yet been confirmed. In this study, the effects of different binders and different pre-curing times on the curing characteristics of mortar were investigated. The results showed that the strength was enhanced by water sprinkling curing even when the pre-curing time was short. Therefore, in Japan, where 2–3 h of pre-curing time is required, it may be possible to reduce the pre-curing time even more by applying water sprinkling curing.

Keywords Precast concrete · Pre-curing time · Water sprinkling curing · Compressive strength enhancement

1 Introduction

In recent years, the decrease in the number of young construction workers and aging of skilled workers have become problems for Japanese construction companies. As one approach to improve productivity, precast concrete (hereafter referred to as PCa) has been attracting attention [1–4]. PCa products are generally manufactured in

Y. Ito (✉) · N. Katsuoka · T. Sato
Master Course of Civil Engineering, Tokai University, Hiratsuka City, Japan
e-mail: yuta090703973@gmail.com

S. Date
Department of Civil Engineering, Tokai University, Hiratsuka City, Japan
e-mail: sdat@tokai-u.jp

T. Kang (ed.), *Proceedings of 5th International Conference on Civil Engineering and Architecture*, Lecture Notes in Civil Engineering 369,
https://doi.org/10.1007/978-981-99-4049-3_12

factories by steam curing, which is an accelerated curing method [5–8]. One of the advantages of using PCa products is that the quality of the products is not affected by the environment because they are manufactured in advance at the factory [9–12]. In addition, in on-site concrete construction, it is necessary to set up a formwork and reinforcing bars and then pour concrete, and a relatively small number of people can carry out the construction process [13–16]. However, steam curing has some disadvantages, such as cracking due to the rapid temperature increase and water loss in the concrete due to drying of the surface, which stagnates the hydration reaction and prevents densification of the microstructure [17–20].

To alleviate these factors, studies have been conducted on underwater curing as a secondary curing process after steam curing [21–23], but it is not easy to create water curing pools in an actual plant due to the limited space available. Therefore, we thought that the loss of strength in PCa members could be prevented by using a water sprinkling curing method that does not require a water tank for curing and is relatively easy to use. Previous studies [24–27] have found that concrete cured with water spray has a compressive strength similar to that of concrete cured in water. In fact, at a Japanese site, there is an example of applying water sprinkling curing using a sprinkler 6 h after casting for the purpose of suppressing cracking of concrete [28]. Further, the higher the maximum temperature during steam curing, the coarser the micro structure inside the mortar, which may allow water supplied by water sprinkling curing to penetrate more easily.

Various other studies have been conducted on PCa products, and it has been found that among the steam curing conditions, the pre-curing time has a significant effect on the compressive strength and micro-structure [29]. However, the relationship between pre-curing time and water sprinkling curing has not been clarified. In addition, high-early-strength Portland cement (hereafter referred to as "H-cement"), which hardens more quickly and has higher initial strength than ordinary Portland cement (hereafter. "N-cement"), is often used in PCa products, but there have been few reports on the use of H-cement and the application of water sprinkling curing to it with different blends. Therefore, in this study, compressive strength tests of mortar were conducted to determine the effect of water sprinkling curing with different binders (H-cement versus N-cement) and pre-curing times.

2 Outline of Experiment

2.1 Experimental Conditions

Tables 1 and 2 show the materials used and the mixing proportions, respectively.

A superplasticizer was added as necessary to achieve the set air volume and flow. Figure 1 shows the steam curing conditions. Before steam curing, the specimens were pre-cured at room a temperature of 20 °C and a humidity of 60% for a specified time (0.5, 2.5, 4.5 h). Steam curing was performed in a constant-temperature and

Table 1 Materials used

Material	Symbol	Properties	Density (g/cm^3)
Cement	N	Ordinary portland cement	3.16
	H	High-early-strength portland cement	3.14
Fine aggregate	S	River sand from Kanagawa (water absorption: 1.46%)	2.69
Superplasticizer	Ad	High range water reducing agent AE type (Polycarboxylic acid ether compounds)	–

Table 2 Mixing proportions

W/C (%)	S/C	Air content (%)	Mini slump (mm)
40	2.0	5.5 ± 1.0	100 ± 10

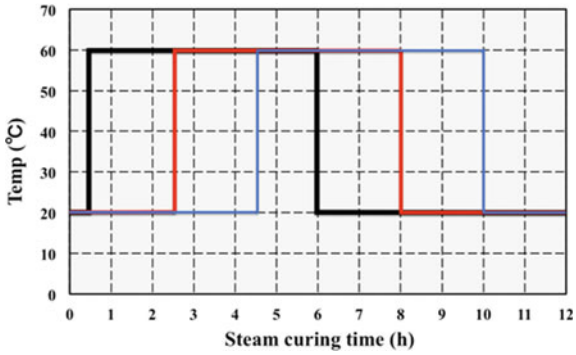

Fig. 1 Steam curing conditions

humidity chamber with no temperature gradient. The maximum steam temperature was set to 60 °C because previous studies [24] found that watering is more effective at higher maximum temperatures. After steam curing at the maximum temperature for 5.5 h, the mold was demolded and subjected to secondary curing.

2.2 Secondary Curing Conditions

Figure 2 shows the secondary curing conditions. After steam curing and atmospheric curing (ambient temperature of 20 °C, humidity of 60%) for the times shown in Fig. 1, water curing (water temperature: 20 °C), water sprinkling curing, or additional atmospheric curing was applied for secondary curing. Figure 3 shows the arrangement of the sprinkler system and specimens for water sprinkling curing. Regardless of the material age, 10 min after demolding, water sprinkling curing was performed for 10 min, and then atmospheric curing was performed until the specified age was

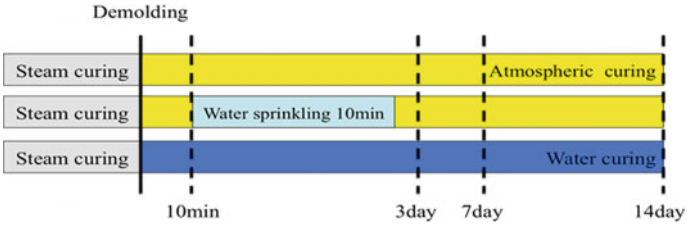

Fig. 2 Secondary curing

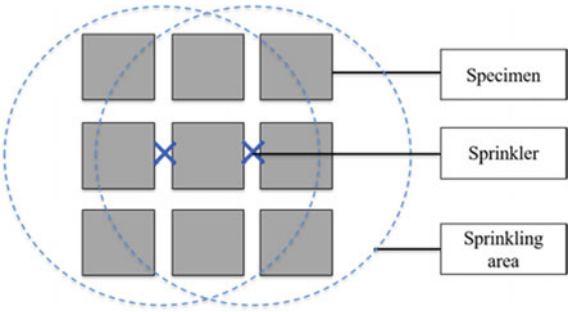

Fig. 3 Arrangement for water sprinkling curing

reached. A sprinkler system was used for water sprinkling curing, with a flow rate of 0.68 L/min. The specimens were moved periodically for even coverage by the water.

2.3 Test Items

To determine the identity of the mortar at the time of the experiment, air-content and mini-slump tests were conducted at the time of freshening in accordance with JIS A 1128 and JIS R 5201. Compressive strength tests were conducted in accordance with JIS R 5201 on prismatic specimens measuring 40 × 40 × 160 mm. The material was aged for 3, 7, or 14 days.

2.4 Evaluation Method

The compressive strength enhancement effect was determined using Eq. (1) as the index value for the effect of water sprinkling curing. The compressive strength enhancement effect is based on atmospheric curing, which is generally used as a secondary curing method, and there is a clear enhancement of the compressive strength after water sprinkling curing.

$$e = (s\sigma - a\sigma) \div (w\sigma - a\sigma) \times 100 \quad (1)$$

e: Compressive strength enhancement effect (%)

$s\sigma$: Compressive strength after water sprinkling curing (N/mm^2).

$a\sigma$: Compressive strength after atmospheric curing (N/mm^2).

$w\sigma$: Compressive strength after water curing (N/mm^2).

3 Results and Discussion

Figure 4 shows the legend for Figs. 5, 6, and 7. Figures 5, 6, and 7 show the relationship between compressive strength and pre-curing time for materials with an age of 3 to 14 days, and Figs. 8, 9, and 10 show the relationship between the compressive strength enhancement effect and the pre-curing time for materials aged 3–14 days. Figures 5, 6, and 7 show that the compressive strength of the H-cement mix is higher than that of the N-cement mix. Figure 5 shows that, for a material age of 3 days, there is a large difference in compressive strength between the specimens that combined H-cement with water sprinkling curing and the combination with atmospheric curing. Figure 7 shows that there is a difference in compressive strength for a material age of 14 days between the H-cement specimen cured by water sprinkling and the specimen with a material age of 3 days. These results can be attributed to the larger specific surface area of H-cement compared to N-cement and the higher tricalcium silicate content [30].

When compared with the secondary curing conditions, regardless of the material used or the steam curing conditions, 10 min of water sprinkling curing resulted in a higher compressive strength than that for atmospheric curing. For example, Fig. 5 shows that regardless of the material used and the steam curing conditions, the compressive strength after water sprinkling curing and water curing was similar. Figure 6 shows that the compressive strength of the H-cement mixture after 2.5 and 4.5 h of pre-curing and secondary water sprinkling curing was higher than that of the

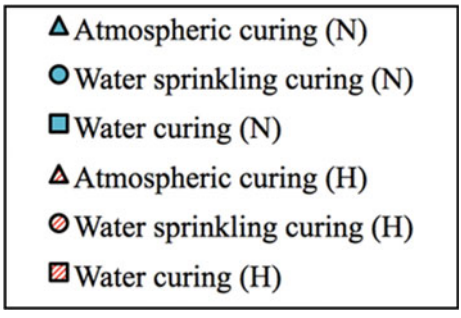

Fig. 4 Legend for Figs. 5–7

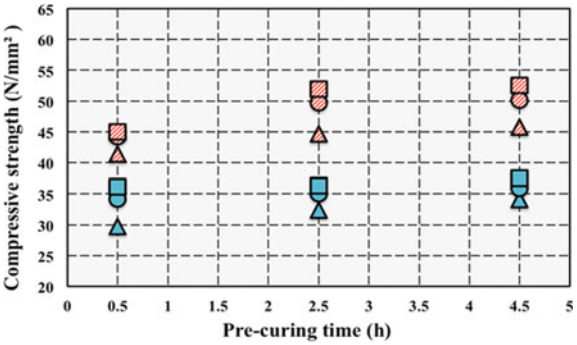

Fig. 5 Relationship between pre-curing time and compressive strength (3 days)

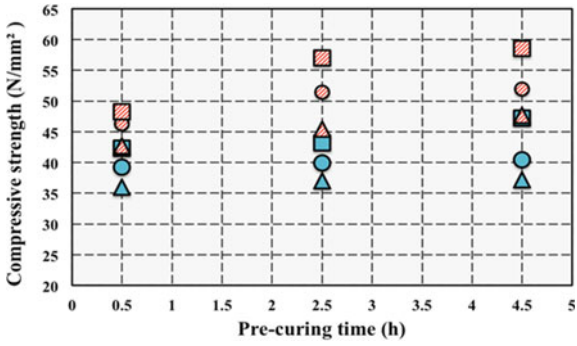

Fig. 6 Relationship between pre-curing time and compressive strength (7 days)

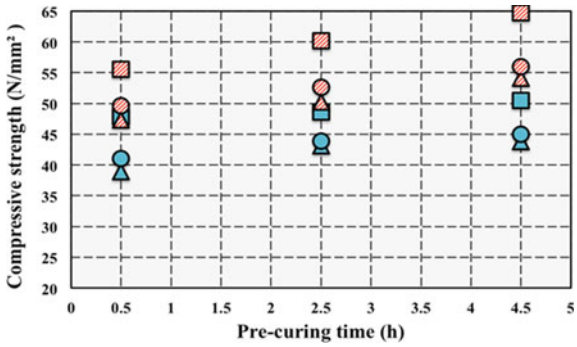

Fig. 7 Relationship between pre-curing time and compressive strength (14 days)

H-cement mixture after 0.5 h of pre-curing and water curing. This is considered to be due to the fact that watering after demolding counteracted the drying of the specimens during the secondary curing period and the stagnation of the hydration reaction [31]. Furthermore, when the pre-curing times were compared, it was found that specimens with a shorter pre-curing time exhibited higher compressive strength regardless of the material used. For example, for the pre-curing times shown in Figs. 5 and 6, the N-cement and H-cement blends showed the same or higher compressive strength

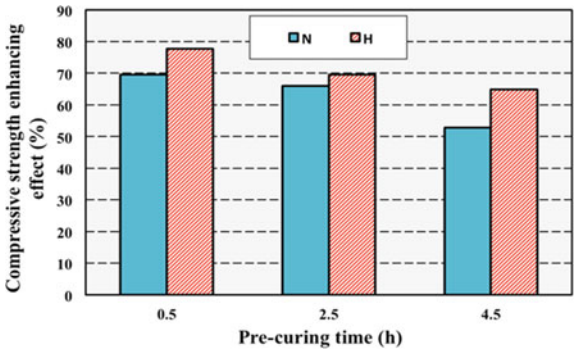

Fig. 8 Relationship between pre-curing time and compressive strength enhancement effect (3 days)

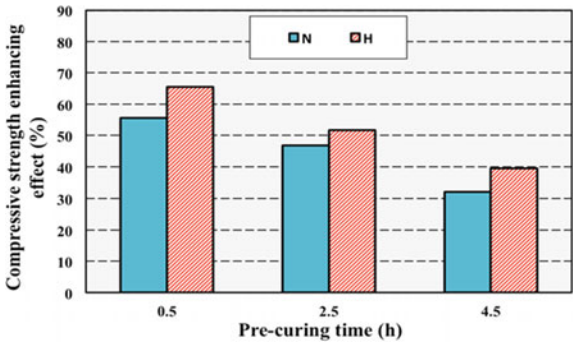

Fig. 9 Relationship between pre-curing time and compressive strength enhancement effect (7 days)

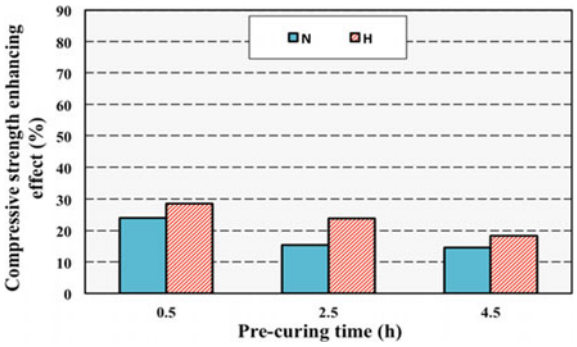

Fig. 10 Relationship between pre-curing time and compressive strength enhancement effect (14 days)

at material ages of 3 days and 7 days, respectively, compared to the specimen with 4.5 h of atmospheric curing after water sprinkling curing and pre-curing for 0.5 h. The compressive strength of the specimens was as high as or higher than that of the specimens cured in the atmosphere for 4.5 h.

Figure 7 shows that the compressive strength of the N-cement and H-cement blends at 14 days of age was as high as or higher than that of the N-cement and H-cement blends following 4.5 h of atmospheric curing after water sprinkling curing

and 2.5 h of pre-curing time. These results indicate that 10 min of water sprinkling curing can shorten the pre-curing time by 4 h for material aged 3 and 7 days, and by 2 h for a material aged 14 days of material age. In Japan, a pre-curing time of 2–3 h is stipulated for steam curing in order during the manufacture of PCa products [32], and we believe that water sprinkling curing can shorten the manufacturing process and lead to improved productivity.

Figures 8 through 10 show that the H-cement blend had more compressive strength enhancement than the N-cement blend for all pre-curing times. This is because the specific surface area of H-cement is larger than that of N-cement [29], and the moisture supplied by water sprinkling accelerates the hydration reaction, resulting in a greater strength than is obtained from atmospheric curing alone. Furthermore, it was found that specimens with a shorter pre-curing time exhibit higher compressive strength regardless of the material used. This may be due to the fact that the short pre-curing time tended to coarsen the micro-structure, allowing the water supplied during water sprinkling curing to penetrate more easily. The difference between the N-cement and H-cement blends was about 10% from 0.5 to 4.5 h of pre-curing time at 14 days of age, which is the standard for shipping PCa products, suggesting that water sprinkling curing would be effective if it is incorporated into actual PCa plants.

4 Conclusion

In this study, the following findings were obtained. It was found that the compressive strength enhancing effect is high when the material age is low, the pre-curing time is short, and H-cement is used. The pre-curing time is specified to be 2 to 3 h, but it was found that pre-curing can be shortened by following it with water sprinkling curing, which leads to improved productivity.

From the above, it is considered that the greatest increase in compressive strength can be expected by using H-cement and shortening the pre-curing time, assuming that short-duration water sprinkling is incorporated in actual precast concrete plants. However, detailed tests on the pore structure inside the mortar to support the above results were not conducted in this study and should be considered in the future.

References

1. Choi H, Taehoon K, Choi H, Hama Y (2019) Performance evaluation of precast concrete using microwave heating form. Materials 12:2–18
2. Wu P, Low S-P (2012) Lean management and low carbon emissions in precast concrete factories in Singapore. Archit Eng 18:176–186
3. Ho DWS, Chua CW, Tam CT (2003) Steam-cured concrete incorporating mineral admixtures. Cem Concr Res 33:595–601

4. Liu H, Qi Y, Chen Z, Tong H, Liu C, Zhuang M (2021) Ultrasonic inspection of grouted splice sleeves in precast concrete structures using elastic reverse time migration method. Mech Syst Signal Process 148:2–10
5. Zhang Z, Zhang B, Yan P (2016) Hydration and microstructures of concrete containing raw or densified silica fume at different curing temperatures. Constr Build Mater 121:483–490
6. Aldea C-M, Young F, Wang K, Shah SP (2000) Effects of curing conditions on properties of concrete using slag replacement. Cem Concr Res 30:465–472
7. Eedem TK, Turanli L, Erdogan TY (2003) Setting time: an important criterion to determine the length of the delay period before steam curing of concrete. Cem Concr Res 33:741–745
8. Rostami V, Shao Y, Boyd AJ (2012) Carbonation curing versus steam curing for precast concrete production. Mat Civil Eng 24:1221–1229
9. Zhong Y, Xiong F, Chen F, Deng A, Chen W, Zhu X (2019) Experimental study on a novel dry connection for a precast concrete beam-to-column joint. Sustain 11:2–22
10. Shufeng L, Qingning L, Hao Z, Haotian J, Lei Y, Weishan J (2018) Experimental study of a fabricated confined concrete beam-to-column connection with end plates. Constr Build Mater 158:208–216
11. Feng B, Xiong F, Chen F, Chen W, Zhang Y (2018) Effects of postcast connection locations on the seismic performance of precast concrete frame joints. Struct Design Tall Spec Build 27:208–216
12. Hsien TY (1997) The economic implications of subcontracting practice on building Prefabrication. Autom Constr 6:163–174
13. Bi L, Long G, Ma C, Xie Y (2020) Mechanical properties and water absorption of steam—cured mortar containing phase change composites. Conc Build Mat 248:2–13
14. Potal G (2008) Factors Affecting the use of precast concrete systems in the United States. Con Eng Manage 134(3):169–178
15. Kurama YC, Sritharan S, Fleischman RB, Retrepo JI, Henry RS, Cleland NM, Ghosh SK, Patricio B (2018) Seismic-resistant precast concrete structures: state of the art. Struct Eng 144(4):1–18
16. ToPcu IB, Toprak MU (2005) Fine aggregate and curing temperature effect on concrete maturity. Cem Concr Res 35:758–762
17. Otabe Y, Terano I, Suzuki Y (1998) Application of expansive concrete to the products by steam curing. Proc Japan Con Inst 20(2):145–150 (in Japan).
18. Oluokun FA, Burdette EG, Deatherage JH (1961) Rates of development of concrete at early ages. Am Conc Inst 58(38):281–298
19. Oluokun FA, Burdette EG, Deatherage JH (2010) Concrete physical property development at early ages: the influence of steam curing. Transp Res Record, 31–36
20. Xiang Y, Long G, Xie Y, Zheng K, He Z, Ma K, Zeng X, Wang M (2020) Thermal damage and its controlling methods of high-speed railway steam-cured concrete: a review. Struct Concr 22:1074–1092
21. Liu B, Jiang J, Shen S, Zhou F, Shi J, He Z (2020) Effects of curing methods of concrete after steam curing on mechanical strength and permeability. Constr Build Mater 256:1–10
22. Li X, Niu W-Y (2016) Effect of supplementary curing after steam-curing on performance of concrete. Mater Sci Forum 852:1376–1382
23. He Z-M, Long G-C (2012) Influence of subsequent curing on water sorptivity and pore structure of steam-cured concrete. Central South Univ 19:1155–1162
24. Katsuoka N, Yokokawa R, Uno Y, Date S (2021) Effect of initial water sprinkling curing on strength development of precast concrete. Ann Meet Cement Conc Eng 75:132–133 (in Japan)
25. Kolo SS, James O, Ndoke PN (2013) Effect of different curing methods on the compressive strength of concrete. Cem Con Comp, 12335–12339
26. Raheem AA, Soyingbe AA, Emenike AJ (2013) Effect of curing methods on density and compressive strength of concrete. Appl Sci Tech 3(4):55–64
27. Ullah N (2020) Effects of cold and hot water curing on compressive strength of concrete, 2–14
28. LNCS Homepage. https://www.pref.yamaguchi.lg.jp/uploaded/attachment/65789.pdf, last accessed 2022/8/19

29. Japan Cement Association: Report of the Technical of the Technical Committee on Concrete (2006) A study on the strength development of concrete under different steam curing conditions, 1–59
30. Eskandarsefa S (2018) Investigation on the effects of mix water temperature on high-early-strength cement concrete properties—an experimental work and a case study. Build Eng 20:208–212
31. Mannan MA, Basri HB, Zain MFM, Islam MN (2002) Effect of curing conditions on the properties of OPS-concrete. Build Env 37:1167–1171
32. Japan Society of Civil Engineers: Standard Specification for Concrete Structures (2002) Mat Const, 252–253

Influence of Polymer on the Coating of Hydroxypropyl Methyl Cellulose and Redispersible Polymer Mortars

Nahomi L. Castro, Pablo J. Hidalgo, Wilson A. Lazo, and Katherine W. Toralva

Abstract A common problem of concrete coating is the setting, in addition to the resistance and among other common factors that influence the workability of the material in the coatings, in the investigation it is desired to add to the coating mortar the hydroxypropyl methyl cellulose and redispersible polymer looking for the improvement in the behavior of mortar in the coating, for a long time the coating mortar has been evolving to improve the quality of the designs of the constructions. This process led to creation of constant improvements in mortars, on the other hand cellulose and redispersible polymer are polymers that have had a good reaction in the behavior with concrete for constructions, the present research focuses on measuring resistance and setting of a mortar with polymers and a traditional mortar for coatings, comparing both mortars demonstrate the workability and mortar quality. The results show that the mortar with polymers has better quality and is more workable than traditional mortar, giving positive results in the resistance tests and setting. At the end of the research, it was possible to verify through the resistance test and setting that mortar with polymers is better when it is used in the lining of the internal and external walls.

Keywords Coating · Polymers · Mortar · Endurance · Forge

1 Introduction

Over the years, buildings and constructions showed an evolution in their internal and external coating, the coatings intervened not only for design but also for human protection. Some historical currents place that coating use is deep from England in the sixteenth century, mainly for interior sections of stone walls, thus, these can

N. L. Castro (✉) · P. J. Hidalgo
Professional Academic School of Architecture, Universidad Continental, Huancayo, Junín, Perú
e-mail: 70400298@continental.edu.pe

W. A. Lazo · K. W. Toralva
Faculty of Engineering, Universidad Continental, Huancayo, Junín, Perú

T. Kang (ed.), *Proceedings of 5th International Conference on Civil Engineering and Architecture*, Lecture Notes in Civil Engineering 369,
https://doi.org/10.1007/978-981-99-4049-3_13

to counteract external effects such as cold and humidity [1]. On the other hand, exterior coatings are also important for buildings protection. Brick, marble and tile are among the most popular materials. From the nineteenth century onwards, the covering concept and building protecting cannot longer do without the new instance of the truth of structures and materials [2]. In addition, from a circular economy point of view, an economically viable and environmentally friendly method must be developed to recover these industrial wastes efficiently for materials development [3]. The growing interest in the maintenance of built heritage has led to the development of specific materials for this work. In repair projects, damaged concrete must be removed and replaced with a material that improves or at least reproduces substrate performance; this performance is measured in terms of resistance and also protection against entry of aggressive agents [4]. It can be stated, without any doubt, that components and techniques for elaboration and execution of mortars in ancient times have been the basis of raw materials used today, always taking into account the existence of an unquestionable improvement in qualities of the materials and a technological evolution that has modernized the construction process [5]. Under this problematic and being the cement-sand mortar the main component used in the union of masonry and buildings cladding, it is necessary to study an alternative to improve the quality, strength and impermeability, in order to protect the building and mainly the health of its occupants [6]. As for the basic constructive functions that mortars have performed in ancient times, it can be said that they have not changed substantially with respect to the current ones. Therefore, mortars were used as bonding materials for the construction of various models of masonry, protective coatings, decoration of masonry and other elements of certain types of constructions [7]. The first standard mortar of cement and sand, was dosed using the abacus application methodology with a cement-sand ratio of 1:3. The second standard mortar of cement, lime and sand in a ratio of 1:1/2:21/4 for type N mortars, was dosed according to the volumetric method established in the NTE INEN 2518 standard [8]. In general, cement repair mortars with polymers have better adhesion and greater resistance to the penetration of aggressive agents [9]. The time during which a mortar has sufficient workability to be used without further addition of water in order to counteract the effects of hardening by the setting principle. It is determined in accordance with the operating procedure of the European Standard UNE-EN 1015-9 [10]. It also resulted in a better interfacial transition zone with a more homogeneous distribution, as well as a microstructure with lower porosity around the internal curing material [lightweight fine aggregate] in the case of the thermally cured mortar [11]. The boom in recent years in the repair of concrete buildings and structures has led to the development of increasingly technological repair mortars. In the development of these mortars by manufacturers, a dilemma arises in the use of polymers in their formulations, as the performance/price/time trinomial is sometimes not justified [12]. A recurring problem in block and mortar walls is humidity, which affects not only the aesthetics of homes and buildings, but also people health who live in them [13]. On the other hand, in the hardening process, mortar may suffer cracks due to plastic or thermal shrinkage, which contribute to greater ease of water absorption [14]. Therefore, in this project, it is desired to make a mortar for the coating, with greater resistance

that helps to improve construction process in workability behavior before mortar setting. In addition, the quality in terms of resistance and homogeneity of final finish is demonstrated, thus differentiating polymer coating from traditional coating.

2 Materials and Methods

Research method demonstrates the traditional mortar performance [cement and fine sand] compared to a polymer composite mortar [fine sand, cement, cellulose [HPMC] and re-dispensable]. Since the fibers must be added in adequate percentages in relation to mortar volume, without diminishing the workability of the mixture, and giving good results [15]. There is some research that promotes fibers use in mortars either cement or with lime additions to improve their characteristics [16], for wall coating of 16 m2 with 1 year of age, composed with the same dosages for a traditional mortar is used, 320 kl of sand, 80 kl of cement, 0.280 of hydroxypropyl methyl cellulose [HPMC] and 0.32 kl of redispersible polymer. Test methods and procedures are detailed for determining the rebound number strength of hardened concrete under sclerometer test [ASTM C805/C805 M-08] and the setting time of concrete mixtures for their resistance to penetration under the standard [ASTMC403/C403M-08]. The strength standard ASTM C805—NTG 41,017 h11 and the setting test under ASTM C 403 NTG 41,017 h12 in which strength is measured over time for significant improvement in mortar performance [NTE INEN 2518] [6].

2.1 Fine Aggregate [Sand]

Fine aggregates are hard and inert materials used to prepare concretes or mortars that pass through the 4.75 mm sieve, also called fine sand [17]. The aggregate used comes from the Pilcomayo quarry located in the province of Huancayo, Junín region. It has a specific weight of 2.60 g/cm3 [NTE INEN 858], unit weight 1,649.13 kg/cm3 [NTE INEN 856], absorption capacity 0.75% [NTE INEN 856], fineness modulus 1.79% [NTE INEN 862], and organic matter content 5%. The determination of organic impurities in the fine aggregate was also carried out, following the NTEINEN 855 standard, obtaining a small amount of organic matter in the aggregate, which does not influence the mechanical properties of the mortars.

2.2 Cement

Portland cement Type I NTE INEN 152, called ANDINO, was used, which meets the requirements of the NTC 321 and ASTM—C150-07 standards and comes in 42.5 kg per bag. Since natural fibers continuously lose their properties once they are immersed in a cement-based matrix, in fact, the hydrophilic character of cabuya and the alkaline aggressiveness of the cementitious matrix can lead to fiber degradation of the mechanical properties of the composite [18]. Therefore, with the development of polymer science and technology, many polymers were used to modify cement or mortar to improve its properties [19].

2.3 HPMC [Cellulose] Hydroxypropyl Methylcellulose

HPMC is a nonionic polymer, a semi-synthetic derivative of cellulose, obtained by reacting alkyl cellulose with a mixture of methylene chloride and propylene oxide [20]. Since hydroxypropyl methyl cellulose [HPMC] is a cellulose ether polymer, ASTM C1438-11 mentions that powdered polymers improve the bond and reduce the permeability of concrete.

2.4 Redispersible Polymer

A polymer is a type of material based on compounds of natural or synthetic macromolecules, which is plasticized and formed at high temperature and pressure with appropriate fillers and additives, and maintains the shape of products unchanged at normal temperature and pressure [21]. Through a study in which the redispersible polymer powder was used, whose polymers are encapsulated and upon contact with water are released from the capsule for the use of repair mortars whose hydraulic compound is cement. As they are superplasticizers, their action as water reducers results in a greater durability of the mortar, which is why they are dosed in a proportion of less than 5% [22].

2.5 Dosage

In order to compare both mortars in terms of workability and quality of a traditional mortar with the polymer composite mortar, the following dosage is considered. The addition of some functional additives can make them have better performance and applications [23]. This parameter is normally used for the design and dosage of mortar, which is why it is important to know the compressive strength values of the

mortar for different values of the same [24]. In addition, in some dosages, cement: sand 1:3 and 1:4 were used, with percentages of ground porcelain tile as a substitute for sand for each dosage with a constant water/cement ratio of 0.65 [25]. Therefore, for the testing of mortars in a 16 m^2 wall, the dosage of,320 kl of sand, 80 kl of cement, 0.280 of cellulose [HPMC] and 0.32 kl of re-dispensable component was used.

2.6 Essay

Setting. The setting process was performed on traditional mortar and mortar with polymers, as a first step a sample of the mortar passed through the sieve #4 was obtained, then mold was completed in 01 layer that was compacted 25 times the mixture with a steel rod and the mold with the rubber hammer 10 to 15 times, the time required for the penetration of each needle 25 mm was 10 ± 2 s as shown in Fig. 1. In which each measurement was recorded at the time, calculating setting time by dividing the applied force by needle contact area and temperature, making eight intercalated and varied measurements according to behavior of mortar between 0.30, 1, 2 (h/min) until the penetration resistance is at least 27.6 MPa or 4000 psi. The setting time test followed NTP 339.082 and ASTM C-403 [26].

Resistance. Measurement of strength of traditional mortar lining with polymer composite mortar lining was performed. The indication value obtained from the rebound tests performed with a Schmidt hammer type L (sclerometer) as mentioned in ASTM C805/C805 M-08 [27], after the impact, pressure is maintained on the instrument to read the rebound number on the scale, and the average reading of 10 rebounds on a point is recorded, so that reading of 12 points was taken on the coating of a 16 m^2 wall in the mortar with polymers and in the traditional mortar as shown in Fig. 2.

Fig. 1 Setting measurement instruments

Fig. 2 Resistance measuring instruments

3 Results

Two mortars have been tested and placed under the same conditions, proportions, processes, times and operators for results reliability of both.

3.1 Setting

The consistency and setting time of mortar were tested in accordance with ASTM C187 [28]. and ASTM C191 [29]. Table 1 shows the results of the setting time of the mortar with polymers to compare the workability of the mortar.

In mortars with polymers case, the material consistency is denoted by time intervals of 0.30, 1.10, 0.40, 1.30 (h/min) in which it is understood that there is a constant setting time, however, from hour 6.42 (h/min) the qualitative exponential behavior begins, reaching rapidly its maximum capacity as shown in Fig. 3.

The setting time ratio for a traditional mortar under ASTM C403/C403M-08 is maintained as shown in Table 2.

In Fig. 4, there is a constant change from 3.40 (h.min).

The traditional mortar begins its setting process immediately, with significant hardening occurring after 3 h from the beginning of the mixing with constant growth, reaching a permanent resistance. Unlike mortar with polymers, it begins its setting process immediately, with significant hardening occurring 6 h after the start of mixing, with qualitative exponential growth, rapidly reaching its maximum capacity.

Table 1 Setting time results for polymer-based mortar NTP 339.082—ASTM C403

Setting time—additive									
Real time (h:min)	Absolute accumulated time (seconds)	Absolute accumulated time (h:min)	Needle diameter		Needle area used (pulg2)	Strength (libras)	Penetration resistance (PSI)	T° Concrete (°C)	T° environmental (°C)
			Fraction	Whole					
12:30	0:00	0:00			0	0	0	–	–
14:45	3240:00:00	2:15	1 1/8	1.125	0.994	135	135.81	12.8	10
15:16	3984:00:00	2:46	1 1/8	1.125	0.994	166	167	12.9	11
15:40	4560:00:00	3:10	1 1/8	1.125	0.994	190	191.14	13	11
16:20	5520:00:00	3:50	13/16	0.813	0.518	230	443.6	13	9.7
17:11	6744:00:00	4:41	13/16	0.813	0.518	281	541.96	13.1	8.7
19:12	9648:00:00	6:42	3/8	0.375	0.11	402	3639.76	13.4	10.5
20:12	11.088:00	7:42	1/4	0.188	0.028	462	16.732.03	13.3	9.4
21:12	12.528:00	8:42	3/16	0.188	0.028	522	18.905.02	13	9
Initial setting time						444	minutes	4:06	Hours:min
Final setting time						397	minutes	6:36	Hours:min

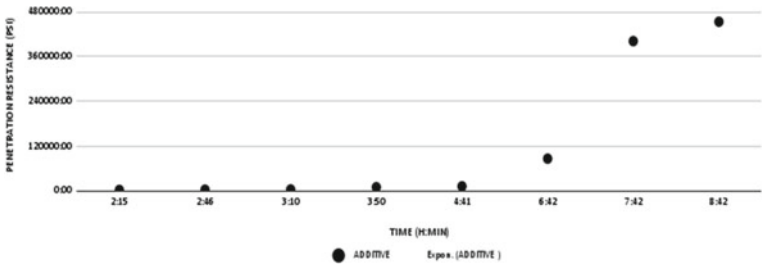

Fig. 3 Setting time—polymer coating

3.2 Resistance (Sclerometry)

After the rebound hammer has contact with the coating as mentioned in ASTM C805/C805 M-08, pressure is maintained on the instrument to read the rebound number on the scale with the surface of the coating, taking the average of 10 rebounds on a point, the reading of 12 points was taken on the coating of a wall of 16 m^2 of area with polymer mortar and traditional mortar as shown in Table 3.

The relationships between rebound number and concrete strength are used to give indications of the relative strength of concrete in different regions of the wall as stated in ASTM C805/C805 M-08, and the strength is constant as shown in Fig. 5.

The constant change differs in the traditional mortar resistance and a mortar with polymers, being so that maximum traditional mortar capacity is 291 kg/cm^2 unlike the mortar with polymers which is 318 kg/cm^2, also shows traditional mortar homogeneity and the mortar with polymers final finish as shown in Fig. 6.

Figure 6a shows the wall with cement and fine sand in the lining. Figure 6b shows the wall with cement, fine sand, hydroxypropyl methyl cellulose and redispersible polymer in the coating, giving this mortar the quality in the homogeneity of the result.

Table 2 Setting time results of traditional mortar

Setting time—pattern									
Real time (h:min)	Absolute accumulated time (seconds)	Absolute accumulated time (h:min)	Needle diameter		Needle area used (pulg2)	Strength (libras)	Penetration resistance (PSI)	T° concrete (°C)	T° environmental (°C)
			Fraction	Whole					
12:00	0:00	0:00			0	0	0	-	-
14:14	3216:00:00	2:14	1 1/8	1.125	0.994	135	135.81	12.8	10
14:45	3960:00:00	2:45	1 1/8	1.125	0.994	165	166	12.9	11
15:16	4704:00:00	3:16	13/16	0.813	0.519	195	376.08	13	11
15:40	5280:00:00	3:40	13/16	0.813	0.11	266	2409.42	13	9.7
16:20	6240:00:00	4:20	5/9	0.563	0.049	300	6109.98	13.1	8.7
17:11	7464:00:00	5:11	1/4	0.25	0.028	351	12.717.39	13.4	10.5
19:12	10.368:00	7:12	1/4	0.188	0.028	468	16.956.52	13.3	9.4
20:12	11.808:00	8:12	13/16	0.188	0.028	503	18.216.9	13	9
Initial setting time						313	minutes	2:53	Hours:min
Final setting time						319	minutes	5:19	Hours:min

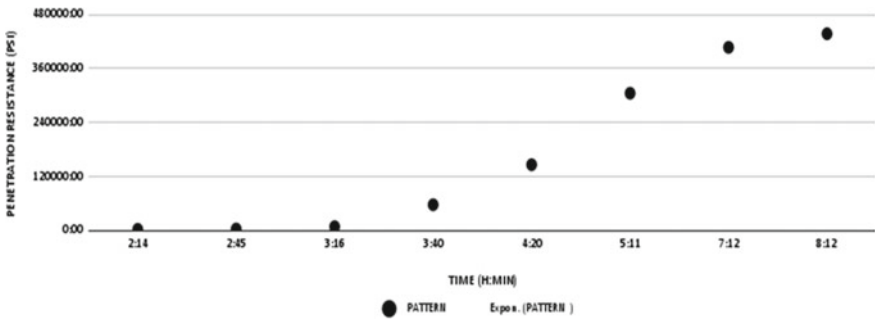

Fig. 4 Setting time for coating with traditional mortar

Table 3 Average of each rebound number per point

Point	Resistance (traditional mortar) (kg/cm^2)	Resistance (composite mortar) (kg/cm^2)
1	291	316
2	288	311
3	280	314
4	274	315
5	278	314
6	280	314
7	282	318
8	282	317
9	276	318
10	273	313
11	276	312
12	284	314

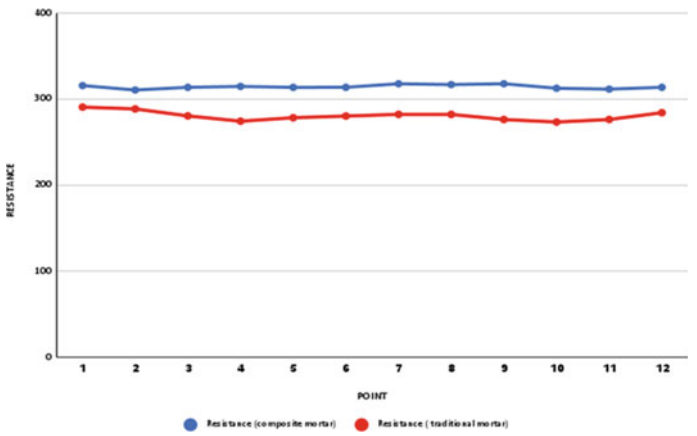

Fig. 5 Comparison of traditional mortar and composite mortar

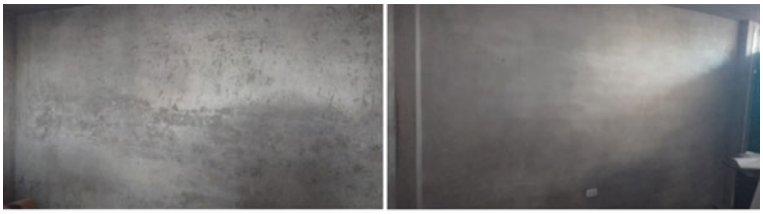

Fig. 6 Comparison of the quality of traditional mortar and polymer-based mortar

4 Conclusion

In the two tests carried out, both in the setting time test of concrete mortar for its resistance to penetration and in the rebound number test in hardened concrete, different results were obtained. In the setting time test, it was shown that there is a difference in the hardening of both mortars. The mortar with polymers shows a hardening behavior around 6 h after the starting time, presenting a qualitative exponential growth. This indicates that mortar with polymers has more resistance to penetration, being a more workable compound especially in the construction process of the coating, unlike a traditional mortar since it presents a hardening reaction about 3 h after the beginning of the preparation of the mortar having a constant growth, in which it is concluded that the mortar with hydroxypropyl methyl cellulose and redispersible polymer present a favorable trend in terms of the workability of the material. Comparing both results we can know that it is convenient to use mortars with polymers since it presents more resistance to penetration and has twice the performance capacity to the hardening time of a traditional mortar. The tests were carried out to learn about the influence of polymers on the construction materials and the need for them in terms of man-hour reduction for this construction process.

On the other hand, the rebound number test in hardened concrete shows the quality of the mortar with polymers, since it presents a higher resistance with a minimum range of 311 kg/cm^2 and a maximum of 318 kg/cm^2 of resistance as opposed to the traditional mortar with a minimum range of 273 kg/cm^2 and a maximum of 291 kg/cm2 with the specified dosage. The aforementioned data show that for a better performance of the mortar placed on site, a dosage of 0.1% hydroxypropyl methyl cellulose and 0.2% redispersible polymer of 100% of the dosage of the traditional mortar is necessary, thus being a constant for any area to intervene that significantly helps to improve the workability performance and quality of the mortar for the coating.

5 Discussion

Just as adding any type of fiber to a mortar makes it much more susceptible to the passage of water under pressure conditions than synthetic polypropylene fibers, so natural cabuya fibers added to a mortar influence the permeability of mortars [9]. It is demonstrated that the influence of polymers in a mortar or others is significant in saving time / labor as for example, the hydroxypropyl methyl cellulose and redispersible polymer that through the test of the setting time of concrete mortar for its resistance to penetration and in the test of the number of rebound in hardened concrete shows a favorable behavior in the workability and quality in the development of the coating in a work.

References

1. Origins and history of the coating (Internet). Continuous coatings. Tuesday, 7 July 2015. Available in: http://revestimientos-continuos.blogspot.com/2015/07/origenes-e-historia-del-revestimiento.html
2. Fannelli G, Gargiani R (2001) The Principle of the coating. Akal Ediciones
3. Kuok CH, Dianbudiyanto W, Liu SH (2022) A simple method to valorize silica sludges into sustainable coatings for indoor humidity buffering. Sustain Environ Res 32:8. https://doi.org/10.1186/s42834-022-00120-3
4. Quian J, You C, Wang Q, Wang H, Jia X (2014) A method for assessing bond performance of cement-based repair materials. Constr Build Mater 68:307–313
5. De Guzman DS (2001) Concrete and mortar technology. Bhandar Editores, Bogotá
6. Viera P, Morales L, Monzó JM (2019) Design and characterisation of a composite based on lime, cement and natural fibres for buildings. In: Proceedings of the VII REDU Congress. Retrieved from https://issuu.com/yyachaytech/docs/redu2019_-royectos_completos
7. Zaruma L (2018) Waterproof mortar based on recycled PET plastic for building cladding in the city of Zamora [Master's thesis]. Retrieved from
8. American Concrete Institute (2002) ACI 544.1R-96. Report on Fiber Reinforced Concrete. Recuperado de http://indiafiber.com/Files/ACI%20report.pdf
9. Viera P, Morillo D, Parion J (2022) Influence of natural and synthetic fibres on the permeability of cement-sand and cement-lime-sand mortars. FIGEMPA: Res Develop 13(1):59–71. https://doi.org/10.29166/revfig.v13i1.3410
10. National Association of Mortar Manufacturers [AFAM] (2018) Characteristics of mortars. Retrieved from https://www.construmatica.com/construpedia/Caracter%C3%ADsticas_de_los_Morteros
11. Liu Y, Wang J, Hu S, Cao S, Wang F (2022) Enhancing the mechanical behaviour of concretes through polymer modification of the aggregate-cement paste interface. J Build Eng 54:104605. https://doi.org/10.1016/j.conbuildmat.2016.05.159
12. Lucas AG (2014) Durability performance of polymer-modified cement repair mortars. Thesis [Doctoral], E.T.S.I. Roads, Canals and Ports [UPM]. https://oa.upm.es/33130/
13. Girón A, Ramírez F (2016) Surface waterproofing in building construction [Degree thesis]. Retrieved from http://hdl.handle.net/11349/4982
14. Castilla FJ (2022) Coatings and surface finishes in contemporary earthen constructions. infconstr [Internet]. September 30, 2011 [cited June 16, 2022] 63(523):143–52. Available from:https://informesdelaconstruccion.revistas.csic.es/index.php/informesdelaconstruccion/article/view/1260

15. Bustos A (2018) Mortars with improved ductility properties by addition of glass, carbon and basalt fibres [PhD thesis]. Retrieved from https://oa.upm.es/54114/
16. Castro J (2016) Glass, steel and polypropylene fibres in the form of lint, applied as reinforcement fibres in the manufacture of cement mortars. Recovered from https://repositorio.uta.edu.ec/jspui/handle/123456789/23307
17. Halinco de (2022) Materials [online] Available at: Accessed 16 June 2022. http://www.halinco.de/html/proy-es/tec_const/Horm-Armado/Materiales.html
18. Coudert L (2022) Influence of the surface treatment of fique fibres on the mechanical properties of the fibre-cementing matrix composite [online], 2020110 [Date consulted: 16 June 2022]
19. Shen J, Liang J, Lin X, Lin H, Yu J, Yang Z (2020) Recent progress in polymer-based construction materials. Int J Poly Sci, Article ID 8838160, 15 p.https://doi.org/10.1155/2020/8838160
20. Kumar V, Banker G (1993) Drug Dev Ind Pharm 19:1–31. https://doi.org/10.3109/03639049309038760
21. Fu H, Xu H, Liu Y et al (2020) Overview of injection moulding technology for processing polymers and their composites. ES Mat Manufact 8:3–23. http://www.espublisher.com/journals/articledetails/285
22. González Á, Villanueva P, Fernández J, Rubio M (2016) Analysis of the porous structure and life cycle of cement-based repair mortars with polymers. XII Congresso Internacional sobre Patologia e Reabilitaçao de Estruturas [CINPAR 20016], 26/10/2016–29/10/2016, Porto, Portugal. pp 1–12.https://oa.upm.es/46403/
23. Xie J, Teng L, Yang Z et al (2013) A polyethylenimine-linoleic acid conjugate for antisense oligonucleotide delivery. BioMed Res Int, Article ID 710502, 7 p. https://www.hindawi.com/journals/bmri/2013/710502/
24. Correa RA (1985) Mortar dosing. In: g. investment [Internet], January 1 [cited 2022 June 16] 11:17–23. Available from: https://revistas.unal.edu.co/index.php/ingeinv/article/view/19502
25. Villarroel JA (2017) Evaluation of recycled porcelain tile and dosage in bedding mortar on compressive strength, absorption, density and flow, Trujillo 2017 [Thesis]. Universidad Privada del Norte Repository. Retrieved from http://hdl.handle.net/11537/10191
26. ASTM C403/C403M-08, Testing method. Determination of the setting time of concrete mixtures for their resistance to penetration
27. ASTM C805/C805 M-08, Testing method. Determination of the rebound number in hardened concrete
28. STM C187, Standard Test Method for Amount of Water Required for Normal Consistency of Hydraulic Paste
29. ASTM C191, Standard Test for Time of Setting of Hydraulic Cement by Vicat Needle

Comparison of Autoclaved Aerated Concrete (AAC) Blocks and CHB Using Life-Cycle Cost Analysis

Aldrine Paul P. Bornales, Mark Arvin P. Velasco, Jomar A. Layderos, and Orlean G. Dela Cruz

Abstract Concrete hollow blocks (CHB) have been used worldwide, especially in the Philippines, due to their cost-saving and lightweight features. Moreover, the energy-efficient CHB promotes faster construction process thereby expediting construction project schedule. However, continuous development in masonry construction introduces more potential masonry products like Autoclaved Aerated Concrete (AAC) blocks. The simplicity of installation and its ability to be part of the structural system make it a more excellent choice over the conventional CHB. In this study, performing life-cycle cost analysis (LCCA) can compare the costs involved between AAC blocks and CHB throughout its service life. Initial fees and future fees of CHB and AAC blocks construction complete the parameters to be evaluated in LCCA. Using a residential building located in Malabon City, Philippines with CHB as the base case, it was found that AAC blocks can be a cheaper choice than the CHB blocks by a slight margin. Nearly negligible difference in the total life-cycle cost (LCC) between CHB and AAC blocks in a 50-year consideration, was discovered in this research. Initial cost of masonry construction dominated the total LCC

A. P. P. Bornales (✉) · M. A. P. Velasco · J. A. Layderos · O. G. Dela Cruz
Graduate School, Polytechnic University of the Philippines, Manila, Philippines
e-mail: aldrine.bornales09@gmail.com

M. A. P. Velasco
e-mail: markarvinpvelasco@gmail.com

J. A. Layderos
e-mail: engr.jalayderos@gmail.com

O. G. Dela Cruz
e-mail: ogdelacruz@pup.edu.ph

A. P. P. Bornales
APB Planning & Design Engineering Services, Rizal, Philippines

J. A. Layderos
Philippine Atmospheric, Geophysical, and Astronomical Services Administration, Quezon City, Philippines

M. A. P. Velasco
Engineering Department, International Design Services, Inc., Quezon City, Philippines

T. Kang (ed.), *Proceedings of 5th International Conference on Civil Engineering and Architecture*, Lecture Notes in Civil Engineering 369,
https://doi.org/10.1007/978-981-99-4049-3_14

which make it the most significant percentage of LCC. Due to minor difference in LCC, a non-cost related analysis between CHB and AAC blocks might show a more comprehensive comparative analysis.

Keywords Autoclaved aerated concrete blocks · Concrete hollow blocks · Life-cycle cost analysis · Low-cost structure · Masonry construction

1 Introduction

Construction of buildings worldwide usually uses concrete blocks due to their energy-efficient, easy-to-install, and lightweight characteristics [1]. Moreover, applying concrete hollow blocks (CHB) enables a faster construction process while reducing construction costs [2]. In the Philippines, using CHB masonry structures has always been a top priority in residential buildings [3]. In other countries like Lebanon, CHB has been a wise choice in masonry units as it has excellent advantages, including lifespan, resistance to fire, low cost and maintenance, and simplicity in implementation [4]. However, due to emerging technologies and modern inventions, the continuous development of masonry construction is unending. Hence, introducing new products that promote cost-saving and resilient structures has continued throughout the decades.

A frontrunner as an alternative to CHB in modern construction is the Autoclaved Aerated Concrete (AAC) blocks. Promising attributes of AAC blocks have been shown in modern buildings to bring efficiency. Thus, it is also a significant concern to study AAC blocks to replace CHB. Primarily, AAC blocks are much lighter and stronger than CHB. Hence, the lightness and stiffness it characterizes could lead to easier handling and optimal structural member sizing, respectively, which may lead to more practical and efficient construction techniques on a large scale. Furthermore, in academic literature, AAC blocks were proposed as an adequate replacement in renovations or retrofits as they lessen disturbances to occupants [5]. However, smooth surfaces of usual AAC blocks lead to lesser bond strength than conventional masonry units like bricks [6].

CHB that the AAC blocks have edge and other commonly used masonry blocks around the world, especially on the environmental effects. Bricks, also known as masonry, pose a more significant concern for the environment than other masonry blocks. Several types of blocks can be utilized as an alternative to red bricks to alleviate pollution and global warming issues. AAC blocks could be a viable option for replacing clay bricks, a relative phenomenon in the Indian construction business. Even though AAC manufacture has increased dramatically, its market share is still relatively tiny compared to red bricks. The production of AAC blocks has no negative impact on the environment. In addition, AAC blocks are smooth and almost eight times larger than red clay bricks, as well as lighter. The bricks are standard in size, but compared to aerated concrete blocks, they are not as strong. The increased size of AAC blocks allows for speedier masonry construction and lower project costs. AAC

has an outstanding feature that makes it a superb insulator, allowing for easier maintenance of the interior environment. Lightweight, high strength, strong durability, heat preservation, sound insulation, fireproofing, impermeable, and good anchoring capabilities characterize AAC blocks. AAC is a certified green building material that is porous, nontoxic, reusable, renewable, and recyclable and can use in commercial, industrial, and residential construction [7].

Achieving construction success is sometimes defined by the project cost or budget limit. Since the use of CHB significantly plays a significant portion of construction cost, it might be valuable to analyze and perform value engineering over it. This study examines the efficacy of using AAC blocks over CHB in terms of efficiency and project cost.

Because of its numerous advantages, lightweight autoclaved aerated concrete (AAC) block masonry in earthquake-resistant infilled reinforced concrete (RC) frame buildings is gaining favor. As a result, a thorough understanding of the strength qualities of AAC block masonry requires an accurate assessment of the seismic behavior of such structures. Using laboratory tests, evaluate the uncertainties associated with the two most essential factors that determine the resistance capacity of infilled brickwork and the proposed best-fitted probability density functions. Furthermore, the in-plane seismic performances of typical RC frame structures infilled with AAC block masonry are analyzed in a probabilistic framework using specified probability density functions, demonstrating that an assumed normal distribution is inadequate for this purpose. Although the reduced strength qualities of lightweight AAC block masonry marginally enhance the building's seismic risk compared to traditional brick masonry. It may be utilized safely as an infill material in locations with high seismicity since it meets the code-required dependability index [8].

Meanwhile, Life-Cycle Cost Analysis (LCCA) is a recognized method of determining the cost of the building throughout its life [9]. However, recent literature has limited research on LCCA, especially on comparative analysis of CHB and AAC blocks in the Philippines. Therefore, this study aims to compare the life-cycle costs (LCC) of CHB and AAC blocks using LCCA. The residential building that used CHB on masonry walls is the base case since it is the conventional masonry unit in the Philippines. After LCCA calculation, cost savings are determined to determine which CHB and AAC blocks are the more economical option in the long run.

2 Conventional Process of Masonry Construction

In most construction, the bounding walls encompassing a building is a product of CHB laying. The simplicity of the process of CHB laying makes it the standard choice in building walls. Inside the CHBs, adding steel reinforcing bars vertically and horizontally to strengthen their resistance to lateral loads. In addition, cement can plaster a brick wall in preparation for painting. The CHBs installation is relatively inexpensive compared to other materials, but it is pretty hefty. CHB construction also offers rooms for secluding conduits, soil, and water pipes [10].

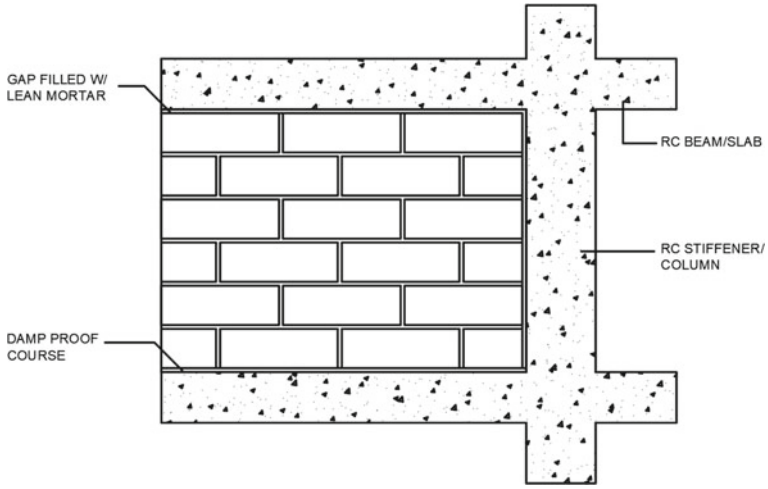

Fig. 1 Finished installation of AAC blocks

Meanwhile, for the setting of the AAC block, vertical alignment strings are first installed at least at each wall end, or corner alongside a 10 mm to 30 mm thick bed cement/ sand mortar leveling course (1:7 to 1:8 mix ratio) over DPC and a damp proof course (DPC)/slip joint at the ground level/wet area, precast/prestressed reinforced concrete slabs. The next step is setting the first block 10 mm to 30 mm away from the edge of the column or stiffener; then, tapping the block with a rubber mallet should be done to align it with the leveling string. Also, check the spirit level; apply the adhesive to the block perpendicular before laying subsequent blocks. ST2 Tie is afterward tied to a column or stiffener & bedded into the adhesive at the block horizontal joint and the remaining first course blocks. Cut block to 300 mm length should then be done to achieve stretcher bond laying pattern (100 mm min., block overlap). Next is applying adhesive to the top of the first course and all perpends of adjacent blocks before placing subsequent blocks in the position. STE2 Tie spaced at 1200 mm centers horizontally should be established, and the first and last blocks of the final course. A 20 mm to 50 mm minimum gap filled with thin mortar cementing the sand ratio of 1:7 or 1:8, as shown in Fig. 1.

3 Concrete Hollow Blocks (CHB)

Since their development in 1890, concrete hollow blocks (CHB) have changed construction for decades. Concrete hollow blocks (CHB) have been one of the most widely utilized walling materials in the Philippines. Because it is resistant to weather, vermin, mold, and fire, it has become one of the most extensively used materials for masonry walls. Additionally, CHBs are inexpensive compared to other materials, and

semi-skilled laborers can install them easily. CHB is a widely available product with excellent thermal and sound insulation, great fire resistance, and a 20+ year lifespan. However, it is hampered in specific ways by the difficulty of obtaining acceptable quality raw materials for its products locally.

Masonry hollow blocks frequently use in construction due to their favorable physical characteristics (mechanical resistance, thermal and acoustic insulation, fire resistance, lifespan), low cost, convenience of use, and low maintenance requirements. In addition, numerous scientific and industrial efforts have been made to develop masonry units to satisfy today's energy-saving standards due to the constantly expanding international interest in building energy efficiency [11].

Concrete Hollow Block (CHB) has two types: load-bearing and non-load-bearing blocks. Load-bearing blocks are those that carry loads aside from their weight. Its thickness ranges from 15 to 20 cm. On the other hand, non-load-bearing blocks use as partitions, fences, dividers, and walls with a thickness of 7–10 cm [12].

Concrete Hollow Blocks (CHB), according to the American Society of Testing and Materials C126-71, are a unit made from Portland cement, water, and suitable mineral aggregate that has a core area of 40–50% of the gross area that provides air space in the concrete hollow block walls. It can be classified as Load Bearing or Non-Load Bearing Concrete Hollow Blocks. Load-bearing CHBs can carry superimposed loads, dead and live loads, while non-load bearings use as interior walls above grade. Concrete hollow blocks can also be considered average, lightweight, or heavyweight.

4 Autoclaved Aerated Concrete Blocks

AAC blocks might be the next phenomenal move in the construction industry. It brings another dimension to masonry construction without sacrificing structural integrity and project cost. A Swedish architect 1924 established AAC when he searched for an alternative material that characterizes excellent thermal insulation while having identical properties to wood [13]. Manufacturing projects of AAC blocks can be found in more than 40 countries and employed across 70 nations [14]. AAC blocks produce prefabricated panels and cuboid units [15]. AAC Blocks provide evident advantages over some conventional materials and processes in masonry. These blocks have the advantage of being around three times lighter than traditional bricks, reducing buildings' dead weight and the need for additional concrete and steel during construction. It offers lower handling and shipping costs as a result. They also reduce dead loads, improving earthquake resistance and lowering building costs. As a result of the lower dead load, foundation and structural cost savings may be more significant.

Moreover, AAC blocks are more prominent than traditional bricks, resulting in fewer joints and cost savings in cement and mortar. Due to their bigger size, AAC

blocks may be built more quickly than clay bricks, resulting in a quicker project timeline. Architecturally speaking, precast AAC components that have been machine-polished provide AAC blocks with accurate architectural design dimensions. AAC blocks are factory-made with completed edges and shapes, resulting in lower plaster costs. Because of the low density, the dead load was reduced, resulting in a reduction in structural steel consumption. AAC blocks cover a larger area for the same quantity of brick, resulting in lower shipping costs.

AAC blocks might also be a better option than other traditional masonry units in terms of cost savings for a construction project's thermal insulation. It is because these blocks have a lot of air bubbles, which improve thermal insulation and reduce the cost of cooling and heating. After all, they do not conduct heat well. As a result, it keeps the room cozy during the winter and relaxed throughout the summer. In addition, it conserves energy by lowering air conditioning needs by 25–30%.

As they are noncombustible and have a melting point of roughly 1500 degrees Celsius, which is substantially higher than that of standard building materials, AAC blocks have the potential to resist fire, which is exceptionally advantageous for future occupants of the building. Also, a fire doesn't emit toxic fumes, which helps to protect lives. Moreover, regarding insulation ability, AAC blocks' sound insulation qualities are more significant than those of traditional bricks.

A more straightforward methodology in construction also promotes a more straightforward execution. AAC blocks are easier to work with than wood. As a result, cutting it is simple, resulting in less cutting waste. Aside from construction execution, AAC blocks also support an eco-friendly setting. AAC's lightweight saves energy in transportation, lowering CO2 emissions from vehicles. Due to their higher density, clay bricks are more prone to fracture during shipping, while AAC blocks do not suffer. Fly ash waste is used in AAC to overcome the problem of disposal. As a result, it is an environmentally friendly building material.

When a violent ground motion occurs, AAC blocks perform better than other masonry units in terms of structural benefit. Because AAC blocks are a function of mass, they offer dead load to the structure, minimizing seismic forces.

AAC blocks presumably require less upkeep as well. AAC blocks are better than clay bricks in places with many slats in the topsoil because clay bricks frequently experience salt efflorescence, which is a problem with AAC blocks. AAC blocks are also a wise choice for masonry buildings because of their long-term usage. AAC does not need frequent maintenance because it does not deteriorate over time [16].

5 Methodology

This study, which focuses on comparing conveniently used CHB and AAC blocks, utilizes the LCCA to assess the total cost throughout its service life. The competitive global market continuously tries to improve product designs by reducing costs and time using emerging life cycle engineering [17]. Usually, Life-Cycle Cost Analysis (LCCA) is generally employed when alternatives to a project or material with a

similar purpose differ in terms of initial and operating costs in evaluating to choose which maximizes the net savings [18]. In the computation using LCCA, initial fees and future charges over a specified time frame are determined first [9]. Therefore, the lowest life-cycle price was determined in this research to measure the economic evaluation between AAC blocks and CHB.

A residential building located in Malabon City, Philippines, which applies CHB as the masonry wall unit, was selected as the base case in this study. Since AAC blocks affect structural members, geometry would change as the cost will also be affected. Thus, the consideration of beams and columns are considered in the construction costs. Since this is a comparative analysis, the construction cost parameters that are entirely identical between CHB and AAC blocks are omitted. Construction costs estimated in this study include material and labor costs. Construction materials or parameters considered are those with significant differences when assessed. All building materials' unit rates and installation rates were also estimated by experienced estimators using a 529 square meters area.

Meanwhile, maintenance and replacement costs are challenging to assess in masonry construction. These masonry units are seldom maintained even after long periods; hence, exact prices are unknown. The maintenance and replacement costs of CHB and AAC blocks are derived from the accurate estimators that quoted the initial construction costs. It is assumed that every ten years, the replacement will be done on the masonry walls; hence, included in the maintenance costs are the repainting and finishing works and labor costs. The estimated useful life of AAC blocks is almost 100 years [19]. However, in this study, a period of 50 years was used.

LCCA evaluates all substantial costs throughout building life [20]. A reasonable discount and inflation rates are applied to get the present value (PV) from future expenses. Future costs were solved using Eq. (1) by considering the recommended inflation rate. The future prices were then discounted using Eq. (2) to PV using a recommended discount rate.

$$\mathrm{FC} = \mathrm{PV}(1 + f)^n \tag{1}$$

$$\mathrm{DPV} = \mathrm{FC}(1 + r)^n \tag{2}$$

where FC is the future cost, PV is the present value, f depicts the inflation rate, DPV indicates the discounted current value, r is the discount rate, and n corresponds to the number of years [9]. Discount rates were taken as 10%, as adapted by most countries [21]. The inflation rate forecasted by [22], which is 3% in 2024, was adopted throughout the service life since it is the latest available prediction in academic literature. SIR (Savings-to-Investment Ratio), which is used to measure the efficacy of investment, was calculated [23]. On the other hand, Salvage value is not considered in this research because there is no data found in available academic literature.

Results of computed LCC were converted from Philippine Peso (₱) to US Dollar ($). After that, values were compared, and the implications of obtained data were

interpreted. In addition, to satisfy the aim of this research, the critical questions listed below need to be answered:

- Does using AAC blocks as masonry units of a building more cost-effective than CHB in terms of life cycle costs?
- Does the cost of AAC blocks as masonry units and CHB in terms of LCC significant?
- What parameter of building estimate contributes most to life-cycle costs?

6 Results and Discussions

This study seeks the comparative analysis between CHB and AAC blocks which was determined using LCCA. After the computations of LCC and savings, the results were tabulated as shown and interpreted.

Table 1 shows the initial cost of AAC blocks and CHB. A slight margin of 28.48 $/m^2 between the initial price of AAC blocks and CHB was determined, which is a 3.63% excess.

Meanwhile, Table 2 shows the estimated energy and water consumption costs of AAC blocks and CHB. A 0.01 $/m^2 difference or a 5.88% excess between the base case and the alternative one.

Table 3 shows the operation, maintenance, and repair costs of AAC blocks and CHB. Again, a significant margin of 0.26 $/m^2 between the initial price of AAC blocks and CHB was determined, which is a 35.00% excess.

Table 4 shows the life-cycle cost of AAC blocks and CHB. A negligible 0.05% increase in savings was found by using AAC blocks over CHB. SIR is calculated as 0.96, marginally less than 1, indicating that the investment is not cost-effective.

It is clearly shown in Table 5 that the initial costs dictate the life cycle cost. Therefore, garnering 99.850% and 99.898% of the total life-cycle cost is the most critical parameter for masonry construction costing.

Table 1 Initial Costs of AAC blocks and CHB

		Initial cost ($)	Unit rate ($/m^2)	Difference ($/m^2)	% excess
Base case	CHB	415,097.14	784.68	−28.48	3.63
Alternative	AAC	430,162.30	813.16		

Table 2 Energy and Water Consumption Costs of AAC blocks and CHB

		Energy and water cost ($)	Unit rate ($/m^2)	Difference ($/m^2)	% excess
Base case	CHB	62.05	0.12	−0.01	5.88
Alternative	AAC	58.40	0.11		

Table 3 The operation, maintenance, and repair costs of AAC blocks and CHB

		OM & R cost ($)	Unit rate ($/m^2)	Difference ($/m^2)	% excess
Base case	CHB	400.00	0.76	−0.26	35.00
Alternative	AAC	260.00	0.49		

Table 4 Life-cycle costs of AAC blocks and CHB

		Initial costs ($)	Life cycle costs ($)
Base case	CHB	415,097.14	15,524.83
Case 1	AAC	430,162.30	16,080.61
Difference		−15,065.16	−555.78
% savings		−3.63	−3.58
SIR			0.96

Table 5 Percentage of parameters in life-cycle costs

	Base case	Case 1
	CHB (%)	AAC (%)
Initial costs	99.850	99.898
Energy costs	0.030	0.027
OM & R costs	0.120	0.075
	100.000	100.000

7 Conclusion

This study aims to compare the cost efficacy of the conventional way of masonry construction, which is by using CHB, and the emerging Autoclaved Aerated Concrete (AAC) blocks using Life-Cycle Cost Analysis (LCCA). After assessing the comparison, it was concluded in this study that:

1. Emerging AAC blocks have no significant difference (nearly negligible) compared to CHB in life-cycle costs. Hence, AAC blocks are just as economical as the CHB.

2. The almost-the-same LCC of AAC blocks and CHB throughout a 50-year life depicts no dominant masonry units in terms of cost. Hence, it is recommended to perform a comparative analysis of non-cost-related parameters to prove that one is more effective than the other.
3. Initial costs of masonry construction remain the most important among the LCC. Thus, an alternative to these masonry units must possess a low-cost structure or initial costs to be significantly cost-effective.

References

1. Deng M, Zhang W, Li N (2020) In-plane cyclic loading tests of concrete hollow block masonry walls retrofitted with high ductile fiber-reinforced concrete. Constr Build Mater 238:117758. https://doi.org/10.1016/j.conbuildmat.2019.117758
2. Jonaitis B, Zavalis R (2013) Experimental research of hollow concrete block masonry stress deformations. Procedia Eng 57:473–478. https://doi.org/10.1016/j.proeng.2013.04.061
3. Imai H, Minowa C, Lanuza AG, Penarubia HC, Narag IC, Soridum Jr RU, Okazaki K, Narafu T, Hanazato T, Inoue H (2015) A full-scale shaking table test on Philippine concrete hollow blocks (Chb) masonry houses. J Disaster Res 10(1):113–120. https://doi.org/10.20965/jdr.2015.p0113
4. Sassine E, Cherif Y, Dgheim J, Antczak E (2020) Experimental and numerical thermal assessment of EPS concrete hollow blocks in Lebanon. J Mat Civil Eng 32(8). https://doi.org/10.1061/(ASCE)MT.1943-5533.0003335
5. Artino A, Evola G, Margani G, Marino E (2019) Seismic and energy retrofit of apartment buildings through autoclaved aerated concrete (AAC) blocks infill walls. Sustain 11(14):3939. https://doi.org/10.3390/su11143939
6. Raj A, Borsaikia AC, Dixit US (2019) Compressive and shear bond strengths of grooved AAC blocks and masonry. Mater Struct 52(6):116. https://doi.org/10.1617/s11527-019-1428-8
7. Tam VWY (2011) Cost effectiveness of using low cost housing technologies in construction. Procedia Eng 14:156–160. https://doi.org/10.1016/j.proeng.2011.07.018
8. Ylanan JL, Utilization of autoclaved aerated concrete (AAC) blocks as the better alternative for concrete hollow blocks (CHB) for masonry all—a case study using DMAIC & DMADV Framework. https://doi.org/10.13140/RG.2.2.12173.41449
9. Islam H, Jollands M, Setunge S, Bhuiyan MA (2015) Optimization approach of balancing life cycle cost and environmental impacts on residential building design. Energy Build 87:282–292. https://doi.org/10.1016/j.enbuild.2014.11.048
10. Thorat PK, Papal M, Kacha V, Sarnobat T, Gaikwad S (2015) Hollow concrete blocks—a new trend. Int J Eng Res 5(5):9–26
11. Sassine E, Cherif Y, Dgheim J, Antczak E (2020) Investigation of the mechanical and thermal performances of concrete hollow blocks. SN Appl Sci 2(12):2006. https://doi.org/10.1007/s42452-020-03881-x
12. Fajardo MB (1980) Simplified construction estimate. 5138 Merchandizing
13. Jain U, Jain M, Mandaokar S (2018) Comparative study of AAC blocks and clay brick and costing. Int J Res Eng, Sci Manag 1(9):539–543
14. Chauhan V, Pundir R (2021) Comparative analysis of multi-storey RCC building with AAC blocks and conventional blocks
15. Kamal MA (2020) Analysis of autoclaved aerated concrete (AAC) blocks with reference to its potential and sustainability. J Build Mat Struct 7(1):76. https://doi.org/10.34118/jbms.v7i1.707
16. Netula O, Singh SP, Bhomia ER (2017) Study and comparison of structure having different infill material (Bricks, AAC blocks and hollow concrete blocks) using ETABS. IJETSR 4

17. Asiedu Y, Gu P (1998) Product life cycle cost analysis: state of the art review. Int J Prod Res 36(4):883–908. https://doi.org/10.1080/002075498193444
18. Fuller S (2010) Life-cycle cost analysis (LCCA). National Institute of Building Sciences, An Authoritative Source of Innovative Solutions for the Built Environment, vol 1090
19. Thakuri LS, Poudel L (2020) Life cycle cost analysis of external walls: a comparative study of AAC and CSEB blocks
20. Islam H, Jollands M, Setunge S, Ahmed I, Haque N (2014) Life cycle assessment and life cycle cost implications of wall assemblages designs. Energy Build 84:33–45. https://doi.org/10.1016/j.enbuild.2014.07.041
21. Zhuang J, Liang Z, Lin T, de Guzman F (2007) Theory and practice in the choice of social discount rate for cost-benefit analysis: a survey. ERD working paper series
22. Castañares SJA, Keeping the inflation target unchanged for 2022–2024
23. Wong NH, Tay SF, Wong R, Ong CL, Sia A (2003) Life cycle cost analysis of rooftop gardens in Singapore. Build Environ 38(3):499–509. https://doi.org/10.1016/S0360-1323(02)00131-2

Application of Recycled Concrete in Construction Based on Environmental Sustainable Development

Yisheng He, Weiqun Cao, and Xiang Zhang

Abstract The development of the construction engineering industry has caused damage to the natural environment and living environment to a certain extent. In recent years, with society's widespread awareness of environmental protection, the use of recycled concrete in construction projects has generally been praised by society and industry insiders and has been valued by relevant government departments. The use of recycled concrete in construction can reduce the damage to the environment to a certain extent. Therefore, this article will discuss and study the application of recycled concrete in construction.

Keywords Environment · Sustainable development · Recycled concrete · Construction

1 Introduction

Recycled concrete is a kind of applied material in construction engineering. The research and development of this building material is a new type of building material based on the concept of environmental protection and recycling. The application of this new building material is conducive to promoting the sustainable development of society, reducing damage to the natural environment and living environment, and the application of recycled concrete materials in construction projects greatly reduces the loss of resources in the construction industry, which is beneficial to people harmonious development with nature [1]. However, with little understanding of this new type of material, recycled concrete has not been explored a lot. There are not many papers discussing about this environmentally friendly construction material. Thus, in this paper, the author compared the new material with traditional concrete materials, found out that the recycled concrete makes the construction industry look new, and can adapt the concept of harmonious coexistence. With the use of recyclable

Y. He · W. Cao (✉) · X. Zhang
Qingdao University of Technology, Qingdao, Shandong Province, China
e-mail: cwqinfo@163.com

T. Kang (ed.), *Proceedings of 5th International Conference on Civil Engineering and Architecture*, Lecture Notes in Civil Engineering 369,
https://doi.org/10.1007/978-981-99-4049-3_15

concrete, the construction industry is becoming less polluting and can add to the sustainability of this industry in the new era.

2 Characteristics and Classification of Recycled Concrete

2.1 Characteristics of Recycled Concrete

As a new type of building material, recycled concrete is not well understood by many people. The most important thing about recycled concrete is that it embodies the word "recycled". Recycling and environmental protection is the basic concept of recycled concrete [2]. The main characteristics of this new building material are saving natural resources, reducing environmental pollution, scientifically and rationally, realizing sustainable development, and realizing harmonious development between man and nature, as shown in Fig. 1. Compared with traditional concrete materials, recycled concrete makes the development concept of the construction engineering industry look new and puts forward the sustainable development concept of harmonious coexistence between man and nature [2]. On the one hand, the construction industry has been better developed and has a broader expansion capacity. On the other hand, it reduces the damage to the natural environment and reduces the loss of natural resources.

The application of recycled concrete in construction projects can make rational use of industrial waste and realize the renewable and effective recycling of natural resources [3]. The use of recycled concrete for construction can to a large extent improve the quality of concrete through new technology and equipment and reduce the waste and loss of engineering materials during construction. In addition, recycled concrete also has environmental coordination and adaptability to the environment. Its environmental compatibility means that in the entire use project of recycled concrete, it can reduce the consumption of resources and can effectively form an organic recycling cycle. The adaptability of recycled concrete means that it can meet the needs of construction projects, has the functions of self-perception and self-repair, and can improve the environment to a certain extent [3].

2.2 Classification of Recycled Concrete

Green concrete can be divided into four categories in construction projects: recycled high-performance concrete recycled aggregate concrete, environmentally friendly concrete and intelligent concrete [4].

Recycled high-performance concrete has excellent properties. This type of concrete is energy-saving concrete, and the concrete can recycle wastes in life and improve resource utilization.

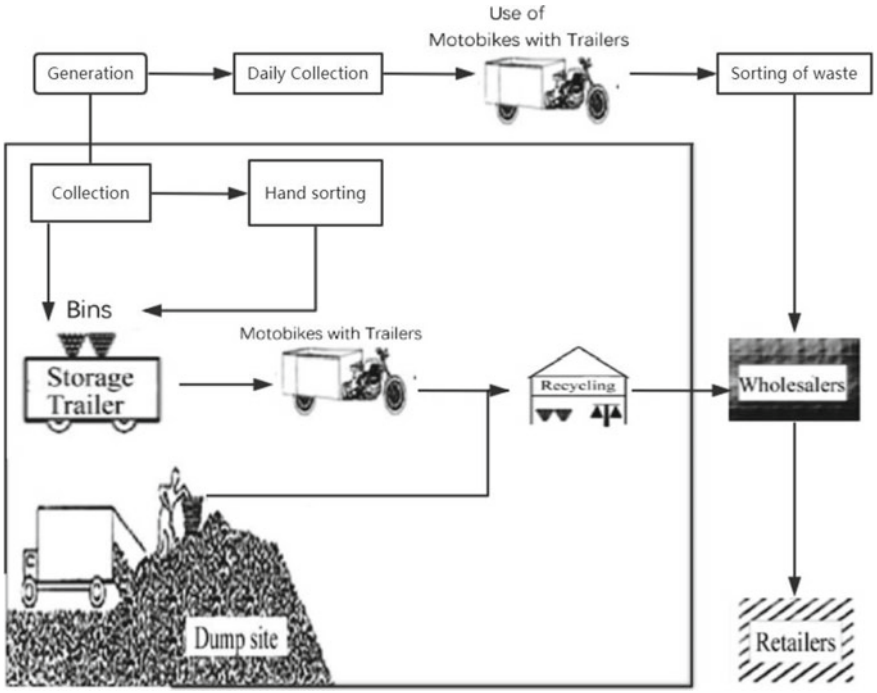

Fig. 1 Production of recycled mixture

Recycled aggregate concrete refers to the use of discarded concrete blocks, mortar, or bricks in construction projects as construction aggregates, and adding water sand and mud for re-mixing [4]. Therefore, the use of recycled aggregate concrete can effectively save building materials, reduce resource loss, protect the ecological environment, and promote ecological development.

Environmentally friendly concrete refers to low-alkaline concrete, which can effectively protect the steel bars from rust and corrosion and increase the service life.

Intelligent concrete refers to the addition of intelligent materials based on traditional concrete [5]. There are many types of concrete, such as temperature-controlled concrete and damage self-diagnosing concrete. Smart concrete has a certain self-repair function and perception function.

3 The Development and Application of Recycled Concrete in Construction Engineering

3.1 Increase Environmental Awareness and Reduce Waste of Resources

In the application process of recycled concrete in construction projects, it is necessary to strengthen the environmental protection awareness of recycled concrete technology researchers and increase their awareness of environmental protection, and relevant construction companies must actively respond to the national call to vigorously promote and promote the environmental protection of recycled concrete technology and environmental awareness of construction projects. Then formulate a corresponding recycling and environmental protection system to implement recycling and environmental protection, and you cannot just stop at shouting slogans [5]. By establishing a system, forming certain corporate norms, and cultivating good environmental protection habits, project designers and construction personnel will have a full understanding of resource conservation, resource reuse, and the use of recycled building materials, and train engineering designers and the construction staff's awareness of regeneration responsibility.

In the development and use of recycled concrete, it is necessary to continuously improve the performance and quality of recycled concrete. Enterprises must organize relevant engineering and technical personnel to strengthen the improvement and learning of supporting technologies [6]. Through the accumulation of construction engineering experience, we have overcome technical difficulties such as cracks and shrinkage in recycled concrete. In addition, relevant government departments and project supervisors should pay attention to the supervision of construction behavior and construction quality and avoid waste of resources and quality problems in the production process of recycled concrete.

3.2 Pay Attention to the Recycling of Resources

In construction projects, we must pay attention to the recycling of resources, continue to research and develop new technologies, and improve the level of technology based on the current level of environmental protection technology. In addition, increase the research on new equipment; improve the production level of new equipment, thereby improving the quality of concrete production, as shown in Fig. 1. In the technical research and development of recycled concrete, resource conservation and environmental protection are still the main concepts to achieve the goal of sustainable development of resources. For example, using recycled aggregate concrete in recycled concrete and processing waste in construction projects can effectively prevent

resource waste, reduce the loss of stones, bricks, and water and sand, and form a scientific and practical concrete chain, to achieve the reuse of resources [7].

3.3 Increase the Use of Recycled Concrete

In the current building construction, it is necessary to increase the construction of recycled concrete and strengthen the execution of the use of recycled environmentally friendly materials [8]. The use of recycled concrete can be divided into three aspects.

(1) Vigorously develop clinker cement in construction projects, improve the quality and performance of traditional clinker cement by studying the mineral composition of clinker cement, and reduce the consumption of clinker cement on resources, as shown in Fig. 2. Based on recycled cement, develop recycled high-performance cement with environmental protection performance, reduce the use of concrete, and improve the efficiency of use. Through the research of cement production technology and production equipment, the performance of cement is improved, and the purpose of saving resources and protecting the environment is realized [9].
(2) Improve and formulate construction standards and acceptance standards for recycled concrete, and strictly control the quality of the project [10]. In addition, set up a recycled concrete technology research institution to conduct research and promotion on recycled concrete.
(3) Government departments should strongly support the use of recycled cement to reduce obstacles in the development and promotion of recycled cement [10]. In addition, the relevant engineering supervision department should increase the

Fig. 2 Environmental bricks made of clinker cement

inspection of recycled concrete to prevent the use of fake and inferior products in construction projects.

3.4 Development and Use of Recycled Concrete at China and Abroad

Some developed countries have many years of experience in researching construction waste, such as the United States, Japan, and Europe. Under the promotion of laws and regulations, they have achieved good research results and can effectively recycle construction waste. It paid attention to the disposal of construction waste earlier and has vigorously promoted the recycling of construction waste in the early stage, reducing construction production costs, saving resources and energy, and improving overall benefits. Table 1 shows the recycling rate of construction waste and the ratio of recycled concrete to recycled resources in various countries.

Research on waste recycling abroad is relatively early, but most of them still focus on the improvement of waste recycling and classification technology and reuse technology, and there are relatively few systematic studies on the effect evaluation of waste recycling. However, due to differences in production levels and resources and environments in different regions, the methods and analysis results cannot be directly applied to China. Therefore, China's research on solid waste should be based on a level that conforms to China's national conditions, economy, and technology.

The research on recycled aggregate concrete in China started 40 to 50 years later than in developed countries. Currently, there is no systematic application of recycled aggregate concrete. Waste concrete needs to be collected, processed, separated, and transported before it can be used. The process of making recycled concrete in China is shown in Fig. 3. The high cost of the process hinders the further research, research, and engineering reuse of waste concrete. With the rapid development of China's economy and the increasing awareness of environmental protection, the waste of resources and environmental pollution caused by waste concrete have attracted more and more attention.

At present, China's concrete pavement reconstruction and recycling applications are mainly completed on-site, which can save transportation costs and solve the problem of local natural aggregate resource shortage. This technique is to dismantle

Table 1 Recycling rate of buildings and concrete in some countries

Country	National construction waste utilization rate (%)	Recycling rate of waste concrete (%)
The United States	45	52
The United Kingdom	45	52
Japan	60	92
Denmark	75	97

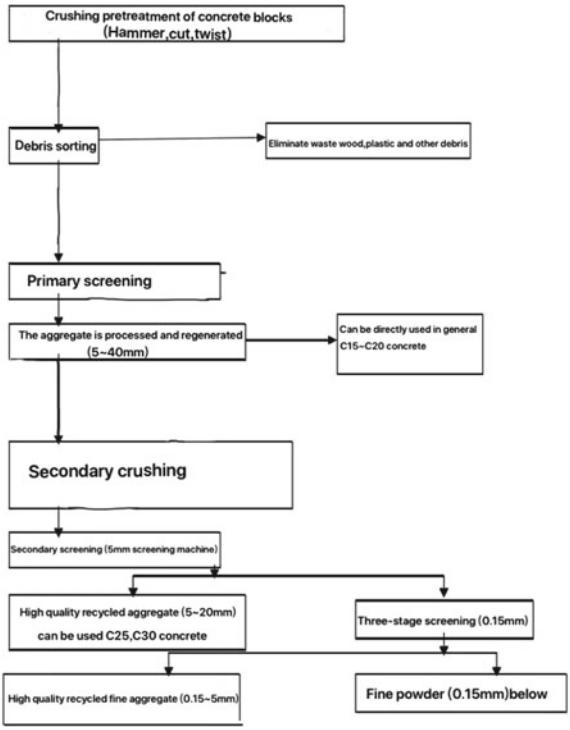

Fig. 3 Process of making recycled concrete in China

the pavement concrete, break it, make it into aggregate, and use the recycled aggregate to the base or subbase in the newly built pavement structure. This method is commonly used in the field of road maintenance in China.

4 Advantages of Recycled Concrete

4.1 Advantages of Various Indicators of Recycled Concrete

The application characteristics of concrete materials in road engineering require that concrete materials must have a certain bearing capacity, which is mainly reflected by its mechanical properties. For green concrete, its mechanical properties are related to its recycled bone crushing method, the strength of waste concrete, water-to-binder ratio, and the specific construction environment. After research, the strength of recycled concrete is inversely proportional to the replacement rate of recycled aggregates, that is, the smaller the replacement rate of recycled aggregates, the greater the

strength; it is proportional to the water–binder ratio, that is, the greater the water–binder ratio, the greater the strength; and the strength of waste concrete is proportional, that is, the greater the strength of waste concrete, the greater the strength of recycled concrete.

The workability of recycled concrete is related to the replacement rate of recycled aggregates and the ratio of water to cement. Compared with ordinary concrete, recycled concrete is crushed and reshaped from waste concrete. The surface of recycled aggregate is rough, and its water absorption performance is greater than that of ordinary concrete. As a result, the slump of recycled concrete is smaller than that of ordinary concrete. Specifically, the slump of recycled concrete is inversely proportional to the content of recycled aggregate, that is, the less recycled aggregate, the greater the slump of recycled concrete. In addition, the slump of recycled concrete is proportional to its water–binder ratio, that is, the smaller the water–binder ratio, the smaller the slump of recycled concrete. Under normal circumstances, the two types of concrete materials with similar conditions have better crack resistance, but their freeze–thaw resistance and permeability resistance are not as good as ordinary concrete materials. For recycled concrete, its anti-permeability can be improved by adding fly ash, etc., and its freeze–thaw resistance can be improved by reducing its water–binder ratio. However, improving the performance of recycled concrete will inevitably lead to an increase in its preparation cost. This requires engineering builders to select the best balance point based on comprehensive considerations such as road engineering application requirements and costs (see Fig. 4).

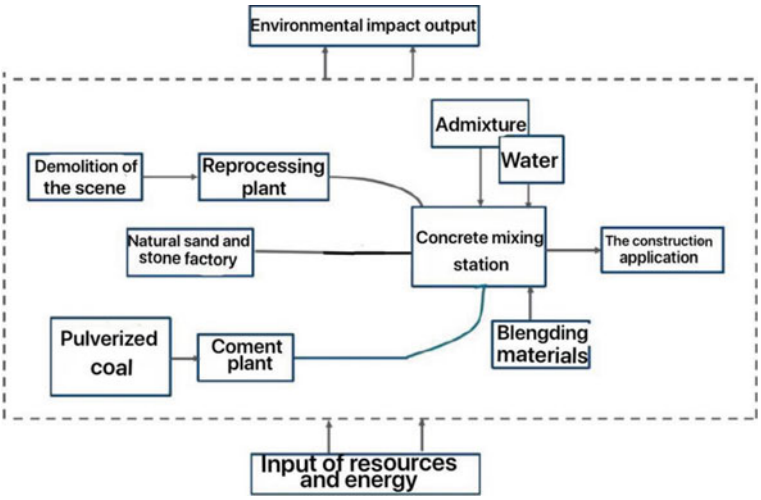

Fig. 4 Production process of recycled concrete mixed with fly ash

4.2 Advantages of Recycled Concrete in China's Construction Projects

At present, a large amount of fly ash will be generated during the construction of China's construction projects, and it will cost a lot of money to process it. Research has found that adding fly ash to concrete will improve the performance of recycled concrete, making recycled concrete develop in the direction of high performance, and there will be more room for use in the future. Compared with ordinary concrete, recycled concrete consumes less energy and has less environmental load, which is inseparable from recycled aggregate. When using fly ash as recycled aggregate for mixing, it can effectively inhibit the alkali-aggregate reaction in concrete, reduce the heat of hydration, reduce drying shrinkage, and improve the durability of recycled concrete. At the same time, fly ash can replace part of recycled concrete. Cement reduces the amount of cement, so as to reduce pollution and cost.

From the perspective of environmental protection, the recycling of construction waste can reduce the removal of rocks from mountains, while reducing the emission of waste gas and solid waste, which is of great significance to the protection of natural energy and the ecological environment.

5 Conclusion

In summary, the development and use of recycled concrete not only reduces the waste of natural resources, but also prevents environmental damage to a certain extent. The excellent performance of recycled concrete realizes the sustainable development of the environment and plays a positive role in the construction of the human living environment. Therefore, we must vigorously promote the use of recycled materials in future engineering construction, establish environmental protection awareness, and promote the sustainable development of natural resources.

Acknowledgements Project: 2019 University Student Innovation Training Project of Shandong Province "Investigation Report on the Status Quo of Green Construction in Modern Construction Industry", Project number: S201910429097; 2020 University Student Innovation Training Project of Shandong Province "Research on Economic and Environmental Evaluation of Recycled Concrete Based on LCA-LCC Integration", Project number S202010429124.

References

1. Ma HY (2018) Development and application of recycled concrete in construction engineering. Recyc Environment Friend Build Mat 12(04):198–201
2. Ji F, He B (2018) Research on the application and development prospects of recycled concrete in architectural engineering design. Doors Wind 7(02):153–156

3. Li QW (2016) Application and development prospects of recycled concrete in construction engineering. Techn Style 11(10):162–165
4. Zhang B (2014) Application of recycled concrete in construction engineering. Const Tech 10:78–81
5. Guo F (2009) Talking about the development and research prospects of recycled concrete. Shanxi Architect 15(23):68–70
6. Zheng Y (2010) Research on the strength of recycled concrete. Low Temp Build Tech 11(04):108–110
7. Liu W (2015) Application and promotion of construction waste recycled aggregates in green concrete. Jiangxi Build Mat 12:27–32
8. Xu YW (2016) Experimental study on mechanical properties of construction waste recycled concrete and its application in highway surface. Nanchang Univ 13(02):44–47
9. Liu WB (2015) Application and promotion of construction waste recycled aggregates in green concrete. Jiangxi Build Mat 12(05):27–32
10. Tian PP, Guan T, Liang R (2016) Application research and prospect of construction waste recycled aggregate in concrete. Guangdong Build Mat 9(08):21–25

Mix Design for High-Strength Lightweight Concrete Using Fly Ash Cenospheres

Hung Viet Le, Thanh Trung Le, and Tuan Van Nguyen

Abstract This paper presents a proposed method of mix design for high-strength lightweight concrete using fly ash cenospheres (FAC-HSLWC) with the required density and compressive strength. The basic steps of this design method include optimizing the binder composition based on the calculation of the maximum packing density of the mixture, selecting suitable binder paste content (through the binder/aggregate ratio-B/A), and the ratio water/binder (W/B) to achieve the required workability and compressive strength; calculating the ratio of cenospheres to replace sand (ratio of cenospheres/aggregate-FAC/A) to achieve the required density of concrete. To develop this method, a series of trial mixes of FAC-HSLWC with different ratios of B/A, W/B, FAC/A were experimented to establish the parameters for the proposed design method. The validation results confirm that the unit weight and compressive strength are relatively close to the calculation results based on the design method. The proposed design method can be used effectively to calculate the optimum mix proportion of FAC-HSLWC.

Keywords Mix design · High-strength · Lightweight concrete · Fly ash · Cenospheres

1 Introduction

Besides popular lightweight concrete using porous aggregates (LWAC) such as expanded clay, shale, slag, or lightweight volcanic materials (pumice, scoria, tuff), concrete using fly ash cenospheres (FAC LWC) has been interested and developed

H. V. Le (✉) · T. T. Le
Vietnam Institute for Building Materials, 235 Nguyen Trai, Thanh Xuan District, Hanoi 100000, Vietnam
e-mail: lvhung210@gmail.com

T. Van Nguyen
Hanoi University of Civil Engineering, 55 Giai Phong, Hai Ba Trung District, Hanoi 100000, Vietnam

T. Kang (ed.), *Proceedings of 5th International Conference on Civil Engineering and Architecture*, Lecture Notes in Civil Engineering 369,
https://doi.org/10.1007/978-981-99-4049-3_16

for more than a decade. FACs are lightweight particles in thermal power fly ash, their particle density is usually in the range of 0.4–9.0 g/cm^3, particle size in the range of 1–300 μm, with the majority of 20–300 μm, and they are the large particles in fly ash compared to other fly ash particles whose particle size is mainly below 20 μm, and their shell thickness in the range of 1–18 μm [1, 2]. In some previous studies, cenosphere particles have a shell that can be resistant to gas and water [3], the crushing strength is about 15.6–17.5 MPa [4], much higher compared with the common lightweight aggregate such as expanded clay aggregate about 0.82–5.6 MPa [5]. FAC LWC has been reported to have lower density and higher strength than popular lightweight aggregate concrete. FAC LWC can meet the required strength in standards for structural lightweight concrete with a density about of 1100 kg/m^3 or more [2]. A study by Du [6] reported that FAC LWC with a density of about 1075 kg/m^3 has a compressive strength of about 20 MPa at 28-day age. A recent number of studies on FAC LWC have shown that FAC LWC could gain compressive strength of 55–69.4 MPa with a density less than 1500 kg/m^3, corresponding to the specific strength (ratio of strength and density) of this type of concrete in the range of 40–47 kPa/kg.m^{-3}, which is equivalent to that of high-strength concrete using conventional aggregates with a density of 2400 kg/m^3 and a compressive strength of about 110 MPa (Huang et al. [7], Wang et al. [8], Wu et al. [9]). These mean that FAC LWC can achieve high strength with low density, which is difficult for normal lightweight aggregate concrete.

For conventional lightweight aggregate concrete (LWAC), numerous studies have been carried out to propose mix design methods [10–14]. ACI 211.2-98 and FIB (1983) provided simple mix design methods for LWAC with an approach similar to that of conventional concrete. The mix proportioning parameters are selected based on relationships between concrete performance and the mix parameters which have been established from numerous experimental results of the previous studies. Most of the recent studies on mix design methods for the LWAC approach have been based on optimizing the particle packing density of particles in the mixture, by optimizing the packing density of the cementitious materials, aggregates, or both to reduce water, paste, or mortar consumption. With this approach, the designed mixture therefore would reduce W/B ratio and intergranular voids in the mixture thereby increasing the strength and durability of LWAC. Costa et al. [12] proposed a method based on optimizing the packing density of concrete mixture including cementitious materials and aggregates. Another mix design method for self-compacting LWAC proposed by Li et al. [13] was also based on the optimization of the packing density of aggregates in the mixture in combination with the selection of the optimal mortar firm thickness surrounding aggregate particles. In general, the LWAC design methods apply only to certain types of lightweight aggregates covered by the method (common is coarse, fine, or both from expanding products of clay, shale, slag, or lightweight volcanic materials). When the properties and particle grading of aggregates change, it will have a certain influence on the optimization of the mix proportions of LWAC.

Research on the development of a design method for lightweight concrete using lightweight materials in the form of hollow microspheres such as FAC particles (FAC LWC) is currently very limited. Most of the current studies on FAC LWC mainly

select the mix proportion of FAC LWC similar to that of conventional concrete with partial or all replacement of fine aggregate (sand) by FAC. Note that unlike normal weight concrete or the conventional LWAC, the aggregate of FAC LWC contains only fine aggregates, not coarse aggregates. This is a remarkable feature in the mix composition of FAC LWC. Wang et al. [8] proposed a method to design lightweight concrete mixes using cenospheres with a density < 1500 kg/m^3, which the author called ULCC. This mix design method was based on the particle size distribution of FAC to calculate the cement paste thickness of cementitious material paste and W/B ratio for the mixture to achieve the required workability and unit weight of ULCC. However, this method does not allow the design of the ULCC with target compressive strength. In addition, this method only applies to FAC LWC with the maximum size of material particles being cenospheres, and the method does not apply to FAC LWC using materials larger than cenospheres such as sand. The objective of this research is to develop a mix design method for high-strength lightweight concrete using fly ash cenospheres partially or fully replacing sand as aggregate, with desired density in the range of 1300–2000 kg/m^3, and compressive strength greater than 40 MPa. The method was established by optimizing the particle packing density of binder composition and the binder to aggregate ratio in the mixture based on the concept of optimal packing density.

2 Proposed Mix Design Method

FAC-HSLWC is commonly a fine-grain cement lightweight composite composed of binder typically including cement and mineral admixtures, aggregates including FAC, sand, and other materials such as chemical admixtures, fiber, and water. In addition, the composition of FAC-HSLWC contains a high content of fine particles (sand particles are the largest size grains in the mixture) so the total surface area of the particles in the system is large, which requires a high amount of mixing water, thus water reducing admixtures such as superplasticizer usually used to reduce the amount of mixing water. The mixture of FAC-HSWLC is also required to achieve appropriate workability without bleeding and segregation for facilitating the construction process such as pumping and compaction. To solve the issues, the approach in the mix design here is the optimization of the mix proportion of FAC-HSLWC by increasing the packing density of the particle material mixture of sand and FAC and the mixture of binder and aggregates (sand and FAC). This would reduce the amount of mixing water, W/B ratio, and binder paste, and maximize the presence of aggregates in the FAC-HSLWC with the target of improving the strength, and durability of concrete but also achieve the required workability of the mixture. To obtain the purpose, the method of designing mix proportion for FAC-HSLWC with the target unit weight and compressive strength is proposed according to the following steps:

- Optimize binder composition including Ordinary Portland Cement (OPC) and Supplementary Cementitious Materials (SCM). SCM consists of silica fume (SF), ground granulated blast furnace slag (GGBFS) or both. The principle of the method is optimizing constituent materials of the binder to obtain the maximum packing density and minimizing the amount of cement used (or maximum SCM content) but the workability of the mixture and strength of concrete have to meet the requirements;
  - Select the ratio of B/A (by volume) to ensure the material mixture has optimal packing density and achieves the required workability of the concrete mixture;
  - Select the ratio of W/B to ensure the required compressive strength of lightweight concrete;
  - Calculate the ratio of FAC to replace sand (ratio of FAC/A) to ensure the required unit weight of lightweight concrete;
  - Use dispersed fiber and shrinkage reducing admixture (SRA) when the concrete strictly required shrinkage reduction, crack resistance, or improving tensile strength.
  - Use superplasticizers to adjust the workability of the mixtures as required (usually in the range of 180–200 mm).

A schematic diagram of the steps of the proposed mix design method for FAC-HSLWC in this study is shown in Fig. 1

3 Establishing Parameters in the Proposed Mix Design Method

3.1 Materials

Ordinary Portland Cement (OPC) 52.5R from Nghi Son Cement Corp., undensified silica fume (SF) from Elkem, ground blast furnace slag (GGBFS) from CHC Vietnam Ltd., a fly ash cenosphere (FAC) from Pha Lai, Hai Duong Vietnam, river sand (RS) with particle size 0–0.63 mm was used in this research. Their physical properties and chemical compositions are presented in Tables 1 and 2, respectively, and the particle size distribution is shown in Fig. 2. A polycarboxylate-based superplasticizer (SP) from Sika Ltd. was used to adjust the workability of FAC-HSLWC mixes.

3.2 Test Method

Workability of fresh FAC-HSLWC mixtures was determined by a flow table test according to BS EN 1015–3:1999. Compression test was carried out on 40 × 40 × 160 mm specimens according to BS EN 1015–11:1999. The specimens were cast in

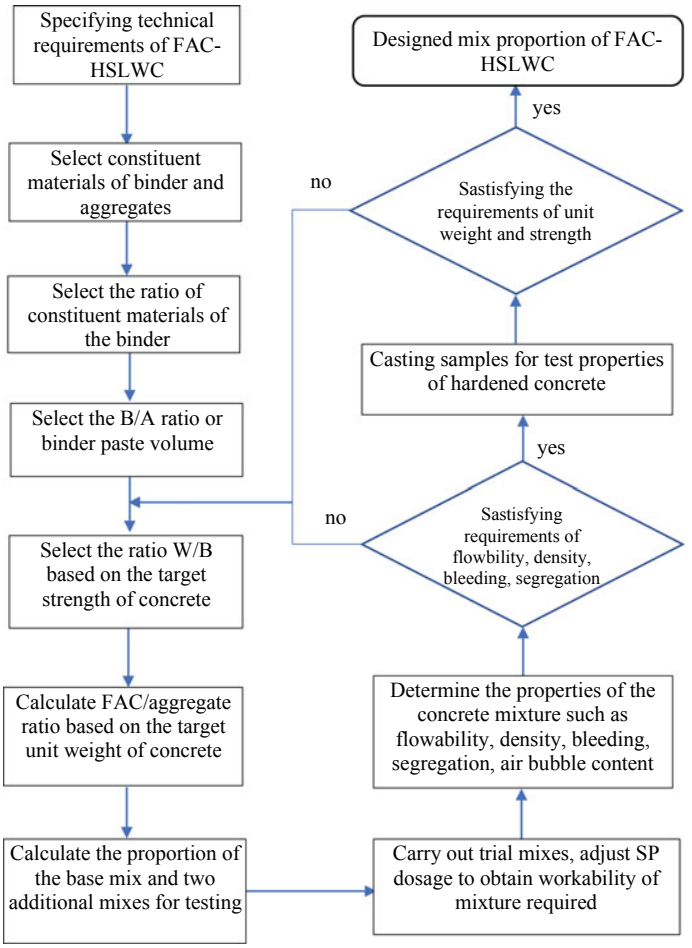

Fig. 1 Schematic diagram of steps in the proposed mix design method for FAC-HSLWC

Table 1 Physical properties of cement, silica fume, cenosphere, and sand

Properties	OPC	GGBFS	SF	FAC	Sand
Specific gravity, g/cm^3	3.10	2.90	2.16	0.786	2.62
Water absorption, %	–	–	–	10.3	3.2
Specific surface area, cm^2/g	3820	5090	29,900	–	–
Mean particle size, μm	16.68	7.84	0.15	116	225

Table 2 Chemical compositions of the materials on the study

	LOI	SiO_2	CaO	Al_2O_3	Fe_2O_3	MgO	SO_3	K_2O	Na_2O	TiO_2
OPC	1.23	19.40	63.50	5.22	3.40	1.61	2.07	0.91	0.00	0.45
GGBFS	–0.49	33.02	39.2	14.02	0.17	8.16	0.05	0.21	0.28	0.12
FAC	0.27	61.40	0.28	26.61	2.79	1.81	0.01	3.91	0.82	–

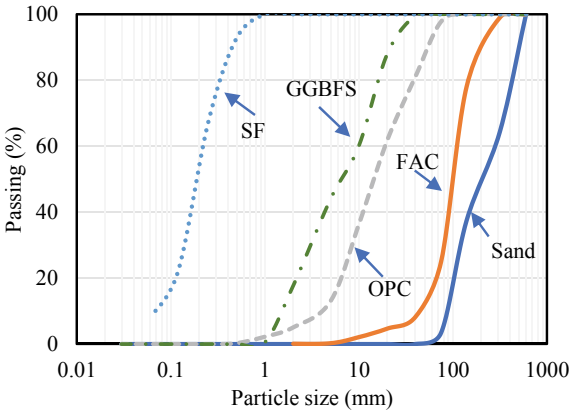

Fig. 2 Particle size distribution of materials

steel molds and compacted by a vibration table and then stored in the moist room at more than 95% relative humidity and a temperature of 27 ± 2 °C. The specimens were demolded after casting 23 ± 1 h and then cured in water at 27 ± 2 °C until testing ages.

3.3 Establishing Parameters in the Mix Design Method

Step 1: Specifying technical requirements of FAC-HSLWC

The main technical requirements include workability of the concrete mixture (tested by flow table method) normally required in the range of 180–200 mm, unit weight (1300–2000 kg/m^3), and 28-day compressive strength in the range (40–80) MPa. Note that the compressive strength is determined on the 40 × 40 × 40 mm specimens taken from the cast prism of 40 × 40 × 160 mm. Compressive strength on 40 × 40 × 40 mm specimen can be converted to that of 150 × 150 × 150 mm cube by multiplying with a conversion coefficient of 0.83.

Step 2: Select constituent materials of binder and aggregates

Binder consists of OPC and SCM, SCM is SF, GGBFS, or both; aggregate including FAC and sand. Determine the particle size distribution and particle density (PD) of each constituent material. The particle size distribution of the sand is determined by

the sieving method, of the FAC by the sieving or laser scattering method, of cement, SCMs is determined by the laser scattering analysis method. Figure 1 shows the grain distribution of the materials used for FAC-HSLWC.

Step 3: Select the ratio of constituent materials to optimize the particle size distribution of the binder.

The optimal particle size distribution of the binder is obtained by optimizing the packing density of the material mixture. The packing density is calculated based on the Compressible Packing Model (CPM) proposed by De Larrard [15]. Binder has the optimal composition when the mixture has the maximum CPM. CPM is determined by virtual packing density (γ_i) and taken into account the actual compressive effect through the compression factor (K). Virtual packing density is the maximum packing density obtained by combining the particle classes of constituent materials at certain ratios to achieve a mixture of minimum intergranular void or maximum density. The calculation formula for virtual packing density of the material mixture when the particle class i is dominant in the mixture with n particle classes, γ_i is as follows:

$$\gamma_i = \frac{\beta_i}{1 - \sum_{j=1}^{i-1} \left[1 - \beta_i + \left(1 - \left(1 - \frac{d_i}{d_j} \right)^{1.5} \right) \right] y_i - \sum_{j=i+1}^{n} \left(1 - \left(\sqrt{1 - \left(1 - \frac{d_j}{d_i} \right)^{1.02}} \right) \right) \frac{\beta_i}{\beta_j}} \quad (1)$$

where β_i, β_j: : the maximum packing density (MPD) of the ith and jth class; y_j is volume fraction retained in each class j; d_i, d_j is the mean size of the ith and jth class, respectively. Maximum packing density of the material mixture with n grain classes according to De Larrard is the minimum value of γ_i as follows:

$$\text{MPD} = \min_{1 \le i \le n} \gamma_i \quad (2)$$

The actual packing density is lower than the maximum packing density because it depends on the compaction energy. Therefore, De Larrard [15] introduced CPM to calculate the actual packing density from the maximum packing density by introducing the compression coefficient K to account for the effect of compaction energy. For a particle class, β_j can be determined by the following formula:

$$\alpha_j = \beta_j / (1 + 1/K) \quad (3)$$

For the mixture of fine particles such as the binder composed of OPC and SMC, the value of K is taken as 12.5. This value is adopted from the works of Jones et al. [16].

By applying de Larrard's CPM model to the binder consisting of OPC and SCM (SF, GGBFS, or both) with particle distribution shown in Fig. 1, PD values of the binder with different OPC and SCM ratios were obtained as shown in Fig. 3. It can be seen that PD of the binder consisting of OPC and SF gain the greatest when the

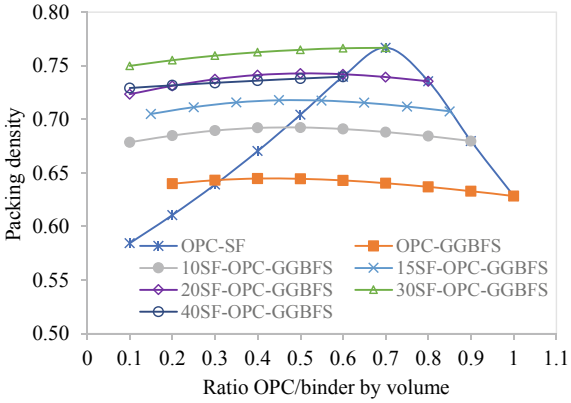

Fig. 3 Packing density of the binder comprising OPC and SCMs with various ratios

ratio of SF is 30% (by volume), with the binder consisting of OPC and GGBFS, the PD fluctuating in a narrow range, the largest PD with GGBFS ~50% by volume, the binder consists of OPC and either SF and GGBFS has the greatest PD with SF and GGBFS at about 30% and 50%, respectively.

Step 4: Select the B/A ratio (by volume) or the volume of the binder paste

Binder paste content in concrete is one of the main factors affecting concrete strength. When the volume of the binder paste is too small compared to the volume of the voids between the aggregate particles, it reduces the workability of the concrete mixture and also reduces the compactness ability of the concrete mixture, reducing the bonding between aggregate particles and paste matrix leads to reduce concrete strength. On the contrary, if the content of binder paste is too large, it would also reduce the strength of the concrete because the aggregate particles are not able to form a stable solid skeleton to resist external compressive forces. Compressive stress will act mainly on the paste matrix part which is usually lower strength than that of aggregate particles.

By conducting a series of trial mixes to determine the compressive strength of FAC-HSLWC with various ratios of binder to a total of binder and aggregate by volume (B/(B + A) ratio) in the range of 0.25–0.5, the relationship between the ratio of B/(B + A) and 28-day compressive strength (28-day f_c') can be represented as a parabolic curve as shown in Fig. 4. Therefore, there exists an optimal ratio among the dry constituent materials, namely sand, FAC, and binder so that 28-day f_c' of FAC-HSLWC is the largest. From the graphs of the relationship of B/(B + A) and 28-day f_c', the optimal B/(B + A) ratio (for maximum compressive strength) can be found in a range of 0.40–0.45 when the W/B ratio is from 0.5 to 0.3. This result can be converted to the optimal range of B/A ratio of 0.667–0.819. It can be seen that the optimal B/(B + A) ratio tends to increase slightly when W/B ratio decreases but the fluctuation is in a narrow range. This is attributed due to a lower ratio of W/B as a result of the higher strength of binder paste, therefore concrete mixture can contain more paste volume by increasing binder content but still give a comparative strength.

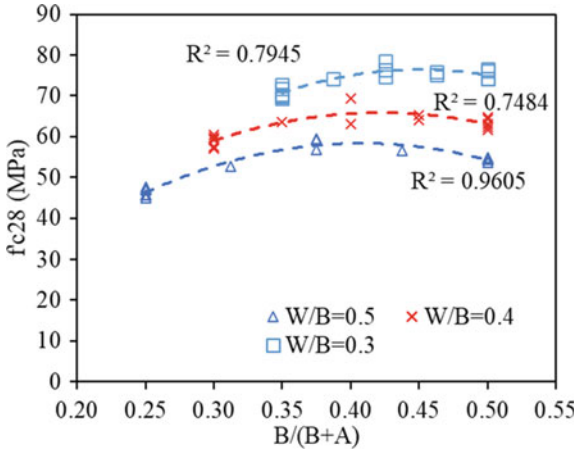

Fig. 4 Relationship between B/(B + A) ratio and f'c28 of FAC-HSLWC

In addition, the high W/B ratio results in an easy-to-compact concrete mixture due to the cement paste having higher flexibility than the concrete mixture with a low W/B ratio.

Based on the research results, the optimal B/A ratio is preliminary taken as 0.667–0.819, corresponding to the W/B ratio from 0.5 to 0.3 has been selected in the design of the basic mix proportion for FAC-HSLWC.

Step 5: Select the W/B ratio to meet the desired Compressive strength of concrete

From the dataset of 28-day compressive strength test results of FAC LWC with W/B ratio from 0.3 to 0.7, aggregate 100% FAC (all sand replaced by FAC), binder including 3 types of OPC, 90% OPC + 10% SF, and 60% OPC + 40% GGBFS. The relationship between W/B ratio and the 28-day compressive strength of FAC-HSLWC can be expressed as a linear line in Fig. 5. Based on these results, the W/B ratio can be preliminarily selected based on the required 28-day compressive strength of FAC LWC.

Step 6: Calculate FAC content used or FAC/A ratio by volume

The FAC content or FAC/A ratio is determined through the requirement of the target unit weight of concrete.

Because FAC is used to replace part or all of sand to reduce the unit weight of concrete to the target value, the relationship between the unit weight of lightweight concrete and the ratio of lightweight aggregate to total aggregate (V_{fac}/V_a) needs to be determined. Dry unit weight of lightweight concrete (γ_{lwc}) can be calculated by the following equation:

$$\gamma_{\text{lwc}} = M_{\text{fac}} + M_s + (1 + \alpha \cdot a)M_b \tag{4}$$

$$\gamma_{\text{lwc}} = M_{\text{fac}} + M_s + 1,2M_{\text{lwc}} \tag{5}$$

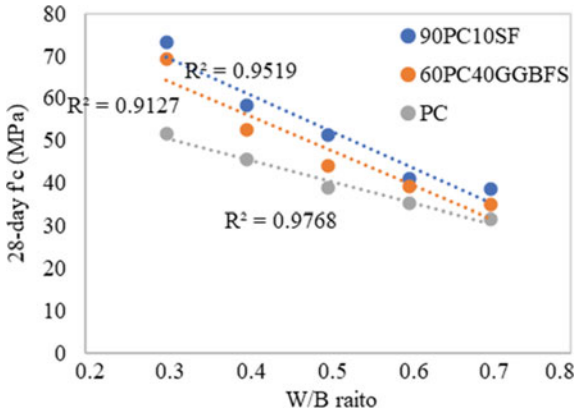

Fig. 5 Relationship of W/B ratio and 28-day compressive strength of FAC LWC

where M_{fac}, M_s, and M_b are the volumes of FAC, sand, and binder, respectively, used for one cubic meter of concrete. α is the coefficient of bound water of the cement hydration product, α is usually taken as 0.25; a is a coefficient related to the degree of hydration of the cement, usually in the range of 0.6–0.8. In formula (5), degree of hydration is taken as 0.8, a is taken as 0.25. Equation (5) can be written as follows:

$$V_{\text{fac}} \cdot \rho_{\text{fac}} + V_{\text{cat}} \cdot \rho_s + 1.2V_b \cdot \rho_b = \gamma_{\text{lwc}} \tag{6}$$

where V_{s} and V_{fac} are the volume fraction of sand and FAC in lightweight concrete, ρ_s and ρ_{fac} are the particle density of sand and FAC, respectively.

In this lightweight concrete, sand and FAC are considered as aggregate phase, therefore:

$$V_a = V_s + V_{\text{fac}} \tag{7}$$

When the ratio of V_b/V_a (B/A by volume) is known, donated by Γ_b, , then the volumetric fraction of binder (V_b) in the lightweight concrete can be calculated via the volume of the aggregate (V_a) by the following equation:

$$V_b = \Gamma_b \cdot V_a \tag{8}$$

Total absolute volumetric fractions of the constituent materials of the lightweight concrete can be calculated by the following equation:

$$V_s + V_{\text{fac}} + V_b + V_w + V_{\text{sp}} + V_v = 1000 \tag{9}$$

With W/B (by weight) known, the volume of water V_w be calculated as follows:

$$V_w = \frac{W}{B} \cdot V_b \cdot \rho_b \tag{10}$$

where V_{sp} and V_v are volumetric fractions of superplasticizer, entrained air, and V_{sp}, and V_v are taken by assumed values (Example $V_{\text{sp}} = 5$–8 L/m^3, $V_k = 40$–45 L/m^3).

Combining Eqs. (6–10) to obtain the formula for calculating the volumetric fraction of the aggregate (V_a) and FAC (V_{fac}) in the lightweight concrete as follows:

$$V_a = \frac{1000 - V_{\text{sp}} - V_v}{1 + \Gamma_b + \frac{W}{B} \cdot \rho_b \cdot \Gamma_b} \tag{11}$$

$$V_{\text{fac}} = \frac{\gamma_{\text{lwc}} - 1,2 \cdot V_a \cdot \Gamma_b \cdot \rho_b - V_a \cdot \rho_s}{\rho_{\text{fac}} - \rho_s} \tag{12}$$

Step 7: Calculate the proportion of the base mix

From the parameters of the ratio of B/A, FAC/A, and W/B, along with the contents of other materials are assumed, the content of constituent materials in the concrete mix is calculated by the absolute volume method according to the following formula:

$$\frac{C}{\rho_c} + \frac{\text{SCM}}{\rho_{\text{scm}}} + \frac{\text{FAC}}{\rho_{\text{fac}}} + \frac{S}{\rho_s} + \text{W} + \frac{\text{SP}}{\rho_{\text{sp}}} + V_v = 1000 \tag{13}$$

where

C is the weight of OPC, kg/m^3;
SCM is the weight of cementitious materials, kg/m^3;
FAC is the weight of cenospheres, kg/m^3;
S is the weight of sand, kg/m^3;
SP is the weight of superplasticizer, liter/m^3;
W is the weight of mixing water, liter/m^3;
V_v is entrained air, liter/m^3.

ρ_c, ρ_{scm} , ρ_{fac}, ρ_s, ρ_{sp} are the particle density of FAC, sand, OPC, SCM, FAC, sand, and superplasticizer, respectively, kg/m^3.

Step 8: Calculate additional mix proportions for trial mixes

Along with the base mix, two additional mix proportions will be calculated by adjusting up and down the B/A ratio in the base mix by 0.1 unit (by volume) for trial mixes. The mix proportions of the two additional mixes are calculated in the same way as the base mix starting from step 6.

Step 9: Carry out trial mixes

Three trial mix proportions are calculated in batches to ensure an adequate amount for testing of properties of concrete. The dosage of superplasticizer in each batch is adjusted so that the concrete mixture obtains the required workability. Carry out trial mixes to determine the properties of the concrete mixture such as flowability, density, bleeding, segregation, air bubble content, and properties of the hardened concrete as required. From test results of trial mixes, a graph of relationship between compressive strength and B/A ratio will be plotted. Based on the required compressive strength and unit weight, choose the appropriate B/A ratio from the graph. The actual mix

proportion of concrete is adjusted based on the measured density of the concrete mixture compared to that of the calculation and the measured entrained air content.

4 Validation of the Proposed Mix Design Procedure

The proposed mix design method was tested with 4 trial mixes of FAC-HSLWC at different unit weights, namely 1300, 1400, 1500, and 1600 kg/m^3, and target compressive strength > 50 MPa. The objective is to compare the theoretical calculation results of the proposed mix design method with the experimental results. Materials used in the trial mixes of FAC-HSLWC include cement OPC, SF, FAC, and natural sand 0–0.63 mm, superplasticizer. The particle size distribution of the materials is shown in Fig. 2. With the required compressive strength > 50 MPa, W/B ratio was assumed to be 0.4 for all 4 trial mixes. The mix proportions calculated by the proposed mix design and test results of properties of FAC-HSLWC are given in Tables 3 and 4, respectively. The results show that to achieve the workability of 180–200 mm, the amount of superplasticizer increases gradually when the aggregate with 1600 kg/m^3 is reduced to 1300 kg/m^3, corresponding to the volume ratio FAC/A increasing from 0.47 to 0.9. The experimental results of experimental results are quite close to the set target, and the deviation is in the range of 1.1–2%. The compressive strength of the trial mixes in the range of 63.0–69.1 MPa tested on 40 × 40 × 40 mm specimens. This result is equivalent to 52.2–57.4 MPa when converted to the compressive strength on the 150 × 150 × 150 mm cube, all of them are higher than the target strength > 50 MPa. The experimental results also show that the compressive strength of concrete decreases gradually when the unit weight of concrete decreases, in other words, the concrete strength decreases when increasing the ratio of FAC/A from 0.47 to 0.9.

Table 3 Mix proportions of FAC-HSLWC calculated by the proposed mix design

Mix ID	Binder composition (%wt)		W/B ratio (by wt)	B/A ratio (by vol)	FAC/A ratio (by vol)	Mix proportion for one cubic meter (kg/m^3)					
	OPC	SF				OPC	SF	FAC	S	SP	W
1300	90	10	0.4	0.667	0.90	688	76	267	103	5.0	306
1400	90	10	0.4	0.667	0.76	688	76	225	247	5.0	306
1500	90	10	0.4	0.667	0.61	688	76	182	390	5.0	306
1600	90	10	0.4	0.667	0.47	688	76	140	534	5.0	306

Table 4 Experimental results of properties of FAC-HSLWC in trial mixes

Mix ID	W/B ratio (by wt)	B/A ratio (by vol)	FAC/A ratio (by vol)	Experimental results						Converted f'c28 on 150 mm-cube (MPa)
				Actual SP dosage (L/m^3)	Flow (mm)	Unit weight (kg/m^3)	Compressive strength (MPa)			
							3 days	7 days	28 days	
1300	0.4	0.667	0.90	5.4	186	1308	39.5	49.1	63.0	52.2
1400	0.4	0.667	0.76	4.7	188	1414	42.0	50.8	65.4	54.3
1500	0.4	0.667	0.61	4.4	191	1520	43.3	52.7	67.8	56.2
1600	0.4	0.667	0.47	4.2	190	1626	45.0	53.8	69.1	57.4

5 Conclusions

A method to design the mix proportion of FAC-HSLWC is proposed with a target unit weight of 1300–2000 kg/m^3 and compressive strength of 40–70 MPa. This mix design method is performed based on the optimization of the packing density of constituent materials and selecting the optimal B/A ratio in the range of 0.667–0.819 based on the test result dataset; calculating the ratio of sand replacement by FAC to achieve the required unit weight of concrete and selecting the ratio of W/B in the range of 0.3 to 0.5 based on the requirement of compressive strength.

The results of validation of the proposed mix design method with concrete mix with unit weight from 1300 to 1600 kg/m^3 confirm the followings:

1. Binder paste content affects the compressive strength of FAC-HSLWC. An optimal binder paste for each FAC-HSLWC mix can be obtained to give the maximum compressive strength. With FAC-HSLWC, the ratio of binder to total dry materials by volume is in the range of 0.4–0.45 when the W/B ratio is from 0.5 to 0.3.
2. Unit weight of FAC LWC can be obtained as required by calculating the ratio of FAC to replace sand. The verification results show that the formula for determining the unit weight of FAC-HSLWC as proposed gives results close to the experimental results, and the difference between the two methods is less than 2%.
3. To obtain a lower unit weight of FAC-HSLWC, FAC/A ratio needs to be increased and this also results in decrease of the compressive strength of FAC-HSLWC.
4. The proposed mix design method can be applied to reduce the number of trial mixes in designing mix proportion for FAC-HSLWC with target unit weight and compressive strength.

For further development of this mix design method, it is necessary to investigate different sources of materials to improve the parameters in the proposed mixing design method. In addition, the relationship between water to binder ratio and the 28-day compressive strength of FAC-HSLWC with different binders and aggregates needs to be established as an empirical equation to predict the compressive strength

of FAC-HSLWC when the water-to-binder ratio is selected to attain the desired compressive strength.

Acknowledgements The authors would like to express our thankfulness to Vietnam Ministry of Science and Technology for the financial support to this research through the project No.21/2019/HD-NDT dated 30/12/2019.

References

1. Ranjbar N, Kuenzel C (2017) Cenospheres: a review. Fuel 207:1–12
2. Hanif A, Lu Z, Li Z (2017) Utilization of fly ash cenosphere as lightweight filler in cement-based composites—a review. Constr Build Mater 144:373–384
3. Bartake SDN (2005) Determination of crushing strength of cenospheres. J ASTM Int 2(7):1–9
4. Liu F, Wang J, Qian X, Hollingsworth J (2017) Internal curing of high-performance concrete using cenospheres. Cement Conc Res 95:39–46
5. Zukri A, Nazir R, Said KNM, Moayedi H (2018) Physical and mechanical properties of lightweight expanded clay aggregate (LECA). In: MATEC Web of Conferences, vol 250, p 01016. EDP Sciences
6. Du H (2019) Properties of ultra-lightweight cement composites with nano-silica. Constr Build Mater 199:696–704
7. Huang Z, Padmaja K, Li S, Liew JR (2018) Mechanical properties and microstructure of ultra-lightweight cement composites with fly ash cenospheres after exposure to high temperatures. Constr Build Mater 164:760–774
8. Wang J-Y, Yang Y, Liew J-YR, Zhang M-H (2014) Method to determine mixture proportions of workable ultra lightweight cement composites to achieve target unit weights. Cement Concr Compos 53:178–186
9. Wu Y, Wang J-Y, Monteiro PJM, Zhang M-H (2015) Development of ultra-lightweight cement composites with low thermal conductivity and high specific strength for energy efficient buildings. Constr Build Mater 87:100–112
10. ACI 211.2 (2004) Standard practice for selecting proportions for structural lightweight concrete
11. FIP Manual of Lightweight Aggregate Concrete (1983) Published by The Surrey University Press, Bishopriggs, Glasgow G64 2NZ, Scotland. Elsevier, 259 pp. ISBN 0-903384-43-4
12. Costa H, Júlio E, Lourenço J (2010) A new mixture design method for structural lightweight aggregate concrete. In: 8th fib PhD Symposium
13. Li J, Chen Y, Wan C (2017) A mix-design method for lightweight aggregate self-compacting concrete based on packing and mortar film thickness theories. Constr Build Mater 157:621–634
14. Bogas JA, Gomes AJM, Structures (2013) A simple mix design method for structural lightweight aggregate concrete, 46(11):1919–1932
15. De Larrard F (1999) Concrete mixture proportioning: a scientific approach. CRC Press
16. Jones M, Zheng L, Newlands M (2002) Comparison of particle packing models for proportioning concrete constitutents for minimum voids ratio. Mater Struct 35(5):301–309

Experimental Study on the Shrinkage of Concrete

Mary Williams, Devdas Menon, and A. Meher Prasad

Abstract The long-term behavior of concrete structures is affected significantly by the shrinkage phenomenon. To study the effect of autogenous and drying shrinkage independently, specimens with and without drying need to be investigated. The most commonly used sealant for prevention of drying is aluminum foil. This study investigates alternative options like paraffin for sealing, which is more durable and reliable. The surface strains in two plain concrete prisms, one sealed with aluminum foil and the other with paraffin wax, were monitored and compared to the control specimen without any sealant, for a duration of 5 days. It was observed that paraffin wax yielded similar results to that of aluminum foil. The long-term shrinkage strains in two standard cylinders with and without wax seal were monitored for 365 days and the results were compared with standard prediction models. The B3 model is able to accurately predict the total shrinkage strains in the cylinder.

Keywords Shrinkage · Concrete · Wax · Aluminum

1 Introduction

Shrinkage of concrete can be defined as the increase in strain in an unloaded specimen over time, when the temperature is kept constant. It is one of the key factors that control the long-term behavior of concrete structures as it causes an increase in strains over time. In pre-stressed concrete structures, shrinkage will lead to loss of pre-stress and if differential shrinkage happens, it will result in excessive long-term deflections. Any restraint to shrinkage will generate secondary moments and stresses and result in cracking, if not adequately designed for. Therefore, it is crucial to study the long-term strains in concrete due to shrinkage and the various factors that affect it.

There are different types of shrinkage in concrete [1, 2] as described briefly below:

M. Williams (✉) · D. Menon · A. M. Prasad
Indian Institute of Technology Madras, Chennai, India
e-mail: mary.williams.p@gmail.com

T. Kang (ed.), *Proceedings of 5th International Conference on Civil Engineering and Architecture*, Lecture Notes in Civil Engineering 369,
https://doi.org/10.1007/978-981-99-4049-3_17

(i) Plastic shrinkage—develops on the surface in fresh concrete due to water evaporation.
(ii) Drying shrinkage—reduction in volume due to loss of water during the drying process.
(iii) Autogenous shrinkage—consequence of self-desiccation in pores of cement paste during hydration.
(iv) Thermal shrinkage—result of temperature changes in concrete during hydration.
(v) Carbonation shrinkage—caused by chemical reactions due to carbon dioxide from the environment.
(vi) Chemical shrinkage—consequence of using water in the hydration process.

The autogenous shrinkage occurs even if there is no drying in the specimen and is normally termed as basic shrinkage. The shrinkage due to drying is termed as drying shrinkage. Numerous studies have been reported in literature on the effect of different parameters like drying, reinforcement, concrete strength, etc., on the shrinkage strains in concrete [3]. In order to study the effect of drying, the control specimen should be completely sealed from drying. This can be achieved by sealing the surface of the specimen with a suitable material, thereby avoiding the exchange of moisture with the environment. Experimental studies on shrinkage reported in literature have mostly used aluminum foil as a sealing material. However, utmost care is required to ensure that there are no tears or holes in the aluminum foil due to its fragile nature.

The present study investigates the effect of using wax and aluminum foil as sealants, by comparing the strains observed with that of a control specimen subject to drying. The long-term shrinkage strains in two standard cylinders (one sealed with wax and the other unsealed, exposed to ambient temperature and humidity conditions) were monitored for a duration of one year and compared with the predictions from standard models. Since there are very limited studies on shrinkage in the Indian ambient temperature and humidity conditions, with the use of local materials for concrete mix, this study is a major contribution to the experimental database of shrinkage in concrete.

1.1 Overview of Prediction Models

Six prediction models for shrinkage have been considered for comparison with the experimental data. All the models consider the effect of different parameters like age of drying, volume to surface area ratio, etc., by multiplying the ultimate or notional shrinkage coefficient with factors that depend on the corresponding parameters.

To model the variation of shrinkage with time, the ACI [4] model, B3 [5] and B4 [6] model adopt a hyperbolic function, whereas the GL 2000 [4] model uses power law. The MC10 [7] and EC2 [8] model are similar and use exponential function for basic shrinkage and hyperbolic function for drying shrinkage. Studies on specimens

subject to varying environmental conditions show that the fib MC2010 model slightly underestimates the shrinkage strains of specimens stored in ambient conditions [9]. Comparison of autogenous and drying shrinkage of concrete was done by Khairallah [10] and it was observed that among different prediction models, only B3 and ACI yield appropriate results for concrete of 28 days old. However, B3 and ACI model cannot be used for prediction of shrinkage in a sealed specimen as they can predict only total shrinkage that includes drying. Only MC10, B4 and EC2 can be used to predict shrinkage of a sealed specimen as they distinguish between basic and drying shrinkage.

2 Experimental Program

The experiment has been done in two parts. Firstly, two different sealants were used to monitor the shrinkage strains in prism, and based on this, one sealant was chosen to monitor the shrinkage strains in a standard cylinder for a period of one year. The results were compared with that of the unsealed cylinder, of the same concrete mix.

2.1 Study on Effect of Different Sealants

For the study of the effect of different sealants on the shrinkage behavior, a nominal mix of concrete was adopted to cast three prisms of size 150 × 200 × 500. The concrete mix proportion used for these prisms is given in Table 2. One prism was kept unsealed, while the other two were sealed, one using aluminum foil (FS, 2 layers of wrapping) and the other using paraffin wax (WS, 1 coat). The strains were monitored using fiber optic sensors at mid-height of the specimen (Fig. 2) and variation in temperature was recorded by fiber optic temperature sensors for a duration of 5 days (Fig. 3).

Table 1 Expression for shrinkage strain in prediction models

Model	Shrinkage strain	Remarks
ACI 209R-92 (ACI)	$\varepsilon_{sh}\,(t, t_c) = ((t\text{-}t_c)^{\alpha}/(f + (t\text{-}t_c)^{\alpha})\,\varepsilon_{shu}$	No differentiation between basic and drying shrinkage
GL 2000 (GL)	$\varepsilon_{sh} = \varepsilon_{shu}\,\beta(h)\,\beta(t)$	
B3	$\varepsilon_{sh}\,(t, t_s) = -\varepsilon_{sh\infty}\,k_h\,S(t)$	
MC 2010 (MC10)	$\varepsilon(t,t_s) = \varepsilon_{cas}\,(t) + \varepsilon_{cds}\,(t)$	Separates basic and drying shrinkage
Eurocode (EC2)	$\varepsilon_{cs} = \varepsilon_{cd} + \varepsilon_{ca}$	
B4	$\varepsilon_{sh,\,total}(t,t_0) = \varepsilon_{sh}\,(t,t_0) + \varepsilon_{au}\,(t,t_0)$	

Table 2 Concrete mix proportion for study on sealant

Composition	Quantity (kg/m^3)
Ordinary portland cement	350
Water	175
12.5 mm aggregate	1050
Sand	525

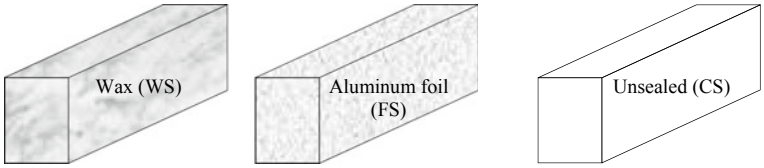

Fig. 1 Representative picture of the sealed and unsealed specimens

2.2 Results and Observations

It was observed that the unsealed specimen showed higher shrinkage strains initially compared to the sealed specimens (Fig. 2). Over time, the rate of shrinkage in the sealed and unsealed specimens converged, with the magnitude becoming almost same. The shrinkage strains observed in the specimens sealed with wax and aluminum foil were similar throughout the test duration, except for minor fluctuations. The temporary fluctuations may be attributed to the local temperature variations (Fig. 3) and vibrations due to local disturbances. If the local fluctuations are ignored, both the sealed specimens (FS and WS) showed a linear increase of strain with time. Even though the sealed specimens had lesser strains initially, it is seen that the variations in temperature affected the strains in both the specimens. This shows that the sealing was not fully effective.

2.3 Study on Long-Term Shrinkage Strains

Based on the observations from study on sealants, it was decided to use paraffin wax as a sealant for the long-term shrinkage study on cylinders, owing to its durability and higher resistance to local wear and tear. Two cylinders of standard size (150 dia $\times$ 300 mm) were cast using the concrete mix (of mean cylinder compressive strength at 6 days 22.8 MPa) given in Table 3. They were cured for 6 days after which one cylinder was kept unsealed (CS) and the other cylinder was sealed using paraffin wax (AS). To make sure the sealing is fully effective, two coats of paraffin wax were applied initially, and after 24 h, a third coat of wax was again applied.

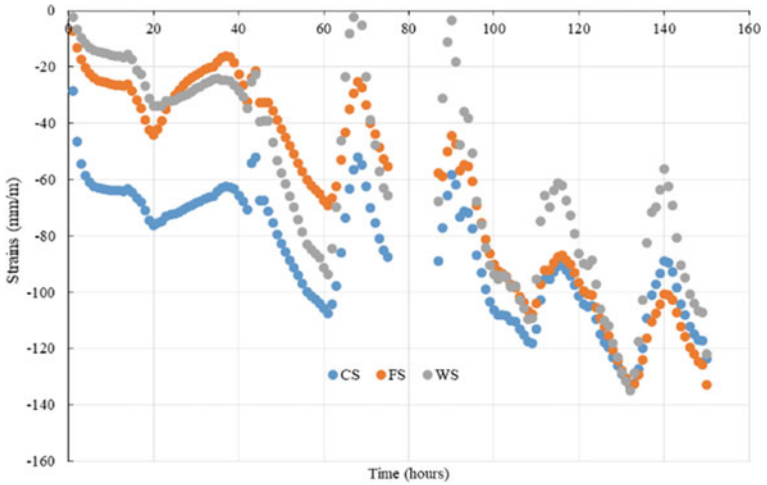

Fig. 2 Shrinkage strains in the sealed and unsealed specimens

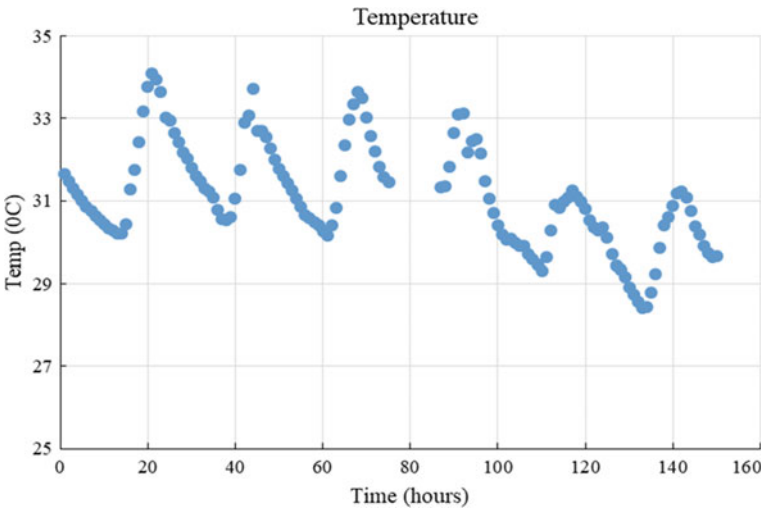

Fig. 3 Variation of temperature during the test duration

Table 3 Concrete mix proportion for study on shrinkage

Composition	Quantity (kg/m^3)
Ordinary portland cement	420
Water	192
12.5 mm aggregate	828
Sand	953

To monitor the strains, electrical resistance strain gauges of 120Ω resistance and 60 mm gauge length were mounted on the surface of the cylinder specimens at mid-height. For each cylinder, two set of readings were taken at symmetrically opposite locations for redundancy. The sampling interval was one hour.

2.4 Results and Observations

The strains observed in both the cylinder specimens (AS and CS) are plotted in Fig. 4.

It was observed that the sealed specimen (AS) had some swelling initially (Fig. 4) and over time, the strain in both the specimens showed an increasing trend. The magnitude of strains are higher in the unsealed specimen (~20%), as expected. However, after 300 days, the observed strains in the unsealed specimen (CS) started showing a decreasing trend, whereas this behavior was not exhibited by the sealed specimen (AS). The reduction in strains in the CS specimen may be attributed to the reduction in temperature around 300 days (Fig. 5), thereby resulting in a decrease in the shrinkage. The AS specimen owing to its surface seal was not affected by the temperature variation and hence does not show any reduction in strains. The minor fluctuation seen in both the graphs plotted in Fig. 4 may be attributed to the noise in electrical strain gauges (due to temperature and humidity variations).

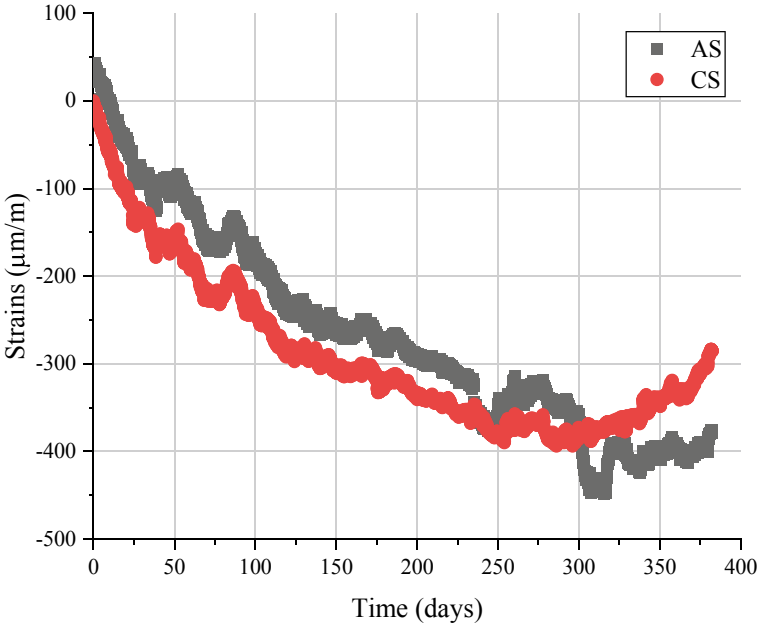

Fig. 4 Shrinkage strains in cylinders

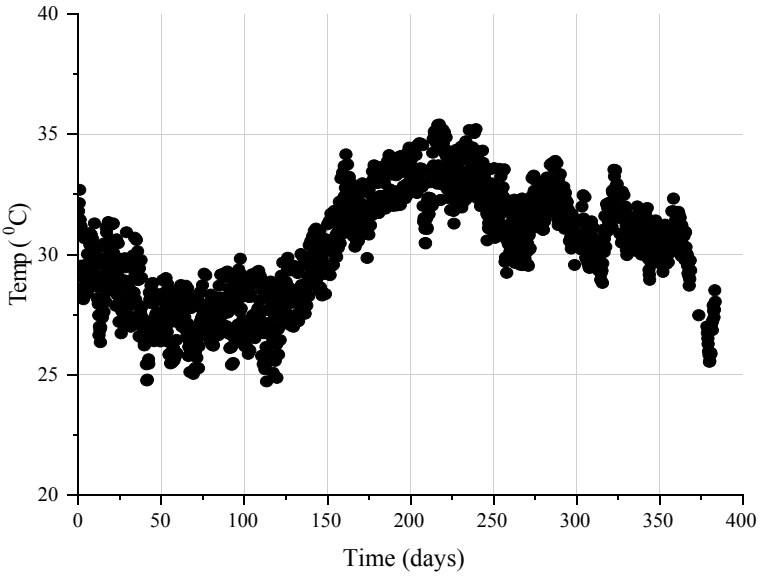

Fig. 5 Temperature variation with time

2.5 Prediction of Shrinkage Strains

The shrinkage strains in the both the AS and CS specimens have been predicted using the standard models and plotted in Figs. 6 and 7.

Of all the models considered for the prediction of shrinkage strains in the unsealed specimen, the B3 model yields the best results, followed by ACI model (Fig. 6). The maximum deviation is seen in the B4 model, where the strains are over predicted by around 32%.

In the sealed specimen, only those models that separate autogenous and drying shrinkage in their prediction model can be used to estimate the strains (EC2, MC10 and B4). The predictions based on these models are plotted below in Fig. 7. It is observed that B4 model shows the least error in predicting the autogenous shrinkage strains, with the deviation from observed strains reducing to 22% at 350 days. MC10 and EC2 model severely underestimate the strains in the sealed specimen.

3 Conclusions

The experimental results indicate that the use of wax as a sealant is effective in preventing exchange of moisture in the specimen with the environment. With respect to the magnitude of strains, autogenous shrinkage causes about 20% lesser strains than

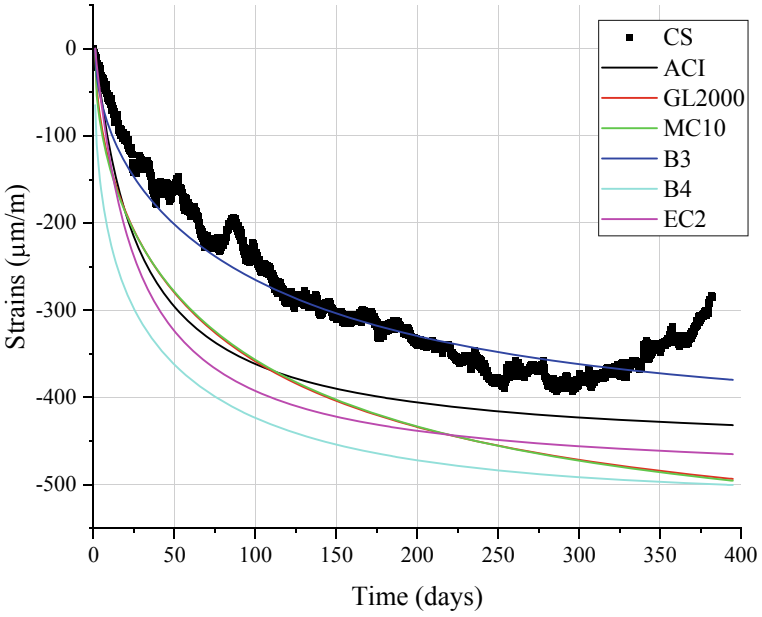

Fig. 6 Predicted v/s observed strains in the CS specimen

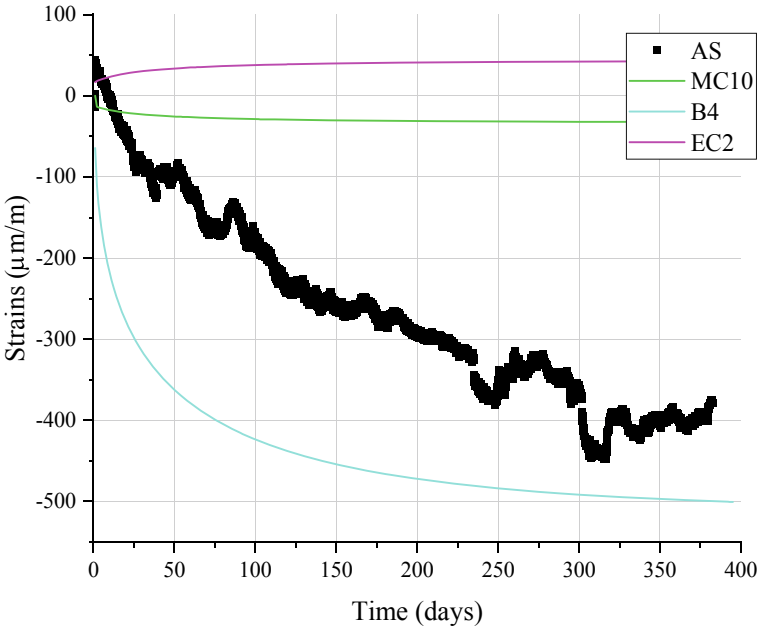

Fig. 7 Predicted v/s observed strains in the AS specimen

combined shrinkage. However, the rate of increase of strain is similar in both autogenous and combined shrinkage. The B3 model is able to predict the total shrinkage strains with good accuracy compared to the other five models considered. Among the three models (B4, MC10 and EC2) that can predict autogenous shrinkage, the B4 model has the least error (22%).

References

1. Šahinagić-Isović M, Markovski G, Ćećez M (2012) Shrinkage strain of concrete-causes and types. Građevinar 64(9):727–734
2. Gilbert RI, Castel A, Khan I, South W, Mohammadi J (2018) An experimental study of autogenous and drying shrinkage. In: Hordijk DA, Lukovic M (eds) High tech concrete: where technology and engineering meet. Springer International Publishing (AG 2018), pp 33–41
3. Sule M, Breugel K (2004) The effect of reinforcement on early-age cracking due to autogenous shrinkage and thermal effects. Cement Concr Compos 26(5):581–587
4. American Concrete Institute (ACI) (2008) Guide for modelling and calculating shrinkage and creep in hardened concrete. ACI-209.2R-08, ACI Committee 209, Detroit
5. Bazant ZP, Baweja S (2000) Creep and shrinkage prediction models for analysis and design of concrete structures—model B3. ACI Spec Publ 194:1–84
6. RILEM Draft Recommendation (2015) TC-242-MDC: model B4 for creep, drying shrinkage and autogenous shrinkage of normal and high-strength concretes with multi-decade applicability. Mater Struct 48(4):753–770
7. CEB-fib (2013) *fib* model code for concrete structures 2010. Lausanne, Switzerland
8. EN 1992-1-1 (2003) Eurocode 2: design of concrete structures-Part 1
9. Nastic et al (2019) Shrinkage and creep strains of concrete exposed to low relative humidity and high temperature environments. Nucl Eng Design 352:110154
10. Khairallah RS (2009) Analysis of autogenous and drying shrinkage of concrete. McMaster University, Ontario

Design of Concrete Structures and Mechanics of Reinforced Concrete Structures

Shear Design Optimization of Short Rectangular Reinforced Concrete Columns Using Deep Learning

Raushan Utemuratova, Aknur Karabay, Dichuan Zhang, and Huseyin Atakan Varol

Abstract This paper aims to show the effectiveness of artificial intelligence (AI) for structural design optimization. Design optimization of rectangular reinforced concrete (RC) columns using a deep neural network (DNN) results in a reduction of both time and monetary resources. The utilization of the DNN model prevents the iterative design process, which is common in a conventional approach. To create the necessary dataset of designs, parametric RC column designs are generated and analyzed automatically using a finite element model (FEM) of the OpenSeesPy Python library. The dataset spans five heights and six concrete classes. The data is pre-processed using equal-sized filtration to preserve the most economical column designs for specified ranges of loading conditions. Based on the given constraints of axial load, bending moments, and shear loads, the NN model predicts cross section geometry and longitudinal and transverse reinforcement. To evaluate the accuracy of the NN model predictions, thirty cases are run through the model and checked for compliance with the Eurocode building standard. A comparative analysis of the NN performance with manual designs demonstrates the overall effectiveness of the NN by 11.3% in terms of monetary price. As for the time aspect, the NN is faster by 8.57 min and 96% more efficient than manual design.

Keywords Reinforced concrete column · Shear design · Deep neural network · Price optimization

R. Utemuratova (✉) · A. Karabay · H. A. Varol
Institute of Smart Systems and Artificial Intelligence (ISSAI), Nazarbayev University, 010000 Nur-Sultan, Republic of Kazakhstan
e-mail: raushan.utemuratova@nu.edu.kz

D. Zhang
School of Engineering and Digital Sciences, Nazarbayev University, 010000 Nur-Sultan, Republic of Kazakhstan

T. Kang (ed.), *Proceedings of 5th International Conference on Civil Engineering and Architecture*, Lecture Notes in Civil Engineering 369,
https://doi.org/10.1007/978-981-99-4049-3_18

1 Introduction

AI in engineering has been developing in the recent years and revolutionizing problem-solving approaches. The application of AI in the real world anticipates unknowns in processes, enhances effectiveness in terms of resources, facilitates operations and minimizes associated risks. For example, in process systems engineering, AI forecasts energy consumption during production and detects potential faults and cracks in oil refineries [1]. In mining engineering, AI predicts the maximum fracture height after coal drilling and reduces post-processing damages [2].

The application of AI in civil engineering varies drastically. For instance, machine learning (ML), a subfield of AI, forecasts traffic flow in transportation and prevents congestion and delays during travel [3]. In addition, a deep learning (DL) model can detect and classify cracks in the pavement to identify the causes of damage by cutting down human involvement [4]. Another area where AI has promising potential is structural health monitoring, such as bridge quality checks and crack detection in structures [4]. In geotechnical engineering, an AI optimization algorithm can predict groundwater levels and pile settlement [5]. In construction, an AI random forest model can explore soil interaction with metallic pipes [6]. A DL model designed to detect personal protective equipment instantly amplifies occupational safety and health quality by reducing the risks of severe injuries in the workplace [6]. AI can also reduce construction expenditures by automating and optimizing construction planning and scheduling [7].

AI is demonstrating its effectiveness in structural engineering as well. For instance, AI can predict the strength of deep beams made of different concrete types and the relative displacements of building floors [8]. A self-tuning ML model can provide load-bearing capacity for concrete beam-column joints [9]. Afzal et al. summarize that intelligence optimization, hybrid optimization, and conventional optimization methods are implemented to make RC structures more sustainable, cost-effective, and durable [10]. The NN model is implemented in carbon footprint optimization by RC columns under axial load and bending moments [11]. Hong et al. propose a concrete column optimization model using an artificial neural network that designs geometry parameters and loading capacity forwardly and reversely without considering shear design [12].

Even though there are several studies on concrete column optimization, detailed column design is still a topic of interest to researchers. Our project proposes a rectangular concrete columns design under shear and bending moments using a DNN model. Our approach shows advantages in terms of time and money criteria compared to manual design. The rest of the paper consists of the following sections: Sect. 2 presents a methodology for tabular data preparation according to the Eurocode 2 building code standard and the NN model. Section 3 discusses the results of the model for 30 different cases in comparison with the ordinary design calculations. Section 4 summarizes the paper and discusses further work.

2 Methodology

2.1 Model Parameters

Table 1 provides a list of material and geometric design parameters and their units. The cross section and longitudinal design configurations of the rectangular column are illustrated in Fig. 1.

The section geometry is defined by the width w and the depth d. The cover c represents the distance from the outer edge of the column to the transverse reinforcement. Longitudinal and transverse reinforcement bars are designated D_l and D_{tr}, respectively, and placed at certain spacings s_l and $s_{\text{tr,}}$ as specified in Eurocode 2 [13]. To locate the longitudinal rebars parametrically, two parameters, n_w and n_d, are introduced to define the number of gridlines along the width and depth. The longitudinal bars are placed along the perimeter at the cross section of these gridlines.

The total number of longitudinal reinforcements N_l is calculated as follows:

$$N_l = 2n_w + 2(n_d - 2) \tag{1}$$

For the concrete material, a parabola rectangle model is used (see Fig. 2a). For the steel material, a linear biaxial model with zero strain hardening ratio is utilized as shown in Fig. 2b. The theoretic stress–strain relationship for both materials is reduced by the safety factor γ.

2.2 Parametric Data Generation and Preprocessing

The parametric dataset is generated using the OpenSeesPy library in Python. To create a column design for analysis, we randomly sample geometric and model parameters, which are h, w, d, D_l, N_l, D_{tr}, s_{tr}, and f_{ck}. In this work, we consider five different column heights, $h = [3.0, 3.5, 4.0, 4.5, 5.0]$ m. The column width w and the depth d vary from 0.2 m up to one-third of the column height with a step size of 0.05 m, and the depth does not exceed four times its width, according to Eurocode 2 [13]. For a column height of 3.0 m, the maximum allowable width and depth are one meter. The clear cover c mentioned in Sect. 2.1 is set at 0.05 m. The longitudinal rebar diameter D_l is randomly selected from the list [12, 14, 16, 20, 25, 28, 32, 40, 50] mm. The number of longitudinal rebars is restricted by the maximum and minimum allowable reinforcement area (see Eqs. 2, 3, 4, and 5), according to the Eurocode.

$$N_{l,\max} = A_{l,\,\max}/(\pi D_l^2/4) \tag{2}$$

$$A_{l,\,\max} = 0.04A_c \tag{3}$$

Table 1 Geometric and material parameters, their descriptions, and units

Parameter	Description	Unit
H	Column height	m
W	Column width	m
D	Column depth	m
C	Concrete cover	m
A	Total section area	m^2
A_c	Concrete area	m^2
A_l	Total longitudinal reinforcement area	m^2
D_l	Longitudinal rebar diameter	m
s_l	Longitudinal rebars spacing	m
N_l	Number of longitudinal rebars	-
n_w	Number of gridlines along a width	-
n_d	Number of gridlines along a depth	-
V_{tr}	Volume of transverse reinforcement	m^3
D_{tr}	Transverse rebar diameter	m
A_{sw}	Cross-sectional area of shear reinforcement	m^2
s_{tr}	Transverse rebars spacing	m
f_{ck}	Characteristic strength of concrete	MPa
f_{cd}	Design strength of concrete	MPa
E_c	Concrete Young's modulus	GPa
ε_0	Concrete strain at maximum strength	-
ε_u	Concrete strain at crushing strength	-
γ_c	Concrete safety factor	-
f_{yk}	Characteristic strength of steel	MPa
f_{yd}	Design strength of steel	MPa
E_s	Steel Young's modulus	GPa
β	Strain-hardening ratio of steel	-
γ_s	Steel safety factor	-
P	Design axial load	MN
M_i	Design moment ($i = y$ or z axes)	MNm
V_i	Design shear load ($i = y$ or z axes)	MN
Z	Lever arm of internal forces	m
θ	Angle between the concrete compression strut and the beam axis perpendicular to the shear force	rad
P_M	Price of a manual design	€
P_{NN}	Price of a column design by NN	€
Δ	Relative difference in manual and NN prices (Eq. 2)	%

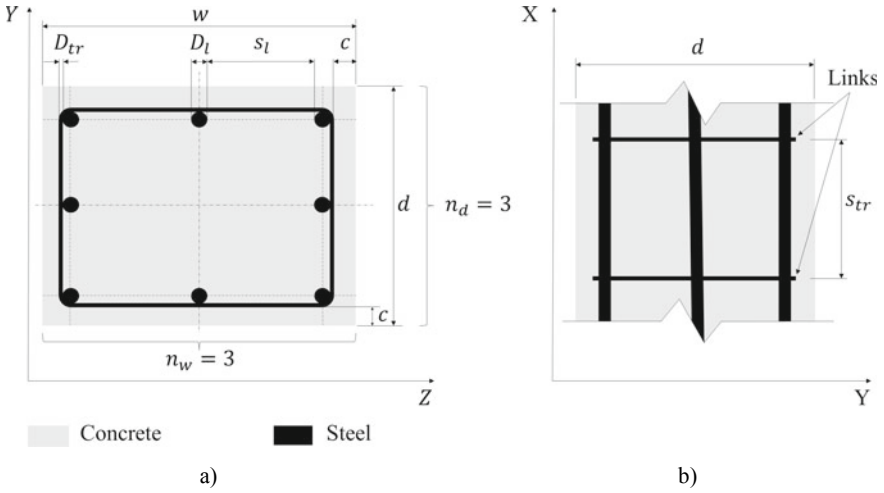

Fig. 1 Geometric parameters of the rectangular RC column: **a** cross section; **b** longitudinal section

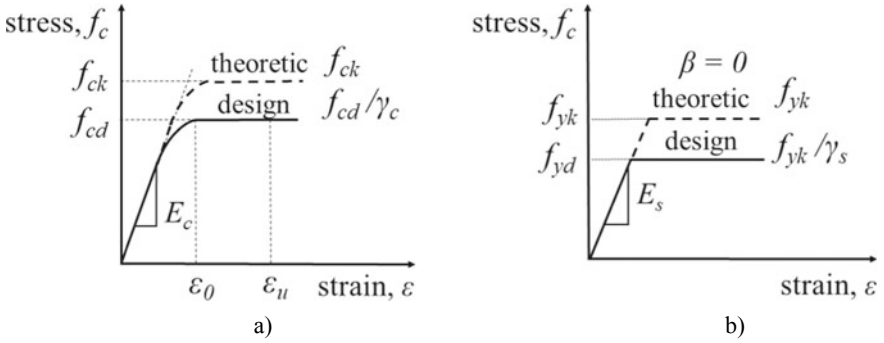

Fig. 2 **a** Stress–strain curve for concrete; **b** stress–strain curve for steel

$$N_{l,\min} = \max\left(4,\ A_{l,\min}/(\pi D_l^2/4)\right) \tag{4}$$

$$A_{l,\min} = \max\left(0.002A_c,\ 0.1P/f_{yk}\right) \tag{5}$$

The transverse rebar diameter D_{tr} is selected from the list [6, 8, 10, 12, 14, 16, 20, 25, 28, 32, 40, 50] mm, with a minimum limitation defined by one-quarter of D_l. The spacing between transverse rebars is regulated by the maximum value obtained as follows:

$$s_{tr,\max} = \min\left(20D_{tr},\ w,\ d,\ 0.4\right) \tag{6}$$

The minimum shear reinforcement is checked using Eq. (7.)

$$A_{sw}/s_{tr}w^3 \geq 0.08(f_{ck})^{1/2}/f_{yk} \tag{7}$$

For the parametric dataset, we consider six normal strength concrete classes with a compressive strength f_{ck} of [25, 30, 35, 40, 45, 50] MPa. Concrete material properties for all classes are presented in Table 2. For the steel material, we use steel with a characteristic strength f_{yk} of 500 MPa, Young's modulus E_s of 210 GPa, and zero strain-hardening ratio $\beta = 0$.

After randomly generating a column cross section and material parameters, the P-M_y-M_z interaction diagram is generated. To obtain the diagram, the section is analyzed under 50 random axial loads from zero to axial load capacity and 30 random moment loads from zero to moment capacity in each direction using finite element analysis in OpenSeesPy resulting in $50 \times 30 \times 30 = 45{,}000$ cases. An example of the interaction diagram is shown in Fig. 3. Next, shear capacity is calculated using Eqs. (8) and (9). The cotangent of an angle between the concrete compression strut and the beam axis perpendicular to the shear force $\cot\theta$ mentioned in the equation is limited from one to 2.5.

$$V = zA_{sw}f_{yd}\cot\theta/s_{tr} \tag{8}$$

$$z \approx 0.9d \tag{9}$$

To filter the data and keep the most optimal designs, the price of each design is calculated using the concrete price given in Table 2 and the steel price of 2,944 €/m^3 [15]. Next, the input loads P, M_y, M_z, V_y, and V_z are normalized from 0 to 1. The five-dimensional input space, where the designs are distributed based on the input loads, is split into equal ranges and the one with the minimum price is kept. The equal-sized filtration step is 0.04. The total number of data points (i.e., filtered designs) after filtration is 3,657,300.

Table 2 Properties of concrete material [14]

f_{ck} (MPa)	E_c (GPa)	ε_0 (%)	ε_{cu} (%)	Price (€/m^3)
25	31	2.10	3.5	72.6
30	33	2.20	3.5	76.2
35	34	2.25	3.5	87.1
40	35	2.30	3.5	96.8
45	36	2.40	3.5	108.9
50	37	2.45	3.5	115.0

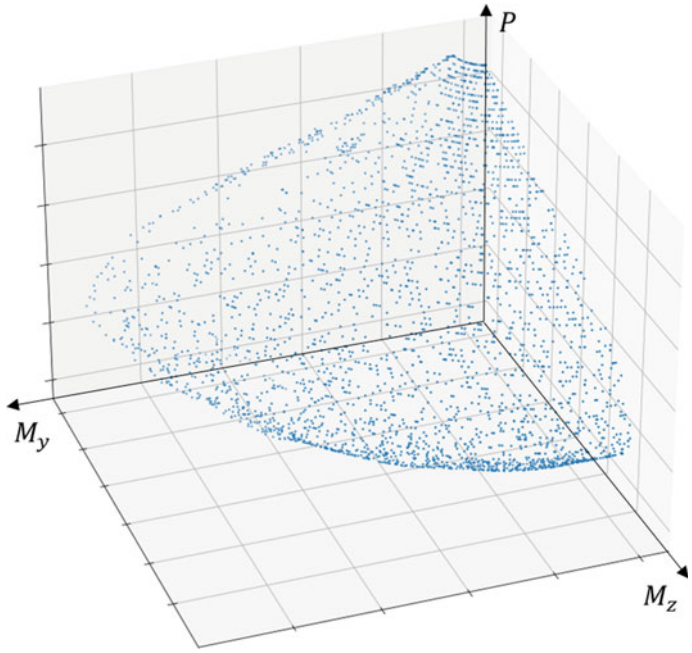

Fig. 3 P-M_y-M_z interaction diagram generated using OpenSeesPy Library

The data generation and preprocessing codes are written in the Python programming language and are publicly available on the GitHub repository under the MIT license.[1]

2.3 Network Architecture

To train the DNN model, the dataset is split into three parts: 80% train set, 10% validation set, and 10% train set. The model architecture consists of 18 fully connected layers: one input layer, 16 hidden layers, and one output layer, as shown in Fig. 4. The model takes seven inputs and predicts four design parameters. The inputs are axial load P, the moments in two directions M_y and M_z, the shear loads in two directions V_y and V_z, the column height h, and the concrete compressive strength f_{ck}. The outputs are the column width w, the depth d, the total longitudinal reinforcement area A_l, and the transverse reinforcement volume V_{tr}. The total number of learnable parameters is 2,033,024. The batch size is 16,384, the learning rate is 0.0001, and the number of epochs is 250. Adam optimizer and the ReLU activation function are used. The total training time of the model is around two hours on a single Tesla V100 GPU card of

[1] https://github.com/IS2AI/Shear-Design-Optimization-of-RC-Column

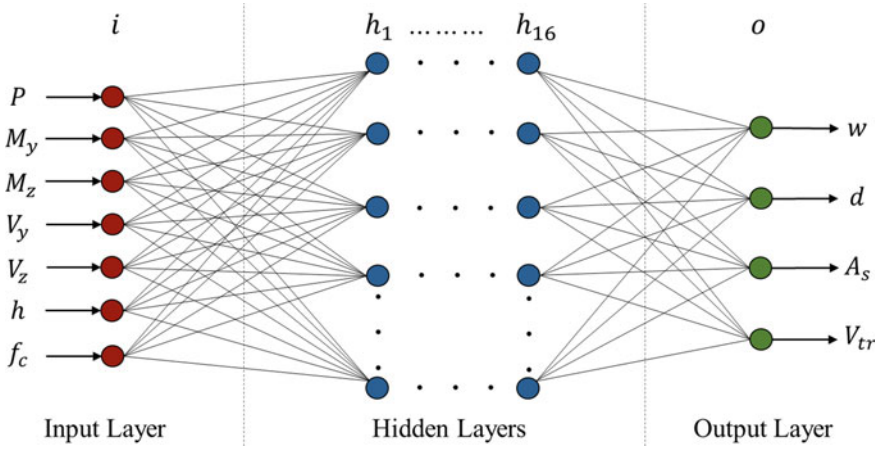

Fig. 4 DNN architecture for shear design optimization of RC columns

the Nvidia DGX-2 server. The network model is available on the GitHub page under the MIT license.[2]

3 Results and Discussion

The NN training and validation losses are presented in Fig. 5. The mean squared error (MSE) loss is 0.00524. To evaluate the performance of the NN, a series of test cases are performed and compared with the manually optimized design by a structural engineer. The six loading cases presented in Table 3 are tested for 5 column heights. For comparison, manual designs and NN outputs for these 30 cases are presented in Table 4. The inference time for all test cases is 8.5 s. The time required to check the validity of the results according to Eurocode 2 is 760.5 s. Overall, 769.0 s or approximately 13 min is required to obtain the final NN results for 30 cases. As a result, the time spent per design by the model is 0.43 min. For hand calculations performed by the structural engineer, about nine minutes are spent per design. The results highlight that the NN is more advantageous than the conventional calculation procedure by 8.57 min per design which is 96% effectiveness.

For the cost comparison of the two approaches, the price of materials used for the designs is calculated. The relative difference Δ between the NN and the manual designs is calculated using Eq. 10 and presented in Table 4. It can be seen from the table, the DNN provides a cheaper design in 26 out of 30 cases. Overall, the NN is 11.3% more economic than the conventional design approach.

$$D = (P_{\mathrm{NN}} - P_M)/P_M \tag{10}$$

[2] See Footnote 1.

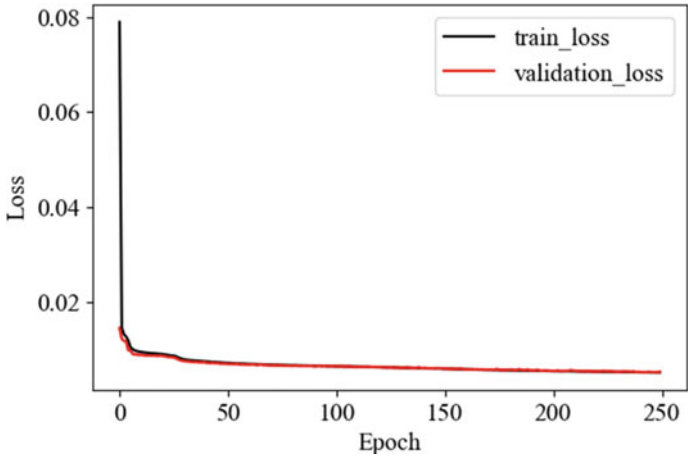

Fig. 5 DNN train and validation losses for the filtration size of 0.04

Table 3 Manual and NN designs comparison based on monetary price

Case	Concrete property	Loading conditions				
	f_c (MPa)	P (MN)	M_y (MNm)	M_z (MNm)	V_y (MN)	V_z (MN)
1	25	0.6	0.1	0.1	0.2	0.2
2	30	0.6	0.1	1.0	0.2	0.2
3	35	0.6	1.0	1.0	0.2	0.2
4	40	6.0	0.1	0.1	2.0	2.0
5	45	6.0	0.1	1.0	2.0	2.0
6	50	6.0	1.0	1.0	2.0	2.0

4 Conclusions

Rapidly developing data-driven technologies are penetrating different areas to facilitate the labor-intensive and time-consuming processes in the industry. This study presents a DNN model for the optimization of rectangular RC column designs under axial load, biaxial bending, and shear forces. The model outputs the cross section geometry and longitudinal and transverse reinforcement for five different column heights and six concrete classes. Since DNN requires a vast number of training data, we generated a parametric dataset using FEM in the OpenseesPy library. To evaluate the network performance, we performed a comparative analysis on 30 test cases for different loading cases, column heights, and material properties. The results show the effectiveness of the NN performance by 11% compared to the manual designs in terms of material cost. As for the time criteria, it takes 0.43 min for the model to predict and check a single column design, while a structural engineer performs a

Table 4 Manual and DNN designs comparison based on monetary price

Height	Manual designs				NN designs				Diff
h (m)	w (m)	d (m)	A_l (10^{-6} m^2)	V_{tr} (10^{-6} m^3)	w (m)	d (m)	A_l (10^{-6} m^2)	V_{tr} (10^{-6} m^3)	Δ (%)
3.0	0.40	0.40	2513	3764	0.45	0.45	2941	3705	−19.4
	0.50	0.80	11,084	3958	0.50	0.80	6158	6443	**17.5**
	0.85	0.85	12,868	7660	0.70	0.70	13,685	6250	**17.8**
	0.70	0.70	1608	33,583	0.80	0.80	1810	33,458	−19.6
	0.80	0.85	1608	40,510	0.60	0.60	3217	30,658	**32.9**
	0.80	0.80	3217	33,458	0.60	0.75	6434	36,871	**7.1**
3.5	0.40	0.40	2513	4391	0.35	0.35	2281	3687	**17.3**
	0.50	0.80	11,084	4486	0.50	0.90	6158	8111	**10.9**
	0.85	0.85	12,868	8810	0.65	0.85	11,197	9001	**18.0**
	0.70	0.70	1608	39,180	0.85	0.55	1527	40,393	**0.4**
	0.80	0.85	1608	47,262	0.65	0.65	2413	35,341	**29.4**
	0.80	0.80	3217	39,034	0.65	0.65	6434	35,948	**15.1**
4.0	0.40	0.40	2513	5019	0.30	0.45	1885	5469	**14.2**
	0.50	0.80	11,084	5278	0.55	0.95	5429	11,111	**3.8**
	0.85	0.85	12,868	9959	0.70	0.70	12,566	8333	**20.7**
	0.70	0.70	1608	44,777	0.65	0.65	1608	41,083	**9.8**
	0.80	0.85	1608	54,014	0.65	0.65	2011	47,930	**25.6**
	0.80	0.80	3217	44,611	0.65	0.70	4825	42,930	**14.6**
4.5	0.40	0.40	2513	5646	0.40	0.40	1810	5646	**8.6**
	0.50	0.80	11,084	5806	0.45	0.85	8042	9537	**11.4**
	0.85	0.85	12,868	11,491	0.70	0.70	14,726	9375	**15.1**

(continued)

Table 4 (continued)

Height	Manual designs				NN designs				Diff
h (m)	w (m)	d (m)	A_l (10^{-6} m^2)	V_{tr} (10^{-6} m^3)	w (m)	d (m)	A_l (10^{-6} m^2)	V_{tr} (10^{-6} m^3)	Δ (%)
	0.70	0.70	1608	50,375	0.65	0.65	1608	46,218	**11.0**
	0.80	0.85	1608	60,766	0.60	0.75	2155	52,645	**23.4**
	0.80	0.80	3217	50,187	0.65	0.70	4310	47,474	**16.3**
5.0	0.40	0.40	2513	6273	0.30	0.65	2941	5610	-15.5
	0.50	0.80	11,084	6597	0.50	0.50	11,781	10,355	**10.8**
	0.85	0.85	12,868	12,640	0.65	0.90	11,197	6642	**18.8**
	0.70	0.70	1608	55,972	0.55	1.00	1608	55,972	-8.4
	0.80	0.85	1608	67,517	0.60	0.90	1810	49,480	**20.4**
	0.80	0.80	3217	55,763	0.70	0.70	4021	55,011	**12.4**

nearly optimal design using a spreadsheet in around nine minutes. Hence, the NN time efficiency is 96%.

References

1. Shi T, Yang A, Jin Y, Ren J, Shen W, Dong L, Man Y (2021) Chapter 1—Artificial intelligence in process systems engineering. In: Ren J, Shen W, Man Y, Dong L (eds) Applications of artificial intelligence in process systems engineering, pp 1–10. https://doi.org/10.1016/B978-0-12-821092-5.00010-3
2. Miao L, Duan Z, Xia Y, Du R, Lv T, Sun X (2022) Analysis of factors influencing mining damage based on engineering detection and machine learning. Sustain 14. https://doi.org/10.3390/su14159622
3. Abduljabbar R, Dia H, Liyanage S, Bagloee SA (2019) Applications of artificial intelligence in transport: an overview. Sustain 11. https://doi.org/10.3390/su11010189
4. Lagaros ND, Plevris V (2022) Artificial intelligence (AI) applied in civil engineering. Appl Sci 12(15):7595. https://doi.org/10.3390/app12157595
5. Zhang W, Li H, Li Y, Liu H, Chen Y, Ding X (2021) Application of deep learning algorithms in geotechnical engineering: a short critical review. Artif Intell Rev 54:5633–5673. https://doi.org/10.1007/s10462-021-09967-1
6. Xu Y, Zhou Y, Sekula P, Ding L (2021) Machine learning in construction: from shallow to deep learning. Develop Built Environ 6. https://doi.org/10.1016/j.dibe.2021.100045
7. Abioye SO, Oyedele LO, Akanbi L, Ajayi A, Delgado JMD, Bilal M, Akinade OO, Ahmed A (2021) Artificial intelligence in the construction industry: a review of present status, opportunities and future challenges. J Build Eng 44. https://doi.org/10.1016/j.jobe.2021.103299
8. Yücel M, Nigdeli SM, Bekdaş G (2021) Artificial intelligence and machine learning with reflection for structural engineering: a review. In: Nigdeli SM, Bekdaş G, Kayabekir AE, Yucel M (eds) Advances in structural engineering—optimization. Studies in systems, decision and control. Springer, Cham, p. 326. https://doi.org/10.1007/978-3-030-61848-3_2
9. Alwanas AAH, Al-Musawi AA, Salih SQ, Tao H, Ali M, Yaseen ZM (2019) Load-carrying capacity and mode failure simulation of beam-column joint connection: application of self-tuning machine learning model. Eng Struct 194:220–229. https://doi.org/10.1016/j.engstruct.2019.05.048
10. Afzal M, Liu Y, Cheng JCP, Gan VJL (2020) Reinforced concrete structural design optimization: a critical review. J Cleaner Prod 260. https://doi.org/10.1016/j.jclepro.2020.120623
11. Karabay A, Utemuratova R, Zhang D, Varol HA (2022) Carbon footprint optimized design of sustainable reinforced concrete columns using deep learning. In: Holschemacher K, Quapp U, Singh A, Yazdani S (eds) Proceedings of international structural engineering and construction, p 9. https://doi.org/10.14455/10.14455/ISEC.2022.9(1).SUS-14
12. Hong W, Nguyen MC, Pham TD (2022) Optimized interaction P-M diagram for rectangular reinforced concrete column based on artificial neural networks abstract. J Asian Architect Build Eng. https://doi.org/10.1080/13467581.2021.2018697
13. EN 1992-1-1:2004 (2004) Design of concrete structures. https://eurocodes.jrc.ec.europa.eu/showpage.php?id=132
14. JC Betons Prices. https://jcbetons.lv/cenas-en/?lang=en
15. Metali. https://www.metali.lv/en/products/rebars

Effect of Different Forms of Force Transmission Members on the Performance of Rectangular Concrete-Filled Steel Tubular Columns under Axial Compression

Na Xu and Guiman Wang

Abstract Based on the study of the mechanical properties of the rectangular concrete-filled steel tube (CFRT) column with I-steel section and rectangular inner ring plate as the force transmission member, this paper designed four other force transmission measures: rectangular steel plate, T-shaped steel beam, channel steel beam, box steel beam. The model of CFRT column with transmission components (different structural measures) was established by general finite element software ABAQUS, and the finite element numerical simulation analysis was carried. They were studied that the effect of different forms of transmission components on the performance of CFRT column under axial force and the interaction behavior of CFRT column. The results show that the CFRT column with T-shaped steel beam can not only improve the bearing capacity of the column, but also achieve better interaction behavior, and save the amount of steel, which provides a basis for the reasonable effective selection of force transmission members in engineering.

Keywords CFRT column · Force transmission members · T steel beam · Work together · The bearing capacity

1 Introduction

It is the key to give full play to the excellent mechanical properties of concrete-filled rectangular steel tube columns to ensure that the steel tube wall and the core concrete in concrete-filled rectangular steel tube columns work together and jointly resist the external load. To ensure that the external load acting on the steel tube wall of concrete-filled rectangular steel tube columns can be effectively transmitted to the core concrete and shorten the shear transmission path between the steel tube

N. Xu (✉) · G. Wang (✉)
Guangdong Polytechnic of Science and Technology, Zhuhai 519090, Guangdong, China
e-mail: 174600556@qq.Com

T. Kang (ed.), *Proceedings of 5th International Conference on Civil Engineering and Architecture*, Lecture Notes in Civil Engineering 369,
https://doi.org/10.1007/978-981-99-4049-3_19

and the core concrete, a new type of concrete-filled steel tubular column joint is characterized in that the steel tube in the floor node area of concrete-filled steel tubular column is provided with force transmission members, namely distribution beam and inner ring rib, wherein the distribution beam is the main force transmission member, and the inner ring rib is arranged at the height of the upper and lower flanges of the distribution beam and communicated with the upper and lower flanges of the distribution beam. The inner ring rib is the secondary force transmission member, which can coordinate the deformation and stress of the steel tube wall and the internal concrete of the concrete-filled steel tubular column, so that the steel tube wall and the internal concrete can bear the external load together. The application of force transmission members can effectively solve the potential safety hazards of concrete-filled rectangular steel tube columns [1–8].

Different forms of s have different transmission characteristics and stress characteristics, thus they naturally have different influences on columns. The research group has designed four other structural measures for force transmission, namely rectangular steel plate, T-beam, channel steel beam and box beam, which are the main force transmission members. It also has studied the influence of different types of force transmission members on the mechanical properties of concrete-filled rectangular steel tube columns under axial force and the combined working performance of concrete-filled rectangular steel tube columns, thus solving the problem of reasonably and effectively setting up force transmission members in practical projects.

2 Design of Force Transmission Members with Four Structural Measures

To investigate the combined working performance of concrete-filled rectangular steel tube columns with different structural measures, and compare and analyze the combined working performance under different structural measures of force transmission, a model of concrete-filled rectangular steel tube columns without considering friction is established by using ABAQUS [9]. It includes four different structures with rectangular steel plates, T-beams, channel steel beams and box beams as main force transmission members, respectively.

2.1 Rectangular Steel Plate

Rectangular steel plates are arranged on the steel tube walls in the concrete-filled rectangular steel tube columns in the floor node area as force transmission members, and the structural form is shown in Fig. 1.

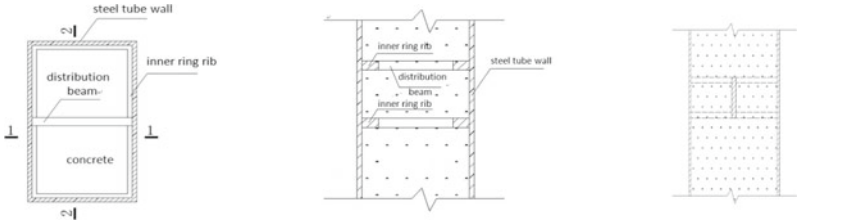

(a) Plan view of single distribution beam (b) Section view of single distribution beam 1-1. (c) Section of single distribution beam 2-2

Fig. 1 Structure and arrangement of rectangular steel plates

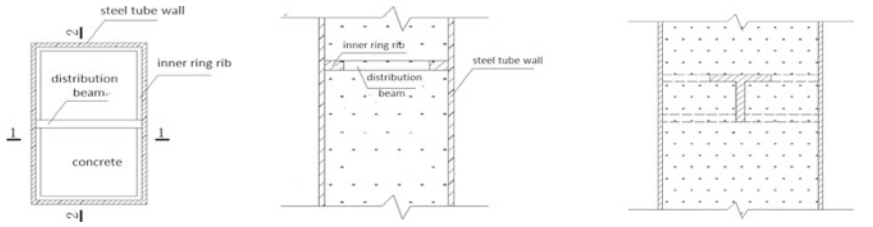

(a) Plan view of single distribution beam (b) Section view of single distribution beam 1-1 (c) Section of single distribution beam 2-2

Fig. 2 Structure and layout of T-beam

2.2 T-Beam

T-beams are arranged on the steel tube walls in the concrete-filled rectangular steel tube columns in the floor node area and are directly used as force transmission members. The structural form is shown in Fig. 2.

2.3 Channel Beam

Channel beams are arranged on the steel tube walls in the concrete-filled rectangular steel tube columns in the floor node area to directly serve as force transmission members, and the structural form is shown in Fig. 3.

2.4 Box Beam

Box beams are arranged on the steel tube walls in the concrete-filled rectangular steel tube columns in the floor node area to directly serve as force transmission members, and the structural form is shown in Fig. 4.

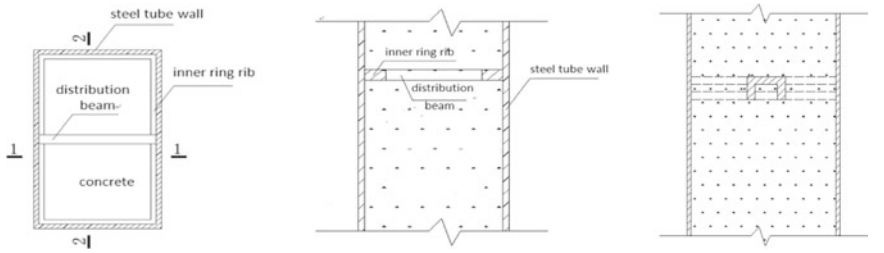

(a) Plan view of single distribution beam

(b) Section view of single distribution beam 1-1

(c) Section of single distribution beam 2-2

Fig. 3 Structural arrangement of channel steel beam setting

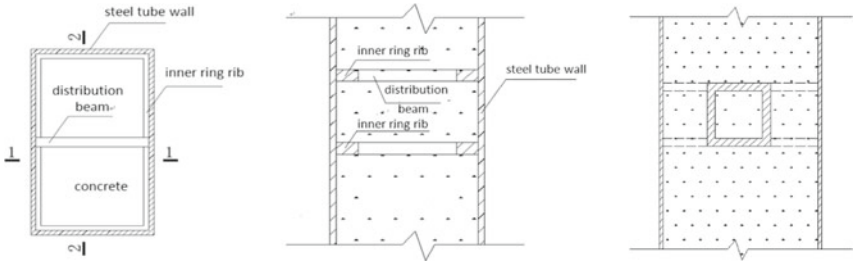

(a) Plan view of single distribution beam

(b) Section view of single distribution beam 1-1.

(c) Section of single distribution beam 2-2

Fig. 4 Structural arrangement of box beams

3 Establishment of Finite Element Model

The selected concrete-filled rectangular steel tube columns have a cross section size of 800 mm × 1200 mm, and a steel tube wall thickness of 16 mm. It is single layer, with a height of 5 m.

3.1 Constitutive Relation Model of Steel

Isotropic elastic plastic model provided by finite element software ABAQUS is adopted, which satisfies Von Mises yield criterion. Q345 is selected. The Poisson's ratio in elastic stage is 0.3, and the elastic modulus $E_s = 2.06 \times 10^5$ MPa. Double-fold line model is adopted, including elastic section and reinforced section. Among it, the modulus of reinforced section is 0.01 E_s. The constitutive relation curve of steel is shown in Fig. 5.

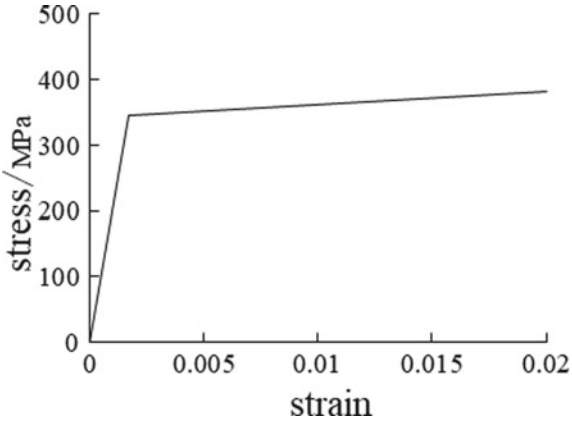

Fig. 5 Constitutive model of steel

3.2 Constitutive Relation Model of Concrete

The plastic damage model provided by ABAQUS software is adopted. Among it, the expansion angle is 30 degrees by default and the viscosity coefficient is 0.0003. C80 is selected. The Poisson's ratio in elastic stage is 0.2, and elastic modulus $E_c = 3.8 \times 10^4$ MPa. Han Linhai [10] proposed the stress–strain relationship of core concrete considering the confinement effect of steel tubes. Based on this, the compression constitutive relation curve of core concrete is shown in Fig. 6. The tensile constitutive relation of concrete adopts the constitutive relation given in Appendix C of *Code for Design of Concrete Structures* (GB50010-2010) [11], and the representative value of uniaxial tensile strength of concrete is 3.5 MPa. The uniaxial tensile constitutive relation curve of concrete core is shown in Fig. 7.

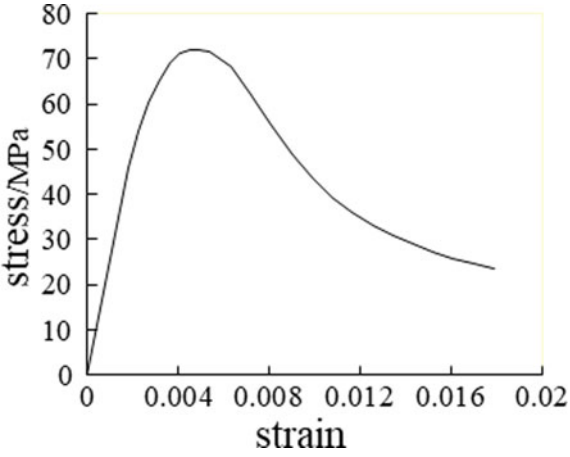

Fig. 6 Compression constitutive relation of concrete

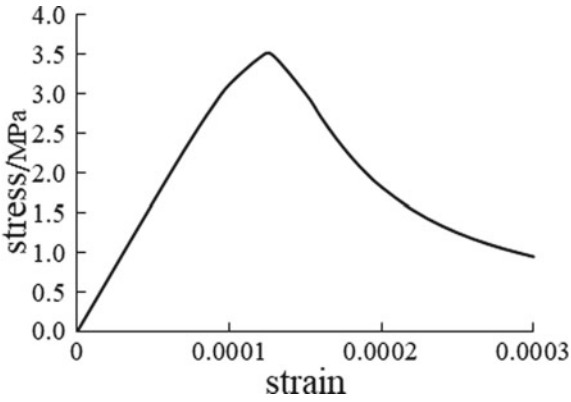

Fig. 7 Tensile constitutive relation of concrete

3.3 Unit Selection

For all finite element models in this paper, to accurately simulate the contact relationship among steel pipe, core concrete and force transmission members, the steel tube wall, circumferential stiffener, force transmission members and core concrete are all simulated by C3D8R solid element.

3.4 Cell Meshing

Figure 8 is a schematic diagram of column section meshing in this paper.

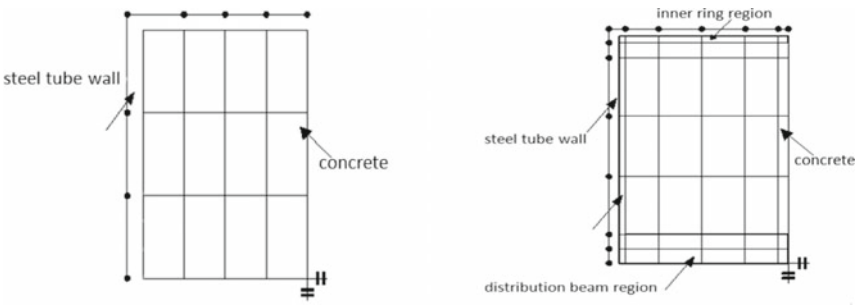

(a) Cross section without force transmission members

(b) Cross section of part with force transmission members

Fig. 8 Schematic diagram of meshing of concrete-filled rectangular steel tube columns section

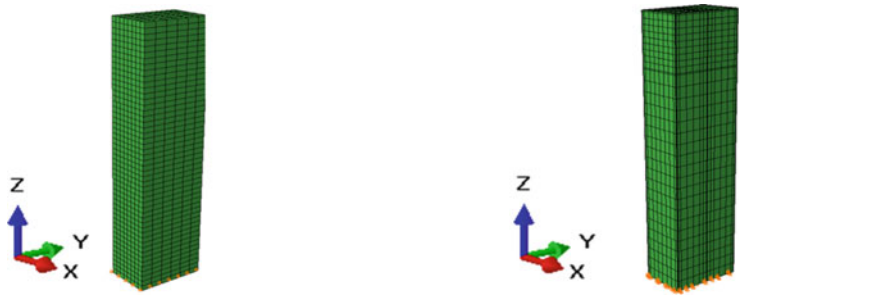

(a) Model without force transmission members

(b) Model with force transmission members

Fig. 9 Finite element model of concrete-filled rectangular steel tube columns

3.5 Interface Model of Steel Tube and Core Concrete

The interface model of the inner wall of steel tube and the core concrete consists of the contact in the normal direction of the interface and the bond slip in the tangential direction. In all the calculation models in this paper, the normal contact between steel tube and core concrete interface is hard contact. Regardless of friction and bonding, for the tangential interaction between steel tube and core concrete, the friction coefficient $\mu = 0$ and the bonding strength $\tau_{\text{bond}} = 0$ are defined.

3.6 Boundary Conditions

The degrees of translation freedom of the concrete at the bottom of the column and the steel tube wall in x, y and z directions are restricted. See Fig. 9 for the finite element model of concrete-filled rectangular steel tube columns.

3.7 Loading Mode

To obtain the load displacement curve, the axial displacement load is applied to the steel tube wall according to the actual engineering situation.

3.8 Solution of Nonlinear Equation

In this paper, the calculation includes three kinds of nonlinear problems of finite element analysis, namely nonlinear problems of steel and concrete materials,

geometric nonlinear problems and nonlinear problems of boundary conditions caused by the change of interface contact between steel tube and concrete in the process of stress. In this paper, Newton–Raphson method is used for iterative calculation.

4 Comparative Calculation and Analysis

Referring to the calculation results of previous research and analysis by the research group, when the friction and bonding between the steel tube wall and the core concrete interface are not considered in the analysis, and there are no force transmission members, the bearing capacity of the concrete-filled rectangular steel tube columns is equivalent to that of the steel tube column. At this time, the concrete hardly participates in the work, and the steel tube wall and the core concrete cannot work together well [8].

When only the concrete-filled rectangular steel tube columns with circumferential stiffeners is arranged in the floor node area of the concrete-filled rectangular steel tube columns, the ultimate bearing capacity of the core concrete $N_{\mathrm{cmax}} = 2.211 \times 10^4$ kN and the bearing capacity of the steel tube wall $N_s = 2.418 \times 10^4$ kN. The ultimate bearing capacity of the concrete-filled rectangular steel tube columns with circumferential stiffeners $N_{\mathrm{max}} = 4.629 \times 10^4$ kN. In the elastic stage, the concrete work bearing coefficient $\alpha_c = 0.546$, which gradually decreases after entering the plastic state; when the maximum bearing capacity is reached, the working bearing coefficient of concrete is $\alpha_c = 0.478$ [8].

When concrete-filled rectangular steel tube columns with I-beams and circumferential stiffeners are arranged in the steel tube wall of the floor node area of concrete-filled rectangular steel tube columns, the ultimate bearing capacity of core concrete $N_{\mathrm{cmax}} = 3.019 \times 10^4$ kN, and the bearing capacity of the steel tube wall $N_s = 2.334 \times 10^4$ kN. The ultimate bearing capacity of concrete-filled rectangular steel tube columns with force transmission members $N_{\mathrm{max}} = 5.354 \times 10^4$ kN. In the elastic stage, the concrete work bearing coefficient $\alpha_c = 0.674$; after entering the plastic state, the work bearing coefficient of concrete gradually decreases. When the maximum bearing capacity is reached, the work bearing coefficient of concrete $\alpha_c = 0.564$[8].

On this basis, the combined working mechanical properties of concrete-filled rectangular steel tube columns under the following four different structural measures of force transmission are studied and analyzed.

4.1 The Main Force Transmission Member is Rectangular Steel Plate

According to the force transmission members proposed in this paper, a single distribution beam and an internal stiffening rib are arranged in the steel tube wall of the floor node area of the concrete-filled rectangular steel tube columns, in which the distribution beam is a rectangular steel plate of 1000 mm × 24 mm; the inner ring rib is 50 mm wide and 24 mm thick. It communicates with the upper and lower ends of the distribution beam, as shown in Fig. 10.

According to the finite element analysis, the axial force-vertical displacement curve of concrete-filled rectangular steel tube columns with rectangular steel plate is shown in Fig. 11. It can be seen from Fig. 11 that the ultimate bearing capacity of core concrete $N_{cmax} = 2.234 \times 10^4$ kN, and the bearing capacity of steel tube wall $N_s = 2.402 \times 10^4$ kN. The ultimate bearing capacity of concrete-filled rectangular steel tube columns with force transmission members $N_{max} = 4.636 \times 10^4$ kN. In the elastic stage, the concrete work bearing coefficient $\alpha_c = 0.574$; after entering plastic state, the work bearing coefficient of concrete gradually decreases. When the maximum bearing capacity is reached, the work bearing coefficient of concrete $\alpha_c = 0.482$.

The results show that rectangular steel plates and circumferential stiffeners are arranged in the steel tube wall of the floor node area of concrete-filled rectangular steel tube columns. Under the ideal situation of concrete pouring at the corner of the steel tube stiffeners, some external loads acting on the steel tube wall can be transferred to the core concrete through the rectangular steel plates and circumferential stiffeners, forcing the core concrete to participate in some work. The bearing capacity of concrete-filled rectangular steel tube columns can be improved. Rectangular steel plates and circumferential stiffeners improve the mechanical performance of concrete-filled rectangular steel tube columns. However, the bearing capacity is lower than that of concrete-filled rectangular steel tube columns with I-beams and circumferential stiffeners. Rectangular steel plate, as a distribution beam, has poorer force transmission effect than I-beam.

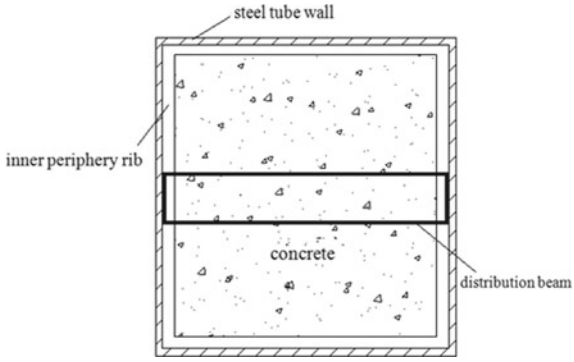

Fig. 10 Section of concrete-filled rectangular steel tube columns with force transmission member

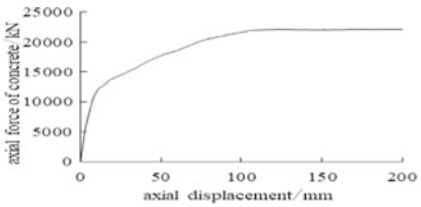

(a) Axial force-displacement curve of concrete

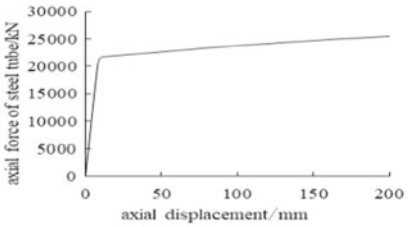

(b) Axial force-displacement curve of steel pipe

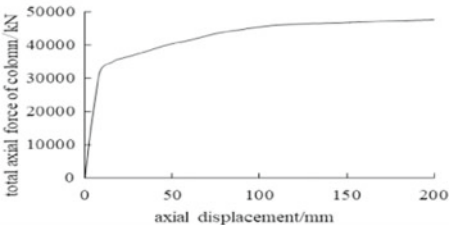

(c) Total axial force-displacement curve

Fig. 11 Axial force–displacement curve of concrete-filled rectangular steel tube columns

4.2 The Main Force Transmission Member is T-Beam

According to the force transmission member setting proposed in this paper, a single distribution beam and an internal stiffening rib are arranged in the steel tube wall of the floor node area of concrete-filled rectangular steel tube columns, among it, the distribution beam is the T-beam of 1000 mm × 300 mm × 13 mm × 24 mm; the inner ring rib is 50 mm wide and 24 mm thick.

According to the finite element analysis, the axial force-vertical displacement curve of concrete-filled rectangular steel tube columns with T-beam is shown in Fig. 12. It can be seen from Fig. 12 that the ultimate bearing capacity of core concrete $N_{\text{cmax}} = 3.012 \times 10^4$ kN, and the bearing capacity of steel tube wall $N_s = 2.324 \times 10^4$kN. The ultimate bearing capacity of concrete-filled rectangular steel tube columns with force transmission members $N_{\text{max}} = 5.336 \times 10^4$ kN. In the elastic stage, the concrete work bearing coefficient $\alpha_c = 0.674$; after entering the plastic state, the work bearing coefficient of concrete gradually decreases. When

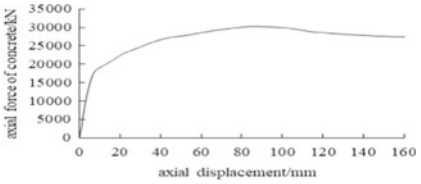

(a) Axial force-displacement curve of concrete

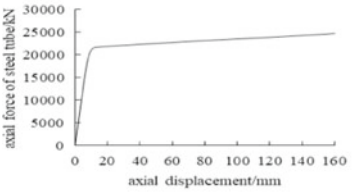

(b) Axial force-displacement curve of steel pipe

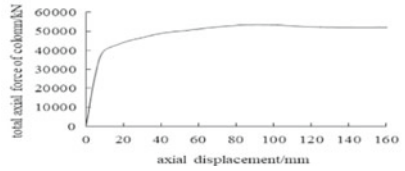

(c) Total axial force-displacement curve

Fig. 12 Axial force–displacement curve of concrete-filled rectangular steel tube columns

the maximum bearing capacity is reached, the work bearing coefficient of concrete $\alpha_c = 0.564$.

The research results show that setting T-beams and circumferential inner ring ribs in the steel tube wall of the floor node area of concrete-filled rectangular steel tube columns can effectively transfer the external load acting on the steel tube wall to the core concrete and force the core concrete to participate in the work. Concrete-filled rectangular steel tube columns can work together well and their bearing capacity is greatly improved. Compared with the I-beam of the same size, the steel consumption is less, but the force transmission effect is almost equivalent to that of I-beam as distribution beam. Under the same force transmission effect, the steel consumption and engineering cost are saved. It is suggested to adopt this force transmission structural measure.

4.3 The Main Force Transmission Member is Channel Steel

According to the force transmission member setting proposed in this paper, a single distribution beam and an internal stiffening rib are arranged in the steel tube wall of the floor node area of concrete-filled rectangular steel tube columns. Among it, the

distribution beam is channel steel # 30A: 300 mm × 85 mm × 7.5 mm; the inner ring rib is 50 mm wide and 24 mm thick.

According to the finite element analysis, the concrete-filled rectangular steel tube columns with channel steel beam have smaller leg width, and the connection surface with the steel tube wall is shorter and smaller in the concrete-filled rectangular steel tube columns with larger cross section and higher height. In the finite element model calculation, with the increase of load, the joint between the steel tube wall and channel steel beam first has a larger stress concentration phenomenon. When the concrete-filled rectangular steel tube column does not reach the ultimate bearing capacity, the component part has been damaged. Thus, it is not recommended to adopt this force transmission structural measure.

5 The Main Force Transmission Member is Box Beam

According to the force transmission member setting proposed in this paper, a single distribution beam and an internal stiffening rib are arranged in the steel tube wall of the floor node area of concrete-filled rectangular steel tube columns. Among it, the distribution beam is a box beam of 1000 mm × 300 mm × 12 mm; the inner ring rib is 50 mm wide and 24 mm thick. According to the finite element analysis, the axial force-vertical displacement curve of concrete-filled rectangular steel tube columns with box beam is shown in Fig. 13.

It can be seen from Fig. 13 that the ultimate bearing capacity of the core concrete $N_{\text{cmax}} = 3.124 \times 10^4$ kN, and the bearing capacity of the steel tube wall $N_s = 2.215 \times 10^4$ kN. The ultimate bearing capacity of the concrete-filled rectangular steel tube columns with force transmission members $N_{\max} = 5.339 \times 10^4$ kN. In the elastic stage, the concrete work bearing coefficient $\alpha_c = 0.690$; after entering the plastic state, the work bearing coefficient of concrete gradually decreases. When the maximum bearing capacity is reached, the work bearing coefficient of concrete $\alpha_c = 0.585$.

The results show that arranging the box beam and the circumferential inner ring rib in the steel tube wall of the floor node area of the concrete-filled rectangular steel tube columns can effectively transfer the external load acting on the steel tube wall to the core concrete and force the core concrete to participate in the work. The concrete-filled rectangular steel tube columns can work together well, and their bearing capacity is greatly improved. However, under this structural measure, the steel consumption is larger than that of I-beam, T-beam and channel beam of the same size. The force transmission effect is 3.2% higher than that of channel beam, 3.6% higher than that of T-beam and 3.6% higher than that of I-beam, all of which are less than 5%. Therefore, under similar force transmission effect, the steel consumption is larger, which increases the engineering cost. In conclusion, it is not recommended to adopt this force transmission structural measure.

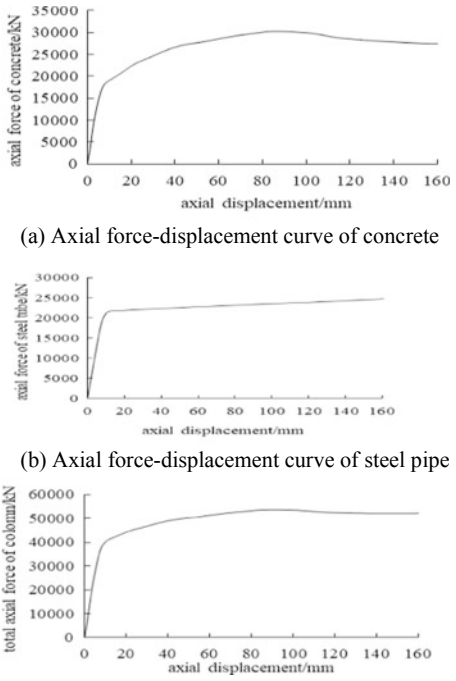

(a) Axial force-displacement curve of concrete

(b) Axial force-displacement curve of steel pipe

(c) Total axial force-displacement curve

Fig. 13 Axial force–displacement curve of concrete-filled rectangular steel tube columns

6 Comparison of Numerical Simulation Results

According to the above finite element calculation results, it can be seen that concrete-filled rectangular steel tube columns with different force transmission structures show different combined working performance. See Table 1 for specific data comparison and analysis.

As can be seen from Table 1, the setting of connecting members improves the bearing capacity of concrete-filled rectangular steel tube columns, enhances the mechanical performance of concrete-filled rectangular steel tube columns and realizes the combined working of steel tubes and core concrete; the concrete-filled rectangular steel tube columns with box beam has the largest bearing capacity, which effectively realizes the combined working of concrete-filled rectangular steel tube columns. However, under this structural measure, the steel consumption is the largest, and the maximum force transmission effect is only increased by 3.6%. Concrete-filled rectangular steel tube columns with T-beam have larger bearing capacity, better force transmission effect and less steel consumption. The force transmission effect of concrete-filled rectangular steel tube column with rectangular steel plate is poor; the structure of concrete-filled rectangular steel tube columns with channel beam is damaged at the contact surface between steel tube wall and channel beam due to

Table 1 Comparative analysis of finite element calculation results

Analysis index	Bearing capacity of concrete (kN)	Bearing capacity of steel pipe (kN)	Total load (kN)	Concrete work bearing coefficient	Steel consumption (cm^2)
The main force transmission member is I-beam	30,190	23,340	53,540	0.564	267.76
The main force transmission member is rectangular steel plate	22,340	24,020	46,360	0.482	240
The main force transmission member is T-beam	30,120	23,240	53,360	0.564	198.88

stress concentration, so that the ultimate bearing capacity of the component is not reached.

7 Conclusions

To sum up, it is suggested that T-beam force transmission structural measure with better force transmission effect and less steel consumption should be adopted. It can not only improve the bearing capacity of the column, but also force the core concrete to bear more external loads and participate in joint working, and greatly save the steel consumption. It is economical and applicable. This paper has solved the problem of reasonably and effectively setting up force transmission members in practical engineering projects, greatly reduced the actual amount of steel used in the project and effectively saved the project cost. The setting of T-beam can not only strengthen the performance of concrete-filled rectangular steel tube columns in combined working, but also save steel consumption, thus promoting the development and application of concrete-filled rectangular steel tubular structures.

Acknowledgements The research was supported by JG201943 (Teaching Reform of Road, Bridge and Tunnel Survey Based on MSMT Mobile Phone Software); 202105Y07 (Teaching Reform of Engineering Survey Based on Virtual Simulation Survey System); J61102009 (Practical Research on the Development of Textbooks for Civil Construction).

References

1. Fu XY, Shen ZY, Li YQ et al (2015) A concrete filled steel tubular column with force transmission members. China, ZL 20111018029 3.2. July 22
2. Fu XY, Xu N (2012) Study on the mechanism of axial compression force transmission of new concrete-filled rectangular steel tube columns joints. J Shen Univ (Sci Tech Edition) 29(4):283–289
3. Shen ZY, Li YQ, Fu XY et al (2011) Experimental research report on mechanical properties of distribution beams with super-large cross-section concrete-filled rectangular steel tube columns. Tongji University, Shanghai
4. Zhang YZ, Li YQ, Luo JH et al (2016) Study on the vertical load transfer mechanism under the structure of giant concrete filled steel tubular column distribution beam (I): experimental research. Chin Civil Eng J 11:1–10
5. Zhang YZ, Luo JH, Li YQ et al (2016) Study on the vertical load transfer mechanism under the structure of giant concrete filled steel tubular column distribution beam (II): numerical analysis. Chin Civil Eng J 12:16–26
6. Luo JH, Li YQ, Zhang YZ et al (2014) Experimental study on axial compression load transfer under structural joints of super-large concrete filled steel tubular columns and distribution beams. Chin Civil Eng J 10:49–60
7. Fu XY, Li YQ, Lei M et al (2013) Reasonable structural measures for steel-concrete interaction of super-large cross-section concrete-filled rectangular steel tube columns. Chin Civil Eng J 12:33–42
8. Xu N (2012) Study on static performance of large cross-section concrete-filled rectangular steel tube columns with force transmission members. Harbin Institute of Technology, Harbin
9. Zhuang Z (2005) ABAQUS nonlinear finite element analysis and examples. Science Press, Beijing
10. Han LH (2007) Theory and practice of concrete-filled steel tubular structure. Science Press, Beijing
11. National Standard of the People's Republic of China (2010) Code for design of concrete structures (GB50010-2010). China Construction Industry Press, Beijing

Review on Seismic Design and Shock Absorption Methods of Reinforced Concrete Frame Structures

Sixiang Jing

Abstract The earthquake brings great threat to both people's life and property, since the reinforced concrete structure is facing various complicated factors. To this end, the thesis takes reinforced concrete frame structure as an example and mainly illustrates the huge damage to building structural. The characteristics of various damage types are analyzed, and the seismic design methods are summarized in combination with the seismic design code. In this thesis, it will mainly discuss the technology of shock absorption. Based on the existing research results, the shortage of current seismic technology is pointed out, and the development trend of future research is prospected.

Keywords Reinforced concrete · Frame structure · Seismic design · Shock absorption

1 Introduction

The seismic waves produced by crustal movement are the common feature of a natural earthquake. In the twentieth century, China totally suffered two earthquakes that killed more than 200,000 people, especially the Haiyuan earthquake in 1920 and the Tangshan earthquake in 1976. The earthquake in 2012, which happened in Yunnan Province, caused a direct economic loss of 4.980 billion yuan. From 1993 to 2017, earthquakes in mainland China caused a total of 740,000 people died and 474,000 people were injured, resulting in a direct economic loss of 1.1 trillion yuan [1]. It can be seen that the frequent appearance of earth has been the major threat to people's personal safety and the whole country's economy.

In order to reduce the harm of earthquake, scientists all over the world have conducted extensive and in-depth research on the seismic performance of buildings. There are many forms of building structures, including masonry, wood, steel

S. Jing (✉)
School of Architectural Engineering, Northeast Electric Power University, Jilin 132012, China
e-mail: 627298720@qq.com

T. Kang (ed.), *Proceedings of 5th International Conference on Civil Engineering and Architecture*, Lecture Notes in Civil Engineering 369,
https://doi.org/10.1007/978-981-99-4049-3_20

and reinforced concrete. In the recent years, many scientists have carried out extensive research on various structures. Lixue [2] and Madhavi et al. [3] studied the seismic resistance and strengthening of masonry structures, and used measures such as increasing the cross section of walls and columns, reducing the floor height and using fiber composite materials to enhance the overall stability of masonry structures. Gao et al. [4] and Pan et al. [5] studied the force performance of joint nodes such as mortise and tenon and loosely connected timber frames under lateral loads. Xi et al. [6], Junshuai et al. [7] conducted seismic analysis of extended arm truss steel structures and high-strength steel structures. Yanfei [8], Zuo et al. [9] analyzed and studied the seismic performance of reinforced concrete frame structures. The above-mentioned results show that the seismic analysis and seismic measures at this stage aim to achieve the corresponding seismic protection objectives. With the development of seismic technology, people have a new understanding of the seismic performance of reinforced concrete structures in buildings. Therefore, in order to explore the seismic design methods and shock absorption techniques for reinforced concrete frame structures, this article summarizes a large number of relevant domestic literature and foreign literature, taking the reinforced concrete frame as an example, combined with the code, summarizing the research results and looking forward to the next focus of the research to be conducted.

2 Types of Damage to Reinforced Concrete Frame Structures

Reinforced concrete frame structures have different types of damage, and integral damage occurs when the structure collapses as a whole. The overall damage of columns in general is more dangerous to the structure because of the low strength of reinforced concrete, the actual axial compression ratio exceeds the limit, etc., and it is more easier to form a plastic column mechanism under strong earthquake action. In the Wenchuan earthquake, there were multiple instances of extremely severe damage due to column damage leading to tilting or even overall collapse of the house [10]. If classified according to the local component damage, the damage of frame structure mainly occurs in local parts such as beams, columns, nodes and infill walls [11–17].

2.1 Frame Beam Damage

The damage of frame beams is mainly distributed at the beam ends and node areas, with vertical cracking, usually accompanied by diagonal cracks. The damage of framed beams is relatively mild, with slight cracking usually appearing at the ends and the crack length is about half of the beam height [11]. As the damage deepens, cracks gradually develop to the top of the beam, and the number of cracks increases. The

Fig. 1 Damage to frame beams

longitudinal reinforcement at the negative bending moment of the beam is susceptible to yielding and the concrete is easily crushed, thus showing bending damage. Local concrete crisp cracking, main reinforcement bending and even reinforcement slippage can occur at the end of beams with severe damage [14], as shown in Fig. 1.

2.2 Frame Column Damage

Since the large internal force at the column end of the joint, under the combined action of bending moment, shear force and pressure, horizontal cracks, diagonal cracks or cross cracks appear around the top of the column, and in serious cases, the concrete is crushed or peeled off and the longitudinal reinforcement yields, this damage form is ductile damage, which can absorb a considerable part of seismic energy [12]. If the axial compression is large, hoop restraint is insufficient, the concrete strength is insufficient, the concrete at the end of the column will be crushed and affect the shear resistance. When the vertical load is too large and the cross section is too small, the concrete strength is not enough, the longitudinal tendons are crushed into a lantern shape, the hoop bars in the column are pulled off or fall off and the column loses bearing capacity in the form of crushing damage [15]. As shown in Fig. 2, the seismic damage of the bottom of the column is mainly manifested by the partial loss of the protective layer of concrete at the bottom of the column, the partial exposure of the column main reinforcement and its hoop reinforcement, the tilting of the bottom column, the horizontal cracks and diagonal cracks cross each other [11].

2.3 Beam-Column Joint Damage

The joint damage is mainly manifested as follows: when the beam end becomes the weak part, the damage occurs at the beam end first, the top part of the beam is subjected to negative bending moment and the tensile reinforcement yields and

(a) (b)

Fig. 2 (**a**) Example 1 of damage to frame columns (**b**) Example 2 of damage to frame columns

Fig. 3 Frame joint damage

the bottom part of the compressed concrete is crushed. When there are cracks or cross cracks, the concrete protective layer falls off, the reinforced concrete part is outward, the beam end is provided with plastic hinges and the frame joints are declared damaged [12]. When the column end becomes weak, the concrete at the end of columns is crushed and the plastic hinge is easily formed at the end of columns, the column longitudinal tendons are flexed or even bulged and the hoop bars are deformed or even broken by outward expansion. Once the number of plastic hinges at the end of the column reaches a certain scale, the whole structure may not have the performance of absorbing earthquake energy [16, 17]. Therefore, as shown in Fig. 3, such damage should be avoided as far as possible.

2.4 Infill Wall Damage

The damage of infill walls is mainly manifested as cracking. The infill walls and perimeter enclosure walls in frame structures are prone to cracking under earthquake action because of their own in-plane stiffness, low bearing capacity and poor deformation capacity. The infill walls are non-load-bearing elements and do not cause damage to the main structure, but the results of previous earthquake investigations

(a) (b)

Fig. 4 (**a**) Example 1 of infill wall damage (**b**) Example 2 of infill wall damage

show that the infill walls and perimeter enclosure walls of multi-story frame structures are more heavily damaged in earthquakes [11]. Especially, the large aperture multi-hollow brick infill walls, as shown in Fig. 4, due to their light mass and low strength, are prone to failure of tie bars due to block splitting in earthquakes, thus producing large cracking or even collapse of the walls [13].

3 Seismic Design Method Based on the Specification

3.1 Determination of Design Seismic Effects

The current design method used in the Chinese Code for seismic design of buildings (GB50011-2010) (2016 edition) [18] is the known structural design seismic force for structural elastic displacement verification, which is called the bearing capacity design method. In the code-based structural seismic design method, considering the combined action of amplification factor and seismic attenuation factor, the design seismic effect is obtained from the effective vibration peak acceleration with the increase of intensity. The formula is as follows [19].

$$F = k\beta \frac{1}{R} G \tag{1}$$

where F is the total horizontal seismic action of the building structure.

k is the seismic coefficient (the ratio of effective peak acceleration of ground motion or peak acceleration of ground motion to gravitational acceleration taken by different seismic zones corresponding to the level of fortification intensity, which reflects the strength of earthquakes of different areas of fortification intensity).

β is the dynamic amplification coefficient (the fitted value of the ratio of the peak acceleration of structural response corresponding to different cycles to the effective peak acceleration or peak acceleration of ground motion, which reflects the dynamic amplification effect of different cycles of the system on seismic action).

I is the building importance coefficient.

R is the seismic action reduction coefficient.

G is the representative value of the structural gravity load (taking the sum of the constant load and the live load that may occur simultaneously with the design seismic action).

3.2 Calculation Based on Seismic Measures

3.2.1 Strong Columns and Weak Beams

In order to reduce vibration more effectively, it has always been advocated to design buildings into strong columns and weak beams, so as to make the structure with plastic hinges at the beam end stronger. In order to prevent earthquake and reduce its damage, the bending moment of the column is larger than that of the beam end, so as to increase the deformation strain force of the structure [17]. The method is to artificially increase the design bending moment of the column. Compared with before and after the change, the flexural strength of the column is much stronger than that before the change, while the beam remains unchanged. That is, the seismic resistance of column is much higher than that of beam [19]. In this way, when the beam and column face the external force together, the beam will yield first, and the column will remain strong.

3.2.2 Strong Shear Capacity and Weak Bending Capacity

Strong shear and weak bend is to avoid non-ductile damage in the parts of the member (beam, column, wall) with high shear before the limit of plastic deformation capacity is reached at the end of the beam to control the occurrence of brittle forms of damage [18]. The shear force is derived from the calculated bending moment to prevent shear damage in beams and columns before bending yields, and such damage can be improved by appropriately increasing the steel reinforcement resisting shear.

3.2.3 Strong Joints and Weak Components

Strong joints and weak members mean that the bearing capacity of nodes should be higher than that of connected members, and the joint failure means that the beams and columns connected to it are failed, and the design value of combined shear force in the core area of nodes should be increased when calculating [18].

"Strong columns and weak beams, strong shear and weak bending, strong joints and weak members" are significant principles to be observed in structural design. The frame structure will be destroyed only when plastic hinges appear at all beam ends and force yielding deformation at the bottom of the structure, and a lot of energy input from ground vibrations is consumed by elastic-plastic deformation. Their yielding mechanism is what we expect, but there are many factors in reality

that make its realization less likely. Therefore, it is necessary to further study the damage of columns and nodes, so that the building can achieve the goal of "strong columns and weak beams, strong shear and weak bending, strong joints and weak members".

3.3 Foreign Specification Calculation Comparison

3.3.1 U.S. Specifications

The American Code ACI 318-02 [20] classifies structures as "general frame structures", "medium frame structures" and "special frame structures". It is stipulated that "general frame structure" and "medium frame structure" do not need to consider the load-bearing capacity difference of members, while "special frame structure" should meet the following formula:

$$\Sigma M_{\mathrm{sc}} \geq 1.2 \Sigma M_{\mathrm{sb}} \tag{2}$$

where ΣM_{sc} indicates the sum of bending capacity at the upper and lower column ends of the node core; ΣM_{sb} indicates the sum of bending capacity at the left and right beam ends of the node core.

The U.S. code achieves "strong shear and weak bend" through different safety factors of bending and shear, which has higher reinforcement rate, higher reliability and greater safety factor.

3.3.2 European Norms

Euro code 8 [21] classifies structures into "high ductility class DCH", "medium ductility class DCM" and "low ductility class DCL". For "low ductility grade DCL" structure, no adjustment of member bearing capacity difference is required, only the design according to static method; while "medium ductility grade DCM" structure and "high ductility grade DCH "DCM" structure and "high ductility grade DCH" structure, the grade difference is required to meet the following relationship:

$$\Sigma M_{\mathrm{cu}} \geq \gamma \Sigma M_{\mathrm{bu}} \tag{3}$$

where ΣM_{cu} indicates the sum of bending capacity at the upper and lower column ends of the node area; ΣM_{bu} indicates the sum of bending capacity at the beam end considering the reinforcement of the floor; $\boldsymbol{\gamma}$ indicates the magnification coefficient of the column end moment, which is 1.35 for "high ductility grade DCH" structure and 1.2 for "medium ductility grade DCM" structure is 1.2.

It can be seen that our code is similar to the American code and European code, by multiplying the beam end bending moment design value by a certain amplification factor to control the column end cross-sectional reinforcement, to ensure that the actual bending capacity of the column end in the node area is greater than the actual bending capacity of the beam end, the difference is that the calculation method of the beam end bending moment design value is different. The highest ductility reserve of reinforced concrete frame structure real under structural measures in the ACI code of the U.S., due to its reinforcement rate and hoop rate is greater, the U.S. code safety factor is high and more reliable. China's seismic code using the column end moment increase coefficient value is slightly insufficient, although the overall level of safety setting is on par with Europe and the U.S., but the code's action effect design value is lower.

3.4 Design Based on Seismic Construction Measures

The seismic structural measures of frame structure include reinforcement rate, anchorage length, lap length, axial pressure ratio, encryption of beam-column hoop reinforcement and seismic structural measures of non-structural members. The seismic structural measures for frame structures are as follows.

3.4.1 Axial Pressure Ratio

The axial pressure ratio is controlled to prevent brittle damage due to small eccentric compression of the column, and the axial pressure ratio is essentially the degree of concrete compressive strength exerted. Our code [18] specifies the limit value for the axial pressure ratio of columns according to the seismic level and structural form, while the American code [20] does not propose the limit value of axial pressure ratio for seismic design, but considers the limit value of axial pressure of columns from the perspective of accidental eccentricity of columns.

3.4.2 Stirrup Ratio

In order to have sufficient safety reserves, in addition to increasing the column section size and improving the concrete strength grade, the configuration of stirrups is also a measure to improve the ductility of columns, because stirrups restrict the transverse deformation of concrete, enhance the ultimate deformation capacity of concrete and improve the ductility of columns. The greater the amount of stirrups and the denser the spacing, the greater the constraint on the concrete.

3.4.3 Stirrup Restraint Form

In the seismic structure, using more stirrups in the easily damaged areas such as beam end and column end can improve the performance of members in failure, effectively improve the ductility and energy dissipation capacity of members and improve the seismic performance of the structure. Different stirrup restraint forms have different effects on the ductility of columns, the restraint effect of compound hoop and spiral hoop is better and the effect of ordinary rectangular hoop is worse.

4 Shock Absorption Technology

4.1 Shock Absorption Technology Concept

In the application of damping technology, on the one hand, it is the improvement of reinforced concrete frame structure. Many scholars have also studied the damping technology and discussed their views. As we all know, shock absorption is to reduce the damage caused by earthquake. The principle of improving building structure to achieve shock absorption is that it is to deal with the damage of earthquake with the damage of structure as mentioned above. In addition, install dampers at relevant parts. It is also known as isolation device, which is a method to achieve the deformation between floors and the internal force of components [22]. Xingjun also pointed out that [23], the damping principle of damper is to reduce structural seismic damage through isolation, energy consumption, application of external force or adjustment of structural dynamic characteristics, so as to achieve building safety. In this regard, other scholars at home and abroad have also conducted a lot of research and proposed a variety of effective damping technologies [24–27]. Domestic and foreign research shows that structural vibration control can reduce the response of buildings under strong earthquakes and effectively improves the seismic performance of structures. Structural energy dissipation and damping technology can absorb most of the energy input from the earthquake and reduce the seismic response of the structure.

4.2 Structural Shock Absorption Control

In fact, structural damping is to counteract the destructive force of earthquake by structural force, which can be divided into four ways: passive control, active control, semi-active control and hybrid control.

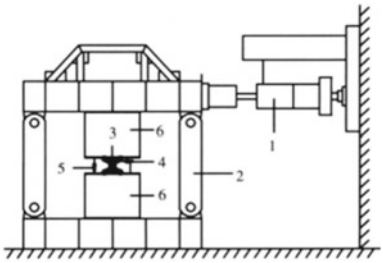

Fig. 5 Schematic diagram of the new stiffened soft steel damper. 1. Hydraulic servo actuator; 2. Loading rack; 3. Damper; 4. Horizontal displacement sensor; 5. Vertical displacement sensor; 6. Steel beam

4.2.1 Passive Control

Passive structural control is a passive control method. It uses the methods of reducing, transmitting and consuming energy to reduce structural vibration. It mainly includes three types: foundation isolation, energy dissipation and damping and tuning damping. Base isolation is to select the relevant vibration isolation damping device installed between the superstructure and the foundation, so that the energy generated by the earthquake cannot be transmitted to the main structure, or reduce the energy input to the superstructure generated by the earthquake, so as to achieve the purpose of reducing the superstructure [23]. Energy dissipation damping is to connect some parts of the structure (such as support, shear wall, node, main structure and auxiliary structure) through damper (or energy dissipation element). When the structure has relative displacement during earthquake, the damper will also be stretched or compressed to produce certain deformation [23].

Tuned damping technology is to connect the substructure to the main structure, so as to transfer the vibration of the structure and redistribute the energy between the original structure and the substructure, so as to reduce the vibration of the original structure [23]. As shown in Fig. 5, these include tuned mass damper (TMD) and tuned liquid damper (TLD).

4.2.2 Active Control

Active control of structure refers to the use of external energy to apply control force to the structure or change the dynamic characteristics of the structure in order to quickly reduce the vibration response of the structure, as shown in Fig. 6. The active control system consists of three main components: sensor, controller and actuator [28–30]. At present, some buildings have successfully applied active control technology. For example, Kyobashi Seiwa, an 11 story building in Tokyo, Japan [31].

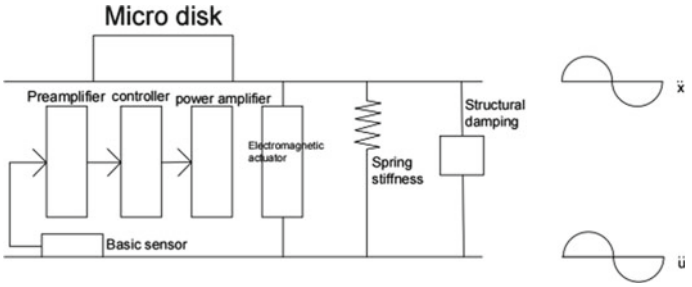

Fig. 6 Active control device based on electromagnetic action

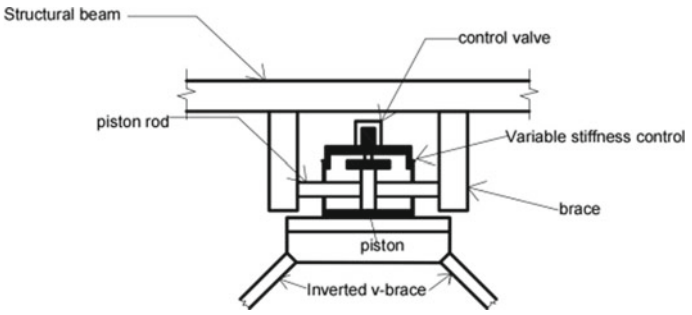

Fig. 7 SAVS semi-active control system

4.2.3 Semi-active Control

Semi-active control mainly includes two types: active variable damping control system and active variable stiffness control system. The active variable stiffness control system consists of a control device that enables the damping of the controlled structure to be switched between various damping states within each sampling period to further achieve the purpose of shock absorption. The active variable damping control system consists of an active variable stiffness control device to cause the stiffness of the controlled structure to be switched between various stiffness values at each sampling period in combination with the external load spectrum characteristics, which enables the controlled structure to move away from the resonance state at each sampling period to further achieve the purpose of shock absorption [23–28] as shown in Fig. 7.

4.2.4 Hybrid Control

Hybrid control is a form of structural damping control in which both active and passive controls are applied to the same structure. Hybrid control includes the hybrid control of active mass damping system (AMD) and tuned mass damping system

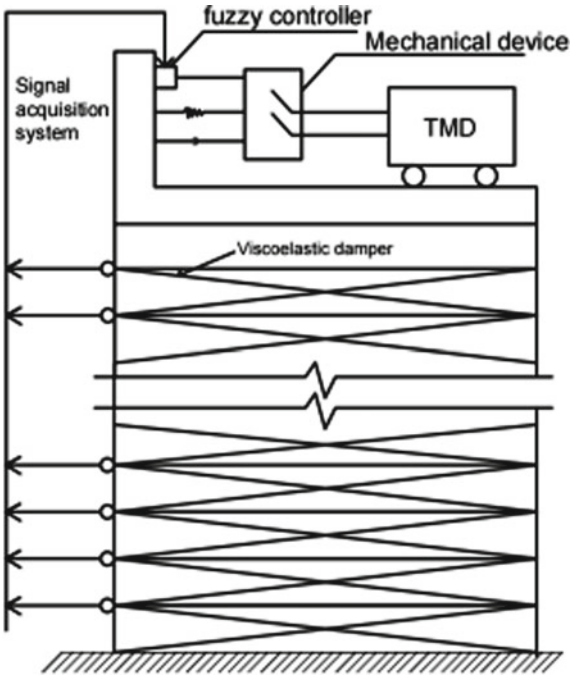

Fig. 8 Schematic diagram of the hybrid control system

(TMD) or tuned liquid damping system (TLD), the hybrid of active control and foundation vibration isolation, the hybrid of active control and energy dissipation damping and the hybrid of liquid mass control system and active mass damping system [23]. As shown in Fig. 8, a hybrid control system combining AMD and TLD was used to control the wind vibration response of the structure for the Nanjing TV tower in China [32].

5 Conclusion and Prospect

This paper summarizes the seismic damage of reinforced concrete frame structures, the corresponding seismic design methods and the development and application of shock absorption reduction technology and makes suggestions on the development direction and research content of future building seismic reduction technology.

(1) In view of the damage types mentioned in the paper, the code stipulates the design objectives of "strong columns and weak beams", "strong shear and weak bending" and "strong nodes and weak members". Through theoretical analysis and experimental research, new effective structural types are created,

which make such structures have better seismic performance when encountering earthquakes and are of great significance for the future development of performance-based seismic design research.

(2) This paper also introduces shock absorption technology applications, including passive control, active control, semi-active control and hybrid control. It is recommended to develop new dampers with good performance, improve the efficiency and quality of dampers and adopt new ideas such as "multiple energy-consuming elements working together and multiple energy-consuming lines of defense".

References

1. Zhenbo W, Xianxiang Z, Wei X (2010) Quiet and smiling. Investigation and statistics of earthquake damage to buildings and consideration of earthquake resistant design in Wenchuan County. Architect 40(S2):144–148. 10.19701J.Jzjg.S2.041
2. Lixue J, Zhuo-Lin W, Fu-Wen Z, Jiang L (2021) Seismic performance assessment method of existing regular multi-story masonry structures based on displacement and ductility. J Build Struct 42(03):72–79
3. Madhavi K, Vinay GN, Devi MVR, Basutkar SM (2020) Shear behavior of brick masonry strengthened with jute fiber reinforced composite. Mat Today: Proceed
4. Gao YL, Tao Z, Liaoyuan Y, Miao Y, Hexian S, Wenzheng Y (2016) Shaking table test of traditional through-drawer wood structure with additional viscoelastic dampers at mortise and tenon nodes. J Civil Eng 49(2):59–68
5. Pan Y, Qingshan Y, Siu-Seong L (2021) Lateral behavior of heritage timber frames with loose nonlinear mortise-tenon connections. Struct 33
6. Xi C, Dong BD, Kun SY, Lin XL, Hong WL, Feng LW, Qisong M (2021) Seismic performance analysis of a super high-rise steel structure using BRB extension truss. Build Struct 51(8):37–42
7. Junsai Q, Shujie Y, Chen C, Yanbo W (2021) Seismic performance analysis and economic evaluation of high-strength steel structures. Build Struct 51(7):73–98
8. Yanfei H (2014) Research on performance-based seismic design method for multi-story concrete frame structures. Chang'an University
9. Zuo Z, Gong M, Sun J, Zhang H (2021) Seismic performance of RC frames with different column-to-beam flexural strength ratios under the excitation of pulse-like and non-pulse-like ground motion. Bulletin of Earthquake Engineering, 2021(prepublish)
10. Qiuping W (2016) Damage modes and seismic design of reinforced concrete frame columns. Jiangxi Build Mat (20):104
11. Na W (2011) Research and analysis of damage mechanism of concrete frame structure. Hebei Engineering University
12. Lingsheng H, Honan L, Shiyun X, Dongsheng W (2009) Investigation and insight into the seismic damage of reinforced concrete frame structures in Wenchuan earthquake. J Dalian Univ Tech 49(05):718–723
13. Leping Y, Zhe Z, Qianli M, Xuchuan L, Xinzheng L, Peng P (2008) The realization of "strong column and weak beam" yielding mechanism from Wenchuan earthquake frame structure damage. Build Struct (11):52–125
14. Xiaoyong L, Zhiwu Y, Zhi S (2021) Seismic behaviour of frame structures with assembly of prefabricated concrete beam. J Build Eng 40
15. Tapia-Hernández E, Guerrero-Bobadilla H (2021) Design demands on columns of inverted-V braced steel frames. Int J Civil Eng (prepublish)

16. Murashko O, Kubiiovich M, Bezushko D, Arsiriy A (2021) Nonbearing wall infill under seismic impacts in terms of non-linear static analysis. In: IOP Conference Series: Materials Science and Engineering 1164 (1)
17. Gao JD, Du XX, Yuan HX, Theofanous M (2021) Hysteretic performance of stainless steel double extended end-plate beam-to-column joints subject to cyclic loading. Thin-Wall Struct 164
18. GB50010-2010 Code for Seismic Design of Buildings (2016 Edition)
19. Yuejun Z (2009) Comparative analysis of different seismic design methods for building structures. Chongqing University
20. Building Code Requirements for Structural Concrete (ACI 318-95) and Commentary (ACI 318R-02) (2002) ACI Committee 318
21. Eurocode 8, Design Provisions for Earthquake Resistance of Structure (1994) ENV1998-1, CEN, Brussels, 34–88
22. Fulin Z (1997) Seismic control of engineering structures. Earthquake Press, Beijing
23. Qi X, Li X, Liu P (2006) Review of seismic control methods for civil engineering structures. Indust Archit (8):59–163
24. Zhou Y, Wu H, Anqi G (2019) Earthquake engineering: from seismic resistance and isolation to recoverability. Eng Mech 36(6):1–12
25. Hong-nan L, Yong-wei Y, Su-yan W (2003) Studies on seismic reduction of story-increased buildings with friction layer and energy-dissipated devices. Earthquake Eng Struct Dynam 32(14):2143–2160
26. Shimazaki D, Nakagawa K (2015) Seismic isolation systems incorporating with RC core walls and precast concrete perimeter frames. Int J High-Rise Buildings 4(3):181–189
27. Jie-Min D, Yu T, Hong-Lei W, Shi-Yu W (2019) Study on the application of combined seismic isolation techniques in high intensity seismic protection zones. J Build Struct 40(02):77–87
28. Jinping O (2003) Structural vibration control-active, semi-active and intelligent control. Science Press, Beijing, pp 1–540
29. Honsner GW (1997) Structural control: past present and future. J Eng Mech ASCE 12(4):134–141
30. Dyke SJ, Spencer BF, Quast P et al (1995) Role of control structure interaction in protective system design. J Eng, Mech 121(2):322–338
31. Mitsuo S, Norihide K (1992) Special issue on control technologies in civil engineering. vibration control effect of Kyobashi Seiwa building. J Soc Inst Cont Eng 31(4)
32. Guiyun Y, Jianxun Z, Jianfeng Y (2009) Research dynamics of seismic control technology for civil engineering structures. J Fujian Eng Coll 7(1):1–23

Structural Behaviours of a Concrete Façade Panel Prototype Facilitated by 3D Printed Formwork

Ziyue Gao, Jun Xia, Deyan Quan, Christiane Herr, and Davide Lombardi

Abstract Façades are key building components, determining building performance and forming the interface between inhabitants and the general public. Accordingly, façades should integrate high aesthetic value with the capability to bear relevant loads. Contemporary architectural façade design strategies often employ complex shapes, which presents civil engineering challenges in terms of assessing structural performance as well as determining effective fabrication strategies. Using 3D concrete printing for fabrication can achieve freeform shapes but has several limitations including limited structural performance. Instead of directly 3D printing concrete elements, this paper presents an approach to fabricating geometrically complex façade elements in ultra-high-performance fibre-reinforced concrete using 3D printed formwork to achieve greater accuracy and cost efficiency compared to conventional fabrication methods. Following compression test and flexural test to examine the feasibility of using 3D printed formwork for concrete fabrication, a façade prototype with a non-standard shape using 3D printed polymer formwork and UHPFRC is examined for its structural behaviours. Results show that compressive strength and flexural strength are not affected negatively by the exterior 3D printed formwork. Meanwhile, the proposed façade prototype demonstrates good concrete flowability and load test results, promising a new construction method for concrete fabrication.

Keywords 3D printing · Concrete fabrication · Façade element

Z. Gao · J. Xia (✉)
Department of Civil Engineering, Design School, Xi'an Jiaotong-Liverpool University, 111 Ren'ai Road, Suzhou, China
e-mail: Jun.Xia@xjtlu.edu.cn

D. Quan · D. Lombardi
Department of Architecture, Design School, Xi'an Jiaotong-Liverpool University, 111 Ren'ai Road, Suzhou, China

C. Herr
School of Design, Southern University of Science and Technology, Xueyuan Dadao 1088, Nanshan District, Shenzhen Guangdong Province, China

T. Kang (ed.), *Proceedings of 5th International Conference on Civil Engineering and Architecture*, Lecture Notes in Civil Engineering 369,
https://doi.org/10.1007/978-981-99-4049-3_21

1 Introduction

Building façades are essential self-load-bearing structural elements in buildings to protect interior structures from deterioration under aggressive environmental conditions. Facades are primarily functional in that they bear relevant mechanical and environmental loads such as wind load and earthquake load [1]. At the same time, building facades are important to how buildings are perceived by both inhabitants and the general public and thus carry a significant aesthetic role. Concrete such as ultra-high-performance concrete (UHPC) is a common building material for facades due to the high strength, workability and ductility [2]. However, there are some limitations for casting concrete façade panels designed with complex and unique geometries due to the requirement of special formworks. Even in conventional building elements, the cost of traditional formworks for concrete casting can be very high, accounting for approximately 50% of the overall costs for a concrete structure [3]. For complex and non-standard concrete elements, this number can be significantly higher and is the reason for few architects and clients to pursue such building facades.

3D concrete printing technology (3DCPT) is a growing field of research, in part motivated by attempts to improve current concrete fabricating methods. Compared with traditional casting technologies, 3DCPT offers several advantages [4]. First, the manufacturing process can be robotized, potentially saving time and human labour. Additionally, it offers greater geometric design flexibility as well as 3D printing-based construction without formwork for increased material economy and sustainability. Already in 2016, the world's first 3D printed concrete bridge of 12-m length was successfully constructed in Castilla-La Mancha Park in Alcobendas, Madrid [5], where 3DCPT helped to achieve maximum structural performance and optimal material distribution. Gosselin et al. [6] conducted flexural tests on the prismatic samples made of ultra-high-performance printed concrete. Results indicated that the flexural strength of the specimens could vary from 11.7 to 16.9 MPa, and the conservatively estimated compressive strength was 120 MPa. Zhu et al. [7] fabricated permanent formwork using 3DCPT for concrete column construction and concluded from compression tests that the composite column employing 3D printed formwork had higher bearing capacity and stiffness than a comparable cast-in-place column. Nevertheless, 3DCPT is still in its initial stages and has faced several essential issues and challenges. First, structural failure such as elastic buckling or plastic collapse easily occurs during the 3D concrete printing process because the geometry is instable or the maximum stress reaches yield strength of the material [8]. Moreover, during the layered material deposition process of 3D concrete printing, weak interlaminar bonding may be incurred due to surface moisture evaporation and differing curing rates. This phenomenon impairs the uniformity and integrity of 3D printed concrete, which thus negatively influences the mechanical properties, stiffness and durability of the concrete elements [9–12]. Additionally, during the printing process, excess deposition of concrete will lead to poor surface quality while insufficient material deposition will result in voids, which can be trapped and weaken the structure

[13]. Consequently, utilizing 3DCPT to manufacture complex concrete structures especially in large-scale construction can be difficult.

In addition to 3DCPT, utilizing 3D printed polymer formwork for concrete casting has also been explored in recent years as polymer-based 3DPT possesses various advantages such as high precision and customized geometry [14]. Jipa et al. [15] successfully conducted concrete casting in 3D printed PLA formwork with complex tubular geometries. After concrete casting, a favourable enclosure for concrete curing is provided by the exterior PLA formwork, preventing the development of cracks owing to water loss. However, yet, there are no load tests to analyse the structural behaviours of the hybrid material. Katzer and Szatkiewicz [16] studied the properties of concrete beam elements facilitated by 3D printed plastic formwork, featuring ribs with different dimensions at the bottom to substitute steel reinforcement. The results indicated that formwork-matrix specimens without ribs can achieve almost twice the flexural strength of traditional mortar samples and specimens with 3D printed formwork and ribs can achieve four times the flexural strength of the plain mortar element. However, only regular rectangular shapes of formwork were investigated in the study. Han et al. [17] compared 3D printing to two conventional methods such as utilizing wooden formworks for fabricating customized concrete structures. After analysing, they concluded that the method of using 3D printed polymer formwork to fabricate concrete can be more accurate, cost-efficient and time-saving than comparable conventional methods for the mass production of highly complex or customized prefabricated concrete structures. In summary, 3D printed polymer formwork offers promise in the fabrication of geometrically complicated concrete elements as the properties of concrete can be improved and fabrication can be more efficient.

As outlined above, previous studies indicate that 3D printed polymer formwork supports the fabrication of freeform concrete façade panels. In 2018, Herr et al. [18] proposed an architectural design approach to integrate parametric design of sculptural concrete facade elements with the fabrication of 3D printed formwork for complex concrete elements. However, much remains unknown regarding structural properties of complex concrete façade panels cast in 3D printed polymer formworks in the field of civil engineering. No previous study has investigated the suitability of this method in the context of high-performance concrete to fulfil the requirement of both freeform architectural design and excellent mechanical performance for concrete façade panels. In this paper, load tests on specimens with basic geometries made of 3D printed polymer formwork. Ultra-high-performance fibre-reinforced concrete (UHPFRC) matrix composite are first conducted to preliminarily analyse the feasibility and mechanical properties of the hybrid material. Then, a prototype of façade panel with a non-standard shape fabricated by 3D printed formwork is employed to investigate its structural behaviours through load testing and finite element analysis (FEA). The presented approach to fabricating the prototype façade panel is the result of a close cross-disciplinary collaboration between civil engineering and architecture and offers an innovative method to design and fabricate concrete façade panels with non-standard geometries that also informs related architectural design approaches.

2 Materials

2.1 3D Printed Formwork

Polyethylene terephthalate glycol (PETG) was used as the 3D printed formwork material as it can offer chemical resistance when combined with concrete and higher ductility to improve the flexural strength of concrete compared to other thermoplastics [19]. The mechanical properties of PETG are summarized in Table 1 [20].

A UR10 Robot with a 2-mm-diameter extruder was used for formwork 3D printing. As mentioned above, PETG was utilized as the printing material with 230 °C melting temperature. Printing speed (ps) and extrusion speed (es) varied to print different thickness moulds. About 1.5-mm thickness is achieved by ps14.4 mm/s, es 60 r/min, and 2.5 mm thickness is achieved by ps14.4 mm/s, es 80 r/min. In total, three categories of formwork were prepared for casting including cylinder and cuboid formworks and the mould for one unit façade panel at a small scale (Fig. 1). The dimensions of printed formwork elements for different specimens are presented in Tables 2, 3 and Fig. 2.

Table 1 Mechanical properties of PETG 20

Material	Density (kg/m^3)	Tensile strength (MPa)	Elongation (%)
PETG	1270	41.7	165.5

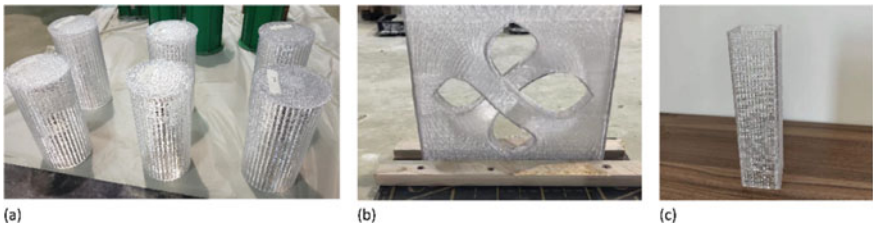

Fig. 1 3D printed formworks **a** cylinder formwork **b** façade panel formwork **c** cuboid formwork (designed and printed by the third author)

Table 2 Dimensions for 3D printed cylinder formworks

Type	Diameter (mm)	Length (mm)	Mould thickness (mm)	Number
3DP-1.5	100	200	1.5	3
3DP-2.5	100	200	2.5	3

Table 3 Dimensions for 3D printed cuboid formworks

Length (mm)	Width (mm)	Height (mm)	Number
200	50	50	3

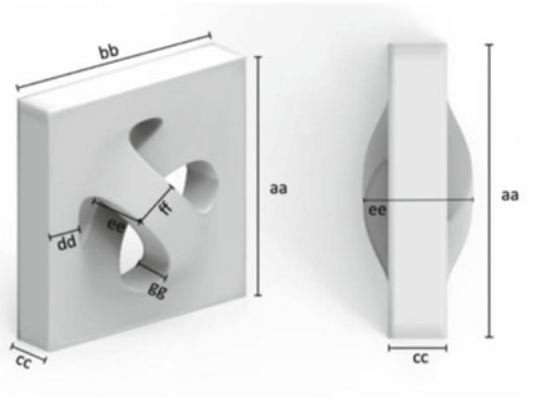

aa(mm)	bb(mm)	cc(mm)	dd(mm)	ee(mm)	ff(mm)	gg(mm)
225	225	45	30	120	45	35

Fig. 2 Dimension for 3D printed mould of one unit façade panel (designed and printed by the third author)

2.2 Concrete

UHPFRC was used in the experiment with the mix design listed in Table 4. The density and elastic modulus of UHPFRC are shown in Table 5 [21]. During mixing, fibres were incrementally added and the adding of superplasticizer was postponed to improve the workability of concrete [21]. After mixing, concrete was poured into the 3D printed formworks (Fig. 3). Traditional plastic or wooden formwork elements with same dimensions were used to cast conventional concrete using the same method. The experiment demonstrated that the above mix design can satisfy the workability requirement for casting concrete in non-standard façade formwork. For concrete curing, cylinder and cuboid specimens were placed in 60 °C water for 72 h and façade specimen were put in a steam box at a condition of 60 °C for 72 h.

Table 4 Mix design of UHPFRC (for 1 m^3)

Component	Quantity (kg)
Premix UHPC powder	2232
Superplasticizer	35
Water	206
PVA fibre (12 mm length)	26

Table 5 Properties of UHPFRC [21]

Density	2650 kg/m^3
Elastic modulus	48.8 GPa

Fig. 3 Fabrication of concrete specimens: **a** cylinder samples **b** façade panel sample

3 Methods

3.1 Compression Test

Before the test, the bottom surfaces of cylinder specimens with 3D printed formwork were ground to be smooth and even. Compression tests were conducted on the cylinder specimens at a speed of 10 kN/s as shown in Fig. 4.

3.2 Flexural Test

Flexural tests were performed using two supports and two loading points as shown in Fig. 5. The span between the two supports is 150 mm. The distance between loading points is 50 mm. The tests were performed at a displacement rate of 5 mm/min. The sampling frequency is 10 Hz.

3.3 Load Test on the Façade Specimen

The 3D printed formwork was dismantled before load testing. Rhino model was rendered to demonstrate the support condition for the concrete panel clearly as shown in Fig. 6. The concrete façade panel was supported by four steel supports, whose dimensions are all 30 × 30 × 60 mm. One point load was added on the middle part of the façade sample as shown in Fig. 7. The specimen was sprayed with white colour

Fig. 4 Compression test on cylinder specimens

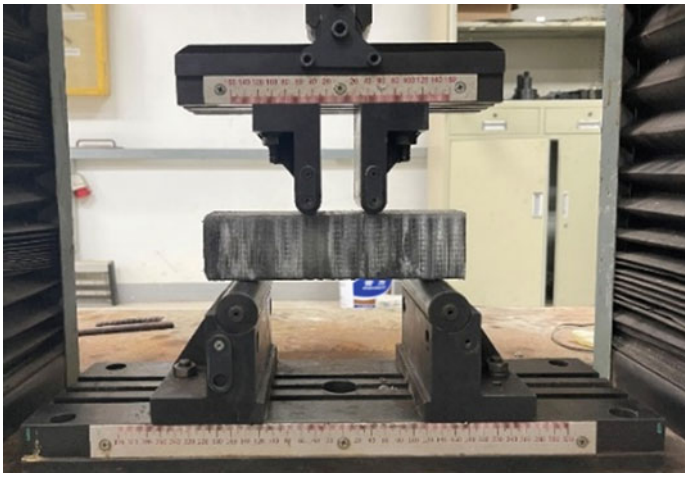

Fig. 5 Flexural test on concrete specimens

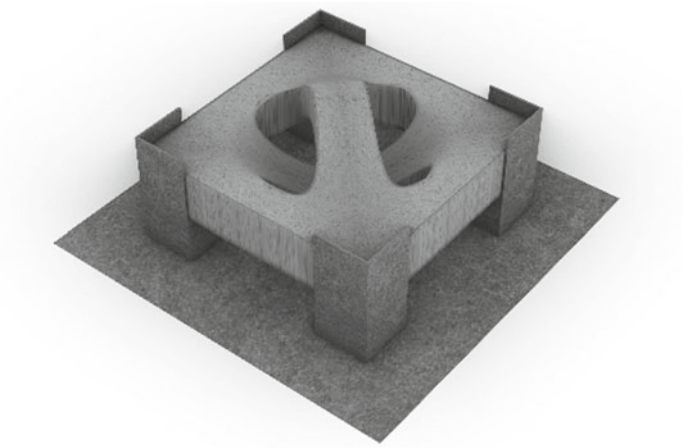

Fig. 6 Support demonstration in the Rhino model

Fig. 7 Load testing on the façade specimen

in advance in order to better observe the crack patterns. The load was applied at a speed of 0.5 mm/min.

3.4 Finite Element Analysis

ABAQUS software was used to perform Finite element analysis. Concrete damage plasticity model is used for simulation. The elastic properties used for FEA are presented in Table 5. After importing the model from Rhino software into Abaqus, several parameters in Abaqus were adjusted in order to properly mesh the complex geometry and analyse the generated mesh. First, the model was meshed by using Tet elements. Meanwhile, it was found that if the number of elements is too large, the mesh could not be analysed successfully. The number can be reduced by increasing the size of interior elements through adjusting parameters such as non-standard interior element growth rate. After decreasing the element number to approximately

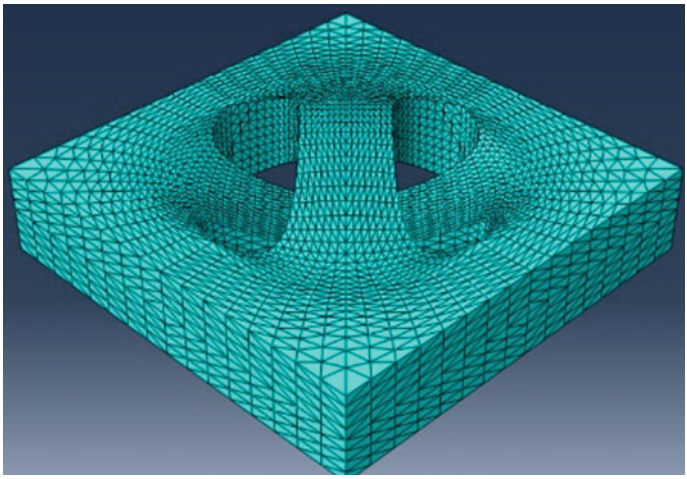

Fig. 8 Mesh of the façade panel in Abaqus

30,000, the mesh could be analysed successfully. The final mesh of the model is shown in Fig. 8.

4 Results and Discussion

4.1 Compression Test Results

Table 6 shows the results of compressive test. For each type, three specimens were tested. For 3DP-1.5 (concrete specimen with 3D printed mould of 1.5-mm thickness), the compressive strength is 69 MPa, which increases to 89 MPa for 3DP-2.5 (concrete specimen with 3D printed mould of 2.5-mm thickness). The compressive strength of the concrete sample cast in traditional moulds is 82.8 MPa. The results indicate that the compressive strength will not be influenced negatively to a large extent and can be even improved by the exterior 3D printed formwork.

Table 6 Compressive strength[a]

Type	Compressive strength (MPa)
3DP-1.5	69.0
3DP-2.5	89.0
Cast-1	82.8

[a] Average compressive strength is presented in the above table

4.2 Flexural Test Results

Three specimens were tested for flexural strength. For concrete specimens with 3D printed formwork, the flexural strength is 13 MPa, which is approximately equal to the strength for samples cast in conventional formwork. The results indicate that the flexural strength will not be influenced negatively by the exterior 3D printed formwork.

4.3 Façade Panel Test Results

Figure 9 illustrates the load–deflection curve of the façade panel sample. The ultimate load is approximately 6.5 kN. According to Fig. 10, an elastic response is first observed. After the elastic phase, load drop related with onset of cracks was observed in the curve followed by load increase due to fibre reinforcement. After reaching the load capacity, no sudden drop of the load was observed, which indicated good ductility of the material. Cracks associated with the drop of load–deflection relationship on the side and arch part of the sample were observed during the testing (the cracks are highlighted by red dotted circles in Fig. 10).

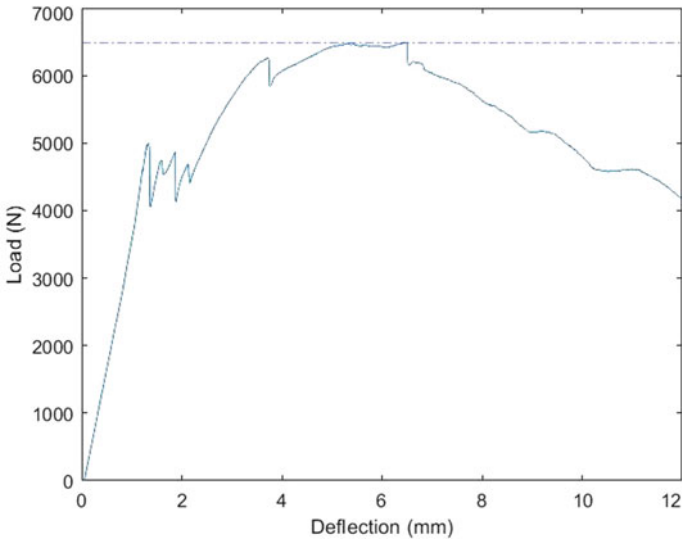

Fig. 9 Load–deflection curve for the façade panel

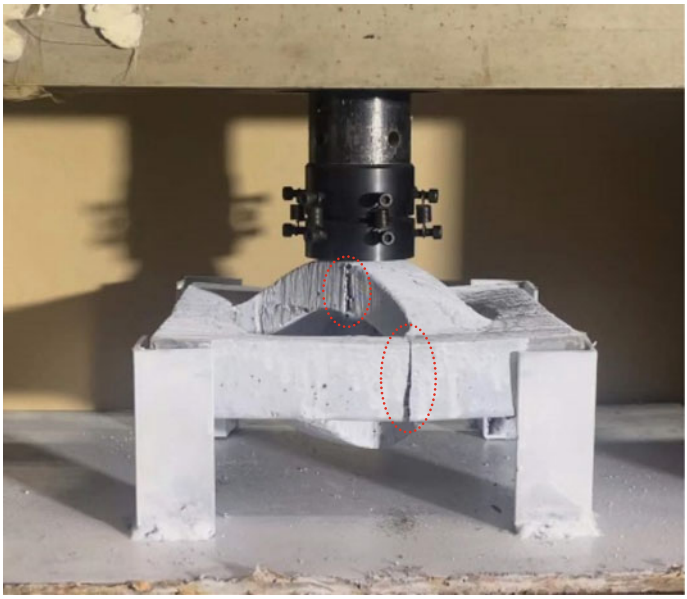

Fig. 10 Crack development during the load testing

4.4 Façade Panel Simulation Results

The deformation and stress distribution of the model under point load are shown in Fig. 11. Stress concentrates on the part where load is added. The preliminary analyses within the elastic stage shows that the model is acceptable for further analyses considering the material nonlinearity.

5 Conclusions

This study employed innovative 3D printed formwork instead of conventional moulds in combination with UHPFRC to fabricate a concrete façade panel prototype with complex geometry. This paper outlines in detail initial tests on the prototype's structural behaviour. Experimental results indicate that the exterior 3D printed formwork presents no obvious negative influences on the flexural strength and compressive strength of the UHPFRC elements. Compressive strength can be even improved lightly by including the 3D printed formwork. A prototype for a UHPFRC façade panel using 3D printed formwork is proposed in the paper, offering a novel construction method for fabricating non-standard concrete façade elements as satisfying workability of concrete and test results are observed in the experiments. Future research in this project will include the testing of prototype façade panels at a 1:1 scale

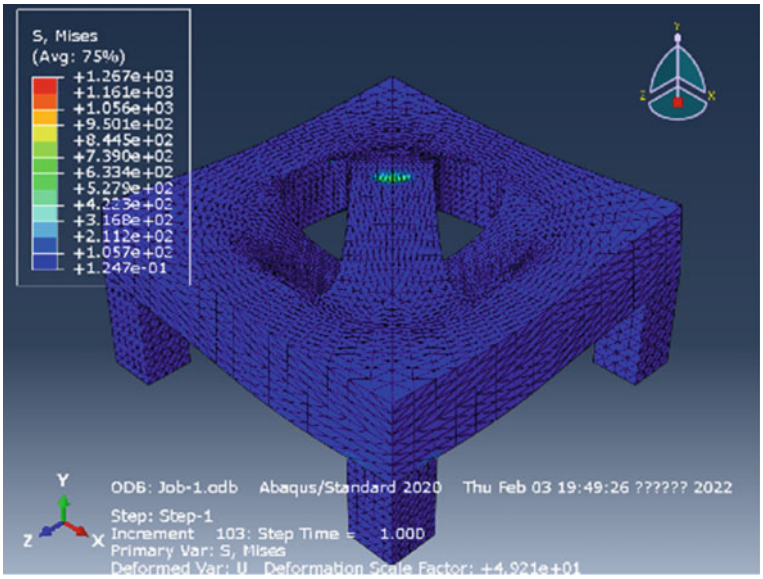

Fig. 11 Deformation and stresses of the façade panel model

to examine the feasibility of the construction method at larger scales. Meanwhile, façade panels with other shapes will be cast and tested in the future.

References

1. Moghtadernejad S, Mirza MS, Chouinard LE (2019) Façade design stages: issues and considerations. J Archit Eng 25(1)
2. Kim S, Kang TH-K, Hong S (2021) Impact performance of thin prefabricated ultra-high-performance concrete Façade. ACI Struct J 118(1):167–177
3. Jipa A, Bernhard M, Ruffray N, Ruffray N, Wangler T, Flatt R (2017) SkelETHon formwork—3D printed plastic formwork for load-bearing concrete structures. In: Proceedings of the 21th conference of the Ibero-American society of digital graphics. SIGRADI, Chile, pp 379–387
4. Nematollahi B, Sanjayan J, Xia M (2017) Current progress of 3D concrete printing technologies. In: Proceedings of the 34th international symposium on automation and robotics in construction. IAARC Publications, Taiwan, pp 260–267
5. World's First 3D Printed Bridge Opens in Spain, https://www.archdaily.com/804596/worlds-first-3d-printed-bridge-opens-in-spain. Last Accessed 20 Mar 2022
6. Gosselin C, Duballet R, Roux P, Gaudillière N, Dirrenberger J, Morel P (2016) Large-scale 3D printing of ultra-high-performance concrete—a new processing route for architects and builders. Mater Des 100:102–109
7. Zhu B, Nematollahi B, Pan J, Zhang Y, Zhou Z, Zhang Y (2021) 3D concrete printing of permanent formwork for concrete column construction. Cement Concrete Compos 121
8. Suiker ASJ (2018) Mechanical performance of wall structures in 3D printing processes: theory, design tools and experiments. Int J Mech Sci 137:145–170

9. Tay YWD, Ting GHA, Qian Y, Panda B, He L, Tan MJ (2019) Time gap effect on bond strength of 3D-printed concrete. Virtual Phys Prototyping 14(1):104–113
10. Sanjayan JG, Nematollahi B, Xia M, Marchment T (2018) Effect of surface moisture on inter-layer strength of 3D printed concrete. Constr Build Mater 172:468–475
11. Xu J, Ding L, Cai L, Zhang L, Luo H, Qin W (2019) Volume-forming 3D concrete printing using a variable-size square nozzle. Autom Constr 104:95–106
12. Marchment T, Sanjayan J, Xia M (2019) Method of enhancing interlayer bond strength in construction scale 3D printing with mortar by effective bond area amplification. Mater Design 169
13. Panda B, Tay YWD, Paul SC, Tan MJ (2018) Current challenges and future potential of 3D concrete printing. Mater Sci Eng Technol 49:666–673
14. Wang X, Jiang M, Zhou Z, Gou J, Hui D (2017) 3D printing of polymer matrix composites: a review and prospective. Compos B 110:442–458
15. Jipa A, Bernhard M, Dillenburger B (2018) Submillimeter formwork 3D-printed plastic formwork for concrete elements. In: TxA 78th annual conference and design Expo, USA
16. Katzer J, Szatkiewicz T (2019) Properties of concrete elements with 3-D printed formworks which substitute steel reinforcement. Constr Build Mater 210:157
17. Han D, Yin H, Qu M, Zhu J, Wickes A (2020) Technical analysis and comparison of formwork-making methods for customized prefabricated buildings: 3D printing and conventional methods. J Archit Eng 26(2):1–13
18. Herr C, Lombardi D, Galobardes I (2018) Parametric design of sculptural fibre reinforced concrete façade components. In: Proceedings of the 23rd international conference of the association for computer aided architecture design research in Asia. Beijing, pp 319–328
19. Burger J, Lloret-Fritschi E, Scotto F, Demoulin T, Gebhard L, Mata-Falcon J, Gramazio F, Kohler M, Flatt RJ (2020) Eggshell: ultra-thin three-dimensional printed formwork for concrete structures. 3D Print Add Manuf 7(2):48–59
20. Shweiki A, Junaid MT, Barakat S (2019) Flexural characteristics of mortar cement reinforced with 3D-printed polymer. In: Proceedings of the 4th world congress on civil, structural, and environmental engineering, Italy
21. Othman H, Marzouk H (2018) Applicability of damage plasticity constitutive model for ultra-high performance fibre-reinforced concrete under impact loads. Int J Impact Eng 114:20–31
22. Wang W, Shen A, Lyu Z, He Z, Nguyen KTQ (2021) Fresh and rheological characteristics of fiber reinforced concrete—a review. Constr Build Mater 296

Mechanical Behavior of Concrete Bridge-Deck Slabs Reinforced with Hybrid Reinforcement

Yahia M. S. Ali, Xin Wang, Shui Liu, and Zhishen Wu

Abstract Recently, hybrid reinforcement by combining steel with fiber-reinforced polymer (FRP) bars has emerged as a new system in reinforced concrete structures to overcome the ductility and serviceability problems of purely FRP-reinforced structures. This paper presents an experimental study aimed at understanding the structural behavior and serviceability performance of concrete bridge-deck slabs reinforced with hybrid bars. Nine full-scale bridge-deck slabs were constructed and tested under four-point loading up to failure. The parameters investigated were reinforcement type, ratio, arrangement, and slab thickness. The test results showed that hybrid-reinforced slabs exhibited ductility leading to an ample warning before failure and avoided catastrophic failure rather than brittle shear failure exhibited by FRP-reinforced slab. In addition, hybrid reinforcement managed to control the crack width and deformations of slab specimens.

Keywords Basalt fiber-reinforced polymer (BFRP) bar · Concrete bridge · Hybrid reinforcement · Shear behavior

1 Introduction

Bridge-deck slabs are the most critical infrastructure exposed to harsh environments (deicing salts, humidity, freeze–thaw cycles, and chlorides) that make these structures very susceptible to corrosion by steel reinforcement. The associated deterioration can accelerate such failure or reduce the expected lifespan of the structure [1]. Within the past two decades, the most effective way to diminish maintenance costs and extend the service life of structures has been to use fiber-reinforced polymer (FRP) composites as an alternative to traditional steel reinforcement in structural components, especially where steel corrosion is a major concern. In addition to the corrosion

Y. M. S. Ali · X. Wang (✉) · S. Liu · Z. Wu
Key Laboratory of C&PC Structures Ministry of Education, Southeast University, Nanjing 210096, China
e-mail: xinwang@seu.edu.cn

T. Kang (ed.), *Proceedings of 5th International Conference on Civil Engineering and Architecture*, Lecture Notes in Civil Engineering 369,
https://doi.org/10.1007/978-981-99-4049-3_22

resistance of FRP composites, FRP composites have many characteristics over steel reinforcement, such as a high strength-to-weight ratio, excellent fatigue resistance, and nonmagnetic and nonconductive nature, which can be used in harsh environments for civil structures. Unfortunately, FRP composites have some drawbacks: a low elastic modulus compared to steel (E_f/E_s = approximately 0.25) and their linear elastic behavior up to failure without exhibiting any yielding plateau, which leads to the brittle failure of the structure [2]. Various design codes such as ACI 440.1R [3], CSA S806 [4], and CSA S6:19 [5] permit using carbon FRP (CFRP) bars, aramid FRP (AFRP) bars, and glass FRP (GFRP) bars, as primary reinforcements in concrete constructions and including design procedures for these type of structures. Recently, basalt fibers have been introduced as a promising addition to the current family of FRPs. Basalt-FRP (BFRP) bars have a relatively higher strength and modulus, comparable costs, and greater chemical stability than GFRP bars [6]. Using BFRP bars with a relatively high elastic modulus, compared to GFRP bars, would significantly decrease the amount of reinforcement required and reduce the crack width [7]. Moreover, BFRP-reinforced concrete beams were investigated in flexural and shear [8]. It was demonstrated that BFRP-RC beams exhibited acceptable deformability. Additionally, the J–factor for steel-reinforced beams was about 50% lower than that of BFRP-reinforced beams due to the lower load capacity at service. However, there is still a lack of BFRP research, and their applications, codes, and guidelines have not yet been formulated for designing concrete structures reinforced with BFRP bars.

In the FRP RC members, deeper cracks decrease the contribution of uncracked concrete to the shear strength due to the lower concrete depth in compression. Moreover, the lower strength and stiffness of FRP bars in the transverse direction resulted in wider cracks and lower aggregate interlock and dowel action contribution of the tensile reinforcement compared to that of an equivalent steel area. Finally, the total shear capacity of FRP-reinforced concrete members is lower than the total shear capacity of steel-reinforced concrete members. However, conventional stirrups are not practical for constructing slab bridges; consequently, the failure mode may be dominated by shear. Slabs reinforced with GFRP or CFRP bars failed in shear failure, while the control steel-reinforced slabs failed in flexure mode by steel yielding followed by concrete crushing [9]. In addition, increasing the flexural reinforcement ratio significantly increased the shear capacity and the post-cracking stiffness [10]. Thus, the reinforcement type and axial stiffness of the reinforcement can be confirmed to have a pronounced effect on the shear capacity of the reinforced concrete sections without shear reinforcement.

Gradual failure can be obtained by utilizing a combination of FRP and steel reinforcements. Therefore, steel reinforcement improves the ductility through the yielding of steel bars and enhances serviceability by reducing crack width and spacing. While FRP-reinforcement maintains the load-carrying capacity even after yielding of steel bars [11]. In addition, hybrid reinforcement resulted in lower crack spacing and smaller widths [12]. From a durability approach, the FRP bars were placed on the outer layer to attack the harsh conditions, and the steel bars were placed on the inner layer with an adequate cover to keep it away from corrosion. However, placing FRP and steel bars in the same layer presented higher flexural

strength than placing steel bars in the inner layer and FRP bars in the outer layer [13]. It is found that the effective reinforcement ratio (ρ_{eff}) has a significant impact on the flexural capacity compared with axial stiffness between GFRP and steel reinforcement (R_{f}) [14]. GFRP-steel RC beams showed slightly lower flexural capacity than steel-reinforced concrete beams. However, the deflection and maximum crack width were larger than beams reinforced with steel reinforcement under service load [15]. Furthermore, the ductility of hybrid-reinforced beams can satisfy the specifications of serviceability limits by adequately regulating the reinforcement ratio and the $A_{\text{f}}/A_{\text{s}}$ value [16]. In addition, the maximum load and moment for serviceability increased with the GFRP-to-steel ratio. At the ultimate stage, the deflection obviously increases and provides a good prefailure warning [17]. Applying the principle of equal stiffness, the overall performance of the hybrid-RC beams was superior when $A_{\text{s}}/A_{\text{f}} \leq 1.0$; however, it declined intensely when $A_{\text{s}}/A_{\text{f}} > 1.0$ [18]. Recently, hybrid (BFRP and steel bars) RC beams designed as under-reinforced section exhibited large deflections and crack widths, and the deformability factors of these beams were noticeably larger than those of over-reinforced concrete beams with hybrid bars [19].

To the authors' best knowledge, no research has been conducted to study the performance of concrete bridge-deck slabs reinforced with hybrid bars. Therefore, there is necessary to comprehend how these hybrid-reinforced concrete bridge-deck slabs behave and later to allow and incorporate this concept into bridge design codes and guidelines. This study investigates the structural behavior of concrete deck slabs reinforced with hybrid steel and BFRP bars compared to a control slab reinforced with BFRP bars.

2 Experimental Program

2.1 Design Concept

The sum of the steel reinforcement ratio, ρ_{s}, and the FRP reinforcement ratio, ρ_{f}, cannot be used to directly reflect the reinforcement of hybrid-RC sections due to the differences in mechanical properties between steel and FRP bars. Thus, an effective reinforcement ratio ρ_{eff} was defined to account for combinations of the elastic modulus in Eq. 1 [19]. The corresponding balanced reinforcement ratio expressed by the elastic modulus and the steel strength, $\rho_{\text{eff,b}}$, could be identified as the ratio where concrete crushing and steel yield occur simultaneously, as shown in Eq. 2.

$$\rho_{\text{eff}} = \rho_{\text{s}} + \frac{E_{\text{f}}}{E_{\text{s}}}\rho_{\text{f}} \tag{1}$$

$$\rho_{\text{eff,b}} = \alpha_1 \beta_1 \frac{f_c'}{f_y} \frac{\varepsilon_{\text{cu}}}{\varepsilon_{\text{cu}} + \varepsilon_y} \tag{2}$$

where ρ_s and ρ_f are the steel and FRP reinforcement ratios, respectively, E_s and E_f are the elastic moduli of the steel and FRP bars, respectively, f_y is the yield stress of the steel bars, α_1 is the ratio of the average stress of the rectangular stress block to the cylinder compressive strength of concrete f_c', β_1 is the ratio of the depth of the rectangular stress block to the depth of the neutral axis, ε_{cu} is the ultimate concrete strain, and ε_y is the yield strain of the steel bars. Hybrid-RC members are preferred to design as under-reinforced section; thus, $\rho_{sf,s} < \rho_{s,b}$. Accordingly, the failure mode is demonstrated by steel bars yielding then concrete crushing, thereby revealing the plastic deformation of concrete. Hence, this section was adopted in the design of hybrid-RC sections.

2.2 Material Properties

The deck slab specimens are fabricated using normal-weight ready-mixed concrete. The average compression strength was evaluated by testing three standard 150 mm concrete cubes after 28-days of curing. The concrete cubes yielded an average compressive strength of 52 MPa. The reinforcement bars used in this paper included ribbed steel bars and BFRP bars, as shown in Fig. 1. BFRP bars are made of basalt fibers and epoxy resin, and basalt fiber content by weight is 70% according to the manufacturer. Axial tensile tests were carried out to evaluate the mechanical properties of the different reinforcement bars according to ASTM D7205/D7205M [20], as applicable. The results of average three specimens of reinforcement bars are reported in Table 1.

2.3 Test Specimens

Nine large-scale reinforced concrete slabs with a total length (L_t) of 2900 mm, a width (b) of 1000 mm, and a depth (h) of 200 mm were used. These dimensions of slabs were chosen to represent the most common size of the concrete deck slabs for girder-type bridges in North America. The test parameters were the reinforcement type, effective reinforcement ratio, ρ_{eff}, ratio between the area of FRP and steel bars, A_f/A_s, and reinforcement arrangement. All slabs have identical steel reinforcement in all directions 12 mm with spacing 225 mm except the bottom reinforcement in the main direction. Clear concrete cover of 50 mm and 25 mm were used for the longitudinal reinforcements at the top and bottom, respectively. The slabs were identified according to the amount and type of longitudinal reinforcement (XB or XBXS), where the letters X, B, and S, indicate the number of bars, BFRP rebar, and steel rebar, respectively.

The test program was categorized into three groups according to the parameters studied. Group A (reference group) consists of two slabs (8B and 5B3S) studying the effect of reinforcement type. In Group B, slabs (5B7S, 6B7S, and 10B6S) were

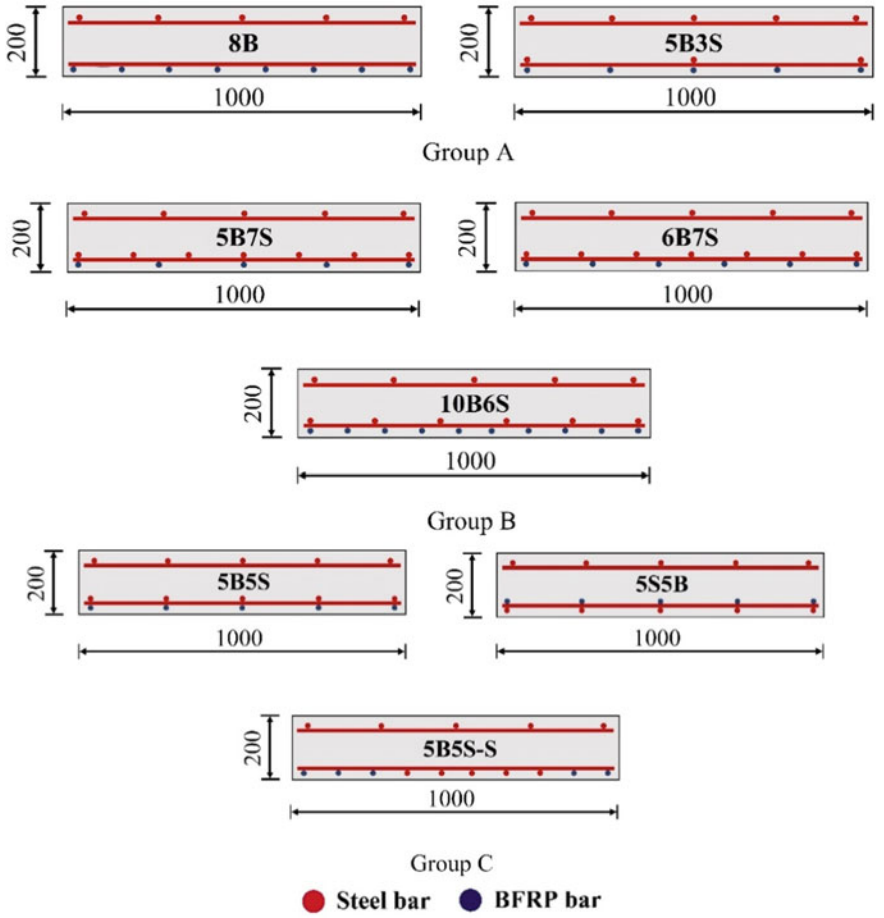

Fig. 1 Reinforcement details of tested deck slabs. *Note* Dimensions in mm

Table 1 Properties of reinforcement bars

Bar type	D (mm)	E (GPa)	f_y (MPa)	f_u (MPa)	ε_u (%)
Steel	12	200	452	667	3.16
	16	200	494	688	3.50
BFRP	16	55	–	1163	2.12

Where: D bar diameter, E elastic modulus, f_y yield strength, f_u ultimate strength, ε_u ultimate strain

Table 2 Details of tested slabs

Group no.	Slab	A_f/A_s	ρ_f %	ρ_s%	ρ_{eff} %	$\rho_{eff}/\rho_{eff,b}$
A	8B	–	0.89	–	0.25	0.09
	5B3S	1.58	0.57	0.43	0.59	0.20
B	5B7S	0.68	0.57	1.01	1.18	0.40
	6B7S	0.81	0.69	1.01	1.19	0.41
	10B6S	1.58	1.11	0.87	1.18	0.40
C	5B5S	0.95	0.57	0.72	0.88	0.30
	5S5B		0.69	0.60	0.79	0.27
	5B5S-S		0.57	0.60	0.76	0.26

designed with similar effective reinforcement ratios to study the effect of increasing the effective reinforcement ratio, ρ_{eff} and A_f/A_s ratio. Group C includes slabs (5B5S, 5S5B, and 5B5S-S) that vary in reinforcement arrangement, where S (last letter in Slab 5B5S-S) represents that reinforcement is arranged in a single layer. Regarding slab (5S5B), which placed steel bars at the outer layer, it is not efficient from the durability point of view; this system is examined only to evaluate the influence of reinforcement arrangement on the structural performances of hybrid deck slabs. Table 2 summarizes the details of the slabs. Figure 1 shows the cross sections of all deck slabs.

3 Test Program and Instrumentation

The slab specimens were tested under four-point bending loading until failure. Figure 2 provides the actual setup and schematic diagram of the test. A steel spreader beam was used to transform the two concentrated loads 900 mm apart, yielding a shear span (a) of 900 mm on both sides with a support-to-support distance (L) of 2700 mm. The load was applied with displacement control at a constant rate of 0.6 mm/min by the hydraulic jack 500 kN capacity to measure the applied loads with a displacement sensor to measure the corresponding deflection. Three LVDTs were positioned at the bottom midspan and the two loading points of each slab, and two LVDTs were installed at the supports to offset their settlements. Five electrical strain gauges were attached to the slab surface to measure the concrete strain along the depth of the slab, and four strain gauges were also attached to the surface of the tensile reinforcement. The applied loads, deflections, and strain readings at a frequency of 10 Hz were automatically recorded using a System 5000 data acquisition system. The crack width was measured using a handheld readout microscope (10085-240X) with a magnification factor of 40x with an accuracy of 0.01 mm.

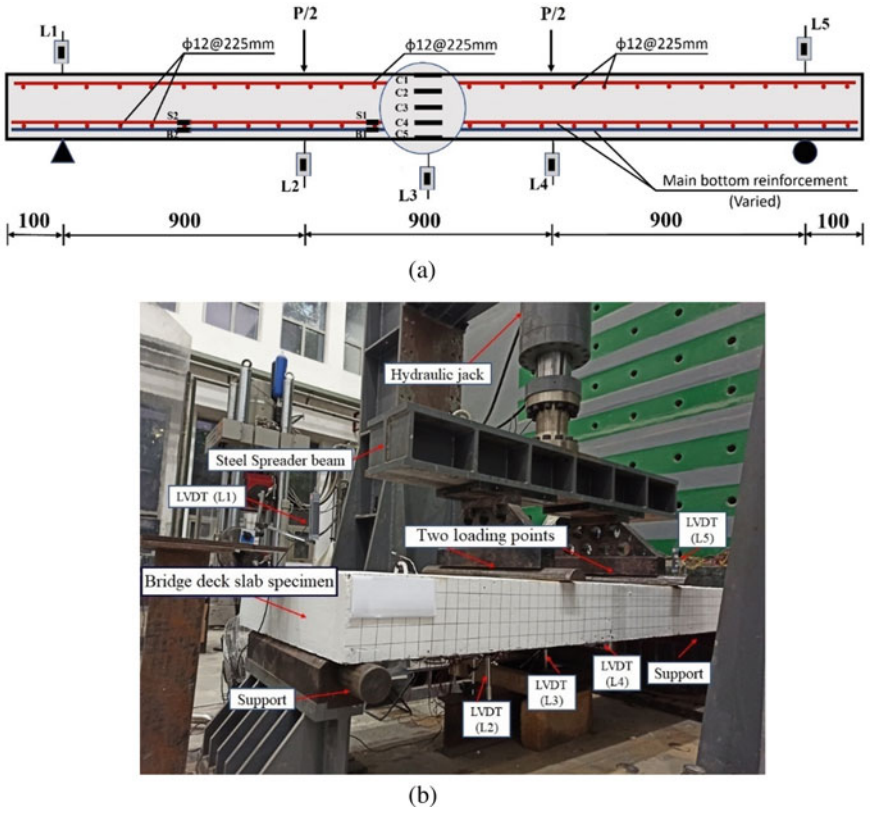

Fig. 2 Test setup: **a** schematic drawing (dimensions in mm); **b** slab specimen ready for testing

4 Test Results and Discussion

4.1 Crack Patterns and Propagation

Figure 3 shows the crack distribution of the tested deck slabs upon failure. The first crack was initiated in the pure bending moment zone. Generally, the cracking load was recorded at a similar load level for slabs of the same thickness, while increasing the slab thickness increased the cracking load, as listed in Table 3. As the load increased, more flexural cracks began to develop below or between the point loads. With further loading, flexural-shear and shear cracks appeared and spread in the shear spans, demonstrating the shear stresses in the shear span. For slab 8B, at a high load level, the shear cracks continued to widen due to the absence of shear reinforcement. A large shear crack opened up until failure occurred. However, in the hybrid deck slabs, shear stresses in the shear spans allowed the flexural cracks to become progressively more inclined and propagated toward the load points. Once

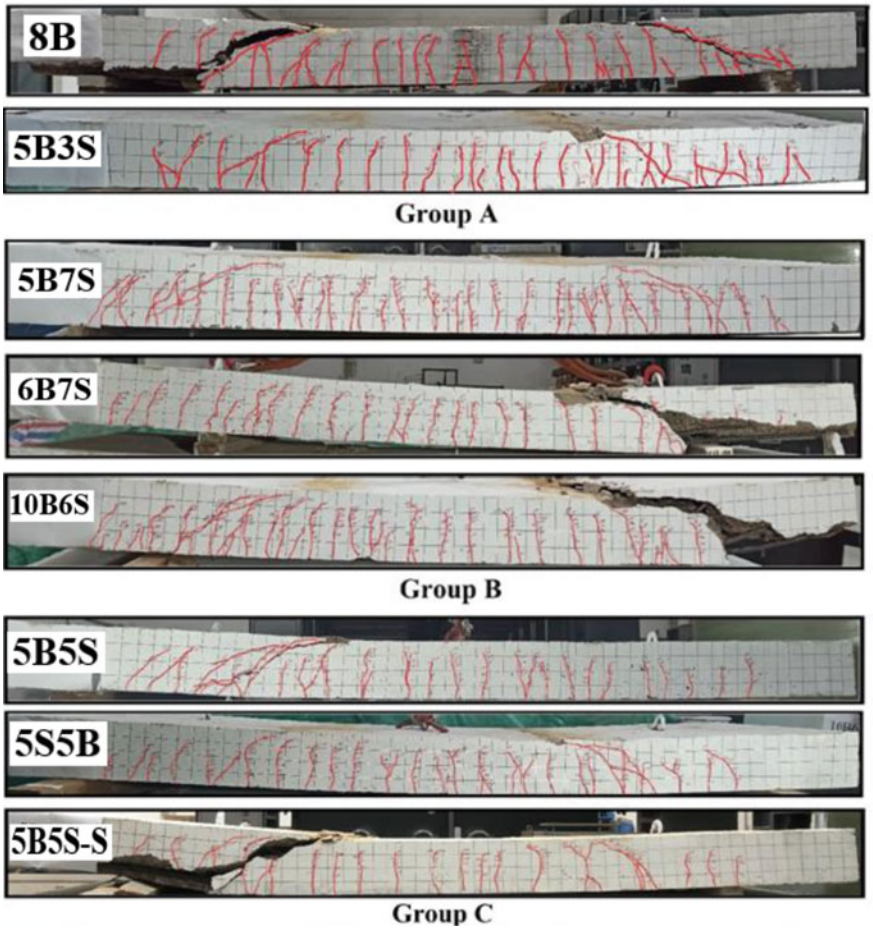

Fig. 3 Cracking patterns and the failure modes of the tested slabs

steel yielded, the number of cracks increased and propagated, accompanied by the widening of the existing cracks. All hybrid slabs failed by one of these cracks, finally causing the slab to fail.

4.2 Mode of Failure

The combined effect of high shear force and bending moment leads to a spatially high stressed area; hence, failure occurs in the shear span. Four different failure modes were observed in the experimental tests and are listed in Table 3. Mode I: Diagonal tension failure (DTF); this mode was observed only for slab 8B reinforced with BFRP

Table 3 Test results of tested slabs

Group no.	Slab	Δ_{cr} (mm)	Δ_y (mm)	Δ_u (mm)	P_{cr} (kN)	P_y (kN)	P_u (kN)	Failure mode
A	8B	2.3	–	63	36	–	295	DTF
	5B3S	1.7	19.1	78	41	179	314	FSF
B	5B7S	1.2	22.3	67	42	260	414	FF
	6B7S	2.0	20.1	49	46	251	437	SCF
	10B6S	1.9	20.3	45	47	294	470	SCF
C	5B5S	2.3	20.6	68	43	190	325	FSF
	5S5B	2.3	18.4	73	38	190	335	FSF
	5B5S-S	3.7	16.5	58	49	211	396	SCF

Where: Δ_{cr} cracking deflection; Δ_y yielding deflection; Δ_u ultimate deflection; P_{cr} cracking load; P_y yielding load; P_u ultimate load

reinforcement owing to the low stiffness of BFRP bars, as shown in Fig. 3. Mode II: Flexural-shear failure (FSF) was observed for slabs 5B3S, 5B5S, and 5S5B, which initiated as a flexural crack closer to the loading point and then propagated inclining upward to the loading point. As shown in Fig. 3, the failure was gradual, and the hybrid slabs displayed some ductility before reaching the ultimate load rather than the brittle shear failure observed by slab 8B, which may be attributed to the higher load levels reached, which confirms enhancement of the shear resistance by the improved dowel action of the double layer reinforcement [21]. Mode III: Shear–compression failure (SCF); the compression zone in the slab was reduced by the inclined flexure–shear cracks; thus, the concrete was crushed in slabs 6B7S, 10B6S, and 5B5S-S as shown in Fig. 3. Additionally, the failure was accompanied by concrete-cover spalling on the tension side without FRP bars shearing off, and the slab maintained its integrity even after failure, which can be attributed to the high reinforcement ratio and A_f/A_s ratio in these slabs. Accordingly, a minimum amount of steel reinforcement with a reasonable value of A_f/A_s is recommended to ensure ductility and to prevent devastating failure of concrete bridge-deck slabs. However, the slab failure mechanism changes between the BFRP RC slab and hybrid-RC slabs could be due to the difference in the shear crack location. Mode IV: Flexural failure (FF) was observed for slab 5B7S by steel yielding where the main crack was approximately under the point load. These slabs did not display any bond-splitting cracks, which shifted the crack location closer to the loading point. Generally, using hybrid reinforcement to reinforce the deck slabs could achieve some plastic deformations of concrete before total failure; thus, this type of section is admissible in the design of hybrid-reinforced concrete members without shear reinforcement.

4.3 Ultimate Capacity

The ultimate capacity for all tested slabs is listed in Table 3. The test results revealed that hybrid slab 5B3S showed a slight increase of 6% in the ultimate capacity compared with slab 8B reinforced with pure BFRP bars. This is attributed to the amount in BFRP bars in slab 5B3S is less than that of slab 8B, whereas BFRP bars are responsible for carrying the additional load after steel yielded. In addition, the ultimate capacity increased, as did the reinforcement ratio. Slab 6B7S showed an increase in the ultimate capacity of 39% compared to control slab 5B3S. This increase in carrying capacity may be due to increasing the amount of reinforcement and decreasing the crack width. Moreover, slab 10B6S contains the highest FRP to steel content ($A_f/A_s = 1.58$) showed an improvement in ultimate capacity by 13% compared with slab 5B7S ($A_f/A_s = 0.68$). The reinforcement arrangement affects the ultimate capacity since slab 5B5S-S reinforced in a single layer exhibited higher ultimate capacity than slabs arranged in double layers. The ultimate capacity of slab 5B5S-S is approximately 1.22 and 1.18 times the ultimate capacity of slabs 5B5S and 5S5B, respectively. From the mechanical point of view, placing the BFRP and steel bars at the outer layer is more effective than placing the BFRP bars at the outer layer.

4.4 Load–Deflection Response

Figure 4 shows the load-midspan deflection curves for the tested deck slabs. All slabs showed a steep linear behavior at the precracking stage with low deflection values. In the post-cracking stage, slab stiffness was significantly degraded due to flexural cracks, which reduced the moment of inertia. Slab 8B exhibited a bilinear load-midspan deflection curve and degraded faster than hybrid RC-slabs due to the lower elastic modulus of the BFRP bars, as shown in Fig. 4a. Conversely, hybrid RC-slabs exhibited trilinear load–deflection curves owing to the presence of steel bars. As shown in Fig. 4, after steel yielded, a pronounced reduction in the slope of the load–deflection curves as the load increased to high levels means that steel reinforcement cannot resist any load, and only the BFRP reinforcement carried the load upon failure. In this stage, the deflection of hybrid deck slabs was lower than the deflection of slab 8B, attributed to the efficiency of the BFRP bars restricting the excessive deflection even after steel yielding. Hence, using hybrid bars to reinforce the concrete bridge-deck slabs keeps the load growing with a reasonable deflection value.

In Group A, slab 8B suffered a larger deflection than slab 5B3S under the same load level, as shown in Fig. 4a. This is attributed to the high elastic stiffness of steel bars compared to BFRP bars, which increased the rigidity of the hybrid slabs. At the yielding load of slab 5B3S, the deflection decreased by 43% compared to slab 8B. For Group B, increasing the effective reinforcement ratio increased the loading

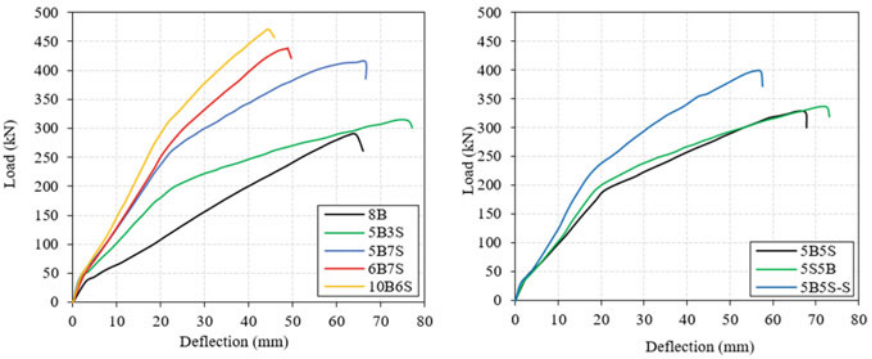

(a) Group A and B. (b) Group C.

Fig. 4 Load–deflection curves of tested slabs

capacity and decreased the deflection at similar load levels. The load–deflection relationship of the hybrid slabs is influenced by the ratio of the FRP to steel ratio, A_f/A_s especially after steel yielded. As A_f/A_s increases, the deflection decreased for example, at the load of 294 kN, the deflection of slab 10B6S was 30% lower than the deflection of slab 5B7S because the former had a high A_f/A_s ratio, which enhanced the slab rigidity by restricting the excessive deflection after steel yielded. The above results proved the significant influence of the A_f/A_s ratio on the postelastic strength of bridge-deck slabs with sufficient deformability and stiffness.

Considering the reinforcement arrangement in Group C, both slabs reinforced in double layers developed larger deflection than slabs arranged in a single layer, as shown in Fig. 4b. At a load of 200 kN (approximately the yielding load of this group), the deflections of slabs 5B5S, 5S5B and 5B5S-S were 23.9 mm, 20.2 mm and 15.7 mm, respectively. At serviceability state, placing the steel reinforcement at the outer layer in slab 5S5B develops less deflection than Slab 5B5S; however, the former showed higher deflection at the ultimate state than the latter.

4.5 Crack Width

Figure 5 shows the applied load–crack width curves. The load–crack width relationship was almost linear for the pure BFRP-RC slab; however, all hybrid deck slabs exhibited a bilinear curve owing to the yielding of steel bars. In Group A, replacing the BFRP bars with steel bars could restrain crack depth and fast propagation due to the higher elastic modulus of the steel bars. As shown in Fig. 5a, the crack widths were inversely proportional to the effective reinforcement ratio. Thus, the measured crack width was lower in the case of slab 6B7S than in slab 5B3S. Moreover, a higher ratio of FRP to steel amount A_f/A_s led to better secondary stiffness and hence

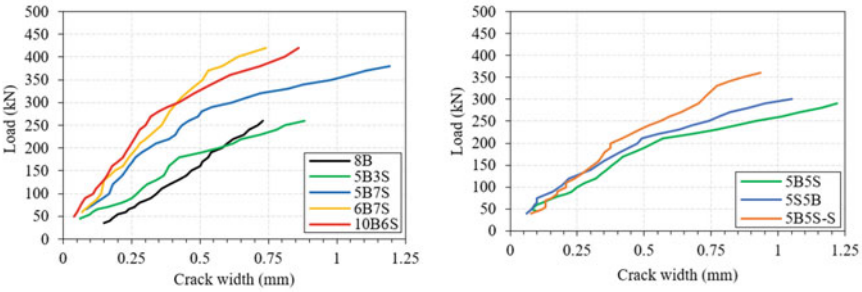

(a) Group A and B. (b) Group C.

Fig. 5 Load-maximum crack width relationship of the tested slabs

narrower crack widths. Placing BFRP reinforcement in the outer layer recorded a wider crack width for slab 5B5S followed by slabs 5S5B and 5B5S-S.

4.6 Reinforcement and Concrete Strains

The applied load versus measured strains at the midspan of both concretes at the top fiber, and the tensile BFRP bars are shown in Fig. 6. Before cracking, all the tested deck slabs showed approximately similar concrete and reinforcement strains. After cracking, the BFRP strain of slab 8B showed a rapid linear increase, increasing the load up to failure. Using steel bars instead of BFRP bars, slab 5B3S yielded a significant reduction in BFRP strain compared to slab 8B, as shown in Fig. 6a. The influence of the reinforcement ratio can be realized in slabs 5B3S and 10B6S; high reinforcement and lower strains were recorded at the same load levels. Increasing the steel reinforcement controlled the BFRP bar strain development in hybrid deck slabs, as demonstrated by the lower tensile strain readings in the BFRP bars of slab 5B3S compared to slab 5B7S. These results tend to indicate the effect of increasing the effective reinforcement ratio to improve the serviceability performance of the hybrid slabs. Moreover, as the A_f/A_s ratio increased, the BFRP strains decreased, as shown in Fig. 6a. The BFRP strain in slab 10B6S ($A_f/A_s = 1.58$) recorded 2422 $\mu\varepsilon$ which was considerably lower than the BFRP strain of slab 6B7S ($A_f/A_s = 0.81$) of 4273 $\mu\varepsilon$ at the yielding load. The secondary stiffness provided by BFRP bars can restrict the strain development of tensile reinforcements after steel is yielded [22]. As shown in Fig. 6b, there was no clear effect of the reinforcement arrangement on the yielding load, while slab 5B5S read a high value of BFRP strain of 1932 $\mu\varepsilon$ followed by slabs 5S5B and 5B5S-S of 1518 $\mu\varepsilon$ and 1198 $\mu\varepsilon$, respectively. Therefore, the BFRP reinforcement undergoes more tensile stress when placed in the outer layer.

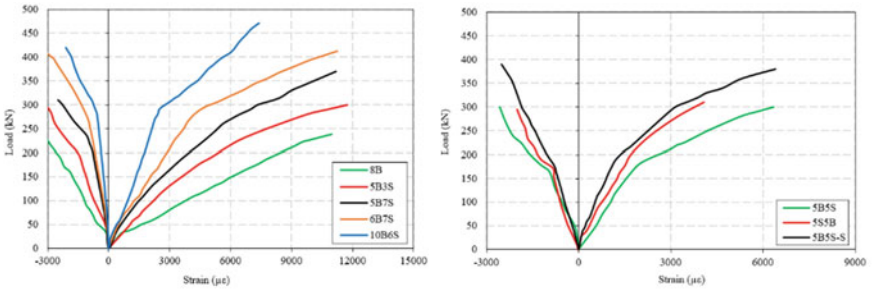

(a) Group A and B. (b) Group C.

Fig. 6 Load-BFRP reinforcement and concrete-strain relationships

5 Conclusions

Nine deck slabs were constructed and tested up to failure to study the mechanical behavior of hybrid deck slabs. The test parameters are reinforcement type, ratio and arrangement, A_f/A_s ratio and slab thickness. Based on the results and discussions presented herein, the following conclusions are obtained:

1. Using hybrid reinforcement, either SFCB or steel and BFRP bars, effectively prevented the brittle shear failure to gradual flexural-shear failure and enhances the deformability and the shear capacity compared to FRP reinforcement. The failure of the hybrid-RC slabs is significantly affected by the ratio of A_f/A_s, and it becomes more severe when increasing the value of A_f/A_s.
2. The flexural reinforcement ratio had a considerable influence on the shear capacity and the post-cracking stiffness of the hybrid deck slabs. Increasing the reinforcement ratio by 100% increased the shear capacity by 50% and the post-cracking stiffness by 54%. This increase in the post-cracking stiffness significantly reduced midspan deflections and crack widths.
3. Improvement of shear capacity is depending on the FRP to steel content A_f/A_s. An increase of the maximum shear capacity of 14% when increasing A_f/A_s from 0.68 to 1.58, respectively.
4. The deflection and crack width of the slab with reinforcement arranged in single layer were lower than those of slabs arranged in double layers.

References

1. Abdul-Salam B, Farghaly AS, Benmokrane B (2016) Mechanisms of shear resistance of one-way concrete slabs reinforced with FRP bars. Construct Build Mater Elsevier Ltd 127:959–970. https://doi.org/10.1016/j.conbuildmat.2016.10.015
2. Goldston M, Remennikov A, Sheikh MN (2016) Experimental investigation of the behaviour of concrete beams reinforced with GFRP bars under static and impact loading. Eng Struct Elsevier Ltd 113:220–232. https://doi.org/10.1016/j.engstruct.2016.01.044
3. American Concrete Institute (ACI) (2015) Guide for the design and construction of concrete reinforced with FRP bars. ACI 440.1R-15. Farmington Hills, MI
4. Canadian Standards Association (CSA) (2012) Design and construction of building components with fibre reinforced polymers. CAN/CSA S806-12. CSA, Mississauga, ON, Canada
5. Canadian Standards Association (CSA) (2014) Canadian highway bridge design code. CSA, Canada, Mississauga, ON
6. Wu G, Dong Z, Wang X, Zhu Y, Wu Z (2014) Prediction of long-term performance and durability of BFRP bars under the combined effect of sustained load and corrosive solutions. J Compos Constr 19(3):1–9. https://doi.org/10.1061/(ASCE)CC.1943-5614.0000517
7. Elgabbas F, Ahmed EA, Benmokrane B (2016) Experimental testing of concrete bridge-deck slabs reinforced with basalt-FRP reinforcing bars under concentrated loads. J Bridge Eng 21(7):1–16. https://doi.org/10.1061/(ASCE)BE.1943-5592.0000892
8. Duic J, Kenno S, Das S (2018) Performance of concrete beams reinforced with basalt fibre composite rebar. Constr Build Mater 176:470–481. https://doi.org/10.1016/j.conbuildmat.2018.04.208
9. El-Salakawy E, Benmokrane B (2004) Serviceability of concrete bridge deck slabs reinforced with fiber-reinforced polymer composite bars. ACI Struct J 101:727–736
10. El-Sayed A, El-Salakawy E, Benmokrane B (2005) Shear strength of one-way concrete slabs reinforced with fiber-reinforced polymer composite bars. J Compos Constr 9:147–157
11. Qin R, Zhou A, Lau D (2017) Effect of reinforcement ratio on the flexural performance of hybrid FRP reinforced concrete beams. Compos Part B Eng 108:200–209. https://doi.org/10.1016/j.compositesb.2016.09.054
12. Aiello MA, Ombres L (2002) Structural performances of concrete beams with hybrid (fiber-reinforced polymer-steel) reinforcements. J Compos Constr 6:133–140. https://doi.org/10.1061/(ASCE)1090-0268(2002)6:2(133)
13. Yinghao L, Yong Y (2013) Arrangement of hybrid rebars on flexural behavior of HSC beams. Compos Part B Eng Elsevier Ltd 45(1):22–31. https://doi.org/10.1016/j.compositesb.2012.08.023
14. Qu W, Zhang X, Huang H (2009) Flexural behavior of concrete beams reinforced with hybrid (GFRP and steel) bars. J Compos Constr 13(5):350–359
15. Ruan X, Lu C, Xu K, Xuan G, Ni M (2020) Flexural behavior and serviceability of concrete beams hybrid-reinforced with GFRP bars and steel bars. Compos Struct 235. https://doi.org/10.1016/j.compstruct.2019.111772
16. Ge W, Zhang J, Cao D, Tu Y (2015) Flexural behaviors of hybrid concrete beams reinforced with BFRP bars and steel bars. Constr Build Mater Elsevier Ltd 87:28–37. https://doi.org/10.1016/j.conbuildmat.2015.03.113
17. Xingyu G, Yiqing D, Jiwang J (2020) Flexural behavior investigation of steel-GFRP hybrid-reinforced concrete beams based on experimental and numerical methods. Eng Struct Elsevier 206. https://doi.org/10.1016/j.engstruct.2019.110117
18. Wang X, Liu S, Shi Y, Wu Z, He W (2022) Integrated high-performance concrete beams reinforced with hybrid BFRP and steel bars. J Struct Eng 148
19. Liu S, Wang X, Ali YMS, Su C, Wu Z (2022) Flexural behavior and design of under-reinforced concrete beams with BFRP and steel bars. Eng Struct Elsevier 263. https://doi.org/10.1016/j.engstruct.2022.114386
20. ASTM (2016) Standard test method for tensile properties of fiber reinforced polymer matrix composite bars. ASTM D7205/D7205M-06. West Conshohocken (PA)

21. Yoo DY, Banthia N, Yoon YS (2016) Flexural behavior of ultra-high-performance fiber-reinforced concrete beams reinforced with GFRP and steel rebars. Eng Struct Elsevier Ltd 111:246–262. https://doi.org/10.1016/j.engstruct.2015.12.003
22. Yang Y, Sun ZY, Wu G, Cao DF, Pan D (2020) Experimental study of concrete beams reinforced with hybrid bars (SFCBs and BFRP bars). Mater Struct Constr 53(4):1–15. https://doi.org/10.1617/s11527-020-01514-8

Seismic Fragility Analysis of a Reinforced Concrete Frame Structure with a High Aspect Ratio Plane Based on Double-Index Limit States

Zuojie Wang, Shi Yang, and Xiangyu Gao

Abstract The finite element models are established for a reinforced concrete frame structure with a high aspect ratio plane. This building is the podium of a complex commercial project located in Jinan, China. By inputting three-way seismic waves, the structural fragility research is carried out based on comparing the fragility curves with consideration on the inter-story drift and the inter-story torsion angle separately (single-index) and comprehensively (double-index with translation-torsion coupling effect). After adding buckling-restrained braces (BRB) into the structure, seismic fragility analyses are done by the same method. The improvements in the structural seismic performance are investigated, and the contributions from BRBs to reducing the structural seismic fragility are quantified. The results show that the translation-torsion coupling effect should be seriously considered in the fragility assessment of reinforced concrete frame structures with a high aspect ratio plane. In addition, the contributions from the BRBs in controlling the translation-torsion coupling effect and improving the structural seismic performance and collapse resistance are very significant.

Keywords Seismic fragility analysis · Reinforced concrete frame structure with a high aspect ratio plane · Double-index limit states

1 Introduction

With the rapid growth of the economic level in the world, the number of complex commercial projects is increasing. Scholars worldwide have paid more attention to the seismic performance of high-rise buildings in complex building groups. In contrast, relatively little research has been conducted on podiums. Due to the restrictions of the site and commercial use, the podiums are mostly made of reinforced concrete (RC) frame structures with high aspect ratio plane. At the same time, the

Z. Wang (✉) · S. Yang · X. Gao
Faculty of Architecture and Civil Engineering, Beijing University of Technology, Beijing, China
e-mail: Wzj_1210@126.com

T. Kang (ed.), *Proceedings of 5th International Conference on Civil Engineering and Architecture*, Lecture Notes in Civil Engineering 369,
https://doi.org/10.1007/978-981-99-4049-3_23

podiums are mostly shopping malls, restaurants, and other crowded places, and their seismic performance should not be neglected.

Seismic fragility analysis can evaluate the seismic performance from a probabilistic point of view. The commonly used fragility analysis method is the incremental dynamic analysis (IDA) method, widely used for seismic demand calculation and seismic performance assessment of structures. Most scholars use the inter-story drift as the damage measure (DM) in the existing research on seismic fragility analysis. Reference [1] shows that it is necessary to consider the influence of torsional response on the assessment results when performing fragility analysis of structures with irregular planes. As for the podium with high aspect ratio plane, the inertial force at the center of mass under an earthquake will form a significant torque on the rigid center due to its large accidental eccentricity. The structure will have an apparent translation-torsion coupling effect.

In this paper, the finite element models (FEM) are established for the podium with a high aspect ratio plane, reinforced concrete frame structure in a complex commercial project in Jinan, China, the fragility analyses with three-way seismic wave input are carried out, and the single-index fragility curves considering the inter-story drift and the inter-story torsion angle separately and the translation-torsion coupling fragility curves considering both are obtained for this structure. The influence of the translation-torsion coupling effect on the results of fragility assessment of such structures is studied. By adding BRBs to the original structure and performing seismic fragility analysis using the same method, setting BRBs to reduce the seismic fragility of the structure, suppressing the translation-torsion coupling effect, and improving the seismic performance of this structure are investigated.

2 Introduction of Research Object

2.1 Basic Information

The research object of this paper is a podium in a complex commercial project in Jinan, China, with a seismic intensity of 7 degree (0.1 g), Group III, Class II site, characteristic period of 0.45 s. The structure's total height is 21.2 m, and each floor is 5.3 m high, a total of 4 floors. The section of the frame column of the original structure (S-1) is 700 mm × 700 mm, the section of the frame beam is 300 mm × 600 mm, and the thickness of the floor is 120 mm. The concrete strength grade of the frame column is C60, the concrete strength grade of the beam, slab is C40, and the rebar is all HRB400 grade. The layout plan of each floor is shown in Fig. 1. Based on the S-1, by adding BRBs at the marked position in Fig. 1, the energy dissipation podium structure (S-2) is obtained, the BRBs' arrangement is all in an inverted V-shape, the core section of BRB is designed as 150 × 150 × 10 × 10 cross-section, and the material is Q235B steel. The remaining indexes are shown in Table 1.

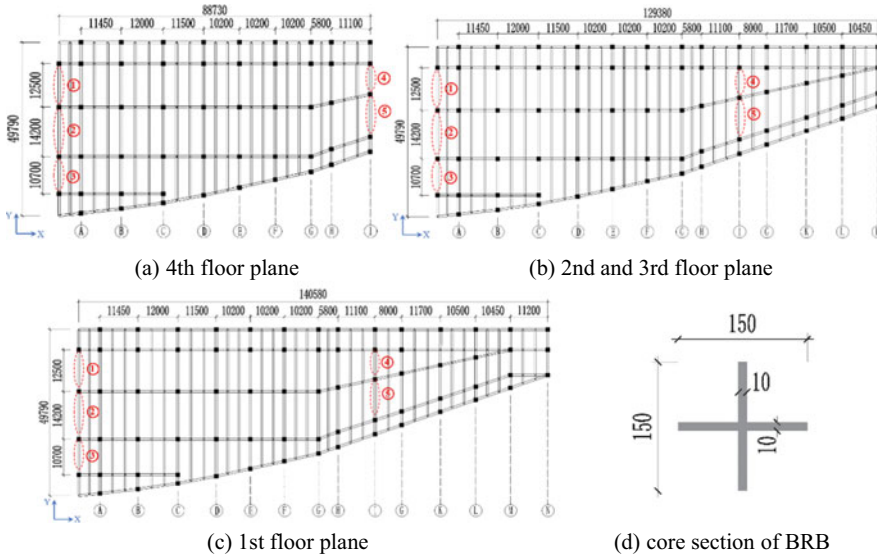

Fig. 1 Layout of the structure

Table 1 Parameters of BRBs

No.	Length (mm)	Design load capacity (kN)	Yield bearing capacity (kN)	Yield displacement (mm)	Ultimate load capacity (kN)
1	8195.01	613.35	783.725	11.48	1175.588
2	8861.30			12.27	
3	7531.15			10.68	
4	6897.76			9.89	
5	8080.39			11.34	

2.2 Finite Element Models

The YJK software was used to establish the design model of the S-1, and the seismic calculations in the elastic phase were carried out. The seismic bearing capacity and structural requirements of the structure met the relevant provisions of the Ref. [2]. The damping ratio is taken as 0.05 for the seismic calculation, taking into account the accidental eccentricity (±5%) and bi-directional translational seismic effects.

This paper established the nonlinear finite element models of the S-1 and S-2 using Etabs software, as shown in Fig. 2. The modeling used frame elements to simulate structural beams and columns, membrane elements to simulate floor slabs, and the nonlinear behavior of the members was considered by specifying discrete plastic hinges [3]. The P-M-M plastic hinges were set at both ends of the frame

column. The M plastic hinges were set at both ends of the frame beam. The BRBs were simulated using axial nonlinear connection units, the Plastic(Wen) model [4] was specified, the elastic stiffness and yield force were set according to the actual size of each BRB, the post-yield stiffness coefficient was uniformly set to 0.05, and the yield index was uniformly set to 2. The loading is the same as the S-1's YJK model.

From Table 2 and Fig. 3, it can be seen that the modal analysis results of the S-1 calculated by the two software are basically the same, and the displacement ratio analysis results are also approximately the same, which can indicate that the models established by the two software are equivalent to each other.

As shown in Table 2, the period ratios of S-1 and S-2 are 0.75 and 0.66, respectively. The torsional coefficient of S-1 is 0.38 in the first vibration mode, which is a coupled vibration of "Y-directional translation + torsion". The maximum values

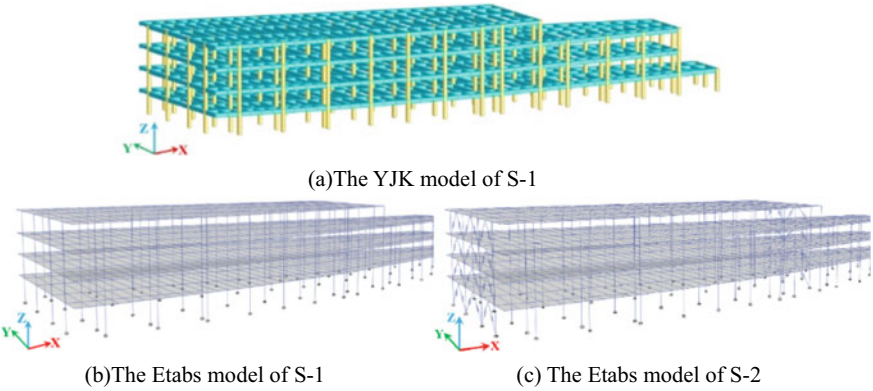

(a)The YJK model of S-1

(b)The Etabs model of S-1

(c) The Etabs model of S-2

Fig. 2 YJK model and Etabs finite element models

Table 2 Results of modal analysis

Structure	Mode of vibration	Period(s)	X-directional translational coefficient	Y-directional translational coefficient	Torsional coefficient
S-1 (YJK)	1	1.206	0.04	0.58	0.38
	2	1.099	0.94	0.05	0.01
	3	0.879	0.05	0.24	0.71
S-1 (Etabs)	1	1.185	0.04	0.59	0.37
	2	1.088	0.95	0.04	0.01
	3	0.883	0.05	0.24	0.71
S-2 (Etabs)	1	0.933	0.98	0.02	0
	2	0.852	0.02	0.94	0.04
	3	0.616	0	0.05	0.95

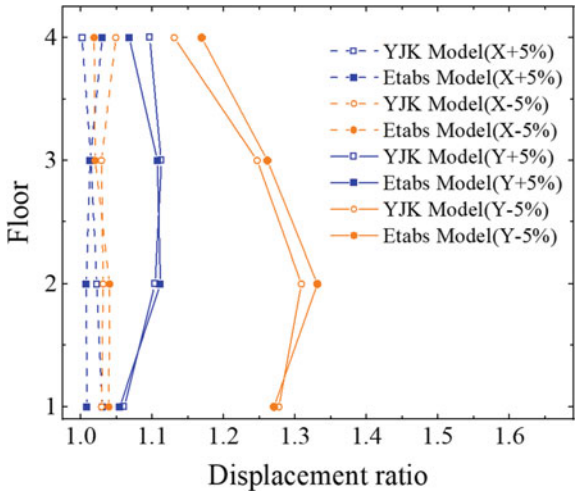

Fig. 3 Displacement ratio of S-1's each floor

of displacement ratios for S-1 and S-2 are 1.33 and 1.09, respectively, both of which are located on the second floor. It can be seen that the addition of BRBs effectively improves the elastic torsional stiffness of the structure and reduces the translation-torsion coupling effect, which is beneficial to the structural seismic resistance.

3 IDA Calculation and Seismic Fragility Analysis

3.1 Selection of Seismic Waves

The 20 seismic waves recommended by Ref. [5] for IDA calculations in this paper were selected, and amplitude modulation was performed using the hunt&fill algorithm [6]. The selected seismic waves' response spectrums are compared with the design code spectrum in Fig. 4.

3.2 Intensity Measures and Damage Measures

In the Ref. [7], IDA calculations were performed using PGA and Sa(T1, 5%) as IM, respectively, and the results showed that the IDA curves were less discrete when Sa(T1, 5%) was used as IM, so Sa(T1, 5%) was chosen as IM in this paper. Since the seismic wave input direction of the IDA in this paper is three-way (X:Y:Z = 0.85:1:0.65), the combined value of the maximum inter-story drift of the floor (θmax) is selected as the first DM and calculated as Eq. (1), where t is the time, and the $\theta x(t)$

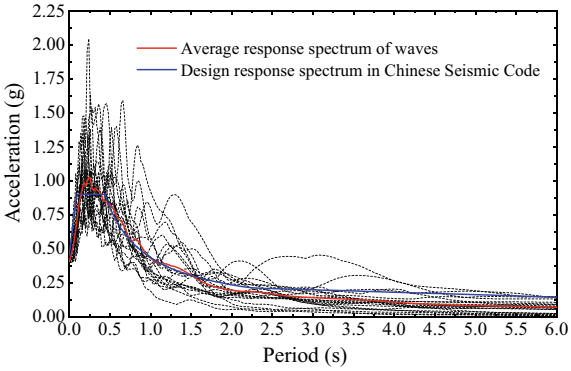

Fig. 4 Comparison of the spectrums between the selected waves and the code

and $\theta y(t)$ are the inter-story drift along the x- and y-direction at t, respectively.

$$\theta_{\max} = \max\left(\sqrt{(\theta_x(t))^2 + \left(\theta_y(t)\right)^2}\right) \tag{1}$$

The maximum inter-story torsion angle ($\alpha_{\max}$) is selected as the second DM [Eq. (2)]. Where the $\delta 1(t)$ and $\delta 2(t)$ are the minimum and maximum values of the inter-story displacement of the vertical members of the floor at t, respectively, λ is the displacement ratio, and L is the distance between the vertical members at the two ends of the structure, see Fig. 5.

$$\alpha_{\max} = \max\left(\frac{\delta_2(t) - \delta_1(t)}{L}\right) \tag{2}$$

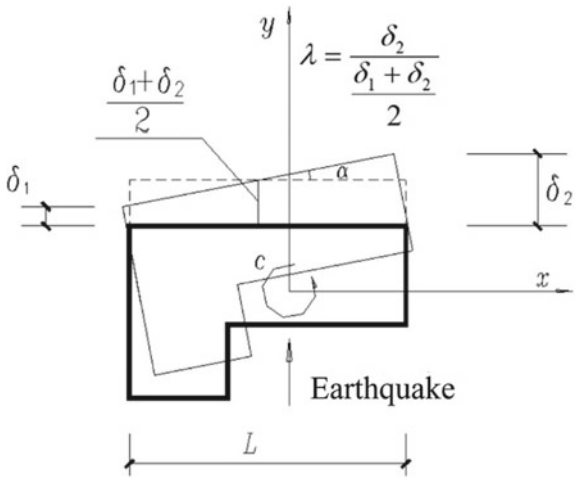

Fig. 5 Inter-story torsion angle and displacement ratio

3.3 The Limit States of the Seismic Fragility Analysis

As two DMs are selected in this paper, the corresponding limit states (LS) must be defined separately. In this paper, four inter-story drift limit states ($\theta_{\text{LS-i}}$) are defined as shown in Table 3, where the 1/550 is the elastic deformation limit of RC frame structure defined in [2]. The 1/100, 1/50, and 1/25 are the limiting states which is immediate occupancy, life safety, and collapse prevention defined in [3], respectively.

According to the definition and calculation equation of the displacement ratio (λ) and inter-story torsion angle (α), the relationship equation of α and δ_2 can be obtained after deduction, see Eq. (3). In addition, δ_2 can be converted into the product of inter-story drift (θ) and floor height h. Thus, Eq. (3) can be further derived as the relationship between θ and α [Eq. (4)] to obtain the limit value of the α in each limit state.

$$\alpha = \frac{2 \cdot \delta_2 \cdot (\lambda - 1)}{\lambda \cdot L} \tag{3}$$

$$\alpha_{LS-i} = \frac{2 \cdot \theta_{Ls-i} \cdot h \cdot (\lambda - 1)}{\lambda \cdot L} \quad (\text{i} = 1, 2, 3, 4) \tag{4}$$

Based on the $\theta_{\text{LS-i}}$ (Table 3), the displacement ratio envelope of S-1 (Fig. 3), and Eq. (4), the inter-story torsion angle limit ($\alpha_{\text{LS-i}}$) of the S-1 in each limit state can be obtained (Table 4).

Table 3 Limit states of the inter-story drift

Limit states	Description	The value of $\theta_{\text{LS-i}}$ (rad)
LS-1	Intact	1/550
LS-2	Minor damage	1/100
LS-3	More severe damage	1/50
LS-4	Collapse	1/25

Table 4 Limit states of the inter-story torsion angle

Floor	Displacement ratio (envelope)	The value of $\alpha_{\text{LS-i}}$ (rad)			
		LS-1	LS-2	LS-3	LS-4
4	1.15	1.69E−05	9.28E−05	1.86E−04	3.71E−04
3	1.26	2.67E−05	1.47E−04	2.94E−04	5.87E−04
2	1.33	3.21E−05	1.76E−04	3.53E−04	7.06E−04
1	1.27	2.75E−05	1.51E−04	3.02E−04	6.05E−04

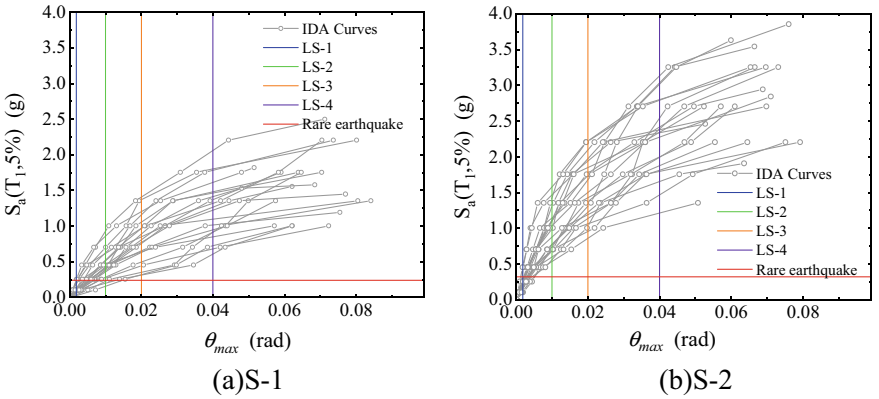

Fig. 6 IDA curves of $\theta_{\max}$

3.4 The Calculation Results of IDA

The seismic waves after amplitude modulation were input sequentially for IDA calculation, and the calculations were terminated when convergence was not possible. Since the displacement ratios of the second floor are greater than the others, the IDA results of the second floor were used for analysis in this paper. As shown in Figs. 6 and 7, the $\theta_{\max}$ and $\alpha_{\max}$ of S-2 are significantly lower than those of S-1 at the same seismic intensity. The reason is that the BRBs are added to S-2, whose lateral stiffness and torsional stiffness in the elastic phase are significantly higher than those of S-1, and the IDA curve dispersion is reduced. The BRBs yield and dissipate energy during the nonlinear stage, reducing structural damage and significantly controlling the translation-torsion coupling effect. In contrast, the translation-torsion coupling effect of S-1 is obvious, and the seismic energy is entirely dissipated by the damage to the structure itself, so its lateral capacity and torsional capacity are reduced significantly, and the degree of structural nonlinearity develops at a faster rate.

3.5 Seismic Fragility Analysis

3.5.1 The Fragility Equation for a Single DM

Seismic fragility can be interpreted as the conditional probability Pf that the seismic demand D of a structure exceeds its seismic capacity C under the action of an earthquake. When only a single DM ($\theta_{\max}$ or $\alpha_{\max}$) is considered, the fragility equation is Eq. (5) according to the Ref. [8]:

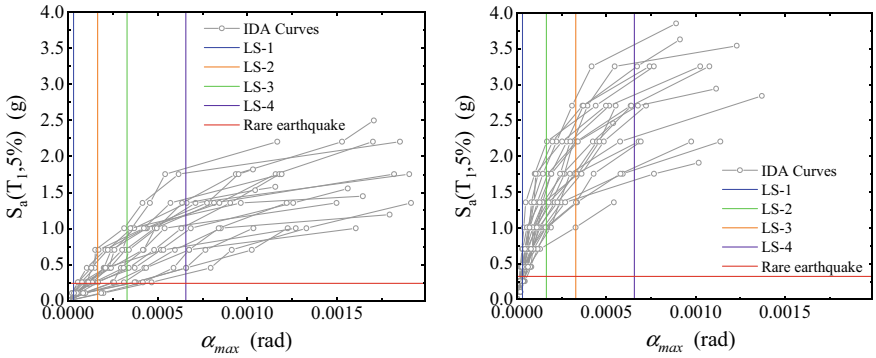

Fig. 7 IDA curves of $\alpha_{\max}$

$$P_{\mathrm{f}} = P(C \le D|\mathrm{IM} = \mathrm{im}) = \Phi\left(\frac{\ln(\mu_{\mathrm{D}}) - \ln(D_{\mathrm{LS-i}})}{\sigma_{\ln \mathrm{D}}}\right)$$
$$= \Phi\left\{\frac{\ln(\mu_{\mathrm{D}}) - \ln(D_{\mathrm{LS-i}})}{\sqrt{\sigma_{\ln \mathrm{D}}^2 + \sigma_{\ln \mathrm{D_{LS-i}}}^2}}\right\} \tag{5}$$

where the μ_{D} is the mean value of the structural seismic demand, and the $D_{\mathrm{LS-i}}$ is the limit value of the structural seismic demand at the *i*th limit state. The σ_{lnD} and $\sigma_{\ln \mathrm{D_{LS-i}}}$ are the logarithmic standard deviation of the structural seismic demand and the logarithmic standard deviation of the structural seismic demand's limit value at the *i*th limit state, respectively. Reference [9] shows that the $\sqrt{\sigma_{\ln \mathrm{D}}^2 + \sigma_{\ln \mathrm{D_{LS-i}}}^2}$ is 0.4 when IDA is calculated with Sa(T1, 5%) as IM.

3.5.2 The Fragility Equation for Double DMs

When considering both $\theta_{\max}$ and αmax as the DMs of the IDA, i.e., considering the translation-torsion coupling effect, the fragility equation can be expressed as

$$P_{\mathrm{f}} = P(\theta_{\max} \ge \theta_{\mathrm{LS-i}} \Leftarrow \alpha_{\max} \ge \alpha_{\mathrm{LS-i}}|\mathrm{IM} = \mathrm{im}) \tag{6}$$

Reference [1] shows that when $\theta_{\mathrm{LS-i}}$ and $\alpha_{\mathrm{LS-i}}$ are fixed values, $\theta \ge \theta_{\mathrm{LS-i}}$ and $\alpha \ge \alpha_{\mathrm{LS-i}}$ two independent events with failure probability can be expressed as

$$P_{\mathrm{f}} = \Phi\left\{\frac{\ln\left(\mu_{\theta_{\max}}\right) - \ln(\theta_{\mathrm{LS-i}})}{\sqrt{\sigma_{\ln \theta_{\max}}^2 + \sigma_{\ln \theta_{\mathrm{LS-i}}}^2}}\right\} + \Phi\left\{\frac{\ln\left(\mu_{\alpha_{\max}}\right) - \ln(\alpha_{\mathrm{LS-i}})}{\sqrt{\sigma_{\ln \alpha_{\max}}^2 + \sigma_{\ln \alpha_{\mathrm{LS-i}}}^2}}\right\}$$

$$-\Phi\left\{\frac{\ln\left(\mu_{\theta_{\max}}\right)-\ln\left(\theta_{\mathrm{LS-i}}\right)}{\sqrt{\sigma^2_{\ln\theta_{\max}}+\sigma^2_{\ln\theta_{\mathrm{LS-i}}}}}\right\}*\Phi\left\{\frac{\ln\left(\mu_{\alpha_{\max}}\right)-\ln\left(\alpha_{\mathrm{LS-i}}\right)}{\sqrt{\sigma^2_{\ln\alpha_{\max}}+\sigma^2_{\ln\alpha_{\mathrm{LS-i}}}}}\right\} \tag{7}$$

where the μ_θ and μ_α are the mean values of the $\theta_{\max}$ and $\alpha_{\max}$, respectively. The $\sigma_{\ln\theta_{\max}}$ and $\sigma_{\ln\alpha_{\max}}$ are the logarithmic standard deviations of $\theta_{\max}$ and the logarithmic standard deviations of αmax, respectively. The $\sigma_{\ln\theta_{\mathrm{LS-i}}}$ and $\sigma_{\ln\alpha_{\mathrm{LS-i}}}$ are the logarithmic standard deviation of the $\theta_{\mathrm{LS-i}}$ and the logarithmic standard deviation of the $\alpha_{\mathrm{LS-i}}$ at the *i*th limit state, respectively.

3.5.3 The Results of the Fragility Analysis

Figure 8 shows the results of the fragility analysis. It can be seen that the fragility curves of S-2 corresponding to each limit state are significantly lower than those of S-1. The αmax's fragility curve of S-1 is slightly higher than the $\theta_{\max}$'s fragility curve at each limit state. In comparison, the αmax's fragility curve of S-2 is significantly lower than the $\theta_{\max}$'s fragility curve. This is due to the higher torsional performance of S-2 due to the addition of BRBs and the lower percentage of torsional displacement of S-2 under earthquakes.

Reference [5] suggested using collapse margin ratio (CMR) as the evaluation index of structural collapse resistance, defined in Eq. (8). Among them, the $S_a(T_1, 5\%)_{50\%}$ is the value of Sa corresponding to the collapse probability equal to 50% (orange arrows in Fig. 7b and c), and the $S_a(T_1, 5\%)_{\mathrm{rare}}$ is the value of Sa corresponding to the rare earthquake (Fig. 7a). As can be seen from Table 5, the CMR of S-2 is 1.34 times higher than that of S-1, indicating that the addition of BRBs can significantly increase the collapse resistance of the structure.

$$\mathrm{CMR} = S_a(T_1, 5\%)_{50\%}/S_a(T_1, 5\%)_{\mathrm{Rare}} \tag{8}$$

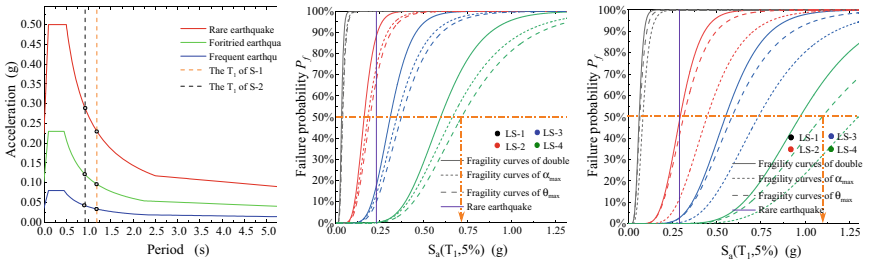

(a) The values of the Sa(T1,5%)

(b)The fragility curves of S-1

(c) The fragility curves of S-2

Fig. 8 Results of seismic fragility analysis

Table 5 Collapse margin ratio of the structures

Structure	$S_a(T_1, 5\%)_{50\%}$ (g)	$S_a(T_1, 5\%)_{Rare}$ (g)	CMR
S-1	0.71	0.24	2.96
S-2	1.11	0.28	3.96

After considering the translation-torsion coupling effect, the failure probability of the two structures at each limit state is increased to different degrees compared to that of considering only θ_{max}. The failure probabilities of LS-2 and LS-3 under rare seismic increased by 18.5% and 8.7% for S-1 and 3.8% and 0.3% for S-2, respectively. Therefore, for such structures with high aspect ratio plane, it is dangerous to use only the θ_{max} as a single DM for fragility analysis. The addition of BRBs can significantly reduce the effect of translation-torsion coupling effect on structural fragility and improve the collapse resistance.

4 Conclusions

In a complex commercial project, this paper studied a podium (RC frame structure) with high aspect ratio plane. The fragility curves of single DM considering the inter-story drift and inter-story torsion angle separately and the fragility curves of double DMs considering both (i.e., considering the translation-torsion coupling effect) were obtained for this structure by the fragility analysis of the three-way seismic waves input. The influence of the translation-torsion coupling effect on the results of the fragility analysis of such structures and the contribution of additional BRBs to reduce the seismic fragility and improve the seismic performance of this structure were investigated. The main conclusions are as follows.

(1) Due to their large accidental eccentricity, the structures with high aspect ratio plane have obvious translation-torsion coupling effect under earthquakes. If only the inter-story drift is used as the damage measure for fragility analysis, it is dangerous. It is suggested that the translation-torsion coupling effect should be considered in the fragility analysis of structures with high aspect ratio plane.
(2) The addition of BRBs can improve the lateral stiffness and torsional stiffness of the structures, effectively reduce the influence of the translation-torsion coupling effect on the vibration mode and seismic response, increase the seismic capacity, reduce the probability of failure of the structure in different limit states, and help achieve the seismic performance-based prevention goals.
(3) The addition of BRBs can reduce the rate of plastic development in the nonlinear phase of such structures, improve the collapse resistance and structural seismic toughness, reduce structural damage, facilitate seismic relief, and improve the investment efficiency of the whole life cycle.
(4) According to Eq. (4) derived in Sect. 3.3 of this paper, combined with the displacement ratio of each floor of the structure and the limit value of the inter-story drift at each limit state leads to the limit value of the inter-story torsion

angle at each limit state, which can be used for the assessment of the torsional performance of the structure.

References

1. Huang XN, Du YF, Li H (2017) Performance-based seismic fragility analysis of plane irregular structure. J Central South Univ (Sci Technol) 48(6):1645–1650
2. China Ministry of Construction (2016) Code for seismic design of buildings (GB50011-2016). China Architecture and Building Press, Beijing
3. FEMA 356 (2000) Prestandard and commentary for seismic rehabilitation of buildings. Federal Emergency Management Agency, Washington, DC
4. Cameron B, Nicos M, Ian A (2002) Component test, stability analysis and characterization of buckling-restrained unbounded braces. PEER Report 2002/08, Berkeley
5. FEMA P695 (2009) Quantification of building seismic performance factors. Federal Emergency Management Agency, Washington, DC
6. Vamvatsikos D, Cornell CA (2002) Incremental dynamic analysis. Earthq Eng Struct Dynam 31(3):491–514
7. Ye LP, Ma Q, Miu Z (2009) Study on earthquake intensities for seismic analysis of structures. J Earthq Eng Eng Vibrat 29(4):9–22
8. Cornell CA, Jalayer F, Hamburger RO, Foutch DA (2002) Probabilistic basis for 2000 SAC federal emergency management agency steel moment frame guidelines. J Struct Eng 128(4):526–533
9. FEMA HAZUS99 (1999) Earthquake loss estimation methodology: user's manual. Federal Emergency Management Agency, Washington, DC

Architectural Design and Theory

The Progression and Shift from Sustainable to Regenerative Architecture Design Concept

Marcelo Villacis-Ormaza

Abstract The buildings' development and construction have contributed negatively over the years to the increase of the environmental footprint and have also affected the biosphere and society's quality of life. For several decades the architectural discipline has studied various concepts and methods to mitigate and reduce these effects through sustainability until the concept of regenerative development. This process has been categorized by analyzing each era's different paradigms, attributes, methodologies, and challenges through a timeline that allows us to know the causes of the evolution of sustainability in architecture. The literature review shows that another vision of how to understand sustainable architecture has emerged, making the concept serve as a relative means of raising awareness for the solution of environmental problems, where it is not the building regenerated as such, but rather the habitat processes that collectively focus on improving people's lives through resilient ecological systems.

Keywords Regenerative architecture · Sustainability · Restorative architecture · Biophilia · Climate crisis

1 Introduction

Human progress has encouraged communities, cities, and territories only to a reformist development, producing global damages such as the increased temperature all over the earth, environmental affectation, production of harmful gases, and social disparities. Therefore, numerous regional and global symposia and conventions have been held to debate the reasons for these impacts and look for an answer to remedy them. In these conventions, which began in the 1970s, the importance and the need to establish techniques, guidelines, or processes to react to these problems, especially for planning, architectural design, and urban planning, was established.

M. Villacis-Ormaza (✉)
Universidad Tecnológica Indoamérica, Quito, Ecuador
e-mail: marcelovillacis@uti.edu.ec; estudioemequito@gmail.com

T. Kang (ed.), *Proceedings of 5th International Conference on Civil Engineering and Architecture*, Lecture Notes in Civil Engineering 369,
https://doi.org/10.1007/978-981-99-4049-3_24

The turn of the millennium prompted UNESCO to take the lead as the principal United Nations office advancing sustained prosperity for people and the planet. However, the wide-ranging discussions on design, construction, economics, public policy, and the search for agreement on sustainability procedures seem to have had not one path but several. As Hagan mentions, environmental architecture is a term that refers to various environmental architectures; "a plurality of approaches in which some emphasize performance over appearance and others some of the appearances of performance" [1].

This effort by architects, planners, urban planners, and organizations linked to the development of territories has produced a change in design thinking, where sustainability is becoming mainstream, a change of mindset, and a positive impact through eco-efficient and sometimes eco-effective sustainable buildings [2]. This paradigm shift is brought about by new architectural practices in building design and urban planning and influenced mainly by a new ecological worldview of architecture that seeks balance, reconnection, and restoration of nature.

The intention of this research is to analyze the evolution of the sustainability design concept through a literature review which summarizes the most relevant paradigms, events, approaches and the challenges that arised in the architecture and building's construction until these days. The aim is to stablish what are the main knowledge gaps and resolutions nowadays in this field.

1.1 The Appeasement of the Climate Crisis. Sustainable Architecture

In recent decades, several conventions and publications (the UN Conference on the Human Environment held in Stockholm in 1972, the Brundtland Report in 1987, AGENDA-21 in 1992, and the World Summit on Sustainable Development held in Johannesburg in 2002) have opened debates on the first issues of environmental change and degradation in urban areas, seeking to reconsider metropolitan planning, the generation of architecture and human development. However, as Cook and Golton put it, sustainable development is extensive, encompassing many points of view and open to broad interpretation, making sustainable architecture an essentially debatable concept [3].

Sustainability was perceived worldwide as a controversial idea with various interpretations; however, a large part of the discussion on sustainable architecture was generally focused on ecological methodologies, using technological innovation and efficiency as the primary response to the climate crisis.

1.2 Change and Flexibility of Sustainable Design Process

The main references agree on the obligation to define all sustainable design characteristics in the first phase of architectural planning. However, the process that allows generating sustainable architecture should be a constant analysis, as mentioned by Hajer, "a specific set of ideas, concepts, and categorizations that are produced reproduced and transformed into a particular set of practices through which meaning is given to social and physical realities" according to the particularities of the environment of intervention [4].

These concepts are constantly evolving and adapting to people's needs not to stagnate; as Keeley and Benton-Short suggest, "sustainability discourses are never static and are rarely stable." They will constantly evolve. Thus, form, design, and technical specifications will constantly change and improve throughout the design process [5].

1.3 Sustainability as a Constant in Architecture

What is significant in the whole process mentioned above is that it has been creating another vision of how to understand and conceive sustainable architecture, renouncing the search for a definition calculated in an efficient and neutral building. Instead, it has been sought that the concept takes a relative rather than absolute sense to raise awareness to solve social and environmental problems. Reevaluating that propensity only to technological innovation that governed most environmental research projects and that disregarded the social and cultural aspects associated with the act of sustainable architecture.

As a result, sustainable architecture ceases to be an option or alternative and becomes a constant in every building process. As Maxman mentions, "sustainable architecture is not a recipe, it is an approach, an attitude. It really should not even have a label. It should just be architecture" [6].

2 Chronology of Paradigm Shifts. From Vernacular Architecture to Regenerative Architecture

In recent decades, the interest has developed in adding to the adaptive and responsive objectives of sustainable architecture a restorative character as a condition to stop the increase of the ecological footprint and seeking to fix the environmental, social, and economic affectations of the past through the regenerative design with approaches that help the joint advancement of social and ecological frameworks holistically. Where it is not the building that is regenerated, but the processes of living that focus on the improvement of the existence of individuals, lasting over time and offering

not only not to affect the natural conditions of the environment, but that the work has a positive impact concerning its initial state.

As Du Plessis suggests, "regenerative design challenges the orthodoxy of current green building practice and the design tools that support it, where methods of environmental assessment of construction have to evolve" [7], as well as understanding that any project enables sustainability enhancement on a large or global scale.

To understand the progressions that have taken place in the field of architecture, jointly in design, building plans, and urbanization trials over the last hundred years, one must follow the historical thread of sustainability in the built environment. According to Shady Attia, "one can classify this history into major phases that shaped architectural discourse and practice, where these phases were mainly influenced by a major reductionist paradigm that defines the sustainability of architecture and building design" [8] (Table 1).

The first phase and, therefore, worldview could be said to be born of a way of looking at the habitat of human beings, reflecting their way of understanding life, where their way of the building does not respond to styles or eras but responds to a autochthonous architecture native to the place that is built based on local needs, materials, and traditions [19].

Unlike the subsequent phases, this one is characterized by having been developed throughout several centuries of observation and experimentation processes of relating the project with its natural environment and regional cultural traditions of its designers and builders. Belonging to the autochthonous traditions of a particular people, many theorists agree, such as Torres Balbas, that "architecture is deeply linked to the soil, the climate, and the landscape, molded by factors in immediate dependence on the environment, perfectly adapted to it, being true geographical responses, resulting from a transformation in which the soil provides the primary material and man the transforming activity" [20].

The second worldview was forged by the thoughts of Frank Lloyd Wright (1906) on organic architecture, Corbusier and Breuer (1906) on solar protection, Hans Meyer (1926) on the organic model, Neutra (1929) on bioregionalism, Aalto (1935) on welfare, and the preparatory guideline to the plan of Bioclimatic Architecture as the worldview of the Olgyay brothers (1953). Where Shady Attia explains, in the best way, "that the buildings of these architects showed a tendency of rationalism and functionalism while being fascinated by the beauty of nature, they developed bioclimatic adaptation, hygiene, safety, and the notion of experimental and empirical design." Until the Olgyay brothers founded the first architectural atelier in 1950, where academic, experimental, and practical processes on sustainability were combined, on this basis, sustainability began to be measured through more precise operations and processes, connecting architecture with the scientific world [11].

The third worldview was affected by the thoughts of Ian McHarg (1963) on planning with nature, McHarg and Mumford (1969) on systems design, Christian Smuts (1926) on Holism and Evolution, and Ron Mace (1972) on universal design, where the structures of the time reflected a rational impact of the use of climate in their ideas as an element of preparation and scale. Ian McHarg mentioned the following: "Ecology provides the single indispensable basis for architecture and planning. It

Table 1 Sustainable architecture events chronology

Phase paradigm years	Influencers and attributes	Approach or methodology	Challenges/issues
	No singular author		
Vernacular architecture Intuition Before 1900	– Local needs – Environmental adaptation – Thermal comfort [9]	– Cultural identity – Local materials – Local construction methods	– Before environmental footprint – The system is effective only in specific circumstances or extents
	Victor Olgyay, Frank Lloyd Wright, Hannes Meyer [10]		
Bioclimatic architecture Discovery 1908–1968	-Climatic Approach: temperature, radiation, and wind effects [11] -Health, hygiene, and precautionary principle -Sun shading -Biological research [10]	-Weather records -Bioclimatic charts -Psychometric chart	-It is not based on performance and simulations
	Ian McHarg, Lewis Mumford		
Ecological architecture Bio-architecture Harmony 1969–1972	– Inspired by a biologically informed vision [12] – Designing with natural and not capital forces – The biotic community concept [12] – Eco humanism – Understanding of natural process [13]	– Observation of natural systems and the complex array of human systems	– Limited cultural, aesthetic, and social values – Limited geographic information systems (GIS) [13]
	AIA, Douglas Balcomb, ASES, PLEA, W. M. Kroner and D. S. Haviland		

(continued)

Table 1 (continued)

Phase paradigm years	Influencers and attributes	Approach or methodology	Challenges/issues
Energy conscious architecture Energy Efficiency 1973–1983	– Passive Design Concepts – Integration of renewable energy technologies – Technological concern – Passive design ideas for the Energy Conscious Architect. (National Solar Heating and Cooling Information Center). – Implementation in architecture school's core curriculum for improving the educational experience – Stimulate Recognition of Energy Conscious Designer by annual Energy Conscious Design Competition [14]	– Energy consumption and conservation based on efficiency – Research-oriented architecture design subjects in academia – Assessment based on standard practice house model or case studies	– Rely on fossil fuels-based or non-renewable energies – Limited to housing projects
	Brundtland, Report of the World Commission on Environment and Development: Our Common Future IEA (UN), Feist, Passive House		
Sustainable architecture Resource Efficiency 1984–1993	– Sustainable development regarding; equity, international economy, Human resources – Food security – Extinction, species, and ecosystems – Fossil fuels awareness – Urban challenge	– Policy framework – Legal principles for environmental protection and sustainable development – Venn diagram and triple bottom line	– Still allowing the ideas of growth not restricted by the biosphere's capacity – The report was very extensive and does nott define what's required and how to value variables in different context
	USGBC, Van der Ryn, EPA, John Elkington		

(continued)

Table 1 (continued)

Phase paradigm years	Influencers and attributes	Approach or methodology	Challenges/issues
Green architecture/ green building Neutrality—triple bottom line 1993–2006	– Efficiency – Performance management system – Ecological design – Quality of life – Green building certification or rate systems – Integrates design with living systems	– Cost effective – Point-scoring systems for certification of buildings – Quantitative method approach	– They only go so far as to use the concept of mitigating or reduce
	UN IPCC, Mazria, 2030 Agenda, 2030 Challenge		
Carbon neutral Architecture Resilience 2006–2015	– Restorative design [15] – Renewable energies – Tracking of data and scenarios related to climate change bounds and intensifying – Database of sustainable design principles, strategies, tools, and resources to achieve zero-carbon projects.	– Climate change assessment reports Cf, O. D. D. S. (2015). Transforming our world: the 2030 Agenda for Sustainable Development. United Nations: New York, NY, USA. – Simulation software for building energy, heating, cooling, daylighting, and solar radiation	– Some published results and predictions have not been very accurate – Some results come not from an independent body but certain governments [16]

(continued)

Table 1 (continued)

Phase paradigm years	Influencers and attributes	Approach or methodology	Challenges/issues
	Lyle, Braungart, Mc Donough, Benyus, Lodder, Marleen & Lijnis Huffenreuter, Roebin, John Wiley, Du Plessis & Hes		
Regenerative architecture Recovery Thrive 2016–2022	– Regenerative Sustainable Development. – Positive impact development – Awakened sustainability – Orange Economy – Circular Economy – Eco-effectiveness – Concept of no waste – Closed circular-flow of goods and services – Projects and actions take place within the biological and physical boundaries of the earth's ecosystems. – Placemaking processes [17]	– Public policy – Triple Top Line – Cradle-to-cradle design [18]. – The upcycle: beyond sustainability-designing for abundance – Biomimetic approach	– Critique of the economic model that underlies the vision – Inconsistencies across urban regenerative thinking and practice – Application of regenerative principles in high-density Urban environments remains a challenge

Source Marcelo Villacis

now has, and will increasingly have, a profound relevance to both urbanism and architecture" [21]. As Renee L. Ripley and Bharat Bhushan explain, "Bioarchitecture is an approach that evidences the theory behind the overall design, the careful choice of materials for construction or creation, the extraction and adaptation of principles, and the cohesion of the parts into the whole. It inspires from living nature to drive architecture's design, function, and materiality" [22].

The fourth worldview started from the primary energy emergence, and it was overwhelmed by the reflections of the American Institute of Architecture (AIA-1972) about the energy-conscious design, the American Solar Energy Society (ASES), including the work of Balcomb (1972) on inactive and dynamic engineering of solar energy, the Passive and Low Energy Architecture Society (PLEA-1980); where Shady Attia explains clearly "the buildings of the time showed a trend toward the inclusion of energy-saving and solar energy design strategies, with the first ideas of energy-neutral buildings and integrated renewable energy systems being introduced in various prototypes and building concepts. In addition, a simulation and empirical

measurement technique was used to quantify building performance based on the energy codes and standards created in this phase" [8].

The fifth sustainable worldview was dominated by the ideas of the Brundtland Report (1987), congruently where the definitions of sustainability were based, as Ceridwen Owen & Kim Dovey say, on promoting a notion of development within environmental limits, defining the concept of sustainability based on the acceptance of the scientific method as a continuum development, influencing various regulations by governments and institutions around the world" [23]. Directing them in a certain way toward architectural biomimicry, as Renee L. Ripley and Bharat Bhushan say, "Biomimetics, or the copying of living nature, is a highly interdisciplinary field involving the understanding of the biological functions, structures, and principles of various objects found in nature by scientists. Biomimetics can lead to biologically inspired design, adaptation, or derivation from living nature" [22].

The sixth worldview was dominated by the ideas of the US Green Building Council (1993) on green and intelligent design, on the design of ecological communities by Van der Ryn (1995), and ARUP (1996) on integrated design. Thus with the emergence of this paradigm, the greening of architecture spread worldwide with environmental considerations, as defined by Phillip James Tabb and A. Senem Deviren; the emergence of the postmodern architectural discourse was addressed as a response to the lack of a place of architecture and urbanism, with environmental solutions to the problems produced by modern architecture and globalization [24].

The seventh partisan carbon-neutral worldview was articulated by the Kyoto Protocol's (1997) reflections on carbon impartiality and the UN IPCC's (2006) report on environmental change. Notwithstanding the work done by Bill Dunster in Zero Energy Development and Ed Mazria in the 2030 Challenge, which affected both exploration and design practice, where they proposed near-zero energy targets for what was to come. In this sense, energy-neutral architecture became a way of thinking that embraces strength, dynamism, and combination. Helen Carruthers explains, "The report's definition of the carbon-neutral building follows the common theme of the various definitions attached to carbon-based building policies that have emerged worldwide. For example, a *carbon-neutral building* is defined as one with significantly reduced energy consumption combined with increased use of low-carbon energy sources to meet remaining demand." This definition led to developing policies, standards, and certifications for designing new and existing buildings [25, 26].

The eighth worldview is influenced by the ideas of Lyle (1996) on regenerative design, the ideas of McDonough and Braungart (2010) on cradle-to-cradle design, and Benyus (2002) on Biomimicry, having several nuances such as permaculture that is currently spreading as an alternative movement. As Katja Rothe explains, "permaculture design is a concept that aims to transform agriculture and urban planning, architecture, development, among others. To summarize, it aims to change human habitats" [27, 28]. In conclusion, this change of ideology essentially seeks to reduce the impact of construction through environmental efficiency, understanding the habitat processes, and at the same time, having cohesion with nature through ecological systems [8, 27, 29].

3 Discussion

The discussion arises from different issues, for example, the energy emergency of 1973 that prompted the advancement of energy effectiveness measures, considering the approach to the requirements of existing structures, where state elements needed to change the vision of their destinies on energy utilization. So, it was essential to create change through practical development with energy productivity goals, considering the climate with standards for using assets effectively.

However, this vision shift focused on energy efficiency as part of sustainable design, thinking only about reducing consumption through zero-energy buildings and zero-carbon buildings to maximize efficiency with a clear goal of neutralizing resource consumption. Marszal and Heiselberg explain that "The economic balance approach is limited. Restricting building impact limits to "zero" or "net zero" is a mistake; the "zero" target limits achieve unsustainable building practices in the long term. If site-generated energy happens to be an abundant resource, why should we limit our goals to zero? In addition, the efficiency paradigm discourages the potential for fossil fuel-independent buildings. The declining availability of oil, gas, and coal and the danger of nuclear power means that the cost of black fuels will be increasingly volatile. Peak oil will have a major impact on the entire economy. Thus, the energy efficiency paradigm has reached its limit in proposing zero energy or zero emissions as the "holy grail" [25].

Consequently, it has become evident to mainstream researchers that the vision of efficiency, which considers it simply from the perspective of decrease and performance, does not address this issue, making sustainable architecture in need of development in its standards and, consequently, in its limits. Moreover, in the mentality of progress, toward another new ecological worldview that seeks to minimize the negative impact of the built environment, thinking beyond just absolute parameters.

Seeking a positive development, as Lyle says, "to achieve a positive constructive footprint, we must move from the cradle to the grave paradigm that aims to reduce, avoid, minimize, or prevent the use of fossil energy to a regenerative paradigm. It aims to increase, support, and optimize the use of renewable energies, leaving aside previous efficiency strategies that have been operating within a carbon-negative or neutral approach that will never achieve a positive and beneficial constructive footprint" [27]. According to a self-sufficient renewable vision, buildings should seek efficiency in resource management combined with ecological habitat systems, which collectively focus on improving people's lives in cohesion with nature. In pursuit of positive development, as Attia and De Herde say, "To increase the carrying capacity to reverse the ecological footprint, building resource management should emphasize the feasibility of harnessing renewable resources, enabling energy exchange and microgeneration within urban boundaries" [8, 29] and providing regenerative architecture more influence in the world and being considered more in the vision of evolution as architecture itself.

4 Conclusion

One of the fundamental resolutions found is that another vision of how to understand sustainable architecture has emerged, leaving aside the conceptual vision handled only by theoreticians or construction professionals but making the concept serve as a relative means of raising awareness for the solution of environmental problems. Reinterpreting the vision that dominated most discussion parameters and emphasizing technical primarily approaches.

A difference in approach has been created through the development of the idea, where it is not the building regenerated as such, but rather the habitat processes that collectively focus on improving people's lives through resilient ecological systems. Imagine that the development and construction of a building should be an essential solution within a socio-ecological system to generate regenerative architecture that meets all parameters such as flows, habitat, energy consumption, community, culture, construction systems, and materials.

In the current practice of ecological construction and design, no environmental assessment methods can verify whether the ideal objectives of ecosystem regeneration are being met. As a result, there is an ambiguous measurement where it can be recognized that buildings cannot exist in isolation from their surrounding contexts, as they must understand and contribute to smaller and larger-scale systems and ecosystems.

References

1. Hagan S (2007) Taking shape: a new contract between architecture and nature. Tak Shape A New Contract Between Archit Nat. https://doi.org/10.4324/9780080518411
2. Barbiroli G (2006) Eco-efficiency or/and eco-effectiveness? Shifting to innovative paradigms for resource productivity. Int J Sustain Dev World Ecol 13(5):391–395. https://doi.org/10.1080/13504500609469688
3. Cok SJ, Golton BL (1994) Sustainable development: concepts and practice in the built environment. Sustain Constr CIB 16:677–685
4. Hajer MA, Pelzer P (2018) 2050—an energetic Odyssey: understanding 'techniques of futuring' in the transition towards renewable energy. Energy Res Soc Sci 44:222–231. https://doi.org/10.1016/j.erss.2018.01.013
5. Keeley M, Benton-Short L (2018) Urban sustainability in the US: cities take action. Urban Sustain. US Cities Tak. Action, pp 1–337. https://doi.org/10.1007/978-3-319-93296-5
6. Guy S, Farmer G (2001) Reinterpreting sustainable architecture: the place of technology. J Archit Educ. https://doi.org/10.1080/10464883.2001.11878703
7. Du Plessis C, Cole RJ (2011) Motivating change: shifting the paradigm. Build Res Inf 39(5):436–449. https://doi.org/10.1080/09613218.2011.582697
8. Attia S (2016) Towards regenerative and positive impact architecture: a comparison of two net zero energy buildings. Sustain Cities Soc 26:393–406. https://doi.org/10.1016/j.scs.2016.04.017
9. Foruzanmehr A, Vellinga M (2011) Vernacular architecture: questions of comfort and practicability. Build Res Inf 39(3):274–285. https://doi.org/10.1080/09613218.2011.562368
10. Tomita H (2008) Hannes meyer's biological concept and its loosening influence on form. J Asian Archit Build Eng 7(2):179–185. https://doi.org/10.3130/jaabe.7.179

11. Olgyay V, Olgyay A, Lyndon D, Olgyay VW, Reynolds J, Yeang K (2019) Climatic elements. Des Clim 32–42. https://doi.org/10.2307/j.ctvc77kqb.8
12. Anker P (2005) The closed world of ecological architecture. J Archit 10(5):527–552. https://doi.org/10.1080/13602360500463230
13. Cohen WJ (2019) The legacy of design with Nature: from practice to education. Socio-Ecol Pract Res 1(3–4):339–345. https://doi.org/10.1007/s42532-019-00026-2
14. Villecco M (1977) Energy conscious design in schools of architecture. Jae 30(3):6. https://doi.org/10.2307/1424301
15. E. Mazria, "It's the architecture, stupid!. World and I.," 2003.
16. Vaughan A (2021) Will the IPCC report matter? New Sci 251(3348):8–9. https://doi.org/10.1016/s0262-4079(21)01442-1
17. Hernandez-Santin C, Hes D, Beer T, Lo L (2020) Regenerative placemaking: creating a new model for place development by bringing together regenerative and placemaking processes, pp 53–68. https://doi.org/10.1007/978-3-030-54686-1_4
18. Braungart M, McDonough W, Bollinger A (2007) Cradle-to-cradle design: creating healthy emissions—a strategy for eco-effective product and system design. J Clean Prod 15(13–14):1337–1348. https://doi.org/10.1016/j.jclepro.2006.08.003
19. Sayigh A (2019) No title how the past can enrich the future. Springer. https://doi.org/10.1007/978-3-030-06185-2
20. Tillería González J (2006) La Arquitectura Sin Arquitectos, Algunas Reflexiones Sobre Arquitectura Vernácula. Aus 8:12–15. https://doi.org/10.4206/aus.2010.n8-04
21. McHarg IL (2014) An ecological method for landscape architecture. In: The ecological design and planning reader, pp 341–347
22. Ripley RL, Bhushan B (2016) Bioarchitecture: bioinspired art and architecture-a perspective. Philos Trans R Soc A Math Phys Eng Sci 374(2073). https://doi.org/10.1098/rsta.2016.0192
23. Owen C, Dovey K (2008) Fields of sustainable architecture. J Archit 13(1):9–21. https://doi.org/10.1080/13602360701865373
24. Tabb PJ, Deviren AS (2014) The greening of architecture. Routledge
25. Marszal P, Heiselberg AJ (2009) A literature review of zero energy buildings (ZEB) definitions
26. Carruthers H, Casavant T (2013) What is a 'carbon neutral' building? Light House Sustain Build Cent Soc
27. Lyle JT (1996) Regenerative design for sustainable development. Wiley
28. Rothe K (2014) Permaculture design: on the practice of radical imagination. Laura Commun +1 3(1). https://doi.org/10.7275/R58913S2
29. Attia S, De Herde A (2011) Defining zero energy buildings from a cradle to cradle approach. In: PLEA 2011—architecture sustainable development conference and proceedings of the 27th international conference on passive low energy architecture, pp 205–210

Implementation of Social Criteria in Atrium Design of Commercial Buildings in Malaysia

Wardah Fatimah Mohammad Yusoff and Foo Jessie

Abstract The studies of social aspect in atrium design are still lacking compared to the environmental aspect. Therefore, this study was conducted to identify social criteria in atrium design and their application in commercial buildings located in Klang Valley, Malaysia. There are two research methods conducted, namely the literature study and the qualitative descriptive research. A list of social criteria in atrium design had been made based on the previous studies. Four commercial buildings in Klang Valley that have atriums were examined via the qualitative descriptive method. The checklist of the social criteria listed from the first method was referred in examining the implementation of these criteria at the selected atriums. The findings of the study show that the implementation of social criteria in the atrium design of the selected buildings still need improvement. The atrium space needs to be designed for visual and physical accessibilities by all groups of users. It must also have flexibility to cater for various space functions and activities. The high consideration of social criteria in atrium design will enable the continuous usage of atrium and eventually provide great social benefits to the users. The findings of this study can be used as a reference in designing an atrium in commercial building, especially for the tropical climate.

Keywords Atrium design · Social criteria · Commercial building

1 Introduction

Atrium is derived from a Latin word that refers to the main room or central courtyard space that has a fireplace. This has caused the wall surface of the room or space to always be filled with black dirt after a period of time. Due to that, the title of atrium is given to that space or room [1]. In building, atrium is normally defined

W. F. M. Yusoff (✉) · F. Jessie
Department of Architecture and Built Environment, Faculty of Engineering and Built Environment, Universiti Kebangsaan Malaysia, Hulu Langat District, Malaysia
e-mail: wardahyusoff@ukm.edu.my

T. Kang (ed.), *Proceedings of 5th International Conference on Civil Engineering and Architecture*, Lecture Notes in Civil Engineering 369,
https://doi.org/10.1007/978-981-99-4049-3_25

as a top-lit internal space that is surrounded by multi-floor levels [2]. The design of the atrium in the modern era has undergone considerable changes. The atrium nowadays mostly uses glass wall and roof, and it is connected to many adjoining spaces. The use of atrium has become increasingly popular and universal regardless of local culture and climate [3]. Atriums are used in various building typologies such as institutional, office, commercial and residential buildings. The large-scale buildings often use atrium as a design concept. The atrium building has become a new norm around the world.

There are many advantages of atrium that contribute to the increase of its usage in buildings. The benefits of atrium can be classified into three main categories, namely the social, environmental, and economic benefits. These benefits are actually interrelated. For example, one of the environmental benefits of atrium is the provision of ample daylighting penetration into the building. This can result in electrical energy saving and eventually provide the economic benefit. Sufficient daylighting at the atrium area also encourages the usage of atrium for gathering and socializing, as well as conducting activities and events. This has led to the social benefit of atrium. In addition, atrium can also be used as a design to revive an old building. An atrium can be integrated to an existing building or created by placing a roof between several buildings as a consolidation [4].

Atrium is commonly applied at the office and commercial buildings. Examples of previous studies that investigated the atrium application at such building typologies are Abdullah et al. [5], Abdullah and Wang [6], Ghasemi et al. [7], Huang et al. [8], Mohsenin and Hu [9], Wang et al. [10], Yusoff et al. [11], and Asfour [12]. However, many previous studies of atrium focus on environmental benefits compared to the social benefits, such as the studies by Yusoff [13], Acosta et al. [14], Vethanayagam and Abu-Hijleh [15], Chu et al. [16], and Lu et al. [17]. The environmental aspects that have been investigated are also various, which cover the daylighting, ventilation, energy usage, and indoor thermal environment. The investigation of social benefits of atrium is still lacking especially in term of its implementation and effectiveness. What are the social criteria need to be considered in ensuring that the atrium is able to fully maximize the social benefits to the users? Are all the required criteria applied in the atrium design? Hence, this study aims to identify the social criteria that are recommended by the previous studies to be implemented in the atrium design. In addition, this study also analyzes the application of the identified criteria at the selected atriums in commercial buildings. The commercial building is selected instead of other building typologies because it has wider accessibility to public compared to the atriums at office, institutional or residential buildings. Hence, its social benefits can be obtained by various groups of users.

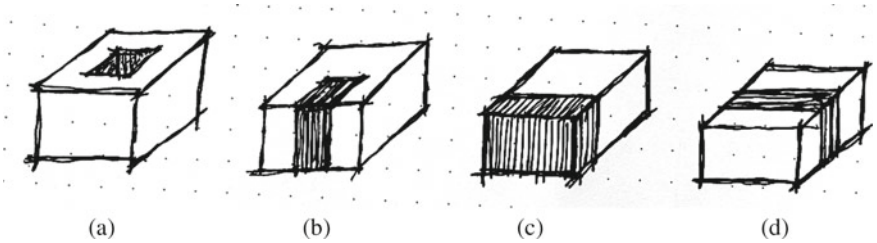

Fig. 1 Four types of atrium design, namely the **a** centralized, **b** semi-enclosed, **c** attached, and **d** linear

2 Common Types of Atrium Design

In general, the design of atrium is based on the climatic condition, architectural approach, and building function. The location of an atrium in a building is a major factor in determining the potential of the atrium. There are four types of atrium design based on the location in the building, namely the centralized, semi-enclosed, attached, and linear [4], as depicted in Fig. 1. Each type of atrium has certain advantages according to the environmental condition, ventilation expectation, and lighting. For example, in a temperate country, the position of the atrium is usually on the side of the building as in Fig. 1c. The reason is to allow heat gained in the winter and enable the users to enjoy the scenery in each season. A glass facade is normally used to maximize the surrounding scenery. For a tropical climate country, the centralized and linear types of atria as in Fig. 1a and d are the most effective in controlling the rate of temperature changes, especially during the summer [18]. Therefore, the centralized and linear types of atria are the most common types of atrium design used in the tropical climate countries.

3 Research Methodology

There are two methods employed in this study, namely the literature study and qualitative descriptive research. The literature study was executed to identify the criteria that relate to the social aspect in the atrium design. Previous studies from various sources such as journal and proceeding articles, books, technical reports, and many others had been referred. From these sources, the social criteria related to the atrium design had been listed. The qualitative descriptive method was conducted in identifying the implementation of the listed criteria at the atriums of buildings that had been selected for the case study. The qualitative descriptive was executed by using the technique of observation.

For this study, there is a limitation where the methods conducted focus only on the criteria derived from the previous studies and the observation. It is planned in the

future to validate the social criteria listed in this study with the expertise to confirm their validity.

3.1 Description of the Selected Atriums

There are four commercial buildings that had been selected for the case studies, namely KL Gateway Mall, Platinum Central, 1 Mont Kiara Mall, and Publika Mall. These buildings were selected as they have atriums which are actively used by the visitors and workers of the buildings. Their locations are within the Klang Valley area in Malaysia, which is well-known as the area with high population density. Figure 2 depicts the atriums that had been selected for the case studies.

KL Gateway Mall is located in Bangsar South which is directly connected by the Federal Highway, Kerinchi Link, and the New Pantai Highway. The mall, which has the total gross floor area of 500,000-square-foot, encompasses the restaurants, fashion stores, and a children's education center. There is an iconic central atrium within the mall that becomes the focal point of local and international arts and crafts exhibitions and also the entertainment activities. This centralized atrium which covers the area of 1600 ft^2, has become the connection point of the green landscapes, shopping malls, recreational parks, and tropical gardens.

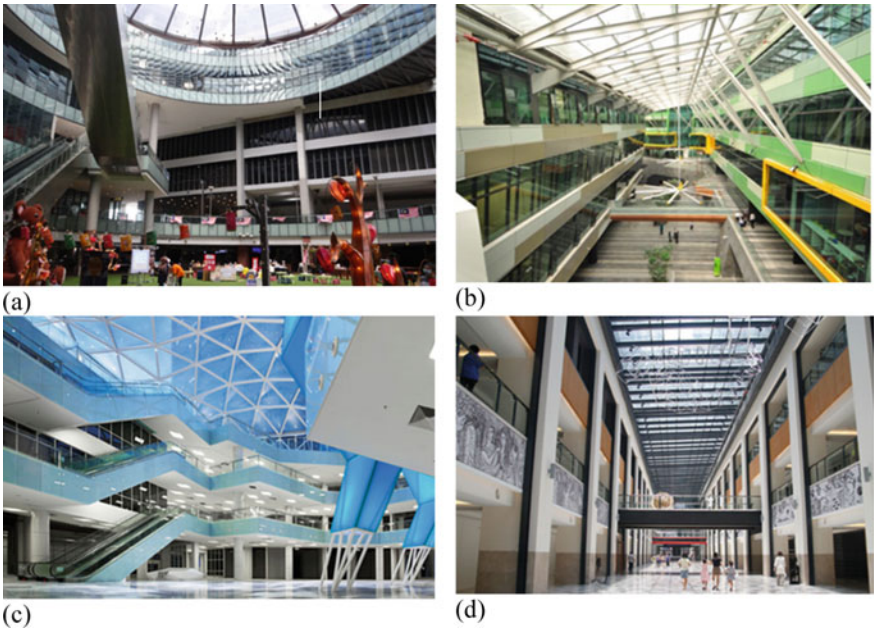

Fig. 2 Atrium at the **a** KL gateway mall, **b** platinum central, **c** 1 Mont Kiara mall, and **d** Publika mall

Platinum Sentral is located opposite the KL Sentral Station Arrival Hall and next to Le Meridien Hotel in Kuala Lumpur. Platinum Sentral is the first commercial development in Malaysia that receives a platinum rating under the Singapore Green Mark rating scheme. It is a retail and commercial development with a net floor area of 94,000 ft^2. It comprises of five office blocks, shops, and green space. The retail space is around 86,251 ft^2. The atrium, which is categorized as the attached type, is designed to create a network of pocket gardens along the building's internal linear path, which is surrounded by the shops and stalls.

1Mont Kiara Mall is a six storeys shopping mall development that is located in Kuala Lumpur. The mall is surrounded by residential buildings, offices, and international schools. The atrium is centralized, and it is designed to be oval shaped. One of the attractions at the atrium is the presence of spacious front plaza with a grand staircase. Due to its location and design, the atrium has become the focal point for the family-oriented community events.

Publika Mall is part of Solaris Dutamas, which is a development that includes office, residential and commercial buildings. The atrium at Publika Mall is categorized as the linear type. The mall is designed with the concept of welcoming the community participation and interaction. As a result, Publika has become the center where the art and culture integrate with the commercial elements. Due to its unique concept, the mall has managed to attract many creative designers and innovative entrepreneurs to actively participate in the activities conducted at the mall.

4 Results and Discussion

The results are presented and discussed in two sub-sections, namely the social criteria of atrium design and the social criteria that are applied at the selected atriums. The first section presented the results that are derived from the literature. Meanwhile, the second section are the results that are obtained from the qualitative descriptive method.

4.1 Social Criteria of Atrium Design

From the literature study, the social criteria of atrium design can be categorized into two aspects, namely the visual and physical accessibilities and the function. There are nine criteria that have been listed under the category of visual and physical accessibilities, as shown in Table 1. The visual and physical accessibilities are the state of being connected or interconnected. The visual communication is the ability to see across one space, and in turn, creating a visual chain. This will then create a visual connection. Meanwhile, a physical contact is something different. On the same level such as a single-storey building, the physical contact is almost identical to the visual contact [19]. This means that when a person sees a space on the same

Table 1 Criteria of social aspect at the atrium listed by the previous studies

	Visual and physical accessibilities
1	Have horizontal and vertical circulations [3]
2	Easy access of staircase, elevators, or escalators [22]
3	Have main staircase for movement and physical connection in atrium that exceeds one level [23]
4	Have elevator that the door is opened up to the atrium [24]
5	Have escalator that allows the safe and continuous flow of users across building levels [19]
6	Have sky bridge across the atrium space [19]
7	Have flexible circulation to accommodate the needs of various user groups and space functions [22]
8	Have a clear visual relationship of different floor levels from the atrium edge [20]
9	Able to see the activities occurred near the atrium space by standing in the middle of the atrium [20]
	Function
10	Used as informal meeting space where the intellectual or social discussion can occur [25]
11	Adequate space for various activities [25]

level, he or she can walk up to the space. However, in multi-storey building such as building with atrium, the visual and physical contacts are disconnected.

One of the common reasons for the adoption of atrium in building by architect is the function of atrium as a social space [20]. Atrium functions as a social space to meet, greet and even a space that allows users to meet others to exchange information and increase creativity. The spacious area provided by an atrium has made it as a node and focal point of a building. Besides being as a strategic place for activities and events, atrium also functions as initial point in distributing the horizontal and vertical circulations within the building [21]. Based on the literature study, there are two criteria that can be classified under the function category, as shown in Table 1.

4.2 Social Criteria Applied at the Selected Atriums

The qualitative descriptive method was conducted in identifying the social criteria applied at the selected atriums. Observation was executed to identify whether the listed criteria in Table 1 were implemented at the atriums of the case study buildings. The buildings that were selected for the case studies are KL Gateway Mall (KLGM), Platinum Central (PC), 1 Mont Kiara Mall (1MKM), and Publika Mall (PM). The findings from the observation at each case study building are tabulated in Table 2.

From Table 2, it can be concluded that none of the atriums in the case study buildings have implemented all the social criteria needed for the atrium design. For the criterion no. 1, though all atriums have the horizontal and vertical circulation elements such as elevator, staircase, and sky bridge, but the 1MKM is found to have

Table 2 Criteria of social aspect at the atriums of case study buildings

	Social criteria	Case study 1: KLGM	Case study 2: PC	Case study 3: 1MKM	Case study 4: PM
	Visual and physical accessibilities				
1	Have horizontal and vertical circulation elements [3]	/	/	/	/
2	Easy access of staircase, elevators, or escalators [22]	/	/	/	/
3	Have main staircase for movement and physical connection in atrium that exceeds one level [23]	X	X	X	X
4	Have elevator that the door is opened up to the atrium [24]	X	X	X	X
5	Have escalator that allows the safe and continuous flow of users across building levels [19]	/	X	/	/
6	Have sky bridge across the atrium space [19]	/	/	X	/
7	Have flexible circulation to accommodate the needs of various user groups and space functions [22]	/	X	X	X
8	Have a clear visual relationship of different floor levels from the atrium edge [20]	/	/	/	/
9	Able to see the activities occurred near the atrium space by standing in the middle of the atrium [20]	X	X	/	/
	Function				
10	Used as informal meeting space where the intellectual or social discussion can occur [25]	X	/	X	/
11	Adequate space for various activities [25]	/	/	/	/

escalator only. There is no main staircase and sky bridge at the atrium that can connect the atrium with the other spaces and floor levels. Meanwhile, for the criterion no. 2, it seems that the circulation elements in all atriums are easy to be accessed by the users. This criterion is very important in ensuring the smooth and fast distribution of people at the same level or different levels.

For the criterion no. 3, it is found that all the atriums have no main staircase that connects the different floor levels. Basically, the main element for vertical circulation at all case study atriums is an escalator. The criterion no. 4 also indicates that all atriums have no elevators that the doors are opened up to the atrium. This is common in commercial building design where the elevators are placed together at one side of the buildings. The criterion no. 5 indicates that the atrium at PC has escalator which connects the ground floor to the first floor level only. Hence, the escalator does not provide continuous vertical circulation to the users in reaching the other floor levels.

For the criterion no. 6, 1MKM does not have any sky bridge across the atrium space. Meanwhile, it seems that only KLGM meets the criterion no. 7 which is the provision of flexible circulation to accommodate the needs of various user groups and space functions. Example of flexibility provided by atrium at KLGM is the availability of ramp, which can be used by people with wheelchair, children on strollers, and users with shopping trolleys. For the criterion no. 8, all the atriums are found to have a clear visual relationship of different floor levels from the atrium edge. The open design of atrium is good as it allows the user to see the entire atrium area and the surrounding spaces. In addition, it also provides a clear visual access to each space [4].

However, for the criterion no. 9, only 1MKM and PM allow the atrium users to be able to see the activities occurred near the atrium space by standing in the middle of the atrium. For the other two atriums, there are certain obstructions that block the view. In term of function aspect, which are the criteria no. 10 and 11, it seems that all the atriums meet the listed criteria except for KLGM and 1MKM, which do not fulfill the criterion no. 10. This is because there is no seating provided for the intellectual or social discussion to occur in the atrium. Furniture such as benches should be placed in the atrium to allow for informal gathering. This can maintain the flow of users even when there are no specific events or activities conducted in the atrium space.

For example, the PC has food and beverage stalls in the atrium space. These stalls able to generate continuous social interaction between users. In addition, this space can also be used as area for informal meetings and gatherings. The visitors can relax for a while in the atrium space, by using the seats provided. Meanwhile, the office workers can spend time there to dine. The spacious space at the atrium is also able to accommodate the needs of various events. The use of necessary technological equipment such as projection screens, audio systems, and monitors as well as speakers should also have suitable placement area in the atrium. For the atrium that allows events such as entertainment and performance, the acoustic aspect should also be taken into consideration in the design.

5 Conclusion

This study has listed the social criteria that have been recommended by the previous studies to be implemented in the atrium design. These criteria are essential in ensuring that the atrium provides benefits to the users in term of social aspect. Besides the function of atrium as a place for meeting, gathering, and socializing, it also becomes a space for any activities and events, either for commercial, educational, or community. To ensure the maximum utilization and social benefits of atrium, it must also provide good visual and physical accessibilities, in term of horizontal and vertical connections. The atrium design must also provide flexibility to cater the needs of various groups of people and space functions.

The investigations executed at four selected atriums in commercial buildings have indicated that some of the criteria have not been implemented in the design. Hence, it shows that there is still improvement need to be executed to the atrium design for commercial building in ensuring that the social benefits are fully obtained by the users. This study is significant as it encourages awareness on the importance of considering the social criteria in the design of atrium. The emphasis of social criteria in atrium design is able to ensure the continuous usage of atrium by the users. In the future, it is recommended that the perception of atrium users should be integrated to the studies in evaluating how significant the listed criterion to them.

Acknowledgements The authors would like to thank the National University of Malaysia (UKM) through the research grant GUP-2019-017 and the Ministry of Higher Education Malaysia through the Fundamental Research Grant Scheme (FRGS/1/2019/TK10/UKM/02/4), and for the financial support.

References s

1. Moosavi L, Mahyuddin N, Ab Ghafar N, Azzam Ismail M (2014) Thermal performance of atria: an overview of natural ventilation effective designs. Renew Sustain Energy Rev 34:654–670
2. Curl JS (2006) Oxford dictionary of architecture and landscape architecture, Second. Oxford University Press, Oxford
3. Saxon R (1986) Atrium buildings development and design, Second. The Architectural Press, London
4. Hung WY, Chow WK (2001) A review on architectural aspects of atrium buildings. Archit Sci Rev 44(3):285–295
5. Abdullah AH, Meng Q, Zhao L, Wang F (2009) Field study on indoor thermal environment in an atrium in tropical climates. Build Environ 44(2):431–436
6. Abdullah AH, Wang F (2012) Design and low energy ventilation solutions for atria in the tropics. Sustain Cities Soc 2(1):8–28
7. Ghasemi M, Noroozi M, Kazemzadeh M, Roshan M (2015) The influence of well geometry on the daylight performance of atrium adjoining spaces: a parametric study. J Build Eng 3:39–47
8. Huang Y, Borong L, Yao N, Yingxin Z (2015) Functional relationship between lighting energy consumption and the main parameters for double atrium offices. Proc Eng 121:1869–1879
9. Mohsenin M, Hu J (2015) Assessing daylight performance in atrium buildings by using climate based daylight modeling. Sol Energy
10. Wang L, Huang Q, Zhang Q, Xu H, Yuen RKK (2017) Role of atrium geometry in building energy consumption: the case of a fully air-conditioned enclosed atrium in cold climates, China. Energy Build 151:228–241
11. Yusoff WFM, Sulaiman MKAM, Muhsin F (2019) Preliminary evaluation of air flow in atrium of building in hot and humid climate. Int J Sustain Trop Des Res Pract 12(1):43–52
12. Asfour OS (2020) A comparison between the daylighting and energy performance of courtyard and atrium buildings considering the hot climate of Saudi Arabia. J Build Eng 30:101299
13. Yusoff WFM (2021) Indoor thermal environment of various semi-enclosed atrium configurations of institutional building in tropical climate. Int J Built Environ Sustain 8(2):35–48
14. Acosta I, Varela C, Molina JF, Navarro J, Sendra JJ (2018) Energy efficiency and lighting design in courtyards and atriums: a predictive method for daylight factors. Appl Energy 211:1216–1228
15. Vethanayagam V, Abu-Hijleh B (2019) Increasing efficiency of atriums in hot, arid zones. Front Archit Res 8:284–302

16. Chu G, Sun Y, Jing T, Sun Y, Sun Y (2017) A study on air distribution and comfort of atrium with radiant floor heating. Proc Eng 205:3316–3322
17. Lu Y, Xiang Y, Chen G, Wu Y, Sun C, Liu J (2019) Summer dynamic thermal environment for isolated atrium in the severe cold region: on-site measurement and numerical simulation. Appl Therm Eng 160:114108
18. Yunus J, Ahmad SS, Zain AA (2010) Analysis of atrium's architectural aspects in office buildings under tropical sky conditions. In: Proceedings of the IEEE international conference on science and social research, pp 536–541
19. Marriage GLG (2012) Significant social space: connecting circulation in atrium design. Te Herenga Waka-Victoria University of Wellington
20. Bednar MJ (1989) Interior Pedestrian places. Whitney Library of Design, New York
21. Adams A, Theodore D, Goldenberg E, McLaren C, McKeever P (2010) Kids in the atrium: comparing architectural intentions and children's experiences in a pediatric hospital lobby. Soc Sci Med 70:658–667
22. Gritch T, Eason B (2022) Atria systems. WBDG: Whole Building Design Guide, 2016. [Online]. Available: https://www.wbdg.org/guides-specifications/building-envelope-design-guide/atria-systems. Accessed 03 Feb 2022
23. Jensen MK (2010) Space unfolded—space as movement, action and creation", mind your behaviour—how architecture shapes behaviour. Dansk Arkitektur Centre, Copenhagen
24. Tregenza P (1976) The design of interior circulation: people and buildings. Crosby Lockwood Staples, London
25. Hung WY (2003) Architectural aspects of atrium. Int J Eng Perform Based Fire Codes 5(4):131–137

Key Elements Performance-Based Building Design on Construction Project Indonesia

Sulfiah Dwi Astarini, Christiono Utomo, and M. Arif Rohman

Abstract Providing a high-performance building is inseparable from its complex process during the design phase. For the design process to achieve better performance, it is important to establish a strategy for managing participants and designing objects. Performance-based building design (PBBD) is a design concept where a designer has the same perception of performance goals as a result of design. This paper reports on the key elements that characterize performance-based building design. A literature review was used to find key elements of PBBD. A survey questionnaire is used as a data collection method to empirically confirm the findings of the literature review. The quantitative method through descriptive mean and standard deviation is used for data analysis. The result of the study found eleven key elements in the design performance process. The most important elements are participant satisfaction, communication of quality, and client involvement. The results of this study are expected to be a basis related to how the PBBD is implemented so that the design results can be by the planned expectations and objectives.

Keywords Performance-based building design · Strategy design · Success design · Construction

1 Introduction

Performance-based building design (PBBD) is growing rapidly in providing high-performance buildings. This design concept integrates various aspects of performance that have been translated from performance requirements into performance objectives. Setting performance goals from the early stages of the design provides designers with a shared understanding so that throughout the design process, designers focus on achieving goals as design success. Because PBBD emphasizes

S. D. Astarini · C. Utomo (✉) · M. Arif Rohman
Department of Civil Engineering, Institut Teknologi Sepuluh Nopember, Surabaya 60111, Indonesia
e-mail: christiono@ce.its.ac.id

T. Kang (ed.), *Proceedings of 5th International Conference on Civil Engineering and Architecture*, Lecture Notes in Civil Engineering 369,
https://doi.org/10.1007/978-981-99-4049-3_26

the various performance criteria integrated into building design, then the PBBD is the basis of a design process that illustrates how well the building can fulfill its function in supporting user/occupant activities [1].

Designing high-performance buildings is a complex activity so the involvement of multidisciplinary design experts is needed to work together and interact with each other as the exchange of data, information, and decision-making processes increases [2]. Although the involvement of a multidisciplinary design team is important for design success, this remains a challenge, especially if the design team that is part of the design team has never been involved in the same project before. This phenomenon can trigger a conflict of interest between each of the designers involved because they have different goals for design results [3]. On the other hand, poor communication amidst the fragmented nature of construction adds to the problems that can hinder the success of the project, even though communication is one of the most influences the implementation of the project from inception to the handover [4].

To support the PBBD process, the client's role in stating performance requirements is fundamental to the design. There are often obstacles in managing the requirements of the client need [5]. These obstacles arise when the client does not have a sufficient understanding of building design, even though the client's understanding and knowledge are needed to identify their requirements clearly [6]. In addition, designers are also required to have good knowledge and understanding, especially in carrying out building performance analysis techniques [1]. Lack of knowledge can hinder designers in providing solutions and decision-making [2]. According to Zhikun and Fungfai [7], knowledge sharing is a factor that can facilitate the creation of a learning environment to improve best practices in the design process.

Furthermore, this research aims to identify key elements that play an important role in the success of the performance-based design. By using a survey of design actors from the construction industry in Indonesia, the most dominant factor was found based on the value of mean and standard deviation ratings. The results of this study are expected to provide theoretical and managerial implications, especially in the field of design management in construction projects.

2 Literature Review

2.1 Performance-Based Building Design (PBBD)

The most commonly used definition of performance-based design in the field of research is the process of designing buildings based on performance requirements that translate into performance objectives and are integrated into building design [8]. Setting performance goals during the design phase helps the designer focus on achieving predetermined performance so that it has the opportunity of design success. Building performance in this case refers to various performance criteria, such as thermal performance, acoustic performance, lighting, structural safety and security,

etc., where these aspects are grouped into several performance categories. These buildings are designed to provide benefits to their occupants, in terms of increasing productivity and health, as well as for the community in terms of environmental well-being.

Applying performance aspects to buildings requires special attention, especially in analyzing building systems, studying building behavior, to prevailing climatic conditions [1]. Based on this, the completion of the design depends on the experience of the designer, because it contributes to a better performance process. According to Ataman and Dino [2], lack of experience and limited knowledge possessed by designers can hinder the design process, so this condition often leads to design errors [9]. Design errors, apart from coming from the individual designer, can also come from the level of team/organization, and at the project level [9]. To achieve an increase in the design performance process in PBBD, it is necessary to have effective management at these various levels so that the design achieves optimum results.

2.2 Elements of Performance-Based Building Design

Designing performance-based buildings is a complex activity because it involves specialized designers with different goals for the design results. This causes a high level of fragmentation, so it is important to manage the designer so that project objectives can be achieved, as well as individual goals can also be met. Achieving design performance goals requires the integration of various participants from the design phase to the operational phase. Based on the literature, these supporting factors need to be considered to achieve the design objectives as project success, as discussed below:

Client Involvement: The researcher [6] discusses client involvement in terms of client quality and its impact on design and project team performance. Client involvement plays a major role to achieve the goals of high-performance building. This is because the client plays a role in selecting the design team, and conveying the necessary information, including the project budget in realizing a high-performance building [2]. Client involvement will lead the multidisciplinary design team to collaborate, followed by the design team's ability to understand and clarify client needs throughout the design process. Client involvement in leading, assessing, and changing requirements has direct effects on design performance [6].

Participant Satisfaction: According to Lehtiranta et al. [10] project, success requires the processes and performance of various multi-stakeholders that are interconnected, coordinated, and work together satisfactorily. Researchers [12] conducted performance evaluations of clients, designers, and contractors to measure the satisfaction of the participants involved. Participant satisfaction is an important factor in achieving project objectives. This is because the participants involved in addition to achieving individual goals, on the other hand, are also required to achieve common goals. Participant satisfaction in the design process can be measured if expectations match the planned final results [11].

Teamwork: Wang et al. [12] identify critical factors related to building efficient teamwork during design collaboration. The study uses the input-process-output (IPO) theory, where efficient teamwork does not only depend on the characteristics of team members but is also influenced by the process. It was further found that team efficiency depends on a team-working atmosphere, followed by collaboration skills, a comfortable working environment, and the use of design technology. A study by Wang et al. [13] added that teamwork concerns how team members work, namely integrating ideas/understandings, acting as individuals in a team, coordinating, and adapting to achieve common goals.

Integrated Design: Design integration is a framework that brings together multi-disciplinary experts to share and develop knowledge to improve building performance from the very beginning of design [14]. In terms of meeting design performance requirements, often the selection of building components/elements can affect other design components, so all design decisions must be considered together or as an interrelated system. A study by Lu et al. [15] states that design integration encourages project participants to be actively involved in evaluating all important decisions related to project progress, from pre-design to the operational phase.

Interoperability: Interoperability is defined as the process of working together between people with people, people with systems, and systems with systems [16]. Researchers Poirier et al. [17] formulated three dimensions of interoperability, namely the dimensions of technology, process, and organization. The technological dimension relates to the dissemination and exchange of data or information carried out between two or more different digitalization tools. The process dimension relates to strategies that link and unify processes throughout the project life cycle. The organizational dimensions are the ability between organizations to collaborate, remove structured barriers, and set common goals.

Communication Quality: The quality of communication is seen as an important factor because it indicates the availability of information that is easy to access openly [18]. Communication quality is concerned with how information can be conveyed by the sender to the right recipient and at the right time [19]. The quality of communication between the design team depends on the use of design technology, the effectiveness of decision-making, and the adequacy of information during design activities [20].

Completeness of Media Communication: Communication media is also considered to contribute to the success of the performance-based design process. This is based on the completion of design work carried out by each design team not always in the same location so high design activities require the use of design technology as a communication media [20]. According to Norouzi et al. [21], communication tools/media are one of the factors that can improve communication performance in the design process.

Frequency of Communication: This refers to appropriate and frequent communication between participants with the aim of identifying design problems and finding solutions to design problems [22]. Researchers Cheng et al. [23] stated that the best communication is face-to-face communication because it provides an opportunity for the recipient to clarify meaning, thereby reducing misunderstandings.

Knowledge-Sharing Behavior: In the design process, knowledge sharing is a factor that encourages the creation of a learning environment and increases the ability to produce the best designs [24]. One of the determining factors in knowledge sharing is knowledge-sharing behavior. Knowledge-sharing behavior refers to the actions taken that affect the designer's willingness to share knowledge [7]. The information and knowledge shared can improve the quality of the designer's work during the design process [25].

The motivation of Knowledge Sharing: Minimizing design errors and increasing innovation thinking through knowledge sharing require strategies where knowledge shared can be rewarded. Motivating team members to share knowledge is an approach used as a strategy to build social networks [24]. Knowledge-sharing motivation is the underlying drive for designers to share knowledge [26]. Researchers [27] argued that motivation in sharing knowledge depends on the organizational culture where the formation of mutual trust can support the practice of sharing knowledge.

Designer Performance: According to Lehtiranta et al. [10], there is a significant influence between designer performance and project success. Designer performance is the designer's ability to complete design work [11]. There are three attributes in predicting the designer's performance, namely the designer's ability to solve problems, the designer's speed in producing designs, and the designer's level of enthusiasm in handling difficult jobs [28].

3 Method

This study uses two research methods that combine qualitative and quantitative studies. The first method is to conduct a literature review to understand the issues in the PBBD area of the construction project. From the literature review, it is found that the relationship between the factors that are considered relevant and become variables investigated in this study. The questionnaire survey method is used to empirically confirm the variables obtained from the results of the literature review. Figure 1 presented the flow of the method in the research.

Eleven variables were verified. The survey process is carried out through an online system, where the questionnaire distributed consists of two parts. The first part contains the respondent's data including experience, the type of building design, and membership professional followed. While the second part contains statements

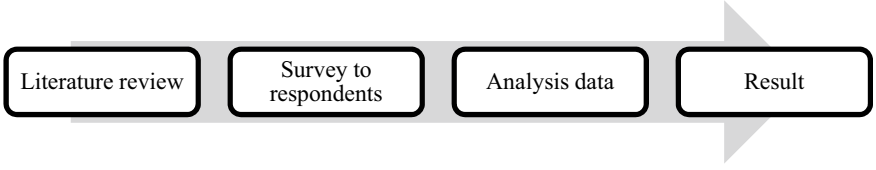

Fig. 1 Flow of research methodology

regarding the key elements of PBBD. A total of 50 respondents were involved. Data analysis was carried out descriptively through the assessment value of the mean and standard deviation.

Respondents involved in this study are design experts on construction projects and have generally been involved in building design. The following shows Fig. 2 of the respondent's experience in the design process, and Fig. 3 is the function of the building designed by the respondent.

Based on Fig. 2, as many as 22 respondents have 10 years of experience in the design process. Sixteen respondents had 11–20 years of experience, and 12 respondents had more than 20 years of experience. Next, Fig. 3 shows that the respondents most involved in the design process were residential buildings with 16 respondents, followed by shopping centers with 8 respondents. Office and industrial buildings 6 respondents. While other building functions designed by respondents include airports, hospitals, schools, and others as many as 14 respondents.

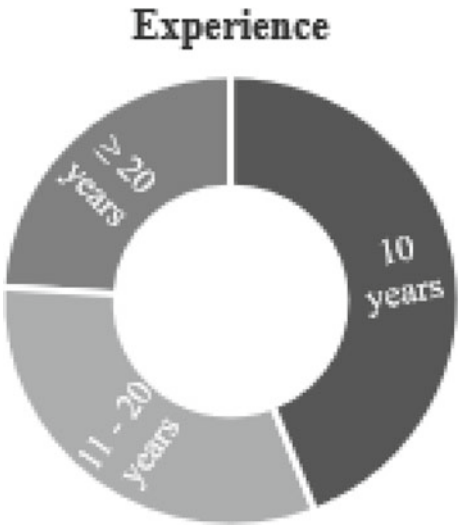

Fig. 2 Characteristics of respondents' experiences in the design process

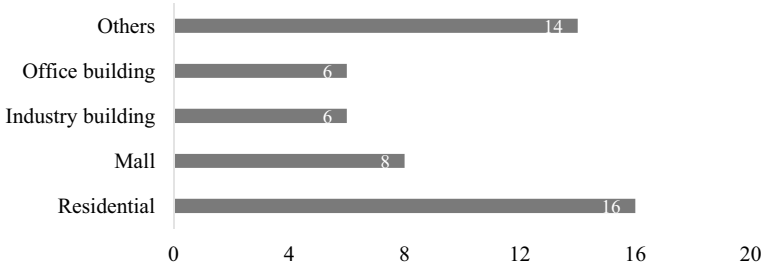

Fig. 3 Function of the building designed by the respondent

4 Result and Discussion

Table 1 summarizes the average value and standard deviation, where the value is the basis for performing the ranking of each factor found as a key element of performance-based design in a construction project.

Based on Table 1, the top ranking of the key elements of performance-based design is team satisfaction (mean = 4.36). This finding is in line with research [11] that team satisfaction is an important indicator of project success. Achieving team satisfaction is highly dependent on how well the team can manage the design process effectively through smooth collaboration, to achieve the design goals that have been set.

The second rank is the communication of quality is considered a key element of design performance (mean = 4.28). Researchers [19] stated to improve the quality of communication requires the role of teamwork where collaboration can support the distribution of information that reaches all participants involved; the existence of awareness and individual development; and organizational support in establishing clear roles and contracts to encourage communication between teams/organizations.

The third rank is client involvement plays an important role in producing high-performance buildings. According to Elforgani and Rahmat [6], the client is actively involved during the initial design phase aiming to identify all the design requirements. Client participation in communicating and coordinating the design process is an important aspect of client quality that affects design performance.

Next, this study found that the communication frequency obtained a low value based on the mean value (mean = 3.68), which confirmed the findings [22]. The study states that the frequency of communication that is too often such as formal face-to-face meetings, and informally conducted between designers during the design phase will only waste time if the design problem does not find resolution solutions, so it only triggers a conflict between designers. The next lowest rank is knowledge-sharing

Table 1 Summary value of mean and standard deviation

Code	Indicator	Mean	SD	Rank
X1	Client involvement	4.28	0.74	3
X2	Team satisfaction	4.36	0.64	1
X3	Teamwork	4.12	0.60	6
X4	Design integration	4.24	0.93	5
X5	Interoperability	4.04	0.79	8
X6	Communication quality	4.28	0.68	2
X7	Completeness of media communication	4.28	0.84	4
X8	Communication frequency	3.68	1.07	11
X9	Knowledge-sharing behavior	3.88	0.97	10
X10	Motivation to share knowledge	4.12	0.78	7
X11	Designer performance	3.96	1.06	9

behavior gets a mean value = 3.88 and has a different variation of respondents' answers based on the value of standard deviation. This confirms that the behavior of sharing knowledge is not so important based on respondents' responses as a key element.

This research then conducts scatter plot analysis to determine the factors that have been applied during the performance-based design process. The results are presented in Fig. 4.

Based on Fig. 4, four quadrants are divided based on the differences in the mean and standard deviation values. In quadrant 1, the value of the mean is large, and the standard deviation is small; meaning that, almost all respondents agree to apply the key element factors in the PBBD process. Quadrant 2 shows the value of a large mean and standard deviation; the meaning, although not all respondents apply the key elements factor, most respondents still agree to apply these factors in the PBBD process. For quadrant 3, which has a small mean value and a large standard deviation, it shows that respondents tend not to do it—but there are still some who apply key elements in the PBBD process. Finally, quadrant 4 has the value of a small mean and standard deviation, meaning that all respondents agree not to apply these factors in the PBBD process. Based on the results of the scatter plot diagram, it was found that the key element factors tend to be applied in the PBBD process. However, the interoperability factor is not applied, as can be seen in quadrant 4. These findings indicate that the design process is still very fragmented due to the high level of specialization between designers which requires work to be divided. Interoperability problems arise because of the support approach or technology that allows individuals to work together in the system [16]. In this case, the interoperability factor has not been applied because it relates to the relationship between systems or technology, and

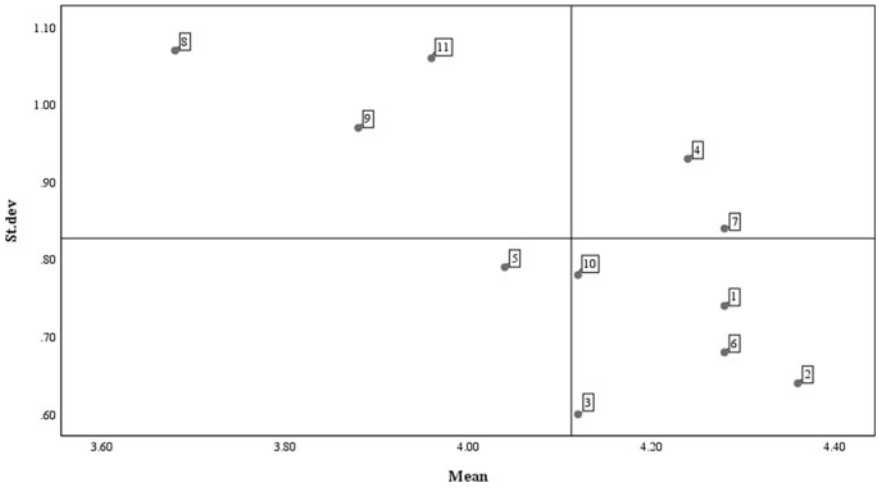

Fig. 4 Scatter plot analysis applying key elements of performance-based design

the relationship between organizations in business processes that can create social networks through trust, collaboration, and common goals.

5 Conclusion

This study identifies eleven key elements that support the practice of implementing PBBD. Through a literature review, the factors used in the research were identified. The questionnaire survey was conducted to obtain empirical data, with descriptive data analysis based on the value of mean and SD. The results showed that team satisfaction, quality of communication, and client involvement. Furthermore, the frequency of communication and knowledge-sharing behavior are considered less important factors based on respondents' responses in the practice of implementing PBBD.

The limitation of this research is that the identified factors may not be complete so further research can update these factors through an in-depth review. The limitation of further research is on respondents who are in Indonesia, so this research cannot be generalized. Future research can expand the research area and verify the results of research on design consultants.

Acknowledgements The authors would like to thank full for the 2022 Doctoral Research Grant based on contract number 1384/PKS/ITS/2022 and all of the respondents involved in this study.

References

1. de Wilde P (2019) Ten questions concerning building performance analysis. Build Environ 153:110–117
2. Ataman C, Dino IG (2021) Performative design processes in architectural practices in Turkey: architects' perception. Arch Eng Desain Manage
3. Dixit S (2020) Study of factors affecting the performance of construction projects in AEC industry. Organiz Technol Manage Construct 12(1):2275–2282
4. Abdul Rahman I, Gamil Y (2019) Assessment of cause and effect factors of poor communication in construction industry. In: IOP conference series: materials science and engineering, Vol 601. IOP Publishing
5. Jallow AK, Demian P, Baldwin AN, Anumba C (2014) An empirical study of the complexity of requirements management in construction projects. Eng Constr Archit Manag 21(5):505–531
6. Elforgani MS, Rahmat I (2012) The influence of clients' qualities on green design performance of building projects in Malaysia-descriptive study. Am J Appl Sci 9(10):1668–1677
7. Zhikun D, Fungfai N (2009) Knowledge sharing among architects in a project design team: an empirical test of theory of reasoned action in China. Chin Manag Stud 3(2):130–142
8. Becker R (2008) Fundamentals of performance-based building design. Build Simul 1(4):356–371
9. Lopez R, Love PED, Edwards DJ, Davis PR (2010) Design error classification, causation, and prevention in construction engineering. J Perform Constr Facil 24(4):399–408

10. Lehtiranta L, Kärnä S, Junnonen JM, Julin P (2012) The role of multi-firm satisfaction in construction project success. Constr Manag Econ 30(6):463–475
11. Kärnä S, Junnonen JM (2017) Designers' performance evaluation in construction projects. Eng Constr Archit Manag 24(1):154–169
12. Wang J, Yuan Z, He Z, Zhou F, Wu Z (2021) Critical factors affecting teamwork efficiency in BIM-based collaborative design: an empirical study in China. Buildings 11(10)
13. Chiocchio F, Forgues D, Paradis D, Iordanova I (2011) Teamwork in integrated design projects: understanding the effects of trust, conflict, and collaboration on performance. Proj Manag J 42(6):78–91
14. Leoto R, Lizarralde G (2019) Challenges in evaluating strategies for reducing a building's environmental impact through integrated design. Build Environ 155:34–46
15. Lu Y, Sood T, Chang R, Liao L (2020) Factors impacting integrated design process of net zero energy buildings: an integrated framework. Int J Construct Manage 1700–1712
16. Turk Ž (2020) Interoperability in construction—mission impossible? Develop Built Environ 4
17. Poirier EA, Forgues D, Staub-French S (2014) Dimensions of interoperability in the AEC industry. Construct Res Congr 1987–1996
18. Maier AM, Eckert CM, Clarkson PJ (2021) Factors influencing communication in collaborative design. J Eng Des 32(12):671–702
19. Hölttä V (2010) Enabling efficient communication of quality design information in a design process. In: Marjanovic D, Storga M, Pavkovic N, Bojcetic N (eds) Proceedings of design 11th international design conference 2010, Croatia, pp 1533–1542
20. Ikudayisi AE, Oviasogie AC (2020) Building design team communication: implications for project success in Nigeria. Asian J Adv Res Rep 13(4):12–23
21. Norouzi N, Shabak M, Bin Embi MR, Khan TH (2015) The architect, the client and effective communication in architectural design practice. Proc Social Behav Sci 172:635–642
22. Listyaningsih D, Utomo C, Rohman MA (2020) The influence of communication on the success design of high-rise residential building on Surabaya. In: Mohamed Nazri F (eds) Proceedings of AICCE'19. AICCE 2019. Lecture Notes in Civil Engineering, pp 1537–1547
23. Cheng EWL, Li H, Love PED, Irani Z (2001) Network communication in the construction industry. Corp Commun Int J 6(2):61–70
24. Bashouri J, Duncan GW (2014) A model for sharing knowledge in architectural firms. Constr Innov 14(2):168–185
25. Che Ibrahim CKI, Mohamad Sabri NA, Belayutham S, Mahamadu A (2019) Exploring behavioural factors for information sharing in BIM projects in the Malaysian construction industry. Built Environ Project Asset Manage 9(1):15–28
26. Javernick-Will A (2012) Motivating knowledge sharing in engineering and construction organizations: power of social motivations. J Manag Eng 28(2):193–202
27. Issa RRA, Haddad J (2008) Perceptions of the impacts of organizational culture and information technology on knowledge sharing in construction. Constr Innov 8(3):182–201
28. Ling YY (2002) Model for predicting performance of architects and engineers. J Constr Eng Manag 128(5):446–455

Bioclimatic Design Strategies in Rural Dwelling in the Chucuito District—Puno 2021

Doris Esenarro, Giancarlo Vargas, Pablo Cobeñas, Vanessa Raymundo, Walter Morales, and Jesus Manuel Prado Meza

Abstract This paper aims at advancing bioclimatic design strategies in a rural house in the Chucuito district, Puno. The town of Juli's temperature is usually −1 °C (30 °F), reaching as low as −8.9 °C (16 °F) and −15.6 °C (4 °F) in the most remote areas with the highest altitude. Housing was built with a contemporary confined masonry system and pitched roofs made of metal calamine. The house's functions were assessed using modeling in specialized software such as DesignBuilder where changes were made on the façade's materials and internal distributions. First, the surrounding climate conditions, the prevalence of lighting toward the façades and the wind's direction will be considered. Finally, the house's thermal comfort was stressed. As a result, it reached an air average temperature between 21 and 23 °C (70 and 73 °F) and outdoor air temperature from 10 to 13 °C (50–55 °F).

Keywords Design strategies · Bioclimatic design · Bioclimatic design strategies · Rural housing

1 Introduction

In the Puno region, one of the most worrisome climatological problems is frost, which is described as the phenomenon in which the air temperature near the earth's surface reaches 0 °C or below, after which ice crystals are formed by the freezing of dew or phase changes from water vapor to ice [1]. This phenomenon can affect crops and create respiratory diseases that affect the population. According to statistics from the Ministry of Health, from 2015 to 2018, Cusco and Puno were the regions with the most deaths from pneumonia in southern Peru. In 2019, Cusco registered 106

D. Esenarro (✉) · G. Vargas · P. Cobeñas · V. Raymundo · W. Morales · J. M. P. Meza
Faculty of Architecture, Ricardo Palma University, Lima, Peru
e-mail: doris.esenarro@urp.edu.pe

D. Esenarro
Instituto Especializado de Investigación de Ecosistemas Recursos Naturales, INERN, UNFV, Lima, Peru

T. Kang (ed.), *Proceedings of 5th International Conference on Civil Engineering and Architecture*, Lecture Notes in Civil Engineering 369,
https://doi.org/10.1007/978-981-99-4049-3_27

and Puno 48 deaths. Of the total number of deaths, most were children under 5 years of age and older adults [2, 3].

According to a SENAMHI report, during the winter of 2020, temperatures in the city of Puno dropped to −1 ℃ (30 °F), in Juli they reached −8.9 ℃ (16 °F) and in the most remote and higher areas temperatures reached −15.6 ℃ (4 °F) [4]. In Juli, meteorological frosts generally begin in April and end in September and is more frequent in the months of June and July. The most intense fall is usually recorded at night and in the early morning before sunrise with clear sky conditions or low cloud cover. It was also observed that solar radiation in Puno is very high [5]. The province of Chucuito has seven districts, five population centers and four rural communities, according to data from the INEI's National Population and Housing Census. It had a population 1,172,697 inhabitants in 2017 [6]. In the district of Juli, houses built under the contemporary system of confined masonry were identified, with gabled roofs of metallic corrugated iron, stone houses with mud and straw roofs, and "cake" mud as the locals call it. It is thought that this type of construction is merely idiosyncratic due to its western configuration and does not fulfill the functions of air conditioning and environmental comfort. It was observed that the application of fired clay masonry units, traditionally known as King Kong 18-hollow bricks, is frequent in the construction of buildings, mainly in load-bearing walls, confined masonry, parapets or partitions, etc. However, for the study region, this is not feasible, since it requires a material with improved thermal properties, i.e., reduced thermal conductivity that is capable of retaining the cold or warm temperature in a medium of low temperature [7]. The common brick used is King Kong 18-hollow brick, which has a compressive strength (Kg/cm^2) > 130.0, an absorption < 18% and no efflorescence [8]. The ancestral adobe constructions with thick walls and pitched roofs have allowed them to a certain degree to prevent the cold from affecting the interior too much and also help the internal bonfires to keep the heat [9]. Pitched roofs have prevented the rains to weaken the adobe constructions. These houses have managed to remain in the area for many years due to their lithic configuration, losing only their coverage [10].

2 Literature Review

2.1 Bioclimatic Design Strategies

The fundamentals are put into practice at the time of design to take advantage of the climate and environmental conditions in order to achieve a situation of thermal comfort inside. It plays exclusively with the design and architectural elements, without the need to use mechanical systems and taking advantage of natural energy [11].

2.2 Bioclimatic Architecture

A set of architectural, constructive and passive elements, capable of transforming the microclimate conditions to achieve values that bring them closer to the conditions of thermo-physiological well-being of human beings, preferably using passive energy, in pursuit of reducing energy consumption and minimizing negative impacts on the environment [12]. It is also defined as an alternative that tries to solve buildings' environmental problems through a logical design that maximizes natural factors and optimizes the use of traditional energy systems.

2.3 Thermal Comfort

A sense of satisfaction of building users with the thermal environment; therefore, buildings have the function of providing indoor environments that are thermally comfortable [13]. Thermal comfort is one of the most important variables to take into consideration in the bioclimatic conditioning of dwellings, this means the conditions of human well-being [14].

2.4 Rural Dwelling

A dwelling located in a rural place. Therefore, it includes rooms and productive areas, since there are activities that are carried out inside with the participation of several or all family members. Their location in rural settlements is related to accessibility and adequate distance to farmland. It is also a cultural, ritual space of knowledge because it occupies a central place for ceremonial activities, sociability and community relations, and solidarity [15].

2.5 Adobe

A solid block of unfired earth, which may contain straw or other material that improves its stability against external agents. When other materials (asphalt, cement, lime, etc.) are added to the adobe to improve its compressive strength and stability in the presence of moisture, it is called stabilized adobe [16]. The mixtures are generally made by adding materials, mixing with an amount of water from 15 to 35% and spraying in order to avoid the formation of clay lumps [17]. The benefits are that it is low cost and has less environmental impact [18]. The thermal conductivity and specific heat of adobe and brick, made of a mixture of clay and straw measured by a thermal probe technique, determined that adobe with straw and brick have a thermal

conductivity lower than 0.35 W/m^{2}K [19]. In addition, it could be said that it is a hygroscopic material because it has the ability to keep the heat or cold [20, 21].

3 Materials and Method

Figure 1 the materials and methods used in the research divided into three stages are observed.

3.1 Study Site

Figure 2 shows the town of Juli, located in the Puno region, in the province of Chucuito. The area of intervention is the town of Juli, which belongs to the High-Andean bioclimatic zone.

The geographic coordinates of the Juli town center are latitude 16° 12′ 48″ South, longitude 69° 27′ 33″ West and 3 888 m of altitude with UTC-5:00.

3.2 Climatology

Figure 3 shows the maximum temperature (red line) and minimum temperature (blue line) in Juli. The thin dotted lines are the average perceived temperatures. The warm season lasts 1.9 months, from October 19 to December 15, and the average

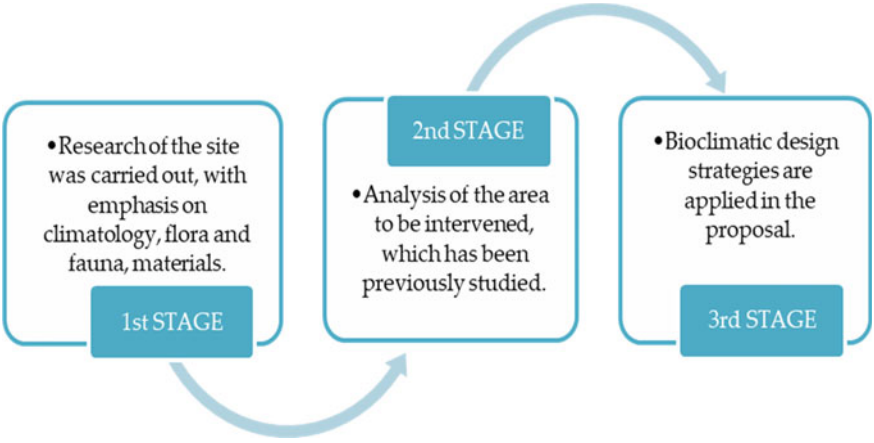

Fig. 1 Research methodological process

Fig. 2 Map of the Puno Region, the Chucuito District and the town of Juli

daily maximum temperature is more than 16 °C (61 °F) [24]. The cool season lasts 1.7 months, from June 10 to July 31, and the average daily maximum temperature is less than 14 °C (57 °F) [22].

Figure 4 shows the maximum, average and minimum relative humidity for a whole year in Juli. The maximum relative humidity corresponds to the month of December with 81.5%, and the minimum relative humidity corresponds to the month of August with 8.7% [22]. Finally, the average annual humidity is 40.5% [23].

Figure 5 shows the average hourly mean wind speed (dark gray line). The windiest part of the year lasts 7.4 months, from August 30 to April 10, with average wind speeds of more than 11.7 km/h [24]. The calmest time of the year lasts 4.6 months, from April 10 to August 30. The day with the highest wind speed is February 15

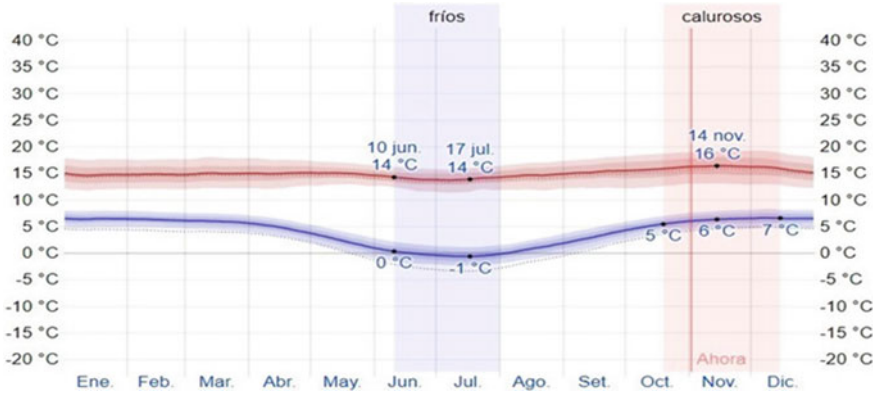

Fig. 3 Maximum temperature and minimum temperature

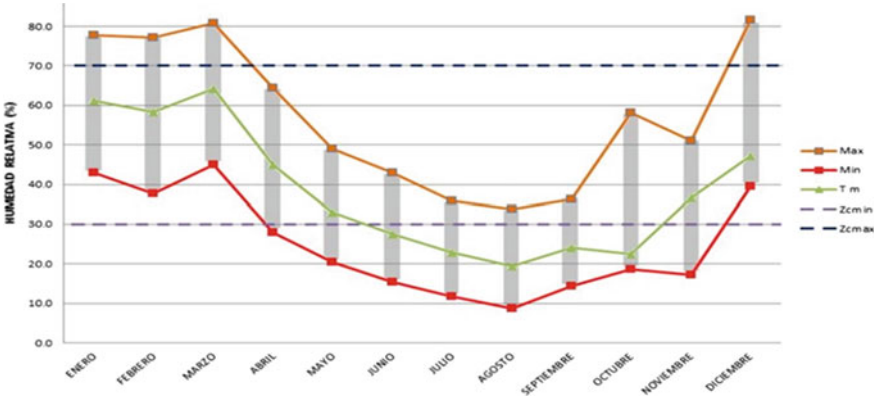

Fig. 4 Comfort zone graph, max, mean and min relative humidity

with a speed of 13.8 km/h, and the day with the lowest speed is May 20 with a speed of 9.6 km/h.

Figure 6 shows the percentage of days in different types of precipitation. The wettest season lasts 3.4 months, from December 15 to March 27, with a probability of more than 22% that a certain day will be a wet day [24]. The driest season lasts 8.6 months, from March 27 to December 15.

Figure 7 shows the percentage of time that each cloud cover band lasts, categorized according to the percentage of the sky covered with clouds. The clearest part of the year in Juli begins approximately on April 20; it lasts 5.3 months and ends approximately on September 29 [24]. The cloudiest part of the year begins approximately on September 29; it lasts 6.7 months and ends approximately on April 20.

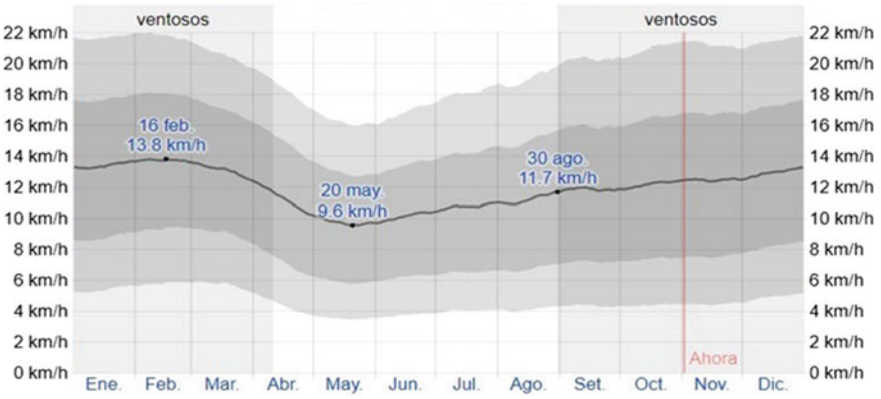

Fig. 5 Graph of winds, direction, frequency and speed

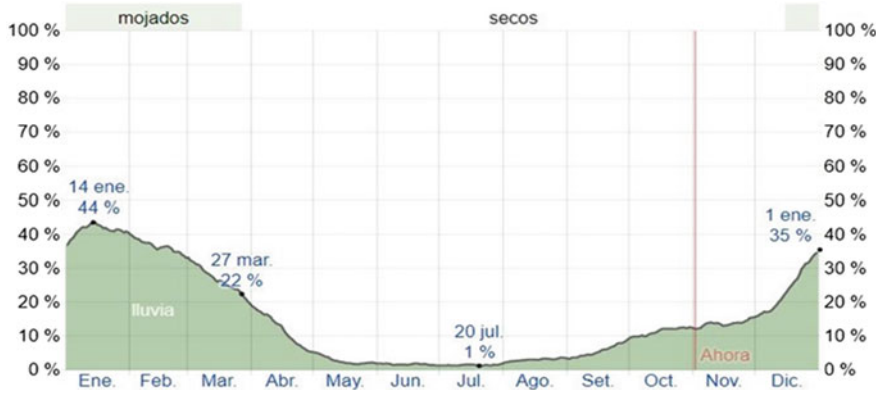

Fig. 6 Precipitation graph

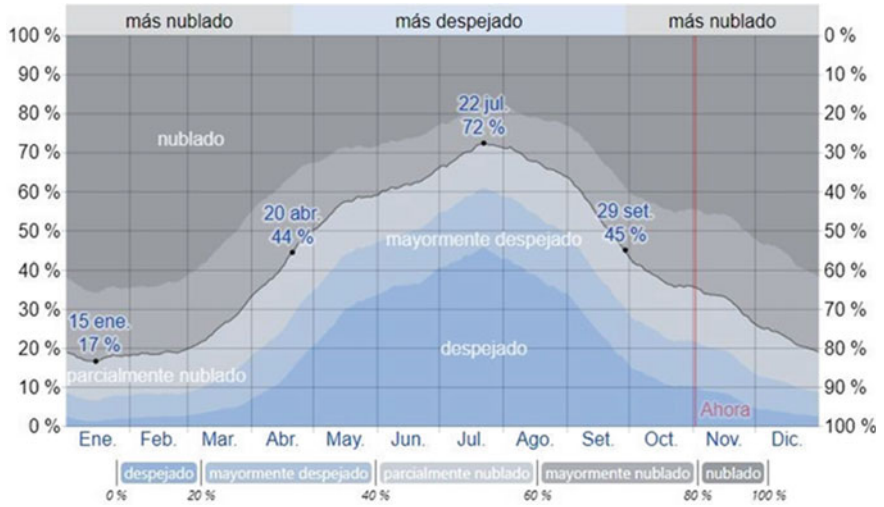

Fig. 7 Cloud cover percentage

4 Results

4.1 Location of the Architectural Proposal

Figure 8 shows the area of the project proposal. The chosen tract of land has 8 linear meters in the front and 24 linear meters in the back, making a total of 192 m^2. It is located in Ilave Street, on a strategic axis due to its proximity to Lake Titicaca.

Figure 9a shows the crosscut that is goes between 3857 m high and approximately 3854 m high. In Fig. 9b, a longitudinal cut that begins at 3859 m high up until 3851 m

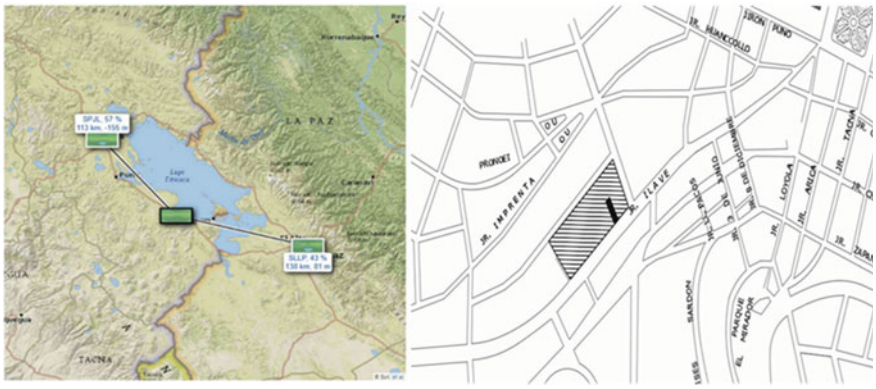

Fig. 8 Proposed land area

high with a more pronounced slope can be observed. Both cases show the unevenness of the land.

Figure 10a shows the analysis of the solar chart with a Lat: −16.2132873 Lon: −69.4591568 Date: 12/10/2021 Azim: 283.51º Elev: 60.7º [25]. On the other hand, Fig. 10b shows all the months of the year drawn on the psychometric chart (3800 m above sea level) as recommended by Givoni, based on the extreme points of temperature and relative humidity. This shows that it is not in the comfort zone so it will be necessary to implement design strategies to achieve thermal, lighting and acoustic comfort.

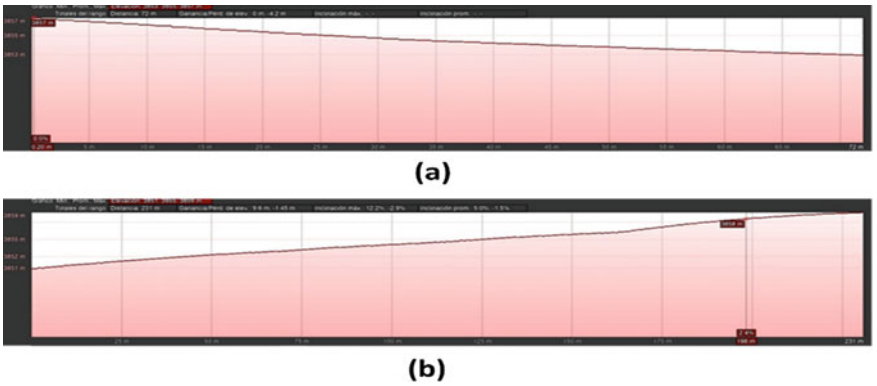

Fig. 9 Land area cuts

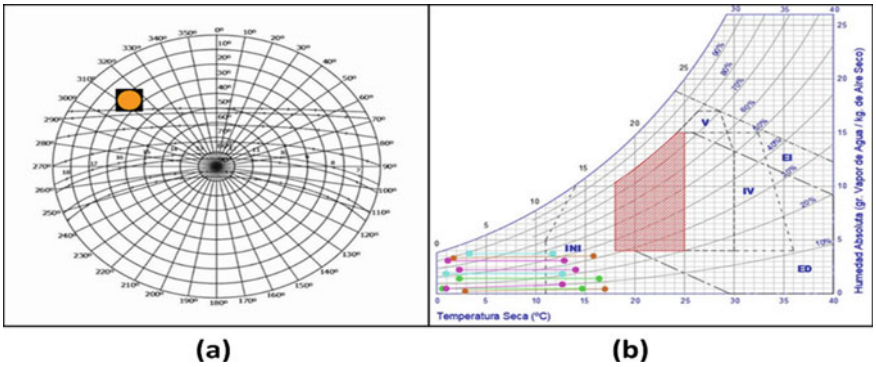

Fig. 10 Solar analysis

4.2 Architectonical Proposal

Figure 11 shows a housing configuration with three notable zones, the first is the commercial space proposed as a consequence of the preexisting residential traditions. There are two greenhouses and a kitchen that will be located in the center of the house since people who cook with gas or wood will emit heat energy that can be maintained and radiated into the house.

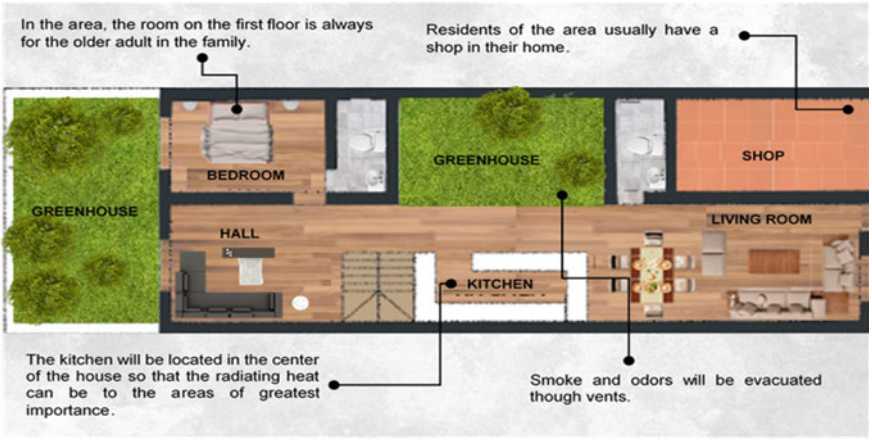

Fig. 11 First floor plan

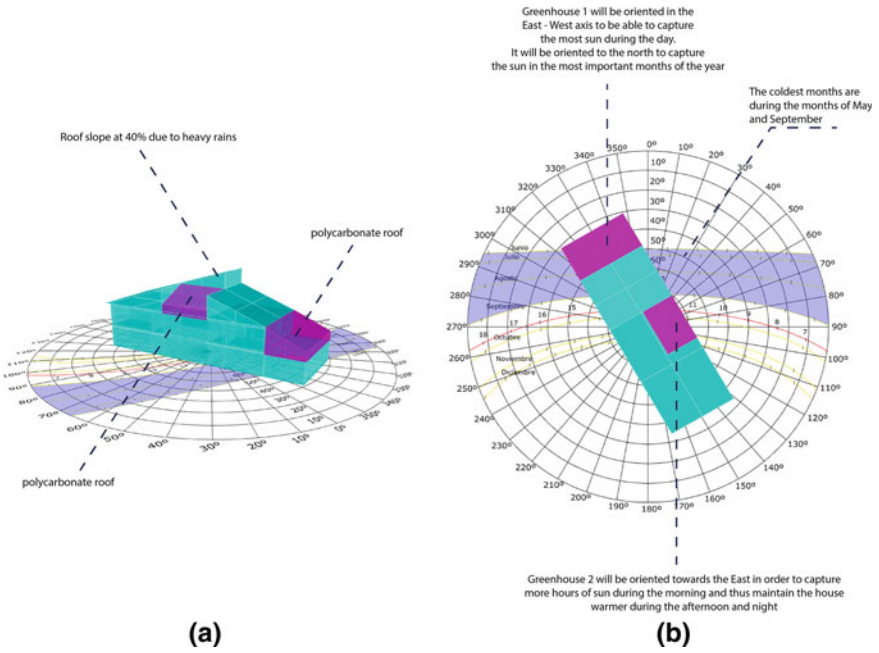

Fig. 12 Sun path with the proposed volume

4.3 Sun Path

Figure 12a shows the perspective position of the volume of the house (cyan), which will have two sunlight inlets where the two greenhouses will be located to provide thermal comfort.

In Fig. 12b, note the location of the house on the ground plan, which will have its solar contributions (magenta) oriented mainly to the northeast to receive the rays of the morning sun.

4.4 Solar Incidence

Figure 13 shows the solar incidence analysis through the proposed openings in the house. This analysis was carried out in the morning hours to show the direction and the solar heat input that will be used mainly by the greenhouses proposed in the project.

Figure 14a shows the analysis of daily solar gain through the spans proposed in the project. The heat graph shows a higher temperature starting from red (warmer), going through green and ending in blue (cooler), and Figure 14b shows the analysis of the annual solar gain through the spans proposed in the project. The heat graph shows a higher temperature starting from red (warmer), passing through a green and ending in blue (cooler).

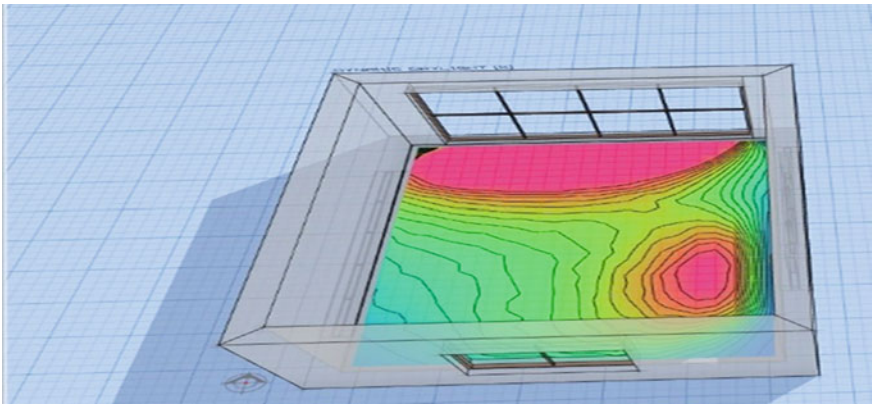

Fig. 13 Path with solar incidence

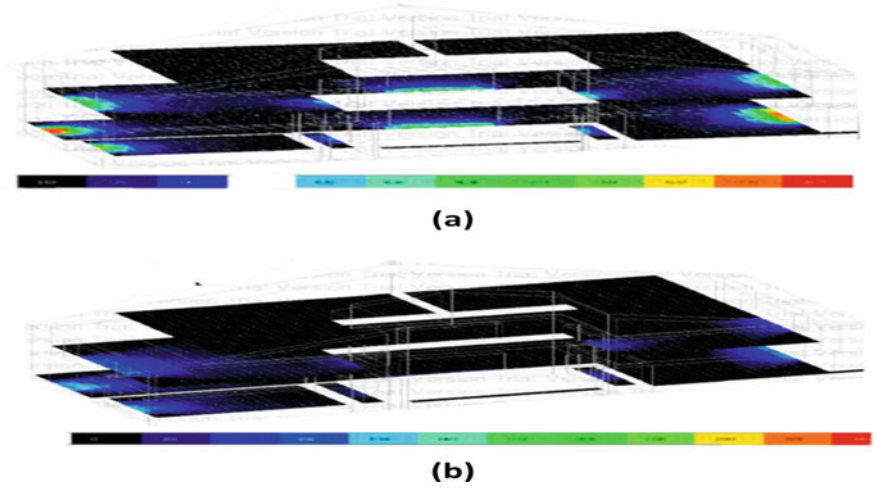

Fig. 14 Sun path

4.5 Result: Applied Strategies

Figure 15a shows the solar collection elements such as solar panels. 320 W 24 V Csun Polycrystalline Solar Panel type will be used. The rural dwellings' energy demand will be covered by 5 units, as well as a solar water heater since the radiation in Juli is high. The capacity of the solar water heater is 310 L. Figure 15b also shows the treatment of rainwater collection through storage tanks [25].

For the energy demand of a rural house in the town of Juli, the following analysis was made:

Table 1 shows the monthly energy demand in a house which is 284,270 W/month. This will cover the demand in a rural house.

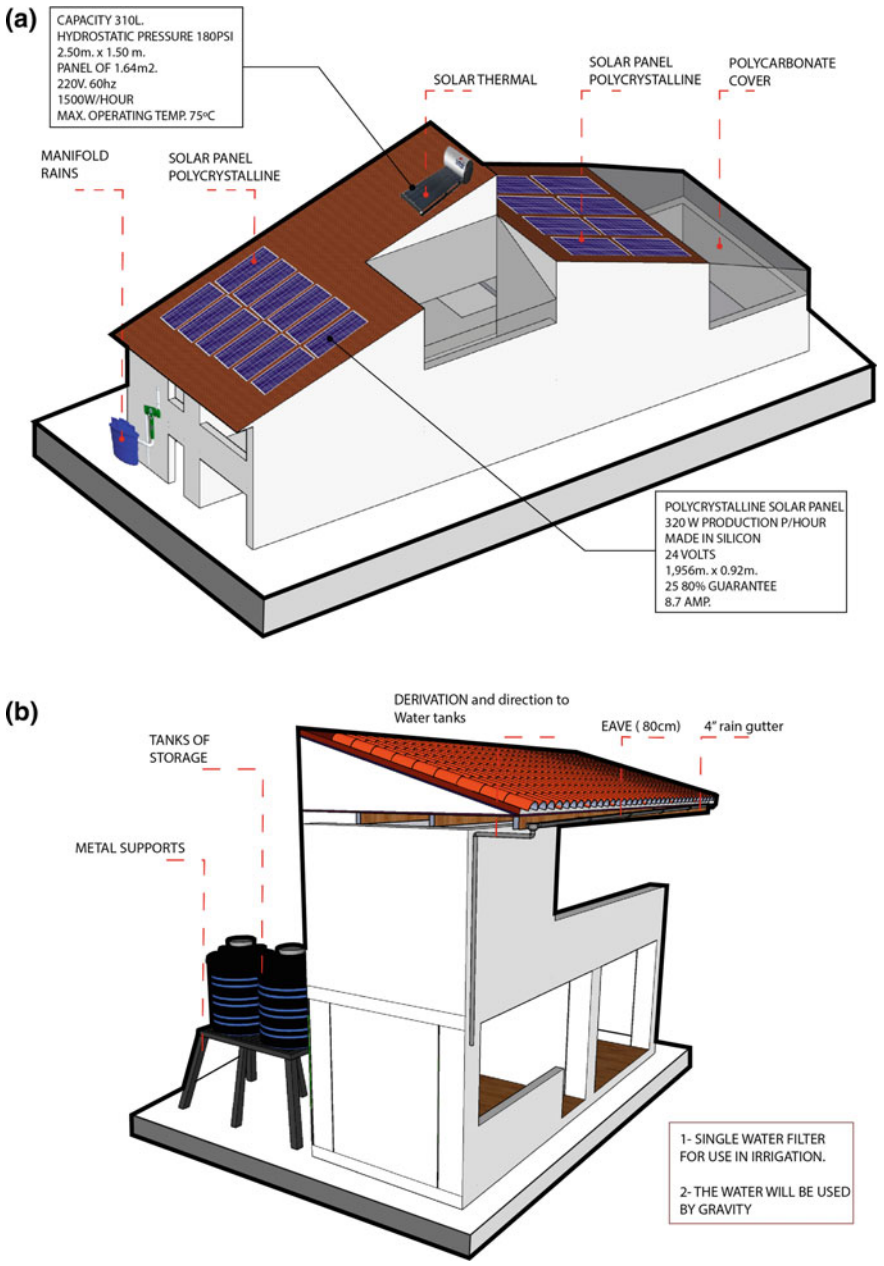

Fig. 15 Image of water collection and energy treatment, made by the authors

Table 1 Calculation of energy demand, made by the authors

Item	Description		Installed power (W/day)
1	Consumption monthly		284.5
		Total	284.5

Table 2 shows the energy demand met by a polycrystalline panel that has an energy production of 320 watts per hour, 1920 watts per day and 57,600 watts per month. In order to meet the energy demand of the house, it is necessary to install 5 polycrystalline solar panels 320 W 24 V, producing a total of 288,000 watts per month.

Figure 16a shows the general guidelines and construction details that must be followed to obtain a better result in terms of thermal management, drainage and structural system.

Figure 16b shows the proposed load-bearing wall based on reinforced adobe, which will be used to obtain a more stable, safe and earthquake-resistant house.

In Fig. 17a the final treatment of the internal spaces is observed, in the dining room and the living room, and Fig. 17b the link established between the kitchen, the dining room and the winter garden is observed.

In Fig. 18a, the spatial relationship between the greenhouse and the intimate space of the house is observed, which will serve to reduce the loss of heat that the house receives from the sun.

In Fig. 18b, the influence that the greenhouse and its landscape treatment will have on the thermal and visual comfort of the residents is observed.

In Fig. 19a the final proposal for the kitchen is observed, where the stove will be inside a brick oven to retain as much heat as possible while cooking, to be used in the house's radiator heating system, and Fig. 19b the piping proposal for the radiator heating system is observed, which will serve to improve thermal comfort in the rooms.

Figure 20 shows the operation of the heating system, which will have a water reservoir (covered with rock wool, porcelain and metal to keep the heat) that will be heated when the stove is on. This reservoir will have a thermostat and an exhaust valve for safety, as well as a 1/2HP water pump to circulate the hot liquid to the house's radiators.

Table 2 Solar panel calculation

Solar panel collection capacity						
Item	Description	Quantity	Installed potency (W)	Usage time (h/day)	Installed power (W/day)	Installed power (W/month)
2	Polycrystalline panel	1	320	6	1920	57,600
			Total			57,600

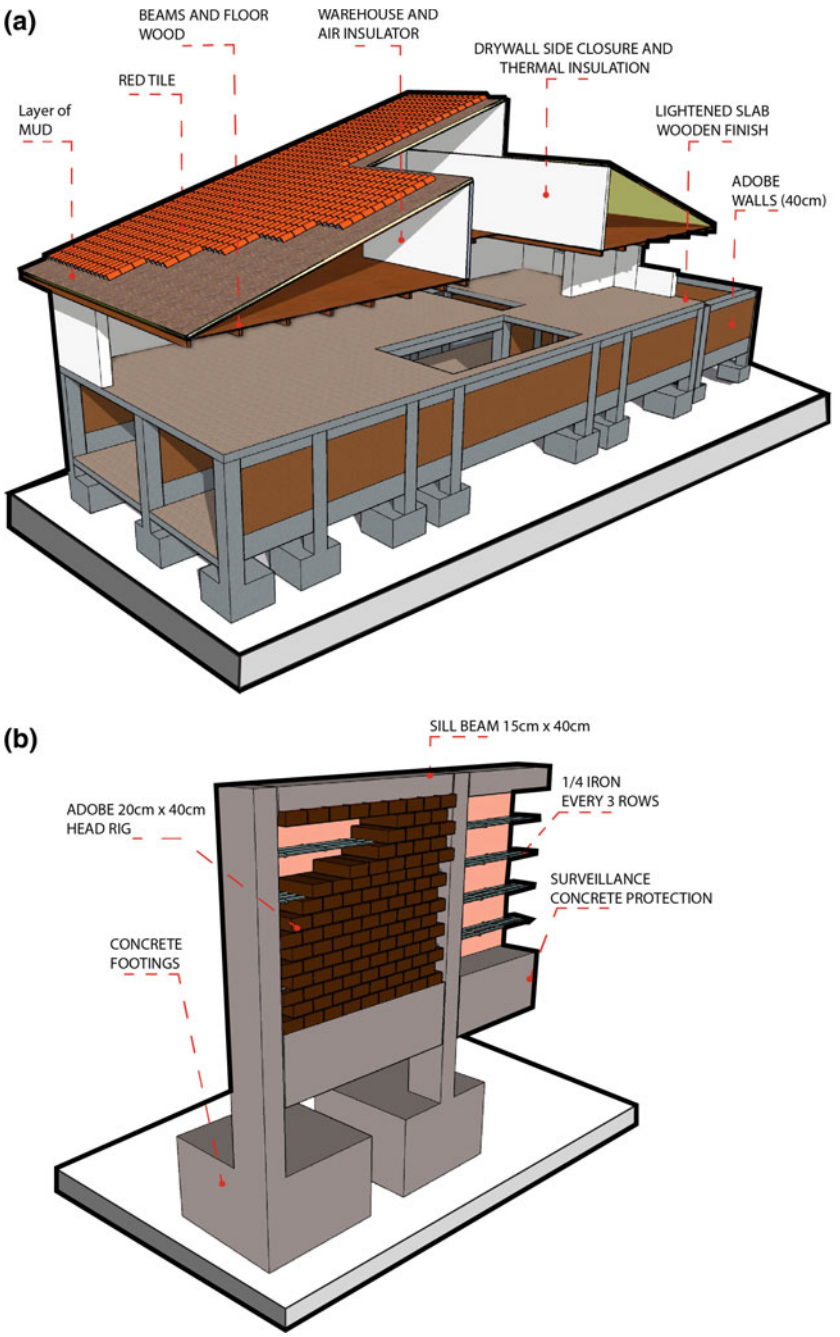

Fig. 16 Construction system image—prepared by the authors

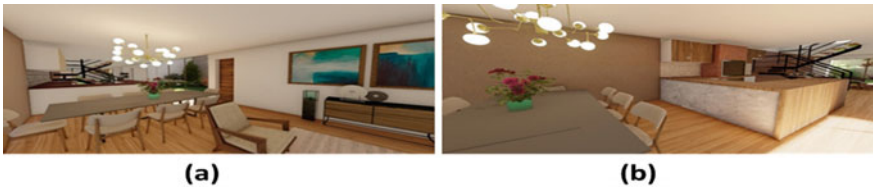

Fig. 17 Interior treatment prepared by the authors

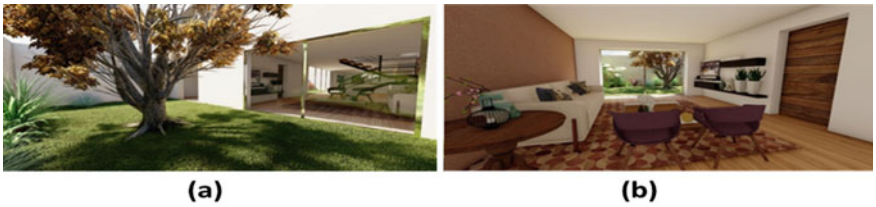

Fig. 18 Interior treatment and greenhouse prepared by the authors

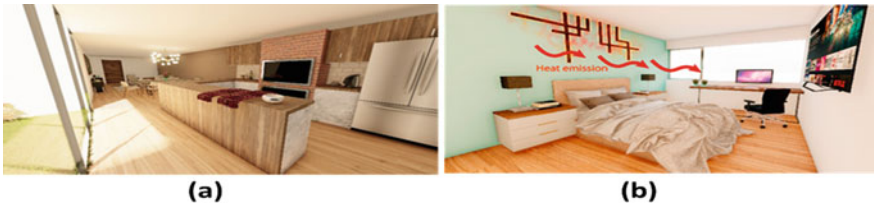

Fig. 19 Oven in kitchen and radiator in bedroom, prepared by the authors

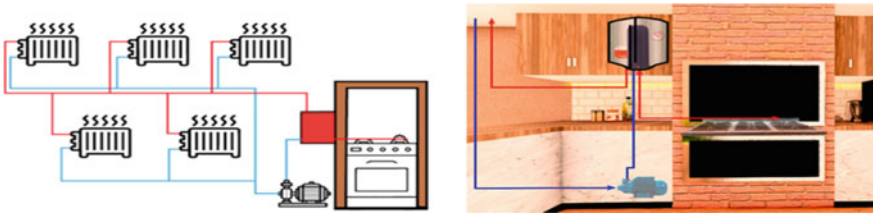

Fig. 20 Water treatment and heating system, prepared by the authors

4.6 Data Analysis

Figure 21 shows the result of the DesignBuilder program's analysis, which considers the materials to be used in the walls, roofs, span sizes and also the greenhouses. The image shows that the average temperature inside the project should be around 23 ºC (73 °F).

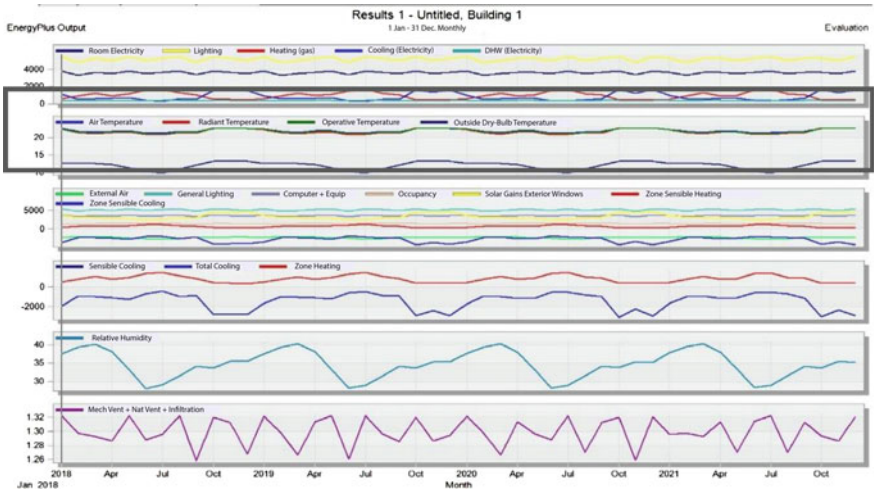

Fig. 21 Results of thermal analysis inside the project, prepared by the authors

4.7 Carbon Footprint

Table 3 shows the result of the DesignBuilder program's analysis, which considers the materials used in the house and makes visible the carbon footprint that will result from building this project where the embodied energy is from carbon (kg CO_2) 102,899.10, [26].

5 Discussion

The millenary technique of adobe is reassessed as an important ecological construction technique since it requires little energy for its manufacture and its carbon footprint is very low. It also has a good seismic-resistant capacity.

The research is focused on evaluating the different techniques of application used with this material, the different organic or inorganic aggregates to achieve a quality final product, which has an excellent thermal and humidity-insulating capacity with an improvement in its duration or lifetime. This is achieved through an analysis of the relationship between the curing times and amounts of liquid used during its application. [14, 27].

This research is of great value since it fosters the creation of a new culture in constructive and architectural development in the different areas of Peru, especially where greater thermal insulation capacities are required, such as Juli, Puno.

Thus, this paper contributes to achieving the inhabitant's better quality of life, dignified and within their reach with the necessary comfort to achieve their well-being.

Table 3 Carbon footprint analysis, prepared by the author

Materials embodied carbon and inventory	Area (m^2)	Embodied Carbon (kg CO_2)	Equivalent CO_2 (kg CO_2)	Mass (kg)
Brick mud at 50C degrees	541.8	80,263.5	83,911.8	364,834
Roof Tile	160.3	1540.8	1607.8	3349.6
Polyurethane (PU) foam	160.3	6731.2	6731.2	2243.7
Timber flooring	153.2	1302.3	1330.6	2831.1
External rendering	9.6	31.2	31.2	312.0
Floor/roof screed	14 3.6	1929.8	1929.8	12,061.3
Plasterboard	160.3	2216.8	2333.5	5833.7
Urea formaldehyde foam	143.6	339.2	365.8	190.5
MW stone wool (rolls)	9.6	44.8	47.8	42.7
MW glass wool (rolls)	160.3	425.2	466.9	277.9
Cast concrete	143.6	2297.4	2297.4	28,717.4
Cast concrete (dense)	299.2	5026.8	5026.8	62,834.9
Sub total		102,149.00	106,080.7	483,529.0
Constructions embodied carbon and inventory	Area (m^2)	Embodied Carbon (kg CO_2)	Equivalent CO_2 (kg CO_2)	Mass (kg)
Project external floor	9.6	90.4	93.7	
Project internal mass	27.8	467.5	467.5	
Techo Tejas	160.3	10,914.00	11,139.4	
Adobe intern	58.3	6655.00	6957.5	
Project ground floor	143.6	5854.3	5909.00	
Adobe intern	483.5	73,608.5	76,954.3	
Project internal floor_reversed	135.7	2279.7	2279.7	
Project internal floor_reversed	135.7	2279.6	2279.6	
Sub total	1154.5	102,149.01	106,080.67	
Glazing embodied carbon and inventory	Area (m^2)	Embodied Carbon (kg CO_2)	Equivalent CO_2 (kg CO_2)	Mass (kg)
Project external glazing	40.1	750.1	750.1	
Local shading				
Window shading				
Sub Total	40.1	750.10	750.1	
Building total	1194.6	102,899.10	106,830.7	

6 Conclusions

The research focuses on addressing the problem of housing in the Andes and, as such, provides a first approach to new alternatives when considering designs and constructions for the residents of the area. The research makes special emphasis on making visible the negative consequences of the western impact on the idiosyncrasy of the residents that encourages them to build inadequate and unsuitable dwellings for the climate of the area [28, 29].

It is proposed to use local building materials and improve adobe construction techniques with contemporary structural applications to achieve earthquake-resistant housing. It is also proposed to conserve and use as much energy as possible that the kitchen produces.

The final product is considered to be able to contribute in an ecologically responsible way to satisfy the needs of housing design and construction in cold climates [30, 31].

References

1. Provincial Municipality of Chucuito (2012) Strategic plan for sustainable development of the district of Juli
2. Málaga X (2011) Juli, the Rome of America: memory, construction and perceptions of the Jesuit past in a highland town
3. Esenarro D, Rodriguez C, Arteaga J, Garcia G, Flores F (2021) Sustainable use of natural resources to improve the quality of life in the Alto Palcazu population center, Iscozazin-Peru. Int J Environ Sci Develop 12(5)
4. Snyder R, Melo-Abreu J (2005) Frost protection: fundamentals. Pract Econom
5. General Edition (2020) Frost and cold weather hit high Andean communities in the midst of the pandemic. https://ojo-publico.com/1924/comunidades-del-sur-enfrentan-el-friaje-en-medio-de-la-pandemia
6. Rpp News (2020) Frost and Friaje season began in Puno. https://rpp.pe/peru/puno/heladas-y-friaje-en-peru-puno-bajas-temperaturas-afectan-a-la-poblacion-noticia-1269101?ref=rpp
7. Senamhi (2020) Frost and cold. https://www.senamhi.gob.pe/main.php?dp=puno&p=heladas-y-friajes-preguntas
8. Flores L (2019) Proposal for locating and determining the capacity of warehouses for the distribution of humanitarian aid in the main departments of Peru affected by frost and cold through the use of operations research tools
9. Bonifacio B (2020) Sustainable island-type houses to mitigate the damage caused by floods in the rural area of Ilave—Puno
10. Weatherspeaker (2015) The weather in Juli, the weather by month. https://es.weatherspark.com/y/27056/Clima-promedio-en-Juli-Per%C3%BA-durante-todo-el-a%C3%B1o#Figures-Humidity
11. Cuéllar J (2017) Study for the thermal conditioning of houses subjected to frost. Case: Santa Rosa populated center (Puno). http://repositorio.lamolina.edu.pe/handle/UNALM/2778
12. Fortón S (2017) Evaluation of thermal conductivity, physical-mechanical properties of 18-hole king kong brick added with pozzolana from the Raqchi quarry in different percentages, compared to a traditional brick

13. International Trade in Endangered Species of Wild Fauna and Flora (2013) Convention on international trade in endangered species of Wild Fauna and Flora. Appendices I, II, and III. https://cites.org/esp/app/appendices.php
14. Reynel C (2016) Identification guide for the common plants of the Peru LNG pipeline right-of-way. https://perulng.com/wp-content/uploads/2016/06/Guia_identificacion_plantas.pdf
15. SENAMHI (2017) Average climatological parameters in Chucuito
16. Evans JM (2000) Bioclimatic design techniques: Mahoney tables and comfort triangles
17. Arhuire I (2020) Characterization of solar radiation in Puno for the design of a solar thermal hot water system for a hotel with 50 people. http://repositorio.unap.edu.pe/handle/UNAP/13167
18. Gama J, Cruz T, Alcalá R (2012) Earthen architecture: adobe as a construction material in pre-Hispanic times. México
19. Barranco O (2015)Bioclimatic architecture. Architect Module CUC 14(2):31–40
20. Pérez M (2015) Methodological guide for the design of bioclimatic and sustainable housing complexes of social interest in the hot humid tropics, pp 75–78
21. Flores N, Domínguez M (2012) Measurement of the energy efficiency of silicon solar panels
22. Ortiz I (2012) Thermal comfort. https://www.academia.edu/37022669/Confort_t%C3%A9rmico
23. Roze J (2000) Conceptualization of rural housing. In: González J, Villar M (Eds) II Ibero-American seminar and workshop on rural housing and quality of life in rural settlements, Vol I. Autonomous University of San Luis Potosí, Mexico, pp 12–15
24. Quispe L, Huillca M, Sotomayor G (2018) Estimation of global solar radiation in the city of Puno by applying the Bristow and Campbell model, pp 27–34
25. Rodriguez C, Esenarro D, Alburquerque C, Vega M, Ramirez V (2020) Theme Park of renewable energies for mitigation of CO_2 in the urban area of the district of Chorrillos, Peru, IOP Conference Series: Materials Science and Engineering
26. Montes CAE (2015) Solar heating system to reduce cold in Alto Andinas Homes
27. Higuera JDLC (2017) Grid Connected Photovoltaic Systems
28. Department of civil engineering and Architectura, University of Catania, 64 Santa Sofia Street, 95125 Catania, Italy
29. Faculty of Civil Engineering, National University of San Agustín de Arequipa, Arequipa 04001, Peru. Department of Architectural Technology, Barcelona School of Building Construction (EPSEB), Universitat Politécnica de Catalunya, 08028 Barcelona, Spain. https://www.osinergmin.gob.pe/calcula-tu-consumo-de-luz
30. Esenarro D, Santos J, Teodoro C, Pandey B, Rodriguez C (2021) Impact of tourist demand, from COVID-19, on the sustainable Inca infrastructure of Ollantaytambo, Urubamba—Cusco I—Peru. In: 10th IEEE international conference on communication systems and network technologies (CSNT)
31. Esenarro D, Escate I, Anco L, Tassara C, Rodriguez C (2020) Proposal for an ecological research center for the recovery and revaluation of biodiversity in the town of Quichas-Lima, Peru. Int J Environ Sci Develop. ISSN 2010–0264

The Optimal Proportion in Construction Quantity Analysis for Reinforced Concrete Structures of Detached Housing Projects

Nattasit Chaisaard, Grit Ngowtanasuwan, and Satawat Dougpan

Abstract Reinforced concrete structures (RC structures) have been widely adopted for a long time, particularly in the widespread constructions of single detached houses. Nevertheless, quantity surveying (QS) to find out a proportion of RC usage per a unit of structural components such as concrete, reinforced steel, and formwork is still limited and inappropriately determined, particularly with only the use of existing numerical data to describe the statistical results in term of possible numerical ranges. The objective of this research is to study in detail an overview of the proportion values by assessing the proportion values in construction quantity analysis for RC structures of detached housing projects under construction. Hence, the researchers perform data collection, verification, and investigation, and classify the results into five groups as follows: (1) an average proportion of the lean concrete volume to a construction area versus that of the compacted sand volume to a construction area, (2) an average percent proportion of the concrete-beam volume to the total concrete volume versus that of the concrete-slab volume to the total concrete volume, (3) an average proportion of the concrete volume to a construction area, (4) an average proportion of the reinforced steel weight to the concrete volume and that of the reinforced steel weight to a construction area, (5) an average proportion of a formwork usage to the concrete volume versus that of a formwork usage to a construction area. Presumably, only a single mean value is insufficient for further consideration. Hence, using mean value ± standard deviation (SD) value together with a boxplot diagram can increase a level of confidence by displaying in graphic the data distribution through their quartiles and interquartile range (IQR) sections, covering more than 50% level of confidence based on basic statistical theory. And the value can be further applied more appropriately.

N. Chaisaard (✉) · S. Dougpan
Construction Management Program, School of Management Science, Sukhothai Thammathirat Open University, Nonthaburi 11120, Thailand
e-mail: nattasit.chaisaard@gmail.com

G. Ngowtanasuwan
Construction Management Program, Faculty of Architecture, Urban Design and Creative Arts, Mahasarakham University, Maha Sarakham 44150, Thailand

T. Kang (ed.), *Proceedings of 5th International Conference on Civil Engineering and Architecture*, Lecture Notes in Civil Engineering 369,
https://doi.org/10.1007/978-981-99-4049-3_28

Keywords Construction materials · Reinforced concrete structures · Descriptive statistics · Construction quantity

1 Introduction

Reinforced concrete structures have been widely adopted for a long time. Nonetheless, quantity surveying (QS) on the amount of construction materials, particularly the proportion unit of the components of RC structures, is still limited and inappropriately determined, particularly with only the use of existing numerical data to describe the statistical results in term of possible numerical ranges. Contextually, the QS on the amount of building materials is an important step in early phases of the construction projects like bidding and proposal processes. However, a focus on controlling and monitoring the amount of core construction materials such as concrete, reinforced steel, and formwork in term of volume or quantity per unit is the most important element in RC structures like detached housing projects in this research. Yet, the accuracy of QS from repeated measurements on the amount of construction materials depends on time constraints, experiences, and expertise on QS skills. So, an estimation procedure is vital to the main success. Laterally, an optional mathematical or statistical model is used to verify the construction QS, depending on preference of the construction operators or researchers [1]. To demonstrate the importance and ongoing development in past researches, models such as regression analysis, neural network, and Monte Carlo have been developed to estimate the amount of building materials [1]. Also, Chaivijarn et al. [2] study and compare unit quantity estimations on residential RC buildings classified into two groups: 5–8-story buildings with areas of 1136–7510 m^2 from six projects, and 3–5-story buildings with areas of 690–2775 m^2 from other six projects. The aim of the study is to find proportion values of concrete, steel reinforcement, and formwork in five building components: footing and ground column, beam, column, slab, and other items referred as miscellaneous items such as stair and fin. By comparing percent proportions of any material amounts of a structural item to a whole and proportions of any material amounts of structure items to a building area or the concrete volume, the researchers focus on average proportions of the amount of concrete, reinforced steel or formwork to a construction area (building usable area, m^2), for footing and ground column, beam, column, slab, and miscellaneous items of 5–8-floor and 3–5-floor residential RC buildings. The researchers found that an average proportion of the concrete volume to a construction area is approximately 0.215 (m^3/m^2). An average proportion of the reinforced steel weight to a construction area is approximately 27.30 (kg/m^2), and the average proportion of a formwork usage to a construction area is approximately 2.53 (m^2/m^2) [2]. Then to prepare a rate analysis for a reinforced concrete work, first the estimator estimates labor, material, equipment, and miscellaneous items for the specific quantity of reinforced concrete of that RC structure. Second the estimator determines components of the structure of the reinforced concrete construction (RCC) to do rate analysis, as the quantity of

reinforcement steel required varies among slabs, beams, columns, foundation, RCC roads, etc. [2, 3]. Nevertheless, there are two methods to estimate the steel required. The first method, with a construction drawing available, is dividing the total weight of steel required with the total concrete volume of different components to determine the weight of reinforcement steels for every cubic meter of concrete [3]. The second method is assuming the reinforced steel percentage for various components. The proportions of reinforcement steels needed for various components are listed below. And the values differing among structures can be inferred from prior encounters with similar structures [3].

- For slabs = 1% of concrete volume.
- For beam = 2% of concrete volume.
- For column = 2.5% of concrete volume.
- For RCC roads = 0.6% of concrete volume.

All of the above literatures make the researchers interested to study and build upon by finding out the optimal proportion of the construction quantity analysis for reinforced concrete structures of detached housing projects. The researchers want to explore beyond typically used average (mean) value by applying statistical principles in the descriptive analysis such as finding mean ($\overline{x}$), , standard deviation (SD), maximum and minimum values, range, skewness, and kurtosis of an analysis on distributed data [4]. Generate data report in term of $\overline{x} \pm$ SD with a certain level of confidence. Essentially analyze the results in a form of a boxplot or a box-and-whisker diagram [5]. And finally interpret results with increased in-depth characteristics of statistics. Given a small number of samples, the data was collected from 17 detached houses of a specialized housing construction company and cannot be used to widely interpret the results in terms of inferential statistics, but can be analyzed in detail with a descriptive analysis and the boxplot method to demonstrate in graphic the locality, spread, and skewness of the numerical data through their quartiles [5, 6]. So, the objective of this research is to perceive a more detailed overview of the proportion values and, specifically, to find outliers that differ significantly from the rest of the dataset. All of which will provide a certain level of confidence and credibility for agencies to audit and assess proportions of the construction quantity analysis for RC structures of detached housing projects under construction.

2 Research Background

As aforementioned, QS and construction cost estimation are very important tasks particularly in the construction management. They are used to obtain important information in decision making on the implementation of the construction project to achieve the goal set. In Thailand, quantity surveying and construction cost estimation are carried out in residential, commercial building projects, a type of building construction commonly constructed by the private sector like small construction companies, with the construction of residential projects accounting for 53.10% of

the total private construction value [7]. Two types of estimations in construction work are rough and detailed price estimations. The most common method of rough estimation is an estimation of the price per a building unit area. It is often used in the initial design work during the construction project budgeting and in the feasibility study for a designer and a project owner to know their budget as realistically as possible and use the budget in decision making on the project investment and the continuing design to develop the projects [2]. Nonetheless, the investigation tracking and result assessment from QS and cost estimation during the construction phase are very vital in designating construction responsibilities to both project manager and project engineer. The responsibilities are monitoring the status of cost performance and especially the utilization of core materials in RC structures consisting of the concrete, reinforced steel, and formwork. The previous studies in Thailand estimate proportions (with a shortcut method) on the amount of building materials of 3–8-story buildings as follows [8]. The proportion of the concrete volume to a building area is 0.289 m^3/m^2. The proportion of the reinforcement weight to a construction area is 63.40 kg/m^2. The proportion of the wooden-formwork volume to the concrete volume is 17.08 ft^3/m^3. The proportion of the reinforcement weight to the concrete volume is 206–221 kg/m^3 [8]. Another study estimates proportions of a residential 5–8-story building as follows [9]. The proportion of the concrete volume to a construction area is 0.22 m^3/m^2. The proportion of the weight of a reinforced steel to a construction area is 33.20 kg/m^2. The proportion of a wooden formwork to the concrete volume is 12.17 m^2/m^3. The proportion of a reinforced steel to the concrete volume is 147.60 kg/m^3. Then, Prapaporn [1] provides a study conducted with linear regression method to define relationship among building materials as a guideline for validation on price estimation. The researcher found that the concrete volume (m^3) correlates to a construction area (m^2) in a range of 0.196–0.246. The reinforced steel weight (kg) correlates to the concrete volume (m^3) in a range of 126.62–205.92. The quantity of formwork (m^2) correlates to the concrete volume (m^3) in a range of 7.16–8.78. While Chaivijarn et al. [2] study and compare proportion estimations of concrete, reinforced steels, and wooden formworks to a construction area on column, beam and floor system of similar reinforced concrete buildings from six projects of 5–8-story buildings with an approximate area of 1136–7510 m^2, and six projects of 3–5-story buildings with an approximate area of 690–2775 m^2. The researcher found that the proportion of the concrete volume to a construction area is 0.215 m^3/m^2 that of the reinforced steel weight to a construction area is 27.30 kg/m^2 and that of a wooden-formwork area to a construction area is 2.53 m^2/m^2. Formerly, the ideas of elemental cost analysis on buildings serve as a foundation for the quantity and cost modeling of structural systems. This strategy divides the entire building system into large groups of fundamental elements including architectural, structural, and building system works. Each of smaller-group elements that make up a large-group element undergoes thorough quantity and cost examinations [10]. One of the large-group elements is the structural system, which is further broken down into substructure group and superstructure group elements. The superstructure is then divided into slab, beam, column, and shear wall elements. Then, the quantities and costs of each element have to be established [10]. And from previous studies, the researchers

are required to study construction project samples of 17 detached houses with data collected from a specialized housing construction company. The researchers gather details from the collected data to:

- compare the average volume of lean concrete (m^3/m^2) to a construction area with the average volume of compacted sand (m^3/m^2) to a construction area [2];
- calculate the average percentages of the volume of concrete in the concrete slab and the concrete beam in proportion to the total volume of concrete [2]. The sum of concrete from both beams and slabs accounts for more than 78.21% of total concrete as shown in the results of our research study with a specified sample dataset;
- assess a typical proportion of concrete volume in a construction area (m^3/m^2);
- verify the average proportions of the weight of reinforcement steel to concrete volume (kg/m^3) and to a construction area (kg/m^2) [2];
- verify the average proportions of the formwork usage to concrete volume (m^2/m^3) and to a construction area (m^2/m^2) [2].

Then, the researchers use statistical principles in the section of descriptive analysis including finding mean ($\overline{x}$), , standard deviation (SD), maximum, minimum, range, skewness, and kurtosis to analyze data distribution [4], generate a data report in term of $\overline{x} \pm$ SD, determine a level of confidence, and analyze the results with a boxplot diagram [5]. The detail steps of this research are described in the research method.

3 Research Method

In this section, the researchers are interested in studying the optimal proportion of construction quantity analysis for reinforced concrete structure of detached housing projects. The researchers not only focus on a typically used average values in the previous studies but also use statistical principles of the descriptive analysis to find key results to be analyzed with a boxplot or a box-and-whisker diagram as described in the next section on the result analysis. And the researchers perform the following steps:

3.1 Data Collection

(1) Verify and study supporting documents composed of construction drawings, specifications, BOQs (bill of quantities), and some record documents on the actual amount of construction materials really used in 17 detached houses to summarize the actual record data, especially in the structural engineering section comprising foundations, columns, beams, floors, and miscellaneous parts such stairs and fin beams around the building, and to calculate construction areas.

3.2 Data Verification

(2) (2) Verify the detail data from BOQs and memorandums (the record documents) on the actual amount of construction materials used in the construction of 17 detached houses, focusing on numerical data details such as the lean concrete volume, the volume of structural concrete, an amount of compacted sand, steel reinforcements, and formworks used.
(3) Finish important data analysis and meanwhile prioritize data for the next step.

3.3 Data Investigation

(4) Report the results of the sequential analysis with a summary and discussion by comparing the research results with those from previous studies.

From the research methodology in the steps above, the results of the study to be further explained:

- the average proportion of the volume of lean concrete at a construction area compared to the volume of compacted sand to a construction area,
- the average percent proportions of the volume of concrete in the concrete slab and the concrete beam in proportion to the total volume of concrete,
- the average concrete volume per square meter of construction area,
- the average proportion of the weight of reinforcement steel to the volume of concrete and to a construction area,
- and the average formwork usage in proportion to concrete volume and to the construction area.

Then, the researchers compare the results through a descriptive statistical procedure with the graphic method to demonstrate locality, spread, and skewness from groups of numerical data in their quartiles, and explain the results with boxplot diagrams.

4 Results

4.1 A Comparison Between the Average Proportion of the Lean Concrete Volume to a Construction Area Versus that of the Compacted Sand Volume to a Construction Area (m^3/m^2)

From the data collection, verification, and analysis, the researchers compare between the average proportion of the lean concrete and that of the compacted sand of footings, ground beams, and slabs in 17 detached houses and show comparisons in Fig. 1 and

Table 1. The researchers found that the average proportion of the lean concrete and that of the compacted sand have a common relationship. The average proportion of the lean concrete is 0.044 m^3/m^2 while that of the compacted sand is 0.087 m^3/m^2. Hereby, the proportions are shown in terms of $(\overline{x} \pm SD)_{lean}$ and $(\overline{x} \pm SD)_{sand}$.

$(\overline{x} \pm SD)_{lean} = \mathbf{0.044} \pm 0.008 = \mathbf{0.052}, \mathbf{0.036}$ m^3/m^2, covering approximately 68% of the result range.

$(\overline{x} \pm SD)_{sand} = \mathbf{0.087} \pm 0.017 = \mathbf{0.104}, \mathbf{0.070}$ m^3/m^2, covering approximately 68% of the result range.

Both the distributions of the average proportion of the lean concrete versus that of the compacted sand are left skewed distributions because of minus values of the skewness. The distributions of kurtosis are greater than those of the normal distributions, which are called "leptokurtic."

From the outcome of descriptive statistics and a boxplot diagram showing comparison of two data groups in Fig. 2, $(\overline{x} \pm SD)_{lean} = \mathbf{0.044} \pm 0.008 = \mathbf{0.052}, \mathbf{0.036}$ m^3/m^2, covering approximately 68% of the result range. And $(\overline{x} \pm SD)_{sand} = \mathbf{0.087} \pm 0.017 = \mathbf{0.104}, \mathbf{0.070}$ m^3/m^2, covering approximately 68% of the result range. The proportions of the lean concrete from both the normal distribution and the boxplot diagram are the same values at **0.044** m^3/m^2, as well as those of the compacted sand at **0.087** m^3/m^2. In the boxplot diagram, the proportions of the lean concrete are indicated in term of Q_1, Q_2, and Q_3. At the 25th percentile, lower quartile $(Q_1)_{lean} = \mathbf{0.040}$. At the 50th percentile, median $(Q_2)_{lean} = \mathbf{0.046}$. At the 75th percentile, upper quartile $(Q_3)_{lean} = \mathbf{0.048}$. And the interquartile range (IQR) is a distance between the 75th and the 25th percentiles, the width of the square box covering approximately 50% of the result range. Then, the researchers found that the minimum value of 0.023 is an outlier, accounting for 1/17 or 5.88% of all values. The proportions of the compacted sand are shown at Q_1, Q_2, and Q_3. At the 25th percentile, lower quartile $(Q_1)_{sand} = \mathbf{0.079}$. At the 50th percentile, median $(Q_2)_{sand} = \mathbf{0.091}$. At the 75th percentile, upper quartile $(Q_3)_{sand} = \mathbf{0.096}$. The interquartile range (IQR) is a distance between the 75th and the 25th percentiles, the width of the square box covering approximately 50% of the result range. The minimum value of 0.043 is an

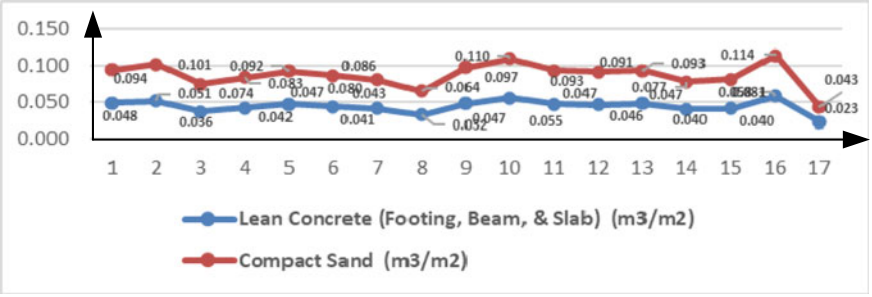

Fig. 1 Comparison between the average proportion of the lean concrete volume to a construction area versus that of the compacted sand volume to a construction area (m^3/m^2)

Table 1 Descriptive results of the average proportion of the lean concrete volume to a construction area and that of the compacted sand volume to a construction area

The proportion of the lean concrete, i.e., footing, beam, and slab (m^3/m^2)		The proportion of the compacted sand (m^3/m^2)	
Mean	**0.044**	**Mean**	**0.087**
Standard error	0.002	Standard error	0.004
Median	0.046	Median	0.091
Mode	#N/A	Mode	#N/A
Standard deviation	**0.008**	**Standard deviation**	**0.017**
Sample variance	0.000	Sample variance	0.000
Kurtosis	1.488	Kurtosis	1.851
Skewness	−0.786	Skewness	−0.907
Range	0.035	Range	0.071
Minimum*	0.023	Minimum*	0.043
Maximum	0.058	Maximum	0.114
Sum	0.740	Sum	1.475
Count	17.000	Count	17.000
Level of confidence (95.0%)	0.004	Level of confidence (95.0%)	0.009

outlier, accounting for 1/17 or 5.88%. Consequently, the boxplot diagram shows in-depth results at a greater level than usual, particularly by demonstrating the specific an outlier value unnecessary to consider because it is too small out of ordinary finding.

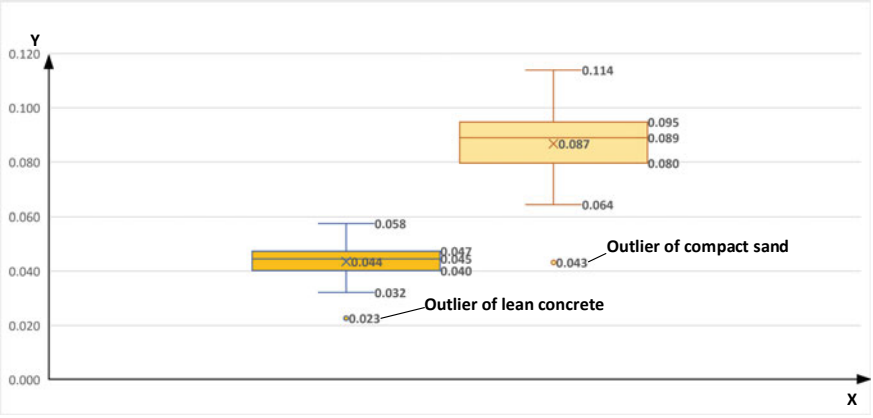

Fig. 2 Boxplot diagram compares the average proportion of the lean concrete volume to a construction area versus that of the compacted sand volume to a construction area (m^3/m^2)

4.2 An Average Percent Proportion of the Concrete-Beam Volume to the Total Concrete Volume Versus that of the Concrete-Slab Volume to the Total Concrete Volume

From the data collection, verification, and data analysis, the researchers compare between the average percent proportion of the concrete-beam volume and that of the concrete-slab volume. From data calculations and analyses from all 17 detached houses, the researchers found the importance in the average percent proportion of a concrete beam and that of a concrete slab. In 17 detached houses, the entire quantity of concrete used for floors and beams corresponded to 78.21% of the total structural concrete. So, the contractor must pay attention to concrete pouring on beams and floors. From the outcome of descriptive statistics compared with the boxplot diagram,

$(\overline{x} \pm \text{SD})_{\text{beam}} = \mathbf{0.351} \pm 0.078 = \mathbf{0.429}, \mathbf{0.273}$, covering approximately 68% of the result range.

$(\overline{x} \pm \text{SD})_{\text{slab}} = \mathbf{0.431} \pm 0.089 = \mathbf{0.520}, \mathbf{0.342}$, covering approximately 68% of the result range.

The percent proportions of the beam concrete in both the normal distribution and the boxplot diagram are the same value at **35.10%**, as well as those of the slab at **43.11%**. In the boxplot diagram, the average percent proportions of a concrete beam are shown as Q_1, Q_2, and Q_3. At the 25th percentile, lower quartile $(Q_1)_{\text{beam}} =$ **30.79%**. At the 50th percentile, median $(Q_2)_{\text{beam}} =$ **34.56%**. At the 75th percentile, upper quartile $(Q_3)_{\text{beam}} =$ **40.80%**. The interquartile range (IQR) is a distance between the 75th and the 25th percentiles, the width of the square box covering approximately 50% of the result range. The minimum value of **15.43%** from the 16th house of 17 detached houses is an outlier, accounting for 1/17 or 5.88% of all values (Fig. 3 and Table 2).

In the boxplot diagram, average percent proportions of the concrete-slab volume are shown as Q_1, Q_2, and Q_3. At the 25th percentile, lower quartile $(Q_1)_{\text{slab}} =$ **36.24%**. At the 50th percentile, median $(Q_2)_{\text{slab}} =$ **44.41%**. At the 75th percentile, upper quartile $(Q_3)_{\text{slab}} =$ **47.53%**. The interquartile range (IQR) is a distance between the 75th and the 25th percentiles, the width of the square box covering approximately

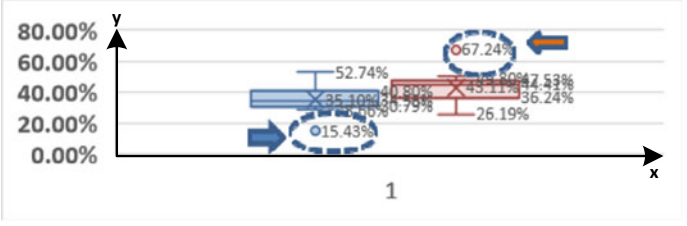

Fig. 3 Boxplot diagram shows the average percent proportion of the concrete-beam volume (blue shape) to the total concrete volume versus that of the concrete-slab volume (red shape) to the total concrete volume

Table 2 Descriptive results of the average percent proportion of the concrete-beam volume to the total concrete volume versus that of the concrete-slab volume to the total concrete volume

The average percent proportion of a concrete beam		The average percent proportion of a concrete slab	
Mean	**0.351**	**Mean**	**0.431**
Standard error	0.019	Standard error	0.021
Median	0.345	Median	0.444
Mode	#N/A	Mode	#N/A
Standard deviation	**0.078**	**Standard deviation**	**0.089**
Sample variance	0.006	Sample variance	0.008
Kurtosis	2.556	Kurtosis	2.657
Skewness	−0.262	Skewness	0.797
Range	0.373	Range	0.410
Minimum*	0.154	Minimum	0.261
Maximum	0.527	Maximum*	0.672
Sum	5.967	Sum	7.328
Count	17.000	Count	17.000
Level of confidence (95.0%)	0.040	Level of confidence (95.0%)	0.045

50% of the result range. The maximum value **67.24%** from the 16th house of 17 detached houses is an outlier, accounting for 1/17 or 5.88%. So, the boxplot diagram shows in-depth results at a greater level than usual, particularly by demonstrating the specific outlier value unnecessary to consider because it is too great out of ordinal findings. The outlier might result from a human error and subject to reconsideration on record necessary data.

4.3 An Average Proportion of the Concrete Volume to a Construction Area (m^3/m^2)

From the data collection, verification, and analysis, the researchers stress on the average proportion of the structural concrete volume to a construction area. From data calculations and analyses of all 17 detached houses, the researchers found consistency in proportions of a concrete volume to a construction area (m^3/m^2), and the average proportion is to **0.459** m^3/m^2. From the outcome of descriptive statistics compared to the boxplot diagram, $(\overline{x} \pm \text{SD})_{\text{conc/area}} = \mathbf{0.459} \pm 0.084 = \mathbf{0.543}, \mathbf{0.375}$ m^3/m^2, covering approximately 68% of the result range.

The distribution of the average proportion of concrete volume is left skewed distribution because of the minus value of skewness in the data analysis. The distribution of kurtosis is greater than that of the normal distribution, which is called "leptokurtic". The average proportions of the concrete volume to a construction area from both

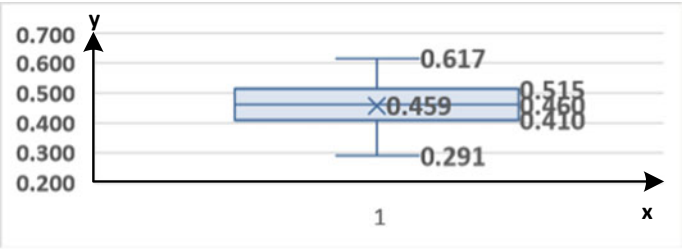

Fig. 4 Boxplot diagram shows the average proportion of the concrete volume to a construction area (m^3/m^2)

the normal distribution and the boxplot diagram are the same values at **0.459** m^3/m^2. In the boxplot diagram in Fig. 4, the proportions of the concrete volume are shown as Q_1, Q_2, and Q_3. At the 25th percentile, lower quartile $(Q_1)_{conc/area} = \mathbf{0.410}$. At the 50th percentile, median $(Q_2)_{conc/area} = \mathbf{0.460}$. At the 75th percentile, upper quartile $(Q_3)_{conc/area} = \mathbf{0.515}$. The interquartile range (IQR) is a distance between the 75th and the 25th percentiles, the width of the square box covering approximately 50% of the result range. The average proportion of structural concrete volume to a construction area from all 17 detached houses is **0.459** m^3/m^2.

4.4 An Average Proportion of the Reinforced Steel Weight to the Concrete Volume (kg/m^3) and that of the Reinforced Steel Weight to a Construction Area (kg/m^2)

From the data collection, verification, and analysis, the researchers stress on the average proportion of the reinforced steel weight to the concrete volume (kg/m^3), and that of the reinforced steel weight to a construction area (kg/m^2). From data calculations and analyses of all 17 detached houses, the researchers found consistency in proportions of the reinforced steel weight to the concrete volume (kg/m^3) and those of the reinforced steel weight to a construction area, and the average proportions of both are **129.513 kg/m³** and **60.422 kg/m²**, respectively. From the outcome of descriptive statistics compared to the boxplot diagram,

$(\overline{x} \pm \text{SD})_{steel/conc} = \mathbf{129.513 \pm 18.285 = 147.798}$, **111.228** kg/m^3, covering approximately 68% of the result range.

$(\overline{x} \pm \text{SD})_{steel/area} = \mathbf{60.422 \pm 17.723 = 78.145}$, **42.699** kg/m^2, covering approximately 68% of the result range. The standard deviations of both proportions are somewhat dispersed. The average proportions of the reinforced steel weight to a concrete volume in both the normal distribution and the boxplot diagram are the same value at **129.51** kg/m^3. In the boxplot diagram in Fig. 5, the average proportions of the weight of reinforce steels to a concrete volume are shown as Q_1, Q_2, and Q_3. At the

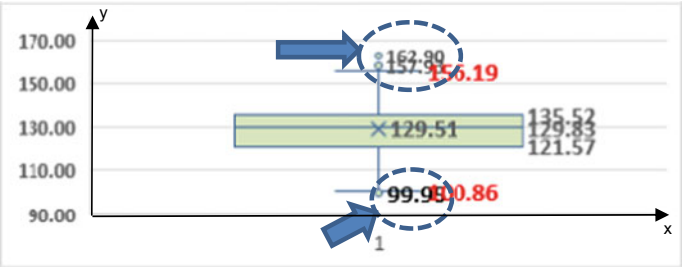

Fig. 5 Boxplot diagram shows the average proportion of the reinforced steel weight to the concrete volume (kg/m^3)

25th percentile, lower quartile $(Q_1)_{\text{steel/conc}} = \mathbf{121.57}$. At the 50th percentile, median $(Q_2)_{\text{steel/conc}} = \mathbf{129.83}$. At the 75th percentile, upper quartile $(Q_3)_{\text{steel/conc}} = \mathbf{135.52}$. The interquartile range (IQR) is a distance between the 75th and the 25th percentiles, the width of the square box covering approximately 50% of the result range. The maximum value is **162.90**. Outliers of **162.90**, **157.93** come from the fourth and the ninth house of 17 detached houses accounting for 2/17 or 11.76% of all values. By the way, the minimum value is **99.95** from the second house of 17 detached houses. So, the boxplot diagram shows in-depth results at a greater level than usual, especially by demonstrating the specific outlier values. The proportions of the reinforced steel weight to a construction area (kg/m^2) are described in the same manner. At the 25th percentile, lower quartile $(Q_1)_{\text{steel/area}} = \mathbf{50.79}$. At the 50th percentile, median $(Q_2)_{\text{steel/area}} = \mathbf{61.03}$. At the 75th percentile, upper quartile $(Q_3)_{\text{steel/area}} = \mathbf{67.47}$. The interquartile range (IQR) is a distance between the 75th and the 25th percentiles, the width of the square box covering approximately 50% of the result range. Extreme outliers are the maximum value **97.47** and **94.54** from the fourth and ninth houses of 17 detached houses, accounting for 2/17 or 11.76%. The outliers might result from an inaccurate QS or estimation. So, the boxplot diagram shows in-depth results at a greater level than usual, especially by demonstrating the specific outlier values.

4.5 An Average Proportion of a Formwork Usage to the Concrete Volume (m^2/m^3) and that of a Formwork Usage to a Construction Area (m^2/m^2)

From the data collection, verification, and analysis, the researchers focus on the average proportion of a formwork usage to the concrete volume (m^2/m^3) and that of a formwork usage to a construction area (m^2/m^2). From the result analysis on all 17 detached houses, the researchers found consistency in proportions of a formwork usage to the concrete volume and those of a formwork usage to a construction area, and the average proportions of both are **6.789 m^2/m^3** and **3.064 m^2/m^2**. From the outcome of descriptive statistics compared to the boxplot diagram,

$(\overline{x} \pm \text{SD})_{\text{formwork/conc}} = \mathbf{6.789 \pm 1.116} = \mathbf{7.905}, \mathbf{5.673}$ m^2/m^3, covering approximately 68% of the result range.

$(\overline{x} \pm \text{SD})_{\text{formwork/area}} = \mathbf{3.064 \pm 0.504} = \mathbf{3.568}, \mathbf{2.560}$ m^2/m^2, covering approximately 68% of the result range. From Figs. 6 and 7 and the boxplot diagram, the average proportions of a formwork usage to the concrete volume in both the normal distribution and the boxplot diagram are the same values at **6.79** m^2/m^3. In the boxplot diagram, in Fig. 6, the proportions of a formwork usage to the concrete volume are shown as Q_1, Q_2, and Q_3. At the 25th percentile, lower quartile $(Q_1)_{\text{formwork/conc}} =$ **6.130**. At the 50th percentile, median $(Q_2)_{\text{formwork/conc}} =$ **6.630**. At the 75th percentile, upper quartile $(Q_3)_{\text{formwork/conc}} =$ **7.420**. The interquartile range (IQR) is a distance between the 75th and the 25th percentiles, the width of the square box covering approximately 50% of the result range. The maximum value of **9.52** from the 17th detached house is an outlier, accounting for 1/17 or 5.882%. The outlier may be a result of an inaccurate QS or estimation, especially in term of quantities of a formwork usage. So, the boxplot diagram shows in-depth results at a greater level of than usual, especially by demonstrating the specific outlier value which requires the stakeholders to review the past data. From Fig. 7, the average proportions of a formwork usage to a construction area in both the normal distribution and the boxplot diagram are the same values at **3.06** m^2/m^2. In the boxplot diagram in Fig. 7, the average proportions of a formwork are shown as Q_1, Q_2, and Q_3. At the 25th percentile, lower quartile $(Q_1)_{\text{formwork/area}} =$ **2.650**. At the 50th percentile, median $(Q_2)_{\text{formwork/area}} =$ **2.970**. At the 75th percentile, upper quartile $(Q_3)_{\text{formwork/area}} =$ **3.410**. The interquartile range (IQR) is a distance between the 75th and the 25th percentiles, the width of the square box covering approximately 50% of the result range. No outliers are found.

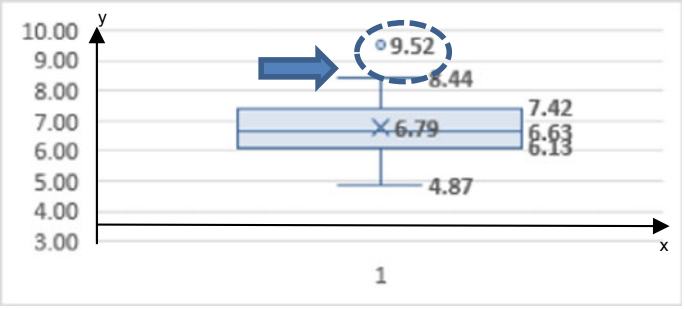

Fig. 6 Boxplot diagram shows the average proportion of a formwork usage to the concrete volume (m^2/m^3)

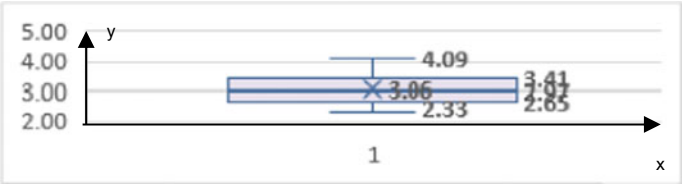

Fig. 7 Boxplot diagram shows the average proportion of a formwork usage to a construction area (m^2/m^2)

5 Conclusions

From the result analysis of the above items 4.1–4.5, the researchers described the entire conclusion in Table 3.

The average proportion of the concrete volume to a construction area is **0.459** m^3/m^2, 0.459 ± 0.084 = **0.543**, **0.375**, covering approximately 68% of the result range. The proportion is greater than 0.289, 0.22, (**0.196**, **0.246**) and **0.215** m^3/m^2 of [1, 2, 8, 9], respectively. A combination of the range of mean and the standard deviation give a greater level of confidence than the normal mean ($\overline{x}$) alone. Especially when combined with the boxplot diagram showing upper and lower outliers, the result can provide a greater level of reliance. The outliers in the upper or lower limit are to be omitted from further consideration. Next the average proportion of the reinforced steel weight to a construction area is **60.422** kg/m^2, close to **63.40** kg/m^2 of [8] but very different from **33.20** kg/m^2 of [9] and **27.30** kg/m^2 of [2]. The outliers from the upper limit were 97.47 and 94.54 kg/m^2, causing excessively high mean values. Next the average proportion of the reinforced steel weight to the concrete volume is **129.51** kg/m^3 (between **121.57–135.52** kg/m^3 in the boxplot diagram), less than **206–221** and **147.76** kg/m^3 of [8, 9], respectively, and close to **126.62–205.92** kg/m^3 of [1]. However, the outlier from the lower limit is **99.95** kg/m^3, and those from the upper limit are **162.90** and **157.93** kg/m^3. If these three values are eliminated, the proportion is reduced to **127.21** kg/m^3 close to the lower-boundary value of [1]. Thus, the average proportion of the reinforced steel weight (kg) to the concrete volume (m^3) is one of the important constraints that the contractors are widely interested. Next, the average proportion of a formwork usage to the concrete volume is **6.79** m^2/m^3 (between **7.420** and **6.130** m^2/m^3 from the boxplot diagram), less than 12.17 m^2/m^3 of [9] close to **7.16–8.78** m^2/m^3 of [1]. The average proportion of a formwork usage to a construction area is **3.06** m^2/m^2 (between **3.41**0and **2.650** m^2/m^2 from the boxplot diagram), close to 2.53 m^2/m^2 of [2]. So using one mean alone may not be sufficient for consideration. With mean ± SD value and the boxplot diagram, the level of confidence can be increased. And with quartile and interquartile range (IQR) sections, the result can cover a 50% level of confidence based on basic statistical theory.

Table 3 Comparison between descriptive statistics ($\overline{x} \pm$ SD) and results of boxplot diagrams with parameters (Q_1, Q_2, and Q_3)

Descriptive Statistics ($\overline{x} \pm$ SD)	Boxplot Diagrams with Parameters
5.1a The average proportion of the lean concrete volume to a construction area versus that of the compacted sand volume $(\overline{x} \pm \text{SD})_{\text{lean}} = \mathbf{0.044} \pm 0.008 = \mathbf{0.052}, \mathbf{0.036}$ m^3/m^2, covering approximately 68% of the result range $(\overline{x} \pm \text{SD})_{\text{sand}} = \mathbf{0.087} \pm 0.017 = \mathbf{0.104}, \mathbf{0.070}$ m^3/m^2, covering approximately 68% of the result range	**5.1b** The boxplot diagram is a comparison between the average proportion of the lean concrete and that of the compacted sand $\overline{x}_{\text{lean}} = \mathbf{0.044}$ m^3/m^2 $(Q_1)_{\text{lean}} = \mathbf{0.040}$, $(Q_2)_{\text{lean}} = \mathbf{0.046}$, and $(Q_3)_{\text{lean}} = \mathbf{0.048}$, covering approximately 50% of the result range $\overline{x}_{\text{sand}} = \mathbf{0.087}$ m^3/m^2 $(Q_1)_{\text{sand}} = \mathbf{0.079}$, $(Q_2)_{\text{sand}} = \mathbf{0.091,}$ and $(Q_3)_{\text{sand}} = \mathbf{0.096}$, covering approximately 50% of the result range
5.2a The average percent proportion of the concrete beam to the total concrete versus that of a concrete slab $(\overline{x} \pm \text{SD})_{\text{beam}} = \mathbf{0.351} \pm 0.078 = \mathbf{0.429}, \mathbf{0.273}$, covering approximately 68% of the result range $(\overline{x} \pm \text{SD})_{\text{slab}} = \mathbf{0.431} \pm 0.089 = \mathbf{0.520}, \mathbf{0.342}$, covering approximately 68% of the result range **Remark**: A proportion has to be converted to %	**5.2b** The boxplot diagram is a comparison between the average percent proportion of a concrete beam and that of a concrete slab $\overline{x}_{\text{beam}} = \mathbf{0.351}$ **(35.10%)** $(Q_1)_{\text{beam}} = \mathbf{30.79\%}$, $(Q_2)_{\text{beam}} = \mathbf{34.56\%,}$ and $(Q_3)_{\text{beam}} = \mathbf{40.80\%}$, covering approximately 50% of the result range $\overline{x}_{\text{slab}} = \mathbf{0.431}$ **(43.11%)** $(Q_1)_{\text{slab}} = \mathbf{36.24\%}$, $(Q_2)_{\text{slab}} = \mathbf{44.41\%,}$ and $(Q_3)_{\text{slab}} = \mathbf{47.53\%}$, covering approximately 50% of the result range **Lower outlier is **15.43%**, upper outlier **67.24%**
5.3a The average proportion of the concrete volume to a construction area $(\overline{x} \pm \text{SD})_{\text{conc/area}} = \mathbf{0.459} \pm 0.084 = \mathbf{0.543}, \mathbf{0.375}$ m^3/m^2, covering approximately 68% of the result range	**5.3b** The boxplot diagram is the average proportion of the concrete volume to a construction area $\overline{x}_{\text{conc/area}} = \mathbf{0.459}$ m^3/m^2 $(Q_1)_{\text{conc/area}} = \mathbf{0.410}$, $(Q_2)_{\text{conc/area}} = \mathbf{0.460,}$ and $(Q_3)_{\text{conc/area}} = \mathbf{0.515}$, covering approximately 50% of the result range **Remark:** No outliers

(continued)

Table 3 (continued)

Descriptive Statistics ($\overline{x} \pm$ SD)	Boxplot Diagrams with Parameters
5.4a The average proportion of the reinforced steel weight to the concrete volume (kg/m^3) and that of the reinforced steel weight to a construction area (kg/m^2) $(\overline{x} \pm \text{SD})_{\text{steel/conc}} = \mathbf{129.513} \pm 18.285 = \mathbf{147.798, 111.228}$ kg/m^3, covering approximately 68% of the result range $(\overline{x} \pm \text{SD})_{\text{steel/area}} = \mathbf{60.422} \pm 17.723 = \mathbf{78.145, 42.699}$ kg/m^2, covering approximately 68% of the result range **5.5a** The average proportion of a formwork usage to the concrete volume (m^2/m^3) and that of a formwork usage to a construction area (m^2/m^2) $(\overline{x} \pm \text{SD})_{\text{formwork/conc}} = \mathbf{6.789} \pm 1.116 = \mathbf{7.905, 5.673}$ m^2/m^3, covering approximately 68% of the result range $(\overline{x} \pm \text{SD})_{\text{formwork/area}} = \mathbf{3.064} \pm 0.504 = \mathbf{3.568, 2.560}$ m^2/m^2, covering approximately 68% of the result range	**5.4b** The boxplot diagram is the average proportion of reinforced steels in kg/m^3 and that of reinforced steels in kg/m^2 $\overline{x}_{\text{steel/conc}} = \mathbf{129.51}$ kg/m^3 $(Q_1)_{\text{steel/conc}} = \mathbf{121.57}$, $(Q_2)_{\text{steel/conc}} = \mathbf{129.83,}$ and $(Q_3)_{\text{steel/conc}} = \mathbf{135.52}$, covering approximately 50% of the result range **Lower outlier is **99.95**, upper **162.90**, **157.93** kg/m^3 $\overline{x}_{\text{steel/area}} = \mathbf{60.42}$ kg/m^2 $(Q_1)_{\text{steel/area}} = \mathbf{50.79}$, $(Q_2)_{\text{steel/area}} = \mathbf{61.03,}$ and $(Q_3)_{\text{steel/area}} = \mathbf{67.47}$, covering approximately 50% of the result range **Upper outliers are **97.47**, **94.54**. kg/m^2 **5.5b** The boxplot diagram is the average proportion of a formwork usage in m^2/m^3 and that of a formwork usage in m^2/m^2 $\overline{x}_{\text{formwork/conc}} = \mathbf{6.79}$ m^2/m^3 $(Q_1)_{\text{formwork/conc}} = \mathbf{6.130}$, $(Q_2)_{\text{formwork/conc}} = \mathbf{6.630,}$ and $(Q_3)_{\text{formwork/conc}} = \mathbf{7.420}$, covering approximately 50% of the result range **Upper outlier is **9.52** kg/m^2 $\overline{x}_{\text{formwork/area}} = \mathbf{3.06}$ m^2/m^2 $(Q_1)_{\text{formwork/area}} = \mathbf{2.650}$, $(Q_2)_{\text{formwork/area}} = \mathbf{2.970,}$ and $(Q_3)_{\text{formwork/area}} = \mathbf{3.41}0$, covering approximately 50% of the result range **Remark**: No outliers

References

1. Prapaporn W (2018) The ratio of construction quantity analysis for reinforce concrete building. In: Conference: the 23rd national convention on civil engineering at Nakhon Nayok Thailand
2. Chaivijarn C, Jarusbumrungroj P, Woracharoensin T, Sirisonthi A, Wongsopit K (2017) The Comparison study of unit quantities estimation for 5–8-and 3–5-storey residential buildings. Kasem Bundit Eng J 7(2)
3. Quantity and rate analysis for reinforced concrete construction. https://theconstructor.org/practical-guide/rate-analysis-for-reinforced-concrete/6954/
4. Vetter TR (2017) Descriptive statistics: reporting the answers to the 5 basic questions of who, what, why, when, where, and a sixth, so what? Anesth Analg 125(5):1797–1802
5. Hintze JL, Nelson RD (1998) Violin plots: a boxplot-density trace synergism. Am Stat 52(2):181–184
6. Lem S, Onghena P, Verschaffel L, Van Dooren W (2013) The heuristic interpretation of boxplots. Learn Instr 26:22–35
7. Business/Industry Outlook 2021–2023: Construction Business 08 February 2021. https://www.krungsri.com/th/research/industry/industry-outlook/Construction-Construction-Materials/Construction-Contractors/IO/io-Construction-Contractors-21
8. Suntornsamai P (2003) Guide for estimating building works (roughly method), 1st edn. Technology Promotion Association (Thailand-Japan)
9. Dangprasert S, et al (2010) A study of unit quantities estimation for 5–8 torey residential building. In: 15th National Civil Engineering Conference. Ubon Ratchathani University
10. Thiruvengadam V, Guite T (2017) Quantity and cost modelling of reinforced concrete buildings of 12–20 storey designed for seismic effects. In: 16th World conference on earthquake, Santiago Chile

Performance-Based Building Design: A Review

Sulfiah Dwi Astarini and Christiono Utomo

Abstract High-performance buildings have become a topic of interest and are constantly undergoing research developments. One of the design concepts for achieving high-performance buildings is known as performance-based building design (PBBD). PBBD is a design concept that facilitates integrated construction actors from the design stage to the operational stage. In the performance-based building design literature, research conducting a literature review on this topic is still scarce, so the purpose of this study is to conduct a review of the performance-based building design literature for a period of 15 years (2006–2021). Based on the literature review methodology, a total of 66 Scopus indexed research papers were identified. The findings show that there are three themes that interest researchers in discussing PBBD research, namely the definition of performance goals, design performance processes, and BIM support in performance-based design. The results of this study are expected to increase understanding in the area of performance-based building design through a literature review and contribute to design science in construction project management.

Keywords PBBD · Performative design · Literature review

1 Background

High-performance buildings have become a topic of interest recently and have developed among researchers and practitioners in the construction field. This is due to the awareness of environmental impacts that mostly come from the construction sector and the concern of industry players to provide healthy and safe buildings for building users/occupants, e.g., buildings consume 40% of global energy and produce 1/3 of GHG emissions [1]. The emergence of a design strategy known as performance-based

S. D. Astarini · C. Utomo (✉)
Department of Civil Engineering, Institut Teknologi Sepuluh Nopember, Surabaya 60111, Indonesia
e-mail: Christiono@ce.its.ac.id

T. Kang (ed.), *Proceedings of 5th International Conference on Civil Engineering and Architecture*, Lecture Notes in Civil Engineering 369,
https://doi.org/10.1007/978-981-99-4049-3_29

building design (PBBD) has received special attention due to its practice of using a building performance approach. In this context, the use of a performance approach guides the project implementation process, so that the resulting building can perform its functions in accordance with expectations and objectives. In its implementation, PBBD practice involves various design experts to translate the needs of clients and building users into performance goals. Furthermore, the performance objectives are integrated into the building design and their achievement is evaluated through the performance simulation measurement method.

According to de Wilde [2], building performance depends on the analysis of building performance which is an important factor for the design, construction, and operational processes that can realize the expectations of the various stakeholders involved. High-performance buildings among researchers refer to sustainable buildings or green buildings that have certificates such as LEED, BREAAM, and ASHRAE, where these buildings are generally energy efficient and have low operating costs. Various design strategies are developed to support the achievement of a set of performance requirements that meet the ratings of the certificate assessment. On the other hand, PBBD is a design concept whose practice is based on a framework of objectives. Researcher Kalay [3] mentions PBBD as a design approach that focuses on the function and aesthetics of the building, while at the same time ensuring that environmental performance is met. To achieve high-performance buildings, actors in this sector cooperate and integrate, which leads to the achievement of the planned objectives starting from the design to the operational stages [4].

In theory, researchers have studied the field of PBBD research, such as on research Ercan and Elias-Ozkan [5] study which explored the ability to generate design alternatives in a short time based on performance-based design workflows. Researchers Astarini et al. [6] analyze the relationship between PBBD theory and retail property management strategies. Other researchers show how to improve PBBD practice through the use of BIM [7], and automation systems using a multi-agent system (MAS) in the architectural design process [8]. There were challenges found related to the implementation of PBBD, where the fundamental problem was the lack of knowledge and skills of designers in providing solutions related to building performance [9], as well as interoperability issues that obstruct the exchange of data, information, and knowledge during the design process [10]. Overcoming these problems, researchers Bashouri and Duncan [11] developed a knowledge-sharing model between designers, where the resulting model facilitates the creation of a learning environment, thereby increasing innovation and minimizing the occurrence of design errors. Researcher Jin et al. [12] summarize the proposed approach, including using programming, ontologies, and semantics, as well as plug-in systems, in overcoming interoperability problems. However, currently, there is still not much research that has been done to verify whether the proposed approach can affect the successful implementation of performance-based design.

Furthermore, the purpose of this study is to conduct a literature review of PBBD research. This is based on the limited number of studies that have conducted a literature review in this research area. The literature review is a method that can be used to summarize research on one topic, identify knowledge gaps, and provide an overview

of future research directions [13]. The literature review carried out in this study was to review studies on the topic of PBBD published in the period 2006–2021. First of all, this study describes the methods used in the research, then discusses the PBBD research found through the exploration process, and finally concludes the research results.

2 Method

This paper conducts a literature review related to the topic of PBBD from 2006 to 2021. In conducting a literature review, the first step of this research focuses on selecting a search engine to select journals and papers that match the keywords. After that, the next step is to set limits on keywords that match the research topic. The last stage is to classify the studies found based on the search results. The following Fig. 1 is the stage of the research screening process.

2.1 Database and Keyword Selection

This study investigates PBBD articles published by searching various databases. Searches were made on databases including Science Direct, Wiley Online, Taylor & Francis, ASCE, and Scopus. The database is widely used by researchers in conducting similar literature reviews [14]. The search was conducted based on different title keywords, which included: "performance-based building design," "high-performance design," "architectural design performance," and "performance design strategy." Following the method used by Bao et al. [15], the focus of the search for articles was limited to titles and abstracts published in journals of architectural design, engineering design, and construction project management, so journals that were not related to the specified ones could be excluded. A total of 186 relevant articles were found based on keyword searches, and after going through the title

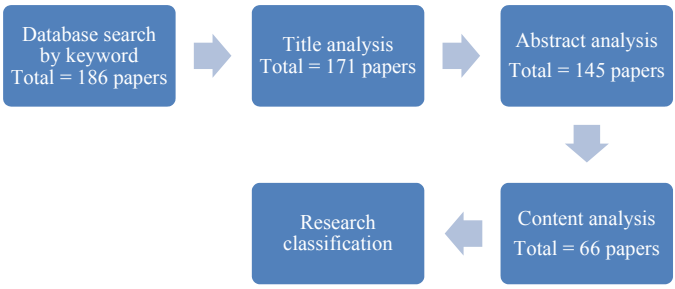

Fig. 1 Stages of the research article screening process

screening process, 15 papers were excluded, resulting in 171 papers. The next step is to carry out the abstract analysis process, resulting in 145 articles. Based on the abstract review, as many as 79 research articles were excluded, so 66 papers were obtained that were further analyzed based on the content of the research.

2.2 Content Analysis and Research Classification

Following the methodology developed by Ahmed et al. [14], before classifying research, the articles reviewed must have the following criteria: (1) articles published in English, (2) published articles, namely before classifying research, the articles being reviewed must have several criteria. The following criteria: (1) articles published in English, (2) articles published in peer-reviewed journals, (3) related to science in architectural design, engineering design, and construction project management, (4), published articles in Scopus indexed journals, and (5) containing specific keywords. Based on these criteria, 66 articles were found for further analysis.

Articles that meet the criteria are then analyzed based on the content that discusses the point of view of performance-based design on construction projects. Research classification is done by identifying the themes discussed in PBBD research topics. Research that discusses the same theme is assigned to the appropriate group. Furthermore, the research being reviewed is given a code that best describes the research theme discussed by the researcher.

3 Result and Discussion

Based on the literature search, there are 66 articles relevant related to performance-based building design. The articles collected are from 2006 to 2021. Next, grouping is carried out based on the name of the journal that publishes related research, and the year of publication based on suggestions [14]. Table 1 shows a summary of publications by journal name and where the article was published, and Fig. 2 shows the number of papers published each year.

Based on Table 1, it can be seen that the journals that publish research papers that most discuss the topic of PBBD are the journal of automation construction, followed journal of architectural engineering and design management, and energy and buildings.

Based on the results of content analysis, it was found that three themes dominated research related to performance-based design for 15 years. The three themes are performance objectives, process design performance, and BIM support for design performance, as illustrated in Fig. 3. The three themes are further discussed as follows.

Table 1 Summary of journals publications

Publisher/database	Journal	No. of article
Wiley	Earthquake Engineering and Structural Dynamics	2
	Fire and Materials	1
ASCE	Journal of Performance of Constructed Facilities	1
	Journal of Architectural Engineering	1
	Journal of Construction Engineering and Management	3
	Journal of Structural Engineering	1
	Journal of Management in Engineering	1
ScienceDirect	Automation in Construction	10
	Design Studies	3
	Probabilistic Engineering Mechanics	1
	Procedia Engineering	4
	Energy Procedia	1
	Engineering Structures	2
	Building and Environment	3
	Journal of Wind Engineering and Industrial Aerodynamics	1
	Journal of Building Engineering	1
	Structural Safety	2
	Energy and Buildings	5
	Structures	1
	International Journal of Sustainable Built Environment	1
Taylor & Francis	Architectural Engineering and Design Management	8
	Construction Management and Economics	1
	Journal of Civil Engineering and Management	1
	Advances in Building Energy Research	1
	Journal of Building Performance Simulation	1
	Building Research and Information	1
	Journal of Earthquake Engineering	1
	Architectural Science Review	1
Tsing Hua University	Building Simulation	2
Springer	International Journal on Interactive Design and Manufacturing	1
MDPI	Sustainability	3
Scopus	ARPN Journal of Engineering and Applied Sciences	1
	Total	66

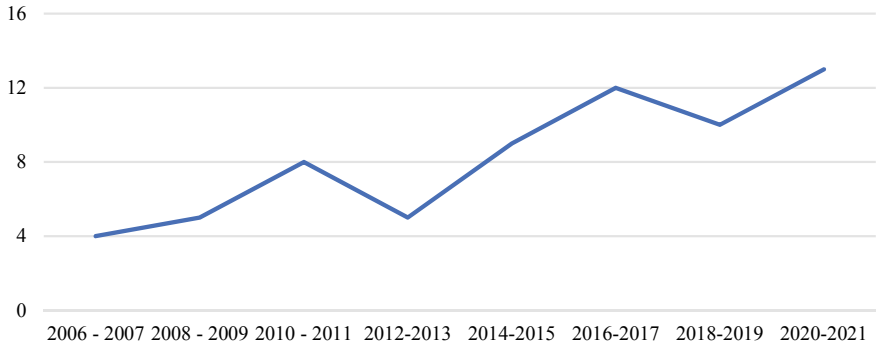

Fig. 2 Summary of the year publication the articles PBBD

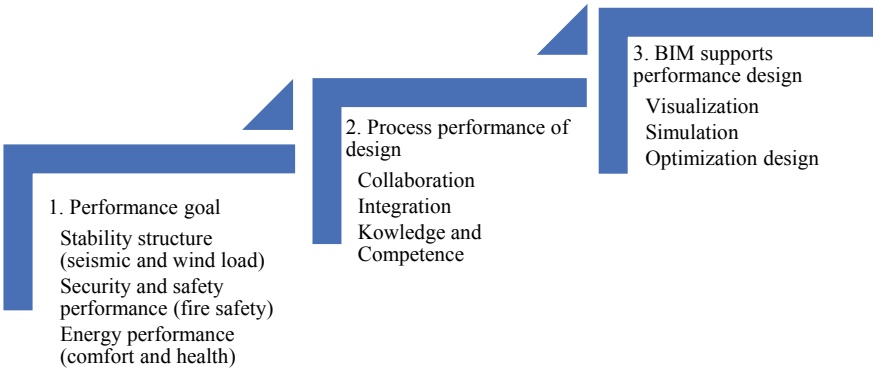

Fig. 3 PBBD main theme

3.1 Performance Goal

The success of the current project is not only focused on cost, time, and quality but also emphasizes specific goals, where the interests of building users/occupants have been considered along with the sustainability of the building. Formulating performance requirements in the design phase is the first stage taken in setting performance objectives as a measure of project success. Performance requirements are the key point where the user/occupant requirements of the building are translated and integrated into the design [16]. PBBD research related to design performance objectives is currently still focusing on the design process that takes into account the analysis of building structures with the aim to minimize economic losses and loss of life due to natural hazards such as earthquakes and/or hazards due to human negligence such as fire. According to Thompson and Bank [17], concern about the function of the building is increasing along with the decline in facility performance due to unexpected events. In addition, the safety of users/occupants is a priority due to the high

level of worry and risk felt by building users occupying the building. Not only is the reliability of the building structure taken into account with the aim of building security and occupant safety, but the PBBD concept is also used as a method in building design to reduce greenhouse gas emissions and create healthy buildings for users/occupants during the life of the building. In the process of achieving these goals, researchers Turrin et al. [18] develop a design that includes energy performance where the results can measure energy efficiency and take into account user/occupant comfort related to building thermal comfort and daytime comfort through the required level of illumination based on visual aspects. Thus, various set performance goals are targeted for the designer to ensure that the planned performance of the building can be achieved.

3.2 Process of Performance Design

Several studies within the scope of PBBD also investigate the performance processes that drive the achievement of design results that are in line with expectations and objectives. The study conducted by Syamil et al. [19] found that process performance can be seen based on teamwork behavior or activities carried out in a team/organization during design development. One of the designer activities that is considered to increase client satisfaction as a project success criterion is how designers can work together through collaboration [20]. Collaboration has been considered one of the factors that affect quality in the design process, because of its function in distributing design tasks based on the roles and responsibilities of the designer [21]. The existence of a division of tasks during the design process can improve communication because design actors know what and where the information can be obtained, so that there is an opportunity for design integration. In addition, researchers Arayici et al. [10] state the importance of collaboration and its relation to integration, especially with regard to the technological tools used by designers in analyzing building performance. In this context, building performance analysis is an important element to ensure that the building meets the needs of users/occupants through performance requirements. In other words, performance analysis is carried out to ensure that the design team sets performance goals before carrying out design activities, and further checks the resulting design whether has met the achievement of these goals [2]. In addition to design collaboration and integration, knowledge and competence are also highlighted as factors influencing process performance in design. According to Dubois et al. [22], these factors form the basis of the problem-solving process and the ability to develop design solutions. The knowledge and experience of participants (clients and designers) on the project being carried out can improve design performance, so that it has a chance of project success [20].

3.3 BIM Supports Performance Design

The performance-based design approach is supported by the use of BIM, which in the process requires a building performance analysis system. BIM has been recognized as a method that integrates processes and information based object throughout the building life cycle. BIM in modelling building performance during the design process plays an important role in providing the information needed by designers, so as to improve design performance and overall building performance [10]. Researchers Jung et al. [7] summarized the benefits of BIM that supports design performance, there are facilitating joint design development, accurate information as a basis for decision making, facilitating information sharing, increasing collaboration, communication, coordination, quality of design, and minimizing risk throughout the project life cycle. Researchers Oduyemi and Okoroh [23] stated that, through the use of BIM, designers can detect design errors early and provide solutions that can minimize the possibility of project failure. The ability of BIM is therefore utilized by designers to improve their design processes through optimal design selection. One of the uses of BIM in a performance-based design approach is as a visualization tool, building performance simulation, and design optimization. Visualization techniques provide shared understanding and minimize the occurrence of interdisciplinary problems, and thereby increasing effective communication between designers [24]. Design simulation is used to explore and predict several aspects of building performance which is implemented into the design to achieve design alternatives [23]. Design optimization is used because of its role in considering trade-offs in complex design processes [25].

4 Conclusion

This study conducted a literature review within the scope of PBBD during the period 2006–2021. The purpose of this study is to identify related studies and provide researchers with an understanding of interesting themes on the topic of PBBD. Based on the literature analysis, as many as 66 papers were reviewed in detail and classified based on each of the themes raised. The results of the literature review show that the achievement of performance goals, process design performance, and BIM support in PBBD practices are themes discussed by many researchers. There are research gaps found in the PBBD study. The various studies reviewed are generally limited to designer stakeholders, and the role of stakeholder property management and facility management in responding to PBBD has not been widely highlighted by researchers. However, the involvement of all stakeholders based on their role is a bridge to integrating all participants, from design to operation in producing high-performance buildings.

Furthermore, this research is expected to contribute to the development of science, in particular, to pave the way for related research to understand the various techniques and strategies used in the PBBD process. The limitation of this research is that the

reviewed papers are based on Scopus-indexed publications, so research outside this scope is excluded, which allows for research bias. Future research could focus on one theme and review it in depth to provide a better understanding of PBBD practice.

Acknowledgements The authors would like to be thankful for the research grants given by the 2022 Doctoral Dissertation Research Grant, Program of Riset Dasar Kompetitif Nasional 2022 of the Ministry of National Education, and Riset Keilmuan ITS.

References

1. Economidou M, Todeschi V, Bertoldi P, Agostino DD, Zangheri P, Castellazzi L (2020) Review of 50 years of EU energy efficiency policies for buildings. Energy Build 225:110322
2. de Wilde P (2019) Ten questions concerning building performance analysis. Build Environ 153:110–117
3. Kalay YE (1999) Performance-based design. Autom Constr 8:395–409
4. Bakens W, Foliente G, Jasuja M (2005) Engaging stakeholders in performance-based building: lessons from the performance-based building (PeBBu) network. Build Res Inform 33(2):149–158
5. Ercan B, Elias-Ozkan ST (2015) Performance-based parametric design explorations: a method for generating appropriate building components. Des Stud 38:33–53
6. Astarini SD, Utomo C, Negoro NP, Sari AF, Rohman MA (2020) The influence of performance-based building design on the strategy of retail property in indonesia. Sustainability 12(21):1–15
7. Jung N, Häkkinen T, Rekola M (2018) Extending capabilities of BIM to support performance based design. J Inform Technol Constr 23:16–52
8. Gerber DJ, Pantazis E, Wang A (2017) A multi-agent approach for performance based architecture: design exploring geometry, user, and environmental agencies in façades. Autom Constr 76:45–58
9. Ataman C, Dino İG (2021) Performative design processes in architectural practices in Turkey: architects' perception. Archit Eng Design Manage
10. Arayici Y, Fernando T, Munoz V, Bassanino M (2018) Interoperability specification development for integrated BIM use in performance based design. Autom Constr 85:167–181
11. Bashouri J, Duncan GW (2014) A model for sharing knowledge in architectural firms. Constr Innov 14(2):168–185
12. Jin R, Zhong B, Ma L, Hashemi A, Ding L (2019) Integrating BIM with building performance analysis in project life-cycle. Autom Constr 106:102861
13. Muller MF, Esmanioto F, Huber N, Loures ER, Canciglieri O (2019) A systematic literature review of interoperability in the green building information modeling lifecycle. J Clean Prod 223:397–412
14. Ahmed R, Philbin SP, Cheema FEA (2021) Systematic literature review of project manager's leadership competencies. Eng Constr Archit Manage 28(1):1–30
15. Bao F, Chan APC, Chen C, Darko A (2018) Review of public-private partnership literature from a project lifecycle perspective. J Infrastruct Syst 24(3):04018008
16. Becker R (2008) Fundamentals of performance-based building design. Build Simul 1(4):356–371
17. Thompson BP, Bank LC (2007) Risk perception in performance-based building design and applications to terrorism-resistant design. J Perform Constr Facil 21(1):61–69
18. Turrin M, Von Buelow P, Kilian A, Stouffs R (2012) Performative skins for passive climatic comfort: a parametric design process. Autom Constr 22:36–50
19. Syamil A, Doll WJ, Apigian CH (2004) Process performance in product development: measures and impacts. Eur J Innov Manag 7(3):205–217

20. Kärnä S, Junnonen JM (2017) Designers' performance evaluation in construction projects. Eng Constr Archit Manag 24(1):154–169
21. Müller R, Jugdev K (2012) Critical success factors in projects: Pinto, Slevin, and Prescott—the elucidation of project success. Int J Manag Proj Bus 5(4):757–775
22. Dubois S, Maranzana N, Gartiser N, De Guio R (2017) A global approach to manage the performance of the problem solving process in innovative design. Int J Interact Des Manuf 11(2):351–363
23. Oduyemi O, Okoroh M (2016) Building performance modelling for sustainable building design. Int J Sustain Built Environ 5(2):461–469
24. Korkmaz S, Messner JI, Riley DR, Magent C (2010) High-performance green building design process modeling and integrated use of visualization tools. J Archit Eng 16(1):37–45
25. Oxman R (2007) A PERFORMANCE-based model in digital design: per-formative—design beyond aesthetic. Archit Eng Design Manage 3(3):169–180

Application of BIM Technology in Optimal Design under EPC Mode

Xin Zou, Rong Guo, and Chen Gong

Abstract To get rid of the predicament of prefabricated building design under the EPC mode, solve the lack of related standardized design system and the problem of mutual restriction among the participants, reduce the workload of the design team, and give full play to the advantages of prefabricated buildings, it is necessary to introduce the BIM technology into the industry of prefabricated buildings. By establishing standardized design modules for prefabricated buildings based on the BIM technology platform, and establishing a BIM information design management system, it is possible to realize information and data sharing through the project database which is helpful to analyze and discuss the optimization plans for each control part, and in-depth integration with other majors. Based on practical verification, the types of component specifications can be reduced and the construction period can be shortened, meanwhile, the communication efficiency of each major will be improved and the construction costs will be reduced, and the problems of integration among various majors can be solved effectively. Under the EPC mode, by introducing BIM technology into the prefabricated building design, it is possible to promote the collaborative design of all participants at all stages and give full play to the advantages of prefabricated buildings, and also, provide a certain convenience for later procedures.

Keywords Prefabricated building · BIM · Standardized module · EPC

X. Zou · R. Guo
Guangdong Innovative Technical College, Dongguan, China

C. Gong (✉)
Guangzhou City University of Technology, Xuefu Road, Guangzhou, China
e-mail: 836835368@qq.com

T. Kang (ed.), *Proceedings of 5th International Conference on Civil Engineering and Architecture*, Lecture Notes in Civil Engineering 369,
https://doi.org/10.1007/978-981-99-4049-3_30

1 Introduction

With the continuous development of China's urbanization and rural construction, the construction industry, especially prefabricated buildings, has developed rapidly while the number of prefabricated buildings has also been increasing in recent years [1]. A prefabricated building refers to a building whose structural components are standardized and prefabricated in the factory, and are assembled at the construction site using the specified assembly process for construction [2]. The prefabricated buildings have the following advantages: short construction period, high production efficiency, high resource utilization, environmental protection, and matching the concept of sustainable social development. The features of prefabricated building construction include a large number of components, complex procedures, difficulties, and dynamic changes in information management [3]. In the construction industry, prefabricated building construction has become the mainstream of the current construction field in China. As a new architectural form, from a practical point of view, prefabricated buildings will fundamentally change the construction mode of traditional buildings, to respond to the new requirements of being green, environmentally friendly and safe, and provide people with more scientific livable space [4]. In recent years, many cities across the country have explored and practiced actively in the field of prefabricated buildings [5–8] and achieved initial results.

The domestic research on the issues related to prefabricated buildings began in the 1950s. During that period, China proposed to learn from the experience of the Soviet Union and other countries to promote prefabricated components and prefabricated buildings domestically. Since then, the prefabricated buildings in China have developed rapidly, and its application has been developed gradually from industrial buildings and public buildings to residential buildings [9]. There are many researches about prefabricated buildings in China: Sun [10], took Shenyang Honghui Garden as an example, carried out a project research on carbon emission evaluation in the physical and chemical stage, based on the established carbon emission evaluation model and carbon emission accounting method of prefabricated buildings; Xu [11], in the view of application advantages of prefabricated building construction technology, put forward three suggestions to optimize the technology effectively: learning and absorbing foreign advanced experience, increasing technical exchanges, and setting up special personnel to carry out on-site management; He [12] studied the building components procurement information integration, retrieval, and decision making under the building information modeling (BIM) environment, based on the development of e-commerce in the construction industry, as well as the characteristics of the building information and industrialization development; Zhang [13] mainly analyzed the application of BIM technology from the perspectives of cost control, cost accounting, and cost analysis, and verified the feasibility of cost management of BIM technology through taking one prefabricated building as research object. Zhou [14] studied the specific application of BIM technology in the

implementation of construction, from the points of four different stages of construction: project design, components production, components transportation, and installation. Cao [15] made comparative research between prefabrication technology and traditional technology with two typical residential buildings. Zhao [16] combined with the status and existing issues of prefabricated building management, proposed to build an engineering procurement construction (EPC) general contracting model which is suitable for prefabricated buildings, applied BIM technology in the EPC mode, studied the whole-process information management of designing, production, construction, operation, and maintenance of prefabricated buildings, and researched the possibilities of BIM technology in the EPC mode.

This article mainly aims at the dilemma of the prefabricated building design under the EPC mode, and proposes several applications of BIM technology in the optimal design of the prefabricated building under the EPC mode, and takes a commercial and residential integration project in Dongguan as an example to further explore the feasibility of the proposed applications, introduces the application of the information management platform at each stage, and analyzes various costs in the process of construction, so as to give better play to the advantages of prefabricated buildings.

2 The Dilemma of Prefabricated Building Design

2.1 Lack of Standard System of Prefabricated Building Design

The development of prefabricated buildings in China is currently in its infancy. In addition to showing great interest in prefabricated buildings, more and more companies start to practice. In recent years, China has also vigorously called for the development of prefabricated buildings and has issued several policies to encourage its development. Prefabricated buildings are facing golden opportunities for their development. Many companies are also actively exploring the development of prefabricated buildings, and however, most of them are doing this just to respond to related policies. They integrate the prefabricated building based on the overall design idea of the original cast-in-place building. In order to meet the so-called assembly rate, some of the cast-in-place components of the buildings are adjusted and split into prefabricated ones.

However, in the process of splitting, the various companies do not have the same standards, what is worse, there is no fixed splitting standard even between projects of the same enterprise, as a result, the design team needs to spend a lot of time to compare and analyze multiple designs, which greatly increases their work, and the final design scheme determined in practice will also have many problems such as lack of rationality. Many companies directly carry out the overall design on the basis of

traditional architectural design standards and then split it into prefabricated components, so the prefabricated design is not based on the advantages of prefabricated buildings.

The reason why this happens is that the development of prefabricated buildings in China is still in its infancy, and the design standard system is not perfect. The design teams do not have relatively unified design standards that can be based on. Instead, the prefabricated split is only carried out to increase the assembly rate in response to national policies. So as a result, the prefabricated buildings do not apply ideally and their development encounters a bottleneck.

One of the purposes of developing prefabricated buildings is to realize industrialized production in the field of architecture, which requires that the split prefabricated components conform to the characteristics of industrial production, which means they have to be repeatable and can be produced on large scale. At present, there is no unified standard to design prefabricated buildings in China. The enterprises design prefabricated buildings only based on the experience of the designers. And the rationality of splitting the prefabricated components varies a lot due to different designers. Since the development of prefabricated buildings in China is still in its infancy, most of the design teams lack relative experience. In addition to considering the safety, comfort and stability of the building during the splitting process, issues such as component production, transportation, hoisting, installation, and connection must also be comprehensively considered. If the design teams focus more on improving the assembly rate, it is easy to come out with split components with low rationality, which will result in poor convenience and poor operability during transportation, hoisting, and installation of components, and increase the difficulty of operation and construction. The prefabricated components must truly realize the standardized and large-scale modern production in order to truly give full play to the advantages of prefabricated buildings and realize the industrial revolution of the construction industry.

2.2 Designs of Various Disciplines Restrict Each Other

Engineering procurement construction (EPC) mode refers to a mode in which the owner entrusts the company to contract the procurement, design, construction, and other parts involved in one project. It has a high economic value which can greatly improve investment efficiency [17]. The application of EPC model for prefabricated buildings helps to fully consider the integration with procurement and construction during the design. This requires that the contracting company can fully integrate the design requirements of each participant in all stages of the EPC model and integrate various professional designs during the design stage. In traditional design mode, the design team needs to use the drawings as the carrier to communicate with the prefabricated component manufacturers, transportation and hoisting teams, construction teams, and other participating majors to solve the practical operability of the design scheme, and comprehensively consider the characteristics of each disciplines in the

design process. The drawings are used as the carrier, due to the large amount of project information and data and the design scheme involves a lot of majors, often there is a delay in information transmission during the communication process. As the participants in each stage cannot communicate with the design team in a timely manner, with the situation of low communication efficiency between the various majors within the design team, there is a certain lag in the communication, transmission, and feedback of information between the participants in each stage and each specialty. The design of prefabricated buildings is a dynamic change process that is constantly improving.

Due to the untimely information transmission, the efficiency of information communication between all parties involved is low, which increases the workload of the design stage and delays the design progress. It is necessary to adjust the communication carrier and communication channel to improve the communication efficiency and realize the sharing of information and data among all majors participated, thereby reduces the workload in the design stage due to untimely information communication.

3 The Application of BIM Technology in the Optimization Design of EPC Prefabricated Buildings

Building information modeling (BIM) is a new technology that is composed of various information and applied to development and management. Introducing BIM technology to the construction of prefabricated buildings can greatly improve the overall efficiency of engineering assembly construction [18]. In the EPC mode, the engineering data of each stage of the prefabricated building project can be effectively simulated in the project design stage. Through the sharing of this information and data, the participants at each stage can communicate effectively with the design team, and the majors within the design team can also communicate on the BIM information management platform, so as to promote fully communication among project design, procurement, and construction of prefabricated buildings during the design stage, and realize the sharing of project information and data, and improve the operability of the design scheme in production, transportation, hoisting, and installation in the future, so as to establish and provide a good foundation for the large-scale standardized production of prefabricated buildings.

3.1 Establish Standardized Design Modules

At present, there is no standardization system for prefabricated building design in China. In order to fully take advantage of prefabricated buildings, such as low cost, fast construction, and good quality, it is necessary to put forward higher requirements

for the rationality and practicability of prefabricated building design, and to establish a prefabricated building design standard system which the prefabricated building design can rely on for the modular design.

As the BIM technology is introduced into prefabricated buildings, enterprises can rely on the BIM technology platform to establish standardized design modules for projects at the design stage, thereby simplifying the whole design process. In the design stage, first of all, need to standardize the module design, appropriate adjustment of parameters can make it meet the design requirements, and at the same time meet the requirements of subsequent manufacturing, transportation, installation, etc., and then optimize and improve other design contents. The establishment of standardized design modules can be implemented according to the following ideas: first, the design team conducts a comprehensive analysis of the overall content of the prefabricated building design scheme, and sorts out all the standardized design modules that can be established for the prefabricated building; second, each major carries out the design of standardized modules and uses the BIM platform to establish a standardized design module to analyze its rationality; third, use the BIM platform to share information of the standardized design module and analysis results, and adjust the revision opinions proposed by each major on the original standardized design module scheme; at last, use the BIM information platform to share information with component manufacturers, hoisting, and transportation professionals and construction personnel, and make adjustments according to the suggestions from these participants to better ensure the operability and the economy of the prefabricated building design scheme in the component production and transportation stage, the convenience, and rationality of hoisting and installation in the construction stage, so as to maximize the optimization of standardized design modules. Modularization and standardization should be considered in the design process of standardized modules to reduce the number and types of standardized designed modules, in order to use as many prefabricated components of the same type and specification as possible during the design deepening stage, so as to reduce the kinds of prefabricated components and mold expenses, as well as reduce manufacturers' production lines and unify production standards, thereby to reduce the cost of prefabricated components.

3.2 Multi-discipline, Multi-stage, and Multi-agent Collaborative Design

Under the traditional contracting model, each major designs independently, and there is a lack of communication among the participants in all stages. Under the EPC mode, the contractor is responsible for the design, the procurement, and the construction of prefabricated projects, although it can increase the participation and communication of each major to a certain extent, due to the limitations of communication channels and communication methods, the communication of information is not timely. In the design stage, each major should fully consider the design suggestions of different

subjects, which requires improving communication channels and communication efficiency.

It is important to fully consider the operability and rationality of fabrication in the design stage of prefabricated buildings, and transportation and hoisting in the procurement stage of prefabricated buildings. The design team should actively communicate with prefabricated component manufacturers to avoid inconvenient production, transportation, hoisting difficulties, and other problems during subsequent stages due to unreasonable design components.

Therefore, the development of multi-professional, multi-subject, and multi-stage collaborative design can effectively give full play to the advantages of prefabricated buildings. With introduction BIM technology (Fig. 1), information sharing can be carried out and each participant at each stage participates into a collaborative design. The BIM technology is used at the design stage to determine the overall goals of design, procurement, and construction, and then comprehensive simulation analysis will be carried out to identify deviations and errors in advance, and multi-professional and multi-subject data will be carried out simultaneously corrected and updated to quickly feedback information to each professional design team, and correct the corresponding component parameters in the model in time, and then rely on the BIM platform to immediately carry out the revised risk inspection in order to feedback the inspection results quickly. Several rounds of cyclical dynamic collaboration like this can provide technical assurance and data support for the realization of the overall goals of the project (see Fig. 1).

For example, during the design of prefabricated components, as the data of the components is shared in the BIM software, the component manufacturer can propose corresponding plans for the production process and transportation plan of the component and provide reasonable suggestions for the component design. The construction party can submit operating specifications for hoisting, installation, and other processes and make professional suggestions for component design. Each professional design team uses the BIM model to analyze and inspect the plans and suggestions submitted by the manufacturer and the construction party, so as to realize

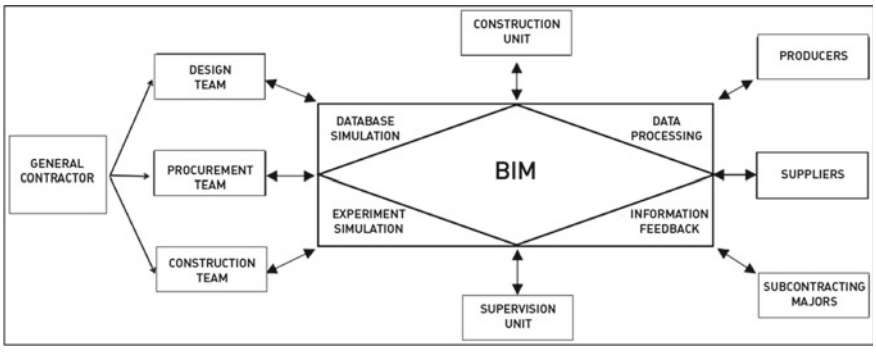

Fig. 1 Prefabricated building information design management platform under EPC mode

effective communication to adjust and modify component parameters to achieve the collaborative design as the ultimate goal.

3.3 Dynamic Deepening Design

The in-depth design of prefabricated buildings should be carried out through the BIM information platform according to the overall goals of the project and the standardized production and construction requirements. The whole design procedure can be divided into several steps: first of all, each professional carries out the initial in-depth design of each specialty based on the suggestions at each stage fades on the preliminary design results; second, use the BIM platform to establish preliminary design models of prefabricated buildings for each specialty and conduct comprehensive analysis; third, propose an overall optimization plan of the initial design results for each major, deepen the integration of one major with the others, and use the BIM platform to check and analyze the design scheme in order to solve the unreasonable design parameters at each stage of each major, and give feedback in time; last, use the BIM platform for dynamic tracking after adjusting the design professionally, and then recycle for further dynamic deepening design to achieve the final goal.

For example, in the design of mechanical and electrical majors, it is necessary to solve the problem of pipeline and equipment collision with other majors, optimize the design content in time, reasonably arrange the directions of equipment and pipelines, reserve reasonable space, and use the BIM platform for inspection and verification, adjust and re-inspect to complete the final design.

4 Engineering Application Practice

There is a commercial–residential integrated project in Dongguan which covers an area of about 19,000 m^2, and its total construction area is about 68,000 m^2. It is planned to have four residential buildings and one commercial office building. The residential units are apartments of 86–120 m^2 with three to four bedrooms. It is representative because the design scheme fully considers the characteristics of prefabricated buildings and take full advantages of prefabricated buildings: fast construction, good quality, and low cost. The project adopts the EPC contracting model, and the winning company is responsible for the design, procurement, and construction. In the design stage, contractors make full use of BIM technology to establish overall goals, which are quality goals and striving for high-quality provincial projects, for the integration of design, procurement, and construction. Meanwhile, the goal of the construction period is 450 days, the goal of cost is to reduce the production, transportation, hoisting, and construction costs of prefabricated building components and increase profit of the contract price by 3%, by adopting a reasonable design scheme

and ensuring quality. In the EPC mode, designs can be optimized from the initial so as to achieve the overall goals of the project.

4.1 Standardized Module Design

Using the BIM platform to establish the standard design module library, so that each design module has a certain uniformity and variability. The residential project uses three standardized design modules for the floor plan, three standardized design modules for the facade design, and eight standardized design modules of components including balcony, staircase, bay window, floor, wall panel, etc. With the use of standardized design modules, the types of component specifications can be reduced and the design efficiency can be improved. The combination of standardized modules can also meet the design diversity and variability. Meanwhile, with the application of prefabricated components increasing and the types of prefabricated components reducing, the cost of production can be controllable to a certain extent. The design team of this project carried out a standardized module optimization design of the original 35 prefabricated components through the BIM platform, and finally reduced the number of prefabricated components to 24 after repeated integration, and the cost per square is reduced by 374 RMB.

4.2 Multi-Professional and Multi-Subject Collaborative Design

This project established a database through the BIM platform and realized the sharing of project information and data. The contractor's design team, procurement team, construction team, construction unit, supervision unit, and prefabricated component manufacturers and suppliers can achieve multi-party communication through the BIM platform. Multi-subjects can analyze the design scheme and immediately give professional suggestions to the designers for further optimization, and then each major optimizes and adjusts their design accordingly and communicates with other majors in time to modify the BIM model data together and feedback the optimized design scheme to each participant for further inspection.

For example, in this project, the construction team analyzed the BIM platform and found that a fire water pipe in a basement crossed the fire shutter, they fed back this information to the design team in time and suggested that it should be changed to parking space laying. Meanwhile, the electro-mechanical design major adjusted the design plan in a timely manner and conducted integrated communication with other majors to finally determine a new adjustment plan accordingly, changing the parameter on the BIM platform and feedback to all participants.

4.3 Using BIM for Deepening Design

Each major of the project made detailed designs based on the preliminary design documents and then used the BIM platform to build a model, analyzed and discussed the optimization plan in the three-dimensional model, proposed a sub-item optimization plan for each control part, and then combined other majors for in-depth integration, solved the problem of integration and matching between various majors, and then applied BIM technology to adjust data in the model to achieve the design goal, e.g., the electro-mechanical major in this project needed to use the BIM platform to analyze the results and propose sub-item optimization schemes for electro-mechanical majors such as water, electricity, and heating, and then combined other majors to deepen the integration in architecture, structure, and decoration, so as to avoid the collision of various pipelines and equipment among different majors and arrange the pipelines more reasonable.

5 Conclusion

In the EPC mode, by introducing BIM technology into the design of prefabricated buildings, the general contractor can promote the collaborative design of all participants in multiple majors and stages, shorten the process of information transmission, improve communication efficiency, and provide technical support for the standardized module design of prefabricated buildings. The prefabricated building design is based on one overall goal to integrate design, procurement, and construction during the entire design process. With this goal achieved, the construction cost can be effectively reduced and the construction period can be shortened impressively. At the same time, the design scheme can also provide certain convenience and operability for the later production, transportation, hoisting, and installation of prefabricated components.

References

1. Li Z (2021) Discussion on the application of prefabricated building construction technology. Prefabricated Build Construct Technol 51(22):140–150
2. Liu X, Li C (2021) Research on the application of BIM technology in the construction of prefabricated buildings. Green Environm Protect Build Mater 4(11):98–99
3. Xue R, Wang X, Shi K (2018) Analysis of construction problems and countermeasures of prefabricated buildings based on building information modeling technology. Indust Architect 550(11):207–210
4. Chen Z, Wang X, Chen C (2021) Development and application of prefabricated buildings under the background of intelligent construction. Build Struct 12(22):160–168
5. Xue Q, He J, Fan C, Li X (2020) Research on the formulation of special planning for the development of prefabricated buildings in the Tibet autonomous Region. Indust Architect 568(05):94–101

6. Cui Y, Guo L (2021) Research on cost management under EPC management mode. Indust Architect 5(29):131–132
7. Liu M, Li W, Cao Y, He J (2021) Comparative analysis of demand guidance policies for Urban district-level prefabricated building industry chain. Build Struct 12(12):1–6
8. Chen G, Ma Y, Liu J, Sheng J (2021) Thinking and application of digital design and intelligent manufacturing of prefabricated buildings. Inform Technol Civ Construct Eng 11(24):1–9
9. Li W, Zhang T, Liu M (2022) Industrial policy simulation of prefabricated building based on system dynamics and evaluation of energy saving and emission reduction benefit. Indust Build 1(22):1–15
10. Sun Y, Liu J, Xia B (2017) Research on carbon emission evaluation of prefabricated buildings in the stage of construction. J Shenyang Jianzhu Univ 34(176):881–888
11. Xiaoming X (2021) Research on construction technology of prefabricated concrete residential buildings: comment on <construction technology of prefabricated concrete buildings>. Indust Architect 51(576):207–218
12. He D (2019) Research on information integration, retrieval and decision-making of building parts procurement under BIM environment. Dalian Univ Technol 17(4):67–73
13. Xinyu Z (2021) Application of BIM technology in cost control during the stage of production and transportation of assembly building. IOP Conf Ser Earth Environm Sci 769(4):439–446
14. Zhou J (2021) Research on lean construction of prefabricated buildings based on BIM. Construct Econom 42(03):41–46
15. Cao X, Li X, Zhu Y, Zhang Z (2015) A comparative study of environmental performance between prefabricated and traditional residential buildings in China. J Clean Prod 12(05):109–114
16. Zhao N (2021) Research on the management mode of EPC project of prefabricated building based on BIM technology. Open Access Library J 08(07):56–60
17. Liang X, Wang D, Dai J, Yan T (2021) Research on cost control of prefabricated building projects under EPC mode—taking an affordable housing project as an example. Construct Econom 42(11):56–60
18. Wang X, Tang Q, Dong Z, Wang R (2021) Research on the application of BIM+ technology in the construction management of prefabricated buildings. Construct Econom 42(11):19–24

Easing the Construction of Bubble Deck System—A Value Engineering

Francis Cayanan, John Robert D. Gabriel, Jener Kris T. Herrera, Josephine Rosette E. Uy, and Orlean G. Dela Cruz

Abstract The bubble deck system is one of the innovations that has benefited the construction sector globally for several decades. The bubble deck slab had been designed and constructed with hollow plastic bubbles in the middle to eliminate the concrete that does not perform any structural function while reducing the slab's self-weight. Value engineering is a technique used to examine how products and services function to provide users with the features they need at the lowest possible cost without compromising the necessary level of quality or performance, i.e., customer contentment. A product or service's value is determined by how appropriate its performance and price are; according to this definition, value can be raised by either improving performance or reducing costs; however, if a product lacks either adequate performance or cost, it is seen to have little value, and therefore, the technical aspect that affects its performance and cost should be taken into account while identifying it. This paper uses value study process flow diagram as the main scheme of the entire procedure, with the function analysis system technique (FAST) application to identify the critical components that can be modified. Compared to the existing process, the innovative product results improve the ease of applicability of the bubble material, where a smooth transition from storage, delivery, and distribution is a significant challenge both to the manufacturers and builders. Future researchers may use this

F. Cayanan · J. R. D. Gabriel · J. K. T. Herrera · J. R. E. Uy · O. G. Dela Cruz (✉)
Graduate School, Polytechnic University of the Philippines, Manila, Philippines
e-mail: ogdelacruz@pup.edu.ph

F. Cayanan
e-mail: engrkikocayanan2@gmail.com

J. R. D. Gabriel
e-mail: gabrielsteelconcrete1707@gmail.com

J. K. T. Herrera
e-mail: herrerajener96@gmail.com

F. Cayanan · J. R. D. Gabriel
Don Honorio Ventura State University, Bacolor, Philippines

J. K. T. Herrera · J. R. E. Uy
Department of Public Works and Highways, Bonifacio Drive, Port Area, Manila, Philippines

T. Kang (ed.), *Proceedings of 5th International Conference on Civil Engineering and Architecture*, Lecture Notes in Civil Engineering 369,
https://doi.org/10.1007/978-981-99-4049-3_31

paper as a reference to look further into alternative value engineering techniques or equivalent materials.

Keywords Bubble deck · Slab · Value engineering · Function analysis · Construction

1 Introduction

The slab has the most crucial role in any structure, carrying permanent and temporary objects and transmitting the loads to other structural elements. The slabs are the plate elements forming floors and roofs of the buildings supported by beams or walls [1]. In other literature, a slab is defined as an essential structural component in constructing an area inside a building. Monolithic reinforced concrete is commonly used in the construction of multi-story buildings. Buildings typically employ reinforced concrete for their slabs, and they are made of one piece of concrete and feature a cross-sectional design [2]. Under compression, concrete is strong; in tension, it is weak. This demonstrates that the tension zone's concrete is of limited usefulness, making the slab heavier and lessening its overall efficiency. Adding extra thickness in slabs will increase the dead load on the structure, and this weight, which is excessive and has no beneficial function, may be eliminated by adding voids to the slab [3]. A biaxial hollow core slab created in Denmark is a bubble deck slab. Jorgen Breuning developed a method of connecting air space and steel within a voided biaxial concrete slab. It is a new, durable, self-supporting concrete floor technology that may be utilized for story floors, roof floors, and ground floor slabs [4]. The invention of the bubble deck slab was revolutionary at the turn of the twentieth and twenty-first centuries. During the first decade, numerous kinds of research have been conducted on the use of the bubble deck innovation [5]. The same advantage was observed by Fatma et al., which stated that the bubble deck slab technique significantly lowers dead loads by removing concrete from the middle of a floor slab, which serves no structural purpose. In the middle of the slab, inefficient concrete is swapped out for hollow spheres made of high-density polyethylene (HDPE), which reduces dead loads and improves performance [6]. The bubble deck slab carries less weight but is very much satisfactory in slab construction considering the negligible difference in load-bearing capacity between them and the conventional [7]. Also, the same can be used in various structures, including residential, office, utility, and industrial systems. Offices, apartments, villas, hotels, schools, parking lots, hospitals, laboratories, and factories are just a few examples [8].

This study aims to evaluate the value engineering aspect of the existing bubble deck system and introduce potential significant modifications to ease its applicability both on the micro and macro scale of the construction industry. This can be effectively done by investigating its: construction time, durability, productivity, economy, accuracy system, environmental impact, safety, labor saving, seismic performance, and maintainability [9]. Value engineering is defined "as an analysis of the functions

of a program, project, system, product, item of equipment, building, facility, service, or supply of an executive agency, performed by a qualified agency or contractor personnel, directed at improving performance, reliability, quality, safety, and life-cycle costs". It can be successfully implemented at every stage of a product, system, or procedure's life cycle [10]. The outputs acquired from the study show that applying VE as a tool in enhancing the quality of a design, product, or service contributes positively to the efficiency and cost minimization of the overall project.

2 Related Literature

2.1 Essential Components, Installation, and Construction of the Bubble Deck System

The basic components of the bubble deck slab are portrayed in Fig. 1. These are the project-specific sizes of the top and bottom reinforcement meshes. They stand upright, joined by vertical grid braces called lattice girders, with the bubble void formers located in between them to keep up with their ideal position. A "bubble-reinforcement sandwich" is cast into the bottom layer of precast concrete to enclose the bottom mesh reinforcement and serve as permanent formwork within a portion of the finished slab depth [11]. A nonporous substance, high-density polyethylene bubble, does not chemically react with reinforcement or concrete [12]. As a result, due to the decreased concrete in the slab, the quick curing time may save additional time [13].

Depending on the manufacturer, there are two main ways to build plastic voided slab systems: a filigree approach, where some of the systems are precast off-site, and a method, where the complete system is built on site [15]. In either case, the production costs for the bubble deck slab have slightly increased due to the manufacturing and assembly of the HDPE spheres [5].

2.2 Advantages and Disadvantages of the Existing Bubble Deck System

Slab self-weight is reduced by 35% when spherical balls are used to fill voids in the middle of a slab, compared to a solid slab of the same thickness, without affecting bending strength or deflection behavior [8]. Additionally, presented a study on a bubble deck slab with elliptical balls. They discovered that the ratio of bubble diameter to thickness influences the behavior of bubble deck slabs [7]. Moreover, a separate experiment demonstrates that bubble deck has only 66% of the concrete volume due to the HDPE balls taking up space, and still having 87% of the bending stiffness of a comparable solid slab [5]. With beams and limited formwork, the bubble deck

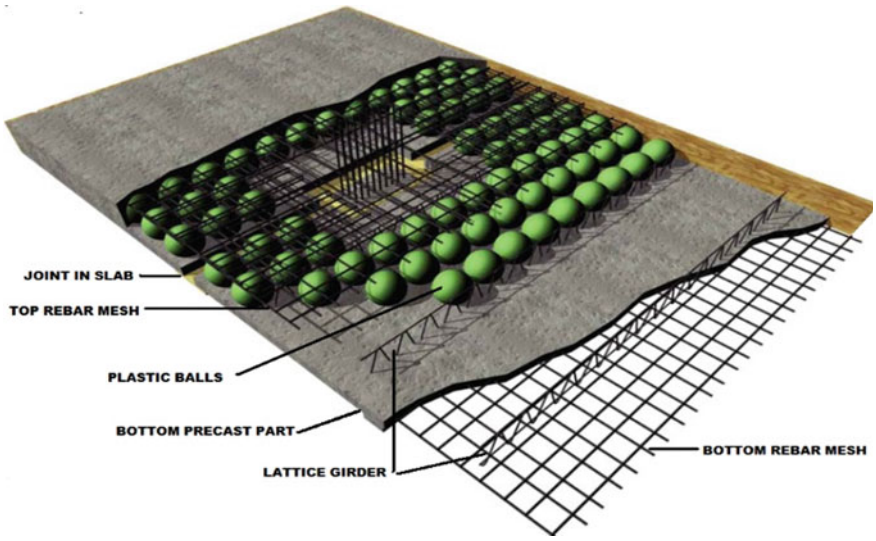

Fig. 1 Basic components of a bubble deck slab [14]

slab produces floors 20 percent faster in terms of construction time, resulting in a 12 percent reduction in construction costs and a 32 percent reduction in concrete use [6]. Furthermore, the bubble deck slab's load-bearing capacity versus the conventional RC slab with various bubble size to slab thickness ratios was assessed. The substantial amount used for traditional slab and bubble deck slab was compared, and it was found out that using a bubble deck ball of 60 mm diameter could save approximately 14% of money, while, for 70 mm diameter is 9.41% [16].

2.3 Existing and Proposed Alternatives for Bubble Material

The plastic balls, also known as void formers, are the most important component of the bubble deck slab system. It is typically a hollow sphere made of recycled high-density polyethylene (HDPE) or recycled polypropylene. Polypropylene and polyethylene were discovered to be ideal because they are lightweight and act as useful crack arresters. Polypropylene and polyethylene differ that the first has a greater melting point, is less heavy, and is not as strong as the latter [17]. Surendar and Ranjitham reported in a separate study that, in most instances, fully recyclable balls are used instead of burning plastics to reduce waste and environmental harm. A plastic ball is inexpensive when compared to HDPE [18]. However, these materials must be manufactured, delivered, and applied to the slab as a "whole" object. In effect, the transportation procedure from the production site to the actual project location will be a significant challenge due to the nature of the volume and shape of the object. If a more portable material will be used as a replacement but serves the

equivalent purpose and provides comparable strength, the logistics challenges can be considerably less if not resolved.

Isobutylene-isoprene rubber (IIR), also identified as butyl rubber, is widely used in the industry of tire, primarily for tubeless tires and inner tubes. Aside from the tire industry, butyl rubber-based elastomers exhibit excellent gas barriers as well as resistance to UV, oxidation, and ozone degradation [19]. In addition to this, polyvinyl chloride (PVC) has a greater economic advantages not only because of its inexpensive manufacturing expenses, but also because of its excellent properties, the most notable of which are relatively high resistance [20].

2.4 Value Engineering Scheme

VE is a method used to evaluate an item's or process's functions in order to identify the best value, or the strongest correlation between worth and cost. In other words, the "best value" can be expressed by a product or process that consistently performs the necessary essential function while having the lowest life-cycle cost [10]. Figure 2 depicts the flow diagram of the value study process.

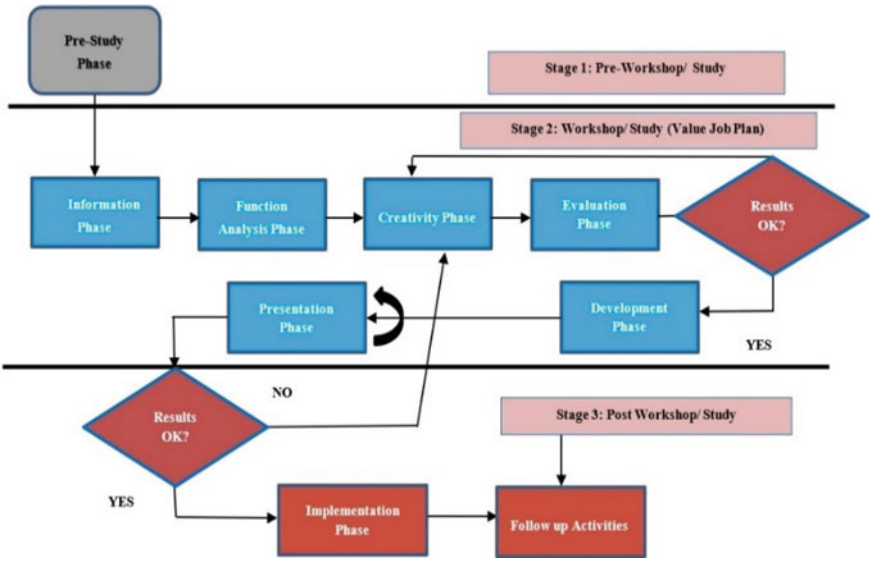

Fig. 2 Value study process flow diagram [9]

2.5 *Factors Affecting the Bubble Deck System*

The Pre-Study Phase. In this step, the study criteria that will help achieve the goal of value engineering are determined. These criteria reflect the priorities of the customer. There are a large number of parameters (non-measure criteria) that affect the bubble deck system, as given in Table 1.

By using the study area selection matrix to establish the VE study's requirements, it was discovered that the items in Fig. 3 that belong to the concerned cycle are those located in the hatched area, which has "high importance" and "high satisfaction", and also, these are the parameters that express the study's priorities; as a result, they will be taken into consideration when comparing the alternatives in terms of how they will affect the VE study.

The parameters that will be chosen for the VE study are those outlined in the hatched area; these criteria are listed in Table 2.

Table 1 Parameters that have impact on the bubble deck system

(A) Construction time	(F) Environmental impact	(K) Seismic performance
(B) Durability	(G) Safety	(L) Ease of operation
(C) Productivity	(H) Labor saving	(M) Maintainability
(D) Economy	(I) Architectural	
(E) Accuracy system	(J) Workability	

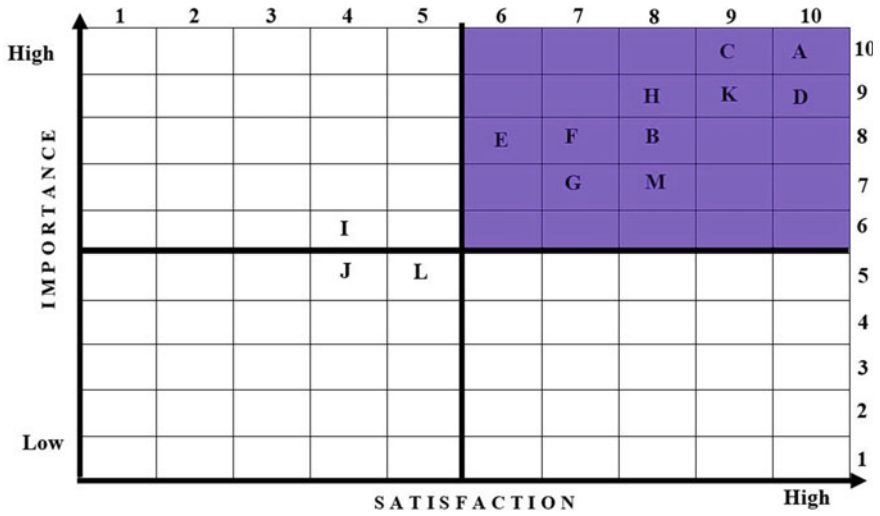

Fig. 3 Area selection for matrix criteria

Table 2 The VE studying ranking criteria

ID	Criteria	Ranking	ID	Criteria	Ranking
A	Construction time	10	F	Environmental impact	5
B	Durability	8	G	Safety	6
C	Productivity	7	H	Labor saving	4
D	Economy	6	K	Seismic performance	9
E	Accuracy system	8	M	Maintainability	5

3 Application of Value Engineering to the Bubble Deck System

3.1 Information Phase

The main idea in this phase is to identify the high-cost areas for detailed study in the subsequent stages of the VE study.

3.2 Function Analysis Phase

The FAST diagram process is used in this phase to comprehend the functions of the bubble deck system and determine the study's scope, as shown in Fig. 4. First, the process must respond to the query of how to accomplish the primary function, going from left to right. Next, it was performed by determining the goals of the value analysis, the high-order function, the primary function, and the essential secondary functions that support the immediate and low-order tasks by utilizing the how-and-why logic path method.

Function Analysis for the Bubble Deck System

From the scope of the study, it was found that the bubble material and bubble size and shape are the most considered variables of the value engineering study. So, function analysis for each item should be studied separately, as shown in Figs. 5 and 6.

Function Analysis for Bubble Material

From the FAST diagram for the bubble material, it was found that the high-order function is: improve adaptability or applicability; the essential process is: withstand load; and the low-order function is: prepare chemical ingredients by engaging in some of the critical path actions that are necessary to complete the essential process. Therefore, it should be kept in mind when selecting the alternatives of the chemical synthesis that will be studied in the next phase, like the alternatives that should meet the characteristic of a good bubble material.

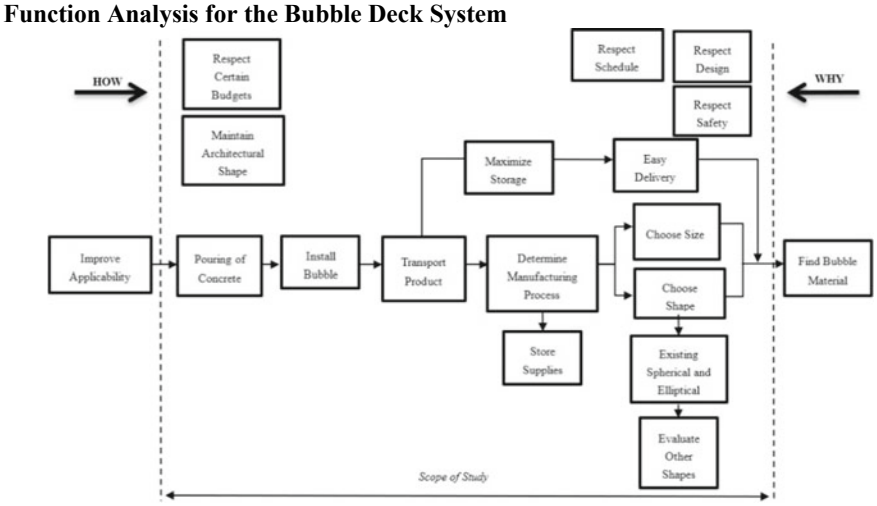

Fig. 4 FAST diagram for the bubble deck system

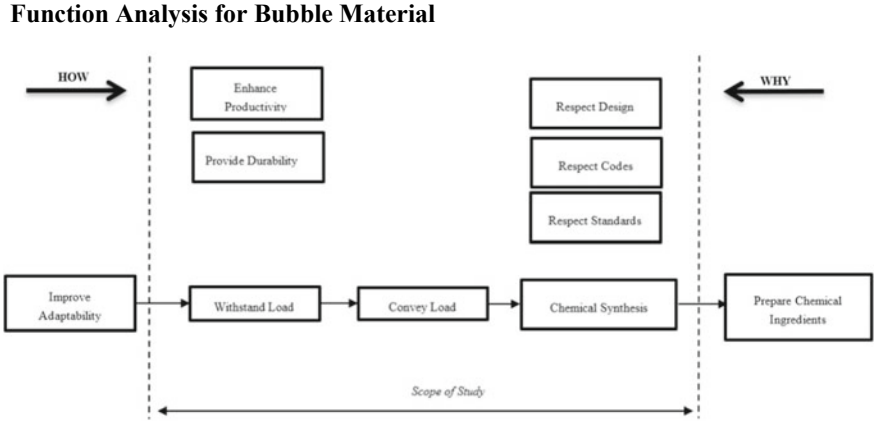

Fig. 5 FAST diagram for the bubble material

Function Analysis for the Bubble Size and Shape

From the FAST diagram for the bubble size and shape, the high-order function is: optimize installation; the primary function is: improve serviceability; the low-order function is: prepare the mold and include some ancillary secondary activities that may be accessible by the study's introductory section and objectives. Therefore, in the creativity phase, alternatives that could be available by the qualities needed in accordance with the primary function and the higher order function from ease of operation, flexibility in work, availability of the market, and the need for fewer

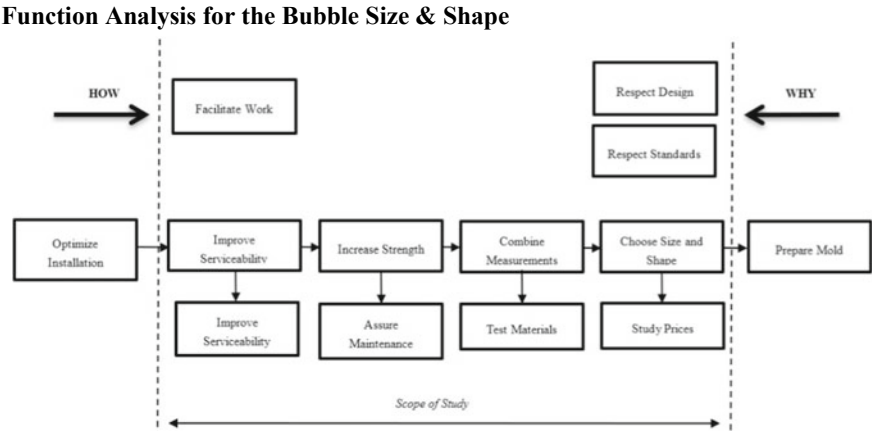

Fig. 6 FAST diagram for the bubble size and shape

laborers must be filtered out in the following stages, and the best alternative among them that achieves the study's objectives must be chosen.

3.3 Identification Phase

Comparing the critical variables mentioned, significant benefits are more likely to be acquired when modification is aligned to the improvement of the bubble material rather than the bubble size and shape. Various kinds of research have been done before, but only specific parameters are involved, and in some cases, although it improves one aspect (e.g., structural behavior) produces a negative impact, such as bubble deck system constructability and other criteria.

In line with this, an "inflatable bubble" that will serve the equivalent function made from an alternative material that can enhance numerous elements is aimed to determine using value engineering technique.

4 Results and Analysis

4.1 Weighted Evaluation Matrix for the Bubble Material Alternatives

By contrasting each alternative with the non-measure criterion for measuring the quality of the bubble material, it was discovered that butyl rubber has the highest value index when using the value equation $(\mathrm{VI} = Q/C)$, next is the high-density

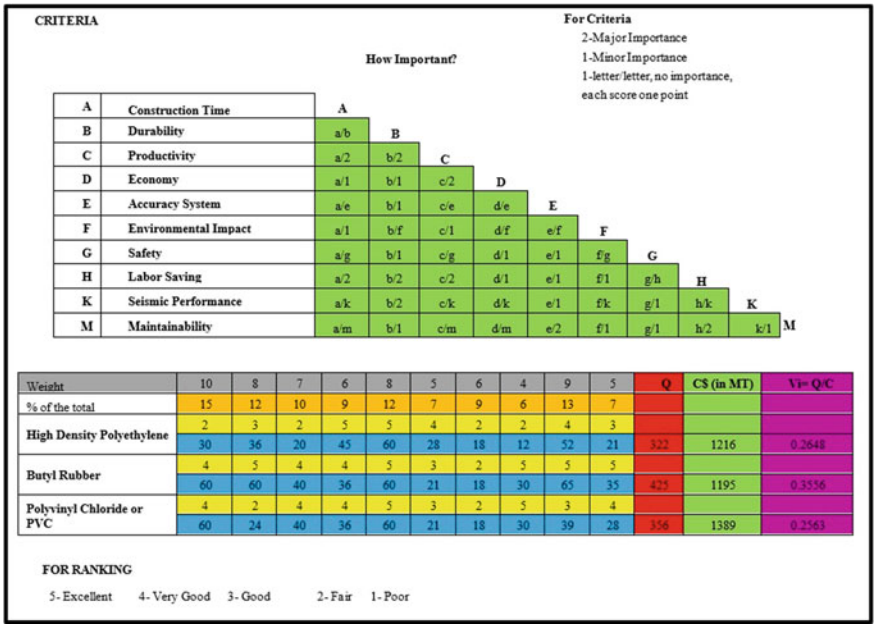

Fig. 7 Weighted evaluation matrix for bubble material alternatives

polyethylene (HDPE), and polyvinyl chloride (PVC) has the lowest value Index. As shown in Fig. 7, upon an investigation of the quality box, it was found out that the polyvinyl chloride (PVC) is the one that follows the butyl rubber in position, not the high-density polyethylene (HDPE), and however, when we refer to the cost element and compare, we discover that the value will differ, and this is the procedure's goal: access to an alternative that achieves compatibility between the desired quality and the cost incurred.

4.2 Bubble Deck System Potential Modifications

When the VE study was applied to the research subject, it was found that the bubble material's applicability had a substantial impact on the existing process because it is considered a crucial component of the system. So, after conducting a FA to determine how well the bubble was made of the new material (butyl rubber), we discovered that:

Material The primary component of the system, bubble material, has the most influence on various factors, including construction time, productivity, economy, accuracy system, seismic performance, and labor-saving, as listed by [9]. Hence, it is a vital part of the system that, once improved, will make a direct and indirect

positive impact on the totality of the project. In addition, using "butyl rubber" as a prominent chemical ingredient makes the properties of the ball more suitable for ease of application.

Installation The output also demonstrates the necessity for stakeholders to take into account the VE study's objective because it affects the system's cost as a whole, as the challenges in the logistics (manufacturing, storage, and transportation) mentioned in Sect. 2.3 [17] takes part in the large percentage of the budget. Making the bubbles "inflatable" using the recommended material, "butyl rubber", will resolve the problem mentioned earlier, as these materials can be delivered in a very minimal shipment requirement due to the decreased initial size(deflated) and mass (lightweight material).

5 Conclusions

The cost model makes it evident that employing the proposed bubble material can result in the following:

a. Savings of $21 per metric ton when compared to the costs of the traditional material.
b. The portion of 18% that increases the labor-saving effectiveness of the butyl rubber application shows the reduction in the cost and effort, the implementation, and the level of acceptability that discuss the proposed and conventional material of the bubble deck system.
c. It is possible to identify the things that need to be studied using the FAST diagram technique during the project study or system.

6 Recommendations

Recommendations are made during the study's last stage, which includes the follow-up phase and the final report creation. The study's results revealed many topics that must be considered in future studies. Thus, the following advice is provided as follows:

a. Consider the possible improvements of the "lattice", as this component is another essential element of the bubble deck system that serves a significant role in its construction for ball location stability and ease of applicability.
b. Benefit vs. cost analysis may be further studied and improved by searching for a supplier offering a lower price for the raw materials needed.
c. The choice of search terms could limit the search results; future researchers are suggested to find more related keywords.

d. The selection of the articles included by the researcher is subjective; individual experiences and knowledge affect the basis of choosing literature.
e. Use another value engineering technique (e.g., numerical evaluation and combinex method).

General Research Recommendations for the Future Studies and Universities

a. When analyzing a project or system, using the FAST diagram increases the possibility of identifying the items that require research and innovation to come up with alternatives and adjustments for the variables connected to the study, which may result in a shorter project timeline or cost-savings.
b. Include VE in university courses or through specialized educational/training programs to support the concept and the value of VE in enhancing our ability to succeed in the market, regardless of the national or international setting. This professional development aims to improve the engineers' and employees' talents and performance. As a result, the construction sector could raise its professional level and fulfill specific demands in the market if provided with specialized courses.
c. Explore other alternative materials that are more ecofriendly to lessen the carbon footprint during its production.
d. Develop a systematic way of inflating the bubble through a portable inflating machine or long-range host with multiple inflating nozzles.

References

1. Varshney H, Jauhari N, Bhatt H (2017) A review study on bubble deck slab. Int J Res Appl Sci Eng Technol 5(X):2136–2139. https://doi.org/10.22214/ijraset.2017.10314
2. Valivonis J, Jonaitis B, Zavalis R, Skuturna T, Šneideris A (2014) Flexural capacity and stiffness of monolithic biaxial hollow slabs. J Civ Eng Manage 20(5):693–701. https://doi.org/10.3846/13923730.2014.917122
3. Jathar A, Pharate S, Warhate K, Nandre P, Tanpure M (2021) Structural behaviour of bubble deck slab. Int J Innovative Res Sci Eng Technol 10(6):6514–6516. https://doi.org/10.15680/IJIRSET.2021.1006120
4. John R, Varghese J (2015) A study on behavior of bubble deck slab using ansys. Int J Innovative Sci Eng Technol (IJISET) 2(11):560–563
5. Ali S, Kumar M (2017)Analytical study of conventional slab and bubble deck slab under various support and loading conditions using ansys workbench 14.0. Int Res J Eng Technol (IRJET) 4(5):1467–1472. Retrieved from https://www.irjet.net/archives/V4/i5/IRJET-V4I5288.pdf
6. Syah TYR, Kusumapradja R, Erni N (2018) Pre-operational business planning: program for improving general hospitals of pademangan class D be a class C. IARJSET 5(11):1–5. https://doi.org/10.17148/IARJSET.2018.51101
7. Biradar R, Nikam V (2020) A review of comparative study between conventional slab and bubble deck slab. Int Res J Eng Technol 7(1):470–472. Retrieved from https://www.irjet.net/
8. Chandekar SD, Chavat SB, Khaple TJ, Pal SG, Kerkar S (2020) A review on bubble deck slab. Int Res J Eng Technol (IRJET) 7(3):1566–1569
9. Mahdi IM, Heiza K, Elenen NA (2015) Value engineering and value analysis of vertical slip form construction system. Int J Appl Innov Eng Manage (IJAIEM) 4(6):200–212. Retrieved from www.ijaiem.org

10. Atabay S, Galipogullari N (2013) Application of value engineering in construction projects. J Traffic Transp Eng 1(1):39–48. https://doi.org/10.17265/2328-2142/2013.12.005
11. Parmar RS (2016) Understanding the concept of "division": assessment considerations. Exceptionality 11(3):177–189
12. Ali MS, Babu SA (2019) A structural study on bubble deck slab and its properties. Int J Res Rev (IJRR) 6(10):352–357. Retrieved from www.ijrrjournal.com
13. Lai T (2010)Structural behavior of BubbleDeck® slabs and their application to lightweight bridge decks, p 41. Retrieved from https://dspace.mit.edu/handle/1721.1/60774
14. Pulikonda S (2018) Bubble deck slab, Slide 31
15. Bhowmik R, Mukherjee S, Das A (2017) Review on bubble deck with spherical hollow balls. Int J Civ Eng Technol (IJCIET) 8(8)979–989
16. Hashemi SS, Sadeghi K, Vaghefi M, Siadat SA (2018) Evaluation of ductility of RC structures constructed with bubble deck system. Int J Civ Eng 16(5):513–526. https://doi.org/10.1007/s40999-017-0158-y
17. Aziz ZA, Chan LH (2021) Bubble deck slab system: a review on the design and performance. Int J Innov Educ Res 9(9):575–588. https://doi.org/10.31686/ijier.vol9.iss9.3397
18. Surendar M, Ranjitham M (2016) Numerical and experimental study on bubble deck slab. Int J Eng Sci Comput 6(5):5959–5962
19. Mandlekar N, Joshi M, Butola BS (2022) A review on specialty elastomers based potential inflatable structures and applications. Adv Ind Eng Polym Res 5(1):33–45. https://doi.org/10.1016/j.aiepr.2021.05.004
20. Lewandowski K, Skórczewska K (2022)A brief review of poly(vinyl chloride) (PVC) recycling. Polymers 14(3035):1–14. https://doi.org/10.3390/polym14153035

Analysis of Architectural Design Factors to Enhance Safety of Public Building Users in Thailand

Porntip Ruengtam

Abstract Public building architectural design factors that promoted user safety were studied on Koh Yor Island, Songkhla Province, Thailand. Relevant factors were investigated through a literature review, including COVID-19 prevention measures in Thailand. Survey data were collected by a questionnaire. The research sample comprised 360 people who used public buildings in the study area and included building owners, building occupants, tourists, and entrepreneurs or related persons. Data were analyzed using two statistical techniques as exploratory factor analysis (EFA) and confirmatory factor analysis (CFA). Four architectural design factors enhanced user safety in public buildings including (1) general architectural facilities, (2) fire safety, (3) COVID-19 prevention measure regulations, and (4) COVID-19 space provision prevention measures. Results can be used to formulate architectural design guidelines to promote community safety in Thailand.

Keywords Architectural design · Public building · Safety · Exploratory factor analysis · Confirmatory factor analysis

1 Introduction

Safety and security are key issues for building users who may be at risk of bodily injury due to various hazards including potential unsafe conditions such as crime, terrorism, or accidents. These insecurities can cause both physical and mental trauma to the victims. Preventive measures against COVID-19 are another issue that has recently come into play in the daily life of public building users in Thailand, causing a change in usage dynamics. Designing public buildings to ensure safety and security is the responsibility of the architect. The principles of design must take into account all building users [1]. In Thailand, public building design guidelines [2] have been

P. Ruengtam (✉)
Interior Architecture Program, Faculty of Architecture, Urban Design, and Creative Arts, Mahasarakham University, Maha Sarakham 44150, Thailand
e-mail: porntip.r@msu.ac.th

T. Kang (ed.), *Proceedings of 5th International Conference on Civil Engineering and Architecture*, Lecture Notes in Civil Engineering 369,
https://doi.org/10.1007/978-981-99-4049-3_32

established, whereby the safety of building users must be considered to promote tourism potential and support sustainable future growth. Songkhla Province is one of the main tourist areas in Thailand, with large numbers of both Thai and foreign tourists. Koh Yor Island in Songkhla Lake has many homestays and resorts. The environment on the island is beautiful, and there are important tourist attractions such as museums, temples, and local Thai houses. This research studied and analyzed factors that promoted the safety of public building users in Thailand. Members of the local community participated in formulating guidelines for building safety consisting of building occupants, tourists, entrepreneurs, and other stakeholders, using Koh Yor Island as the study area.

2 Research Background

Architectural design focuses on the construction of cost-effective buildings and facilities to meet user needs [1]. Good architectural design must take into account the safety of building occupants to mitigate the occurrence of accidents from falling on slippery floors and the collapse of walls and ensure provision of adequate fire escapes [1]. Safety can be defined as protecting people from unintended and unwanted consequences, e.g., a fire is a safety issue while arson is a security issue [3]. Public buildings are used by many people during the day or night according to their purpose. Safety and security are of the utmost importance in the design of all parts of the building including stairs, walkways, doors, windows, handrails, and bathrooms [4]. Facilities are tangible items that are part of a property or building, especially additional amenities that make people feel more comfortable [5]. Facilities are basic requirements for building users such as accommodation, parks, swimming pools, gyms, billboards, communication systems, utilities, transportation, and other services. The COVID-19 epidemic has resulted in a change in the use of public buildings in Thailand [6]. To reduce the risk of spreading the epidemic, people who use the building must follow the measures that the building owner or building caretaker has set, such as wearing a mask, washing hands frequently with gel alcohol, and social distancing. Changes in the use of public buildings also include improvements such as one-way passageways, ventilation, contactless systems, and building entry registration points.

Fire safety regulations in buildings establishes standards for having necessary protective equipment in the event of an accident, such as smoke-heat detectors, fire extinguishers, emergency lights, and fire exits, which must be inspected and ready for use [4]. Universal design has stipulated that design and its environment must be concerned with considering factors including safety concerns, environmental issues, engineering options, aesthetics, prices, and industry standards for all people [7]. Universal design means designing products and environments that can be used by everyone at the greatest possible level without the need for special modifications or designs [8]. The Center for Universal Design [8] has established seven universal design principles to provide guidance in product and environmental design. The principles are (1) equal usability (design is useful and marketable for

multi-talented people), (2) flexibility of use (design supports a variety of preferences and capabilities), (3) simplicity and intuitive use (easy to understand, regardless of user experience, knowledge, language skills, or current level of concentration), (4) perceived information (design effectively communicates essential information to the user regardless of the user's environment or sensory abilities), (5) tolerance for error (design eliminates the dangers and consequences of accidental or unintentional actions), (6) low physical effort (design can be used efficiently and comfortably with minimal fatigue), and (7) space and size for use and approach (appropriate size and space are provided for approach, manipulation, reach, and use regardless of body size, posture, or mobility). These seven universal design concepts were considered and combined in the analysis of various factors in this research.

3 Research Method

3.1 Factor Identification

A list of factors enhancing the safety of users in public buildings was compiled from a literature review. In-depth interviews [9] were conducted with related field experts covering every factor on the list. In-depth interviews allow for detailed discussion and investigation of specific issues. They were repeated continually until a consensus was reached to confirm factors and items [9]. Then, the list of all factors was summarized. Three experts in related fields were selected based on their experience, comprising a professor from an educational institution, an architect, and a project owner. Each expert had over 10 years of experience in the design and maintenance of public buildings in Thailand. The three experts carefully considered the meaning of every statement for each factor at least three times until a consensus was reached. The initial factors and items for architectural design to enhance user safety in public buildings were then improved and modified to be suitable in the Thai context. The items in each factor were classified and confirmed by the three experts and then analyzed, as outlined in Table 1.

In Table 1, the factors were classified into four groups as (1) general architectural facilities (10 items), (2) warning systems (4 items), (3) fire safety (5 items), and (4) COVID-19 prevention measures (11 items).

3.2 Questionnaire Design

A questionnaire survey was designed for data collection to confirm the items and factors enhancing the safety of users in public buildings The questionnaire consisted of two parts as (1) demographics of the respondents including gender, age, education level, and income totaling four questions measured by frequency (percentage) of the

Table 1 Questionnaire items

Factor	Item
General architectural facilities	Q1 Handicap parking
	Q2 Ramps
	Q3 Stairs
	Q4 Handrail or fall protection wall
	Q5 Entrance/walkway/corridor wide enough for wheelchairs
	Q6 Toilet for the disabled
	Q7 Non-slip textured walking surfaces and able to give directions to the disabled
	Q8 Signs and symbols are clearly visible day and night
	Q9 Contact counter information service point that the disabled can access
	Q10 Doors are wide enough for wheelchairs to enter and exit
Warning systems	Q11 Warning signboard/symbol
	Q12 Notification sound
	Q13 CCTV
	Q14 Safety officer
Fire safety	Q15 Fire extinguisher
	Q16 Heat or smoke detector
	Q17 Emergency lighting
	Q18 Fire exit
	Q19 Assembly area
COVID-19 prevention measures	Q20 Hand sanitizer gel or alcohol at various service points
	Q21 Dust-trap carpet from the shoes at the entrance–exit
	Q22 Announcement of codes of conduct for building occupants
	Q23 Good waste management
	Q24 First aid room convenient for entry and exit and ambulance parking
	Q25 Touch less or automatic door opening and closing system
	Q26 Indoor ventilation systems by natural or mechanical methods
	Q27 Air filter/purifier or other method of disinfection system
	Q28 Clearly defined boundaries of the usable area according to distance measures
	Q29 Determine a one-way walking path to avoid passing each other
	Q30 Waiting area in front of the building, as an open space with spaced seats

respondents, and (2) architectural design factors to enhance safety totaling 30 questions measured on a five-level Likert scale from "strongly disagree" to "strongly agree". Validity and reliability tests were performed to ensure that the items and questions in the questionnaire were appropriate for data collection. For the validity test, the three experts were interviewed to reconfirm the items and factors in the questionnaire. They reviewed and commented on whether the questions were valid representative measures of architectural design factors that enhanced safety in public buildings, and suggested more appropriate recommendations for public buildings in the Thai context. This technique improved the clarity and relevance of the questionnaire content. Cronbach's alpha [10] was used for the reliability test to check the reliability of the questionnaire by conducting a pilot group study with 30 target samples (respondents from people in Kho Yor target areas) to test the 30 items consisting of four factors. Results showed that the Cronbach's alpha coefficient for general architectural facilities was 0.990, for warning systems 0.988, for fire safety 0.993, and 0.981 for COVID-19 prevention measures. All four factors gave a Cronbach's alpha coefficient of 0.986. All Cronbach's alpha values were higher than 0.8, proving that the questionnaire was reliable [10].

3.3 Data Collection

The respondents were selected using convenience non-probability sampling, targeting people in the community with safety experience in public buildings such as building occupants, tourists, entrepreneurs, and all stakeholders in the area of Koh Yor, Songkhla Province, Thailand. Three months were spent collecting data through face-to-face and online interviews. Some questions were explained in detail to allow the respondents to understand the content more clearly. Out of the 400 completed questionnaires, 40 were discarded due to incomplete and biased responses, leaving 360 that were used for data analysis.

4 Results

4.1 Descriptive Results

Demographic characteristics of the 360 samples are given in Table 2.

Table 2 showed the demographic characteristics of the respondents in the study including gender, age, education level, and income.

Table 2 Demographic characteristics

Description	Frequency	Percentage
Gender		
– Male	137	38.1
– Female	223	61.9
Age		
– Less than 30 yrs	60	16.7
– 30–39 yrs	73	20.3
– 40–49 yrs	128	35.6
– 50–59 yrs	45	12.5
– More than 60 yrs	54	15.0
Education level		
– Lower than primary school	7	1.9
– Primary school	60	16.7
– High school	148	41.1
– Bachelor degree	137	38.1
– Higher than bachelor degree	8	2.2
Income/Month		
– Less than 10,000 baht	138	38.3
– 10,000–30,000 baht	186	51.7
– 30,001–50,000 baht	25	6.9
– 50,001–100,000 baht	8	2.2
– More than 100,000 baht	3	0.8

4.2 Exploratory Factor Analysis

Exploratory factor analysis (EFA) [11] is a statistical technique for grouping or combining variables with similar characteristics into the same group. Those groups of the variables are called factors [11]. EFA was implemented in this research with a varimax rotation method using statistical software to group the variables. Results showed that Bartlett's test of sphericity had a significant value of 0.001 (less than 0.05), KMO (Kaiser–Meyer–Olkin) measure of sampling adequacy was 0.956 (KMO > 0.6) [12]. Results of the analysis are given in Table 3.

Table 3 showed the factor loading score of EFA. Results of EFA categorized the 30 variables of the architectural design factors to enhance safety into four factors by factor loading scores. The four factors comprised factor 1 consisting of Q1, Q2, Q3, Q4, Q5, Q6, Q7, Q8, Q9, Q10, Q11, and Q12, factor 2 consisting of Q13, Q14, Q15, Q16, Q17, Q18, and Q19, factor 3 consisting of Q21, Q22, Q23, Q24, Q25, Q26, and Q27, and factor 4 consisting of Q20, Q28, Q29, and Q30.

Table 3 Factor loading score of EFA

Item	Factor			
	1	2	3	4
Q2	**0.831**	0.187	0.208	0.209
Q1	**0.817**	0.214	0.255	0.201
Q7	**0.806**	0.247	0.269	0.079
Q6	**0.799**	0.226	0.300	0.154
Q4	**0.785**	0.245	0.312	0.095
Q8	**0.782**	0.200	0.356	0.081
Q5	**0.761**	0.251	0.316	0.144
Q3	**0.760**	0.253	0.273	0.118
Q10	**0.755**	0.242	0.343	0.009
Q11	**0.711**	0.199	0.457	0.088
Q12	**0.628**	0.139	0.525	0.217
Q9	**0.612**	0.218	0.467	0.095
Q24	0.150	**0.873**	0.187	0.128
Q25	0.341	**0.814**	0.115	0.090
Q23	0.258	**0.795**	0.086	0.202
Q26	0.238	**0.783**	0.249	0.231
Q27	0.272	**0.776**	0.240	0.290
Q21	0.234	**0.757**	0.244	0.274
Q22	0.210	**0.730**	0.226	0.327
Q19	0.375	0.242	**0.806**	0.136
Q18	0.429	0.265	**0.784**	0.119
Q16	0.422	0.251	**0.778**	0.095
Q17	0.464	0.243	**0.751**	0.135
Q14	0.422	0.187	**0.741**	0.239
Q13	0.436	0.147	**0.737**	0.227
Q15	0.565	0.252	**0.647**	0.142
Q30	0.163	0.315	0.158	**0.863**
Q28	0.142	0.272	0.171	**0.855**
Q29	0.177	0.469	0.157	**0.684**
Q20	0.126	0.524	0.167	**0.576**

Kaiser–Meyer–Olkin (KMO) = 0.956 (KMO > 0.6), p-value = 0.000 (Sig.)

4.3 Confirmatory Factor Analysis

Confirmatory factor analysis (CFA) [13] is a statistical technique used to verify and confirm the factor structure of a group of variables whether those variables are grouped as fit factors [13]. In this research, CFA was used to confirm the clustering of variables classified into four factors according to the EFA results using statistical software. The first results show that the CFA results are incomplete (not fit), and the software recommends excluding some variables from the analysis. After eliminating the variables suggested by the software, the CFA results fit perfectly, with Chi-square = 41.151, df = 38, p = 0.334 (>0.05), CMIN/DF = 1.083 (<3), GFI = 0.979 (>0.90), and RMSEA = 0.015 (<0.08) [14, 15], as shown in Fig. 1.

Figure 1 showed results of CFA grouping into four factors as factor 1 consisting of Q3, Q4, and Q7, factor 2 consisting of Q17 and Q18, factor 3 consisting of Q21, Q22, Q23, and Q27, and factor 4 consisting of Q28 and Q30.

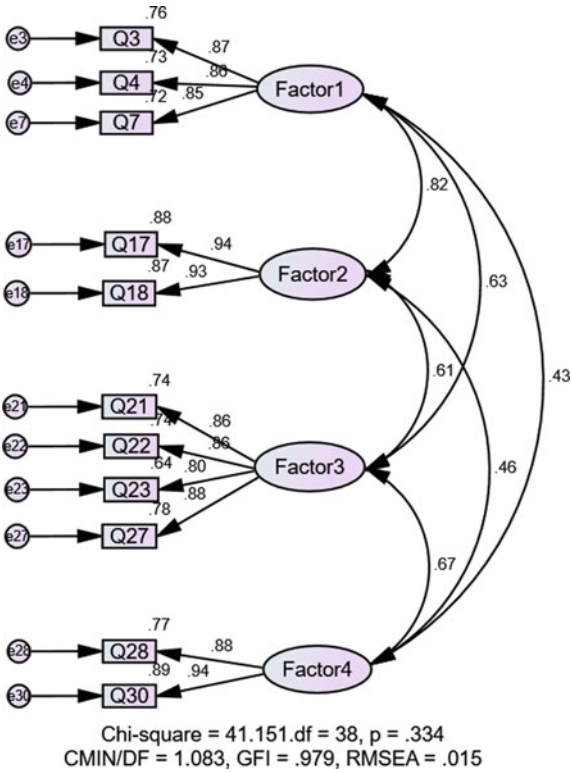

Fig. 1 CFA of public building design factors

5 Conclusions

Factors of architectural design were examined to enhance the safety of 360 users of public buildings in the case study area. Results revealed that four factors of architectural design enhanced the safety of public building users. These factors were (1) general architectural facilities consisting (1.1) stairs as the most important, followed by (1.2) handrail or fall protection wall, and (1.3) non-slip textured walking surfaces and able to give directions to the disabled; (2) fire safety consisting of (2.1) emergency lighting as the most important, followed by (2.2) fire exit; (3) COVID-19 prevention measures in terms of regulations consisting of (3.1) air filter/purifier or other method of disinfection system as the most important, followed by (3.2) dust-trap carpet from the shoes at the entrance/exit, (3.3) announcement of codes of conduct for building occupants, and (3.4) good waste management; (4) COVID-19 prevention measures in terms of space provisions consisting of (4.1) waiting area in front of the building, as an open space with spaced seats as the most important, followed by (4.2) clearly defined boundaries of the usable area according to distance measures. Findings were consistent with [4, 6], who indicated that architectural design factors for public buildings include architectural functional aspects, fire safety aspects and measures for COVID-19 prevention. Our results can be used to formulate guidelines for safety in the community to enhance the safety of users in public buildings in Thailand. These guidelines will help those involved in the architectural design of public buildings such as design architects and project owners, as well as building occupants, to better understand the safety requirements of public building use.

Acknowledgements This research project was financially supported by Mahasarakham University, Thailand.

References

1. Hayes RL (2014) The architect's handbook of professional practice, 15th edn. Wiley, Hoboken, New Jersey
2. Committee for Design, Construction and Inspection (2011) Design standards for buildings and locations. Office of Physical Systems Management, ChulalongkornUniversity, Bangkok
3. The Standards Setting Committee of the IFSSC (2020) International fire safety standards: common principles. Safe buildings save lives, 1st edn. The International Fire Safety Standards Coalition (IFSSC), UK
4. Tarlow PE (2014) Tourism security: strategies for effectively managing travel risk and safety. Elsevier Inc., Waltham, MA
5. Emmitt S, Prins M, Otter AD (2009) Architectural management international research and practice. Wiley, West Sussex, UK
6. Oxford Policy Management and United Nations Thailand (2020) Social impact assessment of COVID-19 in Thailand. Oxford Policy Management Limited, Oxford, UK
7. Burgstahler S (2015) Universal design: process, principles, and applications. University of Washington, College of Engineering. Information Technology, College of Education, Washington

8. NCSU Homepage. Retrieved https://www.ncsu.edu/ncsu/design/cud/about_ud/udprinciples.htm. Accessed 18 Dec 2021
9. Boyce C, Neale P (2006) Conducting in-depth interviews: a guide for designing and conducting in-depth interviews for evaluation input. Pathfinder International Tool Series Monitoring and Evaluation-2. Pathfinder International, MA
10. Nunnally JC (1978) Psychometric theory, 2nd edn. McGraw-Hill, New York
11. Norris M, Lecavalier L (2010) Evaluating the use of exploratory factor analysis in developmental disability psychological research. J Autism Dev Disord 40(1):8–20
12. Kaiser HF (1958) The varimax criterion for analytic rotation in factor analysis. Psychometrika 23(3):187–200
13. Byrne BM (2010) Structural equation modelling with AMOS: basic concepts, applications, and programming. Taylor & Francis Group, Routledge, New York
14. Arbuckle J (2011) IBM SPSS Amos 20 user's guide. IBM Corporation, NY, USA
15. Tabachnick BG, Fidell LS (2001) Using multivariate statistics, 4th edn. Allyn and Bacon, Needharm Hights, MA

Analysis of the Plan Form of Prefabricated Buildings Based on the Space Syntax—A Case Study of the Son Lei House in Macau

Hoi Ian Tam, Liang Zheng, Yile Chen, and Xiaoxiao Wang

Abstract Son Lei House was the first building complex in Macau to adopt prefabricated building technology. Due to the early construction time, the building has gradually encountered problems such as ageing and insufficient facilities, poor environmental sanitation, and outstanding fire safety hazards. Based on Macau Iao Hon estate of Son Lei house as an example, depending on the quantitative analysis of space syntax in the old local-style dwelling houses building space zoning regularity of plane space form, each space in the old residential building is quantified by using nine indicators of the convex space of space syntax, five indicators of the field of viewshed analysis, and simulation of pedestrian stream, and suggestions for the plane optimisation of the building are put forward. The analysis process and optimisation suggestions apply to the same type of buildings, providing a reference for the urban renewal work of the government and enterprises.

Keywords Space syntax · Old residential buildings · Urban renewal · Optimisation strategy · Prefabricated buildings

H. I. Tam · L. Zheng · Y. Chen · X. Wang (✉)
Faculty of Humanities and Arts, Macau University of Science and Technology. Avenida Wai Long, Taipa, Macau 999078, China
e-mail: 2009853aat30002@student.must.edu.mo

H. I. Tam
e-mail: joycethimo@gmail.com

L. Zheng
e-mail: 2009853gat30002@student.must.edu.mo

Y. Chen
e-mail: 2009853gat30001@student.must.edu.mo

T. Kang (ed.), *Proceedings of 5th International Conference on Civil Engineering and Architecture*, Lecture Notes in Civil Engineering 369,
https://doi.org/10.1007/978-981-99-4049-3_33

1 Introduction

Space syntax is to describe the space geometry, topology, and distance of the theoretical system; since the 1970s Bill Hillier puts forward the space syntax theory system that has been widely used in space network structure, space structure, the relationship between human activities, the urban land use and urban form, and architectural interior space analysis specific applications [1]. With the development of modern urbanisation, people pay more and more attention to healthy, convenient, and safe life. The needs of urban space meet the diverse needs of people and solve practical problems in people's daily life. In recent years, various space types have been analysed and optimised using space syntax. The related research includes the study of the identifiability of indoor spaces [2], planning of public spaces for the elderly [3], analysis and optimisation of space line-of-sight [4], crime prevention [5], and the improvement of the urban island effect [6]. Recent research has resulted in many findings and enriched the application scenarios and numerical meanings of the space syntax. In particular, the application scenarios of residential space can be roughly divided into indoor space and outdoor space. Previous studies on the indoor space have used various indicators of the space syntax to interpret the indoor space of residential buildings with different architectural styles and have summarised the cultural differences in the residential space from the level of spatial topology [7]. However, there has still been a lack of qualitative research to support the conclusions of quantitative studies. The research on the outdoor space has quantitatively analysed the spatial permeability, accessibility, and aggregation of the public space in old urban areas. Many strategies for renewing public space in old urban areas have been proposed [8], but they require many indicators for verification [9]. Some of the previous studies have evaluated the use of space using the space syntax, but they lack empirical field evidence.

In this paper, based on the above research present situation, in order to take Macau Son Lei House as the research object, aiming at Son Lei House the interior space of the quantitative research of space syntax, based on the original floor plan of Son Lei House, the optimisation strategy of old residential buildings is put forward by on-site investigation to correct the actual space condition and supported by multi-index numerical simulation, to provide a more scientific basis for the spatial optimisation of residential buildings in urban renewal.

2 History and Spatial Characteristics of Son Lei House

Son Lei House is located on Rua Três do Bairro Iao Hon on the Macau peninsula. It was built in about 1976. It is one of the building complexes that forms Bairro Iao Hon, the complex had eight buildings, four of them were demolished in 2009, and four are still in existence (Fig. 1).

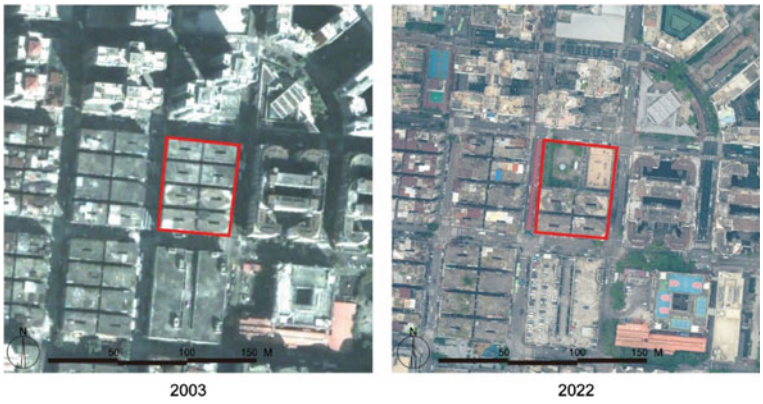

Fig. 1 Before and after the redevelopment of Son Lei House

The seven-storey Son Lei House was originally a residence but some of the residences on the ground floor were used for commercial purposes such as takeaways, renovation companies, and real estate. Some of the floors above have been converted into hair salons, traditional Chinese medicine and western medicine clinics. Son Lei House has the same layout as the surrounding Hong Tai House and Kat Cheong House. The block is 70 m wide. Each building is rectangular shape with a length of 25.8 m and a width of 15 m, with eight units per floor.

Son Lei House was built with prefabricated building technology. The walls and floors are made of pre-cast uniform concrete slabs, and then assembled with hooks and connectors. This method is advantageous for buildings with many units, the process is fast and low cost. Unlike today's pre-fabrication, prefabricated building method back then was not as safe as framed buildings due to technical limitations at that time. The construction and use of Son Lei House spanned over two time periods—before and after the return of Macau to China; it grew from vegetable fields to bringing about a new trend in real estate, and was once a habitat for Chinese refugees. It was an early exploration of prefabricated buildings. It has representative significance in the history of construction engineering of residential buildings in Macau, and the historical process is given in Table 1.

In terms of road planning, there are 1.89 m-wide north–south alleys and 3.45 m-wide east–west alleys between each building in Son Lei House. The north side is Rua Oito do Bairro Iao Hon, the south side is Rua Seis do Bairro Iao Hon, and the east side is Avenida da Longevidade, on the west side is Rua Dois do Bairro Iao Hon (Fig. 2). The surrounding area of Son Lei House is rich in business forms. The north side is the all-day leisure area of Rua Quatro do Bairro Iao Hon, with children's play facilities and a series of fitness and physical exercise equipment to meet the fitness needs of users of different ages; the south side is Centro Commercial Vong Kam, built in the 1980s, is a comprehensive shopping mall integrating selling leather shoes, clothing, small commodities, as well as food and beverage; the east and west sides are multi-storey residences.

Table 1 Historical process of Son Lei House [10]

Time	Event
1930	The location of Son Lei House was originally a racetrack. Affected by the war, refugees poured into Macau, and the racetrack was changed to farmlands to resettle the refugees
1973	"Iau Heng Investment and Construction Co., Ltd." purchased the farmland to build Bairro Iao Hon, including the construction land for Son Lei House
1976	Son Lei House of Bairro Iao Hon was built. It consists of eight buildings of the same specifications, each with seven floors and eight units with two staircases. The Social Welfare Institute purchased four of these buildings to be used as settlements for refugees from Fai Chi Kei and Travessa das Pedrinhas in Ilha Verde
1999	Quality problems started appearing in Son Lei House, a large piece of the cement structure of the communal staircase peeled off, the windows at the communal corridor were severely rusted, and there were cracks in the façade of the building. However, due to insufficient funds for maintenance, no systematic maintenance has been carried out
2001	The four buildings in Son Lei House, which is government property (The Social Welfare Institute), have been rebuilt with a new look, eliminating the hidden danger of accidents due to long-term disrepair
2005	DSSOPT launched the reconstruction plan of Bairro Iao Hon. Seven residential units over 30 years old, including Son Lei House, were planned for demolition and replaced with several 30-storey buildings. In the initial stage, an inter-departmental team would mainly collect the needs and opinions of the residents of Bairro Iao Hon on "Old Districts Redevelopment"
2006	The Macau SAR government proposed a bill on "Regime Jurídico do Reordenamento dos Bairros Antigos". DSSOPT completed a resident survey on "Old Districts Redevelopment". According to the survey analysis, the main reason why residents prefer the government to restructure the old neighbourhoods is that they are dissatisfied with the current living environment, including poor sanitation, serious public security problems, and rampant sexual crimes among others
2008	The "Survey on the Current Situation of Residents in Bairro Iao Hon" was completed. The survey shows that the proportion of tenants in Bairro Iao Hon is high, with owners accounting for 41.2% and tenants accounting for 58.8%. At the same time, the usage of a considerable number of residential units has been changed. Among the 304 industrial and commercial units, 176 have been converted from residential units and only 128 were registered as industrial and commercial units in the government property registry. Nearly 60% of the respondents want the district to be restructured
2009	DSSOPT demolished four of the eight Son Lei House that are government properties and replaced them with a leisure area and a one-storey temporary office of the Old District Redevelopment Consultative Council in Iao Hon as a place to collect opinions and hold talks as part of the follow-up work on old district redevelopment for the government
2012	As many properties in Bairro Iao Hon had unclear ownership issues and difficulty in raising funds, redevelopment came to a standstill
2013	The Macau SAR government withdrew the bill on "Regime Jurídico do Reordenamento dos Bairros Antigos"
2015	The Macau SAR government adopts the concept of urban renewal to replace old district redevelopment

(continued)

Table 1 (continued)

Time	Event
2019	The Macau SAR government promulgated the "Regime de benefícios fiscais para a reconstrução de edifícios" and the "Regime jurídico de habitação para alojamento temporário e de habitação para troca no âmbito da renovação urbana", and Macau Urban Renewal Limited (MUR) was established
Present	The renovation and redevelopment of Son Lei House is under preparation, which has practical significance for the study of Son Lei House

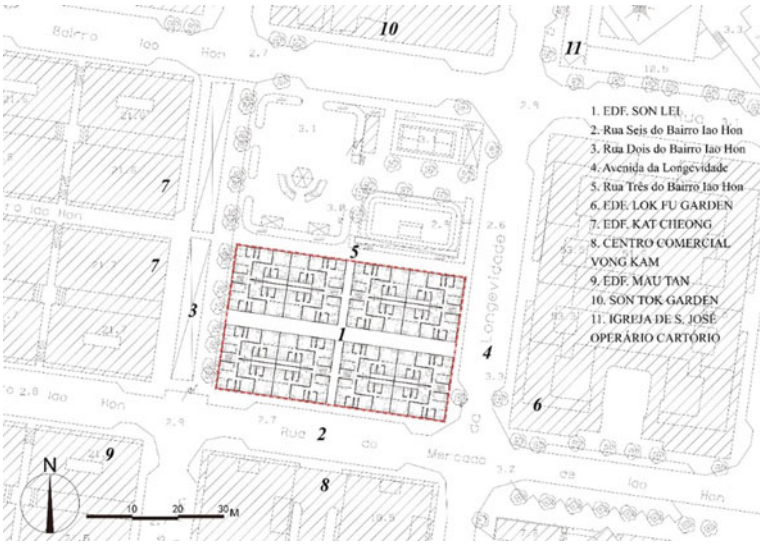

Fig. 2 Location of Son Lei House

In terms of architectural design, a rectangular parallelepiped is used as the shape of the building, with the sides facing the north and south as the main façades of the building. Influenced by modernist residences, the design is simple, and the façades' decoration is mainly composed of concrete square strips and paint, long windows and square windows that are built-in on the prefabricated walls. As it is a prefabricated construction, the architectural elements form a visual rhythm in repetition (Figs. 3, 4).

3 Analysis of the Spatial Form of Son Lei House

Based on the recent research progress and taking the Son Lei House in Macau as a research object, this study conducts a quantitative investigation of the space syntax for the interior space of the Son Lei House. Based on the original floor plan of the

Fig. 3 Façade

Fig. 4 Renderings of Son Lei House

Son Lei House, the actual spatial conditions are corrected through the field survey. Finally, based on the numerical simulation results of multiple indicators (Table 2) and the current situation, an optimisation strategy for old residential buildings is proposed to provide a scientific basis for the spatial optimisation of residential buildings in urban renewal.

3.1 Site Morphological Characteristics

Prefabricated construction in Macau is where prefabricated parts are assembled on the construction site. The prefabricated parts mainly include the main structure above the ground, retaining walls, inner partitioning walls, decoration, equipment and pipelines among others, so the level of repetition of the site morphology is relatively high, and most of them are composed of two- to four-unit types. In the case of Son Lei House,

Table 2 Indicators of space syntax

Indicator	Concept	Meaning	Expression
Spatial structure	Spatial connectivity mode	A measure of spatial independence and mobility	In this study, indicators of the space syntax are represented both graphically and in a tabular form. The values represented graphically are color-coded using the warm and dark and cold and light colours to indicate high and low values, respectively
Choice	The number of shortest topological paths from a particular space to the other spaces	A measure of the attraction potential of spatial walking. A higher choice indicates higher feasibility of walking	
Connectivity	The number of adjacent elements of a space element	Judgement of the permeability of space. A higher connectivity indicates better permeability	
Mean depth	The distances of a space to the other spaces are added and divided by the number of spaces in a system	A space has poor convenience when it has a large mean depth and a large number of spatial transformations, and good convenience when it has a small mean depth	
Intensity	The relative asymmetry of a spatial network is measured by calculating the change rate of entropy with respect to the total depth	Determination of the distance and efficiency of the passage. A higher intensity indicates a greater travel distance and efficiency	
Integration [HH]	The degree to which a space is aggregated with or separated from the other spaces in a space system	An indicator to measure the accessibility of spatial nodes. A higher integration indicates higher accessibility	

(continued)

Table 2 (continued)

Indicator	Concept	Meaning	Expression
Entropy	A measure of spatial location distribution based on the spatial depth, expressing topological differences between spatial layouts	If a space is close to many other spaces, then it has an asymmetric depth and low entropy. The entropy is higher if the depth is more evenly distributed	
Harmonic mean depth	The reciprocal of the depth of a space to the other spaces	Contrary to the mean depth, a larger harmonic mean depth indicates a lower distance cost	
Control	The reciprocal of the number of spaces directly connected to a space, which is then summed across the spaces	A measure of the choice of a space with respect to its adjacent spaces. A value greater than one indicates a strongly controlled space, and a value less than one suggests a weakly controlled space	
Total depth	The sum of topological depths from a particular node to all other nodes	Judgement of the distance cost of a space. A smaller mean depth indicates a lower distance cost	

the floor plan is composed of two main unit types: units with three bedrooms and a living room and units with two bedrooms and a living room (originally, they were one-bedroom units that have been converted into three- or two-bedroom units), with an area of 43.35 square metres (Fig. 5). Each building of Son Lei House is composed of the above two types of units, with eight units on each floor, four of the units share a staircase on the east side of the building, and the other four share another staircase on the west side, which are not connected to each other.

The disadvantage of Son Lei House's floor plan is the unreasonable design of the courtyard. According to on-site research and interviews, residents on the upper floors of Son Lei House would occasionally throw garbage in the courtyard, and as the courtyard has no entrance and exit, it requires residents on the ground floor to enter the courtyard from their window to clean and remove the garbage, but residents on the ground floor are not willing to clean the courtyard, resulting in poor sanitary in the courtyard. With the increase in the number of residential buildings on the ground floor being converted into shops, shop owners would block off the courtyard

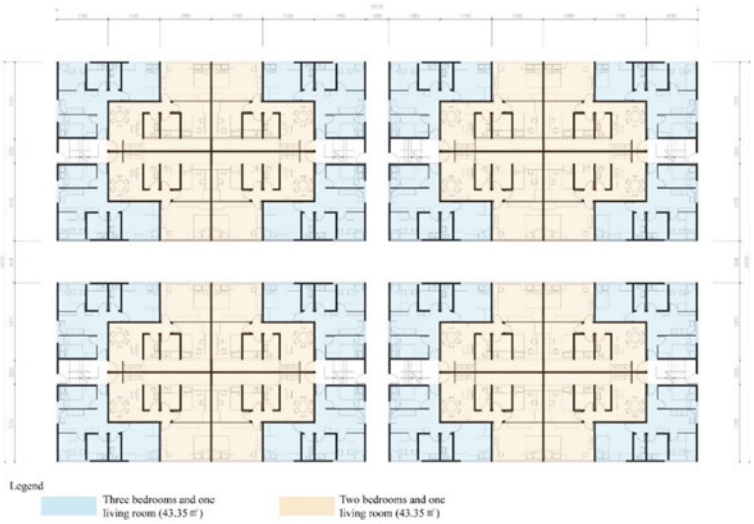

Fig. 5 Interior floor plan of Son Lei House

spaces and turn them into unauthorised spaces in order to increase their shop area, and residents on the upper floors followed suit and made home extensions with the unauthorised spaces (Fig. 6). The unauthorised space is usually used as a utility room in Son Lei House. Although it affects the lighting and ventilation of the rooms surrounding the courtyard, it prevented environmental pollution caused by littering in the courtyard and increased the indoor space (23.1 m^2). Most households have remodelled the space and made use of it.

For residential units on the ground floor that have been converted into shops, units of three bedrooms and a living room have been converted into two shop units, namely shop unit A (27.2 m^2) and shop unit B (16.15 m^2); units with two bedrooms and a living room have been converted into one shop unit which is shop unit C (43.35 m^2). This is determined by the width of the street-facing façade (Fig. 7). In addition, there are also cases where owners who own multiple units combined the units to convert the space into one single large shop unit.

3.2 Numerical Analysis of Space Syntax

Since the east and west sides of each building of the Son Lei House have the same plan forms and are spatially unconnected with each other, the west side of the Son Lei House was selected as a sample for numerical analysis of the space syntax to extract its spatial structure (Fig. 8). There were 25 spaces in this sample, which were numbered from zero. The space No. 19 was the common staircase; spaces Nos. 21, 12, 18, and 6 denoted the living rooms of various units; spaces Nos. 24, 23, 8, 9, 2,

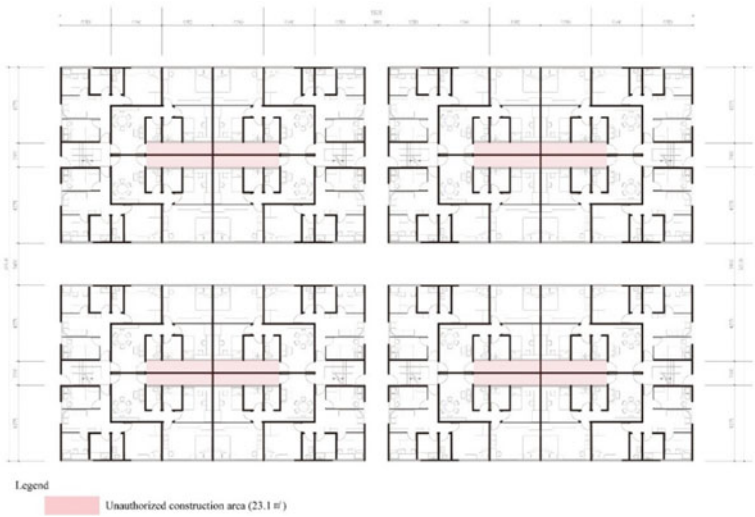

Fig. 6 Unauthorized construction area

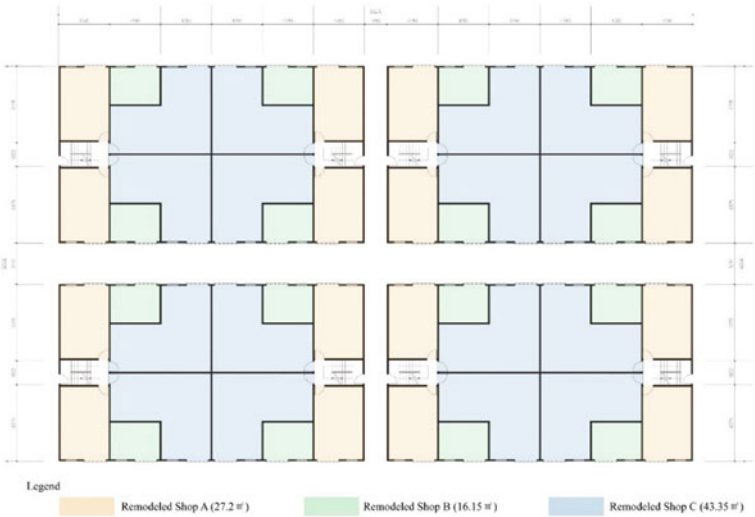

Fig. 7 Floor plan of the Son Lei house ground floor residential converted into a shop

3, 15, and 14 included the bathrooms and kitchens of various units; the remaining spaces were bedrooms of various units (Table 3).

To make this study relevant, nine variables were selected as data sources in the numerical simulation stage of the space syntax, and the specific values of these variables are shown in Table 2 (Figs. 9, 10, 11, 12, 13, 14, 15, 16, 17). As can be observed from the simulation results of these variables, space No. 19 was the

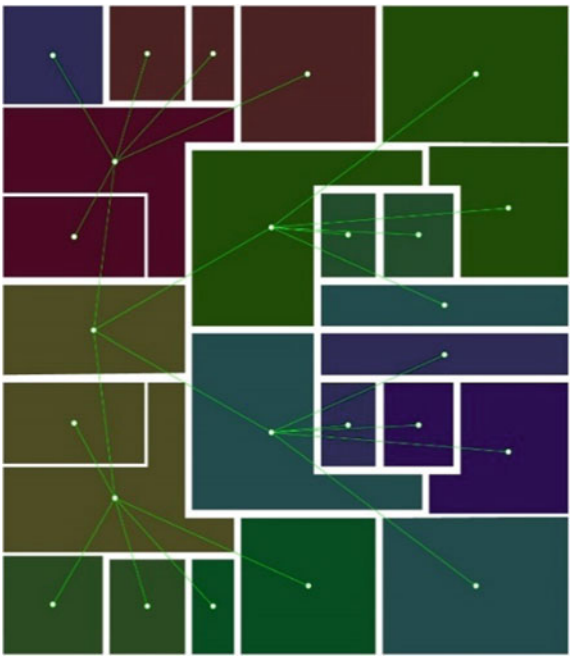

Fig. 8 Spatial structure

centre of the whole space system, and other spaces were distributed in a fan-shaped configuration, having space No. 19 as the starting point and showing an axisymmetric structure with spaces Nos. 19, 7, and 1 as the axis separating the south and north sides. The living room space of each unit had an I-shaped structure.

(1) Choice: The common staircase space No. 19 was red, the living room spaces Nos. 21, 12, 18, and 6 were green, and the rest spaces were blue, having the values of 432, 210, and zero, respectively. The colours indicated that the common staircase was an important walking space, followed by the living room space.
(2) Connectivity: The connectivity of the living rooms of the units was the highest, with a value of six, followed by that of the common staircase with a value of four, and that of the other spaces with a value of one. The connectivity suggested that the living rooms of the units had good permeability while the other spaces had poor permeability. The value of connectivity was closely related to the function of a particular space.
(3) Mean Depth: The mean depth of spaces Nos. 21, 12, 18, and 6 was moderate, with a value of 2.375. The mean depth of space No. 19 was the lowest, having a value of 1.833, and that of the other spaces was high, having a value of 3.333. This indicated that the bedrooms, kitchens, and bathrooms of the units had numerous spatial transformations and poor convenience while living rooms and the common staircase had small mean depths and good convenience.
(4) Intensity: The intensity of spaces Nos. 21, 12, 18, and 6 was the highest, with a value of 1.018, followed by that of space No. 19 with a value of 0.895, while

Table 3 Space syntax numerical simulation numerical

Room	Choice	Connectivity	Control	Entropy	Harmonic mean depth	Integration [HH]	Intensity	Mean depth	Total depth
0	0	1	0.166667	1.459387	3.75	0.986574	0.663358	3.333333	80
1	0	1	0.166667	1.459387	3.75	0.986574	0.663358	3.333333	80
2	0	1	0.166667	1.459387	3.75	0.986574	0.663358	3.333333	80
3	0	1	0.166667	1.459387	3.75	0.986574	0.663358	3.333333	80
4	0	1	0.166667	1.459387	3.75	0.986574	0.663358	3.333333	80
5	0	1	0.166667	1.459387	3.75	0.986574	0.663358	3.333333	80
6	210	6	5.25	1.303381	8.823529	1.674186	1.018266	2.375	57
7	0	1	0.166667	1.459387	3.75	0.986574	0.663358	3.333333	80
8	0	1	0.166667	1.459387	3.75	0.986574	0.663358	3.333333	80
9	0	1	0.166667	1.459387	3.75	0.986574	0.663358	3.333333	80
10	0	1	0.166667	1.459387	3.75	0.986574	0.663358	3.333333	80
11	0	1	0.166667	1.459387	3.75	0.986574	0.663358	3.333333	80
12	210	6	5.25	1.303381	8.823529	1.674186	1.018266	2.375	57
13	0	1	0.166667	1.459387	3.75	0.986574	0.663358	3.333333	80
14	0	1	0.166667	1.459387	3.75	0.986574	0.663358	3.333333	80
15	0	1	0.166667	1.459387	3.75	0.986574	0.663358	3.333333	80
16	0	1	0.166667	1.459387	3.75	0.986574	0.663358	3.333333	80
17	0	1	0.166667	1.459387	3.75	0.986574	0.663358	3.333333	80
18	210	6	5.25	1.303381	8.823529	1.674186	1.018266	2.375	57
19	432	4	0.666667	0.680559	13.33333	2.762406	0.895473	1.833333	44
20	0	1	0.166667	1.459387	3.75	0.986574	0.663358	3.333333	80
21	210	6	5.25	1.303381	8.823529	1.674186	1.018266	2.375	57

(continued)

Table 3 (continued)

Room	Choice	Connectivity	Control	Entropy	Harmonic mean depth	Integration [HH]	Intensity	Mean depth	Total depth
22	0	1	0.166667	1.459387	3.75	0.986574	0.663358	3.333333	80
23	0	1	0.166667	1.459387	3.75	0.986574	0.663358	3.333333	80
24	0	1	0.166667	1.459387	3.75	0.986574	0.663358	3.333333	80

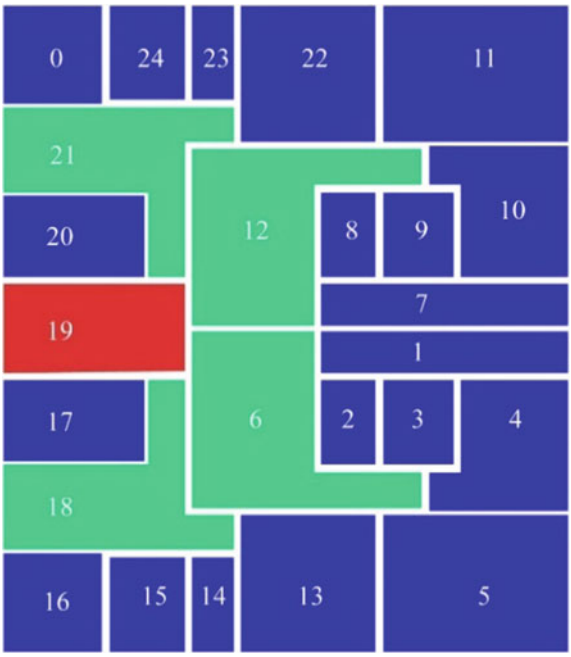

Fig. 9 Choice

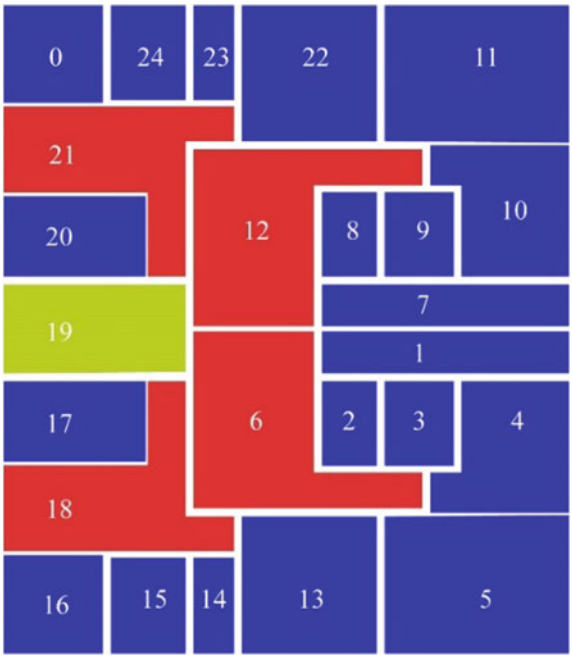

Fig. 10 Connectivity

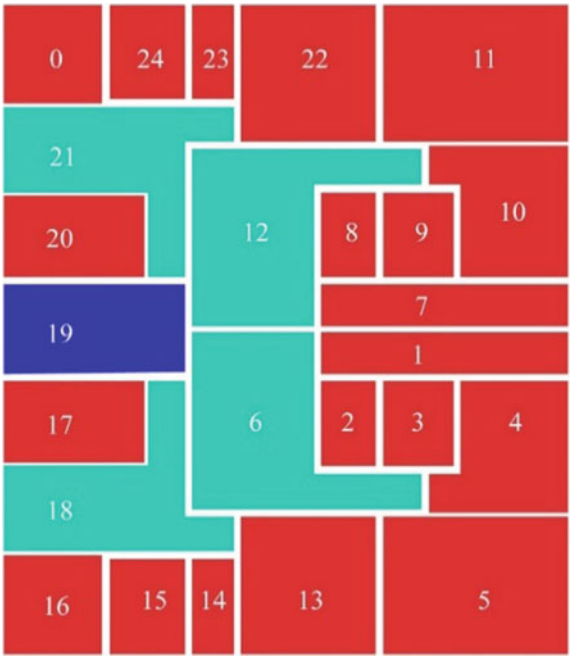

Fig. 11 Mean depth

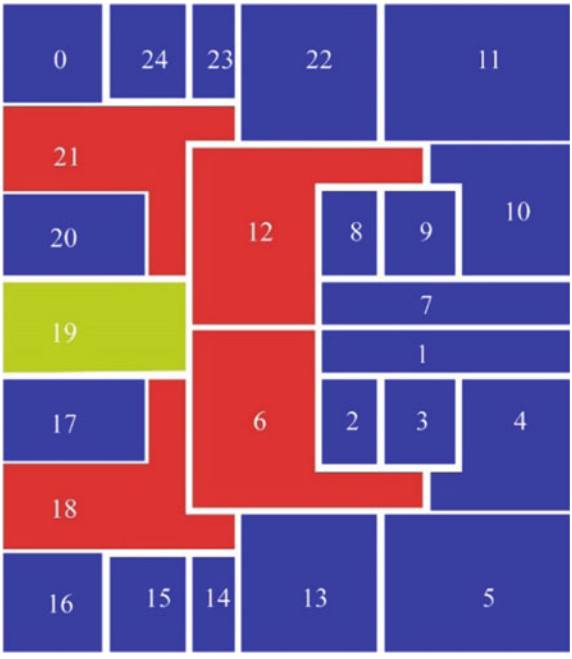

Fig. 12 Intensity

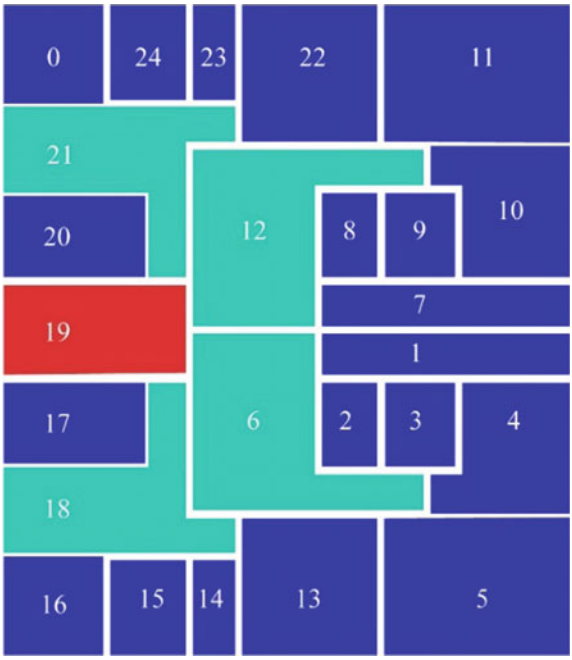

Fig. 13 Integration

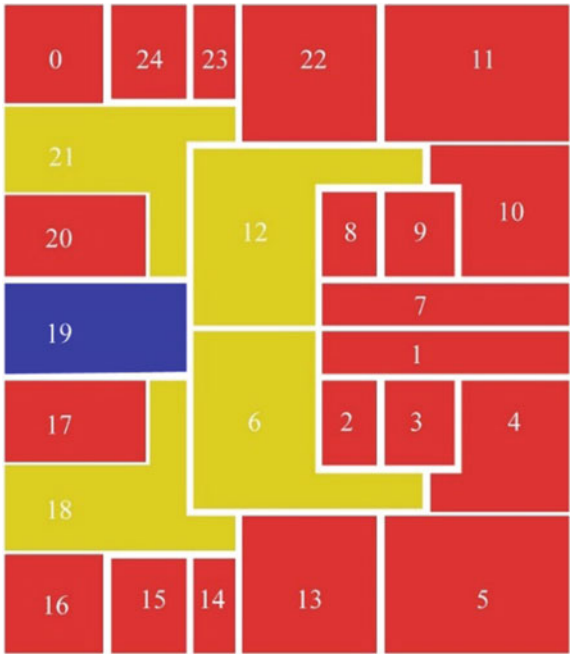

Fig. 14 Entropy

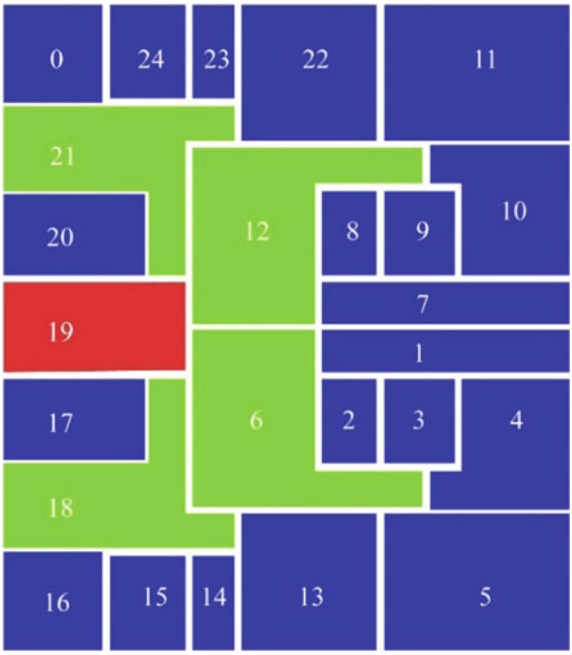

Fig. 15 Harmonic mean depth

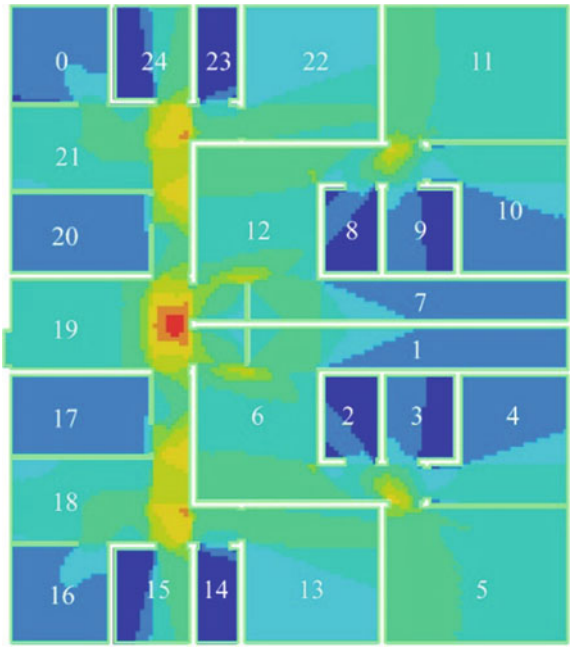

Fig. 16 Connectivity

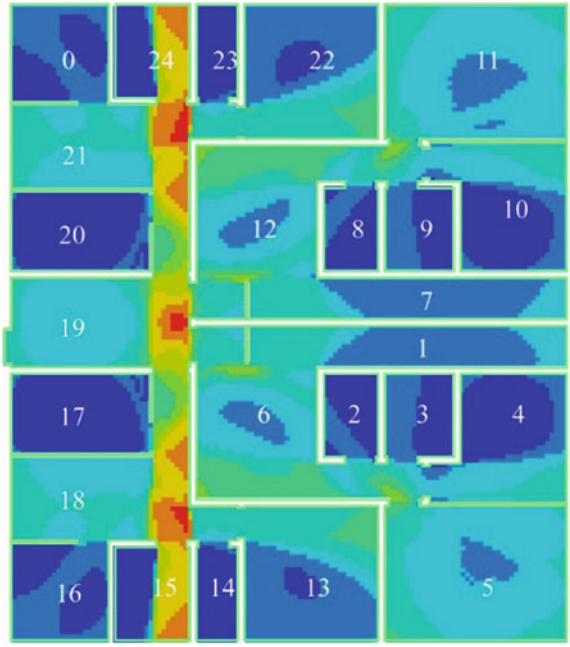

Fig. 17 Point first moment

the intensity of the other spaces is the lowest, having a value of only 0.663. This suggested that the distance and efficiency of access to the living rooms of the units were the highest and were followed by those of the common staircase, while those of bedrooms, kitchens, and bathrooms were the lowest.

(5) Integration [HH]: The integration of space 19 had the highest value, which was 2,762. It was followed by the values for spaces 21, 12, 18, and 6 with a total of 1,674. Other spaces had the lowest in intensity, with a value of 0.986. This indicated that the common staircase was the most accessible, followed by living rooms, while bedrooms, kitchens, and bathrooms were the least accessible. The integration was closely tied to the requirement for privacy in a particular space.

(6) Entropy: The entropy of spaces Nos. 21, 12, 18, and 6 was moderate with a value of 1.303. The entropy of space No. 19 was the lowest, with a value of 0.680, while that of the remaining spaces was the highest, with a value of 1.459. This suggested that the spatial layout of the spaces of the common staircase and living rooms of the units was asymmetrical, while that of bedrooms, kitchens, and bathrooms was more uniform and highly similar.

(7) Harmonic Mean Depth: The harmonic mean depth of space No. 19 is the highest, with a value of 13.333, followed by that of spaces Nos. 21, 12, 18, and 6 with a value of 8.823, while that of the other spaces was the lowest, with a value of 3.750. This indicated that the distance cost of the common staircase was the lowest, followed by that of living rooms, while that of the other spaces was the highest.

(8) Control: The control of the floor space of the Son Lei House was polarised. The control of spaces Nos. 21, 12, 18, and 6 was the highest, having a value of 5.250, while that of the other rooms was the lowest, with a value of 0.166. This suggested that the living rooms of the units were strongly controlled spaces, while the other spaces were weakly controlled spaces.
(9) Total Depth: The total depth of spaces Nos. 21, 12, 18, and 6 was moderate and had a value of 57. The total depth of space No. 19 was the lowest, having a value of 44. The total depth of the other spaces was the highest, with a value of 80. This indicated that the bedrooms, kitchens, and bathrooms had a high distance cost while living rooms and the common staircase had a low distance cost and good convenience.

To summarise, the common staircase No. 19 had the highest values of variables of choice, integration [HH], and harmonic mean depth and denoted the most important walking space in the Son Lei House, with the highest walking possibility, high workability, and the minimum distance cost. Living rooms Nos. 21, 12, 18, and 6 had the highest values of connectivity, intensity, and control and denoted the strongly controlled spaces of the Son Lei House, with high permeability and optimal distance and efficiency. The other spaces had the highest values of mean depth, entropy, and total depth and denoted spaces with the highest privacy level in the Son Lei House, with the best spatial symmetry and high distance cost. Therefore, the spatial quality of the common staircase in the Son Lei House needs to be paid attention to. The common staircase is not only the area with the highest possibility of walking for occupants but also the fire escape with the smallest distance cost. Thus, focusing on the spatial optimisation of the common staircase can effectively improve the occupants' living comfort.

3.3 Isovist Analysis

The visual experience is also an important indicator of occupants' space usage experience and is closely related to human perceptions, such as spatial recognisability and spatial attractiveness. In the isovist analysis (Table 4), based on the plan of the west side of the Son Lei House used in the previous space syntax numerical simulation, the plan was divided into 100 × 100 square cells, and parameters such as connectivity, point first moment, point second moment, visual integration, and visual mean depth were calculated for each cell using the spatial syntax to obtain the analysis results of each parameter (Figs. 18, 19, 20, 21, 22). The values were presented using warm to cold colours to indicate high to low values.

(1) Connectivity is related to the number of spaces in a directly connected system, reflecting the recognisability of spaces and the difficulty of finding them. As shown in Fig. 18, the connectivity at the junction of space No. 19 and spaces Nos. 21, 12, 18, and 6 was the highest, followed by that at the corridors of spaces Nos. 21 and 18, while that of spaces Nos. 24, 23, 8, 9, 2, 3, 15, and

Table 4 Indicator of isovist analysis

Indicator	Concept	Meaning	Expression
Connectivity	The cumulative number of other cells within the line-of-sight depth from a cell in a space looking outward	A cell with a higher value indicates that a larger number of cells in its adjacent region can be seen, thus a better line of sight This variable is for analysing the quality of the line-of-sight of a region	The indicators of the isovist analysis are represented graphically, where the values are colour-coded using warm and dark and cold and light colours to indicate high and low values, respectively
Point first moment	Calculation of the ratios of distance, form, and area of a cell with other cells in the space	A cell with a higher value has a greater potential for human wandering in that space	
Point second moment		A cell with a higher value has a greater potential for human wandering in that space and longer forms of isovists	
Visual integration [HH]	The reciprocal of the cumulative number of turns on the shortest path from a cell to any other cell	A higher value indicates that fewer turns are needed to see the cells in the space from a particular cell	
Visual mean depth	The mean of the cumulative number of line-of-sight depths starting from the selection set to the end-point cell	A higher value indicates a larger number of line-of-sight turns and a longer distance	

14 was the lowest. This indicated that the common staircase had the highest recognisability, followed by the living rooms on the south and north sides, and kitchens and bathrooms had the lowest recognisability.

(2) The point first moment and the point second moment are related to the form and area of the isovist and represent indices for judging the potential of human wandering in a particular space. They are calculated using the distance of visible cells; the point second moment index is the square of the visible cell distance of the point first moment index. The longer the shape of the isovist, the greater the potential for human wandering in space will be. As shown in Figs. 19 and 20, the areas with the highest point first moment index and point second moment index

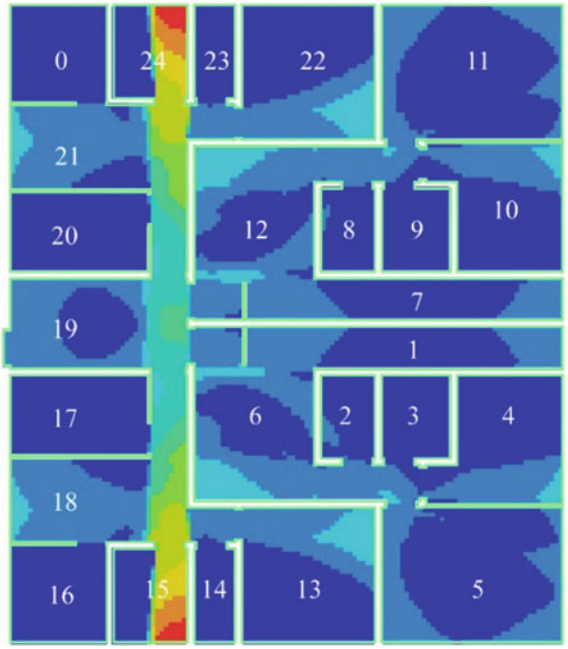

Fig. 18 Point second moment

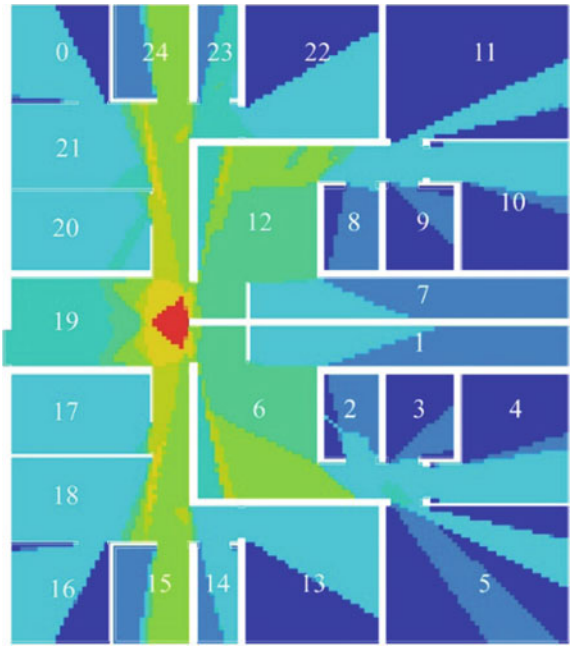

Fig. 19 Visual integration [HH]

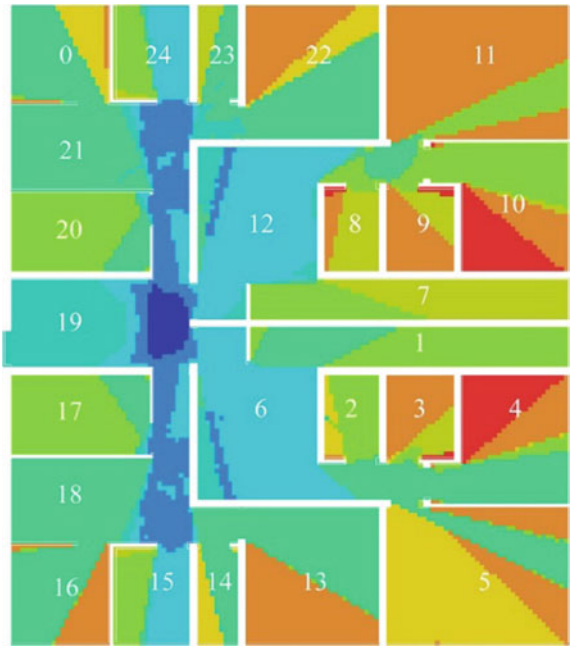

Fig. 20 Visual mean depth

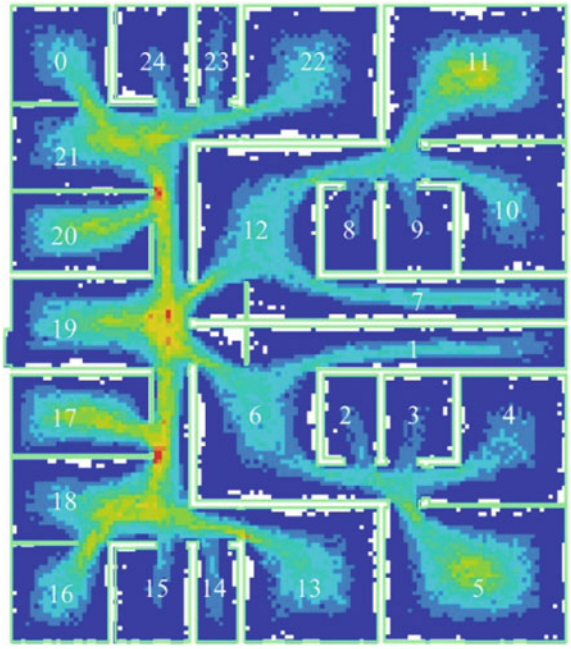

Fig. 21 Crowd flow analysis

were concentrated in the corridors where spaces Nos. 24, 21, 19, 18, and 15 were connected to each other. The second highest point first moment index occurred in spaces Nos. 11, 12, 6, and 5, suggesting that the corridors consisting of the common staircase and living rooms on the south and north sides had a great wandering potential. In addition, large bedrooms also had a certain wandering potential.

(3) Visual integration is a measure of the visual distance from a location to other spaces and is expressed as a degree of visibility and recognition of the space and thus can be used as an indicator of the visual attractiveness of the space. As shown in Fig. 21, the junction of space No. 19 with spaces Nos. 21, 12, 18, and 6 had the highest visual integration, and spaces on the west side had generally higher visual integration than spaces on the east side. This indicated that the common staircase was recognisable and attractive and that the closer a space was to the common staircase, the higher its visibility was.

(4) The visual mean depth indicates the accessibility of a location from other spaces. The depth value represents the number of spatial transformations and can reflect the space convenience. The larger the visual mean depth is, the more steps it is required to reach this space and the lower the convenience is. As shown in Fig. 22, spaces Nos. 10 and 4 had the highest visual mean depth, while space No. 19 had the lowest visual mean depth. This result suggested that the common staircase had the highest convenience, and the bedrooms on the east side required more relative steps to reach other spaces and had lower convenience than staircase.

In summary, the common staircase in the Son Lei House had the highest connectivity, point first moment index and visual integration, which indicated that the common staircase had significant advantages in spatial recognisability, wandering potential, and spatial attractiveness. Therefore, when optimising the design of a house, the environment of the common staircase should be particularly optimised. Kitchens Nos. 24 and 15 had the highest point second moment index, suggesting that these spaces had the deepest isovist, and the unobstructed state of the space should be enhanced to avoid obstruction of the interior furniture. Further, bedrooms Nos. 10 and 4 had the highest visual mean depth, which indicated that these spaces required more relative steps to reach the other spaces and hence had low convenience. This suggested their disadvantages in situations requiring rapid evacuation, such as fire escape, and indicated a need for enhancing the fire escape arrangement of this type of space.

3.4 Crowd Flow Analysis

An agent model was used to simulate and analyse the indoor crowd flow. In the space syntax field, agent models simulated the personalised movement behaviour of a person. The agent determined the line-of-sight range based on the isovist analysis

results, selected its own movement direction, pre-calculated the visual information of a given location, and simulated the crowd gathering condition in space. Based on the previous isovist analysis, the crowd flow analysis was performed (Figs.18, 19, 20, 21), and the crowd gathering was colour-coded using warm and cold colours to indicate high and low levels, respectively. As shown in Fig. 21, the areas with the highest crowd gathering included spaces Nos. 21, 19, and 18, especially the junctions of these spaces, followed by large bedrooms Nos. 11 and 5, while small spaces Nos. 24, 23, 8, 9, 2, 3, 15, and 14 had the lowest crowd gathering. This indicated that people were the most likely to gather in the staircase and living rooms, followed by gathering in large bedrooms, while they were at least likely to gather in bathrooms and kitchens. Accordingly, attention should be paid to the conditions of security and fire protection in areas with a high crowd gathering.

4 Conclusion

Prefabricated embedded buildings are one of the construction types of old residential buildings in Macau. Due to the relatively fixed model of its house type, there is a high demand for environmental improvement and optimisation. Numerical analysis of space syntax, isovist analysis, and crowd flow analysis can effectively judge the shortcomings of its plane form and optimisation potential. This paper takes Son Lei House of Iao Hon estate as an example, and the research process and conclusion can also be applied to the prefabricated embedded buildings with similar plane shape, which has universal applicability.

Taking the Son Lei House as a case study, the numerical simulation of various indicators of the space syntax of the plan form of the prefabricated building was conducted. Based on the obtained simulation results, the following conclusions can be drawn: (1) priority should be given to the optimal design for environmental quality improvement and age-friendliness of spaces of the common staircase in the Son Lei House, which have the highest values of variables of choice, integration [HH], harmonic mean depth, connectivity, point first moment index, visual integration, and crowd flow simulation; (2) occupants in units with living rooms having the highest or second-highest values of variables of connectivity, intensity, control, and crowd flow simulation should be instructed to improve the security measures of their living rooms; (3) occupants in units with bedrooms Nos. 10 and 4, which have the highest visual mean depth, should be instructed to improve the fire protection measures in these bedrooms.

Using space syntax as the main research method in conjunction with field investigation, this study performs the spatial analysis and interpretation and conducts the isovist analysis and crowd flow analysis through computer simulations. Despite certain limitations, the research findings can predict the isovist range and the possibility of crowd gathering. In the future, the analysis results could be corroborated using multi-source data such as those from eye-trackers, GPS positioning, and cell phone signalling, to improve the accuracy of the analysis.

References

1. Xiaorui Z, Zhigang C, Yan B (2014) Research progress and prospects of space syntax. Geogr Geogr Inf Sci 30(3):82–87
2. Jingnan H, Haowu G, Mengwei D (2014) Research on the recognizability of indoor space in shopping malls based on space syntax: taking Wuhan optics valley pedestrian street as an example. Urban Probl 6:46–52
3. Yi D, Bin H (2016) Aframework for planning and design of urban public space for aging based on space syntax. Urban Issues 6:53–60
4. Xi Z, Fang Z (2021) Sightline analysis and optimization strategy of underground space based on space syntax. Chin J Undergr Space Eng 4:1008–1014
5. Yige Z, Fangrong Y, Mengyao W (2022) Analysis of crime prevention and control in urban parks based on CPTED theory and space syntax: Taking Zhengzhou people's park and Zijingshan park as examples. J Southwest Univ (Natural Science Edition) 44(1):202–212
6. Yuetao W, Jingwen S, Binxia X, Yuanjing Z (2021) Research on the improvement strategy of "island effect" in historical cities based on space syntax. Urban Dev Res 4:99–107+2+37
7. Chuqian Y, Daping L (2019) Interpretation of modern Russian-style residential culture in Harbin based on space syntax. In: Proceedings of the 2019 annual meeting and academic symposium of the architectural history branch of the architectural society of China (Part 2)
8. Xiaoxu L, Jin L, Peng W, Jie L (2021) Research on urban public space renewal in the central area of Shihezi Old City, Xinjiang based on space syntax. J Northwest Normal Univ (Natural Science Edition) 134(5):83–88
9. Dayu Z, Lai F, Yang L (2021) Research on the evaluation and improvement countermeasures of public space use of Zhanzhan Road Street in Beijing based on space syntax. Urban Dev Res 11:38–44+173
10. Jornal "Va Kio". Retrieved from http://www.vakiodaily.com/. Accessed on 19 Mar 2022

Structural Health Monitoring and Construction Surveying

Deployment of Self-Powered Structural Health Monitoring System for Highway Bridges

Hoang Minh Ngo Le and Saiji Fukada

Abstract The development of the wireless sensor network has provided an effective tool for building a structural health monitoring system that can monitor the condition of civil structures and infrastructure in real time. However, the power supply for data acquisition components and wireless data communication modules becomes a challenge when the traditional power supply—the electrochemical battery—is limited to short-time operation and the wireless data communication modules must operate with a high frequency to meet the terms "in real time". This study first proposes a self-powered structural health monitoring system using a magnetostrictive vibration energy harvester. A field test was conducted to evaluate the performance of three wireless data communication technologies: IM920, long-range (LoRa), and Sigfox. According to the observation results, Sigfox is the most appropriate wireless data communication technology for the proposed self-powered structural health monitoring system with inexpensive, reliable, and low power consumption advantages. Subsequently, two long-term energy harvesting tests were conducted using the magnetostrictive vibration energy harvester to evaluate the device's performance. Finally, the proposed self-powered structural health monitoring system was deployed at an actual highway bridge and operated stably with the data frequency transmitted four times a day. These results proved the potential for developing a real-time self-powered structural health monitoring system.

Keywords Wireless data communication · Self-powered · Structural health monitoring system · Magnetostrictive materials · Vibration energy harvester

H. M. N. Le (✉)
Graduate School of Natural Science and Technology, Kanazawa University, Ishikawa, Japan
e-mail: ngolehoangminh97@gmail.com

S. Fukada
Faculty of Geosciences and Civil Engineering, Kanazawa University, Ishikawa, Japan
e-mail: saiji@se.kanazawa-u.ac.jp

T. Kang (ed.), *Proceedings of 5th International Conference on Civil Engineering and Architecture*, Lecture Notes in Civil Engineering 369,
https://doi.org/10.1007/978-981-99-4049-3_34

1 Introduction

The recent implementation of the structural health monitoring (SHM) system using a wireless sensor network (WSN) is a big step for applying the Internet of things (IoT) technologies to structure management. Monitoring and maintaining the functional value of the infrastructure continuously can increase the structural lifetime, provide public safety, and reduce the maintenance cost significantly. A typical SHM system generally consists of three steps: data acquisition, data communication, and health evaluation [1]. Data acquisition or data sampling is a technique to measure the current functional value of the target structure through destructive testing techniques (DT) and nondestructive testing techniques (NDT). DT aims to completely deform or destroy a sample to analyze its failure point. Conversely, NDT uses inspection methods that do not damage the testing sample. Testing techniques are selected appropriately in different scenarios based on the measure factor and damage detection strategies and keep economic, environmental, and operational conflicts in mind. However, the most significant advantage of NDT techniques is that it is appropriate to apply WSN technologies, potentially developing a continuous data acquisition system for monitoring structural health.

Data acquisition is an essential step in SHM undertaken by various sensing units. In the past decade, data acquisition technology has shifted from the traditional wired sensor to the advanced wireless sensor because of the advantage of being economical and safe. Wireless sensor networks allow inspectors to sample on-site data remotely when data is transferred over a radio frequency or the Internet. WSN consists of the following hardware components for on-site data sampling: a sensor, wireless data communication module, and power supply unit. From the early twenty-first century, long-term monitoring systems comprising acceleration meters, displacement sensors, and strain gauges were installed on various bridges around the world to assess bridge health conditions [2]. However, these systems face challenges of limited power supply of electrochemical batteries [3]. Although the power requirement of each WSN has been reduced to only tens of milliwatts recently, the batteries require recharging or replacing. The power supply unit can reach thousands of batteries for a large-scale infrastructure such as an over-sea bridge or highway route. Consequently, recharging or replacing these thousands of batteries may increase the maintenance cost significantly and endanger the engineers.

Researchers tried to seek alternatives to an electrochemical battery with many different approaches. The key technology behind the potential power supply unit is an energy harvester that can generate electrical power from ambient sources. The power supply unit of an SHM system, which can commercialize, has to guarantee features like high stability, high durability, and low cost. Potential energy sources include solar, wind and structural vibration. Solar energy harvesters can convert solar energy to electrical energy directly with an efficiency of approximately 20% in general and reach 46% in some scenarios [4]. For wind energy, the current wind turbines can extract electrical power with the actual power coefficient ranging from 0.2 to 0.5 [5].

Regarding the structural vibration energy harvesting technology, many types of vibration energy harvesters (VEH) are proposed, such as piezoelectric vibration energy harvesters (PE-VEH) [6], electrostatic vibration energy harvesters (ES-VEH) [7], electromagnetic vibration energy harvesters (EM-VEH) [8], and magnetostrictive vibration energy harvesters (MS-VEH) [9]. Since solar and wind energy harvesters are expensive and vulnerable to weather and location, structural vibration energy harvesting technology is a promising approach as an alternative to the traditional electrochemical battery because of the advantages of a high coupling coefficient, no depolarization/aging, easy installation, wide-range application, and low cost [10]. However, the ability to power a real-time SHM system remains to be elucidated.

The bridge vibration energy harvesters are classified into EM-VEH [11, 12], PE-VEH [13, 14], and MS-VEH [15–17] based on their energy conversion mechanism. These energy harvesters required calibrating to resonant to the vibration source to reach the best performance [15, 16, 18]. The output capacity of the PE-VEH is from 0.6 to 7700 μW, with the resonant frequency range from 1 to 120 Hz. The output capacity of the EM-VEH is from 0.7 to 1,450,000 μW, with the resonant frequency range from 0.13 to 27 Hz [18]. In 2022, Khan and Ahmad proposed a self-powered vibration-based structural health monitoring system (SV-SHM) with the power supply of an MS-VEH [18]. The operation of this system was tested by installing it on an actual bridge. The results show that the small-sized MS-VEH device proposed by Koganezawa [19] can generate 30.3 mJ per hour in conditions of non-resonance. This 30.3 mJ energy can ensure the SV-SHM operates at least once every two days. Another MS-VEH, proposed by Ueno and Yamada [9], was tested in the laboratory under the actual vibration condition of a highway bridge by Kita et al. [20]. The results show that this MS-VEH generated a peak voltage of 7 V, an instantaneous maximum power of 36 mV, and total energy of 52 mJ in five minutes.

Applying the appropriate wireless data communication technologies is another approach to making the SHM system using WSN operate more efficiently and become a real-time SHM system. The rapid development of communication technologies allows humans, devices, and software to connect through the Internet, known as the Internet of things (IoT). This significant benefit has led to the advent of many applications and solutions serving humanity. The remarkable communication technologies can be listed as WiMAX and long-term evolution (LTE) of the fourth-generation mobile communication networks (4G); or the low-power wide-area network (LPWAN) technologies of the fifth-generation mobile communication networks (5G). However, communication technologies still face many challenges regarding a power source, performance, security, and quality of service (QoS), e.g., the applications of wireless data communication technology in monitoring structural health are still in the study process and have not yet become widespread. Infrastructure such as highways and bridges commonly pass through mountainous or forested areas, where electrical power is not readily available, and the cellular or radio coverage is lacking [21]. Therefore, the wireless data communication solutions need to conduct a field test to examine the practical performance before being applied to the SHM system using WSN.

In this study, the authors first introduced a self-powered structural health monitoring system (SSHM) using an MS-VEH proposed by Ueno and Yamada [9]. Then, the actual performance of three wireless data communication technologies, low-power wide-area (LPWA), long-range (LoRa), and Sigfox is examined in the field test. Finally, the performance, oscillation characteristic of the MS-VEH device, and stability of this SSHM system were reported.

2 Self-Powered Structural Health Monitoring System

2.1 Outlines of the Self-Powered Structural Health Monitoring System

To enhance the efficiency of structural health monitoring and maintenance, the authors propose a self-powered structural health monitoring system (SSHM) using an MS-VEH device. This SSHM system was developed with the following keywords:

- Bridge-vibration-based power supply unit (MS-VEH),
- Applying wireless sensor networks technologies in data acquisition,
- Real-time data and cloud database,
- Ability to apply artificial intelligence (AI) in SHM in the future, and to become a closed-loop automation SHM system.

Figure 1 shows the schematic diagram of the developed self-powered structural health monitoring system. This SSHM system consists of four components: an MS-VEH device and a rechargeable battery in the role of a power supply unit, a titanium wire sensor (TiWS) and a temperature sensor in the role of a monitoring sensor, a wireless data communication unit, and a cloud database. The MS-VEH device extracts electrical energy directly from structural vibration. This energy is stored in a rechargeable battery before being supplied to the TiWS and wireless data communication unit. The details of each component in this SSHM system are described in the following sections.

2.2 Power Supply Unit: Magnetostrictive Vibration Energy Havester

This study utilized a large-sized MS-VEH device (150 × 60 × 50 mm and 0.6 kg in weight with a Fe-Ga alloy plate of 50 × 16 × 2 mm) proposed by Ueno [22] as a power supply unit. Figure 2 shows the structure and principle of this MS-VEH device. The MS-VEH device consists of a U-shaped frame, Fe-Ga alloy plate, copper coil, permanent magnet, and weight fixed to the upper arm tip of the frame. The Fe-Ga alloy, a low-cost magnetostrictive alloy, is rolled laminate before being attached

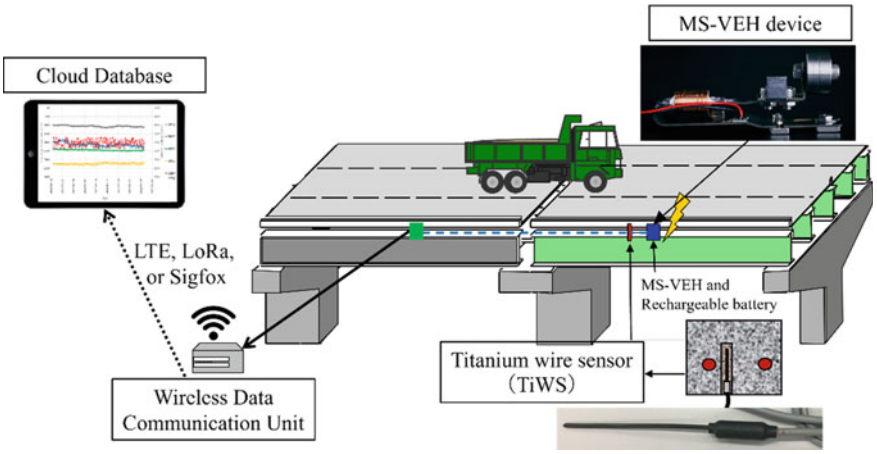

Fig. 1 Outline of the self-powered structural health monitoring system

to the upper arm of the U-shaped frame. Then, the copper coil is wound around the Fe-Ga plate and upper arm. The permanent magnet is placed inside the frame to magnetize the Fe-Ga alloy appropriately by the magnetic bias.

To harvest energy, the lower arm of the U-shaped frame is fixed to the vibration source, while the upper arm operates as a unimorph. An inertial force is applied to the weight when this device vibrates in the vertical direction along with the vibration source. As a result, the upper arm is bent, and the tensile-compressive stress occurs alternately in the longitudinal direction of the Fe-Ga alloy plate. Simultaneously, the magnetic flux increases and decreases via the inverse magnetostrictive effect. The magnetic flux change leads to an electromotive force occurring in the copper coil.

Theoretically, the MS-VEH device will reach the maximum performance when this device resonances to the vibration source. However, in practice, the device's performance also depends on the installation position at the structure. In the previous study, Ha et al. calibrated the weight to make this device resonate with the lateral

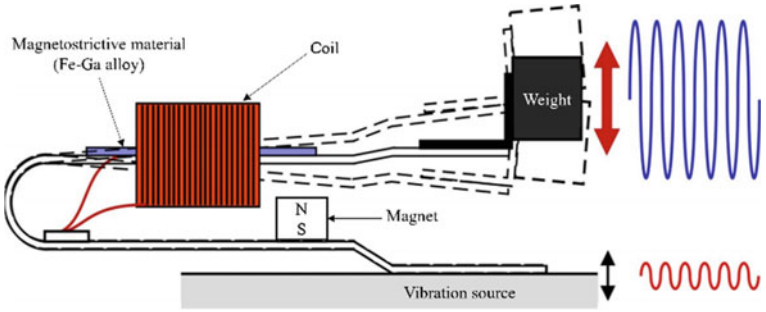

Fig. 2 Outline of the magnetostrictive vibration energy harvester proposed by Ueno [22]

bracing of an actual bridge and enhance the device's performance [15]. Le et al. then conducted a study to find the optimal placement in an actual highway bridge to install the device [16]. These studies made this MS-VEH device perform at its best in the field test. Then, Kita et al. succeeded in utilizing a large-sized MS-VEH device to power an LPWA module [20].

2.3 Data Acquisition: Titanium Wire Sensor and Temperature Sensor

The proposed SSHM system was deployed at a highway bridge in the Hokuriku area, a frosty region located in the northwestern part of Japan. The previous studies confirmed that steel corrosion caused by spraying anti-freezing agents is a leading cause of premature deterioration of the bridge. To mitigate the steel corrosion, Ha et al. proposed a steel corrosion mitigation method using galvanic anode materials [23]. The performance of this corrosion mitigation method is evaluated by monitoring the rebar potentials according to the ASTM C876 Standard [24]. Subsequently, Tran et al. embedded a titanium wire sensor (TiWS) (Fig. 3) into this bridge's reinforced concrete slab (RC slab) to measure the rebar potentials [25].

In this study, the authors decided to continue using these embedded TiWS to monitor the steel corrosion of the test bridge. While the conventional reference electrode was expensive and unsuitable for a wide-range measurement, the TiWS had many advantages, e.g., with a size of only 3 mm in diameter and a varied length, the TiWS can easily be embedded into the structure by a 10 mm diameter drill hole. Furthermore, the 50 mm-long TiWS sensor costs only 1/20 of the conventional reference electrode's price [25]. The TiWS can measure the rebar potentials automatically and is suitable for a WSN system.

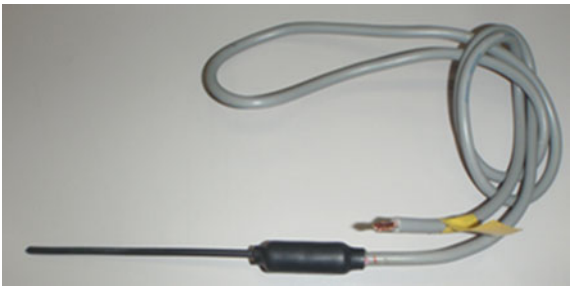

Fig. 3 Titanium wire sensor (TiWS)

Fig. 4 Wireless data communication modules

2.4 Wireless Data Communication: Sigfox

To seek an appropriate wireless data communication solution for the SSHM system, the authors conducted a transmission capacity test of the current data communication technologies. After considering the energy consumption, QoS, transmission range, and cost, it was found that long-range (LoRa) and Sigfox are the potential wireless data communication solutions. Therefore, the authors decided to use those solutions to conduct a transmission capacity test at the actual bridge. Specifically, the IM920XL module (interplan Co., Ltd.), ES920B module (LoRa, EASEL, Inc.), and WF923 module (Sigfox, SMK Corporation) were used in the field test (Fig. 4).

According to interplan Co., Ltd., the transmission range of the IM920XL module is 400 m in high-speed mode and can reach 7 km in long-range mode. Although EASEL, Inc. did not report the transmission range of the ES920B module, previous studies confirmed that LoRa technology could transfer data with a range of 5 km in urban areas and 45 km in rural areas. However, the field test results showed that the IM920XL module could operate stably in a 200 m-radius area with a successful reception rate of 100% and a received signal strength indication (RSSI) in the range of 119 to 135. In comparison, the ES920B module could operate stably in a 2000 m-radius area with a successful reception rate of 88.8% and minimum receiver sensitivity of − 142 dBm. Regarding the WF923 module, because data is transferred to the back-end servers and storage with Sigfox technology, the WF923 module can transfer data in the service area (coverage area) provided by the SMK Corporation (see Fig. 5) [26]. The maximum power consumption of the IM920XL, ES920B, and WF923 is 10, 20, and 20 mW, respectively.

After considering the transmission capacity, power consumption, and stability, the authors decided to utilize the Sigfox WF923 module as the wireless data communication for the proposed SSHM system.

2.5 Off-Site Data Monitoring: Cloud Database System

In this study, the monitoring data collected via TiWS and temperature sensors is transferred to the back-end servers and storage of Sigfox. However, when the SSHM system officially operates, monitoring data will be synchronized to the cloud

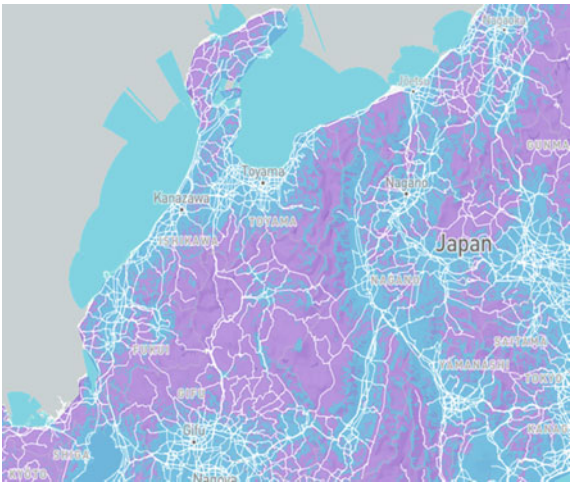

Fig. 5 Sigfox coverage area in the Hokuriku Area, Japan [26] (*Blue* Coverage Area; *Purple* Under Roll-Out area; *Grey* Non-Coverage Area)

database system. This database system allows the engineers access to the location, general information, maintenance history, and real-time monitoring data of many infrastructures.

3 Deployment of the Self-Powered Structural Health Monitoring System to an Actual Highway Bridge

3.1 The Target Bridge

The target bridge in this study is a part of an elevated line in the Hokuriku Expressway. With an average daily traffic volume of approximately 20,000 vehicles, this elevated line has been in service since 1978 and has become a vital regional route. The elevated line was built with various structures with a total length of 8.6 km. The test bridge was constructed as a continuous bridge with the reinforced concrete slab (RC slab) supported by four main steel girders and five concrete piers at the test site. After 44 years in service, the test bridge was degraded with many potholes, cracks, and efflorescence on the road and concrete surface. Furthermore, salt damage due to anti-freezing agents (de-icing salts) was also confirmed (Fig. 6) [23].

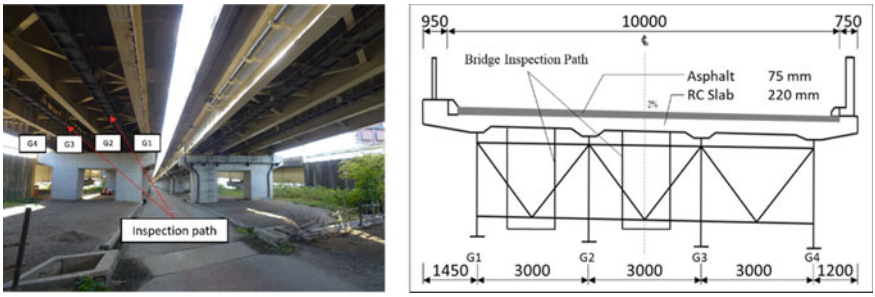

Fig. 6 Test bridges and section plan

3.2 Oscillation Characteristics of the MS-VEH Device

As mentioned above, the target bridge has a complex structure with many components, and each component vibrates at different frequencies and amplitudes. Therefore, the installation location impacts the MS-VEH device performance significantly. For example, in 2021, Le et al. [16] confirmed that the lateral bracing between main girders G1 and G2 at the test area with a frequency of 19.7 Hz was the optimal place to install the MS-VEH device. However, previous studies reported structural frequency changes under different ambient temperatures [27]. The difference in average temperature in summer and winter in the Hokuriku area can reach 30°C. Therefore, in this study, the authors installed the MS-VEH device at the optimal location in February (one week) and July (two weeks) to evaluate the MS-VEH device operation and oscillation characteristics during the winter (February) and summer (July). Figure 7 shows the experimental setup.

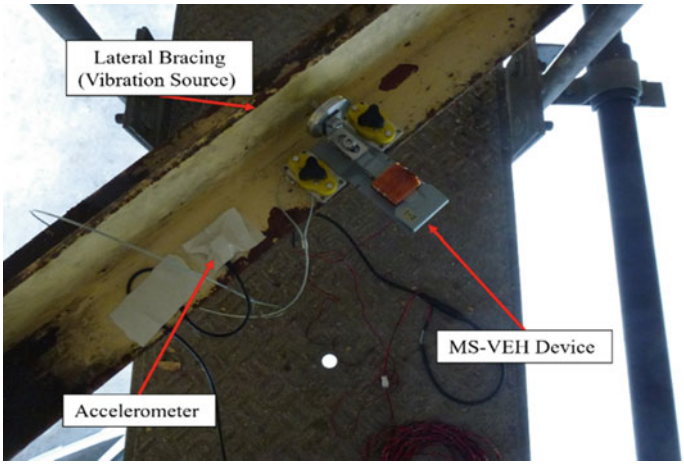

Fig. 7 Experimental setup

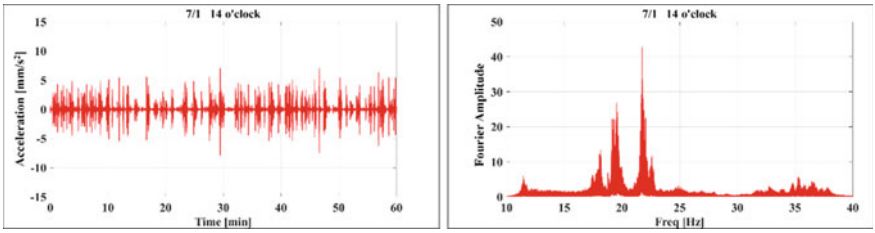

Fig. 8 Example of acceleration response and its frequency response

In the long-term energy harvesting tests, the vibration source acceleration, MS-VEH device acceleration, and voltage generated by the MS-VEH device were collected continuously during the experiment duration with a sampling frequency of 200 Hz. Subsequently, the dominant oscillation frequency of these factors was identified using the fast Fourier transformation algorithm (FFT). Figure 8 shows an example of the acceleration response and its frequency response. The generated power of the MS-VEH device was computed from the collected voltage and system resistance. The dominant oscillation frequency of the MS-VEH device and vibration source was recorded every five minutes and plotted in Fig. 9 for comparison. In addition, the peak value of the vibration source acceleration and the peak value of the generated power were also recorded every five minutes (maximum instantaneous value) (Fig. 10).

Figure 9 shows the frequency of the vibration source and MS-VEH device in February and July. In February, with an average ambient temperature of 6.5°C, the dominant oscillation frequency of the MS-VEH device was approximately 17.6 Hz, while the lateral bracing vibrated with a dominant frequency of roughly 20 Hz. Based on these results, the attached weight on the MS-VEH device was calibrated to make the device resonate with the vibration source. Subsequently, the authors conducted the field experiment again in July. With an average ambient temperature of 25.6°C, the dominant oscillation frequency of the MS-VEH device after calibration was approximately 19.6 Hz, while the lateral bracing vibrated with a dominant frequency of approximately 21.8 Hz. These results showed that the oscillation frequency of the lateral bracing increased when the ambient temperature increased. Consequently, although the attached weight was calibrated, the MS-VEH device could not resonate with the vibration source. In this case, the change in lateral bracing frequency contradicts the previous studies when the reported structural frequency decreases as the ambient temperature increases [27].

Figure 10 shows the correlation between the maximum instantaneous power (in five minutes) of the MS-VEH device and the maximum instantaneous acceleration level of the vibration source. Since it is difficult to find the tendency only by plotting the maximum instantaneous power and maximum instantaneous acceleration, a nonlinear trendline for each scenario was calculated. Regarding the acceleration level of the vibration source, approximately 89% of the maximum instantaneous acceleration in February ranged from 2 to 6 mm/s^2, while approximately 85% of the

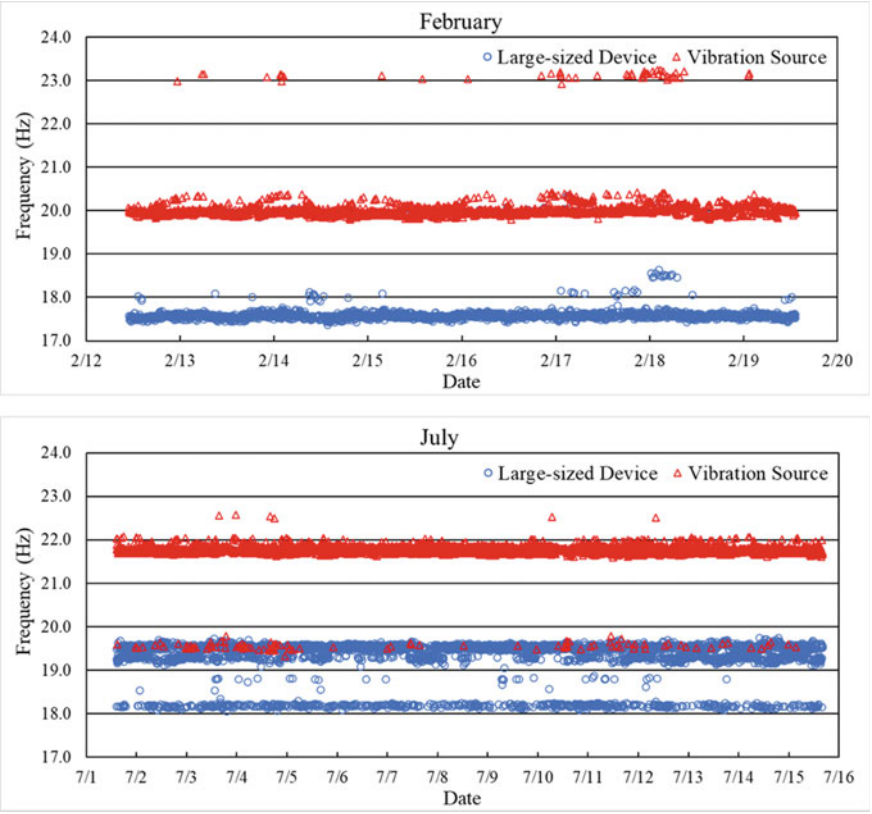

Fig. 9 Oscillation frequency of the MS-VEH and the lateral bracing in February and July

maximum instantaneous acceleration in July ranged from 4 to 8 mm/s^2. These results conclude that the oscillation frequency and amplitude of the vibration source (the lateral bracing) in July are higher than in February. Regarding the output power of the MS-VEH device, most of the maximum instantaneous power in both February and July ranged from 0 to 15 mW. However, when focusing on the power-acceleration trendline, the performance of the MS-VEH device was better in February, with an oscillation frequency of 17.6 Hz.

Figures 11 and 12 show the variation of the maximum instantaneous acceleration and power in a day and a week, respectively. The vibration source acceleration increases from 7 o'clock to 10 o'clock and from 12 o'clock to 17 o'clock before decreasing in the evening. This variation agrees with the daily traffic volume changes and leads to the variation of the generated power of the MS-VEH device during the day (Fig. 11). Similarly, both the acceleration and generated power tend to increase on weekdays and decrease on weekends (Fig. 12). These results confirmed the relationship between the traffic volume and generated energy of MS-VEH device.

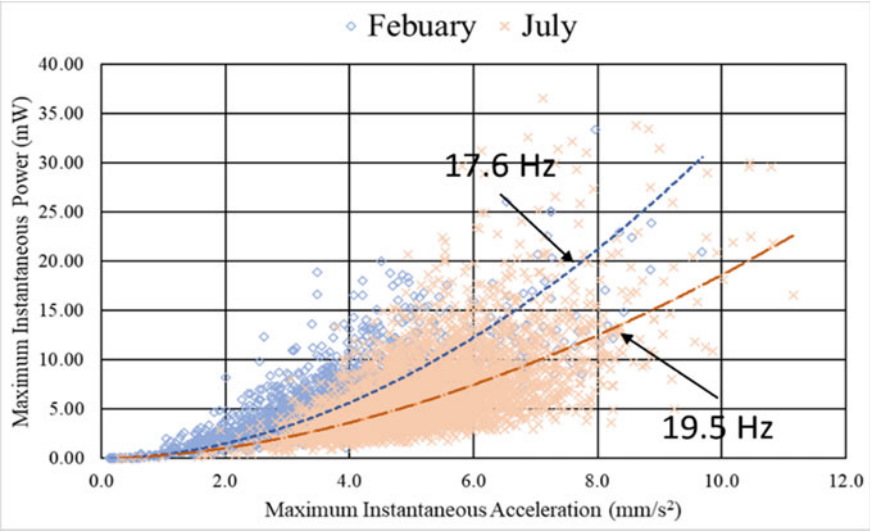

Fig. 10 Correlation between the maximum instantaneous power of the MS-VEH device and the maximum instantaneous acceleration of the vibration source

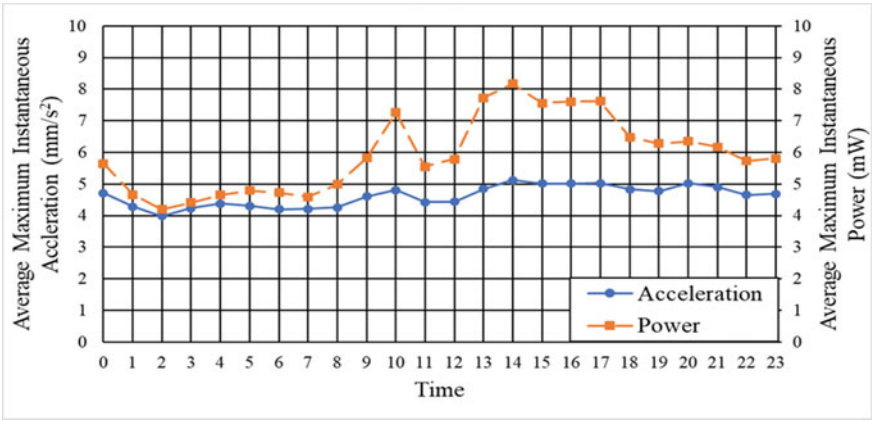

Fig. 11 Variation of the vibration source acceleration and the generated power of the MS-VEH device during the day

3.3 Stability of the SSHM System

With the aim of evaluating the power supply ability of the MS-VEH device and the stability of the WF923 Sigfox wireless data communication modules, the SSHM system was deployed over two months at the target bridge with one MS-VEH device and one WF923 Sigfox module installed at the lateral bracing between main girders

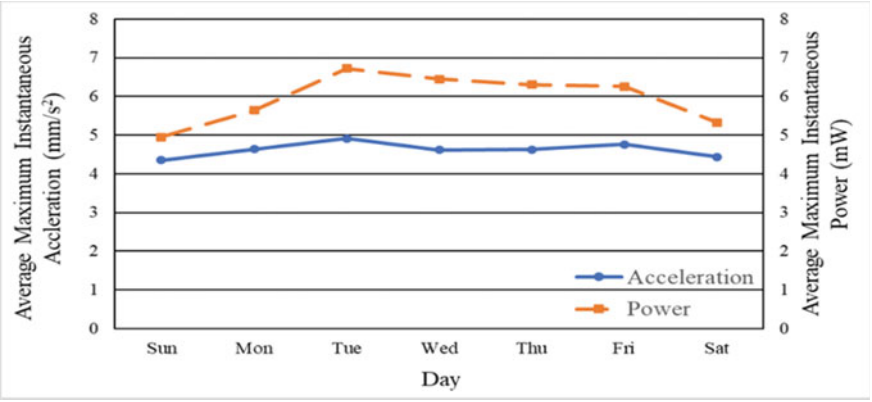

Fig. 12 Variation of the vibration source acceleration and the generated Ppwer of MS-VEH device during the week

G1 and G2. The monitoring data included the battery voltage, ambient temperature, and assumed rebar potential. The data was in hexadecimal format and transferred four times a day due to the Sigfox limitation of daily downlink (DL) message numbers (with a maximum payload length of eight bytes).

After 74 days, the SSHM system sent 294 messages to the Sigfox back-end server with a successful transfer ratio of 100%. Furthermore, the link quality indicator of all messages was in "good" status. Ambient temperature variations and battery voltage tendency from early September to middle November are shown in Fig. 13. Because the battery current is constant, the battery voltage variation can be considered the battery capacity variation. During the experiment, the battery voltage tended to increase while the WF923 Sigfox module sent four messages daily with a transmitted power of 25 mW [28].

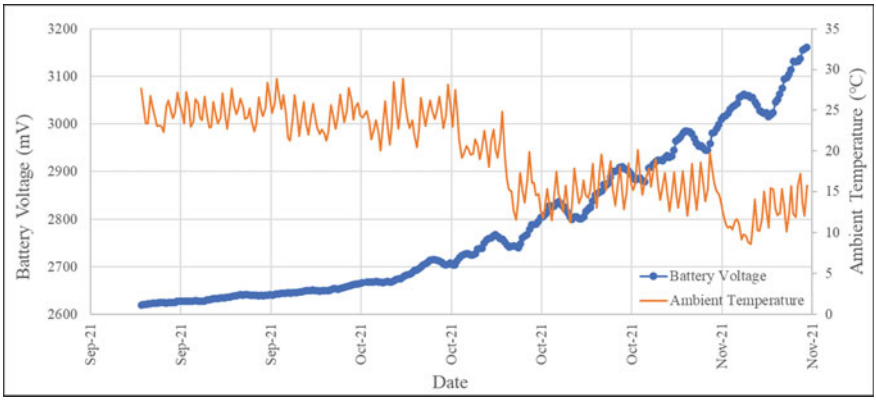

Fig. 13 Tendency of battery voltage and variation of ambient temperature

The experimental results have proven the stability of the proposed SSHM system and the energy harvesting and powering ability of the MS-VEH device.

4 Conclusion and Discussion

This study first proposed and deployed a self-powered structural health monitoring system at a highway bridge. The transmission capacity test was conducted to evaluate the performance of three wireless data communication technologies: IM920, long-range (LoRa), and Sigfox. Lastly, the MS-VEH device's oscillation characteristics and the SSHM system's stability were also reported. The noticeable results obtained from this study are as follows:

1. The transmission capacity test results confirmed that Sigfox is the most appropriate wireless data communication technology for the proposed SSHM system, with advantages in transmission capacity, power consumption, and stability. Consequently, the WF923 Sigfox module was utilized as a wireless data communication unit of the SSHM system in the deployment process at an actual highway bridge.
2. The long-term energy harvesting test results show that in February, with the average ambient temperature of 6.5°C, the dominant oscillation frequency of the MS-VEH device was approximately 17.6 Hz, while the lateral bracing vibrated with a dominant frequency of approximately 20 Hz. In July, after being calibrated, the dominant oscillation frequency of the MS-VEH device was approximately 19.6 Hz. However, the lateral bracing, at that time, vibrated with a dominant frequency of approximately 21.8 Hz. Therefore, the MS-VEH device could not resonate with the vibration source in both scenarios.
3. Regarding the generated power, most of the maximum instantaneous power in February and July ranged from 0 to 15 mW in the acceleration level under 8 mm/s^2. In the non-resonant condition, the MS-VEH device performs better with an oscillation frequency of 17.6 Hz than with an oscillation frequency of 19.5 Hz. In addition, the energy harvested by the MS-VEH device tends to increase on weekdays in the daytime.
4. After 74 days of deploying at an actual highway bridge, the SSHM system sent 294 messages to the Sigfox back-end server with a successful transfer ratio of 100% and the link quality indicator of all messages was in "good" status. During the experiment, the battery voltage increased while the WF923 Sigfox module sent four messages daily. These results have proven the stability of the proposed SSHM system and the energy harvesting and powering ability of the MS-VEH device.

References

1. Li H-N, Ren L, Jia Z-G et al (2016) State-of-the-art in structural health monitoring of large and complex civil infrastructures. J Civil Struct Health Monit 6:3–16
2. Ko JM, Ni YQ (2005) Technology developments in structural health monitoring of large-scale bridges. Eng Struct 27(12):1715–1725
3. Haldar A (2013) Health assessment of engineered structures: bridges, buildings, and other infrastructures. World Scientific Publishing Co. Pte. Ltd, Singapore
4. Dhilipan J, Vijayalakshmi N, Shanmugam DB et al (2022) Performance and efficiency of different types of solar cell material–a review. Mater Today: Proc 66(3):1295–1302
5. Ilhan A, Sahin B, Bilgili M (2021) A review: diffuser augmented wind turbine technologies. Int J Green Energy 19(1):1–27
6. Jeon YB, Sood R, Jeong J-h, Kim S-G (2005) MEMS power generator with transverse mode thin film PZT. Sens Actuators A Phys 122(1):16–22
7. Mitcheson PD, Miao P et al (2004) MEMS electrostatic micropower generator for low frequency operation. Sens Actuators A Phys 115(2–3):523–529
8. Chiu M-C, Chang Y-C, Yeh L-J, Chung C-H (2012) Optimal design of a vibration-based electromagnetic energy harvester using a simulated annealing algorithm. J Mech 28(4):691–700
9. Ueno T, Yamada S (2011) Performance of energy harvester using iron-gallium alloy in free vibration. IEEE Trans Magn 47(10):2407–2409
10. Deng Z, Dapino MJ (2017) Review of magnetostrictive vibration energy harvesters. Smart Mater Struct 26:103001
11. Kwon S-D et al (2013) Electromagnetic energy harvester with repulsively stacked multilayer magnets for low frequency vibrations. Smart Mater Struct 22:055007
12. Galchev T, Kim H, Najafi K (2011) Micro power generator for harvesting low-frequency and nonperiodic vibrations. J Microelectromech Syst 20(4):852–866
13. Sazonov E, Li H, Curry D, Pillay P (2009) Self-powered sensors for monitoring of highway bridges. IEEE Sens J 9(11):1422–1429
14. Peigney M, Siegert D (2013) Piezoelectric energy harvesting from traffic-induced bridge vibrations. Smart Mater Struct 22:095019
15. Ha TM, Fukada S, Ueno T, Ho DD (2020) Practical performance of magnetostrictive vibration energy harvester in highway bridge. In: Proceedings of the international conference on sustainable civil engineering and architecture (ICSCEA 2019). Lecture notes in civil engineering, vol 80. Springer, Singapore, pp 767–775
16. Le HMN, Ha TM, Fukada S, Ueno T (2021) Power generation from bridge vibration under ordinary vehicle load. Int J Struct Civ Eng Res 10(4):165–171
17. Koganezawa S et al (2021) Magnetostrictive vibration sensor for a self–powered structural health monitoring system. J Adv Mech Des Syst Manuf 16(1):1–12
18. Khan FU, Ahmad I (2016) Review of energy harvesters utilizing bridge vibrations. Shock Vib 2016(1340402):1–21
19. Koganezawa S et al (2020) Development of vibration sensor using giant magnetostrictive material for self-powered structural health monitoring system. In: 2020 IEEE SENSORS, pp 1–4
20. Kita S, Ueno T, Fukada S (2021) Highway implementation test of battery-free health monitoring system using magnetostrictive vibration power generation. J Jpn Soc Appl Electromagnet Mech 29(3):570–575
21. Moribe J, Fujimoto A, Tokita Y (2019) Development of a data notification system using GEO-WAVE. IEICE Commun Express 8(12):536–541
22. Ueno T (2019) Magnetostrictive vibrational power generator for battery-free IoT application. AIP Adv 9:035018
23. Ha TM et al (2020) Corrosion mitigation of steel rebars using galvanic anode materials for salt-deteriorated RC slabs in snowy regions. Int J Struct Civ Eng Res 9(2):127–137
24. ASTM C876-15 (2015) Standard test method for corrosion potentials of uncoated reinforcing steel in concrete

25. Tran TT et al (2021) Long-term corrosion monitoring by titanium wire sensor and vibration-based energy harvester. Int J Struct Civ Eng Res 10(1):17–25
26. 0G NETWORK COVERAGE. In: Sigfox. Retrieved from https://www.sigfox.com/coverage/
27. Xia Y, Chen B, Weng S et al (2012) Temperature effect on vibration properties of civil structures: a literature review and case studies. J Civ Struct Health Monit 2:29–46
28. Almuhaya MAM, Jabbar WA, Sulaiman N, Abdulmalek S (2022) A survey on LoRaWAN technology: recent trends, opportunities, simulation tools and future directions. Electronics 11(1):164

Effects of Wall Angle between Small Strip Areas by Using Point Cloud Data

Vachara Peansupap and Khine Zin Zin Theint

Abstract Floors, walls, and ceilings in building construction projects are essential to inspect for checking the quality. The internal wall inspection mainly includes evaluation criteria, measuring techniques, and evaluation items. Traditionally, measuring the right angles between two walls has only been done visually or with a traditional ruler approach, which takes a lot of time. This paper applies point cloud technology to analyze the evaluation of the angles with the use of the MATLAB programming platform. In contrast to the conventional approach, the tools that are typically used to identify the angles include an L-squared ruler that is 30 and 50 cm long. Therefore, this research focus is on the comparison of angle measurement from the full point cloud and partial point cloud (strip model). This research was mainly conducted in two approaches. Firstly, to evaluate the angle between the walls and floors by using the MSAC algorithm with full plane model input and then the second approach automatically cuts the input model again into smaller sizes and then measures its angle. Then the full model and the cut model are compared to check the effect of the angle results depending on the plane size. This research also attempted to examine the distance effect on the laser scanner between the wall and the scanner for extended analysis. From the analysis result, the proposed conceptual framework can be used to check the angle values by automatically cutting the full plane model and their effect on the different distances.

Keywords Geometric quality inspection · Laser scanning · Point cloud technology · Plane detection

V. Peansupap · K. Z. Z. Theint (✉)
Construction Engineering and Management Program, Department of Civil Engineering, Chulalongkorn University, Bangkok, Thailand
e-mail: 6370425021@student.chula.ac.th

T. Kang (ed.), *Proceedings of 5th International Conference on Civil Engineering and Architecture*, Lecture Notes in Civil Engineering 369,
https://doi.org/10.1007/978-981-99-4049-3_35

1 Introduction

Nowadays, in many construction industries, it is essential to rely on an efficient and effective management program to avoid losses or errors in the project execution stage. Mostly, the companies have developed systems such as project managing and controlling to make sure the best quality of products and services for every building is fundamental for all construction companies [1]. This quality inspection of the building must be performed by inspectors to fulfill the drawing and specification of the building construction. In order to achieve a successful project, quality of work is one of the key success factors. Thus, unprecise measurements and specifications may cause unintended issues during the inspection process [2]. For construction inspections in both private and public projects, many authors have been examined for topics including planning, coordinating, and controlling inspection activities and creating an automated system to support inspection processes [3]. Most furnishings and construction materials presume that walls' corners will have right angles, yet some walls don't, whether by accident or purpose. Strange angles create a design difficulty, particularly if is needed to fit storage or furniture into the corners. To fit snugly into corners of walls, wall shelves are normally cut at right angles. Wall construction is based on architecture and this work has the most total areas, both internal and external walls of the building [2]. The internal wall inspection consists of checking the smoothness of the wall and geometric shape of the wall corners. Since it is important in aesthetic perception, these kinds of works mainly focus heavily on precision which consumes most of the time. For instance, the customers can easily access the quality of the wall by touching or with eyesight. Therefore, quality inspection of the finishing walls is one of the main important procedures in the quality control phase.

2 Importance of the Research

2.1 Quality Inspections in Architectural Works

Traditionally, inspectors with experience perform thorough visual inspections of the infrastructure as part of the inspection and safety reviewing process for civil and environmental engineering infrastructure. Manual observation, despite being the accepted method, is labor- and time-intensive [4]. A major lack of competent engineers, which occurs when the number of buildings does not match the number of trained engineers, is a factor that seriously undermines the overall effectiveness of human visual inspection [5]. Since rework of defective components discovered late in the construction process loses 6 to 12% of construction costs, effectively recognizing defects early in the construction process is essential for quality control [6]. The aesthetic parameters of architectural works which is subjective visual quality examination are not dependable. Due to the limitations of visual senses, subjective

quality inspection is unreliable since it cannot measure defect levels and identify all potential defect places. Only subjective visual inspection is used in this area of quality inspection. The limitation of a person's aesthetic judgment is that it cannot measure the value of a particular fault. Conflicts still arise in the existing quality inspection process involving the determination of acceptable defect levels between the contractors, clients, and inspectors [7]. Based on this research, a few elements are considered when evaluating the quality of interior walls. Engineers from consulting firms should visually verify an angle by placing an angle bar at the corner or by looking up from the finished tile floor, baseboard, or ceiling. Then, at random, the primary and subcontractors should check the top, middle, and bottom to see if it forms a right angle [2]. Moreover, very little research has been done related to physical or natural units of measurement (dimensions, locations, and alignments) of the wall quality inspections. Therefore, focusing on these kinds of physical measurements is in need to improve with technology. Thus, quality inspection of the walls is necessary with the use of a point cloud-based algorithm which can reduce inspection time.

2.2 Point Cloud Technology in Quality Inspections

The use of laser scanning for quality control is shown to be successful. It is effective to build as-built models using laser scanning. New 3D data collecting methods have recently been made possible by the development of laser scanning technologies. Different kinds of laser scanners have been developed and using them to assess 3D processes has significantly increased the time and cost of data collecting [8]. Some studies have suggested employing point cloud technology to inspect precast wall panel dimensions and look for surface defects and flatness. Some studies have suggested utilizing point cloud technology to evaluate the size, flatness, and surface faults of precast wall panels. Additionally, laser scanning can capture precise and objective high-density geometry data on objects [9]. There has been research that also proposed about using BIM and Lidar to check the geometric quality of the prefabricated units [10]. In order to detect problems in the wall inclination, this paper proposes on developing a new system that can automatically produce a 3D point cloud model to check the quality of walls in the finishing process. It takes only unstructured 3D point clouds collected by a laser scanner as the input, and the output is a reconstruction of the 3D point cloud model in PLY format. For this process, the data collection will be conducted on a real construction site in Thailand Construction Company. The process would take place in the finishing phase of a construction project. Unlike the other studies that used a region growing algorithm to segment the plane, this study will use the MSAC algorithm together with the mathematical theories to achieve the goals which are to detect the walls and planes automatically and acquire the angles. Without the use of these algorithms, it will not get the result automatically when inputting the point cloud model. An efficient model and algorithm MSAC are proposed to conduct this research. Since the traditional measurement of the right cornered angle of the wall is with L-squared bar rulers,

the small area of the wall can only be measured. Therefore, this research tries to analyze the angle evaluation of the wall as a first step and then check the effect of the small area angle result with the result from the point cloud data by cutting the 3D model automatically in strips. After the size that can compare with the manual measurement is obtained from the system, it is used to check the system accuracy.

3 Developing the Research Framework

In this research, there are mainly six steps to conduct. These steps consist of (1) Preliminary research starting with the literature review (2) Collecting required data and processing for the system (3) Developing and designing the system (4) Testing the system with sample data (5) Applying the system on site (6) Validate the system. The more detailed framework of the proposed system will be presented (see Fig. 1).

3.1 Data Collection and Data Processing

For this data collection process, point cloud data has been collected as a base input data by using FARO 3D laser scanner equipment. In this study, the scanner was positioned around 2 to 3 m from the object that needs to be measured. The scanner resolution is adjusted according to the object of interest, the level of detail needed,

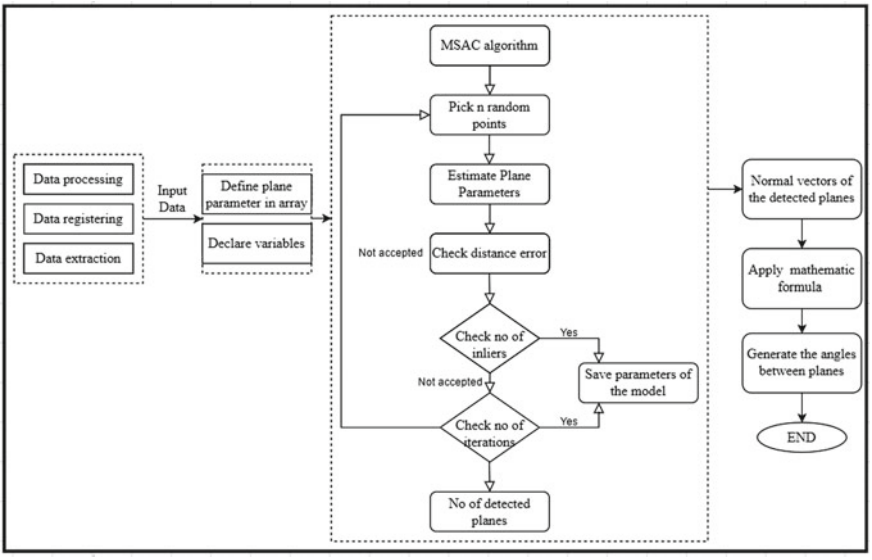

Fig. 1 Proposed system development framework

and the distance to the wanted targets. For the data collection, the scan was set to a full 360-degree scan with a resolution of 1/4, and a quality setting of 4 × has also been used for the internal validation of the system. For the case study, the data has been collected on real construction site in Thailand. The global positioning system (GPS) function has been turned off since it is an indoor setting. The average time of the scanned data is around 10 min for each scan according to the set resolution. However, it took around 6, 7, or 8 min for each scan, and for each target of interest total of 2 scans is conducted and used to process the data. These settings were appropriate for this research as well as consistent with the previous literature. A total of 26 wall corners are collected to use as input data to test in the developed system.

3.2 Developing the Proposed System

According to the framework, there will be data processing to input the data to implement in the MATLAB program. Then, the proposed algorithm which is MSAC will be used to obtain the detected number of planes and from that, the necessary angle results will be generated.

For this data collection process, point cloud data has been collected as a base input data by using FARO 3D laser scanner equipment. For preliminary testing, the sample data from the fourth floor of the Civil Engineering Department building has been collected to test the system as an input.

4 Design and Development of the Automated Cutting Model Strips

4.1 Main Mathematical Concept

Generally, a plane in a 3D space can be defined as a set of points that satisfies the 3D equation which is

$$ax + by + cz + d = 0 \tag{1}$$

where a, b, and c are given constant values. This formula is called the implicit formulation of a plane. With this formula, it is possible to see that the vector $n = (a, b, c)$ is the normal vector to the plane and any point (x_0, y_0, z_0). As for the coefficient d, the expression can be written as

$$d = -(ax_0 + by_0 + cz_0) \tag{2}$$

Normally, the angle between two planes can be identified by computing the normal vectors of the planes and after that, it can use the below cosine theta equation to find the angle between the two planes (corner angle). However, in this case, this study would like to define the precise angle in one of the four quadrants. Since the orientation of the vectors is unknown that is produced from the MSAC algorithm, the exact angle of interest where the quadrant which has the red point needs to be calculated as extended.

$$\cos(\theta) = n_1 \cdot n_2 / |n_1||n_2| \tag{3}$$

In this part of the article, the proposed system is explained with a flowchart and some outputs (see Fig. 2). The main concept in this system is finding the intersection line to create an edge model which is closer to the origin. Moreover, this proposed system creates a strip of a full plane model automatically instead of extracting the cut model from the user itself.

Firstly, the full plane model is used as an input, and by using the MSAC algorithm the planes were detected (see Fig. 3). Then, it started to compute the angle of the full plane model. Then, it used the full plane model again to create an edge by using the method of 5×5 matrix linear equation which is $Ax = b$ for intersecting planes. From

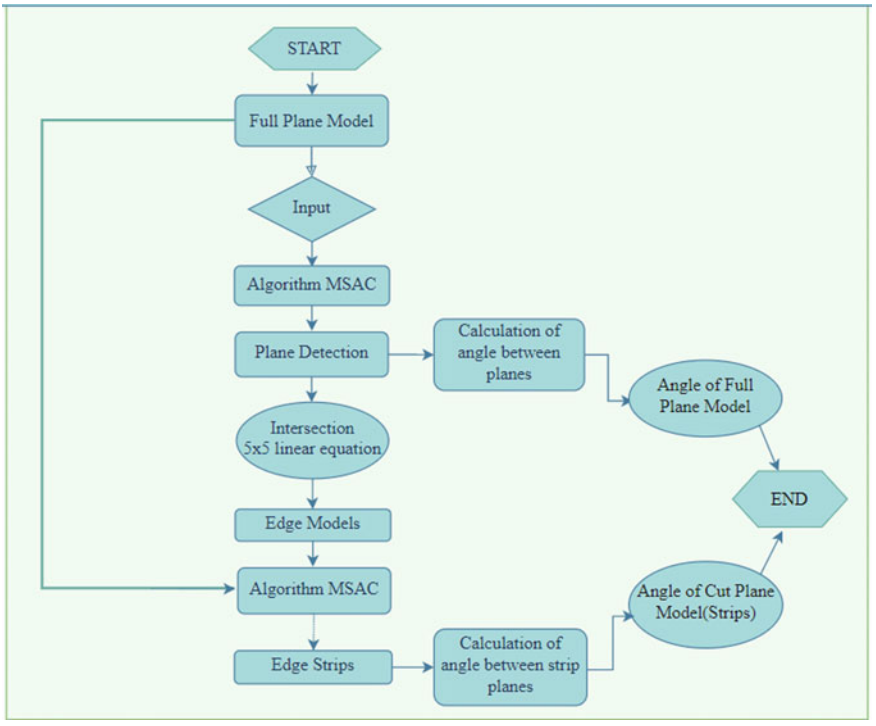

Fig. 2 Flowchart of the proposed system

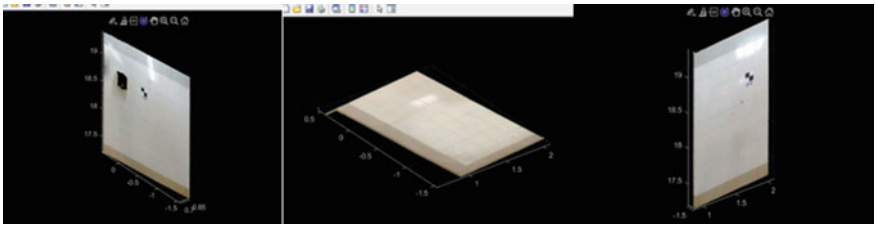

Fig. 3 Sample of plane detection

that, the edge models are obtained as shown in the flowchart. After computing the edge models, cutting 40 cm strips analysis from the edge is performed. In this analysis, the angle between each pair of strips is connected to the same edge. However, the angle between two-point clouds cannot be calculated directly, thus the intermediate step is an estimation of the plane models by using the MSAC algorithm. Moreover, the edge model that is computed from above only has the information of the line equation for the intersection of planes and the information of which pair of planes is generated and which points belong to each plane. So, by visiting the point cloud again the ones that are closer to 40 cm are selected. After that, the main loop visits each edge in the model and by using the two subset of points for each of the two planes, it estimates the plane model using MSAC. Then, finally, with the two planes model for each edge, the angle between the 40 cm strip planes can be obtained.

4.2 Validation of the System

After system fitting, the assessment of the performance of these systems is needed by comparing the system prediction results with the actual (true) data. To check the accuracy of both proposed systems, the results from the traditional measurement and the systems are compared. When comparing the system for accuracy, root mean squared error (RMSE), mean square error (MSE), and mean absolute percentage error (MAPE) are conducted.

5 Testing the Automated System and Its Results

5.1 Reliability Test

This section intends to ensure each proposed system has reliable results and measurements. Since the algorithm that is used in this system is an MSAC algorithm which is a stochastic algorithm that includes the random numbers in its components. Therefore, it is necessary to check the reliability of all these measurements. The system

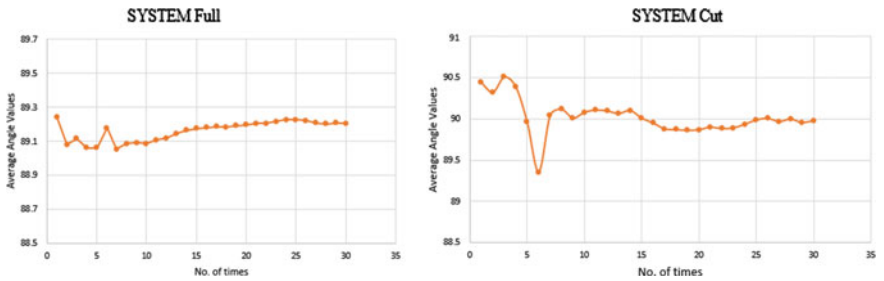

Fig. 4 Average angle values after running for different number of times

will run 30 times for each model and examine the variance of these results values. As can be seen from Fig. 4, the values of the proposed system seem to be steady in the values after running more than 15 times for the proposed system with the input full plane model. The input of the cut model also shows that when running after 20 times the average angle values become stable. Therefore, thirty times testing is used to check the reliability of this research analysis.

5.2 Results of the System

The aim to develop this system is mainly concerned with extracting the model automatically. Basically, all the models are needed to be extracted manually from the SCENE software as explained in the above chapters. Both the full plane model and the cut plane model are needed to be extracted manually to input into the system. Therefore, the main objective here is to automatically cut the input of the full plane model into small strips such as a 40 cm strip which will be known as the cut plane model.

Few of the angle results that are obtained from the 26 corners of the proposed system can be seen in Fig. 5. It shows the angle between each plane with the numbers and its value.

The Fig. 5 are the results of the testing with the case study that is conducted on a real construction site.

5.3 Validation Result of the System

The summary in Table 1 shows the validation of the system by checking its performance using the RMSE, MSE, and MAPE methods. In compliance with the results, the proposed system shows good results with the value of RMSE between 0.2 and 0.5 for all models. Whereas MSE and MAPE showed that automatically cutting

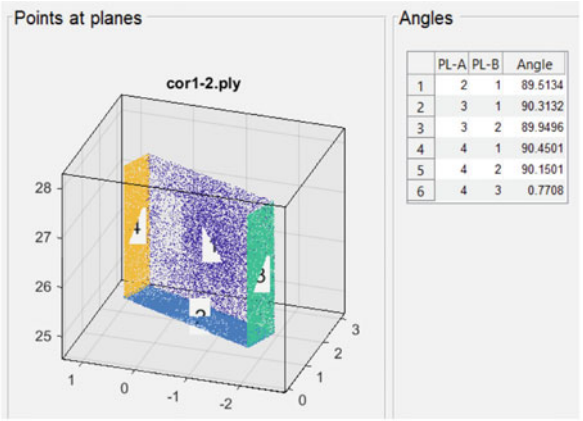

Fig. 5 Experimental results **a** Results of angles between the walls and floors from system **b** Results of angle in 40 cm strip model

models are not strong enough compared with others. However, it is still in the range of reasonable range, thus these values can be defined as acceptable values.

In Table 2, the results of running 30 times in each scan for one corner are described. Different distances such as 100 and 200 cm are set to test the effect on the output result. According to the table, the system gave slightly different results where it can be said that almost no effect on the output from the system at these particular distances.

Table 1 Validation result of the system and manual measurement

	Model	RMSE	MSE	MAPE
1	Results of system (full plane model)	0.2466	0.0608	0.1827
2	Results of system (cut plane model)	0.4076	0.1662	0.3449

Table 2 Summary result for testing different distances and 30 times average of each scan

Scan no.	36	37	38	39	40	41	42	43
Distance (cm)	100	100	100	100	200	200	200	200
No								
1	89.195	89.491	89.350	89.633	89.448	89.828	88.572	88.701
2	89.271	89.025	89.404	89.348	90.498	90.143	89.124	90.049
3	89.561	89.394	89.579	89.374	90.426	89.799	89.140	89.703
4	89.577	89.153	89.347	89.531	88.700	89.970	89.627	89.855
5	89.450	89.329	89.575	89.250	89.730	88.520	88.848	89.767
6	89.288	89.188	89.503	89.146	89.764	89.362	89.154	89.649
7	89.551	89.344	89.505	89.557	89.351	89.485	89.673	89.326
8	89.361	89.291	89.454	89.123	88.796	89.910	88.603	89.015
9	89.674	89.192	89.253	89.325	89.462	89.152	88.885	89.005
10	89.385	89.405	89.535	89.624	89.570	89.537	89.968	89.840
11	89.398	89.503	89.586	89.518	89.202	90.176	89.428	89.691
12	89.648	89.362	89.350	89.588	88.682	89.516	89.386	88.808
13	89.450	89.367	89.646	89.437	89.057	90.062	89.186	89.383
14	89.328	89.168	89.663	89.650	89.692	90.106	88.605	89.034
15	89.356	89.424	89.652	89.264	88.405	90.098	89.898	90.169
16	89.655	89.096	89.548	89.250	88.471	89.868	89.338	89.083
17	89.207	89.440	89.648	89.084	88.822	88.556	88.806	90.238
18	89.498	89.610	89.660	89.023	90.052	89.109	89.476	88.628
19	89.679	89.273	89.550	89.644	88.883	89.246	89.299	88.912
20	89.273	89.496	89.688	89.400	89.418	88.780	89.250	90.271
21	89.345	89.242	89.666	89.465	89.056	89.387	90.077	89.833
22	89.545	89.631	89.579	89.211	88.906	88.873	89.440	89.806
23	89.374	89.307	89.312	89.202	89.053	88.916	89.321	89.399
24	89.413	89.121	89.474	89.520	89.372	89.814	90.243	88.655
25	89.360	89.324	89.228	89.088	89.097	89.367	88.822	89.023
26	89.363	89.453	89.504	89.070	89.547	89.763	89.042	89.367
27	89.378	89.109	89.202	89.250	88.602	89.332	89.292	88.594
28	89.400	89.489	89.445	89.317	90.392	88.919	89.366	88.674
29	89.474	89.594	89.666	89.480	89.100	89.539	89.679	89.969
30	89.668	89.086	89.567	89.127	89.310	90.241	88.675	89.198
Average	**89.438**	**89.330**	**89.505**	**89.350**	**89.295**	**89.512**	**89.274**	**89.388**

Table 3 Results of the correct percentage of the system

	Correct result	Total sample	Correct (%)
System (full)	23	26	88
System (cut)	12	26	54

6 Discussion and Conclusion

The results of verification and reliability analysis of the two components of the proposed system allow us to summarize that the concept of applying point cloud technology, MSAC algorithm, and automatically calculating the angles reduce the subjective attributes in visual quality inspection of walls can be successfully implemented in actual construction projects. Moreover, the system can measure the angle values to reduce the subjective attribute of visual quality inspection. It can help reduce conflicts from differences of perception between the people involved in quality evaluation. Because a person's capacity to assess aesthetic faults is restricted, the idea of implementing an angle detection system can boost the reliability of visual inspection of defect placements. Quantifying defect values is not without its restrictions for people. Therefore, inspectors utilizing a visual inspection method may not be able to detect every problem position, particularly when dealing with big regions like high-rise buildings or massive objects. Compared with an unaided human visual inspection, the proposed system is capable of computing the angle measurement more accurately and consistently. Moreover, it is used to improve construction quality continuously. As can be seen from Table 3, the results of the accuracy of the system can be seen. There is a total of 26 samples to test the proposed system and the results which are close to actual measurement are shown in Table 3.

However, the system still needs improvement to overcome limitations such as making some adjustments with suitable algorithms to measure the angle of the strips (cut model) automatically and accurately. Furthermore, the overall results show that the proposed system can support the human inspection processes of wall quality. Our research conclusions demonstrate that the proposed systems can be implemented, although it requires improvement to overcome their limitations for more accurate angle detection in an actual construction site.

References

1. Giacomello H, Stumpf MAG, Kern AP (2014) Implementation of an integrated management system into a small building company. Rev Constr 13(3):10–18
2. Nititerapad C, Tongthong T, Mokkhamakkul T (2019) Perception of key stakeholders on the internal wall quality inspection process for high-rise residential building construction projects in Thailand. PSAKU Int J Interdisc Res 8(2):12–22
3. Czemplik A (2015) Inspection of construction works according to polish construction law. IOP Conf Ser Mater Sci Eng 96(012057):1–6

4. Spencer BF Jr, Hoskere V, Narazaki Y (2019) Advances in computer vision-based civil infrastructure inspection and monitoring. Engineering 5(2):199–222
5. Chow JK, Liu K-f, Tan PS, Su Z, Wu J, Li Z, Wang Y-H (2021) Automated defect inspection of concrete structures. Autom Constr 132:103959
6. Akinci B, Boukamp F, Gordon C, Huber D, Lyons C, Park K (2006) A formalism for utilization of sensor systems and integrated project models for active construction quality control. Autom Constr 15(2):124–138
7. Laofor C, Peansupap V (2012) Defect detection and quantification system to support subjective visual quality inspection via a digital image processing: a tiling work case study. Autom Constr 24:160–174
8. Haddad NA (2011) From ground surveying to 3D laser scanner: a review of techniques used for spatial documentation of historic sites. J King Saud Univ Eng Sci 23(2):109–118
9. Kim M-K, Thedja JPP, Wang Q (2020) Automated dimensional quality assessment for formwork and rebar of reinforced concrete components using 3D point cloud data. Autom Constr 112:103077
10. Tan Y, Li S, Wang Q (2020) Automated geometric quality inspection of prefabricated housing units using BIM and LiDAR. Remote Sens 12(15):2492

Evaluation of Vibrations in Simple Structures Using the Laser Photo Deflection Method (LDP): Part 2

Anibal Valera, Gelacio Tafur Anzualdo, Irene Tafur Anzualdo, and Doris Esenarro

Abstract The objective of this research is to continue with the results of the first part of our project, the evaluation of vibrations in simple structures using the laser photodeflection method (LPD): in part 2 we present the results of the evaluation of vibrations of a pure concrete column. As stated in a previous report (part 1), the method that was applied is again a combined optoacoustic (non-destructive) procedure, whereby the vibration of the structure is induced by sound and vibrations are detected optically. The reflected laser beam deflects around the sensor in tune with the produced vibration (LPD). Experimentally, the first 12 resonant frequencies are obtained and the results are discussed within the framework of the known basic theoretical approaches. As initially indicated, the column has a length $L = 1.75$ m from the ground (earth), however, the column in turn has an embedment in the ground of about 30 cm, so the total effective length of the column is 2.05 m, which would significantly modify the evaluation of E to almost 11 GPa.

Keywords Vibration modes · Laser evaluation · Structure diagnosis · Laser photo deflection

A. Valera (✉)
Faculty of Sciences, National University of Engineering UNI, Lima, Peru
e-mail: avalera@uni.edu.pe

G. T. Anzualdo · I. T. Anzualdo · D. Esenarro
Postgraduate School, Federico Villarreal National University, Lima, Perú

D. Esenarro
Grupo de Investigación en Sostenibilidad Ambiental, GISA, UNFV, Lima, Perú

Faculty of Architecture and Urban Planning, Ricardo Palma University, URP Lima, Lima, Peru

T. Kang (ed.), *Proceedings of 5th International Conference on Civil Engineering and Architecture*, Lecture Notes in Civil Engineering 369,
https://doi.org/10.1007/978-981-99-4049-3_36

1 Introduction

In a previous work /1/, we discussed the actual problematic of applying the method of vibration evaluations in the study of structural diagnostic, remarking the advantage and actual limitations of the standard procedures [1–13]. Faced to these facts we introduced a new alternative: the optical laser photo deflection (LPD) method, remarking the simplicity and precision of the technic, just confirmed by the results obtained in this work.

Since 2006, our laboratory has systematically applied and innovated the laser photo deflection (LPD) method in the evaluation of structures vibrations (walls, ceilings, buildings). However, the experimental results obtained and published [14–18] did not have much application since it was not possible to establish a clear correlation with the existing theories, managed almost exclusively by the civil engineers.

It should be noted that in one of our latest works [14], comparative evaluations were made between the traditional method (accelerometers) and at the other side our optical method (LPD), highlighting the optical method, basically for the best resolution and the highest range of spectral sensitivity, which confirmed the potential of the optical method in the structural evaluations.

Faced with the problem of interpretation of the experimental results obtained by us in the evaluation of buildings [15, 17, 19], we decided to apply the method systematically to different simple structures such that the participation of each of them in the building vibration can be clearly identified. This is the reason for which we limit ourselves in the present work to the optical evaluation of vibration of the concrete column.

The present work is essentially experimental, based on known techniques and foundations; so, for example, the theory applied in this work is the classical theory of the cantilever beam [20–22], where the equation of motion can be described as:

$$\frac{d^2}{dx^2}\left\{EI(x)\frac{d^2}{dx^2}Y(x)\right\} = \omega^2 m(x)Y(x) \tag{1}$$

where E is the modulus of rigidity of the material, I is the moment of inertia, $Y(x)$ is the displacement in the perpendicular direction (y) at the distance x from the fixed point, ω is the angular frequency and $m(x)$ is the mass per unit length $m(x) = \rho A(x)$.

$I = \frac{b}{12}d^3$ is the moment of inertia of a rectangular section bar (sides b, d).

From Eq. (1) we obtain the solution of the proper modes of vibration of the bar, defined by the frequencies:

$$f_n = \frac{\alpha_n^2}{2\pi}\sqrt{\frac{EI}{\rho AL^4}} \tag{2}$$

2 Experimental

Experimental setup (Fig. 1) schematizes the applied experimental setup (simplified model): There is a concrete column, fixed to the floor, with a small mirror fixed at the top. The mirror is made to hit a laser beam from a certain distance; the reflected laser beam goes to the detector (deflection sensor). In this experimental setup, any movement of the column up to the range of a few nanometers will be detected by the optical system, particularly its vibrations.

The column has magnitudes: $L = 1.75$ m, $b = d = 0.257$ m.

A vibration of the column will produce an alternating voltage response in the detector with the same wave characteristics of the vibration. The signals are sent to a PC to be stored and analyzed.

Experimental Procedure. If the spontaneous vibration signals of a structure are measured in time, we will detect small displacements of the structure, which are usually generated by random movements of the ground (nearby traffic, small earthquakes, wind, etc.). However, these movements are very weak and overlapping such that they do not allow an accurate and prompt evaluation.

Our experimental method consists of selectively inducing (forcing) the column to vibrate, in particular in two ways: a first one consists of hitting the column and a second way consists of subjecting the column to sound waves at specific frequencies, using a speaker.

Shocks Vibration. By means of blows produced on the back of the column, approximately every ½ second, we obtain the wave response shown in Fig. 2.

The FFT analysis of the wave pattern presented in Fig. 2 results in a characteristic frequency of the order of 21.3 Hz (Fig. 3).

The vibration frequency of 21. 3 Hz generated by the blows at the top of the column is associated with the first proper vibration of the column, similarly to the results obtained in a previous work /1/ by our group in the case of a steel bar.

Sound Excited Vibrations. Our second method of forced excitation consists of subjecting the column to sound waves of defined frequencies (by means of a wave generator and a speaker) and observing the vibration response of the column on an

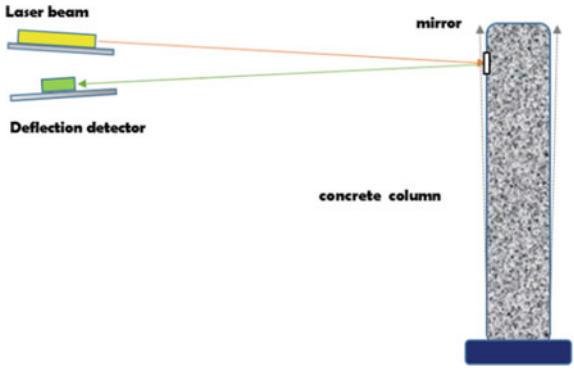

Fig. 1 Experimental diagram of the basic optical array (LPD) was used to evaluate the vibrations of a concrete column on the floor

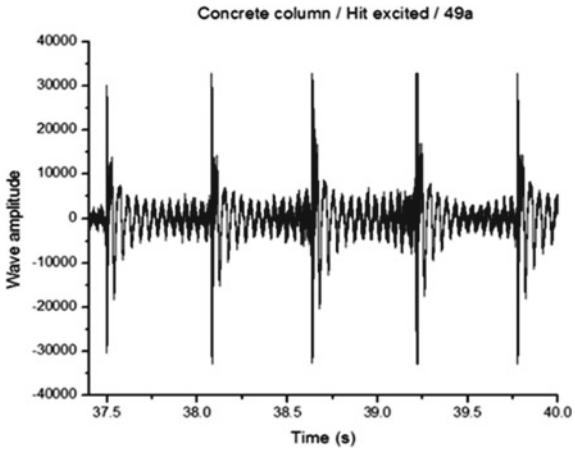

Fig. 2 Partial response of the column when induced to vibrate by shocks

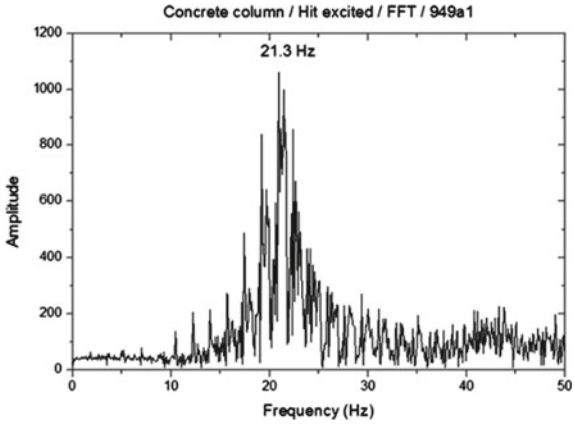

Fig. 3 FFT spectral analysis of the signal shown in Fig. 2

oscilloscope. As soon as one encounters a resonance, the signal from the oscilloscope will be noticeably amplified, showing a train of sine waves at the reference frequency. At this point, the response is recorded for later FFT analysis.

This procedure was developed for our group in late 2006 and constitutes so far, our best alternative for evaluating and confirming the vibration modes of a structure.

In order to be concise, we limit ourselves to show here only the first one of the results obtained at 22 Hz (Fig. 4, Table 1).

Taking into account a referential concrete density value of $\rho_{\text{ref}} = 2300$ kg/m^3, we evaluate the corresponding E_n (Young Modulus) values, which are shown in the graph in Fig. 5.

According to the results shown in Fig. 5, an average value of the Young Modulus is obtained:

$$E_{\text{Average}} : 5.72 \text{ GPa}$$

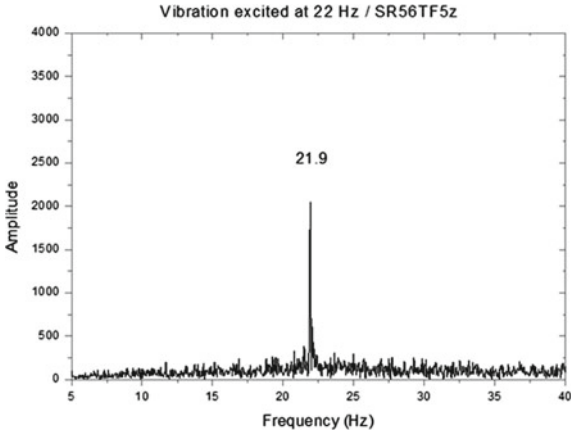

Fig. 4 Vibration induced by forced excitation at 22 Hz

Table 1 Summarizes all obtained resonances, which are explicitly shown in attachment 1

Mode	Frequency (Hz)	File
1	21.9	SR56TF5z
2	133	SR56TF5a
3	375	SR56T5b
4	730	SR56TF5c
5	1196	SR56TF5d
6	1774	SR56TF5e
7	2621	SR56TF5f
8	3379	SR56TF5h
9	4317	SR56TF5i
10	5444	SR56TF5j
11	6570	SR56TF5k
12	7884	SR56TF5l

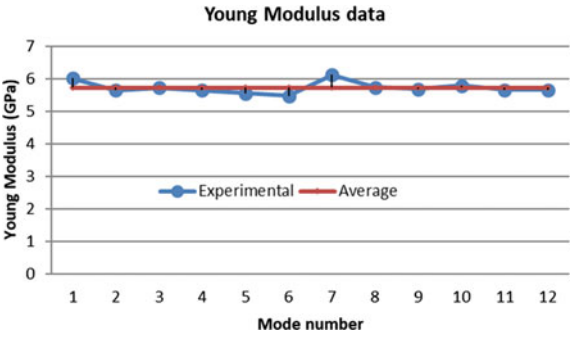

Fig. 5 Evolution of the E_n (Young Modulus) values obtained for the modal frequencies shown in Table 1

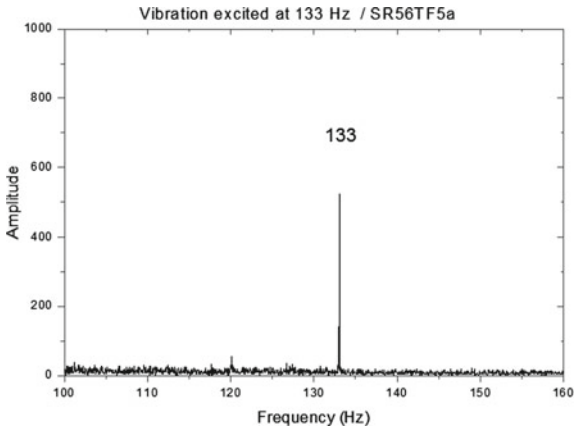

Fig. 6 Vibration induced by forced excitation at 375 Hz

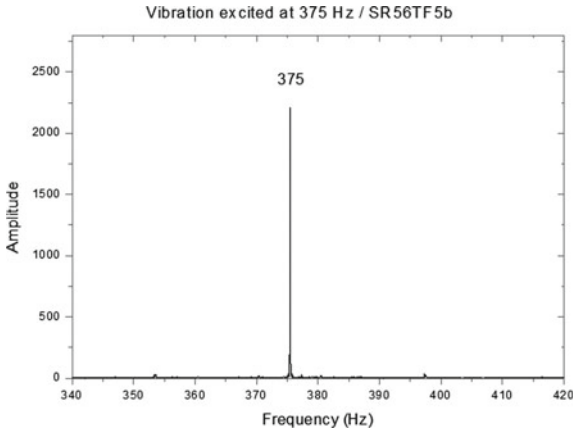

Fig. 7 Vibration induced by forced excitation at 133 Hz

Attachment 1

In this section, we show the explicit data of the resonant vibrations obtained experimentally and used in this work (Figs. 6, 7, 8, 9, 10, 11, 12, 13, 14, 15, 16).

Experimentally, the first resonant frequencies are obtained.

3 Discussion

In this work, we have used a ready-to-mix concrete mixture (Topex), to which water is added, in the amount specified by the manufacturer, to obtain the required concrete mixture.

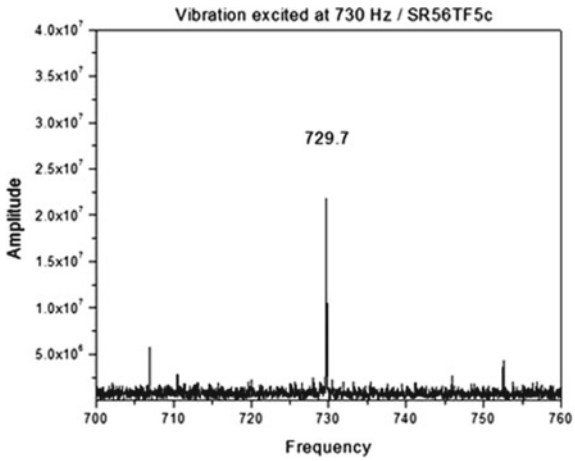

Fig. 8 Vibration induced by forced excitation at 730 Hz

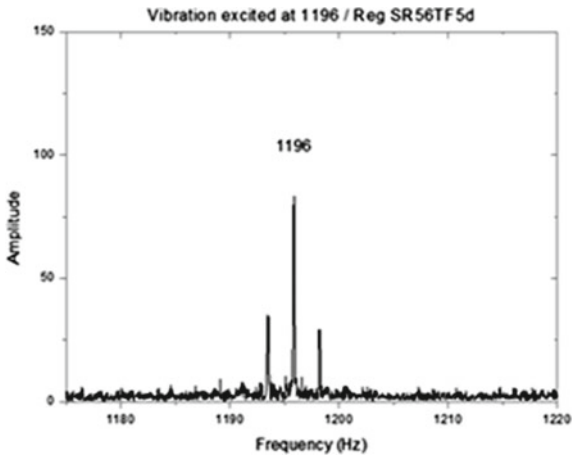

Fig. 9 Vibration induced by forced excitation at 1196 Hz

We do not have specific data on this material. The value of the concrete density used in our calculations was taken: $\rho = 2300$ kg/m^3 as the average value of the references (Engineering toolbox).

The value of 5.72 GPa found experimentally for the concrete column in this report differs markedly from the known standard values. Thus, for example, the reference (Engineering Box) gives the value of E of different concretes, a range of values: from 14 to 41 GPa. This discrepancy was observed at the end of the global evaluation; however, some previous details of the experiment are now displayed.

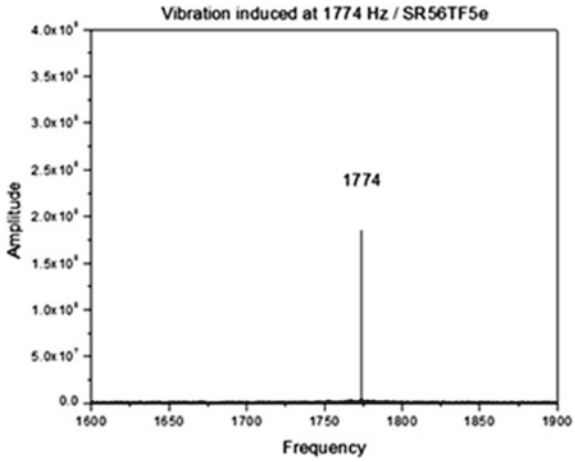

Fig. 10 Vibration induced by forced excitation at 1774 Hz

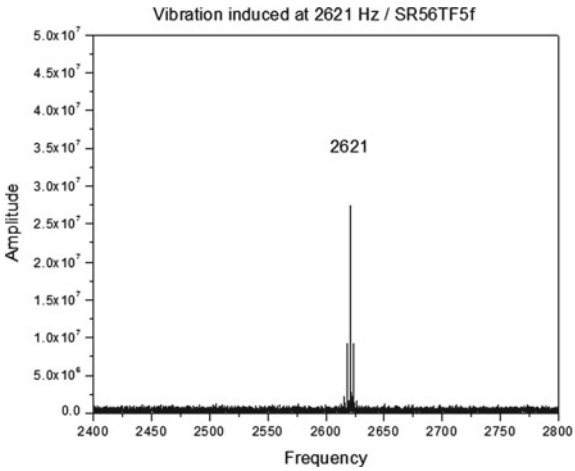

Fig. 11 Vibration induced by forced excitation at 2621 Hz

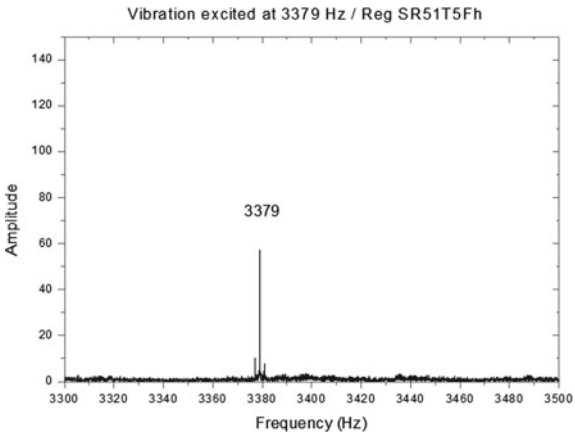

Fig. 12 Vibration induced by forced excitation at 3379 Hz

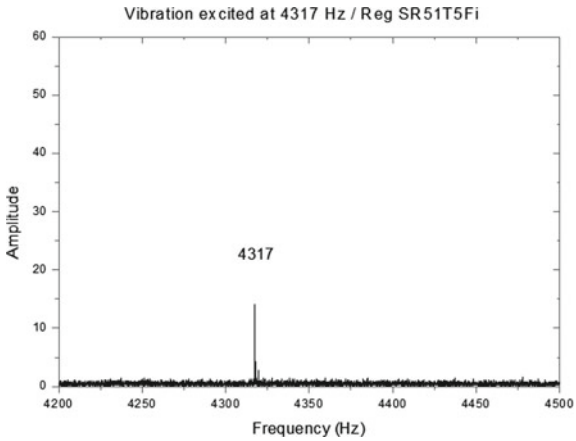

Fig. 13 Vibration induced by forced excitation at 3379 Hz

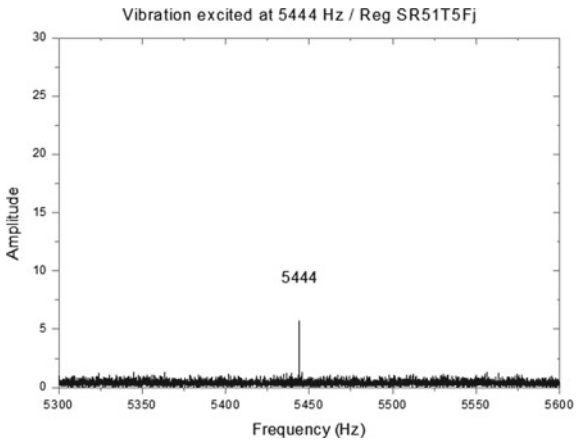

Fig. 14 Vibration induced by forced excitation at 6579 Hz

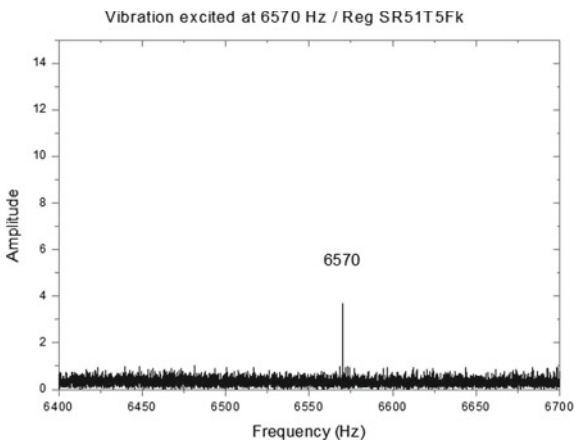

Fig. 15 Vibration induced by forced excitation at 5444 Hz

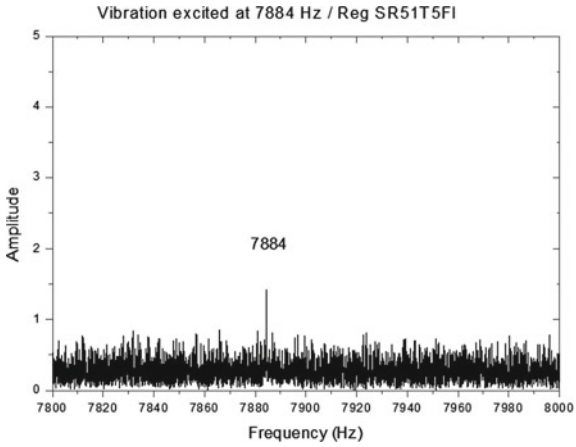

Fig. 16 Vibration induced by forced excitation at 7884 Hz

4 Result

As initially indicated, the column has a length $L = 1.75$ m from the ground (Earth), however, the column in turn has an embedment in the ground of about 30 cm, so the total effective length of the column is 2.05 m, which would significantly modify the evaluation of E to almost 11 GPa, a value that is remarkably close to the expected value [30]. If the floor were not made of Earth, but with a concrete base, the height from the floor could be taken as the effective height.

These details must be definitively clarified in successive evaluations; however, the optical evaluation results are consistent and the method will definitely help us in subsequent structural evaluations.

References

1. Valera V, Castillo G, Tafur G (2018) Evaluation of vibrations in simple structures using the Laser Photodeflection Method (LPD): part 1. In: Research Gate. Retrieved from https://www.researchgate.net/publication/325768375_EVALUATION_OF_VIBRATIONS_IN_SIMPLE_STRUCTURES_USING_THE_LASER_PHOTODEFLECTION_METHOD_LPD_Part_1
2. Lu X, Chruscicki S, Schukar M, Münzenberger S, Krebber K (2022) Application of intensity-based coherent optical time domain reflectometry to bridge monitoring. Sensors 22(9):3434
3. Hoła J, Schabowicz K (2010) State-of-the-art non-destructive methods for diagnostic testing of building structures–anticipated development trends. Arch Civ Mech Eng 10(3):5–18
4. Beben D, Maleska T, Bobra P, Duda J, Anigacz W (2022) Influence of traffic-induced vibrations on humans and residential building—a case study. Int J Environ Res Public Health 19(9):5441
5. Chen M, Ning X, Zhou Z, Shu Y, Tang Y, Cao Y, Shang X, Han X (2022) LMS/RLS/OCTAVE vibration controls of cold orbital forging machines for improving quality of forged vehicle parts. World Electr Veh J 13(5):76
6. Luo L, Mei Y, De Battista N, Kechavarzi C, Soga K (2021) Repeatability precision error analysis of the distributed fiber optic strain monitoring. Struct Control Health Monit 28(8):e2768

7. Moreno-Gomez A, Perez-Ramirez CA, Dominguez-Gonzalez A, Valtierra-Rodriguez M, Chavez-Alegria O, Amezquita-Sanchez JP (2018) Sensors used in structural health monitoring. Arch Computat Methods Eng 25:901–918
8. Oskoui EA, Taylor T, Ansari F (2019) Method and monitoring approach for distributed detection of damage in multi-span continuous bridges. Eng Struct 189:385–395
9. Puzrin AM, Iten M, Fischli F (2020) Monitoring of ground displacements using borehole-embedded distributed fibre optic sensors. Q J Eng Geol Hydrogeol 53(1):31–38
10. Zhao M, Yi X, Zhang J, Lin C (2021) PPP-BOTDA distributed optical fiber sensing technology and its application to the Baishuihe landslide. Front Earth Sci 9(660918):1–12
11. Zhang H, Wang Y, Wang L, Liu Y, Chen H, Wu Z (2022) Process control monitor (PCM) for simultaneous determination of the piezoelectric coefficients d_{31} and d_{33} of AlN and AlScN thin films. Micromachines 13(4):581
12. Xie Q, Duan J, Ban Y, Fu X, Liu S (2022) Laser vibration characteristics of marble specimens and failure criterion. Appl Sci 12(4):2223
13. He Z, Xie M, Huang Z, Li Y, Sui Z, Lu Y, Golosov AM (2020) Experimental hazardous rock block stability assessment based on vibration feature parameters. Adv Civ Eng 2020(8837459):1–11
14. Melchor M (2016) Analysis of vibrations in simple structures using the laser photodeflection method. Master's thesis, UNI/FC Lima, Perú
15. Wang Y, Zhang W, Wu Z, Kong X, Zhang H (2021) Speckle noise detection and removal for laser speech measurement systems. Appl Sci 11(21):9870
16. Xia H, Wei PB, Cao YM, De Roeck G (2005) Traffic-induced vibrations of ground environments and buildings. In: Takemiya H (ed) Environmental vibrations: prediction, monitoring, mitigation and evaluation,1st edn. Taylor and Francis Group, London, UK, pp 529–539
17. Erkal A (2019) Impact of traffic-induced vibrations on residential buildings and their occupants in metropolitan cities. Promet Traffic Transp 31(3):271–285
18. Germonpré M, Degrande G, Lombaert G (2017) A study of modelling simplification in ground vibration predictions for railway traffic at grade. J Sound Vib 406:208–223
19. Hernandez FR, Esenarro DO, Rodriguez CI, Vela LO, Calvo RO (2020) Earned value method management applied to the construction of the multifamily building—Lima, Peru. J Contemp Issues Bus Gov 27(3):838–848
20. Erkal A, Kocagöz MS (2020) Interaction of vibrations of road and rail traffic with buildings and surrounding environment. J Perform Constructed Facil 34(3):04020038
21. Feng D, Feng MQ (2018) Computer vision for SHM of civil infrastructure: from dynamic response measurement to damage detection—a review. Eng Struct 156:105–117
22. Dong C-Z, Celik O, Catbas FN, OBrien E, Taylor S (2019) A robust vision-based method for displacement measurement under adverse environmental factors using spatio-temporal context learning and taylor approximation. Sensors 19(14):3197
23. Oh T-H, Jaroensri R, Kim C, Elgharib M, Durand F, Freeman WT, Matusik W (2018) Learning-based video motion magnification. In: Proceedings of the European conference on computer vision (ECCV), pp 633–648
24. Wadhwa N, Chen JG, Sellon JB, Wei D, Rubinstein M, Ghaffari R, Freeman DM, Büyüköztürk O, Wang P, Sun S et al (2017) Motion microscopy for visualizing and quantifying small motions. Proc Nat Acad Sci (PNAS, USA) 114(44):11639–11644
25. Mendrok K, Dziedziech K, Kurowski P (2020) Detection of structural abnormality of industrial rotary machine using DRS-aided operational modal analysis. Measurement 164:108098
26. Molina-Viedma ÁJ, López-Alba E, Felipe-Ses´e L, Díaz FA (2019) Operational deflection shape extraction from broadband events of an aircraft component using 3D-DIC in magnified images. Shock Vibr 2019(4039862):1–9
27. Shang Z, Shen Z (2018) Multi-point vibration measurement and mode magnification of civil structures using video-based motion processing. Autom Constr 93:231–240
28. Harmanci YE, Gülan U, Holzner M, Chatzi E (2019) A novel approach for 3D-structural identification through video re-cording: magnified tracking. Sensors 19(5):1229

29. Fioriti V, Roselli I, Tatì A, Romano R, De Canio G (2018) Motion magnification analysis for structural monitoring of ancient constructions. Measurement 129:375–380
30. Won J, Park J-W, Park K, Yoon H, Moon D-S (2019) Non-target structural displacement measurement using reference frame-based deepflow. Sensors 19(13):2992

Development of System for Detecting Railway Surface Defects by Using Deep Learning Technique

Vachara Peansupap, Pyae Phyoe, and Tawat Jewbunchu

Abstract Realizing the importance of early prevention of railway deterioration in the railway maintenance, inspection of railway should be carried out regularly. As the railway surface defects can accelerate the deterioration of rail, inspection of railway surface defects becomes a critical task for railway maintenance engineers. Previously, inspection of railway surface defects is conducted by experienced inspectors. However, this subjective visual inspection is labor-intensive, time consuming and costly. So, researchers are finding another alternative to inspect the railway surface defects, and computer vision becomes another alternative to overcome the drawbacks of manual inspection. Previous studies attempted to improve the defect detection of railway surfaces by applying computer vision (CV) based techniques and deep learning; however, there are still limitations. Firstly, the previous research can only conduct the classification of the railway surface defects, but they could not located the defects in the images. Moreover, object detection, which can both classify and locate objects in the image has mainly focused on detecting railway components. Therefore, this paper aims to propose a system that utilizes deep learning techniques to automatically detect railway surface defects within the images. In this research, CNN is trained by using images in which different kinds of railway surface defects include. You Only Look Once (YOLOv4) object detection algorithm is used when the training is conducted. Regarding the collection of image dataset, railway surface defects images are collected from the railway department of Thailand. The system is validated by the testing image dataset, and it can give the result in terms of evaluation matrices. The finding from this research will provide a railway surface defects detection system which can save time and cost and increase the performance.

V. Peansupap (✉) · P. Phyoe (✉)
Department of Civil Engineering, Faculty of Engineering, Chulalongkorn University, Bangkok 10330, Thailand
e-mail: vachara.p@chula.ac.th

P. Phyoe
e-mail: 6370434721@student.chula.ac.th

T. Jewbunchu
Thung Song Maintenance Division, Civil Engineering Department, State Railway of Thailand, Nakhon Si Thammarat 80110, Thailand

T. Kang (ed.), *Proceedings of 5th International Conference on Civil Engineering and Architecture*, Lecture Notes in Civil Engineering 369,
https://doi.org/10.1007/978-981-99-4049-3_37

Keywords Computer vision · Railway surface defects inspection · Deep CNN

1 Introduction

Railway infrastructure, one of the transport infrastructures, is the crucial means of transportation in any countries. It plays a major role of facilitating economic and social needs of a country such as promoting economic growth and cutting greenhouse gas emission [1]. Besides, having enough railway networks can affect the industry, logistics, and mobility of goods, and it can lead to the persuasion of the foreign investment and then increase the gross domestic product (GPD) of the country [2]. Being the importance of railway structure, railway tracks become deteriorate when they are used for ages. Moreover, wheel load, environmental impact, and errors in design and construction stage and imperfection of material quality can influence the railway deterioration [3]. Therefore, it is necessary to maintain the railway track in the proper condition as the railway defects can lead to the acceleration of the deterioration of rail that can cause the rail fracture and derailment accident. Realizing the importance of railway track maintenance, inspection of railway surface defects should be carried out regularly. Previously, railway surface defects are inspected by visual inspection using humans, but this kind of inspection mainly depends on the expertise and the condition of the inspectors. Besides, it takes times and cost, and may expose health and safety of the inspectors in the field [4]. To overcome these drawbacks of visual inspection, many studies are trying to replace visual inspection with computer vision-based railway defects detection as computer vision tasks are becoming popular with the improvement in the technology. CV-based defect detection using a designated computer algorithm can be more reliable and objective. The railway surface defects can be detected automatically by a computer with a proper algorithm, and so, it can considerably save time and cost. Moreover, CV-based inspection can reduce the risk to the inspectors in the field [5]. So, computer vision is applied as another technique to detect the railway surface defects.

2 Literature Review

Realizing the development of computer vision, previous research applied this in the detection of railway surface defects. Besides, researcher can classify the railway defects by using the images with the advancement of CNN architectures. Firstly, railway surface defects such as normal, weld, light squat, moderate squat, severe squat, and join were classified by using deep neutral network [6]. Then, convolutional neutral network combined with traditional object localization algorithm was applied to classify the rail as defect and intact [4]. Besides, [7] conducted the classification of four different types of rail surface defects (healthy, light squat, severe quat, and joint) through the combination of image preprocessing and deep learning network.

Classification in the computer vision task means that the classification model can only describe the types of the objects in the images. It cannot locate where the defect is in the image. Moreover, many studies were carried out the detection tasks in the railway industry with the improvement in CNN and object detection. It means that they tried to achieve the models that can both classify and localize the instances in the images. Regarding the object detection in the railway industry, researchers tried to detect the components or parts of the railway. Firstly, bent rail, loosing ballast, switch, and signals were detected by using different kinds of CNN [8]. Then, different railway components such as rail, bolt, and clip were detected in which the researcher applied three different version of YOLO algorithm and conduct the comparison of the evaluation results [9]. Moreover, there was research in which railway surface defect was tried to detect as defect by using YOLOv3 [10]. Besides, [11] conducted the detection of corrugation, fatigue block, and stripping off block by using deep learning networks in which MobileNet and YOLO were applied as backbone and detection layers, respectively. Despite there were previous research conducted to detect the railway surface defect, there are still limitations to overcome. Firstly, previous research focus on classification of the railway defects as defect. It means that it can only describe the name of the instance in the image when there is only one object in the image. Classification cannot be applied when there are two or more objects in the image. Besides, another drawback of image classification is that it cannot describe where the object is in the image. Then, with the emergence of object detection algorithms, researchers can perform the detection tasks. Although previous research conducted the object detection task, they mainly focused on the detection of railway components. So, this study focuses on the detection of the railway surface defects by using YOLOv4 object detection algorithm in which it can detect the different kinds of railway surface defects.

3 Methodology

3.1 You Only Look Once (YOLOv4)

One stage object detection algorithm, YOLOv4, divides the input image into S $\times$ S grid cell, and each cell is responsible for the detection and localization of the object include in this grid cell. Simultaneously, these grids predict B bounding box coordinates which is relative to their cell coordinates, along with the object label and probability of the object being present in the cell. Intersection over union (IoU) is applied to know whether the predicted bounding boxes are equal to the real boxes of the objects, and it can eliminate unnecessary bounding boxes that do not meet the characteristics of the objects. The non-maximum suppression (NMS) is applied to get the final detection box [12]. Figure 1 shows how YOLO algorithm detects the object.

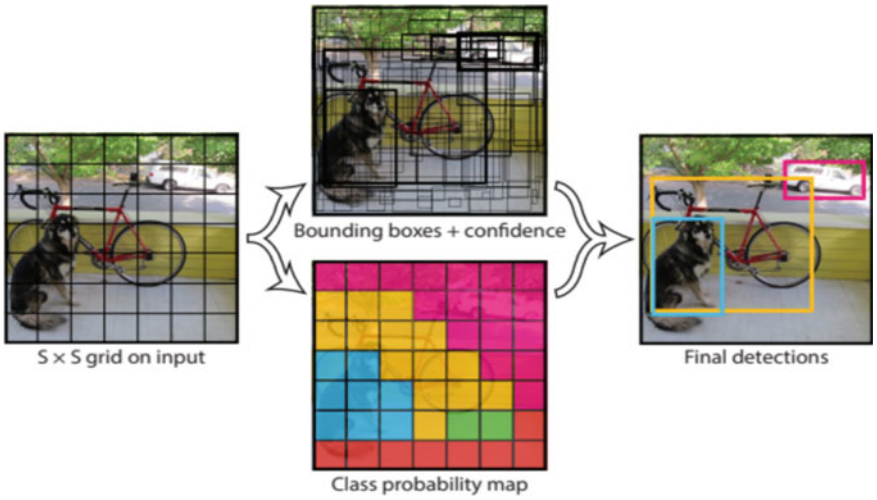

Fig. 1 How YOLO algorithm detects the object

3.2 Data Collection and Labelling

Regarding the development of railway surface detection model, it is necessary to collect the images so that these data can be used in training the models. In this study, the required images regarding the railway surface defects are obtained from the railway department of Thailand. Railway surface defects tried to detect are spalling, squat, corrugation, and wheel burn. Figure 2 shows the sample railway surface defect images used in the training process.

After collecting the required images, the labelling process is carried out before the training process. Labelling means the drawing of the boundaries of the defected

Fig. 2 Sample images of railway surface defects

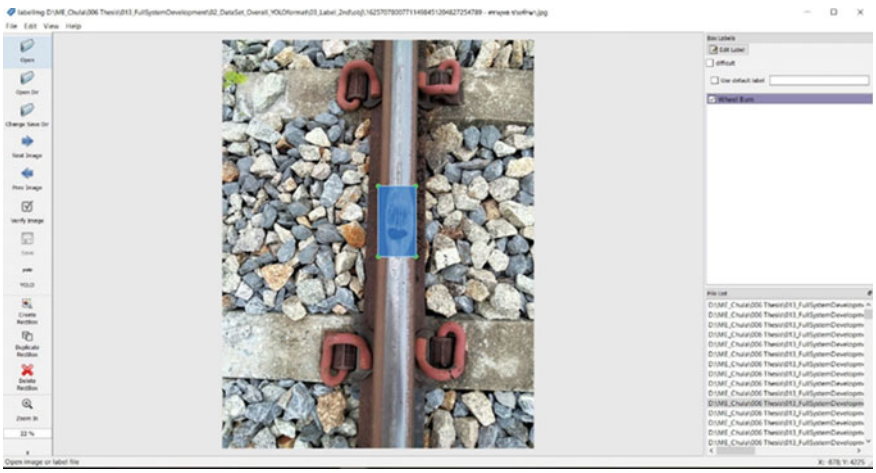

Fig. 3 User interface of LabelImg

area and giving the name of the defects according to the defect types included in the images. For carrying out the labelling process, the labelling tool "LabelImg" is applied in this study. Figure 3 describes the user interface of LabelImg.

4 Experiment and Result

Railway surface dataset is split into 90% for training and 10% for validation. This study focuses on the detection of two types of railway surface defects (spalling and wheel burn) and applies total 150 images where 134 images are used for training and the rest for validation. Moreover, data augmentation techniques like saturation, exposure, hue, and mosaic are also applied in this study. The input image size used for training is 416 × 416, and every image will be resized to this defined size. Other training parameters are also set up such as momentum = 0.949, learning rate = 0.001, and batch size = 64. The training iteration is set up to 60,000. After all the necessary parameters are set up, the training process will be started through Google Colab. In this paper, mean average precision (mAP@0.50) is used to estimate the performance of the proposed model. It is observed that the mAP of the proposed model is 79.16%. The test results of railway surface defect detection of the proposed model are shown in Fig. 4. It can be found that the types and position of the defects can be correctly predicted by distinctive bounding box in images. It is clear that the model can detect and locate the railway surface defects with high accuracy.

Fig. 4 Test sample images

5 Conclusion

This study provides new perception into the railway surface detection. The traditional ways of railway surface inspection take time and cost. Moreover, it may be harmful to the inspectors in some conditions. So, with the advancement of computer vision, this proposed model can detect the railway surface defects with high accuracy. The experiment results show that the proposed model can both detect and locate the railway surface defects in the image. It can save time and cost compared with traditional way of inspection.

References

1. ADB (Asian Development Bank) (2013) Thailand: supporting railway sector reform final report
2. Gnap J, Senko Š, Kostrzewski M, Brídziková M, Cződörová R, Říha Z (2021) Research on the relationship between transport infrastructure and performance in rail and road freight transport—a case study of Japan and selected European countries. Sustainability 13(12):6654. https://doi.org/10.3390/su13126654

3. Xu P, Liu R-K, Wang F, Wang F-T, Sun Q-X (2013) Railroad track deterioration characteristics based track measurement data mining. Math Probl Eng 2013(970573):1–7
4. Shang L, Yang Q, Wang J, Li S, Lei W (2018) Detection of rail surface defects based on CNN image recognition and classification. In: 2018 20th International conference on advanced communication technology (ICACT). IEEE, pp 45–51. https://doi.org/10.23919/ICACT.2018.8323642
5. Kim B, Cho S (2020) Automated multiple concrete damage detection using instance segmentation deep learning model. Appl Sci 10(22):8008. https://doi.org/10.3390/app10228008
6. Faghih-Roohi S, Hajizadeh S, Núñez A, Babuska R, De Schutter B (eds) (2016) Deep convolutional neural networks for detection of rail surface defects. In: Proceedings of the 2016 international joint conference on neural networks (IJCNN 2016), pp 2584–2589
7. Aydin I, Akin E, Karakose M (2021) Defect classification based on deep features for railway tracks in sustainable transportation. Appl Soft Comput 111:107706. https://doi.org/10.1016/j.asoc.2021.107706
8. Mittal S, Rao D (2017) Vision based railway track monitoring using deep learning. arXiv:1711.06423, arXiv:1711.06423v2, https://doi.org/10.48550/arXiv.1711.06423
9. Wang T, Yang F, Tsui K-L (2020) Real-time detection of railway track component via one-stage deep learning networks. Sensors 20(15):4325. https://doi.org/10.3390/s20154325
10. Yanan S, Hui Z, Li L, Hang Z (2018) Rail surface defect detection method based on YOLOv3 deep learning networks. In: 2018 Chinese automation congress (CAC). IEEE, pp 1563–1568. https://doi.org/10.1109/CAC.2018.8623082
11. Feng JH, Yuan H, Hu YQ, Lin J, Liu SW, Luo X (2020) Research on deep learning method for rail surface defect detection. IET Electr Syst Transp 10(4):436–442
12. Świeżewski J (2020) YOLO algorithm and YOLO object detection. Retrieved from https://appsilon.com/object-detection-yolo-algorithm/

Comparison of Optimal Sensor Placement Technics for Structural Health Monitoring Application

Mohamed Oualid Mghazli, Zineb Zoubir, Mohamed Elmankibi, and Nouzha Lamdouar

Abstract The information value of high-rise structural health monitoring applications relies significantly on optimal sensor placement (OSP) technics as it aims to deploy optimally, for economical and data management considerations, a limited number of sensors to obtain structural modal and vibration characteristics. Thus, the reliance and the efficiency of three optimal sensor placement methods: modal assurance criterion (MAC), effective independence (IE), Fisher information matrix (FIM), have been investigated in this paper using a high-rise building as a numerical case study. The detailed finite element model (FEM) served to extract the mode shapes of the reduced FEM model that served as an input for the optimal sensor placement problem. The three OSP technics were mutually evaluated in order to identify the most suited technic based on two criterions: the root mean square (RMS) index and the determinant of the Fisher information matrix (FIM). The results demonstrate that the joint objective function of MAC-FIM delivers satisfying performances in both OSP criteria as it provides the largest amount of mode shape information.

Keywords Optimal sensor placement · Structural health monitoring · Optimization problem

M. O. Mghazli (✉) · Z. Zoubir
Green Energy Park (IRESEN, Km2 R206, UM6P) Benguerir, Morocco
e-mail: mghazli@hotmail.com

M. O. Mghazli · M. Elmankibi
LTDS UMR CNRS 5513, ENTPE, Univ Lyon, Vaulx-en-Velin Cedex, France

M. O. Mghazli · N. Lamdouar
Civil Engineering Laboratory, Mohammadia School of Engineers, Mohammed V University, Rabat, Morocco

Z. Zoubir
EMINES, School of Industrial Management, VI Polytechnic University, Salé, Mohammed, Morocco

T. Kang (ed.), *Proceedings of 5th International Conference on Civil Engineering and Architecture*, Lecture Notes in Civil Engineering 369,
https://doi.org/10.1007/978-981-99-4049-3_38

1 Introduction

In order to ensure the ecological transition toward smart and resilient cities, the latter must take advantage of the technological progress made possible by the Internet of Things to tackle environmental challenges [1] through resources preservation and disasters mitigation. The structural health monitoring (SHM) is one of the Research and Development topics that has emerged as a solution that ensures infrastructures and buildings resiliency through real-time safety assessment and their life cycle extension through early anomalies detection capacities [2–4]. The development of the sensors technology has massively contributed to the development of SHM applications that is slowly starting to replace the classic visual inspection. Unlike the classical technics, the goal of the SHM technology presents various strengths: (a) Post disaster mitigation (b) Provide immediate safety assessment (c) Allow cost-effective maintenance strategies (d) Preserve natural resources preservation through building life span extension (e) Provide insurance firms with reliable data for accurate risk analysis. However, the SHM cost is still high that this technology widespread is still limited [5].

The balance between the cost effectiveness and the reliability of an OSP technic relies mostly on the provided information. The latter is limited by a finite number of sensors that needs to be installed optimally on specific locations within the structure, then needs to be processed and evaluated. The goal is to identify the structure's vibration and modal information's which accuracy is raising with the increase of the number of sensors to be deployed. Unfortunately, the installation of enormous quantities of sensors will complicate the operational cost of such a solution. Hence, the optimal sensor placement technics are, then, introduced as a decision methodology for sensor installation. In fact, the OSP plays a key role in digital twins for structural health monitoring applications as they intend to give the best configuration of sensor deployment in limited number of structural nodes based on criterions related to mode shape orthogonality, modal energy. The question that arises is about which method to adopt in order to guarantee accuracy and efficiency of the damage detection system in the given acquisition points.

Researchers, worldwide, have shown serious interest in R&D topics related to optimal sensor placement as they have addressed IOT components and infrastructures. Mishra et al. [6] presented a review on the IOT infrastructure and how different sensing systems can be deployed in SHM applications, Abner et al. [7] have focused on edge computing technics to expand battery lifespan used in Bluetooth experimented edge computing for Bluetooth. Researchers also attempted to increase algorithms efficiency and accuracy in combinatorial optimization through metaheuristic [8–10] and genetic algorithms [11]. In the literature, several studies discussed the performance of different sensor placement methods: methods based on modal energy like modal kinetic energy (MKE) [12], modal strain energy (MSE) [11, 13], and methods that aim to minimize mode shapes interdependency like Fisher information matrix (FIM) [14, 15], modal assurance criterion (MAC) [3], effective independence (EI) [16].

Huge efforts have been made by the research community to overcome the previous issues, but the relevance and the comparison of optimal sensor placement technics have not been fully addressed. In this paper, we focused our comparative study on Fisher information matrix (FIM), modal assurance criterion (MAC) and effective independence (EI) as they all aim to identify sensor placement that will provide mode shape interdependency. The objective of this study is therefore, to compare the three optimal sensor placement methods based on the same criterions: the root mean square index usually used for MAC and the determinant of the Fisher information matrix.

2 Sensor Placement Objective Functions

The aim of optimal sensor placement is to localize nodes where sensors will record maximum information in terms of vibration and structural modal characteristics [17]. Three objective functions are to be studied and compared: a- MAC, b- Fisher information matrix c-effective independence.

2.1 Modal Assurance Criterion (MAC)

The modal assurance criterion (MAC) describes the mode shapes interdependency

$$\mathrm{MAC}_{i,\,j}(v) = \frac{\left[\emptyset_i^T(v)\,.\,\emptyset_j(v)\right]^2}{\left[\emptyset_i^T(v)\,.\,\emptyset_i(v)\right].\left[\emptyset_j^T(v)\,.\,\emptyset_j(v)\right]}$$
$$i,\ j = 1,\ 2,\ 3\ldots\ldots,\ m \tag{1}$$

$$F_1(v) = \min f_1(v) \tag{2}$$

$$f_1(v) = \sum_{1 \le i,\, j \le m,\, i \ne j} \left\{\mathrm{MAC}_{i,\,j}(v)\right\}^2 \tag{3}$$

$$\mathrm{RMS} = \sqrt{\frac{1}{m(m\,-\,1)} \sum_{j=0}^{m} \sum_{i=0}^{m} \mathrm{MAC}_{\mathrm{ij}}^2} \tag{4}$$

φ_i and φ_j denotes as ith and jth vector in mode shape matrix. T transcripts denotes for transpose matrix.

v denotes as the sensor location vector, m denotes number of mode shapes considered in the OSP problem.

The goal is to minimize the objective function (Eq. (1)) and the RMS (Eq. (4)) which means less correlated mode shapes, thus better results.

2.2 Fisher Information Matrix

The goal of Fisher information matrix criterion is to avoid mode shape collinearity. This mathematically translates in maximizing the FIM matrix rank by finding a sensor configuration which maximizes the det (FIM).

The FIM matrix is defined in Eq. (5) where $\emptyset = (\emptyset_1, \emptyset_2, \ldots, \emptyset_m)$ is the mode shape matrix.

$$\text{FIM} = \emptyset^{\text{T}} . \emptyset = \begin{bmatrix} \emptyset_{11} & \cdots & \emptyset_{s1} \\ \vdots & \ddots & \vdots \\ \emptyset_{1m} & \cdots & \emptyset_{sm} \end{bmatrix} \begin{bmatrix} \emptyset_{11} & \cdots & \emptyset_{1m} \\ \vdots & \ddots & \vdots \\ \emptyset_{s1} & \cdots & \emptyset_{sm} \end{bmatrix} \tag{5}$$

S denotes for the number of sensors.
m denotes number of mode shapes to be considered in the OSP problem.

2.3 Effective Independence

The effective independence is an iterative process that aims to ensure sensor configuration that will secure mode shape interdependency. Based on the Fisher information matrix (FIM), contribution to the linear independency of each degree of freedom is calculated.

The DOFs contribution to the interdependency can be calculated based on Kammer [16, 18]:

$$E_S = \text{Diag}\left(\emptyset . \text{FIM}^{-1} . \emptyset^{\text{T}}\right) = \text{Diag}\left(\emptyset . \left[\emptyset^{\text{T}} . \emptyset\right]^{-1} . \emptyset^{\text{T}}\right) \tag{6}$$

The minimum value will be deleted, and the corresponding degree of freedom will be eliminated until we reach the number of sensors that was set as input.

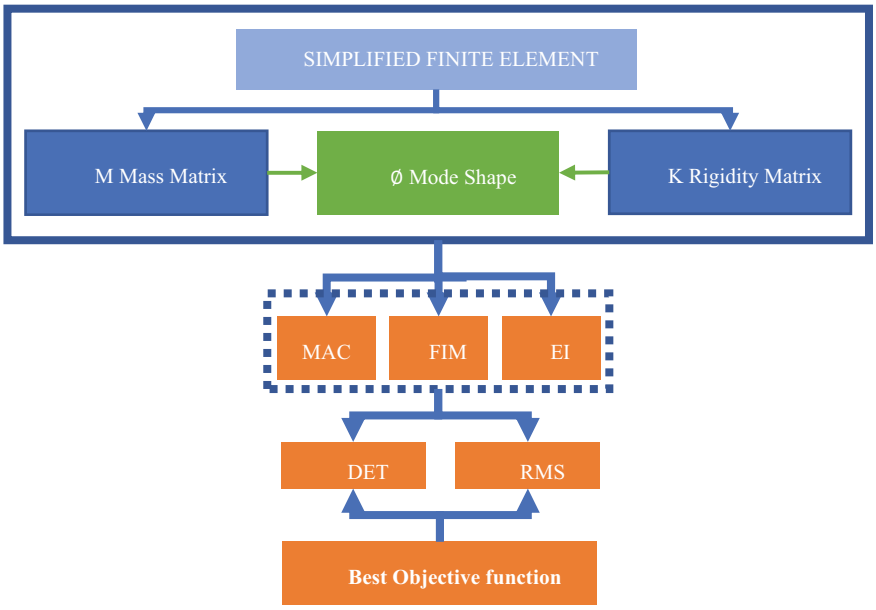

Fig. 1 Methodology

3 Methodology

The methodology that was adopted in this paper follows the following steps (Fig. 1):

(a) Conduct a finite element model analysis;
(b) Extract rigidity and mass matrix;
(c) Calculate mode shape matrix;
(d) Elaborate a simplified beam FEM model;
(e) OSP problem formulation using MAC, FIM and EI as objective functions;
(f) Compare the results based on the same criterions: determinant of the FIM and root mean square (RMS);
(g) Identify the most suited objective function.

4 Model

In this paper, we considered a high-rise structural model with a 410 m tall as a prototype building. The full-scale FEM model, elaborated to provide the OSP with input data, contains 10,720 nodes each with 3 degrees of freedom. A rigid diaphragm assumption was made and no live loads were considered. This FEM model allowed to have the mode shape matrix of the simplified FEM model which was used as

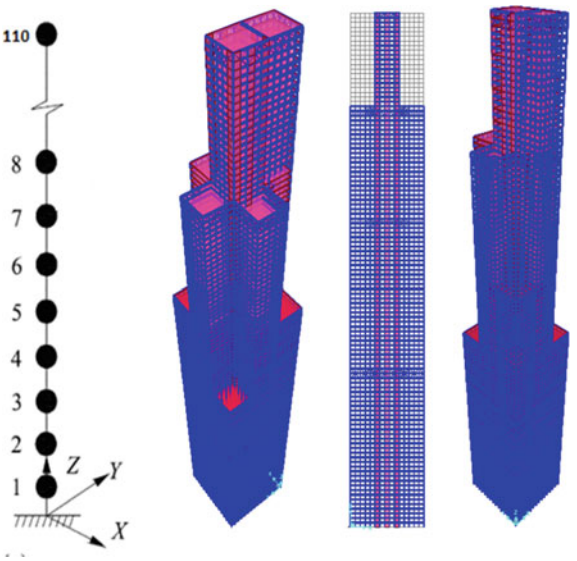

Fig. 2 **a** Reduced FEM model, **b** Full-scale FEM model

an example to investigate the proposed methodology to identify the most suitable optimal sensor method (Fig. 2).

The goal of this paper is to identify the most suited objective function in an optimal sensor placement problem using a reduced numerical FEM model [19] that will provide data for our OSP study. Therefore, the first 15 modes are used.

5 Results and Discussion

The three investigated OSP technics show different performances depending on the index based on which the comparison was made. For both criteria, the det (FIM) and RMS, the Fisher information matrix and the effective independence show similar performances while the modal assurance criterion shows clearly different results. When the det (FIM) is considered as an OSP criteria, the FIM and the EI have better performance than the MAC as they present higher values of the det (FIM) (Figs. 3 and 4).

When the root mean square (RMS) index is adopted as the basis of the comparison, the modal assurance criterion (MAC) presents the best results as it tends to decrease when we increase the number of the deployed sensors. Moreover, the FIM and the EI methods show unstable performance as they fluctuate when the number of sensors increases, but still present results in the same range.

Figure 5 shows the MAC performances simultaneously for the RMS and the DET indexes for different sensor configurations. The graph shows that the MAC performance is increasing in both indexes when the number of sensors is augmented.

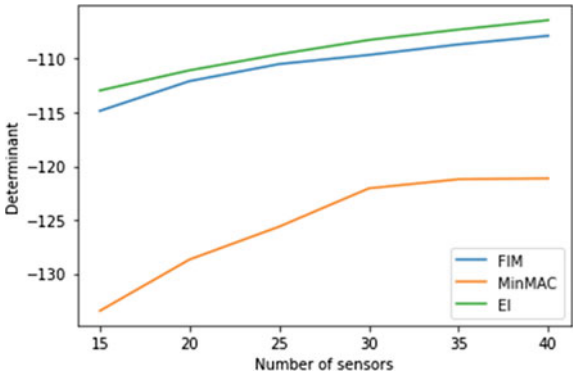

Fig. 3 FIM determinant in logarithmic scale as a function of number of sensors

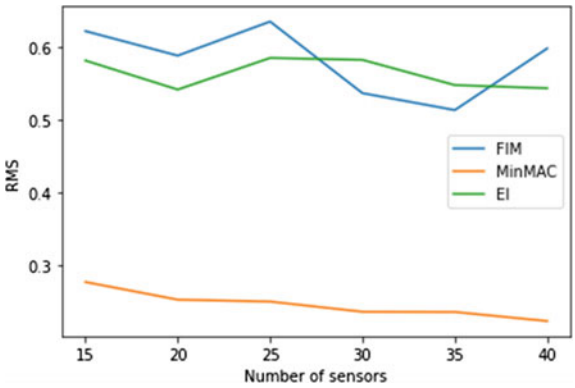

Fig. 4 RMS as a function of number of sensors

In fact, RMS is minimized while the DET increases when the sensor number is augmented.

According to Figs. 6 and 7, FIM and EI show unstable results for RMS criterion when the number of sensors changes from 15 to 40 sensor unlike for the MAC that minimizes the RMS and increases the det (FIM) if we increase the number of sensors.

Unfortunately, the MAC, FIM and EI results depend on the criterion RMS or det (FIM) that was adopted.

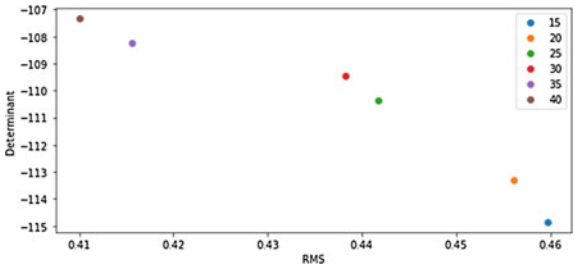

Fig. 5 FIM determinant and RMS for MAC method using different sensor configuration

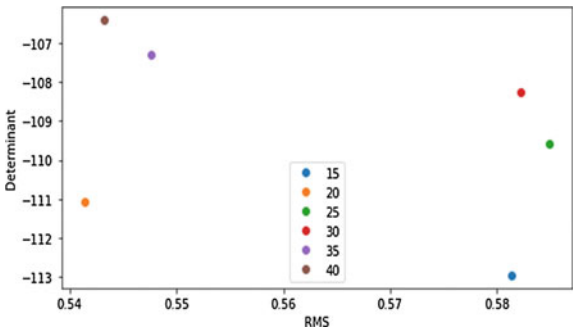

Fig. 6 FIM determinant and RMS for FIM method using different sensor configuration

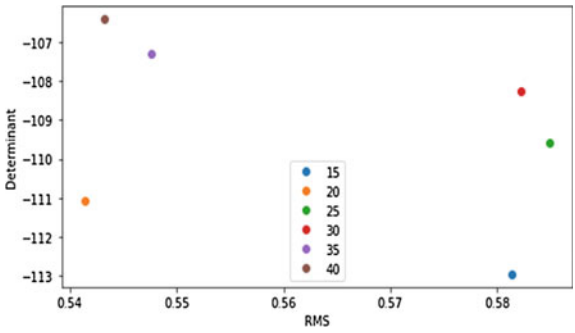

Fig. 7 FIM determinant and RMS for EI method

As the effective independence (EI) has only one solution, it cannot be improved in both indexes (RMS and DET), we explored a joint MAC- and FIM-based objective function and assessed its performance based on RMS and det (FIM) (Figs. 8 and 9).

The MAC-FIM-based objective function has the results in the same range as FIM and presents better performances than MAC when considering det (FIM) as an OSP criterion. When the RMS is considered as an OSP criterion, the MAC-FIM objective

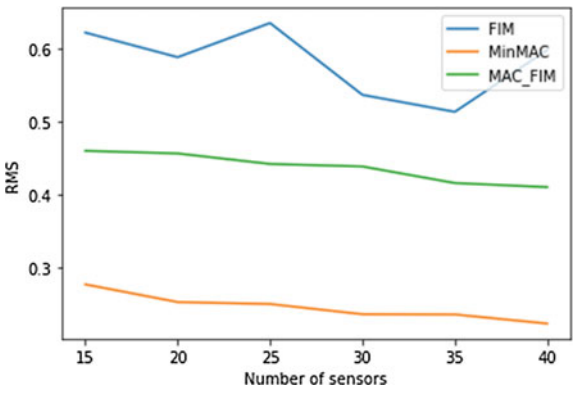

Fig. 8 RMS as a function of number of sensors with MAC-FIM results

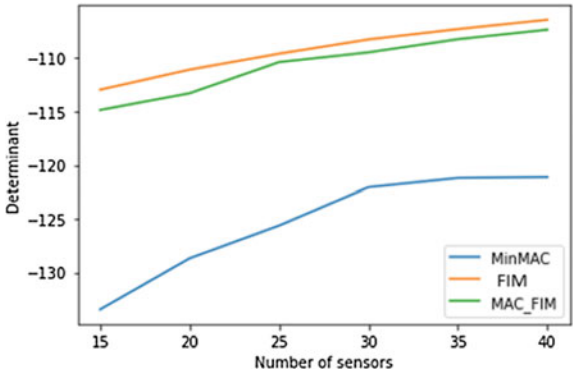

Fig. 9 Det FIM as a function of number of sensors

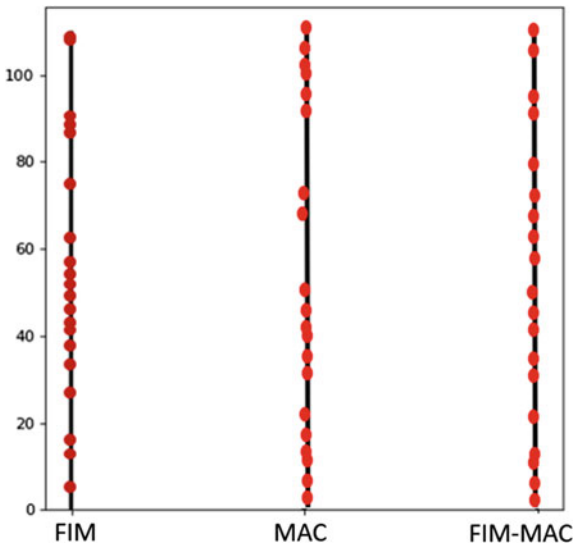

Fig. 10 Example of 20 sensor configurations for FIM, MAC and FIM-MAC

function performed better than the FIM but still underperforming than the MAC (Fig. 10).

6 Conclusions

This study proposes the comparison of three sensor placement methods: modal assurance criterion, Fisher information matrix and effective independence applied on a reduced finite element model of a high-rise building. The three technics have the same goal which is to maximize the mode shape interdependency in the corresponding

nodes where the triaxial accelerometers are placed for structural health monitoring application.

This study revealed that the three technics show different performances depending on the criterion based on which the comparison is made. Modal assurance criterion (MAC) has shown better performances based on RMS criterion while the FIM and EI showed better and similar results based on det (FIM).

For reliable results in both criteria, a novel FIM-MAC-based objective function has been investigated. The performances that were obtained were satisfying in both and helped identify future research topics:

The MAC-FIM-based objective function showed a result improvement based on DET method compared with FIM and MAC separately, but still less performant than the MAC in terms of RMS. This is mainly due to the algorithm efficiency that needs to be increased. Metaheuristic genetic algorithms and machine learning technics can be studied to solve the OSP optimization problem using a bi-objective function based on FIM and MAC jointly.

References

1. Dashkevych O, Portnov BA (2022) Criteria for smart city identification: a systematic literature review. Sustainability 14(8):4448. https://doi.org/10.3390/su14084448
2. Vilaseca ML, Rius JRC (2020) Optimal sensor placement methods and criteria in dynamic testing. Comparison and implementation on a pedestrian bridge. In: Proceedings of the international conference on structural health monitoring of intelligent infrastructure. Advanced research and real-world applications. SHMII-10, Porto, Portugal, pp. 1065–1072
3. Mahjoubi S, Barhemat R, Bao Y (2020) Optimal placement of triaxial accelerometers using hypotrochoid spiral optimization algorithm for automated monitoring of high-rise buildings. Autom Constr 118:103273. https://doi.org/10.1016/j.autcon.2020.103273
4. Amezquita-Sanchez JP, Adeli H (2014) Signal processing techniques for vibration-based health monitoring of smart structures. Arch Comput Methods Eng. 23(1):1–15. https://doi.org/10.1007/s11831-014-9135-7
5. Yi T-H, Li H-N (2012) Methodology developments in sensor placement for health monitoring of civil infrastructures. Int J Distrib Sens Netw 8(8). https://doi.org/10.1155/2012/612726
6. Mishra M, Lourenço PB, Ramana GV (2022) Structural health monitoring of civil engineering structures by using the internet of things: a review. J Build Eng 48:103954. https://doi.org/10.1016/j.jobe.2021.103954
7. Abner M, Wong PK-Y, Cheng JCP (2022) Battery lifespan enhancement strategies for edge computing-enabled wireless Bluetooth mesh sensor network for structural health monitoring. Autom Constr 140:104355. https://doi.org/10.1016/j.autcon.2022.104355
8. Johari NF, Zain AM, Mustaffa NH, Udin A (2013) Firefly algorithm for optimization problem. Appl Mech Mater 421:512–517. https://doi.org/10.4028/www.scientific.net/AMM.421.512
9. Satapathy S, Naik A (2016) Social group optimization (SGO): a new population evolutionary optimization technique. Complex Intell Syst 2:173–203. https://doi.org/10.1007/s40747-016-0022-8
10. Karaboga D, Basturk B (2007) A powerful and efficient algorithm for numerical function optimization: artificial bee colony (ABC) algorithm. J Glob Optim 39:459–471. https://doi.org/10.1007/s10898-007-9149-x
11. He C, Xing J, Li J, Yang Q, Wang R, Zhang X (2013) A combined optimal sensor placement strategy for the structural health monitoring of bridge structures. Int J Distrib Sens Netw 9(11). https://journals.sagepub.com/https://doi.org/10.1155/2013/820694

12. Li DS, Li HN, Fritzen CP (2007) The connection between effective independence and modal kinetic energy methods for sensor placement. J Sound Vib 305(4–5):945–955. https://doi.org/10.1016/j.jsv.2007.05.004
13. Liu W, Gao W-c, Sun Y, Xu M-j (2008) Optimal sensor placement for spatial lattice structure based on genetic algorithms. J Sound Vib 317(1–2):175–189. https://doi.org/10.1016/j.jsv.2008.03.026
14. Guo HY, Zhang L, Zhang LL, Zhou JX (2004) Optimal placement of sensors for structural health monitoring using improved genetic algorithms. Smart Mater Struct 13:528–534. https://doi.org/10.1088/0964-1726/13/3/011
15. Sajedi SO, Liang X (2020) Vibration-based semantic damage segmentation for large-scale structural health monitoring. Comput Aided Civ Infrastruct Eng 35(6):579–596. https://doi.org/10.1111/mice.12523
16. Kammer DC (1991) Sensor placement for on-orbit modal identification and correlation of large space structures. J Guidance Control Dyn 14(2):251–259
17. Feng S, Jia J (2018) Acceleration sensor placement technique for vibration test in structural health monitoring using microhabitat frog-leaping algorithm. Struct Health Monit 17(2):169–184. https://doi.org/10.1177/1475921716688372
18. Kammer DC, Tinker ML (2004) Optimal placement of triaxial accelerometers for modal vibration tests. Mech Syst Sig Process 18(1):29–41
19. Sun H, Büyüköztürk O (2015) Optimal sensor placement in structural health monitoring using discrete optimization. Smart Mater Struct 24:125034. https://doi.org/10.1088/0964-1726/24/12/125034

Structural Diagnosis of a Building by Means of Destructive and Non-destructive Tests

Rolando Mamani, Mariel P. Ramos, Hernan Chavez, Wilson A. Lazo, and Omar A. Hidalgo

Abstract This study presents the structural diagnosis of the clock tower building of the Plaza de Armas in the district of Huaro, province of Quispicanchi, Cusco Region—Peru in which compressive strength tests of concrete cores were carried out according to MTC E 704 with field and laboratory tests. As for the destructive tests, two concrete cores were extracted from level 1 and level 2 of the clock tower with diamond drills, and as for the non-destructive tests, the sclerometer measuring instrument was used in four columns, two columns from level 1 and two columns from level 2 of the clock tower. The results of the destructive and non-destructive tests diagnosed that the structure does not have the necessary compressive strength to withstand a possible earthquake in the area, therefore, the building must be reconstructed; also comparing this result with other research shows that at the time of evaluating and making decisions it is better to reconstruct the building, which will be shown in future research.

Keywords Structure · Building · Sclerometer · Concrete cores · Diamantina

1 Introduction

The structural analysis tools used for diagnosis have allowed the creation of better buildings with higher strength, which often makes it difficult to intuitively predict their behavior under extreme seismic stresses. This makes it very difficult to identify potential design weaknesses at an early stage [1]. In addition, structural monitoring plans are rarely implemented to compare the actual behavior of the structure with that estimated by numerical modeling [2]. There are tests and methods that allow to verify the structural behavior, some are recognized as destructive and non-destructive

R. Mamani (✉) · M. P. Ramos · H. Chavez
Professional Academic School of Civil Engineering, Universidad Continental, Huancayo, Peru
e-mail: 70380248@continental.edu.pe

W. A. Lazo · O. A. Hidalgo
Faculty of Engineering, Universidad Continental, Huancayo, Peru

T. Kang (ed.), *Proceedings of 5th International Conference on Civil Engineering and Architecture*, Lecture Notes in Civil Engineering 369,
https://doi.org/10.1007/978-981-99-4049-3_39

tests. An example of non-destructive testing that was developed in this research is sclerometry, the non-destructive test is an existing test method to evaluate the strength and durability of concrete structures. In the non-destructive test method, without loading the specimen to failure [i.e., without destroying the concrete] we can measure the strength of concrete [3]. Non-destructive testing of concrete is a very simple method of testing but requires trained and experienced people who have some special expertise to interpret and analyze the test results. Several non-destructive methods have been developed to test concrete [4]. The application of non-destructive testing [NDT] offers many advantages, such as time and cost savings for engineers to evaluate structures compared with destructive testing. Among the studies on MEAs incorporating debris, there are few non-destructive testing applications [5]. Many NDE models have been developed using non-destructive technologies to be more accurate, reliable and not dependent on humans [6]. This study provides an avenue for non-destructive detection of damage in polymer matrix composites by analyzing polymer-water interactions and damage-dependent hysteresis [7]. This test method covers the procurement, preparation and testing of: perforated concrete cores to determine their length, or their length strength, or their compressive strength, or their compressive tensile strength, or their indirect tensile strength and sawn concrete beams to determine their flexural strength [8]. For this reason, the present research will use as a destructive control method the extraction of concrete specimens by means of diamond and as a non-destructive method the use of the sclerometer, a tool that evaluates the surface hardness of concrete [9]. The reliability of the results that can be obtained from these models depends on the underlying assumptions, i.e., the constraint conditions, the mechanical model adopted for the materials, the internal constraints, etc. For this reason, it is important to study data reprocessing techniques and their results that allow structural identification and related parameters [10]. The most interesting methods are based on experimental data obtained by non-destructive testing. The latter is a necessary condition especially when the analysis is performed on historic and important buildings [10]. The present investigation was carried out in an important square in the district of Huaro. In order to better design this type of interventions, it is advisable to proceed to the structural monitoring before its execution to obtain useful information about the building under examination [11]. To this end, older structures are analyzed to understand the structural behavior and related cracking patterns [12].

2 Methodology

2.1 Location

The project is located in the district of Huaro, province of Quispicanchi and department of Cusco—Peru. The study area is located at 13°41′24.49″ south latitude and 71°38′26.77″ west longitude in geographic coordinates and 214,353 east, 8,484,984

Fig. 1 Reference location of the study area

north, zone 19 and southern hemisphere in UTM coordinates—WGS84 system at an elevation of 3166 m (Fig. 1).

2.2 Location of Study Points

The existing structure "Torre de Reloj", located in the Plaza de Armas of the district of Huaro, which has two levels and four columns, is being evaluated (Figs. 2, 3, 4, Table 1).

In addition, since seismicity describes the seismic quality or characteristic of an area and expresses the number of earthquakes per unit area or volume and per unit time, mode of occurrence and effects on the surface [13], it is shown that the intervention point is located on the edge of the northeastern area of high concentration of intermediate earthquakes, whose western edge follows the coastline from Lima to the border with Chile whose eastern edge passes near the northern shore of Lake Titicaca, following the boundary of the departments of Cusco and Apurimac of Peru.

2.3 Destructive Testing

The procedures and calculations required for this study were carried out in accordance with the following standards:

- MTC E 707 Taking of cores and beams in hardened concrete, with reference to the following standards, ASTM C 42: Standard test method for obtaining and testing drilled cores and sawed beams of concrete and AASHTO T 24: Standard

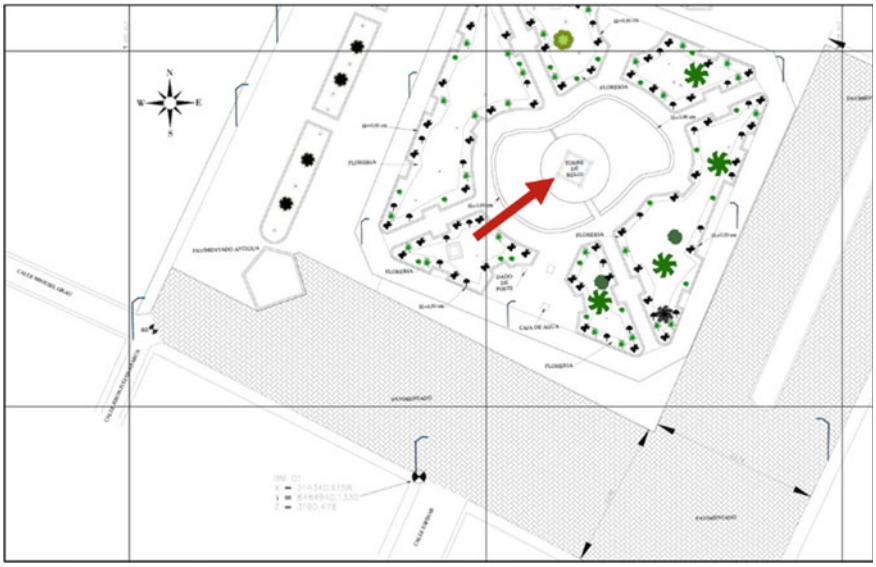

Fig. 2 Location of the clock tower structure

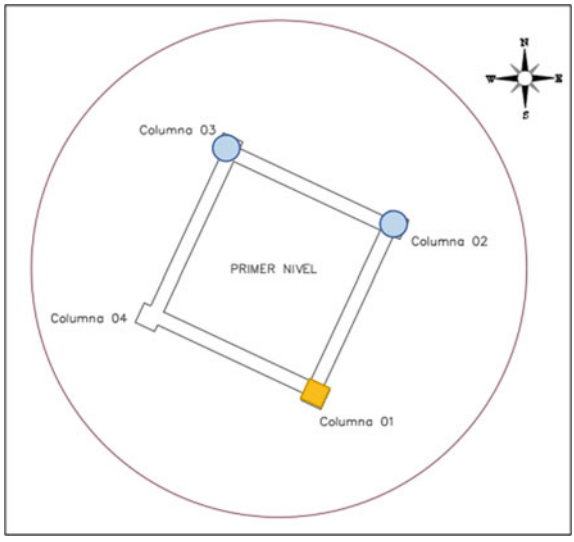

Fig. 3 Floor plan—first level

test method for obtaining and testing drilled cores and sawed beams of concrete [14].

- MTC E 712 Measurement of the length of concrete cores, with reference to ASTM C 17: Standard test method for measuring thickness of concrete elements using

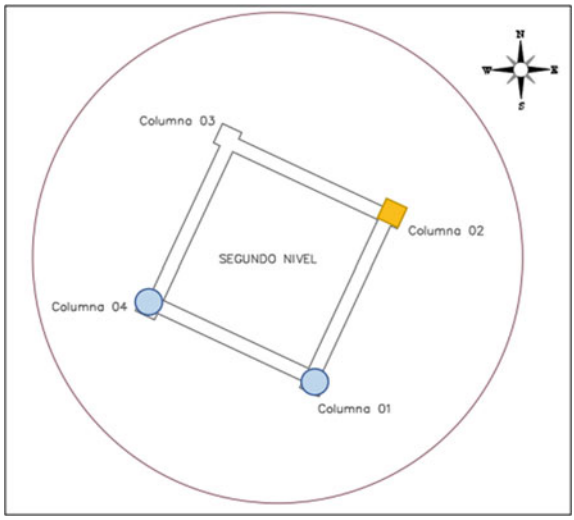

Fig. 4 Floor plan—second level

Table 1 Legend of symbols for location of study points

Legend	
Coring test	
	Column coring
Sclerometry test	
	Sclerometry in columns

drilled concrete cores and AASHTO T 148: Standard test method for measuring length of drilled concrete cores [15].

- MTC E 704 Compressive strength of cylindrical cores, with reference to ASTM C 39- 39 M-2005e2: Standard test method compressive strength of cylindrical concrete specimens and AASHTO T 22–2005: Standard test method for compressive strength of cylindrical concrete [16].

- MTC E 703 Facing of concrete cylinders, with reference to ASTM C 617: Standard practice for capping cylindrical concrete specimens and AASHTO T 231: Standard practices for capping cylindrical concrete specimens [17].
- MTC E 725 Test method for determining the rebound number of hardened concretes [sclerometry], with reference to ASTM C 805:1997: Standard test method for rebound number of hardened concrete and NTP 339.181:2001: Concrete [Concrete]: Test method for determining the rebound number of hardened concrete sclerometer [18].
- E 060 Reinforced [19].

ASTM C42M-13, which is the test method for diamond-drilled concrete cores to determine the compressive strength of the structure and NTP 339.059 assist in obtaining diamond cores, both criteria apply to concrete coring of the existing structure. The concrete core is put to compressive strength to determine the strength of the structural elements [20], in addition, adequate strength ranges are established according to the E 060: Standard for reinforced concrete [21] (Table 2).

Figure 5 shows the diamond coring test performed on 01 column of the first and 01 column of the second level of the clock tower.

Table 3 gives the compressive strength of the concrete cores extracted from the first and second level column.

Table 2 Compressive strength ranges

Denomination	Criteria
Compliance	Briquette strength is equal to or greater than 85% of the design strength
In the range	Briquette strength is equal to or greater than 75% of the design strength
Not complying	Briquette strength is less than 75% of the design strength

Fig. 5 Removal of concrete cores on the first and second levels of the clock tower

Table 3 Concrete core strength summary

Core	Element	Location	Compressive strength (kg/cm^2) × core
T-01	Column 01	First level	55.9
T-02	Column 02	Second level	79.2

2.4 Non-destructive Testing (Sclerometer)

Sclerometry is an inexpensive and rapid technique for assessing dynamic hardness and strength [22]. For this test the surface must be completely smooth, clean and free of surface moisture and it must be ensured that the rebound is taken at 90° to the plane [23]. Then the test is performed under ASTM C805M-13a, which is the standard method for the rebound number in hardened concrete and NTP 339.181, which is the test method for determining the rebound number of hardened concrete, so we have the average of 10 rebound numbers as shown in Fig. 6 in the column of the first and second levels in the clock tower of the Plaza de Armas.

Table 4 gives the non-destructive testing summary in column 02 and 03 of the first level and column 01 and 04 of the second level of the clock tower.

Fig. 6 Sclerometer test in the clock tower

Table 4 Summary of sclerometry tests

Essay	Element	Location (level, axes)	Compressive strength (kg/cm^2) × witness
E-01	Column 02	First level	100.7
E-02	Column 03	First level	111.4
E-03	Column 01	Second level	64.6
E-04	Column 04	Second level	94.3

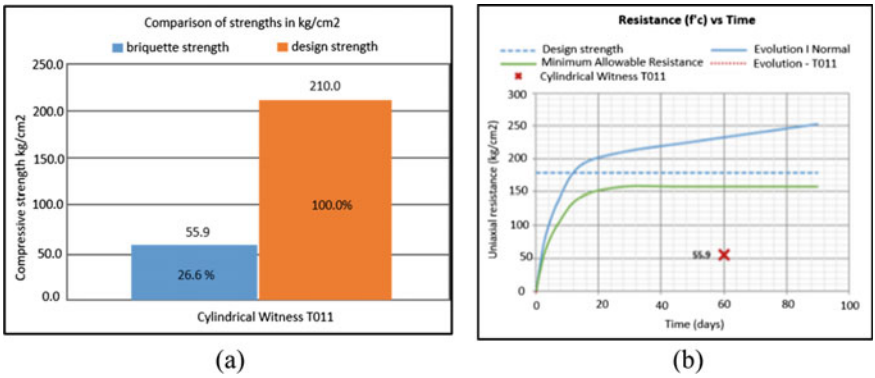

Fig. 7 Plots of results by diamond test in the first level columns

3 Results

3.1 Diamantina (Concrete Cores)

Figure 7 shows the graphs of the results obtained from the extraction of the concrete cores in the columns of the first level and Fig. 7a shows the comparison of the compressive strength of a design of 210 kg/cm^2 with the briquette strength of 55.9 kg/cm^2. On the other hand, Fig. 7b shows the comparison of the compressive strength over time where the briquette is 55.9, which is below the minimum admissible strength.

Figure 8 shows the graphs obtained from the extraction of the concrete core of the second level column. Figure 8a shows the comparison of the compressive strength in kg/cm^2 under a design strength of 210 kg/cm^2 with a briquette result of 79.2 kg/cm^2. On the other hand, Fig. 8b shows the comparison of the compressive strength over time, where the briquette is 79.2, which is below the minimum admissible strength.

Table 5 gives the results obtained from the concrete cores extracted from the columns with diamond drill bits from level 1 and level 2 of the clock tower.

The concrete coring test showed that the column of the first and second levels did not have the required compressive strength of the standard design.

3.2 Sclerometry

The number of 10 bounces on the columns of the first and second level of the clock tower was read, taking the average on the same point of the four columns: two columns of level 1 and two columns of level 2. Figure 9 shows the graph obtained from the sclerometry test at the first level.

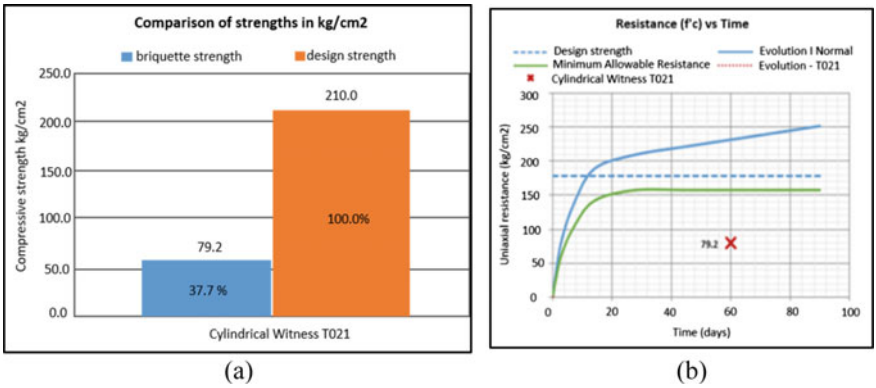

Fig. 8 Diamond test results graphs at level 2

Table 5 Specific data from the first and second levels, where concrete cores were extracted

N° briq	Code witness	Element	Breakage	Carga max. (kN)	Resistance (kg/cm^2)			Percentage f'c (%)		
					x witness	Average	Must have	*x* witness	Average	Must have
1	T011	C 01–1 level	18/10/21	23.05	55.9	55.9	210.0	26.6	26.6	100.0
1	T021	C 02–2 level	18/10/21	31.76	79.2	79.2	210.0	37.7	37.7	100.0

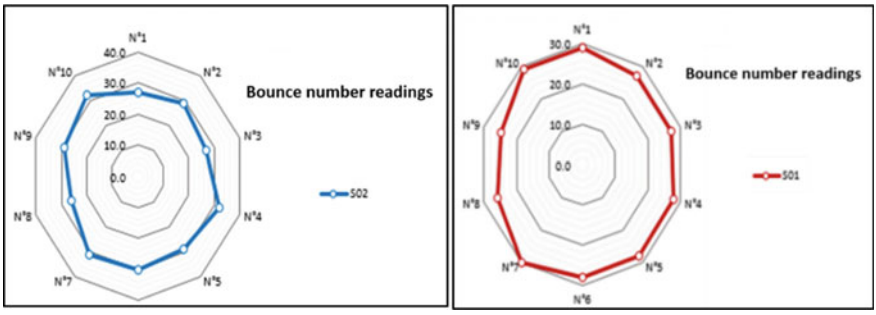

Fig. 9 Sclerometry test on the S01 and S02 spine of the first level

Table 6 gives the total average number of rebounds on column S01 reaching 48% of the design compressive strength and on column S02 reaching 53% of the design compressive strength.

The results of sclerometry on the second level columns are shown in Fig. 10.

Table 6 Compressive strength in sclerometry of the first level columns

Nº	Code	No. of reb. average	Orient. de aplic	Resistance (kg/cm^2)		Percentage of f'c (%)	
				By briquette	Design strength	By briquette	Design strength
1	S01	27.7	0°	100.7	210.0	48.0	100.0
2	S02	29.2	0°	111.4	210.1	53.0	100.0

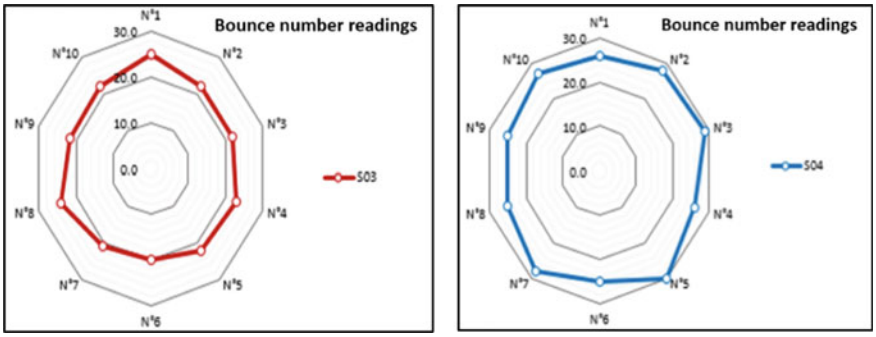

Fig. 10 Sclerometry test on the S03 and S04 spine of the second level

Thus, column S03 reaches 30.8% of the design compressive strength and column S04 reaches 44.9% of the design compressive strength (Tables 7 and 8).

Table 7 Compressive strength in sclerometry of the second level columns

Nº	Code	No. of reb. average	Orient. de aplic	Resistance (kg/cm^2)		Percentage of f'c (%)	
				By briquette	Design strength	By briquette	Design strength
1	S03	22.25	0º	64.6	210.0	30.8	100.0
2	S04	26.9	0º	94.3	210.1	44.9	100.0

The sclerometry test showed that columns S01, S02 of the first level and columns S03, S04 of the second level are highly vulnerable since they do not reach the required design to be considered a structure resistant to compression or even a seismic event in the zone.

Table 8 Specific data of the sclerometry test of the first level and second level columns

Code	Structural element	Ubication	Average	Resistance (kg/cm^2)			Percentage f'c (%)		
			N° of rebound	*x* witness	Average	R. design	*x* witness	Average	R. design
S01	Column 02	First level	27.7	100.7	100.7	210.0	48.0	48.0	100.0
S02	Column 03	First level	29.2	111.4	111.4	210.0	53.0	53.0	100.0
S03	Column 01	Second level	22.25	64.6	64.6	210.0	30.8	30.8	100.0
S04	Column 04	Second level	26.9	94.3	94.3	210.0	44.9	44.9	100.0

4 Conclusion

According to the E060 reinforced concrete standard given in Table 2 and by means of the results obtained in the concrete coring test, it is determined that the compressive strength of the destructive test of the second-floor column has 26.6% and that the briquette of the second level has 37.7% of the design strength, therefore, both columns do not comply with the concrete E060 standard and the result is less than 75% of the design strength. In addition, according to the requirements of the ASTM C-805 standard, in the sclerometry test of columns S01 and S02 of the first level show 48 and 53% and in columns S03 and S04 of the second level show 30.8 and 44.9% of the design concrete strength of 210 kg/cm^2. 9% of design concrete resistance of 210 kg/cm^2, therefore it is concluded that by means of the destructive and non-destructive test it is demonstrated the deficiency in the resistance of the concrete and that the structural elements of the first and second level of the building are vulnerable to any natural event such as an earthquake in the area, therefore the non-destructive and destructive test shows a percentage range that the clock tower should be rebuilt.

5 Discussion

In the research of Japan, Portugal and Brazil with the sclerometer test under ASTM C-805 M and NTP 339–181, an average compressive strength of: 327.22 kg/cm^2 was obtained, considering that the strength can be affected by surface roughness, size, shape and stiffness of the surface, maximum size of coarse aggregate, age and moisture condition of the concrete surface [9]. In these investigations, it was demonstrated that the destructive and non-destructive tests determine the knowledge of the state of the structure of a building and is a decisive factor in decision-making as in the clock tower, which took into account the results of the destructive test of concrete coring and non-destructive test of sclerometry, stating that the results obtained are real in a subsequent investigation will focus on the reconstruction of the clock tower of the Plaza de Armas in the district of Huaro, province of Quispicanchi, Cusco Region.

References

1. Olivera-Lopez JJ, Oyarzo-Vera CA (2020) Structural diagnosis of a reinforced concrete building based on its bio-seismic profile and incremental dynamic analysis. In: Works and Projects online, pp 95–106. http://dx.doi.org/10.4067/S0718-28132020000100095
2. Ventura CE, Horyna T (1997) Structural assessment by modal analysis in Western Canada. In: Proceedings of the 15th international modal analysis conference. Society for Experimental Mechanics (SPIE), Orlando, Florida, USA, pp 234–239

3. El Masri Y, Rakha T (2020) A scoping review of non-destructive testing [NDT] techniques in building performance diagnostic inspections. Constr Build Mater 265:120542. https://doi.org/10.1016/j.conbuildmat.2020.120542
4. Ridgley KE, Abouhussien AA, Hassan AAA, Colbourne B (2019) Characterisation of damage due to abrasion in SCC by acoustic emission analysis [in English]. Mag Concr Res 71(2):85–94. https://doi.org/10.1680/jmacr.17.00445
5. Meftahi F, Soliman A (2023) Evaluating the properties of alkali-activated materials incorporating waste materials using non-destructive testing: a review. In: Walbridge S et al (eds) Proceedings of the Canadian society of civil engineering annual conference 2021 (CSCE 2021). Lecture notes in civil engineering, vol 248. Springer, Singapore, pp. 265–276. https://doi.org/10.1007/978-981-19-1004-3_22
6. Elbeheri A, Bagchi A, Zayed T (2023) Defect based condition assessment of steel bridges. In: Walbridge S et al (eds) Proceedings of the Canadian society of civil engineering annual conference 2021 (CSCE 2021). Lecture notes in civil engineering, vol 240. Springer, Singapore, pp .623–632. https://doi.org/10.1007/978-981-19-0507-0_54
7. Idolor O, Berkowitz K, Guha RD, Grace L (2022) Non-destructive examination of polymer composites by analysis of polymer-water interactions and damage-dependent hysteresis. Compos Struct 287:115377. https://doi.org/10.1016/j.compstruct.2022.115377. ISSN: 0263–8223
8. Terrones J (2022) Diamantina internet essay. In: Scribd. Retrieved from https://es.scribd.com/document/345312234/Ensayo-de-Diamantina. Accessed on 4 Jul 2022
9. Rojas Z, Liseth K (2017) Comparison of diamond and sclerometry tests of the paving of jirones Japón, Portugal and Brasil–Cajamarca. National University of Cajamarca
10. Diaferio M, Foti D, Giannoccaro NI, Sabbà MF (2022) Dynamic identification in an irregular structure. Appl Sci 12(7): 3445. https://doi.org/10.3390/app12073445
11. Foti D, Giannoccaro NI, Sabbà MF, La Scala A (2023) Dynamic identification of a strategic building of the sixties with a mixed structure. Procedia Struct Integrity 44:782–789. https://doi.org/10.1016/j.prostr.2023.01.102. ISSN: 2452–3216
12. Vingsbo O, Hogmark S (1984) One-step pendulum grooving: a technique for abrasive testing. Desgaste 100(1–3):489–502
13. National Civil Defense Institution [s/f] (2022) Seismic risk assessment in the districts of ICA, parcona and la tinguiña. Gob.pe. Retrieved from http://sinpad.indeci.gob.pe/IntranetOracle/
14. Tártara LI, Leavi S, Campana VR, Allemandi DA, Palma SD (2018) A comparison of two experimental models of glaucoma in rabbits. J Fac Med Sci, Cordoba, Argentina 75(1):25–31. https://doi.org/10.31053/1853.0605.v75.n1.16811
15. Mtc E 712 [s/f] (2022) 2000 Measuring the length of concrete cores. In: Xdoc.Mx. Retrieved https://xdoc.mx/documents/mtc-e-712-2000-medida-de-la-longitud-de-nucleos-de-concreto-60a33e288bc0e. Accessed on 5 Jul 2022
16. Barboza AD (2017) MTC 704 compressive strength. In: QDOC.TIPS. Retrieved from https://qdoc.tips/mtc-704-resistencia-a-compresion-pdf-free.html
17. MTC 703 [s/f] (2022) In: Scribd. Retrieved from https://es.scribd.com/document/185621552/mtc703
18. MTC Standard E-725 SCLEROMETRY [s/f] (2022) Retrieved from https://es.scribd.com/document/542629360/Norma-MTC-E-725-ESCLEROMETRIA
19. Amambal J [s/f] (2022) E.060 reinforced concrete. In: Slideshare.net. Retrieved from https://es.slideshare.net/jaimeamambalzambrano/e060-concreto-armado-61395931
20. Murrieta SAG, Cachique CMR (2022) Comparison of diamond and sclerometry tests of the rigid pavement of jr. dos de mayo, blocks 4–11, Scientific University of Peru. Retrieved from http://repositorio.ucp.edu.pe/handle/UCP/1760
21. Ministry of Housing, Construction and Sanitation (2022) E060_CONCRETE_ASSEMBLY, Gob.pe. Retrieved from http://blog.pucp.edu.pe/blog/
22. Vecca VC, Lucero SR Parameters influencing the results of non-destructive sclerometry and ultrasonic testing. Faculty of Engineering, National University of Asuncion, Asunción [PAR]

23. Pardo-Herreño MB, Builes-Salazar RA (2016) Correlation between strengths obtained by compression and sclerometry tests in normal concrete cylinders and those modified with synthetic fiber and steel fiber. Degree work, Catholic University of Colombia, Faculty of Engineering, Civil Engineering Program, Bogotá, Colombia. Retrieved from https://repository.ucatolica.edu.co/handle/10983/13979

Development of a System for Measuring Surface Slope with Point Cloud Data

Vachara Peansupap and Aye Myint May

Abstract The article explored the development of a surface slope measurement system using 3D point cloud data. The floor slope condition is important for the residential building floor quality inspection. Insufficient slope can lead to surface deterioration and water pocket formation. Current slope measurement in floor quality inspection has problems: time-consuming because of the forming log for each elevation point to calculate, random area points are chosen to measure, and the result did not cover the whole floor area, the tools used in the conventional methods can produce the close result not the exact result for the floor area. The aim of the research is the developed a system that can be used as an assistant tool in floor slope inspection with 3D point cloud data so that the calculation can be applied to all areas of the floor. 3D point cloud data can be collected using a FARO 3D laser scanner and execution of the system from acquired data will be performed in MATLAB. The system produces the slope value of the inspected room as well as the direction of the slope to decide the correct direction of the drainage of the floor which is important to access the bathroom or balcony in the residential building.

Keywords Point cloud · 3D laser scanning · Inspection · Slope measurement

1 Introduction

1.1 Background

The concrete floor slope condition is the leading factor for the functionality of the floor. The surface slope of the concrete floor has been evaluated not only with the manual method but also with automatic indicators. However, the quality control in

V. Peansupap · A. M. May (✉)
Department of Civil Engineering, Construction Engineering and Management Program, Chulalongkorn University, Bangkok, Thailand
e-mail: 6370437621@student.chula.ac.th

T. Kang (ed.), *Proceedings of 5th International Conference on Civil Engineering and Architecture*, Lecture Notes in Civil Engineering 369,
https://doi.org/10.1007/978-981-99-4049-3_40

the construction site which includes the implementation of floor inspection evaluated as inefficient as there is not much attention to defective conditions earlier in the construction project. A report on the detection of defects in production in 1999 stated that 54% of the defects are associated with human elements including unskilled and poor supervision of the work [1].

Floor inspection is a crucial step because the fabrication of the floor needs to be performed by hand, while other elements such as columns and walls can be modified by the formwork [2]. The floor finishing quality inspection has heavily relied on visual inspection as well as tools depending upon human productivity. Likewise, the size of the machine and finding where to place the tool needs to be considered. The systematic floor inspection method has been identified as the straight edge method which computes the gap between the 10-foot straight edge and the floor to check the level of the floor [3]. According to ASTM standard, the f-number method has been introduced to inspect floor flatness and floor levelness since the straight edge method ignore the floor condition between the shorter distance [4].

To accommodate the f-number method, several tools such as floor profileograph and Dipstick Floor Profiler Fig. 1 have been introduced to measure floor flatness and levelness which can make the surface profile analysis based on the f-number method [5].

However, the slope of the floor cannot be calculated by using the f-number. Certain types of floors such as the toilets and balconies slopes are needed to check not only the value but also the direction of the water to the drainage. The slope is checked by using plumb bob and spirit level (Carpenter level) by measuring the length and elevation of the floor conventionally. Also, the measurement can be done by utilizing a laser line as the reference (Fig. 2).

Fig. 1 Dipstick floor profiler and face profileograph

Fig. 2 Slope measurement on site

1.2 Problem Statement

The issue with manual slope inspection is the longer inspection time, randomly choosing the points in the whole floor and close but not the accurate result. Another drawback is the results of the measured slope depend upon the choice of the selection of inspection points since there are no criteria for choosing the point. The execution time of the inspection is longer because of the repetitive process.

Automated system development is required to improve the floor slope inspection. The system needed to evaluate the floor slope value as well as the water flow direction to avoid poor drainage.

1.3 Objective

This study takes a fresh look at the measurement of the floor slope by developing the slope measurement calculation system using the 3D point cloud data. The system can be applied as the assistant tool in floor finish inspection for slope as well as the interpretation of drainage flow visually.

2 Literature Review

The floor slope is critical not only for the tiling process but also for the concrete flooring to minimize misalignment, unevenness, and bumpiness. A floor slope is needed to provide proper drainage of the bathroom floor. The traditional way for verifying two slope criteria is to evaluate the water flow for direction and the recorded random elevation difference for slope value. To end ponding, forms and screed guides

should be installed with a minimum slope of ¼ in./ft (20 mm/m), where good drainage is necessary [6].

Positive drainage should always be supplied for exterior slabs and can be desirable for some interior slabs. An exception to these positive drainage recommendations for exterior slabs is the accessible landing area and route to the building, where the maximum slope can be limited to 2% [7].

Point clouds are increasingly being used to generate semantically rich 3D models of sites or to compare the as-is state they record to an earlier "as-designed" state represented by a 3D model or even earlier point clouds. The number of scans and the quality of the scanned data both affect the registration outcome. Inadequate data (both number and quality) will not offer enough overlap, making registration impossible. In contrast, performing too many scans wastes a substantial amount of time. As a result, the number of scans and computing efforts must be balanced [8].

The idea of 3D coordinate extraction using TLS is based on monitoring the time it takes the laser pulse to travel from its source to an object and back, and then determining the distance based on the pulse's transit speed (the same as the speed of the light). Unlike camera-based vision systems, using such laser pulses to generate 3D coordinate data eliminates the requirement for extra calculation for coordinate information during picture acquisition. Transmitting 102–106 laser pulses to an object is used to calculate the object's relative 3D coordinates concerning TLS [9].

3 Methodology

3.1 System Development

The slope calculation is based on the data collected from the point cloud 3D data and analysis from the calculation of data in MATLAB. Recent development in point cloud data findings mostly tended to focus on wall surface analysis rather than floor surface. So, the analysis was conducted using the point cloud data in MATLAB combined with the MSAC algorithm to find the proper floor plan to calculate the floor slope.

The previous research is applied to define the proper value for the floor slope for the inspection. The specification and resolution of the point cloud data are learned to have complete knowledge of the point cloud data. The data collection has been done with the FARO 3D laser scanner for the data collection (Fig. 3).

After the data collection, the data is imported into FARO software to acquire the required area to calculate. The combination of two data is required since the scanner needs to be placed on the floor used as the data. The data is combined by using the auto registration from SCENE software by removing the duplicate points from the point cloud. The registered point cloud is imported to MATLAB for calculation (Fig. 4).

Fig. 3 FARO laser scanner

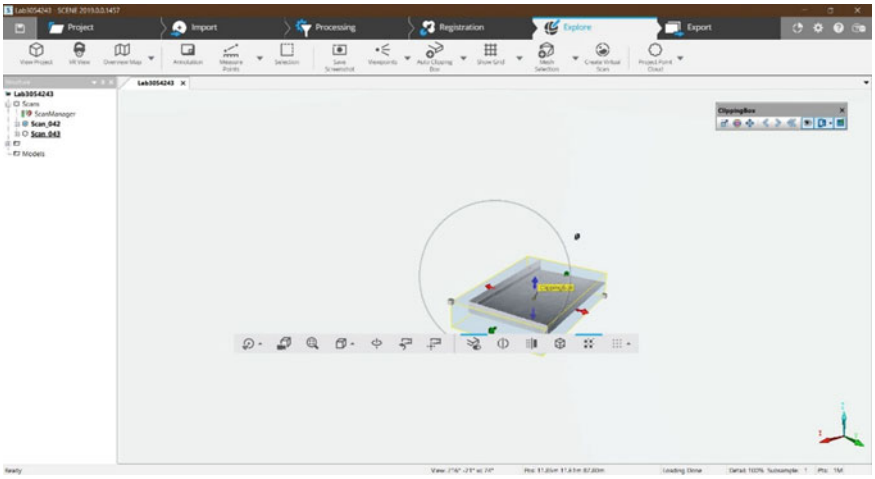

Fig. 4 Registering point cloud

The imported point cloud which includes the information of locations, intensities, and RGB colors to render the point cloud is read in the MATLAB software. The extracted point cloud x,y,z position is specified as the M-by-3 numeric matrix, and the z values normally respond to the elevation of the floor. The z value will be the main number for calculating the direction and value of the slope of the floor.

The original point cloud file which includes the other area (outliers) is extracted by using the using M-estimator SAmple Consensus (MSAC) algorithm to get the fitted plane and also reducing the size of the point cloud. This will allow the point cloud to fit a plane by identifying the constraint and reference vector as an input.

The position matrix of the plane is used to calculate to get the slope value. The slope can be defined as the change in length to the change in elevation in terms of 3D. The change in the y–z plane is calculated which is followed by the change in the x–z

direction. So, the result of the slope value (change of elevation) in the x direction, as well as the y direction, is produced [10]. The results are brought together by using the Pythagoras theorem to get the slope of the whole plane (Fig. 5).

$$m = \sqrt{\left(\frac{dz}{dy}\right)^2 + \left(\frac{dz}{dx}\right)^2} \tag{1}$$

The direction of the slope can be illustrated by the range of the elevation change through the floor. The elevation change can be calculated by making a reference plane over the original plane. The difference between the planes is identified as the elevation difference through the floor. The difference is demonstrated as the color map for the elevation (Fig. 6).

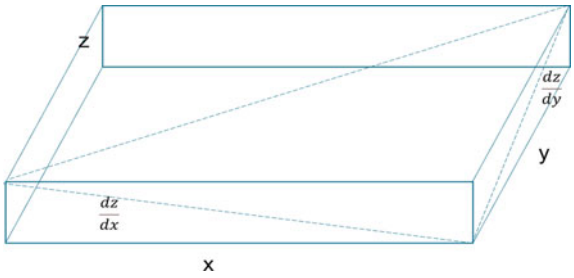

Fig. 5 Slope calculation

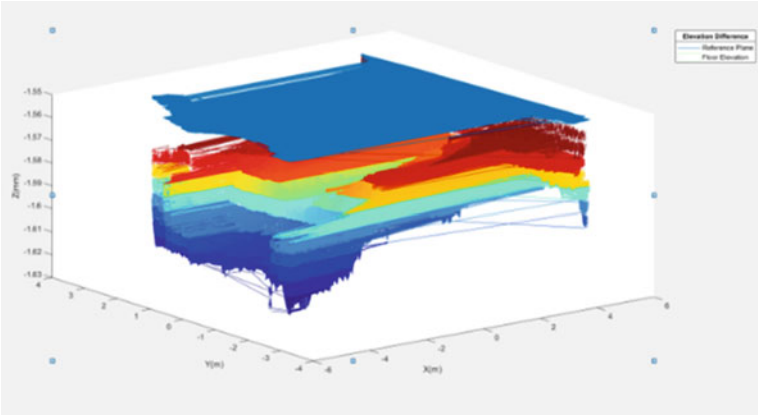

Fig. 6 Extracted floor elevation calculation

Fig. 7 Data collection of point cloud

3.2 Experiment and Result

The data collection is performed inside the Civil Engineering Department building of Chulalongkorn University. The data is retrieved by using FARO 3D laser scanner for the toilet floor to check the drain and center floor to confirm whether the result is consistent. The scanner is positioned two times for the toilet which is at the door and center. For the center floor, the right and left sides of the floor will be used as the station. The resolution of the 3D points will be ¼ and 4x (Fig. 7).

The data processing, registration, and selected plane extraction will be done in the scene software. The two datasets will combine to make the complete floor. The duplicate 3D data points will be removed from the data to form the point cloud. The point cloud will be loaded to MATLAB for calculation. The output generated will include the slope value and color map displaying the direction of the slope.

According to the result, the slope of the toilet is within the needed specification which is 1–2% as well as the manual measurement. The color map showing the direction of the drain is in the same condition as the actual measurement. The center floor can be evaluated as a flat surface since it is under 1% and there is not much difference in elevation difference throughout the floor (Figs. 8, 9, 10, 11).

3.3 Discussion

The system is tested for 30 times in order to make sure the reliability of the automated measurement. The results are 0.16% differential to the average which is 1.93%.

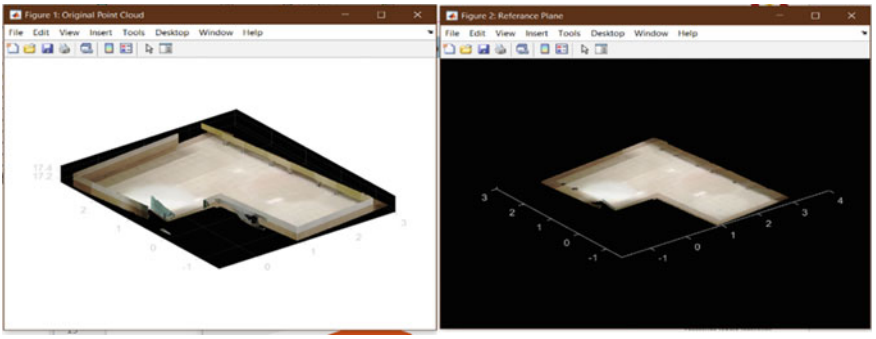

Fig. 8 Point cloud data and extracted plane for toilet

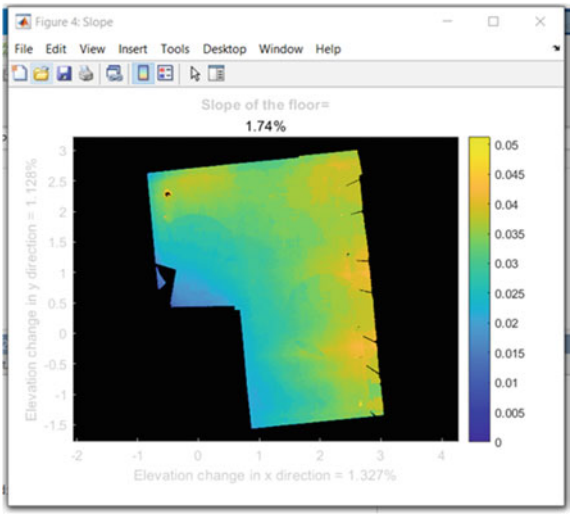

Fig. 9 Slope value and color map for direction

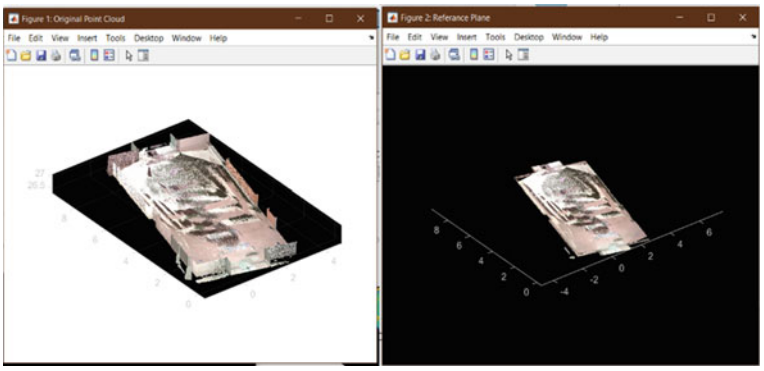

Fig. 10 Point cloud data and extracted plane for center floor

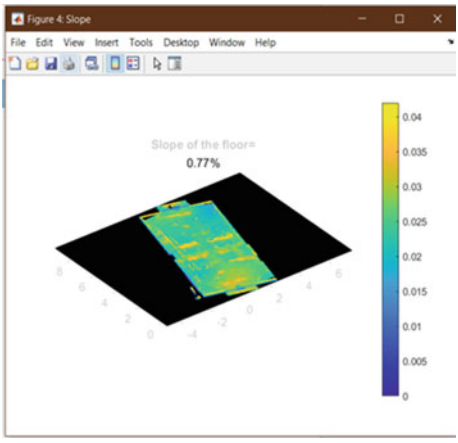

Fig. 11 Slope value and color map for the direction

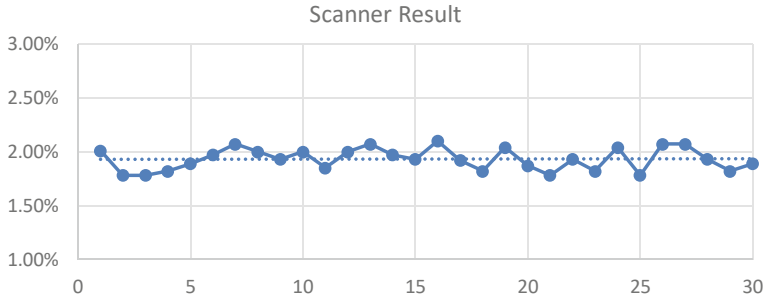

4 Conclusion

Inspection of the slope value is key factor to have the good drainage system for the floor. The conventional way of measuring the slope is time-consuming and repetitive. The study provides a new perspective on slope measurement. By using the 3D point cloud data and MSAC algorithm from MATLAB, the result not only provides the value of the required slope but also but also interprets the direction of the slope from the color map of elevation difference. Application of the proposed system with the help of the point cloud data collection can deliver efficient quality inspection.

References

1. Opfer ND (1999) Construction defect education in construction management. In: ASC proceedings of the 35th annual conference. California Polytechnic University, ASC
2. Garber G (2006) Design and construction of concrete floors. CRC Press
3. ACI (2008) Building code requirements for structural concrete (ACI 318–08) and commentary: an ACI standard
4. ASTM (2008) Standard test method for determining F_F floor flatness and F_L floor levelness numbers
5. Meece A (2017) Laser guided navigation system for the automated floor profiler–string walker edition. Master thesis, University of Cincinnati
6. Witherspoon WT, Taylor J (2004) Slab construction-30 years later. In: GeoSupport 2004: drilled shafts, micropiling, deep mixing, remedial methods, and specialty foundation systems, pp. 993–1003
7. Phelan WS (1989) Guide for concrete floor and slab construction. ACI Mater J 86(3):252–296. https://doi.org/10.14359/2452
8. Aryan A, Bosché F, Tang P (2021) Planning for terrestrial laser scanning in construction: a review. Autom Constr 125:103551
9. Park C-S, Lee D-Y, Kwon O-S, Wang X (2013) A framework for proactive construction defect management using BIM, augmented reality and ontology-based data collection template. Autom Constr 33:61–71
10. Huisman O, de Rolf A (2009) Principal of geographic information systems. The international institute for geo-information science and earth observation (ITC), The Netherlands

GNSS Application in Construction Surveying of High-Rise Buildings with Frame Shear Wall Structures

Yuan Cheng, Renshu Zeng, and Shuliang Guo

Abstract GNSS technology has many features such as all suitable for all-weather condition and high degree of accuracy, which made it a promising method for structural displacement monitoring. In recent years, GNSS has been extensively applied to health monitoring of large civil structures as long-span bridges, dams and high-rise buildings. In the engineering survey, perpendicularity of datum axis and elevation control is one of the most important contents of quality control of building construction. Scientific, rapid and precise measurement method is the foundation of guaranteeing engineering quality and construction period, as well as improving measuring efficiency and precision of positioning. As a new type of measurement method in engineering survey field measurement, GNSS has some particular advantages. For high-rise buildings with frame shear wall structures, construction surveying aims at transmitting axis and elevation. To determine plane and elevation control points of each floor in construction projects, application of GNSS method with static positioning mode is effective. Compared with traditional methods, the accuracy of GNSS method is high enough to meet design requirements. In addition, it is less affected by environment and can improve overall work efficiency. In this chapter, the basic principle of GNSS and the multi-path effect with its process sing method are firstly introduced. Then with the long-period dynamic monitoring data of New Building in Chongqing Industry and Trade and Polytechnic, the performance of GNSS to monitor structural displacements in complex environment is discussed. Finally, the current status of GNSS application in the field of civil engineering is briefly summarized.

Keywords GNSS · High-rise building · Construction surveying · Complex environment · Building construction

Y. Cheng · R. Zeng · S. Guo (✉)
Chongqing Industry and Trade and Polytechnic, Chongqing 408000, China
e-mail: 1035896929@qq.com

T. Kang (ed.), *Proceedings of 5th International Conference on Civil Engineering and Architecture*, Lecture Notes in Civil Engineering 369,
https://doi.org/10.1007/978-981-99-4049-3_41

1 Introduction

With the development of economy and the progress of science and technology, the design of high-rise buildings tends to the ultra-high structure, the wide use of lightweight, high strength and flexible building materials, cable, membrane and other new systems also make the span of space structure is increasing. These large engineering structures are easy to produce large displacement under the action of strong wind, which affects the practical performance of the structure. In addition, for temperature-sensitive structures such as long-span reticulated shells, temperature stress is a role that cannot be ignored. Excessive temperature stress may cause uneven structural force and increase transverse support reaction force, leading to local damage of the structure. Therefore, it is of great significance to monitor the structure in the complex operating environment for a long time and study the changing law of the dynamic response of the structure with time and season to ensure the safe operation of the structure and to check and revise the structural design parameters. The number of high-rise buildings is rapidly growing in China. For these buildings, frame shear wall structures, which require high construction accuracy, are commonly adopted. The aim of construction surveying is the transmission of the axis and elevation of buildings. In traditional construction surveying, laser vertical measuring method is applied in axis surveying and other methods, such as hanging steel rule and total station, are mainly applied for elevation transmission. These methods are relatively mature and easy to apply. However, they suffer from disadvantages such as susceptibility to weather changes and site visibility conditions. Moreover, they are usually time consuming and errors tend to be easily accumulated [1].

The displacement at the top of high-rise building, the top point of long-span bridge tower and the middle span of spatial structure are the key parts for the inspection of large-scale engineering structures. Traditional measurement methods for structural vibration and displacement include displacement sensor method, acceleration sensor method, laser interferometer method and total station method. These methods are often affected by the accuracy and weather conditions and cannot achieve the purpose of long-term structure monitoring. GNSS technology, with its all-weather, automatic, high-precision characteristics, has gradually become a new structure dynamic monitoring method. More importantly, GNSS technology can record the overall deformation of the structure in real time, and the measurement value includes the static displacement component of the structure, such as the structural deformation due to temperature changes, or the structural displacement due to the average wind component, etc., which cannot be done by the widely used acceleration sensors. Figure 1 shows the measuring equipment for GNSS.

At present, the analysis of long-term GNSS test data on structures and the discussion of its feasibility are not sufficient. In this chapter, the working performance of GNSS technology in monitoring dynamic deformation of structures under complex environmental conditions is explored by combining a whole set of long-term dynamic monitoring data of high-rise buildings under construction.

Fig. 1 Measuring instrument

2 GNSS Technology and Its Application in Structure Monitoring

At present, RTKGPS technology is widely used in engineering. RTKGPS full carrier phase real-time dynamic differential technology. A typical RTKGPS system consists of a reference station and a mobile station. The reference station is placed on a relatively stable reference point with known coordinates, and the mobile station is placed on the measured point of the structure. In order to receive stable satellite signals, the height angle around the reference station above 5° should be as far as possible without building occlusion, and there should be no more obstacles above the antenna plane of the mobile station. The base station and the mobile station observe the same satellite synchronously. The reference station transmits its coordinates and observation information to the mobile station through the data link, and the mobile station makes real-time dynamic difference between the data from the reference station and its own observation data, so as to determine the three-dimensional coordinates of the point to be measured. It is important to note that due to the distance between base station and rover that baseline length is very short, so you can think of base station and rover satellite orbit error, receiver differentia and the ionosphere and troposphere delay error brought by the strong correlation and can be eliminated by difference, the premise is the baseline length is not too long, the best control within 10 km, So that RTK GPS has centimeter-level positioning accuracy.

Because RTKGPS technology can reduce most of the systematic errors of GPS measurement, multipath effect has become the most important error source of GPS measurement. The so-called multipath effect means that the receiving antenna may not only receive the satellite signal directly, but also receive the satellite signal reflected by the ground objects around the antenna. The superposition of the two

signals will cause the signal delay of the measurement reference point. Many experts and scholars at home and abroad have conducted in-depth research on multipath effect, summarized the following characteristics of multipath effect, and put forward corresponding countermeasures and elimination measures:

(1) The generation of multipath effect is related to the reflection ability of the surrounding environment. The multipath effect is particularly pronounced in developed urban areas, where smooth glass facade surfaces of high-rise buildings increase signal reflection. In addition, the reflection ability of water surface to GPS signal is the strongest, so in the process of using GPS for bridge dynamic monitoring, the multipath effect is a problem that cannot be ignored.
(2) Repeatability of multipath effect.

    By the hand of a GPS satellite orbit cycle is about 11 h, 58 min, under the condition of the general test, using GPS for consecutive days of observation, the surrounding environment of the multipath effect will not be big change, therefore, at the same point, multipath are 4 min ahead of schedule, the day before that multipath effect has a certain repeatability. The repeatability of multipath effect makes the coordinates between adjacent days have correlation. It is a good method to extract the multipath error in GPS signal by using the strong correlation of multipath effect.
(3) Multipath effect has certain frequency characteristics.

    Due to its own frequency characteristics, the multipath effect has a long period, often reaching tens of seconds or even tens of minutes, which is much higher than the vibration period of the structure. Therefore, in the later data processing process, the multipath effect can be extracted and eliminated by filtering.

Since the 1990s, many large structures have been dynamically monitored by GPS technology. Li Hongnan et al. have made a detailed summary of the application status of GPS technology in structural health monitoring [2]. Celebi et al. conducted field tests on the displacement of a 44-story building in Los Angeles under the environmental vibration of wind load and traffic noise [3]. Breuer et al., Germany, measured the vibration of Stuttgart's 155 m high television tower and 250 m high industrial chimney located in Opole power plant under wind load [4]; Xu Youlin et al. of the Hong Kong Polytechnic University designed a motion simulation table to test the positioning accuracy of GPS in three directions [5]. Li Hongnan et al. designed a GPS-based wind vibration observation system with a super high-rise building as the background and carried out field tests under strong winds [6]. The above research work is mainly based on stage testing, and the long-term monitoring based on GNSS technology, especially under complex environmental conditions, is still less research.

3 Project Overview

The building under long-term monitoring is the relocation housing project of Zhengxinyuan in Fuling District, which is located in the Party School of Jianfulu District, Fuling District, Chongqing. It covers an area of 9338.5 m^2 with total construction area of 46,793.68 m^2. The main construction areas of this project include the main project, auxiliary works, public works and environmental protection works. Specifically, the main project contains two high-rise buildings (i.e., No. 29F/-1F floor of No. 1 Building and No. 28F/-2F floor of No. 2 Building). Auxiliary works are mainly underground garages, equipment houses, and greening. Public works mainly include facilities such as water supply, drainage, and power supply. Environmental protection works include septic tanks and garbage collections. Frame shear wall structure is adopted for the main project, where a certain number of shear walls are arranged. Therefore, it constitutes a flexible and free use space to meet the requirements of different functions of the building. Also, this structure has sufficient shear wall and considerable lateral rigidity.

4 Surveying Methods

4.1 Checking Control Point

Planning department laid three known control points (i.e., GN1, GN2 and GN3) around this project site (Fig. 2) [7]. Three total station instruments (Southern S86s) were simultaneously placed to evaluate the accuracy of GNSS measurements. With static mode alignments, these instruments were placed respectively on GN1, GN2 and GN3 points. 1980 Xi'an coordinate system (3-degree band) was adopted and e Class control network level was applied. Moreover, baseline rejection mode was automatically selected and satellite height angle was set to 15 degrees. Meanwhile, the antenna height of each total station instrument needed to be measured (the height of measured piece of obtained by Southern S86s) [8].

GNSS static positioning accuracy is high and the nominal accuracy of its static measurement can reach $\pm(2.5 + 0.5 \text{ ppm} \times D)$ mm. S86 supports GPS, GLONASS and Beidou systems. For data acquisition, these total station instruments were turned on simultaneously. The observation time of each instrument was not shorter than 45 min, since shorter times could decrease measurement accuracy. Therefore, observation time in this study was about 110 min. All collected data were processed by S86's self-owned solution software. Data processing procedures were as follows: once the consistency of antenna height and measurement method was checked, observation data file was added to data entry. Then, a baseline solution was performed by using the automatic solution module embedded in the software. It was important to note that generally, height cutoff angle and epoch interval have to be set to 15 degrees and 30 s, respectively. Then, baseline condition was set and closed loop

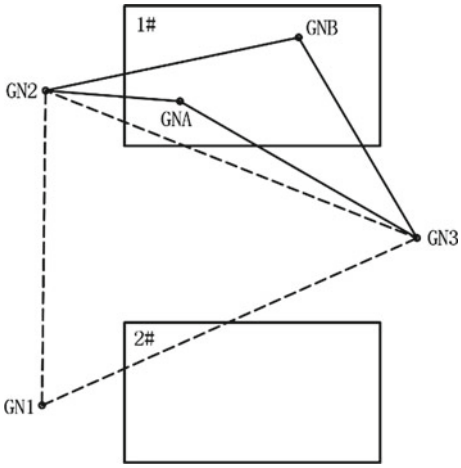

Fig. 2 Plane distribution of control points

Table 1 Resolution of GNSS static observations

Control points	Instruments	Calculated values (m)		Known values (m)		Error (mm)	
		x	y	x	y	Dx	Dy
GN1	2597	3,287,658.0350	521,781.1050	3,287,658.0350	521,781.1050	0	0
GN2	2612	3,287,712.0460	521,781.7230	3,287,712.0460	521,781.7230	0	0
GN3	2584	3,287,686.7334	521,845.6528	3,287,686.7380	521,845.6480	−4.6	+4.8

was checked. Finally, the coordinate of known three points were entered and adjustment was performed. Also, in order to obtain adjustment results, it was necessary to perform automatic processing, three-dimensional adjustment, two-dimensional adjustment, and elevation fitting.

The resolutions of observations are summarized in Table 1.

The error point of GN3 was $f_D = \pm 6.7$ mm, relative error of GN1-GN3 baseline was 1/10600 and relative error of GN2-GN3 baseline was 1/10300.Fig. 3 shows the measured 24-h vibration curve.

4.2 Establishing Horizontal and Elevation Control Networks

Three new elevation control points were laid near the known control points (GN1, GN2 and GN3) and their elevations were measured based on third order leveling by using Southern DL2007 electronic level [9]. Meanwhile, other construction control points (GNA and GNB, shown in Fig. 1) were set on the working surface of building 1#. Together with GN2 and GN3, baseline measurements of these construction control points are collected in static mode and their observation times were all equal to 90 min [10]. According to the above-mentioned method, the coordinates of GNA

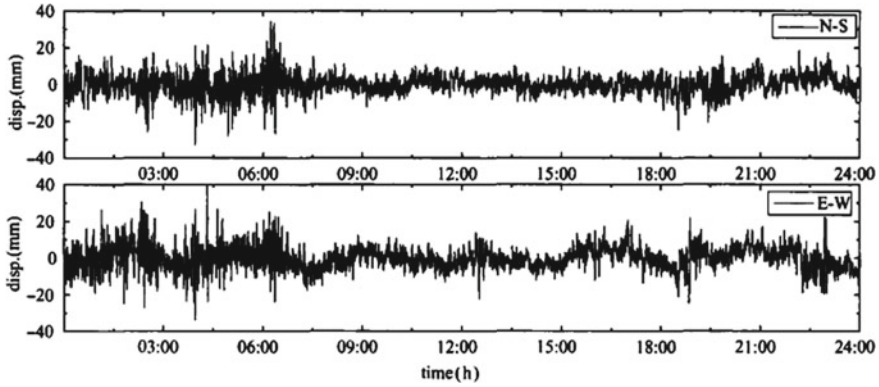

Fig. 3 24 h time history curves in N–S and E–W directions

and GNB were calculated by solution software of S86. According to the axis positions given by control points A and B and design drawings, each axis position was located by southern NTS342 total station [11]. GNA and GNB points were used as control points with known elevation and floor elevation was measured and marked by using Southern DSZ3.

4.3 Determining Control Points for the Construction Floor Based on Traditional Measurement Method

The position of floor axis was transmitted upward by laser vertical gauge. At the same time, leveling instrument and hanging the steel rule were applied to pass the elevation upward. Accuracy and efficiency of traditional methods and GNSS were compared [12].

To be specific, axis at ground floor was passed (building axis at ground floor could directly be laid using total station). Then, some control points at appropriate distances from the axis were set. At the same position on each floor, a hole with dimensions 200 mm × 200 mm was drilled. Then, ML-401 laser vertical gauges were placed at control points on ground level. At the drilled holes on each floor, a cross-shaped target was placed and the position of upward laser on this target was marked. Then, laser vertical gauge was clockwise rotated 90 degrees and the new position on the target was marked again. This procedure was repeated until four points were marked on the target. Then, the intersection point of these four points was determined and considered as axis transmission point. Three axis transfer points were needed in one building at least. Accordingly, the axis position of this building could be set with total station [13].

On the other hand, elevation could be transmitted by hanging steel ruler at a high place (suspended steel ruler). Two leveling instruments were placed on ground floor

Table 2 Comparative analysis of axis point coordinates

Points	GNSS measurements (m)		Traditional measurements (m)		Errors (mm)	
	x	Y	x	Y	Dx	Dy
G2	3,287,706.876	521,798.912	3,287,706.874	521,798.913	+2	−1
M3	3,287,713.376	521,799.012	3,287,713.379	521,799.010	−3	+2
R15	3,287,720.476	521,819.062	3,287,720.472	521,819.065	+4	−3
S17	3,287,722.276	521,822.262	3,287,722.276	521,822.258	0	+4

and construction working floor. Based on readings of level rod and steel ruler on ground floor, elevation on the working floor of construction was calculated. If the floor was high, the same procedure needed to be repeated twice.

Coordinate errors of G2, M3, R15 and S17 at four axes intersection on the 12th floor of Building 1# are summarized in Table 2.

5 Conclusions

In construction surveying of high-rise buildings with frame shear wall structures, GNSS has similar accuracy to traditional methods. Both methods meet design requirements. However, traditional methods were affected by the environment, especially surrounding buildings and inclement weather. On the contrary, errors by using GNSS were not easy to accumulate. Additionally, several holes did not need to be reserved on each floor in GNSS method. With better efficiency, GNSS method required shorter time than traditional methods. Meanwhile, it did not require visibility and could be performed at night and it was not affected by weather conditions. However, the number of devices used in GNSS was high, which meant that equipment investment of GNSS method was higher. In all, GNSS method was simpler and more intelligent. The preliminary exploration of GNSS technology in monitoring structural deformation with time in complex environmental conditions verifies that GNSS has advantages in measuring the static displacement components of structures. However, multipath effect is the main source of error affecting GNSS positioning accuracy. How to identify, extract and reduce the effect of multipath effect is still an important aspect of future research.

References

1. Zhou JW (2017) The application thinking on construction survey of building engineering. Shanxi Archit. 25:199–200
2. Hongnan L, Ting-hua Y, Guo-xin W (2004) Research and application of GPS in structural health monitoring. J Nat Disasters 13(6):122–130

3. Celebi M (2000) GPS in dynamic monitoring of long-period structures. Soil Dyn Earthq Eng 20:477–483
4. Breuera P, Chmielewski T, Gorski P, Konopka E (2002) Application of GPS technology to measurements of displacements of high-rise structures due to weak winds. J Wind Eng Ind Aerodyn 90:223–230
5. Chan WS, Xu YL, Ding XL, Xiong YL, Dai WJ. Dynamic displacement measurement accuracy of GPS for monitoring large civil engineering structures, 2005, Proceedings, SPIE international symposium on smart structures and nondestructive evaluation, CD-ROM, SPIE, Bellingham, Wash
6. Hongnan L, Ting-hua Y, Xiao-dong Y, Guo-xin W (2007) Wind vibration observation of super high-rise structures based on RTKGPS technology. Eng Mech 24(8):121–126
7. Wang ZP (2018) Application of super high-rise building control survey technology in Zhuhai central project. Constr Technol 3:109–113
8. Zhang J (2016) Practice research on GPS measurement technology used in high-rise building construction. Urbanism Archit 17:148
9. Wang Y, Lin CY, Guo JM, Yin CF, Zhang D (2017) Point monitoring analysis of super high rise building based on BDS+GPS technology. Bull Surveying Mapp (6):5–8
10. Zhang X, Wang ZP, Luo B et al (2017) Application of reference line surveying method in setting-out survey of large construction project. Constr Technol 6:136–138
11. Liu CH, Chen H, Zheng J (2016) Discussion on measurement lofting technology of high-rise building construction. Shanxi Archit 5:224–225
12. Zhang JL (2015) On control measures of construction survey for high-rise building. Anhui Archit 3:219–220
13. Ji ML (2015) Quality control of construction survey of high-rise building. Heilongjiang Sci Technol Inf 12:205–205

Urban Planning and Space Design

Inclusive (Healthy and Eco-City) City Planning Prepares for Future Urban Challenges in a Post-pandemic Asian Society

Reazul Ahsan

Abstract The COVID-19 pandemic reshaped the global economy, but it also reshaped urban life. This pandemic pushed a new global standard for urban planning practice incorporating current and future urban planning. It is unambiguous that the current pandemic will significantly impact urban life through healthier eco-city planning, colloquially referred to as "inclusive planning." In light of the post-pandemic situation, future cities must strive to be more inclusive, with eco-friendly development practices and a design that prioritises ecosystem services to coexist with nature. While urban areas in Asian countries have survived numerous disasters in the past, they have not fared when preparing for new ones. This study aims to forecast the future direction of urban planning, revise current practices to prepare for future pandemics and ensure inclusive urban planning practices for healthy and eco-city living. Songdo is a relatively new, well-designed, and rapidly growing city in South Korea. Songdo would be a better case study for a post-pandemic township to analyse urban community problems, specifically the balance between stable and eco-city. This study evaluates Songdo city planning using secondary examples of other new planned eco-cities to determine the gap between being an inclusive city and meeting future challenges induced by the pandemic. The findings of this study were collected, analysed, and represented using desktop research methods. Secondary data sources are used in this method to calculate the existing urban green spaces. The potential sites for redevelopment as urban parks and green spaces for healthy living are then identified using geoinformatics techniques. According to this study, Songdo's current urban green space is significantly less than the global per-person urban space standard. GIS mapping is being used to identify potential urban spaces to promote urban greenspace for healthy living in Songdo. This study examines inclusive city planning practices in a post-pandemic city to meet future needs. Cities today are more concerned with eco-city concepts as a means of adapting to climate change.

R. Ahsan (✉)
Department of City and Metropolitan Planning, University of Utah (Asia Campus), Incheon, South Korea
e-mail: reazul.ahsan@utah.edu

T. Kang (ed.), *Proceedings of 5th International Conference on Civil Engineering and Architecture*, Lecture Notes in Civil Engineering 369,
https://doi.org/10.1007/978-981-99-4049-3_42

COVID-19 provides contemporary thought on eco-city planning, where the environment and climate change should not be the primary focus; public health should be a priority to guide us in a new direction for post-pandemic urban planning.

Keywords Inclusive city · Post-pandemic city · Urban green space · Urban health and Urban challenges

1 Introduction

Global urbanisation processes are creating inequalities, making it more difficult to access resources, and making it more difficult to maintaining human health and well-being in urban areas. As cities become more populous, their energy consumption rises, and their economic activities become more concentrated in urban areas, their significance as economic growth engines cannot be denied. However, many urban areas have social exclusion and limited access to city services and resources. Cities are shaping the future of our planet. There, individuals confront environmental concerns and tackle the obstacles of sustainable development. Modern cities and human settlements must be inclusive, safe, resilient, and sustainable, according to the 11th goal of the Sustainable Development Goalc [1].

Global environmental change and urbanization are major issues on the international political agenda, intending to make cities more livable, ensure equity and justice, and adapt to climate change [2]. Today, urban areas house 54% of the world's population, and more than two-thirds of the world's population is expected to urbanize by 2050 [3]. Preparing urban spaces for an increasing number of people while developing and maintaining cities as sustainable and liveable places is thus one of the major challenges for future urban planning. It is critical to recognize their value when green spaces are increasingly threatened, such as by ongoing urban land conversion for housing and transportation [4].

Cities are shaping our planet's future. There, individuals confront environmental issues and address the challenges of sustainable development. Various city planners and policymakers have proposed and adopted the Smart City (SC) concept to enable efficient transportation systems, sustainable mixed land uses, and high-quality urban services to improve citizens' quality of life [5]. In many instances, SC initiatives failed to address the needs of marginalized groups, such as the elderly, and individuals with disabilities. Even migrants and impoverished communities. For example, New York City installed Samrt City kiosks that were not fully accessible to people with disabilities [6]. Such social or community deprivation heightens the importance of inclusion in SC's efforts to achieve sustainability. Otherwise, disregarding groups such as frail older adults, wheelchair users, and blind or visually impaired individuals could result in unanticipated social and digital exclusion. In addition, COVID-19 makes it clear that urban planning process, health sector, and land-use approaches must be incorporated into SC initiatives to achieve sustainability.

Since at least two decades ago, the concept of the inclusive city has been the subject of extensive academic discourse. Similarly, the United Nations (UN), as outlined in the Sustainable Development Goals (SDG), particularly SDG 11, and the New Urban Agenda (NUA), has prioritised inclusive urban development. Prior to the COVID-19 outbreak, according to the most recent SDG report (2020), sustainable urban development efforts were unequal and slow [7]. Since the COVID-19 pandemic, urban development has thus suffered a significant setback. This crisis reveals the importance of urban green and open space specifically in the hidden only urban areas, to ensure social distance and individuality.

Cities emerged as the epicentres of the COVID-19 pandemic, with approximately 90% of all COVID-19 infections occurring in urban areas. And poor urban neighbourhoods were particularly affected. The vulnerability of cities during the COVID-19 pandemic has highlighted the need to build a healthy, sustainable cities with inclusiveness. Research has identified in highly walkable neighborhoods, COVID-19 spreads at a much slower rate. Residents can travel shorter distances on wider and better-maintained sidewalks, reducing their exposure to the COVID-19 virus.

Similarly, green space mitigates the spread of COVID-19 in low-income neighborhoods, but not in high-income ones. It is probable that housing units in low-income communities are smaller, more crowded, less well-maintained, and have inadequate ventilation. Thus, residents of low-income neighborhoods may find it more challenging to adhere to stay-at-home policies. Large green spaces in such neighbourhoods may provide a safe space for residents to breathe clean air and practice social distancing in a secure environment [8]. Therefore, in an inclusive city approach, it is more important to concern about mixed-income housing instead of low-income housing with open green spaces.

The COVID-19 pandemic has highlighted the need to construct sustainable cities that promote health and reduce their residents' susceptibility to infectious diseases. Future urban planning initiatives should not adopt a one-size-fits-all strategy. Instead, the rebuilding process should be tailored to meet the varied needs of residents of low- and high-income neighborhoods. The COVID-19 pandemic provides the opportunity to reevaluate the significance of inclusive city development, so that cities can flourish for all individuals due to the persistent disruptions that occur in urban areas [9].

Specifically, rebuilding efforts should prioritize low-income neighborhoods, address their high population density, construct more green spaces, and enhance walkability. Nonetheless, this chapter examines the significance of green spaces in inclusive city planning for Songdo, one of the Samrt Cities in South Korea in the aftermath of COVID-19 pandemic. The South Korean government intended to build five smart cities in three provinces: Daegu, Daejeon, and Seoul. Seoul Metropolitan Government has planned three smart cities within the province these three cities are: Songdo, Chungnam, and Gangnam. Songdo is one of the proposed smart cities that has been completed and is operational since 2014. And Songdo is now a fully developed growing smart city with 90,000 residents and is expanding. Due to its location and international business connections, Songdo has become an iconic smart city.

Furthermore, Songdo drew much attention to COVID-19 for its compact urban design and high-density living. This encourages the urban researcher to reconsider

inclusive city planning as part of smart city planning. Therefore, Songdo is considered as a case for this study to assess inclusive city planning to meet future urban challenges.

2 Songdo Planning, Design and Challenges

Songdo's construction began in 2004. Songdo was built on an unprecedented global scale with a $25 billion master plan. Even though it is primarily a private initiative. On the other hand, Songdo is a Korean national project and a one-of-a-kind international collaboration. The government established Songdo to improve the environment by providing more green spaces for urban residents in order to create renewable cities. And, as one of the smart cities, Songdo is currently developing into a sustainable city, with many conditions at stake. Songdo is both a Korean national project and a one-of-a-kind international collaboration. The government established Songdo to improve the environment by providing more green spaces for urban residents to create renewable cities. And, as one of the smart cities, Songdo is currently developing into a sustainable city, with many conditions at stake [10].

Songdo must be more effective, data-driven decision-making, enhanced citizen and government engagement, safer communities, reduced environmental footprint, improved transportation, increased digital equity, new economic development opportunities, and efficient public utilities in order to become a smart city.

Both top-down and bottom-up approaches to urban design have advantages and disadvantages. It is impossible to deny that government-led top-down decision-making is critical in Korea's urban growth and rapid urban development. The Korean government is also still leaning in this direction. However, in terms of emerging smart and green cities, the top-down approach has proven in some ways insufficient.

The case of Songdo demonstrates the importance of citizen involvement in the process of designing or changing cities. Songdo was designed entirely from the top down. The smart and green initiatives reflected precisely what the government desired and intended. However, they do not correspond to residents' perceptions of a green inclusive city. Songdo clearly has some green functions that its residents value, but there is a disconnect between the government's goals and the residents' desires. Songdo could be transformed into a truly smart and green city, showcasing the future of Korean cities, if its well-designed infrastructure and resources accurately responded to the voices of its residents [11] (Fig. 1).

During the COVIS-19 pandemic, it was clear that the community green space designed for Songdo based on the top-down urban design principle was insufficient to ensure healthy community living and maintain a healthy lifestyle. Songdo is envisioned as one of South Korea's smart and green cities. These challenges are caused by a lack of public participation in planning, rapid urbanisation, and economic growth. This indicates that Songod is not designed as an inclusive city, particularly in urban green space.

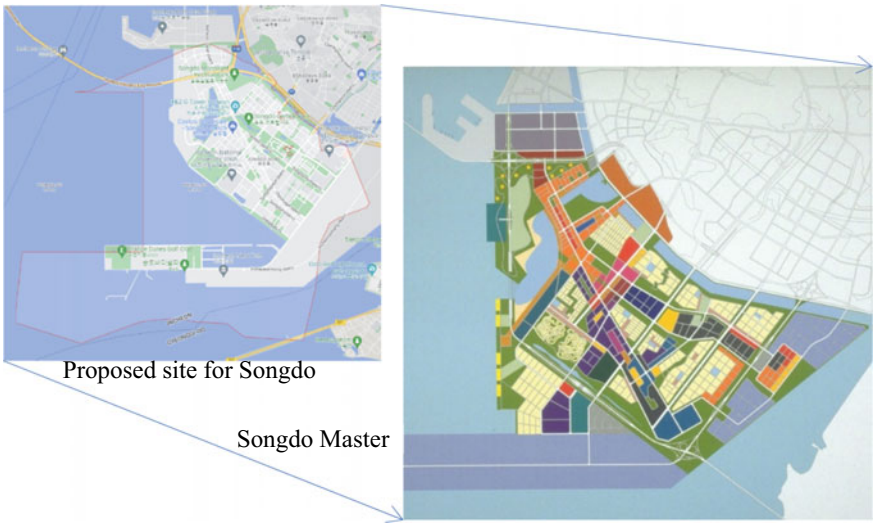

Fig. 1 The proposed site for Songdo smart city and the proposed master plan with urban parks and green spaces [10]

Understanding the challenge of a healthy eco-city planning and how it could be achieved in a post-pandemic scenario to design a healthy, inclusive city with an emphasis on urban green and community space is the primary objective of this study.

Songdo city is a case study because the city was designed with more urban green space for the local community, but it was still insufficient. Therefore, the city will explain the gap and what can be done to promote a healthy lifestyle in the community.

3 Research Design/Method

The majority of this quantitative research is based on secondary data. As a result, the quantitative secondary data for this study was gathered using a desktop research approach. Secondary data gathered from the South Korean Ministry of Land, Infrastructure, and Transport. Secondary urban land-use data are used to compare the amount of green space per person in m^2 in major Korean cities to the global standard.

Secondary data are analyzed and graphically represent the amount of green space per capita in four major South Korean cities: Seoul, Busan, Daegu, and Inchon. This study measured changes in overall urban green space in South Korea and compared urban green space to understand better the importance of urban green space for healthy living.

Later in the study, geographic information system (GIS) was used as part of desktop research to analyze existing urban green space in Songdo and potential urban spaces to improve and increase green space in Songdo. GIS is being used to

assess the amount of urban green space available in Songdo per person and how it could be increased to ensure a global standard and healthy living.

Simultaneously, a geographic information system is used to analyse the current urban green space in Songdo and proposed green space design to ensure healthy living in an inclusive eco-city.

4 Analysis and Description

South Korea is one of the most urbanized and tenth largest economies in the world, respectively. The average rate of urbanization in Korea is 81% (Economic & Social Affairs, Population Division, 1999), which makes Korean cities extremely dense and threatens the availability of urban green space for healthy living. The following diagram presents how per person urban park space decrease in South Korea (Fig. 2).

South Korea's major cities also have insufficient urban park space relative to urban built-up areas. Urban density promotes low-income urban housing in every city in South Korea, which increases urban built-up area and compromises urban green space, negatively impacting urban living during the COVID-19 pandemic and acting as a catalyst for the Coronavirus spread. How these cities must be restructured in a post-pandemic society for inclusive, healthy living is currently a challenge. The following diagram shows the ratio (in percentage) of urban built-up area and urban green space in four major cities in South Korea (Fig. 3).

The above figure indicates high urbanization in major cities. It also indicates that compared to urban built-up areas, the ratio of urban green space is really low and mostly for the upper or high-income group. The medium- and low-income group has limited access [5].

Songdo's total urban built-up area and per capita urban green space are both alarming when compared. The total amount of urban park space and the total amount of urban open space in Songdo can be calculated using the area measurement tool from Navermap (https://m.map.naver.com/) to assess the amount of urban open space per person in the smart city for healthy and inclusive living (Fig. 4).

As per the area measurement, the different urban spaces in Songdo are as follows:

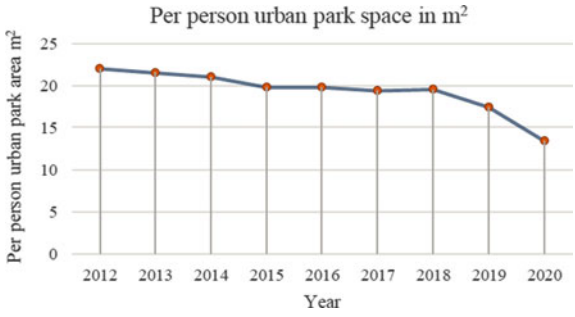

Fig. 2 Per person, urban park space (m^2) decreases over the year in South Korea [12]

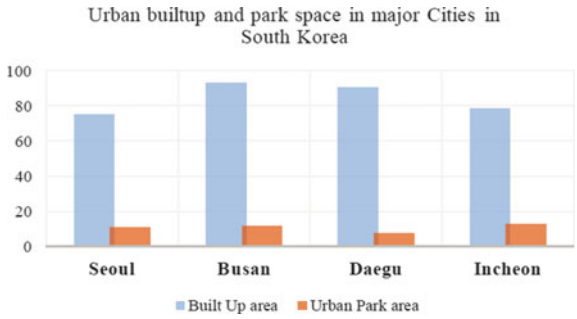

Fig. 3 A ratio of urban built-up area and urban park space in South Korean major cities [13]

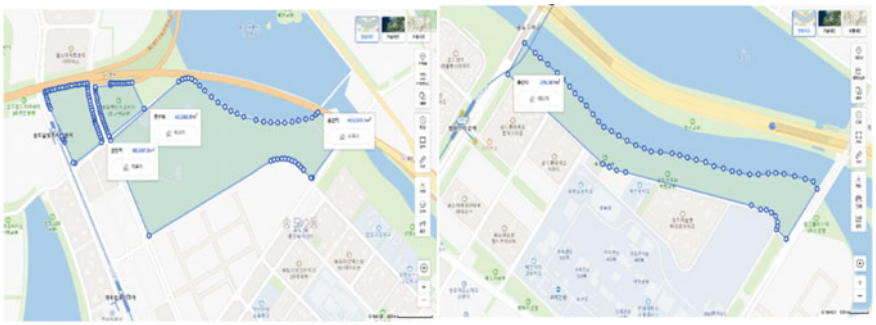

Fig. 4 The Navermap area measurement tool calculates Songdo's urban parks and open space

(i) Total urban park space in Songdo = 1,065,177.3 m^2 (A)
(ii) Total urban open space (not park) = 1,316,828.2 m^2 (B)

Songdo is a rapidly expanding city due to its open layout, economic opportunities, and globalisation. In addition, Songdo's locational advantages make it more appealing for the wealthy to relocate there from the capital and other major cities. Locational advantages and a new urban design make Songdo somewhat inaccessible to middle- and low-income residents.

As of the 2022 public census total population in Songdo is 192,481 (C), and the number keeps on growing.

While calculating per-person green or park space in Songdo.

Green space per person (GP_s) = A/C (A = Total urban park space, C = Total Population)

$$G_s = 1065177.3/192481$$
$$= 5.534\ m^2$$

While the global standard for healthy inclusive living in a compact modern city is 9 m^2 urban green space per person, Songdo has only 5.5m^2 of urban green space

Fig. 5 Comparison between global cities in per person urban green space

per person [14]. As a result, Songdo lags far behind the global standard in ensuring enough open and green space for the residents, which is a disadvantage for a smart city.

The following diagram (Fig. 5) compares urban green/park space per person in major cities worldwide. Per person, green space is very low in Songdo compared to other cities, even the global standard.

Cities are currently dealing with several environmental issues that impact the health and way of life of millions of people around the world. There has been a loss of urban green space (UGS), as well as biodiversity, in Asian cities, as a result of urbanisation and densification, which has resulted in a widening gap between rich and poor, as well as the spread of diseases like COVID-19 [14]. Rather than relying on cutting-edge technology to make a city smart, it is more important to be environmentally and ecologically aware to ensure that the city's diverse population has a healthy quality of life. In a post-pandemic scenario, a key issue for Songdo is how to make it more ecologically smart by increasing urban green space per person to create an inclusive, healthy city for everyone.

5 Designing Songdo a Healthy Eco-City

Urban parks and green spaces have been preplanned for the city of Songdo is a top-down planning approach. Only 1.5 km^2 of the city's 15 km^2 total land is designated as urban parkland, meaning the city uses 10% of urban land for urban parks and green space for the residents. The following diagram shows the planned urban green space for Songdo (Fig. 6).

For this study, CAD maps and GIS tools were used to examine all of the city's parks and other open spaces. This study defines the distinction between urban green space, such as parks, and urban open space differently. Those areas that are used by the local community on a daily basis are known as urban green spaces or parks. Urban open spaces, on the other hand, are unused plots of land within a city that have no other purpose than to sit vacantly. Those areas are off-limits to the general public. Urban open spaces without defined functions, such as areas on the roadside and pockets of land near commercial sites, are referred to as urban open spaces.

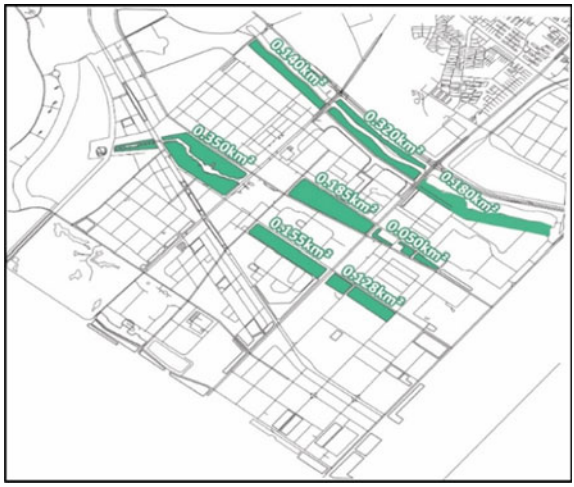

Fig. 6 Planned urban green space in Songdo

This study proposed transforming urban open space in Songdo, South Korea, into urban green ecological corridors and connecting these sites. As a result of this transformation, it is possible to create more urban green space, and the city becomes more inclusive and accessible to all of its residents. The following layer diagram shows the proposed idea of transforming urban open space into urban green space in Songdo.

The proposed design adds the existing urban green/ park space with urban open space that will increase per person urban green space.

$$G_s = \{A + B/C\}$$

where the

A = 1,065,177.3 m^2 Green spaces
B = 1,316,828.2 m^2 Open spaces
C = 192, 481 Population

$$\begin{aligned} G_s &= \{A + B/C\} \\ &= 2, 382, 005.5/192481 \\ &= 12.4\ m^2 \end{aligned}$$

The proposed post-pandemic urban design will increase green space per person from 5.5 to 12.4 m^2, which is more than the global standard to ensure healthy living and inclusiveness in Songdo (Fig. 7).

The principle of smart and compact cities is a high-density, mixed-use pattern that allows for parks and green spaces for healthy living. This practice is thought to limit urban sprawl by increasing activity in densely populated areas, reducing

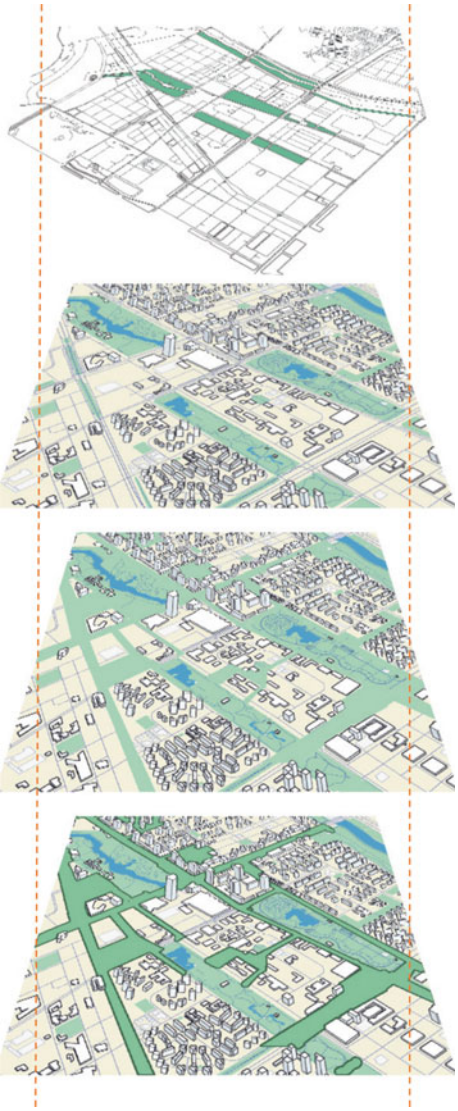

Fig. 7 Transforming urban open space to urban green space in Songdo creates an inclusive and eco-city

personal vehicle trips, and providing diverse services through mixed land use (i.e., discouraging infill development) [15].

Densification has been shown to be largely unhealthy within these urban neighbourhoods, affecting mostly local residents; the permanence of urban built structures means that future residents' health will most likely be affected by conditions resulting from today's urban planning, which is not limited to the short term [16]. To effectively provide ecosystem services in a post-pandemic society, sufficient and high-quality urban green space and/or other greenery elements should be readily available to

urban residents. Improving public health through urban development and greenery renewal in compact cities is an important component of the concept of sustainable development [15, 16].

Every aspect of urban greening can be meticulously examined in order to ensure that cities are both compact and environmentally friendly [17]. A basic human need is to be in touch with nature on a regular basis, and urban green spaces can fulfil this requirement. The question of how much greenery a person needs is especially relevant for urban dwellers because urban green spaces is often the only source of nature-based interaction readily available within any reasonable distance. People who live in cities are happier and healthier if the World Health Organization (WHO)-determined minimums are exceeded [18].

6 Conclusion

The goal of today's compact and dense cities is to incorporate a mixed land use while also increasing the amount of green space available to residents. By incorporating cutting-edge technology, we can improve the quality of life in our cities and make them smarter and more useful. The COVID-19 pandemic, on the other hand, not only affects global health and economics, but also urban planning. Most of all for Asian cities are notorious for rapid urbanization and a consequent lack of green space. High densification facilitated the spread of viral infection at the same time. A post-pandemic scenario necessitates cities being more inclusive and healthy eco-cities to improve their residents' quality of life.

Songdo is one of the smart and compact cities in South Korea, where 10% of the urban land (15 km^2) is preserved as urban green space to promote a healthy and inclusive lifestyle. After COVID-19, it is evident that this green space is insufficient to meet the local community's needs and ensure a healthy lifestyle. Moreover, Songdo urban green space is not designed inclusively from a social perspective. This study examines Songdo's available urban green space and urban open space. Additionally, describe the distinctions between urban green space and urban open space in Songdo. Creating an urban eco-corridor by converting available urban open space into urban green space will increase per capita urban green space in Songdo and promote a healthy lifestyle for all Songdo residents. The same urban planning practises will make Songdo a futuristic smart city both technologically and ecologically.

References

1. Hsu A, Samuel K (2018) How cities are failing to be inclusive—and what they can do about it. Available from: https://www.weforum.org/agenda/2018/12/how-global-cities-are-failing-to-be-inclusive/

2. Ahsan R (2019) Climate change and uncharted social challenge in existing urban setup in Bangladesh. In: Hussain S (ed) Climate change and agriculture. Intechopen, London, pp 169–182
3. Economic UNDO, Social Affairs (1999) Population division, world population prospects: the 1998 revision, vol 180. United Nations Publications
4. Haase D et al (2017) Greening cities—to be socially inclusive? About the alleged paradox of society and ecology in cities. Habitat Int 64:41–48
5. Wang C et al (2021) Is your smart city inclusive? Evaluating proposals from the U.S. Department of transportation's smart city challenge. Sustain Cities Soc 74:103148
6. Woyke E (2019) Smart cities could be lousy to live in if you have a disability. [cited 2nd July 2022]; Available from: https://www.technologyreview.com/2019/01/09/137899/smart-cities-coule-be-lousy-if-you-have-a-disability/
7. Leal Filho W et al (2020) COVID-19 and the UN sustainable development goals: threat to solidarity or an opportunity? Sustainability 12(13)
8. Choi K, Denice P (2022) Inclusion, walkability will be key to rebuilding cities after the COVID-19 pandemic. Available from: https://theconversation.com/inclusion-walkability-will-be-key-to-rebuilding-cities-after-the-covid-19-pandemic-174313
9. Raissa G et al (2021) Rethinking inclusive city development amid COVID-19: the Indonesia context. J Reg City Plann 32(1):71–82
10. Lee SK et al (2016) International case studies of smart cities Songdo, Republic of Korea, Inter-American Development Bank, Seoul pp 1–44
11. Jae-in N, Manning M, Tao JL (2020) What makes a city smart and green in South Korea? Heinrich-Böll-Stiftung, Hong Kong
12. Country Indicator of South Korea (2020) City parks, green spaces, amusement parks. Available from: https://www.index.go.kr/potal/main/EachDtlPageDetail.do?idx_cd=1205
13. Green Division (2021) City parks, green spaces and amusement parks. 2021–09–30. Available from: https://www.index.go.kr/potal/main/EachDtlPageDetail.do?idx_cd=1205
14. Russo A, Cirella GT (2018) Modern compact cities: how much greenery do we need? Environ Res Public Health 15(10)
15. Lin J-J, Yang A-T (2006) Does the compact-city paradigm foster sustainability? an empirical study in Taiwan. Environ Plann B Plann Des 33(3):365–380
16. Næss P (2014) Urban form, sustainability and health: the case of greater Oslo. Eur Plan Stud 22(7):1524–1543
17. Jim CY (2013) Sustainable urban greening strategies for compact cities in developing and developed economies. Urban Ecosyst 16(4):741–761
18. WHO (2012) Health indicators of sustainable cities in the context of the Rio+20 UN conference on sustainable development. Geneva Switzerland, World Health Organization

A Spatial Interpretation on Shopping Center in Urban China

Ting Zhang, Fangqian He, Jienan Ye, and Ying Liu

Abstract Shopping and leisure activities play an important role in contemporary Chinese cities. As a physical space carrier for both activities, shopping center have become an indispensable part of the urban landscape. Over the past few decades, the spatial structure of shopping centers has continued to change in order to meet the consumer demands. Developers and designers have expanded the structure, introducing a variety of services and entertainment, such as cinemas, food, indoor playgrounds, as well as office and residential developments. The aim of these changes is to make this type of areas become an attractive community centers, especially in the suburbs or new towns. Focusing on typology and mode perspective, this chapter examines the main morphological characteristics of shopping centers in contemporary urban China.

Keywords Shopping center · Urban China · Spatial organization · Morphological characteristics

1 Introduction

Retail is an important area of study because of its impact on the economy, its role in distribution, and its relationship to the sale of goods and services to retailers [1]. The shopping center industry, as an important part of the retail industry, it represents a significant portion of the overall retail industry. In Gruen's urbanism, the shopping center has an important role in urban development as a tool for redefining

T. Zhang (✉) · F. He · Y. Liu
Wuxi Taihu University, Wuxi 214064, China
e-mail: zhangt_wxu_edu@163.com

J. Ye
School of Art and Design, Nanjing Forestry University, Nanjing 210037, China

T. Zhang
Polytechnic University of Turin, 10125 Turin, Italy

T. Kang (ed.), *Proceedings of 5th International Conference on Civil Engineering and Architecture*, Lecture Notes in Civil Engineering 369,
https://doi.org/10.1007/978-981-99-4049-3_43

the contemporary city. Some scholars argue that the first shopping center, opened in Detroit in 1954, was a utopian public space designed to bring people together [2], it was a new city [3].

Shopping center is a commercial building space that is surrounded by a complete infrastructure. This hybrid spatial composition is an important factor in attracting customers and enhancing community appeal. Since it is a service-oriented retail activity, it emphasizes a service system to ensure customer satisfaction [4].

In China, shopping center is also a real estate industry that typically combines retail, service, food, beverage, entertainment and leisure complexes, to provide consumers with a wide range of consumer services. The growing maturity and steady prosperity of shopping centers in China has led to their firm dominance in the cities and centers where they are located. As of the end of March 2021, it was reported that there are 7013 shopping centers in 100 cities. (in the CENTER Eagle Eye database).

Previous studies on shopping centers mostly focused on urban economic, customer satisfaction, retail system, project construction etc. [5–8] less research focused on the morphological characteristics of shopping centers in contemporary China. Therefore, this study seeks to examine morphological characteristics of shopping center through multi and descriptive-analytical studies.

2 Literature Reviews

2.1 Concepts of Shopping Center

In previous studies, many scholars have defined the concept of shopping center from various perspectives. Dawson and Lord (1985) define shopping center "*as a group of establishments which is designed, planned, developed, owned, marketed and managed as a unit*." [9] Unlike shopping center, shopping area is a concentration of stores and other commercial establishments. Each establishment has separate ownership and location. That is, one or more shopping centers may be located in one shopping area, or one shopping center may exist independently. They proposed that this distinction is critical because shopping centers are centrally managed and controlled, whereas free competition exists in shopping areas.

According to the International Council of Shopping Centers [10], the shopping center is: "*a group of retail and other commercial establishments that is planned, developed, owned and managed as a single property, with on-site parking provided. The center's size and orientation are generally determined by the market characteristics of the trade area served by the center. The three main physical configurations of shopping centers are centers, open-air centers, and hybrid centers.*"

As the industry and concepts continue to evolve, the definition of shopping center is constantly being updated.

2.2 Types of Shopping Center

According to industry practice, the accepted classification defined by the International Council of Shopping Centers (ICSC 2004) is the most commonly used (Fig. 1). According to the definition, based on their architecture type and design model, shopping centers are divided into two main categories: centers and open-air centers, each category is further divided into sub-categories. First, Centers or Shopping Centers refers to an enclosed shopping centers with controlled air-conditioned and lighted shopping streets and alleys. This type includes neighborhood centers and community centers. Second, the Open-Air Center, which is described as a strip center. It is a row of attached stores or service outlets managed as a coherent retail entity, with an on-site parking lot usually located in front of the store. The strip centers can be configured in a straight line or form an "L" or "U" shape. They can be classified as: regional centers, super-regional centers, fashion/exclusive centers, strength centers, theme/festival centers, and outlet centers.

Another classification is closer to contemporary shopping center, which is proposed by Levy and Weitz's [11]. Nine types are classified based on their physical space and typical anchors: *Neighborhood/community center*; *Power center*; *Shopping mall; Lifestyle center; Fashion/specialty center; Outlet center; Theme/festival center; Omnicenter; Mixed use development* (Table 1).

** The share of the anchor tenants of the Gross Leasable Area (GLA).*

The area that generates 60–80% of the center's sales.

It can be said that there is no unitary method to classify shopping center's definition and typology, and most of the current researches are mainly about geographical location, architecture, shopping type or tenant, retailer type decides in which group a shopping center will be included.

				TYPICAL ANCHOR(S)			
TYPE	CONCEPT	SQ. FT. (Inc. Anchors)	ACREAGE	NUMBER	TYPE	ANCHOR RATIO*	PRIMARY TRADE AREA**
NEIGHBORHOOD CENTER	Convenience	30,000 - 150,000	3 - 15	1 or more	Supermarket	30 - 50%	3 miles
COMMUNITY CENTER	General Merchandise; Convenience	100,000 - 350,000	10 - 40	2 or more	Discount dept. store; super-market; drug; home improvement; large specialty/discount apparel	40 - 60%	3 - 6 miles
REGIONAL CENTER	General Merchandise; Fashion (Mall, typically enclosed)	400,000 - 800,000	40 - 100	2 or more	Full-line dept. store; jr. dept. store; mass merchant; disc. dept. store; fashion apparel	50 - 70%	5 - 15 miles
SUPERREGIONAL CENTER	Similar to Regional Center but has more variety and assortment	800,000+	60 - 120	3 or more	Full-line dept. store; jr. dept. store; mass merchant; fashion apparel	50 - 70%	5 - 25 miles
FASHION/SPECIALTY CENTER	Higher end, fashion oriented	80,000 - 250,000	5 - 25	N/A	Fashion	N/A	5 - 15 miles
POWER CENTER	Category-dominant anchors; few small tenants	250,000 - 600,000	25 - 80	3 or more	Category killer; home improvement; disc. dept. store; warehouse club; off-price	75 - 90%	5 - 10 miles
THEME/FESTIVAL CENTER	Leisure; tourist-oriented; retail and service	80,000 - 250,000	5 - 20	N/A	Restaurants; entertainment	N/A	N/A
OUTLET CENTER	Manufacturers' outlet stores	50,000 - 400,000	10 - 50	N/A	Manufacturers' outlet stores	N/A	25 - 75 miles

Fig. 1 Classification of shopping centers. *Source* ICSC 2004

Table 1 The main types and characteristics of shopping center

Type	Main characteristics-physical space, typical anchor(s)
Neighborhood/ community center	Strip shopping centers Supermarkets or discount food stores Daily shopping trips
Power center	Big-box retailers Located in a closed shopping center Bigger discount stores, off-price retailers
Shopping mall	Closed building with controlled temperature and lights
Lifestyle center	Usually have a well-maintained open-air common square and main street character Denote the aggregation of various specialized stores (mostly fashion apparel), entertainment facilities and restaurants
Fashion/specialty center	Denotes shopping centers in which mostly higher-priced fashion apparel stores, boutiques and gift stores are incorporated, where higher prices mean better quality and brand value
Outlet center	Mostly manufacturers' brand stores and retail outlets, from product assortment point of view they mostly offer fashion apparel with strong brand value, accessories and home furnishings
Theme/festival center	These centers are defined by a certain theme, and the building design and stores are chosen accordingly. It has a tourist attraction character, often a kind of entertainment center is its main anchor tenant, in other cases it attempts to copy a historical place or event
Omnicenter	A new type of shopping center and often combines several of the already described types, for instance, shopping center, lifestyle center or power center. Due to their various characters, provide opportunity for cross-shopping in a single place
Mixed use development (MXD)	Operate within a multi-function building complex. Thus, besides a shopping center, there could be an office building, hotel or perhaps a residential building, cultural center etc. In contemporary cities, retailers prefer this category because it is more attractive than a simple shopping center

By Levy and Weitz's [11]

2.3 Shopping Center in China

In China, according the《Classification of retail formats》GB/T 18106–2004, by ministry of commerce of the people's republic of China. The definition of shopping center is: A variety of retail stores and services in single building or one area, which is developed, managed and operated by a company. It can provide comprehensive services to consumers. The main types are classified into three categories (Table 2).

Differ from the urban business area, the commercial area in the city is developed from the ancient market and retail area. According to the《Principles of Urban Planning》(Third Edition), the modern urban business area is based on commercial retailing and its accompanying catering, accommodation, cultural and entertainment

Table 2 The main types of shopping center

Type	Location	Area (square)
Community shopping center	Regional business center	Less than 50,000 m^2
Urban shopping center	Commercial center of city	Within 100,000 m^2
Super-regional shopping center	Suburb of city	More than 100,000 m^2

services. There are also financial, trade and management industries. It can be seen that the retail industry is the main body of the urban commercial area. The prosperity of the retail industry is also the index that directly reflects the development of the urban commercial area. The healthy development of the retail industry is also a prerequisite for the development of other related industries in the commercial area.

In general, current literature or official documents address the definition and types of shopping centers from various perspectives, few studies focus on spatial organization. Therefore, this study constructs an analysis framework of spatial and morphological characteristics to analyze the case, and proposes the main spatial types of current urban shopping centers in China.

3 Methodology

The methodology is divided into two parts. In the first step, the definitions and types of shopping centers in previous studies were reviewed. Subsequently, according to the morphological characteristics of the shopping center and the type of insertion in the urban environment, five typologies of shopping center were defined.

The second step is multi-case analysis. In this section, the spatial organization and morphological characteristics of nine shopping centers were selected and analyzed, identifying the main categories of urban shopping centers in contemporary China.

Each case was analyzed in depth and spatial analysis framework was produced. A spatial organization atlas of Chinese urban shopping center was redeveloped based on the information provided by Baidu Maps and others database. The spatial maps demonstrate the spatial organization, land use, traffic (entrances and exits and surrounding roads) and other space information of shopping centers in Chinese cities.

4 Case Analysis

This study attempts to understand the relationship between shopping centers and city in terms of spatial organization and morphological characteristics. Therefore, this study provides a spatial interpretation through a multi-case analysis.

Eight cases were selected from different cities in China based on data such as geographic location and overall planning (Table 3). It was analyzed for its

Table 3 The case selection

Case area	Location
Deji Joy city Laifushi	Nanjing Shanghai Hangzhou
Shinkong-place	Suzhou
Wanda (residence) Henglong (office)	Wuxi Wuxi
TaiKoo Li Sanlitun	Beijing
Rongchuang Mall	Wuxi

geographic location, spatial layout and other information, and analysis maps were drawn (Table 4). First, the insertion of different shopping centers in the urban environment is examined; then, several main types of shopping centers are identified based on the spatial organization and the relationship with the surrounding area.

5 Discussion

In China, shopping centers are divided into two main categories based on their geographical location. The first type is located within the inner city. This category emerges with urban transition. The government take back the land property through demolition, and transfer the property to the developer for constructing the shopping center.

According to the case study, there are mainly independent type, integrated type (mall + office) and street/scattered type of this category (Table 5). The independent type refers to demolish the original site and place a shopping center. Its surrounding area often change little with the formation of shopping center. The integrated type is complemented by office buildings that is related with independent type. Because of the land area, the mall with residential area is not generally built in the urban center. Many of the street/scattered types are similar to outlet, with many single buildings built in one area, and commercial model is "not sell, only rent". In China, many urban preservation-led projects are similar to this type, such as the Xintiandi in Shanghai and the Laomendong in Nanjing.

The second type is located in the new town (former suburban area). Most of these areas were formerly farmland and farmer house and are generally far from urban centers, where traffic is often accompanied by viaducts and highways, etc. The spatial structure of this category is large, mainly belongs to mix-use area (Table 5). That is, a shopping mall as the core, surrounded by amusement parks, residential areas, hotels and other settings. The purpose of this type is to build a community model with commerce as the core, and to improve the attractiveness.

Table 4 The spatial organization map of each cases

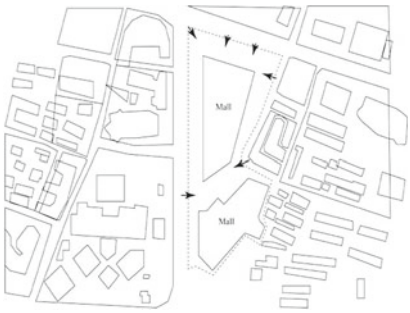	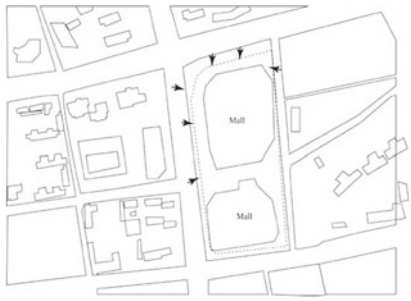
Deji, Nanjing	Joy city, Shanghai
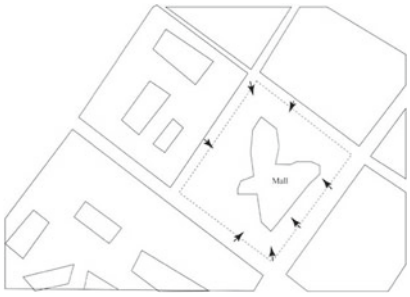	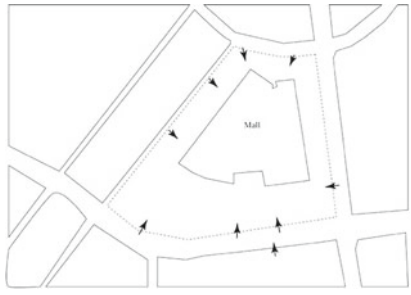
Laifushi, Hangzhou	Shinkong-place, Suzhou
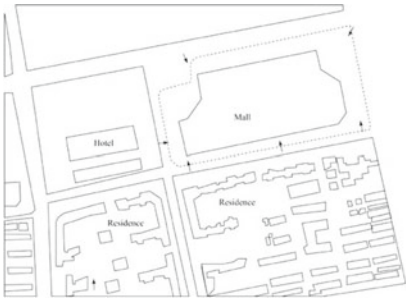	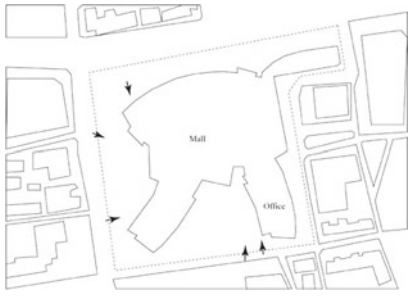
Wanda (residence)	Henglong (office)

(continued)

Table 4 (continued)

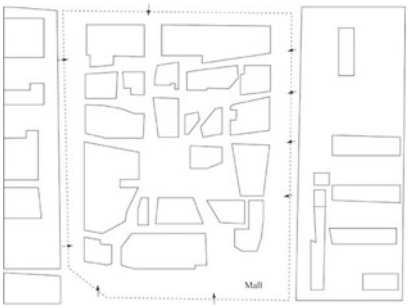	
TaiKoo Li Sanlitun, Beijing	Rongchuang Mall, Wuxi

Source by author

Table 5 The typology of urban shopping center

Typology	Case area
Independent type	Deji; Joy city; Laifushi
Gated type (ground parking)	Shinkong-place
Integrated type	Wanda (+residence); Henlong (+office)
Street/ Scattered type	TaiKoo Li Sanlitun
Mix-use type	Rongchuang Mall

Source author

6 Conclusion

This study analyzes and categorizes the types of urban shopping centers by exploring their physical characteristics and basic spatial organization. Five types were identified through spatial organization analysis and mapping of the atlas (Fig. 2). This classification of types offers the possibility to further understand the study of the relationship between shopping centers and cities in terms of physical space.

The Urban shopping center as a place of urban social life which has a certain interaction with its surrounding urban context. The urban shopping center is forming and being formed by the city. It is an important factor in urban dynamics of the urban development. Urban morphology can be used to understand its relationship with the historical context of city. With the urban development and the gradually changing of urban social life, urban shopping center reflects the various types of integration or separation with the city. This relation effects its function, internal organization, form and character and the relationship with urban morphology. The morphological characteristics of urban shopping center can demonstrate the extent of the interaction of urban shopping center and city. This study focuses on the interaction of urban shopping center and city, it seeks to understand the morphological characteristics of urban

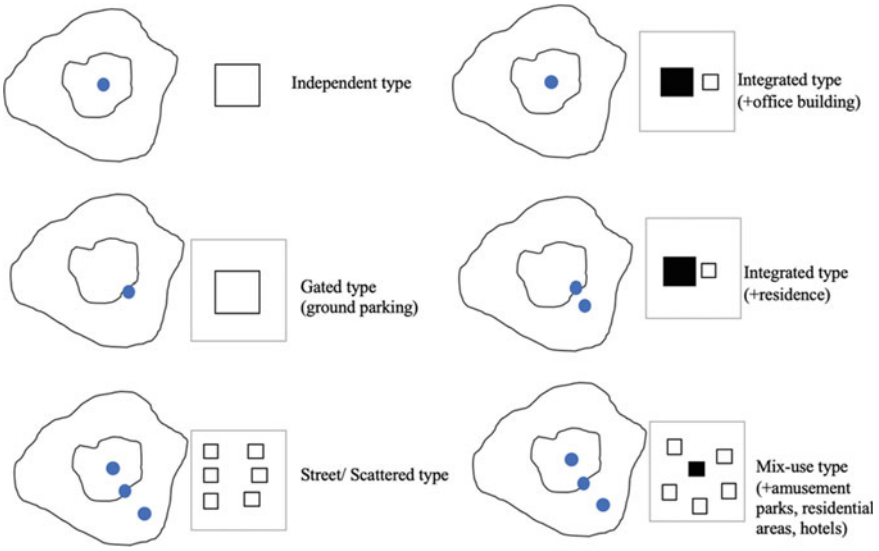

Fig. 2 The scheme of urban shopping center typology

shopping center and its surrounding urban context. It will be attempted to demonstrate the role of urban shopping center in creating urban space in contemporary city.

Funding This study is supported by Philosophy and Social Science of Jiangsu Higher Education (2021SJA0913), the Innovation and Entrepreneurship Training Program for College Students in Jiangsu Province (202313571014Z), and Natural Science foundation of Jiangsu Higher Education (NO. 20KJB560011).

References

1. Berman B, Evans JR (2010) Retail management (A strategic approach). Prentice Hall, Pearson
2. Gruen V, Smith L (1960) Shopping towns USA. The planning of shopping centers. Reinhold Publishing Corporation, New York
3. Bravo L (2013) Open spaces, public spaces, publics, open-minded places. The Public Space of Education, Italy
4. Baker SM et al (2007) How consumers with disabilities perceive welcome in retail servicescapes: a critical incident study. Serv Mark 21:160–173
5. Baker J (1987) The role of the environment in marketing services: the consumer perspective. In: Czepiel J, Congram CA, Shanahan J (eds) The services challenge: integrating for competitive advantage. American Marketing Association, Chicago, IL, pp 79–84
6. Juhari NH, Ali HM, Khair N (2012) The shopping center servicescape affects customer satisfaction. In: 3rd international conference on business and economic research (3rd ICBER 2012), 12–13 March, 2012. Bandung, Indonesia

7. De Simone L, Pezoa M (2021) Urban shopping centers and sustainability approaches in Chilean cities: relations between environmental impacts of buildings and greenwashing branding discourses. Sustainability 13(13):7228. https://doi.org/10.3390/su13137228
8. Zhang T, He F, Wang D (2023) The role of public-private partnerships of project construction—shopping mall as an example. In: Casini M (eds) Proceedings of the 2nd international civil engineering and architecture conference. CEAC 2022. Lecture notes in civil engineering, vol 279. Springer, Singapore
9. Dawson J, Lord D (eds) (2012) Shopping centre development (RLE retailing and distribution). Routledge
10. ICSC shopping center definitions: basic configurations and types (PDF). International Council of Shopping Centers. Retrieved July 15, (2020)
11. Levy M, Weitz BA, Grewal D (2018) Retailing management, 10th edn. McGraw-Hill/Irwin, Burr Ridge, IL

A Numerical Study on Pedestrian-Level Wind Environment in Different Types of Residential Area Streets in Tianjin

Tong Ma

Abstract The spatial morphology of street significantly affects urban pedestrian-level wind environment and further has a great influence on human outdoor thermal comfort. Previous studies usually simplify urban streets as 2D or 3D street canyons with consecutive street interface, which is obvious different from the spatial morphology of Chinese residential area streets. This may cause wind environment difference between them. Taking Tianjin as the research area, this study firstly classified local residential areas into several categories based on its spatial morphological characters. Numerical simulation was then conducted to analyze the pedestrian-level wind environment between each category of street. Key spatial morphological factors that affect pedestrian-level wind were found. Meanwhile, this study figured out the pedestrian-level wind environment difference between Tianjin's actual urban streets and simplified street canyons. Aspect ratio, which is the common morphological indicator used in street ventilation studies, was proved to be unapplicable in ventilation studies for Chinese residential area streets. This chapter suggests several optimization methods according to local climate condition, and provides theoretical references for residential area planning and design for Tianjin and other Chinese cities with comparable climate conditions.

Keywords Ventilation · Spatial morphology · Street canyon · ENVI-met · Numerical simulation

T. Ma (✉)
Beijing University of Technology, 100 Pingleyuan, Beijing, China
e-mail: mtong@163.com

T. Kang (ed.), *Proceedings of 5th International Conference on Civil Engineering and Architecture*, Lecture Notes in Civil Engineering 369,
https://doi.org/10.1007/978-981-99-4049-3_44

1 Introduction

1.1 Existing Studies on Wind Environment of Street Canyon

Street is the fundamental element in urban outdoor space. The spatial morphology of street can significantly affect pedestrian-level wind environment inside street canyon. Therefore, street space that conducive to ventilation is important to improve urban wind environment and outdoor thermal comfort [1–3].

Urban streets have unique wind environment due to its canyon-like space. Existing studies always simplify urban streets as 2D or 3D canyons with consecutive interface on both side of the street. Many studies on 2D street canyons indicate that street width and aspect ratio are key morphological factors that affect wind environment inside the street canyon on wind speed and wind turbulence pattern [4–6]. However, 2D street canyon is too much simplified to reflect the wind condition in actual urban streets [7]. Therefore, studies on 3D street canyons are conducted. Some other factors affect street wind environment beside aspect ratio are summarized as the ratio of street length and building height [8] and the spatial morphology of street intersections [9]. 3D street canyon could be replaced by 2D street canyon only if the street is long enough [10].

However, there are still obvious space morphological difference between simplified 3D street canyon and actual urban street [11]. Therefore, scholars begin to study on generic streets with more complex spatial morphology. It has been proved that street buildings with variant height [12], the consecutiveness of street interface [13] and even balconies along the street interface also affect the airflow inside the street canyon [14]. Beside these parametric studies, other scholars conduct wind studies based on actual urban street spaces. Taleghani [15] figured out the optimal street layout for the Netherland cities. Cui [16] summarized the length of U-shaped street that commonly seen in Shenzhen and Hongkong determines the wind environment inside the street canyon. Chatzidimitriou [17] discussed the orientation and aspect ratio of the street that has best outdoor thermal comfort based on the climate condition of Greece. Nosek [18] studied the influence of courtyard-style street buildings' morphology on the street wind environment in European cities. All these studies demonstrate the importance of using more complex models that are closer to real street spaces for wind environment studies.

1.2 Aim of this Study

Residential area is the widest distributed urban function in cities. Residential areas and adjacent streets in different regions of the world have their unique spatial morphological characteristics. Chinese residential areas are always composed by many independent buildings, which made the adjacent streets lack of continued interface (Fig. 1). As a result, the pedestrian-level wind environment in Chinese residential area

Fig. 1 Street with consecutive interface **a** and street with nonconsecutive interface in Chinese residential areas **b** and **c**

streets may have great differences from simplified 2D or 3D street canyon. However, the wind environment study targeted on Chinese residential area streets is scarce. Therefore, three research questions were investigated in this study as following:

(1) What is the pedestrian-level wind condition in different types of residential area streets in Tianjin?
(2) Is there a significant difference on pedestrian-level wind environment between Tianjin's actual residential area streets and simplified 3D street canyons?
(3) Will the pedestrian-level wind environment show regular changes when street spatial morphology changes in Tianjin's residential area streets?

To answer these questions, this study classified several typical residential area streets according to their spatial morphological characteristics. Then numerical simulations were conducted to assess the pedestrian-level wind condition for each category of residential area street under different street width and different wind direction. Wind environment optimization strategies were discussed at last based on Tianjin's climate and urban condition. This study provides theoretical support for residential area planning for Tianjin and other Chinese cities with comparable weather conditions.

2 Methods and Case Analysis

2.1 Study Area and Weather Condition

Tianjin, a metropolitan located in northern China (Fig. 2), was selected as the study area. Tianjin is located in cold climate region according to Chinese climate zone classification. The meteorological data covering the past 15 years of the city was obtained from local meteorological station. The average monthly temperature is 27.1 °C in July (hottest) and −2.6 °C in January (coldest). The average monthly wind speed is 2.7 m/s, both in summer and winter.

Since 1990, Tianjin started its rapid urbanization. The overall population in Tianjin's urban area exceed 11 million by 2021. Therefore, Tianjin can represent the typical climate conditions and urban development condition in North China, so

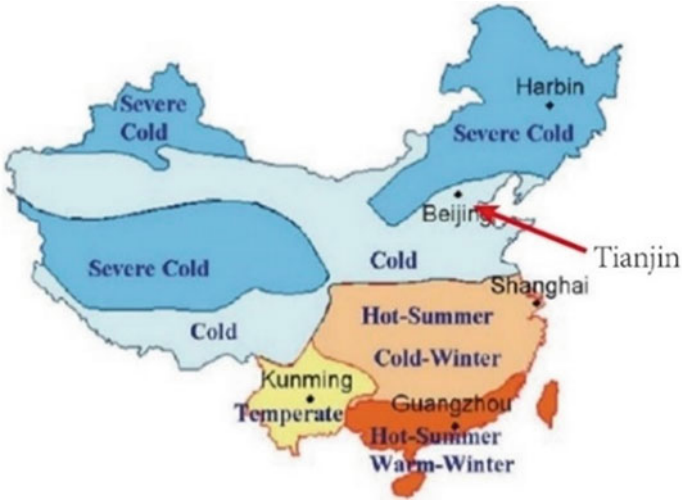

Fig. 2 The location and climate zone of Tianjin

that the conclusions of this study can be applied to other Chinese cities in similar climate regions.

2.2 Wind Criteria Indicators

Wind speed ratio, which is defined as the ratio of pedestrian-level wind speed at measurement point to the input wind speed at 10 m height, was used to assess the pedestrian level wind environment in this study. This indicator can reflect the amplification or blocking effect of buildings on pedestrian-level wind speed. The format is shown in Eq. (1), where R represents the wind speed ratio, V_i represents the wind speed of a measurement point and V_0 represents the input wind speed at 10 m in numerical simulation.

$$R = \frac{\mathrm{V}_i}{\mathrm{V}_0} \tag{1}$$

2.3 Classification and Spatial Morphology of Tianjin's Residential area Streets

The spatial morphology of residential area streets depends on the residential buildings along the streets. Our previous study [19] summarized the spatial morphological

characters of Tianjin's residential areas and classified them into four categories, as Mid-rise, Mid high-rise, High-rise class2 and High-rise class1, respectively. A total of 40 residential areas (10 for each layout pattern) in Tianjin were randomly selected to verify the spatial morphology difference between each category. Featured spatial morphological parameters of these residential areas were selected, including average building height (Avg. BH), average building width (Avg. BW), average building depth (Avg. BD), average north to south distance between buildings (Avg. D-ns) and average east to west distance between buildings (Avg. D-ew), as Fig. 3 shown. The average value of each indicator for each category is shown in Table 1. A one-way ANOVA was conducted on various spatial morphological parameters to verify the morphology difference between each category. Results indicated that there was significant difference on spatial morphology between each group ($p < 0.05$), as shown in Table 1. It proved that this classification method is suitable for Tianjin's residential area streets.

Beside these four categories, there was another featured residential area that has unique spatial morphology. This residential area was "mid-rise enclosed type" and classified into mid-rise category in our past study [20]. However, there was an obvious

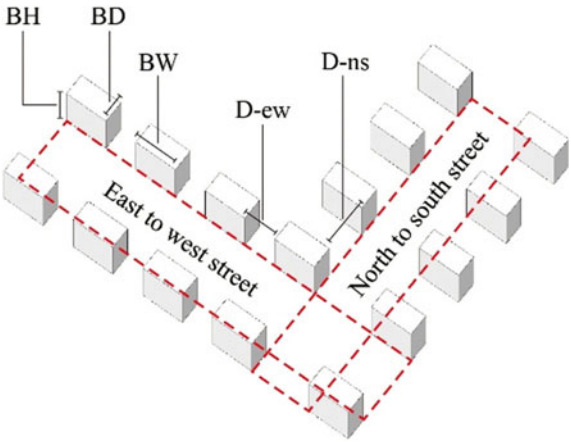

Fig. 3 Each spatial morphological indicator

Table 1 The average value and ANOVA result of each spatial morphological indicators for each category

Layout category	Mid-rise	Mid high-rise	High-rise class2	High-rise class1
Avg. BH (m)	18.1a	33.3b	54.4c	81.1d
Avg. BW (m)	54.2c	45.9b	37.1a	32.7a
Avg. BD (m)	13.9ab	12.9a	16.4b	16.2b
Avg. D-ns (m)	25.5a	44.4b	48.1b	47.5b
Avg. D-ew (m)	12.8a	16.4b	19.7bc	22.2c

spatial morphology difference between mid-rise enclosed type and other layout categories, as the continued building façade along the street. Therefore, this mid-rise enclosed type was classified as an individual street category in this study.

Therefore, Tianjin's residential area streets were classified into five typical categories. They were respectively: mid-rise (type A), mid high-rise (type B), high-rise class2 (type C) and high-rise class1 (type D) and mid-rise enclosed (type E). The satellite map, photograph and 3-D model of each street type is shown in Fig. 4.

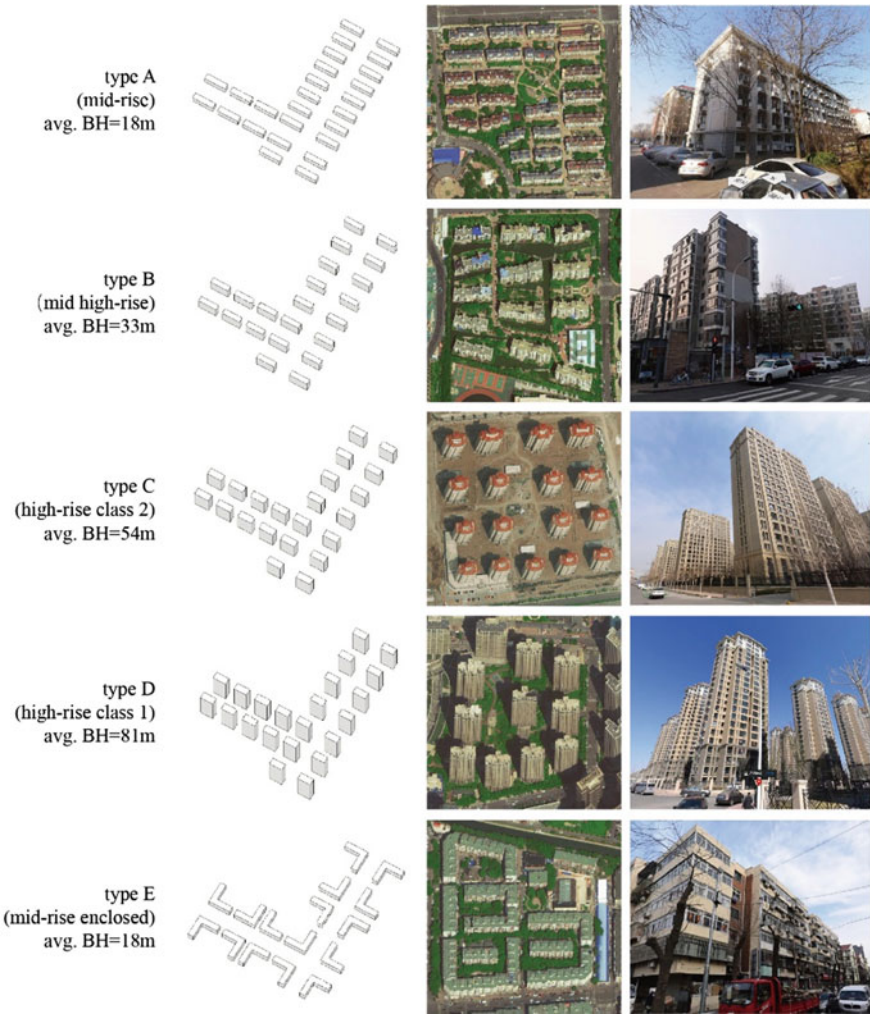

Fig. 4 Satellite map, photograph and 3D model of each type of residential area street

Table 2 Input parameters of ENVI-met simulation

Start time	06:00
Output time	14:00
Grid size	3 m
Simulation time step	2–4 s
Input wind speed (at 10 m)	2.7 m/s
Input wind direction	E/SE/S
Roughness length (at meteorological station)	0.6 m

2.4 Numerical Simulation

ENVI-met 4.4 software was used to simulate the pedestrian-level wind speed for residential area street in this study. Its flow solver is based on the Reynolds-averaged Navier–Stokes (RANS) equation. The reliability and accuracy of this software has been tested by many scholars [15, 19–23]. Table 2 shows the input parameters of ENVI-met simulation in this study.

3 Simulation Results and Analysis

3.1 Simulation Scenarios

Numerical simulations were divided into three groups to explore the relationship between street morphology and pedestrian-level wind speed.

Group 1 discussed the characteristics of pedestrian-level wind environment in five residential streets categories, and how their pedestrian-level wind environment changes with different street widths. 50 residential streets in Tianjin were randomly selected by using satellite images to calculate the street width. The width of most streets was between 22 and 62 m, and the average width was 42 m. Therefore, 42 m was the standard width of simulation cases. The pedestrian-level wind speed of each street type were simulated under three street width: 32, 42 and 52 m. The input wind direction for this group of simulation was fixed in SE.

Group 2 discussed the differences of pedestrian-level wind environment in three different wind directions: E (east), SE (southeast) and S (south). The street width for all simulation cases were fixed in 42 m.

Group 3 discussed the pedestrian-level wind difference between Tianjin's actual residential area street and simplified 3D street canyon. Wind environment between actual streets and simplified streets with same building height were compared. The input wind direction for all simulation cases were fixed in SE, and the street width were also fixed in 42 m.

3.2 Group 1—Wind Environments with Different Streets Widths

Figure 5 wind speed distribution maps for all simulation cases. And Fig. 6 shows the wind speed ratio for five street types in three street widths. Results showed that there were significant differences on pedestrian-level wind speed between each street category, regardless the difference in street width. As building height increased, the average wind speed ratio gradually rose from 0.70 (mid-rise, including type A and E) to 0.79 (type B), 0.86 (type C) and 1.01 (type D). Meanwhile, as building height increased, the areas with low wind speed in leeward side of buildings and high wind speed in windward side of the buildings enlarged simultaneously, which made the wind environment unstable. The simulation results were consistent with our previous research on Tianjin's residential areas [19].

In north–south (N–S) orientation (Fig. 6a), the wind speed increased gradually with the increase of street width for all five street categories. As the street width rose from 32 to 52 m, the wind speed ratio rose 0.09, 0.09, 0.07, 0.07 and 0.05 respectively for type A to E. In east–west (E–W) orientation (Fig. 6b), there was no significant wind speed change under different street width for each street type.

Therefore, it can be inferred that the variation of street width has certain influence on pedestrian-level wind environment of Tianjin's residential areas streets. This influence was mainly on N–S orientation streets, but not on E–W orientation streets.

3.3 Group 2—Wind Environments with Different Wind Directions

Figures 7 and 8 shows wind speed distribution maps and wind speed ratio value for five street types in three wind directions. The wind speed was the highest when the input wind was parallel to the street orientation, the lowest when the input wind was perpendicular to the street orientation, and moderate when the input wind was 45° angle to the street orientation. As a result, there was obvious wind speed difference between two street orientations.

On the other hand, due to the difference of street interface consecutiveness (interface consecutiveness in E–W street is higher than N–S street), there was significant pedestrian-level wind difference between two street orientations even the wind-street angle was the same. In type A and B, the input wind that perpendicular to E-W street was mostly obstructed by buildings (Fig. 7a and d), but fewer obstructed when input wind was perpendicular to N–S street (Fig. 7c and f). As a result, the wind speed ratio of N–S street was 0.24 and 0.20 higher than E–W street in type A and type B. However, this wind speed difference was smaller in type C, the wind speed ratio in N–S street was only 0.05 higher than E–W street. In type D, the wind speed ratio in N–S street was even 0.13 lower than E–W street. This phenomenon could be explained by channeling effect that made strong local wind between tall buildings

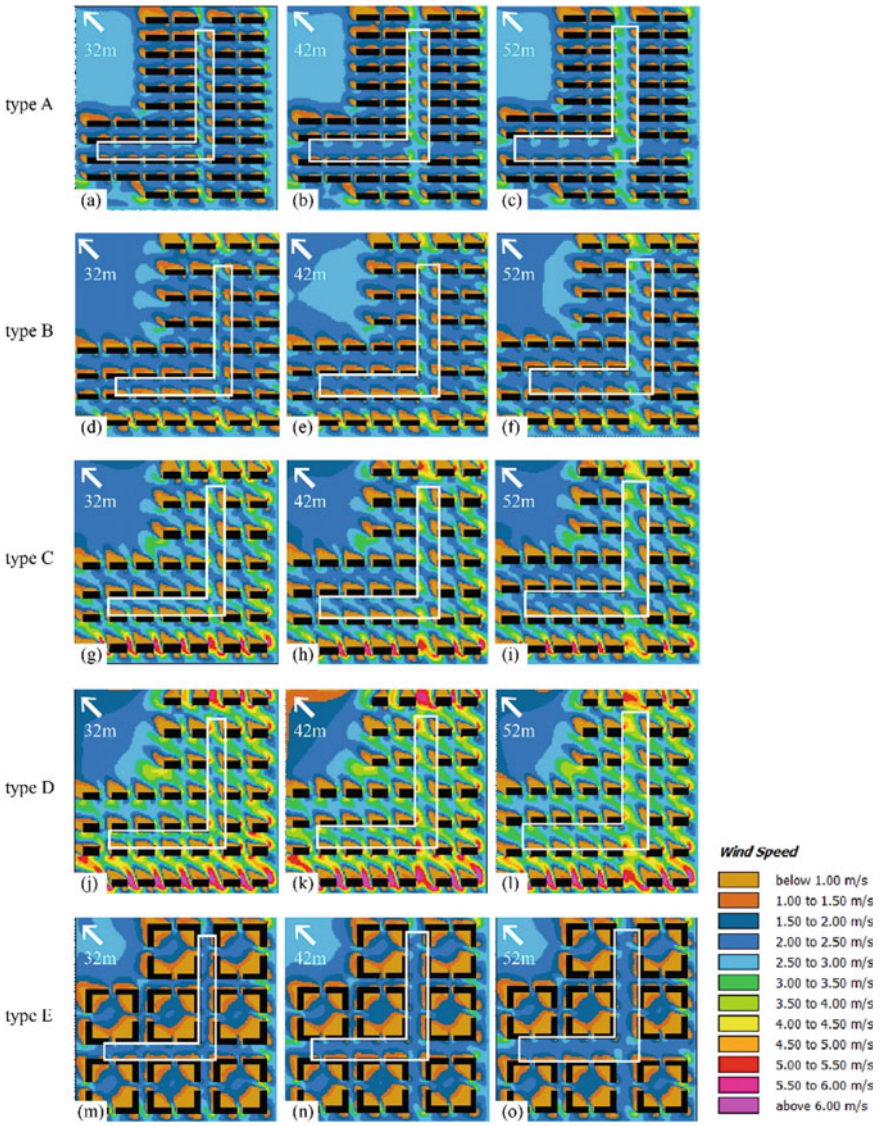

Fig. 5 Wind speed distribution maps of five street types on different street widths

when input wind is perpendicular to E–W street, which is consistent with Kuo's [24] studies. In type E, there was no wind speed difference between N–S and E–W streets due to the similarity of street interface consecutiveness of two street orientations (Fig. 7m and o).

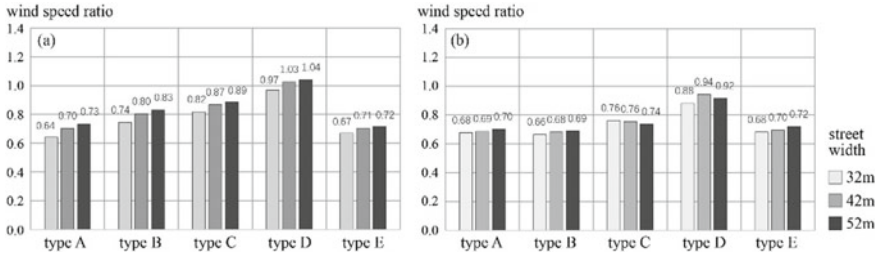

Fig. 6 Wind speed ratio in different street width for N–S **a** and E–W orientation **b** streets

Moreover, considering all three wind directions, the average wind speed of N–S streets was slightly higher than that of the E–W streets. In type A, B and C, wind speed ratio of N–S street was 0.07, 0.11 and 0.07 higher than E-W street respectively.

3.4 Group 3—Comparison Between Actual and Simplified Street Canyons

Figure 9 shows the pedestrian-level wind simulation results of four simplified street canyons (a–d) and four actual residential area streets of Tianjin (e–h). It can be seen that: (1) higher the building height along the street, higher the pedestrian-level wind speed, in both type of streets. (2) Actual streets had more complex wind environment than simplified streets. There were obvious weak wind areas on leeward side and strong wind areas on windward side of buildings in actual streets, which was totally distinguished from simplified street canyon with consecutive street interface. The result is consistent with He's research [9].

4 Discussion

4.1 The Effect of Spatial Morphology on Pedestrian-Level Wind Environment for Tianjin's Residential Area Streets

Simulation results shows that there are three key spatial morphological factors that affect pedestrian-level wind environment in Tianjin's residential area streets. They are (1) building height, (2) street interface consecutiveness, and (3) street width.

Building height is the dominant factor that affect pedestrian-level wind environment. In streets with tall buildings (high-rise class 2 and class 1), the overall wind speed is higher than streets with short buildings (mid-rise and mid high-rise), and there are more local strong wind turbulences which made the wind environment unstable.

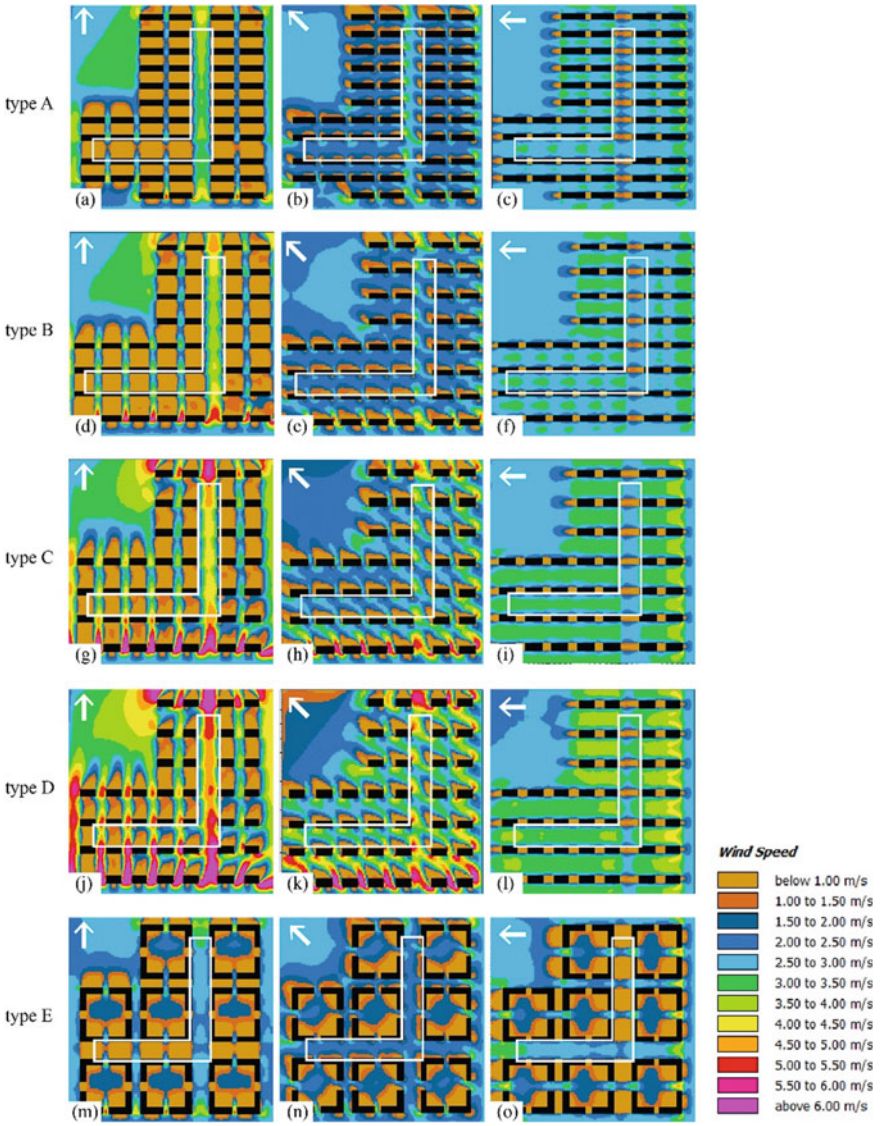

Fig. 7 Wind speed distribution maps of five street types on difference wind directions

Street interface consecutiveness is another reason that caused the wind environment variance, especially in different street orientations. In Tianjin's residential area street, the space between buildings in E–W street is relatively small and the street interface is more consecutive. As a result, inflows perpendicular to the E–W streets are blocked and the wind speeds are relatively low. On the contrary, there are larger spaces between buildings in N–S streets (this is mainly due to daylighting

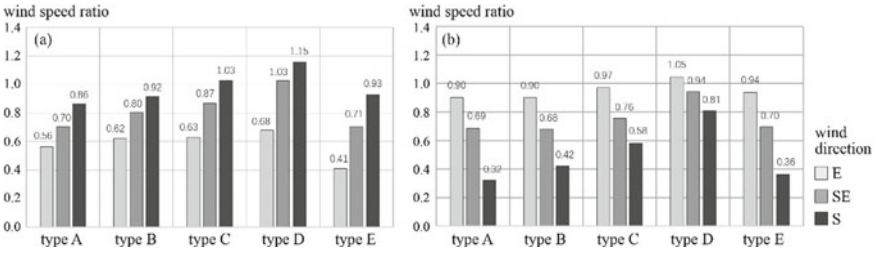

Fig. 8 Wind speed ratio in N–S **a** and E–W street **b** in three different wind direction

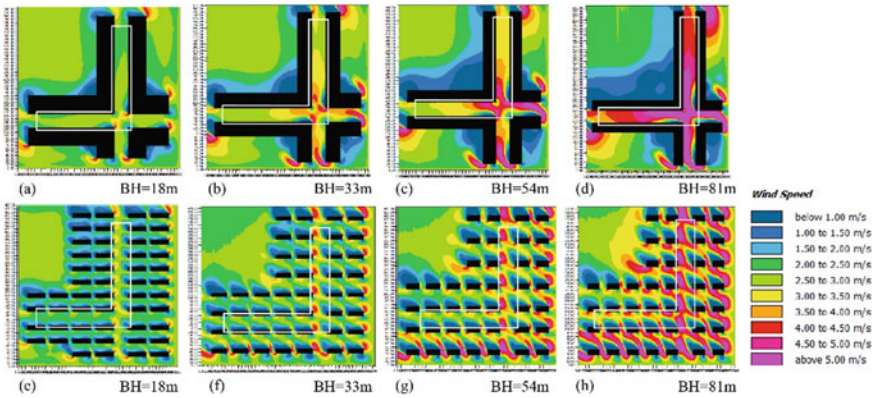

Fig. 9 Wind comparison between simplified street canyons **a**–**d** and actual streets **e**–**h**

requirement in local design regulations), so that the street interface is less consecutive. Therefore, the wind speeds are relatively higher in N–S streets due to less obstructions, as shown in Fig. 10. There is no significant wind difference between two street orientation in type E (enclosed) due to the similarity of street interface consecutiveness in two orientations.

In addition, **street width** is also a factor affect pedestrian-level wind environment, but not as important as above two factors. In all simulated cases, the overall wind speeds are slightly higher in wider street of N–S orientation. With the increase of street width, the wind shadow area behind windward buildings could not cover the whole street gradually, resulting in the increase of wind speed on the downwind side of the street, as shown in Fig. 11.

4.2 Ventilation Optimization Methods

Following optimization methods for Tianjin's residential area streets are proposed in this section according to local climate condition.

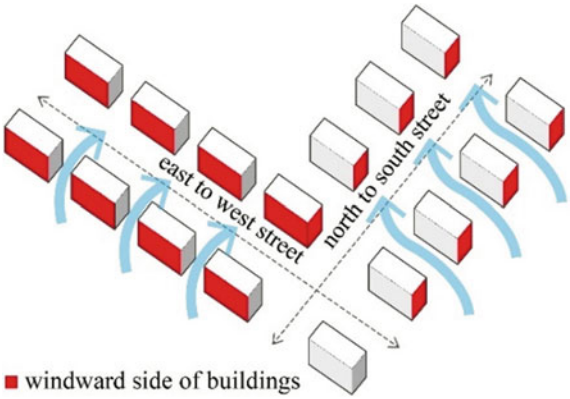

Fig. 10 How wind infiltrated into streets with different orientations

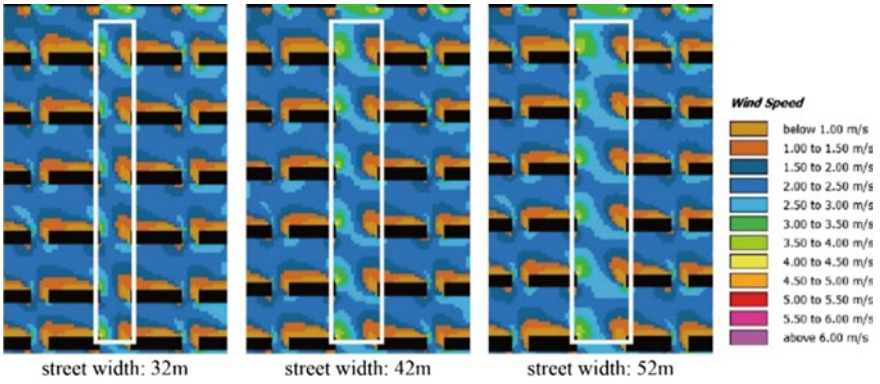

Fig. 11 Wind speed on leeward side of the street rose as street width increased

(1) Mid-rise streets (type A and E), which has the lowest wind speed, is not conductive to summer ventilation but contribute to winter wind protection. Mid high-rise streets (type B) have moderate wind environment. High-rise streets (type C and D), which have the highest wind speed and strong local wind turbulence, are contribute to summer ventilation but worsen the pedestrian-level wind environment in winter. Therefore, mid-rise and mid high-rise residential areas are recommended in suburban area or around large urban open spaces where the ground roughness is relatively low and the overall wind speed is relatively high. On the contrary, in urban core area where ventilation is much needed, streets with high-rise buildings is recommended.

(2) When the angle between input wind and street orientation is large (as 45° in this study) and the building height is tall, wind speed of the windward side of the street is relatively low due to the obstruction of buildings, and the wind speed of the leeward side of the street is relatively high due to the strong wind turbulence caused by downstream (as shown in Fig. 7k). Therefore, when tall buildings are

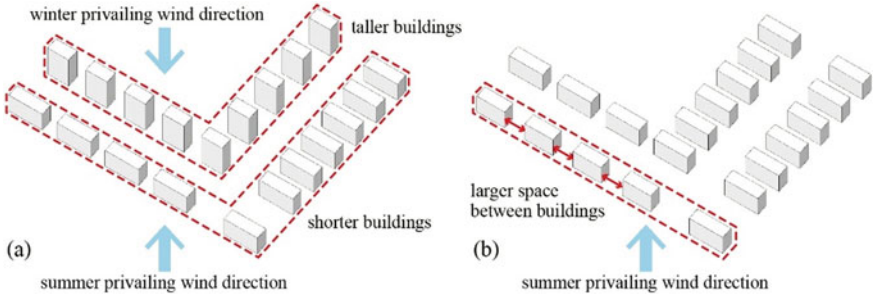

Fig. 12 Changes in building heights **a** and street interface consecutiveness **b**

distributed on windward side of the street and shorter buildings are distributed on leeward side of the street (Fig. 12a), summer ventilation and winter wind protection could be partly achieved based on Tianjin's climate condition, due to the primary wind directions in winter and summer is opposite.

(3) The difference in street interface consecutiveness caused the wind environment variance. Therefore, the space between buildings on south side of E-W street could be increased to allow the input wind less obstructed in order to promote summer ventilation, especially in mid-rise and mid high-rise categories, as shown in Fig. 12b.

(4) Narrow streets led to lower pedestrian-level wind speed and contribute to winter wind protection, so that streets with too much width should be avoided in cold climate region like Tianjin.

4.3 The Necessity of Using Actual Street Model

Section 3.4 compared the pedestrian-level wind environment between simplified street canyons and Tianjin's actual residential streets. Due to the street interface difference, there is significant airflow difference between two types of streets. Therefore, it can be concluded that the simplified 3D street canyon with consecutive street interface is not suitable for pedestrian-level wind study of Tianjin's residential area streets. Street canyon models based on actual urban space is needed due to the unique spatial morphology of Chinese residential area streets.

4.4 The Applicability of Aspect Ratio in Tianjin's Residential Area Streets

Aspect ratio (H/W, H = average building height, W = street width) is a common spatial morphological indicator in street ventilation studies. As can be seen from Fig. 13, there is significant positive correlation between aspect ratio and wind speed

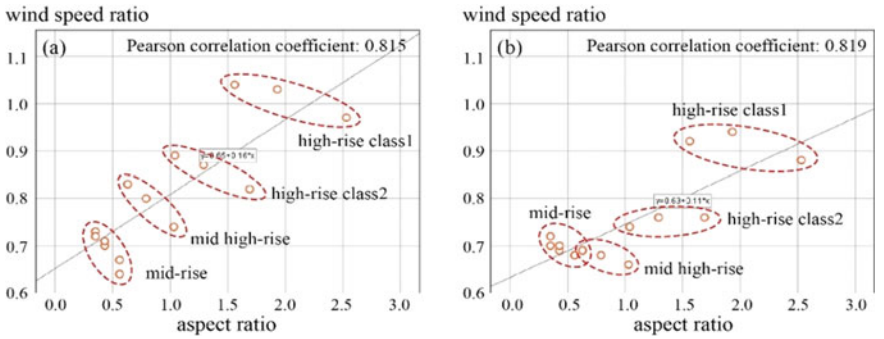

Fig. 13 Correlation between aspect ratio and wind speed ratio of N–S **a** and E–W streets **b**

ratio in five street categories. Does this prove that aspect ratio is an applicable spatial morphological indicator for the ventilation study of Tianjin's residential area streets?

The answer is negative. If we further analyze the relationship between wind speed of each type of street and its aspect ratio, it can be found that wind speed does not enhance with the increase of aspect ratio in E–W street (red dotted circle in Fig. 13b) and even decrease with the increase of aspect ratio in N–S street (red dotted circle in Fig. 13a). This is mainly due to the decrease in street width, as Sect. 3.2 discussed. The rise of wind speed between each type of street is the consequence of building height increase. Therefore, different with simplified street canyon, there is not a clear relationship between aspect ratio and pedestrian-level wind speed in Tianjin's residential area streets. And aspect ratio is not an applicable indicator for similar studies.

5 Conclusion and Limitation

Taking Tianjin as the research area, this study used numerical simulation to analyze the pedestrian-level wind environment in different types of residential area streets under different wind directions and streets widths. The following conclusions are draws.

(1) There is obvious pedestrian-level wind difference in different type of residential area streets. Street with mid-rise buildings has the lowest overall wind speed. The pedestrian-level wind speeds gradually increase as the building height increase on both sides of the street. Also tall buildings along the street generate strong local wind turbulence around buildings.

(2) Average building height is the most influential spatial morphological factor that affect pedestrian-level wind environment for Tianjin's residential area streets. The consecutiveness of street interface and street width also partly affect it.

(3) Several spatial morphological optimization methods are proposed for Tianjin's residential area streets based on local climate condition. Firstly, the type of residential buildings along the street should be considered according to the overall wind speed of the region. Residential areas with tall buildings (e.g., high-rise class2 and class1) should be avoided as much as possible in suburban or around huge urban open spaces and vice versa. Secondly, buildings with different heights could be arranged on both sides of the street according to the prevailing wind direction in winter and summer. Thirdly, street ventilation can be enhanced by controlling the space between buildings.
(4) There is significant difference on pedestrian-level wind environment between Tianjin's actual residential area streets and simplified street canyons. Aspect ratio is not an applicable indicator in ventilation studies of Tianjin's residential area streets. These show the importance of using street models that more closely resemble real urban spaces in ventilation studies.

There are still some limitations in this study. Firstly, only residential streets with single building type were considered. Residential streets with mixed building type (e.g., mid-rise mixed with high-rise) were ignored. Secondly, some residential streets in Tianjin have consecutive podium with commercial or retail function on both side of the street. This type of street was not studied. Finally, there are still some residential streets in Tianjin that do not have a north to south or east to west orientation, which is not included in this paper. These aspects will be analyzed in our further studies.

Funding Information This research is supported by NSFC project: The mechanism and optimization of thermal comfort for urban public space in cold region based on human thermal sensation difference (Grant No. 52208002).

References

1. Ramponi R, Blocken B, de Coo LB et al (2015) CFD simulation of outdoor ventilation of generic urban configurations with different urban densities and equal and unequal street widths. Build Environ 92:152–166
2. Mittal H, Sharma A, Gairola A (2018) A review on the study of urban wind at the pedestrian level around buildings. J Build Eng 18:154–163
3. Wang Q, Zhou T, Liu Q et al (2019) Numerical study of critical re-entrainment velocity of fire smoke within the street canyons with different building height ratios. Environ Sci Pollut Res 26:23319–23327
4. Liu CH, Leung DYC, Barth MC (2005) On the prediction of air and pollutant exchange rates in street canyons of different aspect ratios using large-eddy simulation. Atmos Environ 39:1567–1574
5. Cheng WC, Liu CH, Leung DYC (2008) Computational formulation for the evaluation of street canyon ventilation and pollutant removal performance. Atmos Environ 42:9041–9051
6. Zhong J, Cai XM, Bloss WJ (2015) Modelling the dispersion and transport of reactive pollutants in a deep urban street canyon: using large-eddy simulation. Environ Pollut 200:42–52
7. Allegrini J (2018) A wind tunnel study on three-dimensional buoyant flows in street canyons with different roof shapes and building lengths. Build Environ 143:71–88

8. Chan AT (2001) Strategic guidelines for street canyon geometry to achieve sustainable street air quality. Atmos Environ 35:5681–5691
9. He Y, Tablada A, Wong NH (2019) A parametric study of angular road patterns on pedestrian ventilation in high-density urban areas. Build Environ 151:251–267
10. Mei SJ, Luo ZW, Zhao FY et al (2019) Street canyon ventilation and airborne pollutant dispersion: 2-D versus 3-D CFD simulations. Sustain Cities Soc 50:101700
11. Karra S, Malki-Epshtein L, Neophytou MKA (2017) Air flow and pollution in a real, heterogeneous urban street canyon: a field and laboratory study. Atmos Environ 165:370–384
12. Nosek Š, Kukačka L, Jurčáková K et al (2017) Impact of roof height non-uniformity on pollutant transport between a street canyon and intersections. Environ Pollut 227:125–138
13. Ying XY, Ding G, Hu XJ et al (2016) Developing planning indicators for outdoor wind environments of high-rise residential buildings. J Zhejiang Univ-Sci A (Appl Phys Eng) 17(05):378–388
14. Cui D, Li X, Liu J et al (2021) Effects of building layouts and envelope features on wind flow and pollutant exposure in height-asymmetric street canyons. Build Environ 205:187177
15. Taleghani M, Kleerekoper L, Tenpierik M et al (2015) Outdoor thermal comfort within five different urban forms in the Netherlands. Build Environ 83:65–78
16. Cui D, Hu G, Ai Z et al (2019) Particle image velocimetry measurement and CFD simulation of pedestrian level wind environment around U-type street canyon. Build Environ 154:239–251
17. Chatzidimitriou A, Yannas S (2017) Street canyon design and improvement potential for urban open spaces; the influence of canyon aspect ratio and orientation on microclimate and outdoor comfort. Sustain Cities Soc 33:85–101
18. Nosek Š, Klukova Z, Jakubcova M et al (2022) The effect of courtyard buildings on the ventilation of street canyons: a wind-tunnel study. J Wind Eng Ind Aerodyn 220:104885
19. Ma T, Chen T (2020) Classification and pedestrian-level wind environment assessment among Tianjin's residential area based on numerical simulation. Urban Climate 34C:100719
20. Morakinyo TE, Lam YF (2016) Simulation study on the impact of tree-configuration, planting pattern and wind condition on street-canyon's micro-climate and thermal comfort. Build Environ 103:262–275
21. Salata F, Golasi I, Petitti D et al (2017) Relating microclimate, human thermal comfort and health during heat waves: an analysis of heat island mitigation strategies through a case study in an urban outdoor environment. Sustain Cities Soc 30:79–96
22. Forouzandeh A (2018) Numerical modeling validation for the microclimate thermal condition of semi-closed courtyard spaces between buildings. Sustain Cities Soc 36:327–345
23. Xing Y, Brimblecombe P, Wang S et al (2019) Tree distribution, morphology and modelled air pollution in urban parks of Hong Kong. J Environ Manage 248:109304
24. Kuo CY, Tzeng CT, Ho MC et al (2015) Wind tunnel studies of a pedestrian-level wind environment in a street canyon between a high-rise building with a podium and low-level attached houses. Energies 8:10942–10957

Identifying Boundaries and Open Spaces of the Village Using Bidirectional Buffer Method

Rui Wang and Yanhui Wang

Abstract The study of boundaries helps to understand the relationship between human activities and the natural environment and guides sustainable planning and construction. However, the traditional method of identifying boundaries based on distance thresholds has limited accuracy, so this study aims to propose a more promising approach. The Bidirectional Buffer (BDB) method uses lines and arcs to distinguish solid and open space on the boundary and therefore has a better ability to describe local spatial characteristics. The Geographic Information System (GIS) was used to perform data computation, buffer analysis, and spatial visualization for the case study. By calculating and comparing indicators of Sinuosity, Concavity, and Openness, the new method was proved to be more accurate than the old method in the cross-scale analysis. In addition, the BDB method could identify the open spaces at the edges and inside of villages and distinguish them according to the boundary characteristics, and thus has good application prospects.

Keywords Rural settlement · Boundary · Open space · Bidirectional buffer method · Geographic information system

1 Introduction

With the acceleration of the industrialization process, China's urbanization has experienced a low starting point and rapid development process. By 2020, the urbanization rate has exceeded 60%, and the continuous shrinkage of space and population will be the main development characteristics of rural areas in the future for a long time. The Rural Revitalization Strategic Plan Implementation Report (2018–2019) released in

R. Wang (✉) · Y. Wang
Research Institute of Architecture, Southeast University, 2 Sipailou, Nanjing 210096, PR China
e-mail: wr0624@seu.edu.cn; r.wang@tue.nl

R. Wang
Urban Planning and Transportation Group, Department of Urban Science and Systems, Eindhoven University of Technology, PO Box 513, 5600 MB Eindhoven, the Netherlands

T. Kang (ed.), *Proceedings of 5th International Conference on Civil Engineering and Architecture*, Lecture Notes in Civil Engineering 369,
https://doi.org/10.1007/978-981-99-4049-3_45

June 2020 pointed out that the policy of guiding rural development by classification is an important basis for promoting the spatial construction of production, life, and ecology in rural China[1]. Strategies such as organizing the land transformation of empty villages, enhancing the land-use value of core villages, making full use of the stock space, and preventing the unnecessary spread of construction land are considered important to achieve sustainable rural development. Only by rational use of rural land, can the local agricultural industry and ecological environment be better protected, and accurate boundary delimitation is the premise of planning and policy-making.

The boundary of rural settlement is the result of the aggregation of houses, which has complex, fuzzy, and uncertain characteristics. It not only reflects the relationship between the village and the external environment but also contains the law of self-organization from the bottom to the top and the wisdom of the ancestors in the construction of the living environment. The boundary of the village is a beautiful landscape for the harmonious coexistence of human beings and nature. However, due to the small scale, scattered location, different forms and surrounded by farmland, it is difficult to define a clear spatial boundary in planning. For a long time, the construction land can only be managed from the scale of a township-level administrative region. As a result, some villages expand disorderly and occupy valuable cultivated land and forest land resources, which has caused devastating damage to the ecological environment. Therefore, it is necessary to have a clear understanding of the morphological characteristics and formation mechanism of the boundary between artificial and natural space. In the face of complex village boundary space, the traditional method only using straight lines has limitations, which cannot truly reflect the scale and type of the natural environment, and easily lead to misreading of features. To overcome these difficulties, a boundary identification method based on the Bidirectional Buffer (BDB) is proposed, and its application advantages are proved by quantitative and graphical analysis.

This chapter is structured as follows. Section 2 provides a literature review of the methods and findings related to boundary identification. Section 3 introduces the BDB method for generating boundary graphics. Section 4 carries out a case study of a village and compares the metrics of the old and new methods. Section 5 discusses the application of the new method in identifying and distinguishing open spaces. Section 6 summarizes the main findings and presents limitations and suggestions for further research.

2 Literature Review

The relationship between local and global space has always been an important topic in morphological research. In 1967, the fractal theory was applied to the study of coastline [1, 2], which explained the correlation of complex and irregular boundaries

[1] Source: http://www.moa.gov.cn/xw/zwdt/202006/t20200608_6346078.htm.

at micro and macro levels through mathematical equations. The method was also used to identify morphological boundaries in European metropolitan areas to determine their morphological boundaries and track changes in boundaries in space and time [3, 4]. In the study of space syntax, the curve fitting of integration between local and global is also an important tool to reveal the law of self-organization [5]. The theoretical experience of morphology also tells us that any kind of texture is located in a larger-scale environment, and also contains elements of a smaller scale level. So, the spatial characteristics of adjacent scales should also be considered for the analysis of a certain level of the urban form [6]. These studies are an important basis for cross-scale boundary studies.

Currently, the study of boundaries mostly focuses on large-scale cities and villages located in cities or suburbs [7]. Because the administrative boundary is generated by the needs of planning and management, it is difficult to divide the spatial realm of human living accurately, so the data on building density, land use, and economic development have been used to estimate the boundaries of the built environment [8]. The data commonly used for boundary identification are satellite images [7, 9], but they are difficult to be applied to some areas due to the high accuracy requirements. With the development of remote sensing technology, multi-source data including land use types, nighttime light images, and road networks are also used to determine urban and rural boundaries [10] and have been found to identify settlement patches with reliable accuracy on a regional scale [11]. The Geographic Information System (GIS) is one of the main tools for boundary analysis, and it has been used to determine the urban growth boundary and the expansion of built-up areas [12, 13]. In recent years, machine learning and artificial intelligence have also been used to identify boundaries with the advantages of automation, low cost, and high efficiency [7, 14].

The distance threshold has been always used in the study of rural morphology. The points on the corners of houses whose spacing is less than a specified distance are connected by a straight line. Although this method is widely used for reference, it ignores the self-organization law of traditional settlements from inside to outside and loses the connection and fractal characteristics of boundary morphology [3, 15]. It also has the following limitations:

- Because the method of distance threshold only connects the points on the boundary through straight lines, it cannot distinguish the house and the open space without a building base map.
- The difference in open space morphology caused by different sizes and layouts of houses on the village edge cannot be shown in the results.
- It is difficult to identify the large open space within the village and between the clusters.
- Therefore, it is necessary to optimize the method to generate more accurate graphics of boundaries and retain more morphological information. The current study can provide a reliable tool for future planning and design work.

The rural settlements in China are generally characterized by small scale and high density, and their spatial form is significantly affected by the natural environment. For a long time, most houses and roads have been built without planning guidance,

resulting in irregularly shaped village boundaries. Therefore, the above methods alone cannot assist in small-scale construction on the edge of the village and the methods of boundary identification and quantification need to be adjusted adaptively.

3 Methodology

The relationship between rural settlement and its surrounding environment was fully considered in the initial site selection, and its boundary morphology was affected by topography, waterbody, vegetation, and houses. Although the elements on the edge of villages seem scattered and disordered, their arrangement is closely related to the internal houses and roads, and integrated with the external environment. Therefore, the land space at the edge of the village is interlaced with the adjacent natural areas, resulting in the edge space and boundary morphology being different from those in the system [16]. For example, some villages are close to the main roads and are surrounded by regular fields, so there are fewer concave-convex changes in the edge area, showing a straight-line boundary shape of a continuous solid interface. Some villages are close to woodlands and small ponds, and the layout of houses and natural elements are intertwined with each other, so the boundary features of discontinuous or tortuous changes are presented. It can be seen that the hard boundary (Fig. 1a) and the soft boundary (Fig. 1b) represent different boundary environment characteristics, and the collection of all soft and hard elements on the boundary curve can reflect the complexity of the village edge space. In addition, the square, courtyard, and ridge inside the village sometimes have characteristics similar to the external environment, and their surrounding houses are arranged regularly, forming an inward boundary interface (Fig. 1c). Compared with the old method, the BDB method breaks through the limitation of using only a single line as the boundary element. The generated curve includes two kinds of linearity: straight line and circular arc. The straight line represents the house with a solid interface, and the arc represents a nonsolid open space (Fig. 1).

The research team proposes a cross-scale boundary identification method, that is, the BDB method, which contains both hard and soft fragments. It uses the positive

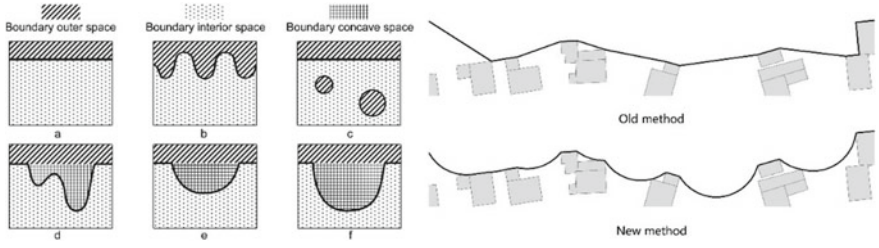

Fig. 1 The BDB method can identify more features of the boundary

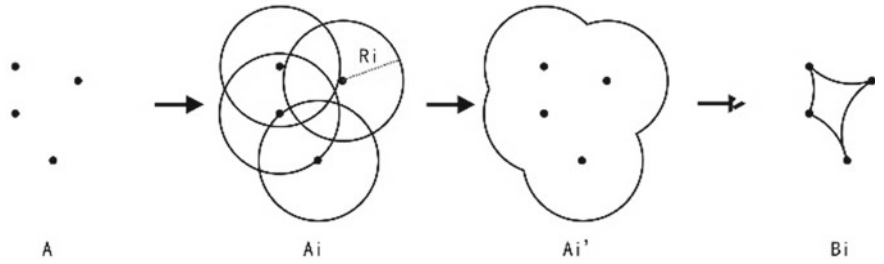

Fig. 2 Steps of the BDB method

and negative transformation of the buffer to complete the integration of the adjacent elements in the base map, simplifies the complex shape, and retains the main spatial features. This method was first applied to the automatic generalization mapping of chart islands and linear elements, with the purpose of merging those islands close to each other or simplifying complex Island boundaries. The solid elements in the settlement exist in various forms, such as columns, walls, and houses, which can correspond to points, lines, and polygons. Since the buffer is the collection of all the point elements within a specified radius around a geospatial element, the buffer transformation of line and polygon elements can be equivalent to the superposition of the transformation results of point elements. The concrete and abstract degree of boundary morphology depend on the selection of buffer distance[2] in the analysis. Although the smaller buffer distance can retain more original graphic features, its ability to integrate adjacent elements is weak, so the generated boundary shape is more complex. Although the larger buffer distance has a stronger integration ability for dispersed elements, it will lose more concave-convex variation features, so the generated boundary is simpler.

ArcGIS software was used for data computation, buffer analysis, and spatial visualization. By setting multi-scale buffer distance, the slice analysis of settlement space can be realized, and the space scale with application value can be selected according to the actual needs. In this study, the BDB analysis was carried out according to the following steps (Fig. 2):

- Transforming the base graph A into Ai by operation of a positive buffer with radius Ri.
- Merging the intersecting parts of graph Ai to obtain the graph Ai'.
- Transforming the graph Ai' into Bi by a negative buffer with radius Ri.
- Extracting the elements including straight lines and arcs in graph Bi as the boundary of graph A.

[2] Under the same analysis scale, twice the buffer distance is equivalent to one time of the threshold distance.

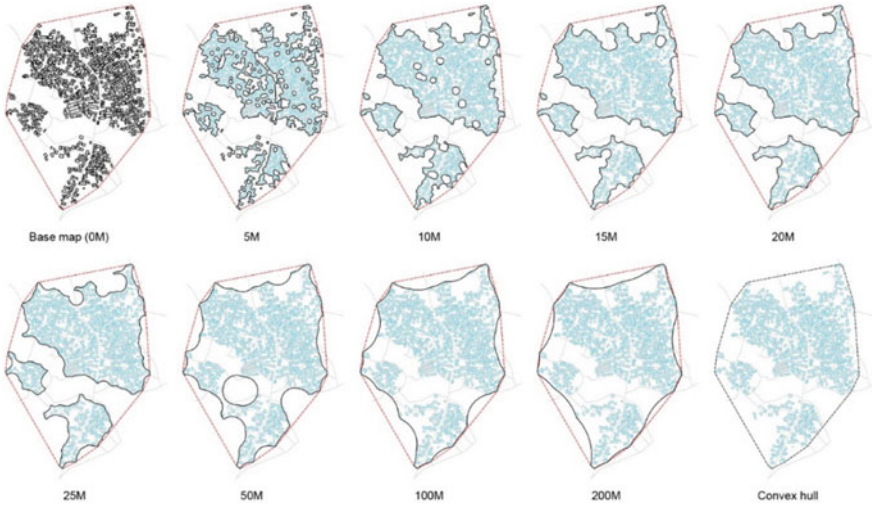

Fig. 3 Village boundary shape from concrete to abstract

4 Case Study and Results

The moderately sized village A was chosen as a case study, which is located on a sloping terrain surrounded by many water ponds and crossed by a valley in the middle. By comparing the overall quantitative indicators and local spatial characteristics of the boundary graphic, the new method is proved to be more accurate and readable than the old method.

The form of boundaries has cross-scale differences from macro to micro, and the macro pattern has a constraint on the micro space [16]. The process of boundary graphics from concrete to abstract is the process of the local features from more to less and the global features from weak to strong. There are two limit states in the set of results: the most concrete solid boundary and the most abstract convex hull boundary[3]. In both traditional and new methods, it is necessary to select the threshold distance or buffer distance of appropriate scale as the generating standard based on different analysis purposes, and abstract the village boundary form appropriately to obtain the boundary curve that can reflect the characteristics of the village. The smaller the analysis scale is, the more concrete the boundary figure is, the smaller the space area enclosed by the boundary is, the larger the total length is, and the closer the shape is to the interface characteristics of the artificial environment such as houses and courtyards. The larger the scale of analysis, the larger the area enclosed by the boundary, the smaller the total length, and the more the shape of the boundary fits the elements in contact with the natural environment (Fig. 3).

Although the environmental conditions of each village are different, as long as the convex hull and solid boundary figure are taken as reference, the spatial correlation

[3] The shortest route around the village.

between the local and the whole of a sample can be judged. The study first calculated the sinuosity (S_i) and concavity (C_i) of the results respectively generated by the two methods with buffer radius from 1 to 15 m, and then judged whether the new method was superior to the old method by comparing the curve trend of the indicators (Table S1).

4.1 Sinuosity

For the local boundary space with the same area of the two depressions, the tortuous change of the longer curve is more obvious (Fig. 1d), while of the shorter boundary curve is smoother (Fig. 1e). Because there is no local depression on the boundary of the convex hull, the change characteristics of concave and convex are the least obvious. The gap between solid boundaries is directly connected with the external natural environment, so it can be considered that it is completely composed of concave space. Therefore, taking the length difference between the solid boundary and the convex hull boundary as a benchmark, the indicator Sinuosity (Si) of different buffer distances can be calculated as:

$$\boldsymbol{S_i} = \frac{\boldsymbol{P_i - P_{ch}}}{\boldsymbol{P_s - P_{ch}}} \tag{1}$$

where P_{ch} represents the total length of the convex hull boundary, P_s represents the total length of the solid boundary, P_i represents the total length of the boundary when the buffer distance R = i. The larger the value of S_i is, the more irregular the boundary curve is, and the closer it is to the solid boundary. The smaller the value of S_i is, the more regular the boundary curve is, and the closer it is to the convex hull boundary. When $\boldsymbol{P_i}$ is equal to $\boldsymbol{P_s}$, $\boldsymbol{S_i}$ is equal to 1, and When $\boldsymbol{P_i}$ is equal to $\boldsymbol{P_{ch}}$, $\boldsymbol{S_i}$ is equal to 0.

4.2 Concavity

For the local boundary space with the same curve length, the smaller area the depression is (Fig. 1d), and the larger area the depression is (Fig. 1f). If the non-solid area within the convex hull boundary of a village is completely filled, then there is no depression in the boundary space at this time. Therefore, taking the area of the area as a benchmark, the indicator Concavity (Ci) of different buffer distances can be calculated as:

$$\boldsymbol{C_i} = \frac{\boldsymbol{A_{ch} - A_i}}{\boldsymbol{A_{ch} - A_s}} \tag{2}$$

where A_{ch} represents the total area of the convex hull boundary area, A_s represents the total area of the boundary area, A_i represents the total area of the boundary

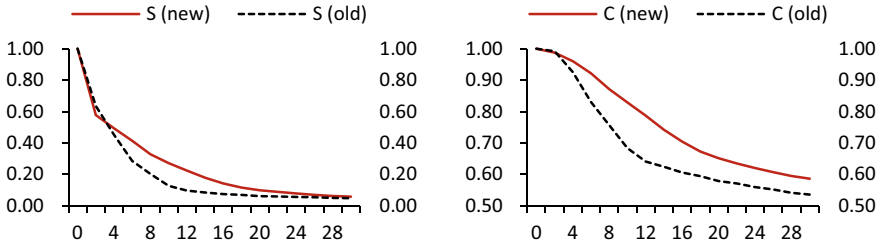

Fig. 4 Indicator S_i and C_i of old and new methods

area when the buffer distance R = i. The larger the value of $\boldsymbol{C_i}$ is, the greater the depression degree of the boundary is, and the closer it is to the solid boundary. The smaller the $\boldsymbol{C_i}$ value is, the smaller the depression degree of the boundary is, and the closer it is to the convex hull boundary. When $\boldsymbol{A_i}$ is equal to $\boldsymbol{A_s}$, $\boldsymbol{C_i}$ is equal to 1, and When $\boldsymbol{A_i}$ is equal to $\boldsymbol{A_{ch}}$, $\boldsymbol{C_i}$ is equal to 0.

By comparing the curves of the new and the old methods (Fig. 4), it can be seen that the new method reaches the maximum later than the old method in the buffer distance range of 0-15 m, indicating that the new method can be applied to a wider range of scale changes. Moreover, the $\boldsymbol{S_i}$ and $\boldsymbol{C_i}$ curves of the new method change more gently, and the slope of the new method is smaller than that of the old method in the range of 0–3 m and more than 10 m, so the identification effect of the new method is better than that of the old method at the micro and macro scales.

5 Discussion

Due to the advantages of multi-scale analysis and more accurate distinguishing ability, the BDB algorithm is suitable for the measurement of complex and changeable open spaces of rural settlements. Based on this, the formation mechanism of its commonness and difference can be further discussed. This method can be applied to more extensive analysis in the future and can assist in planning and design decisions.

5.1 Identification of Open Spaces

Previous studies have demonstrated that the layout of houses at the edge of villages can be adapted to terrain and water conditions, which is one of the reasons for the differences in village boundaries in different natural geographical environments. However, the traditional method cannot distinguish the artificial environment from the natural environment accurately, so it is difficult to further discuss the influence mechanism of this phenomenon at the micro-scale. The advantage of using arc to represent open space is that it cannot only distinguish the boundary elements by line

type but also reflect the opening size and concave degree of the space through its radian and arc length, so that the boundary formed is closer to the real space interface and retains more local feature information. Taking the analysis results of village A in a 15 m buffer radius (corresponding to a 30 m distance threshold) as an example, the new method shows its advantages in four aspects:

Identification of internal open space. In large-scale villages, there are usually some open spaces that retain natural elements. Some of these areas come from the enclosure of the original cultivated land in the process of village expansion, some are ponds that provide domestic water and regulate the local ecological environment, and some provide places for public activities for villagers. As can be seen from area 1 (Fig. 5(1)), the old method can only draw the boundary of the surrounding houses of the village, so it ignores the farmland elements there. However, the new method successfully identifies the inward open space in line with the analysis scale.

Identification of pocket-shape open space. At the southern end of the sample village, there is a concave area connected with the external environment, which forms a semi-open enclosed space around the pond (Fig. 5(2)). Because the old method is based on the span distance, this pocket-shaped area will be sealed, while the new method is based on the relative position of the interface. If the area can accommodate a "circle" with the radius of the analysis scale, it can be identified, so it will not lead to the loss of such spatial information.

Differentiation of local environmental elements. Based on the needs of life and production, ponds and fields are the main environmental elements around the village, and they are usually close to the houses on the border, forming a staggered distribution characteristic. The line graphic generated by the old method will pass through the environmental areas on the boundary (Fig. 5(3)), resulting in the lack of morphological features. However, the arc graphic generated by the new method can bypass these areas and can more accurately divide the artificial and natural elements.

Accurate shape recognition of open space. The old method forms boundary graphics by connecting the corner points of peripheral houses. The disadvantage of this method is that it ignores the wall direction of the edge houses, and the straight

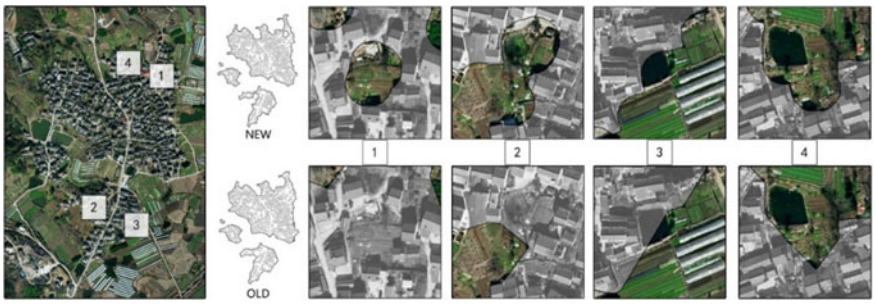

Fig. 5 The BDB method can identify open spaces more accurately

lines formed in some areas will be different from those of the nearby houses, which is easy to mislead the interpretation. For example, in area 4 (Fig. 5(4)), the results of the old method may mislead people into thinking that the area is a rectangular outer space composed of northeast and northwest-oriented houses, but the new method shows that the area is actually composed of an L-shaped hydrophilic space and a concave field.

5.2 Distinction of Open Spaces

The opening degree of rural settlement edge space reflects whether it has a positive attitude to the external natural environment. The measurement process includes two main steps: the first step is to identify and extract the open space on the boundary; the second step is to analyze the spatial openness of different boundary segments.

For the complex house layout and environmental status in the rural settlement edge area, the BDB method can directly distinguish the solid and non-solid spatial elements through straight lines and arcs. In the area with sparse and scattered house layout, there are many open spaces on the boundary, so the proportion of circular arcs is larger than that of straight lines, while in the area with compact and regular house layout, the composition proportion of solid elements is larger, and the number of line segments is more. By calculating and comparing the segment lengths of different elements on the boundary curve of the 25 m buffer radius of samples A and B, it is found that the proportion of solid fragments on the boundary of village B is larger than that of village A (Table 1). This is because village A is located on slope land, and the boundary is mainly composed of small-scale residential buildings. Village B is located on flat terrain, and a large number of industrial buildings are built on the boundary (Fig. 6a). Through field investigation, the research team found that there were indeed differences in perception between these two boundary spaces (Fig. 7a and b).

Different buffer radius analysis results of the same span of boundary fragments contain different information, and their contribution value to the degree of boundary opening is also different. Open space has different scale characteristics. For example, the open interface of a single house with the external environment is closer to the scale of people's living space, while the open space interface of a whole village with the external ecological environment will be affected by a large range of vegetation, terrain, and water. Therefore, the larger the scale, the lower the contribution

Table 1 Percentage of segments in the 50 m buffer radius boundary

	Solid segment (Length/m)	Open segment (Length/m)	Proportion of open segments (%)
Sample A	1182	2376	66.8
Sample B	2122	2653	55.6

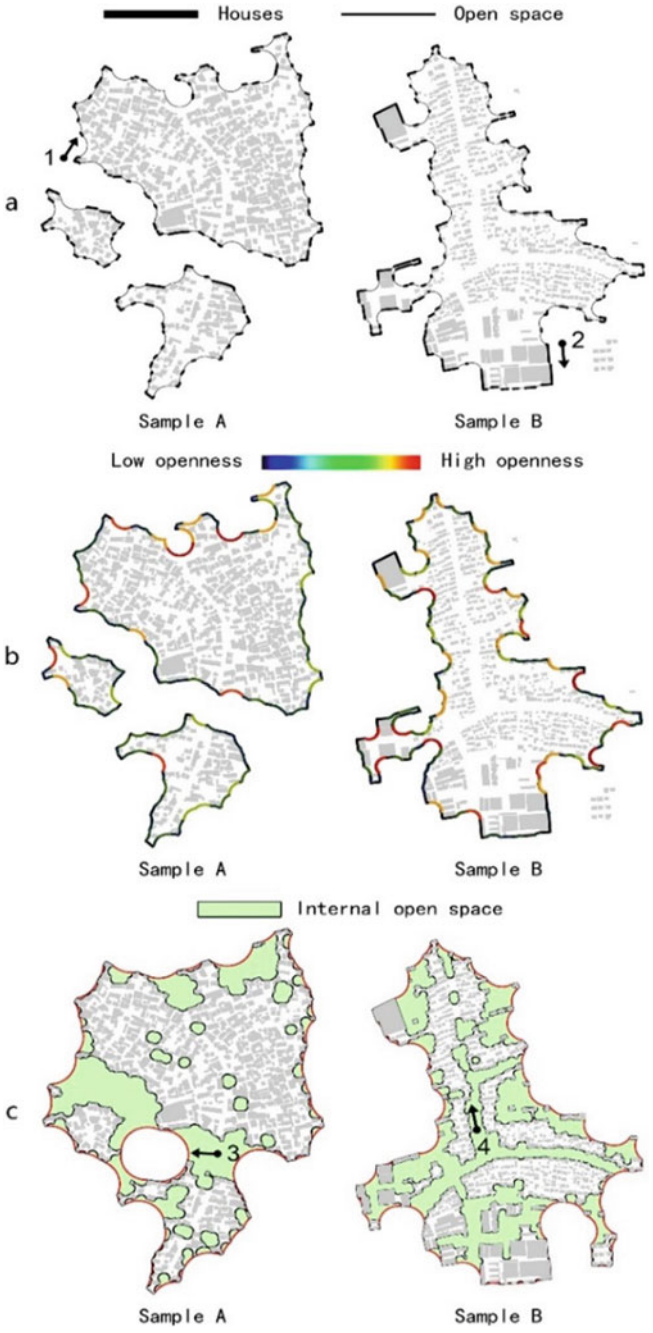

Fig. 6 Using boundaries to analyze the characteristics of open spaces

Fig. 7 Four viewpoints of open spaces

of boundary fragments generated by the local open space to the degree of boundary opening.

If the buffer distance is R, the chord length of a boundary segment is L, and the arc length of the boundary segment is $\mathbf{C} = \sin^{-1}\left(\frac{L}{2R}\right) \times 2\boldsymbol{R}$, and the maximum arc length is $\boldsymbol{C}_{\mathbf{max}} = \boldsymbol{\pi}\mathbf{R}$. Therefore, the Openness indicator (OI) of boundary space is defined as:

$$OI = \frac{\mathbf{C}}{\boldsymbol{C}_{\mathbf{max}}} \tag{3}$$

i.e.

$$OI = \frac{2\sin^{-1}\left(\frac{L}{2R}\right)}{\pi} \tag{4}$$

When $i = 2$R, the maximum of OI is 1. When $i = 0$, the minimum value of OI is 0. When R is constant, the larger L is, the greater the value of OI. When i is constant, the larger the R is, the smaller the value of OI.

To analyze the spatial openness of the boundary segments, the team decomposed the overall boundary of the sample with a buffer radius of 25 m into a set of lines and arcs. The openness indicator of each segment was calculated and distinguished by color (Fig. 6b). The results show that the area with a higher degree of openness is mainly located in the north and west of the village, facing the direction of the increasing slope of the mountain, adjacent to the roads in and out of the village and the ponds scattered on the edge, which indicates that terrain, water, and road factors have a positive impact on the opening of boundary space of village A. On the boundary of village B, in addition to the open space at the intersection with rivers and roads, the surrounding area of factory buildings in the southwest corner also presents an open feature, which is caused by the spatial scale difference of its non-residential function.

The BDB method can also identify the complex open space inside the village. These spaces contain rich natural environment elements and provide places for villagers and tourists to live, produce, and play. They not only reflect the ecological value of rural areas but are an important carrier of village vitality. Because of the lack of accurate boundary identification methods, the quantitative discussion on the layout and shape of the village's internal open space has been ignored in previous studies, while the BDB method can extract the open space within a certain scale range. Taking village A with a ridge crossing in the middle and village B with a river

Table 2 Inward open space between the 50 m and 10 m buffer radius boundaries

	Inward space (Area/m^2)	Total village space (m^2)	Proportion of inward spaces (%)
Sample A	142,110	207,101	31.4
Sample B	182,000	334,575	45.6

crossing in the middle as examples, the boundary graphics of 50 and 10 m buffer radius are calculated respectively, and the open space area within this scale range is obtained by superposition (Fig. 6c). The results show that the proportion of open space area of village B is higher than that of village A, so the overall opening degree of village B's internal environment is better (Table 2). The large-scale open space in village A is concentrated in the middle ridge, and the small-scale open space is distributed in the area with dense houses, while the open space of village B has the characteristics of linear distribution. Through field investigation and comparison of the two kinds of open spaces in current use and scale perception, it can be found that the utilization rate of residents in large-scale open space is low, most of them are for tourism-oriented development, while small-scale open space is generally a place for residents to communicate in daily life (Fig. 7c, d).

6 Conclusion and Prospects

To identify the boundaries and open spaces of rural settlements more accurately, this study proposes a new approach that can compensate for the shortcomings of traditional methods. The BDB method can retain more boundary space information and can distinguish the types of boundary elements and the size of edge space from the building base map. This method firstly expands the positive buffer distance of the base map containing entity elements and then shrinks the merged graphic by a negative buffer distance. By comparing the sinuosity and concavity, this paper proves that the new method has a wider application range in cross-scale boundary analysis. In addition, the new method has advantages in the recognition of concave and convex features of local boundary space, and can more accurately distinguish artificial and natural environmental elements.

The BDB method can deconstruct the spatial base map with different buffer distances and has a good application prospect in the measurement of village boundaries and open spaces. For the small-scale analysis object, it can be used to identify the spatial characteristics such as house layout, street interface, and square shape. For large-scale analysis of objects, it can assist urban design and ecological landscape scope delimitation. Although the current implementation of the algorithm in village boundary identification relies on the ArcGIS software platform, the research team is developing independent software to improve the pertinence and operational efficiency.

Although the current results have demonstrated the significance of the method, a few limitations should be acknowledged. First, the new and old methods can not reflect the impact of terrain on the boundary space in the analysis results, so only flat-terrain villages can be selected as samples. Secondly, low and high walls, soft and hard pavements, eaves of different heights, water surfaces, and cultivated land often have great restrictions on boundary activities. These elements are difficult to distinguish in the analysis base map. Therefore, it is necessary to consider the influence of these elements on the boundary space in the algorithm based on professional knowledge and field investigation.

Acknowledgements This study was supported by the National Natural Science Foundation of China [Award Number: 52178005, 51878143, and 51978142].

References

1. Mandelbrot B (1967) How long is the coast of Britain? Statistical self-similarity and fractional dimension. Science 156:636–638. 10/cn376n
2. Schattschneider JL, Bonetti J (2021) Morphometric characterization of the Brazilian south-southeastern coastline complexity using fractal methods. Rev Bras Geomorfol 22:255–273. https://doi.org/10.20502/rbg.v22i2.1884
3. Tannier C, Thomas I, Vuidel G, Frankhauser P (2011) A fractal approach to identifying urban boundaries. Geogr Anal 43:211–227. https://doi.org/10.1111/j.1538-4632.2011.00814.x
4. Zhao C, Li Y, Weng M (2021) A fractal approach to urban boundary delineation based on raster land use maps: a case of Shanghai. China Land 10:941. https://doi.org/10.3390/land10090941
5. Hillier B (1996) Space is the machine: a configurational theory of architecture. Cambridge University Press
6. Kropf K (2018) The handbook of urban morphology. Wiley
7. Wang X, Xie T, Chen L (2020) Urban village identification from city-wide satellite images leveraging mask R-CNN. In: Ju Z, Yang L, Yang C, Gegov A, Zhou D (eds) Advances in computational intelligence systems. Springer International Publishing, Cham, pp 166–172. https://doi.org/10.1007/978-3-030-29933-0_14
8. Abed J, Kaysi I (2003) Identifying urban boundaries: application of remote sensing and geographic information system technologies. Can J Civ Eng 30:992–999. https://doi.org/10.1139/l03-051
9. Peng J, Hu Y, Liu Y, Ma J, Zhao S (2018) A new approach for urban-rural fringe identification: Integrating impervious surface area and spatial continuous wavelet transform. Landsc Urban Plan 175:72–79. https://doi.org/10.1016/j.landurbplan.2018.03.008
10. Peng J, Liu Q, Blaschke T, Zhang Z, Liu Y, Hu Y, Wang M, Xu Z, Wu J (2020) Integrating land development size, pattern, and density to identify urban-rural fringe in a metropolitan region. Landsc Ecol 35:2045–2059. https://doi.org/10.1007/s10980-020-01082-w
11. Hu X, Qian Y, Pickett STA, Zhou W (2020) Urban mapping needs up-to-date approaches to provide diverse perspectives of current urbanization: a novel attempt to map urban areas with nighttime light data. Landsc Urban Plan 195:103709. https://doi.org/10.1016/j.landurbplan.2019.103709
12. Jiang P, Cheng Q, Gong Y, Wang L, Zhang Y, Cheng L, Li M, Lu J, Duan Y, Huang Q, Chen D (2016) Using urban development boundaries to constrain uncontrolled urban sprawl in China. Ann Am Assoc Geogr 106:1321–1343. https://doi.org/10.1080/24694452.2016.1198213

13. Schuster Olbrich JP, Vich G, Miralles-Guasch C, Fuentes L (2022) Urban sprawl containment by the urban growth boundary: the case of the regulatory plan of the metropolitan region of Santiago of Chile. J Land Use Sci 17:324–338. https://doi.org/10.1080/1747423X.2022.2086312
14. Arribas-Bel D, Garcia-Lopez M-A, Viladecans-Marsal E (2021) Building(s and) cities: delineating urban areas with a machine learning algorithm. J Urban Econ 125:103217. https://doi.org/10.1016/j.jue.2019.103217
15. Tannier C, Thomas I (2013) Defining and characterizing urban boundaries: a fractal analysis of theoretical cities and Belgian cities. Comput Environ Urban Syst 41:234–248. https://doi.org/10.1016/j.compenvurbsys.2013.07.003
16. Forman RT, Forman RTT, Forman RTT (1995) Land Mosaics: the ecology of landscapes and regions. Cambridge University Press

An Examination of the Relationship Between University Facilities and Characteristics of the University's Area Zone: A Case Study of Thammasat University (Rangsit Campus)

Chompoonut Kongphunphin

Abstract University is the heart of the learning society. It serves as a hub for daily living amenities, particularly as a source of knowledge, jobs, trades, and services. Furthermore, the university is a shared living space for a diverse group. The facilities within the university contribute to a one-of-a-kind environment that results in the characteristics of each area zone. This article examines the relationship between university facilities and the characteristic of the university's area zone, which was used by Thammasat University (Rangsit campus) as the research area. The research methodology is based on a survey of key physical facilities' components such as convenience, service, and accessibility. According to the findings, Thammasat University (Rangsit campus) was classified into three distinct area zones: (1) public and service; it was the outer zone that covered a bordering area of the university, which was the highest number of facilities in all dimensions causing to jolly and lively of the area zone, (2) learning, its location was on the center of the university which was the second highest number of facilities, especially as groups of educated buildings supporting learning activities, and (3) residence, it was located in the deepest inner area zone of the university which was the lowest number of facilities in all dimensions that built the restful context suiting for living. The findings of this study can be used as a guideline for policy-making to promote Thammasat University's long-term development (Rangsit campus). They were leading to efficient space management and planning.

Keywords University facilities · Thammasat University (Rangsit Campus)

C. Kongphunphin (✉)
Faculty of Architecture and Planning, Thammasat University, Pathumthani, Thailand
e-mail: kchompoo@ap.tu.ac.th

T. Kang (ed.), *Proceedings of 5th International Conference on Civil Engineering and Architecture*, Lecture Notes in Civil Engineering 369,
https://doi.org/10.1007/978-981-99-4049-3_46

1 Introduction

University is the heart of the learning society. It serves as a hub for daily living amenities, particularly as a source of knowledge, jobs, trades, and services. Furthermore, the university is a shared living space for a diverse group of people [1, 2]. Facilities are a key element in the design and planning of university spaces that facilitate the daily life of students and staff and support the use of people who pass by in the university area [2, 3]. Types and the number of facilities in the various factors, the main influent factors such as users' groups and sizes, and the university's locations and sizes [2–5]. Normally, the university area is divided into different zones based on functions such as education, recreation, service, or residence zones [2, 4]. However, the university facilities in each zone are allocated for supporting activities that represent the zone's character [6]. Besides facilitating daily life for people, university facilities contribute to a one-of-a-kind environment that results in the characteristics of each university's area zone. Moreover, the design and layout of the utility spaces and facilities within the university should be consistent with public transport, roads, parking, buildings, public spaces, and urban landscape management. It also needs to consider the benefits to people and cities in three main aspects: (1) physical and ecological quality, by helping to maintain the original natural environment of the district where the university is located and to enhance the specific characteristics of the district to be clear, (2) behavior and functional quality, by helping to promote the use of facilities by diverse groups of people in the neighborhood and encourage people to have good social interactions with each other, and (3) aesthetic and visual quality, by helping to create a good environment and beautify the university surrounding area that can attract people who pass by to use the area, as well as being able to create good memories for those who come to visit or work in the area [5].

Thammasat University (Rangsit Campus) is located in a suburban area of Bangkok Metropolitan Region: BMA, with various environmental contexts, land uses, building uses, and groups of people. Many facilities support various activities, such as parks and plazas for relaxation, stadiums, and gyms for physical activities, libraries and learning centers for study and research, convenient stores, banks, and pharmacies for convenience in daily life routine, and there are several modes of transportation connecting the university and the city. Thus, it can be said that Thammasat University (Rangsit Campus) is the heart of its neighborhood, social, economic, and environmental development. With a 1,143,853 m^2 area, the university is the biggest education and research center in the northern metropolitan area of Thailand that supports social interaction and doing activities together among the university's crew and people who live around the university by using facilities located in the university [7–9].

This study examines the relationship between university facilities and the characteristic of the university's area zone by analyzing the survey results of the physical features and facilities. The findings of this study can be used as a guideline for policy-making to promote Thammasat University's long-term development (Rangsit campus).

2 Related Research on University Facilities and University Functional Area Classification

2.1 University Facilities

University facilities are public facilities defined as those basic services which cannot be supplied directly to the individual. They satisfy specific public needs—including safety and security, communication, recreation, sport, education, health, public administration, religious, cultural, and social [10]. Several university facilities need to support research, teaching, learning, and other operations for students, faculty, and staff. They can be classed into five types such as (1) educational basic facilities, which are one of the important facilities frequently used by students and faculty to support their learning and teaching needs. It is composed of a lecture room, laboratory, faculty collaboration, administration room, library, student center, university headquarters, and its facilities [11–13]. (2) Support facilities, it is rest and recreational facilities supporting the quality of life for students and staff. It is composed of a gymnasium, auditorium, electronic computing center, training factory, and open spaces or event parks [11–13]. (3) Research facilities, it is a laboratory for research, a graduate school, a research institute affiliated with a university, and auxiliary facilities [11]. (4) Attached facilities, composed of houses or apartments of museums, faculty, staff, graduate students, and researchers. And their auxiliary facilities and affiliated schools many patterns [11, 12]. (5) Transport facilities, this facility is like a lifeline for the university covering all transport such as footpaths, bicycle lanes, streets or roads, and parking [12, 13].

2.2 University Functional Area Classification

A university area composes of three main roles for buildings, open spaces, and facilities and transportation systems [14, 15]. Areas for buildings are planned for groups of buildings supporting educated activities which concluded as administration, education, and learning service. Open space areas are planned for outdoor activities, rest, and recreation. The design of the spaces is related to scenery and perspective that promote the distinctiveness of the university context. Facilities and transportation system areas are the systematization of relationships between elements together in the university by connecting different areas by creating various forms of traffic systems to access areas and buildings.

The university's functional area can be classified into four main basic zones of sharing, educational, residential, and public activity and service. Moreover, service areas are another functional area that appeared in some universities [14–16]. (1) Sharing area zone is a common functional area used by staff and students, including the central library, office of the president, and common faculty buildings. Their locations are located in a position that is easily accessible from other buildings.

The grouping of buildings and the landscape should emphasize the perspective and promote the aesthetic of the area such as the arrangement of the building together with the courtyard in the front aisle. (2) Educational area zone is the area, where buildings are affiliated with various faculties. The location of this zone is related to the common area, where students travel high rate of traffic. Its areas will also have a covered pedestrian system connecting the educational buildings. Its landscape designs are focused on creating an atmosphere that promotes education. (3) Residential area zone is the highest privation zone. This zone is created an atmosphere that is more conducive to living rather than just accommodation, it is organized in the form of a community space by providing common spaces such as recreation, sports, and green spaces. (4) Public activity and service zones are usually arranged around the periphery, and separate access is not mixed with the other zones. This zone is planned to be used to share with the community, usually providing a large parking area to support the use. These functional areas are concluded as sports, arts, and culture sections, and public service areas that generate income for the university such as hospitals, convention centers, and sports complexes. However, there should be a walkway connected to the other zones of the university so that university users can access them.

3 Research Methodology

This study used Thammasat University (Rangsit Campus), with a utility space of 1,143,853 square meters, as a study area. The university is located in a suburban area of Pathumthani province, one of six members of the Bangkok Metropolitan Region: BMA. The adjacent boundary of the university is an open space, group of buildings, and thoroughfare, as presented in Fig. 1.

To get the relationship between the university facilities and characteristics of the university's area zone, there are two steps of the analytic; (1) an identification of physical surroundings and area zones and (2) an analysis of the relationship between roles and facilities in each area zone as showed in Fig. 2.

3.1 An Identification of Physical Surroundings and Area Zones of Thammasat University (Rangsit Campus)

An identification of the university's physical surroundings and area zones can be obtained from an analysis of the physical features survey together with secondary data. The key components of the physical features survey comprise area boundary, building and land use of surroundings, the function of buildings and spaces within the university, and types, locations, and the number of facilities within each zone of the university.

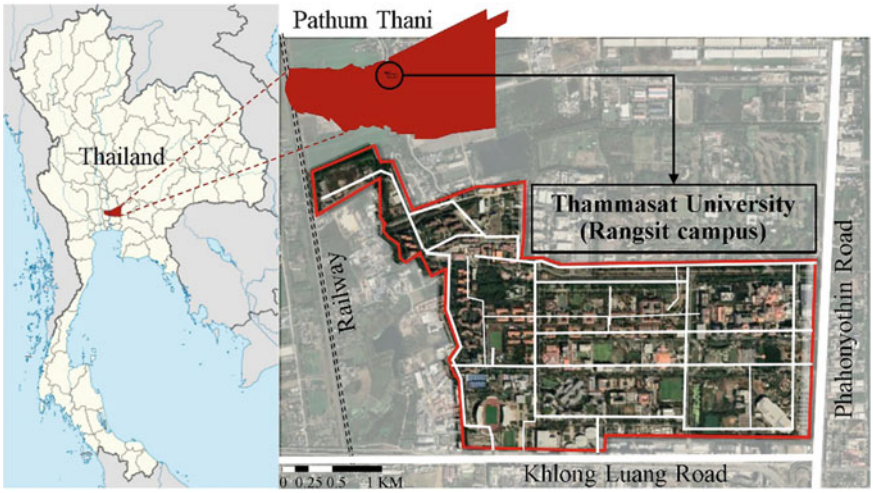

Fig. 1 Study area

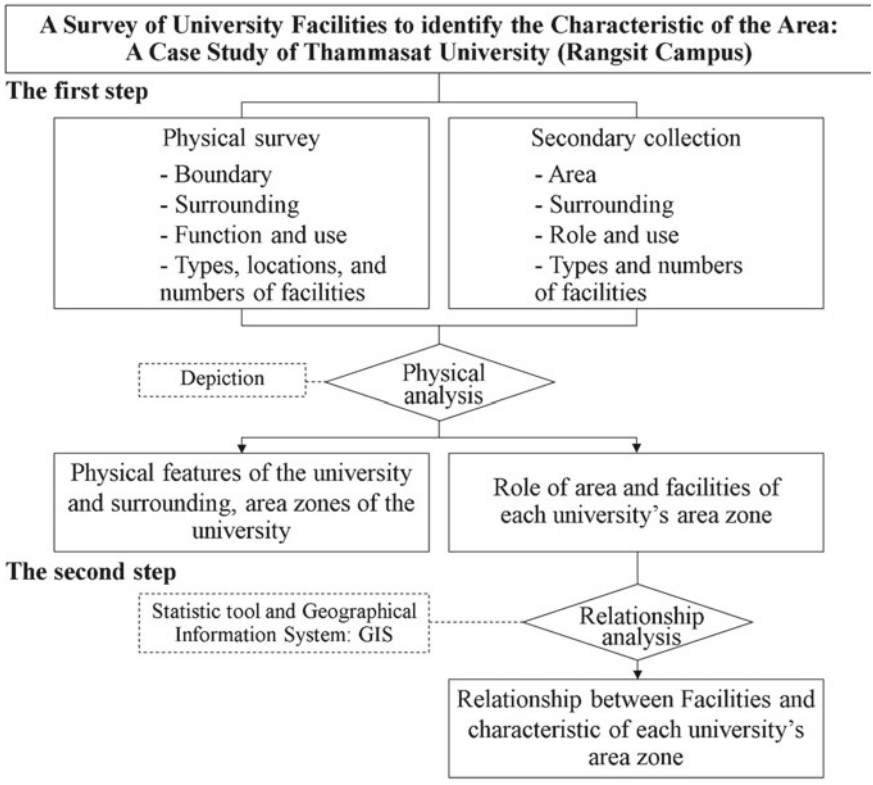

Fig. 2 Analytical framework of the study

The physical features of the surroundings and the university are zoned and used as the base map for the next step.

3.2 An Analysis of the Relationship Between Roles and Facilities in Each university's Area Zone

Each zone of the university obtained from the first step is considered on roles and facilities. The facilities types of the study are classified into three dimensions, covering all kinds of facilities allocated in the university, such as convenience, service, and accessibility.

(1) Convenience covers all facilities that support daily life routines such as food and beverage, convenience store, bank, post office, pharmacy, barber, bookstore, and petrol or gas station.
(2) Service covers all facilities that support quality of life, both physical and mental health, such as hospital, library, learning center, museum, convention hall, drama studio, Buddha hall, sports center, gym, stadium, plaza, park, and landmark.
(3) Accessibility covers all connection routes such as Thammasat University natural gas for vehicle stop (TU NGV stop), parking, shuttle service center, and university gate.

The number of facilities in each zone is calculated by a statistical tool and plotted their locations by the Geographical Information System (GIS). The plotting map of facilities in each zone will represent the relationship between the area characteristics and their facilities.

4 Results and Discussion

4.1 Physical Surroundings and Area Zones of Thammasat University (Rangsit Campus)

According to the consideration of the facilities' components that have been influenced by the character of each zone in Thammasat University (Rangsit Campus), which have been presented in Fig. 3, it has been found that the adjacent boundary of the university was open spaces, group of buildings, and thoroughfare. In the North, it was surrounded by educational and research institutions such as the Asian Institute of Technology: AIT and the National Science and Technology Development Agency: NSTDA and agricultural areas. In the East and South, its boundary was adjacent to the main roads, Phaholyothin and Klong Luang. There were also densely located rental accommodations and food stalls between Klong Luang road and the university in the South. In the East and South, its boundary was adjacent to the main roads,

Phaholyothin and Klong Luang. There were also densely located rental accommodations and food stalls between Klong Luang road and the university in the South. In the west were rental accommodations and Thammasat University train station.

Considering the used area's role, Thammasat University (Rangsit Campus) classified the university area into three zones; public and service, learning, and residence. In terms of the public and service zone, the outer zone covered the most area, 62.45% of all. It was a broader area of the university used for various social activities that various people used together, both open spaces and buildings. Moreover, it had many access connections from its surrounding area, especially the main road in the East

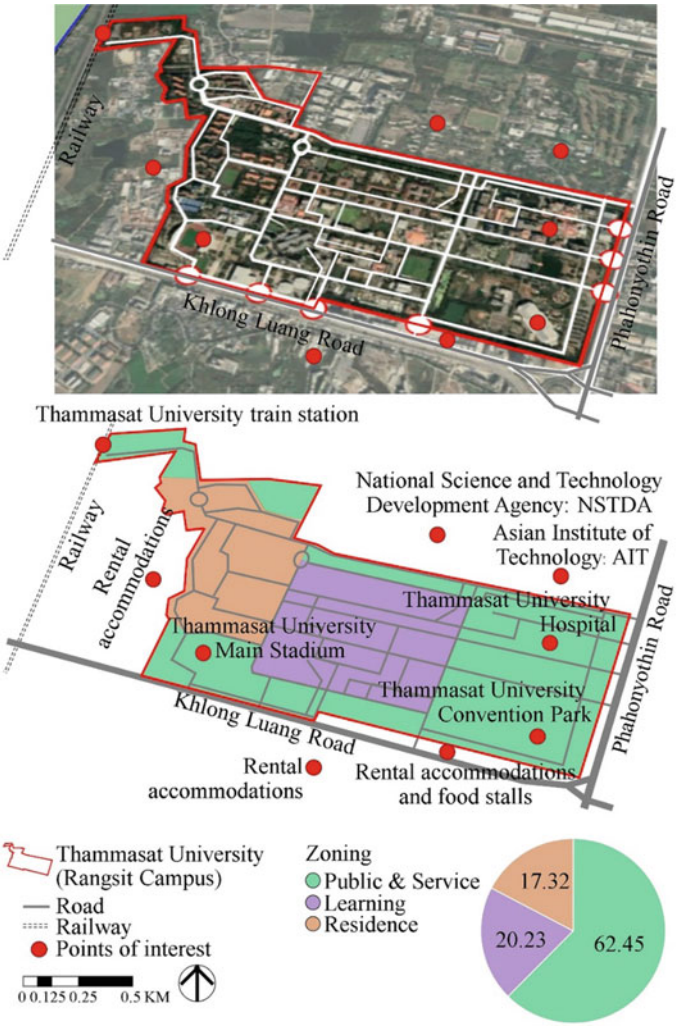

Fig. 3 Physical surroundings and area zones of Thammasat University (Rangsit Campus)

and South. The context of this zone was lively all time, especially in the South, the area connected to Klong Luang road, which was clustered by food booths and private accommodations that service all day and night. In the case of the learning zone, the zone was located in the center of the university. It covered the second most area, 20.23% of all. Most of its area was covered by buildings that students and staff used for educational activities. The context of the zone was lively only during the daytime and working day. The residence zone was located in the deepest inner zone of the university. It covered the smallest area, 17.32% of all. Its area was used as living welfare for students and staff of the university. The context of the zone was restful.

4.2 Relationship Between the Physical Characteristic of Each Zone and Its Facilities

According to the consideration of the facilities' components that have been influenced by the character of each zone in Thammasat University (Rangsit Campus), which have been presented in Figs. 4 and 5, it has been found that the university facilities service in each zone represented to role and function of the university's areas. The public and service zone was the highest number of facilities in all dimensions, followed by the learning and residence zones, the total components were 54, 36, and 24, respectively.

The result of the facilities survey found that in the public and service zone, its 54 facilities' components consisted of 11 components of convenience; food and beverage (5), convenience store (3), bank (1), pharmacy (1), and post office (1), 16 components of service; convenience hall (1), hospital (1), sports center service (2), gymnasium (3), main stadium (1), flick field (1), extreme plaza field (1), plaza (1), park (3), rice field (1), and landmark (1), and 27 components of accessibility; parking (15), shuttle service center (1), TU NGV stop (3), and gate (8). In the learning zone, its 36 facilities' components consisted of 11 components of convenience; food and beverage (6), bank (2), pharmacy (1), post office (1), and bookstore (1), and ten components of service; library (2), museum (1), learning center (1), drama studio (1), landmark (5), and 15 components of accessibility; parking (8), and TU NGV stop (7). In the residence zone, its 24 facilities' components consisted of 8 components of convenience; food and beverage (3), convenience store (3), pharmacy (1), and barber (1), and three components of service; Buddha hall (1), and landmark (2), and 13 components of accessibility; parking (4), shuttle service center (1), and TU NGV stop (8).

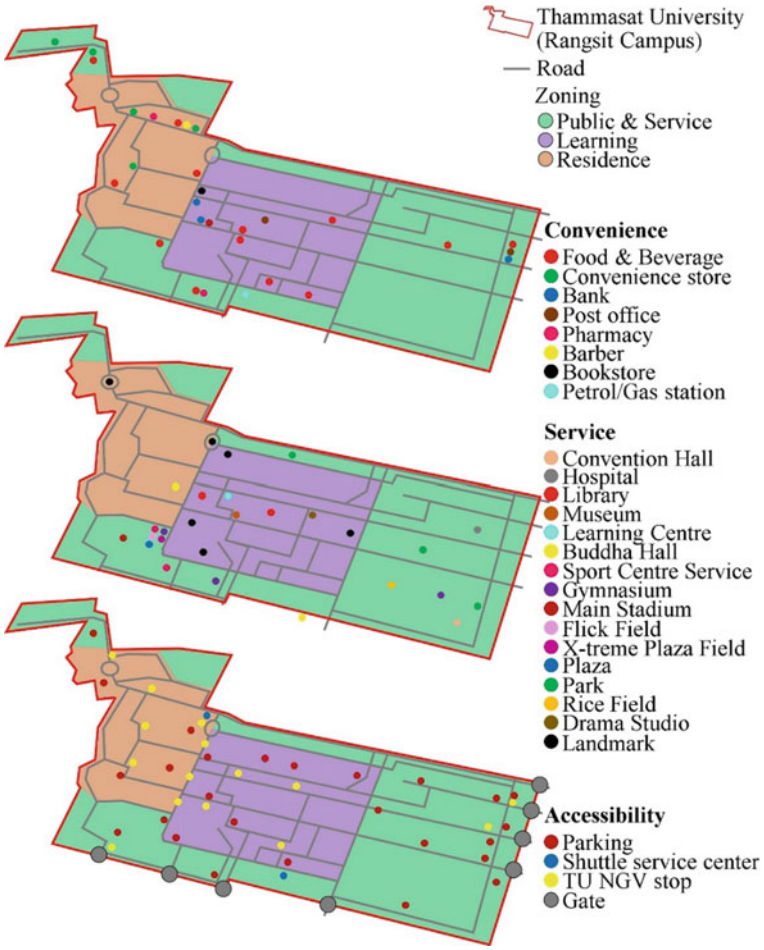

Fig. 4 Components of facilities and their locations in Thammasat University (Rangsit campus)

5 Conclusion and Discussion

It can be concluded that there is a significant relationship between the university facilities service and the characteristic of the university's area zone of Thammasat University (Rangsit campus). The number of facilities in the outer zone of the university public and service was the highest for serving various activities of various groups of users; meanwhile, the context of the zone that lively both in daytime and nighttime. Whereas, the number of facilities in the university's deepest inner zone, which was the residential zone for staff and students, was the lowest, consistently with the area that was the most private zone. Moreover, in the learning zone, most of the facilities

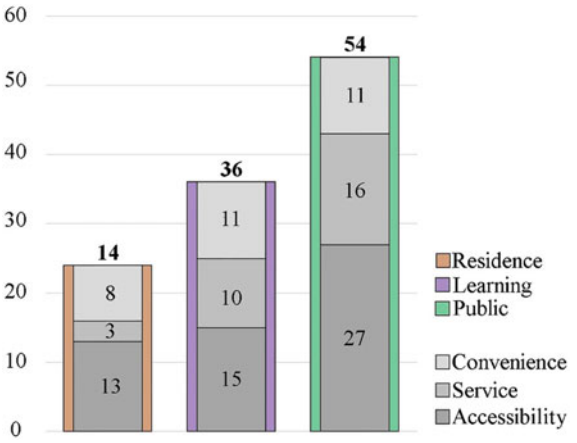

Fig. 5 Bar charts show the number of facilities of Thammasat University (Rangsit campus)

were groups of buildings that supported learning activities; its sense of place was filled with a feel of study and research.

Despite the functional area zones of Thammasat University being classified into three zones, different from the previous study, but their zoning plans were according to the design planning and concept of the university planning of the previous studies. The university facilities located in each university functional area zone promote the notability of characteristics of each area zone.

In addition to the research results, there are considerations from research synthesis as follows: (1) The results of this study are obtained from the analysis that focused on physical factors. For more clear results, economic and social factors should be considered in further studies. (2) The university facilities that appeared at Thammasat University were different from others, this was the limitation of the study that represented the diversity of type, size, and location of the university.

References

1. Center of Innovative Design and Research. A final report of Thammasat university master plan 2034. Thammasat University Press, Pathumthani (2019)
2. Kongphunphin C, Ruangrattanaumporn I, Iamtrakul P (2015) Sustainable road safety towards campus town development. In: Thaneerananont P (ed) Proceeding of the 10th national transport conference. Siam Printing, Bangkok, pp 114–124
3. Thammasat University (Rangsit campus) (2022) Life at Thammasat. https://tu.ac.th/campus life
4. Reed J (2007) Perceptions of the availability of recreational physical activity facilities on a university campus. J Am Coll Health 55(4):189–194
5. Abdullah N, Mohamad N (2016) University recreational facilities service quality and students physical activity level. Procedia Soc Behav Sci 224(15):207–212
6. Lau SSY, Gou Z, Liu Y (2014) Healthy campus by open space design: approaches and guidelines. Front Architectural Res 3(4):452–467

7. Abu-Ghazzeh TM (1999) Communicating behavioral research to campus design: factors affecting the perception and use of outdoor spaces at the university of Jordan. Environ Behav J 10(2):765–804
8. Ojeda O, Yudell M (1997) Campus and community English dictionary, 1989, 2nd edn. Oxford University Press, Oxford
9. Marcus CC, Francis C (1998) People place: design guidelines for urban open space, 2nd edn. Wiley, New York
10. City of Irvine general plan (2019) Public facilities and services. https://legacy.cityofirvine.org
11. Kim MS, Kim JH (2020) Effective university facility management plan proposal reflecting the needs of the main users. Front Psychol 11(219)
12. Han X, Cheng H (2017) Analysis on design principles of public facilities on campus and its adaptability to campus environment. Advan Soc Sci, Educ Humanit Res 124(2017)
13. Creatrixcampus (2022) 10 strategies support university campus facilities management. https://www.creatrixcampus.com
14. Ekabot P, Janjamlha T (2010) Characteristics of the third area of the Thammasat university community (Rangsit campus). National Research Council of Thailand
15. Dober RP (1963) Campus planning. Reinhold Publishing Corporation, New York
16. Schmertz MF (1972) Campus planning and design, 1st edn. McGraw-Hill

The Interactive Effects of Water and Greenery on Landscape Preference in Historic Town

Kunlu Song, Jiang Liang, and Hui Sun

Abstract It has been proved that water and greenery can significantly improve the preference for landscape due to their natural and healing characteristics. However, most previous studies have focused on the independent effects of water or greenery instead of the interactive effects, which have created a gap between theoretical predictions and perceptions of reality. Therefore, this study was designed to quantify the interactive effects of water and greenery on landscape preference. The authors generated four sets of simulated pictures of both Western and Eastern historic townscapes by modifying real-world photos. The combination of "with" and "without" scenarios of water and also greenery was provided, while other landscape elements were kept the same. The pictures were evaluated by 68 participants. It was found that: (1) With greenery presented in initial pictures, the increased degree of landscape preference brought by adding water was significantly better than that without greenery. Similarly, the effects of adding greenery were also greater when water already existed. (2) Furthermore, when water and greenery were both presented in the picture, the increased degree of landscape preference was greater than the sum of the increased degree brought by only water and only greenery. (3) Similar results were shown by four sets of simulated pictures, although they had different cultural styles or spatial structures. When making improvement with a limited budget, the findings of this paper can help townscape planners make low-cost interventions by choosing strategic sites and adding effective elements based on existing landscape resources.

Keywords Landscape preference · Interactive effects · Water · Greenery · Historic towns

K. Song · J. Liang (✉) · H. Sun
School of Architecture and Fine Art, Dalian University of Technology, No. 2 Linggong Road, Dalian 116024, China
e-mail: sunliang@dlut.edu.cn

T. Kang (ed.), *Proceedings of 5th International Conference on Civil Engineering and Architecture*, Lecture Notes in Civil Engineering 369,
https://doi.org/10.1007/978-981-99-4049-3_47

1 Introduction

The historic town is the crystallization of the interaction between human civilization and the natural environment in an area and is an important part of the world's historical and cultural heritage. Historic towns have attracted many people whether as living places or tourist destinations. A more pleasant landscape in historic towns can improve the living quality of residents and enhance the tourism value of historic towns [1]. However, due to naturally declining or commercial erosion, the landscape of a considerable number of historic towns has been destroyed. As a result, people's perception and evaluation of these towns are gradually reduced. In fact, as the economic, cultural, and transportation center of a region, historic towns are often located near the mountains or surrounding water. This makes most historic towns have rich ecological and cultural resources. How to make these precious landscape resources play a greater effect through improvement planning, has become an urgent problem to be solved.

Among the numerous landscape elements that can affect preference, architecture, water, and greenery are the most important three. Architecture is the core element that distinguishes the historic town landscape from the purely natural landscape. The preference for water as a landscape element has been widely proved in previous studies, which is in line with the evolutionary theories that water is one of the most important elements for life [2, 3]. Because of fractal-like and recursive complexity, greenery elements often trigger people's more positive affective responses and decreased mood disturbance compared to the built-up street [4–6]. Previous studies about landscape preference often compared urban and nature as opposites of the dichotomy [7]. However, in historic towns, artificial construction and natural elements are fully integrated, so we need to focus on the combination of the above three kinds of elements. From the perspective of practice, in the process of townscape improvement, protecting buildings, dredging waterways, and increasing greening are all common means in line with the protection policy of the historic town [8]. Therefore, in this study, the building is taken as a fixed element, while water and greening are regarded as variable elements. To study how the addition of water and greenery affects people's landscape preference for a historic town scenery when the architectural elements remain unchanged. This choice has more realistic significance.

Different landscape elements may emphasize each other and resonate, or they may conflict with each other and weaken themselves [9]. Some of the previous studies on landscape preference of historic towns attributed people's preference for the overall scenery to the inherent characteristics of each landscape element in the scenario. The interaction effects such as contrast, setting off, and echo produced when different landscape elements are combined into a whole are not considered [10, 11]. Some studies have compared different combinations of elements, but due to the ordinal measurement methods used to measure preference values, such as the Likert scale, the interactive effects cannot be quantitatively analyzed [12]. At present, the research on the interactive effects of water and greenery in historic towns is still insufficient.

Therefore, the main research purpose of this paper is to quantitatively analyze the influence of two landscape elements, water and greenery, and their interactive effects on landscape preference in historic towns. Thus, it can provide theoretical guidance for townscape improvement and enhance landscape preference more effectively with limited intervention.

2 Methods

To achieve the above research purposes, we generated different historic town landscape simulated pictures and investigated the participant's preference degree for the landscape shown in different pictures. Among them, the preference values of the scenery shown in the picture are the dependent variable. The presence of water elements in the simulated picture is the independent variable 1, including two levels of "with" and "without". The presence of greenery elements in the simulated picture is independent variable 2, which also includes two levels of "with" and "without". The objectives of the experiment are: (1) Test for main effects. For a historic town scenery, how does the presence of water elements affect people's preference of this scenery? How does the presence of greenery elements affect people's preference of this scenery? (2) Test for interactive effects. Is the improvement effects of water or greenery on landscape preference affected by the existing state of each other?

2.1 Stimuli

Simulation experiments with pictures modified by computers are a common method for visual preference investigation [13]. This method makes up for the defect that it is difficult to strictly control environmental variables in field surveys and can accurately observe the changes in the results brought by specific manipulations. The stimuli pictures used in this research were modified according to the real-world photos of the historic town landscape (see Table 1). Four pictures were in a set. The four pictures in a set are identical in their architectural parts. Water and greenery correspond to four variable level combinations of 2*2. picture 1 without water without greenery, picture 2 with water without greenery, picture 3 with water without greenery, and picture 4 with water with greenery. And picture 4 is consistent with the specific forms of water and greenery in pictures 2 and 3. To ensure the reliability of the results, four different sets of stimuli pictures are designed according to this rule. They represent two spatial structures, namely waterfront and street, and two cultural styles, Western and Eastern historic towns. To avoid visual differences between real photos and collaged pictures, the stimuli pictures used in this research were collaged and modified, and all pictures were not original photos.

Table 1 Stimuli pictures for landscape preference test

	Western historic townscapes	Eastern historic townscapes
Structure of edge	 a. 1st set of simulated pictures	 b. 2nd set of simulated pictures
Structure of path	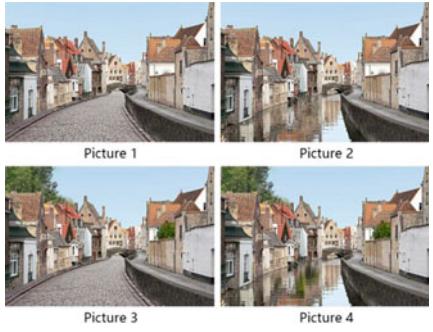 c. 3rd set of simulated pictures	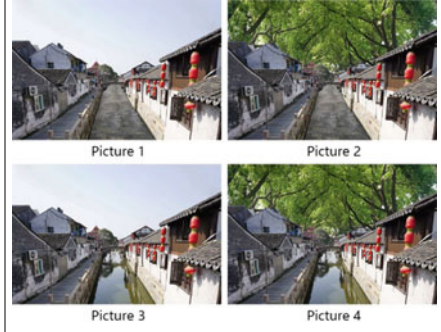 d. 4th set of simulated pictures

2.2 Participants

Previous studies have shown that there is no significant preference difference between the public and designers, men and women, students, and other demographic groups of visual environment preferences [14]. Students are generally considered as acceptable population samples for landscape preference surveys [15, 16]. Therefore, we recruited 68 students from the School of Architecture and Fine Arts of Dalian University of Technology as participants, including 31 males and 37 females.

2.3 Measurements and Calculation

Questionnaire Design. This study pays more attention to the improvement effect brought by the addition of water and greenery to the overall scenery, that is, the difference of preference between different stimuli pictures. Therefore, pairwise comparison was used to score the relative preference of the pictures in this survey. Each picture within the same set was compared with three other pictures separately once, and pictures between different sets were not compared with each other. The guiding question in the survey is as follows: if you visit a historic town and you can only see one of the sceneries in the two pictures, which one would you prefer to see? You only need to make a relative preference assessment between the two pictures that appear together at a time. Participants were asked to indicate their ratings for relative preference on a five-point Likert scale (1: like equally, 2: a weak preference, 3: a clear preference, 4: a strong preference, 5: a very strong preference). In each comparison, participants were required to record two items of relative preference picture and relative preference degree in the questionnaire. A total of six pairwise comparisons can be made between the four pictures in each set, and the four sets of pictures have 4*6 relative preference results.

Data Transformation. During statistical analysis, six relative preference results in each set are transformed into a pairwise comparison matrix (see Table 2). The transform method is as follows: suppose that in the comparison between picture 1 and picture 3, the relative preference picture selected by the participant is picture 3, and the relative preference degree is 4. In the comparison matrix of the current set, the value of $\boldsymbol{a}_{31}$ is 4, and the inverse of $\boldsymbol{a}_{13}$ is correspondingly 1/4. Therefore, the 4*6 comparison scale results of four sets of stimuli pictures can be transformed into four comparison matrices. Then, the researcher calculated the relative preference weight of each participant to the four pictures in the set according to the comparison matrix, which was used as the value of the dependent variable for subsequent analysis.

In this paper, the geometric mean method is adopted to calculate the relative preference weight $W = [w_1, w_2, \ldots, w_n]^T$ of picture 1 to picture N in the pairwise comparison matrix as follows: (1) and (2) are used to calculate the preference weight, and (3) and (4) are used to check the consistency of the comparison matrix.

Table 2 According to the questionnaire data to construct pairwise comparison matrix

	Picture 1	Picture 2	Picture 3	Picture 4
Picture 1	$a_{11} = 1$	$a_{12} = 1/a_{21}$	$a_{13} = 1/a_{31}$	$a_{14} = 1/a_{41}$
Picture 2	$\boldsymbol{a}_{21}$	$a_{22} = 1$	$a_{23} = 1/a_{32}$	$a_{24} = 1/a_{42}$
Picture 3	$\boldsymbol{a}_{31}$	$\boldsymbol{a}_{32}$	$a_{33} = 1$	$a_{34} = 1/a_{43}$
Picture 4	$\boldsymbol{a}_{41}$	$\boldsymbol{a}_{42}$	$\boldsymbol{a}_{43}$	$a_{44} = 1$

- Multiply the elements in each row of the comparison matrix and extract a root to calculate the geometric mean $\overline{w}_i$ of each row:

$$\overline{w}_i = \sqrt[n]{\prod_{j=1}^{n} a_{ij}}, (i = 1, 2, \ldots, n) \tag{1}$$

- The preference weight vector w_i of each picture is normalized by $\overline{w}_i$:

$$w_i = \frac{\overline{w}_i}{\sum_{j=1}^{n} \overline{w}_i}, (i = 1, 2, \ldots, n) \tag{2}$$

- Calculate the eigenvalue $\lambda_{\max}$:

$$\lambda_{\max} = \sum_{i=1}^{n} \frac{(AW)_i}{nw_i} \tag{3}$$

  where A is the comparison matrix constructed as given in Table 2, and W is the weight matrix calculated in step (2). $(AW)_i$ represents the i th scalar of the column vector AW.
- Calculate consistency ratio (CR):

$$CR = \frac{\lambda_{\max} - n}{(n-1)RI} \tag{4}$$

  If CR was less than 0.10, the consistency check was passed, and if CR was greater than or equal to 0.10, it was not passed. Among them, RI is the random index. When $n = 4$, RI $= 0.89$ can be obtained by looking up the table of comparative values from random matrices. Only when the consistency check is passed, the relative preference weight vector of the four pictures obtained in step (2) is effective. On the contrary, it shows that the participant's comparative scoring of this set of pictures is contradictory and inadmissible.

By constructing a pairwise comparison matrix, the ordinal data in the questionnaire, relative preference degree, was transformed into scale data, the relative preference weight of each picture. On the one hand, it can eliminate the influence caused by

different participants' absolute preferences for the same picture. On the other hand, the preference means difference between different pictures in a set can be compared with each other to verify the interactive effect.

2.4 Experimental Procedure

The experiment was conducted in a combination of online and offline. The test pictures were broadcast live through the shared screen function of Tencent Conference to control the display time of pictures and the filling time of questionnaires. Paper questionnaires to record survey results were distributed offline in advance. After the live broadcast, the questionnaire collection can be completed by each participant taking and submitting their questionnaire photos. During the research, each pair of pictures was compared for 15 s. After 15 s, the pictures were randomly switched to two other comparison pictures within the set. After six comparisons in one set, there was a 20-s rest interval with the next set of test pictures.

3 Results

3.1 The Results of Consistency Checks for the Questionnaire Data

A total of 68 questionnaires are collected in the experiment, and each questionnaire evaluated the relative preference scale of four pictures within each set of stimuli pictures through pairwise comparisons. Since there are four sets of stimuli, each questionnaire can be converted into four comparison matrixes. The 272 (68*4) comparison matrixes were checked for consistency ratio. The number and proportion of questionnaires passing the checks are given in Table 3. Only the comparison matrixes that pass the consistency checks will be used for subsequent analysis.

Table 3 Consistency checks results of the questionnaires

Evaluation targets	Number of questionnaires passing the checks	Proportion of questionnaires passing the checks (%)
1st set of pictures	52	76.47
2nd set of pictures	57	83.82
3rd set of pictures	53	77.94
4th set of pictures	54	79.41

3.2 *Descriptive Statistics of the Preference Values by Participants*

The preference value of pictures in each set converted from the questionnaire data is shown in Fig. 1 The abscissa represents the participants' ID number, while the ordinate represents the relative preference of four pictures in a set. Table 4 presents means and standard deviations for preference values of pictures in each set. Four sets of stimuli pictures with different cultural styles or spatial structures showed similar landscape preference rules in Fig. 1 and Table 4, which can be summarized as follows:

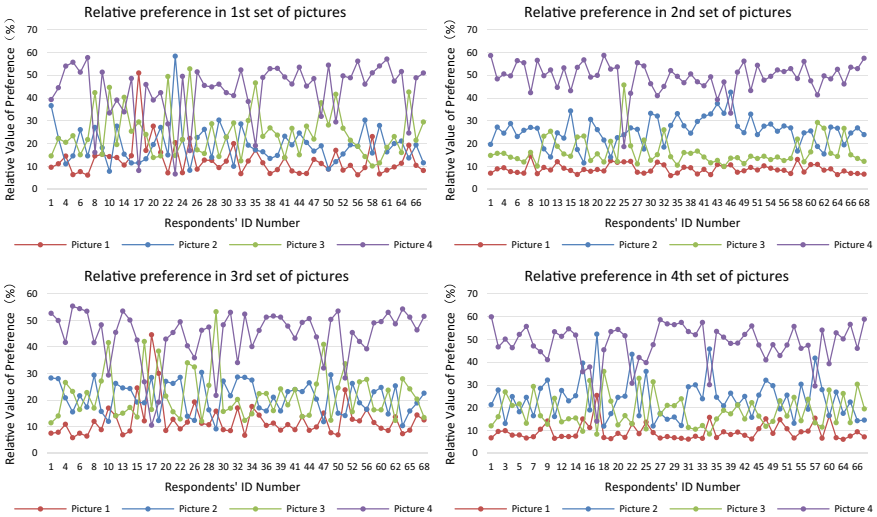

Fig. 1 Relative preference values of all participants who passed the consistency checks

Table 4 Descriptive statistics of the relative preference value (%) between four pictures within each set of stimuli pictures

Source	Mean ± SD			
	Picture 1[a]	Picture 2[b]	Picture 3[c]	Picture 4[d]
1st set (N = 52)	12.73 ± 7.29	19.52 ± 8.45	24.64 ± 10.60	43.11 ± 12.45
2nd set (N = 57)	8.80 ± 1.97	25.49 ± 6.04	16.42 ± 6.11	49.29 ± 6.65
3rd set (N = 53)	12.46 ± 6.60	21.05 ± 5.95	21.93 ± 9.23	44.56 ± 9.71
4th set (N = 54)	9.38 ± 3.67	23.99 ± 8.97	18.46 ± 6.89	48.17 ± 8.71

[a] scenarios without water and without greenery; [b] scenarios with water and without greenery; [c] scenarios without water and with greenery; [d] scenarios with water and with greenery
N number of participants; *SD* Standard deviation

In the four different scenarios shown in stimuli pictures, the lowest preference values consistently correspond to picture 1 in every set (mean = 12.73%, 8.80%, 12.46%, and 9.38%), which have neither water nor greenery in the scenarios.

The preference values of picture 2 (mean = 19.52%, 25.49%, 21.05%, and 23.99%) and picture 3 (mean = 24.64%, 16.42%, 21.93%, and 18.46%) are both higher than picture 1, which indicate that landscapes with water or greenery are more popular in historic towns. In the second and fourth sets, the preference values of picture 2 are higher than that of picture 3, while in the remaining sets, picture 3 is higher than picture 2, which shows that there is no universal phenomenon that water is better than greenery or greenery is better than water. This is in line with the practical experience that preferences of water and greenery are influenced by different forms.

The highest preference values consistently correspond to picture 4, which shows the landscape scenarios with both water and greenery (mean = 43.11%, 49.29%, 44.56%, and 48.17%).

The difference in mean values of the pictures suggests the positive effects of water and greenery on landscape preference. In the next step of our analysis, we aimed to establish the main effects and interaction effects of these two factors through a two-way repeated measures ANOVA.

3.3 Repeated Measures ANOVA on Preference

Two-way repeated measures ANOVA was employed to compare the effects of different scenarios of water and greenery on the participants' townscape preferences. The two independent variables were presence of water and presence of greenery. They all had two levels: with and without, depending on whether there are these two landscape elements in the stimuli pictures. Participants' preference values of stimuli pictures were taken as the dependent variable. SPSS 27.0 was used for all analyses.

Main Effects of Water. The results of the two-way repeated measures ANOVA revealed that there was a significant main effect ($p < 0.001$) of water on landscape preference (Table 5). The effect size $\left(\eta_p^2\right)$ of Adding water in four sets of stimuli pictures was 0.462, 0.927, 0.616, 0.912. All were greater than 0.14, the dividing line of large effects. Ceteris paribus, participants preferred landscape pictures with water over those without.

Main Effects of Greenery. Similarly, Table 5 illustrates the main effect of greenery was also significant ($p < 0.001$), while the effect size in four sets of stimuli pictures was all large ($\eta_p^2 = 0.746, 0.865, 0.795, 0.673$). Ceteris paribus, participants preferred landscape pictures with greenery over those without.

Interactive Effects: Water and Greenery. There was a significant interaction between water and greenery ($p < 0.001$, $\eta_p^2 = 0.272, 0.668, 0.610, 0.646$). Such that the increased degree of landscape preference when water and greenery were both

Table 5 ANOVA results for participants' preference of stimuli pictures[a]

Source		SS	df	MS	F	Sig	η_p^2
1st set	Presence of water	8301.245	1	8301.245	43.768	< 0.001	0.462
	Error	9672.884	51	189.664			
	Presence of greenery	16,381.178	1	16,381.178	149.650	< 0.001	0.746
	Error	5582.643	51	109.464			
	Presence of water * Presence of greenery	1771.864	1	1771.864	19.099	< 0.001	0.272
	Error	4731.323	51	92.771			
2nd set	Presence of water	35,001.125	1	35,001.125	706.035	< 0.001	0.927
	Error	2776.154	56	49.574			
	Presence of greenery	14,075.366	1	14,075.366	358.911	< 0.001	0.865
	Error	2196.142	56	39.217			
	Presence of water * Presence of greenery	3727.705	1	3727.705	112.588	< 0.001	0.668
	Error	1854.118	56	33.109			
3rd set	Presence of water	12,920.513	1	12,920.513	83.579	< 0.001	0.616
	Error	8038.690	52	154.590			
	Presence of greenery	14,417.857	1	14,417.857	201.223	< 0.001	0.795
	Error	3725.862	52	71.651			
	Presence of water * Presence of greenery	2610.829	1	2610.829	81.165	< 0.001	0.610
	Error	1672.678	52	32.167			
4th set	Presence of water	26,508.655	1	26,508.655	547.764	< 0.001	0.912
	Error	2564.898	53	48.394			
	Presence of greenery	14,938.451	1	14,938.451	109.080	< 0.001	0.673
	Error	7258.355	53	136.950			

(continued)

Table 5 (continued)

Source		SS	df	MS	F	Sig	η_p^2
	Presence of water * Presence of greenery	3077.179	1	3077.179	96.613	< 0.001	0.646
	Error	1688.080	53	31.851			

[a] less than 3 levels in the independent variables, so use the value from the sphericity assumed row

presented in the picture was greater than the sum of the increased degree brought by pictures only with water and only with greenery (Tables 4 and 5).

SS Type III Sum of Squares; *df* degrees of freedom; *MS* Mean Square; *F* F ratio; *Sig*. significance; η_p^2 partial eta squared (effect size)

Simple Effects. As shown in Fig. 2, a significant interaction was found in analysis of variance, we need a test of simple effects to reveal the degree to which one factor is differentially effective at each level of a second factor. According to the official support of SPSS software, the test of simple effects can be realized by modifying the syntax code of the "/EMMEANS" clause under the GLM function [17].

The Effects of Adding Water at Different Greenery Levels. Table 6 gives the difference increase in landscape preference caused by adding water at different greenery levels. The results can be summarized as follows:

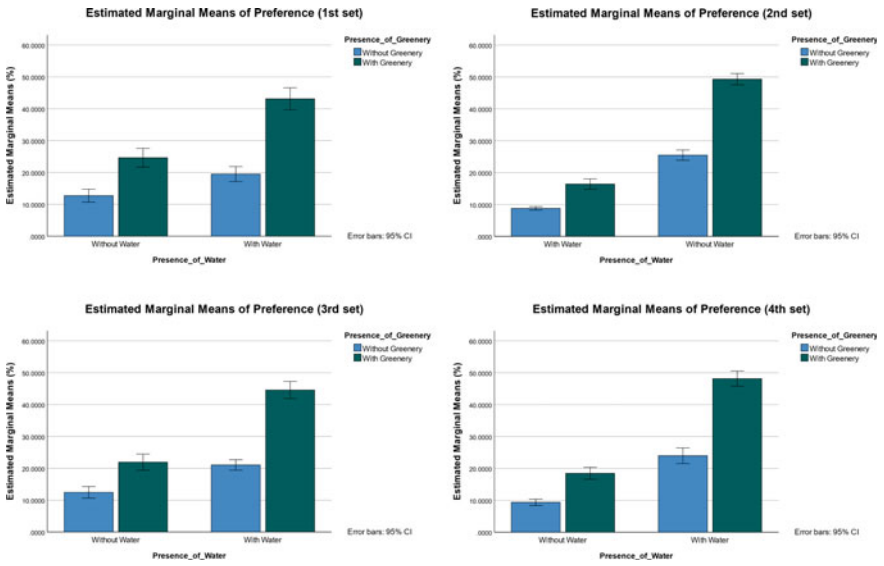

Fig. 2 Means of preference of different stimuli pictures

Table 6 Pairwise comparisons of the effects of water at different greenery levels

Source	Presence of greenery	Presence of water	Mean difference (I–J) (%)	Sig	95% confidence for difference (%)	
					Lower bound	Upper bound
1st set	Without	With (I), Without (J)	6.798	<0.001	3.509	10.087
	With	With (I), Without (J)	18.472	<0.001	12.731	24.214
2nd set	Without	With (I), Without (J)	16.693	<0.001	14.983	18.404
	With	With (I), Without (J)	32.8867	<0.001	29.915	35.819
3rd set	Without	With (I), Without (J)	8.595	<0.001	6.035	11.155
	With	With (I), Without (J)	22.632	<0.001	17.961	27.304
4th set	Without	With (I), Without (J)	14.607	<0.001	12.661	16.554
	With	With (I), Without (J)	29.705	<0.001	26.847	32.563

Firstly, whether there is greenery in the initial picture or not, adding water can effectively improve the landscape preference (all the Mean Difference (I–J) > 0, $p < 0.001$). Secondly, with two different levels of greenery in the initial pictures, adding water can bring a different increase in preference values. Taking the first set of pictures as an example, the difference between means of pictures with water and with greenery and pictures without water and with greenery (I–J = 18.472%) was larger than the difference between pictures with water and without greenery and pictures without water and without greenery (I–J = 6.798%). As can be seen from the stimuli pictures in Table 1, these two different mean differences are caused by adding same water elements into different background environments, which have different levels of presence of greenery. This is an intuitive reflection of the above conclusion that the interactive effect of water and greenery is significant.

The Effects of Adding Greenery at Different Water Levels. Similarly, the results in Table 7 show that: Firstly, whether there is water in the initial picture or not, adding greenery can effectively improve the landscape preference (all the Mean Difference (I–J) > 0, $p < 0.001$). Secondly, when there is water in the initial pictures, the improvement of landscape preference brought by adding greenery is much greater than the improvement brought by adding the same greenery into the initial scenarios without water.

Table 7 Pairwise comparisons of the effects of greenery at different water levels

Source	Presence of water	Presence of greenery	Mean difference (I–J) (%)	Sig	95% confidence for difference (%)	
					Lower bound	Upper bound
1st set	Without	With (I), Without (J)	11.912	<0.001	8.602	15.221
	With	With (I), Without (J)	23.586	<0.001	19.070	28.103
2nd set	Without	With (I), Without (J)	7.627	<0.001	6.106	9.148
	With	With (I), Without (J)	23.801	<0.001	20.996	26.607
3rd set	Without	With (I), Without (J)	9.475	<0.001	6.682	12.268
	With	With (I), Without (J)	23.512	<0.001	20.688	26.336
4th set	Without	With (I), Without (J)	9.084	<0.001	6.746	11.422
	With	With (I), Without (J)	24.181	<0.001	19.744	28.618

4 Discussion

4.1 Effects of Water and Greenery in Historic Towns on Landscape Preference

The results of this study show that the presence or absence of water and greenery will significantly affect c preference for a landscape scenario in historic towns. The influence includes two parts: main effects and interactive effects.

The Main Effects of Water and Greenery. The results of four sets of stimuli pictures in the experiment show that, in a historic town scenario, keeping the building elements unchanged, participants' preference of the scenario can be significantly improved by adding water or greenery. The increase of preference values brought by adding water or adding greenery has no constant difference in effect size, which is related to the specific form of water and greenery in different cases. This is consistent with the empirical cognition and the conclusions of previous studies, which also verifies the reliability of the experimental data [18].

The Interaction Effects. The above analysis of the four sets of stimuli pictures shows that there is a positive interaction between water and greenery on landscape preference. In other words, picture 4, which have both water and greenery, not only have the largest preference values among the four pictures in each set but also has a larger difference from picture 1 than the sum of the difference between picture 2

from picture 1 and picture 3 from picture 1, respectively. This shows that people's perception of a landscape scenario is not equal to the sum of perception of each element in the scenario. In fact, at least as far as the two landscape elements of water and greenery in historic towns are concerned, they inspire and set off each other in people's cognition, forming the effect of $1 + 1 > 2$.

4.2 Practical Implications for Townscape Improvement

Based on the above conclusions, the following suggestions can be made for landscape improvement in historic towns:

Site Selections. Firstly, due to the interactive effects, planners should select a site with a good landscape foundation among the historic town for improvement, which can make the low-cost interventions bring a greater increase of preference. For water and greenery, adding water to the site already with greenery can bring better effects than the site without greenery. Similarly, the effects of adding greenery to the site already with water will also be better than the site without water. Secondly, interactive effects also show that planners should select one site in the historic town for centralized transformation so that the added water and greenery can set each other off, which brings a greater increase of preference than adding them separately in two places. Considering the input–output efficiency, this conclusion is particularly applicable to landscape improvement in towns located in areas lacking water and greenery.

Specific Techniques. Firstly, diverting water and planting greenery are both effective techniques to improve landscape preference in historic towns improvement. There is no obvious advantage or disadvantage between the effects of adding water and adding greenery. Planners can make a flexible choice between them according to the objective conditions of the historic town. Secondly, water is a precious landscape resource in historic towns. The interactive effects show that in addition to repairing the water itself, adding greenery around the water can also play a better value of water. Correspondingly, adding water to the place with perfect greening can further improve the greenery's effects. Thirdly, to be specific, for the waterfront historic towns, where there have natural water elements, attention should be paid to the improvement of greenery. Fourthly, for street space, due to cost considerations, if there was neither water nor greenery originally, greenery should be given priority to increasing. If the greenery is relatively complete, water diversion can be considered if conditions permit. It is originally a river street, which can also better stimulate the value of water by increasing greening.

4.3 Limitations

Firstly, in this research, only two levels of "With" and "Without" have been set for water and greenery elements. But in fact, the effect size will be different according to the specific forms of water and greenery, such as the water surface area, plant color composition, and plant species diversity [19]. Or the water or greenery form is not pleasant, the main effect is negative, what kind of interactive effects will there be? These questions are difficult but valuable and need to be answered in the future research.

Secondly, using simulated pictures in the experiment is a good way to avoid the interference of other factors and focus on the research content. However, it presents a static image of head-up height, which is different from the dynamic visual effects formed by changing the viewpoint at any time when people walk in a real historic town. This may affect the results of the study. In addition, in real historic towns, water and greenery can produce the sound of water flow and leaves, which may increase people's preference for them [20]. In the future research, video with sounds can be used as stimuli to investigate.

5 Conclusions

This study discussed the influence of adding water and greenery on landscape preference. In terms of research methods, the ordinal data of the Likert scale that is easy to be filled in by participants is transformed into scale data that can be used for interactive effects analysis by constructing comparison matrixes. It provides a new method for data collection and statistical analysis of preference surveys. In terms of content, we focus on the interaction when a single landscape element is combined into a whole landscape scenario. The positive interactive effects of water and greenery in the ancient town promoting landscape preference were found, which provides new data support for the in-depth understanding of how people perceive the surrounding environment. In terms of practical application, so we know that by choosing strategic sites and adding effective elements, to cooperate with the surrounding environment, the value of the existing landscape resources in historic towns can be stimulated. Therefore, the preference for townscape can be enhanced with low-cost interventions. This study provides theoretical references from site selections to specific techniques for landscape improvement of historic towns.

References

1. Nicoletta R, Servidio R (2012) Tourists opinions and their selection of tourism destination images: an affective and motivational evaluation. Tourism Manag Perspect 4:19–27
2. Wang R, Zhao J, Meitner MJ et al (2019) Characteristics of urban green spaces in relation to aesthetic preference and stress recovery. Urban For Urban Greening 41:6–13
3. Faggi A, Breuste J, Madanes N et al (2013) Water as an appreciated feature in the landscape: a comparison of residents and visitors preferences in Buenos Aires. J Cleaner Prod 60(SI):182–187
4. Van den Berg AE, Joye Y, Koole SL (2016) Why viewing nature is more fascinating and restorative than viewing buildings: a closer look at perceived complexity. Urban Forest Urban Greening 20:397–401
5. Abdul Aziz NA, Shina LY, Mohamed Mokhtar MD et al (2021) Effectiveness of urban green space on undergraduates stress relief in tropical city: a field experiment in Kuala Lumpur. Urban Forest Urban Greening 63:127236
6. Van den Berg AE, Jorgensen A, Wilson ER (2014) Evaluating restoration in urban green spaces: does setting type make a difference? Landsc Urban Plan 127:173–181
7. Joye Y, Van den Berg A (2011) Is love for green in our genes? A critical analysis of evolutionary assumptions in restorative environments research. Urban Forest Urban Greening 10(4):261–268
8. The website of the Central People's Government of the PRC. http://www.gov.cn/gongbao/content/2021/content_5637945.htm. Accessed 25 Sept 2022
9. Gu C, Song G (2001) The study on the urban image and its application in the urban planning. City Plan Rev 03:70–73+77
10. Lee J, Lee HS, Jeong D et al (2019) The relationship between user perception and preference of greenway T rail characteristics in Urban areas. Sustainability 11:4438
11. Yazawa Y, Furuya K (2020) The relationship between evaluations of water channels landscape and landscape elements in sub-urban residential area in Tokyo, Japan. IOP Conf Ser: Earth Environ Sci 501:012027
12. Cai K, Huang W, Lin G (2022) Bridging landscape preference and landscape design: a study on the preference and optimal combination of landscape elements based on conjoint analysis. Urban Forest Urban Greening 73:127615
13. Stamps AE (2000) Psychology and the aesthetics of the built environment. Publisher, Springer Science + Business Media, LLC
14. Orekhove T, Liang J (2014) The role of greenery, layering, and landmarks in the regulations on urban skylines. China City Plan Rev 23(3):58–65
15. Memari S, Pazhouhanfar F, Nourtaghani A (2017) Relationship between perceived sensory dimensions and stress restoration in care settings. Urban Forest Urban Greening 26:104–113
16. Wang R, Zhao J (2019) A good sound in the right place: Exploring the effects of auditory-visual combinations on aesthetic preference. Urban Forest Urban Greening 43:126356
17. IBM corporation. https://www.ibm.com/support/pages/node/417465?mhsrc=ibmsearch_a&mhq=how%20to%20obtain%20a%20Simple%20Effects%20Test. Accessed 25 Sept 2022
18. Kuper R (2017) Evaluations of landscape preference, complexity, and coherence for designed digital landscape models. Landsc Urban Plan 157:407–421
19. Polat AT, Akay A (2015) Relationships between the visual preferences of urban recreation area users and various landscape design elements. Urban Forest Urban Greening 14:573–582
20. Lindquist M, Lange E, Kang J (2016) From 3D landscape visualization to environmental simulation: the contribution of sound to the perception of virtual environments. Landsc Urban Plan 148:216–231

Study on the Relationship between User Emotions and Spatial Physical Characteristics for Pedestrian Space Design Decisions: A Case Study of Kanazawa and Nomi in Japan

Ruixuan Li, Yuizono Takaya, Huynh Nam-Van, and Xianghui Li

Abstract This paper explores the effects of urban spatial characteristics on users' emotional responses. Two research questions are addressed: (1) Is there a correlation between spatial perceptions and the emotional valences of users? (2) What are the features (especially physical) of a pleasing urban space? To explore these two questions, we conducted experiments in five urban spaces (a university campus, residential area, Japanese garden, modern museum, and traditional pedestrian street) in Japan to obtain data on participants' emotional responses and perception evaluations. The results showed that (1) the factor analysis results showed that the aesthetic characteristics of a space more strongly influence emotional valences than the physical characteristics, and (2) users' emotional valences and scores for perception evaluations are strongly correlated. Moreover, we considered the main physical indexes of pleasant urban spaces, such as the width of the pavement, width-to-height ratio of the tree boundary, vertical boundary, and multi-level boundary.

Keywords Emotional valence · Perception evaluation · Aesthetic characteristics · Physical indexes · Boundary elements

1 Introduction

An important research direction in urban design is optimizing the urban space to meet users' functionality and aesthetic needs. Since the 1960s, researchers have analyzed the effect of the built environment on human psychology and behavior, and they have put forward suggestions for improving environmental quality from the perspective

R. Li (✉) · Y. Takaya · H. Nam-Van · X. Li
Japan Advanced Institute of Science and Technology, Nomi, Ishikawa, Japan
e-mail: s1920040@jaist.ac.jp

R. Li · X. Li
Dalian Polytechnic University, Dalian, Liaoning, China

T. Kang (ed.), *Proceedings of 5th International Conference on Civil Engineering and Architecture*, Lecture Notes in Civil Engineering 369,
https://doi.org/10.1007/978-981-99-4049-3_48

of experts [1–5]. After 2000, some researchers started paying more attention to user perceptions and evaluations. Through data and case analyses, they tried to understand users' general or special needs in different environments, including functionality, physiology, and social conditions. These needs can be separately or comprehensively analyzed through user experiences or emotions.

In the past 10 years, research in this direction has undergone major changes. First, the focus has gradually shifted from method and technology research to applied research [6, 7]. Second, expert perceptual analysis has been progressively replaced by evidence-based user experience analysis [8–10]. Third, the focus has shifted from qualitative to a combination of qualitative and quantitative research [11–16]. Meanwhile, some researchers have investigated the relationship between spatial characteristics and user emotions [12, 14, 17, 18]. However, research results have been mixed. Some researchers combined functional, aesthetic, and physical characteristics as evaluation indexes [11, 17, 18], making it challenging to apply the research results in practice. Physical characteristics are carriers of aesthetic characteristics in urban space, and the extracted physical indexes can directly guide urban spatial design, optimization, and management. Therefore, this study separates the physical and aesthetic characteristics of space and focuses on analyzing the correlation between the physical characteristics of space and the emotional valence of users.

2 Literature Review

Related research on spatial emotion has been conducted mainly in urban design and emotional geography. Related research on emotional geography has focused on emotional maps in large-scale urban spaces [19–21]. In contrast, urban design focuses on studying spatial emotion and aesthetics in small-scale public spaces [6, 7, 22].

Related research in the field of urban design also focuses on the exploration of methods for emotional data acquisition. Shoval et al. [10] used three data collection technologies to conduct a comprehensive survey of the tourism experience, including high-resolution location data obtained through GPS and cellular network location and skin conductance level (SCL) data obtained by physiological sensors. Roberts et al. [23] used the dataset from Twitter as the basis for emotional exploration and analyzed 10,000 tweets to determine individuals' positive or negative emotions. The results show that Twitter data is a viable source of information for researchers studying human interactions with and emotional responses to urban space. Based on the principle of Kansei engineering, Xiang et al. [16] studied the correlation between the urban environment's physical characteristics and pedestrians' emotional responses. They found that open space with visual objects in the distance is the main factor in generating positive emotions. In contrast, a closed refuge space is not a positive factor of happiness, contradicting the results of previous studies.

3 Methods

3.1 Experiment Sites

This study conducted an on-site experiment in urban spaces with different functions to obtain general results. Five-type urban spaces in Japan were selected as experiment sites, including the campus of the Japan Advanced Institute of Science and Technology (JAIST) in Nomi City, the residential area in Yokaichi, Kenroku-en (Japanese garden), the D. T. Suzuki Museum, and the Higashi Chaya District in Kanazawa (commercial pedestrian street in the preserved historical area). The length of the five urban spaces ranged from 0.36 to 1.1 km. Each urban space was divided into four sections with different spatial characteristics, resulting in a total of $5 \times 4 = 20$ sections, ranging from 43 to 300 m in length.

3.2 Data Acquisition

Nine students (aged 23–43) participated in the experiment. During the investigation, participants successively walked through each urban space. Immediately afterward, they filled out the SAM scale (see Fig. 1) and the spatial evaluation questionnaire (see Table 1). A total of 12 pairs of antonym adjectives were used to describe the spatial perception of users. Five semantic levels were designated for each pair.

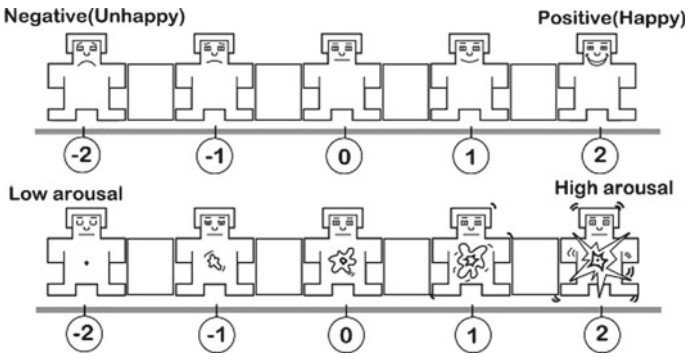

Fig. 1 Self-assessment Manikin (*Source* Lang (1980). Self-assessment manikin. Gainesville, FL: The Center for Research in Psychophysiology, University of Florida)

Table 1 Questionnaire on the perception of spatial characteristics

X_n	Left adj	V_n^{-3}	V_n^{-2}	V_n^{-1}	V_n^0	V_n^{+1}	V_n^{+2}	V_n^{+3}	Right adj
		Entirely	Very	Fairly	Neutral	Fairly	Very	Entirely	
X_1	Public	☐	☐	☐	☐	☐	☐	☐	Private
X_2	Natural	☐	☐	☐	☐	☐	☐	☐	Artificial
X_3	Modern	☐	☐	☐	☐	☐	☐	☐	Historical
X_4	Open	☐	☐	☐	☐	☐	☐	☐	Enclosure
X_5	Diversity	☐	☐	☐	☐	☐	☐	☐	Monotonous
X_6	Easy to identity	☐	☐	☐	☐	☐	☐	☐	Uneasy to identity
X_7	Green-rich	☐	☐	☐	☐	☐	☐	☐	Insufficient green
X_8	Unique	☐	☐	☐	☐	☐	☐	☐	Common
X_9	Beautiful	☐	☐	☐	☐	☐	☐	☐	Ugly
X_{10}	Meaningful	☐	☐	☐	☐	☐	☐	☐	Meaningless
X_{11}	Artistic	☐	☐	☐	☐	☐	☐	☐	Inartistic
X_{12}	Continuous space	☐	☐	☐	☐	☐	☐	☐	Interrupted space

4 Analysis and Results

4.1 Factor Analysis

First, the data on the perceptual evaluations of five urban spaces were normalized. Then, statistical product and service solutions (SPSS) were used to analyze the reliability of the data. The results showed that Cronbach's alpha of the five spatial data was 0.887, indicating good reliability and consistency for the questionnaire results. Then, factor analysis was conducted on the 12 indexes for each space.

The Kaiser–Meyer–Olkin (KMO) test results for all spaces were greater than 0.6 (p-value < 0.001), which met the requirements of factor analysis. The factor analysis reduced the 12 pairs of antonym adjectives to six common factors. The cumulative contribution rate of the six common factors in each space was more than 80%. After analyzing the commonness of the six common factors in each urban space, the obtained common factors were determined as aesthetics, unity, openness, style, nature, and continuity. Because of the negative number in the given factor weight obtained by factor analysis, the range method was used to normalize the data to get the weight of all indexes in the range of 0–1 and to calculate the weight of each common factor in each urban space.

4.2 Correlation Analysis

Table 2 gives the results obtained by calculating the average value of emotional valence and the scores of spatial perception evaluation. The changes in the two variables of the five spaces can be more clearly observed in the line chart (see Fig. 2). Next, the following formula was applied to calculate the total score for each section:

$$F = X_1F_1 + X_2F_2 + X_3F_3 + \ldots\ldots + X_nF_n$$

where F is the total score for each section, X_n is the weight of each index, and F_n is the average of each index.

Next, a correlation analysis was conducted among the total scores for 20 sections and the average value of user emotional valence. The results showed that the Pearson correlation coefficient of the two groups of variables was 0.734 (p-value = 0.001). In other words, there was a strong correlation between the emotional valences of users and the evaluation scores for users' spatial perceptions.

Table 2 Average values of emotional valence and the scores for spatial perception evaluations

Sites	Sections	Scores for each section	Average scores for each space	Valences of each section	Average valences of each space
JAIST campus	Section 1	0.01	−0.04	0.78	0.59
	Section 2	−0.02		0.89	
	Section 3	−0.15		0.11	
	Section 4	0.00		0.56	
Residential Area in Yokaichi	Section 1	−0.05	−0.07	0.44	0.56
	Section 2	−0.01		0.33	
	Section 3	−0.02		1.11	
	Section 4	−0.12		0.33	
Kenroku-en	Section 1	0.11	0.10	0.67	0.67
	Section 2	0.10		0.67	
	Section 3	0.13		0.78	
	Section 4	0.07		0.56	
D. T. Suzuki Museum	Section 1	0.24	0.24	0.11	0.64
	Section 2	0.27		0.78	
	Section 3	0.28		1.11	
	Section 4	0.20		0.56	
Higashi Chaya District	Section 1	0.03	0.03	0.44	0.61
	Section 2	−0.02		0.44	
	Section 3	0.10		0.89	
	Section 4	0.00		0.67	

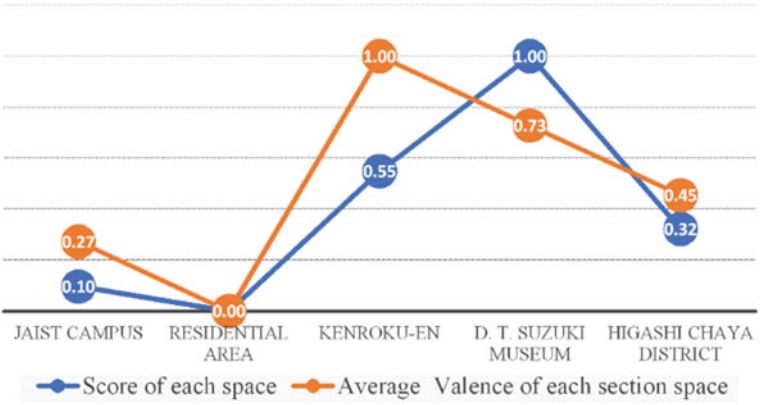

Fig. 2 Line chart of the changes of the two variables in the five experiment sites

4.3 Extraction of Spatial Characteristics

Spatial characteristics generally include physical, aesthetic, and functional characteristics affecting user emotions and perception evaluations. The functional and physical characteristics of space are relatively easy to describe and quantify, while the aesthetic characteristics of space are mainly obtained through questionnaires. Meanwhile, because the functional characteristics of space are often determined by spatial attributes, the spatial physical and aesthetic characteristics were taken as the primary research object.

According to the factor analysis results, the six common factors (aesthetics, unity, openness, style, nature, and continuity) can be divided into aesthetic and physical characteristics (see Table 3). The weights and scores of the six factors were obtained by calculating and summing the scores for each common factor. The total scores for the two main characteristics in different spaces were compared using the histogram shown in Fig. 3.

5 Discussion

Figure 2 demonstrates a correlation between the users' emotional valences and scores of perceptual evaluations. Table 2 and Fig. 2 show the changes in these variables in each of the five urban spaces. The average values of emotional valence are ranked as follows: Kenroku-en (0.67) > the D. T. Suzuki Museum (0.64) > the Higashi Chaya District (0.61) > the JAIST campus (0.59) > the residential area in Yokaichi (0.56). The scores for perception evaluation are ranked as follows: The D. T. Suzuki Museum (0.24) > Kenroku-en (0.10) > the Higashi Chaya District (0.03) > the JAIST campus (−0.04) > the residential area in Yokaichi (−0.07). The top two ranks are reversed in

Table 3 Total scores for physical and aesthetic characteristics for each experiment site

Sites	Items	Pysical characteristics				Aesthetic characteristics			
		Openness factor	Nature factor	Continuity factor	Total	Aesthetics factor	Uniqueness factor	Style factor	Total
JAIST campus	Weight	0.18		0.20	0.38	0.28	0.34		0.62
	Score	0.021		0.000	0.02	−0.036	−0.025		−0.061
Residential area in Yokaichi	Weight	0.18	0.17		0.35	0.23	0.28	0.13	0.64
	Score	−0.026	−0.015		−0.04	−0.026	−0.018	0.011	−0.032
Kenroku-en	Weight		0.17	0.07	0.24	0.29	0.08	0.38	0.75
	Score		0.036	0.006	0.04	0.04	0.008	0.018	0.06
D. T. Suzuki Museum	Weight		0.29	0.19	0.48	0.36	0.15		0.51
	Score		0.023	0.055	0.08	0.11	0.055		0.165
Higashi Chaya District	Weight	0.21	0.14	0.11	0.46	0.30		0.24	0.54
	Score	0.026	−0.019	0.005	0.01	−0.01		0.021	0.015

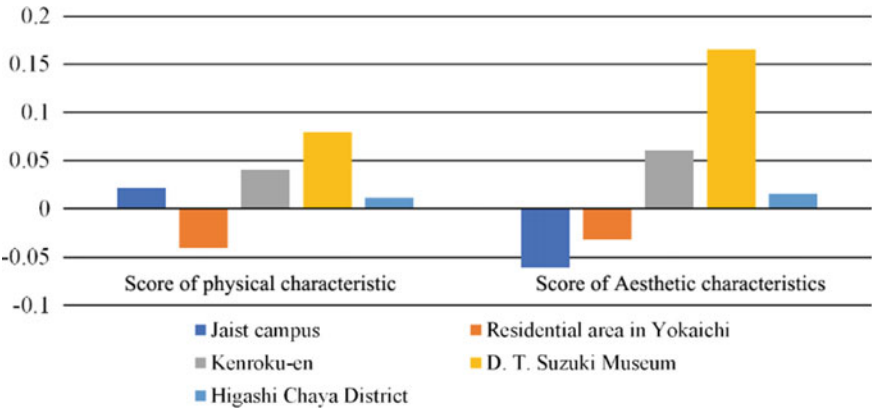

Fig. 3 Histogram of the five sites' scores for physical and aesthetic characteristics

the two rankings. This result indicates that the correlation between emotional valence and scores of perception evaluation is not completely consistent.

Further analysis of the characteristics of these two spaces revealed that the main difference between Kenroku-en and the D. T. Suzuki Museum is spatial consistency. While the differences among the four sections of the D. T. Suzuki Museum were greater than those of the other four spaces, the four sections of Kenroku-en had high spatial unity. Therefore, it may be inferred that user emotions are strongly correlated with the 'unity' of space, while user spatial perceptions correlate strongly with the 'richness' of space.

Table 3 gives the total scores of five urban spaces for physical and aesthetic characteristics. Comparing the data reveals the following:

(1) The scores for aesthetic characteristics of the five urban spaces are all higher than that of the physical characteristics of the same space, which indicates that aesthetic characteristics influence users more than physical characteristics do.
(2) The scores for the physical characteristics of the five urban spaces were ranked as follows: The D. T. Suzuki Museum (0.079) > Kenroku-en (0.04) > the JAIST campus (0.021) > the Higashi Chaya District (0.011) > the residential area in Yokaichi (−0.041). The scores for the aesthetic characteristics were ranked as follows: The D. T. Suzuki Museum (0.165) > Kenroku-en (0.06) > the Higashi Chaya District (0.015) > the residential area in Yokaichi (−0.032) > the JAIST campus (−0.061). The D. T. Suzuki Museum's two characteristics ranked the highest, consistent with the average scores for perception evaluation given in Table 3. However, the physical characteristics of the JAIST campus ranked third, while its aesthetic characteristics ranked fifth, indicating that its physical characteristics were better than its aesthetic characteristics. This result was consistent with the general situation of the campus space. The Higashi Chaya District, a tourist destination, scored low in terms of its physical characteristics, perhaps due to its single-space type.

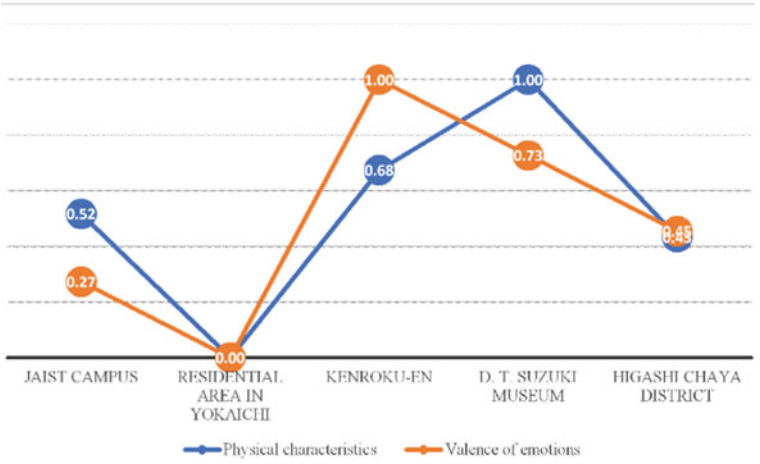

Fig. 4 Line chart of the relationship between physical characteristics and emotional valences in the five sites

(3) After normalizing the data, as shown in Fig. 4, the line chart of the five spaces' physical characteristics and emotional valences was obtained. Comparing Figs. 2 and 4, we found that corresponding to the emotional valences of the five spaces, the changing laws on the physical characteristics and scores for perception evaluations were similar.

Although scores for the aesthetic characteristics of the five urban spaces are all higher than those of the physical ones, there is an undeniable correlation between physical characteristics and emotional valences.

The analysis revealed a strong correlation between users' emotional valences and their scores on perception evaluation. Meanwhile, the weight of the aesthetic characteristics of space was greater than that of the physical characteristics for users' perceptions of space. This result indicates a strong correlation between a space's aesthetic characteristics and users' emotional valence and a relatively weak correlation between a space's physical characteristics and users' emotional valence.

The similarities and differences between these results illustrate the complexity of the relationship between spatial characteristics and user emotions. Thus, research results will differ by field (urban design, architecture, psychology, emotional geography, and landscape architecture), research scale, and research purpose.

6 Conclusion

This study explored the relationship between spatial characteristics and user emotions. Experiment and data analysis revealed a high correlation between the users' emotional valences and their scores on perception evaluation; the aesthetic,

physical, and functional characteristics of urban space jointly affect user emotions and the popularity of a space. In addition to functional characteristics, aesthetic characteristics influence emotional valence more than physical characteristics do. People's emotions and urban spaces are both complex and changeable. The accumulation of multi-case studies will help us gain a more precise and deeper understanding of the relationship between urban space and human psychology.

Acknowledgements This work was supported by the Humanities and Social Sciences project of the Ministry of Education of China (Grant No. 18YJA840006), JAIST Research Grant (Fundamental Research), 'Light of textile' China Textile Industry Federation higher education teaching reform research project (Grant No. 2021BKJGLX313), the Humanities and Social Sciences project of the Educational Department of Liaoning Province (Grant No. J2020062), and the National Natural Science Foundation Project (2021) (Grant No. 32071831).

References

1. Lynch K (1960) The image of the city, vol 11. MIT Press, Cambridge, MA
2. Jacobs J (1960) The death and life of great American cities. Vintage, New York
3. Gehl J (1960) Livet Mellem Husene-Udeaktiviteter og udemiljøer (Life between buildings: Using public space). Arkitektens Forlag, Copenhagen, Denmark
4. Tuan YF (1977) Space and place: the perspective of experience. University of Minnesota Press
5. Whyte WH (1980) The social life of small urban space [Motion Picture]. Direct Cinema Limited. Santa Monica, CA
6. Kanjo E, Al-Husain L, Chamberlain A (2015) Emotions in context: examining pervasive affective sensing systems, applications, and analyses. Pers Ubiquit Comput 19(7):1197–1212
7. Schindler I, Hosoya G, Menninghaus W, Beermann U, Wagner V, Eid M, Scherer KR (2017) Measuring aesthetic emotions: a review of the literature and a new assessment tool. PLoS ONE 12(6):e0178899
8. Gjerde M (2010) Visual aesthetic perception and judgment of urban streetscapes. In: 18th CIB world building congress. Salford, United Kingdom, pp 12–22
9. Wilhelm FH, Grossman P (2010) Emotions beyond the laboratory: theoretical fundaments, study design, and analytic strategies for advanced ambulatory assessment. Biol Psychol 84(3):552–569
10. Shoval N, Schvimer Y, Tamir M (2018) Real-time measurement of tourists objective and subjective emotions in time and space. J Travel Res 57(1):3–16
11. Carmona M, Heath T, Tiesdell S, Oc T (2010) Public places, urban spaces: the dimensions of urban design. Routledge, London
12. Schneider S, Fröhlich J, Bielik M, König R (2014) Space synthesiser-An experimental setup for investigating the relationships between urban form and emotional responses. Des Cogn Behav: Usability Built Environ 23–27
13. Zeile P, Resch B, Dörrzapf L, Exner JP, Sagl G, Summa A, Sudmanns M (2015) Urban emotions—tools of integrating people's perception into urban planning. In from vision to reality for vibrant cities and regions. In: Proceedings of the 20th international conference on urban planning, regional development, and information society. Ghent, Belgium, pp 905–912
14. Cho M, Kim M (2017) Measurement of user emotion and experience in interaction with space. J Asian Archit Build Eng 16(1):99–106
15. Shu L, Xie J, Yang M, Li Z, Li Z, Liao D, Xu X, Yang X (2018) A review of emotion recognition using physiological signals. Sensors 18(7):2074

16. Xiang L, Papastefanou G (2019) Isovist and psycho-physiological stress at the pedestrian level: a real-time measurement case study in a high-density city. In perfect smart cities versus real emotional cities, In: Proceedings of the 24th international conference on urban planning, regional development, and information society. Karlsruhe, Germany, pp 463–471
17. Kalivoda O, Vojar J, Skřivanová Z, Zahradník D (2014) Consensus in landscape preference judgements: the effects of landscape visual aesthetic quality and respondents characteristics. J Environ Manage 137:36–44
18. Zhang F, Zhou B, Liu L, Liu Y, Fung HH, Lin H, Ratti C (2018) Measuring human perceptions of a large-scale urban region using machine learning. Landsc Urban Plan 180:148–160
19. Davidson J, Milligan C (2004) Embodying emotion sensing space: introducing emotional geographies. Soc Cult Geogr 5(4):523–532
20. Resch B (2013) People as sensors and collective sensing-contextual observations complementing geo-sensor network measurements. In: Progress in location-based services Berlin. Springer, Heidelberg, pp 391–406
21. Resch B, Summa A, Sagl G, Zeile P, Exner JP (2015) Urban emotions—geo-semantic emotion extraction from technical sensors, human sensors, and crowdsourced data. In: Progress in location-based services. Springer, Cham, Switzerland, pp 199–212
22. Huang H, Klettner S, Schmidt M, Gartner G, Leitinger S, Wagner A, Steinmann R (2014) AffectRoute: considering people's affective responses to environments for enhancing route-planning services. Int J Geogr Inf Sci 28(12):2456–2473
23. Roberts H, Sadler J, Chapman L (2019) The value of Twitter data for determining the emotional responses of people to urban green spaces: a case study and critical evaluation. Urban Stud 56(4):818–835

Boundary Control Method for Urban Single Congestion Region

Chuanxiang Ren, Zhen Wang, Hui Xu, Juan Teng, and Qiu Meng

Abstract With the rapid development of cities, traffic congestion is more likely to evolve into regional forms of congestion. To alleviate regional traffic congestion in cities while improving the traffic efficiency of road networks, a boundary control method is proposed. This method takes the optimal accumulation of the protected region as the control target and restricts the vehicles entering the protected region when the accumulation exceeds the optimal accumulation. For the optimal accumulation, a macroscopic fundamental diagram (MFD) is constructed. To achieve the control objective of optimal accumulation, the optimal inflow is estimated by a PID control algorithm based on a BP neural network. Then, the signal timing scheme of the boundary intersection is adjusted according to the optimal inflow. Finally, the proposed boundary control method is simulated according to the example road network. The simulation results show that the boundary control method can effectively improve the traffic congestion of the regional road network.

Keywords Macroscopic fundamental diagram · Boundary control · Congestion region · BP neural network · Signal control

1 Introduction

For today's urban traffic, traffic congestion in the urban road network is no longer localized in a certain link or an intersection, but is more likely to evolve into a larger-scale regional traffic problem. Traffic control at the micro level has problems such as insufficient perception and feedback capability, which is no longer able to

C. Ren (✉) · Z. Wang · H. Xu · J. Teng
College of Transportation, Shandong University of Science and Technology, 579 Qianwangang Road, Huangdao District, Qingdao, China
e-mail: renchx@sdust.edu.cn

Q. Meng
College of Electronic Information Engineering, Shandong University of Science and Technology, 579 Qianwangang Road, Huangdao District, Qingdao, China

T. Kang (ed.), *Proceedings of 5th International Conference on Civil Engineering and Architecture*, Lecture Notes in Civil Engineering 369,
https://doi.org/10.1007/978-981-99-4049-3_49

solve the congestion problem more effectively. Regional road network conditions must be analyzed at the macro level, and a combination of macro and micro control is needed to alleviate traffic congestion. Based on this, a boundary control method for urban homogeneous congestion regions is proposed. The signal timing of the boundary intersection is adjusted, so as to restrict the vehicles entering and speed up the vehicles exiting the protected region.

2 Literature Review

MFD is used to analyze traffic flow fundamental diagrams from a macroscopic perspective. Based on the theory of traffic flow fundamental diagram, there is a long history of research to extend the scope of study from a single section to multiple sections or complex networks. Daganzo and Geroliminis et al. [1, 2] proposed the concept of MFD as a way to describe the general relationship between the number of vehicles moving in a network and the level of network operation, and showed that MFD is related to the state of road network operation. They analyzed the simulation data for the Nairobi CBD and obtained a consistent MFD relationship between the average density and the average flow [3]. Gonzales et al. [4] scaled up the traffic demand to obtain MFD about the trip completion flow and accumulation and confirmed that limiting the entering traffic flow to the congestion region can change the mobility of the travelers.

Most of the studies on regional boundary control are based on control methods derived from MFD theory. Haddad et al. [5] studied two regional traffic control problems and proposed an algorithm for determining regional boundaries as well as control strategies. Aboudolas et al. [6] combined MFD with boundary control of several large-scale networks and verified the impact of boundary control on the network. Keyvan-Ekbatani et al. [7] proposed a control strategy based on the concept of feedback gating and verified the strategy is better for improving the average speed and reducing the delay of the road network. Aalipour et al. [8] demonstrated the superior performance of Bang-Bang control form. Sirmatel et al. [9] proposed a nonlinear model predictive boundary control method. Zhu et al. [10] proposed a boundary control strategy based on MFD and divided the urban road network into several sub-regions to control each sub-region.

In summary, with the further study of MFD theory, boundary control based on MFD has received more and more attention. Many boundary control methods have complexity in control or lack intuitiveness. This paper proposes a boundary control method to alleviate the regional traffic congestion problem by calculating the optimal inflow of the road network to adjust the signal timing scheme.

3 Boundary Control Method

An urban single congestion region is defined as a region of the urban road network consisting of multiple intersections with similar congestion conditions, and we call it a protected region, as shown in Fig. 1. Traditional traffic control methods are effective in relieving traffic congestion on local roads, but they tend to cause congestion shifts and are difficult to effectively alleviate regional traffic congestion problems. The traffic operation state of the protected region can be improved by a boundary control method. The regional boundary control method is the signal control of the intersection at the regional boundary. It improves the traffic operation in the region by adjusting the number of vehicles entering and leaving the border.

Data on vehicles entering and exiting the protected region can be obtained by setting up detectors at the entrance and exit lanes of the border crossing. Based on the traffic data, we can evaluate the traffic state of the protected region. There is an optimal accumulation N_o for each protected region in the best operation condition. We use the optimal accumulation of the protected region as the control objective. It is necessary to restrict the vehicles entering the protected region when the accumulation of vehicles exceeds the optimal accumulation.

Firstly, the optimal inflow $q_o(k)$ is calculated based on the traffic state of the protected region, where k is the time step. Secondly, the green time of the entering phase is changed according to the optimal inflow to make it an asymmetric signal phase. At the same time, we add the idea of feedback control to continuously monitor the traffic state of the protected region and adjust the signal timing scheme of the boundary intersection for achieving the control goal. The flowchart of boundary control is shown in Fig. 2.

3.1 MFD

The MFD can be constructed by the accumulation and the trip completion flow. The MFD is usually a non-negative single-peaked curve, as shown in Fig. 3, and

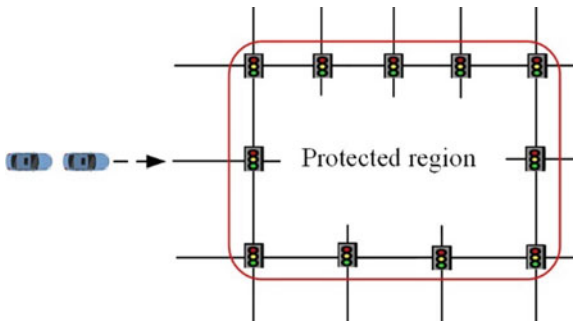

Fig. 1 Protected region with boundary control

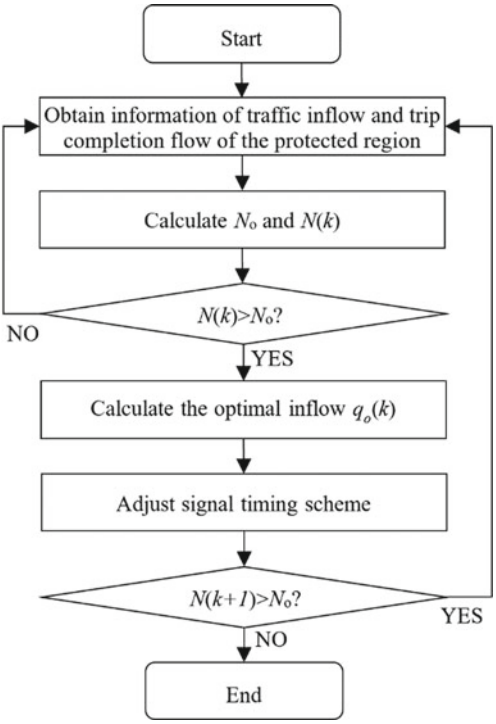

Fig. 2 Flowchart of boundary control

can be divided into three states. The first is the rising phase, which means that the region is in a "free flow" state, and the trip completion flow in this phase is small. The second is the optimal phase, and the region is in the "saturation" state, the trip completion flow reaches the maximum, and the regional traffic state reaches the critical point. The third is the decreasing phase, and the accumulation in the road network is still increasing, but the road network is in the "oversaturation" state, and the trip completion flow gradually decreases.

The MFD is usually fitted with a cubic polynomial [11], as follows:

$$G(N(k)) = aN^3(k) + bN^2(k) + cN(k) \tag{1}$$

where a, b, and c are fitting parameters, $N(k)$ is the accumulation of the *kth* cycle, and $G(N(k))$ is the trip completion flow.

3.2 Traffic Equilibrium Model

There is a dynamic balance between inflow and trip completion flow of the protected region. The accumulation can be calculated by the traffic equilibrium model. Since

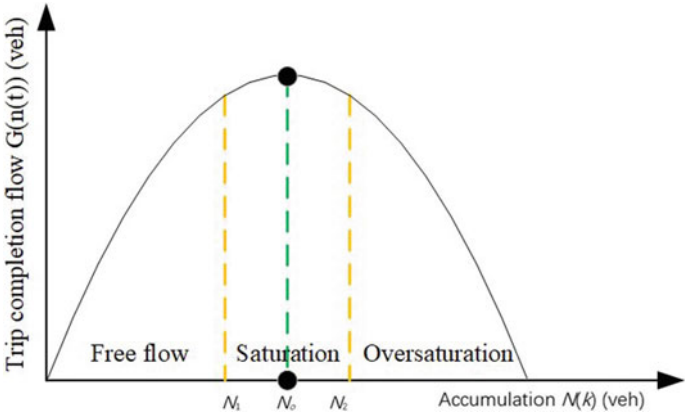

Fig. 3 MFD

the existence of MFD is independent of OD demand [12, 13], this paper assumes that no traffic is generated inside the protected region. Then, the traffic equilibrium model can be expressed as:

$$N(k+1) = N_o + \Delta N(k) \cdot e^{-G'(N_o)\cdot C} + \mu \cdot \Delta q_{in}(k) \tag{2}$$

$$\mu = \frac{1 - e^{-G'(N_o)\cdot C}}{G'(N_o)} \tag{3}$$

where C is the control cycle, $\Delta N(k) = N(k) - N_{\mathrm{o}}$, $\Delta q_{in}(k) = q_{in}(k) - q_{in,o}$, and $q_{in,o}$ is the value corresponding to $G(N_{\mathrm{o}})$.

3.3 Signal Control Method

PID control algorithm based on BP neural network. The optimal inflow is estimated by a PID control algorithm based on a BP neural network. In this case, the optimal inflow of the protected region can be expressed as:

$$q_o(k) = q_o(k-1) + \delta k_p + k_i e(k) + \varphi k_d \tag{4}$$

$$\delta = e(k) - e(k-1) \tag{5}$$

$$\varphi = e(k) - 2e(k-1) + e(k-2) \tag{6}$$

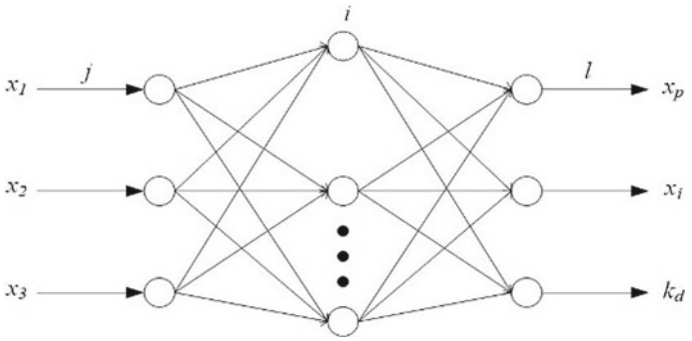

Fig. 4 BP neural network

where K_p denotes the proportionality factor, K_i denotes the integration factor, K_d denotes the differentiation factor, and $e(k)$ is the error between the optimal accumulation and the real-time accumulation.

BP neural network. BP neural network is able to achieve self-adjustment of PID control parameters. BP neural network is a three-layer network which consists of input layer, implicit layer, and output layer [14], as shown in Fig. 4.

The inputs of the input layer can be expressed as:

$$o_j^{(1)} = x(j)(j = 1, 2, 3) \tag{7}$$

The input and output of the hidden layer can be expressed as:

$$net_i^{(2)}(k) = \sum_{j=0}^{3} \omega_{ij}^{(2)} o_j^{(1)}, i = 1, 2, ..., Q \tag{8}$$

$$o_j^{(2)}(k) = f\left(ne_i^{(2)}(k)\right), i = 1, 2, ..., Q \tag{9}$$

where $\omega_{ij}^{(2)}$ is the weighting factor for the input of the hidden layer.

The input of the output layer can be expressed as:

$$net_l^{(3)}(k) = \sum_{i=0}^{Q} \omega_{li}^{(3)} o_i^{(2)} \tag{10}$$

$$o_l^{(3)}(k) = g\left(net_i^{(3)}(k)\right), l = 1, 2, 3 \tag{11}$$

$$\left\{ \begin{array}{l} o_1^{(3)} = k_p \\ o_2^{(3)} = k_i \\ o_3^{(3)} = k_d \end{array} \right\} \tag{12}$$

where $\omega_{li}^{(3)}$ is the weighting factor for the input of the output layer.

The activation function $f(x)$ in the hidden layer and the activation function $g(x)$ in the output layer are denoted as:

$$g(x) = \frac{e^x - e^{-x}}{e^x + e^{-x}} \tag{13}$$

$$f(x) = \frac{e^x}{e^x + e^{-x}} \tag{14}$$

The performance indicator function can be expressed as follows:

$$P(k) = \frac{e^2(k)}{2} \tag{15}$$

The weighting factor of the output layer is adjusted using the gradient descent method, which can ultimately be expressed as:

$$\Delta\omega_{li}^{(3)}(k) = \alpha\Delta\omega_{li}^{(3)}(k-1) + \eta e(k)\frac{N(k) - N(k-1)}{u(k) - u(k-1)}\frac{\partial u(k)}{\partial o_l^3(k)} f'\left(net_l^3(k)\right) o_i^{(2)}(k) \tag{16}$$

where K_p denotes the proportionality factor, K_i denotes the integration factor, K_d denotes the differentiation factor, and $e(k)$ is the error between the optimal accumulation and the real-time accumulation. Where η is the learning rate and α is the inertia coefficient.

$$\left\{\begin{array}{l} \frac{\partial u(k)}{\partial o_1^3(k)} = e(k) - e(k-1) \\ \frac{\partial u(k)}{\partial o_2^3(k)} = e(k) \\ \frac{\partial u(k)}{\partial o_3^3(k)} = e(k) - 2e(k-1) + e(k-2) \end{array}\right\} \tag{17}$$

The weighting factor of the hidden layer can be expressed as:

$$\Delta\omega_{ij}^{(2)}(k) = \alpha\Delta\omega_{ij}^{(2)}(k-1) + \eta e(k) g'\left(net_i^2(k)\right) \tag{18}$$

$$\sum_{l=1}^{3}\left(\omega_{li}^3(k)e(k)\right)\frac{N(k) - N(k-1)}{u(k) - u(k-1)}\frac{\partial u(k)}{\partial o_l^3(k)} o_j^{(1)}(k) \cdot f'\left(net_l^3(k)\right)$$

Asymmetric signal timing scheme. According to the PID control algorithm based on a BP neural network, we can get the optimal inflow $\boldsymbol{q_o(k)}$ of the protected region, and the number of vehicles allowed to enter in the kth cycle can be expressed as:

$$n_o(k) = \frac{q_o(k)}{3600} \cdot C_i \tag{19}$$

where C_i is the signal cycle of the ith intersection.

Thus, the number of vehicles $n_i(k)$ that can be assigned to the ith intersection can be shown as follows:

$$n_i(k) = n_o(k) \cdot \frac{n_{i,in}(k)}{n_{in}(k)} \tag{20}$$

And for the kth cycle, the traffic flow entering intersection i from outside the boundary can be shown as follows:

$$q_{i,in}(k) = \frac{n_{i,in}(k)}{t_{i,in}(k-1)} \tag{21}$$

Therefore, for the *kth* cycle, the optimal green time for the phase entering intersection i can be shown as follows: $t_{i,o}(k) = \frac{n_i(k)}{q_{i,in}(k)}$, then the adjustment amount of the green time entering intersection i at the kth cycle can be expressed as:

$$\Delta t_{i,o}(k) = t_{i,o}(k) - t_{i,o}(k-1) \tag{22}$$

The asymmetric signal timing scheme of the boundary intersection is shown in Fig. 5. At the same time, the green time cannot be increased or decreased indefinitely, and it needs to satisfy the restrictions of minimum value and maximum value. The minimum green time $G_{i,\min}(k)$ uses the pedestrian crossing time, which can be shown as follows:

$$G_{i,\min}(k) = R_t + \frac{W_i}{V_{i,p}} + 2N_{i,p}(k) \tag{23}$$

where R_t denotes the pedestrian reaction time, usually 2–3 s, $N_{i,p}(k)$ denotes the number of people crossing the street, W_i denotes the length of the crosswalk, $V_{i,p}$ denotes the walking speed, usually with an average speed of 1.2 s, and the maximum

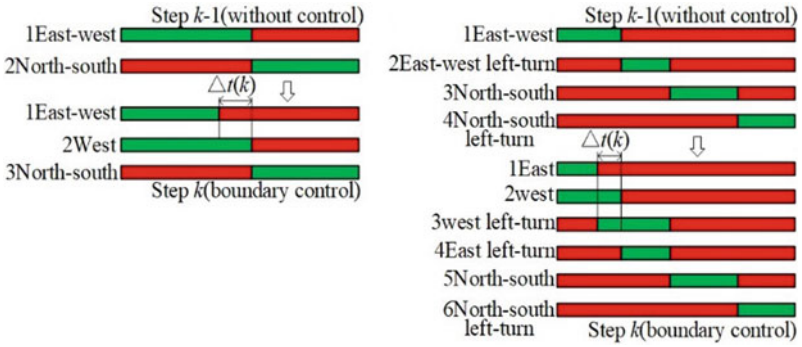

Fig. 5 Asymmetric signal timing schemes

green time $G_{i,\max}(k)$ is calculated based on the signal cycle minus the minimum green time of the opposite traffic signal.

Therefore, the range of optimal signal time to be satisfied for entering boundary intersection i can be shown as follows:

$$G_{i,\min}(k) \leq t_{i,o}(k) \leq G_{i,\max}(k) \tag{24}$$

4 Simulation Experiment

In order to verify the proposed boundary control method, a VISSIM road network model is established with part of the road network in Qingdao as the protected region. The network includes 10 boundary intersections, and each intersection uses a fixed signal timing scheme.

The traffic demand of the protected region can show the process from free flow to congestion, and the traffic distribution of each road within the region can better ensure the homogeneity of the region, so that region can get a well MFD, as shown in Fig. 6, and the expression of MFD is as follows:

$$G(N(t)) = -4.98 \times 10^{-8} N^3(t) - 1.94 \times 10^{-3} N^2(t) + 8.92 N(t) \tag{25}$$

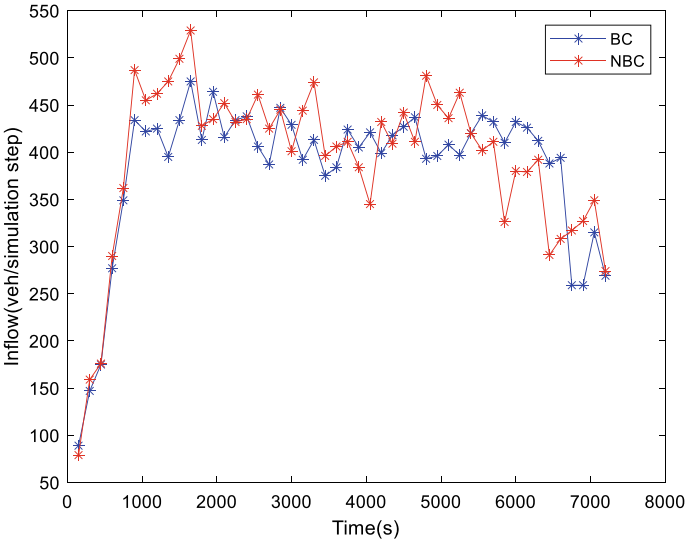

Fig. 6 Inflow versus time for two control methods

Therefore, the optimal accumulation for this region is 2100 (*veh*). Simulation experiments are conducted for the no boundary control method (NBC) and the boundary control method (BC) with a simulation time of 7200 s. The signal period of the boundary intersection and the sampling period is 150 s. Detectors are installed on each road in the road network. Total delay, total travel time, inflow, trip completion flow, average delay, and average driving speed are used as evaluation indicators. The simulation results are shown in Table 1, Figs. 6, 7, 8, 9, and 10.

As can be seen from Table 1, the overall performance of the road network has all improved after the implementation of BC compared to NBC. In particular, the average delay of the road network is reduced by 16.7%, the total delay time is reduced by 18.4%, and the total travel time is reduced by 16.5%.

From Figs. 6 and 7, it can be seen that the variation trends of the inflow and trip completion flow under both methods are similar. Compared with NBC, the variation of trip completion flow under NC is smaller and generally lower than the value that under NBC. The trip completion flow is not always kept at a larger value, which is caused by the excessive traffic demand of the protected region.

Table 1 Results of network evaluation under two methods

Control methods	NBC	BC
Average delay time per vehicle (s)	762.350	635.026
Total delay time (h)	4299.868	3510.282
Total travel time (h)	4818.106	4024.134

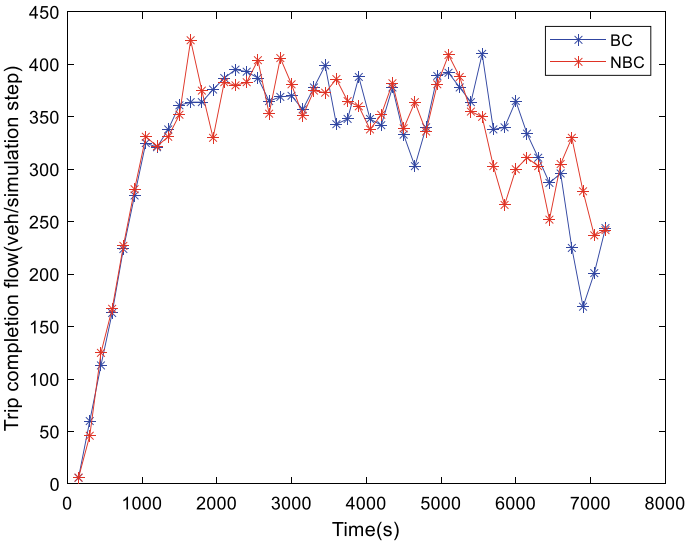

Fig. 7 Trip completion flow versus time for two control methods

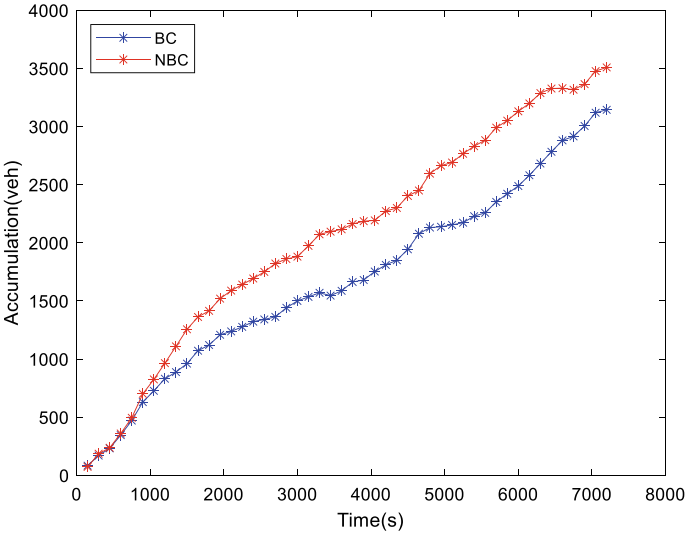

Fig. 8 Accumulation versus time for two control methods

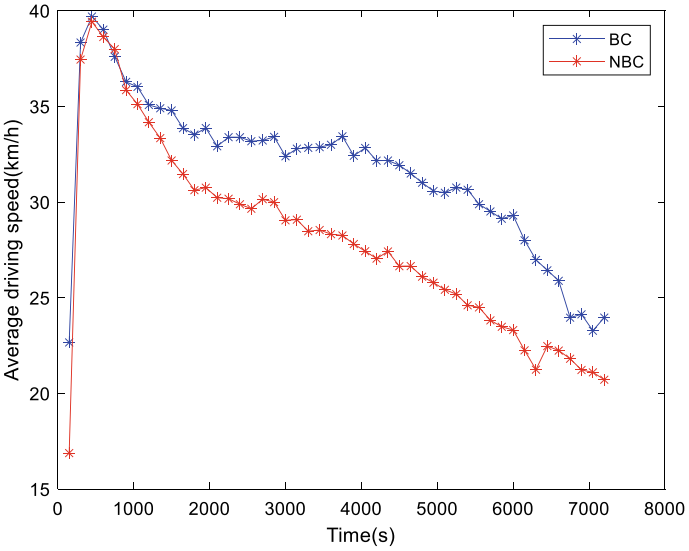

Fig. 9 Average driving speed versus time for two control methods

As can be seen in Fig. 8, the accumulation under BC is generally lower than that under NBC, which indicates that the BC has a better effect. The accumulation does not remain stable but keeps increasing, which is caused by the excessive increase in traffic demand. As can be seen from Fig. 9, the average driving speed under BC is

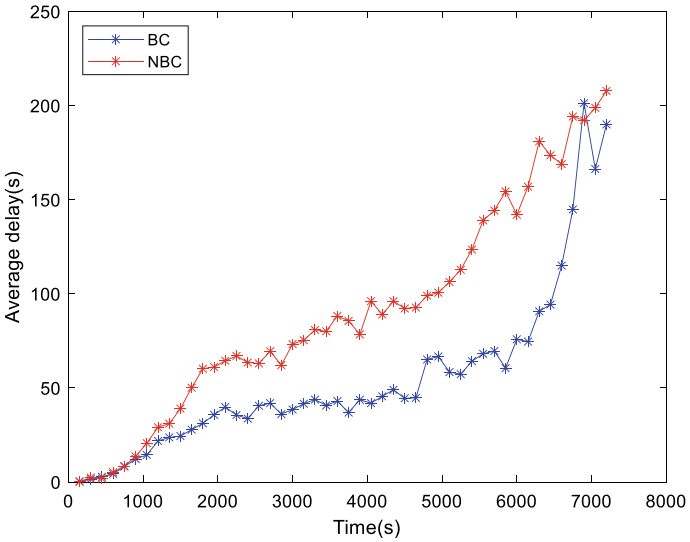

Fig. 10 Average delay versus time for two control methods

greater than 30 km/h until about 6000 s, which is higher than the value under NBC, indicating that BC effectively increases the average driving speed of the protected region. And as can also be seen in Fig. 10, the average delay under BC before 6500 s is much lower than the value under NBC, indicating that BC is effective in reducing the average delay.

5 Conclusion

In this paper, the traffic congestion problem in a region of the city is studied, and the boundary control method for the congestion region is proposed. Firstly, the MFD of the protected region is constructed to determine the optimal accumulation. Secondly, a traffic equilibrium model is developed. Then, the optimal inflow is estimated by a PID control algorithm based on a BP neural network. Finally, the signal timing scheme is designed according to the optimal inflow.

An example region is selected for simulation experiments. The simulation results show that the protected region has a significant improvement in its accumulation, average driving speed, and average delay after the implementation of BC. This proves that the proposed boundary control method can effectively improve the traffic congestion of the regional road network.

References

1. Geroliminis N, Daganzo CF (2008) Existence of urban-scale macroscopic fundamental diagrams: some experimental findings. Transp Res Part B: Methodological 42(9):759–770
2. Daganzo CF, Geroliminis N (2008) An analytical approximation for the macroscopic fundamental diagram of urban traffic. Transp Res Part B: Methodological 42(9):771–781
3. Gonzales EJ, Chavis C, Li Y, Daganzo CF (2009) Multimodal transport modeling for Nairobi, Kenya: insights and recommendations with an evidence-based model, 42
4. Gonzales EJ, Geroliminis N, Cassidy MJ, Daganzo CF (2010) On the allocation of city space to multiple transport modes. Transp Plann Technol 33(8):643–656
5. Haddad J, Geroliminis N (2012) On the stability of traffic perimeter control in two-region urban cities. Transp Res Part B: Methodological 46(9):1159–1176
6. Aboudolas K, Geroliminis N (2013) Feedback perimeter control for multi-region large-scale congested networks. In: 2013 European control conference (ECC). IEEE, Zurich, pp 3506–3511
7. Keyvan-Ekbatani M, Yildirimoglu M, Geroliminis N, Papageorgiou M (2015) Multiple concentric gating traffic control in large-scale urban networks. IEEE Trans Intell Transp Syst 16(4):2141–2154
8. Aalipour A, Kebriaei H, Ramezani M (2019) Analytical optimal solution of perimeter traffic flow control based on MFD dynamics: a pontryagin's maximum principle approach. IEEE Trans Intell Transp Syst 20(9):3224–3234
9. Sirmatel II, Geroliminis N (2021) Stabilization of city-scale road traffic networks via macroscopic fundamental diagram-based model predictive perimeter control. Control Eng Pract 109:104750
10. Zhu WX, Li S (2019) Study on discrete boundary-feedback-control strategy for traffic flow based on macroscopic fundamental diagram. Phys A: Stat Mech Appl 523:1237–1247
11. Ji Y, Mo C, Ma W, Liao D (2016) Feedback gating control for network based on macroscopic fundamental diagram. Math Probl Eng 2016:1–11
12. Aboudolas K, Geroliminis N (2013) Perimeter and boundary flow control in multi-reservoir heterogeneous networks. Transp Res Part B: Methodological 55:265–281
13. Geroliminis N, Haddad J, Ramezani M (2013) Optimal Perimeter Control for Two Urban Regions With Macroscopic Fundamental Diagrams: A Model Predictive Approach. IEEE Trans Intell Transp Syst 14(1):348–359
14. Zhang J, Liu J (2019) BP neural network PID temperature control of beer fermentation tank. J Phys: Conf Ser 1176:052002

Toward an Adjusted Neighborhood Design Combating Future Epidemics Spreading

Samer Abu Ghazaleh and Rawan Abdoh

Abstract This study aims to investigate the impact of the residential neighborhood characteristics on the spread of epidemics diseases, taking COVID-19 disease as a case study, in the neighborhoods of Amman, capital of Jordan. It is conducted using a descriptive and analytical methods, and test hypotheses related to analyzing the relationship between each characteristic of residential neighborhoods and the prevalence of disease. The data of this study was collected by designing a questionnaire directed to the inhabitants of the residential neighborhoods in the city of Amman. The results of the research indicate a significant relationship between the characteristics of residential neighborhoods and the spread of the epidemic, and the study revealed the presence of weaknesses in the design of some residential neighborhoods that caused the varying numbers of cases of infection with the coronavirus among residential neighborhoods. Based on the results, the researchers provided a set of recommendations to decision-makers in order to take into account the optimal residential neighborhood design, which will help in combating the outbreak of potential epidemics in the future whether in Amman City or any other city of World.

Keywords Epidemic diseases · Resilient neighbors · Social distancing

This research is part of a master thesis submitted to the University of Jordan department of Architecture.

S. Abu Ghazaleh (✉)
University of Jordan, Amman, Jordan
e-mail: s.abughazalah@ju.edu.jo

R. Abdoh
Graphic Design Officer at Ministry of Health (UNISEF Contract), Amman, Jordan

T. Kang (ed.), *Proceedings of 5th International Conference on Civil Engineering and Architecture*, Lecture Notes in Civil Engineering 369,
https://doi.org/10.1007/978-981-99-4049-3_50

1 Introduction

1.1 Pandemic Diseases and Neighborhoods

In early 2020, the World Health Organization (WHO) revealed a new outbreak of the COVID-19 pandemic [1]. Jordan, like most countries, witnessed strict curfew measures imposed for the population, where citizens were asked to practice social distancing and stay at home to maintain public health, as a dramatic step to slow the spread of COVID-19 [2]. After a period of imposing a curfew, residents were allowed to walk a few hours a day to meet their basic requirements and purchase goods from shops in their neighborhoods.

Recently, the literature has paid more attention to the impact of neighborhood characteristics on the population's health, especially in times of disasters. Neighborhoods are fundamentally linked to everyday accumulated and long-term health impacts. Almost any disaster, like COVID-19, might provide issues to urban planning and design. The epidemic of COVID-19 caused enormous mortality, damages and widespread loss. Back through history, neighborhoods were established and development motivated to increase their capability to avoid disasters, whereas modern neighborhoods were constructed and grown to increase public health and well-being. As a result, the dilemma of potential disasters would prompt reconsideration of urban design standards. In the post-pandemic era, re-design of resilient residential neighborhoods should be considered to combat the spread of epidemics. This will be achieved by studying the characteristics of residential neighborhoods that affect the spread of epidemics to control them [3].

Urbanization brings with it several public health and infectious disease epidemiological challenges. Epidemics have constantly impacted neighborhoods throughout history. The globe which is faced with a COVID-19 pandemic catastrophe, potentially the worst from more than one hundred years and this has created several issues for urban areas.

The relation between urban planning and public health began simultaneously after the eighteenth century as a response to the epidemiological conditions after the industrial revolution and the conditions of population migration to cities [4]. This led to an abundance of unhealthy conditions. As a result, the layout and design of the built environment have been changed significantly after the deaths caused by the third cholera pandemic [5].

1.2 Residential Neighborhood Concept

Residential neighborhood is a theory or social concept that seeks to create healthy residential environments with their public facilities and necessary services [6]. It may be called a residential neighborhood unit, a social unit, or a planning unit, this unit must be of adequate and sufficient scale, to promote access to public facilities

and to establish a healthy and shared social life [7]. Neighborhoods are described as residences and spatial, social and financial contexts affecting these communities. It is commonly argued that neighborhoods should be big enough to attract members and provide services while remaining small enough for citizens to retain a common neighborhood identity. Conceptualizing a conventional view, a neighborhood is a group of residents in a geographically specific region who share services and a certain degree of solidarity, the concept most recognizable to differentiate neighborhoods from other concepts like community is three main words that describe communities—population, location and solidarity [8]. A neighborhood is a region of a larger society, according to Robert Park and Ernest Burgess, a group of individuals and entities comprising a spatially determined region dominated by ecological, cultural and often political influences [9]. In health studies, the word neighborhood was being described rather broadly, involving units as tiny as block sections and as big as regions. The terms neighborhood and community are often used synonymously in health research to refer to a person's specific residential environment, which is considered to have both material and social features that may be linked to health [10].

1.3 Urban Factors Affecting the Spread of the Epidemic

Human health can be enhanced by living in walkable neighborhoods and access to greenspace. The COVID-19 pandemic has demonstrated the close connection between health and urban areas, highlighting the potential impact of neighborhood characteristics such as population density, public services and transportation infrastructure, which are key drivers of urban growth. To try to keep the epidemic under control, this section outlines urban-specific factors which significantly raise the transmission of pandemics. These aspects are related to both population and urban environment and can vary between neighborhoods. Upward density is the main feature of metropolitan centers worldwide. The city's basic essence is gathering residents and thereby increase density. Building density has long performed a significant role in the aspects that can be affected by urban development. Density has become one of the main features of the urban environment [11]. However, density of population is not a reliable measurement of population density, particularly, in pandemics like coronavirus, where human interaction is the primary explanation for spread, population-based densities are better measured than traditional densities, since variance in sub-area density is more essential than density overall [12]. Given reports of high outbreak rates in townships and informal settlements, many experts have easily implicated population density for the rapid dissemination of the disease, which has intensified government's attempts to "de-densify" specific areas and remove encroaching residences [13]. Larger urban centers, though, have considerably higher infection rates. Ratcliffe et al. found that regions in urban centers exchange transportation and commuting habits, or "movement of residents," within communities and within urban centers, which is a perfect scenario for outbreaks to spread [14].

The second urban factor that affect the spread of epidemic is walkability. A walkable neighborhood where services and products may be accessed easily and safely (i.e., grocery stores, pharmacy, bakery, etc.). Walkable neighborhoods stimulate recreation, increase transit and provide healthy and pleasant roads that serve individuals of all mobility categories. A walkable neighborhood is much than merely an area that allows you to stroll, it must provide the pedestrian sensations that motivate them walk. This requires that the network environment includes features that makes it viable. Walkability is an assessment of how a place is appealing or not enticing to walkers. As shown in Birch research, if neighborhoods become more walkable, neighborhoods can alleviate the extreme crowding in different systems including public transport. Walking is not just a type of human mobility, but also a current social and political practice that may foster physical activity and impact the health of inhabitants as well as maximize the growth of urban areas [15].

The third factor affecting the spread of epidemic is service availability in the neighborhood. The involvement of medical centers can help to mitigate the pandemic's effects, particularly in regards of severity and death count. Insufficient health infrastructure and insufficient levels of public facilities are both seen as major contributors to resource shortages throughout pandemics. The unequal spread of services is extremely significant because it may cause a pause in responding to the outbreak [16].

The fourth factor affecting epidemic spread is public spaces and green parks that lowers stress and enhances the physiological, emotional and spiritual state. The safe usage of green spaces is an obstacle to the prevention of COVID-19 outdoor spread. The importance of parks had never been as clear as it was during the worldwide COVID-19 pandemic. Throughout this disaster, people visited their parks in an unprecedented way—for fresh air, exercise, relaxation, a sense of calm. Particularly now that the information indicates that COVID-19 can be considerably lower in the outside than inside and that public safety officials promote safe, long-distance exercise as part of COVID-19 responses. The way that COVID-19 would affect the potential architecture, utilization and perception of public space are unpredictable [17].

The fifth factor affecting spreading of epidemic spread is land use. Strengthening neighborhoods to cope with pandemic conditions that rely on land use should be taken into account from two major areas: Improving the efficiency and total amount of health and medical facilities through a multi-tiered framework and other services must provide amenities that support health and medical facilities.

1.4 Research Problem

The research and analysis carried out during the time of the COVID-19 pandemic revealed the impact of the characteristics of residential neighborhoods on the spread of epidemics [18]. The problem of this study is that there were several vulnerabilities in the design of residential neighborhoods in Amman, where it has been observed that

the distribution of services in many neighborhoods is challenging as it is difficult to access them on foot during lockdown periods, where many essential services are not accessible within walkable distances which a significant aspect that had previously gone unnoticed since the entirety of Amman's population depend on automobiles. The Mayor of Amman pointed out that there are neighborhoods, where basic services are available planning and technically, and other neighborhoods need to be developed and find special places for commercial services. In addition to the emergence of the problem of the lack of green spaces and public parks in most of the residential neighborhoods in Amman needs solutions [19].

The study also investigating the impact of the population density on the spread of infection epidemics and diseases which occur at the residential neighborhoods. The review of the report of the National Center for Security and Crisis Management showed that there were gathering places in Amman neighborhoods that contributed to the transmission of infection and the increase in the number of infected people in those areas [20].

1.5 Research Hypothesis

The research includes the following hypothesis.

1. There is a significant relationship between neighborhood characteristics and the spread of epidemics in general.
2. There is a significant relationship between population density and the spread of epidemics.
3. There is a significant relationship between designing walkable neighborhoods and the spread of epidemics.
4. There is a significant relationship between providing basic services within walking distance in residential neighborhoods and the spread of epidemics.
5. There is a significant relationship between providing public parks in the residential neighborhood and the spread of epidemics.
6. There is a significant relationship between achieving self-sufficient neighborhoods and the spread of epidemics.

2 Methodology

The methodology is divided into two major sections: the questionnaire for residents of neighborhoods and the case study analysis. A questionnaire is distributed for three selected neighborhoods according to the number of cases of COVID-19 during the period of 16 to March 23, 2020. Three different neighborhoods were selected depending on the number of infected persons. The highest infected neighbor is Al Rawabi neighborhood with 4092 cases, the middle is Al Rashid neighborhood with 1331 cases and the lowest id the Al Ghabeh neighborhood with 104 cases only. The

selection of the neighborhoods is based on the report of the National Center for Security and Crisis Management on the hotspots of corona infection in Jordan [21]. A standard procedure is followed in administering the questions in numerical order to achieve rational results. The sample consisted of 500 users, randomly selected, with an equal percentage of males and females for each neighborhood and determined by Stephen Thompson equation [22], and they are shown in Eq. (1). The questionnaire took almost six weeks to complete. The survey was started by the end of April 2020. The questionnaire was designed and divided into five categories. Density of the neighborhood was the first category, walkability was the second category, services availability was the third category, public open spaces was the fourth category and self-sufficiency were the last one. Eighteen questions were at last resulted for all categories. The thesis hypotheses will be tested for validity and to answer the main thesis question at end.

$$n = \frac{N \times p(1-p)}{\left[\left[N - 1 \times \left(d^2 \div z^2\right)\right] + p(1-p)\right]} \tag{1}$$

where N is the community size, Z is the standard core corresponding to the significance level of 0.95 and is equal to 1.96, D is the error rate of 0.05 and P is feature availability and neutral = 0.50.

2.1 Al Rawabi Neighborhood

Al Rawabi neighborhood is a neighborhood located in Wadi Al Seir district, west of Amman City. It is characterized by large shops on the main streets, such as Abdullah Ghosheh Street, which features services such as pharmacies, restaurants, cafes and supermarkets. But the neighborhood lacks public parks, open spaces and pedestrian paths. The area of the neighborhood is 3.9 km^2, and the number of COVID-19 cases was 4092 for one week from March 16, 2020 to March 23, 2020, with a population of 55,799 inhabitants [23] and a density of 1.41 person per square meters [24]. Walkability and ease of movement in Al Rawabi neighborhood is limited due to the inadequate sidewalk quality. However, through the period of lockdown, residents used the streets despite its poor pedestrian conditions as the streets were mostly empty of cars. Furthermore, walkways proved unsuitable to those with disabilities and those in wheelchairs. Al Rawabi area contains a lot of various services that meet all the needs of the residents, and there are many places that are considered high attractions for the residents. The neighborhood has a small part of the green open spaces and there is no public park (Fig. 1).

Fig. 1 Existing land use of Al Rawabi neighborhood. *Source* Greater Amman municipality, 2021

2.2 Al Rasheed Neighborhood

Al Rasheed neighborhood is within Al Jubeiha district north of Amman City. Al Rasheed neighborhood is close to the city center of Amman. The density of Al Rasheed neighborhood is 2.00 people per square meters with a population of 50,273 [23], and a total area of 2.51 km^2 [25]. Walkability and ease of movement in Al Rasheed neighborhood is limited due to the inadequate sidewalk quality. However, through the period of lockdown, residents used the streets despite its poor pedestrian conditions due to non-existence of cars. Furthermore, walkways proved unsuitable to those with disabilities and those in wheelchairs. In terms of services, it is sufficient and moderate in Al Rasheed neighborhood, where there are shops to buy fruits and vegetables in addition to pharmacies, supermarkets and bakeries (Fig. 2).

2.3 Al Ghabeh Neighborhood

Al Ghabeh neighborhood is within Tariq district northern of Amman. This neighborhood is the International University of Islamic Sciences, in addition to many mosques and pharmacies. The neighborhood is located on a highly elevated and overlooking land. It is one of the new neighborhoods, where construction began nearly four years ago, and it is characterized by its fresh air, especially in summer days. The density of Al Ghabeh neighborhood is 0.29 people per square meter, with a population of 10,784 [26], and an area of 3.70 km^2 [25]. Walkability and ease of movement in Al Ghabeh neighborhood is limited due to the inadequate sidewalk quality. However,

Fig. 2 Existing land use of Al Rasheed neighborhood *Source* Greater Amman municipality, 2021

through the period of lockdown, residents used the streets. Furthermore, walkways proved unsuitable to those with disabilities and those in wheelchairs (Fig. 3).

Fig. 3 Land use of Al Ghabeh neighborhood *Source* Greater Amman municipality, 2021

3 Results

This section is divided into two main parts, the first part will cover the findings of a data descriptive analysis of respondents' perceptions through means, standard deviations, response percentage and level of agreement. The section will also present a correlation study in order to test the relationship between characteristics of neighborhood dimensions such as density, walkability, services availability, public spaces and self-sufficiency and the spread of epidemic as seen in Table 1. Then, comes the hypothesis testing to test the impact of the characteristics of neighborhoods on the spread of epidemic in residential neighborhoods in Amman and their colorations as presented in Table 2. Table 2 will describe both independent and dependent variables from a statistical point of view through means, standard deviations, response percentage and level of agreement. The questionnaire used the five points Likert scale, and in order to calculate the importance, the following equation is used: Interval: (5–1)/3 = 1.33, where low implementation = 1 to 2.33, medium implementation = 2.34 to 3.66 and high implementation = 3.67 to 5.

The average of the five items of density for the 3 selected neighborhoods is 4.01, while the standard deviation is 0.82 which illustrates that the residents in the selected neighborhoods are agreed on a high level of density variables. Furthermore, the results showed that Al Rawabi neighborhood is with the highest mean value of 4.24 and standard deviation value of 0.63, which indicates that there is a high degree of agreement about the effect of density of population on the spread of epidemic. The results showed that Al Ghabeh neighborhood has the lowest mean value of 3.76 and standard deviation value of 0.69, which is probably due to the belief of the population that the reason for the high spread of the virus is the high population density in the neighborhood.

The average of the five items of walkability for the 3 selected neighborhoods is 3.97, while the standard deviation is 0.81, which illustrates that the residents in the selected neighborhoods are agreed on a high level of walkability variables. Furthermore, Table 1 showed that the results of the three neighborhoods are very close together, and it is likely due to the need for the three neighborhoods to develop pedestrian paths, widening sidewalks and adding bike paths. The average of the three items of services availability for the 3 selected neighborhoods is 3.47, while the average standard deviation is 0.76, which illustrates that the residents in the selected neighborhoods are agreed on a medium level of services availability variables. Furthermore, the results showed Al Rasheed neighborhood has the highest mean value of 3.59 and standard deviation value of 0.67, which indicates that there is a medium degree of agreement about the effect of service availability on the spread of epidemic. The results showed that Al Ghabeh neighborhood has the lowest mean value of3.76 and standard deviation value of 0.95. The mean for public spaces for the 3 selected neighborhoods is 4.04, while the standard deviation is 0.82, which illustrates that the residents in the selected neighborhoods are agreed on a high level of public spaces variables. Furthermore, the results showed that providing green spaces in the neighborhood reduces the spread of epidemics as seen from the third

Table 1 A comparison between three selected neighborhoods in terms of the mean, standard deviation, response percentage% and level of agreement of the characteristics of neighborhood

Item	Mean				S.td				Level of agreement			
	All 3 neighborhoods	Al Rawabi	Al Rasheed	Al Ghabeh	All 3 neighborhoods	Al Rawabi	Al Rasheed	Al Ghabeh	All 3 neighborhoods	Al Rawabi	Al Rasheed	Al Ghabeh
Do you think human interaction increase the spread of infection of the Corona virus?	3.94	3.92	4.03	3. 86	0.88	0.87	1.03	0.82	High	High	High	High
Do you think densely populated neighborhoods encourage the spread of COVID-19?	4.35	4.54	4.39	4.12	0.75	0.73	0.86	0.94	High	High	High	High
Do you think maintaining physical distances help preventing the viruses?	4.28	4.40	4.24	4.19	1.02	0.68	0.98	0.74	High	High	High	High

(continued)

Table 1 (continued)

Item	Mean				S.td				Level of agreement			
	All 3 neighborhoods	Al Rawabi	Al Rasheed	Al Ghabeh	All 3 neighborhoods	Al Rawabi	Al Rasheed	Al Ghabeh	All 3 neighborhoods	Al Rawabi	Al Rasheed	Al Ghabeh
Do you think that exposure basic services to enormous pressures because of high density increases the spread of infection?	3.64	4.25	3.53	3.14	0.98	0.86	1.03	1.21	Medium	High	Medium	Medium
Is the increase in population density leads to an increase in cases of COVID-19?	3.84	4.09	3.94	3.48	1.05	0.49	0.86	0.79	High	High	High	Medium
Density	4.01	4.24	4.02	3.76	0.82	0.63	0.78	0.69	High	High	High	High

(continued)

Table 1 (continued)

Item	Mean				S.td				Level of agreement			
	All 3 neighborhoods	Al Rawabi	Al Rasheed	Al Ghabeh	All 3 neighborhoods	Al Rawabi	Al Rasheed	Al Ghabeh	All 3 neighborhoods	Al Rawabi	Al Rasheed	Al Ghabeh
Are the sidewalks in your neighborhood are in good condition, suitable for walking?	3.11	3.04	3.19	3.09	0.80	0.98	0.79	0.63	Medium	Medium	Medium	Medium

(continued)

Table 1 (continued)

Item	Mean				S.td				Level of agreement			
	All 3 neighborhoods	Al Rawabi	Al Rasheed	Al Ghabeh	All 3 neighborhoods	Al Rawabi	Al Rasheed	Al Ghabeh	All 3 neighborhoods	Al Rawabi	Al Rasheed	Al Ghabeh
Is creating more pedestrian friendly neighborhoods reduces congestion on public transport and thus reduces the chances of the virus spreading?	4.24	4.25	4.19	4.28	0.95	0.86	1.03	0.88	High	High	High	High
Is providing wide pedestrian paths reduce the chances of the virus spreading?	4.19	4.22	4.17	4.19	0.67	0.96	1.01	0.74	High	High	High	High

(continued)

Table 1 (continued)

Item	Mean				S.td				Level of agreement			
	All 3 neighborhoods	Al Rawabi	Al Rasheed	Al Ghabeh	All 3 neighborhoods	Al Rawabi	Al Rasheed	Al Ghabeh	All 3 neighborhoods	Al Rawabi	Al Rasheed	Al Ghabeh
Do you think that providing paths for cyclists reduces congestion on public transport and thus reduces the chances of the virus spreading?	4.20	4.19	4.23	4.18	1.02	0.81	0.87	0.76	High	High	High	High
Do you think providing sidewalks with adequate width will prevent overcrowding?	4.12	4.21	4.02	4.13	0.94	0.89	0.87	1.02	High	High	High	High
Walkability	3.97	3.98	3.96	3.97	0.81	0.82	0.98	0.76	High	High	High	High

(continued)

Table 1 (continued)

Item	Mean				S.td				Level of agreement			
	All 3 neighborhoods	Al Rawabi	Al Rasheed	Al Ghabeh	All 3 neighborhoods	Al Rawabi	Al Rasheed	Al Ghabeh	All 3 neighborhoods	Al Rawabi	Al Rasheed	Al Ghabeh
Is your neighborhood having sufficient services and facilities?	4.17	4.54	4.36	3.61	0.88	0.38	0.76	0.65	High	High	High	Medium
Do you think that providing the facilities within reasonable walking distance reduces the chances of infection?	3.21	3.04	3.37	3.22	0.96	1.03	0.74	0.86	Medium	Medium	Medium	Medium

(continued)

Table 1 (continued)

Item	Mean				S.td				Level of agreement			
	All 3 neighborhoods	Al Rawabi	Al Rasheed	Al Ghabeh	All 3 neighborhoods	Al Rawabi	Al Rasheed	Al Ghabeh	All 3 neighborhoods	Al Rawabi	Al Rasheed	Al Ghabeh
Does increasing the provision of basic services in your neighborhood lead to less congestion?	3.04	2.82	3.04	3.27	1.04	0.98	0.67	0.72	Medium	Medium	Medium	Medium
Services availability	3.47	3.45	3.59	3.38	0.76	0.72	0.67	0.95	Medium	Medium	Medium	Medium
Is adding greenery in public areas increases the therapeutic advantages of the open spaces?	4.09	4.16	4.09	4.02	0.91	0.78	1.04	0.36	High	High	High	High

(continued)

Table 1 (continued)

Item	Mean				S.td				Level of agreement			
	All 3 neighborhoods	Al Rawabi	Al Rasheed	Al Ghabeh	All 3 neighborhoods	Al Rawabi	Al Rasheed	Al Ghabeh	All 3 neighborhoods	Al Rawabi	Al Rasheed	Al Ghabeh
Is the availability of parks near your residence helps you cope with the spread of epidemics?	3.93	4.13	4.08	3.57	1.03	0.62	0.97	0.71	High	High	High	High
Is providing small green spaces in the neighborhood allows public health during an epidemic?	4.11	4.20	4.12	4.01	0.89	0.99	0.82	0.88	High	High	High	High
Public spaces	4.04	4.16	4.10	3.87	0.82	0.78	0.84	0.92	High	High	High	High

(continued)

Table 1 (continued)

Item	Mean				S.td				Level of agreement			
	All 3 neighborhoods	Al Rawabi	Al Rasheed	Al Ghabeh	All 3 neighborhoods	Al Rawabi	Al Rasheed	Al Ghabeh	All 3 neighborhoods	Al Rawabi	Al Rasheed	Al Ghabeh
Is the availability of supermarkets in your neighborhood reduces the spread of the epidemic?	4.0	3.87	4.11	4.04	0.66	0.95	0.46	0.67	High	High	High	High
Is the rooftop planting can lead to the stop of spread of epidemic?	3.80	4.02	3.65	3.84	0.91	0.68	0.86	0.61	High	High	Medium	High

(continued)

Table 1 (continued)

Item	Mean				S.td				Level of agreement			
	All 3 neighborhoods	Al Rawabi	Al Rasheed	Al Ghabeh	All 3 neighborhoods	Al Rawabi	Al Rasheed	Al Ghabeh	All 3 neighborhoods	Al Rawabi	Al Rasheed	Al Ghabeh
Is the availability of public services in your neighborhood reduces the spread of the epidemic?	4.02	4.08	4.02	3.96	0.66	0.81	0.92	0.77	High	High	High	High
Is designing self-sufficient neighborhoods will help reduce the transmission of epidemics in the future?	4.15	4.17	4.18	4.11	0.57	0.49	0.72	0.68	High	High	High	High
Self-sufficiency	4.03	4.13	3.90	4.07	0.61	0.55	0.61	0.74	High	High	High	High

Table 2 Correlations between the variables included in the study

		Spread of epidemic	Density	Walkability	Services availability	Public spaces	Self-sufficiency
Spread of epidemic	Pearson correlation	1	−0.096	−0.460**	0.302*	−0.337*	−0.633**
	Sig. (2-tailed)		0.517	0.001	0.037	0.019	0.000
	N	48	48	48	48	48	48
Density	Pearson correlation	−0.096	1	0.195	0.533**	0.460**	−0.136
	Sig. (2-tailed)	0.517		0.183	0.000	0.001	0.358
	N	48	48	48	48	48	48
Walkability	Pearson correlation	−0.460**	0.195	1	0.216	0.214	−0.499**
	Sig. (2-tailed)	0.001	0.183		0.140	0.143	0.000
	N	48	48	48	48	48	48
Services availability	Pearson correlation	0.302*	0.533**	0.216	1	0.555**	−0.380**
	Sig. (2-tailed)	0.037	0.000	0.140		0.000	0.008
	N	48	48	48	48	48	48
Public spaces	Pearson correlation	−0.337*	0.460**	0.214	0.555**	1	−0.178
	Sig. (2-tailed)	0.019	0.001	0.143	0.000		0.227
	N	48	48	48	48	48	48
Self-sufficiency	Pearson correlation	−0.633**	−0.136	−0.499**	−0.380**	−0.178	1
	Sig. (2-tailed)	0.000	0.358	0.000	0.008	0.227	
	N	48	48	48	48	48	48

* indicates a statistical significance for the relationship between variables at 95% confidence level

question on service availability section which has the highest mean value of 4.11 and standard deviation value of 0.95. This is in line with the second question on the same category of service availability with a 3.93 mean value and a 1.09 standard deviation, which again indicates that there is a high degree of agreement on the effect of the availability of parks on the spread of epidemic. The average of the four items of self-sufficiency for the 3 selected neighborhoods is 4.13, while the standard deviation is 0.65, which illustrates that the residents in the selected neighborhoods are agreed on a high level of self-sufficiency variables. Furthermore, the results Al Rawabi neighborhood is with the highest mean value of 4.03 and a standard deviation value of 0.55. This is likely due to the residents' belief in the necessity of achieving a sustainable neighborhood to reduce the spread of epidemics.

4 Discussion and Conclusions

The hypotheses were tested by using the simple regression analysis method and based on the value of (R-Square) that determines the value of the variance in the dependent variable that can be explained through the independent variable. The following table number 3 shows the values of the coefficient of determination of the relationship between the dependent variable (the spread of epidemics) and the independent variables (neighborhood characteristics), on which the hypotheses of this study were tested.

Table 3 gives the results of the multiple regressions analysis to test the first hypothesis which aims to analyze the impact of characteristics of neighborhood represented by (density, walkability, services availability public spaces, self- sufficiency) on the spread of epidemic in the residential neighborhoods in Amman. The fitness of the model for multiple regressions is illustrated by the value of R-squared. Since R-squared is 0.485, the dimensions of the characteristics of neighborhood can explain 0.485 of variance on the spread of epidemic in the neighborhoods of Amman, since (R-squared = 0.485, F-test = 7.9, Sig. = 0.000. So that, the first hypothesis should be accepted and conclude the presence of a significant impact of them on the spread of epidemic in neighborhoods of Amman at a significant level ($\alpha \leq 0.05$).

The results of simple regression analysis to test the second hypothesis are given in Table 3. The dependent variable in the test was the spread of epidemic and the density was the independent variable. The results show that the value of ($R = 0.096$), which indicates that the correlation coefficient between density and spread of epidemic is 0.096. Besides, the value of R-squared (R2) is 0.009, which indicates that density can explain 0.009 of the variances spread of epidemics in residential neighborhoods in Amman. So that, the second hypothesis should be rejected and conclude that there is no significant impact of density on the spread of epidemic in neighborhoods of Amman at a significant level ($\alpha \leq 0.05$).

The results of simple regression analysis to test the third hypothesis are given in Table 3. The dependent variable in the test was the spread of epidemic and the walkability was the independent variable. The results show that the value of ($R = -$

Table 3 Results of the regression analysis of the relationship between the independent variables (neighborhood characteristics) and the dependent variable (the spread of epidemics)

Hypothesis (N)	Characteristics of neighborhood	R	R-square	Degrees of freedom	F	Sig
1	All characteristics of neighborhood	0.637	0.485	5.42	7.9	0.000**
2	Density	0.096	0.009	1.46	0.425	0.517
3	Walkability	−0.46	0.212	1.46	12.359	0.001**
4	Services availability	0.302	0.091	1.46	4.617	0.037**
5	Public spaces	−0.337	0.114	1.46	5.91	0.019**
6	Self-sufficiency	−0.633	0.401	1.46	30.763	0.000**

* indicates a statistical significance for the relationship between variables at 95% confidence level
** indicates the relationship is stronger between variables at 95% confidence level
*** indicates the relationship is more stronger between variables at 95% confidence level
[a] Dependent variable
[b] Predictors (Constant)

0.46), which indicates that the correlation coefficient between walkability and spread of epidemic is 0.46, Besides, the value of R-square (R2) is 0.212, which indicates that walkability can explain 21% of the variance spread of epidemics in residential neighborhoods in Amman-Jordan. So that, the third hypothesis should be accepted and conclude the presence of a significant impact of walkability on the spread of epidemic in neighborhoods of Amman at a significant level ($\alpha \leq 0.05$).

The results of simple regression analysis to test the fourth hypothesis are given in Table 3, the dependent variable in the test was the spread of epidemic and the services availability was the independent variable. The results show that the value of ($R = 0.302$), which indicates that the correlation coefficient between services availability and spread of epidemic is 0.302. Besides, the value of R-square (R2) is 0.091, which indicates that services availability can explain 9% of the variance spread of epidemics in residential neighborhoods in Amman. So that, the fourth hypothesis should be accepted and conclude the presence of a significant impact of the services availability on the spread of epidemic in neighborhoods of Amman at a significant level ($\alpha \leq 0.05$).

The results of simple regression analysis to test the fifth hypothesis are shown in Table 3. The dependent variable in the test was the spread of epidemic and the public spaces were the independent variable. The results show that the value of ($R = -0.337$), which indicates that the correlation coefficient between public services and spread of epidemic is 0.337. Besides, the value of R-squared (R2) is 0.114, which indicates that public services can explain 11% of the variance spread of epidemics in residential neighborhoods in Amman. So that, the fifth hypothesis should be accepted and conclude the presence of a significant impact of the public services on the spread of epidemic in neighborhoods of Amman at a significant level ($\alpha \leq 0.05$).

The results of simple regression analysis to test the sixth hypothesis are given in Table 3. The dependent variable in the test was the spread of epidemic and the self-sufficiency was the independent variable. The results show that the value of ($R = -0.633$), which indicates that the correlation coefficient between self-sufficiency and spread of epidemic is 0.633. Besides, the value of R-squared (R2) is 0.401, which indicates that self-sufficiency can explain 40% of the variance spread of epidemics in residential neighborhoods in Amman. So that, the sixth hypothesis should be accepted and conclude the presence of a significant impact of the self-sufficiency on the spread of epidemic in neighborhoods of Amman at a significant level ($\alpha \leq 0.05$).

The study found that the statistical analysis that population density in itself is not a decisive factor in the spread of epidemics, although respondents from the population believed that there is an effect of population density on the spread of COVID-19. This result is supported by the studies of Rodriguez-Villamizar et al. [27], Amdaoud et al. [28], Sirkeci and Yücesahin [29] and Jamshidi et al. [30].

The study found that the availability of services in itself is good in the residential neighborhood, but the lack of a well-thought-out distribution leads to crowding of residents while obtaining services and increases the speed of the spread of epidemics.

The study found that a walkable neighborhood that enables its residents to access basic services within the appropriate walking distance, and in which, the walking environment is good and has good sidewalks, and paths for pedestrians and bicycles help reduce the number of cases of the virus due to the reduce the need for mobility and reduce opportunities to interact with others in the community. This result is supported by the studies of Moreno et al. [31], Kato and Matsushita [32].

The study found that the availability of green spaces in residential neighborhoods may enhance general health significantly and help satisfy the requirements of people in terms of social contact in addition to combat the spread of epidemic. This result is supported by the study of [33].

The study found that COVID-19 has encouraged many neighborhoods to realize the need of self-sufficiency whether in fundamental household supplies or food supply. This result is supported by the study of [34].

References

1. World Health Organization (2020) Considerations for quarantine of individuals in the context of containment for coronavirus disease (COVID-19): interim guidance, 19 March 2020
2. Al Shawarbeh Y (2020) Amman efforts to contain COVID-19. Smart City J
3. Alshuwaikhat HM (1999) Planning the 2151: century urban neighborhood: learning from previous concepts
4. Leon DA (2008) Cities, urbanization and health
5. Leon DA. op.cit
6. Lawhon LL (2009) The neighborhood unit: physical design or physical determinism? J Plann Hist 8(2):111–132
7. Lawhon LL. op.cit
8. Park Y, Rogers GO (2015) Neighborhood planning theory, guidelines, and research: can area, population, and boundary guide conceptual framing? J Plan Lit 30(1):18–36

9. Park Y, Rogers GO. op.cit
10. Diez Roux AV (2001) Investigating neighborhood and area effects on health. Am J Public Health 91(11):1783–1789
11. Knudsen B, Florida R, Stolarick K, Gates G (2008) Density and creativity in US regions. Ann Assoc Am Geogr 98(2):461–478
12. Baser O (2021) Population density index and its use for distribution of Covid-19: a case study using Turkish data. Health Policy 125(2):148–154
13. Turok I (2020) Cities at the epicenter of the COVID-19 pandemic: density matters
14. Ratcliffe M, Burd C, Holder K, Fields A (2016) Defining rural at the US census bureau. American community survey and geography brief. U.S. Department of Commerce. https://www.census.gov/content/dam/Census/library/publications/2016/acs/acsgeo-1.pdf
15. Wilder-Smith A, Freedman D (2020) Isolation, quarantine, social distancing and community containment: pivotal role for old-style public health measures in the novel coronavirus (2019-nCoV) outbreak. J Travel Med
16. Neiderud C-J (2015) How urbanization affects the epidemiology of emerging infectious diseases. Infect Ecol Epidemiol 5(1):27060. https://doi.org/10.3402/iee.v5.27060
17. Muqueeth S (2021) Parks: a vital community condition. Parks Stewardship Forum 37(1)
18. Sharifi A, Khavarian-Garmsir AR (2020) The COVID-19 pandemic: impacts on cities and major lessons for urban planning, design, and management. Sci Total Environ 142391
19. Tomah AN, Abed A, Saleh B (2017) Assessment of the geographic distribution of public parks in the city of Amman. Eur J Sci Res 144(3):262–275
20. Ministry of Health (2020) Annual statistical report, Amman, Jordan https://www.moh.gov.jo/Echobusv3.0/SystemAssets/04c240a1-dcc8-4df9-bdda-eefca59ad4c3.pdf
21. Ministry of Health, Annual statistical report, op.cit
22. Vincent K, Thompson S (2017) Estimating population size with link-tracing sampling. J Am Stat Assoc 112(519):1286–1295
23. Department of Statistics (2020) Annual Report
24. Greater Amman Municipality (2021) Annual Report, Amman
25. Greater Amman Municipality. op.cit
26. Department of Statistics. op.cit
27. Rodriguez-Villamizar LA, Belalcázar-Ceron LC, Fernández-Niño JA, Marín-Pineda DM, Rojas-Sánchez OA, Acuña-Merchán LA, Ramírez-García N, Mangones-Matos SC, Vargas-González JM, Herrera-Galindo VM (2021) Air pollution, sociodemographic and health conditions effects on COVID-19 mortality in Colombia: an ecological study. Sci Total Environ 756:144020
28. Amdaoud M, Arcuri G, Bourdin S, Costanzo D, Eva M, Iatu C, Ibanescu B, Jeanne L, Levratto N (2020) The early demographic and geographic patterns of the SARS-CoV-2 epidemic in the Netherlands. Tijdschrift voor Economische
29. Sirkeci I, Yucesahin MM (2020) Coronavirus and migration: analysis of human mobility and the spread of Covid-19. Migr Lett 17(2):379–398
30. Jamshidi S, Baniasad M, Niyogi D (2020) Global to USA county scale analysis of weather, urban density, mobility, homestay, and mask use on COVID-19. Int J Environ Res Public Health 1–17. https://doi.org/10.3390/ijerph17217847
31. Moreno C, Allam Z, Chabaud D, Gall C, Pratlong F (2021) Introducing the 15-minute city: sustainability, resilience and place identity in future post-pandemic cities. Smart Cities 4(1):93–111
32. Kato H, Matsushita D (2021) Changes in walkable streets during the COVID-19 pandemic in a suburban city in the Osaka metropolitan area. Sustainability 13(13):7442
33. Xie J, Luo S, Furuya K, Sun D (2020) Urban parks as green buffers during the COVID-19 pandemic. Sustainability 12(17):6751
34. Buheji M, Korže AV, Eidan S, Abdulkareem T, Perepelkin N, Mavric B, Preis J (2020) Global self-sufficiency network-a collaborative approach for addressing post-COVID-19 challenges. Bus Econ Res 10(3):1–22

BIM Technology, Intelligent Building and Information Technology in Building

A System for Evacuation Route Plan Based on the Nature of Terrain and Dynamic Nature of Construction

Thiha Nyimin, Tanit Tongthong, and Vachara Peansupap

Abstract Labors from construction sites are dedicated to working on different activities which could turn into dangerous situations. Moreover, fire in construction and other types of emergencies such as severe or unexpected weather conditions, earthquakes, and partial collision of buildings can also threaten the safety of workers. Therefore, authorities of construction site protection need to have a solid evacuation plan which can provide the fastest evacuation route for laborers. To develop an effective evacuation route plan, it is critical to consider the dynamic nature of construction (material locations, temporary stairs, later, etc.) and the different nature of the terrain in construction (concrete or rebar floors, etc.) that can impact the evacuation time negatively. This paper presents a framework that uses BIM technology and a game engine that can present the object in 3D and provide efficient program to find the fastest evacuation route by considering the velocity on different terrain. The system provides a user-defined form for selecting constraints in order to acquire the fastest evacuation route. These parameters involve the location of the construction materials, complete or incomplete structures of walls or stairs, temporary construction, floor conditions, and exits. The case study using the four-story sample BIM is executed to validate the proposed approach. The proposed system is expected to assist the safety engineers in developing the fastest evacuation route plan.

Keywords Evacuation route planning · Fire safety plan · Pathfinding system · Unity's NavMesh

T. Nyimin (✉) · T. Tongthong · V. Peansupap
Department of Civil Engineering, Faculty of Engineering, Chulalongkorn University, Bangkok 10330, Thailand
e-mail: 6270358621@student.chula.ac.th

T. Kang (ed.), *Proceedings of 5th International Conference on Civil Engineering and Architecture*, Lecture Notes in Civil Engineering 369,
https://doi.org/10.1007/978-981-99-4049-3_51

1 Introduction

Based on the Health and Safety Executive (HSE) statistics, a negative reputation is firmly growing in the construction industry due to the several occurrences of accidents [1]. Moreover, a construction site is regarded as a hazardous and risky workplace, where there are plenty of features that differ from other industries. One main characteristic of the construction industry is physical changes. The changes involve the development of each construction site on a daily basis. The types of machines, crews, materials, and storage of this hardware are mainly making variations in a construction project. Every day, workers from the construction site must know about these environmental changes and alterations of risky locations as well as obstacles on site.

According to the data published by the Federal Emergency Management Agency (FEMA) of the United States (US), approximately 4800 fire accidents happen annually on construction sites [2]. However, surprisingly, the major cause of death and injury on a construction site is not fire accidents, but the safety of workers during an incident is directly proportional to the worker quantity and the evacuation plan, regarding the conduct of the Occupational Safety and Health Administration (OSHA) [3]. Several types of emergency situations need immediate evacuation in a construction site according to the statistics of OSHA (2001). These include severe or unpredicted weather conditions, fractional structure collapse, and earthquakes. For these reasons, evacuation plans should be guaranteed that they are robust enough to handle emergency situations, e.g., there is an emergency evacuation of a high-rise construction site in 2019 because a helicopter collided with a crane from the construction site due to the foggy climate [4].

For safety, it is needed to comprise every emergency, unpredicted, and risky situations that can bring a lost cause either to the people or the environment. A rapid and skilled solution is essential in this case for bringing assurance on the protection of people on the construction site. In case of man-made destruction or natural catastrophes, a suitable fire safety evacuation route plan is necessary to vacate people from the construction site or a building in an effective manner without exposing them to great loss or damage. When it comes to complex and huge factories as well as high-rise constructions, it is even more necessary to consider an evacuation plan. It is stated by Kim and Lee (2019) that evacuation route planning is more challenging in the construction sector due to the dynamic nature of construction [5]. The plan must be considered for individual workers, safety engineers, and construction personnel. In current practice, when planning the moving paths of workers, logistics, and vehicles, safety engineers and construction personnel apply their experience and intuitive understanding of changing workplace conditions [3]. Current practice can produce suboptimal paths since it mainly depends on the subject's judgment, causing human errors. Additionally, since specific fire safety planning practices that focus on each construction site are applied in the construction industry, revises and updates are a must with intervals [6]. However, comprehensive fire safety planning that includes escape route plans, firefighting equipment installation plans, and mandatory education for workers can be an enormously labor-intensive job if done manually. Usually,

Table 1 Movement speeds on different surface conditions and devices [7]

Surface conditions and devices	Average speed (m/s)
Concrete surface	1.89 (horizontal)
Rebar surface	1.41 (horizontal)
Temporary dogleg and parallel stairs	0.68 (slope)
Temporary ladder	0.45 (vertical)
Standard stairs (Male 17–50)	0.935 (slope)

most construction projects rarely provide efficient and practical evacuation plans [5]. Hence, the effective evacuation route planning system is provided in this paper where the construction personnel can generate the fastest evacuation route plan based on the movement speed in different physical characteristics and the dynamic nature of construction.

2 Literature Review

This section will discuss the previous studies related to the movement speed in construction sites, evacuation route-finding systems, and evacuation route planning systems in construction.

2.1 Movement Speed in Different Physical Characteristics

Galea et al., have stated that different surface conditions and devices affect evacuation time [7]. The research has collected the walking speed of a worker on different floor surfaces such as concrete, decking, and decking with rebar. It has also gathered the ascending and descending speeds of the worker on different devices (e.g., temporary dogleg, parallel scaffold stairs, and ladders) from an experiment conducted on a tall construction site. Moreover, Galea has also driven the standard stairs speed based on Fruin [8]. Table 1 shows the movement speed dataset, and these movement speeds will be applied in developing a new approach pathfinding system that can consider the nature of the terrain.

2.2 Evacuation Route-Finding System

The main objective of evacuation pathfinding is to improve evacuation process to reduce the number of fatalities and injuries and accelerate the evacuation process. Gan et al., have mentioned that improving the choices of a route for the evacuees is one aspect of improving the evacuation process [9].

Soltani et al., have discovered the advantages and disadvantages of three algorithms: Dijkstra, A*, and genetic algorithms, in terms of distance, route space, and time consumption [10]. The research uses each algorithm to develop the application of path planning and generates optimized paths in terms of visibility, travel distance, and safety risks. Cui and Shi, have stated that the A* algorithm is appropriate in pathfinding for large spaces since it reduces complexity in search space hierarchy [11]. The path is evaluated based on the following equation;

$$f(n) = g(n) + h(n), \tag{1}$$

where $f(n)$ = the final cost for the path

$g(n)$ = the cost of the path from starting node to node n,

$h(n)$ = the cost of the cheapest path from node n to exit node.

Due to the polygonal structure of the 3D world, a tool that promises a path with the most efficient and shortest route gains popularity, namely Unity's Navigation mesh (NavMesh). Among various algorithms in NavMesh, the A* algorithm gets the spotlight with an output of the ideal shortest path [11]. In addition to this, several authors have used NavMesh in various indoor applications. Some of these applications consist of indoor navigation, indoor evacuation simulation, and evacuation simulation for older adults [12–14]. NavMesh is applied in this paper as a tool for navigating the fastest evacuation route.

2.3 Evacuation Route Planning System in Construction

Khan et al., have introduced a Con-fire safety planning system that uses visual language to generate a fire safety plan. It includes the firefighting equipment installation plan and evacuation route plan [15]. In this system, the evacuation route plan is generated based on the completed building design. Kim and Lee, have developed a platform that can produce a daily evacuation path in 4D BIM [5]. The building structure and evacuation plans will be changed in terms of the progress of the construction, and the A* algorithm is used for route finding. However, this platform does not consider the location of temporary structures and the movement speed of different physical characteristics.

3 Research Gap

Numerous researchers have attempted to improve the evacuation route plan during a construction. Galea et al., tried to improve the evacuation time by evaluating the physical characteristic of different terrains on the route that affects the evacuation process [7]. But, in the study, the authors do not develop the system that provides the fastest evacuation route. Kim and Lee, and Khan et al., introduce the system that can

provide evacuation route [5, 15]. However, their evacuation route planning system do not consider about the nature of terrain on the evacuation route. Therefore, this paper is aimed to fulfill and develop a system that is suitable for construction and can generate the fastest evacuation route plan which consider not only the dynamic change of construction environment but also the nature of terrain on the escape route.

4 Research Methodology

In this section, the development of the proposed system is listed. The literature review and field observation will be carried out in the first stage of the research. This research focused on the case studies of evacuation route planning in construction. According to the explored knowledge from the first stage, the conceptual framework of the proposed system and the system design is produced. To develop the system, the Unity game engine and Visual Studio are mainly utilized. A four-story building is chosen as the case study to test the prototype. One scenario is created in this building, and the concept of the proposed system is tested by using the output from this case study.

5 Development of Prototype

The development environments which are arranged for pursuing the proposed system are discussed in this section. Figure 1 illustrates the step-by-step process of the system. The main software programs that are used to generate the processes are Unity (2019), Navisworks (2019), Visual Studio (2017), and Autodesk Revit (2019). Unity is a cross-platform game engine, supporting more than 25 platforms. The main strength of Unity is that its powerful engine can operate effortlessly. The NavMesh is a building component-making tool, which is used to generate the NavMesh or a polygon mesh of the building. This NavMesh building component is added to Unity for further processes. To generate the script or programming language in Unity game engine, Visual Studio is applied.

5.1 Input

One of the popular BIM software which is used in developing the 3D model of the building is Revit. To use the 3D model in Unity, the FBX file type of this model is needed. However, the acquired FBX file from Revit only shows the name of the components. Hence, FBX files will be exported from Navisworks, which guarantees rich information, showing the components with categories such as levels (floors),

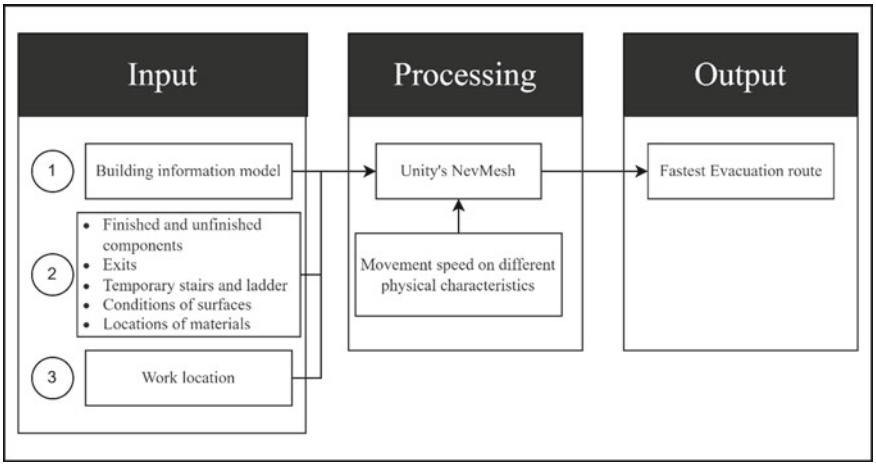

Fig. 1 Process of the proposed system

walls, and doors. Therefore, in this prototype, Revit will be used to export the NWC file, and then Navisworks is applied to generate the FBX file from the NWC file.

Furthermore, the user input model and data will be created which are the main impacts in the evacuation route-finding system. The input models consist of exits, temporary stairs and ladders, work locations, and the location of materials. The usages of these input data are identifying the conditions of the surface and, finished, and unfinished components. These identifications are important in maintaining construction progress for the dynamic building structure on construction sites. NavMesh Surface can create a polygon mesh of the surface that is able to determine the surface conditions and the area that is blocked by a wall or material. The unfinished components are discarded in the user interface.

5.2 System Processing

Before finding the evacuation route, the movement speed on different surfaces and devices is needed to convert to the travel time to find the evacuation routes based on travel time. In this system, the types of temporary stairs have not been classified, and the average speed of temporary dogleg and parallel stairs are used to regard the speed of temporary stairs. Moreover, the walking speed on the slope of the temporary stairs has a disadvantage on the pathfinding system because the angle of the temporary stairs from the system cannot be the same as the real-world angle. To remove the angle of the temporary stair, the walking speed on the slope of the temporary stair is converted to the vertical walking speed in Table 2. By using the travel time in Unity's NavMesh, the fastest evacuation routes from working locations to exits are produced based on the travel time.

Table 2 Average movement speed on different surface conditions and devices

Surface conditions and devices	Average speed (m/s)	Travel time for 1 m (s)
Concrete surface	1.89 (horizontal)	0.53(horizontal)
Rebar surface	1.41 (horizontal)	0.71 (horizontal)
Temporary stairs	0.5 (vertical)	2 (vertical)
Temporary ladder	0.45 (vertical)	2.22 (vertical)
Standard stairs (Male 17–50)	0.935 (slope)	1.07 (slope)

5.3 Output

The main purpose of the output is to support the construction personnel and safety engineers in creating the evacuation route. Therefore, the output includes all useable evacuation routes by arranging in terms of travel time. Moreover, as presented in Fig. 4, the proposed system also provides the travel distance and time.

6 Case Study and Implementation

To investigate the feasibility and applicability of evacuation path planning, a four-story building, which is illustrated in Fig. 2, is used as the case study. In this case study, the work location is chosen on the fourth floor and nine exits are placed. The process of implementation is mentioned below.

Firstly, the NWC file is imported from the Revit architectural model before opening the model on Navisworks. Additionally, the architectural model from Navisworks is exported into an FBX file to use this model in the Unity game engine. The doors and windows from the model are required to be deleted on Unity to carry out the next stage.

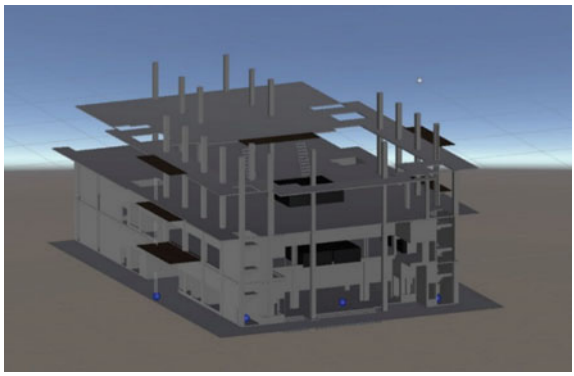

Fig. 2 Four-story construction site condition

Users need to use the user inputs to create the real construction conditions in Unity software. First, building element status is defined by the structural design (e.g., the wall is finished or not) and surface conditions (e.g., concrete or rebar surfaces) in terms of current construction progress. Second, the location of materials, temporary stairs and ladders, and exits should be defined according to the condition of the real construction site. To replicate the real construction site condition in the system, the user needs to use the user input to get the desired construction site conditions. Figure 3 presents how to assign the user input. By clicking on the building object in Unity's scene (green box) and changing the properties by using the layers (blue box), users can identify the finished and unfinished components. To see the other types of inputs such as the locations of material, temporary stairs and ladders, and exits, users can drag the model from the prefab file (yellow box) into the scene and then allocate them to the desired locations. After that, the user has to run the software and fill in the area of work locations (see Fig. 4). The area of the building is divided according to room area from BIM (see Fig. 5). Table 3 represents the result of the fastest evacuation route.

Table 3 shows the result of the prototype system. Regarding the table, the travel distance of the route to exit E1 is longer than the route to exit E2, even though the route to E1 is 10 s faster than exit E2. The result demonstrates that the system chose the evacuation route based on the minimum travel time.

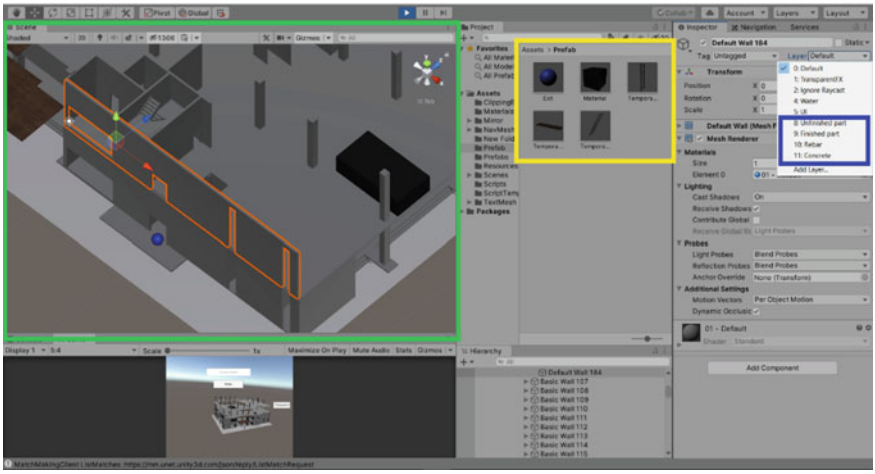

Fig. 3 Input the user input in Unity

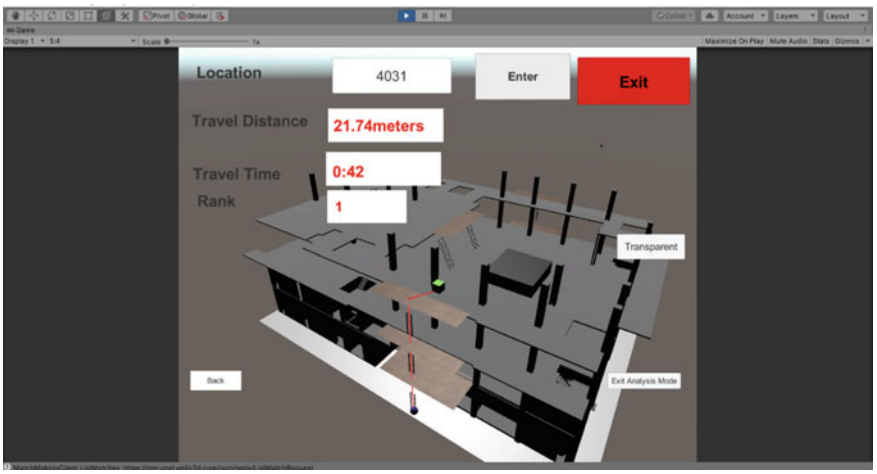

Fig. 4 Output of the prototype

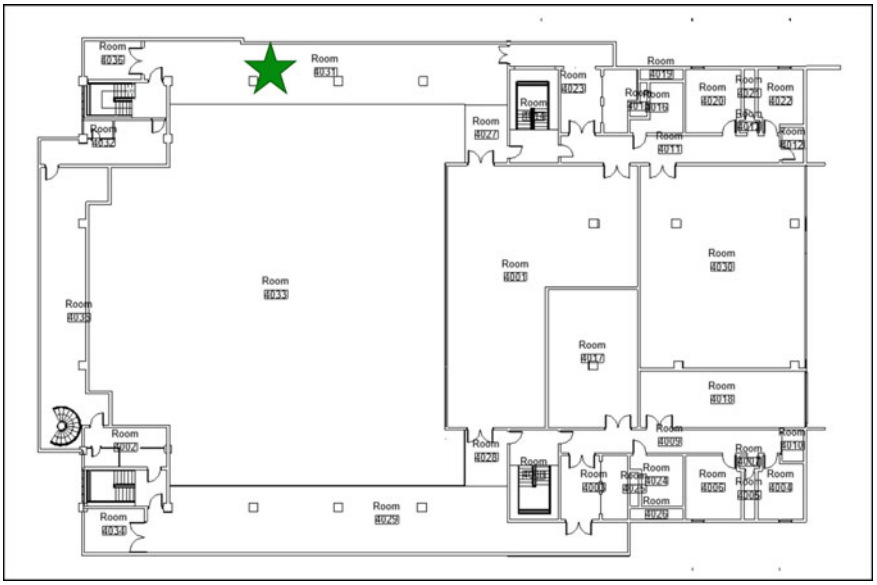

Fig. 5 Floor plan of the fourth floor with respective room numbers

Table 3 Travel distances and time of all useable evacuation routes

Exit	E7	E9	E8	E1	E4	E5	E6	E3	E2
Rank	1	2	3	4	5	6	7	8	9
Travel distance (m)	21.74	43.34	33.55	64.07	47.28	52.36	59.25	60.19	61.93
Travel time (s)	42.47	48.47	48.73	53.75	56.00	58.69	62.60	62.84	63.76

7 Discussion

A lot of information is needed to consider in developing the evacuation route plan for the construction project based on changing construction site conditions. Moreover, when the construction site conditions are changed according to the construction, the evacuation route plan is also needed to be reviewed and updated. It takes a lot of time and human resources to develop an evacuation route plan for a construction project, considering that it is done by hand or from a scratch. Therefore, many researches have tried to develop the system for construction project that can save the time in generating the evacuation route and provide more efficient evacuation route than the conventional methods. To produce the effective evacuation route plan in construction, a system needs to consider the changes of construction sites and physical characteristic of different surfaces. However, the nature of terrain, one of the important factors that has impact on the evacuation time is not addressed in their systems. Therefore, the proposed system has considered not only the dynamic change but also different natures of terrain in the construction site, resulting the effective evacuation route plan.

However, there are some limitations to this study even though this prototype has a positive impact on the evaluation route plan. The first limitation is that users need to update the 3D model from Unity to be similar to the real construction site condition such as building objects and non-building objects. The actual construction site conditions and the site condition from virtual reality should be reflected. Nowadays, not only a variety of sensors can be used in updating the data automatically but also many researchers have attempted automatic data processing, although this sector is not included in the scope of this proposed system. In this study, the pathing finding system is only focused on the travel time, and the system does not consider the reliability of the evacuation route. Therefore, it is recommended that more related factors should be explored based on the project, and a heuristic function should be applied in choosing the evacuation route.

8 Conclusion

The proposed system provides an automatic framework to challenge the generation of evacuation routes, providing the game engine with the required project information. The system also involves user identification of the finished or unfinished building objects, rebar or concrete surface conditions, and input non-building objects to take into account current construction site conditions. The main contribution of this paper is introducing a system that can generate evacuation routes according to the nature of the terrain and construction architectural design, regarding the construction progress. A case study on a four-story construction scenario successfully generated the useable evacuation routes and provided the fastest evacuation route. Moreover, the result of

the prototype shows that the construction personnel should not choose the shortest evacuation route as the optimal evacuation route.

References

1. Health and safety executive (HSE). https://www.hse.gov.uk/statistics. Last accessed 24 Jun 2021
2. Appel Law Firm. Walnut Creek Construction Accident Attorneys. https://www.appellawyer.com/practice-areas/construction-accidents/construction-site-fires. Last accessed 24 Jun 2021
3. Occupational S, Heath A (2001) How to plan for workplace emergencies and evacuations. Occupational Safety and Health Administration, US Department of Labor, Washington, DC
4. Consumer News and Business Channel, https://www.cnbc.com/2019/06/10/helicopter-crashes-into-building-in-midtown-manhattan.html. Last accessed 24 Jun 2021
5. Kim K, Lee Y-C (2019) Automated generation of daily evacuation paths in 4D BIM. Appl Sci 9(9)
6. Choe S, Leite F (2017) Construction safety planning: site-specific temporal and spatial information integration. Autom Construct 84:335–344
7. Galea ER, Deere S, Xie H, Hulse L, Cooney D (2019) Construction site evacuation safety: evacuation strategies for tall construction sites
8. Fruin J (1971) Pedestrian planning and design. Metropolitan association of urban designers and environmental planners, New York
9. Gan H-S, Richter K-F, Shi M, Winter S (2016) Integration of simulation and optimization for evacuation planning. Simul Model Pract Theory 67:59–73
10. Soltani AR, Tawfik H, Goulermas JY, Fernando T (2002) Path planning in construction sites: performance evaluation of the Dijkstra, A∗, and GA search algorithms. Adv Eng Inf 16(4):291–303
11. Cui X, Shi H (2011) A*-based pathfinding in modern computer games. Int J Comput Sci Netw Secur 11(1):125–130
12. Tadepalli SK, Ega PA, Inugurthi PK (2021) Indoor navigation using augmented reality
13. Wächter T, Drögemeier J, Hoffmann M (2021) Simulation of static and dynamic evacuation algorithms in intelligent buildings using unity3D. In: 2021 17th international conference on intelligent environments (IE). IEEE, pp 1–7
14. Du X, Chen Y, Bouferguene A, Al-Hussein M (2020) An agent-based simulation framework for analysing fall risk among older adults in the evacuation procedures. Safety Sci 129
15. Khan N, Ali AK, Van-Tien Tran S, Lee D, Park C (2020) Visual language-aided construction fire safety planning approach in building information modeling. Appl Sci 10(5)

BIM Game: A Testing Ground for Specifying, Modelling, Evaluating and Visualising Information in IFC Formats

Gregor Grunwald and Christian Heins

Abstract The Jade University of Applied Sciences organises digital simulation games to teach students in the department of architecture the networked and digital planning methodology, building information modelling (BIM). BIM is to be the planning standard for construction projects and thus an integral part of university education. The innovative and motivating teaching format "BIM Game" was developed for this purpose. This article describes in detail how the BIM Game is used as a testing ground for the building information process in a BIM workflow. It specifies the project requirements in employer information requirements (EIRs) and checks compliance with the specifications automatically through model checks. In addition, the results of the design competition are read out of the model, visualised and compared as a result evaluation of this architectural design competition. Furthermore, the basic structure of the BIM Game is explained with special attention to the BIM Nuggets. The creation of the BIM Nuggets and their implementation in a new educational structure is funded by Stiftung Innovation in der Hochschullehre.

Keywords Education · BIM Game · Building information modelling · BIM · IFC · EIR · BEP · Information management

1 Introduction

The governments of many countries are calling for digital transformation in the construction industry, thus changing an entire sector of the economy. Universities must meet this changing demand with new educational offers. Building information modelling (BIM) plays a significant role in the digitalisation of construction. BIM is the model-based working methodology for the design, construction and operation of buildings. It is not only about building more digitally, but also about using the digital

G. Grunwald (✉) · C. Heins
Jade University of Applied Sciences, Oldenburg, Germany
e-mail: Gregor.grunwald@jade-hs.de

T. Kang (ed.), *Proceedings of 5th International Conference on Civil Engineering and Architecture*, Lecture Notes in Civil Engineering 369,
https://doi.org/10.1007/978-981-99-4049-3_52

transformation to build or deconstruct better, more resource efficient, more climate friendly and more quality assured.

BIM is offered as a subject at the university, but mostly as a subject isolated from architectural design courses in which BIM could be applied and practised. There is still a way to go before digital planning becomes a natural planning tool [1]. A major hurdle to digital transformation in construction is that "well over half of respondents worldwide (58%) see themselves … still in the 'infancy' of their own digital transformation, 28% in the midfield and 13% already well ahead in the race for tomorrow's projects" [2]. What is true for business and industry is equally true for higher education: the gap between experts and beginners is widening, and the barriers to entry into digital construction planning are becoming increasingly higher.

2 BIM Game

The BIM Game is a learning and teaching format that addresses precisely this problem and attempts to explain and practice the digital planning method [3]. The BIM Game is a digital simulation game that aims to introduce students and interested people from professional practice to the complex world of digitalisation in construction in a playful way. The game is a simulation of an almost real architectural competition in which interdisciplinary planning teams compete against each other and try to solve the set task collaboratively [4], with a special focus on the information process, which will be explored in more detail later in the article. Figure 1 shows a result of such a competition.

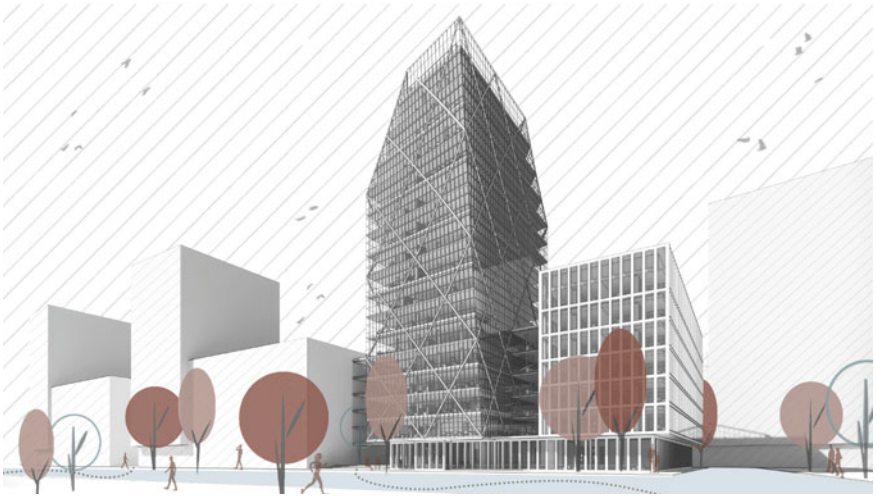

Fig. 1 Example of a project from a one semester teaching course: Business Tower in Hamburg, *Source* Design work by M. B. Buettner

The players are divided into groups and assigned one of the following roles: architect, structural designer, visualiser, cost planner and BIM coordinator. The lecturers take on the role of builders and coach the players groups as needed. The players work together virtually and thus decentral, directly on the 3D model. In doing so, they are in direct competition with the other groups. Regular discussions with the building owners control the progress of the work: the students must deliver partial results. They also find out how far the other groups have progressed in the project—which increases pressure and tension. Results are delivered precisely and, above all, on time. The game ends with a presentation of the results, an assessment of the IFC model, an evaluation of the content and a group comparative visualisation of the most important information. Finally, the best players will be honoured at an awards ceremony. The duration of the BIM Game is usually limited to a short period of one to three days in order to condense work processes and create an intensive game atmosphere [5, 6]. There are also game formats that extend over an entire semester.

2.1 Work Portal and Workflow

The basis of the game is a work portal, a browser-supported pace-setter that asks questions, demands and evaluates answers, sets time limits and guidelines, structures process steps and queries the respective performances. This is ensured by a work portal that controls the entire game.

The business process management system (BPMS), Bizagi, supports the business game from the modelling to the evaluation of the processes. Key elements of this BPMS are a process engine, in which the process models are executed, and a Web-based work portal for interaction with the students. The work portal, based on the modelling notation BPMN2.0 (Business Process Model Notation) [7, 8], guides the participants and the competition organisers sequentially through the competition, oriented towards the following BIM work process (Fig. 2).

The architect and structural engineer, BIM coordinator and all other parties involved, including the client, work together along the BIM process. At the heart of this process is a virtual three-dimensional building model, the coordination model

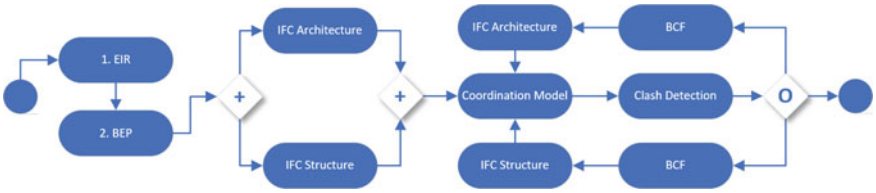

Fig. 2 BIM process. *Source* Own figure based on [3]

that contains all the information about the building—both physical and functional—according to the given specifications. It is generated from the architectural and structural model in an iterative process in which the input of the various planners are coordinated using clash detection and the BIM collaboration format (BCF) for direct communication on the model. Finally, a jury examines the models, evaluates the results and chooses the winner of the competition, bringing the BIM Game to a close after an intensive work phase.

2.2 BIM Nuggets

The BIM Game is complemented by an experimental space for teaching and learning the digital planning methodology BIM. In the form of research-based learning, students develop so-called BIM Nuggets together with experts. These are explanations and tutorials for digital workflows of BIM use cases, such as model creation, model navigation, model visualisation, quantity take-off, rule-based checks, plan creation, clash checking, use of model information, life cycle analysis and others. After understanding, applying and testing the process steps, the students' task is to create the so-called "BIM Nuggets" that explain the BIM use case and to create a—in the sense of the "gamification approach"—playful exercise for this topic. These in turn form the knowledge base for the BIM Game and qualifies the students to participate. Figure 3 shows the concept of the Bim Game in detail.

The Nugget "IFC", for example, contains basic information on IFC model handling topics such as model-based failure analysis, documentation with BCF, collision checks or issue management. The Nugget "model-based handover and warranty

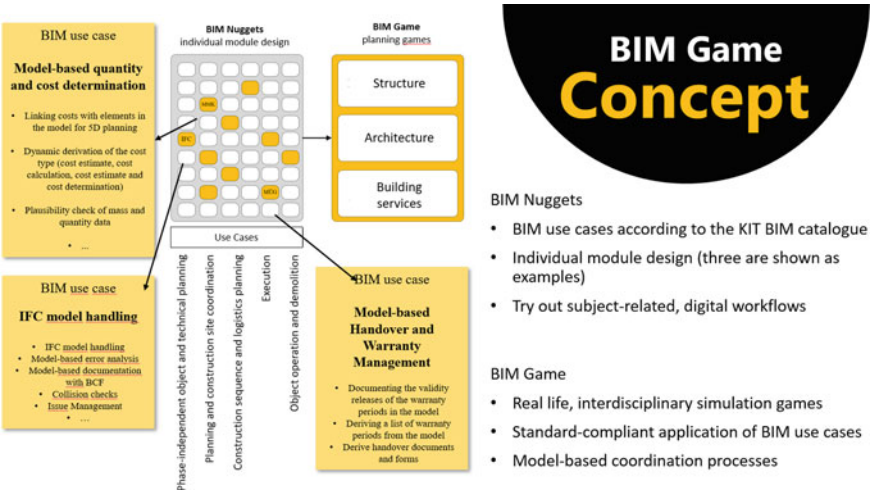

Fig. 3 BIM Game concept including BIM Nuggets and game. *Source* Own figure

Fig. 4 Logo of the foundation. *Source* [9]

management" (MÜG) contains topics such as documenting the validity releases of warranty periods in the model, deriving a listing of warranty periods from the model or deriving handover documents and forms. MMK stands for "model-based quantity and cost determination" and covers topics such as linking costs with elements in the model for 5D planning, dynamically deriving the cost type (cost estimate, calculation, estimate and determination) or plausibility checks of mass and quantity data. The nuggets are characterised by the fact that they deal with self-contained topics, which on the one hand are illuminated theoretically, but on the other hand are also backed up by practical exercises, training the knowledge through applications. The creation of the BIM Nuggets and their implementation in a new educational structure at the university will be funded by "Stiftung Innovation in der Hochschullehre" (Foundation for Innovation in University Teaching). The foundation aims to enable innovation in teaching and learning at universities [9] (Fig. 4).

The funded project is named "CHARGING" (in German: "AUFLADEN") and is briefly summarised below: The journey into the digital future of construction requires ideas, time, courage and energy. The training and further education laboratory for digital design and construction is the place to CHARGE energy and knowledge in order to participate in the digital transformation. The aim of the project is to create a suitable teaching and training concept for teaching BIM, the didactic preparation of learning content and the scientific evaluation of the new concept. The knowledge gained from this will contribute to improving the teaching and further education programmes at the university, to promoting the standardisation of the teaching and further education programmes and to providing impulses and ideas across the university. The project is aimed at students of degree programmes along the entire value chain of the construction and real estate industry, especially prospective architects, civil engineers and specialist planners. The project serves to close the gap between beginners and advanced BIM users, to pick up students who are still looking for access to the topic, and to involve everyone in the digital transformation.

3 Building Information Modelling and Management

Building information modelling (BIM) is the holistic process of creating and managing information for a building object and goes far beyond geometric modelling. The possibilities and advantages of this method of working are to be clarified and demonstrated within the BIM Game and its handling applied. In this respect, the main focus of the event is on the consistent and continuous information management.

3.1 Information Specification

In preparation for the BIM Game, the objectives and the associated requirements are clearly defined at the beginning of the project. These are defined in the Employers Information Requirements (EIR). These describe who has to provide which information on which components and when [10]. The participants receive the EIR, on the one hand to familiarise themselves with the usual set of rules of BIM projects, and on the other hand to define deliverables that can be audited at the end of the competition to prove the quality of their work.

In the BIM Game, the software BIMQ [11] is used to create the EIRs. "BIMQ is a Web-based database that was developed specifically for the requirements and quality management of BIM projects. With BIMQ, the assignment or understanding of LOD requirements [12] in relation to HOAI service phases, service profiles and use cases is no longer carried out via data sheets, but in a database-oriented manner. 'BIMQ follows the Information Delivery Manual (IDM)/Model View Definition (MVD) methodology from building SMART and thus brings all pieces together, namely the actors, phases, use cases, exchange requirements…and last but not least, its representation in the OpenBIM IFC standard'. [13] With the help of BIMQ, comprehensive and well-structured information requirements for a project can be centrally defined, distributed and processed" [14]. BIMQ supports the creation of EIRs according to DIN EN ISO 19650 and makes it easy to tender, control and bindingly accept construction projects. The templates integrated in BIMQ are used as well as individual BIM standards that are freely defined. Figure 5 shows the definition of Key Performance Indicators (KPIs).

BIMQ works in the following nine steps: first of all, basic project settings need to be defined, followed by the creation (or modification) of templates of the project phases, use cases and model components. In the next step, "project setup" use cases are assigned by linking the project phases with BIM use cases. Also, the discipline models need to be assigned. Here, the previously defined model components are

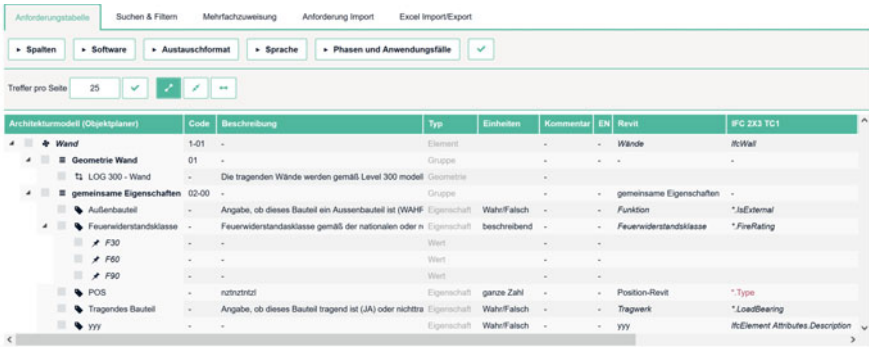

Fig. 5 Creation of the project requirements and mapping of the properties. *Source* BIMQ screenshot [11]

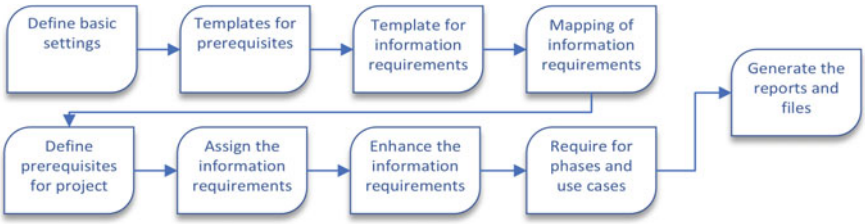

Fig. 6 BIMQ workflow. *Source* Own figure based on [11]

matched to the discipline models and the disciplines are allocated to actors. The final definition step is titled "project requirements" and consists of the actual assignment of the data requirements to the project phases and use cases. For each discipline model and for each object the desired properties, attributes and geometry requirements are assigned. All assignments are relatively defined to the modelling software used in the project and are dependent on the IFC interface format chosen in the application. Finally, in the documentation tab, BIMQ offers the download of written EIRs by project phases and use cases, and offers an IFC mapping file to support a clearly structured IFC export of the planners according to the pre-defined parameters.

In the process, specifications are made for the depth of information required (LOIN) and classifications, and open formats are assigned. The contract annexes created by BIMQ, such as the EIR and the IFC mapping file, are made available to the participants of the BIM Game as the basis for their 3D building modelling to ensure model quality in the project (Fig. 6).

3.2 Execution Planning

BIM execution planning (BEP) is the sum of all specifications for all BIM-related contents, structures, processes and roles that are defined for all participants in a project at the beginning [15]. In the BIM Game, all groups need to prepare a BEP as the response to the Employers Information Requirement (EIR). The requirements of the EIR shall be included in the BEP and implemented in the project. The BEP is a project-related summary of all activities of the project participants in relation to BIM and is understood and demanded during the BIM Game as the first work performance in the entire BIM process.

The BEP documents the procedure for the delivery of information and data and for the fulfilment of the contractually agreed EIR, which was developed by building owners. For this purpose, the players specify the processes, project-related workflows, interfaces and assigns persons to the roles defined in the EIR. Furthermore, requirements for the planning and documentation standards as well as the software and communication tools used are defined. [16]

3.3 Modelling and Model Check

According to the agreed specifications, the groups of the BIM Game start with planning and construction. The architects develop the basic concepts and design approaches, and the structure is deepened by the civil engineers and transferred to a coordination model. Communication takes place via BCF directly on the model. The BIM coordinator of each group monitors and checks the quality of the model. Lecturers provide support when needed. In the course of the game, results as shown in Figs. 1 and 10 arise. These results are to be evaluated and compared with one another.

3.4 Information Evaluation

BIMQ used to generate the starting EIR can also be used to generate the rules for checking the BIM model. It provides rules that can check the models of the BIM Game with a model checker software such as Solibri, Desite MD or BIMcollabZOOM for rule conformity, consistency of content and required properties (Fig. 7).

In the BIM Game, the information requirements are checked during project handover using BIMQ checking rules. In addition, the game uses other automated checking rules, most of which are included in the software as a standard rule set. The rules come from Solibri's architecture and BIM review and check space programme,

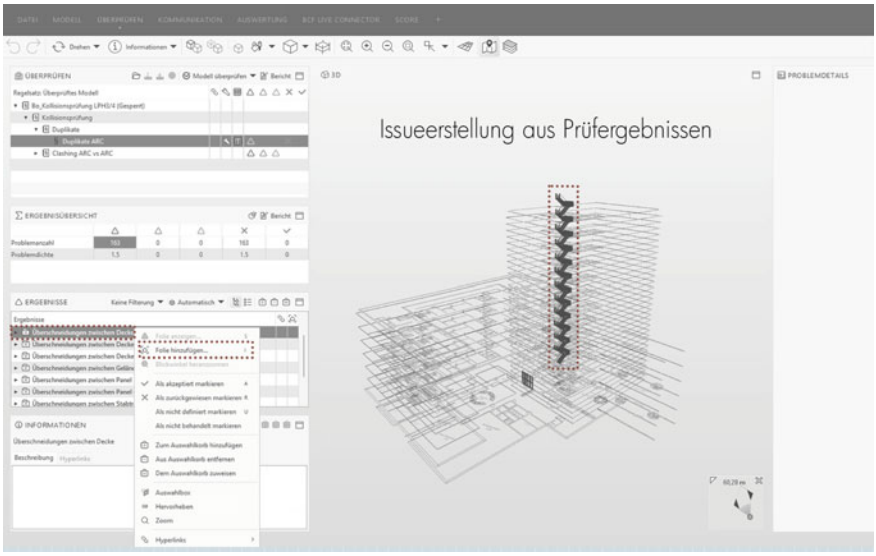

Fig. 7 Solibri model check. *Source* Solibri screenshot of design project by M. B. Buettner

quantities, overlaps and other requirements specified in the EIR. The BIM coordinators of each participating group also receive the respective checking rules and thus have a tool to carry out an internal quality control of the 3D models before submission.

3.5 Information Visualisation

After the rule-based test, a comparative visualisation of the models is carried out. It is used to compare and evaluate the models of the individual groups.

Microsoft's cloud-based Power BI is used for this purpose [17]. The Excel result report of the model check software is provided for the evaluation in PowerBI. This data is now used to visualise the results (Fig. 8).

Another way to evaluate the IFC file with Power BI is to convert the IFC file to Excel. This is done with Bimsheet from Simplebim [18]. Bimsheet extracts and exports model data to Excel and allows visualisation and review of the results. In this way, information from the IFC file can be sorted and compiled in Excel. The data provides information on the room programme and room sizes, on use and area ratios and costs and others.

These design results are compared with the specifications from the EIRs and are checked for compliance, overrun or underrun. In addition, they are compared with

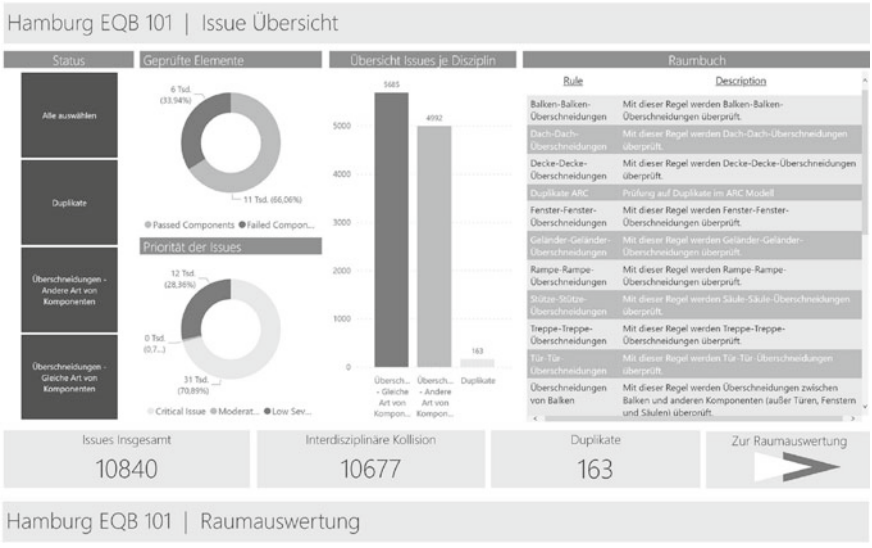

Fig. 8 Visualisation of information. *Source* Screenshot of Power BI Dashboard of design project by M. B. Buettner

the results of the competing groups and thus enable a comparison of the design results in the BIM Game.

In this way, results become visible. IFC files gain transparency and can be used for direct comparisons. Students receive visual feedback on the quality of their design, the degree of compliance with the specifications and the quality of their models.

4 Resume

The aim of the event is to impart knowledge in such a way that all interested parties are taken along on the path to digitisation of construction. The game is a laboratory for experimental, didactic test concepts and serious gaming in the field of digital planning competence to convey know-how, close knowledge gaps and integrate planning methodology into existing curricula. With the two last described process steps of evaluation and visualisation of the results, the IFC models are converted into information that simplifies the evaluation of the designs and brings transparency to the designs. The process model of the BIM Game is therefore updated to include these two additional components (evaluation and visualisation) and is presented as follows (Fig. 9).

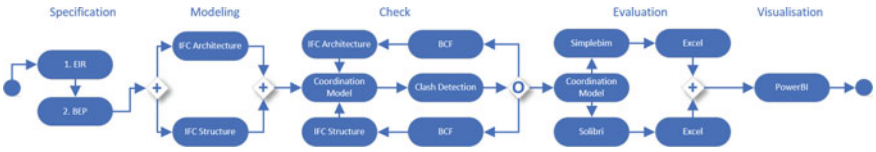

Fig. 9 BIM Game process. *Source* Own figure

Fig. 10 Example of a one semester project: Business Tower in Hamburg, design work by M. B. Buettner

Information management as described in this article goes beyond the "normal" lecture content in the academic training of architects. However, a digital simulation game such as the BIM Game offers ideal framework conditions to train interdisciplinary and parallel cooperation with clearly defined information requirements on the project. In this context, thanks to the structured definition of requirements, automated testing and visualisation of results, the information as "hard facts" are verifiable, visualisable and comparable assessment criteria and, together with the other softer assessment criteria, the "soft facts" (e.g., ideas, activities, decisions and interactions), are ideally created to specifically guide students in a short time and assess their design skills and digital planning competences (Fig. 10).

References

1. Besné Yanguas A et al (2021) A systematic review of current strategies and methods for BIM implementation in the academic field. Appl Sci 11(12)
2. Deutsche Bauzeitschrift DBZ online, Bauverlag, Gütersloh, https://www.dbz.de/artikel/dbz_Die_Digitale_Transformation_des_Bauwesens_Status_Quo_und_Ausblick_auf_die_3601191.html. Last accessed 08 Aug 2022
3. Heins C, Grunwald G, Helmus M (2021) Gamification and BIM—the didactic guidance of decentralised interactions of a real-life BIM business game for higher education. In: ISARC 2021 Conference Paper, 38th international symposium on automation and robotics in construction. https://doi.org/10.22260/ISARC2021/0126
4. Nikolic Dragana, Castronovo F, Leicht R (2021) Teaching BIM as a collaborative information management process through a continuous improvement assessment lens: a case study. Eng Construct Architect Manage
5. Innovative Hochschule Jade-Oldenburg! Homepage, https://ihjo.de/bim-game-jade-work/. Last accessed 08 Aug 2022
6. Innovative Hochschule Jade-Oldenburg! Homepage, https://ihjo.de/55-stunden-spielen-ping-pong-ein-digitales-planspiel/. Last accessed 08 Aug 2022
7. BPMN 2.0 Poster; On-line: http://www.bpmb.de/images/BPMN2_0_Poster_EN.pdf. Last accessed 08 Aug 2022
8. Bundesverwaltungsamt—Kompetenzzentrum Prozessmanagement. Konventionenhandbuch Teil 2 für eine einheitliche Modellierung von IT-Prozessen und Diensten. Version 1.3, Köln, 2016. On-line: https://www.bva.bund.de/SharedDocs/Downloads/DE/Behoerden/Beratung/Prozessmanagement/Konventionen/20160801_Konventionenhandbuch_Teil2.pdf?__blob=publicationFile&v=5. Last accessed 08 Aug 2022
9. Stiftung Innovation in der Hochschullehre Homepage, https://stiftung-hochschullehre.de/. Last accessed 08 Aug 2022
10. Filardo M, Krischler J (2020) Basiswissen zu Auftraggeber-Informationsanforderungen (AIA), bSD Verlag. ISBN 978–3–948742–12–6
11. BIMQ Homepage, https://www.bimq.de/en/. Last accessed 08 Aug 2022
12. Abualdenien J, Borrmann A, König M (2021) Ausarbeitungsgrade von BIM-Modellen. In: Borrmann A, König M, Koch C, Beetz J (eds) Building information modeling. VDI-Buch. Springer Vieweg, Wiesbaden. https://doi.org/10.1007/978-3-658-33361-4_8
13. Armijo A, Elguezabal P, Lasarte N, Weise M (2021) A methodology for the digitalization of the residential building renovation process through OpenBIM-based workflows. Appl Sci 11(21):10429. https://doi.org/10.3390/app112110429
14. BIMQ Homepage, https://bimq.centraldesk.com/de/articles/bY2R-einleitung/. Last accessed 08 Aug 2022

15. Leitfaden und Muster für den BIM-Abwicklungs-plan (BAP), Bundesministerium für Verkehr und digitale Infrastruktur, Homepage: https://bim4infra.de/wp-content/uploads/2019/09/BIM4INFRA_AP4_Teil3.pdf. Last accessed 08 Aug 2022
16. VDI Richtlinie 1552, Blatt 10, Januar 2020, p 7, ICS 35.240.67
17. Roberti F, Ferreira D (2021) Increasing autodesk revit productivity for BIM projects: a practical guide to using revit workflows to improve productivity and efficiency in BIM projects. Packt Publishing Ltd
18. Simplebim Homepage: https://simplebim.com/bimsheet/. Last accessed 08 Aug 2022

Planning for the Use of Crane Towers in High-Rise Multifamily Housing Projects

B. S. Yalan, C. A. Zapata, and A. Hinostroza

Abstract This research article proposes a compilation of the best practices necessary to improve the planning of the use of a crane tower in a construction site, evaluating as a case study, the SIDE Project, a high-rise multifamily housing with the incorporation of a POTAIN MC125 crane tower. The methodology applied is based on the analysis of the current planning processes of this machinery together with the problems presented by resident engineers, to then compile the good practices of the main crane tower suppliers in Peru. These were represented with the BIM modeling tool to study their effectiveness in the case study and capture the correct planning process. Finally, these practices were validated through expert judgment by specialists in this machinery. The results obtained in this research are mainly focused on the validation of the proposed good practices, receiving an approval of almost 100% by the experts in the proposed categories of the improvement processes. In addition, these collected practices received an 80% approval per category by the specialists when affirming that they are essential in the knowledge of resident engineers and builders.

Keywords Crane tower · Best practices · Planning · Management · Operation · BIM

B. S. Yalan (✉) · C. A. Zapata · A. Hinostroza
Facultad de Ingeniería Civil, Universidad Peruana de Ciencias Aplicadas, Prolongación Primavera 2390, Lima 15023, Perú
e-mail: u201711822@upc.edu.pe

C. A. Zapata
e-mail: u201714815@upc.edu.pe

A. Hinostroza
e-mail: pcipahin@upc.edu.pe

T. Kang (ed.), *Proceedings of 5th International Conference on Civil Engineering and Architecture*, Lecture Notes in Civil Engineering 369,
https://doi.org/10.1007/978-981-99-4049-3_53

1 Introduction

In the last decade, the construction of high-rise buildings has experienced a great growth worldwide, becoming a symbol of progress and economic development [1]. High-rise buildings are understood as buildings whose height is much greater in relation to the height of surrounding buildings [2], so that the construction of this type of buildings brings new challenges during the planning and project management stage [3].

Among the most important challenges faced in this type of buildings is the vertical transportation, due to the presence of a great variety of materials, equipment, and labor that must be transferred at high altitude [4]. Therefore, the use of the crane tower is presented as a solution to face tight schedules and avoid delays, becoming a central piece of the on-site production [5]. However, poor crane tower planning during the erection stage is one of the most frequent problems in the industry, since it is common that only 20% of the original project objectives are met [6].

Within the research literature, several positions were found that highlight the importance of planning the implementation of a crane tower. The first of these is based on the BIM modeling tool in crane tower management, through a discrete event modeling simulation based on the workload and capacity of the crane [7]. The second position deals with the management of high-rise building projects, where the aim is to improve the management by means of a planning system based on a regression line [8]. The third research is referred to the management of the crane tower on site by implementing an algorithm to plan the characteristics of the crane tower and its work in the project [9]. The fourth study proposes to establish a critical path on the operation of the crane tower by means of an algorithm that improves its operation time [10].

The objective of this research is to propose a solution to this problem based on the compilation of good practices for planning the use of crane towers in construction, those that allow improvements in the process of analysis of a project in a relationship between the supplier company and the requesting client to enrich the efficiency of the use of this machinery on site.

2 Methodology

In order to correctly analyze the proper planning of the crane tower on site, the research was carried out through a series of steps to cover all the necessary approaches to its characteristics, as shown in Fig. 1. The methodology is developed by first identifying the most frequent problems in high-rise construction projects with the incorporation of this equipment by collecting information in the field with users related to this area. Secondly, the current processes for the management of the crane tower on site are identified by obtaining experimental field information from construction engineers and residents. Thirdly, a construction project with the implementation of

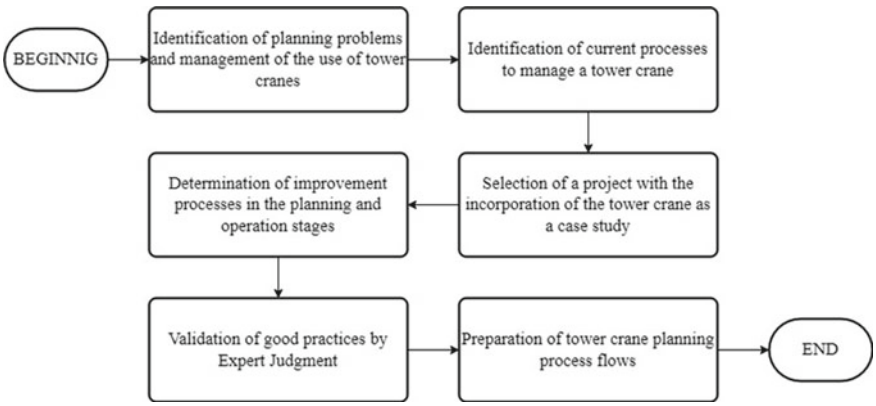

Fig. 1 Flowchart of the methodology. Own elaboration

the crane tower is selected to define its characteristics and to know the details of its on-site planning. Fourthly, the collection of improvement processes or good practices for a correct planning of the crane tower in a high-rise project was carried out, being complemented with a BIM modeling of the case study to define the improvement processes. Fifth, a compilation of best practices will be made to help the construction engineer on the basic technical details to know for the implementation of this equipment on site. Finally, these practices should be validated with input from subject matter experts to determine the approval of the proposed improvement processes.

2.1 Identification of Planning Problems and Management of the Use of Crane Towers

An initial survey was conducted with 24 crane tower professionals and suppliers to identify the failures and nonconformities that occur during the planning and management process of the equipment in a construction project. Also, proposals for improvement that should be applied during the machinery management process were evaluated based on the experience of the respondents, with the purpose of carrying out a study of the most common problems and establishing the root cause with the Ishikawa diagram. However, by regularizing the results obtained, a Pareto diagram was made to define the most frequent problem that occurs when planning the implementation of a crane tower on site.

Table 1 List of interviewees for the identification of the current management processes of the crane tower

Interviewees	Description
N°1	Civil engineer with more than 7 years in the field of civil construction in the occupational safety and environment of the projects
N°2	Civil engineer with more than 22 years in the management of crane towers who considers this a sensitive issue due to the diversity of factors to be taken into account
N°3	Civil engineer risk management analyst, forming part of the planning of the implementation of crane towers in the projects he performs
N°4	Civil engineer specialized in field quality with extensive experience working with crane towers in high-rise construction projects

2.2 Identification of Current Processes to Manage a Crane Tower

A series of interviews were conducted with professional contractors on the different processes currently required to manage the implementation of the crane tower in high-rise construction sites, with a total of four interviewees, including resident engineers, safety engineers, and site supervisors, as detailed in Table 1. This step allowed to know the planning of the use of this equipment from the perspective of the resident engineers, who are the ones who lead with most of the day-to-day work difficulties.

2.3 Selection of a Project with the Incorporation of the Crane Tower as a Case Study

The information was focused on obtaining the information of the "SIDE Multifamily Building" project, since this is a 20-story building plus rooftop, which was built by means of a POTAIN MC 125 crane tower located on a cantilevered reinforced slab supported on the diaphragm wall at street level, whose main characteristics of the equipment are the boom length of 60 m and a height of 62 m.

2.4 Determination of Improvement Processes in the Planning and Operation Stages

The planning improvement processes were identified by means of the best practices obtained from interviews with the technical specialists of the main crane tower suppliers in Peru, as detailed in Table 2, by means of which a comparative analysis

Table 2 List of interviewees for the identification of crane tower planning and management improvement processes

Suppliers	Description
GRÚAS ETAC PERÚ	Civil engineer representative of the operations area with more than 11 years of experience in the field of construction with high-rise equipment
AGRUMAQ	Civil engineer with the position of assistant of the project area in the supplier company
GALIGRÚ	Civil engineer with the position of general manager with more than 12 years of experience

was made with the practices applied in the case study. Likewise, a BIM modeling of the project was carried out with the information obtained from the best practices recommended by the experts to evaluate the improvements in the main management processes of the case study.

2.5 Validation of Good Practices by Expert Judgment

The process flows were elaborated thanks to the compilation of the best practices proposed by the specialists, those that allow to improve the planning of the crane tower with the basic and essential knowledge that the construction engineers do not know and must learn. These were selected by classifying them into categories according to the characteristics of the crane tower in order to provide a better focus on the key processes at this stage of a construction project.

2.6 Preparation of Crane Tower Planning Processes Flows

The validation process of the good practices was carried out by means of the expert judgment method using a rating rubric for the main processes required in the planning of this equipment.

3 Results

3.1 Identification of Planning Problems and Management of the Use of Crane Towers

From Fig. 2, it is possible to determine the most recurrent problems in the planning and management of the use of crane towers, where the most critical is poor coordination between suppliers and customers. It is worth noting that the main problems identified through the survey are, firstly, poor coordination and communication between suppliers and customers with a maximum of 58.3% of respondents. In second place, there is a poor approach to a previously elaborated layout with 45.8%. In third place, there is the lack of maintenance of equipment and accessories with 33.3%. The following is an analysis of the main causes of the main problem in the planning and management of the crane tower.

From Fig. 3, it can be seen that the main problem identified is poor coordination and communication between suppliers and customers, since this kind of problem can lead to an inefficient location of the crane tower, which would not only result in project cost overruns, but could also become a risk to the safety of workers.

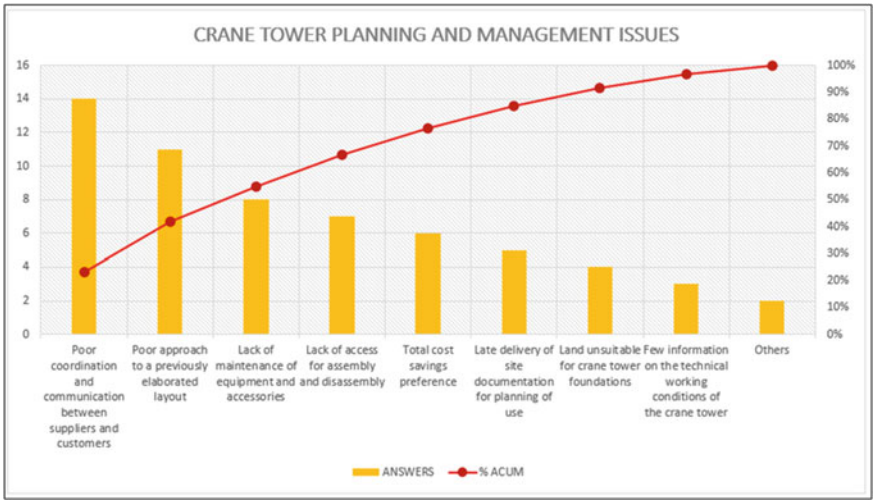

Fig. 2 Problems of planning and managing crane towers. Own elaboration

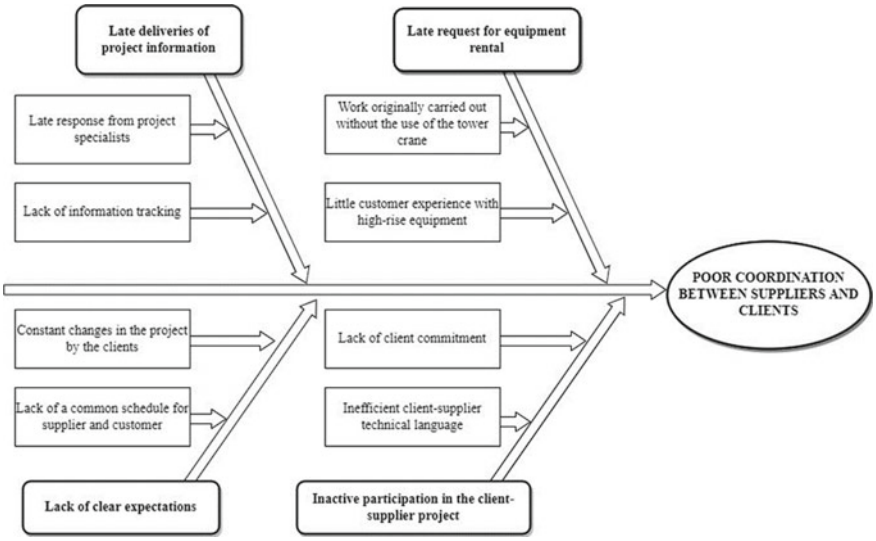

Fig. 3 Ishikawa diagram of poor coordination between suppliers and customers. Own elaboration

3.2 Identification of the Current Processes for the Management of a Crane Tower

In response to the comments received by the professionals, the process diagram in Fig. 4 shows the current activities performed in the planning and management of the crane tower in high-rise construction projects, as follows:

3.3 Description of the Current Characteristics of the Use of the Crane Tower of a Project as a Case Study

The building is composed of 20 floors with 176 apartments plus 01 rooftop plus the construction of 05 parking basements, as shown in Fig. 5, with a height of 56.95 m.

The crane used in the project has an autonomy height of 62 m, which was sufficient for the superstructure of the building, so it could not be founded in the basements and was located at the same level as the street. With this, a beam and a reinforced slab with a thickness of 1.50 m supported on the diaphragm wall were designed, whose design was made considering the parameters of the soil mechanics studies and the loads of the foundation of the equipment and thrusts of the diaphragm wall.

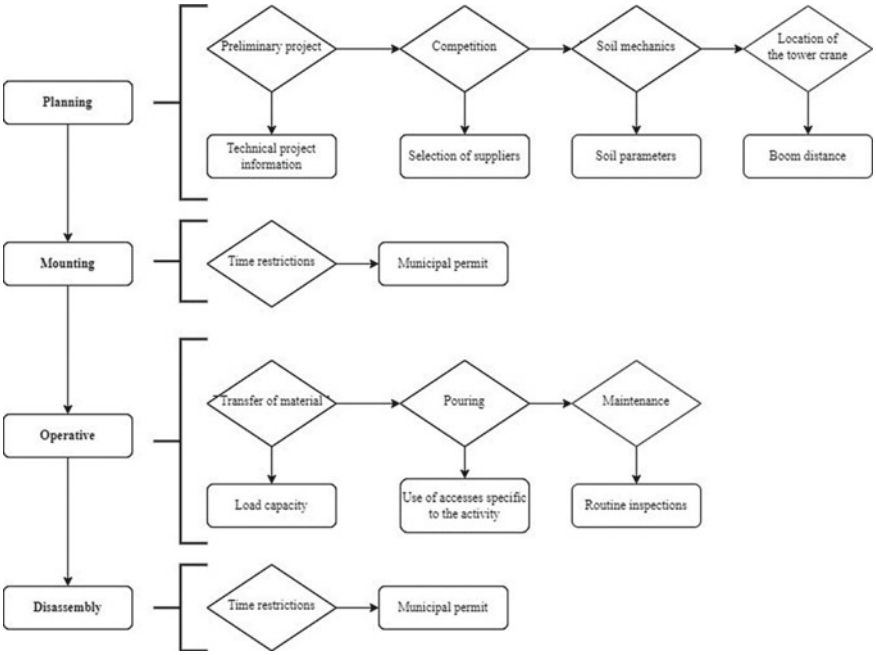

Fig. 4 Flowchart of the current planning and management processes for crane towers. Own elaboration

3.4 Determination of Improvement Processes in the Planning and Management of the Crane Tower by Performing BIM Modeling

Based on the best practices obtained from suppliers, these were grouped into the most relevant categories for the planning and management process of the crane tower, which are shown below:

- Application software
- Application of the BIM methodology
- Choice of the type and model of the crane tower
- Location of the crane tower
- Foundation of the crane tower
- Assembly and disassembly of the crane tower
- Movements of the crane tower.

Next, a BIM modeling of the multifamily housing of the case study detailed in Fig. 6 is made in order to know specifically the correct application of these good practices.

From the interviews conducted, it was possible to obtain different perspectives regarding the practices or processes applied to improve the planning and operation of

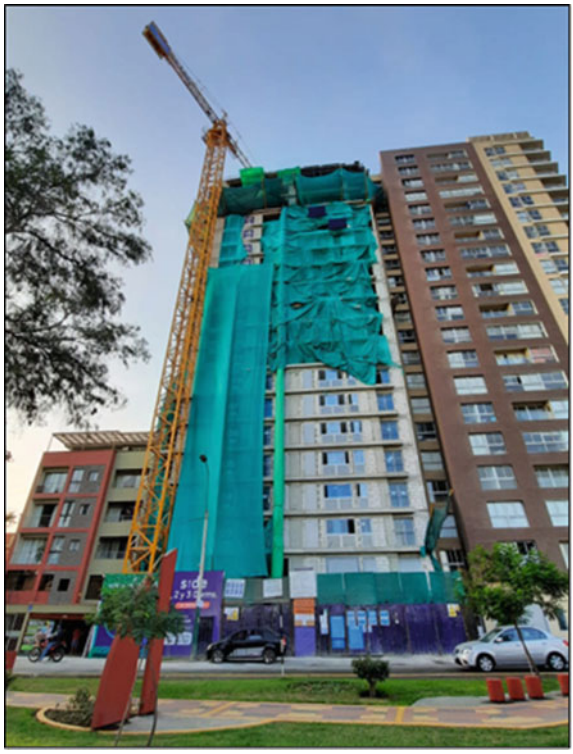

Fig. 5 SIDE multifamily project

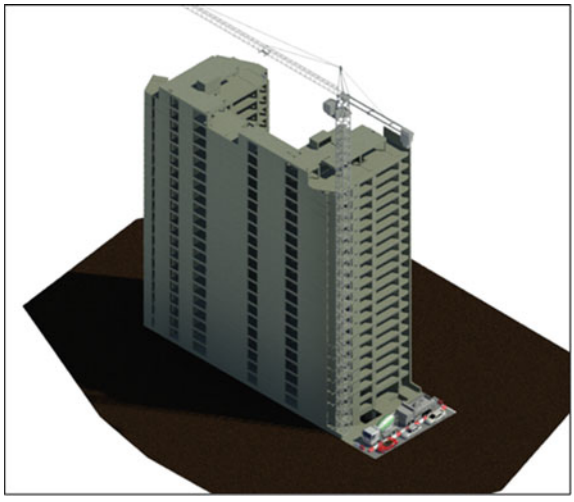

Fig. 6. 3D modeling of the SIDE multifamily housing project

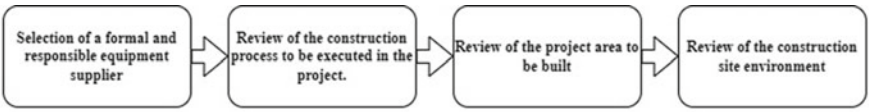

Fig. 7 Flow of the process of choosing the type and model of crane tower. Own elaboration

the crane tower. Likewise, by means of a three-dimensional model of the case study, it was demonstrated that the good practices were effectively applied in the different categories previously mentioned.

3.5 Elaboration and Development of the Process Flows for the Correct Planning of the Use of Crane Towers

The process flows were elaborated by compiling the good practices proposed by the specialists interviewed to organize them into categories on the basic and essential knowledge that every resident engineer or constructor should know when planning this machinery.

3.5.1 Choice of the Type and Model of Crane Tower

From Fig. 7, it can be established that a formal supplier whose equipment complies with minimum safety parameters is required, in addition to a review of the project's construction process. Then, the area of the project is determined, since the turning radius of the equipment must cover the entire project site. Finally, the environment of the construction site is reviewed to determine possible obstacles and access to the crane tower.

3.5.2 Selection of Accessories and Hoisting Elements

Regarding the selection of accessories, it is important to know the main activities that will require vertical transport, for the transfer of ready-mixed concrete, concrete buckets are needed, for the transfer of pallets or pallet racks, baskets will be required, and for the unloading of elements at height, unloading platforms should be installed.

3.5.3 Location of the Crane Tower

Regarding the crane tower location process shown in Fig. 8, it is important to check the surroundings of the project approximately 100 m around, in order to recognize

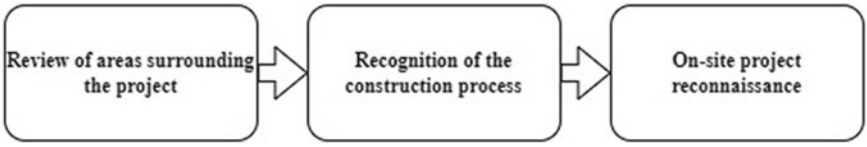

Fig. 8 Crane tower location process flow. Own elaboration

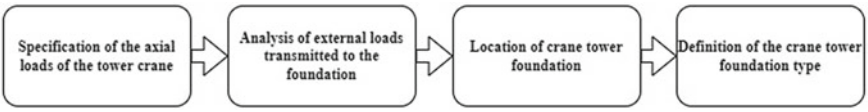

Fig. 9 Crane tower foundation process flow. Own elaboration

possible obstacles, future works to be built, presence of electrical wiring and to establish possible accesses for the assembly and disassembly of the equipment. Likewise, the construction process to be executed must be distinguished, with the purpose of knowing the types of works to be carried out with the machinery. Finally, it is recommended to know the project in situ since it is advisable to locate the crane tower in one of the fronts of the project with access to an avenue or street for supply.

3.5.4 Crane Tower Foundation

Regarding the crane tower foundation process shown in Fig. 9, the first step is to know the crane tower axial load reactions, whose values are established by the manufacturer. Second, an analysis of the external loads transmitted to the foundation must be carried out; it should be noted that the main dynamic load is produced by the wind force. Third, the foundation of the equipment must be located, being advisable to design the foundation at the level of the sidewalk. Fourth, establish the type of foundation.

3.5.5 Assembly and Disassembly of the Crane Tower

In relation to the assembly and disassembly process of the crane tower shown in Fig. 10, a review of the accesses to the site must be carried out. For this purpose, the location of the project with respect to the avenues or streets available for access, as well as its location in the project layout, must be considered. In addition, obstacles and interferences in the area must be evaluated and effective communication between the supplier and the contractor must be maintained. Finally, the appropriate permits must be obtained from the municipality.

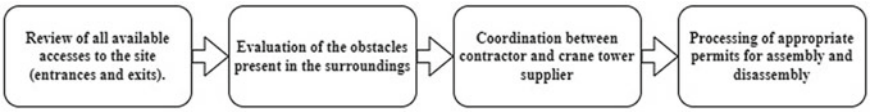

Fig. 10 Flow of the assembly and disassembly process of the crane tower. Own elaboration

3.5.6 Validation of the Methodology Through Expert Judgment of Technical Professionals and Crane Tower Suppliers

The proposed good practices obtained favorable results after the validation by expert judgment, receiving an acceptance by more than 80% in the selected categories for the crane tower planning, as detailed in the graph in Fig. 12. However, these same received an approval from the validating experts with almost 100% in favor to be considered essential in the knowledge of the construction engineer, as detailed in the graph in Fig. 11.

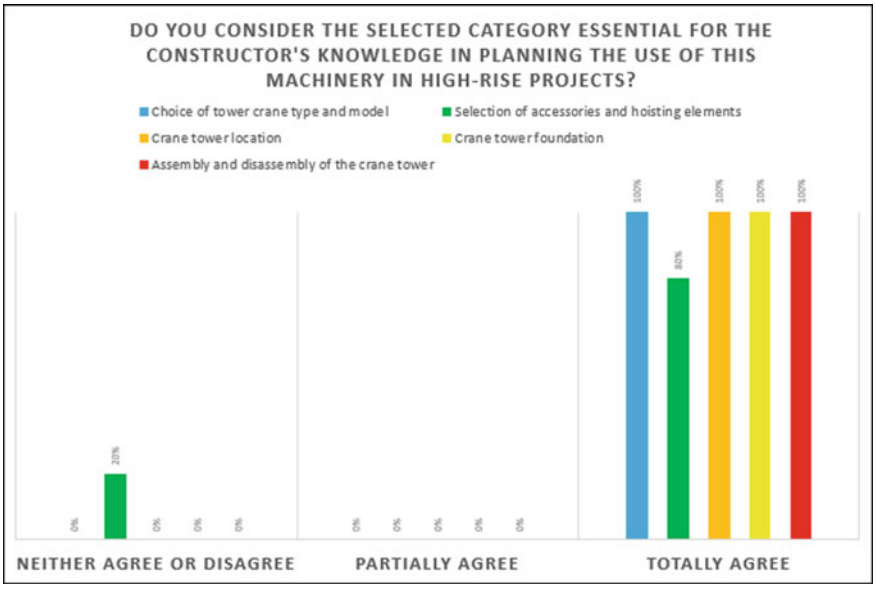

Fig. 11 Validation results regarding the categories selected for good practices. Own elaboration

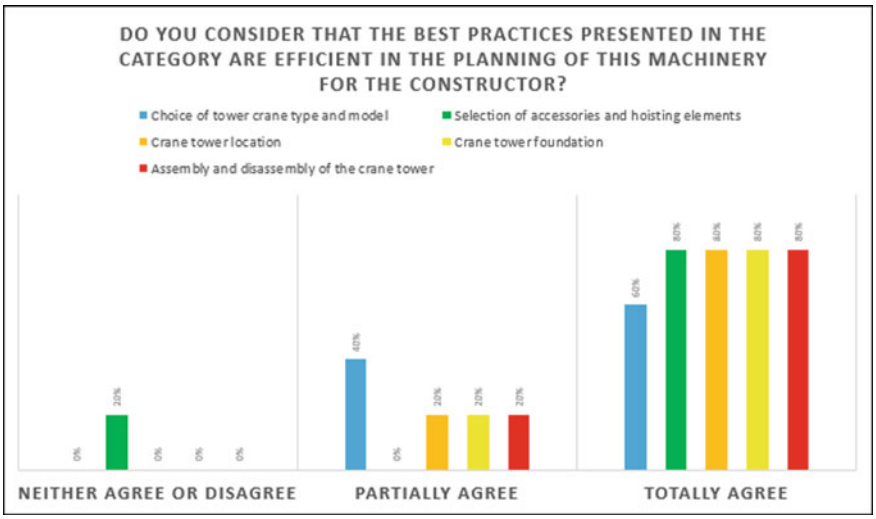

Fig. 12 Validation results regarding the proposed good practices. Own elaboration

4 Conclusions

The main problems identified regarding the planning and management of the use of crane towers on site are: poor coordination between suppliers and clients, poor project layout approach, lack of maintenance of equipment and accessories, lack of access for crane assembly and disassembly, and preference for total cost savings, the first of these being the most critical commented by resident engineers and crane tower experts with 58.3% of the total number of respondents.

Based on the flow chart proposed by the current machinery planning processes mentioned by the resident engineers, the activities related to this stage are fundamental for the correct operation of the crane tower. However, the interview results showed that many builders lacked the technical skills and basic knowledge necessary to better plan the crane tower.

The SIDE project as a case study of the research included the participation of a crane tower model POTAIN MC 125, which is a sufficient and suitable option to fulfill the scope of work activities. It was characterized by a boom length of 60 m and a tower height of approximately 62 m for its correct operation in the construction site. In addition, it meets the minimum crane tower supplier review requirements in the correct process for implementation. This is a project that successfully culminates the work activities with the support of the team.

Through expert judgment verification, the interviewees accepted the best practices in each proposed category, of which 80% were highly recognized and received the highest rating.

The categories selected to classify the good practices obtained were approved by almost 100% of the validating experts, which allows concluding the importance of

these in the planning of the use of the crane tower, as well as their essentiality in the basic knowledge of every resident engineer or constructor.

References

1. Quezada Ramos EN, Serrano Arone Y, Huaco G (2020) A comparative study of the seismic base shear force and story drift ratios using time history and modal spectrum analysis according to peru code E.030 and ASCE 7.16 on high-rise buildings. In: 2020 Congreso Internacional de Innovacion y Tendencias en Ingenieria, CONIITI 2020—Conference Proceedings. https://doi.org/10.1109/CONIITI51147.2020.9240330
2. Ali HM (2018) Site logistics planning for high rise building construction on congested downtown sites
3. Cabrera J, La nueva tendencia del sector construcción: la gestión colaborativa | Inmobiliario | Actualidad | ESAN, https://www.esan.edu.pe/conexion/actualidad/2018/08/17/la-nueva-tendencia-del-sector-construccion-la-gestion-colaborativa/. Last accessed 31 Mar 2021
4. Zhang K, Wang H, Wang K, Cui J, Chen B, Li D (2018) Significant progress in construction equipment of super high-rise building. Int J High-Rise Build 7:243–253. https://doi.org/10.21022/IJHRB.2018.7.3.243
5. Khodabandelu A, Park JW, Arteaga C (2020) Crane operation planning in overlapping areas through dynamic supply selection. Autom Constr 117:103253. https://doi.org/10.1016/j.autcon.2020.103253
6. Cáceres J, Madge A, Perez C, Poma G, Villanueva V (2018) Diseño y construcción del edificio de vivienda multifamiliar Las Cumbres Tesis 1–162
7. Al Hattab M, Zankoul E, Hamzeh FR (2017) Near-real-time optimization of overlapping tower crane operations: a model and case study. J Comput Civil Eng 31:05017001. https://doi.org/10.1061/(asce)cp.1943-5487.0000666
8. Gurmu AT, Aibinu AA (2017) Construction equipment management practices for improving labor productivity in multistory building construction projects. J Constr Eng Manag 143:04017081. https://doi.org/10.1061/(asce)co.1943-7862.0001384
9. Wu K, García de Soto B, Zhang F (2020) Spatio-temporal planning for tower cranes in construction projects with simulated annealing. Autom Constr 111:103060. https://doi.org/10.1016/j.autcon.2019.103060
10. Lee HJ, Lim SY (2020) Development of an optimal path algorithm for construction equipment. Processes 8. https://doi.org/10.3390/PR8060674

Roadmap for the Building Information Modeling Implementation: Structured Plans to Achieve High-Level Strategic Maturity in the Philippines' Construction Industry

Lemuel Lumbera and Dante Silva

Abstract The purpose of the study is to develop a BIM roadmap to assist the Philippines' construction industry in advancing toward a more mature and higher level of BIM implementation. The roadmap will be used to guide the industry in the integration of BIM technology into every construction and architectural project. The study utilizes a quantitative and qualitative approach to create a BIM Maturity Framework to assess the current maturity of the Philippines' BIM industry. The BIM maturity framework consists of five main categories: process, technology, organization, standard, and people. Along with that, sub-fundamental components under BIM capability and competencies were generated to fully measure the maturity of BIM in different areas. Furthermore, the study assesses the current maturity of BIM implementation in the Philippines. The study concluded that among the BIM implementing company based in the country, international companies were already mature enough to use BIM methodologies This suggests that multinational firms have optimal (high maturity) BIM maturity levels when compared to local enterprises which have integrated (mid-high maturity) level. Moreover, several challenges were identified in the difficulties they are facing during the implementation of BIM. Each obstacle on each focus areas was given a proposed strategic plan and actions to overcome hurdles and creates a path for improvement. Furthermore, to fully adopt and integrate the BIM technology in the Philippines, a five-year plan roadmap is introduced to assist the country in achieving a more mature and high-level BIM implementation.

Keywords BIM framework · BIM maturity · BIM roadmap

L. Lumbera (✉) · D. Silva
School of Civil, Environmental, and Geological Engineering, Mapúa University, Manila, Philippines
e-mail: lemuel.lmbr@gmail.com

D. Silva
e-mail: DLSilva@mapua.edu.ph

T. Kang (ed.), *Proceedings of 5th International Conference on Civil Engineering and Architecture*, Lecture Notes in Civil Engineering 369,
https://doi.org/10.1007/978-981-99-4049-3_54

1 Introduction

One of the top contributing sectors to the continuous growth and development of the world economy is the construction industry. It has shown a booming domino effect that any economic movement and condition is directly associated with the status of construction industry project development. Part of the continuous growth and development of the construction industry has been with the integration of different initiatives and innovations intended for its development. One of which is BIM technology, also known as building information modeling. Advanced technologies like BIM to improve design and construction projects in a simulated environment can help the construction industry be more productive and reach its goals [1]. Incorporating BIM and lean construction principles into a structural model increased project scope, timeliness, and total cost while laying the groundwork for rethinking the risks and challenges inherent in the construction industry [2]. Therefore, from the initial concept to the final close, construction projects have been significantly impacted by the merging of BIM and lean.

On the other hand, the BIM maturity model for renovation (BiM^2FR) was created to ease the creative process and encourage widespread adoption of BIM among the companies most likely to carry it out. In addition, the model analysis specifies what features a remodeling industry-specific maturity model (MM) must include [3]. This means that specialized BIM technology has been developed to meet the needs of a specific demographic. To be more explicit, the Building Information Model Capacity Assessment Reference Environment Model (BIM-CAREM) was developed to assess the BIM capability of AEC/FM procedures. It was demonstrated that the model could identify the BIM capabilities of different AEC/FM procedures [4]. The model is important for making sure that all current and future projects and renovations are done in line with ISO standards, which are what BIM-CAREM was built on. Adapting an innovative approach to assess construction project can produce high-quality projects [5].

In addition, a management competence model has been created to foretell the management competency grade and the relative relevance of elements influencing it. With its connection weights, this neural network model was able to accurately predict the management competency rating and figure out how each input parameter affected that rating [6]. Since management has had considerable influence on project implementation as part of the planning committee, this management competency model became relevant to the present study. The BIM roadmap could be set up as a result of the current study, which could help management with strategic planning.

Furthermore, the findings of a study that was carried out on BIM adoption in the Philippines indicated an acceptance level of 64.8%, of which 34.8% were directly engaged in the AEC business [7]. This finding lends credence to the aforementioned assertion. This suggests that the Philippines architecture, engineering, and construction (AEC) business is currently adopting and making use of the most recent developments in technology in order to have an effective method of constructing projects. For businesses to get the most out of building information modeling (BIM), they

need to do an accurate assessment of their current BIM implementation state [8] and commit to using it [9].

Therefore, the goal of this research is to develop a BIM roadmap to assist the Philippines' construction industry in advancing toward a more mature and higher level of BIM implementation and a path for improvement that will be used to help the industry integrate BIM technology into every construction and architectural project.

2 Methods

2.1 Methodology

The study utilized a qualitative and quantitative approach to create the Philippines' BIM roadmap in order to improve the country's current state of BIM implementation and provide a strategic plan and goals to attain a high level of maturity. This study is broken into four phases: Phase 1 encompasses the classification, assessment, and review of BIM maturity assessment tools; Phase 2 entails the creation of a BIM maturity assessment framework. Phase 3 makes it easier to collect, analyze, and report on information, and Phase 4 is the creation of a BIM roadmap for the Philippines construction industry. The researcher used a scored survey and questionnaires to measure the maturity of BIM implementation based on five categories: process, technology, organization, standards, and people. The average score for each category will be the basis for knowing how mature the implementation of BIM in the Philippines is. Also, a Likert scale survey will be used to find out what the biggest problems are for the BIM industry in the Philippines as they use BIM in their projects.

2.2 Data Analysis

During the process of analysis, the replies that were gleaned from the interview were converted into numerical values by making use of the BIM maturity matrix. This allowed for the generation of the BIM maturity index. By collecting the index, the BIM maturity level matrix (Table 1) can be used to classify each case study from the initial level all the way up to the optimal level, and then the maturity level can be found step by step.

Statistical methods, including percentages, frequencies, weighted mean, and comparative analysis will be utilized in the processing of the results. For frequency, each table displays the occurrence of a certain value within a particular demographic or interval. When each of the data points contributes the same amount to the overall average, you get what is known as a weighted mean. In order to calculate the data's weighted mean, we will be using SPSS. Finally, the study used comparative analysis to contrast several BIM evaluation methods, discussing the benefits and drawbacks

Table 1 BIM maturity level matrix (Succar and Williams 2012)

BIM maturity levels			
	Maturity level	Textual definition	Numerical rating (%)
a	Initial	Low maturity	0–19
b	Defined	Mid-low maturity	20–39
c	Managed	Medium maturity	40–59
d	Integrated	Mid-high maturity	60–79
e	Optimized	High maturity	80–100

of each tool and inquiring about respondents' perspectives on the level of maturity (both locally and globally).

3 Results

3.1 Comparing Existing BIM Maturity Assessment Tools that Are Recognized by the Industry

Table 2 shows the BIM assessment tools that are recognized by the industry and have been reviewed and examined through critical analysis. These tools include the maturity tool by BIM Speed, the BIM Profiler by BIM Connect, the BIM maturity matrix (BIM3) by the BIMe Initiative, and the BIM maturity assessment by ARUP. These tools can be used in different ways depending on the needs of the industry, which leads to the creation of new projects and the integration of new technologies.

The strengths, shortcomings, and one-of-a-kind aspects of each BIM evaluation tool are highlighted in Table 3, which demonstrates the various potential benefits that may be realized if the tool were put into use. However, there were also linked flaws in these tools that were offered, which were discussed earlier.

3.2 Categorizing of Assessment Questions on Each Tool that Are Relevant to Measuring BIM Maturity

Figure 1 shows the typical assessment questions each gathered BIM assessment tool has. It was observed that the four BIM maturity tools have different assessment questions depending on the structure and features of the tool and how these tools are being used by various companies to cater to their BIM-based projects. In the same way, different assessment questions have come up in relation to the different categories of BIM maturity tools because each tool has its own set of criteria.

Table 2 Goals and uses of BIM maturity assessment tools

BIM maturity tools	Goal	Uses
BIM maturity tool by BIM Speed	Providing stakeholders with guidance based on their respective BIM maturity levels regarding the implementation of BIM in renovation projects	• Stakeholders involved in renovation projects can use it to approach the renovation with BIM-based methodologies • It defines the scope and facilitate the implementation of BIM in renovation projects • A guide to help achieves specific goals, like reducing energy consumption or enhancing comfort, is provided • It is intended for anyone interested in implementing BIM-based methodologies on their projects
BIM profiler by BIM connect	Providing practical and reliable information on diverse BIM topics to aid in understanding and implementing the concept	• In this test, the user's BIM competency is assessed on the following aspects: strategy, BIM uses, process, data structure, infrastructure, and personnel • In a spider matrix, each competency area is presented to demonstrate BIM Readiness
BIM maturity matrix (BIM^3) by BIMe initiative	Assessing and improving the performance of individuals, organizations, and project teams	• Establishes an international research network that organizes all research activities into knowledge sets • Identify the best steps to improve the performance of the organization based on the results • Competency is measured based on BIM capability and BIM maturity
BIM maturity assessment by ARUP	Creating a common view of BIM best practices across its various projects around the world	• Provide users with a comprehensive overview of how BIM is implemented within a project by assessing its use in different areas • By analyzing the data generated, enterprises can identify gaps in their BIM implementation strategies and shape future investment strategies

Table 3 Strengths, weaknesses, and unique features of BIM maturity assessment tools

BIM maturity assessment tool	Strengths	Weaknesses
BIM maturity tool by BIM speed	(1) The tool excels in managing maturity of facade renovations (2) The assessment question is detailed and easy to understand (3) The tool is cloud-based and easily accessible	(1) The tool mainly focuses on identifying the maturity of renovation type of projects (2) The tool does not give any recommendation to improve the BIM implementation
BIM profiler by BIM connect	(1) It bridges the company need in assessing general information on a firm's constructed BIM structures and systems (2) It helps top management to establish readiness in every project specifically on the strategy, BIM uses, process, data structure, infrastructure, and personnel (3) It measures the maturity in the following aspects: strategy, BIM uses, process, data structure, infrastructure, and personnel and provide a spider matrix as a result	(1) Target value is based on the company standard and not as global standard (2) Few assessment criteria were related to each aspect (3) The tool does not give any recommendation to improve the BIM implementation

(continued)

Table 3 (continued)

BIM maturity assessment tool	Strengths	Weaknesses
BIM maturity matrix (BIM^3) by BIMe Initiative	(1) It follows the four key principles: commitment to openness, grown around a knowledge structure, peer-sourced and peer -tested, and open innovation across boundaries (2) Creates a standardized, modular language for digitalization; learning techniques, tools, and materials based on competency; and the availability of resources, tools, and templates for free (3) Create credible industry-wide competency standards in technology, procedure, and policy; and (4) Facilitates exchange of knowledge	(1) It is just a guideline and will not literally show you the maturity of your BIM implementation (2) The assessment is intended of low-detail organization (3) The assessment question is too broad (4) The tool does not give any recommendation to improve the BIM implementation
BIM maturity assessment by ARUP	(1) Assess the maturity of implementation on each discipline of the project (2) Discovers new methods to magnify its impacts and reap its benefits across all of ARUP's endeavors (3) Offers value from project conception through operation, serving as a foundation for future digital twins and day-to-day asset management tasks	(1) No universal software platform (2) Target value is based on the company standard and not as global standard (3) The tool does not give any recommendation to improve the BIM implementation

3.3 Producing Criterion that Will Measure the organization's BIM Capability, BIM Competencies in Terms of Their Process, Technology, Policy, People, and Standards

The researcher has extracted and used the questions to assess the maturity of BIM implementation across five major categories. The researcher then categorized to form a sub-fundamental component, which is the maturity in terms of BIM capability and BIM competency.

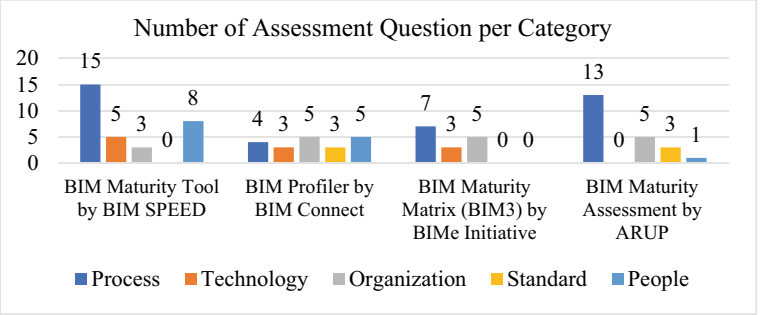

Fig. 1 Number of assessment questions per category

In Table 4, the respondents rate the importance of each sub-fundamental component created by the researcher and put into one of five categories. These categories are based on BIM capability and were used as the BIM criterion for the study.

Table 5 illustrated the BIM competency components as another BIM criteria. Each criterion has been measured according to the identified framework of BIM.

Table 4 BIM criteria under BIM capability

BIM capability		Frequency	Percentage	Total percentage
Process	Coordination working practice	20 25	66.70 83.33	75.01
Technology	System	29	96.70	96.70
Organization	Awareness and motivation	16	53.30	53.30
Standard	Data structure	25	83.30	83.30
People	Roles and responsibilities	23	76.70	66.70
	Qualities and trainings	17	56.70	
Total BIM capability				75.00%

Table 5 BIM criteria under BIM competency

BIM competency		Frequency	Percentage	
Process	BIM use	17	56.70	63.35
	Information flow	21	70.00	
Technology	IT security	14	46.70	46.70
Organization	Organizational requirements	17	56.70	66.70
	Strategy	23	76.70	
Standard	Information exchange	20	66.70	66.70
People	Knowledge management	17	56.70	56.70
Total BIM competency				60.03%

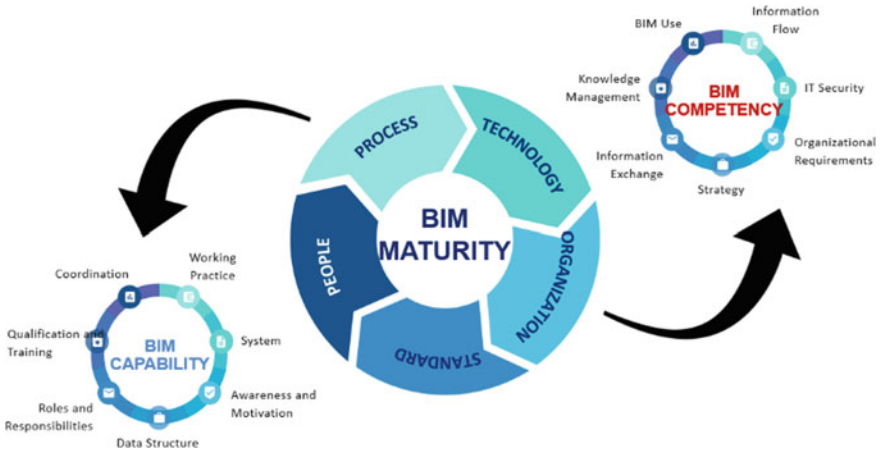

Fig. 2 BIM maturity framework

3.4 Generating a Framework that Will Assess the Maturity of BIM Implementation

BIM maturity is made up of five main categories, as illustrated in Fig. 2. These parts include the process, the technology, the organization, the standards, and the people.

3.5 Assessing the Maturity of Local and International Design and Construction Firms in the Philippines in Terms of BIM Adoption

As given in Table 6, the first case study was conducted among local companies, for which localized organizations have been selected to assess BIM implementation through BIM maturity. By analyzing its BIM maturity matrix, maximum scores are observed for resources (processes) and people. This means that the physical factors of the work environment are reviewed to ensure personal satisfaction and productivity, as well as indicate high levels of collaboration, information flow, working practice, and BIM use on the projects. Also, it manifested that the other physical factors were the human resources (people) that enable us to guarantee that everyone working behind BIM projects clearly knows their roles and responsibilities, has qualified and gained relevant training, and has knowledge management. These have been carried out by interdisciplinary teams, including the majority of stakeholders. With an index of 66.64%, case study number 1 has reached the integrated maturity level (medium–high maturity).

Table 6 BIM implementation maturity among local companies

BIM maturity matrix (Case study 01)						
Granularity level		A (0–19)	B (20–39)	C (40–59)	D (60–79)	E (80–100)
Process	Coordination				65.5	
	BIM use				63.67	
	Information flow				66.17	
	Working practice					79.25
Technology	System				69.33	
	IT security				66.33	
Organization	Organizational requirements				62.50	
	Strategy			54		
	Awareness and motivation				64.66	
Standard	Information exchange			56.5		
	Data structure			51.00		
People	Roles and responsibility				70.33	
	Qualification and training			58.00		
	Knowledge management				63.67	
Subtotal		0	0	54.88	65.80	79.25
Average maturity index						66.64%

On Table 7, the second case study was based on the perspective of the international companies, which is based in the country, on BIM maturity during the implementation of BIM. It showed the results of the BIM maturity level analysis, which showed that the physical factors (processes) and organization got the highest scores. This indicates that the firm strongly aligns to strategies that link architectural production processes in BIM that resolve certain issues related to the company's BIM process and goals which puts it at the optimized (high maturity) level.

3.6 Identifying the Challenges Faced by the company's During the Implementation of BIM Methodologies

Table 8 depicts various challenges encountered by the organization during the implementation of BIM methodologies. These obstacles may affect how ready an organization is to fully implement BIM and get all of its benefits.

Table 7 BIM implementation maturity among international companies

BIM maturity (Case study 02)						
Granularity level		A (0–19)	B (20–39)	C (40–59)	D (60–79)	E (80–100)
Process	Coordination					93.5
	BIM use				78.00	
	Information flow				84.67	
	Working practice					97.00
Technology	System					92.00
	IT security					83.33
Organization	Organizational Requirements					97.00
	Strategy					90.5
	Awareness and motivation					95.33
Standard	Information exchange					85.00
	Data structure					86.67
People	Roles and responsibility					91.33
	Qualification and training					92.00
	Knowledge management					90.00
Subtotal		0	0	0	162.67	1,093.67
Total score						1,256.33
AVERAGE maturity index						89.74%

3.7 Developing the Philippines BIM Roadmap

All of the strategic plans and actions shown in Fig. 3 and described by the researcher are some of the most important ways to help the company in the Philippines deal with the problems it ran into while implementing BIM.

Figure 4 shows the diagram for the Philippines BIM roadmap, which is represented by a five-year plan to fully integrate and implement BIM across the country. The first year's goal will be to set up the Philippine Construction Industry Council. This will lay the groundwork for reaching the goal.

4 Discussions

Each of these tools has a distinct application depending on the needs of the industry, which ultimately leads to the creation of new projects and the incorporation of new technology. Construction companies were able to successfully operate in a virtual environment as a result of their actions taken in this regard. The BIM assessment tools positively aid in achieving the needs of the construction industry, notably in terms of

Table 8 Barriers in BIM implementation

Process barriers	Technical barriers	Organizational barriers	Standard barriers	People barriers
• Risk and challenges of using BIM • Lack of knowledge on BIM and information workflow • Lack of knowledge on BIM uses • Lack of knowledge on defining BIM level of information need • Lack of BIM champion to oversee BIM process • Absence of a solid BIM-based process • Lack of working practice with regards to BIM	• High cost of BIM software • Lack of infrastructure to implement BIM • Lack of compatibility in hardware • Lack of compatibility in software • Inadequate domestic BIM tools • Problems with adjusting to BIM's technology and workflow • Increasing the model's development workload • Lack of IT security system • High cost of BIM software • Lack of infrastructure to implement BIM	• Lack of top management support • Lack of in-house expertise • Lack of other competing initiatives • Lack of cooperation between stakeholders • Lack of knowledge on legal and rights issues on BIM implementation • High costs in changing to BIM process • Lack of research on BIM implementation • Resistance to change • Misunderstanding of BIM • Negative attitude toward working collaboratively • Lack of BIM strategy • Lack of BIM vision and general plans • Lack of top management support	• Inadequate BIM protocols and standards • Insufficient methods for achieving desired results • Problems with industrial property rights and protection • Problems with BIM implementation contracts due to a lack of industry standards • Deficiency in understanding of BIM implementation law and rights • Risks not covered by existing policies during BIM deployment • Inadequate BIM protocols and standards • Insufficient methods for achieving desired results	• Insufficient knowledge of BIM • BIM roles are not clearly defined • Disparity in the provision of BIM-related training and education • Lack of BIM knowledge for actual implementation • Insufficient BIM training • Resistance to change • Lack of knowledge on BIM platforms • Insufficient knowledge of BIM

efficiently planning, designing, constructing, and operating projects. Research done in the past lends credence to the idea that a building information modeling (BIM) system is among the specific innovations that have to do with the application and advancement of an adequate computer model of the way an infrastructure is to be constructed, but can therefore be proffered digitally.

Fig. 3 BIM implementation strategies and actions

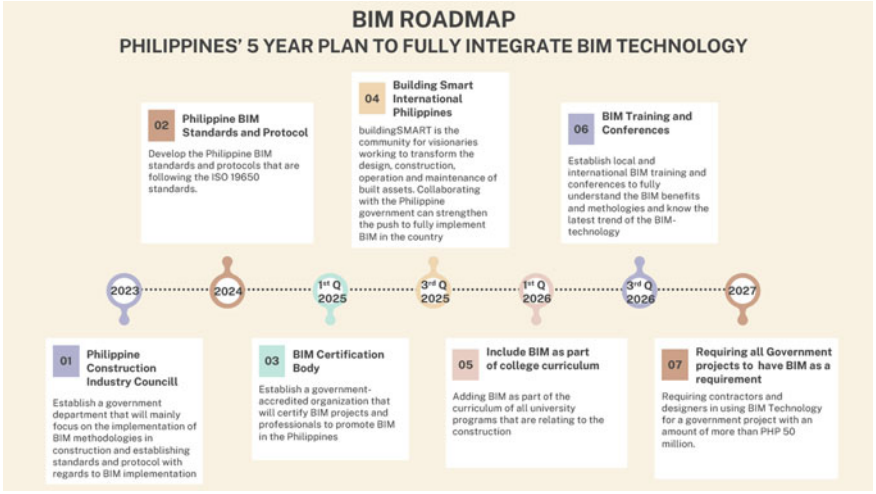

Fig. 4 Philippines' five-year plan BIM roadmap

On the contrary, BIM capability and BIM competency were found to be the two distinguishing characteristics in measuring the maturity of BIM implementation. Technology and standard components dominate in terms of BIM capability, accounting for 96.70% and 83.30% of the five categories and their sub-fundamental components, respectively. When it comes to BIM competency factors, organization, standards, and processes stand out as very important. For the organization, it includes organizational requirements and strategy; for the standard, it incorporates information exchange. On the other hand, the process comprises the utilization of BIM as well as the flow of information with 63.35%. It can be seen that 75% of the respondents agreed that the components under BIM capacity are important in measuring the maturity of BIM implementation compared to 60.03% under BIM competency.

With regards to the BIM maturity framework, it was made up of five main categories, which include the process, the technology, the organization, the standard, and the people. The process category will measure how mature the organization is based on its collaboration and flow of information. The technology category will measure how mature they are in terms of technology management. The organization category will measure the organization's capabilities to implement BIM successfully. The standards category will measure the maturity of the organization in their information exchange and data structure. Lastly, the people category will measure the organization's maturity in their mentality and culture in terms of BIM application.

The analysis and assessment of the BIM maturity level as perceived by both international and local companies support the findings of the analysis. The study pointed out that capacity maturity models highlighted the collection of changes in practices that enable implementers to gain considerable economic benefits [10]. In addition, the technique is summarized in the BIM maturity matrix (BIM3), which includes two axes, which are titled "BIM capability sets" and "BIM maturity index," respectively. In this study, the maturity level assessment requirements were put into five groups: processes, technology, organization, standards, and people. This was used as the basis for making the BIM roadmap, which was made for construction companies in the Philippines that work on BIM-based projects.

Before BIM can be used in practice, there are still issues and challenges that must be addressed. Some of the problems that keep BIM from being as effective as it could be are cultural opposition, high investment costs, uncertainty about return on investment (ROI), and the lack of universal BIM standards [11]. In addition, the obstacles associated with BIM have evolved from those that are technical in nature to those that concern the smooth integration of BIM into regular working procedures. The first thing the organization should do is look at the state of its BIM and see if there are any good ways to improve it to deal with these problems. It was further accentuated that when BIM is used in the building industry, it has a lot of positive effects [12].

In consideration of several challenges encountered, the development of the BIM roadmap, which is specifically designed to guide construction companies in the Philippines, has made a huge contribution in overcoming hindrances that hamper BIM implementation in all projects. In fact, establishing other non-governmental organizations like building smart international Philippines and a BIM certification

body will strengthen the push to fully implement BIM in the country. The inclusion of BIM in the university curriculum will enable students to understand the concept of BIM at an early stage. In addition, BIM training and conferences can be organized to help the country keep up with the latest trends in BIM methodologies and techniques. Lastly, requiring all government projects exceeding PHP 50 million to have BIM as part of the requirement will keep the country on the same page with other Asian countries that are already fully implementing it.

5 Conclusion

The findings revealed that varied applications based on industry demands and the creation of new projects as well as new technologies can be used to meet a wide range of industry needs. So, BIM technologies have helped the construction industry a lot by making it easier to plan, design, build, and run projects.

In terms of each BIM evaluation tool's strengths and weaknesses, it shows the many possible benefits that may be obtained if the tool were used. However, there were also problems with acceptance of technology. Furthermore, the BIM criterion was established to be an organization's BIM capabilities and competencies in terms of its process, technology, organization, people, and standards. BIM tools can be distinguished by their BIM capability and BIM competency. As a result, the company now has the information it needs to properly evaluate and assess the maturity of BIM. Several indicators have come up and been deemed important for figuring out how well BIM is being used.

Furthermore, a number of factors have been taken into account in the evaluation of the BIM implementation by different companies to ensure that the interface and implementation are effective and efficient. So, most companies know how important and helpful it is to focus their business needs on the five core components listed above, but not everyone does.

Based on a critical evaluation and understanding of the maturity level of BIM, it was shown that multinational firms are more mature compared to local enterprises. Importantly, the study found that multinational BIM projects that use BIM methodologies have reached a higher level of maturity than local BIM projects.

On the other hand, BIM implementation posed a variety of obstacles. Barriers to the application's integration within the company were found to have a substantial impact on its performance. Unresolving these issues may lead to an insufficient and low level of BIM implementation across the organization. Providing key strategies and actions to overcome the challenges faced during the BIM implementation can help the organization improve and achieve a high level of maturity. But without proper guidance and implementation from the government, these problems could still come up and make it hard for the country to improve how it uses BIM.

In reality, prior studies have shown how BIM has evolved in tandem with its applications in the construction industry. Yet, the studies lacked information on how the success of BIM deployment was evaluated. Therefore, the focus of the present

research was on how various BIM implementations contributed to the success of the building sector in the Philippines. So, it has the potential to improve the efficiency and effectiveness of solving a wide range of technical and construction-related problems and challenges. It could also help the construction industry by meeting their needs for future improvements with computer-based BIM applications.

This study will concentrate on the process of developing a BIM roadmap for the Philippines. This is something that may be accomplished by determining the present maturity level of BIM implementation in the country based on the many different criteria that have been stated.

Therefore, the BIM roadmap for the Philippines' construction industry provides strategic plans on five key areas: process, technology, organization, standards, and people; and a five-year implementation plan to guide the Philippines and the construction industry. This will help the country get better and reach a high level of maturity in putting BIM into place.

References

1. Sinenko S, Hanitsch P, Aliev S, Volovik M (2020) The implementation of BIM in construction projects. E3S Web Conf 164:08002
2. Silva D, De Jesus KL, Villaverde B, Enciso AI, Mecija AN, Mendoza O (2021) Interdisciplinary framework: a building information modeling using structural equation analysis in lean construction project management. Frontiers Artific Intell Appl 341:234–240
3. Joblot L, Paviot DD, Lamouri S (2019) Building information maturity model specific to the renovation sector. Autom Construct 101:140–159
4. Yilmaz G, Akcamete A, Demirors O (2019) A reference model for BIM capability assessments. Autom Construct 101:245–263
5. Fernandez J, Silva D, De Jesus KL (2021) Hybrid neural—based model for predicting the construction project performance of high—rise building projects in Metro Manila, Philippines. Frontiers Artific Intell Appl 341:274–281
6. Silva D, De Jesus KL, Villaverde B, Adina E (2021) Management competency model: predictive neural network approach for empirical components of construction project proficiency. Frontiers Artific Intell Appl 341:266–273
7. Baccay M, Barbier B, Bagcal O, Rodriguez L (2019) Adoption of building information modeling (BIM) in the Philippines AEC industry: prospects, Issues, and challenges. J Construct Eng Technol Manage 9(2):8–20
8. Miettinen R, Paavola S (2014) Beyond the BIM utopia: approaches to the development and implementation of building information modeling. Autom Construct 43:84–91
9. Liao L, Teo E (2017) Critical success factors for enhancing the building information modelling implementation in building projects in Singapore. J Civil Eng Manage 23(8):1029–1044
10. Stumpp M, Alves R, Manica C (2021) BIM maturity index: analysis and comparison of architecture office's BIM performance in Porto Alegre. Build Manage 5(2):48–56
11. Wu C, Xu B, Mao C, Li X (2017) Overview of BIM maturity measurement tools. J Inf Technol Construct 22:34–62
12. Al-Ashmori YY, Othman I, Rahmawati Y, Mugahed A, Sabah SHA, Rafindadi AD, Mikic M (2020) BIM benefits and its influence on the BIM implementation in Malaysia. Ain Shams Eng J 11(4):1013–1019

Review of Previous Researches' Methodology Stakeholder Integration in Connected Construction

Dewa Made Satriya Wibawa Mertha, Christiono Utomo, Sulfiah Dwi Astarini, Cahyono Bintang Nurcahyo, and Maulita Nahdiyah

Abstract Connected construction is a concept that combines all stages of construction and uses high-end technology to solve problems in the construction industry. Throughout the life cycle's planning, construction, and operation phases, each stage has a different stakeholder and role. The involvement of different stakeholders at each stage of connected construction is still a problem. The discrepancy between planning and output will be a consequence if the interaction between stakeholders at each stage is not properly connected. Several studies on stakeholder integration have been carried out using various methods but are still rarely found in the context of connected construction. So it is important to know the appropriate research method for stakeholder integration in connected construction. This study aims to identify the research methods used in stakeholder integration in connected construction, using determined 20 papers on the topic of stakeholder integration in the construction industry. The result of the study is the mapping of previous research based on the method used. This mapping will be useful for researchers to conduct the methodology of the research, especially on the topic of stakeholder integration in connected construction.

Keywords Stakeholders · Integration · Construction · Connected

1 Introduction

Connected construction is a concept that combines all stages of construction from planning, construction, and operations [1]. Connected construction utilizes today's technologies such as 3D printing, big data, virtual reality, and Internet of Things (IoT) [2]. This technology is designed to integrate each stage of construction. In the connected construction process, each phase requires that stakeholders must be

D. M. S. W. Mertha · C. Utomo (✉) · S. D. Astarini · C. B. Nurcahyo · M. Nahdiyah
Institut Teknologi Sepuluh Nopember, Surabaya 60111, Indonesia
e-mail: christiono@ce.its.ac.id

T. Kang (ed.), *Proceedings of 5th International Conference on Civil Engineering and Architecture*, Lecture Notes in Civil Engineering 369,
https://doi.org/10.1007/978-981-99-4049-3_55

involved. Each phase involves different stakeholders. In the planning phase, the stakeholders involved include architects, engineers, and owners, then in the construction process involving civil engineers, and contractors, followed by an operational phase involving stakeholders such as tenants, buyers, property management, and suppliers, so that at each phase in the construction stage, stakeholders are working together at different stages. Each stage will be completed with respective stakeholders, and hence, the relationship between each stage is not well integrated [3]. The construction industry has characteristics at each stage, so it takes many stakeholders in each sub-process, and therefore, the concept of stakeholder integration in construction at each stage plays a fundamental role [4]. Without the integration of knowledge transfer management, it will certainly impact project outcomes which will affect project objectives such as time, quality, resources, communication, and procurement contracts in the entire project life cycle [3].

Based on these problems, although there have been infrequent discussions related to stakeholder integration in connected construction throughout the whole project life cycle, nevertheless several studies have identified related stakeholder integration in the construction industry. Several studies have been conducted with different methods and objectives, and therefore, it is necessary to identify the research methodology in previous studies to support research related to stakeholder integration in connected construction. This study uses a literature review method, by selecting 20 indexed papers with relevant topics. The results of the research will be a guide for further research to determine methods related to stakeholder integration in connected construction.

2 Conceptual Background

2.1 Stakeholder Integration

The initial statement of the stakeholder concept was triggered by [5] which was standardized at the 1963 Stanford Research Institute, which is a group that can influence or be influenced by the company's goals [6]. Furthermore, the concept is developed from several perspectives into stakeholder integration and understanding of the ability to provide collaborative relationships with various stakeholders [5]. Stakeholder integration becomes important in the industrial world, with this purpose toward the development of strategic capabilities to regulate and carry out corporate management practices. To measure the extent of stakeholder integration in the corporate world, research [7] identified the dimensions of stakeholder integration, including stakeholder capabilities, company interaction with stakeholders, and adaptability between company characteristics and stakeholders. However, in the context of the construction industry, it is not enough just by integrating stakeholders, whereas the behavior of the organization itself will determine how the project performance develops [8]. Therefore, the criteria for stakeholder integration are very important to

identify how far the effectiveness of these criteria contributes to project development [9].

2.2 Connected Construction

There is a lack of definition of connected construction in published papers. However, in published papers, the definition of this concept is related to construction 4.0 which the objectives are connecting all stages of construction by utilizing high-level technology [1]. Cyber-physical systems, BIM, big data, and IoT are the driver for construction 4.0 [1, 10]. According to [10], using BIM become a benchmark for the standard construction 4.0 industry. Construction 4.0 practice is comprehensively described in research [11]. With all the integration of the technology used, monitoring will be easier to do, so that the entire project life cycle information will be well integrated [11]. Indirectly, this will affect the existing organizational structure of a project, changes will lead to a more integrated system [12]. The utilization of technology has not been fully adopted by construction practitioners, due to the low urgency of using technology this is proven in research [13]. IT infrastructure, practitioner knowledge, data management, and organizational resistance are some aspects that will become obstacles when carrying out the practice of technology in the field [14]. The development of adopted technology for BIM in collaborative automation and synchronization real-time monitoring in all phases needs further study, so that the attention and responsibility of stakeholders in each phase can be optimized [15]. Hence, in the future, practitioners will utilize this technology adopted in construction to ensure efficiency [14]. The practice of BIM in the construction industry is controlled by stakeholders who have the ability and willingness to adopt this technology [13]. Therefore, the integration of stakeholders in all phases in the construction that utilizes technology in the practice will be able to maximize the efficiency of the energy used [16].

2.3 Method of Previous Research

Previous research generally used a literature review approach, statistical analysis, interviews, and case studies.

2.3.1 Research Philosophy

Using a two-paradigm approach, the general method used in research is qualitative and quantitative research. The qualitative method begins with data collection and continues with analysis that does not involve calculation with numbers and illustrates the direct perspective of respondents [17]. In the quantitative method, data is collected

using instruments, and the processing uses statistical analysis [17]. In collecting the data, the research data is classified into primary and secondary data [17]. Primary data is obtained directly through informants by researchers who conduct surveys, while secondary data is data obtained through the second person, books, libraries, annual reports, and the Web [17].

2.3.2 Research Technique

a. Literature review is a comprehensive review of articles that have been conducted in previous research. Articles with relevant topics in the scientific literature are sourced from journal articles, conference papers, books, theses, dissertations, and company annual reports [17].
b. Survey is the methodology to explore information with arguments from informants, and this method involves respondents who have knowledge related to the research. So it is important to determine the appropriate informants before conducting the survey [17].
c. Interview is conducting direct discussions by asking respondents questions regarding the research's urgency. [17] acknowledge that there are three characteristics of interviews that can be conducted, including exploratory interviews, design interviews, and in-depth research interviews. Persons from interviews have capable knowledge, so that information can be extracted properly. The interview technique takes a long time, and the number of information is at least 20 [17].
d. Case study, this method uses an event as the object of research. Case studies were conducted to explore problems that occur in the present or the past that have an impact on future events which can be in form of organizations, groups, departments, or individuals [17].

3 Result and Discussion

3.1 Methodology

This research begins by searching for relevant literature on stakeholder integration. It was found that 20 papers with indexed journals were selected for this study to examine the methods. The papers were found published in the range of 2014–2022. The papers are presented in Table 1 containing information about the name of the journal and its respective SJR value.

After determining the 20 papers that have been classified based on the name of the journal and the number of papers along with the SJR value, the paper will be analyzed and explored based on the methodology that was used.

Table 1 Distribution of selected journals and number of papers

No.	SJR	Name of journals	Number of paper
1	2.495	International Journal of Project Management	6
2	1.619	Journal of Management in Engineering	1
3	0.829	Construction Innovation	1
4	0.719	International Journal of Construction Management	2
5	0.717	Engineering, Construction and Architectural Management	5
6	0.512	Journal of Property Investment & Finance	1
7	0.507	Built Environment Project and Asset Management	1
8	0.465	Smart and Sustainable Built Environment	1
9	0.371	Journal of Engineering, Design and Technology	2

3.2 Result

Based on analyzing 20 papers, it was found that there were many studies on the importance of stakeholder integration in construction projects; however, infrequently articles discussed connected construction and identified stakeholder integration at all stages of the project. In line with research [4], research related to the integration of stakeholders in all stages of the project, and conducted interviews to confirm the instruments used in the survey, the purpose of this study was to determine the relationship between integration management and project performance, yet this research was not in a connected construction context. Several studies used the literature review method on stakeholder integration [18, 19] discussed organizational integration management in the construction process, followed by research [20] elaborated on the success factors, project objectives, and project performance into success criteria, and [21] conducted research related to the literature review that discussing stakeholder integration in an off-site construction context. This research aims to provide an understanding of the importance of stakeholder integration in the construction industry. Research on the success factors for achieving successful integration in projects was carried out in research [22] and [23] showed differences in the methods used, in research [22] included interviews to confirm the instrument model and then proceed with statistical analysis or calculation system.

Case studies as research objects were also carried out to investigate and evaluate events related to stakeholder integration. Case study research will generally conduct interviews with respondents [24–26]. Research [26] conducted a comparison of four case studies and conducted semi-interviews to identify variables that affect the design planning stage, and the result of stakeholder integration is the most factor in the design planning process, but the identification of the research is only at the design planning stage. Different from what was done [27] developed a model of stakeholder integration from the entire project stage process, the model was developed with a study literature approach and [16] with the system dynamic method; using case studies as a model approach, the objectives from the model

are to better understand how the process of value creation within the stakeholder integration in the construction industry. The combination of research methods with literature reviews, surveys, and statistical analysis is widely found. Several studies were using a combination of literature review, survey, and statistical analysis; the statistical analysis used included ANOVA [28], principal component analysis (PCA) [29], and Shapiro–Wilk test [23]; the research uses an instrument that was previously compiled through a literature study, and respondents will give an assessment of the instrument made. Sparkling and Mollaoglu [30] have discussed connectivity with all partners in construction projects, success factors in sustainable construction, the framework of the literature in off-site construction, and team integration in the PPP context [31–33]. From several studies that have been explained, the research methods used depend on considerations related to data, information, respondents, and research objectives.

3.3 Discussion

According to the literature review conducted, presented grouping papers based on the method, which are presented in Table 2.

Based on the table above, several combinations of methodologies in the paper are determined. After performing the technical classification in the paper, the classification is continued based on data which includes primary or secondary, and quantitative or qualitative analysis which is presented in the following Table 3.

In Table 3, Y indicates the method used and N methods that are not used in the paper. Based on the table, the next step is to map the paper with four quadrants. The vertical direction quadrant indicates the paper which uses primary or secondary data, while the horizontal direction quadrant uses qualitative or quantitative methods. From the mapping that has been done in Fig. 1, the method most often used in research is the quantitative method with primary data where the data is obtained directly from the respondents.

Table 2 Overview of previous researches technique

No.	Technique	Paper
1	Literature review	[18–21, 30, 32],
2	Case study and interview	[14, 24–26]
3	Model framework and interview	[27]
4	Model Framework, case study, and interview	[16, 33]
5	Literature review, survey, and statistical analysis	[13, 22, 23, 29]
6	Literature review, interview, survey, and statistical analysis	[28]
7	The survey, interview, and confirmatory	[4, 31]

Table 3 Researches classification based on their methods and data sources

No	Methods		Data source		Methods
	Qualitative	Quantitative	Primary	Secondary	
[4]	N	Y	Y	N	Literature review, survey, CFA, any PLS-SEM
[13]	N	Y	Y	N	Survey interview
[14]	Y	N	Y	N	Literature review, case study, and interview
[16]	Y	N	Y	N	Case study, interview causal loop diagram, and system dynamic
[18]	Y	N	N	Y	Peer-reviewed paper
[19]	Y	N	N	Y	Literature review
[20]	Y	N	N	Y	Literature review
[21]	Y	N	N	Y	Literature review, Leximancer, and VOSviewer
[22]	N	Y	Y	N	Literature review, survey, and SEM
[23]	N	Y	Y	N	Survey and Shapiro–Wilk Test
[24]	Y	N	Y	N	Case study and network theory
[25]	Y	N	Y	N	Comparison 4 case study and interview
[26]	N	Y	Y	N	Case study and interview
[27]	Y	N	Y	N	Model framework
[28]	N	Y	Y	N	Literature review, survey, and ANOVA
[29]	N	Y	Y	N	Survey and principal component analysis (PCA)
[30]	N	Y	N	Y	Literature review and meta-analysis
[31]	N	Y	Y	N	Literature review and semi-structural interview, survey, CFA, and PLS-SEM
[32]	N	Y	N	Y	Literature review and social network analysis
[33]	N	Y	Y	N	Interview, survey, and AHP

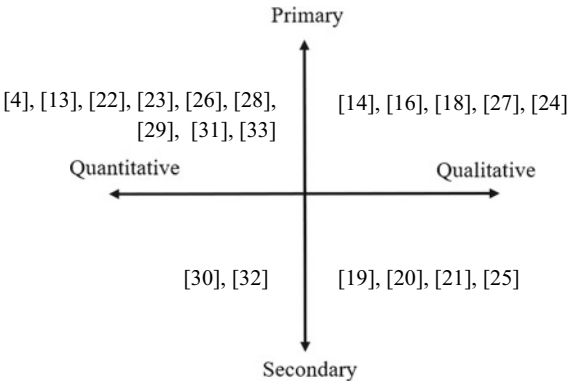

Fig. 1 Mapping of methods used in the previous research

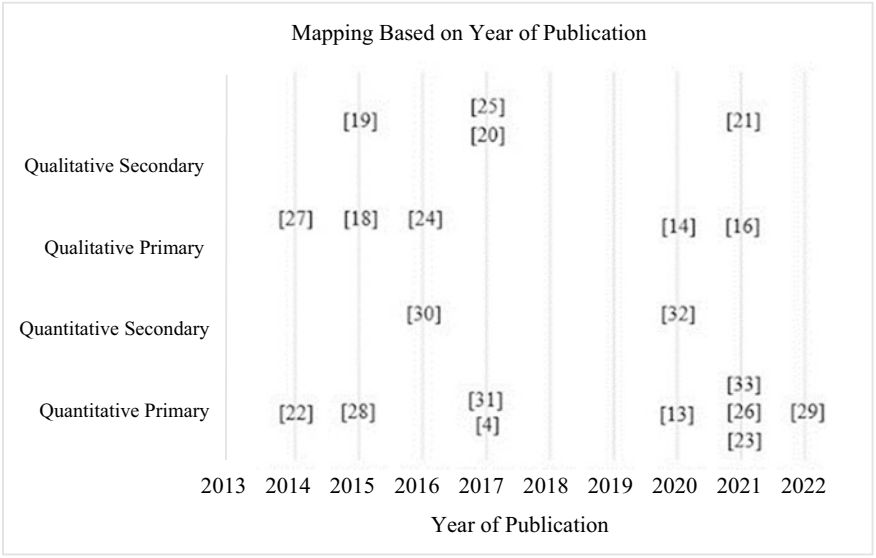

Fig. 2 Mapping based on year of publication

According to Fig. 2, mapping by year of publication shows how often each method is used. Hence, from a sample of 20 papers, it can represent the topic of stakeholder integration that is most often used is the quantitative primary. If the number of review papers increases, the results will not be far from the mapping through historical data. Basically refers to previous research, each construction phase requires many stakeholders to be involved. To develop research on this topic, we must observe the relevance between the empirical data and theoretical ground. We must identify the number of stakeholders involved by conducting research with exploratory or confirmatory modeling ending with statistical analysis. The instrument used will depend on the research model, so the instrument must be understood by respondents in a common language [17]. This really helps us to make decisions from the questions we have, which will represent the situation and conditions in the field especially how to develop integration of stakeholders in construction 4.0. However, the results of primary quantitative research will depend on the characteristics of the respondents being referred to, and therefore, in starting research, the relevance of the topic to the respondents will be very essential [17].

4 Conclusion

Based on the results obtained mapping 20 papers from 2014 to 2022, most of them use primary data and the quantitative method. So it can be concluded that for further research it is recommended to use qualitative methods with secondary data with

having a larger research gap opportunity. The results of this study are expected to be a reference for research methods and data, especially in the context of stakeholder integration in connected construction. For further research, it can be developed by mapping based on the year the paper was published and seeing the development of the research.

Acknowledgements The authors appreciate the recognition and awards in form of a research grant and fellowship from "Penelitian Dasar Kompetitif Nasional" 2022 based on contract number: 1368/PKS/ITS/2022.

References

1. Sawhney A, Riley M, Irizarry J, Perez CT (2020) A proposed framework for construction 4.0 based on a review of literature. In: Associated schools of construction proceedings of the 56th annual international conference. Epic Series in Built Environment, USA, pp 301–309
2. Forcael E, Ferrari I, Opazo-vega A, Arcas JAP (2020) Construction 4.0: a literature review. Sustainability 12:9755
3. Chou JS, Yang JG (2012) Project management knowledge and effects on construction project outcomes: an empirical study. Project Manage J 43(5):46–47
4. Demirkesen S, Ozorhon B (2017) Impact of integration management on construction project management performance. Int J Project Manage 35(8):1639–1654
5. Freeman RE (1984) Strategic management a stakeholder approach. Pitman Publishing, London
6. Rueda-Manzanares A, Correa JAA, Sharma S (2008) The influence of stakeholders on the environmental strategy of service firms: the moderating effects of complexity Uncertainty. British J Manage 19:185–203
7. Ubeda E, Jimenez JDB, Moreno EC (2010) Measuring stakeholder integration: knowledge, interaction and adaptational behavior. Dimensions 93:419–442
8. Baiden BK, Price ADF, Dianty ARJ (2006) The extent of team integration within construction projects. Int J Project Manage 24:13–23
9. Ibrahim CKIC, Costello SB, Wilkinson S (2015) Key indicators influencing the management of team integration in construction projects. Int J Managing Project Bus 8(2):300–323
10. Begic H, Galic M (2021) A systematic review of construction 4.0 in the context of the BIM 4.0 premise. Buildings 11:337
11. Jazzar ME, Urban H, Schranz, Nassereddine H (2020) Construction 4.0.: a roadmap to shaping the future of construction. In: 37th International symposium on automation and robotics in construction (ISARC)
12. Soto BG, Juan IA, Jos S, Hunhevicz J (2019) Implications of construction 4.0 to the workforce and organizational structures. Int J Construct Manage 2331–2327
13. Osunsanmi TO, Aigbavboa CO, Oke AE, Liphadzi M (2020) Appraisal of stakeholders' willingness to adopt construction projects. Built Environ Asset Manage 10(4):547–565
14. Keskin B, Salman B (2021) Airport project delivery within BIM-centric construction technology ecosystems. Eng Construct Architect Manage 28(2):530–548
15. Maskury R, Selamat A, Ali KN, Maresova P, Krejcar O (2019) Industry 4.0 for the construction industry—how ready is the industry? Appl Sci 2819
16. Seki Y, Sutrisna M (2021) Integrating a rich picture diagram and causal loop diagram to model stakeholder engagement in building refurbishment projects. Eng Construct Architect Manage 28(7):1929–1951
17. Adams J, Khan HTA, Raeside R, White D (2007) Research methods for graduate business and social science students. Sage Publication, New Delhi

18. Mok K, Qiping G, Yang J (2015) Stakeholder management studies in mega construction projects: a review and future directions. Int J Project Manage 33(2):446–457
19. Hornstein HA (2015) The integration of project management and organizational change management is now a necessity. Int J Project Manage 33(2):291–298
20. Oppong GD, Chan APC, Dansoh A (2017) A review of stakeholder management performance attributes in construction projects. Int J Project Manage 35(6):1037–1051
21. Nguyen BN, London K, Zhang P (2021) Stakeholder relationships in off-site construction: a systematic literature review. Smart Sustain Built Environ 2046–6099
22. Molwus JJ, Erdogan B, Ogunlana S (2017) Using structural equation modeling (SEM) to understand the relationships among critical success factors (CSFs) for stakeholder management in construction. Eng Construct Manage 24(3):426–450
23. Dithebe K, Thwala WD, Edwards DJ, Hayhow S (2021) Stakeholder management in the alleviation of legal and regulatory disputes in public-private partnership projects in South Africa. J Eng Des Technol 1726–0531
24. Mok KY, Shen GQ, Yang RJ (2016) A network theory-based analysis of stakeholder issues and their interrelationships in large construction projects: a case study. Int J Construct Manage 2331–2327
25. Yang RJ, Gunarthna C, Arashpour M, Xue X, Zhang G (2017) The evolution of stakeholder management practices in Australian mega construction projects. Eng Construct Architect Manage 25(6):690–706
26. Keusters G, Bakker H, Houwing E (2021) Improving the performance of civil engineering projects through the integrated design process. J Eng Des Technol 1726–0531
27. Morrissey J, Dunphy J, Macsweeney R (2014) Energy efficiency in commercial buildings: capturing added-value of retrofit. J Property Invest Finance 32(4):369–414
28. Heravi A, Coffey V, Trigunarsyah B (2015) Evaluating the level of stakeholder involvement during the project planning processes of building projects. Int J Project Manage 33(5):985–997
29. Agyekum AK, Desmond F, Fugar K, Akomea-Frimpong I, Pittri H (2022) Barriers to stakeholder engagement in sustainable procurement of public works engagement. Eng Construct Architect Manage 0969–9988
30. Sparkling AE, Mollaoglu KA (2016) Research synthesis connecting trends in architecture, engineering, and construction project partnering. J Manage Eng
31. Banihashemi S, Hosseini MR, Golizadeh H, Sankaran S (2017) Critical success factors (CSFs) for integration of sustainability into construction project management practices in developing countries. Int J Project Manage 35(6):1103–1119
32. Hu X, Chong H (2020) Integrated frameworks of construction procurement systems for off-site manufacturing projects: social network analysis. Int J Construct Manage 2331–2327
33. Malaeb Z, Hamzeh FR (2022) IPD-inspired framework for measuring stakeholder integration in public-private partnerships. Construct Innovation 22(1):313–326

An Analysis on the Key Influence Factors for Intelligent Construction of Prefabricated Buildings Using DEMATEL-ISM

Hongmin Zhou, Huihui Liu, Shicheng Zhao, and Baohe Zhu

Abstract Intelligent construction refers to a new generation of artificial intelligence and engineering construction that has been naturally integrated into a new construction process. It can be effectively incorporated with prefabricated structures. To scientifically improve the application possibilities of intelligent construction, it is necessary to identify and analyze the key factors influencing its application to prefabricated buildings. This study presents the overall functional architecture of an intelligent construction system for prefabricated buildings and identifies 19 parameters of four aspects from the prefabricated buildings life cycle. To identify the key factors and causal relationships, Decision-Making trial and Evaluation Laboratory (DEMATEL) is employed, in conjunction with Interpretive Structure Modeling (ISM), to construct a multilevel progressive structure model that also clarifies the action pathways of these factors. The feasibility of the proposed methodology has been demonstrated through case analysis. The results show that policies and regulations, technical standard systems, talent quality, and technology and innovation investment are the deep-seated influencing factors in the application of intelligent construction of prefabricated buildings, and the development suggestions are proposed accordingly.

Keywords DEMATEL-ISM · Prefabricated buildings · Intelligent construction · Influence factors

H. Zhou
Shandong Provincial Key Laboratory of Civil Engineering Disaster Prevention and Mitigation, Shandong University of Science and Technology, Qingdao 266590, China

H. Zhou · H. Liu (✉) · S. Zhao
College of Civil Engineering and Architecture, Shandong University of Science and Technology, Qingdao 266590, China

B. Zhu
China Construction Fifth Engineering Division Corp., Ltd, Hunan Changsha 410004, China

T. Kang (ed.), *Proceedings of 5th International Conference on Civil Engineering and Architecture*, Lecture Notes in Civil Engineering 369,
https://doi.org/10.1007/978-981-99-4049-3_56

1 Introduction

As a result of the current labor shortage and increasing environmental restrictions, the central government and local governments have actively promoted prefabricated building policies. A new mode called intelligent construction is emerging with digitization and artificial intelligence. Construction in this new mode is characterized by "Digital Construction," the development from a crude and labor-intensive production to a refined and technologically intensive production that is inevitable for the construction industry. The traditional construction industry is being intelligently transformed and upgraded through this internal impetus.

Jiang [1] proposed the whole process management mode for intelligent bridge engineering assembly type based on the characteristics of bridge engineering prefabricated buildings; Ma and Wang [2] analyzed the superiority of the prefabricated way in achieving intelligent construction of tunnel used mine tunneling and determined that this way is an important component for achieving intelligent construction.

It has been the development of artificial intelligence that has provided the impetus for intelligent construction to be applied, and several scholars have conducted research regarding the application of emerging technologies such as Building Information Modeling (BIM), Digital Twin, and the Internet of Things (IoT) in various phases of building assembly [3–6]. Moreover, the content related to intelligent construction has been gradually enhanced.

Bao and Li [7] presented the research development and applications in the field of intelligent construction. Fan [8] proposed a closed loop control theory for sensing, analyzing, controlling, and optimizing the construction process. It should be noted that almost the studies begin from just certain area of intelligent construction. However, due to the many differences between traditional construction and intelligent construction, there are many conflicts and contradictions in intelligent construction application.

Accordingly, Jia et al. [9] applied ISM and Analytic Hierarchy Process (AHP) to identify the main factors that influence smart construction site; Sun et al. [10] analyzed the characteristics of technological innovation subjects of intelligent construction and developed an evolutionary game model examining the interaction between collaborative innovation subjects of intelligent construction technology. Lee et al. [11, 12] developed an overall architecture for the full life cycle management of industrialized buildings which combines several emerging technologies such as BIM and cloud computing into a single system.

The current research on intelligent construction of prefabricated buildings often focuses only on the perspective of application research of new technologies. The analysis of the system and applied process of intelligent construction and the mechanism of action between the influencing factors is relatively vague. In addition, the traditional path of action of the factors cannot be adapted to the current development model, and there is not yet a clear development path about intelligent construction of prefabricated buildings.

A systematic analysis of the application of intelligent construction across the full life cycle of prefabricated buildings is presented in this paper, which summarizes the concept definition, system construction, and implementation methods. Consequently, a clear and reasonable development path is obtained by analyzing the key influencing factors and hierarchical logical relationships, providing a theoretical basis for developing intelligent construction systems that can be used in prefabricated buildings, and promoting the green development of the construction industry.

2 Intelligent Construction of Prefabricated Buildings

Due to the late start of intelligent construction in China, the concept of intelligent construction of prefabricated buildings has not yet been uniformly defined. So this paper defines it as: In the full life cycle of prefabricated buildings, various artificial intelligences are comprehensively used, such as IoT and intelligent equipment, to replace "Traditional production + Prefabrication." Through the application of industrialization technologies, valueless construction tasks can be reduced or eliminated. As a result, stakeholders and participants' synergy efficiency is improved, the project's construction goals are met, construction costs are reduced, and the construction process is rendered low carbon and highly efficient.

Based on the analysis of the connotation of intelligent construction of prefabricated buildings, combined with relevant references [13–15], The overall functional system architecture of the intelligent construction system of prefabricated buildings is obtained from the major stages of the application of intelligent construction to prefabricated buildings, including intelligent design, intelligent production, smart construction site, and artificial intelligence for IT operations, as shown in Fig. 1.

3 DEMATEL-ISM Model

3.1 Theoretical Definitions

Decision-Making Trial and Evaluation Laboratory (DEMATEL) is a systematic analysis using graphical and matrix tools to analyze the cause and effect relationships among components of a complicated system. This method can be used for converts the inter-dependency relationships and quantitatively determines the key factors.

Interpretive Structure Modeling (ISM) is a combination of qualitative and quantitative methods, which allows the analysis to visualize the degree of influence and internal correlation between the factors in a complex system.

The combination of these two methods allows causal relationships and hierarchical structure between factors in complex systems to be identified with relatively

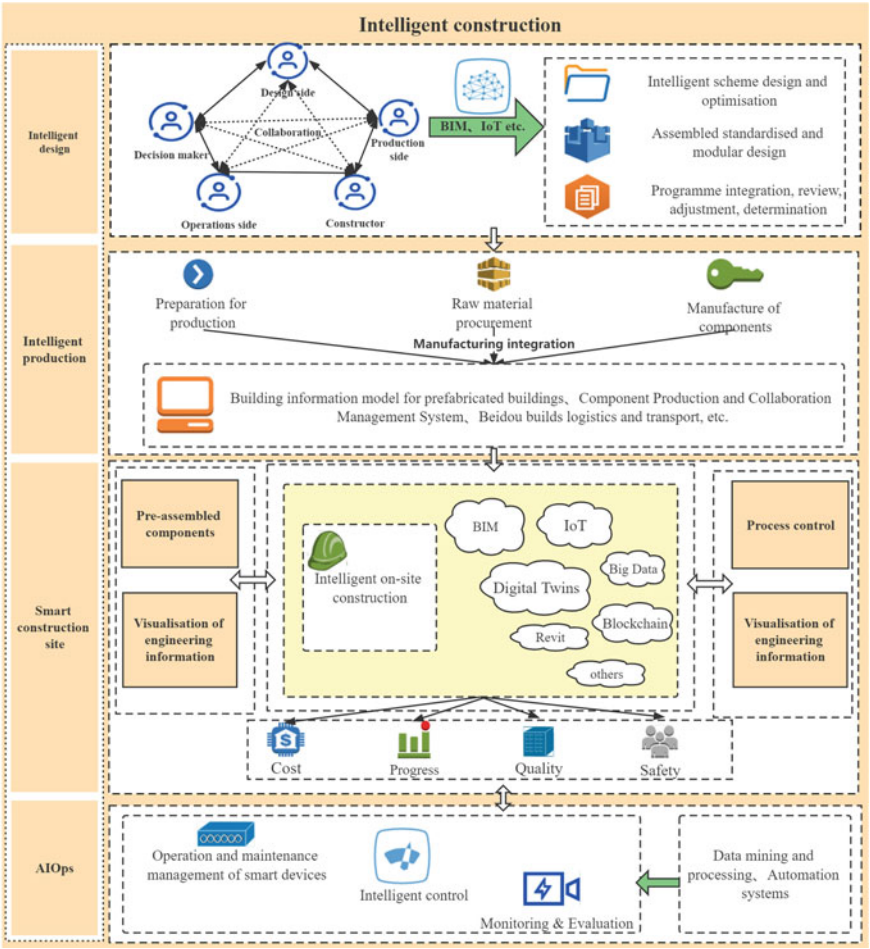

Fig. 1 Overall functional architecture of the prefabricated buildings intelligent construction system

low computational burden, thereby showing the internal correlations between the different influencing factors visually and effectively.

3.2 Model Construction

Constructing a system of indicators. An analysis of the references [14–18] in conjunction with the relevant engineering situation, taking into consideration the entire construction process and five major elements of labor, machine, material, law, and environment of assembly buildings, 19 influencing factors are obtained from four aspects including implementation, organizational, technical, and environmental.

After analyzing the relevant influencing factors with hierarchy and connotation, the 19 influencing factors are summarized in Table 1.

Questionnaires. Several questionnaires were developed to conduct a survey of individuals involved in various aspects of prefabricated buildings and researchers at universities who conduct research on prefabricated buildings. Ten experts were selected to assess the degree of interconnection between the elements on a scale of 0–3 (where 0 represents no influence, 1 represents weak influence, 2 represents average influence, and 3 represents strong influence).

DEMATEL-ISM model construction. The methodological steps of DEMATEL-ISM are shown below.

(1) Setting the system factor set: $S = \{S_i | i = 1, 2, \ldots, \mathrm{n}\}$, n indicates the number of factors.
(2) Based on the questionnaire results, the direct impact matrix B is determined by comparing the impact of S_i on S_j with a diagonal value of 0.
(3) Normalize the direct impact matrix B to eliminate the effects of different magnitudes and obtain the normalized matrix $C = \left[C_{\mathrm{ij}}\right]_{\mathrm{n}\times\mathrm{n}}$ using Eq. (1).

$$C = \frac{B}{\max\limits_{1\le i\le 15} \sum_{j=1}^{15} b_{\mathrm{ij}}} \tag{1}$$

where $\max\limits_{1\le i\le 15} \sum_{j=1}^{15} b_{\mathrm{ij}}$ is the row and maximum value of the influence relationship matrix B.

(4) Using Matlab software, the combined impact matrix was derived to represent the indirect impact of the increase between the elements, with the following Eq. (2).

$$\begin{aligned} T &= \lim_{n\to\infty} (C + C^2 + \cdots C^n) \\ &= C(I - C)^{-1} = \left[t_{\mathrm{ij}}\right]_{n\times n} \end{aligned} \tag{2}$$

where I is the identity matrix and -1 is the inverse matrix

(5) After obtaining the comprehensive influence matrix T, four metric elements are calculated based on the matrix T: influence degree E_i, influenced degree E_j, central degree Z_j, and cause degree Y_i. The cause degree Y_i, which reflects the attributes of the factor, is said to be the cause factor if it is positive, and vice versa for the influence degree of the result factor. The calculation process is given in Eq. (3).

$$E_i = \sum_{j=1}^{n} t_{ij} \quad (i = 1, 2, 3 \cdots n)$$

Table 1 Intelligent construction application index of prefabricated buildings

	Influencing factors	Symbols	Factor explanation
Implementation factors	Intelligent design	S_1	Developing design solutions with technologies
	Intelligent production	S_2	The digital production and transportation of components
	Smart construction site	S_3	Construction processes based on information, such as lifting and visual assembly, are examples of intelligent construction
	Artificial intelligence for IT operations	S_4	Monitoring, service, and visual management, together with data and information to improve site efficiency and decision-making
Organizational factors	Enterprises strategy	S_5	Business development strategy for intelligent
	Multi-disciplinary collaboration efficiency	S_6	The efficiency of multi-disciplinary collaboration, including the flow of information related to project design and construction
	Participant interests	S_7	Cooperation between parties or conflicts arising from interests
	Talent quality	S_8	Ability to operate intelligent equipment, technology, and related intelligent construction knowledge
	Information management level	S_9	Including the aggregation, processing, and analysis of information
Technical factors	Technical advantages	S_{10}	The advantages of intelligent construction technology in the construction and management of buildings
	Technical costs	S_{11}	Costs invested in the introduction of technologies
	Information platform	S_{12}	The platform for communication, collaboration, and information transfer among the participants

(continued)

Table 1 (continued)

	Influencing factors	Symbols	Factor explanation
	Intelligent technology adoption	S_{13}	Willingness of adoption of intelligent technologies
	Technical standards system	S_{14}	A unified standard system for technical data to enable data compatibility, management, and other operations
Environmental factors	Policies and regulations	S_{15}	The government's incentive policies or penalties
	System integration	S_{16}	Ability to integrate various types of data acquisition, analysis equipment, software, and subsystems into a single, coordinated system
	Resource readiness	S_{17}	Resource elements to enable smart construction, such as network facilities
	Competitive pressures	S_{18}	Practices of pilot projects and successful cases, orientation resulting from application of benefits
	Technology and innovation investment	S_{19}	Develop high-tech industries and promote the transformation of technological achievements

$$\begin{aligned} E_j &= \sum_{i=1}^{n} t_{ji} \quad (i = 1, 2, 3 \cdots n) \\ Z_i &= E_i + E_j \quad (i = 1, 2, 3 \cdots n) \\ Y_i &= E_i - E'_j \quad (i = 1, 2, 3 \cdots n) \end{aligned} \tag{3}$$

The calculation results are given in Table 2.

(6) According to the results of the above table, using Matlab software, construct the influence causality diagram, where the horizontal coordinate is the centrality degree, and the vertical coordinate is the cause degree, as shown in Fig. 2.

Multi-level recursive structure modeling. The overall impact matrix F is calculated by substituting the combined impact matrix T into Eq. (4) by further examining the hierarchical and logical relationship between the impact factors. The calculation formula can be expressed in Eq. (4):

$$F = I + T = \left[f_{\mathrm{ij}}\right]_{n \times n} \tag{4}$$

Table 2 Results of each factor calculation

Influencing factors	Influence degree	Influenced degree	Central degree	Cause degree	Attributes
Intelligent design	1.569	0.739	2.308	−0.831	Result
Intelligent production	1.588	0.492	2.08	−1.096	Result
Smart construction site	1.775	0.365	2.14	−1.411	Result
Artificial intelligence for IT operations	1.914	0.188	2.11	−1.735	Result
Enterprises strategy	0.858	0.903	1.791	0.015	
Multi-disciplinary collaboration efficiency	1.742	0.536	2.279	−1.206	Result
Participant interests	0.362	0.757	1.142	0.371	
Talent quality	0.703	1.240	2.005	0.599	
Information management level	1.697	1.030	2.728	−0.667	Result
Technical advantages	0.798	1.244	2.042	0.446	
Technical costs	0.740	1.350	2.131	0.57	
Information platform	0.913	1.190	2.103	0.277	
Intelligent technology adoption	1.440	1.711	3.151	0.27	
Technical standards system	0.199	1.666	1.865	1.467	
Policies and regulations	0.030	1.965	1.995	1.935	
System integration	0.987	1.187	2.174	0.2	
Resource readiness	1.483	1.443	2.925	−0.04	Result
Competitive pressures	0.811	0.912	1.762	0.141	
Technology and innovation investment	0.404	1.098	1.502	0.693	

By introducing a characteristic threshold λ, the overall influence matrix F is refined and simplified.

λ is taken to directly influence the logical relationships of the corresponding influence factors. λ can be taken in two ways: by expert experience, or by calculation based on statistical distributions. In order to make the results more objective and scientific, the second way is chosen here, as given in Eq. (5):

$$\lambda = \alpha + \beta \tag{5}$$

where α represents the mean of all elements in the combined impact matrix T; β represents the standard deviation of the mean of all elements in the matrix T.

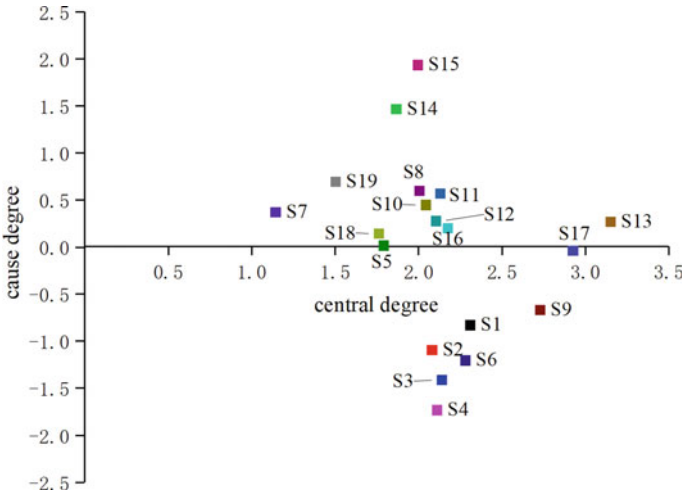

Fig. 2 Influence factor cause result graph

Using Matlab software to solve, the threshold λ is found as follows: $\alpha = 0.0551$, $\beta = 0.0447$, $\lambda = 0.0998$. Based on the following Eq. (6), the onerous factors are crossed out.

$$m_{\mathrm{ij}} = \begin{matrix} 1, f_{\mathrm{ij}} \geq \lambda \\ 0, f_{\mathrm{ij}} \prec \lambda \end{matrix} \tag{6}$$

where 1 indicates a direct effect between the two factors and 0 indicates no direct effect.

The reachable matrix K is given in Table 3.

Reducing the reachability matrix and unfolding the hierarchical division. The reachable set R_i, the prior set S_i, and the common set $C_i = R_i \cap S_i$ are obtained according to the reachable matrix K, and all the factors are divided into different levels.

The four calculated metrics factors and the hierarchical processing results are combined to build a multi-layer recursive structure model, as shown in Fig. 3.

Hierarchical analysis. According to the Fig. 3, the above 19 influencing factors are divided into a complex system with a five-level recursive structure. Based on the logical relevance of the layers of influencing factors, the model structure is further analyzed on three levels: surface, middle, and deep.

(1) Intelligent design, intelligent production, smart construction sites, and AIops in the L_1 and L_2 layers are surface-level direct influencing factors that are driven by the influencing factors in the lower layers and do not actively dominate other factors.

Table 3 Reachability matrix *K*

Indicates	S_1	S_2	S_3	S_4	S_5	S_6	S_7	S_8	S_9	S_{10}	S_{11}	S_{12}	S_{13}	S_{14}	S_{15}	S_{16}	S_{17}	S_{18}	S_{19}
S_1	1																		
S_2		1																	
S_3			1																
S_4				1															
S_5					1								1						
S_6						1			1										
S_7							1												
S_8	1	1	1	1				1	1								1		
S_9	1	1	1	1					1				1						
S_{10}	1	1	1	1						1									
S_{11}						1					1		1			1	1		
S_{12}	1	1	1	1		1			1			1				1	1		
S_{13}	1	1	1	1		1			1	1			1			1	1	1	
S_{14}	1	1	1	1		1			1				1	1		1	1		
S_{15}	1	1	1	1	1	1	1		1		1		1		1		1	1	
S_{16}	1	1	1	1		1						1	1			1			
S_{17}	1	1	1	1		1			1				1				1	1	
S_{18}																	1	1	1
S_{19}					1														1

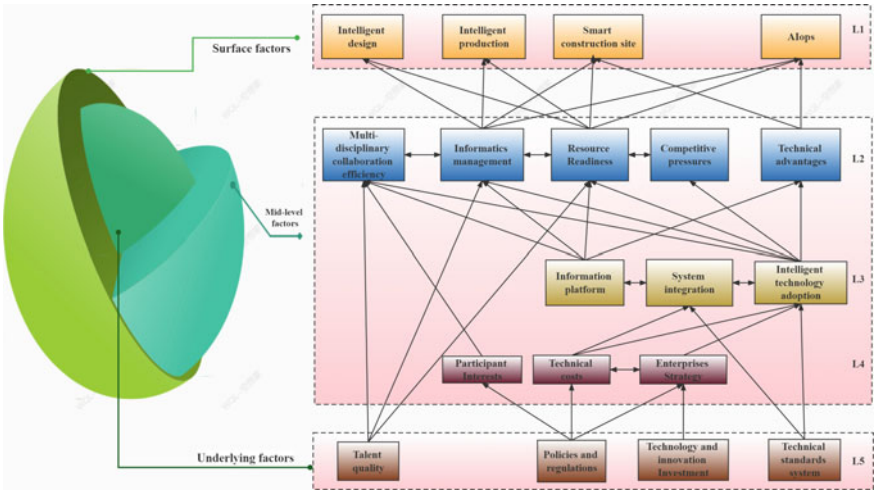

Fig. 3 ISM hierarchical structure model diagram

The loops in the model represent strong linking relationships, taking a loop existing in the L_3 layer as an example. The construction of the information platform provides a platform for sharing, processing, and applying multiple heterogeneous data and site information resources, which is beneficial to further realizing the coordination of data and information in the intelligent construction system, thereby increasing the level of integration of the system. By integrating the systems, the data from each subsystem is incorporated into the platform in a seamless manner. In other words, the construction of the information platform is closely linked to the degree of integration of the system.

(2) Factors such as multi-disciplinary collaboration and information management level are indirect causes that affect the application of intelligent construction at the L_2, L_3, and L_4 levels of the model.

The influencing factors in the lower layer are influenced upwards according to the way shown in the figure, such as the construction of the information platform, which provides an exchange platform for government supervision, tracking, and management, as well as visualization and digitization of engineering product information by the owner, along with the integration of cost, schedule, and quality control objectives, thus enhancing the efficiency of the collaboration between various professions. This factor also affects the level of information technology management, and the development of the information platform provides a resource reserve for data processing and information resources.

(3) Policies and regulations, talent quality, technology and innovation investment, and technical standards are deep influencing factors, which are at the bottom of the model and affect the surface impression factors by influencing the middle

influencing factors. They have a fundamental impact on the application of intelligent construction.

4 Case Application

The construction of the Tiantai mountain tunnel (subsequently referred to as Project A) was carried out in accordance with the design requirements for intelligent and informative construction. Therefore, adjustment factors were identified based on the causal links in the model where the key influencing factors were located. In the actual construction of the Tiantai mountain tunnel, the site space was limited, which made layout and construction organization challenging. Taking advantage of the visualization advantages offered by BIM technology will result in a variety of construction solutions for dynamic simulation and optimization, as well as the use of radio frequency identification technology for component production, identification and tracking, etc. Additionally, Enterprise Resource Planning (ERP) is used to manage the storage logistics of components. The application of all of these technologies together requires interactive data conversion, which involves developing an independent design and production management information system that integrates BIM, RFID, and ERP integration. Establishing an information platform for information flow, determining which level of intelligent construction applications is appropriate for a project [18]. Not only had the site's use rate gone up a lot, but the way it was set up had also been made more sensible as shown in Fig. 4.

Fig. 4 BIM-based construction site layout for the Tiantai mountain tunnel

5 Conclusion

Although prefabricated buildings are evolving toward intelligence, their construction has not yet formed a system for the application of intelligent construction, and the ambiguity of the application has greatly limited its ability and potential. The recommendations based on the model results are as follows:

(1) Implement new policies and regulations, as well as technical standards, and build a strong industrial chain between the government, industry, and enterprises, utilizing government incentives, subsidies, and penalties. The objective is to provide a guiding effect on enterprise organizational strategies related to the implementation of intelligent construction in prefabricated buildings as well as to reduce technical costs associated with equipment procurement, maintenance, and upgrading, so that intelligent construction technology can be adopted more effectively. The coordination of all parties involved in the construction process will enhance organization synergy and information exchange.
(2) It is beneficial to establish an intelligent construction standard system and technical evaluation mechanism, build an information platform, develop relevant standards and technical frameworks to facilitate the delivery and application of various types of engineering data, forming a more mature integrated system for the whole process of construction to link component design, manufacturing, transportation, assembly, and quality control in tandem.
(3) It is important to increase the amount of investment in scientific and technological innovation and improve the quality of personnel training. The successful technological innovation will cause an exponential growth in the number and scale of individuals applying intelligent construction. The intelligent construction innovation network presents point innovation and faceted diffusion, which in turn forms the overall innovative talent quality of the whole industry. The talent gift is closely related to the development of the industry, so focusing on engineering software, engineering machinery and other technical and equipment issues, ensuring that the knowledge update of talent training can keep pace with the times, both to keep up with and lead the development of intelligent construction applications for assembly buildings.

Funding National Natural Science Foundation of China (No.51874189).

References

1. Jiang ZL, Zang GG (2021) Research on full-process management of bridge engineering assembly intelligent construction. Highway Eng 46(04):39–45
2. Ma WB, Wang ZW (2022) Research on prefabrication and assembly of railway tunnels excavated using drilling-and-blasting and prospects of intelligent construction. Tunnel Construct 42(7):1119

3. Liu FX (2019) Prospects for intelligent construction equipment technology innovation and collaborative construction management of railway tunnel. Tunnel Construct 39(04):545–555
4. Liu ZX, Liu ZS, Sun JJ, Du XL (2021) Intelligent construction methods and model experiments based on digital twins. J Build Struct 42(06):26–36
5. Kong L, Ma B (2020) Intelligent manufacturing model of construction industry based on Internet of Things technology. Int J Adv Manuf Technol 107:1025–1037
6. Yi J (2021) Intelligent building construction management based on BIM digital twin computational intelligence and neuroscience 11
7. Bao YQ, Li H (2019) Artificial Intelligence for civil engineering. China Civil Eng J 52(05):1–11
8. Fan QX, Lin P, Wei PC, Ning ZG, Li G (2021) Closed-loop control theory of intelligent construction. J Tsinghua Univ (Sci Technol) 61(07):660–670
9. Jia MS, Xu YQ, Zhao LM, Huang M (2020) Analysis of factors affecting the construction of smart site based on ISM+AHP. Construct Econ 41(03):42–48
10. Sun XL, Sun YC, Xue XL, Wang L, Liu C (2022) Research on interactive relationships between collaborative innovation stakeholders of intelligent construction technology. China Civil Eng J l:1–10
11. Lee S, Kwon SA (2014) Conceptual framework of prefabricated building construction management system using reverse engineering, BIM, and WSN. Adv Construct Build Technol Soc 37
12. Wang ZH (2002) Continual improvement of the engineering quality—a creative model of management for the engineering quality. J Shandong Univ Sci Technol (Natl Sci) 03:58–62
13. Irani Z, Kamal MM (2014) Intelligent systems research in the construction industry. Expert Syst Appl 41(4–1):934–950
14. Zhang H, Ma L, Tian SH, Guo HL (2022) Critical construction scenarios, elements and development paths for intelligent construction platforms. J Tsinghua Univ (Sci Technol) 62(02):215–220
15. Wang HW, Zhong BT, Li YK, Zeng SX, Yuan JF (2022) Management theory and method of Intelligent construction, operation and maintenance for large-scale complex projects. J Manage Sci 35(01):55–59
16. Liu K, Liu YF, Zhou HM, Kou YY, Ji Q, Li D (2020) Evolutionary game and numerical simulation of participants' collaborative behavior in integrated project delivery project. Alexandria Eng J 60(1):373–385
17. Rajput S, Singh SP (2019) Identifying industry 4.0 IoT enablers by integrated PCA-ISM-DEMATEL approach. Manage Decis 57(08):1784–1817
18. Zhang JB (2021) Research on BIM parametric modeling and optimization of constructions schedule management for highway tunnel. MASTER thesis, Shandong university of science and technology

Application of Augmented Reality for Checking Scaffolding Installation in Maintenance Process

Vachara Peansupap, Aye Chann Myint, and Kriengsak Panuwatwanich

Abstract Since special maintenance of the building components requires the thoughtful planning of temporary structures, maintenance technicians have to survey on-site to select the suitable temporary structure for the working environment before conducting the maintenance process. In the current practice, the adoption of the traditional method for checking the safety of scaffolding brings workload and takes time to decide on the appropriate scaffolding. This paper aims to develop an integrated approach for selecting the appropriate scaffolding and assisting in the inspection of scaffolding. It will benefit the user in preparing and planning equipment for maintenance tasks and ensuring safety by giving the guideline to check after installation. In this paper, an augmented reality (AR) system was developed to choose suitable scaffolding based on a work environment and provide a safety inspection checklist of scaffolding. A case study of the scaffolding selection and reporting of temporary structure preparation for maintenance tasks will be conducted in this research. The system will be tested in a real site environment to evaluate the performance and feasibility of the proposed system. The findings from this research will provide how the AR system enables the maintenance profession to make better decisions for the selection of scaffolding and easier safety inspection of scaffolding in the workspace which will ensure the safety of maintenance personnel and reduce the hazards in the working space.

Keywords Augmented reality · Scaffolding installation · Safety inspection · Work environment

V. Peansupap (✉) · A. C. Myint
Department of Civil Engineering, Faculty of Engineering, Chulalongkorn University, Bangkok 10330, Thailand
e-mail: vachara.p@chula.ac.th

A. C. Myint
e-mail: 6272107821@student.chula.ac.th

K. Panuwatwanich
School of Civil Engineering and Technology, Sirindhorn International Institute of Technology, Thammasat University, Bangkok 12120, Thailand
e-mail: kriengsak@siit.tu.ac.th

T. Kang (ed.), *Proceedings of 5th International Conference on Civil Engineering and Architecture*, Lecture Notes in Civil Engineering 369,
https://doi.org/10.1007/978-981-99-4049-3_57

1 Introduction

In recent year, augmented reality is widely used in construction industry. Many researchers believe that bringing the automation in construction can gives the great benefit to the engineering professionals [1]. Augmented reality (AR) is a superimposed technology that overlays digital information into the real environment in real time [2].

Through the assistance of augmented reality, engineering professions and technicians get the accurate information of the process and procedures of maintenance task in order to maintain, repair, replacement, and fix the issues at the site [3].

Since most of the labor force at the sites are working at height, using dangerous equipment, heavy machine and components, maintenance, and construction activities are high-risk activities with specific hazards and risks [4]. It is found that falling from the scaffolding is one of the major accidents leading to fatal accidents and injuries [5]. Olanrewaju, Law, and Preece [6] stated that scaffold accidents are one of the major causes of injury and death on Malaysian construction sites. According to the analysis of 1,630,452 construction accidents in Spain, López et al. [7] presented that scaffold and ladders accidents occurred at 9.4% of total accidents which will serve the highest number of fatal injuries.

Scaffolding is a temporary structure that supports the worker to get access for maintenance or servicing of the components at the existing building [8]. Proper scaffolding is essential to conduct maintenance activities safely and successfully without any hazard. 60% of maintenance professionals have experienced scaffolding accidents during maintenance works [9]. The major causes of scaffolding accidents are people falling, incorrect operating procedures, environmental conditions, improper construction, or work rules and falling materials due to equipment failure [9].

Unsafe environmental conditions in the workspace and improper selection of equipment will hazard to the personnel carrying out the work tasks [10]. Hence, it is noted that the selection of appropriate equipment for maintenance is crucial factor that impacts labor productivity, construction efficiency, and safety of the personnel.

To fulfill the gap, this search will contribute the selection of suitable temporary structure and preparation of temporary structure installation by using augmented reality for maintenance. Moreover, there is still lack of adoption of AR approach for scaffolding installation. Therefore, AR for checking space accessibility is proposed in this research. Therefore, this research will focus on developing integrated approach by using augmented reality in order to help the maintenance professionals.

2 AR-Based System Design and Development

The system is designed to help the maintenance professions in selecting the appropriate scaffolding for maintenance and ensuring the safe installation of the temporary structure during maintenance. The first module is designed to support the selection

of suitable equipment for maintenance and to check the working environment for the installation of the scaffolding. The system allows the user to select the scaffolding which is appropriate for the existing working environment such as space and height. The output of this module will help the maintenance technician in decision-making in the selection of the appropriate scaffolding for maintenance and checking the working environment for scaffolding installation.

The second module was designed to extend module 1 from the selection of an appropriate temporary structure to support the preparation of selected temporary structures for building maintenance and ensure the safety of scaffolding installation. The second module is divided into two parts 2.1 and 2.2 as described in Fig. 1. It reports for temporary structure preparation and records for the safe installation of temporary structure. For module 2.1, a set of data from the model will help to prepare the required quantity set of a temporary structure for the maintenance of building components. As shown in Fig. 2, module 2.1 provides the required set of data that can be utilized for reporting the preparation of the selected temporary structure and aims to reduce the re-input data by utilizing the provided data from the system.

Regarding module 2.2, the inspection checklist for temporary structures showed the general guideline to ensure that the user must check the critical point of scaffolding installation before maintenance. The safety checklist record will help to analyze the repetition and frequency of installation problems for future improvement. The output

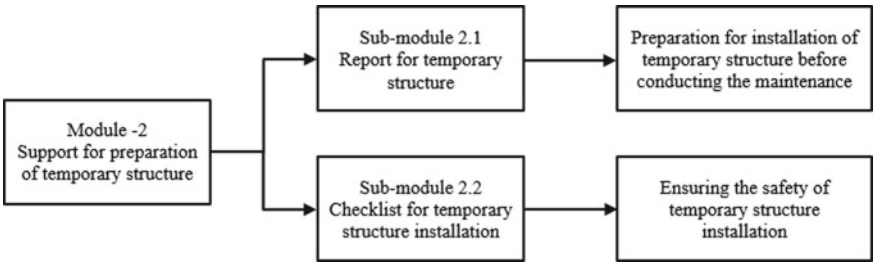

Fig. 1 Framework of second module of the system

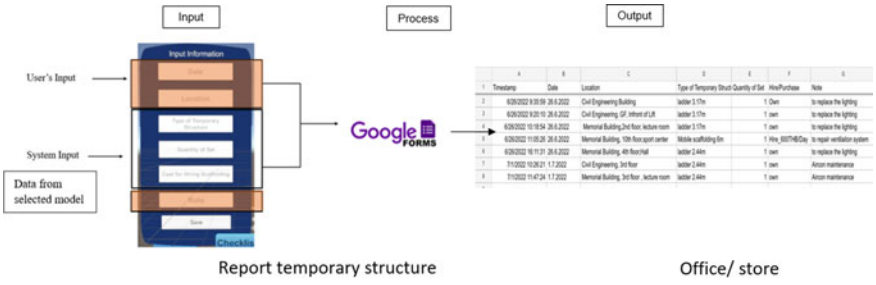

Fig. 2 Conceptual model of module 2.1

allows the user to evaluate the problems and defects in the installation. The instruction guideline for checking the safety of scaffolding is shown in Fig. 3.

For system development, the architecture of the system as shown in Fig. 4 includes three main processes which are input, process, and output. The input data are designed into two parts, which are the space requirement module for module 1 and the scaffolding module for module 2. The imported data are processed in Unity, and AR core is used to detect the ground plane which will support to place the multiple object placement on the ground. Visual studio programming is used for system development. Mobile application is generated as output from Unity in which user interface assists to communicate between the users and the proposed system. It includes the selection of scaffolding, checklist, multiple object placement, and reporting.

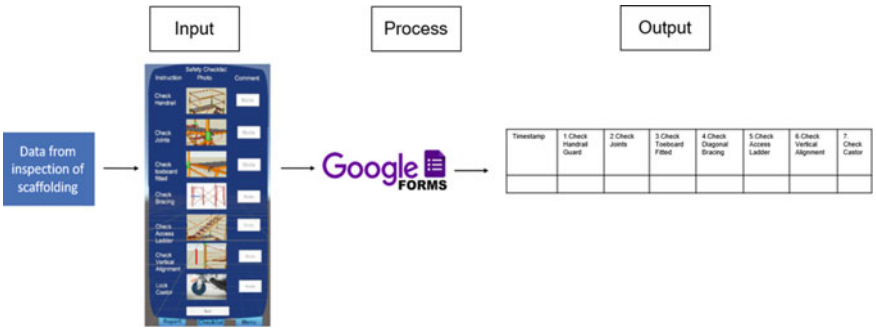

Fig. 3 Conceptual model of module 2.2

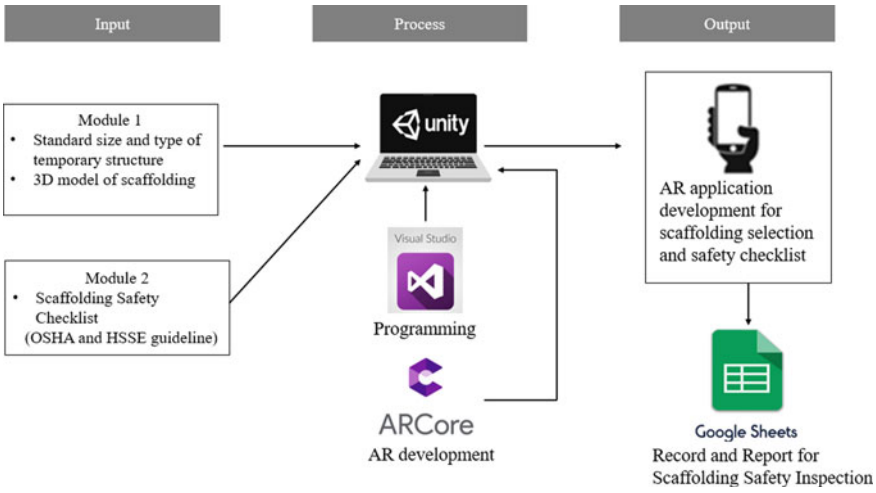

Fig. 4 Architecture of the system

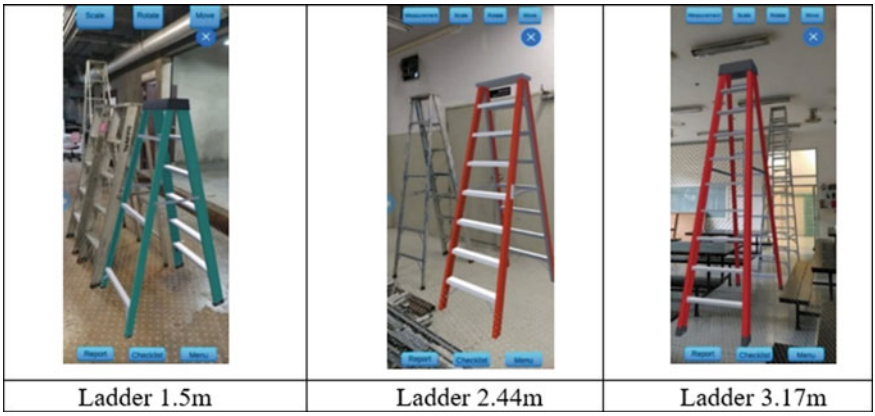

Fig. 5 Verification of height comparing with the actual ladder

3 Verification of the System

The prototype of the system was tested in both laboratory and real-world environments to verify the accuracy and feasibility of the system for selection of suitable equipment and reporting for preparation of temporary structure installation. Firstly, the size and height of virtual 3D objects were verified by comparing with the actual temporary structure since the position and orientation of the camera, movement, and distance of the user can affect the performance of the application. The ladders such as 1.5 m height, 2.44 m height, and 3.17 m height were tested in the lab and compared to the height of the actual ladders. Figure 5 presented the comparison between virtual and actual objects for verification of the system. As a result, it was found that the height and size of virtual ladders were close to the actual ones. Therefore, the external validation in the actual working environment will be conducted.

4 Case Studies

4.1 Case Study 1 Selection of Appropriate Temporary Structure for Replacement of Lighting System

The first module of the system was tested to evaluate the space whether it is enough space to install the temporary structure. Therefore, a set of the temporary structure was trialed to select the appropriate type of temporary structure according to the working space. To test the system, the student lecture room at Chulalongkorn University which has limited space for setting up the ladder was selected. Firstly, the virtual 3D object of 2.44-m ladder was selected and placed in the available space

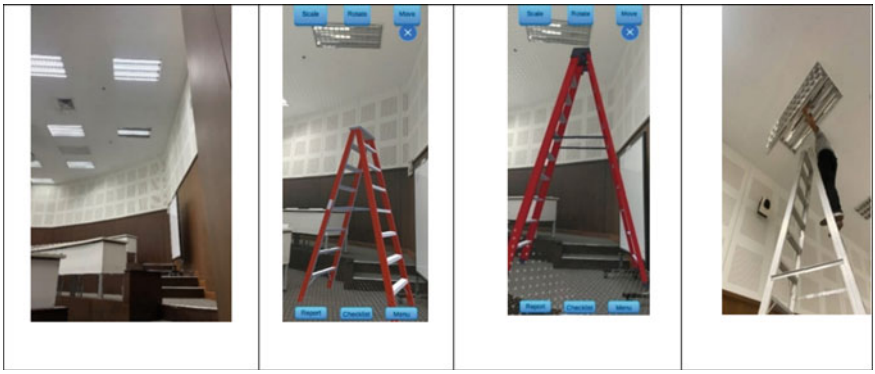

Fig. 6 Section of a temporary structure for replacement of light in the lecture room

where it is needed to install the ladder for the replacement of the lighting as shown in Fig. 6. It is found that the first trail of the ladder was inappropriate as the height of the ladder did not reach to replace the lighting. The second time was trailed to find out the ladder which is suitable with available space and height for maintenance of the lighting in the student lecture room. Thus, it can be concluded that the system can support decision-making for the selection of appropriate temporary structures according to space and height requirements.

4.2 Case Study 2 Selection of Appropriate Temporary Structure for Maintenance of Air Ventilation System

The second case study was conducted sports center at Chulalongkorn centennial memorial building for maintenance of the air ventilation system. Since the ventilation system was installed at the two-story height of the building, there was an unavailable temporary structure that could reach the height to perform the maintenance. Firstly, the technician selected the 4 m height of mobile scaffolding and visualized it in the working space. It was found that the 4 m height of mobile scaffolding was not enough height to reach the component. Then, the second trial was conducted. The user selected the 6 m mobile scaffolding and placed it in the working space as shown in Fig. 7. It was revealed that the 6 m height of mobile scaffolding could reach the air ventilation system and is appropriate for maintenance. Thus, the second type of mobile scaffolding was selected.

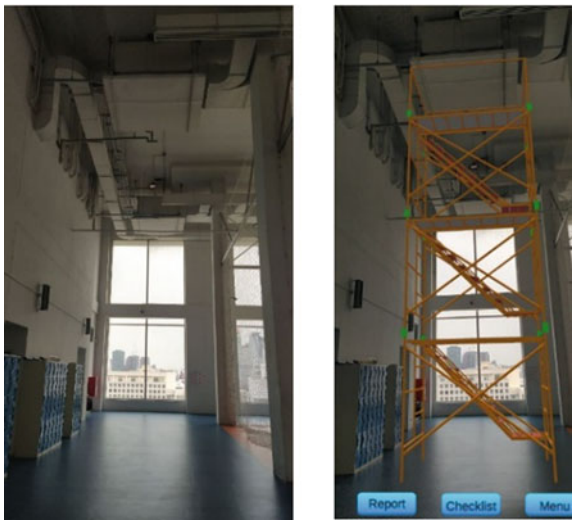

Fig. 7 Selection of temporary structure for maintenance of ventilation system at sport center, Chulalongkorn centennial memorial building

4.3 Case Study 3 Report for the Preparation of Temporary Structure

The second module of the system aims to support module 1 selection of appropriate scaffolding. The system showed the data of selected temporary structure in the input field of reporting panel after the user chose the suitable temporary structure. The system was tested according to the case studies of module 1 and recorded the maintenance task to support the preparation of a temporary structure after selecting the appropriate type. Before conducting the maintenance task, technicians surveyed the on-site where the light was broken. After that, the technician selected the appropriate type of temporary structure for maintenance and reported the information to arrange the required type of temporary structure for maintenance.

From the analysis of the report, as shown in Table 1, the technicians require a 2.44 and 3.17 m ladder for maintenance of lighting, whereas the 6 m mobile scaffolding needs to hire for maintenance of the ventilation system. Therefore, it can be concluded that the system can help the technician to arrange and plan for the preparation of the required temporary structure in the maintenance process.

5 System Validation

The questionnaire survey was conducted to evaluate the system. The centennial memorial building and civil engineering building located at Chulalongkorn University were selected for the projects to test the system. The five maintenance technicians who participated in testing the prototype system for the case studies were recruited to

Table 1 Report for preparation of required temporary structure for maintenance

Timestamp	Location	Type of temporary structure	Qty	Hire/Purchase	Note
6/26/2022 9:35	CE Blg	Ladder 3.17 m	1	Own	To replace the lighting
6/26/2022 9:20	CE, GF, Lift	Ladder 3.17 m	1	Own	To replace the lighting
6/26/2022 10:18	M Building, 2ndF, lecture room	Ladder 3.17 m	1	Own	To replace the lighting
6/26/2022 16:11	M Building, 4F, Hall	Ladder 2.44 m	1	Own	To replace the lighting
7/1/2022 10:26	CE, 3rd floor	Ladder 2.44 m	1	Own	Aircon maintenance
7/1/2022 11:47	M Building, 3F, lecture room	Ladder 2.44 m	1	Own	Aircon maintenance

interview and answer the questionnaires. The ten professionals who have experience in building maintenance were selected to take part in the questionnaire survey.

To validate the system, the respondents were asked to rate the system on 5 scales by using Likert's scale method. The evaluation results for the proposed system are presented in Table 2. As the evaluation of the questionnaire, the experimental results from users' satisfaction and comparison of the performance of the system were between 3.5 and 4. According to the Likert's scale criteria, it is proved that the system is feasible to use in selection of suitable temporary structure for maintenance.

Table 2 Results from the evaluation of questionnaires by respondents

No.	Questionnaires	Average scores
1	The system is easy to use in the selection of temporary structures for maintenance	4.00
2	The system helps to choose the appropriate type of temporary structure for maintenance tasks	3.93
3	The system helps to check the obstructions in the working space for the installation of a temporary structure	4.07
4	The system helps in quantity take-off for the required set of temporary structures to conduct maintenance tasks	3.73
5	The checklist of the system helps in checking the safety of temporary structure installation	3.87
6	The system helps in quantity take-off for the required set of the temporary structure better than the traditional method	3.60
7	The checklist of the system helps in checking the safety of temporary structure installation better than traditional method	3.93

6 Conclusion

This research developed the AR prototype system that can help in decision-making for selection of suitable temporary structure according to the working environment and supporting the preparation of temporary structure for maintenance of the building. Moreover, the system provides the safety checklist and reporting system to ensure the safe installation of temporary structure. To validate the accuracy of the system, the internal validation and external validation were conducted. The overall result from the experiment indicated that AR system could support the maintenance personnel in selecting appropriate temporary structures, preparing temporary structures, and ensuring the safe installation of a temporary structure for maintenance.

However, limitation was found during the testing of the prototype system. Due to the adoption of markerless augmented reality system, the lighting of the environment and the texture of the ground plane impacted to the tracking of the system. Besides, the floating of the objects was found during testing the system. It is noted that the camera orientation can affect the size of the virtual object.

Therefore, the selection of suitable temporary structure and reporting system should be improved in the future. The tracking of the AR system needs to integrate so that the overlaying and floating of the object can be avoided. In this research, the safety checklist of the second module has not tested due to the lack of available of mobile scaffolding in the current project. Thus, testing of safety checklist for installation of temporary structure should be considered in the future research.

References

1. Kangari R, Yoshida T (1990) Automation in construction. Robot Syst 6(4):327–335
2. Patil CB (2016) Overlaying virtual object into real world by using augmented reality. Int Res J Eng Technol 3(3):153–156
3. Palmarini R, Erkoyuncu JA, Roy R (2017) An innovative process to select augmented reality (AR) technology for maintenance. Procedia Cirp 59:23–28
4. Hoła B, Nowobilski T, Szer I, Szer J (2017) Identification of factors affecting the accident rate in the construction industry. Procedia Eng 208:35–42
5. Kim K, Cho Y, Zhang S (2016) Integrating work sequences and temporary structures into safety planning: automated scaffolding-related safety hazard identification and prevention in BIM. Autom Construct 70:128–142
6. Olanrewaju A, Law X, Preece C (2021) Evaluation of scaffold accidents during building maintenance works. In: Proceedings of international structural engineering and construction, 8. https://doi.org/10.14455/ISEC.2021.8(1). CSA-03
7. López MAC et al (2008) Construction industry accidents in Spain. J Safety Res 39(5):497–507
8. Adhikari CS, Singh P, Kumar V, Yadav S, Hussain U, Khan MA (2019) Designing and detailing of scaffoldings. Int J Adv Res Ideas Innovations Technol 5(3):2045–2052
9. Causes of scaffolding accidents. Retrieved from https://www.linkedin.com/pulse/causes-scaffolding-accidents-natverlal-t-jadav/
10. Choudhry RM, Fang D (2008) Why operatives engage in unsafe work behavior: investigating factors on construction sites. Safety Sci 46(4):566–584. https://doi.org/10.1016/j.ssci.2007.06.027

Bridge Engineering and Technology

Survey on the State of Deterioration of Highway Bridge Concrete Slabs in a Snowy Region and Countermeasures Based on the Cathodic Protection Method

Runa Kawajiri, Hoang Minh Ngo Le, Keita Hashimoto, Minh Tuan Ha, Saiji Fukada, Toshiyuki Aoyama, and Kazuyuki Torii

Abstract The replacement of bridge RC slabs has marked the start of expressway renewal work. On the snowy Hokuriku expressway, the deterioration caused by the combination of alkali–silica reaction (ASR) with steel corrosion is accelerated by the application of de-icing salts. Therefore, it is imperative to identify and determine the leading cause of deterioration of each bridge when planning maintenance. In this study, a survey on the amount of chloride penetration into concrete, and the degree of ASR of concrete was investigated using cores taken from RC slabs in a viaduct in the Kanazawa City area. Based on this survey, a new cathodic protection method was applied, and titanium wire sensors monitored its effectiveness. Finally, it was determined that the new cathodic protection method effectively controlled

R. Kawajiri (✉) · H. M. N. Le · K. Hashimoto
Graduate School of Natural Science and Technology, Kanazawa University, Ishikawa, Japan
e-mail: r.kawajiri@stu.kanazawa-u.ac.jp

H. M. N. Le
e-mail: minhngo97@stu.kanazawa-u.ac.jp

K. Hashimoto
e-mail: keitahashimoto@stu.kanazawa-u.ac.jp

M. T. Ha
HUTECH University, Ho Chi Minh, Vietnam
e-mail: hm.tuan@hutech.edu.vn

S. Fukada
Faculty of Geosciences and Civil Engineering, Kanazawa University, Ishikawa, Japan
e-mail: saiji@se.kanazawa-u.ac.jp

T. Aoyama
P.S. Mitsubishi Construction Co., Ltd, Tokyo, Japan
e-mail: t-aoyama@psmic.co.jp

K. Torii
Kanazawa University, Ishikawa, Japan
e-mail: torii@se.kanazawa-u.ac.jp

T. Kang (ed.), *Proceedings of 5th International Conference on Civil Engineering and Architecture*, Lecture Notes in Civil Engineering 369,
https://doi.org/10.1007/978-981-99-4049-3_58

the corrosion of steel bars of reinforced concrete slabs in a saline environment with de-icing salts.

Keywords RC slabs for highways · Steel corrosion by salt damage · Alkali–silica reaction · A new type of cathodic protection method · Monitoring

1 Introduction

Various types of deterioration, such as the sedimentation and depression of reinforced concrete deck slabs (RC slabs), have been reported throughout Japan [1, 2]. Local deterioration in road surfaces and bridge piers has become a safety concern. The alkali–silica reaction (ASR), salt damage due to anti-freezing agents, and frost damage have caused the premature deterioration of many bridges in the Hokuriku region: a snowy coastal area in Northwestern Japan [3, 4]. On the Hokuriku Expressway, salt damage caused by anti-freezing agents and deterioration due to the ASR are more severe than those in other areas. Many anti-freezing agents have been sprayed during the winter, with a cumulative mass per unit road length of 1,000 tons/km. The number of de-icing salts used has increased yearly since studded tires were banned in 1989. The current elevated line in the Hokuriku Expressway, which has been in service for 45 years, is shown in Fig. 1. Conventionally, the potholes on the road surface were repaired using the patching method. However, deterioration continues as the leading cause of premature deterioration has not yet been identified. The second large-scale repair and renewal plan for the expressway is currently being formulated. This study investigates an economical and rational countermeasure that can protect the structure from regional deterioration factors under a budget constraint.

There are only a few studies that have identified the causes of RC slab deterioration, but most of these studies do not correctly distinguish the ASR from frost

Fig. 1 Potholes and cracks on the road surface

damage. On the Hokuriku Expressway, constructed in a delta region (at around 800 m above sea level), frost damage is not detected. In addition, fatigue is not considered a leading cause of deterioration owing to the small traffic volume. For these reasons, the combined deterioration phenomenon due to salt damage and the ASR is suspected to be the main cause of deterioration. The ASR, as first reported in the 1940s, significantly affects the durability of concrete structures [5]. It is a chemical reaction with a multi-stage process entailing reactive silica in aggregates and alkalis in cementitious materials. The product of this reaction is an alkali–silica gel (ASR gel) [6–8]. The ASR gel is not harmful to concrete, but the increase in its volume after absorbing moisture from the surroundings exerts significant pressure on the materials. When the stress induced by the ASR gel exceeds the tensile strength of concrete, spalling, cracking, and loss of strength in the concrete and rebar will occur. The cause–effect relationship between the ASR gel expansion and the reduction in the mechanical properties of concrete has been investigated in many studies [9, 10].

Regarding the ASR in the Hokuriku region, an aggregate of volcanic rocks (andesite, rhyolite, and welded tuff) has been used in concrete for many years. Cracks due to the ASR are found in bridge piers and bridge abutments throughout the region [11]. A close observation of the cross sections of a removed concrete deck from the Hokuriku Expressway is shown in Fig. 2. Many horizontal cracks due to the ASR appeared inside the concrete deck, along with the corrosion of the upper and lower reinforcing bars. As shown in Fig. 3a, the internal cracking of the concrete progressed remarkably owing to the ASR. However, internal observations at the microscopic level are essential for identifying the ASR reactivity of sand particles in the early stages of the ASR (see Fig. 3b).

Notably, the sodium chloride (NaCl) in anti-freezing agents promotes ASR by enabling the permeation of alkaline components [12]. Salt damage by anti-freezing agents is a phenomenon in which sodium chloride permeates into the concrete interior through cracks in the road surface and causes corrosion within the reinforcing bars. Previous studies have investigated countermeasures against salt damage via many different approaches [13–17]. In 2020, Ha et al. confirmed salt damage on the Hokuriku Expressway [18]. A deck slab on the Hokuriku Expressway is considered to have changed from corrosion expansion to the developmental stage. With the primary purpose of preventing steel corrosion in RC decks due to anti-freezing agents, and as a preventive maintenance measure in the large-scale renewal of bridges, a galvanic-anode-based steel corrosion mitigation method was applied to an elevated line on the Hokuriku Expressway [18]. This was the first time that an easily detachable sacrificial anode was applied to the lower surface of the RC decks of a bridge in this expressway. The monitoring of the steel corrosion of the RC decks has continued since 2018.

In this study, with the target structure being a highway bridge in the Hokuriku region, the amount of salt permeation and deterioration owing to the ASR were confirmed by collecting the core from the RC deck of the target bridge. Subsequently, the leading cause of deterioration was clarified based on the experimental results. Finally, the authors examined the workability of the galvanic-anode-based steel corrosion mitigation method.

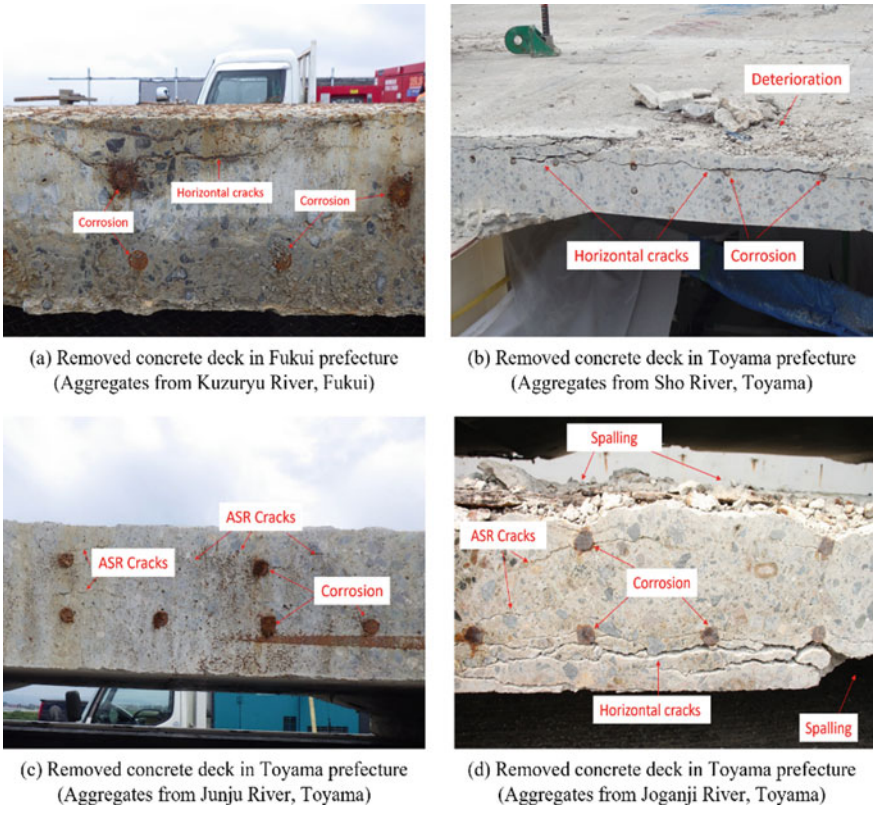

(a) Removed concrete deck in Fukui prefecture (Aggregates from Kuzuryu River, Fukui)

(b) Removed concrete deck in Toyama prefecture (Aggregates from Sho River, Toyama)

(c) Removed concrete deck in Toyama prefecture (Aggregates from Junju River, Toyama)

(d) Removed concrete deck in Toyama prefecture (Aggregates from Joganji River, Toyama)

Fig. 2 Cross sections of removed concrete decks from the Hokuriku Expressway

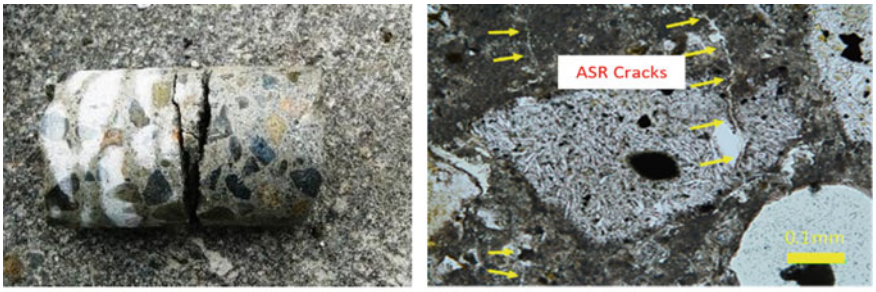

(a) Horizontal cracks in the core collected from the RC deck

(b) Collected core surface under polarizing microscope (Andesite aggregate from Kuzuryu River, Fukui)

Fig. 3 Concrete core observation results

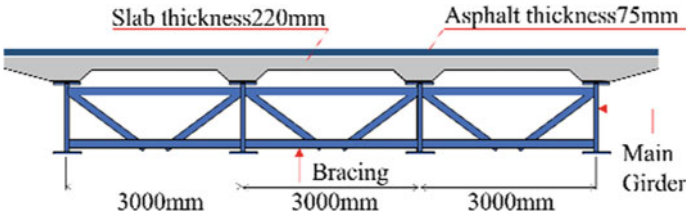

Fig. 4 Cross section of the target bridge

Table 1 Concrete mix design

Water W (%)	Cement C (kg)	W/C (%)	Coarse aggregates G (kg/m^3)	Fine aggregates S (kg/m^3)	Admixture (kg/m^3)
154	300	51.3	1167	701	0.75

2 Outline of the Target Bridge and the Experiment Setup

2.1 Outline of the Target Bridge

The target bridge is a highway bridge located in Kanazawa City. It has been in service since 1978 and passes through an urban area with an extension of approximately 8.6 km and is 3.5 km away from the coast. This highway bridge is a part of the elevated line of the Hokuriku Expressway. The average daily traffic volume is 20,000 vehicles, and the mixing rate of large vehicles is nearly 23%.

The composite bridge has a reinforced concrete deck slab (total width, slab thickness, and asphalt thickness of 11.45, 220, and 75 mm, respectively) supported by four Posten T girders as the main girders (Fig. 4). The cover concrete of the deck slab is 30 mm. The design strength of the concrete is 24 N/mm^2. Table 1 presents the concrete mix design. Regarding the steel material, D19 reinforcing bars are arranged at 125 mm intervals on the lower side of the deck in the center of the span and at 250 mm intervals on the upper side of the deck.

2.2 Overview of the Experiment Setup

Several cylindrical concrete specimens (55 mm in diameter and 110 mm in height) were sampled from both the upper and lower sides of the target bridge deck slab. The sampling positions are shown in Fig. 5. These specimens were subjected to compressive strength and static elastic modulus tests (JIS A 1108) [19], accelerated mortar bar tests (ASTM C 1260) [20], and concrete chloride-content tests.

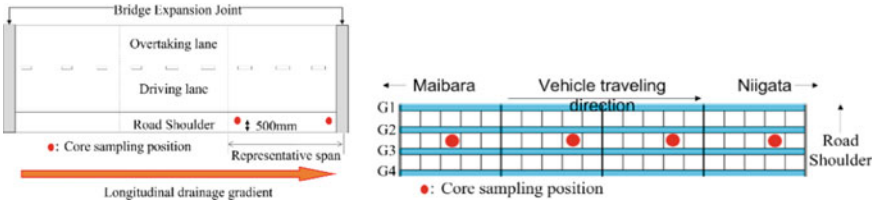

(a) Road pavement surface (b) Lower surface of the slab

Fig. 5 Concrete specimens sampling position

According to initial observations of the collected specimens, horizontal cracks were confirmed at the upper reinforcing bar position. Precipitates and rust stains of the reinforcing bars were observed on the surface of the specimen, but interior cracks were not found in the healthy part of the deck slab.

- Measurement of ASR in Concrete

The specimens collected from the A1 abutment and RC slab were subjected to an accelerated mortar bar test ASTM C 1260 (complete immersion of the specimens in 1N NaOH solution at 80 °C for 14 days). In addition, the specimen surface was observed with a stereo microscope to investigate the current extent of the ASR. The concrete aggregates for the A1 abutment and RC decks were mainly collected from the Tedori River, which is the main river in the Ishikawa Prefecture. However, many aggregates collected from the river in this region have been reported as reactive aggregates [21]. Therefore, the alkali–silica reactivity test of the aggregates was carried out for river gravel and river sand from the Tedori River by a chemical method (JIS A 1145) [22] and the mortar bar method (JIS A 1146) [23].

- Concrete chloride-content test

A concrete chloride-content test was conducted on the concrete specimens collected from the upper and lower sides of the deck slab to confirm the permeation status of chloride ions by spraying an anti-freezing agent. The sampling position on the upper side of the deck was selected on the extra lane, from the center of the span, the pier, or the vicinity of the abutment in the span with the lowest longitudinal gradient in the bridge. The healthy and deteriorated parts of the deck slab were selected and collected for the sampling position on the lower side. Generally, salt permeation by an anti-freezing agent differs depending on the sampling position on the bridge (such as gradient, pothole, or crack). Therefore, the authors analyzed the chloride concentration and its fluctuation value at each measurement position.

3 Deterioration Situation

3.1 Evaluation of ASR

- Compressive strength and static elasticity modulus

The relationship between the compressive strength and the static elastic modulus/compressive strength ratio of the concrete specimens collected from the target bridge is shown in Fig. 6. This figure shows that the deterioration due to ASR progresses as the measurement point approaches the origin from the "healthy curve" [24]. In the case of concrete specimens, the obtained results were considerably close to the healthy curve. Although the design strength was 24 N/mm^2, all the measurement results of the compressive strength exceeded 30 N/mm^2.

- ASR: Expansion rate and observation under a stereo microscope

The results obtained from the accelerated mortar bar test (ASTM C 1260) are shown in Fig. 7. The expansion rate of all specimens was less than 0.05% after 14 days and less than 0.1% after 28 days of complete immersion in the NaOH solution. According to the ASTM C 1260 and ASTM C 1567 standards, an expansion rate of less than 0.1% is considered harmless, and the aggregate is regarded as non-reactive [25].

The core surface under a stereomicroscope is shown in Fig. 8. An extremely low amount of ASR gel was detected in some aggregates. Some of the rocks commonly

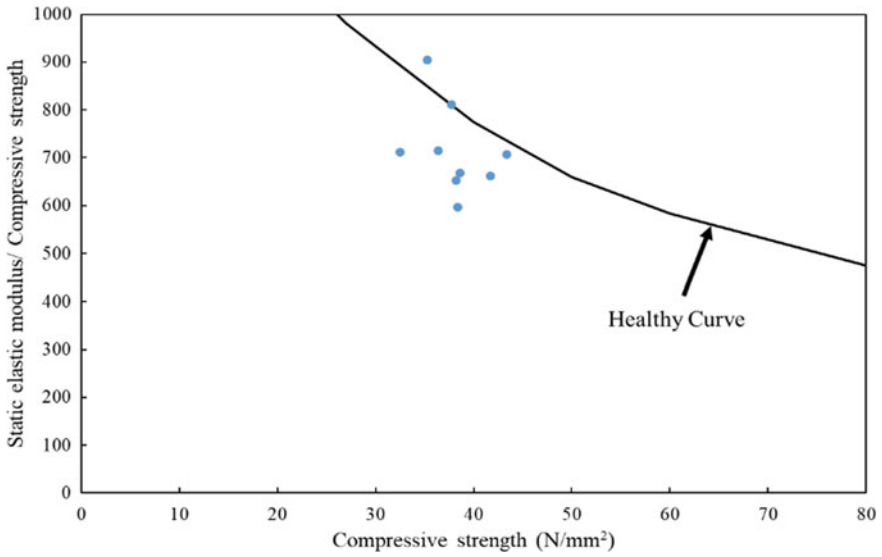

Fig. 6 Relationship between the compressive strength and the static elastic modulus/compressive strength ratio of the concrete specimens

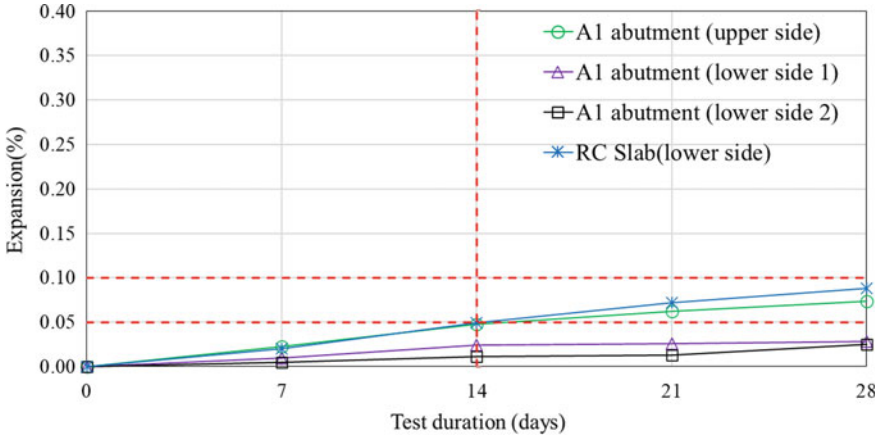

Fig. 7 Results obtained from the accelerated mortar bar test

found in the Tedori River, such as granite, rhyolite, andesite, and basalt, were confirmed as coarse aggregates in the concrete specimens. Reactive aggregates (rhyolite and andesite) were included, but these volcanic rocks had already transformed into stable minerals with crystalline structures (such as quartz) due to their relatively old age. Therefore, the ASR reactivity of these aggregates was extremely low.

Based on the accelerated mortar bar test results, the authors confirmed that the leading cause of deterioration in the target bridge was not ASR.

- ASR reactivity of aggregate in the Kanazawa area

Intending to clarify the ASR reactivity of the aggregate from the Tedori river (downstream in the Kanazawa City area), the authors conducted an ASR reactivity test for the aggregates from this river, and the results are given in Table 2. It has been reported that the aggregates from upstream and downstream of the river have a

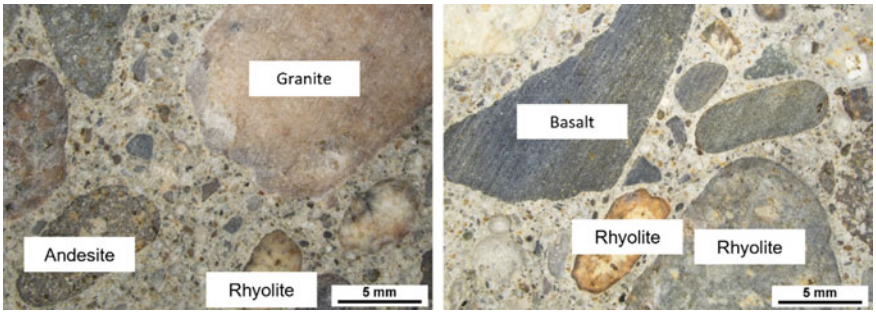

(a) Andesite, granite, rhyolite (b) Basalt, rhyolite

Fig. 8 Core surface under a stereomicroscope

Table 2 ASR reactivity test results

Aggregate	Source	ASR reactivity				
		Chemical method (JIS A 1145)			Mortar bar method (JIS A 1146)	
		Sc	Rc	Result	6 months	Result
Gravel	Tedori River (downstream)	60	124	Non-reactive	0.032	Non-reactive
Sand		105	116	Non-reactive	0.002	Non-reactive

different ASR reactivity. Moreover, there are many cases of ASR deterioration of structures using aggregates from upstream. The aggregates used for the target bridges are river gravel and river sand collected downstream of the Tedori River. Both were considered "harmless" by the chemical method (JIS A 1145) and mortar bar method (JIS A 1146). The ASR reactivity of the aggregates from this river was influenced by the contamination of volcanic and pyroclastic rocks distributed around the Hakusan mountain area (upstream). The aggregates from downstream were non-reactive. This result led to the same conclusion as that from the accelerated mortar bar test result.

In addition, the direct current from the electrochemical corrosion protection method was an ASR promotion factor. Therefore, the effect of the galvanic-anode-type steel corrosion mitigation method was verified before being installed on the target bridge.

3.2 Steel Corrosion Situation

The concrete chloride-content test results are summarized in Table 3. Most concrete specimens have a chloride ion concentration of less than 0.5 kg/m^3 (73% at the surface position, 73% at the upper-side rebar position, and 83% at the lower-side rebar position). A chloride ion concentration higher than 1.5 kg/m^3 was also confirmed at the surface and the lower-side rebar position. At the upper-side rebar position, the chloride ion concentration did not exceed 1.5 kg/m^3, and the standard deviation was smaller than that at the surface and lower reinforcing bar. Although the target bridge was not constructed in a severe salt-damage environment, chloride ions easily permeated inside, either through the cracks on the road surface or the girder end near the expansion joint when sprayed with the anti-freezing agent. Because of the above reasons, the corrosion of the girder end near the expansion joint was serious, and concrete spalling was also confirmed. The corrosion of the upper- and lower-side rebars was considered to have evolved from the advanced period to the early accelerated period.

The average annual spraying amount of the anti-freezing agent in the target bridge is 23 tons/km. After 45 years in service, the cumulative spraying amount reached approximately 1000 tons/km, and the bridge required large-scale repairs. Potholes on the road surface of the target bridge occurred 425 times in the 11 years from 2007

Table 3 Chloride ion concentration test results

Position		Relative frequency (%)		
		Road surface	Upper-side rebar	Lower-side rebar
Chloride ion concentration (kg/m^3)	$Cl^- \leq 0.5$	73	73	83
	$0.5 < Cl^- \leq 1.0$	9	21	7
	$1.0 < Cl^- \leq 1.5$	9	6	3
	$1.5 < Cl^- \leq 2.0$	9	0	7
	Average	0.62	0.44	0.29
	Standard deviation	0.16	0.06	0.23

to 2018 (an average of 49 potholes per kilometer). In addition, the deterioration on the asphalt pavement surface and free lime on the lower side of the deck slab were confirmed.

Furthermore, it has been confirmed that the neutralization depth of the bottom surface of the RC deck ranges from approximately 0 to several mm. Because of the wet weather conditions in the Kanazawa City area, neutralization is difficult. Therefore, the authors have concluded that there was no risk of steel corrosion due to neutralization.

4 Galvanic-Anode-Type Corrosion Mitigation Method

4.1 Outline of the Galvanic-Anode-Type Mitigation Method

For an efficient countermeasure against steel corrosion, Ha et al. proposed a galvanic-anode-type steel corrosion mitigation method, which has been applied to the target bridge since 2018 [18]. Because this method is applied on the lower surface of the RC deck (Fig. 9), traffic restrictions are not required.

The schematic diagram of the corrosion prevention method is shown in Fig. 10. This corrosion mitigation method consists of an anchor, sacrificial anode material, backfill material, holding plate, and storage cover. The anchor is designed to fix the sacrificial anode material inside the drilled hole with a diameter of 40 mm. The galvanic anode material is made by connecting a zinc plate with a 30 mm diameter and 5 mm thickness to a screw bolt with an anti-corrosive coating. The length of the galvanic anode material is adjusted to reach or be close to the neutral axis of the deck slab. Regarding the backfill material, which acts as an electrolyte solution, two types were tested in this method: bentonite- and mortar-type materials. Bentonite-type backfill materials consist of bentonite mixed with LiOH, and a special sponge containing an aqueous solution of LiOH (non-adhesive type). Mortar-type backfill materials consist of mortar material mixed with LiOH (adhesive type). The storage

(a) Installation of the galvanic anode

(b) Galvanic anode-type corrosion mitigation system

Fig. 9 Installation of the galvanic-anode-type corrosion mitigation system

cover with a water retention characteristic is designed to protect the sacrificial anode material and store the measurement terminal with or without energization.

At the target bridge, the test area is the lower side of the deck slab between the G2 and G3 main girder. In this area, after considering the spacing of the rebars, the sacrificial anode materials were installed with a spacing of 500 mm in the bridge axis direction and 450 mm in the direction perpendicular to the bridge axis.

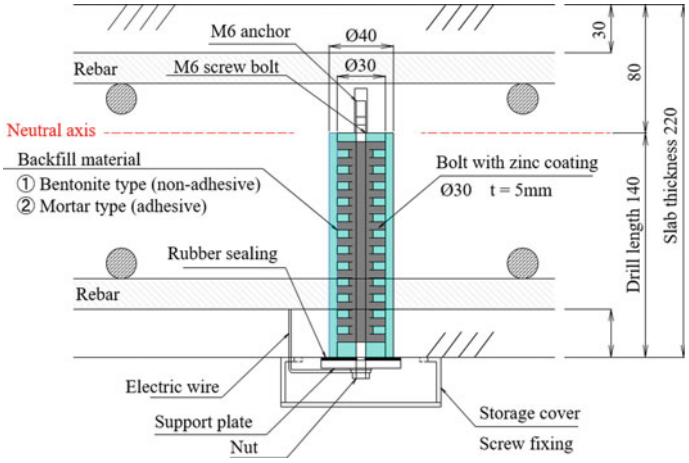

Fig. 10 Outline of the corrosion mitigation method. *Note* From "Corrosion mitigation of steel rebars using galvanic anode materials for salt-deteriorated RC slabs in snowy regions," by 18. Ha, T.M et al., 2020, IJSCER 9(2), 127–137. https://doi.org/10.18178/ijscer.9.2.127-137

4.2 *Effectiveness of the Galvanic-Anode-Type Corrosion Mitigation Method*

Although the electrochemical protection method can suppress the steel corrosion of the reinforcing bar on the upper side of the RC deck slabs even when installed from the lower side, many sacrificial anode materials, and a significant protection current, are required. A good anti-corrosion effect cannot be expected because there is not enough bath voltage to prevent corrosion in the upper-side rebars. After considering the corrosion prevention effectiveness and the maintenance cost, this method was proposed from the viewpoint that the corrosion prevention effectiveness will be ensured at a minimum price. Therefore, this method is not a corrosion prevention method that can completely prevent corrosion but can extend the lifetime of the target structure by approximately 10 to 20 years before being renewed.

A depolarization value of 100 mV or higher has been widely regarded as an anti-corrosion criterion for the electrochemical corrosion prevention method [26–28]. However, many previous studies have reported that the corrosion effect in this corrosion prevention method can occur at a lower depolarization value [29, 30]. Although the experimental conditions in these previous studies varied, the corrosion protection rate was approximately 86–92% at a depolarization value of 25 mV and approximately 92–99% at a depolarization value of 50 mV. Based on these results, the electrochemical corrosion prevention method is assumed to effectively mitigate the corrosion of steel materials at a depolarization value of 25 or 50 mV [18]. In this study, the depolarization value of 25 mV was set as the target for steel material corrosion mitigation.

4.3 *Depolarization Amount, Current, and Corrosion Mitigation Effect After 975 Days Installed*

A titanium wire (TW) sensor [38] was embedded in the concrete to evaluate the performance of the galvanic-anode-type steel corrosion mitigation method by measuring the electric potential of the rebars. TW sensors were installed in the test area to measure the electric potential of the upper rebar (WR1) and the lower rebar (WR2). TW sensors WR3 and WR4 were installed at the portion with the white precipitate in the test area to measure the electric potential of both the upper and the lower rebars. The variation in the depolarization amount over 975 days following the corrosion mitigation method is shown in Fig. 11.

In the case of the bentonite-type backfill material, the depolarization amount increased over the first 200 days before decreasing significantly. Thereafter, it decreased below 25 mV after approximately one year at the upper rebar position and after 563 days at the lower rebar position. Moreover, 975 days after the corrosion mitigation method, the depolarization amount of the galvanic anode using the

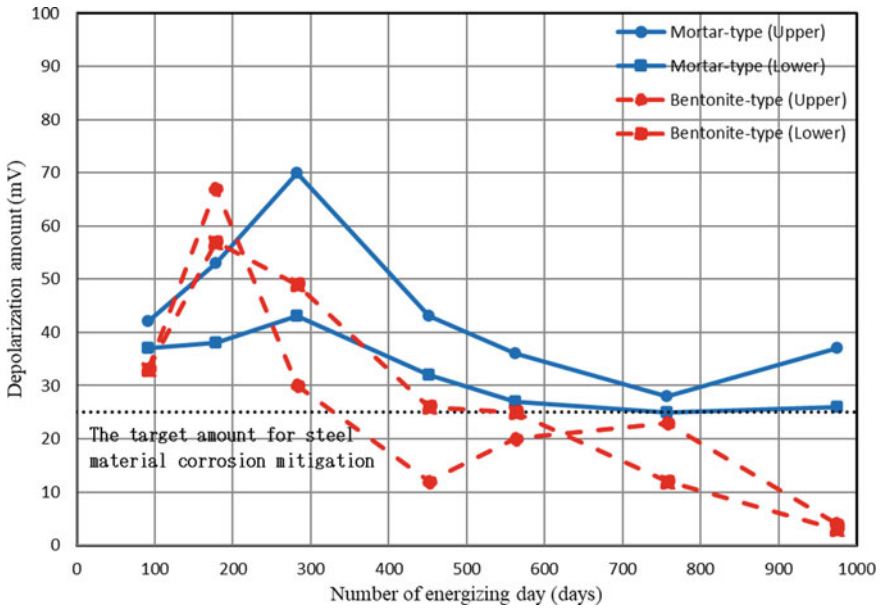

Fig. 11 Variation in the depolarization amount over 975 days

bentonite-type backfill material was nearly zero. In the case of the mortar-type backfill material, the depolarization amount increased over the first 300 days before decreasing significantly; however, it remained above 25 mV even after 975 days at all the positions.

A sponge was placed around the drilled hole for the galvanic anode using the bentonite-type backfill material to facilitate quick replacement. However, the galvanic anode material was less likely to corrode when the sponge dried. Therefore, the effective duration of the galvanic anode utilizing the bentonite-type backfill material was brief. By contrast, for the mortar-type backfill material, as the backfill material undergoes hardening, the alkaline component is retained, and the environment in which the galvanic anode material is corroded is maintained. Consequently, the effective duration exceeds that in the case of the bentonite-type backfill material. However, this backfill material type also suffers from a problem in that it is difficult to replace the sacrificial anode once it is installed. Currently, to ensure the durability of galvanic anode materials and facilitate their replacement, the authors are attempting to identify new suitable backfill materials.

In addition, the current generated by the galvanic anode, AN1–AN4, was also measured using a data logger. These results were utilized to analyze the effect of ambient temperature on the current generated (Fig. 12). Notably, a significant difference was observed between the current generated from the galvanic anodes utilizing the bentonite- and the mortar-type backfill materials, especially after 200 days following the corrosion mitigation method (i.e., AN1 and AN2 versus AN3 and

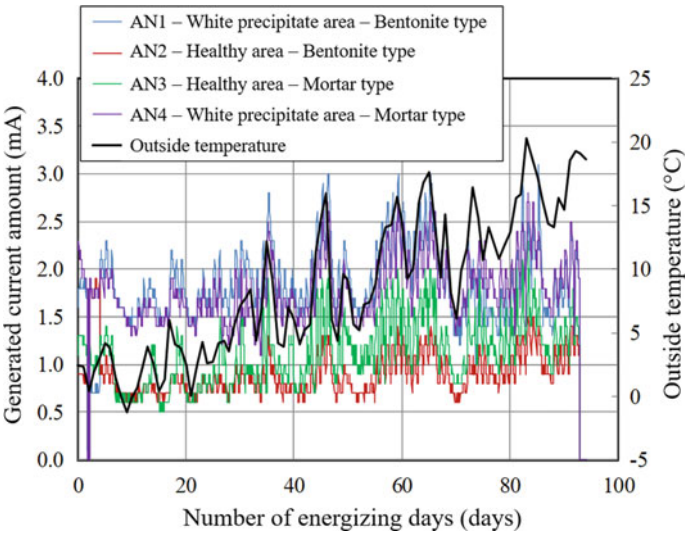

Fig. 12 Variation in current generated by the galvanic anode material over 975 days

AN4). However, in comparing the currents generated at the healthy portion and the portion with the white precipitate, the difference was not apparent (AN1 versus AN2 and AN3 versus AN4).

5 Conclusions

In this study, the leading cause of the deterioration in a target structure was confirmed based on experimental results. The authors also evaluated the performance of the galvanic-anode-type steel corrosion mitigation method. The results obtained in this study can be summarized as follows:

1. The compressive strength and static elastic modulus of the target bridge were significantly reduced owing to the deterioration caused by the combined effects of salt damage and the ASR.
2. Regarding the compressive strength of the target bridge, although the design strength was 24 N/mm^2, all the measurement results for the compressive strength exceeded 30 N/mm^2.
3. According to the results of the accelerated mortar bar test, the leading cause of deterioration in the target bridge was not the ASR.
4. Based on the results for the ASR reactivity of the aggregate, the river gravel and river sand collected downstream of the Tedori River were non-reactive aggregates.

5. Although the target bridge was not constructed in a severe salt-damaged environment, chloride ions easily permeated through the cracks and potholes on the road surface, thereby resulting in the corrosion of the steel material. Owing to this premature deterioration, large-scale repairs may be required in the future as part of the expressway's renewal work.
6. In the case of the mortar-type galvanic anode, the depolarization amount remained above 25 mV (i.e., the target amount for steel material corrosion mitigation under this method) even after 975 days following the corrosion mitigation method. By contrast, in the case of the bentonite-type galvanic anode, it was not possible to maintain the depolarization amount above 25 mV.
7. This study confirmed the effectiveness of the galvanic anode-type steel corrosion mitigation method in terms of mitigating steel material corrosion. However, in the case of the mortar-type galvanic anode, replacing the sacrificial anode once it is installed remains challenging. Considering this disadvantage, new backfill materials need to be developed to improve the workability, stability, and durability of this method.

References

1. Fang J, Ishida T, Yamazaki T (2018) Quantitative evaluation of risk factors affecting the deterioration of rc deck slab components in East Japan and Tokyo regions using survival analysis. Appl Sci 8(9):1470
2. Adel M, Yokoyama H, Tatsuta H, Nomura T, Ando Y, Nakamura T, Masuya H, Nagai K (2021) Early damage detection of fatigue failure for RC deck slabs under wheel load moving test using image analysis with artificial intelligence. Eng Struct 246:113050
3. Maeshima T, Koda Y, Iwaki I, Naito H, Kishira R, Suzuki Y, Ohta K, Suzuki M (2016) Influence of alkali silica reaction on fatigue resistance of RC bridge deck. J Japan Soc Civil Eng Ser. E2 (Materials and Concrete Structures) 72(2):126–145
4. Ishikawa Y, Adachi Y, Aoyama M, Nagai M (2011) Characteristic and structural assessment of damaged RC decks by chloride corrosion of reinforcing bar and fatigue. J Struct Eng A 57A:1263–1272
5. Stanton TE (1942) Expansion of concrete through reaction between cement and aggregate. Trans Am Soc Civil Eng 107(1)
6. Diamond S (1992) Alkali aggregate reactions in concrete, an annotated bibliography 1939–1991. Strategic Highway Research Program, Washington, DC United States
7. Farny JA, Kerkhoff B (2007) Concrete technology: Diagnosis and control of alkali-aggregate reactions in concrete. Skokie, Ill.: Portland Cement Association, United States
8. Kagimoto, Kawamura M (2011) Measurements of strain and humidity within massive concrete cylinders related to the formation of ASR surface cracks. Cement Concrete Res 41(8):808–816
9. Giaccio G, Zerbino R, Ponce JM, Batic OR (2008) Mechanical behavior of concretes damaged by alkali-silica reaction. Cement Concrete Res 38(7):993–1004
10. Ha TM, Fukada S, Torii K (2017) Effects of fly ash on mechanical properties of pc girder using reactive andesite aggregates. J Adv Concrete Technol 15(10):579–594
11. Torii K, Nomura M, Sannoh C, Hirono S (2021) The geological survey on reactive aggregates in the Chubu district and the local effective utilization of fly ash concretes. Concrete J 59(4):321–328
12. Heisig A, Urbonas L, Beddoe RE, Heinz D (2016) Ingress of NaCl in concrete with alkali reactive aggregate: effect on silicon solubility. Mater Struct 49:4291–4303

13. Velivasakis EE, Henriksen SK, Whitmore D (1998) Chloride extraction and realkalization of reinforced concrete stop steel corrosion. J Performance Construct Facilities 12(2):77–84
14. Balonis M, Sant G, Isgor OB (2019) Mitigating steel corrosion in reinforced concrete using functional coatings, corrosion inhibitors, and atomistic simulations. Cement Concrete Compos 101:15–23
15. Calero JC, Llorca MAC, Terradillos PG (2017) Influence of different ways of chloride contamination on the efficiency of cathodic protection applied on structural reinforced concrete elements. J Electroanaly Chem 793:8–17
16. Zhang EQ, Abbas Z, Tang L (2018) Predicting degradation of the anode–concrete interface for impressed current cathodic protection in concrete. Construct Build Mater 185:57–68
17. Lee HS, Yang HM, Singh JK, Prasad SK, Yoo B (2018) Corrosion mitigation of steel rebars in chloride contaminated concrete pore solution using inhibitor: an electrochemical investigation. Construct Build Mater 173:443–451
18. Ha TM, Kameda H, Aoyama T, Mizuno Y, Torii K, Fukada S (2020) Corrosion mitigation of steel rebars using galvanic anode materials for salt-deteriorated rc slabs in snowy regions. Int J Struct Civil Eng Res 9(2):127–137
19. Japanese Industrial Standard: JIS A 1108:2018 Method of test for compressive strength of concrete. Japanese Standards Association, Tokyo, Japan (2018)
20. American Society for Testing and Materials (2021) ASTM C 1260: 2021 Standard test method for potential alkali reactivity of aggregates (Mortar-Bar Method). American Society for Testing and Materials, Pennsylvania, United States
21. Torii K, Nomura M, Honda A (2004) Petrographic features of alkali-silica reactive aggregates in Hokuriku district and compatibility between various test methods determining alkali-silica reactivity of aggregate. Doboku Gakkai Ronbunshu 2004(767):185–197
22. Japanese Industrial Standard: JIS A 1145:2017 Method of test for alkali-silica reactivity of aggregates by chemical method. Japanese Standards Association, Tokyo, Japan (2017)
23. Japanese Industrial Standard: JIS A 1146:2021 Method of test for alkali-silica reactivity of aggregates by mortar-bar method. Japanese Standards Association, Tokyo, Japan (2021)
24. Kobayashi K, Mori Y, Nomura K (1993) Method of diagnosing alkali-silica reaction by compressive loading test. Doboku Gakkai Ronbunshu 1993(460):151–154
25. American Society for Testing and Materials (2021) ASTM C 1567: 2021 Standard test method for determining the potential alkali-silica reactivity of combinations of cementitious materials and aggregate (Accelerated Mortar-Bar Method). American Society for Testing and Materials, Pennsylvania, United States
26. National Association of Corrosion Engineers: NACE SP0169–2013 Control of external corrosion on underground or submerged metallic piping systems. National Association of Corrosion Engineers, Texas, United States (2013)
27. Beavers JA, Garrity KC (2001) 100 mV polarization criterion and external scc of underground pipelines. Corrosion 2001, NACE-01592
28. Funahashi M, Bushman JB (1991) Technical review of 100 mv polarization shift criterion for reinforcing steel in concrete. Corrosion 47(5):376–386
29. Otani S, Caronge MA, Yamamoto D, Hamada H (2017) Fundamental study on depolarization value and protection effects of steel in concrete under cathodic protection. Concrete Res Technol 28
30. Rathod N, Slater P, Sergi G, Seveviratne G, Simpson D (2019) A fresh look at depolarization criteria for cathodic protection of steel reinforcement in concrete. MATEC Web Conf 289:03011

Structural Performance of a Deteriorated Small Bridge due to Poor Construction

Le Trung Kien, Hoang Minh Ngo Le, Toshihiko Minato, and Saiji Fukada

Abstract Many civil engineering structures were built in Japan during periods of rapid economic growth. Some of the existing road bridges are showing signs of age-related deterioration, such as cracking and concrete delamination. This situation is becoming an urgent problem in Japan, and a similar situation is occurring in the Hokuriku region. The causes of the damage vary, and this study focuses on small bridges that have deteriorated due to poor construction. Loading tests were carried out on deteriorated bridges using test vehicles. The main girder strains of the bridge were measured to estimate the structural performance of the present bridge. In addition, the healthy and deteriorated states of the target bridge were analyzed using the finite element analysis (FEA), and the stiffness of the bridge was estimated by comparing the experiment with the results from the analytical model.

Keywords Poor construction · Stiffness · Finite element analysis · Loading test

1 Introduction

For 19 years, from 1954 to 1973, the Japanese economy proliferated. During this period of high economic growth, Japan constructed many civil engineering structures. Some of the existing road bridges have long been built [1]. According to statistics,

L. T. Kien (✉) · H. M. N. Le
Graduate School of Natural Science and Technology, Kanazawa University, Ishikawa, Japan
e-mail: kienle1852140@stu.kanazawa-u.ac.jp

H. M. N. Le
e-mail: minhngo97@stu.kanazawa-u.ac.jp

T. Minato
Tokyo Consultants Co., Ltd, Ishikawa, Japan
e-mail: minato@tokyo-con.co.jp

S. Fukada
Faculty of Geosciences and Civil Engineering, Kanazawa University, Ishikawa, Japan
e-mail: saiji@se.kanazawa-u.ac.jp

T. Kang (ed.), *Proceedings of 5th International Conference on Civil Engineering and Architecture*, Lecture Notes in Civil Engineering 369,
https://doi.org/10.1007/978-981-99-4049-3_59

by 2023, there will be over 700,000 bridges in Japan, and 43% will be more than 50 years old [2]. With more bridges over 50 years old becoming damaged, this situation is becoming an urgent problem in Japan. Inspection and maintenance are required to ensure traffic safety. A similar situation occurs in the Hokuriku region, which is located in the northwest of Honshu Island, Japan. Environmental factors influence damage to many bridges here [3–6], e.g., earthquakes frequently appear in the Hokuriku region. If an earthquake affects a bridge, it will collapse or have large cracks, which is very dangerous. Besides, the region near the sea was the cause of the chloride attack and the alkali–silica reaction (ASR), such as fatigue cracks in the concrete slabs and salt damage to concrete members [7, 8], and in addition, spraying anti-freeze in snowy areas for traffic safety causes salt damage to deterioration on structure [9].

Besides the environment, poor construction is also a significant cause that few people pay attention to the structure of premature deterioration. It can be material separation occurs when the distribution of the constituent materials of the concrete is uneven, or incorrect concrete curing methods can lead to insufficient durability and cracking. In addition, improper mix proportions and poor compaction during construction will lead to low-quality construction and reduced concrete health [10]. Therefore, it is urgent to take appropriate action against these deteriorating structures and efficiently maintain and repair them.

In Japan, all bridges are evaluated by visual inspection once every five years by the periodic inspection guidelines for bridges of the Ministry of Land, Infrastructure, Transport, and Tourism (MLIT) [11]. By visual method, the condition of the outside structure can be evaluated. However, the damage inside the concrete structure is difficult to detect and may not be found. Because it is impossible to determine the stiffness of a deteriorated bridge, a method to properly evaluate the situation of deterioration and the stiffness of structure to understand their current condition is considered essential [12].

For that reason, this study will find an inspection method to evaluate the situation of the structure. The small bridge that has deteriorated due to poor construction is the subject of this research. Loading tests were carried out on the bridge using test vehicles. The test vehicle was loaded statically at a predetermined location to measure the main girder strain on the road surface [13]. The healthy and deteriorated states of the target bridge were analyzed using finite element analysis (FEA) [14]. The stiffness of the bridge was estimated by comparing it with tests conducted on the actual bridge and analytical models.

Fig. 1 Target bridge

2 Current Status of Research Bridge

2.1 Overview of the Target Bridge

The objective bridge in this study is the reinforced concrete bridge on the Nanao-Wajima Line of the leading regional road, which was completed in 1959 (see Fig. 1). In the 63 years since its completion, the daily traffic volume of the bridge is approximately 4900 with the mixing rate of heavy vehicles is about 5.7%.

The target bridge is a small road bridge (skew bridge), which has a length of 15 m, girder length of 14.95 m, and width of 6.5 m. The structural type is a simple reinforced concrete T-girder bridge with a superstructure. The bridge slab has a concrete thickness of 230 mm and an asphalt pavement thickness of 70 mm. The modulus of elasticity was designed at 20.5 GPa for concrete and 200 GPa for steel. Figure 2 shows a general view of the target bridge.

2.2 Deteriorating Condition of the Target Bridge

In Japan, evaluation of bridge conditions based on the Guidelines for Periodic Road Bridge Inspection of MILT [11]. The classification of the soundness conditions will be described in Table 1.

The recently periodic close visual inspections resulted in a judgment of Soundness III for the main girders, bearings, and substructure (abutments). The inspection results show that the results are very close to Soundness IV. Cracks on the underside of the main girder, corrosion of the steel bars on the bottom of the main girder, and deterioration of the steel bearings have occurred (see Fig. 3). Cracks on the underside of the main girder, corrosion of the steel bars on the bottom of the main girder, and deterioration of the steel bearings have occurred. On-site observations revealed numerous delamination and exposed rebar on the underside of the main girder. The exposed rebars were found to be thinning. The abutment has cracks that are suspected

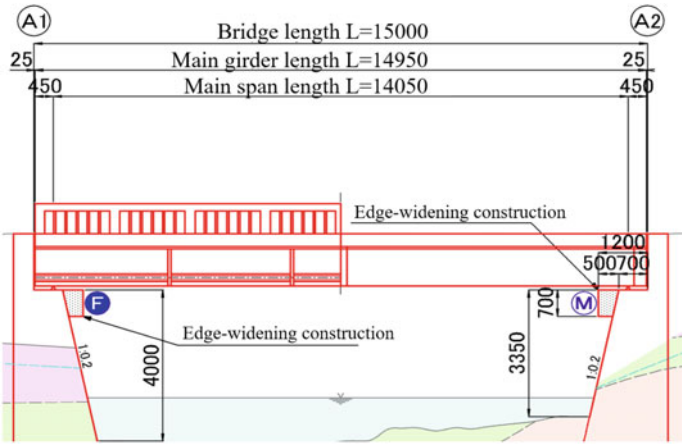

(a) Side view

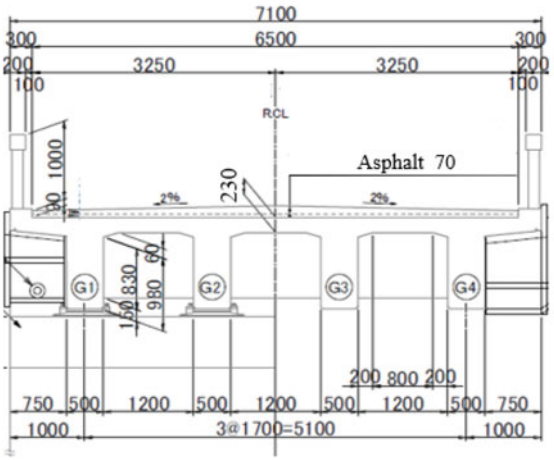

(b) Cross section

Fig. 2 View of the target bridge (Unit: mm)

Table 1 Guidelines for periodic road bridge inspection

Category		Condition
I	Good	No structural deficiency
II	Preventive maintenance	Preventive maintenance is desirable, although no structural deficiency is found
III	Early rehabilitation	The structure needs early rehabilitation, or it can become deficient
IV	Emergency rehabilitation	The structure needs emergency rehabilitation because it is deficient, or it will most likely become deficient

(a) Corroded bearings (b) Corroded rebar of main girder

Fig. 3 Target bridge condition

of having penetrated throughout. Some of them have been discovered to have water leakage and free lime. The bearings are dysfunctional due to severe corrosion. Based on the above phenomenon, it was inferred that poor construction was the cause. The experiment used in this study should verify their load-bearing capacity to ensure soundness.

3 Loading Test

3.1 Measurement Items

As described in Sect. 2, the recently periodic inspection of the target bridge resulted in a Soundness III judgment for the main girders, bearings, and substructure (abutment). The steel bar corrosion, bending cracks at the lower edge of the main girder in the middle of the span, and corrosion of the steel bearings in the bearing section are factors that degrade the structural performance. Therefore, loading tests were carried out to specify the current structural performance after comparing it with the analysis results [15].

Figure 4 shows the sensor arrangement on the bridge. In this test, the main girder strains were measured using strain cages installed on the upper and lower flanges at the center of these girders (G1, G2, G3, and G4). Crack displacement was calculated using a crack displacement meter to measure the bending cracks near the center of the span. The bridge axial displacement (G1 to G3 girder) and vertical displacement (G4 girder) of the movable bearings were measured for bearing displacement.

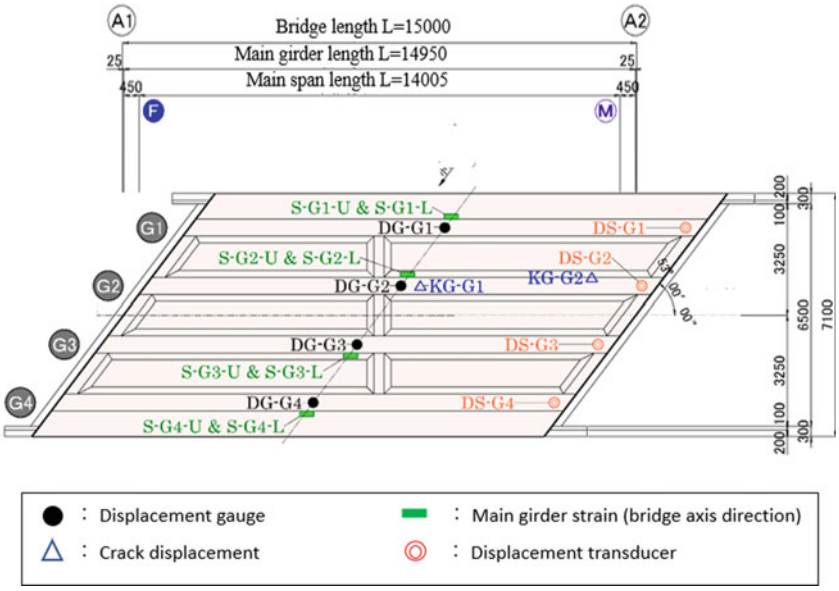

Fig. 4 Sensor arrangement (Unit: mm)

3.2 Loading Test Description

In the research, many methods used trucks in bridge tests; Andrew el at. used weigh-in-motion (WIM) and bridge weighing-in-motion (BWIM) [16]. These two alternatives provide another option to traditional static weighing stations for determining vehicle axle weights. In addition, loading tests are widely used to assess bridge structural behavior and strength, determine damage, or improve repair work efficiency (Endijs et al. [17]; Eva et al. [18]). Field tests are also profitable in determining the bridge's ability to distribute live loads more accurately. Two tri-axle trucks were used in this experiment, as shown in Fig. 5. Table 2 summarizes each test vehicle's shaft weight and dimensions.

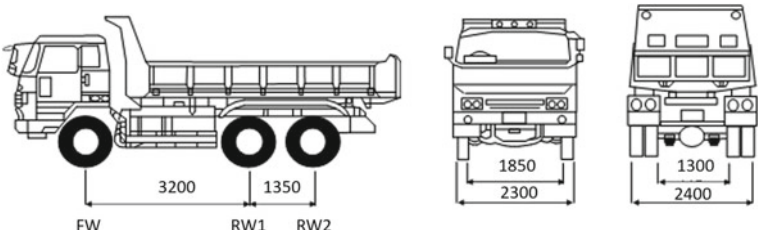

Fig. 5 Vehicle test (Unit: mm; FW, RW1, and RW2 are the wheel axle of the test truck)

Table 2 Weight of test vehicle (Unit: kN)

Vehicle number	No. 1	No. 2
Front axle (FW)	52.087	49.147
First rearmost axle (RW1)	87.857	85.946
Second rearmost axle (RW2)	78.400	82.173
Total weight	218.344	217.266

In the loading test, tri-axle trucks were used to measure the strain by stopping the vehicle at each loading position shown in Fig. 6. The loading was conducted by sequentially moving about 1.75 m (1/8 span length of a bridge) in the direction from A1 to A2 and back. In each loading case, the centers of the two rear wheels of the test vehicle were loaded at the respective target points. The loading case diagrams from the cross-sectional direction are shown in two cases: eccentric and parallel loading (see Fig. 7).

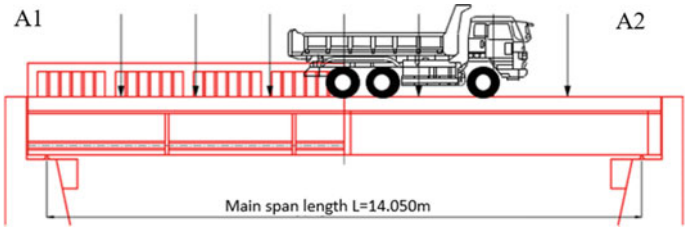

Fig. 6 Loading position in bridge axis direction

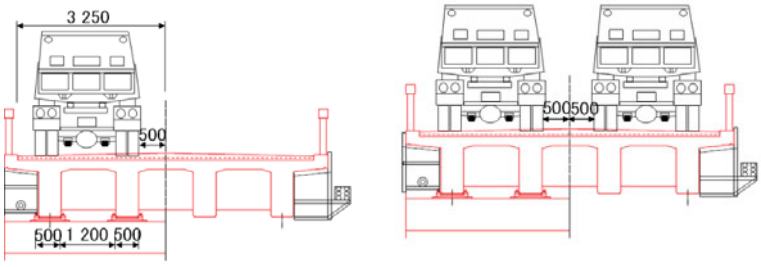

(a) Eccentric loading (b) Parallel loading

Fig. 7 Eccentric and parallel loading (Unit: mm)

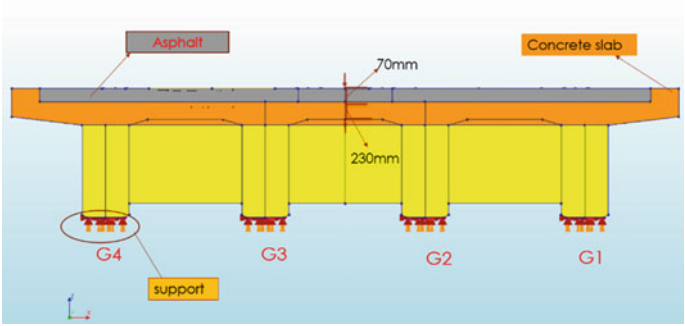

Fig. 8 Analytical models of the target bridge

4 Numerical Analysis

4.1 Analysis Model

A finite element model was created using the general-purpose structural analysis software DIANA 10.5 [19] to evaluate the stiffness and load carrying capacity of the main girders in the target bridge (Fig. 8). The main girders, slabs, ground cover, and pavement were modeled using solid elements, while the rebar was modeled using embedded rebar elements. The Young's Modulus was set to 200 GPa with steel and 20.5 GPa with concrete to reproduce the intact state of target bridge.

Figure 9 shows the case of parallel loading as a reproducible analysis of a loading test. The displacements and strains of the main girders are calculated by applying the wheel loads of each vehicle to the created analytical model of the bridge. The loading plane is 200 mm and 500 mm in the longitudinal and transverse directions to the bridge axis, respectively, based on the specification for Highway Bridges [20]. The experimental and analytical results are compared, the actual bridge is reproduced on the analytical model, and the design stiffness and current stiffness are evaluated. The boundary conditions of the bearings are modeled as the sound state at the time of completion, with the A1 side fixed in the bridge axis direction and the A2 side movable in the bridge axis direction.

4.2 Experiment and Numerical Analysis Results

The strains in main girders G1 and G4 obtained from the loading tests and analysis were compared for the following two case loading patterns. As described in Sect. 2, the inspection results of the main girder and bearings show that the results are close to Soundness IV. Young's Modulus of the material of the main girder is reduced in the order of 100, −80, −60, and −40% for each case, and the degree of deterioration

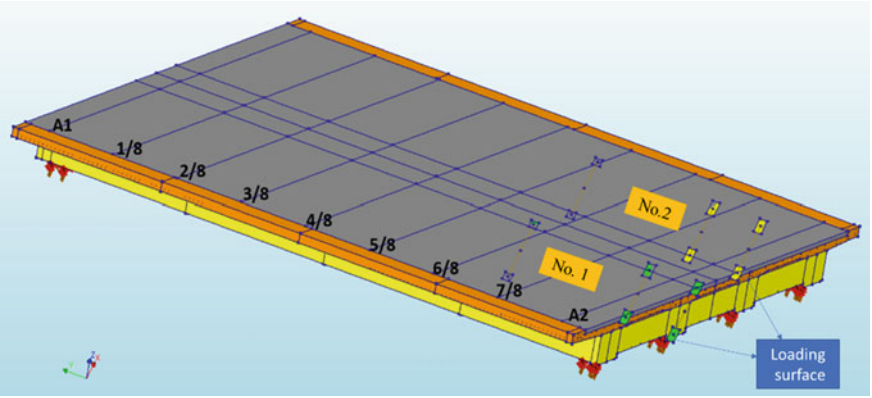

Fig. 9 Reproduced analysis of loading tests (parallel loading case)

of the steel and concrete material is evaluated, so that the current state of the bridge can be accurately grasped.

In the first case, Young's Modulus of steel will be reduced to compare with the test values given in Table 3.

The loading tests and analyses for the first case are compared. Figures 10 and 11 show the results of the strain of G1 and G4 in a parallel loading test, respectively. The analysis value in the first case shows that the strain of girders G1 and G4 was less than half of the experimental value. Model A is a healthy model for the target bridge. However, there is no significant difference in reducing Young's Modulus of steel between the four models. To have a wider assessment of the current state of the bridge, it is necessary to carry out the second case.

In the second case, Young's Modulus of concrete is also reduced to compare with the test values shown in Table 4.

Figures 12 and 13 compare the strain from the load test and the analysis in the second case. As each model decreases in degree and Young's Modulus increases, the analytical values will closely parallel the experimental values. In Model D2 with a Young's Modulus of 40%, the tensile strain of about 80μ is recorded for the lower side of the main girder in G1 and G4. Although the test value is still higher than model D2, this study can also assess the high damage of girders G1 and G4. In the target bridge, the reinforced concrete of the main girder was reduced by approximately 40–50%. When the rate of decrease in Young's Modulus exceeds 60%, it is considered

Table 3 Analysis parameters of young's modulus (GPa) and model name for first case

Scenario		Model A	Model B	Model C	Model D
Deterioration of steel		Intact	Deteriorated	Severely deteriorated	
Young's modulus of material	Steel	200	160	120	80
	Concrete	20.5	20.5	20.5	20.5

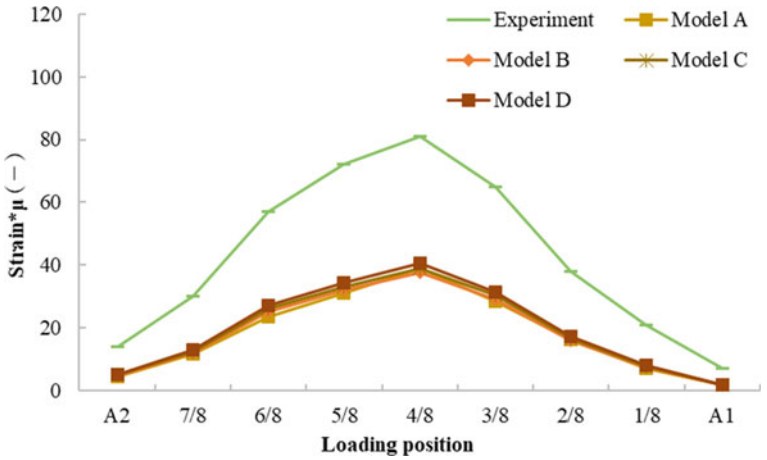

Fig. 10 G1 girder strain in parallel loading test and analysis result of the first case

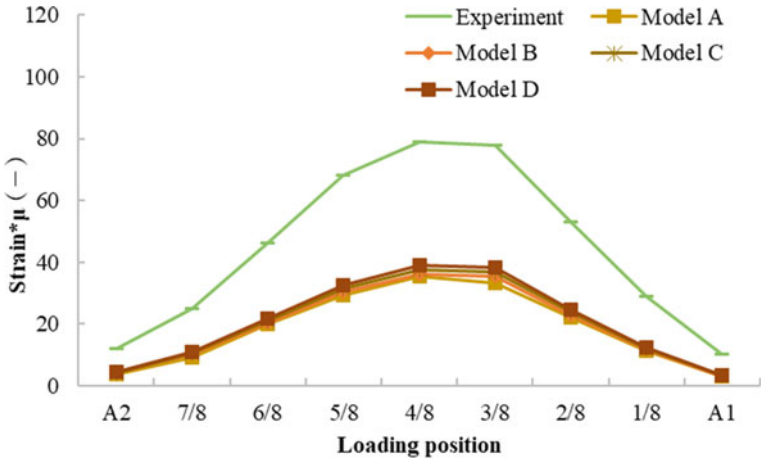

Fig. 11 G4 girder strain in parallel loading test and analysis result of the first case

Table 4 Analysis parameters of Young's Modulus (GPa) and model name for second case

Scenario		Model A	Model B2	Model C2	Model D2
Deterioration of concrete		Intact	Deteriorated	Severely deteriorated	
Young's modulus of material	Steel	200	200	200	200
	Concrete	20.5	16.4	12.3	8.2

that the role of the reinforced concrete is lost. Furthermore, the possibility of sudden displacements in the G4 bearings of the A2 abutment increases. The current condition of this bridge is 40–50% deteriorated, which is thought to result in a low level of safety. For safety reasons, repair methods must be implemented as soon as possible.

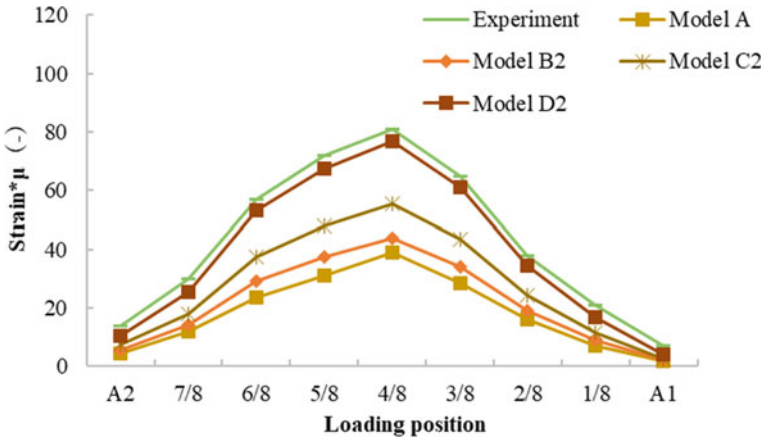

Fig. 12 G1 girder strain in parallel loading test and analysis result of the second case

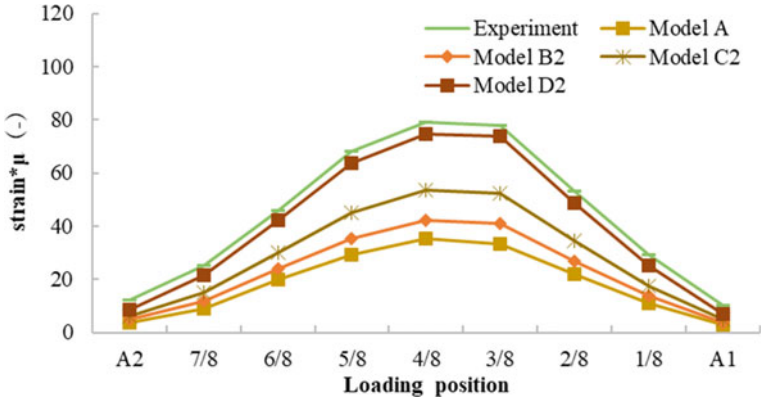

Fig. 13 G4 girder strain in parallel loading test and analysis results of the second case

5 Conclusions

In this study, static loading tests using a test vehicle were conducted to evaluate the stiffness of small bridges that had deteriorated or have damage due to poor construction. An analysis was also conducted to estimate the degree of material deterioration.

The results obtained from this study are detailed below.

(1) In the target bridge, the corrosion of steel bars and bearings on the lower side of the main girder were observed. In addition, numerous concrete spalls and exposed reinforcing bars were also observed. It was noted that poor construction was the probable cause.
(2) The target bridge was modeled using the FEA. The analytical result is relatively close to the experimental value obtained by simulating a sound model and various degrees of deterioration. The state of this bridge was shown in Model D2. It was inferred that Young's Modulus of concrete was close to 40% for the target bridge.
(3) According to the results of this study, the current stiffness of this bridge has deteriorated by more than 60%. It was inferred that the safety of this bridge was low. For safety, it is necessary to implement the repair method as soon as possible.

References

1. Bureau of Construction, Tokyo Metropolitan Government, Maintenance and Repair of Roads and Bridges, https://www.kensetsu.metro.tokyo.lg.jp/english/jigyo/road/07.html. Last accessed 25 May 2022
2. Ministry of Land, Infrastructure, Transport and Tourism, Road Maintenance in Japan: Problems and Solutions, https://www.mlit.go.jp/road/road_e/pdf/RoadMaintenance.pdf. Last accessed 2022/06/28.
3. Minami T, Fujiu M, Nakayama S, Takayama J (2017) Effective analysis of soundness of bridges affected by earthquakes by using bridge inspection data in Hokuriku region. J Eastern Asia Soc Transp Stud 12:1448–1457
4. Hashimoto T, Torii K (2013) The development of highly durable concrete using classified fine fly ash in Hokuriku district. J Adv Concrete Technol 11(11):312–321
5. Fukada S, Ha TM, Torii K, Tsuda M, Ura S, Sasatani T (2017) Long-term monitoring for ASR-deteriorated PC rigid-frame bridge. J Disaster Res 12(3):396–405
6. Ha TM, Ura S, Fukada S, Torii K (2020) Development and application of a highly durable precast prestressed concrete slab deck using fly ash concrete. Maintenance Manage Life-Cycle Des Performance 16(9)
7. Katayama T, Tagami M, Sarai Y, Izumi S, Hira T (2004) Alkali-aggregate reaction under the influence of deicing salts in the Hokuriku district Japan. Mater Character 53(2):105–122
8. PCA: Types and Causes of Concrete Deterioration, PCA R&D Serial No. 2617, Portland Cement Association (2002)
9. Arima N, Fukada S, Ha TM, Moriyama M, Miyashita T (2016) Structural damage identification based on non-destructive and destructive investigation of PCT girder removed due to salt

damage. In: Proceedings of 5th international symposium on life-cycle civil engineering, pp 1559–1565
10. Kovler K, Chernov V (2009) Failure, distress and repair of concrete structures, woodhead publishing series in civil and structural engineering, pp 32–56
11. Ministry of Land, Infrastructure, Transport and Tourism, Road Maintenance in Japan: Problems and Solutions: https://www.mlit.go.jp/road/road_e/pdf/RoadMaintenance.pdf. Last accessed 10 Jun 2022
12. Maki Y, Ha TM, Fukada S, Torii K, Ono R (2019) Stiffness evaluation and current status of a degraded road bridge slab located in a mountainous area. J Adv Concrete Technol 17(1):62–78
13. Chuanzhi D, Selcuk B, Marwan D, Ninel A, Necati FC (2020) Bridge load testing for identifying live load distribution, load rating, serviceability and dynamic response. Front Built Environ
14. Islam N, Miyashita T, Shill SK, Takeda K, Fukada S, Takatsu A, Al-Deen S, Subhani M (2022) Assessment of structural health of an existing prestressed concrete bridge by finite element analysis. Australian J Civil Eng
15. CTL Group Qatar website, https://www.ctlgroupqatar.com/single-post/2017/11/07/bridge-load-testing. Last accessed 30 Jun 2022
16. Andrew L, Wei S, Brandon D (2017) Development and testing of a bridge weigh-in-motion method considering nonconstant vehicle speed. Eng Struct 152:709–726
17. Endijs V, Ainars P, Atis Z (2021) Evaluation of the residual load-bearing capacity of the existing road using plate loading test. In: 30th international Baltic road conference
18. Eva OLL, Ane B, Cor V, Hordijk DA (2019) Optimizing finite element models for concrete bridge assessment with proof load testing. Front Built Environ
19. DIANA FEA Homepage, Diana Finite Element Analysis, https://dianafea.com/index.php/solution. Last accessed 21 Jun 2022
20. Japan Road Association: Specifications for Highway Bridges, part I common, The library of Japan Road Association

Evaluation of the Condition of Prefabricated Pretensioned Prestressed Beam Forming the Load-Bearing Structure of Bridges after About 60 Years of Use

Stanislav Rehacek, David Citek, and Daniel Dobias

Abstract The paper summarizes results of diagnostic work on approximately 6 bridges constructed from prestressed standardized precast elements used in the 1960-1990s for the construction of bridges in the Czech Republic. These are mainly the standardized girders of KA type (Type documents for prefabricated girders KA-73, Dopravoprojekt 11/1973, digital copy) for clearances of 9–18 m and I girders (Type documents for prefabricated girders I-73, Dopravoprojekt 11/1973, digital copy) for clearances of 21–30 m. The assessment focused mainly on the actual strength class of concrete in relation to the design strength, visual inspection of the outer face and inner chambers of the girders with the help of videoscopes, and last but not least, checking the condition of the prestressing reinforcement and the state of cable ducts grouting. The condition of the prestressing reinforcement was checked firstly by means of mechanical probes and secondly by means of the half-cell method in the place of visual defects. Results were supplemented by a corrosion survey of the prestressing reinforcement with regard to content of chloride ions in the grout mixture.

Keywords Bridge · Concrete · Reinforcement · Inspection · Beam

1 Introduction

The objective of this paper is to evaluate the state of the diagnosed bridge structures, where previous bridge inspections have found significant failures affecting the load-bearing capacity of the bridges [3]. Structural condition of the selected structures was V and above on a VII-point scale [3]. The most frequent failures were corroded prestressing cables in standardized girders, failures in transverse joints of the girders,

S. Rehacek (✉) · D. Citek · D. Dobias
Klokner Institute, CTU, Prague, Prague, Czech Republic
e-mail: stanislav.rehacek@cvut.cz

T. Kang (ed.), *Proceedings of 5th International Conference on Civil Engineering and Architecture*, Lecture Notes in Civil Engineering 369,
https://doi.org/10.1007/978-981-99-4049-3_60

and failures under the anchor areas. Possibly also in areas of other failures, such as leakage areas and spots with concrete degradation.

The output was an assessment of the extent of corrosion damage to the prestressing reinforcement, description of the structural condition in terms of chloride ion content in concrete of the supporting structure, and a detailed corrosion assessment of the prestressing reinforcement. Another objective was to propose a possible method of bridge rehabilitation and reconstruction with partial use of new materials (UHPC).

2 Description of the Bridges

The diagnostic surveys focused on single-span to three-span bridges in the Czech Republic, which carry roads mainly over watercourses or roads of lower classes.

The abutments and any supports of the bridges are from reinforced concrete or a combination of plain concrete and reinforced concrete. In the case of KA girders, the supporting structure is mounted on asphalt felt or elastomeric bearings. Type I girders are then mounted on steel bearings.

3 Diagnostic Work

3.1 Destructive Compressive Strength Tests of Concrete

Core borings with the approximate diameter from 50 to 100 mm were taken from the supporting structures of the bridges for the purpose of destructive compressive strength tests of concrete. Smaller bore diameters were chosen in places where there was a risk of damage to the prestressing reinforcement during drilling.

A summary of the results of these destructive compressive strength tests and their corresponding strength classes or concrete classes are specified in the following Tables 1 and 2.

Based on the destructive compressive strength tests of concrete, it is possible to state that the strength class of the structure meets or exceeds the requirements of the type documentation in all cases.

3.2 Comparison of Concrete Carbonation Depth and Rebar Cover Layer Thickness

Determination of the concrete carbonation depth was carried out uniformly over the entire length of the bridge structures. Measurement uncertainty can be estimated

Table 1 Compressive strength test of concrete—results summary

Diagnosed structural elements		Compressive strength of concrete [MPa]		Variation coefficient v*
		Average of the tests	Characteristic	
Bridge no. 1, Ka-73	Destructive	51.2	44.2	4.7
Bridge no. 2, Ka-73	Destructive	49.8	38.2	10.0
Bridge no. 3, Ka-73	Destructive	52.9	43.2	8.8
Bridge no. 4, i-73	Destructive	51.7	39.6	11.7
Bridge no. 5, i-73	Destructive	54.3	44.2	3.3
Bridge no. 6, i-73	Destructive	64.3	47.0	5.7

*ČSN 73 2011 [4] specifies the limit value of the variation coefficient for homogeneous concrete of class C 30/37 and higher as $v = 12\%$ (homogeneity in terms of strength)

Table 2 Strength class or concrete class based on the performed tests

Diagnosed structural elements		Concrete class/strength class of concrete	
		ČSN EN 1992	Requirement of documentation [1 and 2]
Bridge No. 1, KA-73	Destructive	C 40/50	B 500, C 35/45
Bridge No. 2, KA-73	Destructive	C 35/45	
Bridge No. 3, KA-73	Destructive	C 40/40	
Bridge No. 4, I-73	Destructive	C 35/45	
Bridge No. 5, I-73	Destructive	C 40/50	
Bridge No. 6, I-73	Destructive	C 45/55	

within ±2 mm. Rebar in the structure is subject to corrosive processes, which are influenced by a number of factors. The most important factors include.

(a) Humidity of the environment,
(b) Filling the pore system of the concrete with water,
(c) Depth of the rebar below the surface,
(d) Thickness of the carbonated concrete layer, and
(e) Content of certain pollutants in the concrete (chloride ions, presence of acids, and other aggressive media).

If the rebar loses its passivation by the alkalinity of the concrete (carbonation), the presence of moisture will induce corrosive processes leading to known defects such as loss of the concrete surface layers and loss of rebar cross-section.

HILTI PS 1000 radar was used to determine the thickness of the cover layer over the outer surface of the reinforced concrete elements. Function of the device is based on the principle of sending electromagnetic pulses into the structure. The output of the registration of electrical pulses reflected from material inhomogeneities is a planar scan with a cross-section of the particular structure. Hilti PROFIS PS 1000 software interface was used to determine the approximate position and thickness

of the cover layer on the outer surfaces of individual structures. HILTI PS 1000 allows for a maximum detection depth of 300 mm. Accuracy of depth indication is ± 10 mm for depths below 100 mm. For depths over 100 mm, the accuracy is ± 15%. Localization accuracy is ± 10 mm.

Findings show that in most of the monitored bridge structures, only a small portion of the soft reinforcement of the girders (especially the ties) lie in the carbonated concrete layer and are no longer protected against corrosion by its natural alkalinity. Remaining structural rebar, especially the prestressing reinforcement, lie in the non-carbonated concrete layer and are protected by its natural alkalinity.

3.3 Determination of Chloride Content in Concrete

Chloride ion content above a certain limit significantly increases the risk of rebar corrosion and accelerates the corrosion process. For this reason, a chemical analysis of the concrete was carried out as a part of the diagnostic work in order to determine the content of chloride ions in the concrete.

Sampling locations were evenly distributed over the load-bearing structures of the bridges. Three samples from different depths (0–15, 15–30, and 30–45) were always taken at the same location.

Pursuant to ČSN EN 206 + A2 [5], the limit content of Cl- [% wt.] related to the weight of cement is 1% wt. for plain concrete; 0.4% wt. for reinforced concrete and 0.2% wt. for prestressed concrete.

Based on the analysis of the chloride content for 6 monitored bridge structures, it is generally possible to state that the concrete of the investigated structural concrete elements has a relatively high content of chloride ions in the depth range of the sampling (0–15 mm) and does not meet the requirements of ČSN EN 206 + A2 at 4 out of 6 monitored bridge structures. As regards the sampling depth range of 15–30 mm, the chloride ion content is relatively high and does not meet the requirements of ČSN EN 206 + A2 at 2 out of 6 monitored bridge structures.

In the remaining sampling range (30–45 mm, corresponding to the position of the prestressing reinforcement), the chloride ion content is already relatively low and meets the requirements of ČSN EN 206 + A2 for all bridge structures.

The grout mixture used to protect the prestressing reinforcement has a low chloride ion content for the time being and meets the requirements of ČSN EN 206 + A2.

The high chloride ion content corresponds to the sampling locations at the failure points (leakage to the bottom face and sides of the supporting structure). A summary of the results is specified in Table 3.

Table 3 Summary results of the chloride content determination in the concrete of the supporting structure

Diagnosed structural elements	Conversion of Cl- to cement quantity of approximately 420 kg in 1 m3 of concrete [%]		
	Depth: 0–15 mm	Depth: 15–30 mm	Depth: 30–45 mm
BRIDGE NO. 1, KA-73 girders	0.45	0.22	0.15
BRIDGE NO. 2, KA-73 girders	0.25	0.15	0.08
BRIDGE NO. 3, KA-73 girders	0.41	0.31	0.18
BRIDGE NO. 4, I-73 girders	0.14	0.13	0.09
BRIDGE NO. 5, I-73 girders	0.17	0.11	0.06
BRIDGE NO. 6, I-73 girders	0.23	0.15	0.04

3.4 Reinforcement of Structural Elements

Destructive tests of prestressing reinforcement of the supporting structure were carried out on each bridge structure with the aim of determining the position and condition of the prestressing reinforcement.

The evaluation of the condition of prestressing reinforcement is based on the article of the proceedings ISBN 978–80-907,611–2-4 from the 26th Concrete Days (2019) prepared by the Klokner Institute [6]. Condition of the prestressing reinforcement is classified into 6 levels based on the corrosion damage rating scale:

Level 1 Reinforcement without any sign of corrosion.

Level 2 Reinforcement with initial localized surface corrosion. The original non-corroding surface can still be noted. The corrosion does not affect the change in cross-section.

Level 3 Spread surface corrosion of the reinforcement without flaking corrosion products. Its effect on the reduction of the reinforcement cross-section and mechanical parameters is not significant.

Level 4 Fully spread surface corrosion of the reinforcement. The corrosion products are peeling off. However, there is no apparent change to the cross-sectional shape and no reduction in the cross-sectional area. However, the change in the cross-sectional area already occurs at the level of %. This type of corrosion is the borderline in terms of the degree of negative impact on mechanical properties of the reinforcement.

Level 5 Fully spread surface corrosion of the reinforcement. Massive flaking of corrosion products. A uniform pitted "orange peel" type structure forms on the surface of the rebar. Apparent changes and reduction in shape and cross-section of the rebar in some places. Loss of the cross-sectional area is significant and already reaches dozens of % of the original area.

Level 6 Massive flaking of corrosion products. Distinct and apparent change in the shape of the rebar. Some may even be broken or completely corroded. Significant reduction of the rebar cross-sectional area, loss of cross-section at the level of 50% or more of the original area.

Based on the performed destructive tests and other findings, it can be generally stated:

- Probes to the prestressing reinforcement were made on the lower faces of the girders and then on the side of the outmost girders at the locations below the anchors.
- The most problematic locations proved to be the transverse girder joints (bonded or filled with mortar) where the prestressing reinforcement is more susceptible to corrosion due to degradation of the joint material and leakage due to non-functional bridge deck waterproofing, see Figs. 2 and 3.
- Another problematic areas are located under the anchors of the girders. Especially in case of lifted cables, the grouting mixture subsided already at the time of the grouting and the prestressing reinforcement is not thus protected by the mixture and is more susceptible to corrosion, see Fig. 1.

Fig. 1 A look inside the guard. Ungrouted guard, visible subsidence of the grouting material. Corrosion of prestressing reinforcement wires

Fig. 2 A look inside the KA girder's chamber. Visible active leak traces. Corrosion of the exposed reinforcement

Fig. 3 View of the bottom face of the KA girders. The chambers of the girders were flooded with water due to malfunctioning waterproofing

3.5 Corrosion Assessment of Prestressing Reinforcement

Corrosion survey on bridges also included the collection of corrosion products (very often with fine-grained fragments of cement grout) and their elemental analysis by XRF (X-ray fluorescence analysis) and phase representation analysis by XRD (X-ray diffraction analysis) method. Results of the laboratory tests clearly show that in most cases the corrosion damage was induced and mainly stimulated by chloride anions (Cl-), which are contained in de-icing salts (NaCl). The content of chloride anions in the corrosion products was significant. At the same time, akaganeite (β-FeO(OH)), which contains embedded chlorine atoms, was found in several cases in the corrosion products. Furthermore, usually significant amounts of hydrocalumite (the hydration phase of cement containing chlorine atoms) were found in the grouting residues.

The results clearly show that a highly localized and unpredictable corrosion damage stimulated by chloride anions occurs in the prestressing reinforcement cables. Localization depends mainly on the penetration of moisture into the area of the prestressing reinforcement (leakage and condensation).

For citations of references, we prefer the use of square brackets and consecutive numbers. Citations using labels or the author/year convention are also acceptable. The following bibliography provides a sample reference list with entries for journal articles [1], an LNCS chapter [2], a book [3], proceedings without editors [4], as well as a URL [5].

3.6 Half-Cell Potential Method

Destructive tests in the area of the prestressing reinforcement were supplemented with potential measurements, taking into account visual inspections and access to the structures. A network of 100 × 100 mm measuring points was chosen. When

planning the network, the aim was to place the axis in the lain of the cable ducts and/or longitudinal rebar. The measurement orientation was chosen from the origin ± 0 positive in the direction of the chainage. Non-destructive measurements were also used to determine the position of the rebar in the test area with maximal possible accuracy.

While evaluating the results, it is important to keep in mind that this is only an informative measurement which should be supplemented by exposing the examined rebar in order to verify its corrosion state. Criteria for the probability of active corrosion occurrence pursuant to ASTM C876 15[7] are used for the evaluation. The limit values cannot be seen as completely universal, and each measurement needs to be approached individually.

4 Use of Modern Materials in the Rehabilitation

Diagnostics of the structure provides structural engineers and the investor with the groundwork for subsequent rehabilitation of the structure. There are multiple ways of the bridge structure rehabilitation as such. The scope and method of the rehabilitation depend on the character of the structure, and its purpose is to increase the durability and service life of the structure.

Nowadays, ultra-high performance concrete (UHPC) is increasingly used for these remediation interventions on a global scale. This cement-composite, fine-grained material with minimal porosity and homogeneous structure stands out for its high durability, long service life, and material properties. The compressive strength of UHPC is at 150 MPa and above. As regards strengthening or rehabilitation of structural details, this material is particularly suitable due to its favorable consistency. The mixture can be modified and optimized as self-compacting, self-leveling, and thixotropic. The mixture is reinforced with dispersed reinforcement in form of steel, composite, or plastic fibers in order to achieve the required tensile properties and residual strength after formation of crack.

In the case of bridge rehabilitation, the material can be used in several ways. Rehabilitation of the top face of the supporting structure with additional concrete layer and reinforcement of vertical elements (pillars and abutment walls) is very widespread. First, the incoherent and degraded concrete layer is removed from the existing structures by high pressure water jet or by mechanical means, and a layer of UHPC is applied to the surface. Due to the excellent cohesion of both materials, material properties, resistance to frost and chemical deicing agents, this layer forms a protective envelope and increases the durability of the structure. The surface layer of such reinforced elements also increases the resistance against possible vehicle impact.

Another way of UHPC utilization in the rehabilitation and reinforcement of bridge structures is the replacement or strengthening of the bridge deck. The application method is very similar to that used for the pillars. The non-compliant bridge deck or part of it is removed and replaced with a layer of highly resistant UHPC. This layer

is either directly used as the pavement (USA) or serves the base for waterproofing and normal bridge superstructure (Europe).

In special cases, it is also possible to use UHPC as a grouting material for promoting the monolithic character of the structure around supports, joints, or for bonding of precast structural elements. In these cases, a bespoke design is required, which can fully benefit from the use of all excellent properties—compressive strength, residual tensile strength, consistency, and mainly the durability. This material has been developed in the Czech Republic for the last 15 years. Experience with new UHPC structures is now beginning to be used to a greater extent also in the rehabilitation and reinforcement of structures. Also in the case of the described diagnosed bridges, one of the options for the rehabilitation of structural details is the use of UHPC to promote their monolithic character.

5 Summary

Diagnostic surveys of the load-bearing structure on 6 bridges have shown that the structures do not show static failures or other defects that could have a direct effect on their load-bearing capacity. The design strength of the concrete has been demonstrated for all structures. Carbonation has only interfered with the soft reinforcement of the girders so far, and the prestressing reinforcement lies in the non-carbonated layer of concrete and is protected by the natural alkalinity of the concrete.

Content of chloride ions in the prestressing reinforcement depth was also relatively low in most cases and complied with the requirements of the standard. The high chloride ion content corresponds to the sampling locations at the failure points (leakage to the bottom face and sides of the supporting structure).

In most cases, however, the girders are subject to long-term leakage of saline solutions and other corrosive agents into the structure due to non-functional waterproofing.

The identified defects of the supporting structure can be eliminated only by a complete replacement of the waterproofing system, which will prevent the ingress of additional water into the structure and thus extend the life of the girders by another 10–20 years. In case of waterproofing replacement, UHPC can be used to reinforce the bridge deck. This layer is either directly used as the pavement (USA) or serves the base for waterproofing and normal bridge superstructure (Europe). The additional concrete layer significantly increases the durability of the structure, and it can be used to consolidate the monolithic character of the girders and, for example, reduce the height of the bridge deck.

Acknowledgements The paper has been written with the support of the TAČR grant project CK02000329—UHPC as the main load-bearing structure for middle-span bridges.

References

1. Type documents for prefabricated girders KA-73, Dopravoprojekt 11/1973, digital copy
2. Type documents for prefabricated girders I-73, Dopravoprojekt 11/1973, digital copy
3. ČSN 73 6221: Inspection of road bridges
4. ČSN 73 2011: Non-destructive testing of concrete structures
5. ČSN EN 206+A2: Concrete: Specification, performance, production and conformity
6. Effect of corrosion on the properties of steel prestressing reinforcement, team of authors, Klokner Institute, CTU. Proceedings of the 26th concrete days (2019), section CT2B: research and technology 3, ISBN 978–80–907611–2–4
7. ASTM C876–15: Standard test method for corrosion potentials

Research on Urban Crossing Viaduct Bridge Jacking Technology

Chun Yang, Qian Wang, Heng Wu, Mingjin Zhang, and Xu Xin

Abstract Facing the increasingly saturated urban traffic volume to solve the urban congestion situation, the urban viaducts have to be reconstructed to meet the daily traffic requirements. In this paper, taking an urban spanning viaduct reconstruction project as an example, the finite element analysis software Midas Civil is used to set different working conditions to analyze the stress characteristics, and the stability of the whole bridge and the jacking support during the jacking process. Meanwhile, this paper study the difficulties and key technical points of urban viaduct jacking technology and provides technical reference for the application of this technology in similar projects. Research indicates that the main girder stress changes caused by height changes during the jacking process are small within 1 MPa. When the single-side jacking exceeds 60 mm, the jacking support will be bearing empty with varying degrees, ranging from 1 to 3 in this paper. Uneven jacking will cause serious empty of the bridge bearing, the void number of temporary supports near 30 when uneven jacking height up to 10 mm, and it has little influence on the stress variation of the main girder. And it also will cause the phenomenon that the reaction force of some supports is too concentrated, as high as 2000 kN.

Keywords Urban viaduct · Jacking technology · Bridge reconstruction · Finite element · PLC system

C. Yang · Q. Wang · H. Wu
Department of CMCU Engineering Co., Ltd., Chongqing 400041, People's Republic of China

M. Zhang (✉) · X. Xin
Department of Bridge Engineering, Southwest Jiaotong University, Chengdu 610031, People's Republic of China
e-mail: Zhang-Minjin@swjtu.edu.cn

T. Kang (ed.), *Proceedings of 5th International Conference on Civil Engineering and Architecture*, Lecture Notes in Civil Engineering 369,
https://doi.org/10.1007/978-981-99-4049-3_61

1 Introduction

With the development of economy and construction technology to meet the new urban development in the future, the existing bridge design can no longer meet the requirements in terms of line type, and it is urgent to renovate bridges through the jack-up technique. Nowadays, in the wake of old bridge renovation, many studies have been done on the application of bridge jacking technology.

A study on the integral lifting of simply supported girder bridges had been done to meet increased navigation capacity about numerous bridges [1]. Done some research on the bearing jacking method to reduce the tensile stress in the negative bending moment zone of steel concrete [2]. A construction organization was designed to replace bridge bearings without interruption of traffic by applying the jack-up technique [3]. Researched the reliability index of the typical cross-section through analyzing a finite element of the construction stage and bridge completion stage to provide a reference for jacking construction of continuous bridge [4]. The two types of steel brackets as the load carrying platform was designed to study the stability of the support under the jacking beam protection, and it is aim to provide meaning for guidance for similar projects [5]. Studied the calculation method of jacking force and analyzed the influence of different closure temperatures on jacking force and structural deformation and internal force state, and the results show that low-temperature closure is a benefit for the vertical deformation control of the main girder at the jacking stage and the stress gradient of V-shaped pier is less [6]. Based on the programmable logic controller (PLC), synchronous jack-up replacement is a kind of advanced technology to replace the current method, and it can control the displacement accuracy of bridge jacking and determine the stress and strain during the jacking stages and help to digitalize the jack-up construction stage [7]. Optimized the longitudinal linear of the original route based on the synchronous jacking up construction, providing the accurate analyzing threshold and the monitoring step during the construction stage through simulating the limit force of beam by finite element software [8]. To verify the maximum value of the unsynchronized vertical difference and guide the construction and ensure safety, adopted 3D software to study the relationships between the unsynchronized vertical difference and the girder's deformation behavior [9]. Investigated changes in the behavior of the old bridges and temporary support bridges by comparing the calculated management values with the monitoring data, realizing automatic management and monitoring of bridge jacking [10]. The development and implementation of a computer-based remote monitoring system provided a continuous evaluation of data collected on the bridge [11]. Based on the current specification, the bearing capacity and stability of the early-built stone bridge were evaluated by calculation through the theoretical analysis, which is considering the effect of dead load and live load and temperature variation [12].

Under the guidance of numerical analysis, the characteristics of strain and stress distribution in the progress of integral jacking of girder bridges are studied [13]. According to the requirements of synchronous lifting of the bridge, the appropriate

control strategy is selected, and the hydraulic system of synchronous lifting device is designed. And the results show that the control of the system is convenient and the synchronization accuracy is high [14]. The steel hoop is designed as the lifting force platform, and the optimization method of the steel hoop is proposed in the analysis of the results [15]. The note discussed the technical difficulties of integrating a synchronous hydraulic jack-up system into a housing facility [16].

A novel asynchronous analysis method known as single and interlaced points is proposed. And the method is appropriate for analyzing the asynchronous lifting of long-span steel roof structures [17]. Based on the research that the causes which lead to difference displacement in the key parts of the bridge, and a posture adjustment and control algorithm based on average displacement is proposed [18].

2 Project Profile

The superstructure of the overpass viaduct jacking project in this paper is a prestressed simply supported small box girder of the left bridge (29.3 + 30 + 26.3) m and the right bridge (26.3 + 30 + 29.3) m, the bridge plane is located on a downslope of 6.4%, the left and right bridges are arranged symmetrically, and the bridge deck is independent. The main girder height is 1.6 m, and the single width of the bridge deck is 9.5 m. The bridge deck is composed of precast box girders and cast-in-site wet joints. The cantilever length of the flange plate is 40 cm, the horizontal thickness of the side web and the middle web is 18 cm, and the thickness of the top and bottom plates is, respectively, 12 cm and 15 cm. The lower structure adopts cylindrical piers with a diameter of 1.5 m. The pier foundation adopts a pile foundation. The cross-sectional layout of the bridge is composed of four pieces of prefabricated small box girders (see Fig. 1). And the elevation view of the bridge is a crossed shape (see Fig. 2).

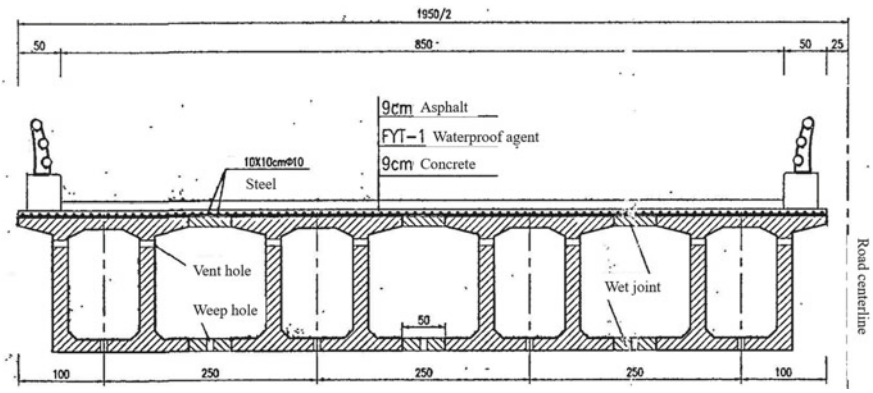

Fig. 1 Cross-sectional view of the bridge

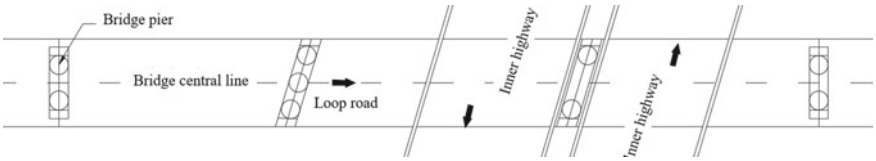

Fig. 2 Elevation view of the bridge (single bridge)

3 Finite Element Model

According to the design data, a full bridge model is established by using the flexible shear lattice method through Midas Civil finite element analysis software, and its force characteristics are calculated and analyzed. This method can simulate the overall stiffness and force behavior of the full bridge more, while reducing the computational workload and taking the computational accuracy and efficiency into account. A total of 1416 main girder elements are used in the full bridge model (see Figs. 3 and 4). Table 1 gives a summary of the physical properties of different materials.

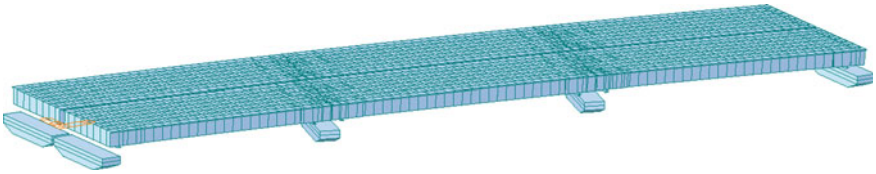

Fig. 3 Spatial geometry model of the bridge

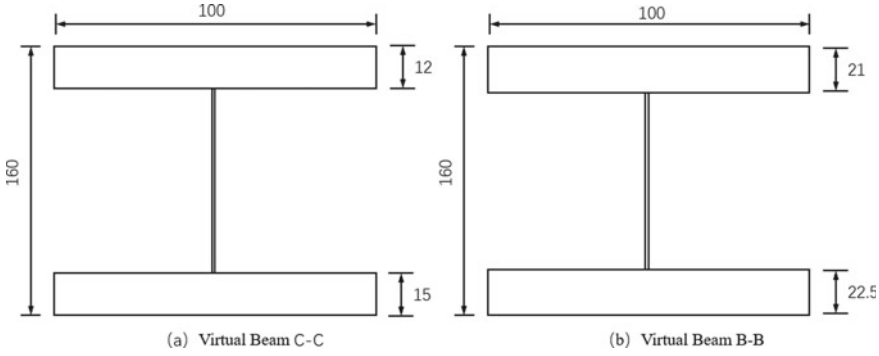

Fig. 4 Virtual beam structures (Unit: cm)

Table 1 Material physical performance index

Materials	Physical index	Parameter	Materials	Physical index	Parameter
Main girder	Compressive design strength	22.4 MPa	Bridge pier	Compressive design strength	13.8 MPa
	Tensile design strength	1.830 MPa		Tensile design strength	1.390 MPa
	Elastic modulus	34,500 MPa		Elastic modulus	30,000 MPa
Cover beam	Compressive design strength	18.4 MPa	Steel strand	Standard strength	1860 MPa
	Tensile design strength	1.650 MPa		Elastic modulus	1.95×10^5 MPa
	Elastic modulus	32,500 MPa		Relaxation ratio	0.03

4 Analysis of Jacking Mechanism

The bridge in this project is a skew bridge with a longitudinal slope. The jacking position is not orthogonal to the bridge central line, so there is a vertical difference between the jacking points from the old bridge to the predetermined height. To ensure contact between the jack and the jacking distribution beam keep each jacking point in the same plane without a void. It is necessary to control the vertical height of jacking to a certain proportion to prevent the jacking deviation from exceeding the allowable value (see Figs. 5 and 6).

4.1 Single-Side Synchronous Jacking

Considering that the absolute synchronization of the jacking process cannot be guaranteed on a construction site, many factors limit the single jacking height, so this section explores the single maximum jacking height during unilateral synchronous jacking, and the right main girder is jacked up with considering the dead load of

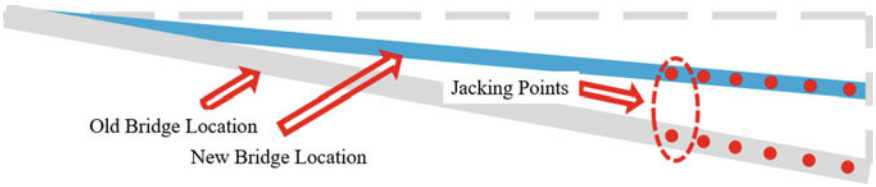

Fig. 5 Vertical position of jacking points

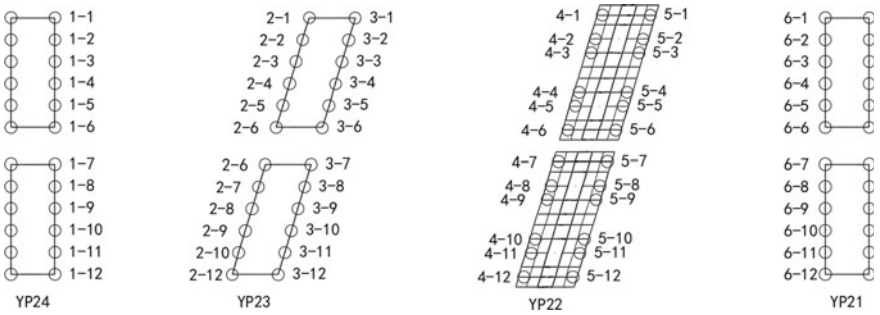

Fig. 6 Vertical layout of jacking points

the main girder and the prestressing force (see Fig. 7). The working cases are set as shown in Table 2.

It can be seen from Table 3 that the maximum tensile and compressive stress of the main girder does not change much during the unilateral synchronous jacking process, and the maximum tensile stress of each girder is within 1 MPa, which is within the

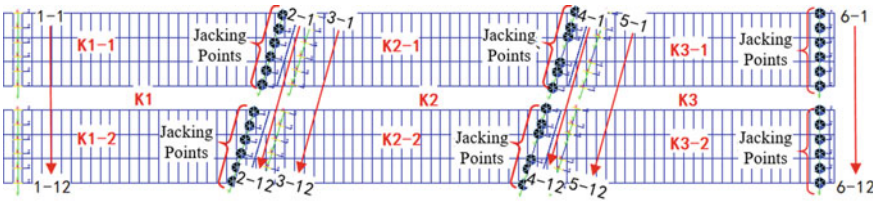

Fig. 7 Jacking position simulation

Table 2 Single-side synchronous jacking cases

Jacking points			Jacking height case No.
2–1 (L1)	4–1 (L1)	6–1 (L1)	1: 10 mm 2: 20 mm 3: 30 mm 4: 40 mm 5: 50 mm 6: 60 mm 7: 70 mm 8: 80 mm 9: 90 mm 10: 100 mm
2–2 (L2)	4–2 (L2)	6–2 (L2)	
2–3 (L3)	4–3 (L3)	6–3 (L3)	
2–4 (L4)	4–4 (L4)	6–4 (L4)	
2–5 (L5)	4–5 (L5)	6–5 (L5)	
2–6 (L6)	4–6 (L6)	6–6 (L6)	
2–7 (L1)	4–7 (L1)	6–7 (L1)	
2–8 (L2)	4–8 (L2)	6–8 (L2)	
2–9 (L3)	4–9 (L3)	6–9 (L3)	
2–10 (L4)	4–10 (L4)	6–10 (L4)	
2–11 (L5)	4–11 (L5)	6–11 (L5)	
2–12 (L6)	4–12 (L6)	6–12 (L6)	

Table 3 Single-side synchronous jacking results (Unit: MPa)

Case No.	Tensile stress of main girder (max)	Compressive stress of main girder (max)	The number of bearing void
1	0.73	10.21	0
2	0.73	10.21	0
3	0.73	10.23	0
4	0.73	10.24	0
5	0.75	10.26	0
6	0.77	10.27	1 (K3)
7	0.78	10.29	2 (K3)
8	0.80	10.30	3 (K3)
9	0.82	10.32	3 (K3)
10	0.83	7.56	3 (K3)

safety reserve of the main girder. When the single jacking height exceeds 60 mm, the temporary jacking support begins to be void to varying degrees. Therefore, it is necessary to strictly control the jacking height during the jacking process for the K3 main girder.

4.2 Single-Point Jacking Analysis

The bridge jacking is caused by the jacking force exerted by the jack at the jacking point, so it is simulated by forced displacement in the model. In this section, jacking each support on one side of each span, the stress change of the main girder is observed. Each jacking point is jacked by 2–10 mm with the interval being 2 mm, considering that the minimum control accuracy error of the jack is 0.1 mm. The jacking points L1, L2, and L3 of each span were selected for analysis due to the symmetry of the jacking points arrangement (see Fig. 8).

Table 4 shows the displacement results of single-point jacking of L1, L2, and L3 from 2 to 10 mm at 2 mm intervals. It can be seen from the table that when the jacking is 2 mm, the number of temporary supports is less, but with the jacking

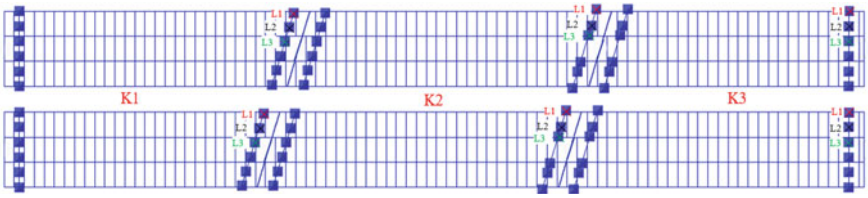

Fig. 8 Separate jacking points arrangement

Table 4 Single-point jacking result (Units: mm, MPa, kN)

Jacking points	Jacking height	Tensile stress of main girder (max)	Compressive stress of main girder (max)	The number of bearing void	Reaction force (max)
L1	2	0.86	10.41	18	1172.58
	4	0.90	10.45	20	1301.28
	6	0.95	10.49	22	1389.13
	8	0.99	10.54	23	1470.81
	10	1.03	7.56	28	1557.23
L2	2	0.73	10.03	2	845.51
	4	0.74	10.01	8	1245.22
	6	0.74	10.06	18	1525.89
	8	0.77	10.09	24	1680.82
	10	0.82	10.14	24	1771.69
L3	2	0.75	10.00	12	1921.54
	4	0.79	9.98	19	2064.79
	6	0.82	10.03	29	2173.03
	8	0.82	10.03	30	2173.03
	10	0.82	10.03	29	2173.03

height increasing of L1, L2, and L3, the void number of temporary supports gradually increases, and the main girder faces the risk of overturning. Therefore, during the jacking process, there is a requirement to strictly control the jacking displacement to avoid the situation of too high jacking. It should be adjusted in time when the temporary supports are emptied during the construction. Meanwhile, the local force of the distribution girder will face the risk of local failure when the reaction force caused by the temporary support lacking is larger. In terms of stress, the maximum tensile stress and compressive stress of the main girder did not change much. And compared with unilateral synchronous jacking, the maximum tensile stress increased, but they were all within the internal force storage range of the main girder.

4.3 Single Jacking Point Void Analysis

As mentioned above, the voiding of the bearing during the jacking process is discussed. Considering the specific conditions in the construction, this section conducts a force analysis on the voiding of a single bearing, and the voiding setting of the specified bearings is shown as L1–L6, respectively (see Fig. 9).

It can be seen from Table 5 that only the L1 support voided will cause other bearings to be emptied, and others do not, so it is necessary to pay more attention to the jacking process. At the same time, it also can be seen that in the voiding

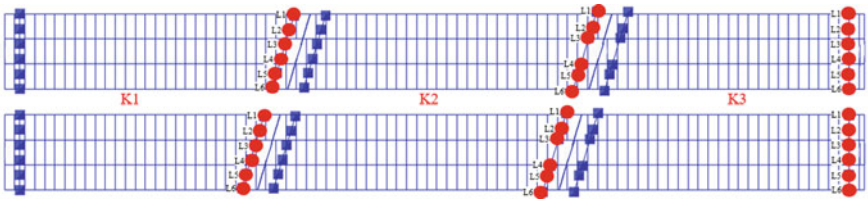

Fig. 9 Appointed bracket with bearing empty

Table 5 Results of appointed bracket with bearing empty (Units: MPa, kN)

Case No.	Tensile stress of main girder (max)	Compressive stress of main girder (max)	The number of bearing void	Reaction force (max)
L1	0.72	9.94	2	1372.16
L2	0.73	10.21	0	853.69
L3	0.73	10.24	0	929.93
L4	0.73	10.19	0	958.48
L5	0.73	10.19	0	871.93
L6	0.74	10.04	0	1004.53

conditions of the six single-point supports, the stress of the main girder does not change much, which is within the safety reserve of the main beam. In sum, the maximum reaction force of the working conditions is relatively uniform except for the L1 support voided, and it will not cause excessive local force. Therefore, the jack pads should be replaced during the jacking process one by one when the height is increased.

5 Jacking Process Scheme

5.1 Bridge Substructure

After jacking up to the design elevation, it is needed to chisel the original cover beams, lengthen the steel, and pour concrete. The renovation design of the old bridge by covering the beam and raising the height can effectively utilize the original structure and reduce the project cost. At the same time, new bridge piers and cover beams are built on one side of the original beam, and steel box beams are hoisted to widen the bridge deck to meet the existing road traffic requirements (see Fig. 10). The soil below the platform is replaced with graded broken stone with a thickness of 1 m. On the foundation of the original platform, the old and new structures are planted and connected, and the concrete platform is poured again, wrapping the tie beams and pier piles (see Fig. 11).

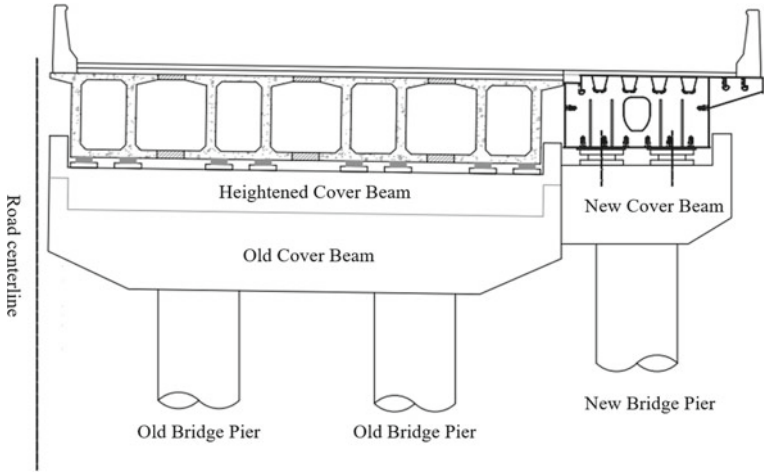

Fig. 10 Reconstruction of bridge piers and cover beams

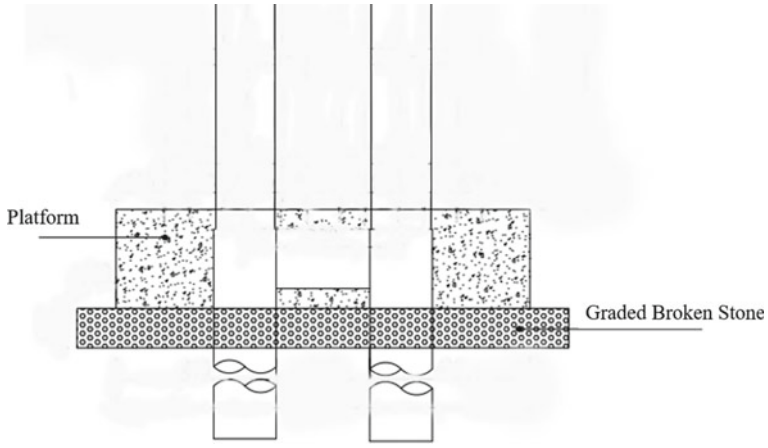

Fig. 11 Reconstruction of pile platform

5.2 Steel Support Structure

The steel support system is connecting the main girder and the bearing platform during the jacking process, and it is the important structure of the entire jacking. At the same time, the stiffness and stability of the steel support are the key factors that determine the success of the jacking. It is necessary to be able to withstand the self-weight load caused by the structure such as the self-weight of the beam, the horizontal load caused by the jack offset in the jacking process, and the temperature load. The whole process maintains the force to meet the overall and local stability

requirements. The steel support system in this paper is composed of supporting steel pipes, transversely connecting steel pipes, oblique connecting members, and temporary pads. The materials used are shown in Table 6.

Considering that the road under the bridge in this paper is inner ring high speed and does not have completely closed working conditions. And two forms of steel support system under the girder are adopted (see Figs. 12 and 13). The main supporting steel pipes are connected to the newly poured platform through the anchor bolt, and the steel pipes are connected through the flange plate. In order to ensure the stability of the steel support system in the jacking process, the B-type steel pipes are connected to the adjacent pier through the hoop.

Table 6 Steel support materials

Materials	Parameter	Materials	Parameter
A-type steel pipe	$\Phi = 30$ cm, $\delta = 1$ cm	16 Mn plate	60 * 60 * 2 cm
B-type steel pipe	$\Phi = 15$ cm, $\delta = 0.8$ cm	16 Mn plate	120 * 120 * 3 cm
C-type steel pipe	$\Phi = 60$ cm, $\delta = 1.2$ cm	Flange plate	$\Phi = 60$ cm
D-type steel pipe	$\Phi = 40$ cm, $\delta = 1.0$ cm	Anchor	M36 * 240

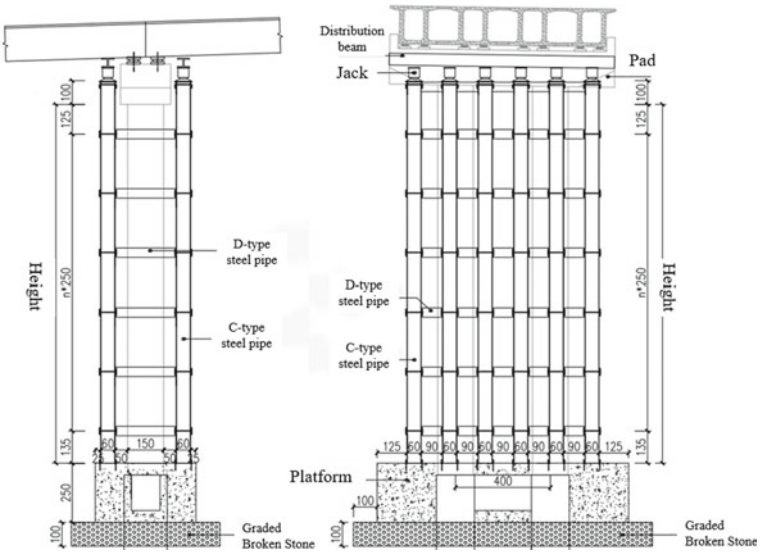

Fig. 12 Steel support structure (A-type)

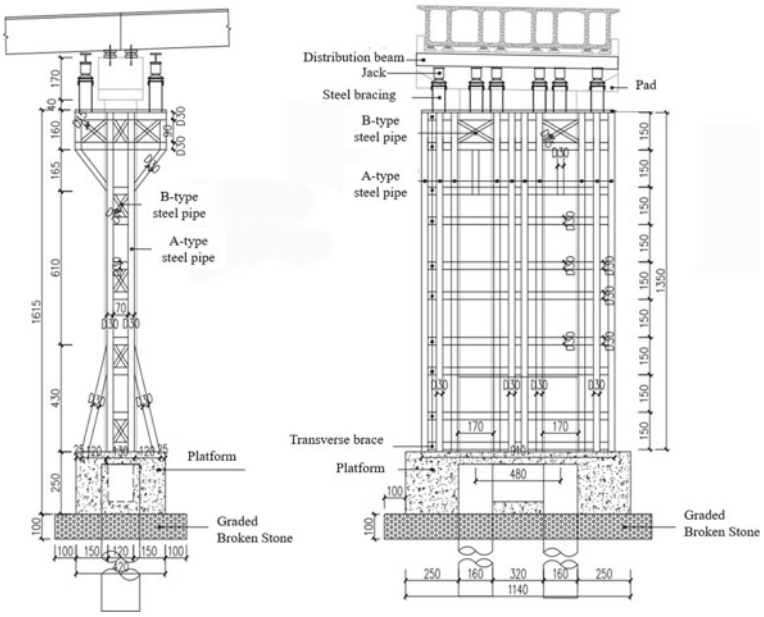

Fig. 13 Steel support structure (B-type)

5.3 PLC Synchronizing Control System

In this paper, the bridge jacking progress needs to strictly control the contents of the main girder, the steel support system under the beam, and the foundation settlement, so as to ensure that the bridge main girder is always in the safe reserve during the jacking process. The conventional jack lifting control system will lead to the settlement of the upper beam with the cylinder closing of the jack, which is difficult to control. At the same time, it will generate additional stress on the beam, resulting in the deformation of the beam. The PLC synchronous control system can make the hydraulic system controlled by a computer, which can fully realize automatic synchronous displacement, and precisely control the change of displacement, reaction force, and load pressure. In the meantime, the cylinder hydraulic one-way valve can prevent the pressure loss of the system and pipeline and protect the effective support of the load.

6 Conclusion

In this paper, the finite element software Midas Civil is used to analyze the whole jacking process of oblique simply bridge with longitudinal slope, and the following conclusions are drawn:

1. The jacking height change of the main girder in the jacking process does not produce the secondary internal force of the structure, and the stress of the main girder changes little, which meets the requirements of the specification.
2. When the unilateral jacking height exceeds 60 mm, the jacking support will be voided to varying degrees, and the adjacent support will have stress concentration.
3. The emergence of uneven jacking will lead to the emptying of jacking bearings and will affect the emptying of adjacent bearings, resulting in the reaction force of some jacks as high as 2000 kN.
4. The void of the bearing has little effect on the stress of the main girder, so the jack can be raised step by step under the condition of maintaining dynamic monitoring.

References

1. Ge XL, Li WY, Jie XC (2013) Jacking technology for a simply supported girder bridge. Appl Mech Mater, 477–478
2. Jinxin L, Xiaowei M, Xin Z (2021) Research on bearing jacking method of steel -concrete composite beam bridge. IOP Conf Ser Earth Environ Science 647
3. Guodong Q, Xin G, Kan R, Jiangjiang T (2021) Research on the application of technology of replacing bridge: bearings without interrupting traffic. J Phys Conf Ser 1865
4. Shen JK (2014) Based on the different specifications of jacking construction of continuous girder bridge reliability analysis. Appl Mech Mater 3309
5. Zhou C, Yan QS, Zheng HB, Wei G (2080) The research of steel bracket jacking experiment in long span continuous beam bridge. Appl Mech Mater 2080
6. Zhang F, Wang Y (2019) Studies on closure jacking force and closure temperature of the continuous rigid frame bridge with V-shaped pier. In: Proceedings of the 2018 7th international conference on sustainable energy and environment engineering (ICSEEE 2018)
7. Cao J (2016) Research on synchronization of jacking up based on programmable logic controller (PLC) to replace bridge bearings. Int J Civil Eng Mach Manuf 1
8. He J, Gao X (2016) Research of synchronous jacking up construction monitoring and control technologies of bridge. In: Proceedings of the 2016 2nd international conference on architectural, civil and hydraulics engineering (ICACHE 2016)
9. Li F, Wu P, Yan X (2015) Analysis and monitoring on jacking construction of continuous box girder bridge. Comput Concr 16
10. Fang YM, Chou TY, Hoang TV, Lee BJ (2019) Automatic management and monitoring of bridge lifting: a method of changing engineering in real-time. Sensors 19
11. Mondal P, DeWolf JT (2007) Development of computer-based system for the temperature monitoring of a post-tensioned segmental concrete box-girder bridge. Comp-Aided Civil Infrastruct Eng
12. Zhao ZM, Wang XL, Chen FJ, Wang ZJ, Yang YJ (2014) Analysis and evaluation on safety of old stone arch bridge based on current specification. Appl Mech Mater
13. Xu C (2015) Integral lifting of a three-span continuous beam bridge. J Perform Constr Facilities
14. Wang J, Zhao J, Li W (2019) The mathematical modeling, simulation, and practice of a multipoint synchronous lifting control case study for bridges. Math Probl Eng
15. Chen Z, Yan QS, Jia BY, Yu XL (2013) Large span continuous girder bridge jacking steel hoop stress analysis. Adv Mater Res
16. Seo J, Yoo WS, Lee U, Kim C, Kang K, Cho H (2016) Case study of a synchronous hydraulic jack-up system for constructing high-rise residential buildings. Can J Civil Eng

17. Tian L, Hao J, Wei J, Zheng J (2016) Integral lifting simulation of long-span spatial steel structures during construction. Autom Constr
18. Qiang ZY, Hua TX, Hua CD, Hai JB (2010) Posture adjustment and control algorithm for integral synchronous lifting of bridge. Adv Mater Res

Geotechnical Engineering and Earthquake Disaster Prevention

Stabilization of Sandy Slopes with Vetiver Grass Using Experimental Method and Mathematical Model

Myrella Surichaqui Contreras, Abeli Rodriguez Oliva, and Rossana Herrera Lopez

Abstract This paper proposes the evaluation of the feasibility of a bioengineering geotechnical solution for the control of natural slope landslides caused by soil susceptibility, because of natural events or human action. The engineering solution with environmental considerations involves using the vetiver plant (*Chrysopogon zizanioides*) to stabilize the natural slope. The methodology applied was the identification of soil characteristics through soil mechanics laboratory tests, knowledge of vetiver grass and slope stability analysis considering the experimental method (EM) and mathematical model (MM). The shear strength parameters obtained in the experimental method consider the cohesion and friction angle resulting from the direct shear test, while the second method only considers the additional cohesion resulting from the mechanical effect provided by the vetiver roots. The results of the research report that, in the experimental method, the safety factor of the global stability presents a smaller increase as the root of the plant grows compared to the mathematical method. Finally, the values of the safety factors obtained from the slope stability analysis modeled in the SLIDE geotechnical software are higher than the minimum values established in the Peruvian EC regulations. 020 Stabilization of soils and slopes under static and pseudo-static conditions.

Keywords Safety factor · Vetiver · Slope stability · Direct shear · Mathematical model

1 Introduction

Landslides on the Peruvian coast are usually recurrent due to natural events or human action [1]. Institutions protecting the safety and well-being of the population in the context of natural disasters have carried out studies expressing numerically the number of areas affected by this problem. The indicators show that there are a total of

M. S. Contreras (✉) · A. R. Oliva · R. H. Lopez
Faculty of Civil Engineering, Universidad Peruana de Ciencias Aplicadas, Lima, Peru
e-mail: u201522348@upc.edu.pe

T. Kang (ed.), *Proceedings of 5th International Conference on Civil Engineering and Architecture*, Lecture Notes in Civil Engineering 369,
https://doi.org/10.1007/978-981-99-4049-3_62

32,036 affected populations, generating losses of material goods and negative environmental impacts [2]. For these reasons, the present research studies the feasibility of using the vetiver plant as an engineering solution to control unstable slopes formed by sandy soil.

Recent research allows identifying solutions with different geotechnical methodologies that are given to the problem according to the global context. On the one hand, among the authors who carried out research applying the experimental method, tested by direct shear in the laboratory on samples of mixed soil with roots in reconstituted and undisturbed conditions, both for clay and sandy soils. They analyzed slope stability in PLAXIS 2D, obtaining as results that the safety factors of sandy slopes with vegetation increased up to 20.6% [3]. So also, in another investigation, performed the direct shear tests on a clayey soil at four depths 0–10, 10–20, 20–30 and 30–40 cm and at three normal stresses equal to 1.0, 2.0 and 3.0 kg/cm^2 concluding from their stability analysis that the soil cohesion and the angle of internal friction of the clayey soil with vetiver can increase up to 119.6% and 81.96%, respectively [4]. Similarly, other authors investigated the root morphology of vetiver grass in sandy soils by measuring root lengths at time intervals to determine shear strength using direct shear tests. They concluded that vetiver can grow up to 97 cm in 3 months in sandy soil and further indicated that the use of this plant increased shear strength [5].

On the other hand, the following researchers developed a mathematical model to estimate the force added to the soil by vetiver roots whose mechanical effect is to increase soil cohesion. Islam et al. developed a mathematical model indicating that the additional shear strength provided by roots is 5.14 the root tensile strength per unit soil area. The relationship obtained between the additional shear strength provided by the roots and the root tensile strength per unit soil area is approximately linear [6]. Based on the same methodology, Badhon et al. developed a mathematical model that increase the shear strength in 5.10 times the tensile stress of root fibers per unit area of soil [7].

Based on the different methodologies used by the previously mentioned authors, this research categorizes the methodologies into experimental and numerical with the objective of comparing their results through the factor of safety (F.S.) using the vetiver plant in its different growth periods to stabilize natural slopes. The results will allow to choose the most viable or optimal method in relation to the evaluation of the limitations of each one.

2 Methodology

2.1 Case Study

Soil sample. The soil was obtained from a field located in the district of Villa Maria del Triunfo, province of Lima, Peru; in which granulometric tests (ASTM D422, [8]) and Atterberg Limits (ASTM D4318, [9]) were performed to determine its soil classification (ASTM D2487 [10]) according to the fines it contains.

Vetiver (Chrysopogon zizanioides). Vetiver is a plant from the Asian continent; among its morphological characteristics is that its roots can grow up to 3 m deep depending on soil conditions and have the property of not being invasive; that is, they grow vertically. Likewise, their fibrous roots contribute to increased resistance to cutting [11]. For this research, the vetiver plantation was extracted from the same field from which the soil samples were obtained. The plant under study obtained a root length of approximately 2 m in 12 months and has been cultivated in an arid climate.

2.2 Direct Shear Test

In the present study, direct shear tests were performed, according to ASTM D3080 [12], for soils with and without roots of the vetiver plant subjected to different normal stresses: 1–2–4 kg/cm^2 with the purpose of determining the variation of the geotechnical parameters of cohesion (c) and friction angle (φ).

Equipment used for the laboratory test. To determine the shear stress of the rooted and unrooted soil samples, they were tested in a direct shearing machine model HM-2560A containing a circular box 5 cm in diameter and 2.5 cm high. Specimens extracted from 30 to 80 cm depth were tested under consolidated and drained conditions (CD).

Sample preparation. In the case of the sample without roots, the soil was remodeled maintaining its initial conditions obtained in the field. In the case of the samples with vetiver, the soil was remolded considering a soil-vetiver ratio of 60% and 40%, respectively, according to what was observed and quantified from the materials extracted in the tubular molds in the field. In addition, 2.5 cm of root length were cut to reconstitute the sample, as shown in Fig. 1.

2.3 Mathematical Model

The mathematical model is a series of empirical formulas that allow direct determination of the additional cohesion based on the morphological characteristics of the

Fig. 1 Vetiver roots

root [11]. The equations for the calculation of the additional cohesion are expressed below.

Root tensile strength. The relationship between root tensile strength and diameter is expressed in the following equation, where T_r is the root tensile strength in MPa, and D is the root diameter in millimeters.

$$T_r = 16.95 \times D^{-0.60} \text{ (MPa)} \tag{1}$$

Root Area Ratio (RAR). Area ratio refers to the ratio of root section area along the area of the soil cutting plane, where RAR is the area ratio in percent, and T is the growing period in months.

$$\text{RAR} = 0.00055T^2 + 0.00993T \text{ (\%)} \tag{2}$$

Additional cohesion due to the presence of roots. Based on the above equations, the additional cohesion derived from the root resistance is obtained.

$$c_r = 1.2T_r \times \text{RAR (kPa)} \tag{3}$$

3 Results and Analysis

3.1 Classification and Sample Parameters

Table 1 shows the soil classification of the tested sample which, according to the Unified Soil Classification System (USCS), was found to be poorly graded sand (SP) with 0.10% gravels, 95.92% sands and 3.98% fine fractions.

Table 1 Results of the granulometric test and classification according to USCS

USCS classification	Granulometry (%)		
SP	Coarse fractions	Gravels	0.10
		Sands	95.92
	Fine fractions		3.98

Table 2 Results of the experimental method

Type of sample	Condition	Test mode	Number of tests	Age (months)	Shear strength parameters	
					Cohesion (c) kPa	Friction angle (φ)
SP	Without vetiver	Consolidated drained (CD)	1	–	2.94	38.6
SP	With vetiver	Consolidated drained (CD)	3	6	29.42	39
				9	30.4	39.6
				12	32.36	40

3.2 Experimental Method (EM)

Four direct shear tests were performed for soils with and without vetiver, the results of which are presented in Table 2. The test modality used was direct consolidated drained shear (CD).

For the soil without vetiver, the results show that the soil has a cohesion of 0.03 kg/cm^2 and a friction angle of 38.6°; while for the soil-vetiver system, there are cohesion results of: 0.30–0.31–0.33 kg/cm^2 and friction angles of: 39°–39.6°–40° at times 6, 9 and 12 months, respectively.

From the results, we have that the soil after being tested with vetiver roots at different times presents an increase in the shear strength parameters c and φ due to the fact that the presence of vetiver roots has allowed the generation of an additional shear strength of the soil.

3.3 Mathematical Model (MM)

After measuring the diameters, with the Vernier calibrator instrument, of approximately 30 roots, we proceeded to develop the equations of the method mentioned to obtain the additional cohesion (C_r). Table 3 shows a summary of the results for each item.

The additional cohesion for the time of 12 months is 0.40 kg/cm^2; while the angle of internal friction (φ) is not affected by root reinforcement [10]. From the results, it

Table 3 Additional cohesion (C_r) of vetiver root (using the empirical formula of Voutipreux et al. [11])

Age (months))	Diameter, D (mm)	Tensile Strength, T_r (Mpa)	Root area ratio (RAR)	Additional cohesion, C_r	
				(kPa)	(kg/cm^2)
6	0.83	18.9	0.079	18.03	0.18
9	0.93	17.7	0.134	28.42	0.29
12	1.03	16.6	0.198	39.59	0.40

is evident that the relation of root diameters is directly proportional to the additional cohesion.

3.4 Slope Stability

Slope stability analysis without vetiver. The static and pseudo-static analysis was performed in the SLIDE program. For this purpose, the following parameters were entered: specific weight of 15.66 kN/m^3, cohesion of 2.94 kN/m^2 and friction angle of 38.6°; obtaining as a result the safety factor of global stability. On the one hand, the static analysis results that the safety factor by the simplified Bishop's method is 1.382 which, when verified by the CE 0.20 standard [13], does not meet the minimum required factor of 1.50. On the other hand, the pseudo-static analysis requires the seismic loading, and the value of the maximum horizontal acceleration is 0.20. This factor is the result of 50% of the PGA acceleration [14], which is obtained from the acceleration map [15] located on the coast of Lima, Peru, resulting in a safety factor for the simplified Bishop's method of 1.101 which, when verified by the EC standard 0.20, does not meet the minimum required factor of 1.25. In summary, the slope is unstable.

Slope stability analysis with vetiver. In the SLIDE program, the slope reinforced with vetiver roots is schematized as a layer represented in Fig. 2. The simulation is developed under static and pseudo-static conditions to obtain the global stability factors of safety by Bishop's simplified method. Table 4 summarizes the parameters of the rooted soil in different periods of vetiver root growth corresponding to both methods of this study. It should be noted that after observing the root growth of the vetiver plant in periods of 6, 9 and 12 months, the depth of the vetiver roots that perpetrated the sandy soil was measured, which were 0.8–1.5–2 m, respectively.

Static analysis. Figure 3 shows an increase in the safety factor in relation to the growth time of the vetiver roots for both methods, whose values are greater than 1.5, thus obtaining a stable slope according to the Peruvian standard CE 0.20. The mathematical model shows that the safety factor in the period from 6 to 9 months increases by 25.29% and in the period from 6 to 12 months it increases by 48.28%.

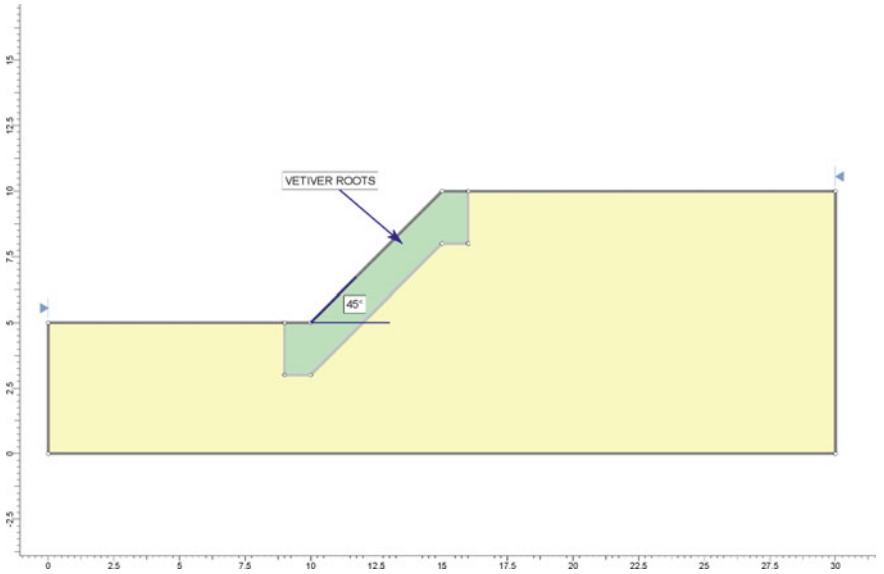

Fig. 2 Diagram of the slope reinforced with vetiver roots

Table 4 Parameters entered in the SLIDE program at different growth periods

Method	Properties	Unit	Age (months)		
			6	9	12
Experimental (EM)	Specific gravity	kN/m^3	15.59	15.67	15.70
	Cohesion	kN/m^2	29.42	30.40	32.36
	Friction angle	degrees	39.0	36.6	40.0
Mathematical (MM)	Specific gravity	kN/m^3	15.59	15.67	15.70
	Cohesion	kN/m^2	20.59	31.38	42.17
	Friction angle	degrees	38.6	38.6	38.6

Note The slope of the modeled slope is 45°

Similarly, in the experimental model, it is observed that in the 6–9 months period it increases by 17.30% and in the 6–12 months period it increases by 29.73%. In summary, at 12 months, it is interpreted that the result of the MM is 7.5% more than the EM.

Pseudo-static analysis. In this research, to know the behavior of the soil with vetiver roots under external acting forces, a seismic load was applied considering the location of the sandy soil. In this case, the value of the maximum horizontal acceleration is 0.20 for slopes located on the coast of Lima. Peru. The results of the analysis are detailed in Fig. 4, which when verified by the CE 0.20 standard complies with the minimum required factor of 1.25, thus obtaining a stable slope. The mathematical

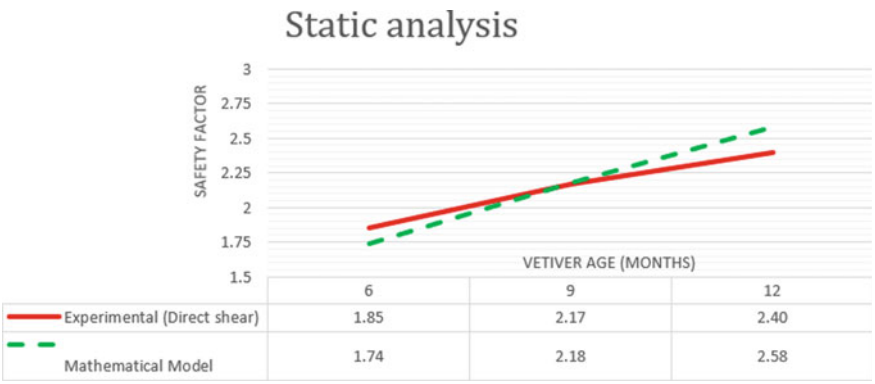

Fig. 3 Safety factor versus vetiver age

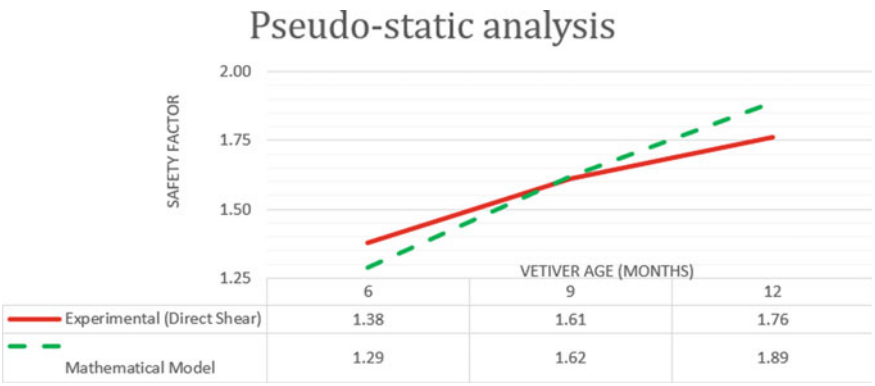

Fig. 4 Safety factor versus vetiver age

model shows that the safety factor in the period from 6 to 9 months increases by 25.58% and in the period from 6 to 12 months it increases by 46.51%. Similarly, in the experimental model, it is observed that in the 6–9 months period it increases by 16.67% and in the 6–12 months period it increases by 27.54%. In summary, at 12 months, it is interpreted that the result of the MM is 7.39% higher than the EM.

4 Conclusions

The growth and functionality of vetiver plants is a function of soil properties. In this case, the sandy soil was key to study the root development of the vetiver plant because its type is highly susceptible to the problem of slope slides. For this reason, it was evaluated in software to validate the feasibility of using vetiver to control landslides

in critical soils, obtaining as a result that the slope is stable even considering the seismic acceleration.

The additional cohesion obtained from the mathematical model made it possible to identify that the roots provide adherence to the soil, preventing the shear zone from failing easily. This is explained by the fact that the average diameter of the roots increases as a function of plant growth time, and this directly affects the tensile strength of the roots. In addition, the length reached by the roots of the vetiver plant provides remarkable resistance to shearing, as evidenced by the safety factors obtained from the evaluation of the overall stability of the slope.

The result of the overall stability of the slope reinforced with vetiver plant in a one-year growth period with the MM is 7.5% more than with the ME in static state and 7.39% in pseudo-static state. The percentage differentiation between methods is mainly due to existing limitations. In relation to the experimental method, the limiting factor is the scale on which it is developed, and in relation to the mathematical method, its application is restricted to maintaining the angle of internal friction uniform, since it is not affected by the presence of roots, according to the authors of the model.

Acknowledgements This research was supported by the agronomist Alois Kennerknecht, member of the Red Vetiver Perú and promoter of the use of vetiver as a natural, economical, and long-lasting solution to multiple problems.

References

1. Servicio Nacional de Meteorología e Hidrología del Perú. https://hdl.handle.net/20.500.12542/261. Last accessed 25 Aug 2022
2. Instituto Nacional de Defensa Civil Homepage. https://www.indeci.gob.pe/direccion-politicas-y-planes/compendios-estadisticos/compendios/2020-2/. Last accessed 25 Aug 2022
3. Badhon FF, Islam MS, Islam MA (2021) Contribution of Vetiver root on the improvement of slope stability. Indian Geotech J 51(4):829–840
4. Hamidifar H, Keshavarzi A, Truong P (2018) Enhancement of river bank shear strength parameters using Vetiver grass root system. Arab J Geosci 11(20)
5. Islam MS, Arif ZU, Badhon FF, Mallick S, Islam T (2016) Investigation of Vetiver root growth in sandy soil. In: BUET-ANWAR ISPAT 1st Bangladesh civil engineering SUMMIT 2016, BUET. Bangladesh
6. Islam MS, Badhon FF (2020) A mathematical model for shear strength prediction of vetiver rooted soil. In: Hambleton JP, Makhnenko R, Budge AS (2020) Geo-congress 2020, American Society of Civil Engineers (ASCE), vol 2020-February, pp 96–105. Geotechnical Special Publication, Minneapolis
7. Badhon FF, Islam MS, Islam MA, Arif MZU (2021) A simple approach for estimating contribution of vetiver roots in shear strength of a soil–root system. Innov Infrastruct Solutions 6(2):1–13
8. ASTM Homepage. https://www.astm.org/d0422-63r07e01.html. Last accessed 25 Sept 2022
9. ASTM Homepage. https://www.astm.org/d4318-17e01.html. Last accessed 25 Sept 2022
10. ASTM Homepage. https://www.astm.org/d2487-17.html. Last accessed 25 Sept 2022
11. Voottipruex P, Bergado D, Mairaeng W, Chucheepsakul S, Modmoltin C (2008) Soil reinforcement with combination roots system: a case study of vetiver grass and *Acacia mangium* willd. Lowland Technol Int 10(2):56–67

12. ASTM Homepage. https://www.astm.org/d3080-04.html. Last accessed 25 Sept 2022
13. Norma CE0.20. http://www3.vivienda.gob.pe/dnc/archivos/Estudios_Normalizacion/Normalizacion/normas/NORMACE020.pdf. Last accessed 25 Sept 2022
14. Instituto Geofísico del Perú. https://repositorio.igp.gob.pe/handle/20.500.12816/783. Last accessed 25 Sept 2022
15. Instituto Geofísico del Perú. https://sigrid.cenepred.gob.pe/sigridv3/storage/biblioteca//11603_estudio-del-peligro-sismico-en-la-zona-de-los-acantilados-de-la-costa-verde-lima.pdf. Last accessed 25 Sept 2022

ANN-Based Seabed Soil Type Classification Economical Impact for Subsea Trenching Process

Khaled A. Hassan, Elbadr O. Elgendi, Ahmed S. Shehata, and Mohamed I. Elmasry

Abstract Applications that involve image analysis frequently make use of an artificial neural network (ANN). It has been established that it is effective in classifying the types of soil that are found on the seabed, which would facilitate the process of trenching for underwater flow lines (pipelines and cables) as subsea trenchers are used to protecting the flow lines, but it still needs to be investigated from an economic point of view. This research is the economic study of utilizing ANN to classify the different types of seabed soil for use in the underwater trenching process. This economic analysis was carried out by computing the difference between the energy consumption levels of two jet trenchers before and after the implementation of this technology. The findings of this study indicated that the use of ANN image analysis successfully reduced trenchers' energy consumption by 14–22%, which unquestionably cause a reduction in the overall cost of the trenching process.

Keywords Soil classification · Jet trenching · Offshore flowlines · Flowlines construction machine learning · ANN · Economical study · Energy · Cost estimation

1 Introduction

With the increase in demand for offshore structures like oil, gas, and wind farms, flow lines such as submarine pipelines and cables have seen also an increase in demand. These flow lines are being laid on the seabed. Due to the hazards that

K. A. Hassan (✉) · E. O. Elgendi · M. I. Elmasry
Construction and Building Engineering Department, College of Engineering and Technology, Arab Academy for Science and Technology and Maritime Transport (AASTMT), Alexandria, Egypt
e-mail: khaled.hassan5@student.aast.edu

A. S. Shehata
Marine Engineering Department, College of Engineering and Technology, Arab Academy for Science and Technology and Maritime Transport (AASTMT), Alexandria, Egypt

T. Kang (ed.), *Proceedings of 5th International Conference on Civil Engineering and Architecture*, Lecture Notes in Civil Engineering 369,
https://doi.org/10.1007/978-981-99-4049-3_63

face these lines, they need protection from these hazards. Submarine flow lines can be seriously damaged by external hazards such as industrial fishing activities, ship anchors, icebergs, and containers that fall from ships [1, 2]. During a study conducted by the U.S. Department of Energy on 1061 submarine cables accidents, it was found that only 18% were damaged due to internal causes, while the major part 82% were damaged due to external events [3]. To protect flow lines, they must be buried in a trench under the seabed [4–9]. Subsea trenches are effective in protecting the flowlines from external hazards, as if they are not protected in an excavated trench, they can be seriously damaged [2, 3]. Jet trenchers are typically used to excavate the subsea trenches [10]. To execute a subsea trench using the jet trenching method, high-pressure water is jetted through nozzles, while the amount of pressure is decided to be suitable for excavation in the hardest type of soil along the flowline trench route [1].

The amount of water pressure may be suitable for trenching in the hardest type of soil along the trenching route, although the types of soil change from hard to soft and vis-versa along that route which leads to an unstraight trench bed causing unwanted free spans that would lead to bending stress on the flow line. The problem of using the maximum jetting pressure of the trencher leads to some challenges, which are the high cost of energy consumed by the trencher leading to higher construction cost, and the extra bending stress due to the free spans leading to higher maintenance cost. Hard soils like rock or clay would require high pumping power to be trenched, while soft soils like sand and silt require less pumping power [11]. All of that comes from that engineers cannot make fast soil classification for the seabed soil, which leads to the key challenge, the seabed soil classification [12].

Seabed soil classification is the base for trenching operations. To classify the type of seabed soil, engineers must collect samples from the seabed using any of the known seabed sampling equipment and then perform laboratory tests on these samples [13]. Although the test results may be reliable, this technique is time-consuming. The sampling technique gets more complicated and time-consuming as trenches are excavated at depths of thousands of meters below the sea surface, raising the cost of the operation [10]. Conventional soil classification methods are not effective enough in underwater trenching procedures because they do not correctly estimate the length of each soil type and rely on human labor, resulting in lower accuracy. So, there must be a quick technique to classify soil at that depth without increasing the project's overall cost.

Artificial neural network (ANN) is a machine learning technique that is being used for image processing [14–17]. Soil classification can be simplified by using image processing [18]. The process of classifying soil types by machine learning techniques has seen a rise in the last years [19]. Much research have been conducted on soil classification by image analysis. Although Rao's (2016) research on image processing for soil classification provides useful information for speedily identifying different types of soil, his findings cannot be applied to underwater soil classification because they were not developed on submerged soils [17]. An automated system for soil classification using image processing was developed by Chandan (2019) in MATLAB; however, it was not trained to classify underwater soils [15]. While

Hassan et al. (2022) have studied the underwater soil classification using ANN image analysis, they have reused a pretrained ANN in MATLAB and retrained it to be able to classify new types of images, this ANN takes an image of the underwater soil as input then analysis this image and finally gives the output which is the soil type with an accuracy reached to 96%, and their results shown that the use of such technology in that field would enhance the subsea trenching process by making a fast soil classification, reducing the free spans in the subsea trenches and increasing the automation in the subsea trenching process [20]. Although the valuable results of Hassan's research about the use of ANN in the subsea trenching process have not included the economic impact of using such technology in this field, which is the aim of this research.

By classifying the seabed soil type, the trencher would be able to change the jetting pressure to be suitable for trenching in every type of soil, which would lead to an almost straight trench bed [20]. Overall, this approach has reduced human control while increasing automation and, as a result, lowering the process's error rate. As a result, this technology would reduce the time spent on soil classification by conventional methods, save money throughout the construction and operation phases of underwater flowlines, and improve the underwater trenching process overall [20].

Costs for flow lines are often broken down into three categories: material, construction, engineering and inspection [21, 22]. The cost of laying offshore flowlines is usually proportionate to the overall time spent on the work, which includes mobilization and flowline laying time [23]. The construction cost consists of vessel day rate, mobilization, and demobilization, laying of flowline, trenching, survey, etc. [23].

This research aims to study how much cost reduction would be achieved in underwater flow line trenching by studying the economics of using ANN in seabed soil classification. In this research, the cost of energy consumed by jet trenchers will be analyzed. This research has a more specific scope that is studying the difference in trenchers' power consumption between the two approaches, the use of maximum jetting pressure of the trencher along the trenching route and using variable jetting pressure depending on the type of seabed soil that is being analyzed by the ANN in which the trencher is excavating.

2 Methodology

Based on the aforementioned, the subsea trenching process is typically done by jet trenchers. To achieve our main objective, a comparison of energy consumption between the two approaches would be done. The first one is using the maximum pumping power of the trencher, and the second is using a variable pumping power according to the type of seabed soil in which the trencher is excavating. Firstly, information about the jet trenchers in the trenching market has been gathered. Then perform an energy consumption estimation for both approaches. Figure 1 illustrates the outline of this research's methodology.

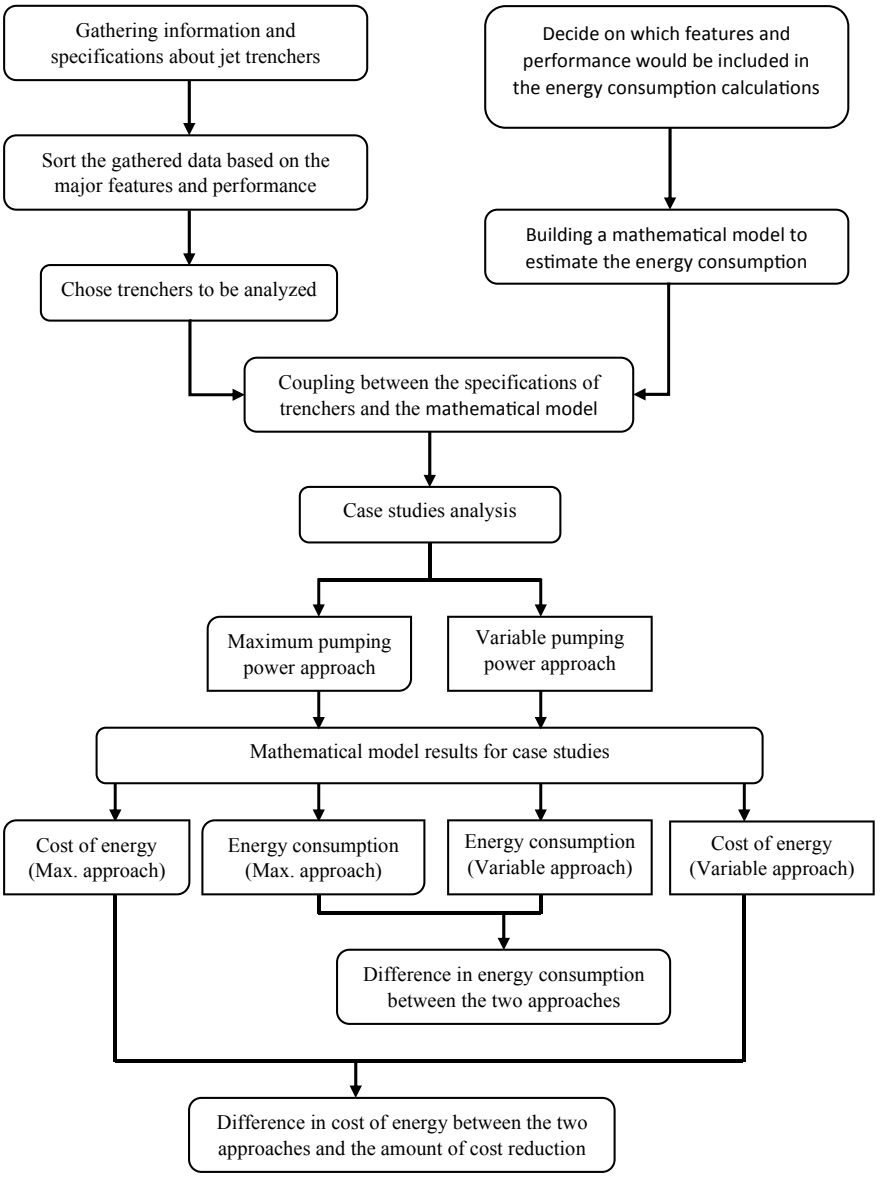

Fig. 1 Outline of the research's methodology

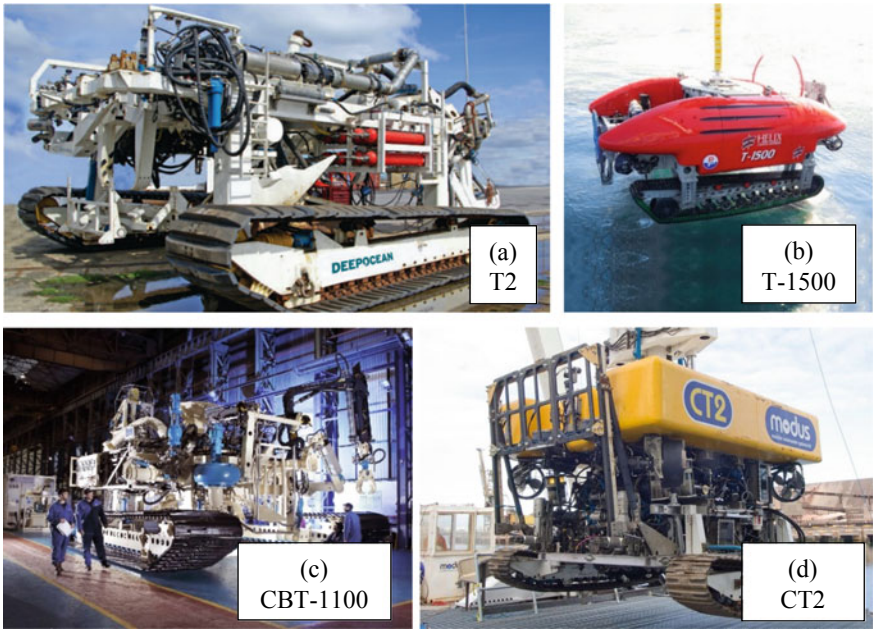

Fig. 2 Remotely operated vehicles (ROVs) jet trenchers used in subsea trenching operations: **a** T2 jet trencher from Deepocean (Photograph source: Machine specification sheet [24]); **b** T-1500 jet trencher from Helix (Photograph source: Machine specification sheet [25]); **c** CBT-1100 jet trencher from SMD (Photograph source: Machine specification sheet [26]); **d** CT2 jet trencher from Modus (Photograph source: Machine specification sheet [27])

2.1 Jet Trenchers in the Market

Many companies in the market develop subsea trenchers such as soil mechanics dynamics (SMD), MODUS, Helix, Reef Subsea, and Deepocean. Every company has several trencher models. Figure 2 shows some of the most common jet trenchers in the market.

2.2 Sort the Gathered Trenchers' Data

Many jet trenchers' specifications have been collected from operators' Web sites and specifications sheets. The major features and performance indicators of regularly used waterjet trenching machines are summarized in Table 1.

Table 1 Major features and performance indicators of regularly used waterjet trenching machines

Available models	Jetting specification				Machine capabilities				Operators
	Installed power (kW)	Pump (kW)	Flow rate (m^3/h)	Jetting pressure (bar)	Operation depth (m)	Soil condition	Burial depth (m)	Trenching speed (m/h)	
CBT-800	2 × 300	2 × 200	600 per sword @10 bar	10–15	1000	All sands Clays from 10 to 400 kPa Rock from 10 to 400 kPa	2 max	0–250	Soil machine dynamics SMD
CBT-1100	2 × 400	2 × 300	800 per sword @10 bar	10–15	1000	All sands Clays from 10 to 4000 kPa Rock from 1 to 40 MPa	3 max	0–250	Soil machine dynamics SMD
CBT-2100	4 × 400	2 × 300	800 per sword @10 bar	10–15	1000	All sands Clays from 10 to 1000 kPa Rock from 1 to 80 MPa	3 max	0–250	Soil machine dynamics SMD
CBT-3200	6 × 400	2 × 400	–	–	1000	All sands Clays from 10 to 1000 kPa Rock from 1 to 80 MPa	2.5	0–250	Soil machine dynamics SMD
CT-1	–	1 × 180	–	5	2500	Sands to medium strength clay	3 max	2000	MODUS
CT-2	–	1 × 300	–	5	3000	Suitable for a range of soil types, including sands and very soft to soft clays	2 max	3000	MODUS
T-1200	–	3 × 281	1050–1800	8–16	3000	Sand, silt and gravel to stiff clay	3 max	780	Helix

(continued)

Table 1 (continued)

Available models	Jetting specification				Machine capabilities				Operators
	Installed power (kW)	Pump (kW)	Flow rate (m^3/h)	Jetting pressure (bar)	Operation depth (m)	Soil condition	Burial depth (m)	Trenching speed (m/h)	
T-1500	281	2 × 281	960–4200	1–20	1000	Sand, silt and gravel to stiff clay	3 max	780	Helix
Q-1000	–	2 × 350	1250	15	2000	Sand to stiff clay	3 max	–	Reef Subsea
T2	–	520	1850	4.5	1500	Suitable for a range of soil types, including sands and very soft to hard clays	3	300	Deepocean

2.3 Building a Mathematical Model

A mathematical model has been built to estimate the energy consumption of different models of jet trenchers in different types of soil. This model has been constructed to estimate the energy consumption of the trenchers along the trenching route considering the distance, seabed soil type, pump power (kW), trencher power (kW), speed of trenching (km/h), and time of trenching (h). The mathematical model is shown in Tables 2 and 3. The time prediction formula is given as:

$$T = D/S \tag{1}$$

where T is the time of trenching; D is the distance of trench of one soil type; S is the trenching speed. While the energy estimation formula is given as:

$$E = PT \tag{2}$$

where E is the energy consumed by the jet trencher; P is the power of which the trencher is using, pumping power and power used by other tools on the trencher such as cameras, lights, and sensors; T is the time of trenching.

2.4 Energy Consumption Estimation (Case Study)

Two jet trenchers would be chosen as a case study to estimate their energy consumption in a trenching route. The two trenchers are CBT-110 from SMD and T-1500 from Helix, as seen in Fig. 2. A trenching route of ten kilometers in length has been assumed. The trenching route consists of different types of soil.

3 Results and Discussion

For the estimation of power consumption, calculations have been done for two jet trenchers. After that, the cost of energy has been calculated, and the cost of every kWh has been assumed to be 0.25 USD. Trenchers CBT-1100 from SMD and T-1500 from Helix are the two examples. Some key specifications have been gathered for these trenchers like pumping power, operation depth, trenching speed, and fixed power that is used for powering tools like cameras, sensors, and lights.

The SMD CBT-1100 jet trencher is using 2 pumps of 300 kW, uses 200 kW for other tools, can operate at depths of 1000 m, and can reach up to 250 m/h of trenching speed. Table 2 shows the results of CBT-1100 estimations. Figures 3 and 4 show the comparison of energy consumption for both approaches, while Figs. 5 and 6 show the cost of energy consumption. After these estimations, it was indicated that the new

Table 2 SMD CBT-1100 jet trencher estimations

Distance		1st km	2nd km	3rd km	4th km	5th km	6th km	7th km	8th km	9th km	10th km
Subsea soil type		Sand	Sand	Clay	Clay	Clay	Rock	Rock	Clay	Clay	Sand
Max. pumping power	Pump power (kW)	600	600	600	600	600	600	600	600	600	600
	Fixed trencher power (kW)	200	200	200	200	200	200	200	200	200	200
	Time of trenching (h)	10	10	10	10	10	10	10	10	10	10
	Energy consumption (kWh/km) Max. pumping power	8000	8000	8000	8000	8000	8000	8000	8000	8000	8000
	Energy cost ($/km) Max. pumping power	2000	2000	2000	2000	2000	2000	2000	2000	2000	2000
Variable pumping power	Pump power (kW)	400	400	500	500	500	600	600	500	500	400
	Fixed trencher power (kW)	200	200	200	200	200	200	200	200	200	200
	Time of trenching (h)	10	10	10	10	10	10	10	10	10	10
	Energy consumption (kWh/km) Variable pumping power	6000	6000	7000	7000	7000	8000	8000	7000	7000	6000
	Energy cost ($/km) Variable pumping power	1500	1500	1750	1750	1750	2000	2000	1750	1750	1500

proposed approach has saved 14% of the energy used by the trencher, which would lead to a 14% cost reduction in the cost of energy.

The Helix T-1500 jet trencher has two 281 kW pumps, utilizes 281 kW for other tools, can trench at depths of 1000 m, and has a trenching speed of up to 780 m/h. The results of T-1500 estimations are shown in Table 3. Figures 7 and 8 illustrate the energy consumption comparison for both systems, while Figs. 9 and 10 indicate

Table 3 Helix T-1500 jet trencher estimations

Distance		1st km	2nd km	3rd km	4th km	5th km	6th km	7th km	8th km	9th km	10th km
Subsea soil type		Sand	Sand	Sand	Sand	Gravel	Clay	Gravel	Sand	Sand	Sand
Max. pumping power	Pump power (kw)	562	562	562	562	562	562	562	562	562	562
	Fixed trencher power (kW)	281	281	281	281	281	281	281	281	281	281
	Time of trenching (h)	10	10	10	10	10	10	10	10	10	10
	Energy consumption (kWh/km) Max. pumping power	8430	8430	8430	8430	8430	8430	8430	8430	8430	8430
	Energy cost ($/km) Max. pumping power	2108	2108	2108	2108	2108	2108	2108	2108	2108	2108
Variable Pumping Power	Pump power (kW)	300	300	300	300	400	562	400	400	400	400
	Fixed trencher power (kW)	281	281	281	281	281	281	281	281	281	281
	Time of trenching (h)	10	10	10	10	10	10	10	10	10	10
	Energy consumption (kWh/km) Variable pumping power	5810	5810	5810	5810	6810	8430	6810	6810	6810	6810
	Energy cost ($/km) Variable pumping power	1453	1453	1453	1453	1703	2108	1703	1703	1703	1703

the cost of energy use. Following these calculations, it was discovered that the new recommended approach saved 22% of the energy required by the trencher, resulting in a 22% savings in energy costs.

Figure 11 shows the results of changing the trenching speed on the energy consumption for the Helix T-1500 trencher. It illustrates that the higher the trenching speed, the lower the energy consumption of the trencher.

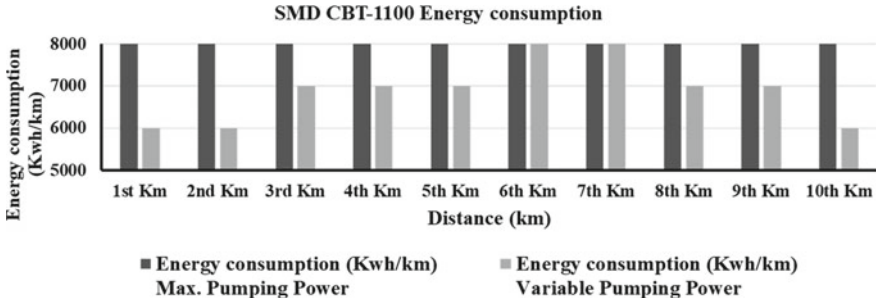

Fig. 3 SMD CBT-1100 energy consumption estimation every kilometer for both scenarios

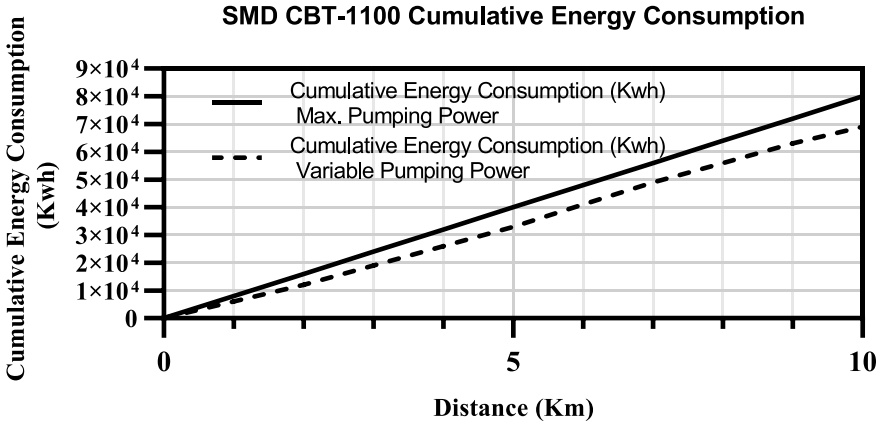

Fig. 4 SMD CBT-1100 cumulative energy consumption estimation for both scenarios along the 10 km trenching route

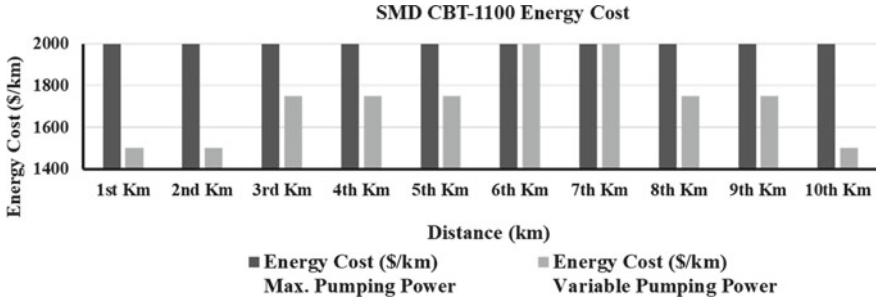

Fig. 5 SMD CBT-1100 energy cost estimations for both scenarios every kilometer

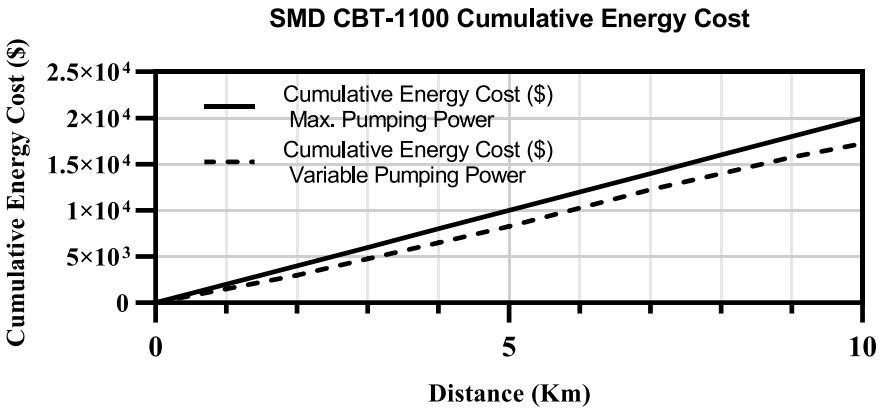

Fig. 6 SMD CBT-1100 cumulative energy cost estimations of energy for both scenarios along the 10 km trenching route

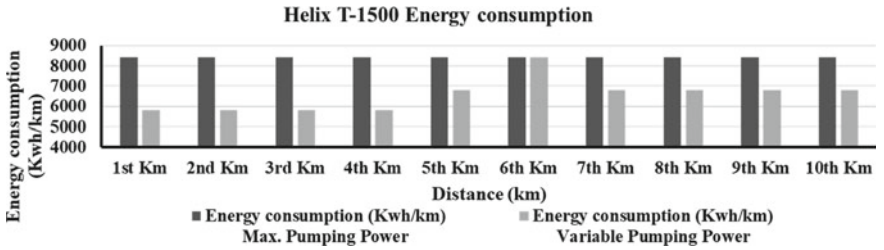

Fig. 7 Helix T-1500 energy consumption estimation every kilometer for both scenarios

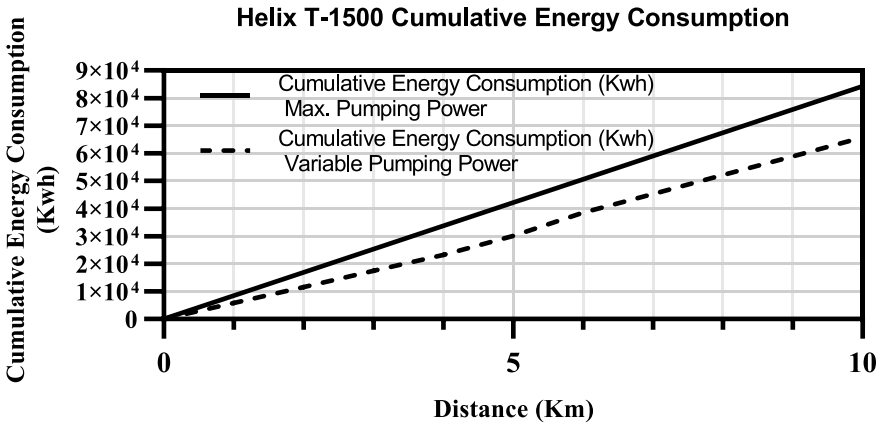

Fig. 8 Helix T-1500 cumulative energy consumption estimation for both scenarios along the 10 km trenching route

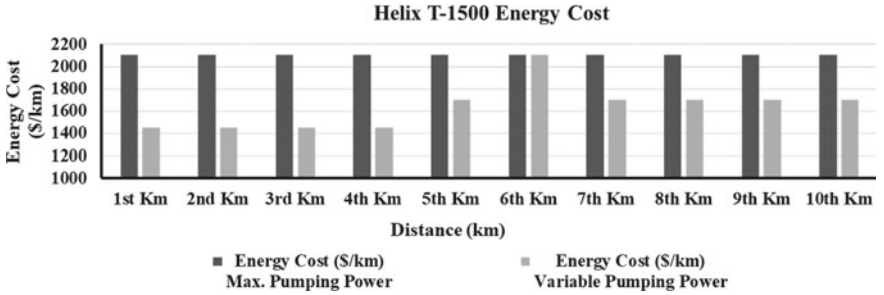

Fig. 9 Helix T-1500 energy cost estimations for both scenarios every kilometer

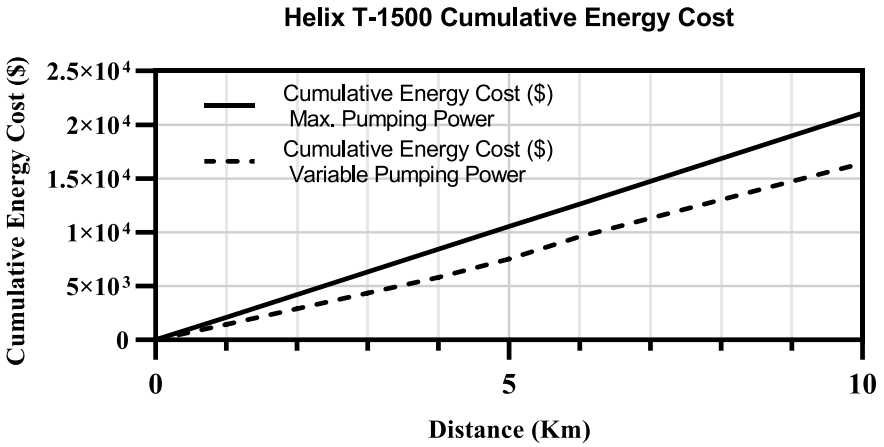

Fig. 10 Helix T-1500 cumulative energy cost estimations of energy for both scenarios along the 10 km trenching route

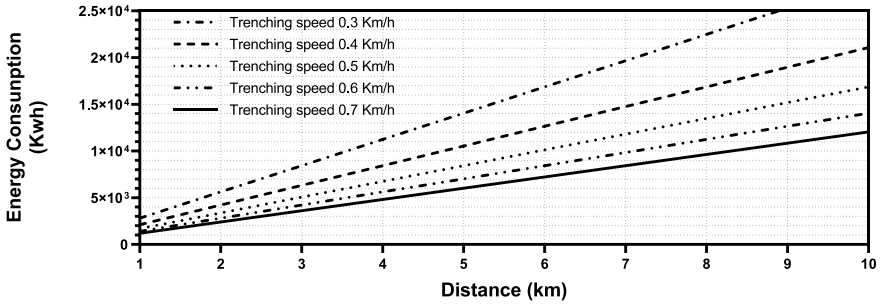

Fig. 11 Cumulative energy consumption for trenching speeds of 0.3, 0.4, 0.5, 0.6, and 0.7 km/h

Based on the aforementioned calculations, it was obvious that the new proposed approach of using ANN for seabed soil classification would decrease energy consumed by the trencher resulting in decreasing the cost of trenching process which is a part of the construction cost of any flow line laying project. Also, this approach would decrease the bending stress on the flow line, which would affect the maintenance in the operation phase of the flow line, as that would lower the probability of failures that are caused by bending stress over the flow line.

4 Conclusion

An economical study has been introduced in this research for a seabed soil classifier based on ANN. The economical study has been done through the estimation of the energy consumption of two jet trenchers before and after using this technology, the jet trenchers are SMD CBT-1100 and Helix T-1500. A mathematical model has been developed for the estimation purpose of a trenching route of a ten kilometers distance with different types of seabed soils (sand, clay, and rock) considering the power of the trencher, speed of trenching, etc. According to the findings of the research, the application of the proposed technology would result in a reduction in the overall cost of the construction of the flowlines. This would be accomplished by lowering the cost of trenching, which would in turn reduce energy consumption by 14% for the SMD CBT-1100 jet trencher and by 22% for the Helix T-1500 jet trencher.

References

1. Njock PGA, Zheng Q, Zhang N, Xu YS (2020) Perspective review on subsea jet trenching technology and modeling. J Mar Sci Eng 8:1–27
2. Bruschi R, Bartolini L (2019) Protecting offshore pipelines from external interference: dropped and dragged anchors. In: Abu Dhabi International Petroleum Exhibition & Conference 2018 (ADIPEC 2018). Society Petroleum Engineers
3. Tate KW, Tudor W, Eaton R (1982) Protecting submarine cables from accidental damage
4. DNV (2010) Risk assessment of pipeline protection. Mater Technol, 1–45
5. Brunning P, Machin J (2014) Applications and performance of trenching technologies in Asia-Pacific. In: Proceedings of annual offshore technology conference, vol 2, pp 1447–1462
6. Guo Xs, Nian Tk, Wang Fw, Zheng L (2019) Landslides impact reduction effect by using honeycomb-hole submarine pipeline. Ocean Eng 187:106155
7. Bai Q, Bai Y (2014) Subsea pipeline design, analysis, and installation
8. Properties M, Mucosa HO (2015) Technical Report : review of cabling techniques and environmental effects applicable to the offshore wind farm industry
9. Zhang S, Ge T, Zhao M, Wang C (2017) The prediction of traveling jet trenching in stiff clay based on the erosion failure mechanism. Mar Georesources Geotechnol 35:939–945
10. Zhang S, Wang C, Ge T (2017) Experimental prediction of the noncontact jet Trencher's excavation depth in clay. Mar Georesources Geotechnol 35:300–304
11. Rui Z, Metz PA, Reynolds DB, Chen G, Zhou X (2011) Historical pipeline construction cost analysis. Int J Oil Gas Coal Technol 4:244–263

12. Thusyanthan I (2012) Seabed soil classification, soil behaviour, and pipeline design
13. Offshore Soil Investigation Forum (2000) Guidance notes on geotechnical investigations for subsea structures
14. Bhattacharya B, Solomatine DP (2006) Machine learning in soil classification. Neur Netw 19:186–195
15. Chandan, Thakur R (2019) An intelligent machine learning model for soil image classification. In: International conference on signal processing, VLSI and communication engineering pp 0–4
16. Thakur R (2018) An intelligent model for Indian soil classification using various machine an intelligent model for Indian soil classification using various machine learning techniques, pp 33–41
17. Rao A, Gowda SAN, Beham MA (2016) Machine learning in soil classification and crop detection. IJSRD-Int J Sci Res Dev 4:2321–2613
18. de Souza WM, Ribeiro AJA, da Silva CAU (2022) Use of ANN and visual-manual classification for prediction of soil properties for paving purposes. Int J Pavement Eng 23:1482–1490
19. Bathula MC, Madiraju SVH (2021) Application of digital image processing to determine the properties of aggregates and soil using MATLAB: a case study. J Adv Chem Sci 7:711–716
20. Hassan KA, Elgendi EO, Shehata AS, Elmasry MI (2022) Energy saving and environment protection solution for the submarine pipelines based on deep learning technology. Energy Rep 8:1261–1274
21. Kaiser MJ (2020) Offshore pipeline construction cost estimation: chapter 9. In: Offshore pipeline construction industry, pp 209–228
22. Kaiser MJ (2020) The offshore pipeline construction industry: activity modeling and cost estimation in the U.S. Gulf of Mexico
23. Kaiser MJ (2017) Offshore pipeline construction cost in the U.S. Gulf of Mexico. Mar Policy 82:147–166
24. Deepocean Deepocean trencher T2 specification sheet
25. Helix T-1500 Trencher Jet trenching system specification sheet
26. SMD SMD CBT-1100 jet trencher specification sheet
27. MOUDUS CT-2 jet trencher specification sheet

Research on the Propagation of Earthquake Disaster Risk in Water Supply System

Tianyang Yu

Abstract Based on the calculation results of the vulnerability and the risk entropy index of the water supply system, the connectivity and risk propagation path of the urban water supply system are analyzed. Through the analysis of the disasters affected by the urban water supply system and different water supply subsystems during the earthquake, the disaster risk propagation mode and mathematical model of the urban water supply system during the earthquake are established, so as to carry out the risk assessment of the urban water supply system. Taking Karamay as an example, the city with refined basic data is used as the application city of the risk propagation model proposed in this paper. Combined with the topological structure of the city's water supply system, the path of earthquake disaster risk propagation in the water supply system and the vulnerability assessment index of the water supply subsystem are studied, and the vulnerability assessment index and risk entropy index of each subsystem of water source, reservoir, building, and pumping station are established.

Keywords Risk propagation path · Urban water supply system · Risk assessment · Risk propagation model · Risk

1 Introduction

The urban water supply system is composed of multiple water supply subsystems. The water supply system meets the user's requirements for water volume, water pressure, and water quality. It has always been its ultimate goal. This requires multiple water supply subsystems to coordinate with each other. Functional failure can cause the entire water supply system to fail to provide normal water supply to users.

T. Yu (✉)
Guangdong Earthquake Agency, Guangzhou, China
e-mail: 821677781@qq.com

Guangdong Earthquake Disaster Risk Control and Prevention Center, Guangzhou, China

T. Kang (ed.), *Proceedings of 5th International Conference on Civil Engineering and Architecture*, Lecture Notes in Civil Engineering 369,
https://doi.org/10.1007/978-981-99-4049-3_64

This paper takes Karamay city as an example and takes the city with refined basic data as the application city of the multiple risk assessment models proposed in this paper. Combined with the topological structure of the city's water supply system, the path of earthquake disaster risk propagation in the water supply system is studied, and the vulnerability assessment index of the water supply subsystem is proposed. Risk entropy index of each subsystem is calculated. The overall risk assessment of Karamay city water supply system under the action of earthquake is given.

2 Propagation Path of Earthquake Disaster Risk in Water Supply System

The urban water supply system is a complex system composed of multiple water supply subsystems from source water to users. The above-mentioned multiple water supply subsystems operate in coordination to provide normal water supply for users.

As can be seen from Fig. 1, although the spatial structure and relationship between different water supply subsystems are complex, they are characterized by mixed complex systems in structure. Water processes, etc. provide energy, and even once the function of the pressurized system fails, the water supply of the entire city will be interrupted. Therefore, functionally, the pressurized system and the above-mentioned water supply subsystem are in a series connection relationship. Therefore, we can simplify the functional relationship of different water supply subsystems of the urban water supply system as shown in Fig. 2 according to the structural characteristics and functional relationship of the series connection system. And the functional relationship of the water supply subsystem at each node in Fig. 2 can be determined according to the structural features and functional relationship of the parallel system. In this way, we have obtained a basic path relationship of the water flow in the water supply system, that is, the risk chain of the earthquake disaster risk propagation in the urban water supply system.

2.1 Basic Model and Mathematical Model of Earthquake Disaster Risk Propagation in Water Supply System

According to the composition, structural characteristics, and risk type factors of the urban water supply system, it can be known that there are the following three basic modes of risk transmission in the water supply system [1]:

(1) Serial mode

The serial propagation mode of risk propagation in the water supply system means that the risks faced by different water supply subsystems enter the propagation nodes in turn and propagate in the water supply system, that is, the different risks faced by

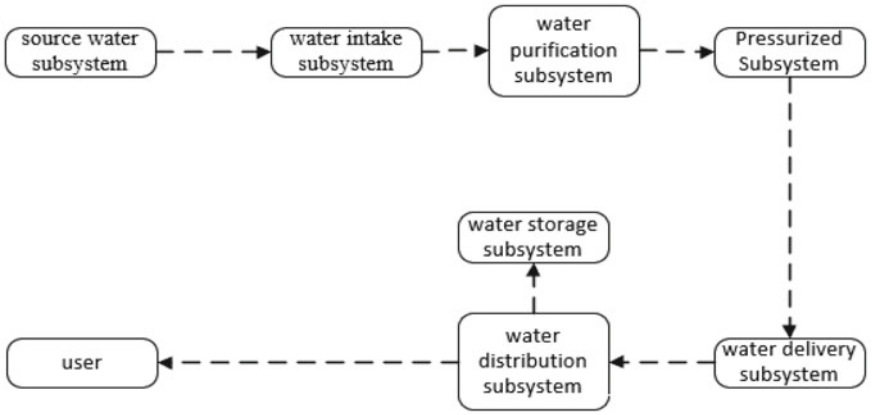

Fig. 1 Functional structure diagram of each subsystem of water supply system

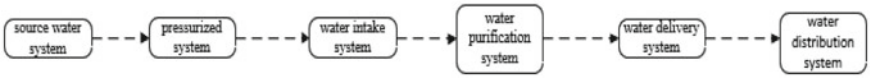

Fig. 2 Basic path of earthquake disaster risk propagation in water supply system

the water supply subsystem do not occur at the same time, then the serial propagation mode. The mathematical model of is:

$$R = \prod_{i=1}^{n} R(i) \tag{1}$$

where $R(i)$ represents the different risks faced by each water supply subsystem.

(2) Parallel mode

The parallel propagation mode of risk propagation in the water supply system means that two or more serial risks of the water supply subsystem enter the propagation nodes at the same time and propagate in parallel in the water supply system. These risks do not affect each other. The mathematical model is:

$$R = \max[R(i)] \tag{2}$$

(3) AND mode

The AND-type propagation mode of risk propagation in the water supply system means that the different risks faced by the water supply subsystem are propagated in a shape similar to a fan. The risks faced by the water supply subsystem are first superimposed and then propagated into the water supply system. The mathematical model of the AND-type propagation model is:

$$R = \sum_{i=1}^{n} f(i) \times R(i) \tag{3}$$

where $R(i)$ represents the different risks faced by each water supply subsystem and $f(i)$ represents the proportion of the water supply volume of each water supply subsystem to the total water supply volume of the water supply system.

After the analysis of the basic model and mathematical model of the risk propagation of the water supply system, we can use Ri to represent the risk of the i-th water supply subsystem of the urban water supply system. In this way, it can be used to represent the water supply function level that the entire urban water supply system can meet the user's water demand within the range of given operating conditions and operating conditions. That is to evaluate the overall risk of urban water supply system under the influence of earthquake threat.

2.2 *Earthquake Disaster Risk Entropy Evaluation Model*

The severity factor E_i, the probability of occurrence of earthquake intensity p_i determined by the earthquake hazard method, and the comprehensive vulnerability index V of the urban water supply pipe network calculated in Ref. [2] are introduced together, and the earthquake disaster risk entropy function of the water supply pipe network is calculated as:

$$H(R) = -\lambda V \sum_{i=1}^{t} E_i \times P_i \ln p_i \tag{4}$$

In the formula: $H(R)$ is the total measurement function of the earthquake disaster risk of the water supply network. $H(R)$ is a statistical average, and its magnitude is the result of the combined action of the probability space P_i and the severity space S_i of the seismic event X_i faced by the water supply network and its own vulnerability V. The smaller the index, the smaller the uncertainty of the water supply network facing earthquakes, that is, the smaller the risk of earthquake disasters, and vice versa.

3 Case Study

According to the data provided by Karamay city Water Co., Ltd., the process of water supply system is given based on the analysis of the source water, water intake, water delivery, and water distribution process of Karamay city water supply system, as shown in Fig. 3.

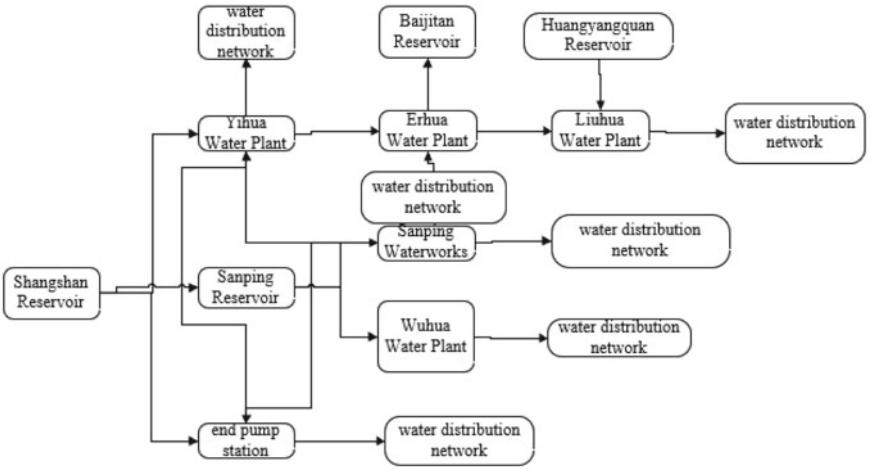

Fig. 3 Karamay city water supply system process

3.1 Vulnerability and Earthquake Disaster Risk Assessment Results of Each Subsystem

According to the basic data of Karamay water supply system (part of the data are listed in Table 1) and the seismic capacity evaluation index system [3] of different water supply subsystems in Ref. [2], the vulnerability [4] of each water supply subsystem is quantified by using the different mutation potential functions described in Ref. [2]. Finally, the vulnerability of each water supply subsystem is given, and the calculation results are shown in Table 2.

Combined with the vulnerability calculation results of each subsystem of the Karamay water supply system in the previous section (see Table 2), according to the earthquake intensity occurrence probability provided in Ref. [5] and the earthquake disaster risk entropy model of the water supply system proposed in this paper (see

Table 1 The basic data of Karamay water supply system

No.	No.	Pipe name	Diameter	Material	Construction	Length (km)
1	C1	Yihua to Shangshan	DN600	Steel	1990s	21
8		The last section to Shanshang	DN300	Steel	1970s	9
9		Baikou Spring to Regulating	DN1000	Cement	1980s	31
34	E7	Shanshang Reservoir to Xijiao Road	DN700	Cast iron	2000s	5.7
43	E6	Mountain Pool to Youquan Road	DN500	Cast iron	2012s	0.75

Table 2 Vulnerability results of each subsystem of water supply system in Karamay city

Water supply subsystem	Vulnerability index	Water supply subsystem	Vulnerability index
Source water subsystem	0.059	Sp Intake pump station	0.119
Water delivery system	0.073	Sp booster pump station	0.089
Water distribution system	0.072	Sp building (structure)	0.067
Yi Intake pump station	0.119	Wu Intake pump station	0.119
Yi booster pump station	0.089	Wu booster pump station	0.089
Yi building (structure)	0.067	Wu building (structure)	0.067
Er Intake pump station	0.119	Liu Intake pump station	0.119
Er booster pump station	0.089	Liu booster pump station	0.089

Table 3 Risk entropy [6] index of each subsystem of water supply system in Karamay city

Water supply subsystem	Risk entropy Index	Water supply subsystem	Risk entropy index
Source water subsystem	0.091	Sp intake pump station	0.184
Water delivery system	0.113	Sp booster pump station	0.137
Water distribution system	0.111	Sp building (structure)	0.103
Yi intake pump station	0.184	Wu Intake pump station	0.184
Yi booster pump station	0.137	Wu booster pump station	0.137
Yi building (structure)	0.103	Wu building (structure)	0.103
Er intake pump station	0.184	Liu intake pump station	0.184
Er booster pump station	0.137	Liu booster pump station	0.137

Eq. 4), the calculation results of each subsystem are calculated. The calculation results of the earthquake disaster risk entropy index are shown in Table 3.

3.2 Overall Risk Assessment of Earthquake Hazards in Water Supply System

(1) Shanshang Reservoir → Yihua Water Plant and the last section of the water intake pumping station → Sanping Reservoir → Water delivery subsystem → Yihua Water Plant and the final section construction (construction) (2) Shanshang Reservoir → Sanping and Wuhua Waterworks Intake Pump Station → Sanping Reservoir → Water Delivery Subsystem → Sanping and Wuhua Water Factory buildings (structures) → Sanping and Wuhua water plant pressurization pump stations → water distribution subsystem; (3) Baijiitan Reservoir → the first station of the second water plant and the pumping station for pumping water → the construction of the second water plant (Structure) Building → Pressurization Pump Station of Erhua Water Plant → Water Distribution Subsystem; (4) Huangyangquan Reservoir → Liuhua

Water Intake Pump Station → Water Transmission Subsystem → Liuhua Water Plant Building (Structure) → 6 Chemical booster pump station → water distribution subsystem.

Because the occurrence of an earthquake is a sudden event, this paper only considers the impact of the earthquake on the water demand of users of the water supply system, and the effect of the earthquake on each subsystem of the water supply system occurs simultaneously, that is, for the same path, the earthquake disaster risk is simultaneous. The propagation into each water supply subsystem belongs to the parallel propagation mode; for different paths of the water supply system, the earthquake disaster risk is an AND-type propagation mode between the above four paths.

For the above four risk propagation paths, the risk entropy of the two risk propagation paths (3) and (4) finally propagated to the user, respectively, takes the maximum risk value of each subsystem; that is, the risk entropy value of the water pumping station subsystem is 0.184. The two paths (1) and (2) have source water from Shanshang and Sanping reservoirs. During the earthquake, the water storage of Sanping Reservoir can meet a certain demand for source water. The risk entropy is 0.184 for resolution and absorption. Therefore, the risk of the two risk propagation paths (1) and (2) finally propagated to the user object is taken as the risk entropy of the booster pump station subsystem of 0.137. Since different risk paths belong to the AND-type transmission mode, the water supply of the four risk transmission paths is 40,000 m^3/d for the first water plant, 300,000 m^3/d for the Sanping and Wuhua water plants, and 300,000 m^3/d for the second water plant. 90,000 m^3/d, Liuhua Water Plant 100,000 m^3/d, the four risk paths account for 7.5%, 56.6%, 17.0%, and 18.9% of the total water supply in the water supply system, respectively. Therefore, according to formula 3, the earthquake disaster risk entropy of Karamay city water supply system is calculated by taking the proportion of water supply as the weight to be 0.154 (0.137 * (7.5% + 56.6%) + 0.184 * (17.0% + 18.9%) = 0.154).

4 Conclusion

(1) The above example analysis and calculation results show that the seismic risk assessment model of water supply pipeline network considering risk propagation proposed in this paper is reasonable and feasible.
(2) Due to the small vulnerability index of each subsystem of the water supply system in Karamay city, although the area will be affected by earthquake disasters in the future, the earthquake disaster risk entropy index of the water supply system is 0.154, and the total earthquake disaster risk entropy is at a low level. Faced with the risk of earthquake intensity VI and VII.

References

1. Li C (2009) Theory and application of project risk element transfer. China Water Resources and Hydropower Press, Beijing, pp 30–31
2. Yu T, Guo E (2021) Comprehensive seismic capacity assessment method of regional water supply network. Earthq Eng Eng Dyn 41(4):102–108
3. Knemeyer AM, Walter Z, Cuneyt E (2009) Proactive planning for catastrophic events in supply chains. J Oper Manag 27:141–153
4. Guo E, Yu T (2017) Emergency assessment method for earthquake damage to water supply pipeline network. In: International collaboration in lifeline earthquake engineering 2016 IRP 1. ASCE, pp 528–535
5. Yu T, Guo E (2020) Study of the earthquake disaster risk assessment of the regional water supply networks. Int J Seismic Eng 37(3):84–105
6. Cornell CA (1968) Engineering seismic risk analysis. Bull Seismol Soc Am 58(5):1583–1606

Green Function for S-Wave from Vertical Propagation at Seismic Events

Huber Nieto-Chaupis and Anthony Alfaro-Acuña

Abstract In this paper, the shear stress originated by a S-wave and with a vertical propagation that produces distributions of stress at time is studied from the view of integer-order Bessel functions as well as the Green's functions. Guided by this mathematical methodology, it is derived a kind of propagator at the frequencies that links two events defined each one by a frequency. Computational simulations are done. Therefore, the seismic event can be seen as decreasing wave at the space of difference of frequencies that in falling at time.

Keywords Shear stress · Civil engineering · Green function

1 Introduction

Despite the fact that a seismic event is totally random [1], most progress has been done at the theoretical modeling and their resulting computational simulations. Basically, it was not targeted to make time predictions but also the energy released by event was focused [2]. Actually, it is of great importance to find links between the amplitude and released energy, so that one makes reliable estimations about these energies more than a speculative policy that would be far from reality. These estimated energies acquire relevance at the civil engineering so that secure buildings are expected to be built [3]. Clearly one can perceive that the energy prediction needs an accurate computational strategy in order to acquire a rough idea of future subsequent scenarios with a direct impact at the urbanism and the implementation of housing projects that demands the construction of tall buildings. In this manner, the gathered knowledge represents a kind of advantageous as to make robust and secure buildings. On the other hand, the accumulated theoretical knowledge of the physics and geophysics of a seismic event emerge as a relevant component for the robust design and the construction of tall buildings nowadays at modern cities that are based at the vertical

H. Nieto-Chaupis (✉) · A. Alfaro-Acuña
Universidad Autónoma del Perú, Panamericana Sur, Km. 16.3 Villa El Salvador, Lima, Peru
e-mail: hubernietochaupis@gmail.com

T. Kang (ed.), *Proceedings of 5th International Conference on Civil Engineering and Architecture*, Lecture Notes in Civil Engineering 369,
https://doi.org/10.1007/978-981-99-4049-3_65

urbanistic growth [4–7]. Thus, the triplet geology, civil engineering and physics play a concrete role at all those cities that are presenting geological fails by which it is deeply believed to be the main cause of the random apparition of earthquakes.

In this manner, one can wonder about the model parameters of a certain theoretical model that might be well encompassing to a real seismic event, so that one has the chance of improving the quality of buildings. Such improving would consist in the projection of model parameter at the design as well as implementation that led to a robust construction of a tall building.

This paper focuses on phenomenological models based by the effect of shear stress to create vertical dynamics giving rise to an earthquake. Essentially, it is based at the consequences of Snell's law by which the S-wave propagates in a vertical manner by crossing different layers of soil and weakening its amplitude. In this manner, one can wonder about the decreasing or increasing of vertical waves yielding horizontal dynamics and their direct impact on the well-established movement that makes a seismic event.

Therefore, this paper has opted by the usage of the well-known green functions whose main purpose in the present context is that of identification of all those values of frequency that makes it null or infinite a wave-like horizontal displacement. For this end, a second-order differential equation is derived. It is noteworthy that although the well-known second law is used, the implementation of disturbs and noise to the S-wave and horizontal displacements is not taken into account.

For example, a model that implements these situations can be formulated through the second law of Newton that for this event consider the sum of "Q" extra forces. Thus from [8], the full formulation can be written as:

$$F = m\frac{\mathrm{d}^2 u}{\mathrm{d}t^2} + \sum_{q}^{Q} \eta_q f_q, \tag{1}$$

where η_q a model parameter denoting the fact that while $\eta_q > 0$ exists a complication at the solution of Eq. 1 since f_q would have to be well-established. Nevertheless, one can appeal to consistent approximations that neglects these extra forces so that $f_q \Rightarrow 0$.

2 Motivation for the Usage of Green's Function

Equation 1 belongs to a family of ordinary differential equations that admits instantaneous solution since all of them are defined at the time domain. A generalization of Eq. 1 can be written as $(\Delta^m + \Delta)u(t) = 0$, where the symbol Δ^m corresponds to the "m" derivative with $m > 1$. The fact that interactions can be instantaneous then one can associate the well-known Dirac-Delta function at the sense that for any function G one gets that: $(\Delta^m + \Delta)G = \delta(t - t')$. Here, one can see the insertion of $\delta(t - t')$ the well-known Dirac-Delta function. Clearly, one can find a kind of complexity in

above. The way as it was written suggests that it can be applied in a straightforward manner for any case, in particular for the 2nd law, it is constitutes the main point of this paper. Following this view, this paper implements the usage of Green's function as a Green's equation [9] that in its more general form has the form for Eq. 1 can be written as:

$$\left(\frac{\mathrm{d}^2}{\mathrm{d}t^2}+\frac{\mathrm{d}}{\mathrm{d}t}+\sigma\right)G(\omega,\omega')=\delta(\omega-\omega'), \tag{2}$$

with σ a constant and $\delta(\omega-\omega')$ the Dirac-Delta function. Methods and schemes to solve Eq. 2 are well-known at the territory of physics [10]. The rest is this paper which is as follows: second section provides the theoretical machinery of the shear stress necessary for this paper. Here is introduced the integer-order Bessel functions in third section the Green's function is implemented. In fourth section, the conclusion is presented.

3 Theoretical Formulation

Consider Fig. 1 an initial time by which exists a single shear stress τ that in terms of mechanical force is written as:

$$F=\tau A \tag{3}$$

it is represented by stress onto the orange color cube of size $\mathrm{d}z$ and area A and volume V. Subsequently at a next time, one has there is an infinitesimal force given yielding as well as an infinitesimal shear stress $\mathrm{d}\tau$ so that one can write down:

$$\mathrm{d}F=\mathrm{d}\tau A. \tag{4}$$

whose geometry is denoted by the indigo color in Fig. 1. For a complete seesaw, the usage of second law suggests to write down:

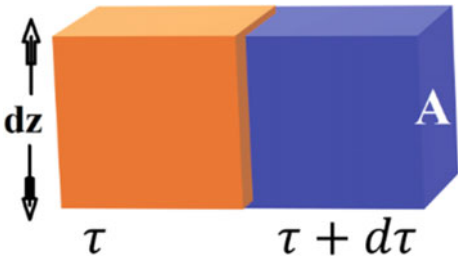

Fig. 1 Basic movement caused by a S-wave at the z direction. It also produces infinitesimal displacement (indigo color) at the shear stress

$$(F + \mathrm{d}F) - F = \mathrm{d}M\frac{\mathrm{d}^2x}{\mathrm{d}t^2}. \tag{5}$$

It should be noted that the seesaw action is done along the perpendicular direction of "z" direction. In this manner, the right side of Eq. 5 contains a second-order derivative of "x" respect to time. Thus, Eq. 5 can be written as:

$$\mathrm{d}F = A\mathrm{d}z\rho\frac{\mathrm{d}^2x}{\mathrm{d}t^2} \tag{6}$$

and from Eq. 3 one has that:

$$\mathrm{d}\tau A = A\mathrm{d}z\rho\frac{\mathrm{d}^2x}{\mathrm{d}t^2} \Rightarrow \mathrm{d}\tau = \rho\frac{\mathrm{d}^2x}{\mathrm{d}t^2}\mathrm{d}z, \tag{7}$$

Thus, one can see that the geometric model given by Fig. 1 yields that a small increment at the "z" turns out to be as an increment in the shear stress. From Eq. 7, one can see that the both sides that can be integrated in a straightforward manner as: $\int \mathrm{d}\tau = \rho\frac{\mathrm{d}^2x}{\mathrm{d}t^2}\int \mathrm{d}z$. It was assumed that $\int_0^\gamma \mathrm{d}z = \gamma$, ... $\tau_0 = z_0 = 0$. Thus, one gets:

$$\tau = \rho\frac{\mathrm{d}^2x}{\mathrm{d}t^2}\gamma. \tag{8}$$

It is noteworthy the next change (it should be noted that G exhibits its inverse as the distance γ), so that one gets below:

$$G = \frac{\tau}{\gamma}, \tag{9}$$

where clearly one has from Eq. 8 and Eq. 9 that:

$$G = \rho\frac{d^2x}{dt^2}, \tag{10}$$

fact that suggests to write Eq. 10 as 2nd grade differential equation:

$$\frac{\mathrm{d}^2x}{\mathrm{d}t^2} - \frac{G}{\rho} = 0. \tag{11}$$

It is clear that there is a certain difficulty to balance the units. In fact, the formulation of Eq. 9 must be consistent with the definitions of force and shear stress. In this manner, it is plausible to define G again inside this context of searching a right mathematical structure in the sense that:

$$G = -x\beta, \tag{12}$$

in this way, from Eqs. 11 and 12 one arrives to:

$$\frac{\mathrm{d}^2x}{\mathrm{d}t^2} + \frac{x\beta}{\rho} = 0, \tag{13}$$

where it is easy to note that β has units of density per time to square. In order to put all definitions in terms of physical variables and to keep the required consistency in the meaning of next equations, the new variable β can be expressed in terms of tangible physics observables. In this manner, one has below:

$$\beta = \frac{\rho}{t^2} = \frac{m}{V}\frac{1}{t^2} = \frac{m}{V\ell}\frac{\ell}{t^2} \tag{14}$$

one can see that last term constitutes an acceleration. Thus, one gets the following:

$$\frac{m}{V\ell}\frac{\ell}{t^2} = \frac{ma}{V\ell} = \frac{f}{\ell\ell A} = \frac{\tau}{A} \tag{15}$$

expressing the fact that β is proportional to the shear stress but inverse of area as seen in Fig. 1:

$$\beta = \frac{\tau}{A} \tag{16}$$

by the which Eq. 13 acquires the following form:

$$\frac{\mathrm{d}^2x}{\mathrm{d}t^2} + \frac{\tau x}{\rho A} = 0, \tag{17}$$

that turns out to be the correct differential equation for the purposes of this paper [11–13].

4 Usage of Integer-Order Bessel Functions

From Eq. 17, it is easy to define the solutions at the complex plane given by:

$$x(t) = x_0 \mathrm{Exp}\left[i\sqrt{\frac{\tau}{\rho A}}t\right] = 0, \tag{18}$$

clearly one can make the change for the term inside the square root through a frequency:

$$\omega = \sqrt{\frac{\tau}{\rho A}} \tag{19}$$

in virtue to Fig. 2, where the initial shear stress comes from below toward up, then the seesaw mechanism can be completed with the implementation of factor $\text{Sin}^2(\theta)$ therefore Eq. 19 can be written as dependent on the angle θ so that one can arrive to:

$$x(t) = x_0 \text{Exp}[i\omega t \text{Sin}(\theta)] = 0, \tag{20}$$

here one can use the expansion of it onto a basis of integer-order Bessel functions at the sense that:

$$\text{Exp}[i\omega t \ \text{Sin}(\theta)] = \sum_n^{\infty} J_n(\omega t)\text{Exp}(i\theta) \tag{21}$$

and the solutions for Eq. 20 are written as:

$$x(t) = x_0 \sum_n^{\infty} J_n(\omega t)\text{Exp}(in\theta), \tag{22}$$

and from Eq. 8 follows that:

$$\tau = \sum_n^{\infty} x_0 e^{in\theta}\left[\frac{\gamma\rho}{4}\omega^2(J_{n-2}[\omega t] + J_{n+2}[\omega t]) - \frac{\gamma\rho}{2}\omega^2 \ J_n[\omega t]\right]. \tag{23}$$

Figure 3 is plotted different distributions for Eq. 23 when the geometrical angle θ is small so that it can be neglected. It was done for the first 5 integer orders. The frequency was established by $n\omega$ and $\omega = 0.1\ \text{s}^{-1}$. Indeed $\frac{\gamma\rho x_0\omega^2}{4}$ was assigned approximately the value of 1000 in arbitrary units. It is noteworthy that in the scenario that the geometrical angle does not vanishes, then the distributions of Fig. 3 are the ones that corresponding to the imaginary part of complex exponential because it is easy to note that all distributions except the case of $n = 2$, have initialized at $t = 0$ [14, 15].

In Fig. 4, it is displayed the case when the frequency $\omega = 0.2\ \text{s}^{-1}$ that is twice of case shown in Fig. 3. In contrast to Fig. 3, here one can argue that it is actually the pure part imaginary since because all orders are sharing same initial time at $t = 0$.

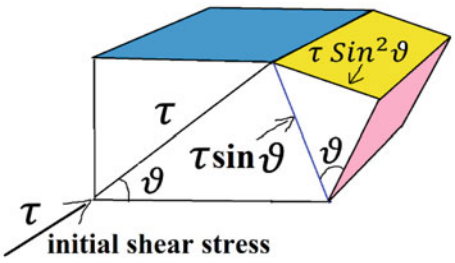

Fig. 2 Propagation of shear stress resulting as the square of Sin of geometrical angle at the upper side of deformed cube

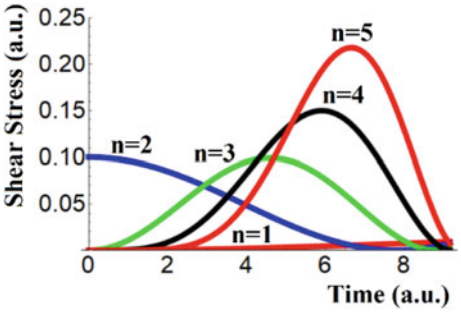

Fig. 3 The square of shear stress when the geometrical angle is negligible. The color of each distribution is associated an integer number of order of Bessel function

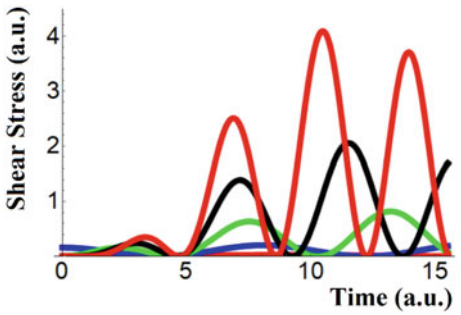

Fig. 4 The square of shear stress as above when the frequency is duplicated. The largest peaks are now shifted to the right side

The fact that the shear stress is vibrating in time can be argued with the basis that not any cancelation of opposite forces over the areas [16, 17]. In other words, the initial shear stress propagates in an asymmetric manner creating different vertical and horizontal components [18, 19], so that at time, each one of them contributes with a sharp wave whose net amplitude can increase or fall in time.

5 Implementation of Green's Function

Turning back to Eq. 17, one can write it in its form of operator given by:

$$\left(\frac{\mathrm{d}^2}{\mathrm{d}t^2} + \frac{\tau}{\rho A}\right)x = 0. \tag{24}$$

The fact of having different frequencies as well as various shear stresses then it can be an argument to write the corresponding Green's function to Eq. 24 as follows:

$$\left(\frac{\mathrm{d}^2}{\mathrm{d}t^2} + \frac{\tau}{\rho A}\right)f(\omega, \omega') = \delta(\omega - \omega') \tag{25}$$

with $\delta(\omega-\omega')$ the well-known Dirac-Delta function depending on the difference of frequencies. A possible solution of such equation is to take the convenient Fourier transform that respect the difference of frequencies of right side. Mathematically speaking one has that:

$$f(\omega,\omega')=\int G(\omega,\omega')\mathrm{Exp}\left[i(\omega-\omega')t\right]\mathrm{d}t. \tag{26}$$

With the integral form of Dirac-Delta function:

$$\delta(\omega-\omega')=\int \mathrm{d}t\,\mathrm{Exp}\left[i(\omega-\omega')t\right] \tag{27}$$

And working out all in the left side of Eq. 25 then one arrives to an integration of form:

$$\int \mathrm{d}t\; e^{i(\omega,\omega')t}\left[G(\omega,\omega')\left\{-(\omega-\omega')^2-\frac{\tau}{\rho A}\right\}-1\right]=0 \tag{28}$$

by which one obtains in a straightforward manner:

$$G(\omega,\omega')=\frac{-1}{(\omega-\omega')^2+\frac{\tau}{\rho A}}. \tag{29}$$

Whose resulting frequencies can be written as:

$$\omega=\omega'\pm i\sqrt{\frac{\tau}{\rho A}}. \tag{30}$$

Now one can define the shifted frequency as:

$$\omega_S=\sqrt{\frac{\tau}{\rho A}}, \tag{31}$$

so that the Green's function is infinite and their poles are given by:

$$\omega=\omega'\pm i\omega_S. \tag{32}$$

that can be interpreted as the transition of having a frequency created by the initial shear stress to one with a frequency with an imaginary component originated again by the S-wave propagation. With Eq. 29 now Eq. 26 can be written in an accurate manner through the Green's function:

$$f(\omega,\omega')=\int \frac{-\mathrm{Exp}\left[i(\omega-\omega')t\right]}{(\omega-\omega')^2+\frac{\tau}{\rho A}}\mathrm{d}t \tag{33}$$

When it is worked out at the denominator of Eq. 33 one can arrive to:

$$\left(\omega-\omega'\right)^2+\frac{\tau}{\rho A}=\frac{1}{\left(\omega-\omega'\right)^2}\left[1+\frac{\tau}{\rho A\left(\omega-\omega'\right)^2}\right] \tag{34}$$

It is plausible that in the scenario that the square of difference of frequencies time the product ρA then one can state that:

$$\rho A\left(\omega-\omega'\right)^2\gg\tau \tag{35}$$

the term inside brackets in Eq. 34 becomes actually an infinite sum given by:

$$1+\frac{\tau}{\rho A\left(\omega-\omega'\right)^2}+\frac{1}{2!}\left(\frac{\tau}{\rho A\left(\omega-\omega'\right)^2}\right)^2+\cdots=\sum_{p=0}^{\infty}\frac{1}{p!}\left(\frac{\tau}{\rho A\left(\omega-\omega'\right)^2}\right)^p \tag{36}$$

that is actually the well-known expansion of exponential function:

$$\mathrm{Exp}\left[\frac{\tau}{\rho A\left(\omega-\omega'\right)^2}\right]=\sum_{p=0}^{\infty}\frac{1}{p!}\left(\frac{\tau}{\rho A\left(\omega-\omega'\right)^2}\right)^p, \tag{37}$$

in this manner Eq. 33 acquires another form:

$$f\left(\omega,\omega'\right)=\frac{1}{\left(\omega-\omega'\right)^2}\times\int-\mathrm{Exp}\left[i\left(\omega-\omega'\right)t\right]\mathrm{Exp}\left[\frac{\tau}{\rho A\left(\omega-\omega'\right)^2}\right]\mathrm{d}t. \tag{38}$$

With this Eq. 33 is simplified to have a single exponential.

$$f\left(\omega,\omega'\right)=\frac{-1}{\left(\omega-\omega'\right)^2}\int e^{\left[i\left(\omega-\omega'\right)t+\frac{\tau}{\rho A\left(\omega-\omega'\right)^2}\right]}\mathrm{d}t. \tag{39}$$

The function $f\left(\omega,\omega'\right)$ can be interpreted as the amplitude between an initial and final state, defined by the initial frequency ω and ω' due to the change of direction of shear stress as seen in Fig. 2. For example, when the real part of complex exponential number is considered, for an integration between 0 and T, Eq. 39 has now the tractable form written as:

$$f\left(\omega,\omega'\right)=\frac{-\mathrm{Sin}\left[\left(\omega-\omega'\right)T\right]e^{\left[\frac{\tau}{\rho A\left(\omega-\omega'\right)^2}\right]}}{\left(\omega-\omega'\right)^3}. \tag{40}$$

It is easy to note that the real exponential has to be finite at the sense that

$$\frac{\tau}{\rho A(\omega-\omega')^2}\approx 0$$

to avoid "runaway" solutions. In this manner, Eq. 40 can be expressed as:

$$f(\omega,\omega')=\frac{-\mathrm{Sin}\big[(\omega-\omega')T\big]}{(\omega-\omega')^3}. \tag{41}$$

It should be noted that the term $(\omega-\omega')^{-3}$ is obtained in a straightforward manner through the usage:

$$\frac{\mathrm{d}^3}{\mathrm{d}T^3}\mathrm{Sin}\big[(\omega-\omega')T\big]=-(\omega-\omega')^3\mathrm{Cos}\big[(\omega-\omega')T\big]. \tag{42}$$

It has implications in Eq. 40 in the sense that solving Eq. 41 and it is inserted in Eq. 40, the one arrives to:

$$\begin{aligned} f(\omega,\omega') &= \frac{-\mathrm{Sin}\big[(\omega-\omega')T\big]\mathrm{Cos}\big[(\omega-\omega')T\big]}{\frac{\mathrm{d}^3}{\mathrm{d}T^3}\mathrm{Sin}[(\omega-\omega')T]} \\ &= \frac{-\mathrm{Sin}\big[2(\omega-\omega')T\big]}{2\frac{\mathrm{d}^3}{\mathrm{d}T^3}\mathrm{Sin}[(\omega-\omega')T]} \end{aligned} \tag{43}$$

So that Eq. 26 from Eq. 25 can finally written as:

$$f(\omega,\omega')=\frac{-\Delta T^3\mathrm{Sin}\big[2(\omega-\omega')T\big]}{2\mathrm{Sin}[(\omega-\omega')T]}. \tag{44}$$

In Fig. 5, the shear stress as function of frequency difference is plotted. The gray color acquires the maximum value as seen at the gray color line. The interpretation is as follows: once the generation of a secondary frequency is contemplated in the sense that is producing a "resonance-like" dynamics. Thus, the gray line tries to form a peaked distribution, fact that might be canceled by the apparition of another frequencies.

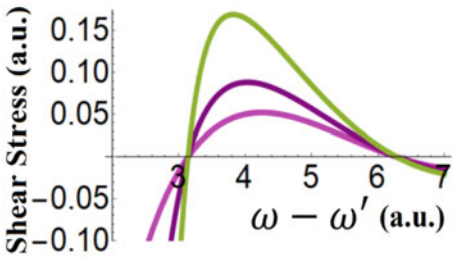

Fig. 5 The amplitude of shear stress from Eq. 40 generated initially for values of $\frac{\tau}{\rho A}=1$ (magenta color), 10 (purple), and 20 (gray), and $T=1$ s

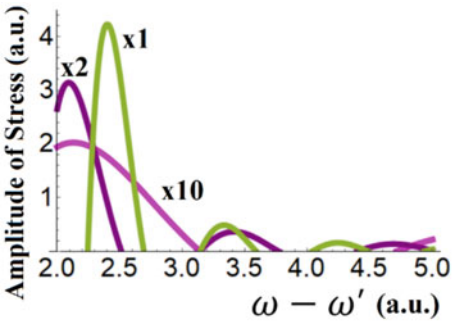

Fig. 6 The amplitude of shear stress from Eq. 40 multiplied by a factor as seen at the plot for values of $\frac{\tau}{\rho A} = 1$ (magenta color), 10 (purple), and 20 (gray), and $T = 2$ s. 5 s and 7 s, respectively, for the order of colors given above. Plot and all done have been achieved with WOLFRAM [23]

In Fig. 6, the amplitude of stress is plotted. Again, the gray line appears to exhibit the highest value of amplitude. However, the amplitude is decreasing with the increasing of frequency difference. This is demonstrating that the resonance (if any) can be only a kind of mechanical stress that is not only a direct manifestation of the 2nd law of Newton, but also a point that contemplates frequencies that are not directly seen in the Newton's theory [20–25]. In other words, because the seismic event is a direct consequence of 2nd law so that the apparition of harmonics would come from the composition of materials that push each other and which one contains much more density [26–28]. Thus, in some materials, the apparition of harmonics can of course produce a strong dynamic that is reflected in the scale of Richter. A robust analysis of this will be done in a next paper.

6 Conclusion

In this paper, a theory of generation of shear stress initialized by a vertical impulse assumed to be an instantaneous response of seismic event has been presented. Basically, it was derived a wave function corresponding to the propagation of energy that is actually released by a common seismic event [29, 30]. Thus, the solutions have turned out to contain a complex, fact that has been advantageous in the sense that from it the integer-order Bessel functions have been derived in closed form. Thus, the perpendicular propagations have been simulated. Subsequently, the Green's function was formulated. Although various systematic changes were applied, the main frequencies were obtained. The shifted of main frequency is done along the complex part. Clearly for practical ends the value ω^2 although was not deeply stressed, in the future, the scenarios that are depending on this quantity shall be studied. Finally, the Fourier transform of Green's function was simulated. This was interpreted as the amplitude of shear stress under dependence of difference of frequencies. Along the

paper, this difference was seen as a kind of transitions between states. Interestingly, this called "frequency's transition" can be well understood as the before and after a peak of a seismic event [31–33]. With respect to this, imminently one robust study is needed to corroborate these preliminary ideas derived from the usage of Green's function.

References

1. Perfettini H, Avouac JP, Tavera H et al (2010) Seismic and aseismic slip on the Central Peru megathrust. Nature 465:78–81
2. Susukida Y, Katsumata K, Ichiyanagi M et al (2021) Focal mechanisms and the stress field in the aftershock area of the 2018 Hokkaido Eastern Iburi earthquake (MJMA = 6.7). Earth Planets Space 73:1
3. Barontini A (2021) Seismic safety assessment of mixed timber-masonry historical building: an example in Lima, Peru. J Earthq Eng 25(5)
4. Beck SL, Ruff LJ (1989) Great earthquakes and subduction along the Peru trench. Phys Earth Planetary Interiors 57(3–4):199–224
5. Guzmán-Speziale M, Molina E (2022) Seismicity and seismically active faulting of Guatemala: a review. J S Am Earth Sci 115:103740
6. Álvarez O et al (2014) Geology. Tectonophysics
7. Álvarez O et al (2019) Reviewing megathrust slip behavior for recent Mw > 8.0 earthquakes along the Peru-Chilean margin from satellite GOCE gravity field derivatives. Tectonophysics 769:22
8. Alva Hurtado JE (2020) Dinámica de Suelos (in Spanish) Edit. EDUNI, Lima, First Ed. November 2020
9. Bostock MG (2004) Green's functions, source signatures, and the normalization of teleseismic wave fields. J Geophys Res 109:B03303
10. Kuzemsky AL (2017) Chapter 5: Green Functions Method in Mathematical Physics. In: Statistical mechanics and the physics of many-particle model systems, pp 121–153 (2017)
11. Munirwansyah M et al (2020) A new empirical equation of shear wave velocity to predict the different peak surface accelerations for Jakarta city. Geodesy Geodyn 11(6):455–467
12. Zhang L et al (2016) Stochastic ground-motion simulations for the 2016 Kumamoto, Japan, earthquake. Earth Planets Space 68:184
13. Katsumata A (2001) Relationship between displacement and velocity amplitudes of seismic waves from local earthquakes. Earth Planets Space 53:347–355
14. Schaeken T, Hoogerbrugge L, Verschuur E (2022) A non-reflecting wave equation through directional wave-field suppression and its finite difference implementation. Sci Rep 12:407
15. Karimpouli S, Tahmasebi P (2020) Physics informed machine learning: seismic wave equation. Geosci Front 11(6)
16. Fazio M, Alparone S, Benson PM et al (2019) Genesis and mechanisms controlling tornillo seismo-volcanic events in volcanic areas. Sci Rep 9:7338
17. Rowley P, Benson PM, Bean CJ (2021) Deformation-controlled long-period seismicity in low-cohesion volcanic sediments. Nat Geosci 14:942–948
18. Posadas KA, Morales J, Ibañez JM, Posadas-Garzon A (2021) Shaking earth: non-linear seismic processes and the second law of thermodynamics: a case study from Canterbury (New Zealand) earthquakes. Chaos, Solitons & Fractals 151
19. Milton Graeme W, Willis John R (2007) On modifications of Newton's second law and linear continuum elastodynamicsc. Proc R Soc A 463:855–880
20. Lippiello E, Giacco F, Marzocchi W et al (2015) Mechanical origin of aftershocks. Sci Rep 5:15560

21. Vallianatos F, Pavlou K (2021) Scaling, properties of the Mw7.0 Samos (Greece), 2020 aftershock sequence. Acta Geophys 69:1067–1084
22. Vassallo M et al (2022) Peak frequency changes from HV spectral ratios in Central Italy: effects of strong motions and seasonality over 12 years of observations. J Geophys Res Solid Earth 127:e2021JB023848
23. https://www.wolframalpha.com/
24. Hwang HS, Hamm SY, Cheong JY et al (2020) Effective time- and frequency-domain techniques for interpreting seismic precursors in groundwater level fluctuations on Jeju Island, Korea. Sci Rep 10:7866
25. Craig TJ, Chanard K, Calais E (2017) Hydrologically-driven crustal stresses and seismicity in the New Madrid Seismic Zone. Nat Commun 8:2143
26. Kato A, Ben-Zion Y (2021) The generation of large earthquakes. Nat Rev Earth Environ 2:26–39
27. McBeck J, Aiken JM, Cordonnier B et al (2022) Predicting fracture network development in crystalline rocks. Pure Appl Geophys 179:275–299
28. Gvirtzman S, Fineberg J (2021) Nucleation fronts ignite the interface rupture that initiates frictional motion. Nat Phys 17:1037–1042
29. Díaz J, Ruiz M, Sánchez-Pastor PS et al (2017) Urban Seismology: on the origin of earth vibrations within a city. Sci Rep 7:15296
30. Chen KH, Yeh TC, Chen Y et al (2022) Characteristics and impact of environmental shaking in the Taipei metropolitan area. Sci Rep 12:743
31. Wu L, Wang D, Lei Z et al (2020) Campus vibration in Nanwangshan Campus, China University of Geosciences at Wuhan monitored by short-period seismometers. J Earth Sci 31:950–956
32. Groos JC, Ritter JRR (2009) Time domain classification and quantification of seismic noise in an urban environment. Geophys J Int 179(2):1213–1231
33. Manea EF, Michel C, Poggi V et al (2016) Improving the shear wave velocity structure beneath Bucharest (Romania) using ambient vibrations. Geophys J Int 207(2):848–861

Building Energy Management and Thermal Comfort

Study on Energy Consumption Influencing Factors of HVAC Systems for Cleanrooms in Semiconductor Fabs

Yiling Chen, Nan Li, Yu Zhao, and Wei Zhao

Abstract To maintain ultra-high air cleanliness, the air changes per hour can be several hundred in semiconductor fabrication plants (fabs) cleanrooms, making HVAC systems for cleanrooms dozens of times more energy intensive than those for public buildings. The study aims to identify the significant energy consumption influencing factors of HVAC systems for cleanrooms and their significance ranking, providing the direction and basis for energy conservation of semiconductor fabs. First, this study compiled 10 primary energy consumption influencing factors using theoretical analysis. Then, the energy consumption of each influencing factor was simulated using a Design Builder model of a semiconductor manufacturing facility at various values. Furthermore, the significance ranking of the 10 influencing factors was also determined using single-factor analysis, orthogonal experiments, and variance analysis. Results show that the significant energy consumption influencing factors are total air changes and COP of chillers. The significance ranking is air changes per hour > COP of chillers > supply air temperature of MAU > outdoor air flow rate > fan efficiency > pump efficiency > process efficiency > lighting equipment efficiency > heat transfer coefficient of roof > heat transfer coefficient of external wall. This study is instructive for the proposal of energy conservation strategies and estimating energy savings.

Keywords Energy conservation · Influencing factors · HVAC system · Semiconductor cleanroom

Y. Chen · N. Li (✉)
Chongqing University, Chongqing 400045, China
e-mail: nanlicqu@126.com

Y. Zhao
Sinopharm Chongqing Pharmaceutical and Medical Industry Design Institute Corporation, Chongqing 400010, China

W. Zhao
The Fourth Construction Co., Ltd. of China Electronics System Engineering, Shanghai 200051, China

T. Kang (ed.), *Proceedings of 5th International Conference on Civil Engineering and Architecture*, Lecture Notes in Civil Engineering 369,
https://doi.org/10.1007/978-981-99-4049-3_66

1 Introduction

The scale of semiconductor fabs has been growing along with the demand for semiconductors in recent years, resulting in a significant increase in energy consumption. Among them, the energy consumption of HVAC systems in semiconductor fabs can account for more than 50% of the total building energy consumption [1]. Due to the strict cleanliness requirements of cleanrooms, the energy consumption of HVAC systems for cleanrooms is 30–50 times more than that for thermal comfort [2, 3]. Therefore, it is undoubtedly essential to research energy consumption influencing factors for energy conservation of semiconductor fabs.

A series of energy conservation works on HVAC systems for cleanrooms has been conducted. Li et al. [4] discussed the main energy characteristics of HVAC systems for cleanrooms. They illustrated the importance of energy saving by treating the clean air volume independently from the air conditioning air volume. Through theoretical analysis and experiment, You et al. [5] verified that controlling variable fresh air volume in a clean air conditioning system is feasible and has an excellent energy-saving effect. Shi [6] found that the energy consumption of the chiller accounted for more than 30% of the total energy consumption of the plant through a year's operation energy consumption data of the HVAC system in the chip factory. Still, the annual full load operation time was less than 20%. In addition, the application of variable frequency pumps in the circulating water system can save 30% of the power. Through simulation and mathematical statistics, Li [7] obtained that the main influencing factors of energy consumption in the pharmaceutical industry are air changes, fan efficiency, fresh air volume, and refrigeration unit COP. Yuan [8] researched 16 electronic industrial buildings in Suzhou and concluded that building energy consumption was significantly correlated with building area, air conditioning energy consumption, air conditioning type, and total lighting power. Tong [9] pointed out that the energy consumption of the wind system designed for 12 h^{-1} air changes in the HVAC system for cleanrooms can be reduced by at least 20% compared to the requirement of 15 h^{-1}. Sun et al. [10] analyzed the energy consumption influencing factor of HVAC systems in the inpatient department of a hospital and obtained the sensitivity order of factors by orthogonal experiment as follows: indoor design temperature > fresh air volume > temperature difference between cold water supply and return water > chiller efficiency > heat transfer coefficient of external wall > pump efficiency. Hu et al. [11] developed simulation software for the energy consumption of high-tech fabs, which featured more detailed characteristics of the subsystems. In the application process, the measured data indicated that the process tool, chillers, and clean dry air systems are three major energy consumers. Yin et al. [12] investigated the indoor environment and the performance of air conditioning systems in semiconductor fabs. The results showed a cold-heat offset and energy loss in MAU. Lin et al. [13] proposed a new fan dry coil recovery unit (FDCU) recirculation system, which effectively ensures the cleanroom's environmental control and shortens the return air path. Compared with the traditional wall return system, it can reduce power consumption by more than 4%. Ma et al. [14] found through measurement that the

cleanliness of chip cleanrooms is often over-guaranteed, and there is a possibility of lowering the design standard for energy-efficient and economical operations.

In conclusion, more recent attention has concentrated on the HVAC systems for cleanrooms in hospitals and pharmaceutical industries or the associated energy-saving technology in semiconductor fabs. There is little research on the energy consumption influencing factors of HVAC systems for cleanrooms in semiconductor fabs. Therefore, the primary and significant energy consumption influencing factors of HVAC systems for cleanrooms in semiconductor fabs and their significance ranking were clarified in this paper using theoretical analysis, simulation, and orthogonal experiment, which can provide some guidance for energy conservation of HVAC systems in semiconductor fabs.

2 Methodology

2.1 Theoretical Analysis of Energy Consumption Influencing Factors

Compared with public buildings, cleanrooms in semiconductor fabs need to ensure higher air changes per hour to maintain ultra-high air cleanliness. The HVAC system for cleanrooms is typically required to operate year-round without breaks. Therefore, there are many differences in the energy consumption characteristics between cleanrooms in semiconductor fabs and public buildings.

To obtain the primary energy consumption influencing factors of HVAC systems for cleanrooms in semiconductor fabs, it is essential to determine the load composition of cleanrooms in semiconductor fabs. Since the energy demand of the semiconductor fabs is mainly the cooling demand, this paper will focus on the cooling part. Through theoretical analysis and related literature [15], the cooling load composition of semiconductor fabs has been determined by:

$$\mathrm{CL} = \mathrm{CL_{Envelope}} + \mathrm{CL_{OA}} + \mathrm{CL_{Body}} + \mathrm{CL_{Lightning}} + \mathrm{CL_{Process}} + \mathrm{CL_{Fan}} \quad (1)$$

where $\mathrm{CL_{Envelope}}$ is the cooling load of the envelope, $\mathrm{CL_{OA}}$ is the cooling load of the outdoor air, $\mathrm{CL_{Body}}$ is the cooling load of human body, $\mathrm{CL_{Lighting}}$ is the cooling load of lighting equipment, $\mathrm{CL_{Process}}$ is the cooling load of process equipment, and $\mathrm{CL_{Fan}}$ is the cooling load of fan.

And the influencing factors of cooling load in semiconductor fabs were further analyzed in Fig. 1.

The energy consumption of HVAC systems in semiconductor fabs is not only related to their load composition but also to the system's energy efficiency. Therefore, it is also necessary to analyze the energy consumption influencing factors regarding system operational energy efficiency. The analysis results are shown in Fig. 2.

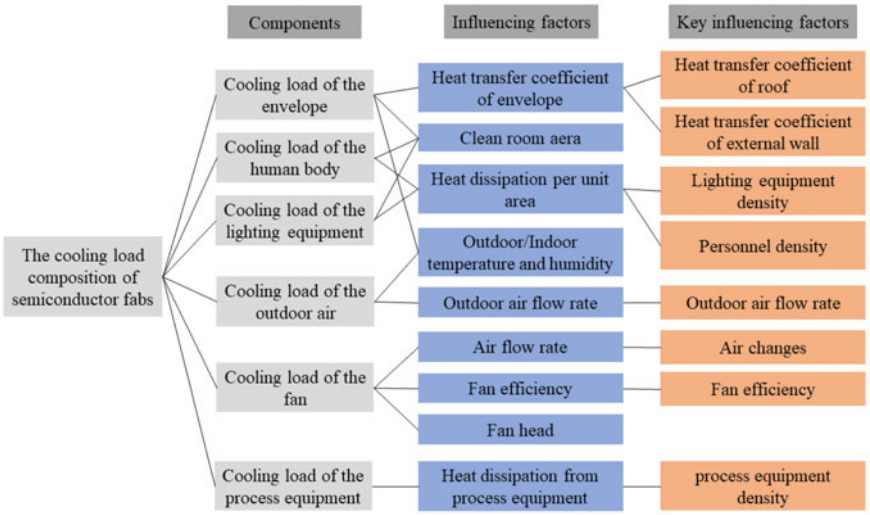

Fig. 1 Components and influencing factors of the cooling load in semiconductor fabs

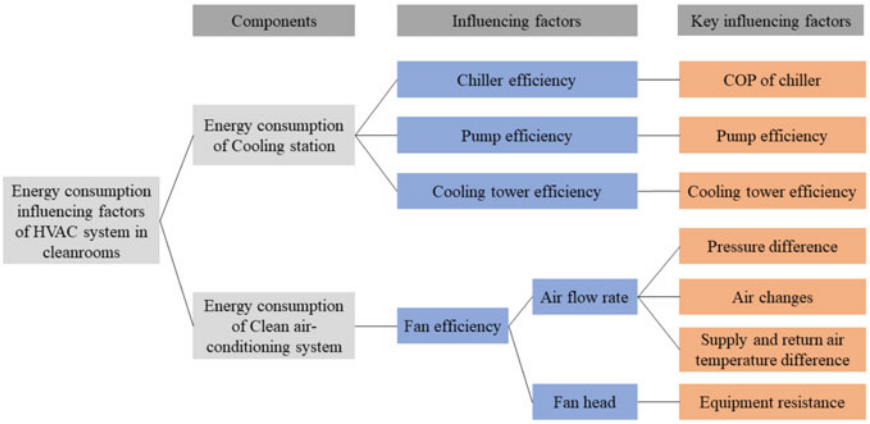

Fig. 2 Components and influencing factors of the operational energy consumption of semiconductor fabs

Based on the analysis results, combined with the results of the on-site investigation done by my research group [16, 17], 10 primary energy consumption influencing factors of HVAC systems in semiconductor fabs were selected. They can be divided into four parts—envelope influencing factors, internal disturbance influencing factors, wind system influencing factors, and water system influencing factors. The results are given in Table 1.

Table 1 Main energy consumption influencing factors of HVAC systems in semiconductor fabs

Source	Categories	Main influencing factors
Cooling load	Envelope	Heat transfer coefficient of roof
		Heat transfer coefficient of external wall
	Internal disturbance	Lighting equipment density
		Process equipment density
Operational energy efficiency	Wind system	Supply air temperature of MAU
		Outdoor air flow rate
		Air changes per hour
		Fan efficiency
	Water system	COP of chillers
		Pump efficiency

2.2 Simulation

To explore the variation of energy consumption of HVAC systems under different values of influencing factors, Design Builder was used to simulate dynamic energy consumption throughout the year of an assembly and testing semiconductor fab in Chengdu. The project model is shown in Fig. 3.

Statistics show that more than 90% of the energy consumption in semiconductor fabs is consumed by HVAC systems. Therefore, instead of taking into account other forms of energy consumption such as spray humidification, this study primarily focuses on power consumption.

The hourly energy consumption data is difficult to collect due to the confidentiality of the semiconductor fabs data. Therefore, to calibrate the model, monthly energy use was employed. Using the monthly energy consumption of HVAC systems in 2019, this model was calibrated in accordance with ASHRAE guideline 14–2014.

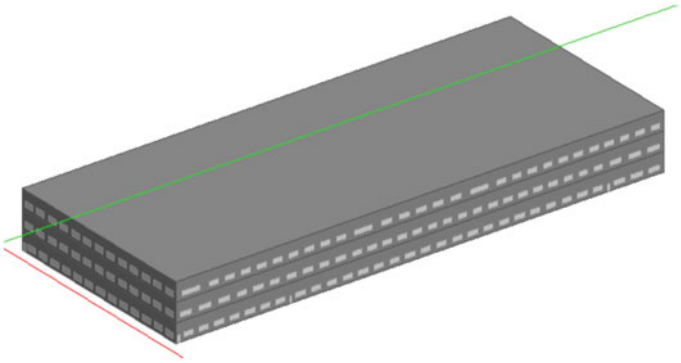

Fig. 3 Design builder simulation model of an assembly and testing semiconductor fab

The calculation formulas of dimensionless error metrics are shown in (2)–(3):

$$\mathrm{MBE} = \frac{\sum_{i=1}^{N_P}(M_i - S_i)}{\sum_{i=1}^{N_P} M_i} \tag{2}$$

$$\mathrm{CV(RMSE)}_P = \frac{\sqrt{\sum_{i=1}^{N_P}((M_i - S_i)^2/N_P}}{\overline{M}_P} \tag{3}$$

where M_i and S_i are measured and simulated data at instance i, respectively, p is the interval (i.e., monthly), N_P is the number of values at interval p (i.e., $N_{\mathrm{month}} = 12$).

ASHRAE Guideline 14 gives the acceptable limits for calibration to monthly data as $-5\% \leq (\mathrm{MBE})_{\mathrm{monthly}} \leq 5\%$ and $\mathrm{CV(RMSE)}_{\mathrm{monthly}} \leq 15\%$. The maximum of $(\mathrm{MBE})_{\mathrm{monthly}}$ of this model is 10.48%, and the $\mathrm{CV(RMSE)}_{\mathrm{monthly}}$ of this model is 5.2%, all within the reasonable range. Therefore, the accuracy of this model is judged to be acceptable.

2.3 Single-Factor Analysis

To initially assess the degree of influence of each factor on the energy consumption of HVAC systems, the impact of the single factor on the system's energy consumption under certain conditions of other factors was first studied.

Each factor is chosen at four optimal values for the energy consumption simulation, with the actual value serving as a benchmark value. The energy consumption of the benchmark value and the optimized value were compared to determine the extent of each factor's influence. The selected values of each factor are given in Table 2.

The maximum energy conversation rate was utilized as the evaluation index to measure the impact degree of each factor on the energy consumption of the HVAC system. The formula is as follows:

$$Q_A = \frac{A_{\max} - A_{\min}}{A_{\mathrm{base}}} * 100\% \tag{4}$$

where Q_A is the maximum energy conversation rate, A_{base} is the electricity consumption benchmark value of the HVAC system.

2.4 Orthogonal Experiment and Variance Analysis

Since there are complex coupling relationships among the energy consumption influencing factors, single-factor analysis is insufficient to accurately reflect each factor's significance degree. Therefore, an orthogonal experiment and variance analysis were

Table 2 Selected value of each influencing factor

Influencing factors	Benchmark	Level 1	Level 2	Level 3	Level 4
Supply air temperature of MAU (°C)	17	17.5	18	18.5	19
Air changes per hour (time/h)	ISO7 = 25	ISO7 = 22.5	ISO7 = 20	ISO7 = 17.5	ISO7 = 15
	ISO8 = 15	ISO8 = 13.5	ISO8 = 12	ISO8 = 10.5	ISO8 = 9
Process equipment density (W/m^2)	60	55	50	45	40
Pump efficiency (%)	70	75	80	85	90
Lighting equipment density (W/m^2)	24	21	18	15	12
Fan efficiency (%)	70	75	80	85	90
Outdoor air flow rate (%)	30	25	20	15	10
Heat transfer coefficient of external wall (W/m^2K)	0.62	0.5	0.4	0.3	0.2
Heat transfer coefficient of roof (W/m^2K)	0.49	0.39	0.29	0.19	0.11
COP of chillers	4.5	4.7	4.9	5.1	5.3

further employed. Two levels are taken for each factor: Level 1: the original model benchmark value. Level 2: the optimized value. The orthogonal experiments were arranged in $L_{12}(2^{10})$ and energy consumption was calculated by simulation. The benchmark and optimized values of energy consumption factors are given in Table 3.

To further give the significance ranking of each influencing factor, the results of the orthogonal experiment were subjected to variance analysis. The calculation formula is shown as (5)–(13):

Table 3 Selected value of energy consumption factors in orthogonal experiment

No.	Influencing factors	Level 1	Level 2
A	Supply air temperature of MAU (°C)	17	19
B	Air changes per hour (time/h)	ISO7 = 25	ISO7 = 15
		ISO8 = 15	ISO9 = 9
C	Process equipment density (W/m^2)	60	50
D	Pump efficiency (%)	70	80
E	Lighting equipment density (W/m^2)	24	18
F	Fan efficiency (%)	70	80
G	Outdoor air changes rate (%)	30	25
H	Heat transfer coefficient of external wall (W/m^2K)	0.62	0.4
I	Heat transfer coefficient of roof (W/m^2K)	0.49	0.29
J	COP of chillers	4.5	5.3

- The total sum of squares of deviations:

$$\mathrm{SS_T} = \sum_{i=1}^{n} y^2 - \frac{\left(\sum_{i=1}^{n} y_i\right)^2}{n} \tag{5}$$

where $\mathrm{SS_T}$ is the total sum of squares of deviations, i is the experiment times, $i = 1, 2, 3 \ldots, n$, y_i is the experimental results, the energy consumption value of the i times; n is the total number of experiments.

- The sum of squared deviations of factors:

$$\mathrm{SS}_j = \frac{1}{r} \sum_{i=1}^{m} K_{ij}^2 - \frac{\left(\sum_{i=1}^{n} y_i\right)^2}{n} \tag{6}$$

where SS_j is the sum of squared deviations of factors, j is the influencing factors serial number, $j = 1, 2, 3 \ldots, k$, m is the number of factor levels, K is the number of factors, and r is the number of horizontal repetitions in the experiment.

- The error sum of square

$$\mathrm{SS_e} = \mathrm{SS_T} - \sum_{j=1}^{k} \mathrm{SS}_j \tag{7}$$

- Freedom

$$df_\mathrm{T} = n - 1 \tag{8}$$

$$df_j = m - 1 \tag{9}$$

$$df_\mathrm{e} = df_\mathrm{T} - \sum_{j=1}^{s} df_j \tag{10}$$

where df_T is freedom of total deviations, df_j is freedom of factor deviation, df_e is freedom of error.

- The order of F distribution

$$\overline{\mathrm{SS}_j} = \frac{\mathrm{SS}_j}{df_j} \tag{11}$$

$$\overline{\mathrm{SS_e}} = \mathrm{SS_e}/df_\mathrm{e} \tag{12}$$

$$F_j = \overline{SS_j}/\overline{SS_e} \tag{13}$$

where $\overline{\mathrm{SS}_j}$ is the variance of factors, $\overline{\mathrm{SS}_\mathrm{e}}$ is the variance of experimental error, df_e is the freedom of error.

3 Results and Discussion

3.1 Single-Factor Analysis

Figure 4 shows the fitted curves for each influencing factor and the power consumption of HVAC systems under different values.

As shown in Fig. 4, the correlation coefficients between the power consumption of HVAC systems and the 10 influencing factors are all greater than 0.9, showing a linear relationship. According to the maximum energy conversation rate, the influence order of 10 energy consumption influencing factors is as follows: air changes per hour (15.04) > COP of chillers (10.04) > supply air temperature of MAU (8.57%) > outdoor air flow rate (7.86) > fan efficiency (7.44%) > pump efficiency (5.66%) > lighting efficiency (4.99%) > process equipment efficiency (3.98) > heat transfer coefficient of roof (0.81) > heat transfer coefficient of external wall (0.54%).

3.2 Variance Analysis

By formula (5)–(13), the value of SS_j, df_j, $\overline{\mathrm{SS}_j}$, F_j can be calculated. The F value and its order were obtained as given in Table.4.

If the F value of the influencing factor is greater than the critical value at a certain significance level, it will be considered a significant influencing factor. The larger the F value, the more significant the impact. The significance level α is often used with values of 0.05, which can be obtained by the table of F critical values. Therefore, the significant energy consumption influencing factors of HVAC systems in semiconductor fabs are total air changes and COP of chillers. The F value of each energy consumption influencing factor is shown in Fig. 5.

4 Conclusion

The primary energy consumption influencing factors of HVAC systems for cleanrooms in semiconductor fabs have been identified by this study with success. Significant influencing factors and their significance rankings were established by simulation, single-factor analysis, orthogonal experimentation, and variance analysis. The following is a summary of the key findings:

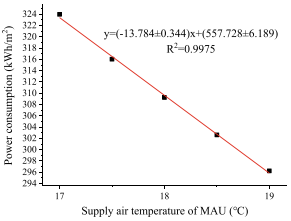

a. Fitting curve of supply air temperature of MAU

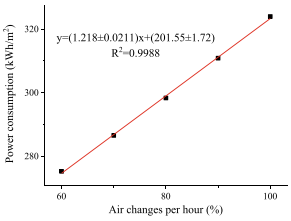

b. Fitting curve of air changes per hour

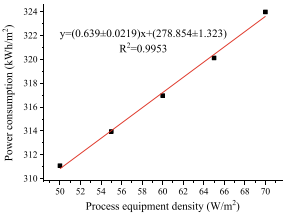

c. Fitting curve of process equipment density

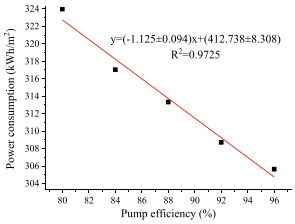

d. Fitting curve of pump efficiency

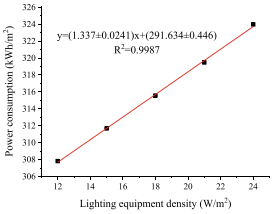

e. Fitting curve of lighting equipment

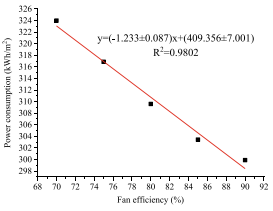

f. Fitting curve of equipment of fan efficiency

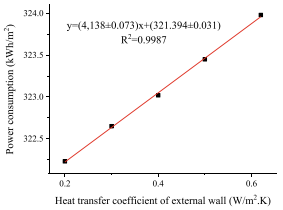

g. Fitting curve of coefficient of external wall

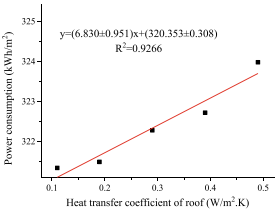

h. Fitting curve of coefficient of external wall

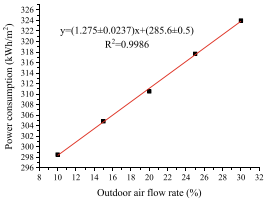

i. Fitting curve of outdoor air flow rate

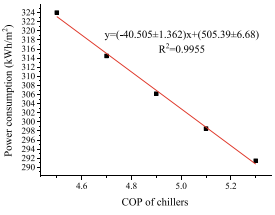

j. Fitting curve of COP of chillers

Fig. 4 Fitting curves of 10 influencing factors and the HVAC system power consumption

Table 4 *F* value and its order in variance analysis

Influencing factors	*F* value	Sort
Supply air temperature of MAU	121.711	3
Total air changes	478.043	1
Process equipment density	23.430	7
Pump efficiency	27.470	6
Lighting equipment density	21.451	8
Fan efficiency	50.581	5
Outdoor air changes rate	58.865	4
Heat transfer coefficient of external wall	7.228	10
Heat transfer coefficient of roof	15.272	9
COP of chillers	205.717	2

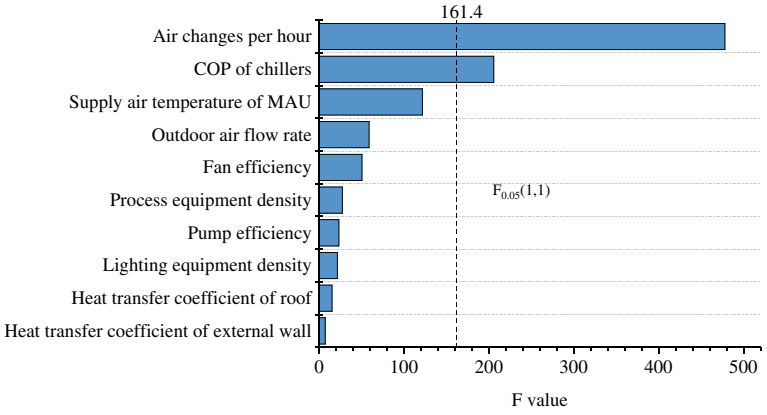

Fig. 5 *F* value of energy consumption influencing factors of HVAC system in semiconductor fabs

- According to theoretical analysis, 10 primary energy consumption influencing factors of HVAC systems for cleanrooms in semiconductor fabs were obtained and can be divided into four parts: The first part is envelope influencing factors including heat transfer coefficient of roof and heat transfer coefficient of external wall. The second part is internal disturbance influencing factors including lighting and process equipment density. The third part is wind system influencing factors including supply air temperature of MAU, outdoor air flow rate, air changes per hour, and fan efficiency. The fourth part is water system influencing factors including COP of chillers and pump efficiency.
- According to single-factor analysis, the influence order and maximum energy-saving rate of 10 energy consumption influencing factors of HVAC systems for cleanrooms in semiconductor fabs is obtained as follows: air changes per hour (15.04%) > COP of chillers (10.04%) > supply air temperature of MAU (8.57%) > outdoor air flow rate (7.86%) > fan efficiency (7.44%) > pump efficiency (5.66%)

> lighting efficiency (4.99%) > process equipment efficiency (3.98) > heat transfer coefficient of roof (0.81) > heat transfer coefficient of external wall (0.54%).

- According to orthogonal experiment and variance analysis, the significance order and F value of 10 energy consumption influencing factors of HVAC systems for cleanroom in semiconductor fabs is obtained as follows: air changes per hour ($F = 478$) > COP of chillers ($F = 205$) > supply air temperature of MAU ($F = 121$) > outdoor air flow rate ($F = 59$) > fan efficiency ($F = 51$) > pump efficiency ($F = 27$) > process efficiency ($F = 23$) > lighting equipment efficiency ($F = 21$) > heat transfer coefficient of roof ($F = 15$) > heat transfer coefficient of external wall ($F = 7$). Air changes per hour and COP of chillers are significant influencing factors at the significance level of 0.05.
- The ranking results of single-factor analysis and variance analysis are typically identical, both pointing to the conclusion that wind system influencing factors have the most significant impact on the energy consumption of HVAC systems in semiconductor fabs. Therefore, it is crucial to focus on the energy conservation of wind systems in semiconductor fabs in future research.

However, the influence of manufacturing processes and exhaust systems on HVAC systems is not examined in this paper's investigation of energy consumption influencing factors. Further research is required in the area of cleanrooms to determine how manufacturing processes and exhaust systems affect HVAC system energy consumption. Additionally, the HVAC system model constructed in this research has received some processing for simplification and equivalent replacement. Nonetheless, future studies may attempt to conduct more accurate simulation studies using different energy simulation tools.

References

1. Zhuang CX (2021) Coordinated demand-controlled ventilation strategy for energy-efficient operation in multi-zone cleanroom air-conditioning systems. Build Environ 191:107588
2. China National Standardization Administration (2018) Guidelines for energy saving in clean rooms and controlled environments. China Standard Press, China, Beijing
3. Zhao WX, Li HX, Wang SW (2022) A comparative analysis on alternative air-conditioning systems for high-tech cleanrooms and their performance in different climate zones. Energy 261:125284
4. Li HX, Ning YS (2009) Characteristics and energy saving of air conditioning system in clean workshop. J Build Energ Effi 37(3):24–27
5. You YW, Cao BS, Li Y et al (2010) Research on energy saving control of variable air volume in clean air conditioning system. Contam Control Air-Condition Technol (2):15–18
6. Shi JY (2014) Research on energy saving of air conditioning system in semiconductor workshop. Xi'an University of Science and Technology, China, Shaanxi
7. Li X (2014) Multi-factor analysis and research on the influence of energy consumption of purification and air conditioning system in pharmaceutical plant. Tianjin University, China, Tianjin
8. Yuan W (2015) Analysis of energy consumption evaluation of electronic industrial buildings in Suzhou region. Suzhou University of Science and Technology, China

9. Tong X (2017) Design of split-level purification air conditioning for tall clean plants. Clean and Air Conditioning Technology, China
10. Sun MZ, Yao JS (2019) Analysis of factors influencing energy consumption of hospital inpatient air conditioning. Heat Ventilat Air Condition 49(1):101–105
11. Hu SC, Lin T, Fu BR (2019) Analysis of energy efficiency improvement of high-tech fabrication plants. Int J Low-Carbon Technol 14(4):508–515
12. Yin JW, Liu XH, Guan BW et al (2020) Performance and improvement of cleanroom environment control system related to cold-heat offset in clean semiconductor fabs. Energy Build 224:11094
13. Lin T, Hu SC, Xu TF et al (2014) Developing an innovative fan dry coil unit (FDCU) return system to improve energy efficiency of environmental control for mission critical cleanrooms. Energy Build 90(1):94–105
14. Ma Z, Guan B, Liu X et al (2020) Performance analysis and improvement of air filtration and ventilation process in semiconductor clean air-conditioning system. Energy Build 228:110489
15. Tao CY (2020) Study on the energy consumption influencing factors of clean air conditioning system and comprehensive evaluation of operation in chip plant. Chongqing University, China
16. Zhao Y (2021) Research on evaluation method of energy-saving operation of clean air conditioning system in chip factory. Chongqing University, China
17. Feng YM (2013) Research on the diagnosis method of cooling station based on hierarchical index system. Tsinghua University, China

Investigating Thermal Bridges in Curtain Walls of High-Rise Building in Indonesia

Muhammad Rafif Cahyadi Agung and Miktha Farid Alkadri

Abstract Thermal comfort plays an important part when considering the performance of the building façade. One strategy to achieve thermal comfort is to reduce the thermal loss in the building envelope, which is often referred to as thermal bridges. Although the issue of thermal bridges has been extensively considered in the building design and construction, its contexts are predominantly addressed in the four-season countries due to the need for insulating materials during winter. In fact, this issue also has great relevance in tropical countries such as Indonesia, especially related to high energy consumption due to the cooling loads system. Thus, this study aims to analyze thermal bridges on curtain walls of high-rise buildings in Indonesia. To do so, a computational simulation workflow is developed by using THERM and Ladybug in Grasshopper. In parallel with that, on-site measurements are also conducted to gather the room and materials temperature by using HOBO temperature logger and FLIR thermal camera. As result, this study reveals that linear thermal bridges are found in the building element junction and they can significantly affect the building performance both interior and exterior. This study recommends addressing the issue of thermal bridges in Indonesian building codes.

Keywords Thermal bridges · Linear thermal transmittance · Curtain wall · High-rise building

1 Introduction

As the capital city of Indonesia, Jakarta is the most populated city and even in Southeast Asia. This makes Jakarta one of the fastest growing cities, surpassing Beijing and Bangkok [1]. Along with the growth of Indonesia's population, annual

M. R. C. Agung · M. F. Alkadri (✉)
Cluster of Architectural Sciences and Building Technology, Department of Architecture, University of Indonesia, Depok, Indonesia
e-mail: miktha@ui.ac.id

T. Kang (ed.), *Proceedings of 5th International Conference on Civil Engineering and Architecture*, Lecture Notes in Civil Engineering 369,
https://doi.org/10.1007/978-981-99-4049-3_67

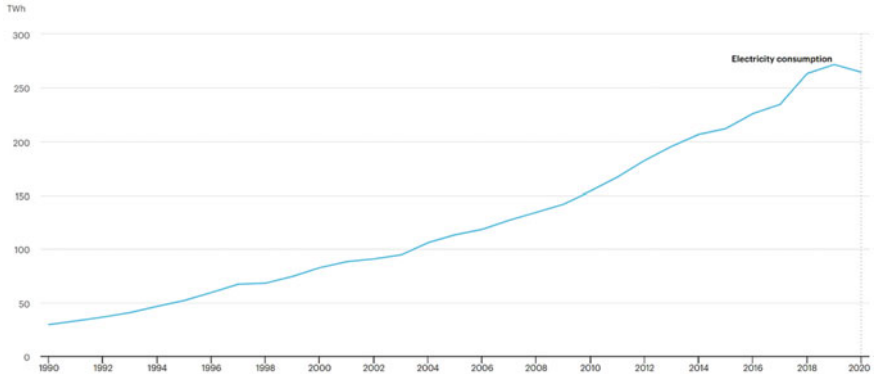

Fig. 1 Indonesia's electricity consumption graph 1990–2020 [2]

Fig. 2 Typical building energy consumption in tropical countries [3]

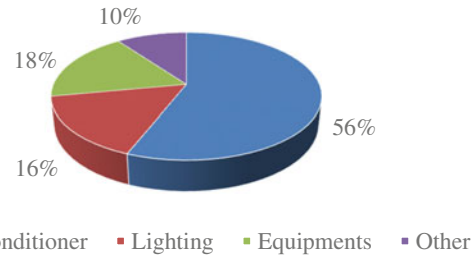

energy consumption has also increased rapidly. As shown in Fig. 1, the total energy use in Indonesia in 2019 reached 271.7 TWh [2].

A study conducted by Katili et al. [3] on cooling methods to achieve thermal comfort shows the typical building energy consumption data in tropical countries (see Fig. 2). This shows that the energy consumption is mainly dominated by the use of air conditioning systems.

Thermal comfort is defined as a state of mind that describes satisfaction with the thermal environment that requires subjective evaluation [4]. Lechner describes three level of methods that can be used to achieve thermal comfort when designing the building [5]. They are the reduction of heat flow through the building envelope, passive systems, and mechanical equipment. In the context of Indonesian buildings, air conditioner (AC) and fans, which are included in the third tier, provide the largest contribution to thermal comfort, while the first tier is often neglected. In this regard, the reduction of heat flow within the building envelope refers to the issue of thermal bridges.

Thermal bridges happen when thermal transmittance of the building component changes significantly [6]. This is often caused by the difference of the material conductivity, and/or changes in material thickness, and/or changes at internal and external areas at junctions of floor/wall/roof [6]. In general, the issue of thermal

bridges has already been considered in building codes in most countries with a four-season of climatic context. It specifically affects the heat flow within the building envelope and the energy usage [7]. For example, Theodosiou et al. [8] investigate thermal bridges on insulated wall configurations of Greek Building to calculate its effect on energy usage. The results show that thermal losses in the building are 35% higher than previously estimated, and the energy required to heat the building is 30% higher compared to calculations that does not consider thermal bridges. Another existing study exemplifies the decreasing of energy consumption in the Mediterranean house around 25% for terrace, 17.5% for semi-detached house, and 3.5% for cooling the building [9].

To the best knowledge of the authors, however, there has been no studies yet that specifically address the issue of thermal bridges in Indonesian building codes SNI 6389 [10]. This is because insulating materials are rarely implemented in building construction. In fact, thermal bridges can principally affect thermal comfort of the building during cooling activities and also the energy usage.

Therefore, this study aims to identify the potential thermal bridge in the building envelope based on Indonesian climatic context. This study specifically investigates a computational method of heat flow and psi-values (linear thermal transmittance) of the selected building components. Furthermore, the following section will discuss the theoretical framework of these aspects.

2 Theoretical Foundation

2.1 Heatflow Within the Building Envelope

In general, heat flows can be categorized into one-, two-, or three-dimensional heat flows. In this regard, when the heat flows perpendicularly to the plane or surface of an element, the process is called one-dimensional heat flow [4]. This usually applies only to infinitely large elements with parallel plane surfaces ad uniform cross sections. On the other hand, two- or three-dimensional heat flows happen when the boundary or materials of plane parallel surfaces are not homogenous [4]. Furthermore, areas with an increased multidimensional heat flow occurs can refer to thermal bridges [4]. According to ISO 14683 [11], the inaccuracy when calculating heat loss of the building envelope can be corrected using the following equation (see Eq. 1)

$$H_{\text{total}} = \sum U_{\text{ext.wall}} A_{\text{ext.wall}} + \sum U_{\text{roof}} A_{\text{roof}} + \sum U_{\text{basement}} A_{\text{basement}} + U_{\text{window}} A_{\text{window}} + \sum U_{\text{door}} A_{\text{door}} + \sum \psi_k l_k + \sum X_j \quad (1)$$

with:

H_{total} heat loss within the building envelope, W/K.
U thermal transmittance of the building component, W/(m^{2}K).

A surface area of the building component, m^2.
ψ_k linear thermal transmittance at joint k, W/(mK).
l_k length of joint k, m.
X_j point thermal transmittance, W/K.

Furthermore, this study will focus on linear thermal bridges. Theodosiou et al. describe that linear thermal bridges can have an overall heat transfer effect on the building envelope up to 30% or higher [12]. Besides, point thermal bridges can also have a significant impact on overall heat loss, although they are rare and very limited to a few building constructions [12].

2.2 Thermal Bridge

Thermal bridge is part of the building envelope, when the uniform thermal resistance is significantly changed by the full or partial penetration of the building envelope by materials with different thermal conductivity, and/or changes in the thickness of the material, and/or the difference between internal and external areas, as occurs at the junction of the wall/floor/ceiling [6].

2.2.1 Types of Thermal Bridge

Thermal bridge according to ASHRAE is classified into three categories: clear field, linear, and point [13]. The clear field is the sum of evenly distributed thermal bridges such as metal studs, brick ties, or connections between claddings. This is usually calculated with the U-Value of the wall or roof. Linear thermal bridge is an additional heat flow caused by a detail that can be defined by a unit length on a building surface. The use of psi-value is usually multiplied by the length of occurrence of the linear thermal bridge, then added to the total heat loss of the building. Point thermal bridge is a heat flow that occurs in one element or discrete point, usually occurs if there is penetration in large areas such as walls, roofs, and floors [13].

2.2.2 Psi-Values (Linear Thermal Transmittance)

According to International Standard ISO 10211 [6], the linear thermal transmittance is defined as the rate of heat flow at steady state divided by the length and temperature difference between the environments on both sides of a thermal bridge. In this regard, the linear thermal transmittance can be described as a quantity of the influence of the linear thermal bridge on the total heat flow. It is further illustrated through the equation below (see Eq. 2):

$$\psi = L_{2D} - \sum_{j=1}^{N_j} U_j l_j \tag{2}$$

with:

L_{2D} numerically defined two-dimensional (2D) technical thermal coupling fact considered for the joints of the building, W/(mK).
U_j thermal transmittance of structure j, W/(m^{2}K).
l_j length of the part of the structural model j, where U_j transmission coefficient can be applied, m.

Furthermore, the overall heat transfer through the two-dimensional components of the building envelope (i.e., wall, roof, floor) can be assessed using Eq. 3, whose sum refers to the linear thermal bridges associated with the component [6].

$$Q = \left(U.A + \sum_j \psi_j.l_j \right).(T_i - T_o) \tag{3}$$

Equation 3 can be rewritten in a different form to Eq. 4. Here, the impact of thermal bridges is represented as an additional thermal transmittance value, U, later defined as Eq. 5 below:

$$Q = (U + \Delta U).S.(T_i - T_o) \tag{4}$$

$$\Delta U = \frac{1}{S}.\sum_j \psi_j.l_j \tag{5}$$

with:

Q heat flow, W.
U thermal transmittance or U-Value, W/(m^{2}K).
S surface area, m^2.
T temperature, °C.
i indoor.
o outdoor.
U_j thermal transmittance of structure j, W/(m^{2}K).
l_j length of the part of the structural model j, m.

3 Method

The proposed method in this study combines two tasks, namely on-site measurements and computational simulations. On-site measurement aims to gather a series of initial datasets such as room and material temperature based on predefined period. These datasets are then inputted to the computational simulation in order to perform the thermal bridge simulation. Furthermore, the detail procedure of each task is discussed below.

3.1 On-Site Measurement

Before conducting on-site measurement, first the radiation analysis simulation was carried out to identify which facades receive the most heat. This step is conducted using a 3D modeling tool, Rhinoceros based on working hours period (from 8 a.m. to 6 p.m.) for 365 days. Afterward, on-site measurements were conducted to record the interior room temperature and exterior facade temperature using HOBO temperature logger and FLIR thermal camera (see Fig. 3).

In this regard, Hobo temperature logger is used to collect the temperature data and determine when the highest temperature difference (ΔT) occurs. Meanwhile, FLIR thermal camera is a thermal imaging camera that captures and visualizes the material surface temperature. In this case, the images were captured from both the inside and outside of the building envelope (see Fig. 4).

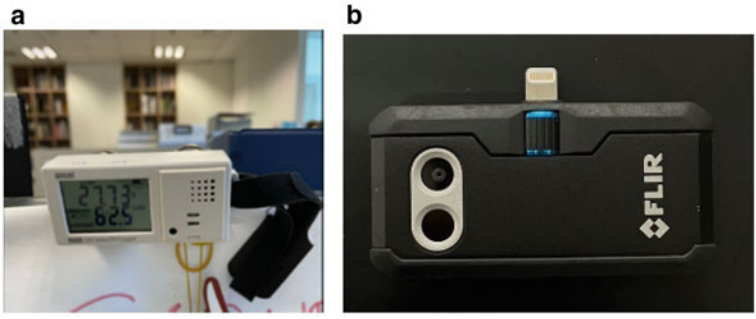

Fig. 3 Tools used for on-site measurement: **a** Hobo MX1101; **b** FLIR One Pro iOS

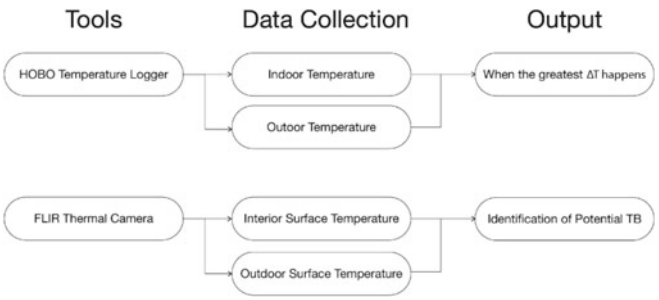

Fig. 4 On-site measurement procedures

3.2 Computational Simulation

This study uses two computational simulation: Radiation analysis simulation and thermal bridge simulation. The first simulation is needed to provide input for the second simulation.

3.2.1 Radiation Analysis Simulation

The objective of the analysis is to determine which façade receives the most heat. The workflow for the overall simulation can be seen in Fig. 5. This workflow uses Rhino 3D [14] and Grasshopper [15]. Rhino 3D is a 3D CAD that is developed by Robert McNeel and Associates. Grasshopper is a visual programming language that is integrated within the Rhino 3D itself. Input used for the simulation is EPW file, the 3D model of the building and its context. The output is visualization of each building faces with color that indicates the amount of heat it receives in kWh/m^2.

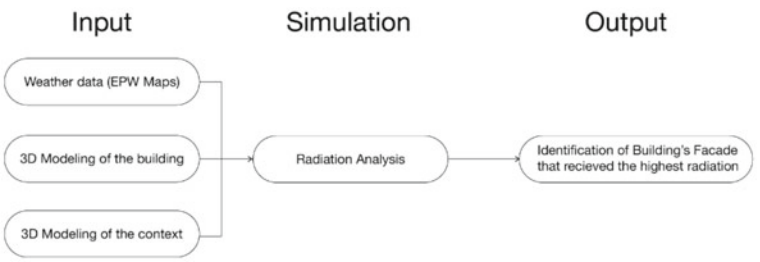

Fig. 5 Radiation analysis simulation workflow

3.2.2 Thermal Bridge Simulation

This study proposes a computational workflow for thermal bridge simulation by using a visual programming language, Grasshopper [15] integrated with THERM [16] for the heat transfer processes (see Fig. 6). This simulation employs two-dimensional conductive heat transfer. The input required for this simulation is the material temperature for the innermost and outermost layers, obtained from field measurements. The goal is to calculate the het flow that occurs with and without a thermal bridge.

3.3 Selected Case Study

The selected case study is an office room at the 23rd floor of a high-rise building located in South Jakarta, Indonesia (see Fig. 7a). The office uses curtain wall as the façade (see Fig. 7a).

The office room of the case study is selected because of its active usage at working hours, high intensity of air conditioner usage that is caused by heavy usage of

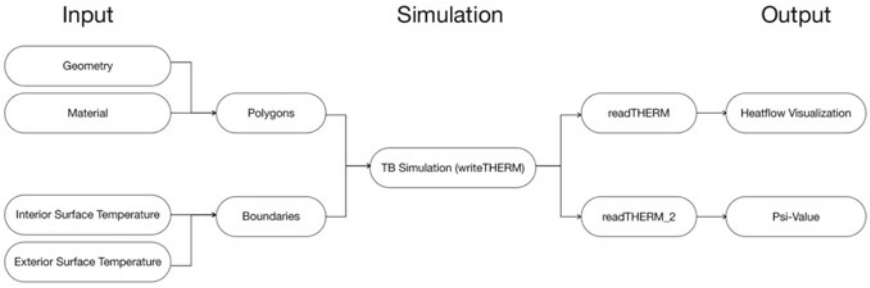

Fig. 6 Computational workflow of thermal bridge simulation

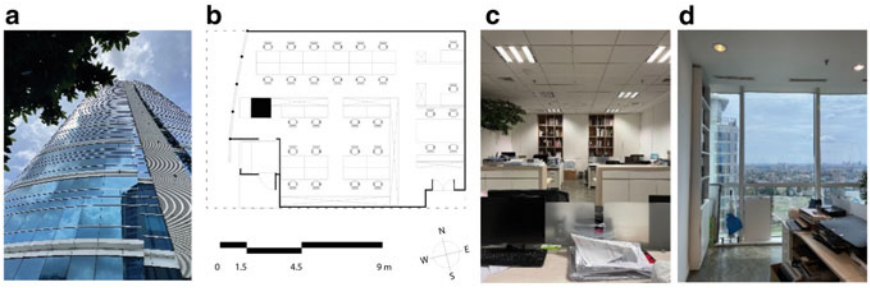

Fig. 7 **a** Façade of the building; **b** Floor plan of the office; **c** Interior atmosphere; **d** View from the office

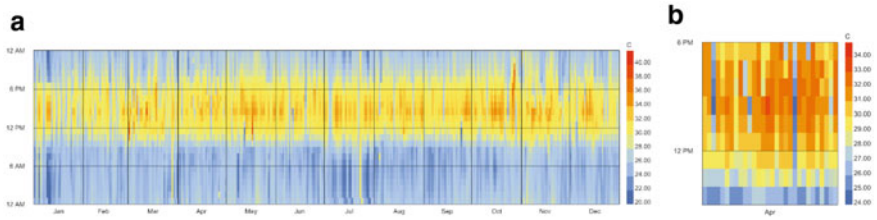

Fig. 8 Dry bulb temperature at the office: **a** Annual; **b** April

computer equipment (see Fig. 7c), and the façade is facing west (see Fig. 7d), which means it is the most exposed face of the building within the office's working hours.

4 Result and Discussion

4.1 DBT Obtained from EnergyPlus Weather Data (EPW)

Yearly dry bulb temperature data will be needed to decide the time step that will be used in the radiation analysis. The EPW of Jakarta City is analyzed with time period from 9 a.m. to 5 p.m. which is taken from the average working hours of employees at the case study site. Data for the whole year is shown (see Fig. 8a). Since the case study was conducted in April, further analysis was then carried out for specific hourly data for 1 month (see Fig. 8b).

Because Indonesia is a tropical country which has two seasons, dry and wet, the yearly dry bulb temperature is rather constant for the whole year. After obtaining the detailed data of dry bulb temperature at the chosen month, the study was conducted (April). It is decided that the time step for the radiation analysis is from 12 to 4 p.m. The selected hours contain a fairly high air temperature at around 33 °C at its highest.

4.2 Radiation Simulation Results

Radiation analysis simulation is then conducted with the chosen timestep (12–4 p.m.). The building surrounding the site is also inputted because it could affect the result. The result is a color coded data of each façade that shows how much radiation it received (see Fig. 9). It can be seen that the west side receives the most solar radiation. Therefore, a thermal bridge simulation will be carried out on the facade facing the west side.

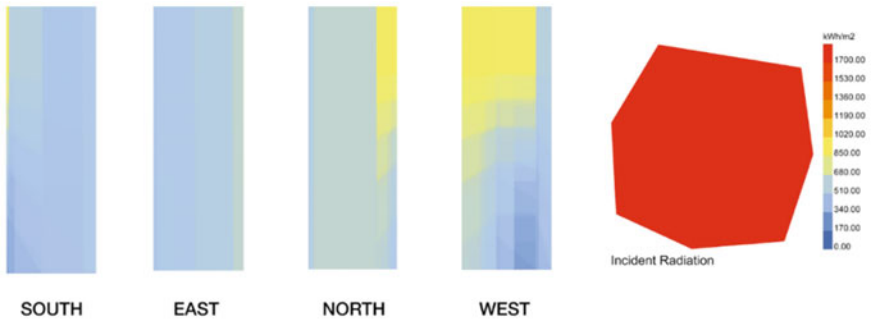

Fig. 9 Radiation analysis of building façade orientation

4.3 Site Observation Result

4.3.1 Room Temperature of Interior and Exterior

There are two sets of data from the HOBO temperature logger, one is from the device that is located outside, and one is inside. The graph (see Fig. 10) shows that the lowest temperature at the exterior is 28 °C which occured at 10:32, and reach its highest temperature at 36 °C which occurred at 15:32. This happened because the west-facing façade receives a lot of heat in the afternoon. The graph (see Fig. 10) shows that the lowest temperature at the interior is 22 °C which occured at 11:46, and reach its highest temperature at 27 °C which occurred at 10:32.

The detailed data is exported into datasheet, where the temperature difference (ΔT) is also calculated to determine at which time has the greatest ΔT. It is found that the largest ΔT occurred at 15:32 which is 10.93 K. Therefore, 15:32 WIB will be the time period chosen for the thermal bridge simulation.

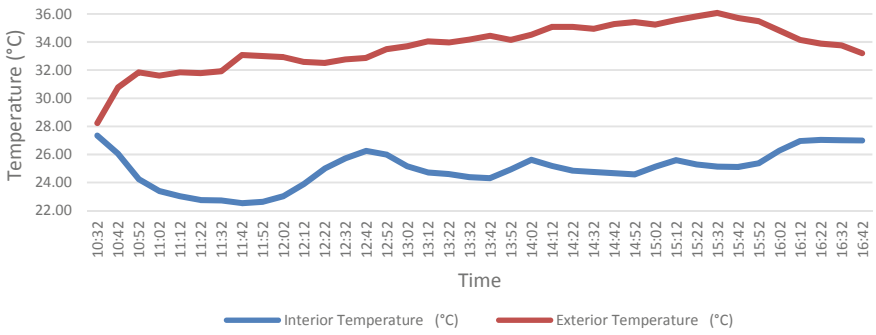

Fig. 10 Graph from HOBO temperature logger located at the exterior and the interior

4.3.2 Surface Temperature of Interior and Exterior Building Components

There are two types of junction that are studied in this paper. These types of junction are chosen because it is one of the main elements of curtain wall (see Fig. 11). These junctions are:

a. Transom and glass
b. Mullion and slab edge.

Images taken in Table 1 are images of the junctions that are going to be simulated. The images are taken at 15.30 which the greatest temperature difference throughout the day happened. It is found that there are some possibilities of thermal bridge because of the significant temperature difference at some parts of the building component.

4.4 Thermal Bridge Simulation Result

The result of the thermal bridge simulation will be explained in this part. The output result is visualization of the heat flow and the *psi-value* (ψ). The *psi-value* (ψ) is then compared to the building codes that consider *psi-value* (ψ) in their guide to decide whether the values are below or above the limit.

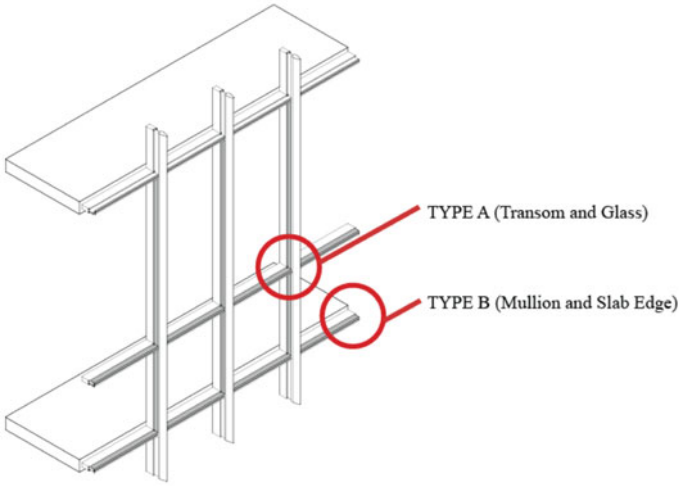

Fig. 11 Main elements of curtain wall

Table 1 Image taken with thermal imaging camera

Junction		Image		Surface temperature (°C)	
Type	Side	IRT camera	Real camera	Highest	Lowest
A	Interior	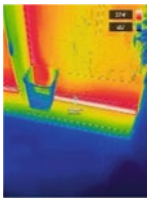		37.5	25
B	Interior	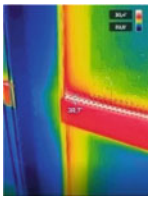	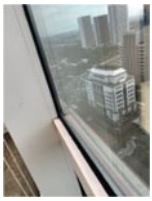	38.7	28.9
A	Exterior	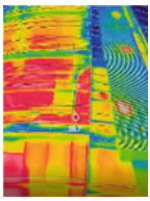		38.7	28
B	Exterior	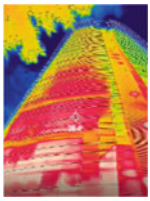		38.4	27.6

4.4.1 Junction A (Transom and Glass)

The simulation results for the visualization of heat flow at the junction of the transom and glass are shown (see Fig. 12). It can also be seen that there is leakage of heat flow at several points. Seen in the green-yellow part that the temperature is 33–34 °C. Meanwhile, when compared with the temperature of the glass surface which is the main structure on the facade of the curtain wall, the temperature is only 33.2–33.5 °C. The simulation results for the visualization of the thermal bridge for junction A show the presence of a thermal bridge.

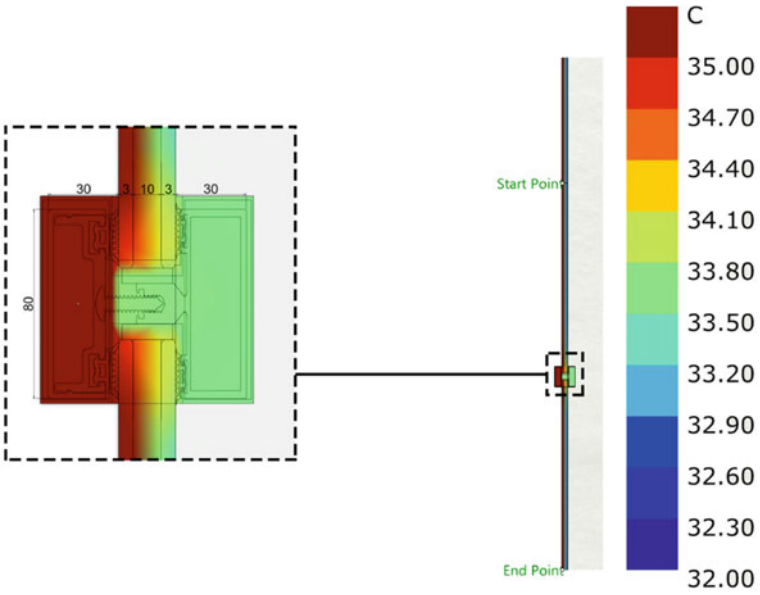

Fig. 12 Heat flow visualization of junction A: Transom and glass

It was found at the junction of the glass and transom for the heat flow through the main structure of 152.7 (W/m), while that through the comparative structure was 150.3 (W/m). The psi-value (ψ) obtained is 0.146668 (W/mK).

4.4.2 Junction B (Mullion and Slab Edge)

The simulation results for the visualization of heat flow at the junction of the mullion and floor slab are shown (Fig. 13). It can also be seen that there is leakage of heat flow at several points. Seen in the green-yellow part that the temperature is 33.8–34 °C. Meanwhile, when compared with the temperature of the glass surface which is the main structure on the facade of the curtain wall, the temperature is only 32.9–33.2 °C. The simulation results for visualization of thermal bridges for this junction B show the presence of a thermal bridge.

It was found at the junction of the mullion and slab edge that the heat flow through the main structure was 101 (W/m), while that through the comparative structure was 97.4 (W/m). The psi-value (ψ) obtained is 0.22354 (W/mK).

The psi-value (ψ) results at both junction that are simulated are then compared with building codes that considers psi-value (ψ) in the handbook.

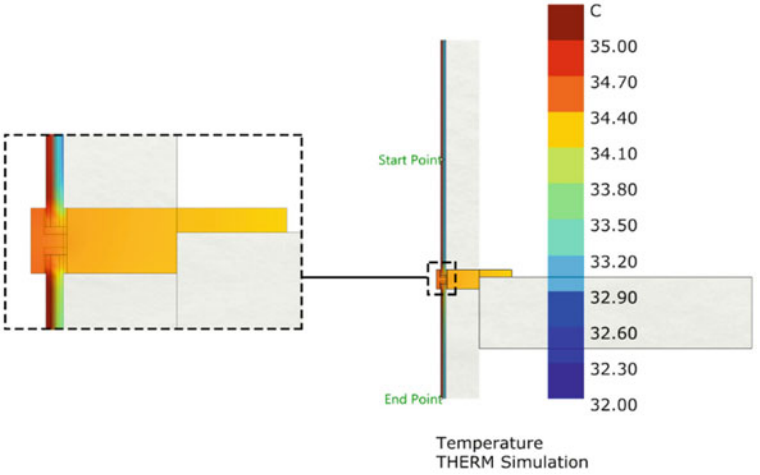

Fig. 13 Heat flow visualization of junction B: Mullion and slab edge

Table 2 Comparison of psi-value (ψ) case study results with building codes

Junction	Psi-value (W/mK)	Psi-Value Limits (W/mK)					
		French Building Code			Denmark Building Code		Passivhaus Organization
		Residential	Apartment	Others	Window Fittings	Building Foundation	
A	0.1466	<0.65	<1	<1.2	<0.06	<0.4	<0.01
B	0.2235	<0.65	<1	<1.2	<0.06	<0.4	<0.01

4.5 Psi-Value (ψ) Comparison

The results of the psi-value (ψ) are then compared with building standards that are available in several countries/regions (see Table 2). Green indicates the psi-value (ψ) is still in accordance with the standard and red does not.

4.6 Additional Thermal Transmittance (ΔU) Evaluation

Additional thermal transmittance (ΔU) that is caused by the thermal bridge is calculated by referring to Eqs. 4 and 5 that is mentioned in theoretical foundation. The calculation of heat gain from the two junctions is given in Table 3. The psi-values

Table 3 Additional thermal transmittance (ΔU) calculation

Junction	Ψ_j (W/mK) Psi-value	Length of junction	Amount of junction	l_j (m) Total length	$\Psi_j . l_j$ (W/K)	S (m^2) Surface area	ΔU (W/(m^2K)) Additional thermal transmittance
A	0.14666	0.08	5	0.4	0.058	0.4	0.146
B	0.22354	1	4	4	0.894	4	0.223
Total additional thermal transmittance caused by junction A and B							0.370

are obtained from the computational simulation, while the length of the junction is obtained from site observation.

It is found that the total additional thermal transmittance U of the two simulated junction types has a value of 0.3702 W/(m^2K). Instead of using psi-values, the Italian building code uses U-Value as unit when determining the qualitative value of thermal bridge. When referring to the Italian building codes, the U-value should not exceed more than 15% of the U-Value of the building components. If the U-Value for the curtain wall discussed in this paper is assumed 2 W/(m^2K), then this U-Value is still within safe limits because it is only 0.3702 W/(m^2K).

4.7 Heat Gain Evaluation

Table 4 gives the calculation for the additional heat gain of the two simulated junction types. Although the psi-value (ψ) of junction B is roughly two times larger than junction A, the additional heat gain caused by junction B is 16 times larger than junction B because of the length and amount of the junctions it has.

Table 4 Calculation of heat gained by thermal bridge

Junction	Psi-value (W/mK)	Length of junction (m)	Amount of junction	Total length (m)	Heat gain (W/K)
A	0.14666	0.08	5	0.4	0.058664
B	0.22354	1	4	4	0.89416
Total heat gain from thermal bridge					0.952824

5 Conclusion and Future Recommendation

This paper aims to identify the phenomenon of thermal bridge on two types of junction at a façade of a building located in Jakarta, Indonesia. Junction A is the junction of transom and glass, while Junction B is the junction of mullion and slab edge. By performing thermal bridge simulations and psi-value (ψ) calculations, these results can be evaluated and compared with several building codes in national building standard that considers thermal bridge in its guidebook.

The output of the simulation is a visualization of the heat flow that occurs in the building construction details and the value for the psi-value (ψ). The psi-value (ψ) is then calculated again into the heat loss/heat gain formula according to ISO 14683 (see Eq. 4). The psi-value (ψ) is also compared with some building codes regarding the standard psi-value (ψ) in some contexts. After conducting simulations on two types of junction on the facades of high-rise buildings in Jakarta, Indonesia, it was found that:

- It is true that there is a thermal bridge phenomenon.
- The psi-value (ψ) is still below the maximum value for the French and Italian building codes, but exceeds the maximum value for the Danish building codes and the Passivhaus organization.
- There is an inaccuracy in measuring the temperature of the surface material using an infrared thermal (IRT) imaging camera. This is due to the selection of building components that have glass, so that the temperature measured is the impact of conduction and radiation heat. In fact, for simulating the thermal bridge, it is only limited to heat transfer through conduction.
- Further discussion is needed to consider thermal bridges in OTTV calculations (Calculation of heat flow within the building envelopes that is used in Indonesian building codes).

The effect of the thermal bridge on the total heat gain/heat loss in a building still needs to be identified to find out how large the role of the thermal bridge is in contributing additional heat gain/heat loss. This is because the selected case study is only limited to 2 types of junctions. If all the junctions are calculated, it can be re-identified how much influence the thermal bridge has on the total heat transfer in the building envelope.

Acknowledgements This research is funded by Directorate of Research and Development, Universitas Indonesia under Hibah PUTI 2022 (Grant No.NKB-1149/UN2.RST/HKP.05.00/2022).

References

1. Jakarta population 2022. Jakarta Population 2022 (Demographics, Maps, Graphs) (n.d.). Retrieved 17 May 2022, from https://worldpopulationreview.com/world-cities/jakarta-population
2. IEA (2021) Indonesia—countries & regions. IEA. Retrieved 17 May 2022, from https://www.iea.org/countries/indonesia
3. Katili AR, Boukhanouf R, Wilson R (2015) Space cooling in buildings in hot and humid climates—a review of the effect of humidity on the applicability of existing cooling techniques. Paper presented at: SET 2015. Proceedings of 14th international conference on sustainable energy technologies, Nottingham, United Kingdom. https://doi.org/10.13140/RG.2.1.3011.5287
4. Szokolay SK, Brisbin C (2004) Introduction to architectural science: the basis of sustainable design. Architectural
5. Lechner N, Andrasik P (2020) Heating, cooling, lighting: sustainable design methods for architects. Wiley
6. ISO (2017) ISO 10211:2017. ISO. Retrieved 19 June 2022, from https://www.iso.org/standard/65710.html
7. Theodosiou T, Tsikaloudaki K, Kontoleon K, Giarma C (2021) Assessing the accuracy of predictive thermal bridge heat flow methodologies. Renew Sustain Energy Rev 136:110437. https://doi.org/10.1016/j.rser.2020.110437
8. Theodosiou TG, Papadopoulos AM (2008) The impact of thermal bridges on the energy demand of buildings with double brick wall constructions. Energy Build 40(11):2083–2089. https://doi.org/10.1016/j.enbuild.2008.06.006
9. Evola G, Margani G, Marletta L (2011) Energy and cost evaluation of thermal bridge correction in Mediterranean climate. Energy and Buildings 43(9):2385–2393. https://doi.org/10.1016/j.enbuild.2011.05.028
10. Loekita S, Priatman J (2015) OTTV (sni 03-6389-2011) and ETTV (BCA 2008) calculation for various building's shapes, orientations, envelope building materials: comparison and analysis. Civil Eng Dimension 17(2). https://doi.org/10.9744/ced.17.2.108-116
11. ISO (2017) ISO 14683:2017. ISO. Retrieved 19 June 2022, from https://www.iso.org/standard/65706.html
12. Theodosiou TG, Tsikaloudaki AG, Kontoleon KJ, Bikas DK (2015) Thermal bridging analysis on cladding systems for building facades. Energy Build 109:377–384. https://doi.org/10.1016/j.enbuild.2015.10.037
13. ASHRAE Research (2016) Standard 55-2013 user's manual: Ansi/Ashrae standard 55-2013, thermal environmental conditions for human occupancy
14. McNeel R (n.d.) Rhinoceros 3D. www.rhino3d.com. Retrieved 25 Aug 2022, from https://www.rhino3d.com/
15. Grasshopper (n.d.) Retrieved 25 Aug 2022, from https://www.grasshopper3d.com/
16. Therm. THERM | Windows and Daylighting (n.d.) Retrieved 24 Aug 2022, from https://windows.lbl.gov/software/therm

Simulation Analysis on the Influence of External Wall Thermal Parameters to the Air-Conditioning Load of Buildings with Internal Heat Sources

Huijie Zhang, Chen Hu, Liping Wang, and Weiping Zhao

Abstract As one of the key factors to maintain a stable indoor thermal environment, building envelope has a very important impact to the air-conditioning load and energy consumption. The thermal process of buildings with steady internal heat source is quite different from that of ordinary civil buildings. The envelope heat transfer progress of such buildings has been analyzed by means of qualitative analysis and theoretical derivation in this paper. An independent equipment room in Hefei area was taken as a referenced to analyzed the relationship between air-conditioning load and external thermal parameters under different indoor heat dissipation conditions with the software DeST. According to the simulation results, the exterior wall thermal parameters are obviously different when the design load and the accumulated load reach the minimum value. When the heat transfer coefficient is small and the thermal inertia index is large, the design load gets the minimum value. It is just the opposite when the cumulative load is minimized. Based on simulation data, the relationship between cumulative load and equipment heat dissipation and exterior wall thermal parameters was obtained. It has certain guiding significance for thermal engineering design of exterior wall of air-conditioning building with strong internal heat source.

Keywords Air-conditioning load · External wall · Thermal parameter

1 Introduction

The main function of air-conditioning system in the building is to maintain a stable indoor thermal environment. The thermal balance of the building is maintained by means of heating or cooling when the indoor temperature is lower or higher than the

H. Zhang · C. Hu
Research Institute of Economics and Technology, State Grid Anhui Electric Power Co., Ltd., Hefei 230009, China

L. Wang (✉) · W. Zhao
College of Civil and Engineering, Hefei University of Technology, Hefei 230009, China
e-mail: lpwang@hfut.edu.cn

T. Kang (ed.), *Proceedings of 5th International Conference on Civil Engineering and Architecture*, Lecture Notes in Civil Engineering 369,
https://doi.org/10.1007/978-981-99-4049-3_68

design condition. The envelope structure, such as exterior wall and roof, as the key factor to cut off the direct heat exchange between indoor and outdoor and to maintain a stable indoor thermal environment, has a very important impact on air-conditioning load and energy consumption. According to the building thermal environment theory, the heat from the outside to the interior through the opaque envelope is not a definite value even if the outdoor air parameters and indoor air temperature remain constant. It is not only related to the indoor and outdoor parameters and thermal parameters of the envelope, but also to the intensity of the indoor radiant heat source [1]. Therefore, it is of great significance to analyze the building envelope thermal parameters and indoor heat source intensity from the angle of air-conditioning load.

The limits of thermal parameters of building envelope of different types are set in relevant design specifications [2]. For example, the heat transfer coefficient limit of external walls of industrial buildings is 1.10 W/(m^2K) in hot summer and cold winter zone. The heat transfer coefficient limits of class A public buildings are 0.60 W/(m^2K) and 0.80 W/(m^2K), respectively. The limits of heat transfer coefficients of exterior walls of residential buildings are 0.60 W/(m^2K) and 1.00 W/(m^2K), respectively, taking thermal inertia index $D = 2.5$ as the dividing line. The influence of thermal parameters of building envelope on air-conditioning load had been studied also. Bai et al. [3] calculated the building air-conditioning cooling load of the residential building in Chongqing by eQUEST and analyzed the influence of the thermal inertia on the cumulative load under different air-conditioning running mode. The results showed that the effect of the thermal inertia index on the air-conditioning cooling load was not significant when the thermal inertia index is less than 3. Yang et al. [4] studied the correlation between average envelope window-wall ratio, atrium sky light ration, average index of the thermal inertia, average coefficient of heat transfer and cooling load of a large space building with atrium in Guangzhou. The results showed that the average heat transfer coefficient was moderately correlated to building load, but less correlated to atrium cooling load. The characteristics of building energy consumption in different envelope structures and building design combinations in Lanzhou and Zhengzhou were studied by Wang et al. [5]. The results showed that the thermal load sensitivity of the same envelope in Zhengzhou was higher than that in Lanzhou.

These researches verified the influence of building envelope thermal parameters on civil building air-conditioning load. There are some buildings with strong concentrated heat sources inside also in engineering practice. The influence of building envelope on building energy consumption is different from that of conventional civil buildings. The influence of heat dissipation density of indoor equipment in control building of a substation in alpine area on energy saving of building envelope was simulated by Lu et al. [6] with DeST. The results showed that the thermal insulation performance of exterior wall should be enhanced under the condition of low indoor heat dissipation density, the optimal heat transfer coefficient of exterior wall was existed under the condition of medium indoor heat dissipation density and the heat transfer coefficient of exterior wall should be appropriately increased under the condition of high indoor heat dissipation density. Cao et al. [7] took a 110 kV indoor substation in Shanghai as an example to simulate the energy consumption of the

substation's air-conditioning under different working conditions. The results showed that the heat transfer coefficient of the external wall and the roof of the substation should be higher than 2.0 W/(m^2K) and 1.4 W/(m^2K). Both of which were higher than the limits of the current design specifications. Taking Guangzhou city as an example, Liu et al. [8] simulated the annual air-conditioning operation energy consumption of a 220 kV indoor substation with DeST. The conclusion showed that in the absence of natural ventilation, building air-conditioning energy consumption would decrease with the increase of heat transfer coefficients of external walls, roofs and Windows. Liu [9] tested outdoor meteorological parameters, internal and external wall temperatures and other parameters of the south wall under 0 W/m^3 and 300 W/m^3 working conditions by establishing a scale experimental model of the industrial thermal workshop in Xi'an in summer. The results showed that heat flow in the south wall was transmitted from the indoor to the outdoor under 300 W/m^3.

These studies analyze the effect of heat transfer coefficient of envelope on air-conditioning load through simulation or experiment. According to the building thermal environment theory, the heat from outdoor to indoor through non-transparent envelope is not a certain value even if outdoor air parameters and indoor air temperature remain unchanged. It is not only related to indoor and outdoor parameters and thermal parameters of envelope, but also related to the intensity of indoor radiant heat source. The power of equipment in general civil buildings is small and intermittent, which has limited influence on the heat transfer process of the envelope. The building with strong internal heat source, such as high-temperature workshop and equipment room, has a strong internal heat source and works continuously. The correlation between building energy consumption and the outer envelope is obviously different from that of ordinary civil buildings. In this paper, the determination of external wall heat transfer direction under the condition of long-term operation of strong internal heat source was analyzed by theoretical deduction. An independent equipment room in Hefei was selected as an example to study the relationship between air-conditioning load and exterior wall heat transfer coefficient and thermal inertia index with the software of DeST.

2 Envelope Heat Transfer Process

To simplify the heat transfer progress, an independent equipment room has been selected as the example. The electrical equipment in the building runs continuously. There is no permanent staff and material transportation and storage in the room. The lighting system is turned on for a short time only during equipment maintenance. The indoor environmental parameters are maintained within a certain range by the continuously operating air-conditioning system. The heat generation of such buildings has the following characteristics.

- Stable single internal disturbance: No human heat dissipation indoors. Lighting heat dissipation is not regular. The heat fluctuation of electrical equipment could be ignored.
- Periodic double disturbance: Solar radiation and outdoor air temperature change periodically.
- Single type of enclosure structure: No internal wall heat transfer. Little influence on building heat of outer window and door because of the limited area.
- Simple sensible heat transfer: No moisture release. The ratio of heat and humidity is infinite.
- No heat transfer delay caused by materials or other furniture.

Due to the complexity of the factors affecting the thermal process of buildings, there are many thermal parameters involved. On the premise of ensuring the application and universality of the analysis results in the engineering field, assumptions and simplifications of external conditions are necessary.

- Steady-state heat conduction: The interior equipment is almost unchanged. The indoor temperature is relatively constant. Solar radiation and outdoor air temperature show periodic changes. The progress could be analyzed by steady-state heat conduction. The heat transfer direction could be determined by qualitative method when outdoor parameters change.
- Heat source heat dissipation: The heat diffuses into the room by means of conduction, convection and radiation. The convection heat dissipation evenly distributed in indoor air. The radiation heat dissipation evenly distributed in all indoor surfaces.
- Physical property condition: The same material and surface have the same physical property parameters (Fig. 1).

The main functions of the air-conditioning system in the building are to maintain a stable indoor thermal environment. When the indoor temperature deviates from the design condition, the system keeps the room temperature constant by heating or cooling. The heat of the room mainly includes heat dissipation of indoor equipment, heat transfer through the envelope and solar radiation. The heat dissipation of indoor equipment is not only the main source of indoor heat, but also affects the indoor and external heat transmitted through the non-transparent envelope, which plays an important role in the load of the air-conditioning system. The equipment heat Q exchanges heat with the indoor air and the inner surface of the envelope by means of convection, radiation and heat conduction. Let the proportions of convection, radiation and heat conduction exchange be α, β and γ.

The common way to analyze heat transfer process of building components such as exterior wall and roof is to list partial differential equations and boundary conditions. Then it is solved by theoretical derivation or numerical calculation. The whole heat transfer process could be expressed in time series by the solution process clearly. On the basis of the assumptions above, the influence of indoor factors on the inner surface of the envelope and outdoor parameters on the outer surface of the envelope could be investigated, respectively.

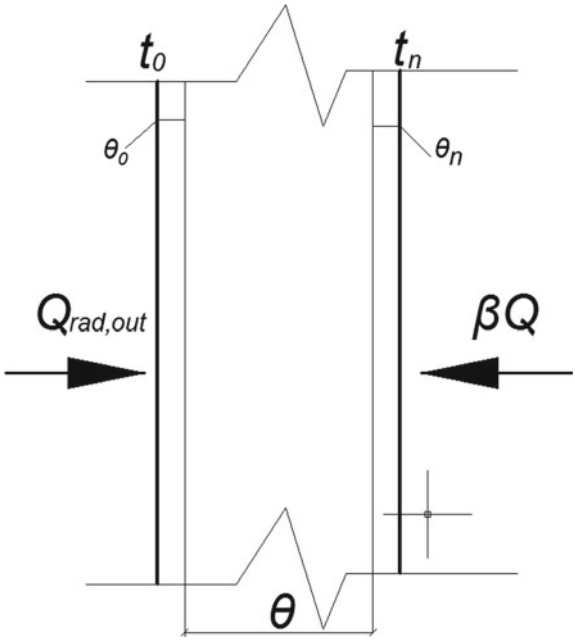

Fig. 1 Schematic diagram of exterior wall

According to literature [9], the temperature of the inner surface of the wall will be increased when the radiation energy produced by the equipment operation falls on the inner surface of the envelope structure. The heat transfer through the wall would be reduced. The heat transfer process of the envelope is affected by indoor heat source radiation energy, outdoor radiation energy and thermal parameters of the envelope. The envelope structure is divided into three parts according to different materials, namely inner surface, intermediate layer and outer surface.

The simulation results of literature [10] showed that the influence of the temperature of each inner wall of high-temperature industrial buildings on the thermal radiation of each indoor wall can be ignored. Assuming that the temperature of each inner surface of the envelope is the same, the radiation heat of the equipment is evenly distributed on each inner surface. Suppose that the initial internal surface temperature of the envelope is equal to the indoor temperature tin, the radiant heat falling on the internal surface of the envelope per unit area makes the internal surface temperature rise, part of the heat exchange with the indoor air through convection, part of the heat transfer to the middle layer through the way of heat conduction. It follows that.

$$\frac{\beta Q}{A}\left(\frac{R_{h,n}}{R_w + R_{h,n}}\right) = \rho_n c_n (t_n - t_{\text{in}}) \cdot \theta_n \tag{1}$$

$$R_h = {}^1\!/_h, \; R_w = \sum {}^{\theta_i}\!/_{\lambda_i} \tag{2}$$

where A is the inner surface area of the envelope and i is the materials types of the intermediate layer.

$$t_n = \frac{\beta Q(h_n R_w + 1)}{A \cdot \rho_n c_n h_n \theta_n} + t_{\text{in}} \tag{3}$$

The same applies to the outer surface of the envelope.

$$t_0 = \frac{Q_{\text{rad},0}(h_0 R_w + 1)}{A \cdot \rho_0 c_0 h_0 \theta_0} + t_{\text{out}} \tag{4}$$

where $Q_{\text{rad},0}$ refers to the radiation heat obtained by the outer surface of the envelope. The air-conditioning load could be obtained as Eq. (5). Equation (6) is the determination basis of heat transfer direction of building envelope.

$$Q_{ac} = 8760Q + \sum_{\tau=1}^{8760} \left\{ HG_{\text{rad}} + \sum_{j=1}^{5} \frac{KA_j}{A} \left[\frac{\beta Q(h_n R_w + 1)}{\rho_n c_n \theta_n h_n} - \frac{(h_0 R_w + 1) Q_{\text{rad},0}}{\rho_0 c_0 h_0 \theta_0} + \frac{t_{\text{out}} - t_{\text{in}}}{A} \right] \right\} \tag{5}$$

$$\frac{1}{A} \left[\frac{\beta Q(h_n R_w + 1)}{\rho_n c_n \theta_n h_n} - \frac{(h_0 R_w + 1) Q_{\text{rad},0}}{\rho_0 c_0 h_0 \theta_0} \right] \geq t_{\text{out}} - t_{\text{in}} \tag{6}$$

3 Simulation Analysis

According to (5) and (6), the air-condition energy consumption is difficult to calculate theoretically, and also not convenient for application in practical engineering. The software of DeST was introduced to simulate the association between the air-conditioning load of the building with internal heat source and thermal parameters of the envelope.

An independent equipment room located in Hefei area was introduced as the example, which is 9 m long, 8.3 m wide and 4 m high. The interior design temperature is 28 °C. The equipment runs steadily and continually. There is no permanent staff in the building. The lighting system runs only during equipment maintenance. There is no storage or transportation of other materials. During the process of simulation, 15 kinds of exterior walls with different heat transfer coefficient K and thermal inertia index D were selected. In the case of different equipment heat dissipation, the relationship between the maximum load and annual energy consumption of the building was investigated.

3.1 Design Load

The indoor heat gain of the building mainly comes from the heat dissipation of indoor equipment, solar radiation and heat transfer through the envelope. As the indoor and outdoor environmental conditions remain unchained, the difference between the design load is determined by the change of the equipment heat dissipation and thermal parameters of the envelope. According to the air-conditioning load theory, all the equipment heat dissipation is converted into indoor heat gain when the equipment runs continually and steadily. The heat transfer direction of the envelope could be qualitatively determined by investigating the relationship between cooling load and the equipment heat dissipation. As shown in Fig. 2, the number of hours when cooling load per unit area is greater than the heat generated by equipment decreases gradually with the increase of equipment heat dissipation. Taking case 14 as an example, the cooling load per unit area is the highest among all the cases. When the heat dissipation $Q = 50$ W/m^2, it is 1264 h, accounting for 13.85% of the annual time. When the heat dissipation $Q = 250$ W/m^2, the value decreases to 943, accounting for 10.33% of the annual time. When Q is between 50 and 100 W/m^2, the lowest cooling load greater than the equipment heat dissipation hours is case 5, when $Q \geq 150$ W/m^2, it is case 1. From the time distribution of the whole year, the time when the design load is higher than the equipment heat dissipation mainly occurs in July and August. It also occurs when the daytime temperature is higher in adjacent months. Accordingly, when indoor has stronger internal heat source, building envelopes play the role of loose heat for about 90% of the year.

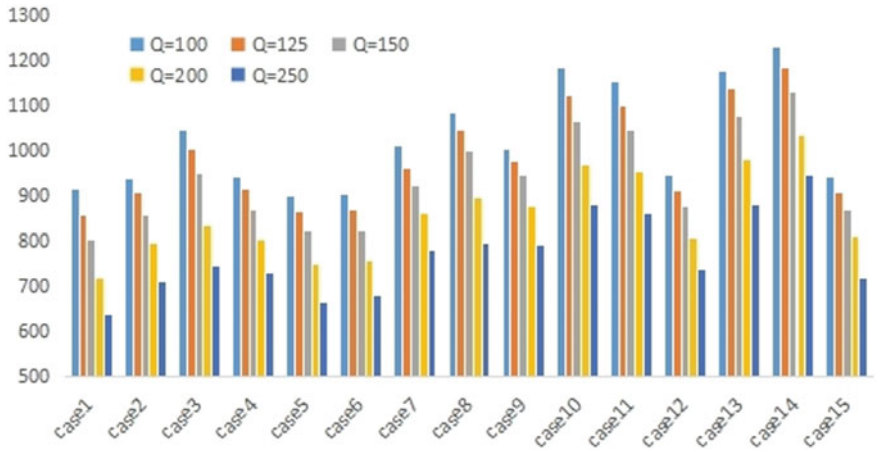

Fig. 2 Statistics of cooling load per unit area greater than equipment heat dissipation hours under different equipment heat dissipation conditions

3.2 Accumulated Load

According to the general rule, the air-conditioning system runs under partial load most of the year. It is impossible to evaluate the annual energy consumption of the system only by examining the design load. It is difficult to analyze the hourly load due to the large number also. The cumulative loads with different equipment heat dissipation and external wall parameters were obtained as shown in Fig. 3.

As can be seen from the figure, when the equipment heat dissipation changes, the cumulative load of the reference building also changes. Take case 14 as an example, which gets the highest cumulative load when the heat dissipation $Q = 50$ W/m^2.

Fig. 3 Diagram of cumulative load and equipment heat

When $Q = 250$ W/m^2, it gets the lowest value. Just the opposite to case 14, case 5 is in a lower level when $Q = 50$ W/m^2, which gets the maximum value when the $Q = 250$ W/m^2. At the same time, the difference of accumulated load under different thermal parameters of external walls is gradually decreasing as Q increases. The difference between the maximum load and the minimum load increases from 26,000 to 60,000 kWh.

3.3 Data Fitting

According to the above analysis, the exterior wall thermal parameters under minimum values of design load and accumulated load was listed in Table 1. Taking the minimum values of design load as the reference index, it could be found that when the external wall heat transfer coefficient K is low and the thermal inertia index D is high, the design load of the air-conditioning system reaches the lowest value. With the minimum values of accumulated load as the reference index, it could be found that with the gradual increase of equipment heat dissipation, the external wall heat transfer coefficient K increases gradually, while the thermal inertia index D decreases gradually.

In order to find the numerical relationship between accumulated load and equipment heat dissipation Q, external wall heat transfer coefficient K and thermal inertia index D, the simulation results were fitted. The fitted result could be seen in Eq. (7) and Table 2 for details. When the indoor heating intensity $Q \geq 50$ W/m^2, the mean relative error of fitting results is less than 10%.

$$f(Q, K, D) = a_1 K^2 + a_2 D^2 + a_3 K + a_4 D + a_5 K D + a_6 \quad Q \geq 50 \text{ W/m}^2 \quad (7)$$

Table 1 Thermal parameters under different operation conditions

	Minimum design load						Minimum accumulated load					
Q	50	75	100	150	200	250	50	75	100	150	200	250
K	0.345	0.486	0.194	0.194	0.194	0.194	0.703	1.491	2.874	3.904	3.904	3.904
D	5.583	3.494	6.413	6.413	6.413	6.413	4.021	2.039	3.999	0.932	0.932	0.932

Table 2 Parameters in Eq. (7)

Parameter	Fitting result	Parameter	Fitting result
$a1$	$a1 = 1454 + 0.9Q$	$a4$	$a4 = -839.3 + 7.6$Q
$a2$	$a2 = 128.7 - 1.1Q$	$a5$	$a5 = -10.7 - Q$
$a3$	$a3 = 3341 - 115.6Q$	$a6$	$a6 = -15{,}470 + 642.8Q$

4 Conclusions

The heat transfer process of the building envelope was analyzed by qualitative analysis and theoretical derivation, the judgment conditions of heat dissipation of the building envelope were obtained. The relationship between air-conditioning load and thermal parameters of building envelope with internal heat source has been derived. The determination method of heat transfer direction of envelope structure was also given.

An independent equipment room in Hefei had been simulated as an example. The design load with a strong internal heat source running continuously and steadily got the minimum value when the heat transfer coefficient value was low and the thermal inertia index value was high. It was just the opposite for the accumulated load.

The relationship between design load and accumulated load of air-conditioning system and external wall thermal parameters was fitted between the air-conditioning accumulated load and thermal parameters, while the equipment heat dissipation was greater than 50 W/m^2. It has certain guiding significance for thermal engineering design of exterior wall of air-conditioning building with strong internal heat source.

References

1. Zhu Y (2010) Building environment. China Architecture & Building Press, Beijing, pp 55–56
2. GB 55015-2021. General code for building energy efficiency and renewable energy use
3. Bai X, Zhang Z, Li W (2013) Impact of building outside wall thermal inertia on air conditioning cooling load. Ind Constr 43(Supplement, 2013):102–105, 119
4. Yang Y, Li F, Zheng L (2017) Correlation analysis of building envelope thermal parameters and cooling load of building and atrium. HV&AC 47(01):46–50
5. Wang Y, Hu W, Sun P et al (2015) Analysis of sensibility of building load to building envelope thermal parameters in cold zone. J Civil Archit Environ Eng 37(03):108–115
6. Lu M, Wang J, Chen J et al (2017) Influence of heat release density in converting station monitor room on energy saving performance of building envelope. Build Energy Efficiency 45(10):128–131
7. Cao L, Han X, Wu Z et al (2013) Study on building envelope energy efficiency design parameters of substation buildings in Shanghai. Power & Energy 04:343–346
8. Liu Y, Zhang Y, Cai Z et al (2020) The influence of thermal performance of building exterior envelope on building energy consumption of substation. Build Energy Efficiency 48(02):29–33
9. Liu T (2016) Studies on the heat transfer of industrial plant's exterior wall under the heat source radiation in summer. Xi'an University of Architecture and Technology
10. Wang Y (2020) Indoor radiant heat distribution on the walls of concentrated heat source building. Xi'an University of Architecture and Technology

Architectural Heritage and Historic Building Conservation

Study on the Protective Reuse Strategy of Noble Mansion Buildings in the Old Urban Area of Lhasa

Qing Qin and Yang Chen

Abstract Tibet possesses unique regional characteristics, a profound cultural heritage, and a rich architectural heritage, all of which have a high importance for preservation. However, due to the low economic level in Tibet, study into the preservation of historical structures was delayed. In the recent years, however, a portion of the ancient buildings has been demolished due to the rapid growth of tourists in the region. Using the noble mansion buildings in the old urban area of Lhasa as the research object and "summarizing the building mode, analyzing the existing problems, evaluating and grading the building value, and proposing specific strategies" as the research process, combined with social and economic needs, this paper discusses reasonable protection measures and sustainable reuse methods for such historical buildings. It gives experience and a point of reference for future studies on the preservation of historic buildings in Tibet.

Keywords Noble mansion buildings · Historic building conservation · Protective reuse · Lhasa region

1 The Value and Current Situation of Noble Mansion Buildings in the Old Urban Area of Lhasa

Tibet is situated on a snowy plateau, which creates a unique natural environment with severe cold and dry winters, cool summers with minimal precipitation, and extreme sun radiation. In the meantime, a distinct human milieu has developed due to the religious beliefs of the Tibetan people throughout history. Under the combined influence of these two, the distinctive design techniques and architectural patterns of

Q. Qin (✉)
Taiyuan University of Technology, Taiyuan 030024, China
e-mail: qinqing_mer@163.com

Y. Chen
Xi'an Jiaotong University, Xi'an 710049, China

T. Kang (ed.), *Proceedings of 5th International Conference on Civil Engineering and Architecture*, Lecture Notes in Civil Engineering 369,
https://doi.org/10.1007/978-981-99-4049-3_69

traditional Tibetan architecture have steadily emerged. As the political, economic, and cultural hub of Tibet, Lhasa is home to the most emblematic examples of Tibetan architecture. Moreover, because the manor system was the primary institutional form throughout the feudal society of ancient Tibet [1], it has resulted in Tibetan territories being peppered with massive manors, which have formed an integral component of the traditional Tibetan architectural system. Among them are the noble mansions in the old urban area of Lhasa [2].

After the formation of New China, the old noble mansions lost their conventional architectural purpose [3]. After being reclaimed by the government, a portion of the buildings was distributed to commoners or descendants of the aristocracy who formerly resided there. As public housing, a portion of the buildings was sublet to tenants. A portion of the buildings was sublet to businesspeople from around the country, and the lower levels were used for commercial purposes, while the top floors were occupied by residents. The street-facing areas were made available to the public for the operation of individual shops or small workshops. The majority of the buildings have been converted into restaurants, inns, hotels, etc., as a result of the tourism boom. There are numerous ways to repurpose the buildings, but the renovation process has destroyed certain historic structures. Combining the demands of users and society to rationalize the utilization of noble house buildings without compromising their original historical appearance and heritage value has become an essential issue.

2 Spatial Models and Existing Problems of Noble Mansion Buildings in the Old Urban Area of Lhasa

As part of Lhasa's traditional residential architecture, the noble mansion buildings exhibit distinctive architectural forms and functions. In order to study the conservation reuse of noble mansion buildings, we must first outline their architectural space models and analyze the challenges in their existing transformation and use as a foundation for investigating more systematic techniques for protective reuse.

2.1 The Spatial Models of Noble Mansion Buildings

Type and scale. As Lhasa has been the political, economic, cultural, and religious heart of Tibet since antiquity, many noblemen have constructed their homes there. In the old urban area of Lhasa, twelve magnificent mansions have been maintained, all of which are located along Barkhor Street [4]. The information given in Table 1 is a summary of the existing noble mansion buildings in the old urban area of Lhasa.

Plane form. *General Layout*. On Barkhor Street, the building density is high, the land area is compact, and the distance between buildings is extremely near. Consequently,

Table 1 Existing noble mansion buildings in the old urban area of Lhasa

Name	Date of construction	Building area (m^2)
Samdrup Podrang	1642	2316
Yabshi Phunkhang	1842	3500
Labrang Nying ba	1407	2000
Phala	1750	3582
Pomdatsang	Early seventeenth century	3000
Kunsangshar	1907	2982
Shatra	1800	3700
Bonsho	1920	1660
Trombasha	?	?
Gimai	Eighteenth century	414
Boutang	1930	566
Podrang Sarba	1930	?

unlike the traditional residential buildings in Lhasa, which are square, the architectural outline of the noble mansion buildings varies according to the street and adjacent buildings. The general layout is courtyard style, with the main building's bigger area, deeper depth, and greater number of levels connected to the veranda building's smaller area, shallower depth, and fewer floors to form the central courtyard. The primary buildings are oriented south to enhance solar gain and heat absorption. The flat layout of ten noble mansions is seen in Fig. 1. The layout forms are identical, establishing a pattern of "front corridor and back building" or "south corridor and north building."

Functional layout. The functional layout of the mansion is directly tied to its "front corridor and back building" type of plane form. This paper examines the three

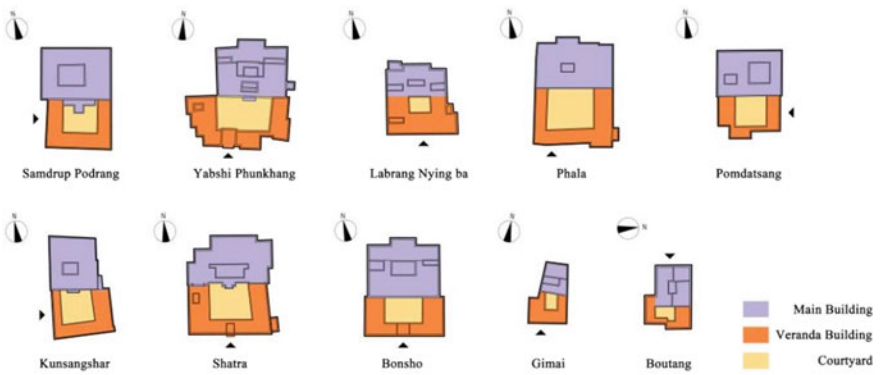

Fig. 1 Layout plan of noble mansion buildings

noble mansions of Pomdatsang, Yabshi Phunkhang, and Shatra and identifies the fundamental principles of functional layout (see Table 2).

The main building of the mansion is mostly three floors tall and expansive. It is typically the master's primary living area and is designed with more crucial functions. The interior of the main building consists mostly of one or two secondary courtyards as well as the lofty atrium on the second and third levels of the Buddhist hall. The veranda buildings are typically two stories tall, positioned on the south side of the main building, and arranged in a "U" configuration, with the hallway on the north side and the rooms on the south side. Comparatively, the depth and area of the veranda building are smaller than those of the main structure.

The building's vertical functional layout is identical to that of traditional Tibetan residential buildings, with rooms of lesser importance and frequency of use, such as storehouses and stops, located on the first floor of the main building and the veranda building. The second floor of the main building is mostly used for auxiliary services, including the Buddhist hall, kitchen, living rooms, and storage rooms. The second floor of the veranda building is utilized for subordinates' bedrooms. The master's living space is on the third floor of the primary building. The building's layout adheres to the design principles of traditional Tibetan architecture. The more

Table 2 Functional layout of noble mansion buildings

Name	First floor plan	Second floor plan	Third floor plan
Pomdatsang		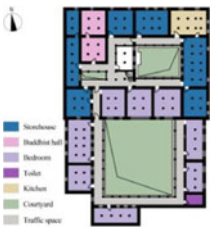	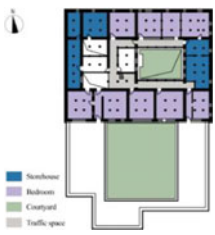
Yabshi Phunkhang			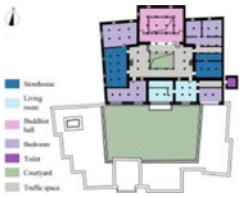
Shatra	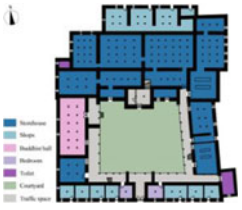		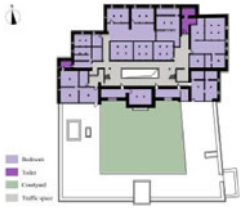

important and often used rooms, such as bedrooms and living rooms, are typically located in the south, while storage rooms and kitchens are often arranged in the north. As a distinctive and essential functional element of Tibetan architecture, the Buddhist hall occupies the largest floor area in the center of the main structure. It is composed primarily of the full height of the second and third levels.

Elevation form. On the original material of soil and stone, the walls of noble mansion buildings are typically painted white. Along with doors, windows, arches, and decorative hanging objects, they comprise the center portion of the building facade. Trapezoidal components are fully utilized on the facade. The walls are masoned with a broad base and a thin apex, and their general outline is trapezoidal. Additionally, the black margins of the doors and windows are also trapezoidal in design. Typically, the facade is symmetrical, with the entrance in the middle and windows on both sides. Doors are relatively low, built of wood and partially embellished with metal. The entrance arches originated in Han architecture and were influenced by Tibetan culture for primarily ornamental purposes [5]. Similarly, window apertures exhibit distinct regularities. Generally, the windows on the ground floor are modest, whereas those on the upper floors are larger. The area and number of windows in the southern direction are considerable, whereas those in the northern direction are tiny. Doors and windows are typically decorated with religious motifs in red, yellow, blue, and green.

2.2 Existing Problems of Noble Mansion Buildings

Existing noble mansions in the old urban district of Lhasa have been partially repurposed, mostly as public rental housing, government office property, hotels, restaurants, and shops, and returned to the nobles' descendants. There are numerous issues with the preservation and repair of buildings, which have caused some harm to the architectural style and originality of the structures.

The original building is in disrepair. Due to the lengthy history and the use of stone, soil, and wood as the principal building materials, the majority of structures have experienced weathering, collapse, and decay in the recent years. For instance, the Aga soil roof has sustained some damage as a result of the substantial maintenance requirements, and its waterproofing capacity has diminished. In addition, the inside timber components of the structures have deteriorated and fractured.

Lack of detailed classification protection and reuse system of ancient buildings. China separates all immovable cultural relics into national, provincial, municipal, and county-level cultural relics protection units in accordance with the "Law of the People's Republic of China on the Protection of Cultural Relics." Nonetheless, each level lacks further subdivisions and tailored conservation and usage guiding regulations for ancient buildings. Samdrup Podrang, Labrang Nying ba, and Pomdatsang, for instance, are three national critical cultural relics protection units of the existing

noble mansions in the old urban area of Lhasa. However, their strategies of reuse are vastly different. One of the buildings is utilized for government offices, while others are converted into hotels, restaurants, and public rental housing. The degree of protection and alteration of buildings also varies drastically. It is evident that the absence of detailed management and guidance policies has resulted in disparate levels of reuse of historic structures.

The public's awareness of the protection of historical buildings is weak. Most reuses of noble mansions involve altering the building's purpose without regard for its historical or social significance. The method of reuse, such as public rental housing, has severely damaged buildings. In order to accommodate the needs of modern life, it is common for residents to alter the internal space of buildings, including arbitrary partitioning, additional construction, and blocking doors and windows, which not only affects the spatial structure of traditional buildings but also poses serious safety risks. In addition, the use of modern building materials, such as concrete, asphalt linoleum for roofing, aluminum alloy doors and windows, and guardrails in the transformation process has ruined the original architectural characteristics and facade shapes.

3 Protective Reuse Strategy of Noble Mansion Buildings in the Old Urban Area of Lhasa

Rather than mindlessly following a single renovation technique, the protective reuse of historic buildings should be customized to the building's individual requirements. Protective reuse stresses "protection prior to use"; therefore, it is required to define the value evaluation system for buildings, obtain the protection grade of buildings based on the evaluation results, and then determine the optimal reuse mode.

3.1 Evaluation of the Architectural Value of Noble Mansions

Presently, countries across the globe employ diverse methods for determining the worth of historical buildings. Based on the existing assessment methodologies and the current laws and regulations on the preservation of cultural relics and monuments in China, this study presents the criteria and contents of value evaluation for both protection and reuse purposes, mainly including ontology value and reuse value (see Table 3).

The reuse method was determined by evaluating the 12 existing aristocratic homes in the old urban area of Lhasa based on the above criteria.

Table 3 Value evaluation criteria of noble mansion buildings

Level I indicators	Level II indicators	Level III indicators
Ontology value	Historical value	Longevity
		Relevance to historical figures and events
	Artistic aesthetic value	Regional characteristics of architecture
		Architectural modeling, style, and space features
		Architectural details and decorative features
	Science and technology value	Rationality of building space layout
		Energy saving design of building area
		Building structure
		Building material
		Construction technology
	Sociocultural value	Religious and cultural values
		Value of residents and the public
		Building type particularity
Reuse value	Environmental value	Location advantage
		Coordination with surrounding environment
		Building external environment suitability
	Use value	Overall preservation and integrity
		Space and function reusability
		Structural safety and reusability
		Comfort level
		Infrastructure status
		Economic benefits of reuse

3.2 Determination of Protective Reuse Strategy Based on Value Evaluation

For noble residence buildings with high ontology value and low reuse value, it is appropriate to adopt the authenticity protective reuse strategy, i.e., to maintain the originality of the buildings to the greatest extent possible, with preservation as the primary focus and restoration as the auxiliary, without altering the form, location, or function of the buildings. Additionally, the conservation and restoration of buildings should be conducted using authentic historical materials. The noble houses with low ontology and high reuse value might explore function replacement as a protective reuse method. On the basis of preserving the original aspect of the neighborhood, the interior and exterior of the building should be modified to accommodate the needs of contemporary society.

Authenticity protective reuse strategy. The three national critical cultural relics protection units of Samdrup Podrang, Labrang Nying ba, and Pomdatsang are the oldest of the twelve noble mansion buildings, having been constructed between 400 and 600 years ago. The original architectural pattern, structure, materials, details, and decoration of the buildings are well conserved and have a high cultural relic value, as determined by the value assessment. Therefore, the authenticity protective reuse strategy is recommended. The method can be used by "collecting basic building information, restoring the original pattern and function, and choosing feasible reuse methods."

Collecting basic building information. The collecting of fundamental building information is a prerequisite for restoring the building's legitimacy. In addition to on-site research and mapping, it is necessary to acquire as much historical knowledge as possible through the collection of historical documents and interviews with locals. Notably, the three noble mansions that qualify for the authenticity protective reuse strategy were constructed long ago and have experienced several repairs and modifications during the course of history. In addition to focusing on historical reconstruction information during collecting, a comprehensive maintenance file must be created.

Restoring the original pattern and function. Samdrup Podrang is currently used as the Barkhor Street Office of the People's Government of Chengguan District in Lhasa, as a result of the author's field investigation. Pomdatsang was transformed into a traditional old hotel. The first story of the main building of Labrang Nying ba is a hotel, the second floor is the dormitory for personnel, and the remaining space is used for public rental housing. Except for the government office, the other two transformation methods have caused some harm to the building's original structure and design. Pomdatsang, which was turned into a hotel, was outfitted with 32 guest rooms, each with an additional private bathroom, partition walls, and a complete water supply and drainage system, which drastically altered the construction of the building. The current mix of personnel and renters in Labrang Nying ba has resulted in severe reconstruction of the building, as well as extensive damage to the architectural style and features. After gathering basic information about the structure, the existing functions should be transferred and the inappropriate interior expansions and alterations should be eliminated. The building should be meticulously restored to its original space, structure, and form. Those whose architectural patterns have been severely destroyed can be repaired and reconstructed in accordance with the spatial layout of historical mansion structures.

Choosing feasible reuse methods. The three noble mansions, which have implemented the authenticity protective reuse method, are of high ontological worth and have for centuries contributed to Lhasa's social, cultural, and religious history. It would be wasteful if they were sealed only after being protected. When reusing them, we should select forms that have minimal impact on the buildings and can preserve the historical appearance and cultural heritage, such as museums, exhibition halls,

and memorial halls, for the primary purpose of showcasing Lhasa's traditional social and religious culture and the evolution of its historical civilization.

Function replacement protective reuse strategy. The ontology value of the remaining nine mansions is ordinary or poor, but their reusability value is considerable. They should implement the function replacement protective reuse strategy in order to incorporate new functions fit for urban development and to stimulate the vitality of the neighborhood without harming the original architectural and street features. This method can be implemented by "selecting reasonable replacement functions, designing and renovating the building, and formulating efficient management strategies."

Selecting reasonable replacement functions. The choice of replacement function is largely influenced by the local social environment, industry demand, and neighborhood style, and its environmental and usage value should be evaluated in a reasonable manner. Lhasa is evidently unique compared with inland cities. It is situated on a plateau and has a poor climate and inconvenient transportation. The primary and secondary industries are largely under developed, however the tourism industry is quite advanced. According to the Lhasa Municipal Government Gazette, Lhasa's total tourism revenue in 2021 was 37.77 billion yuan, representing 50.9% of the city's GDP. Tourism has become one of the city's most vital pillar sectors. The twelve noble mansions analyzed in this research are all located on Barkhor Street in the old urban district of Lhasa, which is the region with the highest concentration of tourists, except the Potala Palace. Therefore, the most suitable replacement functions should fulfill the needs of cultural tourist development, such as hotels, restaurants, cultural innovation or featured product retail, folkloric experiences, bookstores, teahouses, and cafes, as well as other commercial architectural functions. The selection of functions for specific buildings must be determined further by taking into account their specific location, surrounding environment, building area, and building construction, among other criteria.

Designing and renovating the building. All the protection, restoration, and renovation methods used in architectural conservation and reuse should be reversible to the greatest extent possible so that the original building form, function, and materials can be restored to their original state if better methods for historic building conservation are explored in the future. When reusing and transforming, it is vital to maintain architectural compatibility with the surrounding environment, to minimize alterations to the building's internal structure and architectural form, and to maintain and repair the building's components and elements. The inherent cultural and historical ambiance cannot be diminished. In addition, new functional requirements must be met, including spatial arrangement, streamlined design, safety design, amenities, and indoor comfort. The government can establish a fixed amount of special funding to assist operators in attracting top-tier design and construction teams in order to gain enhanced technical support.

Formulating efficient management strategies. After the commercial reuse and functional replacement of historical buildings, effective management approaches are

required. The government should first manage the reused and reconstructed noble mansion buildings, establish a unified regulatory reward and punishment system, and perform frequent inspections to prevent private developers and operators from inflicting development damage by constructing privately. Second, operators and managers must conduct regular training for service employees to improve their awareness of the protection of historical buildings and cultural identity in order to prevent them from unwittingly causing harm to buildings as well as to monitor customers and other users. Finally, a reliable system for fund returns should be devised. In addition to the government's initial investment in special funds for building renovation, operators should be required to invest a specified proportion of their profits in the subsequent maintenance and protection of the building to ensure its sustainability.

4 Conclusion

Tibet has a history of thousands of years and has undergone several governmental and religious transformations as well as ethnic integration, resulting in the formation of a distinct regional culture. Ancient buildings, as essential carriers of the human environment, must pursue a new conservation and renewal strategy. Based on the Lhasa region and focusing on Tibetan architecture with regional characteristics, this paper uses the existing noble mansions in the old urban area as the research object and summarizes the space model of architecture from the perspectives of type, scale, plane and facade form, and structural form as the basis for the subsequent proposal of the protective reuse strategy. In addition, according to the research findings, this paper evaluates the obvious issues with the current reuse process of buildings at the building ontology level, system level, and protection awareness level in order to provide corresponding strategies for protective reuse. Specific strategies are proposed based on the principles and steps of "value assessment, classified protection, and classified building utilization." Two specific measures, namely the authenticity protective reuse strategy and the function replacement protective reuse strategy, have been formulated for the existing noble mansions in the old urban area of Lhasa. These measures can serve as the theoretical basis for the sustainable protection of large-scale manors and mansions in Tibet, and they are also anticipated to serve as a guide for the conservation of historical buildings in Tibet.

References

1. Maojia L (2013) Research on Tibetan Manor System. Tibet University, Lhasa
2. Ziyun J, Yongping W, Tingting N (2009) Study on Tibetan manor architecture from the view of religion culture. Huazhong Architecture 27(03):257–260
3. Junrui L (2009) Primary research on architecture of historical mansions in the old city of Lhasa. Southwest Jiaotong University, Chengdu

4. Yangzong C (2012) The aristocratic families in Tibet, 2nd edn. China Tibetology Publishing House, Beijing
5. Junrui L, Mingjuan L (2011) On the hierarchical characteristics of noble mansions in the old urban area of Lhasa. Tibetan Art Studies 04:58–63

The Correlation Between Sacredness and Architecture in Madaba, Jordan

Jawdat Goussous and Sara Bayyari

Abstract This research is conducted to highlight the prominence of sacred architecture in Madaba, Jordan, by bringing awareness to the tourism sector and the local public regarding Madaba's attraction sites and showcasing its holy significance to the Christian community worldwide and its effect on the public interest. Few of the prominent cases were chosen for the research as they are the main attractions in Madaba of which they are littered with mosaic floorings and walls that have religious, public figures, monarchs, living conditions, and conquest tales. It also discusses what makes Madaba sacred enough through its historical timeline and mosaic art ornamentation significance to encourage tourism and demand recognition from the public. The research uses qualitative and quantitative analysis and the author's perspective from observations as a method of collecting information from the perspective of the public and input into the sacred archaeology of Madaba and the recognition of its existence among locals. The observation resulted in noticing a positive factor between the existence of these historical and religious architectural and artistic sites with it being a tourist attraction. The contradiction stands in how it exists within the referral tourist agencies and governmental action plans to dismantle this negativity.

Keywords Heritage · Conservation · Historical monuments · Mosaic · Christianity · Tourism · Byzantine · Roman era · Jordan

1 Introduction

Madaba's history goes back to the Bronze Age towards the beginning of the 4th millennium B.C. and the Iron Age c. 1200 and appears to be confined to the area of the west acropolis. It dates back to the Nabataeans and the Romans in 106 A.D. when

J. Goussous (✉) · S. Bayyari (✉)
University of Jordan, Amman 11942, Jordan
e-mail: j_goussous@ju.edu.jo

S. Bayyari
e-mail: sara.m.bayyari@gmail.com

T. Kang (ed.), *Proceedings of 5th International Conference on Civil Engineering and Architecture*, Lecture Notes in Civil Engineering 369,
https://doi.org/10.1007/978-981-99-4049-3_70

Christianity became rooted in Madaba as the city expanded to the northern region to reach its furthest in the Byzantine period and shrank in area in the ninth century during the Islamic period. Many archaeologists, researchers, and scholars visited the area of Madaba back in the nineteenth century to discover the magnificent art of the mosaics and interpret, analyse, and link them to the biblical verses that created the city's international reputation. When Madaba was shown to the public, with its ancient history that had been identified, it revealed some architectural characteristics that reflect the events it has gone through religiously, socially, and most certainly geographically (see Fig. 1) as there weren't many available resources back in the day. Much like many of the ruins in Jordan, the untold stories are kept in memory through the mosaic either it be of the rulers of Madaba in said times or a retelling of a biblical story. A typical house would be made of mud bricks or stones. Christian migrants who came from Karak near the end of the nineteenth century situated their homes near their preferred church and the techniques for the finer homes were inspired by Karaki principles.

One of the prime and most notable discoveries in Madaba are the mosaic which have a long history of being either stolen, destroyed, lost, or removed from their original discovered location; some have been found in houses as they were built directly over the mosaics. It is impossible not to be captivated by the scenery; the buildings themselves spoke of an obsolete rich historical architecture, simple yet mesmerizing. Palestinian architects coming from the areas around Jerusalem, Bethlehem, and Nablus designed the fine homes in Madaba which show the uncanny resemblance in the structures between two regions. The Roman influence is evident from how the streets and buildings are structured and presented: "Rome and Italy, for some time the strongholds of western architectural usage, proved impregnable to the Semitic type" [1]. Not only that, but the impressive mosaic art on the floors and

Fig. 1 Memorial Church of Moses, author (2018)

walls tell a story that is the foundation of Christianity, how the colours of the mosaic contrasted from dark coloured texts on bright walls spread among the churches. The survival of some of the rich mosaics, which are being protected by the government of Jordan, show the importance of the heritage of this city which is prideful for Jordanians to maintain the geographical importance of the land. They served the local Christian inhabitants as their place of worship and accommodated the everyday praise, prayer and cultic devotion [2]. While one could expect these buildings to exhibit the daily routine of "religious functions," their spatial organization was more than an architectural determinism of the "form follows function" or an "interaction location" approach [3].

How did these sacred monuments affect Madaba's history? How did the architecture develop throughout the years in the light of natural disasters? How did the Roman Empire inspire sacred architecture in Madaba? What makes Madaba standout as one of the top Christian tourism sites?

This research emerges from the inspiration and visual beauty that a person might experience from visiting a prosperous city that tells many tales of religion, sacredness, architecture, new discoveries and excavations, memorials, and many more flourishing eye-opening sites.

2 Mountain Nebo

One of the most important tourist attractions near Madaba is Mt. Nebo, which is significant in the Christian faith as it perpetuates the last moment of Moses' life as it is recognized by the Roman Catholic Church as a pilgrim site. According to Christian belief, Moses had climbed up the mountain and had a glimpse of the Promised Land man.

On Syagha, the peak, a monastery stands that goes back to the fourth century during Byzantine times, the Memorial Church of Moses. The church went through natural disasters in 749 A.D. that caused some damage to the building, but it was reconstructed during the following years with the same plan using the retaining walls of terraces used in the Byzantine period.

When approaching the façade of the church, what immediately comes to mind is the White Temple in Uruk. Just like the temple, the church stood in all its glory atop the mountain creating a façade for viewers to admire. With its basic contrasting colours, it thrilled tourists to go inside and explore it (see Fig. 1).

To share the importance of the site and of the Church and Madaba in general, and to give a fascinating yet brief historical lesson to visitors, a museum was created to present all the information needed. It displays mosaic pieces from different monasteries, insights on the development and protection of the construction, Greek inscriptions, Palestino-Armanic inscriptions, Roman potteries, maps, architectural plans, and models of the church itself [4].

The entrance to the church goes around the building and will take you to a small court that'll have a point of focality at the edge of the terrace—a symbolic monument

made with metal in the shape of the serpentine cross by Italian artist Giovanni Paolo Fontani. Inspired by the biblical verse when God told Moses to erect the bronze serpent on a pole to protect his people from the poisonous snakes.

> And just as Moses lifted up the serpent in the wilderness, so must the Son of Man be lifted up. John 3:14–3:14

The above verse is carved at the base of the pole in reminder of the meaning behind the sculpture. Knowing the artist understood the stature of the location and the historical background of the mountain provoked him into combining it with this sculpture that gives magnificence to the sacred mountain. The greatness of its location in the middle of the desert overlooking the Dead Sea, the Jordan River, Jericho, and the distant hills of Jerusalem really empowers the mountain, creating a great symbol that is full of historical meaning and significance.

Different patterns and interpretations with their meanings will be found on the guide boards outside the building with a detailed explanation on the foundation and elements of the church. Set out vertically on three sections, the sides are aisles filled with exquisite mosaic art linked back to the fifth century. The middle part has two series of pillars that lead to a baptismal font (see Fig. 2).

An archaeological team, in 1933, lead by Fr. Sylvester Saller who later conducted research excavating the Iron Age tombs in Nebo, Jordan [5], and Fr. Bellarmino Bagatti uncovered the fundamentals for understanding the development in the Byzantine-Omayyad mosaics. The mosaics were layered on top of each other. Fr. Virgilio Corbo and Fr. Michele Piccirillo [6] found mosaic pieces during the removal of the first layers, and they were able to distinguish four time periods from analysing the mosaics.

The scenes of the diakonikon mosaics are rendered with particular attention to details; it receives special attention with its richness in colour and geometric designs of patterns, flowers animals, and a ciborium above an altar flanked by two bulls and gazelles which shows the richness of the Byzantine characteristics in the memorial church with the numerous iconographic that people prize and venerate their depictions of Christ, the Virgin Mary, and other Christian symbols in this site [7].

3 The Greek Orthodox Church of Saint George

The church named after the venerated Roman soldier Saint George lies over the remains of a Byzantine church from the sixth century. The Greek Orthodox church itself prominently stands as a fully designed church in a Byzantine era style located in the heart of Madaba city (see Fig. 3).

It contrasts with the other sacred sites in Madaba that are protected under steel pavilions, and the Orthodox church is still an intact architectural building rather with the Madaba Map covered under it. The ceremonies held in both the Orthodox church and the Memorial church seem to hold more sacred significance to the Christian

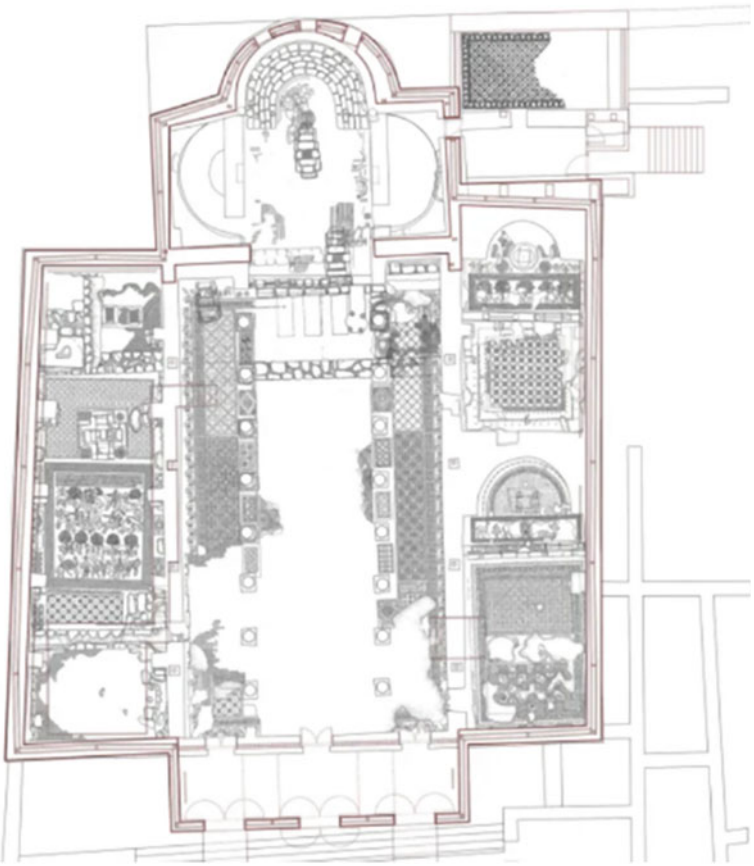

Fig. 2 Memorial church's plan, Pattini, S., Basilica Del Monte Nebo, a place for the meeting *of three religions* (2012)

Fig. 3 Left: the site before the church was built. Middle: the church in 1897. Right: the church currently, author (2021)

tourists and locals as they feel sacredness of the rituals more in a completed structure with sumptuous iconographic interior rather than floorings and columns under shelters that grants more of a completion to a tale.

The Byzantine ruins that the church was built on was taken advantage of as some of the features are of Byzantine relations from the five-bay arcades that divide two aisles from a nave, side rooms at the west end of the south aisle and a western atrium [8].

Unbeknownst to the architects, the church was constructed over the most significant finding in the city's history: the Madaba Mosaic Map (see Fig. 4.) when it was found under debris from the fire in 1897.

Depictions of cities zin floor mosaics in early Christian basilicas continue the Roman tradition in a Christian context. They depict the unified spaces of natural elements, human scenes, and flora and fauna. The map was almost forgotten and uncared for before its value been determined [9]. Gerasimus, a Christian saint, sent an architect from Jerusalem to inspect the map, finding it "unworthy" because pieces of the mosaic were missing. Researchers assumed that the parts of the map went missing due to the construction of the Orthodox church; others assume that the church had gone up in flames, along with the fragmented map.

> Did the Persians cause this catastrophe in 614? We don't know. [10]

One of the reports on the discovery elaborated that:

> What seems even more remarkable, however, is that Schumacher, Séjourné and Bliss showed no awareness of the existence of the mosaic, although all three had been welcomed as guests by town's residents (some of whom must have known of the mosaic's existence) and

Fig. 4 Madaba Map, author (2021)

> had actually taken detailed measurements and described the byzantine structure after the completion of the Greek Orthodox chapel. [11]

These three scholars, who were interested in the mosaic art in houses such as Farid Al-Masri in 1895, traced the line of an ancient city wall, when inspecting the ruins while leading expeditions through the regions of biblical Moab and Gilead and much more. Why was the mosaic art that would mark the identity of Christian Madaba in Jordan concealed?

In 1896, when the map received its due recognition, Kleopas Koikylides, the Librarian of the Patriarchate of Jerusalem, published a report on his visit to Madaba at the time. With it, in 1897, news of the map spread wildly, and international scholars descended on Madaba to conduct research on the map as it became a source for reading Byzantine history; it documents cities within the Holy Land such as Jerusalem and Neapolis during the sixth and seventh century. It also illustrates natural scenes like the landscapes on the sides of the River Jordan.

The mosaic map pinpoints the characteristics and topography of Byzantine Palestine, cities like Jerusalem, Neapolis, Jericho, Bethlehem, Gaza, Karak, lower Egypt, the Mediterranean Sea, the Dead Sea, east and west of the Jordan River—the river which allegedly is the site where Jesus was baptized by John the Baptist. Till this day, with all the other mosaic art around, no other maps or art have been found that have the same accuracy as the Madaba Mosaic Map.

> Both cities and monasteries serve thus to date the map. It seems clear that the author of the map is presenting, not an ideal biblical map, but a map of the country of his day. [12]

Different mosaic pieces in the Madaba Mosaic Map have not been recovered nor restored from thieves until this day, so it remains incomplete where no one can analyse the history and stories it holds to complete the bigger picture. Unfortunately, the chances of retrieving them are almost, if not certainly, non-existent.

4 Church of the Holy Martyrs and the Burnt Palace

The Church of the Holy Martyrs (locally, Al-Khadir) is strategically located alongside renowned churches on the Roman road and can be dated back to the sixth century A.D. Much like the other unique structures noticed in Madaba, the Roman symbolism is indicated in this specific church.

> Succeeding generations of missionaries born and trained in Europe, generally Southern Europe, continued to bring out with them their own traditional ideas as to what was fitting for the House of God, and thus generations of converts became likewise conditioned. In architecture, the result was a great flowering of Southern European building styles outside of Europe. [13]

The name of the church emerged in 1994 when archaeologists found a mosaic inscription that translated to the church's current name. Each section of the church developed due to the difference of functions the users at the time needed. The

entrance, the lobby area or the narthex was an open area towards the city which leads to the nave where worshippers used to hold their rituals. This became a tourist attraction once the mosaic art had been interpreted from the Greek and Roman inscriptions, which is another detail the Romans had contributed to Christianity in Madaba. A captivating series of mosaic sceneries had been disfigured in the eighth century after Emperor Leo orders to ban and destroy living creatures' images, include hunting, animals, herding, winemaking, and geometric patterns that tells tales back to the Byzantine era. The additional rooms on each side of the west and east (which later revealed that one room was for keeping bread, wine and other offerings; the other was for keeping vessels and garments) and the bishop's throne were all added in phases.

In this, compound of churches next to each other, on the northern side of the Martyr's Church, is the first private building of the Byzantine era Madaba to be explored, the Burnt Palace. As predicted from its name, one the private residence rooms had caught on fire giving the palace its notorious name. The aftermath of that disaster is the reason behind the notability of this church. In 1905, under a thick layer of charcoal and ashes in the courtyard, archaeologists found a mosaic pavement (which is yet another piece in the puzzle) which served as a decoration on the floor in the room that went up in flames. This is when they named it the "Burnt Palace" (see Fig. 5).

Another theory said that in the seventh century, an earthquake occurred, demolishing the palace and triggering the fire. This Burnt Palace, from the start of its

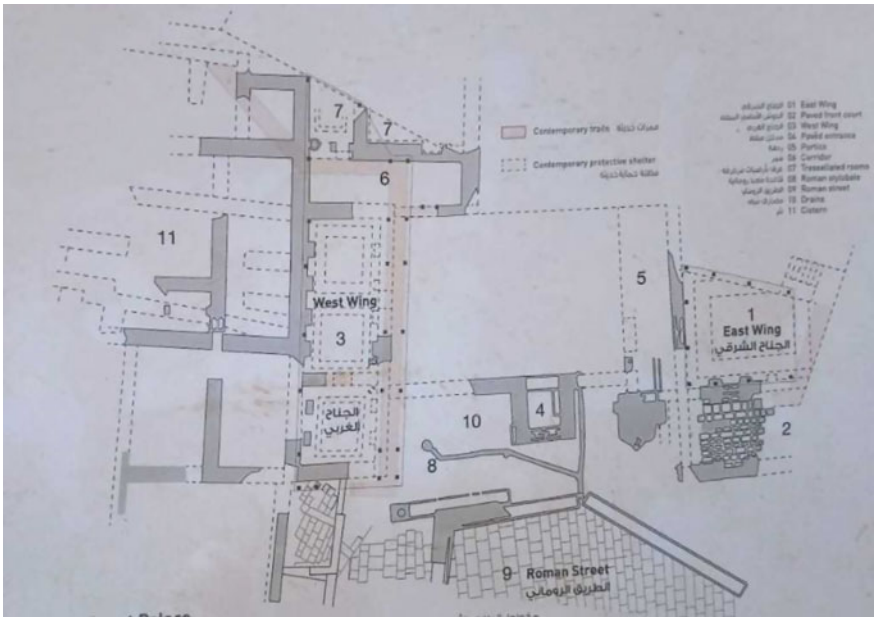

Fig. 5 Map of The Burnt Palace and its surroundings, author (2018)

Fig. 6 Burnt Palace, author (2021)

construction in the late sixth century/early seventh century, also underwent numerous architectural changes through the Umayyad period and beyond. The main entrance's door has door knockers in the form of a lion's head, as did the doors in the interior. A continuous grid of mosaic trees, flowers, animals, and birds, the central panel has a vast range of portraits of shepherds, ewes and lamps, dogs and rabbits. Currently, it is covered under a steel pavilion with curtain walls (see Fig. 6) to preserve it from any natural forces with the mezzanine used as a pathway circulating the palace preventing any interaction with the visitors and the mosaic. The church characteristic in the burnt palace consists of the naves, anthrax, and two rows of Corinthian columns. While it does hold the Byzantine structure of a basilica, there aren't any current ceremonies held in the premise other than showcasing the mosaic and tour guides going over the variations of depictions of the mosaic art.

5 The Hippolytus Hall and Virgin Mary Church

Both of these sacred architectural landmarks were stacked over each other, creating layers of stones and contain a mosaic art piece that was created during the days of Emperor Justinian (527–65 A.D.) in the classical Renaissance depicting more acanthus plants, flowers, trees, and birds. The famous tale of the tragedy that occurred

to Hippolytus can be seen in a series of mosaics along the hall; of course, fragments of the artwork went missing—whether they were stolen or destroyed is unknown. Just like many sacred monuments in Madaba, an act of vandalism in 1981 destroyed the chapel.

The Virgin Mary Church was built over the hall itself. It is the only church in Madaba that follows a centralized plan. The nave took the shape of the circular centre of a Roman temple which tells us that not all the remains of the temple went to waste or was unexcavated; moreover, the nave is supported by underground vaults and arches, with a courtyard in the eastern section of the church (see Fig. 7).

This mosaic can be dated to the sixth century making it the earliest known work from Byzantine Madaba. The Virgin Mary Church was the subject of several debates over the interpretation of the mosaic art laid on its pavement and what date it could lead back to [14]. There is an ongoing investigation of the Greek inscription as some scholars argue over the real translation of the letters, even dismissing theories from renowned researchers that empowered the religious reputation of the church and gains insight on Christian behaviour towards their philosophy and history.

Fig. 7 Diagram of the Hippolytus Hall and the Virgin Mary church, author (2018)

Fig. 8 Top view of the circular inscription in the Church of Virgin Mary, author (2022)

Phaedra and Hippolytus is a Greek mythology portrayed in a large mosaic map discussing the way of living for both the princess and her step son respectively. As mentioned, the mosaic interpretations are still under dispute, however, from what is being gathered from the wide circular inscription spread on the floor and viewed from a structural mezzanine (see Fig. 8) "*the church was rebuilt and beatified by the "care and zeal of the Christ loving people of Madaba*" [6]. The importance of this mosaic derives from its late date after 750 CE, this indicates that there was still a sizable Christian community in Madaba sufficiently prosperous to rebuild the church and decorate it with a new coloured mosaic floor [6] using only locally available stone (limestone, basalt, jasper, and oil shale) as raw materials. What is significant about the elements found at Madaba is that they demonstrate that Madaba benefited from the talents of one of the superior Byzantine mosaic schools in the Levant, specializing in geometrical designs [15].

Following with the mosaic trade, it is heavily encouraged in Madaba most knowingly the institution for mosaic art and restoration adjacent to the Virgin Mary and the Hippolytus Hall that creates religious and non-religious custom pieces, replicas, and mosaic of existing paintings and are being used for deployment as banners for shops, souvenirs, murals, and furniture (see Fig. 9).

6 The Roman Road

What's interesting is the location of monuments that hold significant historical relevance and how close they are to each other, almost making some sort of a nest. Not even a few metres walking distance, a person can find the Martyr's Church to the Burnt Palace, the Virgin Mary's Church, and the King Hussein bin Talal Mosque, which, in a way, feels like it combines the city in some sort of a force, a way to

Fig. 9 Mosaic art deployment, author (2022)

bring dominance and unity at the same time; this is what Madaba calls the Archaeological Park. The Decumanus road runs on an east–west axis which is adapted from the Romanian planning of cities that mimics a chessboard; it intersects with the Cardo, the north–south axis. The Decumanus, built between the second and the third centuries, holds most of the Byzantine churches and Islamic mosques. The changes in the architecture, mosaic art, the continuation of vandalism against these holy structures gave the road its major importance in Madaba's heritage and continued to change during each century with its civilization [13].

Whereas now, these streets are decorated with local stores that invites tourists. They aren't blemished or damaged, so to speak, but rather created an assembly point, a relaxation area after the tour given inside the churches and archaeological park. By observation, non-Jordanian tourists seem to be driven to interact with these new manmade structures from souvenir stores, cafes, standalone markets, and food trucks. Although some of the destination points that are on the Roman road are camouflaged by the shop banners and shop doors that might confuse the user from the exact way to the entrance, they are still very distinguishable from the signs and tour guides paving the way for tourists inside (see Fig. 10).

7 Analysis and Discussion

We have investigated the prominent locations and tourist destinations of Madaba that provide numerous visual arts that represents ways of living, creatures, and mythology with techniques and principals used in the mosaic designs; these artefacts and monuments are partially exploited [16]. Recent study saw that advertising is the most influential promotional mix on the mental image of foreign tourists to Jordanian tourist destinations, while sales promotion is the least influential factor had an effect on mix factors on the foreign tourists' mental images of the Jordanian tourist destinations [17]. It is an important pilgrim that needs to be entangled with a targeted audience in many different languages in popular social media platforms that do not

Fig. 10 Markets covering Roman Road, author (2022)

lack in ways of advertising either in images, texts, infographics, videos, exhibitions, and events to revitalize the governorate on a global scale [18, 19].

To go further in depth into this matter, a survey with a questionnaire was conducted to involve the public's opinion and insight into what specializes Madaba's heritage as a tourist attraction. In consensus, when asked to describe the city of Madaba in three words, it seemed that Madaba has built a reputation of being touristic, spiritual, multi-religious, filled with mosaics, and simple as it resides in the countryside, yet so rich and fast developing. The local residents of Madaba, comprising 14% of the surveyed, and people who visited, 67.4%, were asked in the questionnaire if Madaba's experience differs from other cities in Jordan. There were mixed reactions between the two groups as some agreed with the question, mentioning the enormous number of Christian ruins and mosaics that can't be found in any other city. The minority were those who said that it is similar to other Jordanian cities in terms of its urban planning and architectural fabric, but it stands out for its historical importance.

Of those who never lived or visited 9.3% and of those who only heard of Madaba mostly know about it being a tourist attraction rather than its religious significance. Of these, 81.4% elaborated more on Madaba's importance from the historical and tourism aspects; this audience appreciated Madaba as a remarkable city: it is called Mosaic City for its many magnificent Byzantine mosaics in churches that have stories

to be told and explained. There is also a school for this craft to keep Madaba as a city of mosaic.

To follow up with the last question, participants were asked to suggest ways to better the recognition of Madaba as a tourist site. They mentioned that advertising through national television, radios, newspapers, educational books, giving out brochures, and to support all of this with a new signage system on the roads would make it easy for tourists to reach and to identify these sites. They think organizing the city's buildings to make them harmonious with the historical buildings would make the city a part of the history and the visit to Madaba would become more memorable. Some even suggested filming movies and TV shows in Madaba would increase international and internal tourism. Tourism offices should be urged to add Madaba to trips to Aqaba, Wadi Rum, Petra, Jerash.

Mervat Al-Saidat, a resident in Madaba, elaborated further during an interview:

> Madaba is ancient, although it keeps up with everything new; with its people it'll always keep its authenticity. The mosaics in Madaba are art, and their ability creates a canvas of that material which is extravagant. It preserves the human heritage for the benefit of the future generations and will put Madaba in a historical category for those who are interested in human science and archaeology and architecture. Putting these ruins on the map of the tourism and archaeology world will create international awareness in the holy world and among those who are interested in such rich monuments. In addition, it creates awareness to local and international investors to develop infrastructure and services to both local citizens and tourists. It helps enhance the tourism industry in Madaba and Jordan, thus, will create jobs and participate in increasing the Gross Domestic Product (GDP) of the country.

There is a positive factor between the existence of these historical and religious architectural and artistic sites with it being a tourist attraction [20]. The contradiction stands in how it exists within the referral tourist agencies and governmental action plans to dismantle this negativity.

8 Conclusion

History combines the acts of the people who came before us, their thoughts and studies, their beliefs and arts, their harmony and care, their planning and developing. It has played a huge role in creating an atmosphere filled with quaintness, relaxation, richness in such a small city like Madaba. Its value isn't for nothing if all those archaeologists had excavated it for centuries and bringing awareness to its existence will most certainly be eye-opening for everyone to receive pleasure from visiting it.

In Madaba, the correlation of sacredness combines beliefs before Christianity and representation of deities created from the Byzantine era along with the churches of saints and dedications of Roman emperors (as by another popular belief that they were god sent) to commemorate them and finally the mosques for the Muslim population. Architecture wise, in a panoramic view of the skyline, the slanted red rooftops of the archaeological park and Virgin Mary church, church of the holy martyrs combines with the mosques' minarets shows of the cohesion and coexistence of religions

Fig. 11 Burnt Palace and mosque panoramic view

and cultures (see Fig. 11) that created and imprinted image of Madaba, splendorous journey for self-discovery and education that is taught through illustrations of mosaic till this day are still being discovered and spurs new and completes stories.

> As for really new ideas of any kind—no matter how ultimately profitable or otherwise successful some of them might prove to be—there is no leeway for such chancy trial, error, and experimentation in the high-overhead economy of new construction …. Old ideas can sometimes use new buildings. New ideas must use old buildings. [21]

The survey didn't prove that there is much understanding or motivation from the youth on history in general, let alone knowing what Madaba's identity holds or realizing the name and reputation it could be having for the country if it understood the humbleness of what archaeology showed us throughout the years. Existence of unique historical objects can predetermine successful development of tourism in the region and Jordan literally has one of the biggest attractions for Christians who can live and experience, within hours, the story of a religion.

The lack of investments shadows the cultural heritage almost completely. The essentiality of educating the youth on historical and cultural heritage of the country on the whole is based on understanding important roles of cultural cognitive activity for a person and to enhance it by being a part of it. Despite the obsolete history of Madaba, it is still developing independently but still keeping with its initial rural characteristics and the hidden gem that is missing from international and internal recognition [22].

Another prominent issue is that the perimeter fence and walls of the surrounding environment of sacred placed like The Burnt palace or The Archaeological Park is limited any type from any type of activity from the local community and tourist who pass by cannot have visual access to the entrance of the palace. It does not hold any significance in any form with the local community other than it being a "tourist attraction for Christian tourists." A management plan and managing objectives from public authorities are needed to restore and revitalize the area is needed to maintain a sense of permanency.

Having new technological conservation interventions on Madaba will create a new case to study for archaeologists, architects, and students alike to start an advert on how Madaba adapted new techniques on restoring Emperor Justinian era mosaic and basilicas successfully. Paying attention to the restoration aspects and the tidiness of mosaics is to play a role in the tourism attraction. It is also recommended to take advantage of the age of emanation of social platforms to advert for variable priced touristic programmes to promote the routes of Jordan. Lectures, seminars, and the exploitation of local events and international programmes is deemed important to bring awareness to this sector. It is noted through the reoccurring visits to Mountain Nebo, Madaba became a "honeymoon" destination to religious tourists. When asked why they specifically chose Madaba, it was reasoned with wanting to follow up with the prophet's footsteps and continue the Christian pilgrimage from Makawer to Mountain Nebo to Jesus' Baptism Site.

Stories of martyrs, kingdoms, and crusades are illustrated in detailed mosaic art in every church of Madaba that are being disregarded as these holy sites aren't given the care needed and are left for time to dust over them. There are plenty of incidents where new residents of Madaba have found pieces that either complete a puzzle or begins a new tale of ancient times in Madaba that becomes too damaged for display and restoration from the effect of bulldozing through them without proper inspections in the area.

References

1. Bernheimer R (1939) An ancient oriental source of Christian sacred architecture. Archaeol Inst Am 43(4):647–668
2. Clark D (2007) Viewing the liturgy: a space syntax study of changing visibility and accessibility in the development of the Byzantine church in Jordan. World Archaeol 39(1):84–104
3. Hillier B (2005) Between social physics and phenomenology: explorations towards an urban synthesis? In: 5th international space syntax symposium proceedings, TU Delft, vol 1, pp 3–23
4. Bikai P, Thomas AD (1996) Madaba cultural heritage
5. Staller S (1996) Iron Age Tombs At Nebo, Jordan OFFPRINT of Studii Biblici Franciscani Liber Annuus XV
6. Piccirillo M (1976) New discoveries in Mountain Nebo
7. Piccirillo M (2007) Mount Nebo. Studium Biblicum Franciscam Guide Books
8. Leal B (2018) A reconsideration of the Madaba Map. Gesta 57(2):123–143
9. Saradi H (2010) Space in Byzantine thought. In: Ćurčić S, Hadjitryphonos E (eds) Architecture as icon: perception and representation of architecture in Byzantine Art [Exhibition at the

Princeton University Art Museum: March 6, 2010–June 6, 2010]. Yale University Press, New Haven, Connecticut, pp 73–111
10. Donner H (1992) The mosaic map of Madaba: an introductory guide. Kampen, The Netherlands
11. Harrison T, Batiuk S (2017) The metal trade and Early Bronze Age craft production at Tell Tayinat
12. Gregory C (1897) The Madaba Map. The Biblical World, 12(4)(Oct., 1898):244–250
13. Butler J (1962) Nineteen centuries of Christian Missionary architecture. Soc Archit Historians 21(1):3–17
14. Di Segni L (1992) The date of the Church of the Virgin in Madaba
15. Nassar M (2016) The portrait art during the Byzantine period, Jordan: a comparative study. Mediterr Archaeol Archaeometry 16(3):93–105
16. Bader M (2012) Religious tourism in Jordan: current situation, future developments and prospects. A case study on Islamic and Christian holy sites. A thesis submitted in partial fulfilment of the requirements of Catholic University of Eichstaett-Ingolstadt (KU) for the degree of Doctor of Philosophy in Tourism Management
17. Aldebi H, Aljboory N (2017) The impact of the tourism promotion-mix elements on the foreign tourists' mental images of the Jordanian tourist destinations (a field study). Int Bus Res 11(1):74
18. Al-Makhadmah I (2019) The role of the tourist mix in activating Christian religious tourism in Madaba Governate, Jordan
19. Al-Sarayreh M, Al-Dalaeen M (2012) Historical and religious archaeological sites and their role in the process of touristic attraction in Jordan (Madaba as a case study). Asian Soc Sci 8(3):163
20. Jacobs J (1961) The death and the life of great American cities
21. Wahib M (2004) Discoveries of religious tourism in Amman. The Hashemite University, Jordan
22. Fakhoury L (2009) Mādabā archaeological sites: bridging the gap between the living and once living sites of Mādabā. In: Studies in the history and archaeology of Jordan, vol 10

Influential Factors and Mechanism of Sense of Place in Historic Districts

Hongwei Hui, Benteng Liu, Yuping Sun, and Shunyao Zhang

Abstract As urban renewal becomes an integral part of urban development, the focus of urban planning has risen from environmental qualities to spiritual needs. Improving sense of place helps to activate lost spaces. Therefore, the study of sense of place in historic districts is critical. Taking the Nancang historical and cultural area in Dunhuang as an example, a structural equation model is constructed based on social attributes, built environments, crowd activities, emotional intentions, residence time and sense of place. Collecting subjective evaluation data through questionnaires for model fitting, data analysis and hypothesis testing, and then the mechanism is explored. The results show that there is a hierarchical relationship. Based on social attributes, built environments and crowd activities, emotional intentions are generated through interaction between people and places over time to form sense of place further. Meanwhile, the study confirms that sense of identity and direction are the two most direct and relevant factors. In addition, social attributes have a positive influence on residence time and residence time has no significant influence on sense of place. The study offers a useful guidance for protecting and promoting sense of place in historic and cultural area.

Keywords Heritage protection · Sense of place · Influential factors · Mechanism · Structural equation model

1 Introduction

As the carrier of traditional culture and urban memory, historic districts are essential parts of urban renewal, and their local characteristics give rise to sense of place [1]. With the rapid development of cities, traditional landscapes have been destroyed and local characteristics have been blurred in some areas. At the same time, new intelligent cities are altering traditional cultural systems and lifestyles, affecting people's

H. Hui (✉) · B. Liu · Y. Sun · S. Zhang
Lanzhou University of Technology, Lanzhou, Gansu, China
e-mail: 8998946@qq.com

T. Kang (ed.), *Proceedings of 5th International Conference on Civil Engineering and Architecture*, Lecture Notes in Civil Engineering 369,
https://doi.org/10.1007/978-981-99-4049-3_71

perception of local characteristics. How to pass on sense of place with local characteristics in urban development is considered more important than environmental protections.

Although there are many theoretical studies and empirical summaries about sense of place, most researches are qualitative. It needs to be explored in conjunction with quantitative analysis. At the same time, structural equation modelling can measure latent variables indirectly through observed variables and deal with degree of associations among multiple variables. Taking the Nancang historical and cultural area in Dunhuang as the research object, the study explores the interrelationship among variables based on place theory and further explores the mechanism. The study is conducive to protecting and enhancing sense of place.

2 Theoretical Bases and Research Hypotheses

2.1 Theoretical Bases

Place and sense of place are the core concepts of place theory. Norberg-Schulz (1979) proposes that the place is a meaningful whole that combines natural and artificial environments and argues that sense of place is formed when a place creates and maintains sense of identity and direction over a while [2]. Sense of place is formed through the subjective perception of environments and conscious perception of place, including perceptual feelings and emotional experiences. It is related to historical cultures, social backgrounds and regional characteristics.

The mechanism of sense of place needs to be supported by scientific models. The classical triangular model consists of physical environments, activities and meanings. Ghoomi et al. proposes that sense of place consists of five elements: demographic characteristics, physical characteristics, social characteristics, meanings and ecosystems [3]. Kaya proposes that sense of place consists of four elements: demographic characteristics, physical characteristics, social characteristics and meanings [4]. In essence, physical characteristics and ecosystems belong to built environments. Overall, the study proposes that sense of place includes four elements: social attributes, built environments, crowd activities and emotional intentions.

2.2 Research Hypotheses

Hashemnezhad divides sense of place into three levels: cognition, behaviour and emotion. Cognition leads to spatial perception as a way of understanding form. Behaviour leads to interaction with environments as a mean of satisfying function. Emotion is the highest level, which creates sense of place by giving it meaning [5]. Zhou argues that emotion emerges first and accumulates as the building is used,

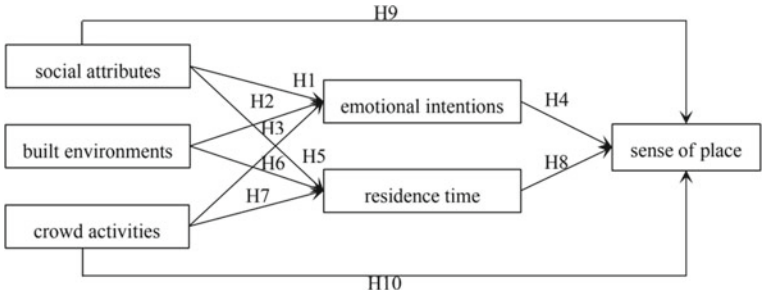

Fig. 1 Hierarchical model of sense of place

finally generating sense of place [6]. The study proposes that there is a hierarchical relationship in the process of generating sense of place. Firstly, social attributes, built environments and crowd activities have positive influences on emotional intentions respectively. And then emotional intentions have a positive influence on sense of place.

When tourists choose a destination, easy access is essential and historical value is a key attraction. Meanwhile, beautiful environments and plentiful activities tend to prolong residence time. Furthermore, Mohammad finds that time also influences sense of place [7]. The paper proposes that social attributes, built environments and crowd activities have positive influences on residence time and residence time has a positive influence on sense of place.

Zhou proposes that sense of place can be influenced by current social developments and human activities [6]. Dameria finds that tourists are likely to develop durable sense of place in seconds when they travel with formerly established impressions [8]. The paper proposes that social attributes and crowd activities have positive influences on sense of place.

Combining the above research hypotheses, a hierarchical model of sense of place is constructed with social attributes, built environment and crowd activities as causal variables, residence time and emotional intentions as mediating variables, and sense of place as the outcome variable (Fig. 1).

3 Questionnaire Design and Data Source

3.1 Questionnaire Design

Firstly, 4 dimensions and 33 influential factors are identified based on theoretical research. Secondly, 10 experts in the field of heritage protection are selected to redetermine (merge, remove or add) the influential factors by using Delphi. Moreover, a Likert five-point scale about the contents is made. Thirdly, 30 questionnaires are carried out first and the contents are adjusted. Final results contain 4 dimensions and

Table 1 Measuring scale

Latent variables	Observed variables
SC: Social attributes	SC1: Significance of historical value
	SC2: Harmony in internal relations
	SC3: Harmony in external relations
	SC4: External accessibility
	SC5: Internal accessibility
BE: Built environments	BE1: Retention of traditional layout
	BE2: Retention of building function
	BE3: Appropriateness of spatial scale
	BE4: Availability of public facilities
	BE5: Representative of plant landscape
	BE6: Peculiarity of architectural form
	BE7: Beauty of natural environment
	BE8: Colour co-ordination
CA: Crowd activities	CA1: The number of visitors
	CA2: Degree of participation of activities
	CA3: Degree of richness of activities
	CA4: Retention of traditional customs
	CA5: Retention of traditional skills
	CA6: Retention of long-established businesses
EI: Emotional intentions	EI1: Sense of security in activities
	EI2: Attraction of spatial nodes
	EI3: Degree of cleanliness
	EI4: Sense of responsibility for protecting the area
SP: Sense of place	SP1: Sense of identity
	SP2: Sense of direction
RT: Residence time	RT: Length of stay

26 influential factors (Table 1) and questionnaires also contain personal information of respondents.

3.2 Data Source

The 400 questionnaires were completed in the Nancang historical and cultural area in Dunhuang from 25 December 2021 to 10 January 2022. Equal numbers of questionnaires were distributed to residents, merchants and tourists because of different

Table 2 Model fitting

	χ^2/df	RMR	GFI	AGFI	IFI	TLI	CFI
Criteria	< 3.000	< 0.050	> 0.900	> 0.900	> 0.900	> 0.900	> 0.900
Result	1.872	0.048	0.895	0.866	0.941	0.930	0.941
Fit	Ideal	Ideal	Acceptable	Acceptable	Ideal	Ideal	Ideal

perceptions of different people [9]. Finally, 400 questionnaires were returned and 59 invalid questionnaires were removed, with an effective rate of 85.3%.

4 Results and Analyses

4.1 Model Computing

Firstly, the reliability and validity of the questionnaire data need to be tested by SPSS. The results suggest that the reliability of five latent variables is more significant than 0.7, representing that there is a good reliability. Meanwhile, the results suggest that KMO is more bigger than 0.9 and the significance reaches 0.000, representing that there is a good validity. Second, the validation factor analysis model is constructed and calculated by Amos. Some of the indicators obtained do not meet minimum criteria and the model is corrected based on place theory. Finally, analysis results are exposed below and most indicators reach minimum standards (Table 2) and standardised coefficients are reflected in path coefficients of the model (Fig. 2).

By looking at the significance levels between the latent and revealed variables, hypotheses H1, H2, H3, H4 and H5 are tested, and other hypotheses are not verified due to the low significance level (Table 3).

4.2 Descriptive Statistical Analysis

Firstly, residents, merchants and visitors fill out similar numbers of questionnaires. There are fewer men (38.4%) than women (61.6%). Most people are aged 31–40(29.6%), followed by 41–50(28.2%). This result indicates that the survey respondents are predominantly young and middle-aged.

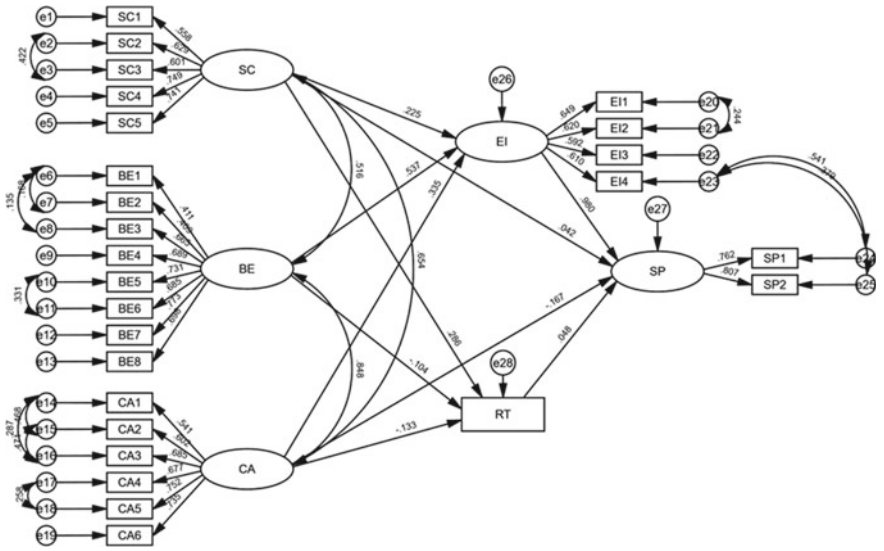

Fig. 2 Structural equation model

Table 3 Operation result

Paths	Standardisation	Non-standardisation	S.E	C.R	PLabel
SP ← SC	0.042	0.064	0.122	0.521	0.602
SP ← CA	− 0.167	− 0.240	0.330	− 0.726	0.468
SP ← EI	0.980	1.061	0.271	3.922	***
SP ← RT	0.048	0.021	0.017	1.228	0.220
EI ← BE	0.537	1.029	0.268	3.843	***
EI ← SC	0.225	0.313	0.104	3.024	**
EI ← CA	0.335	0.446	0.196	2.281	*
RT ← SC	0.286	0.983	0.334	2.94	**
RT ← CA	− 0.133	− 0.438	0.616	− 0.712	0.477
RT ← BE	− 0.104	− 0.491	0.735	− 0.668	0.504

Note ***indicates significance at the 0.001 level; **indicates significance at the 0.01 level; *indicates significance at the 0.1 level

5 Mechanism

The relationships between variables can be explored through effects analysis. If other factors remain constant, a 1-unit increase in social attributes will increase emotional intentions by 0.225 units. Social attributes, built environments and crowd activities significantly affect emotional intentions. Therefore, the effects of all three on sense

Table 4 Effect analysis

	SC	BE	CA	EI	RT	SP
Total effect of standardisation						
RT	**0.286**	− 0.104	− 0.133	0.000	0.000	0.000
EI	**0.225**	**0.537**	**0.335**	0.000	0.000	0.000
SP	**0.276**	**0.521**	**0.156**	**0.980**	0.048	0.000
Direct effects of standardisation						
RT	**0.286**	− 0.104	− 0.133	0.000	0.000	0.000
EI	**0.225**	**0.537**	**0.335**	0.000	0.000	0.000
SP	**0.042**	**0.000**	**− 0.167**	**0.980**	0.048	0.000
Indirect effects of standardisation						
RT	**0.000**	0.000	0.000	0.000	0.000	0.000
EI	**0.000**	**0.000**	**0.000**	0.000	0.000	0.000
SP	**0.234**	**0.521**	**0.322**	**0.000**	0.000	0.000

of place will also be analysed. Bolded numbers are the effects of tested hypotheses or their associated hypotheses (Table 4).

The total effect can make an analysis of combined influence that every variable on sense of place. The direct effect of emotional intentions on sense of place is 0.980. At the same time, other latent variables have no direct effect, indicating that sense of place is generated based on emotional intentions. The indirect effect refers to the influence of causal variables on outcome variables through mediating variables. Social attributes, built environments and crowd activities indirectly affect on sense of place, indicating that sense of place is a very complex system.

Sense of identity and direction have high path coefficients and significance levels, verifying that they are the two most direct and relevant factors that constitute sense of place [2]. Combined with validated hypotheses and effect analysis, the study proposes a hierarchical relationship: Based on social attributes, built environments and crowd activities, generating emotional intentions through people's activities in places over time, further forming sense of place.

5.1 On the Mechanism of Social Attributes

Although there is a weak direct effect (0.042), social attributes have an indirect effect on sense of place (0.234). Social attributes directly affect emotional intentions (0.225) and residence time (0.286). The various factors in the social attributes have vary influence and external accessibility is the most important (0.749), followed by internal accessibility (0.741), significance of historical value(0.558) is the weakest.

The good accessibility could increase people's intentions to visit the area and make it easier to gain sense of identity. In historic districts, streets and alleys are

dominant spatial forms apart from buildings. Meanwhile, they offer the vitality of this place. The survey finds that people are more concerned about the width of streets and parking spaces. Besides, excellent social relations could sustain structures of previous social network and decrease the number of out-migration of local residents and increase visitors' experience. The preservation of the original inhabitants can make the historical and cultural area a living culture rather than a specimen in an exhibition hall. In brief, it is vital to maintain original system and continue the traditional culture and life from past to now.

5.2 On the Mechanism of Built Environments

Although built environments have no direct effect on sense of place (0.000), there is a significant indirect effect on sense of place (0.521) and a significant direct effect on emotional intentions (0.537). An area with a beautiful environment is more likely to attract people to travel or live there, so the three most important factors are beauty of natural environment (0.773), representative of plant landscape (0.731) and colour co-ordination (0.698). In the absence of excellent colour design, it is not easy to express an aesthetic street, even if the architectural forms are varied and the street layout is strictly rational. In contrast, the influence of retention of traditional layout (0.411) and retention of building function (0.409) is weaker.

More and more tourists are choosing destinations with regional identity [10]. Architectural form is an essential factor in reflecting regional identity. For example, the typical layout of traditional dwellings with triple or quadrangle courtyards and inverted sloping roofs, as well as the pergolas that rise above the roof, creates a unique architectural style in Dunhuang. The retention of traditional layout is an essential factor in constituting the texture of the area and reflecting the character of the area. The continuation of the functions of traditional buildings is a reflection of historical authenticity, and the revitalisation of the functions is the key to attracting tourists. Creating a quality living environment in the form of culture and leisure is the primary way to preserve historical and cultural areas.

Public facilities are closely related to population movement, and improving public facilities can make historical and cultural areas more livable and attractive. The results suggest that the clear signs to locate the granaries in the Qing dynasty, car parks and toilets are more concerned. A spatial form with a clear location helps to generate sense of place. Moreover, the appropriateness of spatial scale concerns people's willingness to stop or play in the area. However, the spatial scale of the existing streets is depressing, mainly because some are narrow and hidden.

5.3 On the Mechanism of Crowd Activities

There is a total effect of crowd activities on sense of place (0.156) and emotional intentions (0.335). Of these, retention of traditional skills is the most important (0.752), followed by retention of long-established businesses (0.735), degree of richness of activities (0.685), retention of traditional customs (0.677), and degree of participation of activities (0.602). In comparison, the number of visitors (0.541) is the weakest, with only a weak influence.

The traditional skill is a part of residents' lives, a highlight for visitors and a critical window to show national culture. The survey finds that people are more concerned with famous long-established businesses. Retaining a long-established business is a crucial factor in continuing the cultural lineage. Increasing the variety of activities to enrich residents' daily lives and enhance tourism's attractiveness can contribute to improve sense of place. Moreover, people in tourist cities expect their hometown to be better known for its local performances and related events [10].

5.4 On the Mechanism of Emotional Intentions

Emotional intentions have a substantial direct effect (0.980) and no indirect effect (0.000) on sense of place. Of these, sense of security in activities (0.649) is the biggest effect and degree of cleanliness (0.592) is the weakest effect, probably because clean environment in Dunhuang makes this factor appear less significant.

Sense of safety is a composite judgement formed by people about the level of safety, which is an essential basis for generating other emotions. Spatial nodes generally refer to street ends and corners but can also be unique places (famous trees, ancient wells), which are important places for people to interact and will form shared memory. The survey finds that most people consider the area to be in poor condition. Therefore, there is a need to demolish poor buildings and develop public spaces. In addition, the promotion of cultural heritage protection must be strengthened at all times to increase people's sense of responsibility.

6 Discussion and Conclusion

6.1 Discussion

The study explores influential factors and mechanism of sense of place that are appropriate for the historic districts in the northwest but fails to compare with other areas, which has certain geographical limitations. Moreover, a comparative study of perceptions between different sorts of people was not analysed. In addition, a

comparative study of perceptions of place in the low and high seasons could not be conducted because of the impact of the epidemic.

The study has shown that sense of place is a complex system closely linked to perceptions. Except for individual differences, perceptions may also be affected by geography, time and policy. Therefore, we should continue exploring sense of place in historic areas, conduct horizontal and vertical comparative studies and use more comprehensive and more profound ways to protect and enhance sense of place.

The study is more on the theoretical side. Regarding practical application, Tao creates sense of place in three spatial forms through ecological restoration, preservation of relics and assembling dialogue [11]. Yang establishes an evaluation system for sense of place in tiny public spaces and gives a specific construction strategy [12]. Ge analyses the street types that should create sense of place in urban streets and puts forward the general design methods and evaluation ideas suitable for China [13]. Lin studies the essential characteristics of place and makes them concrete in a new way by correlating landscape types with widely recognised landscape archetypes to create landscape spaces with sense of place [14]. The major orientation of later study is to combine the evaluation system of sense of place with architectural typology and give specific strategies.

6.2 Conclusion

The study verifies that there is the hierarchical relationship: Based on social attributes, built environments and crowd activities, and through interaction between people and places, emotional intentions are generated over time to form sense of place further. Meanwhile, the study confirms that sense of identity and direction are the two most direct and relevant factors of sense of place. On the other hand, social attributes are vital in attracting people to stay or play. In addition, the effect of residence time on sense of place is weak.

References

1. Gu DZ, Zhang Y, Chen G, Yin YC (2020) Research on value assessment and adaptive protecti on of historical buildings in “atypical historical cities.” Ind Constr 50(02):82–88
2. Norberg-Schulz C (2010) Genius loci: towards a phenomenology of architecture, 1st edn. Huazhong University of Science and Technology Press, Wuhan
3. Ghoomi HA, Yazdanfar SA, Hosseini SB, Maleki SN (2015) Comparing the components of sense of place in the traditional and modern residential neighborhoods. Procedia Soc Behav Sci 201:275–285
4. Kaya A (2017) Evaluation of sense of place with respect to demographic changes. Gazi University J Sci Part B: Art Humanit Des Plann 5(3):13–24
5. Hashemnezhad H, Heidari AA, Hoseini PM (2013) “Sense of place” and “place attachment.” Int J Archit Urban Dev 3(1):5–12

6. Zhou K, Yan K, Wang J (2015) The reinterpretation of place spirit: on the protection and reuse of architectural heritage. J Sichuan Normal Univ (Soc Sci Ed.) 42(03):67–72
7. Mohammad-Moradi A, Yazdanfar SA, Norouzian-Maleki S (2020) Exploring the sense of place components in historic districts: a strategy for urban designers and architects. Iran Univ Sci Technol 30(1):30–43
8. Dameria C, Akbar R, Indradjati PN (2018) Whose sense of place? Re-thinking place concept and urban heritage conservation in social media era. In: IOP conference series: earth and environmental science, p 012010. IOP Publishing, Bandung
9. Xiang LL, Dong JJ, Wang KL, Zhao LL (2019) Research on the difference of the sense of place in historical district based on subject perspective: taking Nanluogu lane block in Beijing as an example. Urban Dev Stud 26(07):114–124
10. Li JP (2020) On the feasibility of boosting local tourism through regional customs and performing arts. Technol Wind (14):251+268
11. Tao F, Tang J, Bao YL (2020) The wisdom of traditional human settlements and reshaping of place spirit: inheritance of ancient villages in the sustainable landscape design of urban residential areas in Zhejiang. J Zhejiang Univ (Humanit Soc Sci) 50(05):168–177
12. Yang MN (2020) Research on sense of place construction of micro public space in Mingcheng district of Xi'an. Xi'an University of Architecture and Technology
13. Ge Y, Shen X (2021) Connotation, method and practice of the design of street with a sense of place: the compilation of the group standard street design guide. New Archit (04):35–39
14. Lin Q, Wang XR (2022) Archetype, place, and experience. Chin Lands Archit 38(05):6–13

Transportation Engineering and Management

Comparing Quality of Life between TOD and Non-TOD Areas in Central Business District (CBD) of Bangkok, Thailand

Pawinee Iamtrakul, Pisinee Visuttiporn, Jirattikan Ammapa, Jirawan Klaylee, Sararad Chayphong, and Yoshitsugu Hayashi

Abstract The population of Bangkok has been expanding which is driving up transport demand and housing construction. As a result, metropolitan areas have been urbanizing rapidly and creating critical infrastructure investments. As a result, compact urban development and areas nearby mass transit stations in terms of transit-oriented development (TOD) can help encourage mixed land use, including residential, commercial, and city service systems and improve high-quality facilities and pedestrian pathways easy to access. This study aims to capture the differences in perceptions within cities, especially among resident populations between TOD and non-TOD areas in Sukhumvit district as a Central Business District (CBD) representative. Spatial and statistical analysis was applied to determine the differences between the area within TOD 500 m and outside the TOD area. The perception of the road environment was assessed in terms of wealthy (X_1), safe (X_2), lively (X_3), and beautiful (X_4) aspects. In this study, different perceptions within the city, especially based on the local population, are examined which is of the utmost importance for urban planning to understand perceptions within the study area. Increasing efficiency gains from transport infrastructure investment and development areas, according to the TOD concept, could make the area development in proximity to transit stations more suitable and sustainable while enhancing the quality of life for city residents.

Keywords Transit-oriented development (TOD) · Quality of life · Perception · Satisfaction · Urban transport

P. Iamtrakul (✉) · P. Visuttiporn · J. Ammapa · J. Klaylee · S. Chayphong
Center of Excellence in Urban Mobility Research and Innovation, Faculty of Architecture and Planning, Thammasat University, Pathum Thani, Thailand
e-mail: pawinee@ap.tu.ac.th

Y. Hayashi
Center for Sustainable Development and Global Smart City, Chubu University, Kasugai 487-8501, Japan

T. Kang (ed.), *Proceedings of 5th International Conference on Civil Engineering and Architecture*, Lecture Notes in Civil Engineering 369,
https://doi.org/10.1007/978-981-99-4049-3_72

1 Introduction

The advantages of TOD include greater accessibility to public transportation and consequently more opportunities, the use of serviced land rather than sprawl area, increasing in transit ridership, a reduction in vehicle traffic pollution, a decreasing in the consumption of oil and gas, and healthier lifestyles, to encourage people to walk, bike, and utilize public transportation instead of personal vehicles. This is often accomplished by creating mixed-use communities around transit nodes with moderate to high densities and a walkable environment, except for the usual comfortable walking distance, there is no set of criteria for the appropriate distance. According to the literature, the walkable distance to transit can vary from 250 to 800 m [1, 2], depending on the topography and demographics of the location. The critical elements of TOD have been expanded into the "5D": density, diversity, design, destination, and distance [3]. By implementing the TOD principle, important things can be accomplished, including enhancing metropolitan communities' economic, social, and environmental well-being. These include increasing economic activity, minimizing possible population distribution, and lowering air pollution [4]. Over the past few decades, Bangkok has been characterized by rapid urbanization and the emergence of the TOD concept has resulted in a revolutionary process for urban quality of life, livability, sustainability, and transport. In past research, few studies have been conducted to assess perceptions in the road environment compared to non-TOD and TOD areas. In this regard, the perception of road environment factors that are included in the study can be summarized as follows;

- road environment gives the impression of being a road suitable for travel (Wealthy);
- the traveler feels safe during the journey to the destination (Safe);
- the surrounding road environment makes commuters feel alive (Lively);
- the road environment feels beautiful and pleasant during the journey (Beautiful).

This study provides a new idea for understanding the quality of life by focusing on TOD in the urban area while assessing the success of the TOD area in terms of urban quality of life enhancement.

2 Literature Review

Transit-oriented development (TOD) is an important strategy for urban development that aim to achieve sustainability and smart growth. A high-density, compact, mixed-use development near public transportation services is created based on the TOD urban planning concept, which is suited for urban development and sustainability. The fundamental philosophy appears to be the same in all contexts which can be elaborated as follows;

- constructing transit lines to connect current and planned concentrations of urban growth,
- focusing on urban development around stations to support public transit use, and
- establishing a city suited to pedestrians for better accessibility.

According to NJ Transit [5], the acceptable walking distance of New Jersey residents near transit stations is based on the general notion of willingness to walk for 5–15 min, or 400–800 m, to travel to or from a transit stop. However, it relies on the topography, security, and other activities near a transit stop. In 1997, the 3D framework of TOD included density, diversity, and design, combined with transportation networks and in 2008, expanded the design dimension to include the 2D principle (destination accessibility, distance to transit) to create the TOD area [6, 7]. The economic, social, and environmental well-being of urban areas can be significantly enhanced by implementing the TOD principle, which can also result in increased economic activity, decreased population growth, and air pollution [8].

The impact of residential self-selection on travel behaviour as a confounding element of the built environment has been one of the key discussions. Residential self-selection and travel-related attitudes may impact mode choice behaviors in TOD zones [9]. The results of a study in the Bangkok area on how to decrease car ownership within a 1-km radius of stations revealed that residences located in narrow streets, particularly, have a substantial impact on car use and parking availability and in turn, affect car ownership. These elements might be argued to prevent TOD residents in Bangkok from using public transportation [10]. According to a recent study examining 17 TOD projects of various sizes in four urbanized areas, residents in TOD areas tend to commute by transit two to five times more frequently than non-TOD areas [11]. Transit mode share for business trips has increased among TOD residents over the 30 years from 1970 to 2000, whereas it has declined across other regions. The proportion of TOD inhabitants using transportation for commuting was twice as high as the regional average value in 2000, despite regions growing more dependent on cars for business trips [12]. Before moving to TOD, 52% of people who commuted by car opted to take the train instead after finding housing near a train station [13]. Another study examined whether transit-oriented development (TOD) may reduce vehicle travel miles. Based on the specified measurement criteria, the authors then show results from travel behaviour analysis performed in TOD and non-TOD areas of the two metropolitan areas under consideration. The findings showed that even in locations with similar land use patterns, residents of TOD neighborhoods prefer to drive less with VMT in Washington, D.C., and Baltimore, compared to non-TOD areas [14].

3 Methodology

In this study, both statistical analysis and spatial analysis were applied. The spatial analysis supported the explanation of the difference between an area within a radius of 500 m and an area outside (non-TOD). This section describes the research process which will be divided into 3 parts of explanation as follows:

3.1 The Overall Framework of Methodology

More consideration has been paid to applying the concept of compact urban development and developing areas around mass transit stations (TOD) to promote mixed land use, such as residential, commercial, and city service systems. Furthermore, improving facilities and pedestrian walkways to be of high quality must be performed for more convenient access. The circulation of economic activities must be emphasized, especially in the central business district (CBD) area. Figure 1 represents a diagram showing the study's method structure. The study framework focused on TOD and non-TOD areas for considering the residential quality of life (QoL).

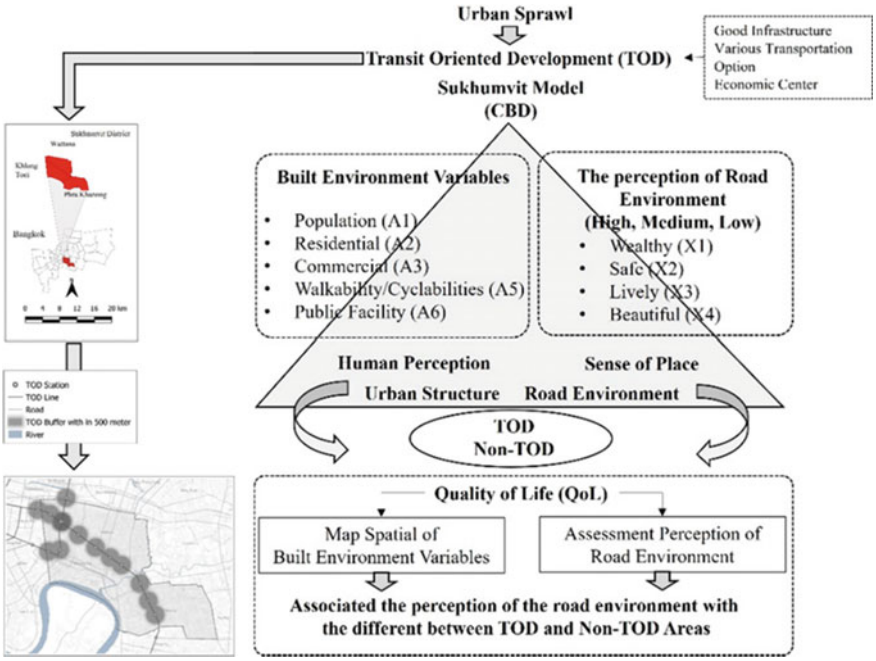

Fig. 1 Framework of study

In the first stage, the Sukhumvit area in Bangkok was selected as a target site, which includes Watthana, Klongtoey, and Phra Khanong districts. It is represented as a central business district (CBD) which has been filled with residential, commercial, employment, and real estate interests. The area is defined by a city form with a boundary of road networks that connects all locations. There are several travel modes for connecting points, e.g., MRT stations, BTS stations, cycling routes, etc., to facilitate travelers. The study area was divided into 500 * 500 grids and specifies the number of sets in each grid to collect the questionnaires of 500 sets, which was used for statistical analysis and its correlation, namely personal data (socioeconomic characteristics), physical characteristics, and perception of the road environment. Population (A_1), residential (A_2), commercial (A_3), bus stop (A_4), walkability/cyclability network (A_5), and public facilities (A_6) are described together with statistical analysis to determine the differences between the areas within TOD of 500 m, and outside the TOD in Sukhumvit area demonstrates the perception of the road environment in terms of wealthy (X_1), safe (X_2), lively (X_3) and beautiful (X_4).

3.2 Identification of Indicators

The specifics and significance of variables which are covered in this section comprises of three categories—social, economic, and access (see Table1). The input data is allocated into spatial data for analysis that are within a radius of 500 m. within TOD and an area outside (non-TOD). On the social side, population (A_1) is applied to present population density, which is returned in population units per square kilometer area (population/km^2). On the economic side, there are two factors which are residential (A_2) represents the residential density, and commercial (A_3) for the commercial density which are returned in units per square kilometer. The final factor of analysis is accessibility which consists of bus stops (A_4), walkability/cyclability (A_5), and public facilities (A_6), where bus stops present the unit of analysis in a kilometer and public facilities were determined by using network analysis for selecting the distance to the nearest transit location (line to hub).

3.3 Spatial and Statistics Analysis

In this research, spatial and statistical analyses were used. The spatial analysis was applied after selecting the study site and determining the built environment factors that affect the perception of the road environment. That will be expressed in 500 * 500 grid cells of totaling 87 grids. After that, each variable was geographically evaluated using the analysis tools to reflect their social dimensions (population factors, A_1). The spatial technique was performed by converting geolocation data from polygon to point using the actual centroid command which creates an internal point of a polygon layer into a new point layer to demonstrate the population density per area.

Table 1 Identification of variables

ID	Categories	Variables	Explanation of variable	Unit
A1	Social	Population	Population density	Population per square kilometers area (population/km^2)
A2	Economic	Residential	Residential density	Per square kilometers
A3		Commercial	Commercial density	Per square kilometers
A4	Access	Bus stop	Bus stop density	Per square kilometers
A5		Walkability/cyclabilities	Total length of walkability/cyclabilities	Kilometers
A6		Public facility	Point of public facility (e.g., hospital, education)	Kilometers

The population is calculated from house type or building data and multiplied by the average household of each building. The transformed data of residential (A_2) and commercial area (A_3) from polygon to point data is converted by using the actual centroid command, which creates an internal point of a polygon layer into a new point layer. After that, to see the densities of both activities inside and outside the TOD region, the same command was applied to convert data from polygon to centroid points by taking to determine the density per grid area. For the accessibility factor, the location of the bus stop (A_4) was retrieved from the open street map method to identify the bus stop network and analyze the density per grid area. For walkability/cyclabilities (A_5), the existing data was combined with the inference of the location of the pedestrian footpaths mostly adjacent to the primary and secondary roads. It is configured by having a sidewalk representing 1 and no pedestrian path for 0. Furthermore, for public facility access (hospital and education, A_6), the spatial analysis was performed by analyzing the network to determine the closest distance to the facility. Given an origin and a destination layer, this algorithm computes the distance between origin features and their closest destination. Distance calculations are based on their specific features and then described by comparing the socioeconomic characteristics in the TOD area and other areas (non-TOD) using cross tabulation and comparing the differences between both classifications. Finally, the level of perception of the road environment in several categories can be analyzed, including wealthy (X_1), safe (X_2), lively (X_3), and beautiful (X_4) aspects by using chi-square statistics.

4 Results

From the socioeconomic data analysis characteristics of respondents, it was found that the majority of both the TOD and non-TOD participants were males (TOD 50.8%, non-TOD 55.4%) with a bachelor's degree (TOD 66%, non-TOD 56.4%), the salary ranges between 10,000 and 25,000 baht (TOD 39.6%, non-TOD 47.2%), housing

character is a detached house/twin house (TOD 40%, non-TOD 47%). However, there is a difference in transportation mode selection in daily life. People in TOD area tends to choose a mode of transportation by walk/bicycle and public transport (buses) (17.3%), followed by public transport (van/taxi/motorcycle) and motorcycle (16.8%), respectively. Non-TOD group prefers to use their private vehicle (passenger car) (20.8%) to travel, followed by motorcycle (19.1%) and public transport (van/taxi/motorcycle) (15.8%), respectively (see Table 2). As for the perception of the road environment, it was found that those in the TOD area had the highest level of wealthy aspect ($X_1 = 2.76$), followed by lively ($X_3 = 2.71$), safe ($X_2 = 2.59$), and beautiful ($X_4 = 2.31$), respectively. For non-TOD residents, the perception of wealthy aspect ($X_1 = 2.4$) presents the highest value, followed by safe ($X_2 = 2.35$), lively ($X_3 = 2.31$), and beautiful ($X_4 = 2.14$), respectively. This section describes the general data for comparison between TOD areas within a radius of 500 m. and the outer radius of the Sukhumvit area using summation and computation as a geospatial analysis.

From the calculation of population density (A_1) within TOD and non-TOD areas, it was found that the population density within TOD was 0.54 population per km^2 and non-TOD was 0.49 population per km^2. In terms of residential density (A_2), it was found that within TOD was about 0.04 population per km^2 and non-TOD was about 0.21 population per km^2. In terms of commercial density (A_3), it was found that TOD was about 0.006 population per km^2 and non-TOD was about 0.009 population per km^2. Regarding bus stop density (A_4), it was found that inside TOD was about 0.009 population per km^2 and non-TOD was about 0.003 population per km^2. The total distance of walkability/cyclabilities (A_5) within the TOD, the mileage was approximately 64.7 km, and the non-TOD was about 133.9 km. Finally, in terms of public facilities (A_6), the total shortage distance to hospitals within the area of 500 m in TOD areas was about 3.06 km. and non-TOD areas was about 9.45 km. The total shortage distance to schools within an area of 500 m in TOD area was about 13.67 km., and non-TOD areas were about 73.83 km. (as illustrated in Table 3). The geospatial analysis results in Fig. 2 show the variables of the built environment within TOD and non-TOD.

The result of hypothesis testing in this study was performed by using chi-square statistics to describe the relationship between the differences in the TOD and outside TOD areas together with the level of perception of the road environment in different areas (wealthy, safe, lively and beautiful aspect). It was found that the difference between within 500 m of the TOD area and outside 500 m in radius (Non-TOD) was related to the perception of the road environment in wealthy aspect (X_1) (*p-value* = 0.002), safety aspect (X_2) (*p-value* = 0.001), and lively aspect (X_3) (*p-value* = 0.000), which were statistically significant at the 0.05 level. However, there was no significant correlation factor with the perception of the road environment which presents in terms of beautiful aspect (X_4) (*p-value* = 0.293), statistically significant at the 0.05 level.

Table 2 Comparing socioeconomic data between non-TOD and TOD area

Variables	TOD		Non-TOD	
	N	%	N	%
Gender				
Male	100	50.8	168	55.4
Female	92	46.7	124	40.9
Others	5	2.5	11	3.6
Education level				
Lower than junior high school	5	2.5	13	4.3
High school	21	10.7	41	13.5
Diploma	29	14.7	48	15.8
Bachelor's degree	130	66.0	171	56.4
Postgraduate	12	6.1	30	9.9
Income level (Average per month per person, baht)				
Less than 10,000	9	4.6	29	9.6
10,001–25,000	78	39.6	143	47.2
25,001–40,000	66	33.5	87	28.7
40,001–55,000	28	14.2	31	10.2
More than 55,000	16	8.1	13	4.3
Housing character				
Detached house/twin house	79	40	143	47
Townhouse	15	8	21	7
Commercial buildings	10	5	27	9
Condominium	71	36	63	21
Dormitory/apartment	21	10.7	48	15.8
Temporary building (wooden shed/galvanized shed)	1	0.5	1	0.3
Transportation mode selection in daily life				
Passenger car	32	16.2	63	20.8
Motorcycle	33	16.8	58	19.1
Walk/bicycle	34	17.3	43	14.2
Public transport (buses)	34	17.3	44	14.5
Public transport (BTS/MRT)	31	15.7	47	15.5
Public transport (Van/Taxi)				
Motorcycle	33	16.8	48	15.8
Total (Respondents = 500 sets)	197	100	303	100

Table 3 Characteristics of variables between TOD and non-TOD

Variables	TOD				Non-TOD			
	Min	Max	Average	Total	Min	Max	Average	Total
Population (A_1) (population/km^2)	0.00	0.01	0.0020	0.540	0.00	0.0110	0.00160	0.490
Residential (A_2) (km^2)	0.00	0.003	0.0007	0.040	0.00	0.0060	0.00100	0.210
Commercial (A_3) (km^2)	0.00	0.005	0.0001	0.006	0.00	0.0010	0.00000	0.009
Bus stop (A_4) (km^2)	0.00	0.0006	0.0001	0.009	0.00	0.0003	0.00002	0.003
Walkability/cyclabilities (A_5) (km)	0.001	7.278	0.1230	64.7	0.00	1.765	0.096	133.9
Public facility (Hospital) (A_{6a}) (km)	0.115	0.914	0.382	3.06	0.702	2.63	1.35	9.45
Public facility (Education) (A_{6b}) (km)	0.088	0.704	0.427	13.67	0.569	3.259	1.57	73.83

5 Discussion and Conclusion

Differences in transportation mode selection in daily life were found in the results of the socioeconomic differences between people who commuted in the area within 500 m of the TOD area and other areas (non-TOD) in the Sukhumvit district (see Table 3). Most commuters enjoy their daily travel by walking/bicycle and public transport (buses), followed by public transport (van/taxi/motorcycle) and motorcycle in the TOD area. When considering the accessibility in terms of the total number of footpaths for walking and cycling, it was found that the total number of paths within the TOD area was more significant than outside (non-TOD). In terms of bus service locations, it was found that the area within the TOD area has a higher density of points than outside the TOD areas; those who lived or traveled within the TOD area had the opportunity to travel and use the facilities more than who commuted in non-TOD areas. For in non-TOD areas, commuters usually use their own car, followed by a motorcycle and public transport (van/taxi/motorcycle), respectively, indicating the opportunity for those living or traveling in non-TOD areas with less access to public transport.

As a result, people who commute outside of TOD tend to use both private cars and motorcycles for most of their transportation mode selection in daily life. The result of analysis on the relationship between different areas in TOD and non-TOD was related to the perceived road environments (see Table 4). This study considered 4 aspects

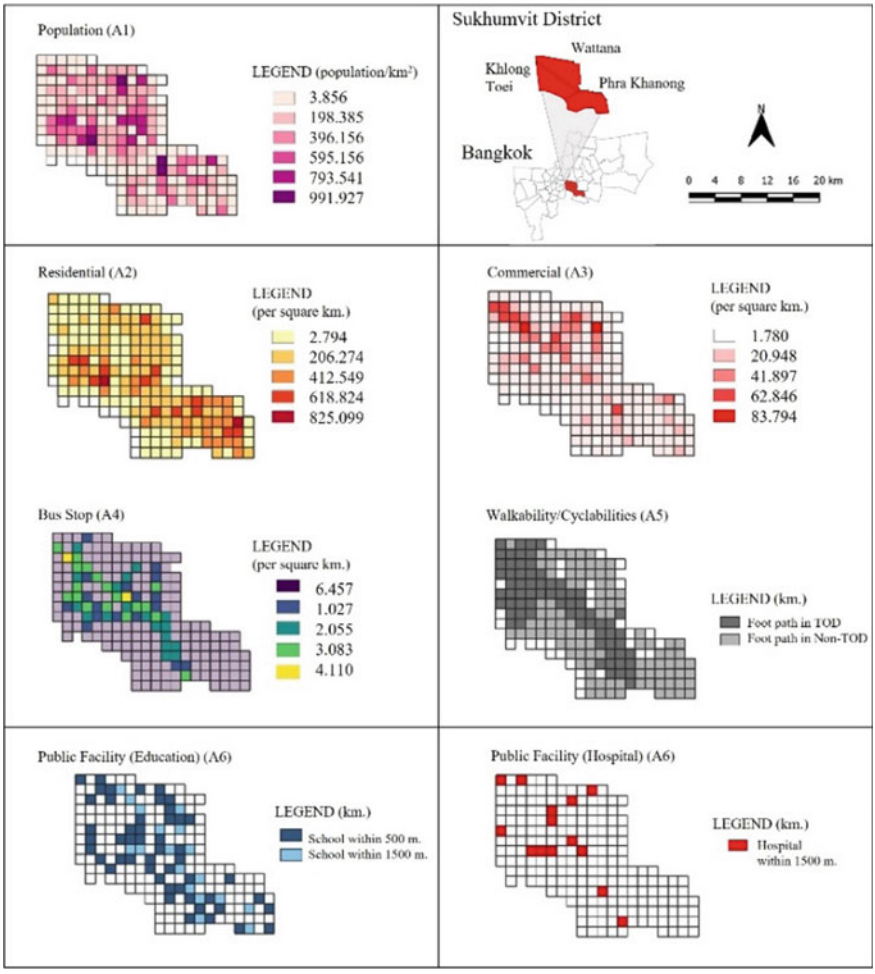

Fig. 2 Built environment characteristics of TOD and non-TOD area

of perception on road environment which are in wealthy (X_1), safe (X_2), and lively (X_3). However, the surrounding road environment makes commuters feel alive but unrelated to beautiful (X_4) and pleasant during the journey. According to this study, differences in perceptions within cities, especially among resident populations, are essential for urban planning [15]. Understanding these perceptions would be valuable for an improving of the efficiency of transport infrastructure investments to design and plan the transit areas according to the TOD concept for appropriate and sustainable urban development [16, 17].

Table 4 Perceptions of the road environment between TOD and non-TOD area

Variables		TOD		Non-TOD		Sig
		N	%	N	%	
1. Wealthy (X_1)	1	29	14.7	84	27.7	0.002
	2	79	40.1	116	38.3	
	3	89	45.2	103	34	
2. Safe (X_2)	1	34	17.3	98	32.3	0.001
	2	88	44.7	103	34	
	3	75	38.1	102	33.7	
3. Lively (X_3)	1	27	13.7	89	29.4	0.000
	2	87	44.2	122	40.3	
	3	83	42.1	92	30.4	
4. Beautiful (X_4)	1	65	33	118	38.9	0.293
	2	69	35	105	34.7	
	3	63	32	80	26.4	
Total		**197**	**100**	**303**	**100**	

Remark Level of significance is 0.05; Level of satisfaction is 1 = Low, 2 = Medium, 3 = High

Acknowledgements The authors gratefully acknowledge the financial support provided by the Science and Technology Research Partnership for Sustainable Development (SATREPS) Project of The Japan Science and Technology Agency (JST) and The Japan International Cooperation Agency (JICA) "Smart transport strategy for Thailand 4.0 realizing the better quality of life and low-carbon society" under Grant JPMJSA1704. It is conducted under the Faculty of Architecture and Planning Research Fund, Thammasat University, contract no. TDS 10/2021, and partially supported by Center of Excellence in Urban Mobility Research and Innovation, Faculty of Architecture and Planning, Thammasat University, Pathum Thani, Thailand.

References

1. Cervero R (1993) Ridership impacts of transit-focused development in California. Monograph 45, Institute of Urban and Regional Development, University of California, Berkeley, CA
2. Institute for Transportation and Development Policy (2017) TOD Standard, 3rd edn. ITDP, New York
3. Jeffrey D, Boulange C. Giler-Corti B., Washington S, Gunn L (2019) Using walkability measures to identify train stations with the potential to become transit-oriented developments located in walkable neighborhoods. J Transp Geogr 76:221–231
4. Iamtrakul P, Padon A, Klaylee J (2021) The study on association between urban factors and walkability of transit-oriented development (TOD). GMSARN Int J 16:388–398
5. NJTransit (1994) Planning for transit-friendly land use a handbook for New Jersey communities. In: U.S. Department of transportation, federal transit administration
6. Iamtrakul P, Ruengratanaumporn I, Klaylee J, Chaypong S (2020) The walkability of transit oriented development (TOD): a case study of Bangkok metropolitan, Thailand.

Lowland Technology International, International Association of Lowland Technology (IALT) 22(4):181–192
7. Riza H, Hayati SH, Ahyahudin S (2021) Carrying capacity of transit-oriented development (TOD) area in Jakarta. In: IOP Conference series: earth and environmental science, Volume 716, The 1st journal of environmental science and sustainable development symposium 28–30 Sept 2020, Jakarta, Indonesia. Earth Environ Sci 716 012131
8. Iamtrakul P, Raungratanaamporn I, Shinpiriya P (2017) Framework of planning and policy analysis for transit oriented development (TOD) towards sustainable Urban Development. J Architectural/Plann Stud (JARS) 14(1):95–122
9. Padon A, Iamtrakul P (2021) Grouping areas around rail transport stations based on the concept transit oriented development (TOD): the green line (Mo Chit—Onnut) and the blue line (Bang Sue—Hua Lamphong). J KMUTNB. 31(3)
10. Iamtrakul P, Zhang (2014) Measuring pedestrians' satisfaction of urban environment under transit oriented development (TOD): a case study of Bangkok metropolitan, Thailand. Lowland Technol Int 16(2):125–134
11. Arrington GB, Cervero R (2008) TCRP Report 128: effects of TOD on housing, parking, and travel. Transportation Research Board of the National Academies, Washington, DC 3
12. Renne J (2005) Transit oriented development: measuring benefits, analyzing trends, and evaluating policy. Dissertation Submitted to Graduate Program in Urban Planning and Policy Development. Rutgers University
13. Cervero R (1993) Ridership impacts of transit-focused development in California. University of California, Berkeley, CA, Institute of Urban and Regional Development
14. Nasri, Zhang (2014) The analysis of transit-oriented development (TOD) in Washington, D.C. and Baltimore Metropolitan Areas. Transp Policy 32:172–179
15. Iamtrakul P, Chayphong S (2021) The perception of Pathum Thani residents toward its environmental quality, suburban area of Thailand. Geographica Pannonica 25(2):136–148
16. Yoshitsugu H, Ikuo S (2003) Dual strategies for environmental and financial goals of sustainable cities De-suburbanization and social capitalization. Built Environ 29(1):8–15
17. Witsarut A, Hayashi Y, Takeshita H, Kii M, Vichiensan V, Theeramunkong T (2021) Can space-time shifting of activities and travels mitigate hyper-congestion in an emerging megacity, Bangkok? Effects on quality of life and CO_2 emission. Sustainability 13(12):6547. https://doi.org/10.3390/su13126547

Research on Application Scenario of Intelligent Road Studs for Smart Highway

Xianglin Yao, Hao Sun, Min Li, and Hongfang Li

Abstract The construction of smart highway in China has developed rapidly in the recent years. Aiming at some problems existing in the information perception and release of smart highway, this paper puts forward a new type of Intelligent Road Stud based on a number of research and market product benchmarking and analyzes the advantages and feasibility of intelligent stud in smart highway. The system architecture and equipment internal structure of intelligent stud are introduced. For the sections with limited sight distance such as highway fog area, small radius curve and highway diversion area, the intelligent stud release and early warning function for the above scenarios are proposed, and a simulation test environment is built in the field to test the application scenarios such as highway fog area and small radius curve. The results showed that using of intelligent stud can realize the accident risk warning to the driver in the section with bad sight distance, make up for the deficiency of variable information board and other equipment, optimize the early warning way and realize the fine prompt of collision risk, so as to reduce the danger of driving safety caused by bad sight distance.

Keywords Smart highway · Vehicle road coordination · Intelligent road studs · Application scenarios · Warning

1 Introduction

In the recent years, the construction of smart highway in China has developed rapidly, especially in terms of expressway. With the arrival of "new infrastructure", smart highways in various provinces and cities, including Zhejiang, Guangdong, Yunnan, Xiong'an and other places, have achieved good phased results.

Up to now, the Ministry of transport has piloted a number of provinces in order to speed up the promotion of the new generation of national traffic control network

X. Yao (✉) · H. Sun · M. Li · H. Li
China Highway Engineering Consulting Corporation, 17th West Third Ring Road, Beijing, China
e-mail: 595039865@qq.com

T. Kang (ed.), *Proceedings of 5th International Conference on Civil Engineering and Architecture*, Lecture Notes in Civil Engineering 369,
https://doi.org/10.1007/978-981-99-4049-3_73

and smart highway, and put forward six demonstration directions such as infrastructure digitization, road transportation integration and comprehensive application of Beidou high-precision positioning [1]. Taking the typical domestic smart expressway project as example, Beijing New airport Expressway has built a series of intelligent contents such as video accurate monitoring system, traffic feature acquisition system, dynamic speed limit system and confluence area early warning system; using Beidou high-precision positioning and vehicle road communication system, Jingxiong Expressway can provide vehicle road communication, high-precision navigation and early warning of key scenario, and has built the first exclusive lane for intelligent driving in China [2]; Yunnan Zhaoyang West Ring Expressway aims to build a national leading smart expressway around the city and has built an integrated management system of construction, management, maintenance and transportation based on digital twins.

However, after the construction of smart highway is completed and put into operation, there are still some problems in vehicle road information perception and release. For example, the current information perception mode based on video and radar has a large blind area, resulting in the lack of perceived information; the release means and content dominated by VMS is single, so it is urgent to expand the ways of information release [3].

Therefore, aiming at the above problems of smart highway, this paper proposed intelligent road stud, which can enhance the information perception range and optimize the early warning means, so as to reduce the potential safety hazards in the process of driving.

2 Description to Intelligent Road Stud

Road stud, also known as raised road beacon, is a raised marking block fixed on the road for marking. It can be used to mark the boundary of opposite carriageway, the boundary of same carriageway, the edge line of carriageway, etc. It can also be used to mark dangerous sections such as curves, entrance and exit ramps, diversion markings, road narrowing.

At present, the transition of traffic safety facilities to intelligence and digitization is a major trend of smart highway construction. Intelligent road stud will be important carrier for vehicle road information interaction on smart highway that can realize multi-source information sending, sensing and publishing by integrating geomagnetic, Bluetooth and other micro-sensing technologies.

Intelligent road stud has strong practicability in smart highway and mainly has the following advantages:

- In terms of information collection, through vibration sensors and geomagnetic sensors, it can collect various traffic parameters such as the speed, length and occupancy of passing vehicles.

- In terms of information transmission, Bluetooth, ZigBee and other communication technologies can be integrated to realize low-power, stable and high-speed wireless communication.
- In terms of information release, intelligent studs are arranged along the lane line, and lane control in different scenarios such as traffic ban, warning and guidance can be realized through the change of light color frequency.
- In terms of cost, compared with high-precision detection equipment such as HD camera and Lidar, it has low manufacturing cost and is easy to be popularized and applied.
- In terms of installation and maintenance, there is no need to build the new poles, and the embedded installation on the road surface is adopted, which is basically parallel with the road surface, does not affect the road snow shovel and other work, and convenient for maintenance.
- In terms of working environment, the intelligent stud can work normally in bad weather such as rain, ice and snow, heavy fog and low visibility at night, with strong stability.

At present, there are relevant standards for road studs (i.e., raised road beacon) in the industry. *GB5768 Road traffic signs and markings* has made rough provisions on their definition, shape and layout position: when used in conjunction with markings, active luminous type or directional reflective type shall be selected, with its color consistent with the color of markings, and the layout interval is 6–15 m [4]; *GB24725 Raised road markings* have detailed provisions on its classification, composition, technical requirements and test methods: it shall have good chemical corrosion resistance, water resistance, UV resistance and weather resistance. Metal materials shall also have good toughness. After being damaged by overload, there shall be no sharp fragments causing traffic injury, generally trapezoidal, circular or oval. The height above the road surface shall not be greater than 20 or 25 mm [5]. In addition, in the subdivision field, *GB19813 Solar raised road markings* stipulate the definition, structure classification, technical requirements and luminous performance of solar protrusion road beacon [6]. *T/CECS 10,076 Geomagnetic induction raised road markings* stipulate the product structure, model and functional requirements of geomagnetic induction raised road marking [7].

In addition to relevant standards, at the level of theoretical research, domestic scholars have also conducted a lot of research on traditional and intelligent stud. In terms of traditional road nails, HE. L. conducted compressive load test and overall impact resistance test to solve the problems of easy damage and rapid failure of reflective performance of Expressway road nails, and obtained the most vulnerable damage point of road nails, which provides a reference basis for improving performance [8]. HE. S. studied the feasibility of using mechanical energy to convert electrical energy, and applied this technology to road studs. The mechanical energy generated by vehicles rolling the pavement on the road is used to realize the active luminescence of road studs, which puts forward a new direction for the sustainable development of the transportation field [9]. In terms of intelligent stud research, HU. H. proposed magnetic induction technology, which determines the relative position

of vehicles through electromagnetic induction generated by magnetic road beacon, and then induces vehicles to drive in the specified Lane [10]. LI. P. proposed the parking lot scheme of intelligent stud management service area, which provides a reference for the application of intelligent stud in smart expressway and intelligent management of service area [11]. In addition, through the research of Bluetooth protocol, some scholars have developed the master–slave node of intelligent stud based on Bluetooth communication, which uses intelligent stud for data acquisition and transmission [12].

To sum up, studs have been applied in the field of smart roads, mainly through geomagnetic sensing, wireless communication and other means to collect and transmit traffic parameters, which has a certain level of intelligence, but there are still some problems to be further studied. Although intelligent studs have been applied in the construction of smart highways in China, their applicable scenarios and functional services have not been clarified. It is urgent to sort out the application scenarios that can be used for intelligent stud early warning.

3 System Architecture of Intelligent Stud

The intelligent stud system are composed of outfield equipment, transmission channel and cloud control center. The outfield equipment mainly includes: intelligent stud, controller, industrial Ethernet switch, etc.

- The intelligent stud integrates sensors such as three-axis geomagnetic detector, IOT communication module and LED lamp, which has multiple functions of information perception, transmission and release. The normal luminous color of intelligent stud is white. When different levels of early warning events occur, the color is yellow and red colors.
- The intelligent stud controller is used to obtain the transmission signal of the visibility detector and other equipment. Then, the luminous state of intelligent studs are controlled in real time by algorithm.
- As the medium of signal transmission, industrial Ethernet switch is used to connect visibility detector and controller. The system architecture is shown in the Fig. 1.

The internal structure of the intelligent stud device is shown in the Fig. 2. The device has built-in power supply module, main control module, perception module, communication module and light-emitting module, which integrates the collection, communication and release of traffic information. In the aspect of acquisition, the sensing module is composed of three-axis geomagnetic sensors to comprehensively obtain a variety of important parameters of traffic information, such as speed, flow, time occupancy, vehicle stop discrimination, vehicle type classification and so on; in terms of communication, the communication module is composed of wireless mesh ad hoc network, which can realize super anti-interference, low-power consumption, low delay and high reliable two-way communication; in terms of release, the light-emitting module is composed of multiple groups of LED light beads to realize the

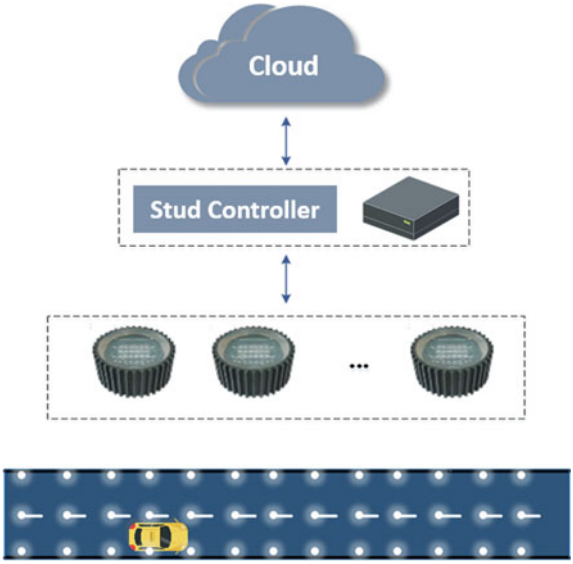

Fig. 1 System architecture of intelligent stud

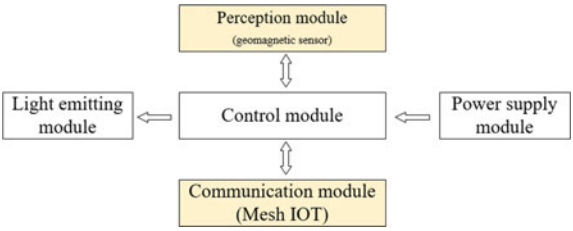

Fig. 2 Internal structure of intelligent stud

early warning release of drivers with different light colors and different flashing frequencies. Compared with the camera, radar and other equipment, the intelligent stud is buried on the road at a certain interval along the road lane line. It has the characteristics of many kinds of acquisition parameters, low manufacturing cost, simple installation and maintenance, strong environmental adaptability, and is not affected by bad weather.

4 Application Scenario of Intelligent Stud

Combined with the advantages of intelligent stud, this paper analyzes the safety early warning requirements of driving in fog area, night, small radius curve, diversion area and confluence area of expressway and combs the early warning functions of the above scenarios on the basis of demand analysis. Take fog scenario of highway as an example.

a. Demand analysis

In case of heavy rain or dense fog, due to low visibility and limited sight distance, it is easy to cause traffic accidents. Therefore, it is very important to take certain early warning measures for high incidence sections of rain and fog, such as fog areas, improve the road sight distance and realize active guidance and early warning.

By setting up an intelligent stud system in the fog area section, the functions of lane contour display, driving guidance, vehicle following warning, parking warning and so on can be realized for the sight distance requirements of low visibility in rainy and foggy weather.

b. Scenario function

After the system is turned on, when a single vehicle is driving, the intelligent stud on both sides will form a sliding belt moving with the vehicle, and there is white light in front of the vehicle to show the lane outline. There is red light in a certain range behind the vehicle to warn the vehicle to the rear. As shown in the Fig. 3.

When two cars follow, due to the limited sight distance in the fog area, the rear car cannot grasp the specific position of the front car. If the distance between two cars is less than the minimum safety distance, there is a hidden danger of rear end collision. Therefore, the vehicle following warning is carried out through the intelligent stud system. As the two vehicles approach, the number of white lights in front of the rear vehicle decreases continuously. Until the two vehicles reach the minimum distance between the two vehicles, all the intelligent studs between the two vehicles turn into red lights. As shown in the Fig. 4.

When there are vehicles parked in the roadside emergency lane, if the rear vehicles are not found in time, there will be rear end collision accidents and other potential safety hazards. The emergency lane parking warning can be carried out through the intelligent stud system. After the vehicle stops in the emergency lane, the red light will be turned on within a certain range behind the vehicle to warn the rear vehicle. As shown in the Fig. 5.

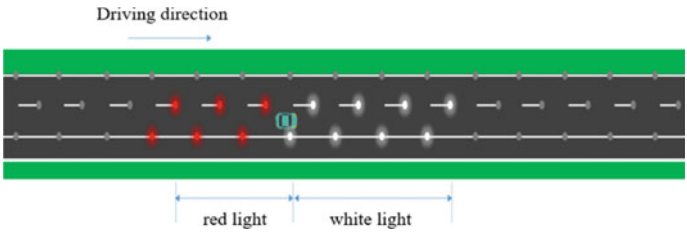

Fig. 3 Sketch map of single vehicle driving in fog area

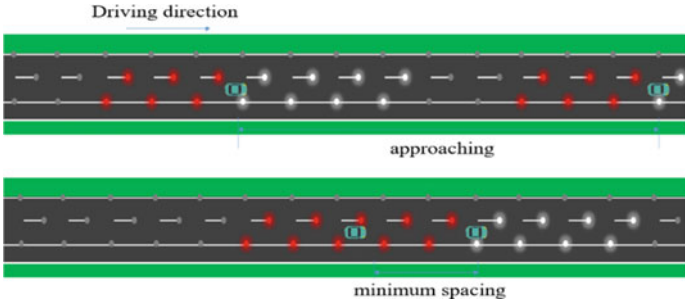

Fig. 4 Sketch map of car following in fog area

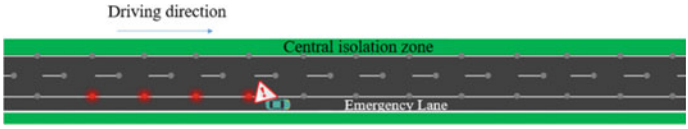

Fig. 5 Sketch map of parking in fog area

5 Test Result

In this paper, in order to verify the function realization effect of the application scenario, a field road is selected to build a simulation test environment, and the on-site tests are carried out for single vehicle driving, car following driving, meeting driving and other scenarios under the road fog area section and small radius curve section. The test results are as follows.

The function realization of single vehicle driving in the fog area scenario is shown in the Fig. 6. When driving with the vehicle, the intelligent stud on both sides of the vehicle will form a sliding belt moving with the vehicle, and the white flashing light will be turned on in front of the vehicle to show the lane outline; Turn on the red flashing light at the rear of the vehicle to give early warning of the safety distance of the rear vehicle.

The function realization of multi-vehicle following driving in the fog area scenario is shown in the Fig. 7. When the two vehicles are far away, they follow the single vehicle driving state; as the distance between the two vehicles decreases gradually, the number of lights in front of the rear vehicle decreases continuously until the distance between the two vehicles reaches the minimum safe distance, all of them become red lights.

The function realization of the parking warning scenario under the fog area scenario is shown in the Fig. 8. After the vehicle stops in the emergency lane, the red flashing light is turned on in a certain range behind the vehicle to warn the rear vehicle.

Fig. 6 Single vehicle driving in fog area

Fig. 7 Car following in fog area

Fig. 8 Parking in fog area

6 Conclusion

Aiming at some problems existing in the current smart highway in information perception and release, this paper puts forward a new type of intelligent stud equipment, analyzes the advantages and feasibility of intelligent stud in smart highway and introduces the system architecture and internal structure of intelligent stud. Then it analyzes the application scenarios of intelligent stud, such as how to warn the vehicle driver in the application scenarios with limited sight distance, such as highway fog area, small radius curve, highway diversion area and so on. Finally, a simulation test environment is built for typical scenarios to test the function realization of different

scenarios. The results show that the intelligent stud can optimize the early warning means and warn the driver of accident risk, so as to reduce the hidden danger of driving safety caused by poor sight distance. Next, aiming at the impact of different lighting forms on driving behavior, combined with the definition of traffic language signals in the current standards and specifications, this paper will study the understanding of different drivers on the light color, frequency and other contents of intelligent stud lights.

References

1. Notice of the general office of the Ministry of transport on accelerating the pilot of a new generation of national traffic control network and smart highway TGH [2018] No. 265
2. Jingxiong SH (2021) Expressway has a smart lane to test driverless. Beijing Daily, 26 Nov 2021
3. G. L. Thoughts on intelligent high-speed construction. China's Transportation Informatization, 38–42 (2019)
4. National standard of the people's Republic of China. Road traffic signs and markings. Highway Research Institute of the Ministry of Transportation (2009)
5. National standard of the people's Republic of China. Raised pavement markers. Highway Research Institute of the Ministry of Transportation (2009)
6. National standard of the people's Republic of China. Solar raised pavement markers. Highway Research Institute of the Ministry of Transportation (2005)
7. National standard of the people's Republic of China. Magnetic induction raised pavement markers. Highway Research Institute of the Ministry of Transportation (2019)
8. H. L. Study on compression and impact resistance of raised road signs on Expressway. Henan Build Mater 26–28 (2017)
9. H. S. Feasibility study on protruding road signs based on road piezoelectric energy acquisition technology. Western Transp Technol (4):3 (2019)
10. H. H. Application of magnetic induction technology in Intelligent Highway. Henan Sci Technol (10):1 (2014)
11. L. P. A parking management system for expressway service area based on intelligent stud. Shandong Indus Technol (5):2 (2018)
12. G. Z. Research on vehicle speed detection and application based on short spacing double node geomagnetism. Harbin Institute of Technology

Enhancement of Aluminum Alloy by Hybridization with BFRP Sheets

Haithm A. M. Al-Shami, Jianxun Liu, Yahia M. S. Ali, Hao Wu, and Zhishen Wu

Abstract This paper presents an enhancement method for aluminum alloy with and basalt fiber-reinforced polymer (BFRP) sheets for application in traffic sign boards industry. The behavior of the hybrid composition between aluminum alloy and BFRP sheets was experimentally studied under static loading. The tested parameters were resin type, arrangement of BFRP sheets and number of BFRP layers and their effect on the ultimate tensile strength. The test results show that hybridization of aluminum alloy and BFRP sheets clearly improves the tensile strength compared to the aluminum alloy alone. Thus, this advantage will benefit hybrid composition reaching integrated great performance in traffic signs boards. Based on the experimental results, utilizing the aluminum alloy with BFRP sheets is efficiently improved the ultimate tensile strength of compared to aluminum alloy. In addition, the hybrid specimens contain two layers of BFRP sheets showed higher tensile strength than their counterparts with one BFRP sheet. Also, using BFRP sheets with 90° direction is recommend for using in the industrial applications owing to its high integrated performance rather than that of 45° direction.

Keywords 5052-aluminum alloy · Hybridization · BFRP sheet · Traffic sign boards

H. A. M. Al-Shami · J. Liu (✉) · Y. M. S. Ali · H. Wu · Z. Wu
Key Laboratory of C&PC Structures Ministry of Education, Southeast University, Nanjing 210096, China
e-mail: 101012467@seu.edu.cn; llljjjxxx@126.com

National and Local Unified Engineering Research Center for Basalt Fiber Production and Application Technology, International Institute for Urban Systems Engineering, Southeast University, Nanjing 210096, China

T. Kang (ed.), *Proceedings of 5th International Conference on Civil Engineering and Architecture*, Lecture Notes in Civil Engineering 369,
https://doi.org/10.1007/978-981-99-4049-3_74

1 Introduction

Aluminum, a silvery-white metal, has unique qualities not seen in other non-ferrous metals. Aluminum is widely employed where a lightweight, non-corrosive metal is required, such as in missiles and vehicle parts, where weight savings are a significant benefit. Aluminum is weak in its pure form and has limited applications, in addition, the demand for materials with high qualities and properties has increased. Thus, aluminum is commonly used when alloyed with small amounts of other metals, resulting in a complex and strong metal. In this case, it will be suitable for the products in which people have expanded their horizons beyond ferrous materials [1]. 5052-aluminum alloy is widely used in traffic sign boards, the manufacture of vehicle components, ships and vessels [2]. In some cases, it can be used in nuclear and marine engineering structural parts due to its strong corrosion resistance, exceptional forming performance and excellent weldability [3].

In the last two decades, fiber-reinforced polymer (FRP) composites have been extensively used in numerous industrial applications, such as aerospace, sporting goods and civil engineering. FRP has superior properties such as, high strength-to-weight ratio and excellent chemical and corrosion resistance compared to both aluminium and steel. Pervious investigations have been carried out on glass FRP (GFRP) and carbon FRP (CFRP). Basalt FRP (BFRP) is a new environmentally friendly fibers have been widely used in various concrete composite structures in the recent years [2, 4–16]. BFRP exhibits higher tensile strength, elastic modulus and chemical stability than GFRP at the same cost [7–10]. Furthermore, basalt fibers are non-combustible and chemically stable [17, 18] and excellent weather, alkaline and acid resistance. Furthermore, basalt fibers can be employed at temperatures ranging from – 200 °C to relatively high temperatures (i.e., in the range of 600–800 °C) [10, 11, 19–22]. It also has a lower cost and wider operating temperature range than CFRP [11–13]. Moreover, the tensile strength of BFRP is more than four times that of steel bars, whereas the density is only one-fourth of that of steel [9]. This indicates that BFRP is highly cost effective. Found that the static strength of the BFRP displays slight deterioration after aging in the salt solution [22].

New and advanced items have been done due to new technologies and advancements in production or manufacturing. These items require a material with distinct to better adapt to the actual environment and perform as expected. In some countries, hurricane storm weather is prevalent, which requests the traffic sign boards could bear high wind pressure-high resistance to the stress. The objective of hybridization between aluminium alloy with fibers is to get the high strength of FRP with the ductile aluminium alloy. Hence, hybridization technique is a reliable way to improve the performance of aluminium alloy, since it has a desired properties with reduced cost. However, to date, the mechanical properties of hybrid aluminium alloy and BFRP sheet have not been investigated. The aim of this study is to investigate the aluminium of hybrid aluminium and BFRP sheets and the aluminium is also studied for comparison.

2 Experimental Program

2.1 Materials

In this paper, BFRP sheets with 45° and 90° orientation were used with areal density of 251 g/m^2 and thickness of 0.35 mm provided by Jiangsu GMV Co., Ltd China, while the density of aluminum alloy was 650 g/m^2, respectively. The mechanical properties of the above materials according to the manufactures are reported in Table 1. Two types of epoxy resin were used in this study one of them is cured at high temperature (E1), while the other one is cured at room temperature (E2). The mechanical properties of the resins were tested according to the ASTM: D1141-98 [6] and the results are listed in Table 1. All materials used are shown in Fig. 1.

2.2 Specimen Fabrication

To study the effect of hybrid technique, hybrid specimens were prepared in addition to, one aluminum alloy (Al alloy) with 3 mm thickness for comparison purpose. The hybrid specimens were made by hand lay-up then the molding was compressed as shown in Fig. 2. The same fabrication steps were carried out by Singh et al. [4]. The hybrid specimen was fabricated by stacking the 2 mm aluminum alloy laminate with BFRP sheet using the corresponding resin and then layered up in a flat-bottomed iron mold. The final thickness of the hybrid specimens differs according to the number

Table 1 Mechanical properties of the BFRP sheets and the resins [23]

Types	Tensile strength (MPa)	Elastic modulus (GPa)	Failure elongation (%)
BFRP fiber	2100	91	2.30
E1	79	3.0	5.4
E2	80	3.05	5.3

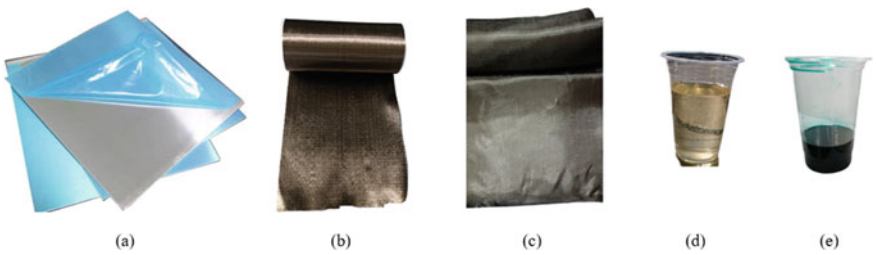

Fig. 1 Materials: **a** Aluminum alloy; **b** BFRP sheet (90°); **c** BFRP sheet (45°); **d** Epoxy resin (E1); **e** Epoxy resin (E2)

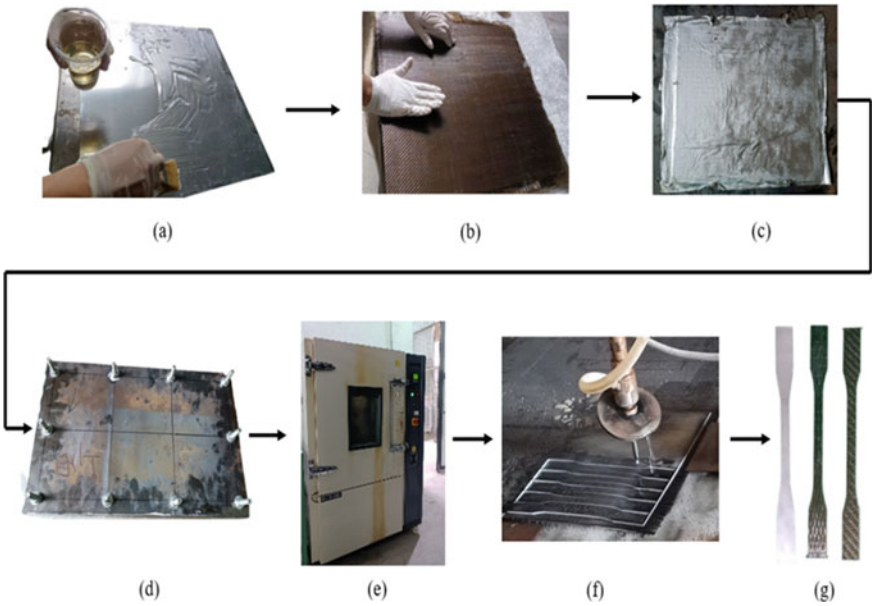

Fig. 2 Fabrication process: **a** paint the aluminum alloy with the according resin; **b** stacking the BFRP sheet with the aluminum alloy; **c** stacked the composite in aluminum foil; **d** Placing the composite between the iron plates; **e** Hot oven curing only for specimens with epoxy resin E1; **f** cutting machine; **g** Specimens with required dimensions extracted from the composite

of stacked sheets. For an excellent surface finish and ease of debonding, the stacked layers were initially placed between the aluminum foil. The fabricated specimens were placed between two 3 mm thick iron plates and bolts were used to connect iron plates. The entire arrangement was dried in a hot air oven for a specific time (145 °C for 2 h) (only for specimens with epoxy resin E1). The fabrication steps are highlighted in Fig. 2. The prepared specimens were left at room temperature for 24 h before cutting them to the required shape which is 200 mm length and 2 mm width with a 100 mm gauge length, as shown in Fig. 3g. The test parameters in this study were fiber arrangement, number of BFRP sheets' layers and type of resin used. The hybrid specimens were identified as follows: (H-X-Y-Z), where the letters X, Y and Z, indicate the angle of arrangement (90°; 45°), number of BFRP sheets' layers (1: one layer in only one side; 2: two layers: one in each side) and type of resin (E1; E2), respectively. For example, H-90-1-E represents to contain of aluminum alloy and one layer of 90° BFRP sheet fabricated by epoxy resin. The specimen details are listed in Table 2. For each case, five specimens were prepared and tested to obtain reliable results.

Test Setup and Procedure. The specimens were tested under static tension test. Tests were done by using the tensile test machine (SHIMADZU), as shown in Fig. 3. The specimens were gripped in between the wedge grips such that entire grip length covers the face of the grips. The pressure in the wedge grips was performed to

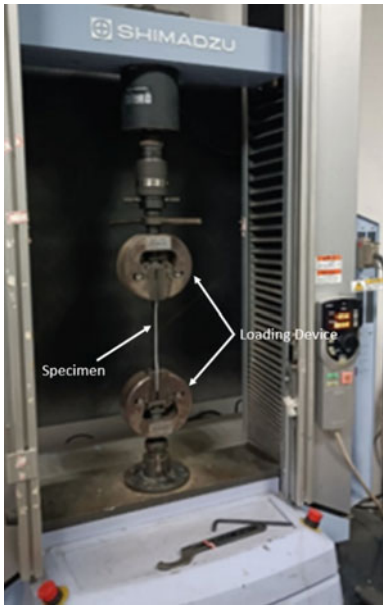

Fig. 3 Tension static test

Table 2 Details of specimens

Specimen	Number of BFRP sheet layers	BFRP sheet orientation	Resin type	Thickness (mm)	Number of specimens
Al alloy	–	–	–	3	5
H-90-1-E1	One layer in only one side	90°	Epoxy resin (E1)	2 + 0.35 = 2.35	5
H-90-1-E2			Epoxy resin (E2)		5
H-90-2-E1	Two layers one in each side		Epoxy resin (E1)	2 + (2*0.35) = 2.7	5
H-90-2-E2			Epoxy resin (E2)		5
H-45-1-E1	One layer in only one side	45°	Epoxy resin (E1)	2 + 0.35 = 2.35	5
H-45-1-E2			Epoxy resin (E2)		5
H-45-2-E1	Two layers one in each side		Epoxy resin (E1)	2 + (2*0.35) = 2.7	5
H-45-2-E2			Epoxy resin (E2)		5

avoid the specimen from slippage and failure at grips during tension. The rate of displacement was 2 mm/min.

3 Test Results and Discussion

3.1 Failure Mode Mechanism

The failure modes of all tested specimens are shown in Fig. 4. The aluminum alloy specimen failed due to rupture, however, the main damage mechanism for all hybrid specimens is interface debonding along the interface between BFRP sheet and aluminum alloy. It is worth mentioned that, the interface debonding appeared only for the BFRP sheets, while no failure was detected for the aluminum alloy itself. In addition, for hybrid specimens contains BFRP sheet with 90° arrangement, a long crack longitudinal matrix cracking was clearly seen in several locations on the surface of the specimen, as seen in Fig. 5. In contrast, rupture of BFRP sheet after interface debonding was observed for the hybrid specimens with BFRP sheet with 45° arrangement. This is attributed to the low transverse strength of the anisotropic fibers and the sensitivity to transverse matrix cracks [12].

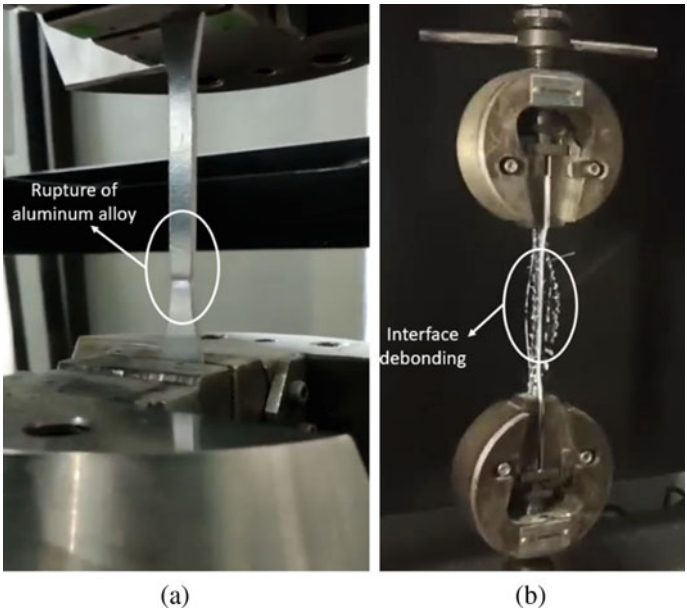

Fig. 4 Failure mode: **a** Aluminums alloy specimen; **b** Hybrid specimen

Fig. 5 Failure mode **a** Aluminum alloy (Al alloy) **b** Hybrid specimens with BFRP sheet (90°); **c** Hybrid specimens with BFRP sheet (45°)

3.2 Static Tensile Strength

The results of tensile test are listed in Table 3. To make full understanding of the effect of hybrid technique and the other investigated parameters on the tensile strength, each parameter will be discussed separately in the following sections.

Effect Hybrid Technique. Using combination between aluminum alloy and BFRP sheet displayed good behavior compared to aluminum alloy alone. The ultimate tensile strength of specimen H-90-1-E1 improved by 87% compared to specimen Al alloy. This percent increased to 138% when using two layers of BFRP sheets. This finding strongly confirms the great role of hybrid method on the tensile strength.

Effect of Resin Type. Table 3 reported that using epoxy resin (E1) which cured in high temperature exhibited better ultimate tensile strength compared to epoxy resin (E2) in all cases. This may be due to epoxy resin (E1) was treated in the heated oven with high temperature (145 °C) as explained in the fabrication process. Thus, the composite matrix becomes much higher than epoxy resin (E2) which cured in the room temperature, as shown in Fig. 6. For example, the average tensile strength of specimen H-90-1-E1 was 204 MPa, however, specimen H-90-1-E2 displayed only 95.6 MPa. This mean the percentage of increase was 113%. The high temperature

Table 3 Results of the tested specimens

Specimen	Tensile strength (MPa)	Avg. tensile strength (MPa)	CV (%)
Aluminum alloy	102	109.2	3.82
	113		
	112		
	107		
	112		
H-90-1-E1	199	204	1.55
	208		
	205		
	206		
	202		
H-90-1-E2	109	95.6	13.4
	85		
	89		
	82		
	113		
H-90-2-E1	236	260.2	4.7
	264		
	266		
	267		
	268		
H-90-2-E2	204	210.6	3.7
	200		
	211		
	217		
	221		
H-45-1-E1	118	127.2	4.0
	126		
	129		
	131		
	132		
H-45-1-E2	85	88.8	5.4
	98		
	87		
	89		
	85		

(continued)

Table 3 (continued)

Specimen	Tensile strength (MPa)	Avg. tensile strength (MPa)	CV (%)
H-45-2-E1	141	141.8	4.0
	145		
	133		
	150		
	140		
H-45-2-E2	85	82.6	3.1
	86		
	81		
	82		
	79		

provides the sufficient curing developing a stiffer composite. This different performance arises from different breakage mechanisms in the matrices [12]. Hence, the static tensile strength greatly depends on the resin types used in the hybrid process.

Effect of Arrangement of BFRP Fibers Sheet Types. Figure 7 demonstrated that the ultimate tensile strength of hybrid specimen with BFRP sheet (90°) is a much higher than that of (45°) of layers. As mentioned before, the lower strength of BFRP in the transverse direction. For instance, the ultimate tensile strength specimen H-90-2-E1 displayed 84% more than specimen H-45-2-E1. The arrangement of BFRP fibers sheet played an important role in the final results of the ultimate tensile strength of the specimens.

Effect of the Number of BFRP Sheet Layers. Increasing the number of BFRP sheets' layers enhanced the tensile strength of the hybrid specimens, as shown in

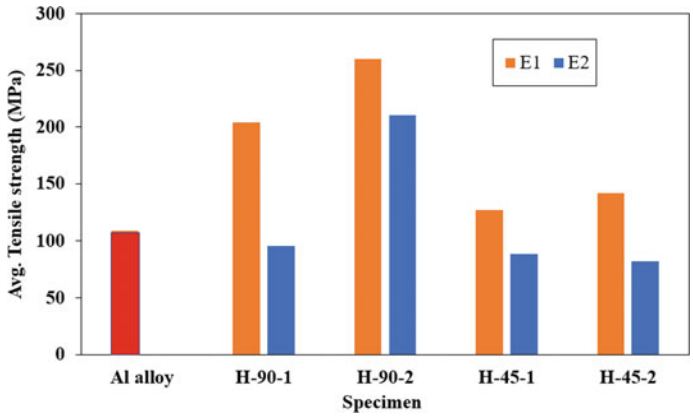

Fig. 6 Effect of resin type on the tensile strength

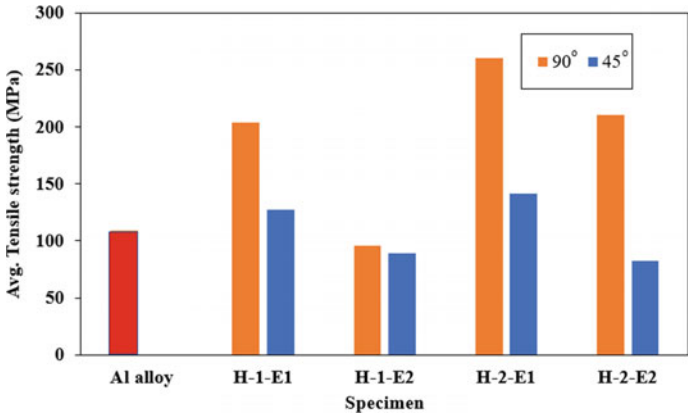

Fig. 7 Effect of BFRP arrangement on the tensile strength

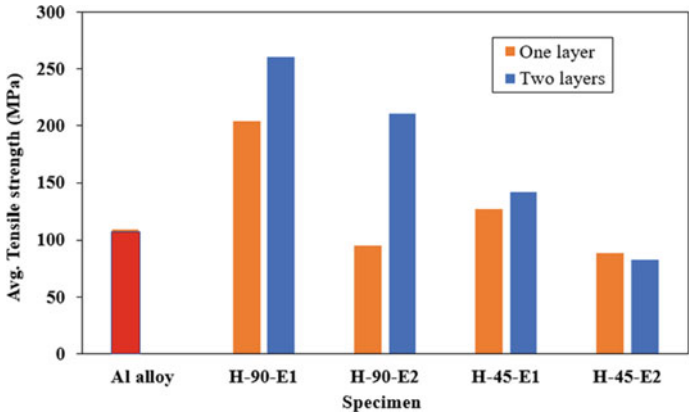

Fig. 8 Effect of number of layers on the tensile strength

Fig. 8. For example, the average tensile strength of specimens H-90-1-E2 and H-90-2-E2 was 95.6 and 210.6 MPa, which means the improvement was 120%. The reason behind this is that BFRP sheets have high tensile strength which improve the whole tensile strength of the composite with increasing the number of layers.

4 Conclusion

This paper has presented a promising new composite material, BFRP with aluminum alloy which offers potential advantages for application in industry of traffic sign boards. The most effective parameters affecting on the hybridization performance

were studied, such as resin types, fiber arrangement and number of BFRP layers. Based on the test results, the conclusion can be drawn as follows:

1. The aluminum alloy exhibited rupture failure, however all the hybrid specimens with BFRP sheets arranged in 90° failed due to interface debonding with a long longitudinal cracking in the matrix, in contrast, for hybrid specimens with 45° BFRP sheets, the interface debonding developed to rupture of fiber sheet due to the lower transverse strength of fibers.
2. Using the aluminum alloy with BFRP sheets is efficiently improved the ultimate tensile strength of compared to aluminum alloy. In addition, the hybrid specimens which contain two layers of BFRP sheets showed higher tensile strength than their counterparts with one BFRP sheet.
3. In hybridization process, using BFRP sheets with 90° direction is recommend for using in the industrial applications; owing to its high integrated performance rather than that of 45° direction.

References

1. Mishra D, Bhowmik A (2020) A comprehensive study of an aluminum alloy AL-5052 SEE PROFILE a comprehensive study of an aluminum alloy AL-5052, May 2018, pp 2349–1108 [Online]. Available: https://www.researchgate.net/publication/325076297
2. Shanavas S, Raja Dhas JE (2017) Weldability of AA 5052 H32 aluminium alloy by TIG welding and FSW process—a comparative study. IOP Conf Ser Mater Sci Eng 247(1). https://doi.org/10.1088/1757-899X/247/1/012016
3. Guo N, Wu D, Wang G, Cheng Q, Fu Y, Yu M (2022) Investigation on underwater wire-feed laser deposition of 5052 aluminum alloy. J Manuf Process 76 (Sept 2021):687–694. https://doi.org/10.1016/j.jmapro.2022.02.050
4. Singh SB, Vummadisetti S, Chawla H (2018) Influence of curing on the mechanical performance of FRP laminates. J Build Eng 16 (Dec 2017):1–19. https://doi.org/10.1016/j.jobe.2017.12.002
5. Shi J, Wang X, Zhang L, Wu Z, Zhu Z (2022) Composite-wedge anchorage for fiber-reinforced polymer tendons. J Compos Constr 26(2):1–11. https://doi.org/10.1061/(asce)cc.1943-5614.0001194
6. ASTM D1141-98, Standard Practice for the Preparation of Substitute wastewater (2013)
7. Su C, Wang X, Ding L, Wu Z (2020) Enhancement of mechanical behavior of FRP composites modified by silica nanoparticles. Constr Build Mater 262:120769. https://doi.org/10.1016/j.conbuildmat.2020.120769
8. C. Su, X. Wang, L. Ding, Z. Chen, S. Liu, and Z. Wu (2021) Experimental study on the seismic behavior of seawater sea sand concrete beams reinforced with steel-FRP composite bars. Eng Struct 248(Apr):113269. https://doi.org/10.1016/j.engstruct.2021.113269
9. Wang X, Wu Z, Wu G, Zhu H, Zen F (2013) Enhancement of basalt FRP by hybridization for long-span cable-stayed bridge. Compos Part B Eng 44(1):184–192. https://doi.org/10.1016/j.compositesb.2012.06.001
10. Wang X, Wu G, Wu Z, Dong Z, Xie Q (2014) Evaluation of prestressed basalt fiber and hybrid fiber reinforced polymer tendons under marine environment. Mater Des 64:721–728. https://doi.org/10.1016/j.matdes.2014.07.064
11. Wang X, Shi J, Liu J, Yang L, Wu Z (2014) Creep behavior of basalt fiber reinforced polymer tendons for prestressing application. Mater Des 59:558–564. https://doi.org/10.1016/j.matdes.2014.03.009

12. Hartwig G, Hübner R, Knaak S, Pannkoke C (1998) Fatigue behaviour of composites. Cryogenics (Guildf) 38(1):75–78. https://doi.org/10.1016/S0011-2275(97)00113-6
13. Wang X, Su C, Deng W, Wu Z (2019) Bond behavior between corrugated BFRP shell and concrete under monotonic and cyclic loads. Constr Build Mater 210:596–606. https://doi.org/10.1016/j.conbuildmat.2019.03.072
14. Vol AM (2018) Tensile properties of FRP composites temperatures. J Appl Mech (11):963–970
15. Shao Y, Okubo K, Fujii T, Shibata O, Fujita Y (2014) Effect of matrix properties on the fatigue damage initiation and its growth in plain woven carbon fabric vinylester composites. Compos Sci Technol 104:125–135. https://doi.org/10.1016/j.compscitech.2014.09.010
16. Dong H et al (2020) Evolution of interface and tensile properties in 5052 aluminum alloy/304 stainless steel rotary friction welded joint after post-weld heat treatment. J Manuf Process 51(June 2019):142–150. https://doi.org/10.1016/j.jmapro.2020.01.038
17. Deák T, Czigány T (2009) Chemical composition and mechanical properties of basalt and glass fibers: a comparison. Text Res J 79(7):645–651. https://doi.org/10.1177/0040517508095597
18. Wei B, Cao H, Song S (2010) Tensile behavior contrast of basalt and glass fibers after chemical treatment. Mater Des 31(9):4244–4250. https://doi.org/10.1016/j.matdes.2010.04.009
19. Sim J, Park C, Moon DY (2005) Characteristics of basalt fiber as a strengthening material for concrete structures. Compos Part B Eng 36(6–7):504–512. https://doi.org/10.1016/j.compositesb.2005.02.002
20. Scheffler C, Förster T, Mäder E, Heinrich G, Hempel S, Mechtcherine V (2009) Aging of alkali-resistant glass and basalt fibers in alkaline solutions: Evaluation of the failure stress by Weibull distribution function. J Non Cryst Solids 355(52–54):2588–2595. https://doi.org/10.1016/j.jnoncrysol.2009.09.018
21. Morozov NN et al (2001) Science for ceramic production materials based on basalts from the European North of Russia. Steklo Keram 58(3):24–27
22. Wang X, Zhao X, Wu Z (2019) Fatigue degradation and life prediction of basalt fiber-reinforced polymer composites after saltwater corrosion. Mater Des 163:107529. https://doi.org/10.1016/j.matdes.2018.12.001
23. Wang X, Zhao X, Wu Z, Zhu Z, Wang Z (2016) Interlaminar shear behavior of basalt FRP and hybrid FRP laminates. J Compos Mater 50(8):1073–1084. https://doi.org/10.1177/0021998315587132

Research on Ice Suppression and Performance Evaluation of Anti-Freezing Pavement

Haining Xu, Zhisong Sun, Jiancun Fu, Fei Yang, and Fangtao Liu

Abstract Under the rainy and snowy weather in winter in the north, the snow and ice on the asphalt pavement have extremely adverse effects on the vehicle driving safety and road traffic capacity, such as the reduction of driving speed and the increase of traffic accident rate. In order to reduce these impacts, a variety of anti-freezing pavement technologies have been developed. At present, the anti-freezing pavement technologies can be divided into active and passive types. As a technology with the advantages of anti-freezing pavement, environmental friendliness, and construction convenience, the chemical material inhibition freezing pavement technology has received extensive attention in recent years. This technology refers to adding a certain amount of salt storage snow melting and ice suppression materials to the asphalt pavement in advance, so that the snow melting components can be actively dissolved and precipitated in the wet environment. In this paper, two different specifications of antifreeze ice modifiers are used to design the mix proportion of antifreeze ice pavement, and the impact breaking test is developed to evaluate the antifreeze effect of the mixture of different antifreeze ice modifiers, the falling rate of asphalt mixture with anti-freezing agent increased obviously, and the falling rate of asphalt mixture with AF-I reached 60%. Finally, the indoor tests show that the high temperature stability and water stability of the mixture meet the performance requirements. The research in this paper shows that chemical inhibiting materials as additives can effectively inhibit the adhesion of ice when the performance of asphalt mixture meets the requirements, it improves the driving safety on bad weather roads and have a positive impact on the practice of anti-freezing pavement technology.

Keywords Anti-freezing pavement · Anti-freezing performance · Road performance · Mix proportion design

H. Xu · Z. Sun
Weihai Highway Development Center, Weihai 264200, China

J. Fu · F. Yang · F. Liu (✉)
Shandong Transportation Institute, Jinan 250102, China
e-mail: 156711993@qq.com

T. Kang (ed.), *Proceedings of 5th International Conference on Civil Engineering and Architecture*, Lecture Notes in Civil Engineering 369,
https://doi.org/10.1007/978-981-99-4049-3_75

1 Introduction

Road icing and snow have always been the key and difficult point in road maintenance. The icing and snow on asphalt pavement will not only affect the road capacity, but also bring hidden danger to traffic safety [1–3]. At present, the road maintenance department mainly adopts the measures of combining mechanical snow removal and deicing salt to ensure the traffic in winter [4]. But the spreading of deicing salt has a certain lag, and with the extensive use of deicing salt year by year, the high concentration salt solution after deicing salt melting not only causes certain damage to the road itself, but also causes certain damage to the traffic safety facilities on both sides of the road [5–7]. Salt storage anti-freezing pavement is a kind of pavement with active snow removal function, which has the advantages of good environment and convenient construction. The salt storage anti-freezing pavement needs to design the ice suppression additive as a part of the pavement materials [8]. When the pavement has a certain humidity, the anti-freezing components will actively precipitate to reduce the freezing point of the pavement [9].

In this paper, two different specifications of salt storage anti-freezing materials are taken as the research object, and SMA-13 anti-freezing pavement design, anti-freezing performance evaluation of mixture, and high and low temperature road performance verification are carried out, respectively.

2 Materials and Methods

2.1 Pavement Foundation Materials

According to the technical requirements of technical specification for highway asphalt pavement construction, the crushing value, density, water absorption, dust content, abrasion value, and other indicators of coarse aggregate, sand equivalent, density, methylene blue, and other indicators of fine aggregate, penetration, softening point, ductility, elastic recovery and segregation, and other indicators of modified asphalt, mineral powder, the technical indexes of fiber materials meet the requirements of the specification.

2.2 Anti-Freezing Additives

ZGHIT low freezing point filler is selected as the anti-freezing powder (AF-II), as shown in Fig. 1. Its maximum nominal particle size is 0.075 mm, which is composed of low surface hydrophobic material and low freezing point material; the main component of anti-freezing particles (AF-I) is chloride salt, and the reinforcement agent

Fig. 1 Anti-freezing modifier

and slow-release agent are added. The particle size is larger and can be replaced by fine aggregate.

Anti-freezing material can reduce the freezing temperature of road surface water [5], while hydrophobic material can reduce the ability of water penetrating into the road surface, improve the wetting state of water and road surface, and reduce the bonding ability of ice and road surface.

3 Results and Discussion

3.1 Mix Proportion Design of Anti-Freezing Pavement

3.1.1 Mixture Production and Test and Determination of Production Temperature

According to the asphalt used in the project and previous engineering experience, the indoor mixing temperature of asphalt mixture is determined as 170–175 °C, and the compaction temperature suitable for the molding of test specimens and initial rolling temperature on site is determined as 160–165 °C [10].

3.1.2 Target Mix Design

The content of anti-freezing additive is 5% of the mass of asphalt mixture. In order to ensure the proper volume index of asphalt mixture, the screening test of two kinds of anti-freezing additives is carried out. The screening test results show that the particle size of anti-freezing ice is in the range of 1.18–2.36 mm, which should be

Table 1 Gradation of anti-freezing asphalt mixture

Size (mm)	19	16	13.2	9.5	4.75	2.36	1.18	0.6	0.3	0.15	0.075
SMA-13 (AF-I)	100	99.7	90.7	71.5	30.6	20.1	15.5	14.5	13.7	12.8	10.7
SMA-13 (AF-II)	100	99.7	90.7	71.5	30.5	21.7	17.5	15.6	14.2	13.1	9.4
SMA-13	100	99.7	90.7	71.5	30.5	21.7	17.5	15.6	14.2	13.1	10.8

Table 2 Summary of test parameters

Types of additives	Void ratio (%)	Aggregate gap rate (%)	Asphalt saturation (%)	Stability (kN)	Flow value (mm)
SMA-13 (AF-I)	3.8	18.8	79.5	8.0	2.8
SMA-13 (AF-II)	3.7	18.6	80.2	7.2	2.7
SMA-13	3.7	17.9	77.8	6.9	3.1

used instead of fine aggregate; the anticoagulant ice powder is basically less than 0.075 mm, so it should be used instead of mineral powder.

According to the grading range specified in technical code for construction of highway asphalt pavement, three gradations are debugged, respectively, in the design process, and (AF-I, AF-II) are used to replace equal amount of fine aggregate and mineral powder. The passing rate of grading design is given in Table 1.

Marshall test was carried out, 75 times for each side. When 0.3% lignin fiber is added in the molding process, the maximum theoretical density of asphalt mixture is designed by calculation method. Marshall test is used to verify the mix proportion, and all indexes of the mixture meet the specification requirements, as given in Table 2. Finally, 5.9% of the three mixtures are selected.

3.2 Evaluation of Anti-Freezing Performance

3.2.1 Freezing Test

In order to verify the anti-freezing effect of pavement materials with anti-freezing modifier, the research group designed comparative experiments to explore. After the completion of the rutting test, the two groups of rutting boards were allowed to stand for 12 h, and the waterproof glue was used to form a circle with a diameter of 5 cm on the surface of the rutting board to ensure that there was no water leakage in the circular area. A layer of clean water is evenly distributed in the circular area by using a spout, and the two groups of specimens are put into a constant temperature and

humidity incubator for preparation. It can be found from the figure that the water distribution of the specimens with modifier is more uniform due to the action of salt in the modifier, while the surface water of the specimens without modifier is agglomerated.

Considering that the freezing temperature of water is 0 °C, firstly, keep the incubator at 0 °C for 2 h, set the temperature from 0 °C to decrease by 0.5 °C every half hour, and use the scraper to check the freezing condition of the surface of the road. It is found that the freezing temperature of water in the mixture without anticoagulant is − 0.5 °C, while that in the mixture with anticoagulant ice particles is − 5 °C. The addition of anticoagulant significantly reduces the condensation temperature of water.

3.2.2 Impact Breaking Test

The impact breaking test design aims to investigate the deicing ability of pavement under extremely cold temperature. The standard Marshall specimens with foundation mix proportion, AF-I and AF-II are, respectively, formed and placed in a mold with a diameter of 11 mm. Water is added to 5 mm above the surface of the specimen. The three groups of specimens were put into the refrigerator for test, and the temperature was set at − 18 °C for 16 h until the specimens were completely frozen. After the specimen is taken out of the mold, knock off the ice at the bottom of the time to ensure that the quality of the three groups of specimens with ice is basically the same, as shown in Fig. 2.

After specimen preparation, record the mass of each group of specimens. Ensure that the test pieces are facing down, and fall freely from the height of 70 cm worktable. Each group of test pieces is tested for five times continuously, and their mass is measured, respectively. The final test data is shown in the Fig. 3.

It can be seen from Fig. 3 that the falling rate of asphalt mixture with anti-freezing agent increases obviously, and the falling rate of asphalt mixture with AF-I reaches 60%. For the road surface with frozen surface, the icing on the road surface can be removed more quickly in the process of vehicle rolling, which is combined with the reducing effect of anti-freezing ice particles on the setting temperature, and it can significantly reduce the icing on the road.

3.3 Pavement Performance Test

3.3.1 Rutting Test

According to the test specification for asphalt and asphalt mixture of Highway Engineering (JTG E40-2011), the dynamic stability of asphalt mixture is determined by forming test pieces according to the optimum asphalt content, so as to test the anti-rutting ability of asphalt mixture [11, 12]. The test results show that the dynamic

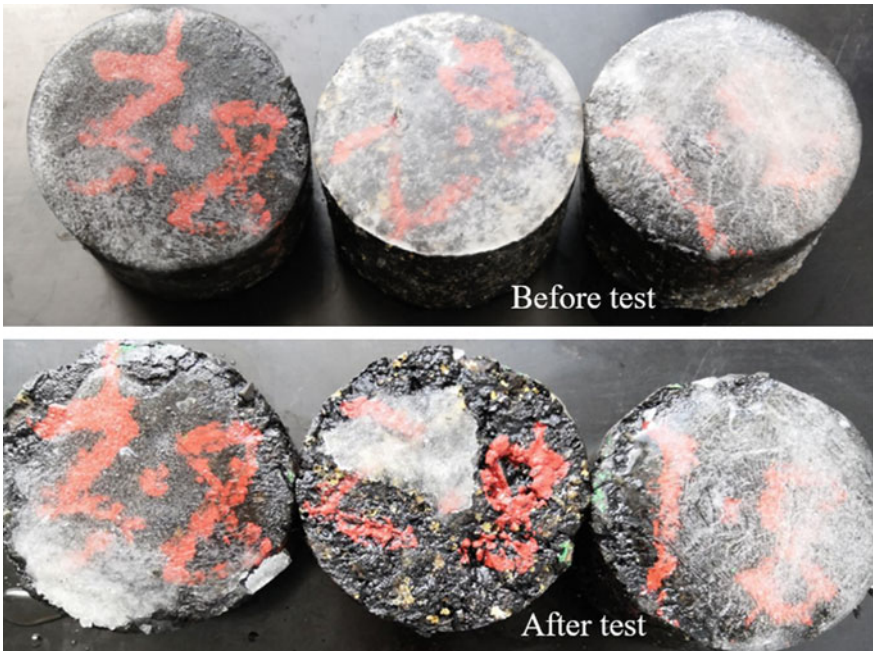

(a) AF-II (b) AF-I (c) Foundation

Fig. 2 Test pieces before and after impact crushing test

Fig. 3 Surface icing of each group of test pieces

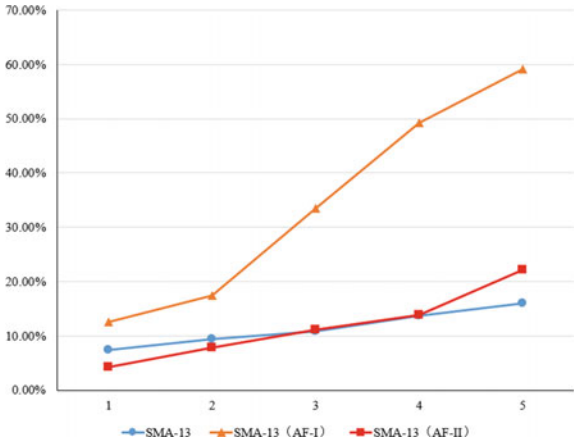

stability of the material with modifier meets the requirements of the specification and design documents that the dynamic stability of asphalt mixture is not less than 3000 times/mm, as given in Table 3.

Table 3 Rutting test data

Test result	Dynamic stability (times/mm)	Requirements (times/mm)
SMA-13 (AF-I)	5676	≥ 3000
SMA-13 (AF-II)	7159	
SMA-13	6631	

Table 4 Results of freeze–thaw splitting test

Test result	TSR	Requirements (times/mm)
SMA-13 (AF-I)	86.6%	> 80%
SMA-13 (AF-II)	89.2%	
SMA-13	87.3%	

It can be seen from the Table 3 that the dynamic stability test results of the three kinds of mixture obviously exceed the specification requirements, and the high temperature stability of the mixture is excellent, in which the mixture with AF-I is lower than that with AF-II. The rutting test shows that the high temperature performance of the mixture will not be affected by the addition of anti-coagulation ice modifier, which can meet the use requirements.

3.3.2 Freeze–Thaw Splitting Test

Marshall test machine was used to carry out freeze–thaw splitting test on Marshall specimens after freeze–thaw treatment. The test results of TSR of freeze–thaw splitting test are given in Table 4.

The test results show that the residual strength ratio of the mixture with anti-coagulation ice modifier meets the specification requirements, and the water stability of the mixture meets the technical requirements.

4 Conclusion

The paper designs two kinds of anti-freezing ice modifier of different specifications and verifies the performance of anti-freezing and pavement. The main conclusions are as follows:

(1) The specifications of the two kinds of anti-freezing modifiers are different. In the design of the ratio, the AF-II should replace some mineral powder and the AF-I should be used for the fine aggregate. After adjustment, the volume index of the mixture can meet the design requirements.

(2) The ice temperature of the mixture without anti-freezing agent is − 0.5 °C, while the ice temperature of the mixture mixed with anti-freezing modifiers is − 5 °C, and the addition of anticoagulant significantly reduces the condensation temperature of water; The falling rate of asphalt mixture with anti-freezing agent increased obviously, and the falling rate of asphalt mixture with AF-I reached 60%.
(3) The high temperature stability and water stability of the anti-freezing pavement can meet the requirements. The addition of the anti-freezing modifier has little influence on the short-term performance of the pavement.

References

1. Wu S, Yang J, Sun X et al (2020) Preparation and characterization of anti-freezing asphalt pavement. Constr Build Mater 236(6):117579
2. Liu H, Jia J, Liu N et al (2019) Influence of the mixing time on the anti-freezing performance of chloride-based asphalt mixtures. Constr Build Mater 213(July 20):637–642
3. Mohsen AE, Ahmad G, Amin R (2017) Effects of deicing and anti-icing materials on resistance of warm mix asphalt
4. Rui C, Hao P (2016) Impact of salt freeze-thaw cycles on low temperature performance of asphalt mixture based on the strain energy density
5. Esfahani MA, Goli A, Rahimipordanjani A (2018) Effects of deicing and anti-icing materials on resistance of warm mix asphalt
6. Wu S, Yang J, Yang R et al (2018) Investigation of microscopic air void structure of anti-freezing asphalt pavement with X-ray CT and MIP. Constr Build Mater 178(July 30):473–483
7. Li S (2018) Experimental study on anti-freezing performance of salt asphalt mixture. Subgrade Eng
8. Cui YN, Chen RP, Han JW et al (2018) Microstructure and low temperature creep properties of SBS modified asphalt and its mixture under salt freezing cycle. Bull Chin Ceram Soc
9. Zhang Z, Luo Y, Zhao F (2018) Review of research on the effect of salt storage deicing material on the preformance of asphalt mixture. Chemical Indus Eng Prog
10. Chang R, Hao P (2017) Impact of salt freeze-thaw cycles on low temperature performance of asphalt mixture based on the strain energy density. DEStech Trans Eng Technol Res
11. Zhengqi Z, Yaofei L, Fuqiang Z (2018) Research progress on the influence of salt storage snow melting and ice suppression materials on asphalt mixture performance. Progr Chem Indus 321(06):267–269
12. Yongjun M, Jiangang S, Xue B (2012) Study on optimal design of anti freezing asphalt concrete. Highway Home Abroad 32(4):256–259

Quality of Life Determination Based on Daily Commuting Experiences in Central Business District (CBD) of Bangkok, Thailand

Pawinee Iamtrakul, Pisinee Visuttiporn, Jirattikan Ammapa, Jirawan Klaylee, Sararad Chayphong, and Yoshitsugu Hayashi

Abstract The evaluation of factors that affect people's pleasure as well as the goodness and well-being of life is known as the study of quality of life. It requires further implication with quantification of these experiences since human beings may interpret context, location, and situational changes through their perception. Thus, this study aims to determine the relationship between socioeconomic profile and the perception of road environment through a statistical and spatial analysis approach. Data was conducted by questionnaire survey of total of 500 sets in Sukhumvit area. Geographic information system (GIS) was applied for visualization through a grid of 500 * 500 m^2 (total of 87 grids) to demonstrate the distribution users' perception of road environment. The results present that only educational levels were associated with wealthy (X_1), lively (X_3), and beautiful (X_4) perceptions. In addition, there was a correlation between marital status and lively (X_3), boring (X_6), and beautiful (X_4) statistically significant at 0.05. Meanwhile, the relationship between grid of study area and perception of the road environment demonstrates that the natural environment and situations in each area are probably consistent with the experience of the road environment perceived by commuters. Finally, the results of this study can be a guideline for the improvements of the CBD of Sukhumvit to strengthen quality of life while traveling of commuters since built environment can improve or impair their quality of life.

Keywords Megacity · Perception · Travel behaviors · Satisfaction · Urban transport

P. Iamtrakul (✉) · P. Visuttiporn · J. Ammapa · J. Klaylee · S. Chayphong
Center of Excellence in Urban Mobility Research and Innovation, Faculty of Architecture and Planning, Thammasat University, Pathum Thani, Thailand
e-mail: pawinee@ap.tu.ac.th

Y. Hayashi
Center for Sustainable Development and Global Smart City, Chubu University, Kasugai 487-8501, Japan

T. Kang (ed.), *Proceedings of 5th International Conference on Civil Engineering and Architecture*, Lecture Notes in Civil Engineering 369,
https://doi.org/10.1007/978-981-99-4049-3_76

1 Introduction

The perspective of people's experience and their interactions with and concerning location is called the sense of place [1]. Sense of place is the way we perceive places like streets, towns, cities, or ecoregions. It reflects our historical and experiential knowledge of a place while improving our ability to create a more sustainable future for that place [2]. Different people might have various definitions of the same city or area while one individual may value a neighborhood's social and ecological qualities, historical, cultural, aesthetic, economic, and other aspects [3]. Without a critical analysis of cities in term of socially built environments that people acquire and create, understanding the sense of place in the urban setting would be insufficient for improving space quality. It can be improved by investigating the feeling of place while considering its function in enhancing the design standard. Thus, it is one of the critical elements in developing harmony between individuals, their surroundings, and their emotional perception [4]. This understanding is affected by the person's intent while entering or leaving one space and entering another. This process is influenced by person's perception and organizational skills for structural space. In order to achieve a sense of perception of the environment, it is necessary to separate the critical aspects and practical elements [5].

Cities' sense of place is influenced by migration, global mobility, and the merging of natural and built environments which also reflects the connections between the economy, environment, politics, culture, and history [6]. The consideration of place in adaptation planning and decision-making is underrepresented [7, 8]. Between architects, designers, and urban planners, there has been an increased focus on the quality of spaces and built environments. Quality of life (QoL) research has gained more attention in several health-related sectors, including medicine, social sciences, health services, and health promotion since the late 1990s. In addition, health, material comforts, personal safety, relationships, learning, and creative expression represent as a key message to help and encourage others, involvement in politics and public life, socializing, and leisure activities. There are a few examples of the many factors in people's lives that make up the concept of quality of life which also has to do with perception.

Thus, this study aims to investigate how the road environment is perceived by categorizing it into 6 groups of wealthy (X_1), safe (X_2), lively (X_3), beautiful (X_4), depressing (X_5), and boring (X_6). Questionnaires based on face-to-face interview were performed for data collection purposes. The study area was the Sukhumvit area which is located in Bangkok and comprises of Wattana District, Khlong Toei District, and Phra Khanong District. Sukhumvit represents as a central business district with various transportation options and good infrastructure and is considered an important economic center. By classifying the six perceptions of the road environment and describing the differences in perceptions across 87 grids, the understanding among the differences in socioeconomic characteristics of commuters can be quantified.

2 Literature Review

A human perception exists a difference in point of view in sensing that senses something is excellent, or a positive perception or bad perceptions influence on human behaviors visible or actual. There are several definitions of perception in the literature, not just one. The word "perception," which denotes "receiving, gathering, the activity of taking possession, and apprehension with the mind or senses," is derived from the Latin words perceptio and percipio [9]. Perception is a person's point of view or viewpoint on an object being observed to comprehend or reach a conclusion about an event or thing which is achieved through exercising one's judgment on items in one's environment by utilizing one's senses. Everyone's perceptions might differ because it all depends on everyone's perception process. The process of perception occurs through the five senses, namely the senses of hearing, sight, taste, touch, and smell. The human brain is a complex system where everything seems connected to everything. Thus, factors that affect perceptions have been studied which specifications of human perception are a range of sensory modalities. Our brain employs a variety of sensory data sources, including information from vision, touch, and hearing, to perceive the exterior environment [9].

The term "sense of place" is frequently used to characterize the distinctness or uniqueness of places and areas [10]. Since the late 1990s, QoL research has received increased interests in various health-related fields, including medicine, social sciences, health services, and health promotion [11]. The study of quality of life is the evaluation of elements that contribute to the goodness and well-being of life and people's happiness. It investigates the interrelationships between these components [12]. However, the quality-of-life concept includes multiple aspects of people's lives, such as health, material comforts, personal safety, relationships, learning, creative expression, and opportunity to help and encourage others, participation in public affairs, socializing, and leisure [13, 14]. It also has to deal with perception, especially regarding feelings or emotions. When the perception of the context, place, and situation changes, human beings can process it through the perception of what they see, touch, hear, and smell, which can positively or negatively affect their quality of life (e.g., safe, lively, boring, depression, etc.) [15].

3 Methodology

This study reviews human perceptions, a component of a person's experience. Furthermore, perception influences the quality of life in good and bad ways [15]. One of them is the environment that can be observed in daily life, such as the environment from traveling, and living. [16, 17]. The research methods of this study are based on statistical analysis to identify the relationship between socioeconomic status and the perception of the travel environment in the Sukhumvit area. The data

was gathered via gathering social, economic, building, and transportation information, as well as collecting 500 sets of questionnaires. The survey is the first source and collects secondary locational based data such as building data, density, land use, and transportation network to set up for further geospatial analysis. Sukhumvit zone has explored the quality of life based on commuting behaviors which include the districts of Khlong Toei, Wattana, and Phra Khanong. The second source is allotted space for storing inquiries. The study area was divided into 500 * 500 m^2 and specifies the number of sets in each grid to collect the questionnaire. In this research, data are based on two parts of the questionnaire, which was used for statistical analysis and its correlation, namely personal data (socioeconomic characteristics), physical characteristics, and perception level of the road environment. The quality of life was determined and categorized into 6 indicators which the relevant assessment indicators were divided into positive and negative terms. Positive indicators include wealthy (X_1), safe (X_2), lively (X_3), and beautiful (X_4). Negative indicators are depression (X_5) and boring (X_6).

The third source of data for analysis is the process of statistical analysis including frequencies distribution, descriptive analysis with crosstabulation, and spatial analysis. Convert the results of statistical analysis into spatial analysis with six indicators which are used to visualize and demonstrate the perception of the road environment in map with mean, maximum, and minimum perception values in each aspect. It begins with a grid analysis to split the average of each area into a 500 * 500 m^2 which will be presented in the blue-red range of color for illustration. The geographical map can help to demonstrate the average perception of each aspect. The results of the spatial study were then utilized to build a 3D model that simulate how the average value of road environment would appear among different dimensions as shown in Fig. 1.

4 Result of Analysis

The results were reported with descriptive statistics, including percentage, mean, standard deviation, and frequencies. The characteristics of the respondents from a total of 500 sets were primarily male (53.6%) with a bachelor's degree (60.2%), income level (average per month, baht) is 10,001–25,000 baht (44.2%), single status (55.6%) among 3 districts of Sukhumvit area. The highest average perception of road environment were wealthy ($\overline{X}_1 = 2.54$; SD = 1.21), safe ($\overline{X}_2 = 2.44$; SD = 1.21), lively ($\overline{X}_3 = 2.46$; SD = 1.19), beautiful ($\overline{X}_4 = 2.26$; SD = 1.18), depressing ($\overline{X}_5 = 2.20$; SD = 1.21) and boring ($\overline{X}_6 = 2.32$; SD = 1.21), respectively.

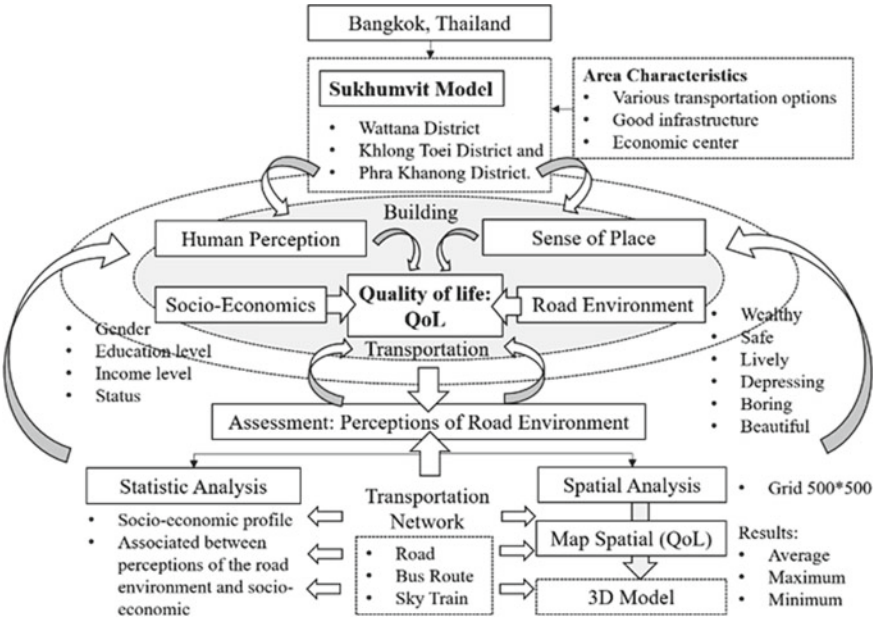

Fig. 1 Framework of study

4.1 Socioeconomic Crosstabulation with Six Perceptions of Road Environment

When considering socioeconomic characteristics of crosstabulation with the average perception of the road environment (Table 1), in positive factors, the highest perception level has belonged to wealthy (X_1) aspect. It can be classified characteristics of socioeconomic as female, with a bachelor's degree, income level (average per month, baht) was between 40,001 and 55,000 baht. In terms of safe (X_2) aspect, the highest perception level was female, with a diploma, income was between 40,001 and 55,000 baht. In terms of lively (X_3) aspect, the highest perception level was other genders with a diploma and their income level was more than 55,000. In terms of beautiful (X_4) aspects, the highest perception level was female with high school and their income level was between 40,001 and 55,000 baht. In negative factors, the highest perception level in depressing (X_5) aspect was other genders with a bachelor's degree and income level was 25,001–40,000 baht. Finally, the highest perception level in the boring (X_6) aspect was other genders with a diploma, and income level was between 40,001 and 55,000 baht. Remarkably, all of them were single status.

In addition, the lowest level of perception, in positive factors, in wealthy (X_1) aspect can be classified characteristics of socioeconomic as male with lower than junior high school and their income level (average per month, baht) was less than 10,000 baht and married. Regarding safe (X_2) aspects, the lowest level was other

Table 1 The perceptions of the road environment indicators and socioeconomic profile

Variables	Perceptions of the road environment (%)																	
	Positive factors												Negative factors					
	Wealthy (X_1)			Safe (X_2)			Lively (X_3)			Beautiful (X_4)			Depressing (X_5)			Boring (X_6)		
	1	2	3	1	2	3	1	2	3	1	2	3	1	2	3	1	2	3
Gender																		
Male	18.4	20.4	14.8	18.0	19.8	15.8	13.6	21.6	18.4	21.0	18.2	14.4	18.4	20.4	14.8	18.0	19.8	15.8
Female	12.8	17.8	12.6	12.6	16.6	14.0	9.2	18.6	15.4	14.6	15.2	13.4	12.8	17.8	12.6	12.6	16.6	14.0
Others	0.4	1.2	1.6	0.4	1.0	1.8	0.4	1.6	1.2	1.0	1.4	0.8	0.4	1.2	1.6	0.4	1.0	1.8
Sig	0.321			0.174			0.691			0.680			0.225			0.177		
Education level																		
Lower than junior high school	2.0	0.8	0.8	2.0	1.0	0.6	1.8	1.4	0.4	2.4	0.6	0.6	1.8	1.2	0.6	2.2	1.0	0.4
High School	2.8	5.6	4.0	3.2	5.0	4.2	4.0	3.8	4.6	3.8	4.6	4.0	4.4	5.2	2.8	3.4	6.0	3.0
Diploma	3.2	6.2	6.0	3.2	6.6	5.6	3.4	6.2	5.8	4.2	7.4	3.8	4.2	7.4	3.8	4.6	5.2	5.6
Bachelor's degree	11.8	23.2	25.2	15.4	21.8	23.0	12.2	26.2	21.8	22.6	19.0	18.6	18.0	22.4	19.8	18.0	22.4	19.8

(continued)

Table 1 (continued)

Variables	Perceptions of the road environment (%)																	
	Positive factors												Negative factors					
	Wealthy (X_1)			Safe (X_2)			Lively (X_3)			Beautiful (X_4)			Depressing (X_5)			Boring (X_6)		
	1	2	3	1	2	3	1	2	3	1	2	3	1	2	3	1	2	3
Postgraduate	2.8	3.2	2.4	2.6	3.8	2.0	1.8	4.2	2.4	3.6	3.2	1.6	3.2	3.2	2.0	2.8	2.8	2.8
Sig	0.022*			0.108			0.049*			0.024*			0.271			0.116		
Income level (Average per month per person, baht)																		
Less than 10,000	2.2	2.6	2.8	2.8	3.2	1.6	3.0	2.0	2.6	2.8	2.6	2.2	2.6	2.8	2.2	2.6	3.0	2.0
10,001–25,000	10.2	18.6	15.4	13.2	15.8	15.2	10.4	17.6	16.2	17.0	15.6	11.6	14.4	19.8	10.0	13.4	16.4	14.4
25,001–40,000	7.2	11.6	11.8	6.8	12.2	11.6	7.4	13.8	9.4	12.0	10.4	8.2	9.0	10.4	11.2	9.6	11.6	9.4
40,001–55,000	1.6	4.0	6.2	2.2	4.8	4.8	1.8	5.6	4.4	2.4	4.8	4.6	3.2	5.0	3.6	3.0	4.8	4.0
More than 55,000	1.4	2.2	2.2	1.4	2.2	2.2	0.6	2.8	2.4	2.4	1.4	2.0	2.4	1.4	2.0	2.4	1.6	1.8
Sig	0.437			0.363			0.111			0.287			0.119			0.915		
Marital status																		
Single	12.0	22.2	22.4	14.3	22.0	20.4	13.2	22.8	20.6	19.1	20.8	16.7	16.3	22.2	18.1	15.9	20.0	20.8
Married	8.8	15.7	13.0	10.6	13.8	13.0	9.0	16.3	12.2	15.9	11.2	10.4	13.2	14.7	9.6	13.0	15.9	8.6
Divorce	1.8	1.6	2.4	1.8	2.4	1.6	1.0	3.5	1.4	2.2	2.9	0.8	2.2	2.4	1.2	2.4	1.6	1.8
Sig	0.320			0.777			0.050*			0.016*			0.596			0.024*		

Remark Level of significance is 0.05; Level of satisfaction is demonstrated by 1 = Low, 2 = Medium, and 3 = High

genders, with lower than junior high school, their income level was less than 10,000 baht and divorce.

In terms of lively (X_3) aspect, the lowest perception level was male, with lower than junior high school, their income level was less than 10,000 baht and divorce. In terms of beautiful (X_4) aspects, the lowest perception level was male with lower than junior high school, their income level was 10,001–25,000 baht and 25,001–40,000 baht and divorce. In negative factors, the lowest perception level in depressing (X_5) aspect was male, with lower than junior high school, their income level was 10,001–25,000 baht and divorce. Finally, the lowest perception level in the boring (X_6) aspect was male, with lower than junior high school, their income level was less than 10,000 baht and married.

4.2 Sukhumvit District Classify into 3 County Crosstabulation with Six Perceptions of Road Environment

The results can be represented in a boxplot graph among six perceptions of the road environment compared with 3 subdistricts which comprise of Khlong Toei, Phra Khanong, and Wattana in Sukhumvit district. Figure 2 can describe that in positive factors, the highest perceived aspect was wealthy (X_1) in Phra Khanong, and the lowest was beautiful (X_4) in Wattana. For negative factors, the highest perceived aspect was boring (X_6) in Phra Khanong, and the lowest was depressing (X_5) in Wattana. In addition, when considering area by grids, the level of perception was visualization shown by 3D Model as depicted in Figs. 3 and 4.

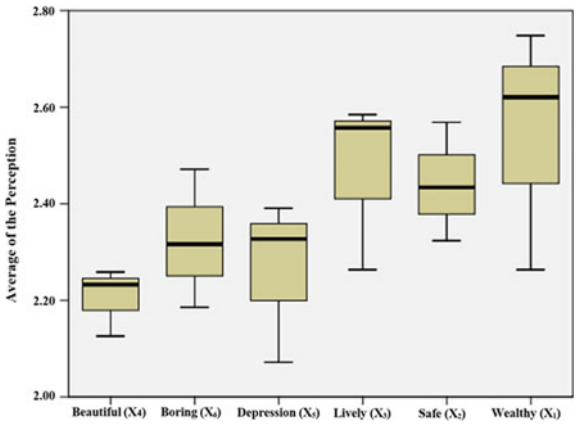

Fig. 2 The average value of six perceptions indicators of road environment

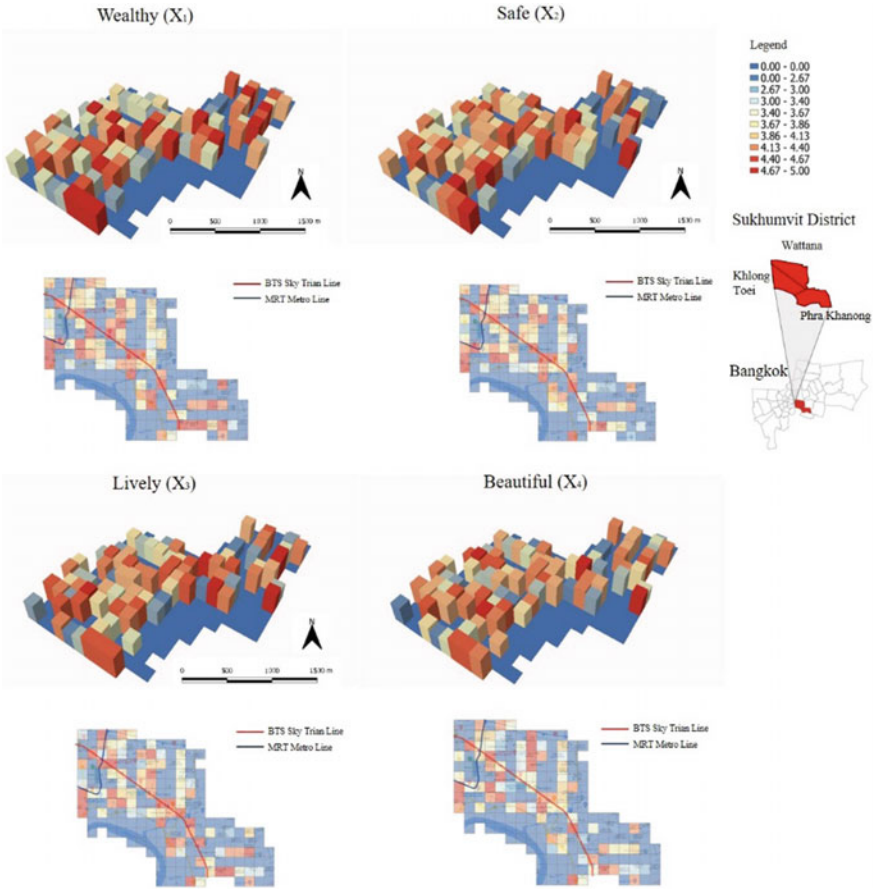

Fig. 3 The average values of positive perception indicators of road environment

5 Discussion

The result found that the highest average level among different perception of road environment in positive factors includes wealthy (X_1), safe (X_2), lively (X_3), and beautiful (X_4) and in negative factors represents boring (X_5) and depressing (X_6), respectively. When classifying Sukhumvit district into 3 subdistricts with six perceptions of the road environment, the result demonstrates that in positive factors, the highest perceived aspect was wealthy (X_1) in Phra Khanong and the lowest was beautiful(X_4) in Wattana.

For negative factors, the highest perceived aspect was boring (X_6) in Phra Khanong and the lowest was depressing (X_5) in Wattana. In addition, the six perceptions of road environments can be compared in terms of spatial analysis. It was found that the highest average in the wealthy (X_1) aspect is located close to On Nut Station

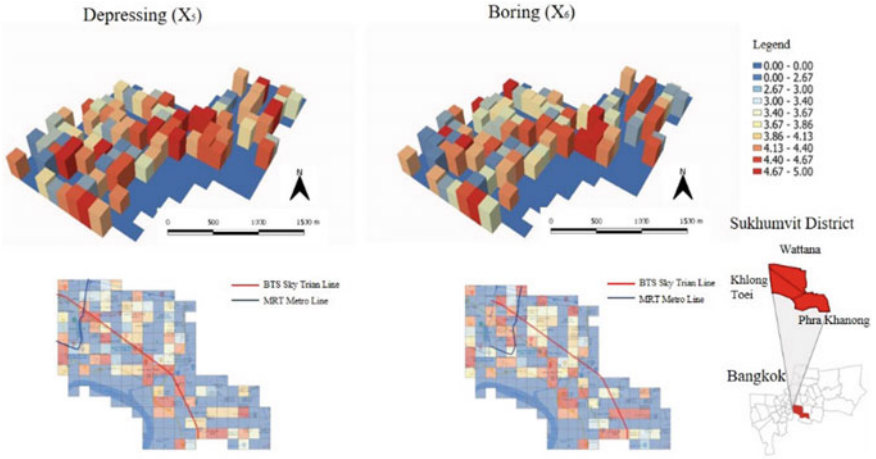

Fig. 4 The average values of negative perception indicators of road environment

of the BTS Green Line; the important places are Phra Khanong District Office. The lowest average in the wealthy (X_1) aspect is located at Samitivej Hospital which is the proximity location of a small community mall, shops, and restaurants. However, the road section has only two traffic lanes, thus the area presents the lowest wealthy (X_1) aspect. In terms of safe (X_2) aspect, it was found that the highest average was located under Chalerm Maha Nakhon expressway, and the lowest level of perception in safety was located close to Udom Suk Station of the BTS Green line. Probably because the area is a very private alley which results to feel insecure during the journey. For the lively (X_3) aspect, the highest average was located covering the area along the canal that has been repainted for a better look and lively to commuters' feelings. The lowest score was located under an expressway coupled with only two traffic lanes which are impossible to create a sense of the vibrancy of the road environment.

In terms of depressing, the highest average in depressing (X_5) aspect was located mostly in the middle of the city center, such as the Asoke intersection, close to Asoke Station and Sukhumvit Station which is the area where a wide variety of commuters. This can lead to congestion in large numbers of people, which makes the environment in this area feel most stressful or depressing during traveling. The lowest level of perception of safety was located near the temple and covered the private alley. In terms of boring, the highest average in boring (X_6) aspects is located in the same area as the highest average in wealthy (X_1) aspects. This is due to the roads being suitable for traveling, but also make commuters feel bored while traveling. The lowest was located at Nana station of the BTS Green Line which represents the location of an important community mall such as Korean town that can attract traveler and create a new impression and experience. Finally, the highest average in the beautiful (X_4) aspect was located in the same highest perceived level of travel suitability. In the wealthy (X_1) aspect, it shows that the area makes people feel beautiful and pleasant.

The lowest value was at the area that covered the private alley for residences, thus it makes the perception of beauty and pleasure at the lowest level.

6 Conclusion

This study aims to identify the relationship between socioeconomic profile and the perception of road environment through a statistical analysis and applied Geographic information system (GIS) for visualization. Sukhumvit area was selected as case study by conducting questionnaire survey of 500 sets. The study divides the perception of road environment into six groups which consist of wealthy (X_1), safe (X_2), lively (X_3), beautiful (X_4), depressing (X_5), and boring (X_6) in order to understand the perception and describe the differences in perceptions. The results demonstrated that Sukhumvit presents an area with a variety of transportation options and infrastructures which represents as an important economic center. When considering the correlations between socioeconomic characteristics and the perception of road environments, only educational levels were found to be associated with wealthy (X_1), lively (X_3), and beautiful (X_4) perceptions. It was found a correlation between marital status and lively (X_3), boring (X_6), and beautiful (X_4) statistically significant at the 0.05 level. The results of this study can be helpful for improvements of Sukhumvit area, particularly at the area of low perception level of wealthy (X_1), safe (X_2), lively (X_3), and beautiful (X_4) aspects. Policy improvements and legislation to strengthen safety provision must be recommended in areas with little awareness of the safety environment to reduce the atmosphere in high depressing and boring areas toward an improvement of the traffic congestion and its surrounding environment.

Acknowledgements The authors gratefully acknowledge the financial support provided by the Science and Technology Research Partnership for Sustainable Development (SATREPS), Project of The Japan Science and Technology Agency (JST), and The Japan International Cooperation Agency (JICA) "Smart transport strategy for Thailand 4.0 realizing the better quality of life and low-carbon society" (Chair: Prof. Yoshitsugu Hayashi, Chubu University, Japan) under Grant JPMJSA1704. It is conducted under the Faculty of Architecture and Planning Research Fund, Thammasat University, contract no. TDS 10/2021, and partially supported by Center of Excellence in Urban Mobility Research and Innovation (UMRI), Faculty of Architecture and Planning, Thammasat University, Pathum Thani, Thailand.

References

1. Adams JD (2013) Theorizing a sense of place in transnational community. Child Youth Environ 23(3):43–65. https://doi.org/10.7721/chilyoutenvi.23.3.0043
2. Iamtrakul P, Teknomo K, Hokao K (2007) A recreational valuation of public preference on park users' willingness to pay. Lowland Technol Inter 9(1):41–49
3. Iamtrakul P, Teknomo K, Hokao K (2015) Interaction between recreation activity and public preference: a case study on public parks in Saga city, Japan. Lowland Technol Int 7(2):45–57

4. Rapoport A (1969) House form and culture, 1st edn. Prentice-Hall, Englewood Cliffs, NJ
5. Ghaffari A (1993) The fundamentals of the design of consecutive space in urban architecture. Soffeh, Architectural Sci Res 6-7-8
6. Iamtrakul P, Klaylee J (2022) Measuring commuters' behavior and preference towards sustainable mobility: case study of suburban context of Pathum Thani, Thailand. In: 4th International conference on renewable energy and environment engineering on IOP conference series: earth and environmental science, vol 897, no 1, pp 012023. IOP Publishing
7. Agyeman J, Devine-Wright P, Prange J (2009) Close to the edge, down by the river? Joining up managed retreat and place attachment in a climate changed world. Environ Plan A 41(3):509–513. https://doi.org/10.1068/a41301
8. Adger WN, Barnett J, Chapin FS III, Ellemor H (2011) This must be the place: underrepresentation of identity and meaning in climate change decision-making. Global Environ Polit 11(2):1–25. https://doi.org/10.1162/GLEP_a_00051
9. Velik R, Bruckner D, Lang R, Deutsch T (2010) Emulating the perceptual system of the brain for the purpose of sensor fusion. In: Human-computer systems interaction, vol 60, pp 17–27. Springer-Verlag, Berlin-Heidelberg
10. Foote KE, Azaryahu M (2009) Sense of place. Int Encycl Human Geogr 2009:96–100. https://doi.org/10.1016/B978-008044910-4.00998-6
11. Noyez L (2013) Quality of life research, it's only the beginning. Neth Heart J 21(1):19–20. https://doi.org/10.1007/s12471-012-0360-0
12. Bidmeshki EA, Heidari M, Azar IA, Forghani F, Basirani N (2008) Multiple roles and women's quality of life: in Iran (Zabol). Iran J Psychiatry 3(3):93–99
13. Iamtrakul P, Chayphong S, Klaylee J (2019) The study on age-friendly environments for an improvement of quality of life for elderly, Asian Mega city, Thailand. Lowland Technol. Int 21(2):123–133
14. Iamtrakul P, Klaylee J, Ruengratanaumporn I (2021) Participatory planning approach towards smart sustainable city development. Proc Int Struct Eng Constr 8(1):1–6. https://doi.org/10.14455/ISEC.2021.8(1).SUS-11
15. Iamtrakul P, Chayphong S (2021) The perception of Pathumthani residents toward its environmental quality, suburban area of Thailand. Geogr Pannonica 25(2):136–148. https://doi.org/10.5937/gp25-30436
16. Ammapa J, Visuttiporn P, Klaylee J, Chayphong S, Iamtrakul P (2022) Using GIS-based spatial analysis: comparing pattern of urbanization and transportation networks. In: 10th International conference on traffic and logistic engineering (ICTLE), pp 17–21. https://doi.org/10.1109/ICTLE55577.2022.9902095
17. Iamtrakul P, Zhang J (2014) Measuring pedestrians' satisfaction of urban environment under transit oriented development (TOD): a case study of Bangkok Metropolitan, Thailand. Lowland Technol Int 16(2):125–134

Construction Project Management and Facility Planning

Value Engineering of Precast Slab to Ease Construction Project Schedule and Cost

Jhun M. Jacinto, Ernie D. Tombado, Henry C. Tan II, and Orlean G. Dela Cruz

Abstract The assembly and erection of structures are a part of building construction. With the typical construction approach, there are numerous issues and challenges. First, conventional construction is a linear process requiring each stage to finish before the next can start. As a result, time is wasted and not utilized effectively. The construction process can also be adversely affected by labor and the weather. Adopting Value Engineering (VE) principles encourages individuals to work more effectively in teams while continuously seeking to enhance their production and service systems. Any firm can examine and optimize its resources with cost optimization. The force field analysis technique of VE is used in this paper to evaluate and resolve some of the force factors that affect the construction delays and possible solutions to shorten the construction project by applying a precast slab structure. Using precast slabs on construction is time efficient, requires less construction time, and is more cost-effective than the traditional cast-in-place approach. Force Field Analysis (FFA) proves that strengthening the forces that resist change can contribute to improving and reducing construction costs and schedules.

E. D. Tombado · H. C. Tan II · O. G. Dela Cruz (✉)
Graduate School, Polytechnic University of the Philippines, Sta. Mesa, Philippines
e-mail: ogdelacruz@pup.edu.ph

E. D. Tombado
e-mail: tombado.ernie@gmail.com

H. C. Tan II
e-mail: henrycruztan1997@gmail.com

J. M. Jacinto (✉)
Engineering Department, Aurora State College of Technology, Baler, Aurora, Philippines
e-mail: jhun.jacinto05@gmail.com

E. D. Tombado
Laguna Lake Development Authority, Quezon City, Philippines

H. C. Tan II
PJ Lhuillier, Incorporated, Quezon City, Philippines

T. Kang (ed.), *Proceedings of 5th International Conference on Civil Engineering and Architecture*, Lecture Notes in Civil Engineering 369,
https://doi.org/10.1007/978-981-99-4049-3_77

Keywords Precast slab · Construction project schedule · Construction project cost · Value engineering · Force field analysis

1 Introduction

The construction of buildings has both beneficial and harmful consequences. The adverse effects of conventional construction include significant energy consumption (up to 40% of total global energy production), use of 12% of the entire global clean water supply, and spending 30% of global resources on the construction phase [1]. The traditional in-situ method used in the construction business is one of the things that has caused the quality of the environment to decline. Construction trash and debris harm the environment by releasing airborne dust particles, clogging drainage systems with soil waste, and disposing waste material [2]. Often concrete slab's formwork is created to provide adequate support for new concrete before it can support itself. Sheathings, joists, stringers, and shores are typically employed as part of the formwork for concrete slabs, utilizing plywood sheets as sheathing, and joists, stringers, and beaches serve as beams and columns [3]. This process of sheathings, joists, stringers, and shores takes much time to finish and needs to be done orderly. Time and cost significantly affect how successfully a building project is completed [4]. According to many experts and developers, the precast concrete technique is one of the most excellent solutions for all these challenges. The "in-situ cast concrete" method and the "precast" approach are the two most popular and traditional methods for casting concrete. In contrast to standard construction technology, it is unique. One of the most popular varieties of composite concrete elements is the precast slabs, a layer of precast concrete that acts as a form or skeleton for a cast-in-place concrete slab [5]. Precast structures are an example of applied advanced construction technology in which concrete construction components are cast in a reusable mold to achieve the desired shape, strength, and cross-section before being cured in a factory under controlled conditions to ensure the highest quality [4]. Off-site building techniques are considered more environmentally friendly and sustainable for conducting business in the construction sector because they result in less material waste, reduce site activities, and shorten construction times [1]. The advantages of composite floors made and concrete slabs are widely known. Still, there is a lack of knowledge regarding these floors' ultimate capacity and flexibility and the behaviour of shear connectors attached to thin-walled components [6]. Prefabricated prefinished volumetric construction (PPVC) would give the industry the much-needed push to embrace productivity in its design and construction process. Besides, precast construction now assumes a more defined and crucial position in our relentless drive for higher productivity [7]. These strategies include prolonging the usable lives of existing structures and creating new ones that are adaptable and easy to disassemble (enabling materials and components to be reused); or substituting building materials and components with those from low-carbon supply chains [8]. It considerably shortens the time a building takes to build and improves the quality and productivity

of the work [9]. It is crucial to find the best solution for the structural system of the building to facilitate quicker and easier construction activities with a smaller amount of construction material while maintaining a satisfactory level of building safety and performance. Moreover, it will maximize return on investments while improving the quality of midrise building construction [10].

2 Review of Related Literature

2.1 The Types of Precast to Ease Construction

Implementing precast construction is quick, simple, and can save a lot of time and labor. Therefore, adopting that structure is heavily favored in most developed nations [4]. In arrangements made of reinforced concrete, a solid slab is a typical slab supported by beams and columns, with the weight distributed to those components. Since slab thicknesses are neglected compared to the other two dimensions, slabs that transmit both vertical load and horizontal load, such as earthquakes, to the vertical bearing elements of the structure are typically considered two-dimensional [11]. For building floors, engineers have a variety of options. The price of the slabs for any building project will naturally vary depending on the various slab construction types.

2.2 Waffle Precast Slab

A reinforced concrete slab with evenly spaced ribs running parallel to the sides that resembles a waffle from below is known as a waffle slab. A waffle slab's bottom has a shape resembling a waffle, but its top is typically smooth, like a conventional building surface. Due to the pockets' ability to trap heat, it aids in floor insulation [12]. Its primary purpose is to handle heavier loads and greater distances than flat floors because these systems are lighter and can be used for both the floor and the roof. Furthermore, waffle slabs are suitable for bridge construction. When a broader span in a building needs covering with the fewest number of columns possible, the waffle slab is a great solution [13]—also used when the beams' depth is restricted to achieve a precise height. In addition to producing a lighter and more affordable building, adopting a waffle slab system has significant advantages over solid slab systems in terms of creating a safer structure with increased seismic performance in seismic design scenarios [10]. The use of approximate analytical techniques in the design and the provision of insufficient reinforcements at the slab sections, while the ribs were occasionally inadequately strengthened, were the causes of the failures seen in the precast waffle slabs [14].

2.3 Hollow-Core Slab

The most popular precast flooring system is a hollow-core slab, a precast prestressed concrete element primarily used for floor, roof, and wall panels. Because of its utilization, buildings can now feature complex floor plans on the top levels and clear, column- and beam-free spaces on the lower floors. The panels are made to support enormous loads [15] due to its design's high level of efficiency and adaptability, as well as the site's ease of implementation and control. Hollow-core slabs are highly developed structural components employed worldwide because of their numerous benefits and extensive uses. It can be utilized with various supporting structures, including prefabricated beams, on-site concrete cast structures, steel structures, brick or concrete walls, and concrete or steel walls. Overall, the tests on prestressed hollow-core slabs demonstrated their high load capacity, resilience to cracking, and stiffness during bending [15]. In addition, less concrete in the neutral zone of the slab is being replaced by holes or voids made in hollow precast floors, reducing the dead weight and increasing the slab's efficiency. These also provide a considerable benefit over traditional solid slabs in terms of reduced material usage (concrete and reinforcement), reduced cost, improved structural efficiency, shortened building time, and innovative technology [16]. A slab is one of the main structural parts. Based on the previous studies, results show that the precast slab construction time is significantly quicker than the cast-in-situ slab since the cast-in-situ slab took around 31 working days and 43 total days, including holidays, while the precast slab only needed about nine working days and 13 entire days [4].

2.4 Solid Precast Slab

Lightweight hollow-core slabs are generally more expensive than solid slabs. In reinforced concrete structures, beams and columns typically support a solid precast slab where the load is transferred. These systems can be either two-way or one-way spanning. Solid slab systems are known to impact the outcomes of modal analyses due to their high diaphragm rigidity, demand for lateral resistance, and translational stiffness [11]. Precast slabs can be reused once, twice, or three times in place of in-situ concrete, saving roughly 43.93%, 64.01%, and 70.70% of the cost, respectively [17]. The results revealed that solid specimens shatter more frequently and have excellent energy absorption rates and ultimate load capabilities [18]. The main benefits of using precast concrete in construction include the potential for increased construction speed, high-quality precast units, improved durability, a decrease in labor requirements on the construction site, and the need for formwork, but perhaps most significantly, social and environmental benefits [19]. Additionally, precast concrete slabs can considerably decrease operation time compared to cast-in-situ concrete [17].

The methods used to manufacture and construct a building's structural components vary widely. Currently, the two basic concrete construction techniques are cast-in-place and precast concrete. Since the early 1960s, precast concrete has been increasingly popular as an alternative to conventional cast-in-place construction techniques [20]. Construction tasks like mixing, laying, and curing are frequently necessary for cast-in-place concrete construction. Along with lengthening the project's timeline, these actions also raise the project's cost by requiring more formwork material, on-site labor, and waste materials during construction. Waffle precast slabs, hollow-core precast concrete panels, and solid precast concrete slabs are a few examples of precast concrete products that are gaining popularity. Precast construction is becoming more popular because it speeds up construction, lowers unit costs, and produces less waste. Using the cast-in-situ approach is less advantageous today, where quality is more crucial in a short amount of time. Precast concrete is a novel way of concreting to get around the problems with the cast-in-situ concreting method and comply with modern standards [21].

2.5 Cost and Time Savings for Precast Construction

A project's timely, affordable, and accurate completion ensures effective project management. The primary indicators for analysing construction projects' general effectiveness are time, cost, quality target, and involvement satisfaction. Precast concrete offers durability and flexibility at a low price. Precast systems also require minimal maintenance [22]. "Prefabrication system of construction" refers to the division of a complete dwelling unit into distinct prefabricated or built-in panels. Known also for standard proportions in a factory part, such as the floors, walls, columns, beams, and roofs. The construction industry has maintained and guaranteed the quality of its work using controlled prefabrication and streamlined installations, resulting in products with a high degree of aesthetic excellence. Using standardized components and reducing on-site labor results in less construction waste, which results in a cleaner job site [23]. Precast panels can support structural building loads, which minimizes the need for additional structural elements and lowers overall costs. Proper time management for the construction project is crucial to reduce the risk of delayed completion [24]. Project completion on schedule, within budget, and following specifications is ensured by effective project management. Precast concrete technology can reduce material waste, frequently occurs with conventional concrete technology.

Consequently, it is a sustainable and environmentally acceptable construction technique [25] through factory-controlled mass production procedures, a high level of material and craft quality, and a significant increase in labor efficiency [26]. Because electrical piping is already installed in precast walls and slabs, precast construction finishes faster than cast-in-situ construction [22]. Precast panel manufacturing efficiency saves the end-user money and time.

2.6 Benefits of Precast Slab

The quality of precast concrete is guaranteed to be consistently good when used in a project because of how created the material is. The construction process has many components, and the fact that it is long term raises the risk factor. VE principles and techniques aim to provide the best value from a whole-life perspective during the project development [27]. Precast technique productivity variation is minimal, suggesting that its production values are more stable over time [22]. Precast concrete technology is also widely used because it decreases material waste, frequently occurs with conventional concrete technology, making it an environmentally friendly and sustainable building technique [28]. Through factory-controlled mass production procedures, significant labor efficiency can be attained, and high standards of material and craftsmanship can also be realized [26]. As precast construction is produced in large quantities, the labor costs, steel wastage, concrete waste, and finishing item costs are lower than for cast-in-place projects of comparable size [22]. Even when the initial formwork cost for a more effective cross-section might be higher than it is for a standard cross-section, by repeatedly using the formwork during mass production, the formwork cost per unit produced would be negligible in comparison to the cumulative material quantity savings in the precast element [29]. Utilizing precast slabs can considerably improve the performance of the sustainable building by reducing obsolescence [17].

2.7 Force Field Analysis in Construction Project Scheduling

VE is a powerful tool for enhancing engineering design, examining and evaluating the function of design aspects, lowering costs, and increasing efficiency to get the best value. The VE methodology is used for almost any construction project because of its generic nature [30]. The goal of VE is to efficiently identify unnecessary costs that do not give quality, use, life, aesthetic, or customer features [31]. A complete cost–benefit analysis for the design is necessary to assist the owner in obtaining helpful information to help them make decisions [32]. Saving money while delivering better value is a winning combination. Value engineering aims to get the best value for money [33]. Integrating VE and sustainability principles aims to solve difficulties in the sustainable process while lowering the cost of sustainability at the design stage. Achieving significant gains in energy utilization for a small additional cost through cost analysis, a wide range of technologies, and design solutions. Furthermore, to find effective quality control, scheduling, planning, and design procedures [33]. Depending on how precise the decisions must be, evaluation methods include: (1) quantitative evaluation methods that rely on precise digital evaluation to achieve high degrees of accuracy and (2) qualitative evaluation methods that rely on subjective experiences before applying numerical evaluations to achieve lower degrees of accuracy [14].

3 Value Engineering Technique and Methodology

Force field analysis is one of the many value engineering techniques focusing on the problem and trying to resolve or provide a particular decision to achieve the desired outcome. This analysis achieved the desired results by using the forces already present in the problem or situation. Two forces were involved in this study the driving forces to change and the forces that resist the change. These forces are already present in the problem or situation. With the force field analysis, it will develop a certain amount of discipline to stop and explain what is seen. Those three words—already what is there—are crucial in fixing the issue. However, those two forces are in an unbalanced state, and to remove this need is either strengthening the forces for change or weakening the forces resisting change. Many forces can be attributed to the precast slab to ease the construction project schedule; however, the researcher will limit the two to five attributes to simplify the study. The state of the art of this research is that this research is based on the different qualitative research studies of precast slabs in easing the construction project schedule and cost [22]. Furthermore, the VE technique used in this study suggested the forces or problems already given and needed resolution for decision-making in using the precast slab in the construction of the building or other structures. The detailed methodology is shown in Fig. 1.

4 Results and Discussions

The fundamental tenet of the force field analysis is that a particular system only persists as it does because of opposing forces that balance one another out or because forces that promote and resist change are in an equilibrium condition. Driving forces are often advantageous, rational, conscious, reasonable, and economical; they also foster advancement. Resisting forces typically limit development and change and are unfavorable, illogical, unconscious, emotional, social, or psychological. Either the driving forces will need to be boosted, or the opposing forces will be reduced to encourage change. The influence of each force will be assessed using a numerical scale, with five being the strongest and one being the weakest. The scores are subjectively assigned based on how each force affects the change initiative.

4.1 Driving Force

The completion of the construction building project is significantly influenced by time and cost. Fewer trade subcontractors are required on-site, resulting in a better work sequence and a less congested construction site during the busiest times of the project. A smaller workforce also translates to less idle time (workers waiting for Alimak, etc.) and less weather-related downtime. Precast concrete slabs are a

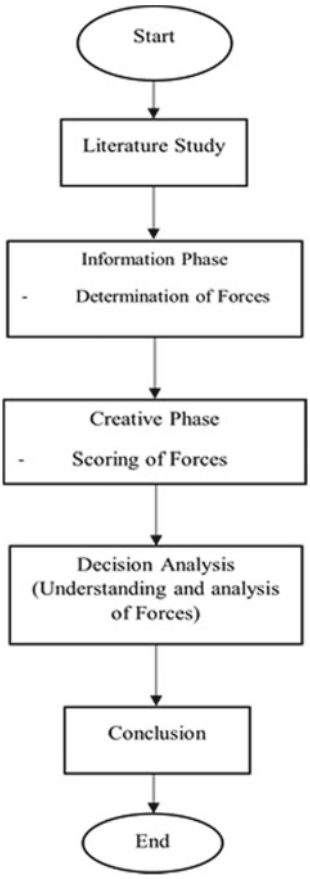

Fig. 1 Research Methodology

viable substitute that can be used for many projects and is affordable and adaptable. Some precast construction methods reduce or eliminate the expense of scaffolding, which accounts for the most significant portion of the cost of building a slab [7]. As a result, the project was completed more quickly; it costs 18% more than it would have if the conventional cast-in-situ process had been used to construct it. In addition, fabrication or production in a controlled setting ensures proper oversight, consistent quality, and the ability to carry out quick corrections. Precast construction uses 20% less concrete, 30% less steel, 50% less labor, and 50% less waste during construction than conventional cast-in-situ construction [2].

4.2 Resisting Force

Precast constructions also have significant drawbacks compared to the conventional approach, such as extra care for connection, challenging transportation, high cost, and storage on the construction site. When more components are employed in the composition, casting or assembly of the composite structure becomes more difficult. The more distinct modules there are, the more expensive each one becomes because each requires a unique mold. Molds are not likely recycled and used for a different project once utilized. Additionally, the increased variety of modules will necessitate more on-site installation work (grouting, jointing, etc.). The panels will be transported on a per-trip basis, and depending on the size of the panels, the truck can only load a certain number of panels at once. Public roadways are subject to Land Transport Authority (LTA) limitations [38].

Additionally, hoisting requires a tower crane with a higher capacity. The 30-tonne tower crane is far more expensive to buy and rent than a tower crane with a representative capacity, and contractors face additional challenges due to the equipment's limited availability. Finally, stakeholders noted that water tightness and leakage are significant concerns with precast concrete despite the enhanced and higher-quality craftsmanship. According to a Construction Industry Development Board (CIDB) study conducted in August 2010, leakage problems in precast concrete structures occur at a higher rate than other defects, with an incidence rate of 11.2% compared to 1.9–3.7% [39]. Suppose a water leak is not correctly fixed; in this case, it will result in excessive defects, including pipe corrosion, concrete spoilage, and steel reinforcement corrosion, which can compromise the structural integrity of concrete buildings.

4.3 Analysis of Forces

The study conducted analyzed precast slabs to ease construction schedule and cost. However, it is also essential that the forces mentioned will be evaluated for their significance. Reducing the overall project cost can lie in cutting construction expenditures during the planning phase. Changing materials or processes is sometimes the best approach to reduce costs in construction. Inadequate planning, poor communication, and simple mistakes that waste labor hours and supplies are just a few of the many things that can cause a construction project to take longer.

Figure 2 below explains the importance of the forces that drives and resists the implementation of the precast slab in the construction project to ease the schedule and cost. As presented in the figure, forces of vital importance, such as structural design issues, are nearly impossible to change. Hence, these forces can neither be weakened nor be strengthened; however, some forces are related to construction management issues that can be supported. When approaching a situation with synergy, it views

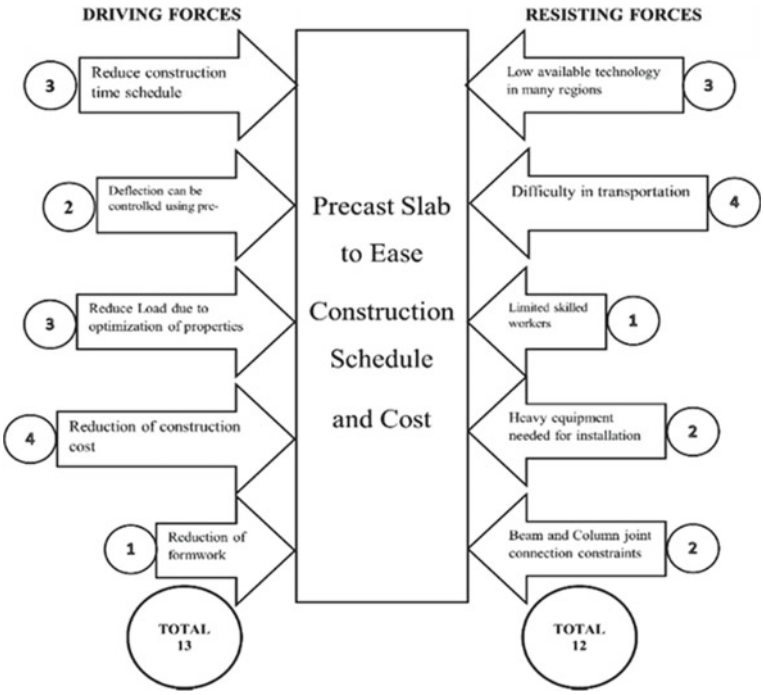

Fig. 2 Force field analysis diagram

differences and difficulties as chances to develop fresh perspectives and opportunities, which converts restraining factors into driving forces. This study has shed light on the forces against employing precast slabs to cut construction costs and schedule delays. It illustrated the VE methodology, where the driving forces account for more than the resisting forces. It means the precast construction system is time efficient, requires less construction, and is more cost-effective than the traditional cast-in-place approach. However, this value engineering also proves that some forces will not change, even if they are vitally important, due to the structural limitations of the precast slab design concerning the deflection and beam-to-column joint connections.

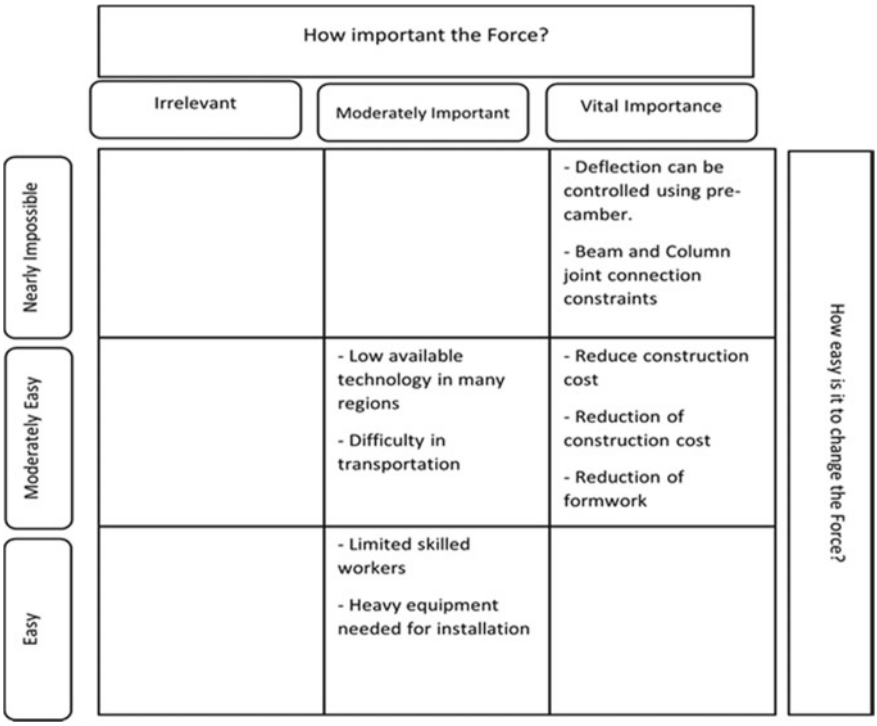

Fig. 3 Analysis of forces

5 Conclusion

Precast concrete is manufactured in another area, such as a factory or a construction site, and then it is hoisted and secured firmly. Compared to cast-in-situ concrete, precast concrete is an alternative. The project's success depends on selecting the right technologies and building techniques, frequently poorly thought out but essential components. Using an efficient, systematic decision-making strategy will improve the quality of the decisions and boost the chances of success. One such technique is force field analysis. According to the theory underpinning force field analysis, situations are maintained by an equilibrium between forces that drive change and others that resist it. For change to occur, intensifying the driving forces or the resisting forces must be lessened. The analysis has suggested that using a precast construction system is time efficient, requires less construction, and is more cost-effective than the traditional cast-in-place approach. Since conventional construction is a linear process, thus each step will be completed first before moving on to the next. Precast construction is simplified and can finish quickly because components have been made beforehand, and it takes place in a facility designed explicitly for precasting.

Additional to the benefits of quality control, factory-cast concrete is produced more cost-effectively and with greater efficiency. Simplified scheduling is done by removing logistical issues, which helps prevent unforeseen costs. Formwork on-site presents logistical challenges. Precast eliminates all the hassles associated with organizing skilled labor and logistics on-site. The accuracy of precast concrete also reduces material waste. Prefabricated systems can reduce on-site waste production, construction time, and equipment consumption. However, this paper only identified some factors that weigh down the forces for change and against change. Thus, using different value engineering techniques is suggested to conduct a full-scale differentiation of precast versus conventional in terms of time and labor quantities.

References

1. Latief Y, Berawi MA, Basten V, Budiman R (2017) Construction performance optimization toward green building premium cost based on greenship rating tools assessment with value engineering method. J Phys Conf Ser 877(1). https://doi.org/10.1088/1742-6596/877/1/012041
2. Abd. Rahman NA, Ahmad S, Zainordin ZM (2013) Perception and awareness of leaking for toilet in pre-cast concrete structure. Procedia Soc Behav Sci 85:61–69. https://doi.org/10.1016/j.sbspro.2013.08.338
3. Kaveh A, Behnam AF (2012) Cost optimization of a composite floor system, one-way waffle slab, and concrete slab formwork using a charged system search algorithm. Scientia Iranica 19(3):410–416. https://doi.org/10.1016/j.scient.2012.04.001
4. Sarhan O, Raslan M, Tallawi G (2021) Hollow-core precast and two-way solid slabs: cost estimation and time duration comparison. Int J Adv Eng Sci Appl 2(1):29–35. https://doi.org/10.47346/ijaesa.v2i1.22
5. Shaban A, Gabr A-H, el Sebai AM, Saleh IM (2019) Inas Mohamed Saleh, behavior of recycled aggregate reinforced concrete composite one way pre-slabs. Int J Civil Eng Technol (IJCIET) 10(06):567–578 [Online]. Available: http://www.iaeme.com/IJCIET/index.asp567, http://www.iaeme.com/ijciet/issues.asp?JType=IJCIET&VType=10&IType=6, http://www.iaeme.com/IJCIET/issues.asp?JType=IJCIET&VType=10&IType=6, http://www.iaeme.com/IJCIET/index.asp568
6. Leal LAAS, Batista EM (2020) Composite floor system with CFS trussed beams, concrete slab and innovative shear connectors. Revista Escola de Minas 73(1):23–31. https://doi.org/10.1590/0370-44672019730049
7. Kong H, Managing M, Jien L, Director P. Pre-fabricated pre-finished volumetric construction (PPVC) for residential projects
8. Abu qadourah J, Al-Falahat A, Alrwashdeh S (2022) Investigate the carbon footprints of three intermediate flooring systems: cross-laminated timber, solid concrete, and hollow-core precast concrete. J Appl Eng Sci 1–6. https://doi.org/10.5937/jaes0-32783
9. Anandh KS, Prasanna K, Priya MGS, Simon SM (2020) An industrial study of just in time (JIT) management in precast construction projects. AIP Conf Proc 2277. https://doi.org/10.1063/5.0025220
10. Idrizi Z, Idrizi I (2017) Comparative study between waffle and solid slab systems in terms of economy and seismic performance of a typical 14-story RC building. J Civil Eng Archit 11(12) https://doi.org/10.17265/1934-7359/2017.12.002
11. Akyol B, Resatoglu R (2019) Investigating the effect of solid and lightweight hollow block slabs on construction cost. Proc Inst Civil Eng Manag Procurement Law 172(2):70–79. https://doi.org/10.1680/jmapl.17.00054

12. Sarita M, Khot R, Professor A. Comparative study of waffle slabs with flat slabs and conventional RCC slabs [Online]. Available: http://www.ijert.org
13. Mary Jose A. Finite element analysis for the behavioral study of composite waffle slab using ANSYS. Int J Eng Trends Appl (IJETA) 5 [Online]. Available: www.ijetajournal.org
14. Akinyele J, Alade G (2014) Application of yield line theory in pre-cast waffle slab. Niger J Technol 33(1):27. https://doi.org/10.4314/njt.v33i1.4
15. Ajdukiewicz A, Kliszczewicz A, Węglorz M. Experimental study on effectiveness of interaction between pre-tensioned hollow-core slabs and concrete topping
16. Dosumu OS, Adenuga OA (2013) Assessment of cost variation in solid and hollow floor construction in Lagos state
17. Shen L, Tam VW, Li C (2009) Benefit analysis on replacing in situ concreting with precast slabs for temporary construction works in pursuing sustainable construction practice. Resour Conserv Recycl 53(3):145–148. https://doi.org/10.1016/j.resconrec.2008.11.001
18. Madhkhan M, Entezam M, Torki ME (2012) Mechanical properties of precast reinforced concrete slab tracks on non-ballasted foundations. Scientia Iranica 19(1):20–26. https://doi.org/10.1016/j.scient.2011.11.037
19. Khare R, Maniyar M. Seismic performance and design of precast concrete building structures: an overview
20. Ramsey D, Ghosh A, Abbaszadegan A, Choi J (2014) School of sustainable engineering and the built environment life cycle assessment of pre-cast concrete versus. Cast-in-place concrete. Course project report series
21. IJETR033358-with-cover-page-v2
22. More SA, Patil A (2008) Time, cost, productivity and quality analysis of precast buildings. Int Res J Eng Technol 9001:1069 [Online]. Available: www.irjet.net
23. Ismail A, Mohamad MI, Yahya A (2010) Time impact of scheduling simulation for high rise building [Online]. Available: http://penerbit.uthm.edu.my/ejournal/index.php/journal/ijscet
24. Chin LS, Hamid ARA (2015) The practice of time management on construction project. Proc Eng 125:32–39. https://doi.org/10.1016/j.proeng.2015.11.006
25. Jayasooriya S, Denagama T, Jayasooriya JMSN, Denagama TD (2019) Comparative analysis of precast construction and conventional construction of small-scale concrete building in terms of cost challenges, trends and opportunities of technical and vocational education and training (TVET) comparative analysis of precast construction and conventional construction of small-scale concrete building in terms of cost [Online]. Available: https://www.researchgate.net/publication/344597542
26. Yee AA, Hon D Eng PE. 34 PCI Journal
27. Price ADF (2005) Exploring conceptual linkages between value engineering and sustainable construction infrastructure project management view project 2013/14 DH national dementia capital investment programme view project [Online]. Available: https://www.researchgate.net/publication/228907643
28. Abdelghany M, Rachwan R, Abotaleb I, Fathy A, Albughdadi A. Building on our growth opportunities
29. Elhegazy H (2020) State-of-the-art review on benefits of applying value engineering for multi-story buildings. Intell Build Int. Taylor and Francis Ltd. https://doi.org/10.1080/17508975.2020.1806019
30. Wei T, Chen Y (2020) Green building design based on BIM and value engineering. J Ambient Intell Humaniz Comput 11(9):3699–3706. https://doi.org/10.1007/s12652-019-01556-z
31. Chakravarthy K, Janani R, Kalyana Chakravarthy PR, Rathan Raj R (2018) A study on value engineering and green buildings in residential construction. A study on value engineering & green building in residential construction. IJCIET_09_01_088 Int J Civil Eng Technol 9(1):900–907 [Online]. Available: http://www.iaeme.com/IJCIET/index.asp900, http://www.iaeme.com/ijciet/issues.asp?JType=IJCIET&VType=9&IType=1, http://www.iaeme.com/IJCIET/issues.asp?JType=IJCIET&VType=9&IType=1, http://www.iaeme.com/IJCIET/index.asp901

32. Arumsari P, Tanachi R (2018) Value engineering application in a high rise building (a case study in Bali). IOP Conf Ser Earth Environ Sci 195(1). https://doi.org/10.1088/1755-1315/195/1/012015
33. Yardim Y (2018) Review of research on the application of ferrocement in composite precast slabs. Periodica Polytech Civil Eng 62(4):1030–1038. https://doi.org/10.3311/PPci.11737

An Analytical Network Process (ANP) Model for Choosing Optimal Public–Private Partnership (PPP) Contract Types for Infrastructure Projects

Su Lae Yee Zaw and Veerasak Likhitruangsilp

Abstract With the rapid social and economic development, a great deal of expenditure is crucial for the nation's infrastructure development. Nevertheless, the governments of many developing nations have been experienced with the limited budget and technical inability to deliver effective public infrastructures. Public–private partnership (PPP) has been adopted as an alternative collaboration arrangement between the government and the private sector in many nations to overcome these challenges. PPP can be defined as a long-term contract between a public agency and a private entity for rendering public facilities, including design, construct, finance, operate, and manage the project. The PPP contract types can be classified by various factors. Different PPP options imply different levels of responsibility and risks to be assumed by the private operator. Deciding an appropriate PPP contact type is always a risk-taking task for the government. This decision-making depends upon several criteria, which directly contribute to project success. This paper proposes a multi-criteria decision-making model based on analytical network process (ANP). The proposed model can be employed to choose a PPP contract type that optimizes important criteria. The main input of the model is the priorities (weights) of the PPP contracts selection criteria, which are obtained from a series of questionnaire surveys. The model is applied to an actual PPP project for verification.

Keywords Analytical network process (ANP) · Multi-criteria decision-making · Public–private partnership contracts · Public–private partnership (PPP)

S. L. Y. Zaw (✉) · V. Likhitruangsilp
Construction Engineering and Management Program, Department of Civil Engineering, Chulalongkorn University, Bangkok, Thailand
e-mail: sulaeyeezaw45@gmail.com

T. Kang (ed.), *Proceedings of 5th International Conference on Civil Engineering and Architecture*, Lecture Notes in Civil Engineering 369,
https://doi.org/10.1007/978-981-99-4049-3_78

1 Introduction

At present, the governments of many developing countries are challenged to fulfill the requirements of public infrastructure services. However, these types of services need high capital investment and advanced technology. Thus, governments need to consider the suitable project delivery methods to meet their objectives and appropriate prices to use this service for users. Theoretically, public–private partnership (PPP) can address the above issues. The term PPP refers to the scope of all possible relations between public and private organizations for delivering infrastructures or other services [1]. Via the PPP approach, the private party is responsible for construction and operation risks, while the public agency is responsible for political risks, project selection, and legal risks. Moreover, users can attain better services due to the competence of a private company with the proper price of the public agency.

To deliver the project with a PPP arrangement, the government needs to consider three main issues. First, the government can strongly support the project politically and socially or not. Second, the government organization must consider legal and regulatory contexts. Finally, decision-makers must consider carefully the most appropriate type of PPP contract that yield the greatest benefit for both public and private sectors financially and commercially [2].

PPP contracts can be categorized into five main types [2]:

1. Design-Build-Finance-Operate (DBFO) or Design-Build-Finance-Operate-Maintain-Finance (DCFM)
2. Build-Operate-Transfer (BOT) or Build-Own-Operate-Transfer (BOOT)
3. Build-Transfer-Operate (BTO)
4. Rehabilitate-Operate-Transfer (ROT)
5. Concession.

However, based on the responsibilities of the private sector and ownership of the facilities, PPP options can be divided into four contract types [3]:

1. Build-Operate-Transfer (BOT) or Build-Own-Operate-Transfer (BOOT)
2. Design-Build-Finance-Operate (DBFO) or Design-Construct-Manage-Finance (DCMF) or Design-Build-Finance-Maintain (DBFM)
3. Build-Transfer-Operate (BOT) or Build-Transfer-Lease (BTL) or Build-Lease-Operate-Transfer (BLOT) or Build-Lease-Transfer (BLT)
4. Build-Own-Operate (BOO)

This paper focuses on four types of PPP contracts based on public and private roles. These PPP contract types are compiled from different reliable and relevant sources, including textbooks, papers, thesis, journals, and websites. Table 1 presents the details of the four PPP contract types, which are examined in this paper.

Table 1 Public and private roles for different types of PPP contracts

Options	Ownership	Design	Build	O&M	Financial responsibility	Source of revenue	References
DBFO DBFM DCMF DBFOM	Public	Private	Private	Private	Public, Public/ Private, Private	Government or user pays	[1–3]
BOT BOOT	Public (Private owns until contract finished)	Private	Private	Private	Public	Government or user pays	[1–3]
BTO BTL BLOT BLT	Public (Private owns during build)	Private	Private	Private	Public	Government or user pays	[2, 3]
BOO	Private	Private	Private	Private	Private	Private, off-taker, public, users	[1–3]

Note
DBFO Design-Build-Finance-Operate; *DBFM* Design-Build-Finance-Manage; *BOT* Build-Operate-Transfer; *BTO* Build-Transfer-Operate; *BTL* Build-Transfer-Lease; *BLT* Build-Lease-Transfer; *BOO* Build-Own-Operate; *DCFOM* Design-Construct-Finance-Operate-Maintain; *BOOT* Build-Own-Operate-Transfer; *BLOT* Build-Lease-Operate-Transfer; *O&M* Operation and Maintenance; *DCMF* Design-Construct-Maintain-Finance

2 Problem Statement

Several past studies investigated critical success factors for PPP projects. Choosing an appropriate PPP contract type for a specific infrastructure project is one of the most important critical success factors [4–9]. A major challenge is that there are various PPP contract types. Different PPP options imply different levels of responsibilities and risks to be assumed by the private operator. Different contract types entail unique disadvantages and advantages, as well as different effectiveness and suitability in different sectoral and project contents [10].

Selecting a suitable PPP option for a certain project is a challenging task for the government and the stakeholders. Stakeholders involve the nomination of PPP options such as political decision-makers who approve decision criteria for selecting preferred and recommended PPP options, investors who provide feedback on the contributions to various PPP options, strategic consultants who furnish an unbiased evaluation of PPP options, as well as review the existing frameworks and propose reforms [1]. This decision must be in accordance with project objectives and many other criteria, leading to project success. However, there is no universal guide for selecting the PPP contract type for a specific infrastructure project. This may limit the success of PPP projects [2].

Several decision-analysis methods have been applied in order to select appropriate PPP contract types. These methods are the analytical hierarchy method (AHP), outranking method (OR), analytical network process (ANP), a simple weighted sum approach (WS), fuzzy set theory (FST), and multi-attribute utility analysis (MAUA). In the past study, an AHP model and sensitivity analysis was developed to select the best form of PPP contract for airport projects in developing countries [11]. Moreover, an ANP model was implemented as a tool to define the most reasonable PPP option for solving the problems of abandoned construction projects in Iraq [12]. By using both AHP and ANP techniques, a multi-criteria assessment model was developed to obtain the optimal solution for the maintenance plan for plumbing services [13].

3 Literature Review

3.1 Concern Criteria for Selecting the Appropriate Type of PPP Options

In general, there is no systematic approach for selecting the procurement method, which is appropriate for a certain project. Thus, it is necessary to identify the procurement selection factors and develop a model for a practical selection process. Both are critical for the efficiency and achievement of the project [14].

Subsequent paragraphs, however, are indented.

In this paper, 28 criteria for choosing an appropriate PPP contract type were first compiled from past literature [1–3, 11, 15, 16] as follows (Table 2).

These criteria were then verified by interviewing a group of PPP experts. The verified results were then used for a pairwise comparison to construct an ANP decision analysis model.

3.2 Analytical Network Process (ANP)

The ANP is an extension of the analytical hierarchy process (AHP). The ANP is considered much more systematic than AHP. It includes a network, which consists of clusters (i.e., components, criteria, and nodes) and elements [17]. The main problem is divided into sub-problems by defining the goal, criteria/sub-criteria, and alternatives as shown in Fig. 1. The goal is what we want to achieve and criteria are the facts that influence the achievements of the desirable decision. The alternatives are the elements upon which a decision must be made. Figure 1 displays the structure of the ANP model.

The development of an ANP model can be broken down into the following four steps.

Step 1 The three parts of the problem are defined: goal, criteria, and alternatives.

Table 2 Contract selecting criteria from literature review

Contract selecting criteria	Contract selecting criteria
1 Risk allocation and sharing 2 Prerequisites to implementing a particular form of PPP 3. The private sector's interest in the option 4. Types of project nature 5. Strong private consortium 6. Available financial market 7. Payment mechanism (the source of revenue stream) 8.The level of private finance involved 9.Political support 10. Technical constraints and goals of the sector 11. Legal and regulatory constraints 12. Institutional issues 13. Commercial, financial, and financing requirements and constraints 14. Type of asset	15. Special requirements of the sector based on characteristics of the system or population 16. What functions the private party is responsible for? 17. Transparent procurement 18. Commitment made by partners 19. Favorable legal framework 20. Efficiency in cost and time management 21. Quality improvement 22. The economic framework developed 23. Financial return 24. Integrated delivery of projects 25. Efficiency of safety management at work 26. Transfer sustainable technologies and methods 27. Percent of completion and 28. Environmental conservation

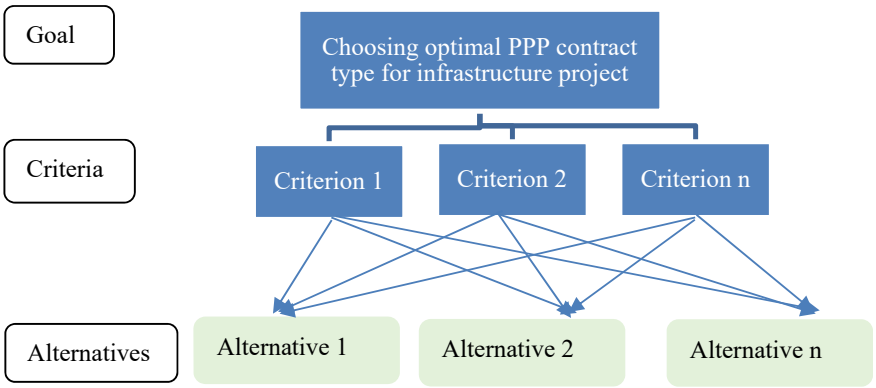

Fig. 1 ANP structure

Step 2 The criteria and alternatives are scaled from 1 to 9 according to Saaty, as shown in Table 1.

Step 3 The weights of the elements are obtained from the results of pairwise comparisons. To assure the reliability of the judgments, it is very important to ensure consistency between the comparisons made. CR is the consistency ratio, and its recommended value is less than 10%. CR is the ratio of the consistency index (CI) and the random index (RI). The consistency index of a matrix is given by

$$CI = (\lambda_{\max} - n)(n - 1) \tag{1}$$

where $\lambda_{\max}$ is the ratio of the total weight of the criteria and the total number of criteria. For the number of criteria which is less than ten, the appropriate random index can be used as shown in Table 3, where n is the number of criteria.

Step 4 If the consistency ratio is less than 10%, the questionnaire result is considered reliable, and the best alternative can be selected which has the highest weight.

The ANP model can be analyzed by using spreadsheet software or commercial software (e.g., super decision software). Figure 2 displays the user interface of the ANP model in super decision software.

Table 3 Definition of the Saaty's scale [17]

Scale	Definition
1	Two options are equally important
3	One option is moderately more important than another option
5	One option is more strongly important than another option
7	One option is very strongly important than another option
9	One option is extremely important than another option
2, 4, 6, 8	Middle values
Can use reciprocals when making comparisons inversely	

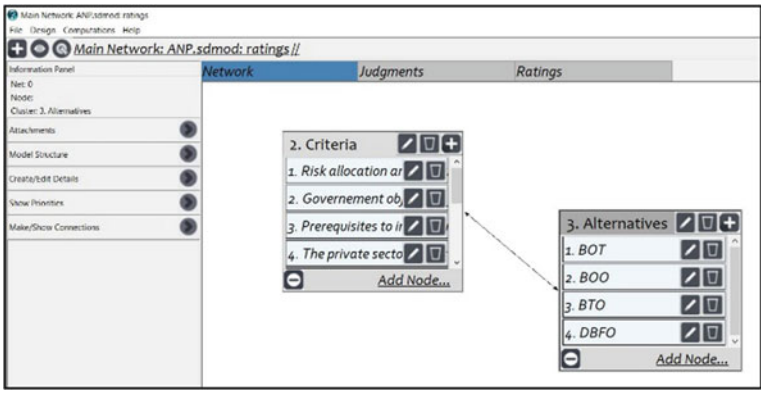

Fig. 2 ANP model in super decision software

3.3 Types of PPP Contracts

Based on our literature review, four PPP contract types are widely adopted in most developing countries.

1. Build-Operate-Transfer (BOT)
2. Build-Transfer-Operate (BTO)
3. Build-Own-Operate (BOO)
4. Design-Build-Finance-Operate (DBFO)

Build-Operate-Transfer (BOT) In the BOT contract, the private partner provides the capital investment required to build a new facility. The private operator will own the assets for a time period set by the contract, which is sufficient to allow the developer to recuperate its investment costs through user charges (e.g., collect the revenue from users). Thus, the private sector's transfer period must be long enough to cover its investment. In some PPP projects, the public sector agrees to purchase a minimum level of output, which is sufficient for the operator to recover its costs during operation.

Build-Transfer-Operate (BTO) In Build-Transfer-Operate (BTO) projects, the government pays the capital investment. Thus, the private company needs to transfer the ownership of assets to the public owner immediately after construction has been completed, rather than at the end of the contract.

Build-Own-Operate (BOO) In Build-Own-Operate (BOO) projects, the developer constructs and operates facilities without transferring the ownership to the public sector. This type of PPP arrangement is similar to privatization, but in BOO projects, the government is still involved.

Design-Build-Finance-Operate (DBFO) The duties of planning, building, funding, and operating are combined in the Design-Build-Finance-Operate (DBFO) strategy. Yet, the public entity is always the owner of the item. The degree of financial obligations, which are often passed on to the private partner, varies substantially among DBFO agreements [1]. The private shareholder's interest in the project is based entirely on the contractual rights to operate the facility and to collect fees from the off-taker, rather than on ownership of the tangible assets, as long as the contracting authority retains legal ownership of the facility throughout.

4 Methodology

This paper proposes a decision-support model that is structured with analytical network process (ANP). The model is designed to identify the criteria that are critical for choosing the most suitable PPP contract type. The priorities of these criteria are assessed by the decision-makers in PPP projects.

The proposed model encompasses seven steps.

Step 1 Review relevant theory and literature to identify the criteria for choosing the appropriate type of PPP contract and explore existing decision-supporting methods.
Step 2 Compile and analyze major PPP contract types, which are widely used in developing countries.
Step 3 Finalize the list of criteria from Step1. Conduct the interviews with PPP experts to verify the criteria that affect the selection process of PPP arrangement.
Step 4 Assess the weights of the criteria and their priorities. The respondents rank the priorities of the criteria with the fundamental scale (1–9).
Step 5 Rank the most appropriate PPP contract type based on the priorities of the weights of the criteria according to analytical network process (ANP).
Step 6 Validate the proposed ANP model using a case study.
Step 7 Identify the limitations of the proposed model and conclude the research study.

5 Result and Discussion

To identify the PPP contract selection criteria, relevant past studies, research works, journals, articles, and textbooks were examined. We listed a total of 28 contract criteria, which are considered while choosing appropriate PPP contract types. These criteria were reviewed by seven PPP professionals experienced in PPP infrastructure projects through in-depth interviews. The experts who participated in these interviews entail one director from the private consulting firm and one from the public consulting firm, one senior executive vice president, and four engineers. Table 4 displays their profile. As can be seen, among the seven respondents, three participants have ten years of experience or more in PPP infrastructure projects and four respondents have five to ten years of PPP experience. Each participant was provided with a list of PPP contract selection criteria and was asked to identify the criteria that affect the contract selection process in infrastructure projects. According to their opinions, twenty-one criteria were removed. Table 5 lists the seven criteria considered in this research.

The final criteria and the alternative PPP options became the inputs of the ANP model to evaluate the pairwise comparison. The ANP model can rank the most appropriate PPP contract type for a specific infrastructure project (Table 6).

Those seven criteria mentioned above become the input of ANP model. They were applied as a case study in the "My Thuan Expressway" project, and the related data were collected for this project to make a pairwise comparison for the expert in this project. In this research, analytical network process (ANP) calculation was done

Table 4 Random index

n	1	2	3	4	5	6	7	8	9	10
RI	0	0	0.25	0.89	1.11	1.25	1.35	1.4	1.45	1.49

Table 5 Profile of the PPP experts

No	Designation	Organization	Experience	Sector
1	Director	Construction supervision	≥ 10 years	Private
2	Director	Consultant	≥ 10 years	Public
3	Senior executive vice president	Consultant	≥ 10 years	Private
4	Engineer	Consultant	5–10 years	Private
5	Engineer	Department of highway	5–10 years	Public
6	Engineer	Consultant	5–10 years	Private
7	Engineer	Consultant	5–10 years	Private

Table 6 Final PPP contract selection criteria

No	Contract selection criteria
1	Risk allocation and sharing
2	Prerequisites to implementing a particular form of PPP
3	The private sector's interest in the option
4	Commercial, financial, and financing requirements and constraints
5	Which function is the private sector responsible for?
6	Efficiency in cost and time management
7	Quality improvement

by super decision software developed by Saaty. The weight of the criteria can be gained by making a pairwise comparison. According to Saaty [17], the result can be assumed to be reliable and consistent if the results of the measurement are less than 10%. Therefore, they can be accepted as the consistency ratio is within the range of 6%. The pairwise comparison in super decision software can be seen in Fig. 3. The priorities of the criteria are shown in (Fig. 4) as well.

According to the results, the main criterion for the choosing of PPP contract type in an expressway project is risk allocation and sharing with a high weight of 0.36094. Thus, 0.36094 can be presumed as risk allocation and sharing between the private sector and public sector is the most important criterion when considering the suitable PPP contract type for this expressway project. Then, commercial, financial, and financing requirement has a weight of 0.17791, while the weight of prerequisites to implementing a particular form of PPP contract type is 0.16816. The private sector interest in the option shows 0.07084, efficiency in cost and time management illustrates 0.05933, and the quality improvement is 0.04589, respectively.

According to the decision-maker's priority, the most suitable contract type for this project is the Build-Operate-Transfer (BOT) contract which meets all the criteria with the highest weight of 0.58965. Build-Transfer-Operate (BTO) and Build-Own-Operate (BOO) are the second and third-rank contract types with a weight equal to 0.21361 and 0.11246, respectively. Design-Build-Finance-Operate (DBFO) contract type can be regarded as the last one for this project which has the least weight

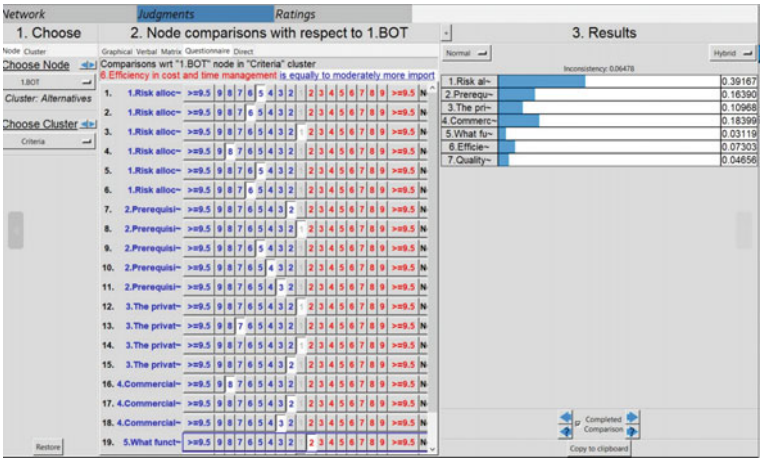

Fig. 3 Pairwise comparison by super decision software

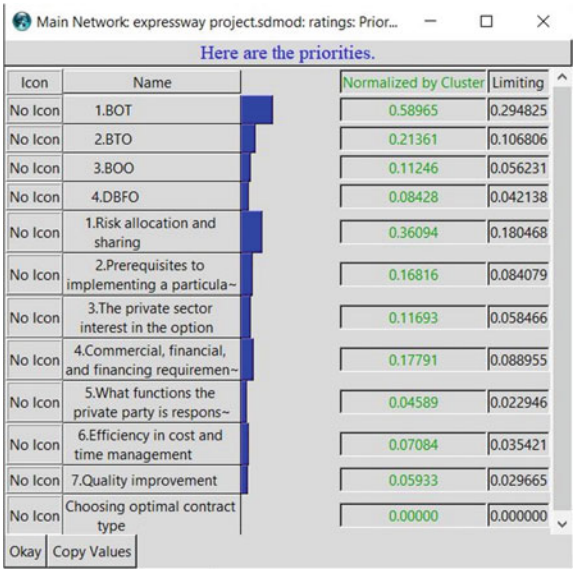

Fig. 4 Priorities for the criteria and alternatives

0.08428. Therefore, Build-Operate-Transfer (BOT) contract can be considered as the most appropriate contract type based on the provided criteria.

This research was focused only on the widely used PPP contract types in Thailand. And most of the respondents have experience in transportation sectors. The same research could be done for the other PPP sectors by investigating the influence of contract selection criteria. However, these contract selecting criteria need to modify based on the unique character of the specific PPP project. Moreover, the proposed

ANP model has limitations. It will be more efficient if the criteria are not over five because the pairwise comparison process for decision-makers is time-consuming. To overcome this limitation, contract selection criteria must be cautiously carried out.

6 Conclusion

The objective of this paper is to establish a conceptual framework for selecting the most appropriate PPP contract type based on the ANP method. In this paper, we discuss the details of the proposed ANP model. The 28 main criteria were compiled from our comprehensive literature review and were verified by the in-depth interviews with seven PPP experts. The 28 criteria were then reduced to seven criteria. These criteria became the input of the ANP model and were pairwise compared. The model incorporates the four PPP options: BTO, BOT, BOO, and DBFO. The model then ranked the most appropriate PPP option for a certain infrastructure project. The weights of these criteria and PPP alternatives are based on the project characteristics. The model thus can recommend the optimal PPP contract type resulting from the priorities of the weight of the criteria. In the future study, the ANP model should be added benefit, opportunity, cost, and risk control hierarchies and it can be developed for practical usage.

Acknowledgements The authors are deeply grateful to the ASEAN and Non-ASEAN scholarship program, Chulalongkorn University, Thailand.

References

1. Felsinger K (2008) Public-private partnership handbook. Asian Development Bank
2. World Bank (2017) Public-private partnerships: reference guide version 3. World Bank
3. Yescombe ER, Farquharson E (2018) Public-private partnerships for infrastructure: principles of policy and finance, Butterworth-Heinemann
4. Abdel Aziz AM (2007) Successful delivery of public-private partnerships for infrastructure development. J Constr Eng Manag 133(12):918–931
5. Chou J-S, Pramudawardhani D (2015) Cross-country comparisons of key drivers, critical success factors and risk allocation for public-private partnership projects. Int J Project Manag 33(5):1136–1150
6. Communities, C. o. t. E (2003) Guidelines for successful public-private partnerships, European Commission
7. Jefferies M, Gameson ROD, Rowlinson S (2002) Critical success factors of the BOOT procurement system: reflections from the stadium Australia case study. Eng Constr Archit Manag
8. Natalia L, Tanzil ND, Sari PY (2021) Critical success factors of public-private partnership from 2000 to 2019: a literature review. J Perspektif Pembiayaan dan Pembangunan Daerah 8(6):531–540

9. Wibowo A, Alfen HW (2014) Identifying macro-environmental critical success factors and key areas for improvement to promote public-private partnerships in infrastructure: Indonesia's perspective. Eng Constr Archit Manag
10. European Union Commission (2003) Guidelines for successful public-private partnerships, Regional Policy Report, European Union Commission, Brussels
11. Mohammed AO, Harputlugil T (2017) Conceptual framework for a decision-making model based on the analytic hierarchy process (AHP) to select the best public private partnership (PPP) model for airports. Nzaar Sci Committee 99
12. Khudhaire HY, Naji HI (2021) Applying network process to the selection of financing method for abandoned construction projects in Iraq. Diyala J Eng Sci 14(2):62–70
13. El Chanati H, El-Abbasy MS, Mosleh F, Senouci A, M.ASCE, Abouhamad M, Gkountis I, Zayed T, Al-Derham H (2016) Multi-criteria decision making models for water pipelines. J Perform Constr Facil 30(4):04015090
14. Ratnasabapathy S, Rameezdeen R (2007) A decision support system for the selection of best procurement system in construction. Built-Environ Sri Lanka 7(2)
15. Ambarsari R, Soehodho S, Sumabrata RJ (2021) Conceptual framework for a decision-making model to select the public-private partnership (PPP) structure for urban rail transit in Jakarta
16. Khudhaire HY, Naji HI (2021) Adoption PPP model as an alternative method of government for funding abandoned construction projects in Iraq. IOP Conf Ser Mater Sci Eng
17. Saaty TL, Vargas LG (2006) Decision making with the analytic network process, vol 282. Springer Science+ Business Media, LLC, Berlin, Germany

The Benchmarking in Facility Management Performance Measurement for the Office Building in Bangkok, Thailand

Wiruj Somsopon and Alita Chaladdee

Abstract Many iconic urban high-rise buildings contain offices, requiring proper management to reduce unnecessary resource waste. Benchmarking in facility management (FM) performance measurement improves operational efficiency by using comparisons with best practices. However, external benchmarking processes have not yet established FM professional standards in Thailand. This study proposes FM performance measurement benchmarking for office buildings in Thailand by field data collection for 14 Bangkok office buildings. Results were that electricity and facility operating expenses should be considered for FM benchmarking. The leading operational cost is average electricity expense of 40.91 baht/square meter (sq m)/month. FM team benchmark or best performance uses techniques and planning in an operations and maintenance (O&M) project to reduce electricity consumption. FM teamwork for other buildings may apply these methods as energy and financial management best practices for improvement plans. If these processes boost continuous exchange of information and knowledge gained, key performance indicators (KPIs) used should be consensus-based and match nationwide organizations with similar backgrounds and contexts to raise FM professional levels in Thailand and abroad.

Keywords Benchmarking · Facility management performance measurement · Office building

W. Somsopon (✉) · A. Chaladdee
Faculty of Architecture and Planning, Thammasat University, Pathum Thani, Thailand
e-mail: wirujsom@ap.tu.ac.th

A. Chaladdee
e-mail: alitactu@ap.tu.ac.th

T. Kang (ed.), *Proceedings of 5th International Conference on Civil Engineering and Architecture*, Lecture Notes in Civil Engineering 369,
https://doi.org/10.1007/978-981-99-4049-3_79

1 Introduction

Office buildings are a group of buildings that directly influence the city. It is often found that the zones for office buildings are defined in the city's center as an economically important area with many infrastructure facilities and often an icon of the area. Besides affecting building occupants' quality of life and health, it also affects cities. For example, the energy demand of buildings is a major cause of urban heat islands, especially in office buildings, the high load range is between 7:00 AM and 7:00 PM [1]. Lima et al. found that reducing heat generation in office buildings can reduce the heat load in a hot and humid climate by an average of 16–18% [2]. Therefore, effective facility management is essential for this type of building.

Facility Management (FM) is a profession that encompasses multiple disciplines to ensure the functionality of the built environment by integrating people, place, process, and technology [3]. Facility management requires knowledge of three areas of management: building and facility knowledge, management knowledge, and financial knowledge. The management and long-term planning deal with the facility, operating system, and building users [4].

Currently, facility management in Thailand is an essential matter for every organization. But in the interest of such work, it found that in each organization, if the organization's executives see the importance of that work, they will support and plan various tasks in their respective departments. But if any organization sees that the matter is unimportant or urgent, it needs to be corrected and improved. The organization's management will not provide adequate support for the development and improvement of facility management operations [5].

The way to motivate each organization to realize the importance of facility management is to evaluate or measure their facility management performance by looking at the performance of that organization. Then compare, show the, and rank each other. When the comparison takes place, if the results show that the performance in our organization is lower than others or below the standards that our organization has set goals, it will create an incentive within the organization to want to develop and improve performance in performing such tasks better. The method mentioned above involves the FM performance measurement and benchmarking process [6–8].

FM performance measurement is the evaluation or comparison of performance against established goals using indicators and measurements based on the nature of FM work. But because each organization has different businesses, policies, functions, and facilities. The performance and quality requirements required to use facilities and FM operations vary.

Benchmarking is the continuous process of measuring products, services, and practices against the toughest competitors of those companies recognized as industry leaders [9]. There are eight steps of benchmarking in facility management [10];

(1) Identify the subject of the exercise
(2) Decide what to measure
(3) Identify who to benchmark both within your sector and outside
(4) Collect information and data

(5) Analyze finding and determine gap
(6) Sets the goal for improvement
(7) Implement the new order
(8) Monitor the process of improvement.

Moreover, Bogan and English mentioned that FM benchmarking starts with;

(1) Deciding what to benchmark (launch)
(2) Finding companies to benchmark (organize)
(3) Gathering the data (reach out)
(4) Analyze data and integrate (assimilate)
(5) Recalibrate and recycle the process (act) [11].

Thus, the benchmarking is a process to help improve and develop operational efficiency by comparing and learning from those with best practices. However, facility management is now more well-known and accepted in Thailand. The external benchmarking processes have never appeared or were setting it up to create standards in the FM profession in Thailand [5]. There is only internal FM performance measurement. Many public and private buildings use methods to measure and compare their internal performance, especially office buildings. They are more expensive in operation and maintenance, and their management thus requires professional knowledge and skills [12].

This study has two research objectives.

(1) To study the benchmarking in FM performance measurement
(2) To suggest the benchmarking in FM performance measurement for the office building in Bangkok, Thailand

2 Research Methodology

The research method used was mixed method. This includes reviewing relevant literature and field data collection from 14 offices in Bangkok. Field data collection includes numerical data on building management and interviews with stakeholders. The literature reviews included theories and concepts of benchmarking in facility management and FM performance measurement from scientific papers, journals, research, and case studies, as well as a review of FM's theories, concepts, scope, and processes.

2.1 Conceptual and Theoretical Boundaries

Chotipanich and Somsopon studied FM performance indicators from 28 academic articles by foreign academics. They found that 326 indicators were used to measure and evaluate the performance of all departments and organizations. They can be grouped into eight groups as follows [13]:

(1) Space and Area Management Performance: 66 indicators
(2) Energy and Utilities Performance: 52 indicators
(3) Environmental Health and Safety (EHS) Performance: 26 indicators
(4) Churn and Relocation Performance: 64 indicators
(5) Service and Maintenance Performance: 56 indicators
(6) Custodial Performance: 28 indicators
(7) Customer Satisfaction: 14 indicators
(8) Financial Performance: 20 indicators.

In assessing the importance of Benchmarking FM Performance Indicators, experts commented that FM performance measurement and evaluation should be done in the Financial Performance category. Electricity consumption and Facility operating expenses are the most important and should be considered because the monthly electricity consumption of every organization is very high. Reducing the amount and cost of using electricity will benefit the organization and directly affect the total building management cost. The amount of electricity consumption per square meter of the same business organization that is well FM performance can bring the indicators of that good organization to be set as the goals and learn practical techniques to reach the goals [5].

The first step in the Performance Management Process was to target the aspects of performance evaluation and create a strategy. When goals and strategies are established, we need to control the variables and factors involved in the process. The next process was measurement. Finally, an assessment must best match the assessment plan and goals [14].

We can compare the results of performance appraisals with the best performing organizations by Benchmarking. The organization can use the results from all the studies to improve its performance as an improvement plan (Fig. 1). In this study, we used data on electricity expense (baht/sq m/month) and facility operating expense (baht/sq m/month) to compare FM performance with other organizations to achieve better performance.

2.2 Conceptual and Theoretical Boundaries

Scope of theories and concepts. This study examines theories and concepts of benchmarking, benchmarking in facility management, KPIs in FM performance measurement, and the Performance Management Process.

Scope of the study area. To suggest a guideline for FM Benchmarking, the researcher studied FM cost data from office buildings for rent in the area surrounding the rail transit station area in Bangkok. All office buildings will be 500 m from the Bangkok Mass Transit Station (BTS) and Metropolitan Rapid Transit Station (MRT), which is a walkable distance. The selected BTS was Sukhumvit Line (from Mo Chit Station to Bearing Station) and Silom Line (from National Stadium Station to Bang Wa Station). The selected MRT was Chaloem Ratchamongkhon Line (From Hua

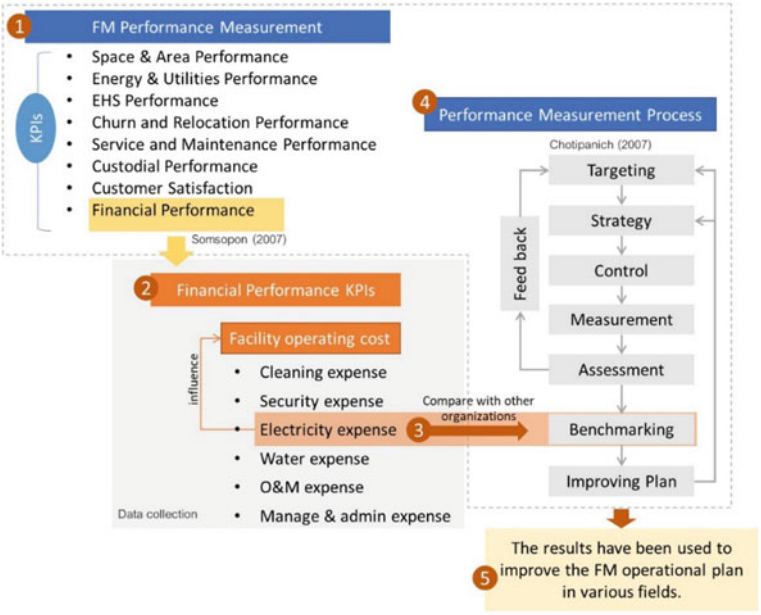

Fig. 1 The conceptual framework of Benchmarking in FM performance measurement

Lamphong Station to Bang Sue Station). Therefore, all case studies will be buildings built after 2005, when both BTS and MRT trains were opened.

The pilot study found that there was a total of 444 office buildings for rent in 11 districts of Bangkok, but some buildings did not meet the criteria. Therefore, there are a total of 81 rental office buildings left. From the 81 office buildings that were the population of this study, the researcher chose 14 different office buildings as a sample size with purposive sampling.

Data Collection and Samples. This study collected FM costs from 14 rental office buildings owned by private organizations and government agencies. They are located in Bangkok (Table 1 and Fig. 2). The details are as follows.

(1) There are two types of building space usage; release of rental space, and using the space by themselves in the whole building (Head Quarter).
(2) There are two types of building ownership; juristic person and single owner.
(3) The building has 3732–66,860 sq m and 3–40 floors.
(4) The data collection was organized based on performance measures in terms of financial performance, and the data is in total cost/area/month. (baht/sq m/month)

Table 1 The rental office building samples in Bangkok, Thailand

Building	Location	Gross area (sq m)
A	Thung Phaya Thai, Ratchathewi District, Bangkok	64,710.00
B	Suriyawong, Bangrak District, Bangkok	47,797.00
C	Silom, Bangrak District, Bangkok	57,068.00
D	Khlong Tan, Khlong Toei District, Bangkok	41,503.00
E	Khlong Toei Nuea, Watthana District, Bangkok	32,000.00
F	Bangrak, Bangrak District, Bangkok	3732.00
G	Thung Maha Mek, Sathorn District, Bangkok	33,898.00
H	Thung Song Hong, Lak Si District, Bangkok	23,164.00
I	Thung Maha Mek, Sathorn District, Bangkok	66,860.00
J	Silom, Bangrak District, Bangkok	60,824.00
K	Thung Maha Mek, Sathorn District, Bangkok	27,467.00
L	Thung Song Hong, Lak Si District, Bangkok	22,777.00
M	Silom, Bangrak District, Bangkok	11,421.00
N	Thanon Phaya Thai, Ratchathewi District, Bangkok	27,629.00

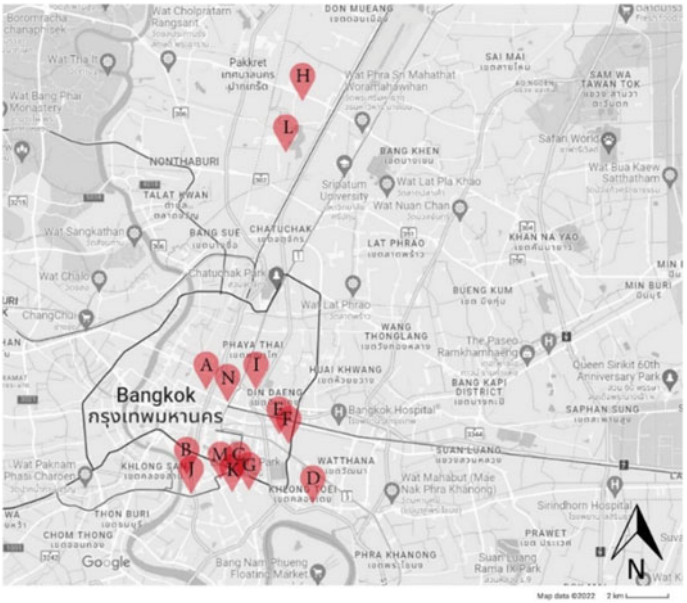

Fig. 2 Map of the rental office building samples in Bangkok, Thailand

3 Results and Discussions

3.1 Benchmarking in FM Performance Measurement

Developing strategies for FM plays an important role in contributing to an organization's business objectives and needs. There are three stages that need to be focused on in developing FM strategies: analysis, solution, and implementation [15]. And benchmarking is one strategy that has a process for improving FM performance.

From the study, benchmarking in FM performance measurement is a comparative analysis process in which the results of measured performance are compared to each organization's level of competence and performance. It will improve and develop FM operations to learn and apply the techniques in the performance of those who perform better.

Benchmarking doesn't just tell you where your organization is. But it will also tell you which organization is the best practice or has the best performance in that field, and it will make it possible to know how much gap exists between our organization and others. And it also makes it possible to understand why our organization is in this position. Suppose the results show that our organization is at a lower level or lower than the organization's goals. In that case, such impressions serve as an impetus that will enable the organization to develop and improve its practices to be as good as or better than other organizations. It also creates cooperation between organizations and exchanges operations in different organizations in the same field of work.

In addition to the benefits of the benchmarking process mentioned above, the advantages of implementing the benchmarking process in FM performance measurement include other advantages, such as reducing costs and the trial-and-error time of each organization's operations. Because benchmarking is the process of making comparisons and learning for the better. These results will help them know in which direction to develop and adjust the operational plan and improve the plan. The benchmarking must be implemented as a dynamic process for continuous improvement.

3.2 Benchmarking in FM Performance Measurement for the Office Building in Bangkok, Thailand

The formulation of techniques that can assess "facilities performance" in terms of quality and cost-effectiveness is critical for organizational and Facilities Management advancements. This study chose the FM financial performance as facility operating expense which reflects the quality and cost-effectiveness in the assessment of FM performance measurement.

The study of FM financial performance of 14 office buildings in Bangkok found that the electricity expense accounts for the largest share. The largest proportion of the electricity expense is building I at 77.68%, while building F has the smallest

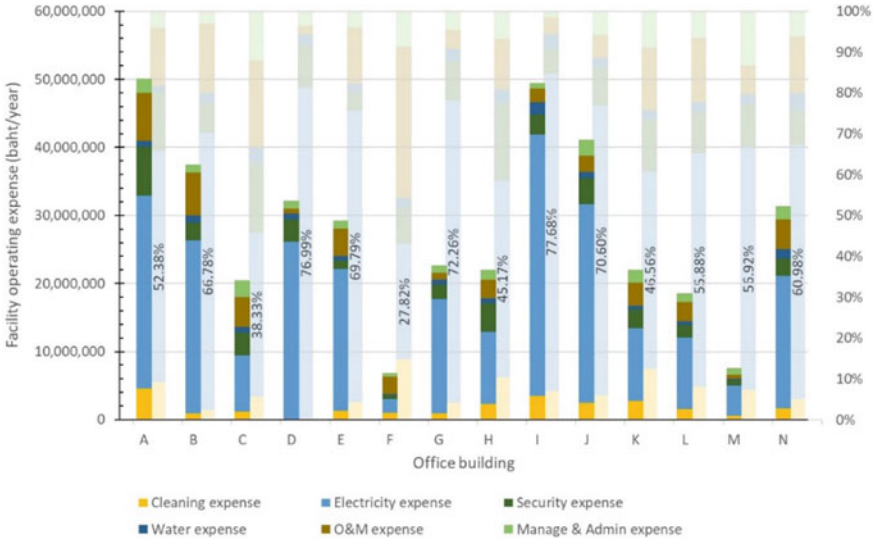

Fig. 3 The proportion of the facility operating expense of 14 office buildings in Bangkok, Thailand

electricity expense at 27.82% of the total facility operating expense. The average electricity expense is 58.37% of the facility operating expense. Thus, the electricity expense is the expense that affects the facility's operating expense the most.

And the minor proportion of expense is the water expense, which is precisely what FM experts mentioned. The water consumption indicator in the building is the least essential KPI because it costs less and does not affect the facility operating expense. The results shown in Fig. 3.

From Fig. 4, the facility's operating expense ranges from 31.28 to 156.42 baht/sq m/month, and the average was 73 baht/sq m/month. While the electricity expense ranges from 11.99 to 58.90 baht/sq m/month, and the average was 40.91 baht/sq m/month. According to the FM cost-effectiveness, building C was the building with the best management of both expenses; the facility operating expense and the electricity expense, as 31.28 and 11.99 baht/sq m/month, respectively.

From the benchmarking process in the conceptual framework, benchmarking process, which in this study means collecting data and analyzing financial performance as the facility operating and electricity expense. This process leads to the search for the benchmark or best performer, herein building C's FM team. The other building's FM team needs to see how the best practices perform and learn how they do it.

According to the study on facility management expenses, utility expenses accounted for the second proportion of expenses after facility operating expenses with the cost of electricity being the highest cost [16]. And it is consistent with the results of this study.

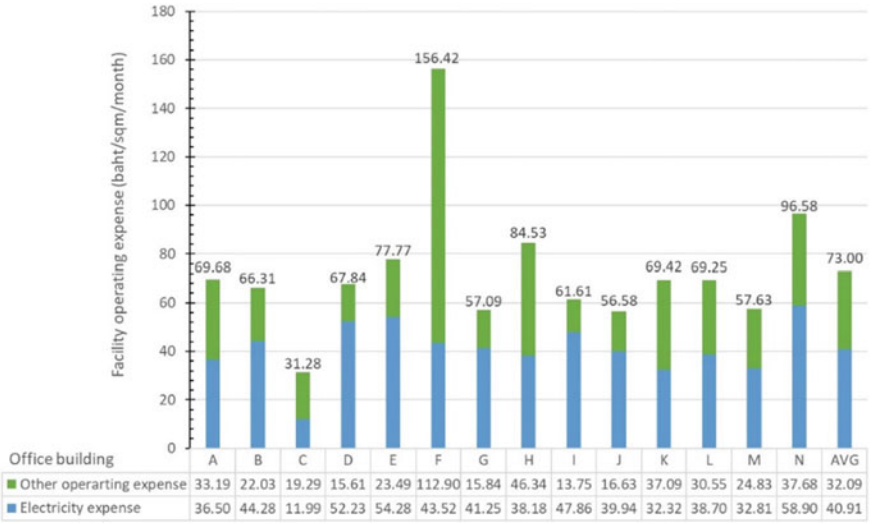

Office building	A	B	C	D	E	F	G	H	I	J	K	L	M	N	AVG
Other operarting expense	33.19	22.03	19.29	15.61	23.49	112.90	15.84	46.34	13.75	16.63	37.09	30.55	24.83	37.68	32.09
Electricity expense	36.50	44.28	11.99	52.23	54.28	43.52	41.25	38.18	47.86	39.94	32.32	38.70	32.81	58.90	40.91

Fig. 4 The FM performance measurement in the facility operating expense of 14 office buildings in Bangkok, Thailand

The study on facility management expenses found that the expenses in the category of utilities were related to the physical characteristics of the building [16]. Such buildings will have high expenses in the category of utilities as well. From Table 1, building C, a high-rise building with 22 floors, has the 4th largest gross area. But Fig. 4 shows the lowest electricity expense (baht/sq m/month). Therefore, the physical characteristics of the building do not always affect the facility operating and electricity expense. Building C's FM team mentioned that maintenance expenses would increase even more if good and proper O&M were performed. But it can reduce the amount of electricity used in the building for various machines and reduce the facility management expenses.

Building C's FM team managed the building using the PDCA concept. P as Plan; there was the operation planning and manual for operation and maintenance management such as the daily operation audit, preventive maintenance, and corrective maintenance. D as Do; there was the quality control system as ISO9001, the international organization standardization, which covered work efficiency and quality controlling and checking in the management system. C as Check; there was monitoring by the supervisor and manager in each operation. And A as Act; there was the annual customer satisfaction survey on O&M and FM performance. The results will reflect the performance and lead to further improvements in operations.

Therefore, from the comparison of financial management performance. If the FM team of other buildings applies the concepts and techniques of best practices as building C's FM team to their way of working, including developing their work plans, it will improve the management of expenses.

From the conceptual framework of the FM performance management process and the concept of cost-effectiveness, FM, which is a work at the management level, needs a management plan to constantly develop and improve the plan. In energy management, additional assessments from data collection such as utility information audits and energy audits should be added to guide the energy conservation plan in the short-term, middle-term, and long-term. And in financial management, budget control should be added to routine operations and annual budgeting. If there is control in both areas, effective cost control will achieve.

4 Conclusions

The benchmarking in FM performance measurement is a comparative analysis process in which the results of measured performance are compared to each organization, which will improve and develop FM operations to learn and apply the techniques in the performance of those who perform better as best practice. The results will be used to develop and adjust the operational plan and improve the plan. Moreover, implementing the FM benchmarking will reduce costs and the trial-and-error time of each organization's operations. The benchmarking must be implemented as a dynamic process for continuous improvement.

According to FM experts from the previous study, the measurement and evaluation of FM performance should be done in the financial performance category, especially electricity consumption and facility operating expense are the most important and should be considered first.

The study of FM financial performance of 14 office buildings in Bangkok found that the electricity expense accounts for the largest share. The average electricity expense is 58.37% of the facility operating expense, and the electricity expense is the expense that affects the facility operating expense the most. The benchmark or best performer managed the building using the PDCA concept for O&M operation to reduce electricity consumption. The FM team of other buildings can use and apply the techniques as best practices and energy and financial management in their improvement plan.

This study has limitations in terms of collecting data from office buildings. Some information is inaccessible due to the confidentiality of the company. The findings of this study should be considered by FM service providers, the building and facility management, and the building owner for information on budgeting in various fields.

For suggestions, further studies should study more on FM performance indicators like environmental health and safety (EHS), service and maintenance, and customer satisfaction. It could increase the population and sample size to provide more comprehensive data for applying the results to enhance the FM profession in Thailand. Building a network of FM organizations and exchanging information on the various functions of each organization are essential to improving performance. Benchmarking processes is one of the FM strategies for improving FM performance, creating added value to FM businesses enhancing the efficiency of each level of FM

management that leads to innovation and business success to Thailand and other countries.

References

1. Meng F, Guo J, Ren G, Zhang L, Zhang R (2020) Impact of urban heat island on the variation of heating loads in residential and office buildings in Tianjin. Energy Build 226:110357
2. Lima I, Scalco V, Lamberts R (2019) Estimating the impact of urban densification on high-rise office building cooling loads in a hot and humid climate. Energy Build 182:30–44
3. IFM. The Benchmarking Process [Online]. IFM: IFM (2006). Available from: http://www.ifm.eng.cam.ac.uk
4. Chulasai B, Chotipanich S (2004) Facility management. Chulalongkorn University, Bangkok
5. Somsopon W (2007) Performance measurement for facility management practice in Thailand. Thesis in Master degree, Department of Architecture, Faculty of Architecture, Chulalongkorn University. Bangkok: Chulalongkorn University
6. Bagchi PK (1995) Role of benchmarking as a competitive strategy: the logistics experience. J. IJPDLM 26(2):422
7. Bernard Williams Associates (2001) Facilities economics incorporating premises audits. Building Economics Bureau, British
8. Monroe LK (2007) Rethinking facility management: the pursuit of best practices gives building a competitive edge [Online]. FM link: FM link. Available from: http://www.fmlink.com
9. White G (2003) Performance Management in Facility Management. J Facility Management Thailand 2002 The validity and essence of facility management 1 (Mar 2003):58
10. Atkin B, Brooks A (2014) Total facility management. Wiley, British
11. Bogan CE, English (1997) MJ benchmarking best practices: winning through innovative adaption. J IJQRM 14(5):516
12. Hyunji Shin SM et al (2018) Facility management process of an office building [Online]. J Infrastruct Syst 24(3). Available from: http://www.ascelibrary.org
13. Chotipanich S, Somsopon W (2007) Performance metrics and benchmarking issues for FM practice in Thailand (VIVID), pp 7–13. Chulalongkorn University, Bangkok
14. Chotipanich S (2007) Documents for facility management course. Faculty of Architecture Chulalongkorn University, Bangkok
15. Maszuwita Abdul W, Syahrul-Nizam K, Mohd-Khairolden G (2015) The significance of strategic planning and management in facilities management. The Professional Journal of Royal Institution of Surveyors Malaysia. Royal Institution of Surveyors Malaysia, Kuala Lumpur
16. Sooksena P (2019) Expenses for repair and maintenance of common area systems, residential condominiums, high building type case study: 4 condominiums in the central business area of Bangkok. J Sarasatr, Faculty of Architecture, Chulalongkorn University, vol 3/2019. Chulalongkorn University, Bangkok

A Study on the Direction for Regional-Linked School Complex Facilities

Ji-Won Jeong and Hae-Yeon Yoo

Abstract It is necessary to study the changes in school facilities in response to social needs. This is because in this process, schools are not only performing existing educational and learning functions, but also symbiotic and linked development with the region. Therefore, the purpose of this study is to identify regional and complex cases for each district for schools in Seoul, analyze the planned characteristics, and suggest the institutional and planned direction. For this study, reports and data analysis, field case studies, and consultations with officials of the Seoul Metropolitan Office of Education were conducted through literature research. The procedure of this study is as follows. First, this study investigated and analyzed the emergence and necessity of school complex facilities in Korea. Second, the current status of school complex facilities conducted at elementary, middle, and high school levels in Seoul was analyzed. Third, the types were divided according to the planning characteristics, and the characteristics and limitations of the main cases were analyzed. Finally, the direction of improvement was proposed in terms of planning and institutional aspects. The results of examining 103 schools in Seoul are as follows. First, the number of projects decreased from a specific year, and second, the complexation ratio was lower than the total number of schools, and there were variations by region. Finally, similar programs were combined. Based on this, the institutional and planned direction of the regional-linked school complex facilities was proposed.

Keywords Regional-linked · School complex facilities · Smart living-lab

This study is part of the results of the 2022 National Research Foundation of Korea's research funding. Task number: NRF-2020R1A2C1006354.

J.-W. Jeong
Department of Architecture, Soongsil University, Seoul, Republic of Korea

H.-Y. Yoo (✉)
School of Architecture, Soongsil University, Seoul, Republic of Korea
e-mail: zenism@ssu.ac.kr

T. Kang (ed.), *Proceedings of 5th International Conference on Civil Engineering and Architecture*, Lecture Notes in Civil Engineering 369,
https://doi.org/10.1007/978-981-99-4049-3_80

1 Introduction

1.1 Background and Purpose

Recently, in Korea, various programs for education, such as education systems and programs, are being developed along with the reorganization of the curriculum in 2022. However, the operation of uniform educational spaces, modular classrooms, and closed school facilities is still emerging as a problem. Therefore, there is a growing demand for improvement in school spaces and uniform facilities that need improvement.

In particular, the "High school credit system" has been introduced at the high school level, and various types of "Optional subjects" are being applied. At the middle school level, the curriculum is being reorganized so that students can decide their own career paths through the "Free school year program." At the elementary school level, children's emotional development, tendencies, and academic ability are promoted, focusing on the introduction of "After-school programs" and "Play-oriented schools." In addition, demands for changes in school space, such as the development of smart devices and response to infectious diseases caused by COVID-19, are continuously being made.

It is also necessary to study the changes in school facilities in response to social needs. This is because in this process, schools are not only performing existing educational and learning functions, but also symbiotic and linked development with the region. In particular, the decrease in the school-age population and the lack of empty spaces in urban spaces were need for changes. So, it is necessary to study the direction of regional-linked facilities and space design using the school's playground, empty classrooms, and spaces.

Therefore, the purpose of this study is to identify regional and complex cases for each district for schools in Seoul, analyse the planned characteristics, and suggest future development directions.

1.2 Methods and Procedures

For this study, reports and data analysis, field case studies, and consultations with officials of the Seoul Metropolitan Office of Education were conducted through literature research.

The procedure of this study is as follows. First, this study investigated and analyzed the emergence and necessity of school complex facilities in Korea. Second, the current status of school complex facilities conducted at elementary, middle, and high school levels in Seoul was analyzed. Third, the types were divided according to the planning characteristics, and the characteristics and limitations of the main cases were analyzed. Finally, the direction of improvement was proposed in terms of planning and institutional aspects. The scope of the study is 103 schools in Seoul.

This is the sum of 60 elementary schools, 30 middle schools, and 15 high schools. In terms of timing, part or all of the facilities were planned through complexation after 2000, and schools shared with the local community were studied.

2 School Complex Facilities in Korea

2.1 Appearance and Necessity of School Complex Facilities in Korea

Total birth rate decreased by 0.852 in 2021(0.808) compared to 1985(1.66), while the school-age population (6–17 years old) also decreased by 4910 in 2021(5442) compared to 1985(10,352) in Korea. As a result, as the extra space of the school increased, the land area for education per student increased, and unused classrooms appeared as problems.

As the number of students decreased, interest in space utilization increased, and the Ministry of Education has been carrying out the "School Space Improvement Project" since 2018 to solve various problems. In addition, since 2015, individual local governments have been carrying out various small and medium-sized space improvement projects considering the characteristics of each region (Fig. 1).

After 2019, as the COVID-19 situation faced, it took on a new aspect, not the existing school and classroom. In this process, other problems were raised, such as the absence of a comprehensive promotion model linked to the curriculum, the demand for fundamental changes in the learning space, and the lack of digital environment-based infrastructure. To solve this problem, a new type of school space improvement project called "Green Smart School (GSS)" was promoted in 2020. At that time, "Green Smart School" was one of the top 10 representative projects of the Korean

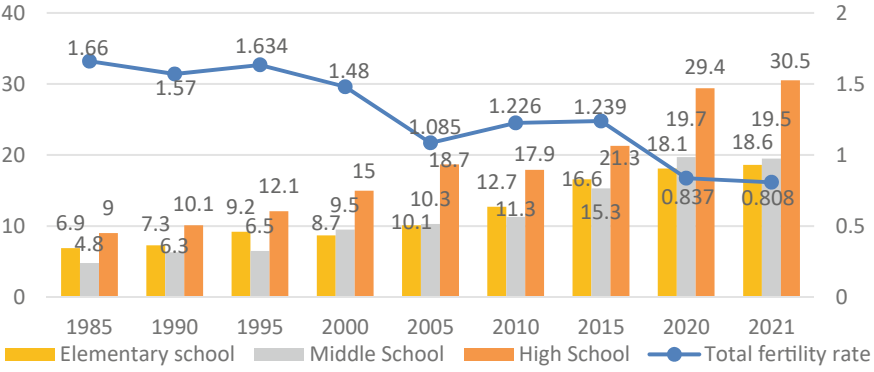

Fig. 1 Total fertility rate and School site area per student by school level [1, 2]

Table 1 Type of living SOC complex facilities [3]

Verticality complex	Horizontal complex	Duplicate complex
		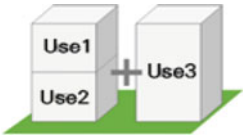

New Deal project, and it was a project to renovate and remodel old schools that have passed more than 40 years.

The core elements of Green Smart School are divided into five areas: "Space Innovation (Restructuring), Smart Classrooms, Green School, School Complexation, and Safety." Among them, school complexation is linked to the Living SOC (Social Overhead Capital) complex project. The Living SOC Complex Project is one of the core tasks of the Living SOC Three-Year Plan ('20 ~ '22'), and the Living SOC project was implemented to alleviate the lack of infrastructure and regional gaps that promote the benefits of the people in daily life. In this process, problems such as difficulty in securing new sites, excessive construction and operation costs, and overlapping functions and programs occurred to expand infrastructure.

In order to solve these problems, "Living SOC Complex Facility" was promoted. The term "Living SOC Complex Facility" means a project to build two or more living SOC-related state-funded projects[1] on one site as a single or linked facility [3]. A total of 530 projects[2] were selected from 2020 to 2022, and the complexation will be carried out through three methods (Table 1). By combining facilities (functions) that existed on different sites into one site and planning them as a complex building, it is easy to secure the site, economical, link functions and programs, and increase the efficiency of movement (Fig. 2).

The Living SOC Complex Facility Project is divided into four categories: (1) specialized in cultural and sports facilities, (2) specialized in welfare facilities, (3) complex of school facilities, and (4) complex of public rental housing. Among them, the aforementioned Green Smart School's core elements, the school complexation and the school facility complexation of the life SOC complex project, are linked. Through school complexation, it was used as a complex facility suitable for local community demand to respond to the decrease in the school-age population and ease the burden of securing local governments sites. The Living SOC Complex Facility is not just a place where functions and facilities are shared and used together, but is meaningful as a place where residents of various classes gather to express life innovation through communication and exchange.

[1] There are 13 types of facilities subject to complexation, including public libraries, small libraries, national sports centers, living and cultural centers, national and public daycare centers, care centers, and parking lots [3].

[2] 289 cases in 2020, 149 cases in 2021, and 92 cases in 2022 [4].

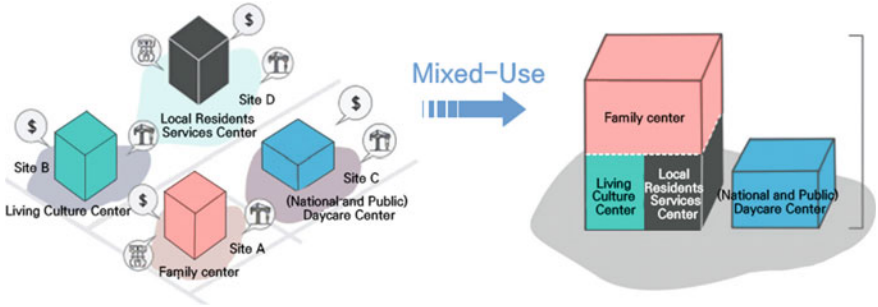

Fig. 2 Concept diagram of living SOC complex facilities [5]

As the school's role as an urban hub facility is re-examined, it is very significant that the shortage of alternative spaces has been resolved through school-community linkage amid rapid urban development.

2.2 A Preliminary Study on the School Complexity in Korea

The following Table 2 shows previous studies conducted in Korea regarding school complexation. As a result of examining previous studies, it was confirmed that the connection between local residents (local facilities) was important through the complexation of school facilities, and safety issues were also being studied.

As the need for school complexation increased, the Ministry of Education enacted the Act on the Installation, Operation, and Management of School Complex Facilities (School Complex Facilities Act) on March 24, 2020. The School Complex Facility Act aims to contribute to the development of schools and communities by installing facilities that students and local residents can use together in accordance with Article 1 (Purpose). In addition, an online matching platform was established on January 2021, which connects the Office of Education with the idle school site and local governments wishing to utilize the school site [10]. Figure 3 shows the current status of the nationwide complexation of school facilities as of January 31, 2021. It can be confirmed on school complexity, and it can be confirmed that school complexity was mainly conducted around elementary school. Accordingly, the school complexity was intended to analyse Seoul.

3 Status of School Complex Facilities in Seoul

As of 2022, the current status of school facilities in Seoul is as follows, and a total of 103 schools have combined school facilities in Seoul (Fig. 4).

Table 2 A preliminary study on school complexity

Author (Year)	Contents
Reigh [6]	• Development of complex sharing of facilities and education programs for local residents through the complexation of school facilities • Based on coexistence and sharing with the community, it is necessary to pursue sharing of communities and facilities, sharing of education, sharing of talents, and sharing of values
Hwang and Park [7]	• Various usage needs are analyzed according to the characteristics of local residents • As demands for various types of facilities appear according to the characteristics of local residents, it is necessary to provide types of facilities not provided in the local community
Lee and Kim [8]	• An analysis of the necessity, operation system, and space of the opening and complexation of school facilities through the connection between school facilities and the community identifies external factors that cause problems and suggests solutions accordingly
Kim and Yoo [9]	• Proposed community-linked school facilities • Emphasize connection within the region through connection with idle spaces in the region

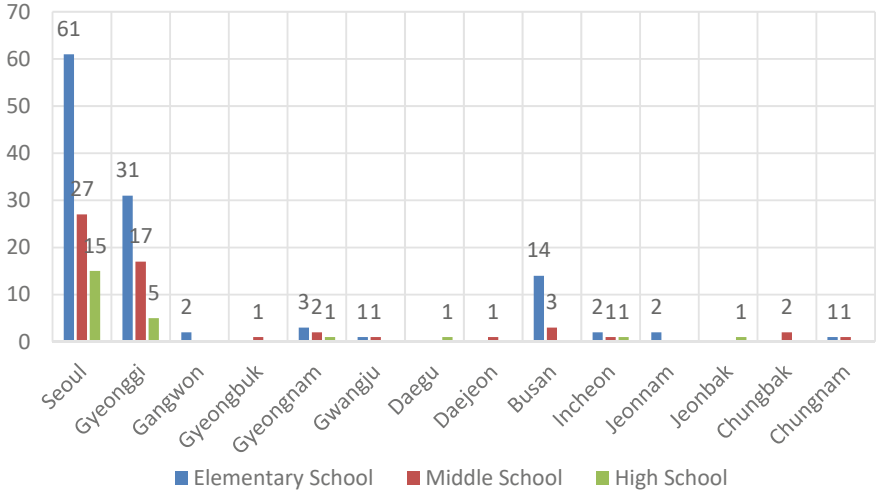

Fig. 3 The status of school complex facilities in Korea [11]

3.1 Current Status of School Complexation by Year

In Seoul, the complexation of school facilities began in 2001 and began in earnest in 2004. Since then, the largest number of complexes has been combined to 19, but the number of complexes has decreased again since 2006 (Fig. 5).

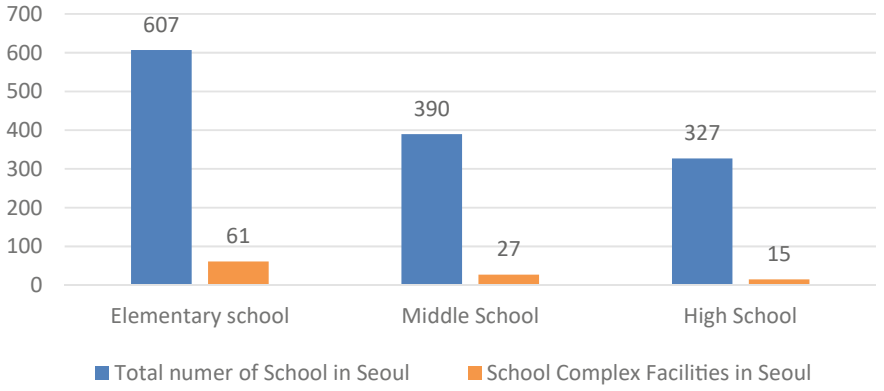

Fig. 4 Total number of school facilities and complex facilities in Seoul

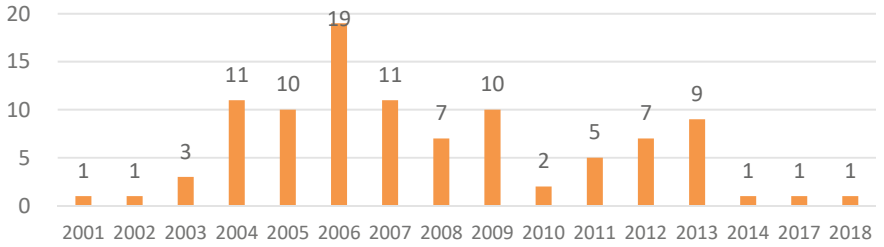

Fig. 5 Number of school complex facilities in Seoul

3.2 Current Status of School Complex Facilities by District

In order to examine the current status of complexation by autonomous district, the ratio of school complexation is summarized as shown in Fig. 6. Three out of 25 autonomous districts in Seoul did not integrate schools, five autonomous districts with less than 5%, four autonomous districts with 10.1–15.0%, and two 15.1–20.0%. There were 10 autonomous districts with 5.1 to 10.0%, and 1 autonomous district with 20% or more was Gangbuk-gu. Through these analysis results, it was found that the progress of school complex facilities varies greatly depending on the region.

3.3 Current Status of School Complexation by Programs

As a result of examining 99 complex facilities, it is divided into three types of complex facilities: underground parking lots, sports facilities, and cultural facilities. Among them, sports facilities are the most common, followed by underground parking lots

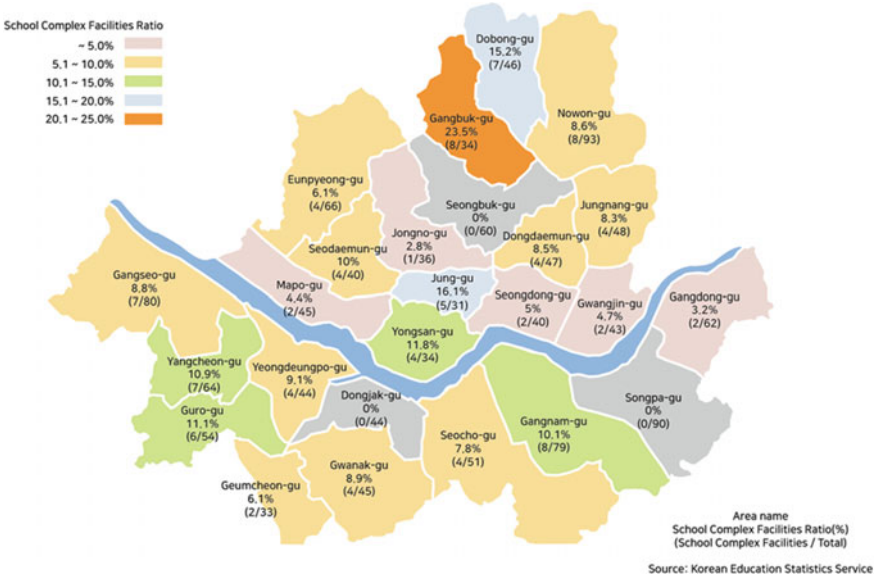

Fig. 6 A Diagram of the school complex facilities by autonomous region in Seoul

and cultural facilities. In the case of sports facilities for all, it occupies the largest number of auditoriums (sports centers) in existing schools.

In the case of cultural facilities, they were created along with other facilities, and there are significantly fewer cases where there are only cultural facilities. In addition, most of the programs configured were similar (Fig. 7 and Table 3).

Fig. 7 Daedeok elementary school auditorium and library/Nanwoo middle school public parking lot [12, 13]

Table 3 Depending on the program and area

Area	A	B	C	A, B	A, C	A, B, C	Total
~ 1000 m^2	13						13
1001–3000 m^2	22	2	2	8	3		37
3001–5000 m^2	1		6	4	2	3	16
5001–7000 m^2			3	1	4	2	10
7001–9000 m^2			3	2	2	4	11
9001–11,000 m^2			1		2	1	4
11,001 m^2 ~						8	8
Total	36	2	15	15	13	18	99

A Sports facilities for all living *B* Cultural facilities *C* Underground parking lot

4 Direction for the Integration of Regional-Linked School Facilities

The results of analyzing the current status of school complex facilities in Seoul are as follows. First, it started in 2001 and proceeded in earnest in 2004, but the number of projects has decreased sharply since 2016. Second, about 5.1–10% of the total school facilities were complexed, but there were significantly fewer places where the complexation took place and the regional variation was severe. Lastly, there were the largest number of sports facilities to utilize existing auditoriums and playground facilities, followed by complex facilities that combine sports facilities, cultural facilities, and underground parking lots. However, most of them consisted of similar programs.

Based on these current statuses and limitations, this study would propose a planned and institutional direction for the complexation of school facilities.

First, institutional incentives for school complex facilities should be provided. Regardless of the species of the zone, it is necessary to ease the floor area ratio and the building and closing rate. In addition, during the construction period of large-scale facilities, for the safety of students, the local education office's policy is also needed to conduct construction with a gap of one to two years after existing students graduate. In this case, cooperation from nearby schools must be made. In addition, it is essential to improve the stability, aesthetics, and environmental aspects of temporary teachers (modular teachers), which have recently become issues.

In addition, the direction in terms of planning is as follows. Appropriate programs should be provided in consideration of regional characteristics. In addition, a participatory design in which local residents participate on their own and set up planning and programs should be applied. In particular, an alternative is needed so that residents and schools can operate the "Living Lab" to proceed with the process and operation after completion. This is to minimize the possibility of civil complaints and to ensure sustainability as a regional hub facility. At this time, when preparing

a hub facility, it shall be carried out in consideration of the safety of students, such as movement plan and opening time.

5 Conclusion

As the Korea's step-by-step education curriculum continues to change, the absence of architectural spaces or uniform educational spaces that support this is becoming a problem. In addition, as the number of students decreases, interest in space utilization is increasing. The school space is changing according to these changes in the times and social demands, and the government has started to carry out the "Green Smart School" project. One of the main areas of this project is school complexation, and this project is linked to the "Living SOC Complexation Project." By compounding various facilities in one building, it is easy to secure a site, link functions, and programs, and the efficiency of movement is high.

Accordingly, school complexation is necessary in that it can be solved by implementing a sustainable city and re-examining the role of the school as an urban base facility, and using insufficient space as a school space.

For this study, the results of examining 103 schools in Seoul are as follows. First, the number of projects decreased from a specific year, and second, the complexation ratio was lower than the total number of schools, and there were variations by region. Finally, similar programs were combined. Based on this, the institutional and planned direction of the complexation of regional-linked school facilities was proposed.

Above all, it is used as a school complex as a regional hub space by incorporating a smart living-lab that allows local residents to continuously participate from planning to post-construction operations and record, maintain, and manage local changes. This study is expected to be used as basic data for the introduction of new programs to complex facilities.

References

1. The Ministry of Education (2021) 2021 Education Statistics Analysis Data Collection, pp 6, 136
2. Statistics Korea Homepage. https://kostat.go.kr/portal/eng/index.action. Last accessed 24 Sept 2022
3. Joint with relevant ministries (2021) Guidelines for selecting a life SOC complex project in 2022, pp. 6, 9
4. Cabinet Office Life SOC Promotion Team: press release-3 years of hard work. Our neighborhood life SOC
5. Life SOC Homepage. https://www.lifesoc.go.kr/main. Last accessed 24 Sept 2022
6. Reigh YB (2011) Everybody's schools, schools as community hubs. J Korean Inst Educ Facil 18(4):39–45
7. Hwang SH, Park SB (2010) A study on the local residents' needs for mixed-use school facilities. J Korean Housing Assoc 21(5):125–135

8. Lee JY, Kim YH (2018) Problems analysis of spatial system and in opening school facilities. KIEAE J 18(5):5–12
9. Kim JS, Yoo HY (2020) A study on the planning direction of local connected school facilities for the neighborhood regeneration. J Archit Inst Korea Plann Des 36(5):71–82
10. Ministry of Education.: Guidelines for the 2022 Living SOC School Facilities Complex Project, 13 (2021)
11. Ministry of Education (2021) The status of school complex facilities
12. Korea Institute of Education Facility Safety, Green Smart Future School Design Guidelines by Core Elements Helping Data Collection, p 55 (2021)
13. DongA ilbo. https://www.donga.com/news/Society/article/all/20100106/25219783/1. Last accessed 24 Sept 2022

Structural Design and Structural Mechanics

Application of Preference Information in Truss Design

Tao Zhang, Weifang Xiao, and Xianzhong Zhao

Abstract Many automated structural design methods have been developed to improve design efficiency and quality. However, most of them can only consider the quantitative objectives and constraints. This may ignore the important qualitative design information, which limits the functionality and efficiency of these methods. To solve this problem, qualitative information needs to be effectively integrated into the design process. To this end, this study aims at modeling the user shape preference to guide the generation of satisfactory truss structures. A prediction model for user preference is proposed by generating the data set and selecting the appropriate machine learning method. Besides, Physical Programming is adopted to combine the prediction model with a grammar-based computational design method. Finally, a new automated design method for truss structures is developed.

Keywords User shape preference · Prediction model · Truss design method

1 Introduction

In recent years, many automated structural design methods have been developed to realize a rapid design process. Satisfactory design results can be achieved due to the improvement in design efficiency and quality. The design of structures is a complicated decision-making process involving multiple factors, which includes not only qualitative but also quantitative parameters. However, most of the current methods can only consider the quantitative objectives and constraints. It is difficult to apply qualitative information during the automatic design process, which limits the functionality and efficiency of these methods.

To solve this problem, qualitative information needs to be transformed into a new form that can be recognized and processed by computers. Different from quantitative

T. Zhang (✉) · W. Xiao · X. Zhao
Department of Structural Engineering, Tongji University, Shanghai 200092, China
e-mail: zhangtao1994@tongji.edu.cn

T. Kang (ed.), *Proceedings of 5th International Conference on Civil Engineering and Architecture*, Lecture Notes in Civil Engineering 369,
https://doi.org/10.1007/978-981-99-4049-3_81

information, e.g., weight and displacement, which can be defined by specific mathematical formulas, the qualitative information is generally empirical and subjective. This makes it difficult to be quantified. User shape preference is one of the typical qualitative design information that deeply affects the design result. Therefore, it is investigated in this study.

Plenty of studies have been carried out to explore an appropriate and efficient way to apply qualitative information in the structural design process. Some of them tend to use humans to replace the evaluation/fitness function in the optimization system [1]. Thus, interactive design methods such as Interactive Evolutionary Computation (IEC) are developed. Von Buelow et al. proposed an interactive design method with IEC for discrete structures. The designers or users can influence the choice of parents for the subsequent generation during the genetic algorithm (GA) optimization process until a satisfactory design is obtained [2, 3]. Muller et al. presented a new computational approach that extends the application range of the existing IEC method to the rigid frame structure design [4, 5]. Interactive Particle Swarm Optimization (PSO) is also an important interactive design method [6]. Felkner et al. presented an interactive framework for the truss design based on the interactive PSO. The framework has been successfully applied in the design of 2D and 3D truss structures [7, 8]. These interactive design methods can obtain satisfactory results because of the direct participation of users. However, the long-time interaction may cause user fatigue problems [9], which reduces the design quality and efficiency.

In other studies, preference information was defined as specific values, functions, or models. Furuta et al. developed a supporting system for the aesthetic design of dam structures which used the Analytic Hierarchy Process (AHP) method to reflect the user preference in a fitness function [10]. Neural networks can also be employed to provide user evaluation information. Chikata et al. conducted the scenery evaluation for concrete retaining walls using neural networks [11]. Bailey and Raich modeled the preference information by using neural networks. Then, the modeled information was combined with GA to generate Pareto-optimal designs [12]. Overall, these methods can quantify the preference information for re-use. Thus, the user dependence is reduced. However, the improvement in the accuracy of the preference functions remains a challenging task.

This study aims at applying user shape preference in the design of plane truss structures to improve design quality and efficiency. An accurate prediction model for user shape preference is proposed. After that, it is integrated with a grammar-based computational design method named Structural Topology and Shape Annealing (STSA) for generating satisfactory structures. In the next section, a brief introduction to STSA is presented. Then, the main steps of preference modeling are described. Finally, the combination of the prediction model with the STSA method is explained.

2 Structural Topology and Shape Annealing (STSA)

STSA is a structural topology generation and optimization technique that combines shape grammars and performance evaluation with a heuristic optimization algorithm [13]. Shape grammars (see Fig. 1) define a set of rules for structural modifications involving size, shape, and topology modifications. The selection probability of each rule is dynamic and based on the merit of the rule. More details on STSA are described in Shea [14]. These grammars can be used to transform the structures more flexibly. Performance evaluation integrates multiple design criteria including objectives and constraints with dynamic weights to evaluate the quality of a structure. A simulated annealing (SA) algorithm with a modified annealing schedule provides an iterative optimization framework for the global exploration of the complex design space. The workflow of STSA is shown in Fig. 2.

When designing a structure by STSA, an initial design with basic design information (e.g., constraints and loading conditions) needs to be given. The input design is modified using the shape grammars to form a new design. Then, the design quality is analyzed and evaluated. The acceptance or rejection of the new design is decided according to the SA schedule. The above-mentioned procedure is repeated in an iterative loop until a satisfactory design is found. Compared with other design methods, STSA is capable of generating more innovative and flexible truss forms which provide more possibilities for structural design. The STSA method has been successfully applied in engineering practice [13, 15].

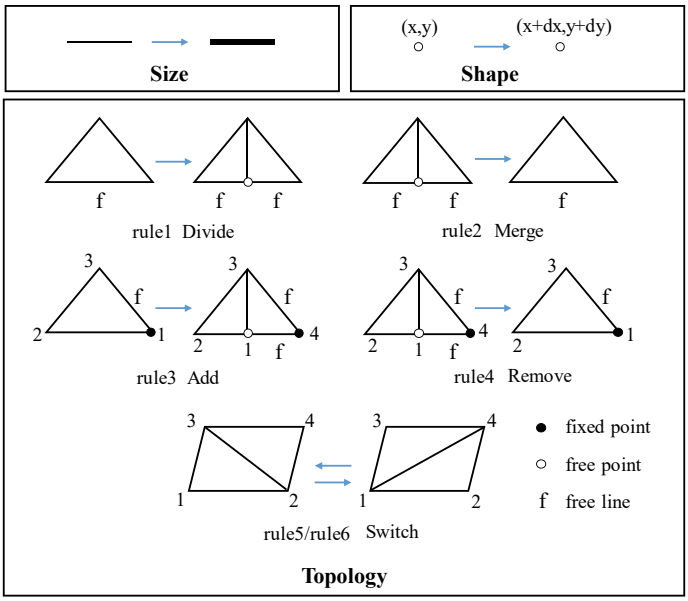

Fig. 1 Shape grammars for plane truss [14]

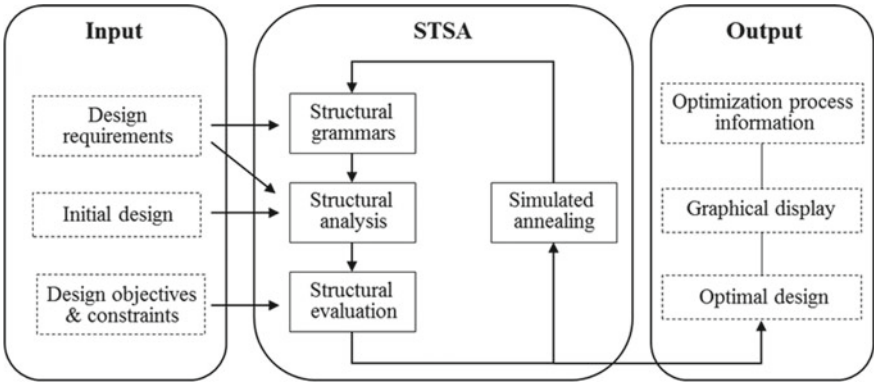

Fig. 2 Workflow of STSA method

Fig. 3 Design area for truss structures

3 Sample Generation and Feature Recognition

3.1 Generation of Random Truss Samples

To ensure the diversity of sample shapes and the generality of the results, the truss samples are generated by the STSA method with random loading conditions. The design area (see Fig. 3) is a rectangle of 2000 units long and 1000 units high. The two ends of a truss sample are hinge supports. Except for these two endpoints, other nodes can be added, deleted, or moved. In the end, a sample population containing 200 plane trusses is obtained. Each of them has less than 50 members.

3.2 Recognition of Truss Features

The visual distinction is the basis to express the user shape preferences for truss structures. The features of samples need to measure the visual information numerically. Therefore, the effective truss features need to be distinguishable and can describe the geometric characteristics of truss shapes accurately. To find such features that

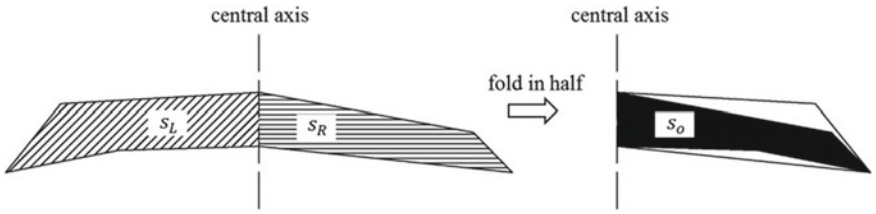

Fig. 4 Definition of symmetry rate

meet the requirements, 26 initial truss features are defined and collected. They are evaluated and verified one by one in the following.

Each initial truss feature has a specific mathematical expression. The result of the expression represents an aspect of the structural geometry such as the structural height or symmetry. Some features can be calculated with fundamental structural information such as Height-Span Ratio (HSR) which uses the maximum height at nodes divided by the span. A more complicated definition of features is also possible. For example, Eq. (1) shows an initial truss feature named Symmetry Rate (SyR) which describes the symmetry of a truss structure. In Fig. 4, a truss structure is folded along the central axis. The overlapping area is divided by the maximum area on both sides of the axis to measure the structural symmetry. If choosing the smaller one as the denominator, it may be completely covered by the larger one. Therefore, the larger area is chosen as the denominator. A higher value of SyR means that the truss structure has a better property of symmetry.

$$SyR = \frac{S_O}{\max(S_L, S_R)} \tag{1}$$

where S_O = overlapping area; S_L = area on the left side of the central axis; and S_R = area on the right side of the central axis.

To identify the effective features, the K-means method is used to classify the truss sample population based on each truss feature. The clustering results are plotted on a graph, in which the truss samples belonging to the same group are drawn together. In addition, the average and standard deviation of each group are calculated. As mentioned before, the primary evaluation standard for a qualified feature is that the truss structures with different geometric shapes can be visually distinguished. Therefore, the truss samples in the same group should possess visual similarities whereas the truss samples in different groups are visually different. Meanwhile, the numerical results provide references for evaluation. The evenly distributed averages and smaller standard deviations imply the validity of the feature. Three structural designers are invited to participate in the evaluation process.

The initial features are evaluated one by one. Nine effective features are selected to constitute a feature vector that describes five geometric attributes of truss shapes, as shown in Table 1.

Table 1 Effective feature vector

Basic size	Complexity	Mid-span width	Flatness	Symmetry
Height-span ratio	Number of members	Truss depth	Top chord height differences	Symmetry rate
Mid-span clear height	Average length of web members	Dispersion of nodes	Bottom chord height differences	

4 Preference Information Acquisition

The labels of samples are generally obtained from a human interactive process based on the user preference information. This section aims at collecting this preference information more easily and effectively.

According to previous studies [16, 17], users prefer grouping the samples before evaluation. This reduces the burden on users. Therefore, the truss samples are grouped based on the similarities before the user's evaluation. The users need to choose a preferred sample group. After that, the samples in the group are evaluated. This will effectively reduce the time needed for user interaction and avoid user fatigue problems.

SOM [18] method is applied in this study to group the truss samples based on the feature vector. The sample population is clustered into nine groups, which is considered beneficial for user evaluation. Then, an interaction system written in C# programming language is developed to collect information on user shape preference, as shown in Fig. 5.

There exist mainly two user interfaces in the system, i.e., the Selection interface and the Evaluation interface. In the Selection interface (see Fig. 5a), the user can preview the groupings of truss samples (the clustering results) in the left window and choose a preferred group. Then, the system jumps to the Evaluation interface (see Fig. 5b), where the user can evaluate the current sample on the right side. The current sample is presented in random order and three simple evaluation options are available: "Preferred," "Acceptable," and "Disliked," which correspond to 1, 2, and 3 points, respectively.

Five students were invited to experience the system. They were asked to choose one preferred group and complete the evaluation. Then, a validation group corresponding to the preferred group, which contains 30 truss samples, is presented for evaluation. In addition, suggestions for improving the system are collected. After that, the students were further asked to complete the evaluation of other groups and their validation groups for the generation of the data sets. The truss samples in the validation group were randomly generated by using the STSA method. Note that their feature values need to lie within the application range of all samples' feature values of the corresponding group.

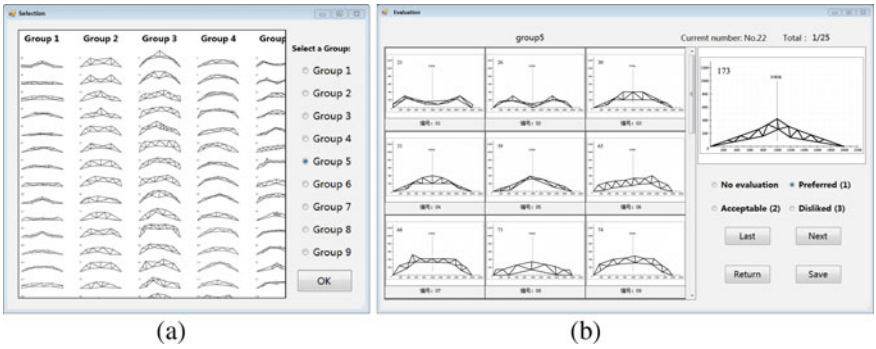

Fig. 5 Screenshots of the interaction system: **a** selection interface; **b** evaluation interface

5 Algorithm Selection for Prediction Model

Two classical machine learning methods, namely Back Propagation Neural Network (BPNN) [19] and Random Forest (RF) [20], are used to develop the prediction model based on the data sets generated in Sect. 4. A numerical experiment is conducted to compare the prediction performance of these two methods.

The validation groups are input for the corresponding prediction models to calculate the outputs which are continuous values between 1 and 3. Mean Square Error (MSE) and Prediction Accuracy (PA) are defined as the evaluation indicators. As shown in Eq. (2), MSE measures the errors between the predicted values and the label values. PA represents the prediction accuracy, which is calculated using Eq. (3).

$$\mathrm{MSE} = \frac{\sum_{i=1}^{N} (y_i - \widehat{y_i})^2}{N} \tag{2}$$

$$PA = \frac{n_c}{N} \times 100\% \tag{3}$$

where N = number of samples; y_i = label value of the ith sample; $\widehat{y_i}$ = predicted value of the ith sample; n_c = number of correct predictions.

Based on the evaluation results using the indicators mentioned above, the RF method gets higher PA values and lower MSE values. This indicates that the prediction models using the RF method have better prediction abilities. Furthermore, the model parameters of the RF method are more universal whereas the model parameters of BPNN need to be adjusted for every group. Therefore, the RF method meets better the needs of this study and is considered more appropriate for developing the prediction models.

6 Combination of Prediction Model and STSA Method

Section 5 has verified the effectiveness of the model construction method which converts the user shape preference into numerical values. However, how to use the numerical information to guide the generation of truss structures remains a problem. This section focuses on the effective combination of the prediction model and the STSA method.

The design process of a structure usually involves trade-offs between multiple factors. Therefore, the optimal design is a multi-objective optimization problem (MOP). The classical methods for solving MOPs, such as the weighted-sum method, usually rely on the user's judgment of the relative importance of different objectives. However, it is generally difficult for users to determine the weighted values which integrate the objectives with different physical meanings and orders of magnitude, especially when a MOP involves qualitative objectives. To overcome this difficulty, Physical Programming (PP) [21] is used in this study.

Instead of setting weights, the users can express their expectations for each objective in a more meaningful way by using the PP method. They only need to specify several ranges such as desirable (D), tolerable (T), undesirable (U), unacceptable (UNA), etc. for each objective and the boundary values. Then, a class function $\overline{g}(x)$ is introduced for each objective. Figure 6 shows a possible class function for the objective function $g_i(x)$ such as the structural weight. The smaller the objective value, the better. The parameters $\overline{g}_i^1$ to $\overline{g}_i^3$ should be the same for different class functions. Thus, different objectives can be mapped to the same solution space. Finally, an aggregate function is obtained by combining all objectives' class functions in the optimization model.

Structural weight, node displacement, and user preference, defined in Eqs. (4)–(6), are selected as the design objectives in this study. Based on the PP method, the aggregate function $G(x)$ is defined in Eq. (7). For the user preference objective, the boundary values are determined as 1.5, 2.5, and 3 according to the evaluation options (see Fig. 5b) and rounding rule. The boundary values of other objectives need to be

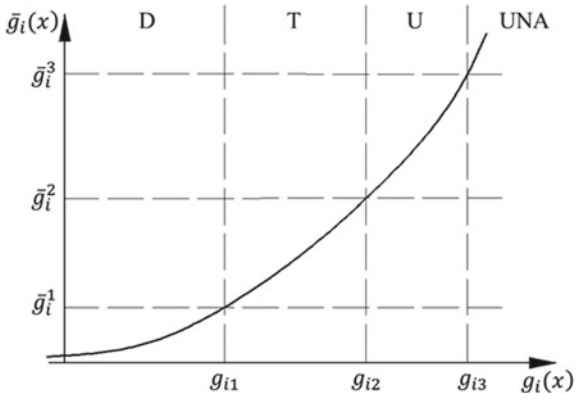

Fig. 6 A possible class function

set by the user or designer.

$$g_1 = \min \sum_{i=1}^{n} \rho l_i s_i \tag{4}$$

$$g_2 = \min \left[\max_{1 \le j \le m} (\text{disp}_j) \right] \tag{5}$$

$$g_3 = \min \text{ pref} \tag{6}$$

$$G(x) = \sum_{k=1,2,3} \overline{g}_k [g_k(x)] \tag{7}$$

where ρ = material density; n = number of members; l_i = length of the ith member; s_i = cross-sectional area of the ith member; m = number of nodes; disp_j = displacement of the jth node; pref = preference prediction value.

The aggregate function $G(x)$ becomes the core part of the performance evaluation of the STSA method, which effectively coordinates the user preference objective with conventional quantitative objectives. In addition, it combines the prediction model and the STSA method.

Embedding the interactive system into the STSA algorithm, an innovative automated design method is obtained. When designing a truss structure with this method, the designer or user needs to complete the evaluation using the interactive system. After that, the prediction model is developed automatically. Then, the optimization process starts and the structural evaluation information is calculated through the aggregate function. Finally, the design result is obtained. If no satisfactory result is obtained, the designer or user can reset the boundary values to restart the design process.

Two students experience the design process based on a simple design case, and both get satisfactory results. Furthermore, their suggestions for improvement are collected to optimize the design process.

7 Conclusions

In this study, an innovative truss design method is presented which incorporates the user shape preference to the automated truss design process. To convert the preference information into a computable design objective, a prediction model for user shape preference is developed. Specifically, a truss sample population is generated randomly. A feature vector is defined to describe the geometrical characteristics of the truss structures. To collect the preference information effectively, an interactive system is designed. Finally, the Random Forest method is used to develop the prediction model. Besides, the Physical Programming method is employed to combine the

prediction model with the STSA method which forms the basis for developing an innovative automated design method for truss structures. Compared to other automated methods, the new design method can consider qualitative design information during the optimization process, which improves the functionality of the method. Meanwhile, the validity of the method is verified by a design case.

References

1. Takagi H (2001) Interactive evolutionary computation: Fusion of the capabilities of EC optimization and human evaluation. P IEEE 89(9):1275–1296
2. Von Buelow P (2008) Suitability of genetic based exploration in the creative design process. Digital Creativity 19(1):51–61
3. Turrin M, Von Buelow P, Stouffs R (2011) Design explorations of performance driven geometry in architectural design using parametric modeling and genetic algorithms. Adv Eng Inform 25(4):656–675
4. Mueller C, Ochsendorf J (2011) An interactive evolutionary framework for structural design. In: 7th International seminar of the IASS structural morphology group. London
5. Mueller CT, Ochsendorf JA (2015) Combining structural performance and designer preferences in evolutionary design space exploration. Automat Constr 52:70–82
6. Madar J, Abonyi J, Szeifert F (2005) Interactive particle swarm optimization. In: 5th international conference on intelligent systems design and applications (ISDA'05). IEEE, pp 314–319
7. Felkner J, Chatzi E, Kotnik T (2013) Interactive particle swarm optimization for the architectural design of truss structures. In: 2013 IEEE symposium on computational intelligence for engineering solutions (CIES). IEEE, pp. 15–22
8. Felkner J, Chatzi E, Kotnik T (2015) Interactive truss design using particle swarm optimization and NURBS curves. J Build Eng 4:60–74
9. Machwe AT, Parmee IC (2009) Reducing user fatigue within an interactive evolutionary design system using clustering and case-based reasoning. Eng Optimiz 41(9):871–887
10. Furuta H, Hase H, Watanabe E, Tonegawa T, Morimoto H (1996) Applications of genetic algorithm to aesthetic design of dam structures. Adv Eng Softw 25(2–3):185–195
11. Chikata Y, Yasuda N, Matsushima M, Kobori T (1998) Inverse analysis of aesthetic evaluation of planted concrete structures by neural networks. Comput-Aided Civil Infrastruct Eng 13(4):255–264
12. Bailey B, Raich AM (2012) Modeling of user design preferences in multiobjective optimization of roof trusses. J Comput Civil Eng 26(5):584–596
13. Shea K, Smith I, Asce F (2006) Improving Full-Scale transmission tower design through topology and shape optimization. J Struct Eng 132(5):781–790
14. Shea K (1997) Essays of discrete structures: purposeful design of grammatical structures by directed stochastic search. Carnegie Mellon University
15. Xianzhong Z, Kristina S (2010) Intelligent generation and design of spatial truss structures. J Build Struct 31(9):63
16. Ohsaki M, Takagi H (1998) Improvement of presenting interface by predicting the evaluation order to reduce the burden of human interactive EC operators. In: SMC'98 Conference proceedings. 1998 IEEE international conference on systems, man, and cybernetics (Cat. No. 98CH36218). IEEE, pp 1284–1289
17. Bailey B, Raich A (2006) Capturing user aesthetic design preferences during multi-objective roof truss optimization. In: Joint int. conference on computing and decision making in civil and building engineering (ICCCBE), Montreal, pp 3374–3384
18. Kohonen T (1990) The self-organizing map. P IEEE 78(9):1464–1480

19. Hecht-Nielsen R (1992) Theory of the backpropagation neural network neural networks for perception. Elsevier, pp 65–93
20. Breiman L (2001) Random forests. Mach Learn 45(1):5–32
21. Messac A (1996) Physical programming: effective optimization for computational design. AIAA J 34(1):149–158

Research on Hysteresis Model of High Damping Rubber Bearings Considering Mechanical Properties Based on Dynamic Loading Test

K. H. Park, T. Mazda, and Y. Kajita

Abstract High damping rubber bearings (HDR) are made by combining natural rubber with carbon fillers. Because of its simple structure can be easily applied to seismic isolation design and is easy to manage. Also, high damping rubber bearings are seismic isolators with excellent damping ability against earthquakes. High damping rubber bearings have high horizontal flexibility against earthquake motion and can dampen seismic energy, but the mechanical dependence resulting from material properties cannot be ignored. This research aims to experimentally reveal the dependence and nonlinearity of high damping rubber based on dynamic loading tests and to propose an advanced accurate hysteresis model. First, a dynamic loading test was performed using a scaled-down high damping rubber specimen, and mechanical properties such as equivalent stiffness, equivalent damping constant, and strain energy were evaluated. Subsequently, based on the mechanical evaluation, a hysteresis curve was modeled considering the characteristics of high damping rubber. In this research, a hysteresis model considering these characteristics was proposed by focusing on the rate dependence due to the Mullins effect and the hardening phenomenon occurring in the region of large shear deformation, such as a large earthquake. Finally, the actual behavior of high damping rubber and the feasibility of the modeling procedure were evaluated by comparing the results of the dynamic loading test using seismic waves assuming real earthquakes and dynamic analysis. As a result, it was possible to propose a hysteresis model that can represent the nonlinear characteristics of high damping rubber.

Keywords High damping rubber · Dynamic loading test · Hysteresis model

K. H. Park (✉) · T. Mazda · Y. Kajita
Kyushu University, 744 Motooka Nishi-Ku, Fukuoka, Japan
e-mail: 3TE21920S@s.kyushu-u.ac.jp

T. Kang (ed.), *Proceedings of 5th International Conference on Civil Engineering and Architecture*, Lecture Notes in Civil Engineering 369,
https://doi.org/10.1007/978-981-99-4049-3_82

1 Introduction

Research in many related fields has been continued to minimize the damage to buildings and structures through earthquake-resistant design to prepare for earthquakes. After the Kobe Earthquake that occurred in Japan (1995), it is true that seismic isolation design, which is a method to further improve stability against earthquakes, has been attracting attention rather than structures built with earthquake-resistant design. The purpose of seismic design is to use seismic isolators to prevent damage to structures as well as to prevent additional secondary damage in case of strong earthquakes. What is required of such a seismic isolator is the ability to have strong vertical stiffness and flexible ability to horizontally at the same time. A laminated rubber bearing is one of the seismic isolators that can be deformed in the horizontal direction between the lower part of the column and the foundation of the structure designed to realize the seismic isolation performance. Laminated rubber bearings are made by stacking thin rubber sheets with steel plates. Since it has high rigidity in the vertical direction, the ability to support the superstructure is excellent. In addition, since it has flexible rigidity and deformability in the horizontal direction when a strong earthquake occurs, the period of the structure is lengthened to minimize the damage from the earthquake. The types of laminated rubber bearings are broadly classified into Natural Rubber Bearings (NRB), Lead Rubber Bearings (LRB), and High Damping Rubber bearings (HDR), depending on the materials used. Since the rubber layer of NRB is made of natural rubber and has no damping ability, it is characterized in that it must be designed in parallel with an energy-absorbing device such as a damper for seismic isolation. The LRB and the HDR are currently the most widely used seismic isolators, and their characteristic is that they not only function as bearings supporting the upper structure but also have the ability to absorb energy against vibration, in contrast to NRB. Therefore, the advantage is that seismic isolation design is possible only with bearings. The LRB exerts its damping ability from a lead plug that is inserted into the center of the bearing. The HDR is a seismic isolator that has the damping ability of the rubber itself by mixing natural rubber with carbon filler. HDR is increasingly used in various fields due to its excellent damping ability against vibration energy, ease of construction and management, and the use of eco-friendly materials. However, the behavior of high damping rubber bearings is highly complex. The dependence and nonlinear characteristics occurring in the material properties cannot be ignored in the design of seismic isolation using HDR. The obvious factors causing the dependence of HDR are temperature, surface pressure, and shear strain. A hysteresis model capable of representing such nonlinearity and hysteresis characteristics is essential for a more accurate and precise design of HDR applied seismic isolating structure. In this research, the hysteresis curve of HDR was modeled for dynamic analysis considering the nonlinearity caused by the dependency of experienced shear strain. At the same time, when a rubber bearing using a rubber material is subjected to a large deformation region, a hardening phenomenon in which shear stiffness is rapidly increased occurs. When the hardening phenomenon occurs, the long periodization and damping performance which are the advantages of seismic isolation rubber are

lost. [1] Currently, the bilinear model is the most widely used as a representative hysteresis model in seismic isolation design. Although the bilinear model is widely used in design as a hysteresis model of seismic isolation bearings, there are many uncertainties about the accuracy of seismic response analysis. The bilinear model is generally limited to the mechanical properties of HDR. In most cases, this model is difficult to represent the hardening phenomenon. In the research on the hysteresis model of HDR isolators so far, TAKENAKA proposed a modified HD model considering the experienced shear strain dependence of HDR [2]. YOSHIDA suggested a hardening damage model by extending the bilinear model [3]. Furthermore, Nguyen Quang Tam modeled the hysteresis model of HDR through nonlinear rheological mechanical behavior, and there is an improved rheology model that considers rate-dependent cyclic behavior based on the load test results using HDR specimens [4, 5]. FUJISAWA presented a double target model by dividing the initial and normal history of HDR [6]. OHTORI proposed an improved double target model that can approximate the restoring force characteristics of HDR [7, 8]. This hysteresis model is complicated in parameter setting and has limitations in its simple application in seismic design. MAZDA proposed a bilinear double target model that eliminated the complexity of parameter setting based on the double target model. The seismic response analysis of the seismic isolation structure to which this model was applied was performed to show the restoring force characteristics of HDR [9, 10]. NAITO modeled the hysteresis curve of the LRB using a trilinear model considering the Mullins effect based on the results of the dynamic loading test [11]. High damping rubber has a nonlinearity in which stiffness is rapidly increased due to hardening that occurs in large shear deformations such as earthquakes, along with dependence on the experienced shear strain. Therefore, in this research, an advanced hysteresis model was developed considering the hardening phenomenon of HDR based on dynamic load tests. Dynamic loading tests were conducted using sine waves and seismic waves based on what was done in NIWA research [12]. Finally, the validity and effectiveness of the hysteresis model were investigated by comparing the results of the dynamic loading test with the results of the dynamic analysis performed by the proposed model.

2 Dynamic Loading Test

Two kinds of dynamic loading tests were performed by sinusoidal wave and seismic wave [11]. The purpose of the test by the sinusoidal wave is to investigate the hysteresis characteristics of HDR and to experimentally prove the dependence and hardening phenomenon. Next, the purpose of the test by the seismic wave is to confirm the actual behavior of HDR using an input wave assuming an actual earthquake. Figures 1 and 2 show the test specimen and test apparatus. HDR specimen of 110 mm × 110 mm × 73 mm produced by the YOKOHAMA RUBBER CO., LTD. was used. Dimension and material properties of HDR specimen are shown in Table 1. This specimen has four steel plates with a thickness of 2.3 mm between high

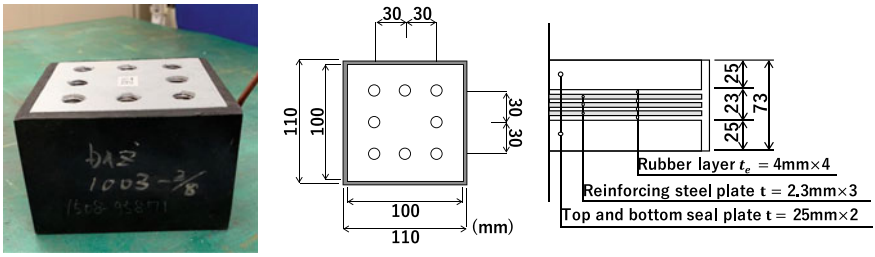

(a) specimen (b) plan view (c) side view

Fig. 1 Test specimen for dynamic loading test

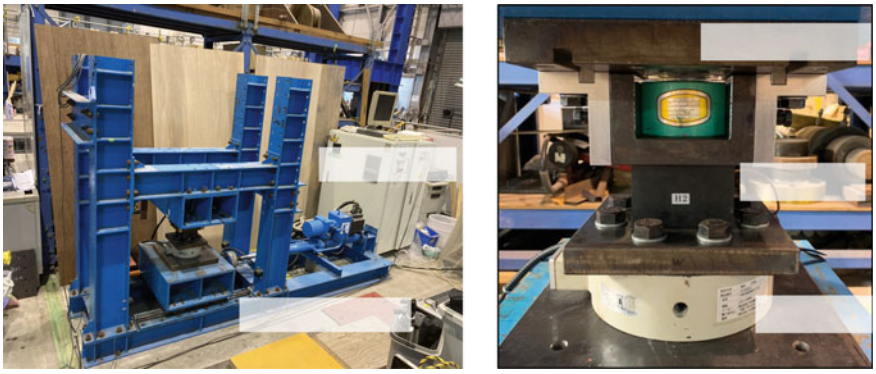

(a) side view (b) mounting of specimen

Fig. 2 Test setup of dynamic loading test

damping rubber layers. The specimen is subjected to shear deformation on the load cell installed in the hybrid actuator. The test specimen is constantly subjected to a vertical load of 60 kN from the hydraulic jack as in the test standard of manual for highway bridge bearings [13, 14]. A displacement measuring device is installed on the actuator and the specimen to measure the displacement of the specimen against shear deformation.

2.1 Sinusoidal Loading Test

The first dynamic loading test was conducted with a gradually increasing sine wave to investigate the dependence of HDR on the shear strain and the hardening phenomenon. Since HDR is characterized by the dependence of maximum shear strain in which the mechanical properties are changed by the shear strain received in the past, the loading conditions that start with a small shear strain were planned.

Table 1 Dimension and material properties of HDR specimen

Name of the material	High damping rubber
Cross-section (mm^2)	10000 mm^2
Number of rubber layers	4
Total rubber thickness (mm)	16
Thickness of one steel plate (mm)	2.3
Shear modulus (N/mm^2)	0.8
Shape factor, S_1	4.0
Aspect ratio, S_2	4.0

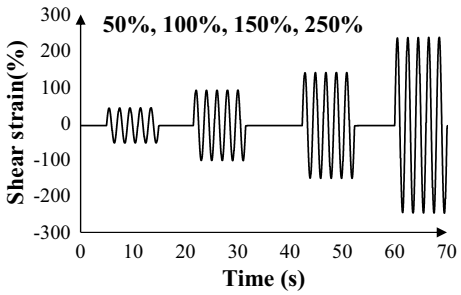

Fig. 3 Strain history of Sinusoidal loading test

The order of shear strain applied in the dynamic loading test is 50%, 100%, 150%, and 250%. The frequency of the sinusoidal wave was 0.5 Hz, and it vibrated five times for each shear deformation. The strain history of the sinusoidal loading test and the result of the sinusoidal loading test are respectively presented in Fig. 3. And Fig. 4. The hysteresis curve of HDR specimen for five cycles was obtained from the sinusoidal loading test. From the hysteresis curve obtained in this loading test, the stress change occurred even in the hysteresis loop of the same shear strain, especially after the first loop. This means that the mechanical properties are different for the same shear strain. In addition, in step 4 of the experimental results, in the hysteresis loop of 250%, which is the most considerable shear strain among the input waves, a hardening phenomenon in which the stiffness is rapidly increased can be confirmed. Overall, the hysteresis curves after the first hysteresis are consistent.

2.2 Seismic Loading Test

The second dynamic loading test is to apply shear deformation using random waves assuming earthquakes to the specimen and obtain a hysteresis curve close to the actual behavior of HDR. This random wave assumes a type 2 design earthquake of type 2 ground prescribed in Japan, and loading tests were conducted on three cases. The strain history of the seismic loading test is shown in Fig. 5. In this research,

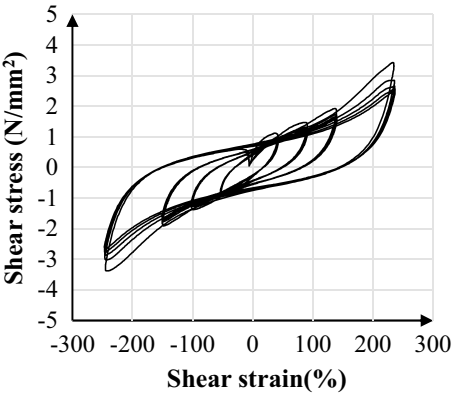

Fig. 4 Result of Sinusoidal loading test

since there is a limit to the number of data that can be input to the hybrid actuator, a part with a clear characteristic of shear deformation within the allowable number of data was used as the input wave. Figure 6 gives the results of seismic loading tests. This is the stress–strain curve of HDR test specimen when a random wave assuming a type 2 design earthquake is input [14]. This result is a hysteresis curve close to the actual behavior of HDR when an earthquake occurs, and from the test results, the dependence and nonlinearity due to the Mullins effect and hardening of HDR can be confirmed.

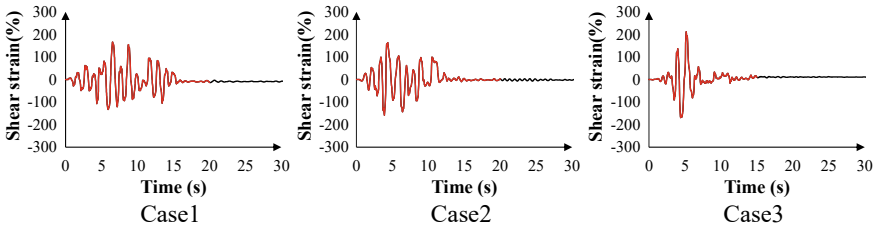

Fig. 5 Strain history of Seismic loading test

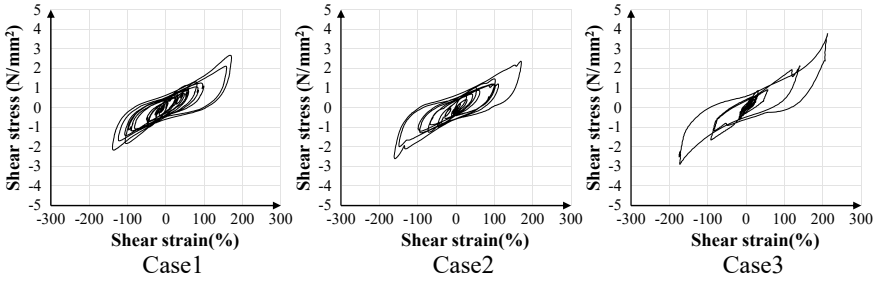

Fig. 6 Results of seismic loading tests

2.3 Dynamic Analysis

Based on the results of the dynamic loading tests, the hysteresis curve was modeled considering the nonlinearity of HDR. In this research, modeling was carried out based on the data of 250% shear strain, which showed the most prominent HDR hysteresis among the test results using increasing sine waves. To evaluate the validity of the modeling, dynamic analysis was performed by setting the same input wave as that of the loading test, and the respective results were compared. In addition, the accuracy of the proposed hysteresis model was evaluated compared to the results of the seismic loading test.

2.4 Modeling Procedure

In this research, a hysteresis model of HDR, which is called the trilinear double target model, is proposed that allows the accurate representation of the stress–strain relationship, including rate dependence for shear deformation. The conceptual diagram of the hysteresis model is shown in Fig. 7. Modeling of the hysteresis curve of HDR was performed based on the experimental data when 250% of shear strain was applied to the specimen from the dynamic loading test. The parameters considering the dependence of the maximum shear strain were determined by separating the experimental data of the initial hysteresis and the experimental data of the typical hysteresis. In addition, the hardening stiffness and the strain at which the phenomenon of hardening occurs within the hysteresis curve were set as parameters based on the experimental results, and rules were established so that the hardening stiffness could be applied in the region where the shear strain exceeds a specific range. Among the five cycles, the data of the first cycle was used for the initial history, and the data of the third cycle, which was relatively stable, was used for the standard history. The parameters include first stiffness, second stiffness, hardening stiffness, and unloading stiffness, which can be objectively determined based on the dynamic loading test results.

3 Analytical Conditions

In this dynamic analysis, the trilinear double target model proposed as a hysteresis model was applied to the single degree of freedom system supported in HDR. Analytical conditions are shown in Fig. 8. For the input wave, two types of waves used in the sinusoidal loading test and the seismic loading test were applied, respectively. Table 2 shows the parameters of the trilinear double target model. The parameters were divided into parameters G1, G3, and G5 for the skeleton curve of initial loading and parameters G2 and G4 for the skeleton curve of steady state to represent the experienced shear strain dependence for the input wave. In addition, the shear strain

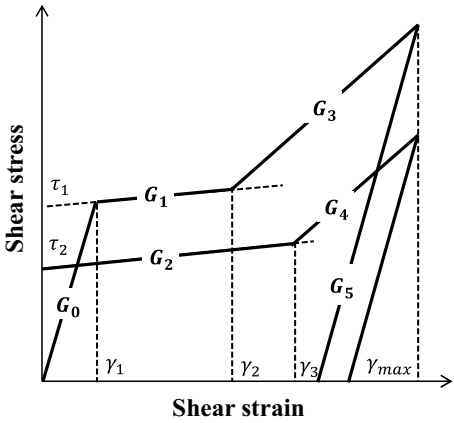

Fig. 7 Conceptual diagram of hysteresis model

at which hardening occurs was set based on experimental data. The hardening stiffness of the skeleton curve of initial loading was applied from a shear strain of 125%, and the hardening stiffness of the skeleton curve of steady state was set to be applied from a shear strain of 150%.

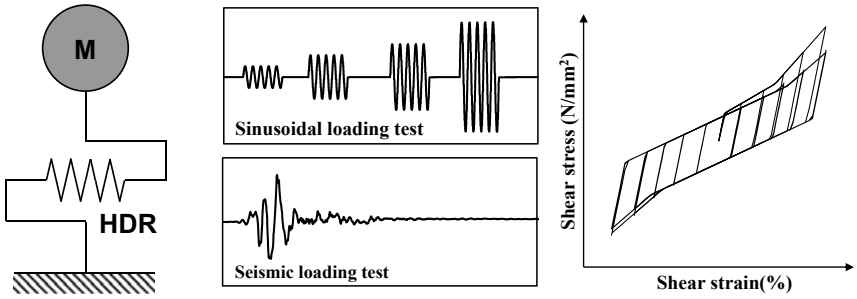

(a) Structural model (b) Input wave (c) Hysteresis model

Fig. 8 Analytical conditions

Table 2 Parameters of the trilinear double target model

G0(N/mm)	G1(N/mm^2)	G2(N/mm^2)	G3(N/mm^2)	G4(N/mm^2)
4385	830	668	1606	1232
G5(N/mm^2)	td1(N/mm^2)	td2(N/mm^2)		
7016	758	706		

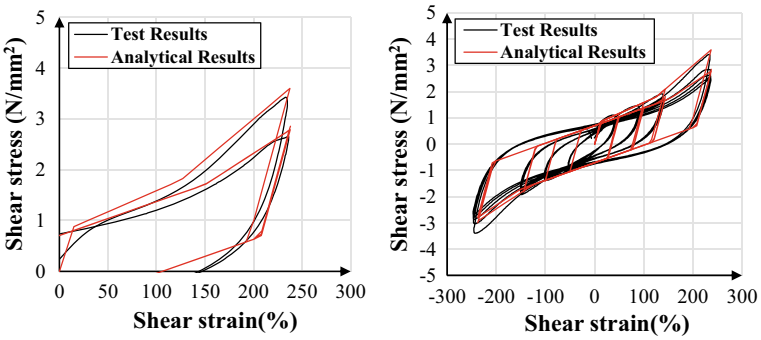

Fig. 9 Experimental and fitted stress–strain curves

3.1 Analytical Results

Figure 9 shows the experimental and fitted stress–strain curves. Analytical results of the trilinear double target model are shown in Fig. 11. This means comparing the test results with the trilinear double target model. From the results of the dynamic loading test, it was possible to distinguish between the initial hysteresis curve and the normal hysteresis curve. In addition, the hardening stiffness was applied according to the proposed modeling procedure so that the results of the dynamic load experiment could be realistically reproduced. As a result of performing dynamic analysis using the input wave of step 4 of the dynamic loading experiment by sinusoidal wave, the high agreement was confirmed for the shear strain of 250% and other cases. From the results of the dynamic loading test and dynamic analysis, the mechanical characteristics of HDR were evaluated. Figure 10 shows the comparison between the experimental and analytical results by calculating the maximum load, equivalent stiffness, damping constant, and strain energy.

4 Conclusions

In this research, dynamic loading tests by sinusoidal wave and by seismic waves were possible to understand the dependence, nonlinearity, and actual behavior of HDR using a hybrid actuator and HDR test specimen. Based on the test results, the modeling procedure of the trilinear double target model, which is a hysteresis model of HDR in dynamic analysis, was proposed. Finally, test results and analytical results considering the nonlinearity of HDR were compared. The following observations were made.

1. Under the sinusoidal loading test, the dependence of experienced shear strain and hardening phenomenon, hysteresis characteristics of HDR, were confirmed. Based on the test results, it was experimentally confirmed that the mechanical

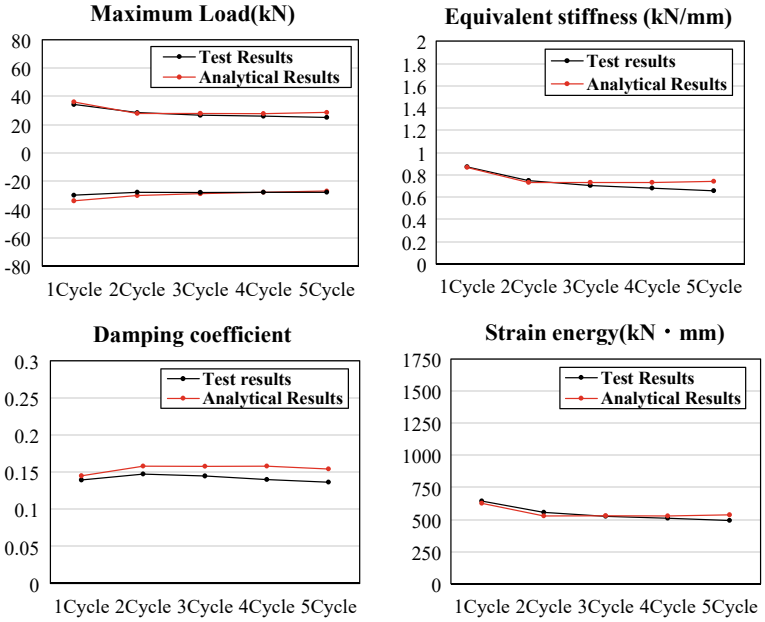

Fig. 10 Evaluation of mechanical properties of test results and analytical results

properties were significantly reduced after the first deformation for the same shear deformation due to the Mullins effect. In addition, it was confirmed that when a shear strain was exceeding a particular strain rate applied to the specimen, the stiffness rapidly increased, and the hardening phenomenon occurred. In the dynamic loading test using seismic waves, the actual behavior and hysteresis characteristics of HDR were confirmed by applying shear deformation of the specimen with random waves assuming the design earthquake motion.

2. The modeling procedure of the trilinear double target model, considering the dependence and hardening of HDR due to the Mullins effect, was proposed based on the test results and the concept of the bilinear model. This modeling procedure focused on improving the versatility and effectiveness of the hysteresis model by suggesting an objective procedure that anyone can set the same parameters. Since each parameter was calculated by separating the experimental data into the initial history and the steady state history, the Mullins effect of HDR could be considered. To model the hardening phenomenon, it was reflected that the strain rate at which each hardening occurred was different in the data of the initial history and the steady state history of HDR.
3. The validity of the trilinear double target model was evaluated by comparing the results of the dynamic loading tests and dynamic analysis. In this research, the analysis was performed using the same input wave as two dynamic loading tests on the SDOF structure to which HDR hysteresis characteristics by the trilinear double target model were applied. As a result, it was possible to reproduce HDR

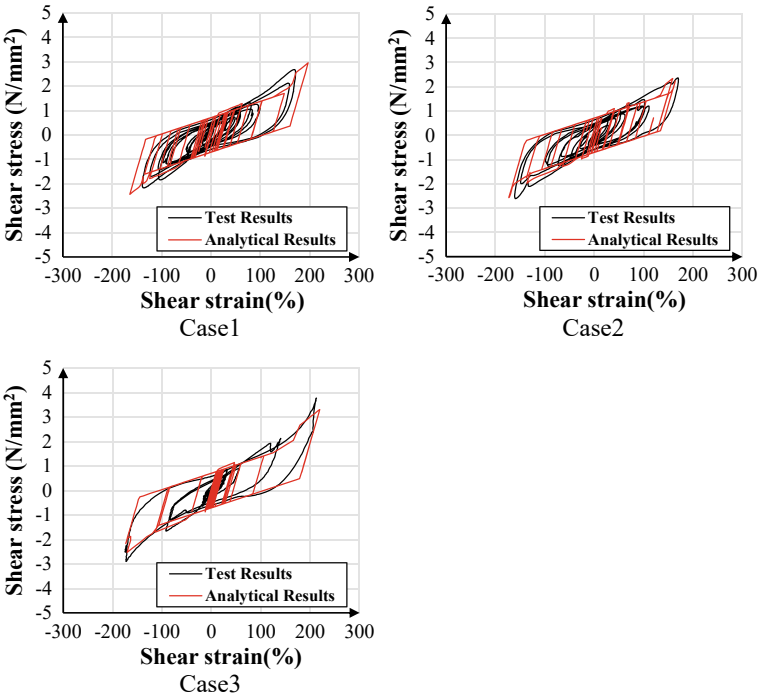

Fig. 11 Analytical results of the trilinear double target model

response in each dynamic loading test accurately. Finally, the evaluation of the mechanical properties between the experimental results and the dynamic analysis results was carried out. The maximum response load, equivalent stiffness, damping constant, and strain energy agree very well with the experimental results, making it possible to consider the nonlinearity of HDR.

Acknowledgments This research is part of the results of research conducted in collaboration with the HDR Study Group (Kawakin Core-Tech Co., Ltd., Sumitomo Riko Company Ltd., NIPPON CHUZO.K.K., Bridgestone Corporation, THE YOKOHAMA RUBBER CO., LTD.).

This research was supported by JST SPRING, Grant Number JPMJSP2136.

References

1. Furukawa A (2007) Seismic reliability analysis of isolated cable-stayed bridge considering hardening effect of seismic isolator and uncertain structural properties. J JSCE 475–484
2. Takenaka Y (2001) Modified H-D model: a new smooth-curve hysteresis model of laminated rubber bearings for base isolation. AIJ J Technol Des 14:87–92

3. Yoshida J (2014) Extended bilinear hysteretic models for laminated rubber bearings. J JSCE 70(2):238–251
4. Nguyen QT (2015) The modelling of nonlinear rheological behaviour and Mullins effect in high damping rubber. Int J Solids Struct 75–76, 235–246
5. Nguyen DA (2015) An improved rheology model for the description of the rate-dependent cyclic behavior of high damping rubber bearings. Soil Dyn Earthquake Eng 77:416–431
6. Fujiisawa K (1993) A study on analytical modeling for seismic isolator. Summaries technical papers of annual meeting architectural institute of Japan. B Struct 1:505–506
7. Ohtori Y (1994) Earthquake response analysis of base isolated building with modified double target model. Summaries of technical papers of annual meeting architectural institute of Japan. B. Struct 1:793–794
8. Ohtori Y (1995) Effect of experienced shear strain dependency of high damping rubber bearing on earthquake response of isolation structure. J Struct Construct Eng (Transactions of AIJ) 60(472):75–84
9. Mazda T (2015) Evaluation on seismic response considering characteristics of high damping rubber bearing. J JSCE 71(4):198–209
10. Park KH (2022) Dynamic analysis of bridge pier considering hysteresis characteristics of high damping rubber bearings. In: Proceedings of 2021 4th international conference on civil engineering and architecture, 281–292
11. Naito N (2017) Seismic performance evaluation of LRB considering Mullins effect and hardening. Proc JSCE 73(4):I_499-I_510
12. Niwa N (2000) Dynamic loading test and simulation analysis of full-scale semi-active hydraulic damper for structural control. Earthquake Eng Struct Dyn 29:789–812
13. Japan Road Association: Manual for Highway Bridges Bearings (2018)
14. Japan Road Association: Design Specifications for Highway Bridges part 5, Seismic Design (2012)

Predicted Equations on Ultimate Bond Load of Strands-Cement System

Shih-Tsung Hsu, Pin-Chan Lee, Yung-Chen Yen, Jr-Hao Liao, Chung-Pin Li, Hao-Wei Yang, and Wen-Chi Hu

Abstract To elucidate the bond behavior of strand-cement system with various parameters, this research manners a sequence of pullout tests. The bond stress-slip relationships are depicted. Additionally, this study establishes predicted equations of ultimate bond load with various parameters. The pullout tests are conducted through MTS (Material test system). Variables in this study contain compressive strength of cement body, bond length, and quantity of strand. The predicted equations for the ultimate bond load under different conditions can be established by using multivariate regression analysis for single strand-in-cement samples. The ultimate bond load estimated by the predicted equation is consistent with the test results. The ultimate bond load reduction factor is created by comparing the ultimate bond load of three and five strand-cement specimens with that a single strand-cement specimen.

Keywords Ultimate bond load · Predicted equation · Reduction factor · Pullout test

1 Introduction

Tied-back anchors are usually to be applied as the retaining structure for slope and excavation. A tieback structure is more economical and offers a larger operating space for deep excavation with large or irregular area.

An anchor consists of three portions, namely anchor head, free end, and fixed end. This study focuses on the loading mechanism of the fixed end, usually the fixed

S.-T. Hsu · Y.-C. Yen · J.-H. Liao · C.-P. Li · H.-W. Yang · W.-C. Hu (✉)
Chaoyang University of Technology, Taichung, Taiwan
e-mail: winniehu@gmail.com

S.-T. Hsu
e-mail: sthsu@cyut.edu.tw

P.-C. Lee
Yuejin Technology Co., Ltd., New Taipei, Taiwan

T. Kang (ed.), *Proceedings of 5th International Conference on Civil Engineering and Architecture*, Lecture Notes in Civil Engineering 369,
https://doi.org/10.1007/978-981-99-4049-3_83

end is made of strands-in-cement. The allowable bond stress for strand-cement is provided for diverged sort of cement strength and strand by the JSSMFE Regulation [1]. Nevertheless, the regulation does not provide the ultimate bond stress under various bond length and quantity of strand for designers. Hence, the factor of safety that relates the bond strength of strands-cement system for permanent and temporary anchors could not be estimated. Consequently, this research adopts the 7-wires strand with 12.7 mm in diameter which commonly be used in Taiwan to study the bond behavior of strands-cement system. The typical bond load/stress-slip curve is launched and explored. The predicted equations for the ultimate bond load under diverse conditions are created by using multivariate regression analysis for single strand-in-cement specimens. Additionally, this study established a reduction equation for the bond load by comparing the ultimate load of three and five strand-in cement specimens with that of single strand-in-cement specimens.

ACI Committee 318 [2] expresses that the bond strength is a sort of shear strength between the strand surface and cement grout. Janney (ACI 1954) [3] demonstrates that the bond stress is combination of the mechanical interlock, relaxing pre-stressed of strand induces dilatant effect (Hoyer's effect), and chemical adhesion between the strand surface and cement grout. The failure types of pulled single strand-cement system can be classified into two modes, the pulled-out strand and several fissures in cement body accompanied with cleavage fracture. Danga et al. [4] use MTS to test the strand-in-cement specimens; the results reveal that the slip displacement of strand-in-cement is more sensitive than that of steel-in-cement, because smooth and mechanical interlocking can be found; the bond stress-slip movement relationship is created by using the nonlinear ordinary differential equation in their research. Lee et al. [5] also employ single strand-cement specimens to perform pullout test, then the bond stress-slip movement is launched absolutely.

2 Laboratory Test

This test employs cement grout which has water-cement ratio W/C of 0.45 and 0.55 to make cylinder samples with 7 days, 14 days, and 28 days. Strand-in-cement specimens are tested to discover the bond behavior in terms of cement's compressive strength, bond length and number of strand. The cement cylinder is 15 cm in diameter; cylinders' lengths are 15 cm, 30 cm, and 45 cm, respectively. The strand with 7 wires and 12.7 mm in diameter has ultimate load of 18.7 kN. The quantity of strand are 1, 3, and 5 respectively, and be inserted into the cement specimen. After curing, strands-cement specimens are pulled via MTS (machine test system) as demonstrated in Fig. 1.

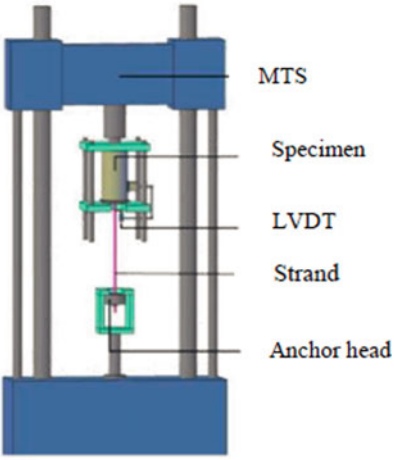

(a) Test equipment

(b) Five strands-in-cement specimens

Fig. 1 Details of test device and specimens

3 Test Result and Analysis

The research draws and discusses the bond load/stress-slip displacement curve in terms of diverse cement cylinder's compressive strength (W/C and age of cement sample), strand's bond length and quantity. The predicted equations for the ultimate bond load are established by multivariate regression analysis for single strand specimens. Moreover, this study creates the reduction equation for the bond strength after comparing the ultimate load of three and five strand specimens with that of single strand specimens.

Theoretically, the elastic elongation of strand plus slip displacement is the total movement of strand. The total movement subtracted the elastic elongation is the slip displacement. However, the elastic elongation of strand is really small. Figure 2a illustrates that the ultimate bond load increases as the bond length increases. Figure 2a,

b depict that the ultimate bond load increases when compressive strength of cement increases ($W/C = 0.45$). Figure 2c depicts the more quantity of strand, the more ultimate bond load. These situations can also be treasured for $W/C = 0.55$. Hsu et al. [6] present more details about the behavior of bond strength.

The following equation could obtain the bond stress, then the study can establish the bond stress-slip displacement relationships as displayed in Fig. 3.

$$\tau = \frac{Q}{\pi d_s l_b} \tag{1}$$

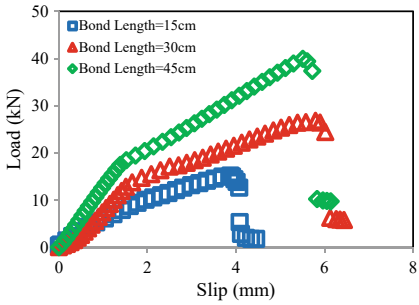

(a) fc'=32.83MPa, one strand

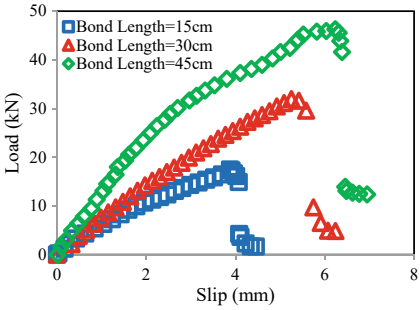

(b) fc'=37.5MPa, one strand

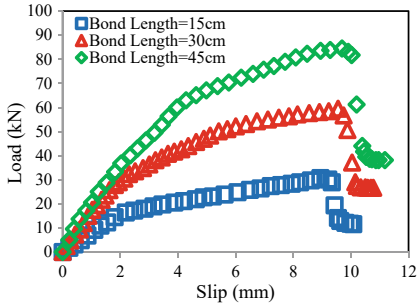

(c) fc'=37.5MPa, five strands

Fig. 2 Bond load-slip relationships for various compressive strength, strands, and bond lengths

Fig. 3 Bond stress-slip displacement relationships

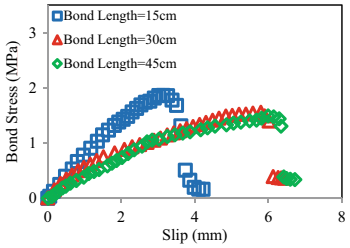

(a) fc'=32.83MPa, one strand

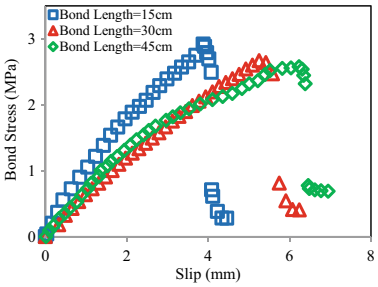

(b) fc'=37.5MPa, one strand

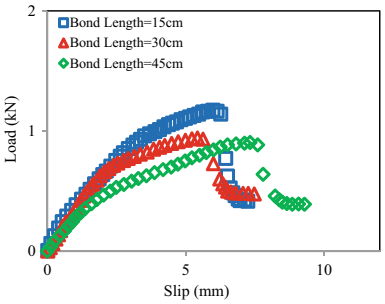

(c) fc'=32.83MPa, three strand

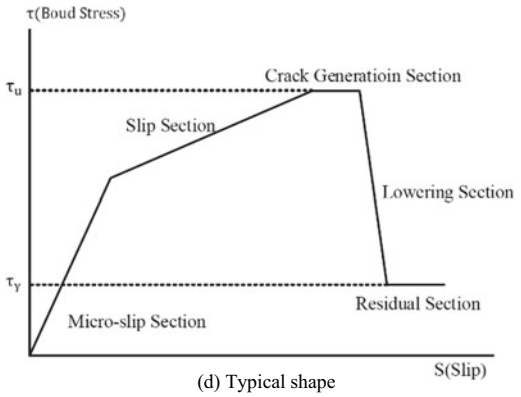

(d) Typical shape

where l_b represents the bond length, d_s is the strand's diameter, and τ denotes the bond stress.

Figure 3a, b reveal that higher bond strength is resulted from the higher compressive strength, the bond strength decreases a slight bit as bond length of strand increases. Figure 3c, d show the peak bond stress decreases with an increase in quantity of strand.

According to the results illustrated in Fig. 3a–c, the study separates the bond stress-slip displacement curve into five stages and demonstrated in Fig. 3d, and are explained as follows:

(1) Micro-slip section: the specimen is stressed to 0.4–0.5 times the ultimate load. In this section, the chemical adhesion between strand and cement is failure, and the micro-slip occurs.
(2) Slip-section: Surpassing the micro-slip section, the relative slip increases until the mechanical interlocking mechanism losses between strand and cement.
(3) Crack generation section: The specimen is stressed to peak load; the bond stress-slip curve appears horizontally. In this stage, the crack occurs nearly by strand initially and extends to the surrounding of cement cylinder.
(4) Lower section: When the stress of specimen surpasses the ultimate bond stress, the cement which located in thread of strand is crushed, the mechanical interlocking mechanism almost losses, the bond stress-slip curve decreases rapidly in this stage, whose bond stress-slip curve decrease more slowly.
(5) Residual section: After the lower stage, the mechanical interlocking mechanism losses completely, only the friction between strand and cement offers the residual stress [6].

The test results exhibit that the compressive strength of cement fc' and bond length of strand l_b are two important factors that govern the ultimate load Q_u of single strand-in-cement specimens. Figure 4 illustrates the relationship among the ultimate load Q_u, compressive strength fc', and bond length l_b of single strand-in-cement specimens. Figure 4 reveals that the ultimate load increase with increases in both compressive strength fc' and bond length l_b. The following two equations could represent the relationship among the ultimate load Q_u (kN), compressive strength fc' (MPa), and bond length l_b (cm) by using multivariate regression analysis.

$$Q_u = (0.1 \cdot l_b - 0.05) \cdot f_c' - (2.75 \cdot l_b - 4.4) \quad \text{, for } w/c = 0.45 \tag{2}$$

$$Q_u = (0.09 \cdot l_b + 0.15) \cdot f_c' - (2.4 \cdot l_b + 1) \quad \text{, for } w/c = 0.45 \tag{3}$$

Figure 4 demonstrates the comparison of predicted and test results on ultimate load Q_u and compressive strength fc' relationship for various water-cement ratio W/C and bond length l_b. The figures present that the values calculated by the predicted equations are consistent with those measured by tests.

For designer-friendly, this study combines Eq. (2) and (3) into Eq. (4) as following equation.

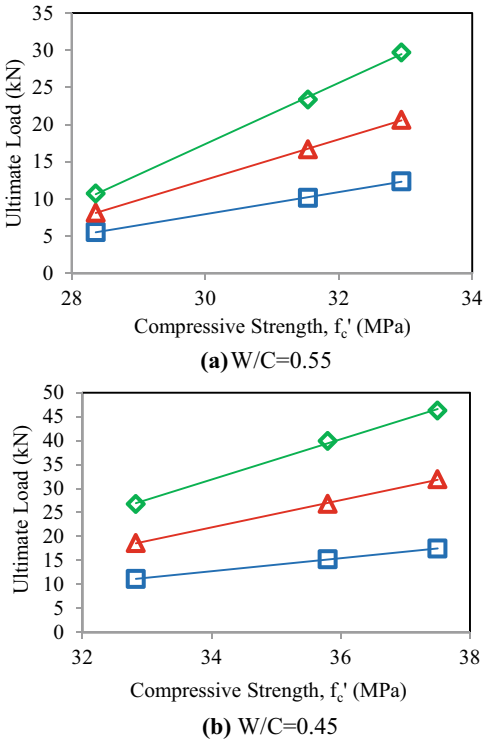

Fig. 4 Comparison of multivariate regression and test results on ultimate load Q_u-compressive strength fc' relationship for various water-cement ratio W/C and bond length l_b

$$Q_u = (0.1 \cdot l_b + 0.06) \cdot f_c' - (2.7 \cdot l_b - 1) \tag{4}$$

Figure 5 shows that the values calculated by the predicted equation (Eq. (4)) are in a good agreement with test values.

Table 1 demonstrates the ultimate load of various cements age and quantity of strand n with the bond length l_b of 30 cm and water/cement ratio W/C of 0.45. The table reveals the ultimate bond load increases with an increase in quantity of strand; however, ultimate bond load per strand is decreased with an increase in quantity of strand. This phenomenon is not only for the bond length of 30 cm but also for the bond length of 15 cm and 45 cm. According to Table 1, this study established the equation of reduction factor for ultimate bond load for specimens with three and five strands as follows.

$$Q_{u(\text{group})} = \varphi \cdot Q_{u(\text{single})} \cdot n \tag{5}$$

where Q_u (group) is the ultimate bond load of multi-strands, Q_u (single) signifies the ultimate bond load of single strand, n denotes the quantity of strand, and the ϕ represents the reduction factor. The reduction factors are calculated and displayed in Table 1 and can be presented as following equation.

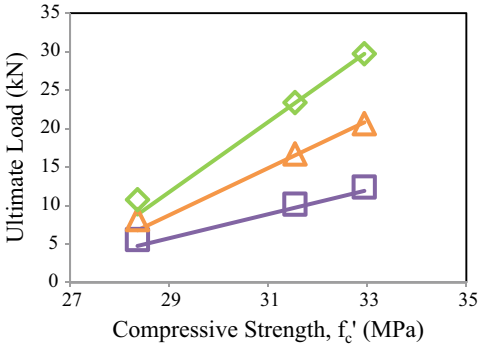

(a) W/C=0.55

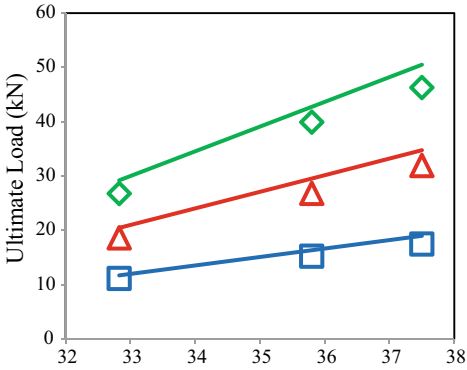

(b) W/C=0.45

Fig. 5 Comparison of the results predicted by using Eq. (4) and test results on ultimate load Q_u-compressive strength fc' relationship for various water-cement ratio W/C and bond length l_b

Table 1 Ultimate load of various conditions with bond length of 30 cm

Cement age (day)	Quantity of strand	Ultimate load (kN)	Ultimate load per strand (kN)	Reduction factor, ϕ(%)
7	1	18.625	18.625	100
	3	33.793	11.264	60.4
	5	32.273	6.455	34.7
14	1	26.793	26.793	100
	3	50.639	16.879	62.9
	5	54.925	10.985	40.9
28	1	31.934	31.934	100
	3	59.397	19.799	61.7
	5	62.271	12.454	39.1

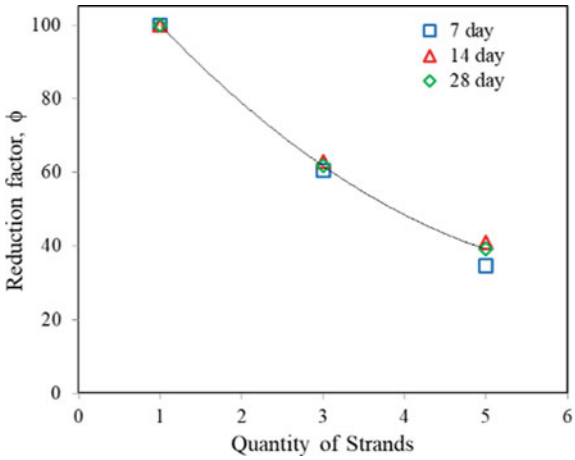

Fig. 6 Comparison of predicted and test results on reduction factor of ultimate bond load

$$\varphi = 125.9 \cdot e^{-0.235 \cdot n} \tag{6}$$

Figure 6 is the reduction factors predicted by Eq. (6) and those calculated by test results. The figure depicts that the predicted results by Eq. (6) are close with calculated results by laboratory tests.

4 Summary

This research manners a series of pull-out tests to study the bond behavior of strand-cement system. The following conclusions were drawn.

1. Increasing cement compressive strength could increase ultimate bond stress; however, ultimate bond stress decreased with increases in both bond length and quantity of strand.
2. This study separated the bond stress-slip displacement curve into five sections, there were micro-slip section, slip section, crack generation section, lowering section, and residual section.
3. The predicted equations for the bond strength under diverse conditions could be established by using multivariate regression analysis for single strand specimens. The values calculated by the predicted equation were consistent with the test values.
4. The ultimate bond load reduction factor can be obtained as well by comparing the ultimate load of three and five strand specimens with a single strand specimen. The reduction factor can be presented as a predicted equation for calculating the ultimate bond load.

References

1. Japan Society for Soil Mechanics and Foundation Engineering (JSSFME): Ground Anchor Design, Construction Standards and Solution. Japan (1990)
2. ACI Committee: Building Code Requirements for Structural Concrete (ACI 318–05) and Commentary (318R-05). ACI, Michigan (2005)
3. ACI: Nature of Bond in Pre-tensioned Prestressed Concrete. ACI (1954)
4. Danga CN, Murraya CD, Floyd RW, Micah-Halea W, Martí-Vargas JR (2014) Analysis of bond stress distribution for prestressing strand by standard test for strand bond. J Eng Struct 72:152–159
5. Lee C, Shin S, Lee S (2017) Modeling of bond stress–slip relationships of a strand in concrete during steam curing. Int J Concrete Struct Mater 11
6. Hsu ST, Shih CH, Chen KT, Yen YC, Chang WC, Li CP (2022) Bond load-slip behaviors of strand assemblies-in-cement. In: Proceedings of 2021 4th international conference on civil engineering and architecture, 271–280

Numerical Investigation of Dynamic Response of a Cross-Fault Tunnel Surrounding Rock Subject to Earthquake Excitation

Wanpeng Shi, Danqing Song, Janwei Zhang, and Mengxin Liu

Abstract Traffic tunnel engineering is an important lifeline engineering in the world, which has a great risk of destruction during earthquakes. It is of great significance to ensure their safe and reliable operation subject to earthquakes. The interaction between seismic loads and complex geological conditions results in complex dynamic responses of tunnels across faults. In this work, the research progress of seismic response of cross-fault tunnel is analyzed, and the influencing factors of earthquake damage are summarized. In addition, three-dimensional dynamic analysis is used to study the dynamic characteristics of a cross-fault tunnel. The results show that the influence factors of earthquake damage of cross-fault tunnel mainly include surrounding rock properties, fault parameters, ground motion parameters and tunnel buried depth. The direction of seismic wave affects the propagation characteristics of wave in tunnel surrounding rock. Geological conditions have impacts on the earthquake response of surrounding rock. The dynamic amplification effect of surrounding rock of cross-fault segment decreases with the increase of tunnel lining elevation, and the dynamic amplification effect of intact surrounding rock is different from that of cross-fault segment. The input directions of ground motion has effects on the seismic amplification effect of surrounding rock, and the dynamic amplification effect of horizontal ground motion is greater than that of vertical ground motion. This research work has reference function for earthquake reinforcement measures of tunnel engineering.

Keywords Cross-fault · Tunnel · Dynamic response · Earthquake excitation

W. Shi · J. Zhang
School of Civil Engineering and Architecture, Henan University, Henan Kaifeng 475000, China

D. Song (✉)
State Key Laboratory of Subtropical Building Science, School of Civil Engineering and Transportation, South China University of Technology, Guangdong 510640, China
e-mail: dqsong@scut.edu.cn

M. Liu
Institute of Cold Regions Science and Engineering, School of Civil Engineering, Northeast China Observatory and Research Station of Permafrost Geo-Environment of the Ministry of Education, Northeast Forestry University, Harbin 150040, China

T. Kang (ed.), *Proceedings of 5th International Conference on Civil Engineering and Architecture*, Lecture Notes in Civil Engineering 369,
https://doi.org/10.1007/978-981-99-4049-3_84

1 Introduction

With the continuous development of social and economic level, the scale and quantity of transportation and engineering construction in China are on the whole showing a trend of continuous growth. As an engineering building of underground passage, tunnel has some incomparable advantages over other projects, so it also presents a very obvious trend of growth, with long tunnels and large tunnel groups constantly emerging. As the Sichuan–Tibet Railway crosses the steep terrain zone, the total altitude difference is over 3500 m, and it crosses 21 snow-capped mountains with an elevation of more than 4000 m, 14 rivers and 5 geomorphic units. Plate collision and tectonic activity along the railway project are strong and seismically active. The topography, geology and climate conditions along the railway construction are extremely complex. The total length of the Sichuan-Tibet railway is about 1800 km, and the length of the tunnel section is about 1200 km, with a ratio of bridge and tunnel being more than 80%. Complex geological and geomorphic conditions make tunnel engineering construction face great challenges.

Tunnel engineering is often faced with various disasters, such as rock burst, gas outburst, water inrush and mud inrush (Fig. 1) which have adverse effects on the construction operation and maintenance of tunnel engineering. Crossing fault is an unavoidable engineering problem in tunnel construction. Because of the existence of fault fracture zone, tunnel seismic damage is more obvious, the extent of tunnel damage is enlarged, and the surrounding rock across the fault segment is prone to problems. For example, a strong earthquake occurred in Kern County, California, USA, in 1952, which caused severe damage to four tunnels crossing the fault in the earthquake area [1]. The Izumi Earthquake in Japan in 1978 caused obvious cracking of the second lining of the Inatori tunnel across the fault, fracture of steel bars, mass concrete falling at the top of the tunnel and serious deformation of the tunnel as a whole [2]. In 2008, the Wenchuan earthquake caused serious damage to highway tunnels in the earthquake area. For example, the Longxi tunnel had multiple lining collapses and dislocations across the fault segment, and multiple cracks appeared around the tunnel [3]. Cross-fault tunnels are highly vulnerable to damage under earthquake action, and this research has practical scientific and engineering significance on seismic damage mechanism, influence factors, dynamic response analysis method, dynamic response law and seismic technology of cross-fault tunnels.

This work summarizes the principal influencing factors of the dynamic characteristics of cross-fault tunnel surrounding rock through literature survey. According to the summary of the existing research results, the problems of seismic response of tunnel and the contents to be further investigated are put forward. In addition, three-dimensional finite element dynamic analysis was carried out for cross-fault tunnel by using finite element method, and the effects of ground motion directions on earthquake response of tunnel surrounding rock were investigated. The effect of geological conditions on the amplification of tunnel surrounding rock is analyzed.

Fig. 1 Damage phenomenon of cross-fault tunnel

The seismic response characteristics of tunnel across faults and intact surrounding rock sections are compared.

2 Analysis of Influence Factors of Cross-Fault Tunnel Seismic Damage

According to the summary of relevant research results, the seismic damage of tunnels across faults under earthquakes can be divided into two parts, including earthquake-induced tunnel damage and shear failure of tunnels across faults caused by fault dislocation. In the process of tunnel construction, it can provide basis for seismic design of tunnel by comprehensively summarizing the influence factors of seismic damage of cross-fault tunnel. Based on previous studies, this work divides the influencing factors of seismic damage of cross-fault tunnels into the following four aspects, including surrounding rock properties, fault parameters, ground motion parameters and tunnel structure types, as shown in Table 1.

2.1 Influence of Surrounding Rock Properties

The seismic response of cross-fault tunnel is greatly affected by the properties of surrounding rock [4–6]. It is difficult to avoid the difference of surrounding rock properties in the fault fracture zone. When lithology and geological structure of

Table 1 Influencing factors of cross-fault tunnel earthquake damage

Type	1	2	3	4
Influencing factor	Surrounding rock properties	Fault parameters	Ground motion parameters	Tunnel buried depth

surrounding rock are poor under the action of earthquakes, the surrounding rock will produce large uneven deformation, causing large damage of the tunnel crossing the fault. The influencing factors of surrounding rock properties on its seismic damage mainly include rock and soil strength, surrounding rock pressure and surrounding rock hydraulic conditions. The tunnel earthquake damage is related to the medium condition of surrounding rock. According to the Hanshin earthquake survey, soft soil tunnel structures are more prone to failure than rock tunnels [7]. Compared with the homogeneous surrounding rock, the existence of bad geological structures such as joints, weak structural planes and weak interlayers aggravates the seismic damage degree of surrounding rock and leads to serious damage of tunnel structure. Chen et al. [8] conducted a field investigation on the seismic damage of cross-fault tunnels and believed that the quality of surrounding rock had an impact on the degree of seismic damage, and the seismic damage generated in tunnels was mainly concentrated in the locations with poor surrounding rock quality and large difference between strata. Qian [9] believes that when the tunnel depth is large and the surrounding strata are complex and changeable, the property of surrounding rock is very uneven. When the tunnel is subjected to earthquake and other catastrophic loads, it is easy to suffer earthquake damage through the weak and broken zone of active fault and under high in-situ stress. Fan et al. studied the earthquake response of surrounding rock across soft and hard surrounding rock and considered that the earthquake response of tunnel lining structure mainly depends on the cross-fault tunnel surrounding rock [10]. Cui et al. analyzed the large deformation and collapse of soft rock tunnel in 2008 Wenchuan earthquake and other influencing factors and their cause mechanism and believed that the poor self-stability of surrounding rock was one of the main causes of tunnel failure [11]. When the horizontal stress is large, the tunnel lining structure will produce a large stress increment, which will easily lead to the damage of the tunnel lining structure [12]. It can be seen that the properties of tunnel surrounding rock have a great influence on the seismic response of cross-fault tunnel, and improving the strength of tunnel surrounding rock has become an effective seismic means. In addition, the hydraulic conditions in surrounding rock have great effects on the dynamic response of cross-fault tunnel. The hydraulic factor in surrounding rock has impact on the propagation characteristics and dynamic response of seismic wave in rock mass [13]. In the multi-geological disaster chain, the hydrodynamic coupling factor plays a very important role, but the current research is insufficient [14].

2.2 Influence of Fault Parameters

According to previous relevant studies, it can be concluded that fault parameters, including fault dip and width, are one of the primary influencing factors of cross-fault tunnels dynamic damage under earthquakes. Under the condition of variable fault dip, the smaller the dip angle of the fault, the larger the displacement and internal force value of the tunnel lining, and the large angle intersection with the fault should be considered in the process of tunnel line selection. Liu et al. explored the seismic

damage mechanism of tunnels under different fault strike, suggesting that faults had a certain amplification effect on seismic response, which became more obvious as the angle between fault strike and tunnel decreased [15]. Jiao et al. adopt FLAC3D to analyze the influence of dip angle of fault dislocation on the seismic response of cross-fault surrounding rock, which the results show that the dip angle of reverse fault is the same, the stress on different parts of lining shows an overall trend of increasing with the increase of dislocation distance [16]. In addition, the width of fault has an influence on the seismic response of cross-fault tunnel. The greater the width of fault, the greater the extreme value of tunnel lining displacement and internal force, but when the range of fault fracture zone increases to a limit value, the vibration effect caused by the fracture zone is not significant [17]. Lin et al. studied the influence of fault width on dynamic characteristics of cross-fault tunnel, indicating that the impact range of strike-slip fault dislocation on lining was different with the fault width, and there was a limit of the impact range of fault dislocation on lining [18]. Gong et al. used field measurement and numerical simulation methods to study the surrounding rock deformation law in the process of tunnel crossing the fault fracture zone with different dip angles [19].

2.3 Influence of Ground Motion Parameters

Earthquake parameters are related to dynamic response of cross-fault tunnels, including ground motion intensity, duration, spectrum characteristics, incident angle and direction of ground motion and ground motion type.

Previous studies have shown that the dynamic response of surrounding rock increases as seismic intensity, and the possibility of cumulative plastic damage increases with the increase of holding time. Chen believes that ground motions with different spectral characteristics have different impacts on structures, and the response of structures under low-frequency ground motions is greater [20]. In the seismic response analysis of underground structures, simple harmonic wave, real ground motion and synthetic ground motion are usually used. However, the time–frequency distribution of ground motion energy of different types is very different, and its influence on the structure is also very different. The structure response under simple harmonic input is very large, which may be an unfavorable ground motion input, and the intensity of ground motion is overestimated [21]. Far-field harmonic ground motions and near-fault pulse-type ground motions are two special long-period ground motions, whose energy is mainly concentrated in the low-frequency band and has a great damage effect on long-period structures. In particular, when the tunnel is subjected to near-fault pulse-type ground motions, the structure is prone to first transcendent failure.

The incident direction and angle of ground motion have influence on the dynamic response of cross-fault tunnel. Huang believed that the incident angle affected the stress characteristics and failure forms of the lining structure, and the incident direction of wave changed little, while the stress and deformation of each point of the

structure could change greatly [22]. Chen believes that when shear wave is incident vertically, the arch shoulder and arch foot of tunnel lining are unfavorable seismic parts. When shear wave incident in 45° direction, the arch and arch wall of tunnel lining are easy to produce large internal force and bending moment [23].

2.4 Influence of Tunnel Buried Depth

The depth of tunnel also affects the seismic dynamic response of cross-fault tunnel. Sunil et al. found that deep buried structure is more advantageous than shallow buried structure. Lin believes that the seismic response of underground structures does not change significantly with the buried depth and is affected by many factors [24]. Chen et al. believe that when the structure buried depth is 0.25 times the wavelength of rock mass, the tunnel lining will be damaged due to the significant increase of stress; that is, the most unfavorable buried depth exists [25]. However, it is still controversial whether the tunnel structure has the most unfavorable dynamic buried depth. Zang et al. studied the influence of tunnel depth on seismic dynamic response of karst tunnel by using finite-element numerical simulation and theoretical analysis method, which the results show that the shallower the buried depth of karst tunnel is, the larger the seismic dynamic response displacement is [26].

3 Dynamic Response of a Cross-Fault Tunnel: A Case Study

3.1 Numerical Model

Taking a cross-fault tunnel in southwest China as an example, the generalized model of underground tunnel is shown in Fig. 2 according to the actual project. Based on the generalized model of underground tunnel, the finite element method is used to establish a three-dimensional numerical model (Fig. 3). The size of the numerical model is 40 m (width) × 100 m (length) × 40 m (height). The diameter of the tunnel is 8 m. The thickness of the lining and fault is 0.4 m and 20 m, respectively. In the numerical model, the tunnel was meshed with C3D8 elements. The total number of elements in the numerical model was 58,905. The number of elements in the surrounding rock and the fault was 42,312 and 10,320, respectively.

In addition, before the dynamic analysis step, ground stress balance should be carried out to reduce the adverse effects of gravity. In order to avoid the distortion of the result caused by the refraction and reflection of the finite element mesh, infinite element elements were set at the bottom and both sides of the model to reduce the specific boundary effect. In order to explore the dynamic response characteristics of cross-fault tunnels under earthquake action, a horizontal and vertical peak ground

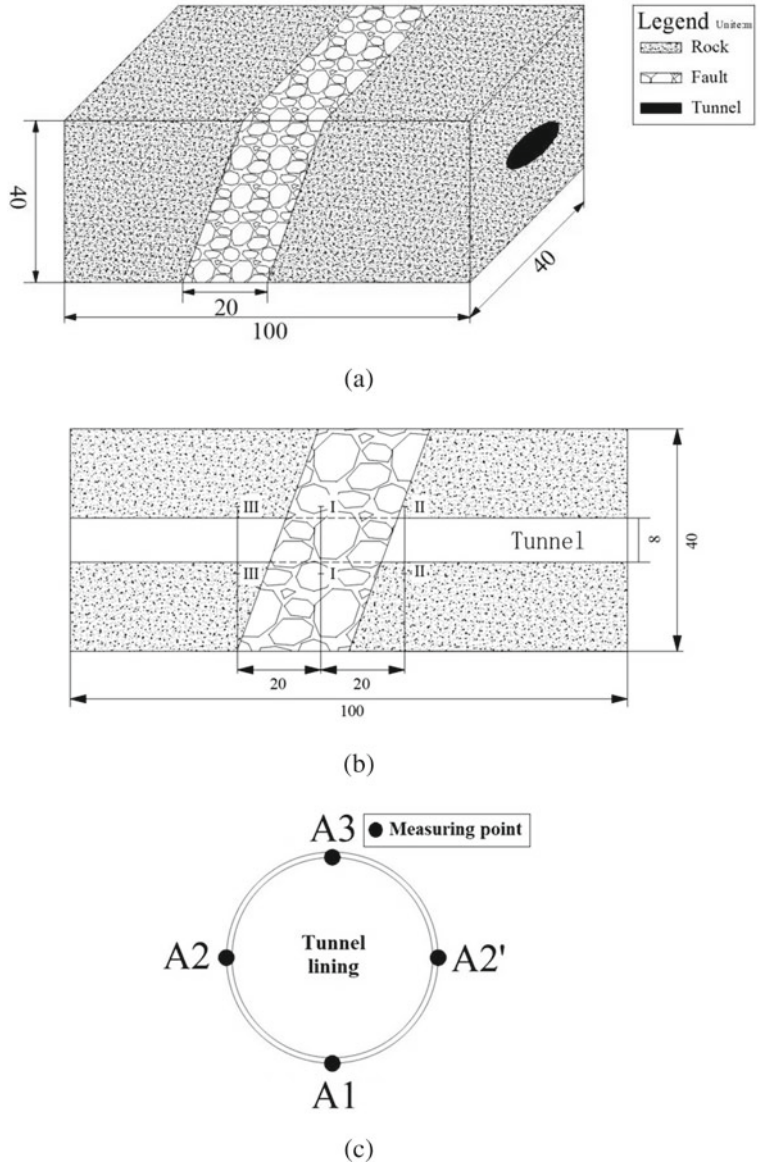

Fig. 2 Schematic diagram of a cross-fault tunnel: **a** three-dimensional stereogram; **b** longitudinal profile; **c** tunnel lining structure (Unit: m)

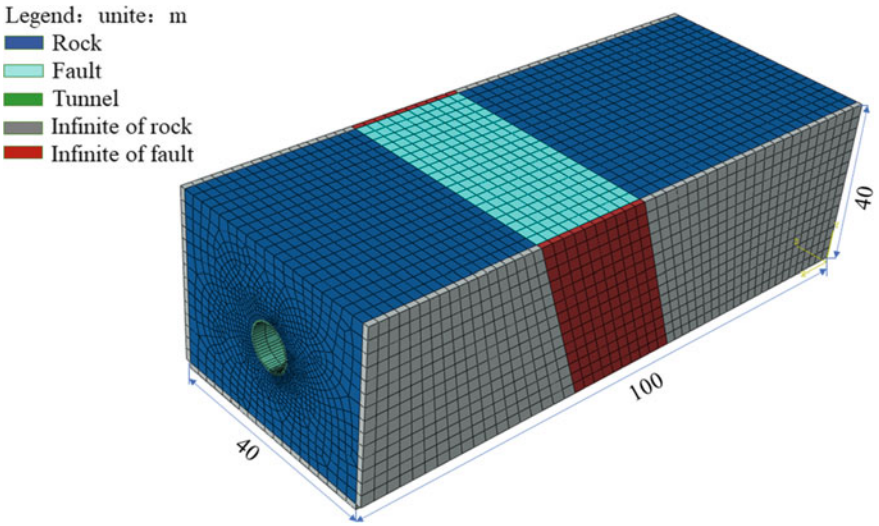

Fig. 3 Numerical model of a cross-fault tunnel

Fig. 4 Ground motion waveform loaded on numerical model

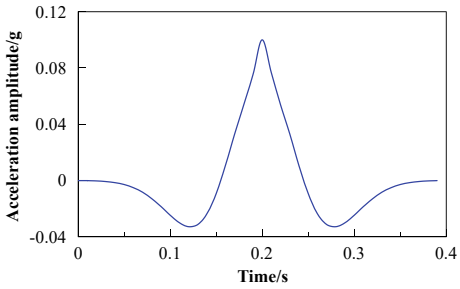

acceleration (PGA) of 0.1 g Ricker wavelet was carried out at the bottom of the model for simulation experiment, respectively. The input time history was 0.4 s, as shown in Fig. 4. The main physical and mechanical parameters of a cross-fault tunnel are shown in Table 2 [27].

3.2 Dynamic Response of Surrounding Rock Subject to Earthquake

Three typical sections of the tunnel were selected, including sections 1–1 '(cross-fault segment), 2–2' (upper wall of fault) and 3–3 '(lower of fault), as shown in Fig. 2b. Tunnel vault (A3), arch waist (A2 and A2') and arch foot (A1) of different sections were selected, as shown in Fig. 2c, to investigate the dynamic response

Table 2 Main physical and mechanical parameters of a cross-fault tunnel

Type	Density (kN/m^3)	Modulus of elasticity (GPa)	Poisson's ratio	Cohesive force (MPa)	Internal friction angle (°)
Surrounding rock	23.5	2.4	0.3	0.65	33.0
Fault fracture zone	19.5	0.8	0.34	0.4	26.5
Lining structure	24	30	0.2	/	/

characteristics of tunnel surrounding rock at different locations. The time-history curves of acceleration of different sections when input horizontal and vertical seismic waves are shown in Figs. 5 and 6. Figure 5 shows that when input horizontal seismic wave, the acceleration waveform of different sections is generally similar to the input Ricker wave, but the PGA of different measurement points is different. Figure 6 shows that when input vertical seismic wave, the acceleration waveform at different measuring points is obviously different from the input wave. By comparing Figs. 5 and 6, it can be seen that the direction of ground motion has an obvious influence on the wave propagation characteristics of cross-fault tunnel surrounding rock, in particular, on the propagation characteristics of the input vertical seismic wave.

In addition, in order to further study the dynamic response characteristics of different sections of the tunnel, the PGA of different measurement points were selected as the analysis index. Change rule of PGA changes of different sections is shown in Fig. 7. Figure 7a shows that, under horizontal seismic wave, the PGA of surrounding rock of cross-fault sections 1–1 'decreases gradually from arch foot to tunnel vault, while that of sections 2–2' and 3–3' increases gradually. This indicates that the dynamic acceleration amplification effect of tunnel surrounding rock of cross-fault segment is closely related to the geological conditions. Figure 7b shows that, under vertical seismic wave, PGA of tunnel surrounding rock of cross-fault sections 1–1' decreases gradually with the increase of elevation, while the PGA of surrounding rock of tunnel sections 2–1'and 3–3' increases firstly and then decreases with the increase of elevation. By comparing Fig. 7a and Fig. 7b, it can be seen that the dynamic amplification effect of tunnel surrounding rock is different under the action of different ground motion directions, which indicates that the directions of ground motion have effects on the variation characteristics of the dynamic amplification effect of tunnel surrounding rock.

In addition, in order to study the influence of ground motion input direction on the dynamic amplification effect of tunnel surrounding rock, the ratio of PGAx to PGAz under horizontal ground motion (PGAx/PGAz) is shown in Fig. 8. Figure 8 shows that the PGAx/PGAz of surrounding rock of three sections are all greater than 1.0, indicating that the dynamic amplification effect of shear wave on tunnel surrounding rock is much greater than that of longitudinal wave. The PGAx/PGAz values of surrounding rock cross-fault sections 1–1 'increase with elevation gradually, and

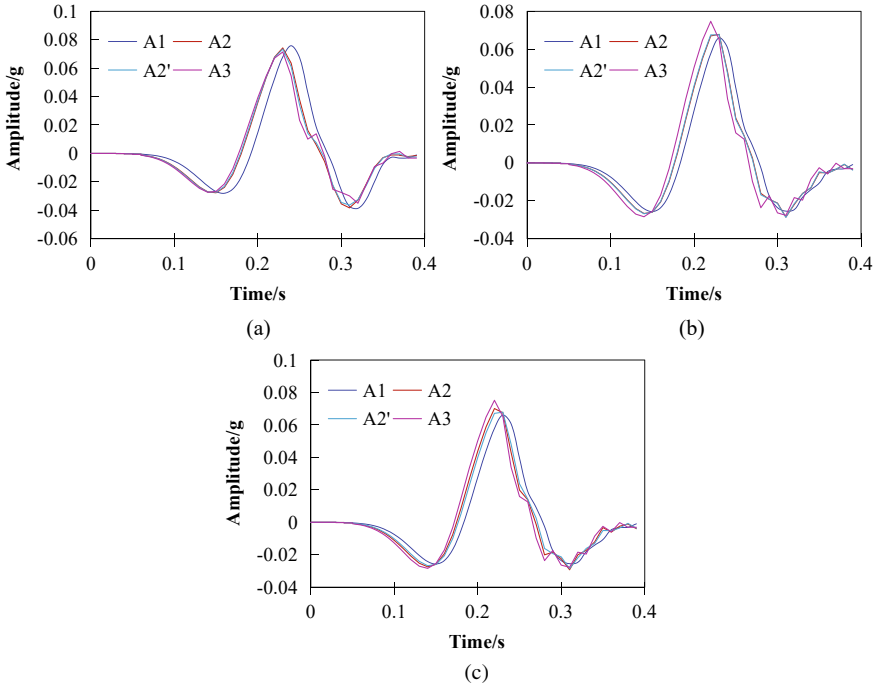

Fig. 5 Acceleration time-histories of different tunnel sections when input horizontal seismic wave: **a** 1–1'; **b** 2–2'; **c** 3–3'

they are much greater than those of cross-section 2–2' and 3–3'. This indicates that the shear wave has a greater effect on the dynamic amplification of the cross-fault tunnel surrounding rock than that of the intact rock. Moreover, the sections 3–3 'and 2–2' are located on the hanging wall and footwall of the fault, respectively. Figure 7 shows that PGA of sections 3–3' is larger than that of sections 2–2', indicating that the dynamic amplification effect of the hanging wall of the cross-fault tunnel is larger than that of the footwall.

4 Conclusion and Prospect

According to the method of detailed literature survey, the influence factors of seismic damage of cross-fault tunnel under earthquakes mainly include surrounding rock properties, fault parameters, ground motion parameters and tunnel buried depth. However, due to the randomness of seismic load and the complexity of the interaction mechanism between fault and tunnel structure, the seismic dynamic response and failure mechanism of cross-fault tunnel become very complicated. The contribution

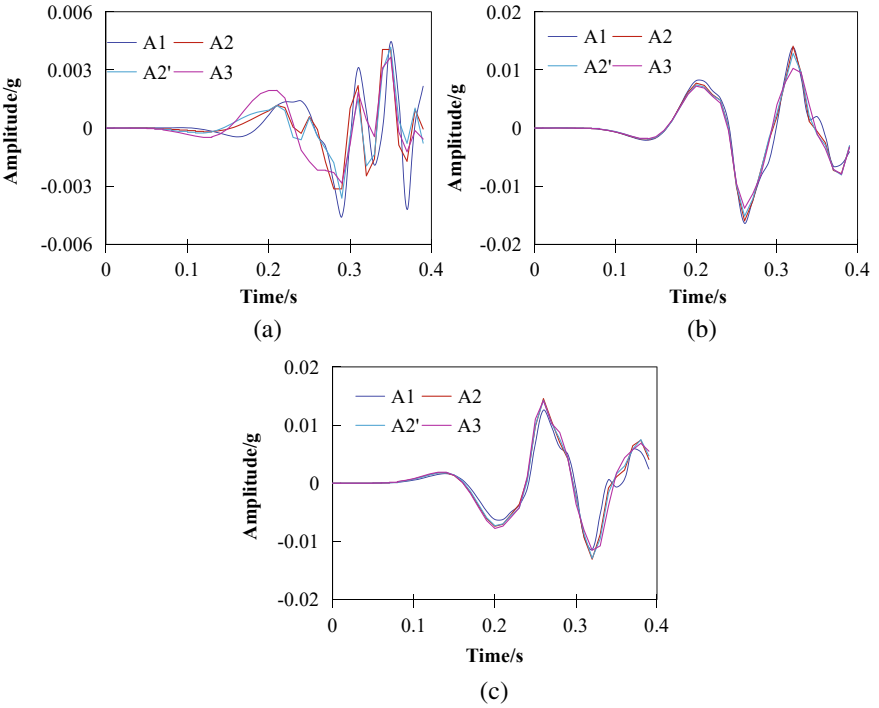

Fig. 6 Acceleration time-histories of different tunnel sections when input vertical seismic wave: **a** 1–1'; **b** 2–2'; **c** 3–3'

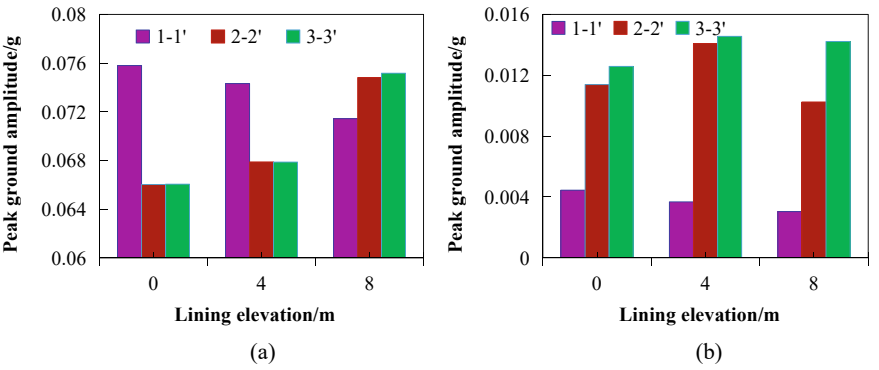

Fig. 7 Change rule of peak ground acceleration with tunnel lining structure elevation of tunnel sections 1–1', 2–2' and 3–3': **a** when input horizontal seismic wave; **b** when input vertical seismic wave

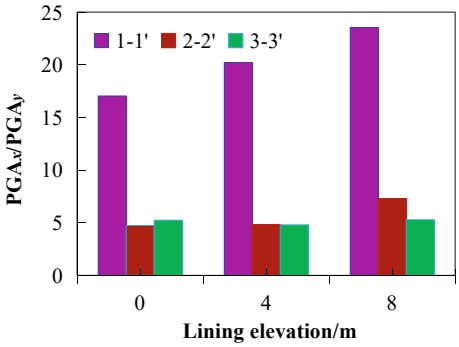

Fig. 8 Ratio of PGA under horizontal seismic wave to that under vertical wave with tunnel lining structure elevation of tunnel sections 1–1', 2–2' and 3–3'

degree of the seismic damage factors and the action mechanism of various factors for cross-fault tunnel still need to be further studied.

In addition, three-dimensional finite element dynamic analysis is used to investigate the dynamic response characteristics of cross-fault tunnel surrounding rock. The directions of ground motion have effects on the wave propagation characteristics in surrounding rock, and P-wave has greater impact on the seismic waveform. The dynamic amplification effect of tunnel surrounding rock is closely related to geological conditions. The PGA of the cross-fault surrounding rock decreases with the elevation, and the PGA of the intact surrounding rock segment is different from that of the fault segment. Under S-wave, PGA of intact surrounding rock increases with elevation. The input direction of ground motion has an effect on the dynamic amplification effect of surrounding rock, and the dynamic amplification effect of surrounding rock is greater under P-wave. In particular, the PGAx/PGAz ratio of cross-fault surrounding rock is much higher than that of intact surrounding rock.

Acknowledgements This study was funded by the National Natural Science Foundation of China (52109125), the National Postdoctoral Program for Innovative Talent of China (BX20200191), the China Postdoctoral Science Foundation (2020M680583) and the Shuimu Tsinghua Scholar Program (2019SM058).

References

1. Prentice CS, Ponti DJ (1997) Coseismic deformation of the wrights tunnel during the 1906 san francisco earthquake: a key to understanding 1906 fault slip and 1989 surface ruptures in the southern Santa Cruz mountains, California. J Geophys Res Solid Earth 102:635–648
2. Yoshikawa K (2010) Geology and swelling rocks of the Izumigoshi tunnel, shin-tokaido line. JNR J Japan Soc Eng Geol 5:191–196
3. Wang B, Zhang Z, He C, Zheng HL (2017) Implementation of a long-term monitoring approach for the operational safety of highway tunnel structures in a severely seismic area of China. Struct Control Hlth 24:1985–1993

4. Song DQ, Liu XL, Huang J, Zhang JM (2021) Energy-based analysis of seismic failure mechanism of a rock slope with discontinuities using Hilbert-Huang transform and marginal spectrum in the time-frequency domain. Landslides 18:105–123
5. Song DQ, Chen Z, Dong LH, Zhu WC (2021) Investigation of the seismic response characteristics of a rock mass slope containing weak structural planes under seismic excitation based on multi-domain coupling analysis. Geomat Nat Haz Risk 12:2776–2802
6. Chen Z, Song DQ (2021) Numerical investigation of the recent Chenhecun landslide (Gansu, China) using the discrete element method. Nat Hazards 105:717–733
7. Yin L, Wei Y (2015) Topology optimization for tunnel support in layered geological structures. Int J Numer Meth Eng 47:1983–1996
8. Chen KZ, Li TB, Ma CC, Zhang H (2020) Simulation of tunnel pressure relief blasting and rock burst suppression based on CDEM. J Eng Geol 28:667–676
9. Qian Q (2017) Main developments and directions of geological prediction and informatized technology of tunnel construction. Tunn Constr 37:251–263
10. Fan L, Chen JL, Peng SQ, Qi BX, Wang F (2020) Seismic response of tunnel under normal fault slips by shaking table test technique. J Cent South Univ 27:1306–1319
11. Cui G, Meng L, Zhang J, Wang M, Zhu C (2018) Study on large-scale shaking table model test for seismic response of soft and hard surrounding rock interface section of tunnel portal part. Adv Eng Sci 50:84–90
12. Lyu D, Chu Y, Sha M, Wang X (2018) Nonlinear seismic response of a hydraulic tunnel considering fluid-solid coupling. Math Probl Eng 2018:1–12
13. Huang J, Song DQ, Liu XL, Zhao J, Wang EZ, Wang SJ (2020) IOP Conference Series: Earth and Environmental Science (Liquid filling auxiliary device for liquid-filled rock joints and its application), p 570
14. Song DQ, Liu XL, Li B, Zhang JM, Bastos V JJ (2021) Assessing the influence of a rapid water drawdown on the seismic response characteristics of a reservoir rock slope using time–frequency analysis. Acta Geotech 16:1281–1302
15. Liu LB, Wang YF, Liu F, Zhou J (2017) Shaking table model tests on the influence of fault strike on the seismic responses of tunnels. J Vib Shock 36:196–202
16. Jiao P, Lai H (2019) Theoretical analysis on the influence of different dip angle reverse faults' dislocation on tunnel structure. China Civ Eng J 52:106–117
17. Zhong Z, Wang Z, Zhao M, Du XL (2020) Structural damage assessment of mountain tunnels in fault fracture zone subjected to multiple strike-slip fault movement. Tunn Undergr Space Technol 104:103527
18. Lin K, Chen X, Zuo J, Zhang P (2013) Numerical simulation of effects of fault width on characteristics of across-fault tunnel due to fault movement. J Nanjing Univ Technol 35:61–65
19. Gong LJ, Ren R, Wang YQ, Wang ZF, Yang RP (2021) Analysis on deformation characteristics of surrounding rock of tunnel crossing fault fracture zone with different dip angles. Highw 66:313–319
20. Chen WZ (2012) Study on the stability of underground engineering under special geological environment. Science Press, Beijing
21. Cui Z, Sheng Q, Leng XL, Zhu ZQ, Zhang YM, Yang JH (2013) A reivew of study on seismic catatrophe of large-scale underground cavern group. J Disaster Prev Mitigation Eng 33:606–616
22. Huang QB, Peng JB (2008) Calculation about earthquake stress for underground pipeline based on the incident angle of earthquake wave. Chin J Undergr Spa Eng 4:979–984
23. Chen ZX, Wang TD, Huang CH (2011) Case study of earthquake-induced damage patterns of rock tunnel and associated reason. Chin J Rock Mech Eng 30:45–57
24. Lin G (1990) Review of underground structure seismic analysis. World Earthquake Eng 2:1–10
25. Chen CH, Wang TT, Jeng FS, Huang TH (2012) Mechanisms causing seismic damage of tunnels at different depths. Tunn Undergr Sp Technol Trenchless Technol Res 28:31–40
26. Zang WJ, Jian CH, Zhang GJ, Wang ZZ, Sun WT (2020) Analysis of influence of buried depth on seismic dynamic response of karst tunnel. J Dalian Univ Technol 60:36–45
27. He C, Li L, Zhang J, Geng P, Yan Q (2014) Seismic damage mechanism of tunnels through fault zones. Chinese J Geotech Eng 36:427–434

Research on Mechanical Properties on Mixed-Tensioned Precast U-shaped Girder in Rail Transit

Yun Li and Yumin Song

Abstract In this paper, the mechanical properties of the mixed-tensioned precast U-shaped girder are analyzed and evaluated by method of FEM and static loading test taking the Rail Transit Line 8 in Qingdao as engineering background. The feasibility of design and construction is verified about the mixed-tensioned precast U-shaped girder which is a type of new product. At the same time, two types of precast U-shaped girder by using pre-tensioning method and post-tensioning method are made up with the same section and quantity of prestressed steel strand of mixed-tensioning method, and their mechanical properties of stress and deformation are compared and analyzed by FEM. The results show that the mechanical behavior of mixed-tensioned precast U-shaped girder meets relevant codes requirement, and its mechanical properties have a certain superiority because of combining the advantages of pre-tensioned U-shaped and post-tensioned U-shaped girder, so the mixed-tensioned precast U-shaped girder has a certain application prospect.

Keywords Rail transit · Prefabricated U-shaped girder · Finite element · Mixed-tensioning method · Pre- tensioning method · Post-tensioning method · Mechanical property

1 Introduction

With the rapid development of urban rail transit, precast U-shaped girders are widely used in rail transit viaducts. As a new type of trough girder which is one type of the through bridges, U-shaped girder has the unique advantages of good effect of sound insulation and noise reduction, high section utilization rate and low building

Y. Li (✉)
Shandong Technology and Business University, Shandong Province, Yantai 264000, China
e-mail: 58046910@qq.com

Y. Song
School of Urban Rail Transit, Shanghai University of Engineering and Technology, Shanghai 201620, China

T. Kang (ed.), *Proceedings of 5th International Conference on Civil Engineering and Architecture*, Lecture Notes in Civil Engineering 369,
https://doi.org/10.1007/978-981-99-4049-3_85

height compared with traditional girder such as box girder, T girder or plate-girder [1–6]. At present, the widely used precasting methods of single line U-shaped girders mainly include mixed-tensioning method, pre-tensioning method and post-tensioning method [7–10]. Among the single line precast U-shaped girders that have been put into operation in China, Shanghai Metro Line 16 and Qingdao Metro Line 13 have used the pre-tensioning method; Shanghai Metro Line 8, Nanjing Metro Line 2, Rail Transit Line 13 in Chongqing and Nanjing Metro Line S1 have used the post-tensioning method; Qingdao Metro Line 11 has used both pre-tensioning method and post-tensioning method. In order to keep the bridge span of Qingdao Metro Line 8 equal to that of adjacent Jinan-Qingdao High-speed Railway, the U-shaped girder with the railway standard span of 32.7 m was adopted, but the construction technology was the mixed-tensioning method which combined pre-tensioning method and post-tensioning method. Although the mixed-tensioned precast U-shaped girder has been put into engineering application, there are few studies on the mechanical properties of it. Meanwhile, there are few studies on the difference of mechanical properties between mixed-tensioning method, pre-tensioning method and post-tensioning method. Taking the Rail Transit Line 8 in Qingdao as engineering background, the mechanical properties of the mixed-tensioned precast U-shaped girder are analyzed. Meanwhile, the mechanical properties and the superiority of the precast U-shaped girders by using mixed-tensioning method, pre-tensioning method and post-tensioning method are compared and analyzed by the method of FEM.

2 Project Overview

The total length of Qingdao Metro Line 8 is about 60.8 km. The viaduct is used in the section from Qingdao Jiaodong International Airport Station to Jiaodong Town Station, and the total length of the bridge is 728.445 m, where the single line precast U-shaped girder taking span of 32.7 m has used the construction technology of mixed-tensioning method which combined pre-tensioning method and post-tensioning method. The U-shaped girder is a straight-line beam with 5.0 m line spacing, and its cross-section is the thin-walled opening U-shaped. The appearance of the outer web and its upper flange plate is T-shaped. The thickness of web is 0.286 m. The top width of web is 1 m. The appearance of the inner web and its upper flange plate is inverted L-shaped. The thickness of web is 0.28 m. The top width of web is 0.72 m. The thickness of the bottom plate is 0.4 m within 1.2 m of the girder end. The height of the girder changes from 2.04 m to 1.9 m. The thickness of the bottom plate changes from 0.4 m to 0.26 m. The length of the transition section is 0.42 m. The upper width of U-shaped girder is 5.42 m. The bottom width of non-plate thickening section is 3.98 M, and that of bottom plate thickening section is 4.52 m. The center line of bearing is 0.6 m away from the girder end. The center line of track is inclined to the inner web side, which is 0.14 m away from the center line of the bottom plate. The section size of middle position and fulcrum position of the mixed-tensioned precast U-shaped girder is illustrated in Figs. 1 and 2.

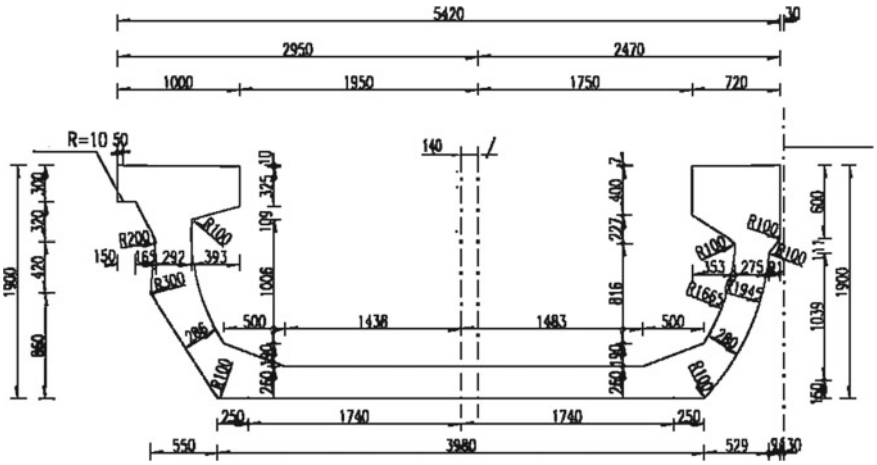

Fig. 1 Selection size of middle position (unit: mm)

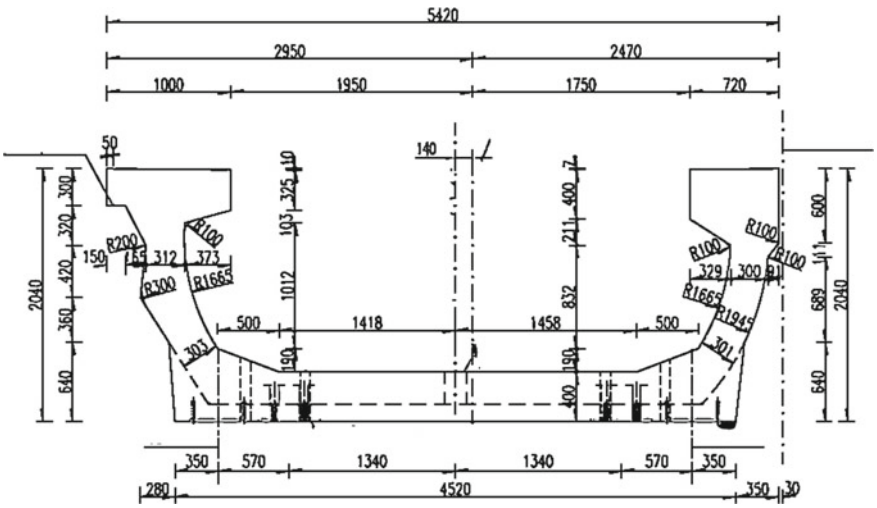

Fig. 2 Section size of fulcrum position (unit: mm)

There are 88 steel strands for prestressed concrete in the mixed-tensioned precast U-shaped girder. In order to avoid excessive tensile stress in the upper edge concrete of girder end due to the steel strands, plastic casings are set at the end of some steel strands. There are 28 bundles of non-casing steel strand N1, 26 bundles of 2.4 m casing steel strand N2 and 26 bundles of 5 m casing steel strand N3. The fptk of steel strands for prestressed concrete is 1860Mpa. Tension control stress of both pre-tensioned and post-tensioned prestressed steel strands under anchor is 1302Mpa.

3 Brief Introduction of Analysis Method of Mechanical Properties of the Precast U-shaped Girder

The FEA and static loading test is still used in mechanical property analysis as usual. The FEM software-Midas FEA has been adopted to establish the beam element model and the solid element model. The calculation and analysis of beam element model is used to guide and formulate the plan of static loading test, and that of solid element model is used to contrastively analyze the mechanical properties.

Figure 3 shows the solid element model of the precast U-shaped girder. There are 20,381 solid elements in the model of the girder. The prestressed steel strands are imitated by the prestressed elements in the FEM software. The pre-tensioned steel strands are divided into 8000 elements, and the post-tensioned prestressed steel strands are divided into 200 elements. The mixed-tensioned steel strands are divided into 6000 elements in the part of pre-tensioning and 80 elements in the part of post-tensioning.

In the static loading test, 6 precast U-shaped girders have been taken to the experiment by the method of reaction loading on the test platform constructed previously. In order to reduce the test cost and save time, the test principle of 'The maximum bending moment at the mid-span section is equal to the most unfavorable bending moment in design, and the maximum shear force at the fulcrum section is approximately equal to the most unfavorable shear force in design' have been established according to the fact of simply supported beam that the maximum bending moment is at the mid-span section and the maximum shear force is at the fulcrum section.

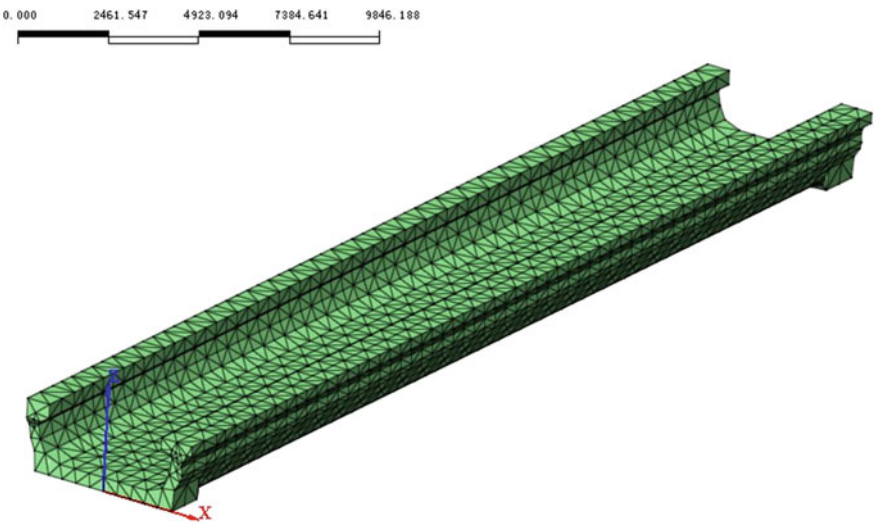

Fig. 3 Solid element model of the precast U-shaped girder

Fig. 4 Site of test

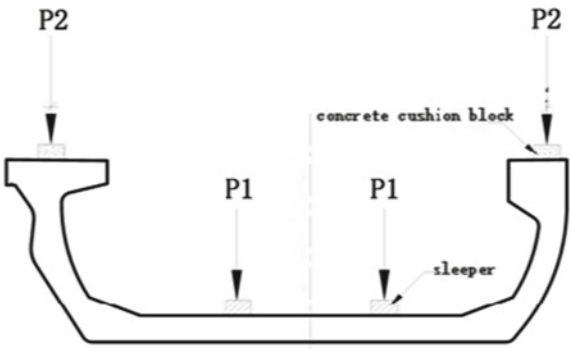

Fig. 5 Loading scheme of U-shaped girders

Under the above conditions, the tests of bending moment loading and shear loading have been completed.

There are 5 gantry reaction frames in the test, and their center distance is 6.8 m. Sleepers or concrete pads have been arranged at the loading point P1 of the bottom plate and P2 of the web. The site of test and the loading scheme of U-shaped girders are shown in Figs. 4 and 5.

4 The Analysis of the Mechanical Properties of Mixed-Tensioned Precast U-shaped Girder

The static loading test mainly tests the strain and deflection at the control section of the 32.7 m-span mixed-tensioned precast U-shaped girder under 1.0 times of design value of load and 1.2 times of design value of load. Meanwhile, the intensity and stiffness are evaluated according to relevant codes. The static loading tests of

three U-shaped girders are completed, and each of them was loaded twice. The main experimental results are as follows:

(1) Under 1.0 times of design value of load, the maximum deflection of the second girder is 10.13 mm, which meet the requirements of the standard of stiffness (< L/2000) in the design code;
(2) Under 1.0 times of design value of load, the residual deflection of all the three girders ranges from 2.49% to 3.10%, which meet the requirements (< 20%);
(3) Under 1.0 times of design value of load and 1.2 times of design value of load, calibration coefficient of the bending normal stress increment of all the three girders is under 1.00, which meet the requirements;
(4) After complete unloading, the residual strains of the three girders are, respectively, 0~17%, 3~18% and 2~17%, all of which are under 20%;
(5) Under 1.0 times of design value of load and 1.2 times of design value of load for 10 min, there are no transverse cracks at the bottom edges of bottom plates, chamfers of girders and arc transition section of three girders, which meet the requirements of crack resistance.

The test results are compared with the results of FEA, and the comparison diagrams of the stiffness and intensity of mixed-tensioned precast U-shaped girders are illustrated in Figs. 6 and 7.

From the above analysis, we can see that.

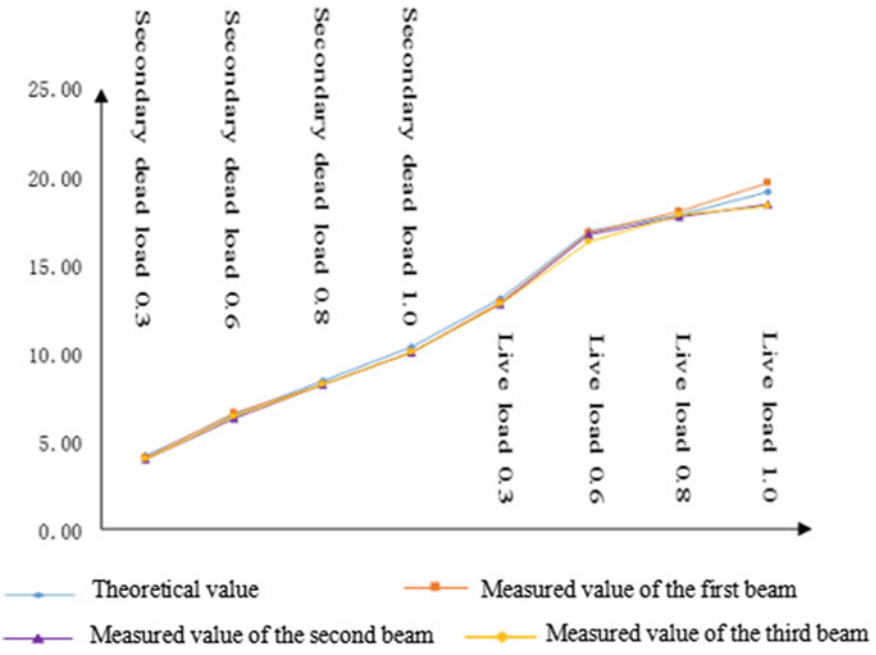

Fig. 6 Comparison diagram of deflection at mid-span section (unit: mm)

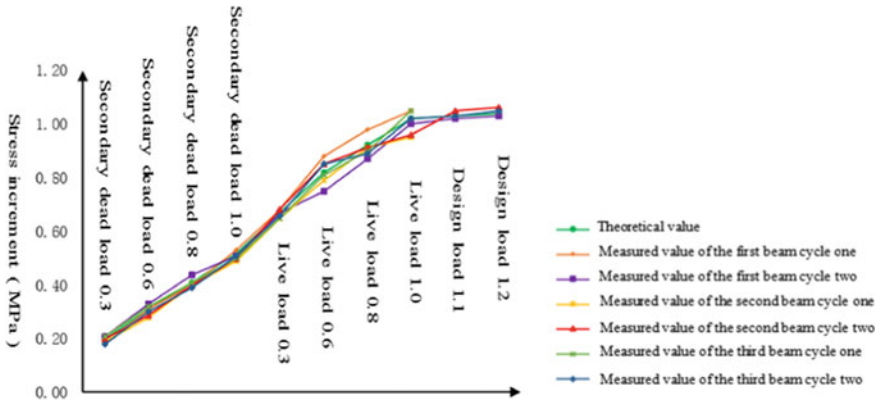

Fig. 7 Comparison diagram of the stress increment at mid-span section (unit: MPa)

(1) The structural design and the construction technology of mixed-tensioned precast U-shaped girders adopted in the Rail Transit Line 8 in Qingdao meet the requirements of the standard in the relevant code, and the structures are reliable.
(2) The FEA is in good agreement with the experimental results, and the test and calculation analysis are mutually verified. The calculation by models is correct, which can be used as the basis of further analysis of the theory of FEA.

5 Comparative Analysis of Mechanical Properties of Precast U-shaped Girders by Mixed-tensioning Method, Pre-tensioning Method and Post-Tensioning Method

By changing the arrangement of prestressed steel strands and construction method, the finite element models of pre-tensioned and post-tensioned precast U-shaped girders at the same condition of the amount of steel strands and the sections have been established for the comparative analysis of mechanical properties.

5.1 Comparative Analysis of Mechanical Properties Under the Load of Prestress

The compressive stress under the load of prestress.

According to experience, the bottom edges of simply supported beams are in the state of compression under the load of prestress. Due to the difference of calculation and analysis, it tends to cause tensile stress in the upper edge of the section. The vertical bending normal stress values of the top edge of the outer web at the

fulcrum, 1/8 span, 1/4 span, 3/8 span and mid-span section of three types of precast U-shaped girders have been recorded in Table 1. The comparison diagram of the vertical bending normal stress values of the U-shaped girders under this condition is illustrated in Fig. 8.

According to Table 1 and Fig. 8, all the top edges of the three U-shaped girders are in the state of compression under the load of gravity and prestress, and the compressive stress of mixed-tensioned precast U-shaped girders is between that of pre-tensioning method and post-tensioning method.

The camber under the load of prestress.

The track irregularity is affected by the camber value of the girder under the load of prestress. Taking the concrete creep in 3650 days into consideration, the maximum cambers of the U-shaped girders under the load of gravity and prestress are recorded as follows: mixed-tensioning method-13.70 mm; pre-tensioning method-13.99 mm; post-tensioning method-13.33 mm. It can be seen from the above that there is not much difference among the three.

Table 1 Vertical bending normal stress values of the top edge of the outer web (unit: MPa)

Type	Fulcrum	1/8 span	1/4 span	3/8 span	Mid-span	5/8 span	3/4 span	7/8 span	Fulcrum
Mixed-tensioning method	0.51	−0.13	−2.36	−3.20	−3.71	−3.20	−2.36	−0.13	0.51
Pre-tensioning method	0.57	−0.06	−2.29	−3.15	−3.68	−3.15	−2.29	−0.06	0.57
Post-tensioning method	0.03	−0.28	−2.50	−3.36	−3.91	−3.36	−2.50	−0.28	0.03

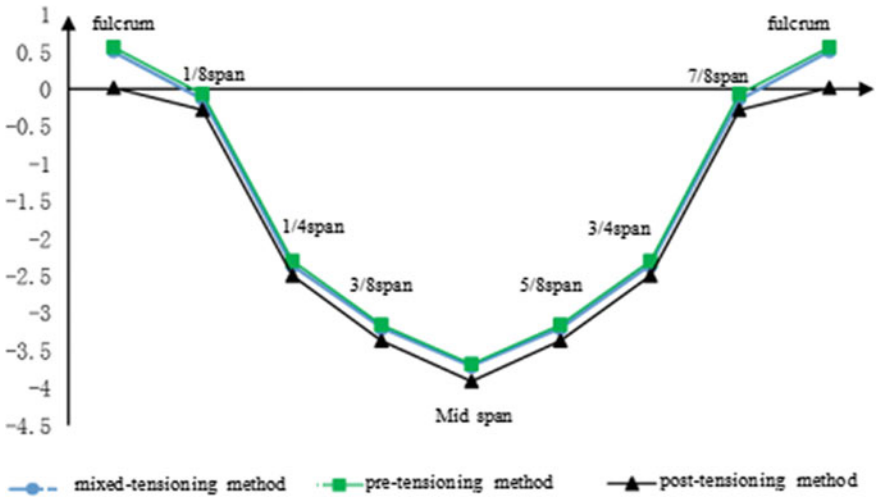

Fig. 8 Comparison diagram of the vertical bending normal stress values of the top edge of the outer web (unit: MPa)

5.2 *Comparative Analysis of Mechanical Properties Under the Most Unfavorable Loading Combination*

Under the most unfavorable loading combination, the compressive stress on the bottom edge of the bottom plate of the simply supported U-beam is low, and even tensile stress occurs. Therefore, under the most unfavorable loading combination of gravity, prestress, secondary dead load and live load of train, the vertical bending normal stress values of the bottom edge of the bottom plate at the fulcrum, 1/8 span, 1/4 span, 3/8 span, mid-span, 5/8 span, 3/4 span and 7/8 span section of three types of precast U-shaped girders have been recorded in Table 2. The comparison diagram of the vertical bending normal stress values of the U-shaped girders under this condition is illustrated in Fig. 9.

Table 2 Vertical bending normal stress values of the bottom edge of the bottom plate (unit: MPa)

Type	Fulcrum	1/8 span	1/4 span	3/8 span	Mid-span	5/8 span	3/4 span	7/8 span	Fulcrum
Mixed-tensioning method	−8.87	−8.43	−7.51	−5.72	−5.37	−5.72	−7.51	−8.43	−8.87
Pre-tensioning method	−9.01	−8.56	−7.63	−5.86	−5.55	−5.86	−7.63	−8.56	−9.01
Post-tensioning method	−8.85	−8.39	−7.46	−5.68	−5.35	−5.68	−7.46	−8.39	−8.85

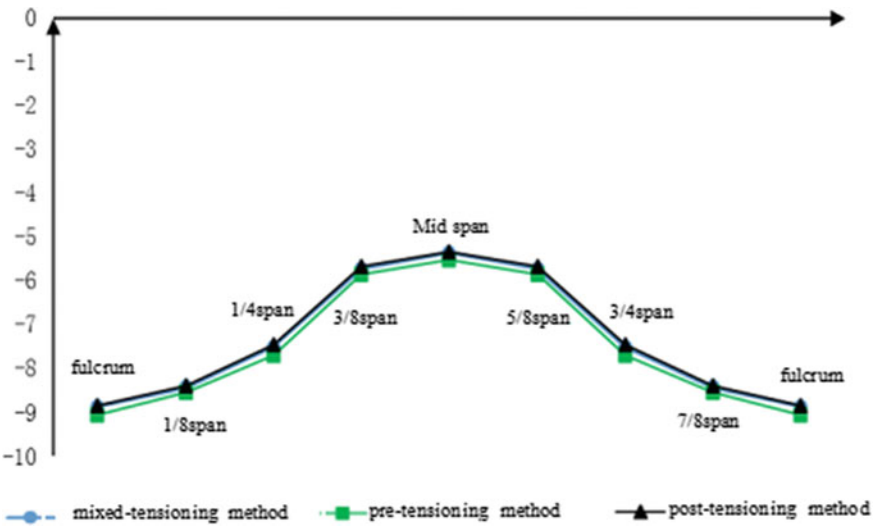

Fig. 9 Comparison diagram of the vertical bending normal stress values of the bottom edge of the bottom plate (unit: MPa)

Obviously, under the most unfavorable loading combination, the compressive stress of the bottom edge of the bottom plate of the mid-span section is almost the same.

Under the most unfavorable loading combination, the shear stress values at the fulcrum, 1/8 span, 1/4 span, 3/8 span, mid-span, 5/8 span, 3/4 span and 7/8 span section of three types of precast U-shaped girders have been recorded in Table 3. The comparison diagram of the shear stress values of the U-shaped girders under this condition is illustrated in Fig. 10.

Obviously, the shear stress values at the fulcrum section of the post-tensioned and mixed-tensioned precast U-shaped girder are lower than that of pre-tensioning method due to the bent prestressed steel strands at the fulcrum section, which is beneficial to improve the shear bearing capacity.

Finally, under the most unfavorable loading combination, the vertical displacements at the fulcrum, 1/8 span, 1/4 span, 3/8 span, mid-span, 5/8 span, 3/4 span and 7/8 span section of three types of precast U-shaped girders have been recorded

Table 3 Shear stress values (unit: MPa)

Type	Fulcrum	1/8 span	1/4 span	3/8 span	Mid-span	5/8 span	3/4 span	7/8 span	Fulcrum
Mixed-tensioning method	−1.12	−0.76	−0.66	−0.39	0.00	0.39	0.69	0.81	1.18
Pre-tensioning method	−1.55	−1.09	−0.68	−0.40	0.00	0.40	0.70	1.10	1.55
Post-tensioning method	−0.99	−0.61	−0.67	−0.39	0.00	0.39	0.69	0.66	1.11

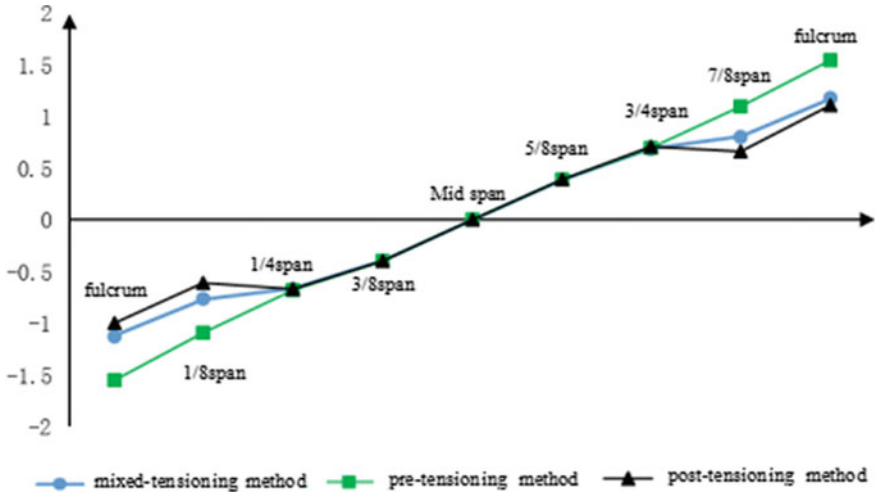

Fig. 10 Comparison diagram of the shear stress values (unit: MPa)

Table 4 Vertical displacements (unit: mm)

Type	Fulcrum	1/8 span	1/4 span	3/8 span	Mid-span	5/8 span	3/4 span	7/8 span	Fulcrum
Mixed-tensioning method	0	−0.51	−2.29	−4.21	−5.20	−4.18	−2.25	−0.47	0
Pre-tensioning method	0	−0.31	−2.06	−3.97	−4.92	−3.97	−2.06	−0.31	0
Post-tensioning method	0	−0.73	−2.52	−4.53	−5.58	−4.53	−2.52	−0.73	0

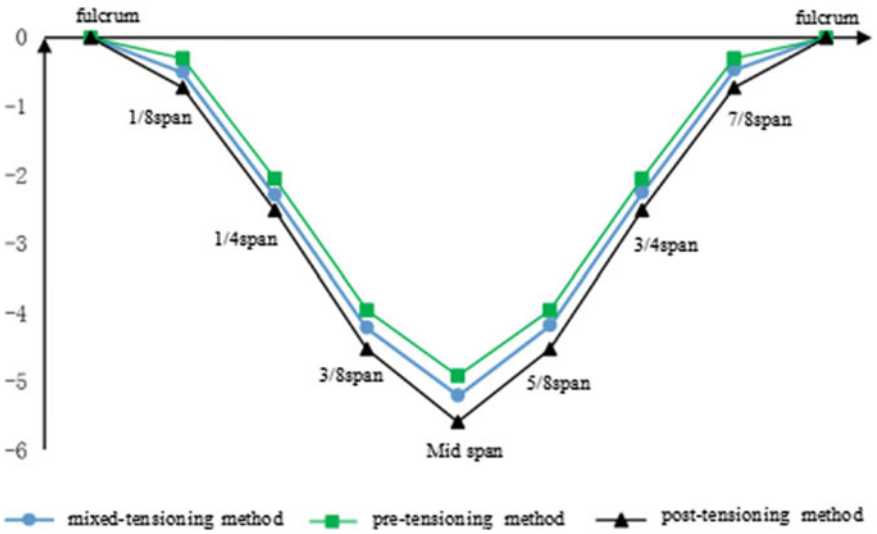

Fig. 11 Comparison diagram of the vertical displacements (unit: mm)

in Table 4. The comparison diagram of the vertical displacements of the U-shaped girders under this condition is illustrated in Fig. 11.

Obviously, the deflection of mid-span section of the mixed-tensioned precast U-shaped girder is between that of the pre-tensioning method and the post-tensioning method. The difference of deflections between Table 4 and Fig. 11 should be due to the construction technology of prestressing.

6 Conclusions

(1) For the first time, the mixed-tensioned precast U-shaped girder has been used in the Rail Transit Line 8 in Qingdao, and the calculation analysis and the loading test show that it meets the service requirements;

(2) Keeping the span, section and material consumption at the same level, the mechanical properties of mixed-tensioned precast U-shaped girders are almost the same as that of the pre-tensioning method and the post-tensioning method. The properties of deformation of mixed-tensioned precast U-shaped girders are between that of the pre-tensioning method and the post-tensioning method;
(3) The mixed-tensioned precast U-shaped girder has the advantages of that of the pre-tensioning method and the post-tensioning method. It can not only control the camber caused by prestressed construction, but also improve the shear bearing capacity of the fulcrum section. It can save materials such as anchors or concrete, which is suitable for the long span precast U-shaped girder and worth popularizing;
(4) The influence and calculation theory of the loss of prestress at the part of pre-tensioning caused by part of post-tensioning remain to be further studied about the mixed-tensioned precast U-shaped girder.

References

1. El-Domiaty AA, Elsharkawy AA (1998) Stretch-bending analysis of U-section beams. Int J Mach Tools Manuf 38(1):75–95
2. Kuangzhang H, Xinyuan J (1987) Channel beam. China Railway Publishing House, Beijing, pp 5–7
3. Qing LI (2009) Structural calculation and experiment of U-beam in Nanjing metre line. Urban Mass Transit 12(8):8–12
4. Xiao-dong S, Ding-Jun W, Qi L (2011) Stress analysis of new U-shape girders for urban rail transit considering warping. Struct Eng 27(5):68–72
5. Yu-Min S, Ding-Jun W, Jian H (2017) Study on static load test of pre-tensioned pre-casted U-beam. Architect Technol 48(8):883–886
6. Yu-Min S, Zhi-Jun W (2007) Analysis on causation and countermeasures for vertical prestress failure of concrete box beam bridges. Railway Standard Design 11:58–60
7. Staquet S, Rigot G, Detandt H et al (2004) Innovative composite precast prestressed precambered U-shaped concrete deck for Belgiums high speed railway trains. PCI J 49(6):94–113, 134
8. Zhang L (2017) Design and research of continuous U-beam in line 13 of Qingdao metro. Railway Standard Des 61(07):81–83, 92
9. Jian-Jun Z, Wei L (2009) Design and construction of U-type beam in elevated area of urban rail traffic in Shanghai. Urban Roads Bridges Flood Control 5:113–116
10. Hong Z, Zhao-Hui L, Zhi-Wu Y et al (2019) Time-dependent camber deformation reliability of high-speed railway PSC Box girder considering creep effect. J China Railway Soc 41(6):107–114

Structural Analyses of RC Buildings with Various Support Types

Gokhan Tunc, Tuğrul Tanfener, and Zainab Kamal Khayyat

Abstract The seismic design of buildings is performed based on dynamic analyses by considering fixed-base supports. The effect of soil's elastic behavior is usually ignored during the analysis and design phases of buildings. Due to differences in the seismic responses of rigidly and elastically supported buildings, it is essential to study the impact of the elastic behavior of soil on overall building design. In this study, the structural behavior of rigid basement walls with various support conditions will be investigated. For this purpose, a parametric study will be conducted on a total of 60 reinforced concrete buildings with two different layouts. For this purpose, five support types will be studied. These supports types in their correct order are as follows: (1) vertical area springs at the base coupled with horizontal area springs all around the basement walls, (2) fixity at the base coupled with horizontal joint springs only at the ground floor level, (3) vertical joint springs at the base, (4) only fixity at the base with no joint or area springs, and (5) vertical joint springs at the base coupled with horizontal joint springs only at the ground floor level. The results revealed that the buildings with support type 2 exhibited the most rigid behavior, while the buildings with support types 1 and 3 exhibited the most flexible behavior. The fundamental periods from support type 5 were always smaller than those from support type 1, pronouncing the significance of the presence of horizontal springs. Based on the results, it was also concluded that the choice of support type had almost no impact on the design of a mat foundation.

Keywords Elastically supported buildings · Rigid basements · Support types

G. Tunc (✉) · Z. K. Khayyat
Department of Civil Engineering, Atilim University, Ankara, Turkey
e-mail: gokhan.tunc@atilim.edu.tr

T. Tanfener
Prota Engineering, Turan Güneş Bulvarı, Galip Erdem Cad. No: 27, Ankara, Turkey

T. Kang (ed.), *Proceedings of 5th International Conference on Civil Engineering and Architecture*, Lecture Notes in Civil Engineering 369,
https://doi.org/10.1007/978-981-99-4049-3_86

1 Introduction

The dynamic behavior of buildings with basement floors has not been widely studied since most of the past research in this field has focused on soil-structure interaction (SSI) and therefore rather overlooked at the presence of basement floors. In finite element (FE) modeling, the foundation of a reinforced concrete (RC) building is generally assumed rigid. However, this assumption might not be valid for buildings if more realistic support conditions are intended to be modeled.

In the past some researches have been conducted in this area. One of the earliest articles related to SSI was published as a conference paper in 1969 [1]. The article discusses the seismic resistance design of nuclear reactor facilities and focuses on the interaction between ground and structure. The article states that during seismic activity, energy absorption between a structure and its supporting foundations occurs specifically for heavy and massive structures resting on soil. This absorption can be incorporated into seismic design as a function of damping, or through general modifications to the input motion, which would eventually help reduce lateral forces transmitted to a structure resting on soil. In 1978, the capability of finite element procedures in capturing the soil-structure interaction effects of a nuclear plant during an earthquake was investigated by comparing analytical and recorded results [2]. The study concluded that finite element procedures could yield results with a high level of accuracy if they were used in conjunction with good engineering judgment. In 1992, a simplified approximate procedure was proposed for the seismic design of tall buildings with multi-level basements [3]. This new procedure included the effects of superstructure–substructure soil interaction and the dynamic earth pressure effects existing on the exterior basement walls. This study concluded that the interactive seismic design of buildings with multi-level basements generated more economical results when compared to those with fixed-base assumption. In 2004, the effect of SSI on the natural period and base shear forces of buildings with frames resting on mat foundation was investigated [4]. In another study conducted in 2008, the seismic performance of RC frame structures, with 6 and 20 stories resting on fixed and flexible bases, was evaluated through a set of 13 near-fault earthquake (NFE) records by conducting two-dimensional nonlinear time history analyses [5]. The study compared the response of flexible-base and fixed-base models and concluded that the characteristics of the NFE records might significantly influence the impact of SSI effects on tall and low-rise structures. The study concluded that soil flexibility lengthened the natural period and decreased the base shear forces. In 2010, similar study was conducted for building frames bearing on strip foundation with and without considering the impact of soil flexibility [6]. The analyses results investigated the change in the lateral natural periods and base shear forces. In 2013, the seismic analysis of frame-shear wall buildings was conducted to determine their dynamic behavior based on a design spectrum generated from the Indian Seismic Code Is: 1893–2002 [7]. The study concluded that the effect of soil flexibility led to a 27% increase in the natural period and some degree of reduction in the bending moments and shear forces. In the same year, SSI effects were studied through nonlinear dynamic analysis

by investigating the seismic response of a 10-story moment-resisting frame, with a shallow foundation, resting on varying soil types [8]. The structure was assumed to have a fixed base, with and without SSI features. The results demonstrated that the soil class significantly influenced the performance level of the model. Specifically, in soft soil, building performance declined rapidly from the life safe level to near collapse, indicating that the consideration of SSI effects on the design of concrete moment-resisting building frames resting on soft soil is essential. In 2014, the effects of soil flexibility on buildings with mat foundation were studied [9]. The study concluded that the natural period increased when SSI was included, and that for a soft soil condition, the impact was more influential when compared to stiffer soils. The study emphasized the importance in seismic design deficiencies of buildings if SSI is not considered. In 2019, the SSI was analytically investigated on tunnel-form buildings. Based on the results, it was concluded that as the building height and earthquake intensity increased, the SSI impacts on the structural responses such as shear forces and story drifts became more pronounced [10].

This article, which is mainly extracted from an MS thesis conducted at Atilim University, Ankara, Turkey, will investigate the structural behavior of rigid basement walls by studying a total of 60 reinforced concrete buildings with two distinct layouts [11]. These buildings, each of which had a different number of floors, are assumed to have mat foundations of differing thicknesses. In the analysis phase, the effects of a total of five support types will be examined. These support conditions are as follows: (a) vertical area springs assigned to the base coupled with horizontal area springs assigned to the basement walls, (b) fixity at the base coupled with horizontal joint springs assigned to the ground floor level only, (c) vertical joint springs assigned to the base, (d) fixity at the base with no other joint or area springs, and (e) vertical joint springs at the base coupled with horizontal joint springs assigned to the ground floor level only. To do that horizontal and vertical spring supports will be assigned to each building's foundations and basement walls to determine the effect of soil's elastic behavior. During the analysis and design phases, following parameters will also be studied in-depth: (a) total building height (low, moderate, and high-rise); (b) soil type (dense and medium-dense sand); and (c) the number of basement floors. The scope of this study is to select the support type that would most closely simulate the actual behavior of buildings. For this purpose, the buildings will be analyzed by using a commercially available software package SAP2000 [12]. In the seismic analysis of the buildings, the response spectrum method generated according to the Turkish Earthquake Code 2007 (TEC07) will be utilized [13]. In order to satisfy the scope of this study, the analyses results will be evaluated through a total of four parameters: (a) modal mass participation factors (MMPF), (b) fundamental periods, (c) foundation forces, and (d) base shear forces.

2 Building Description

In this study, a total of two rectangular floor layouts were used for the 10, 20, and 30 story buildings. The plan dimensions of these layouts were 24 by 42 m. The layouts were identical to each other although the shear wall locations were different. As shown in Fig. 1, the shear walls in the first floor layout were used in the core of the building, while in the second layout, they were located near the building's shorter edge. The layout with central core walls is denoted by "A", while the other layout (with the walls near the building edge) is denoted by "B" (see Fig. 1). In these buildings, the number of basement floor levels was changed. The 2, 3, and 5 basement floor levels were assumed, for the 10, 20, and 30 story buildings, respectively.

All the buildings were assumed to have the same floor height of 3.2 m. The total heights of the buildings varied from 32 m for the 10-story building, to 96 m for the 30-story one. Table 1 lists the dimensions of structural members.

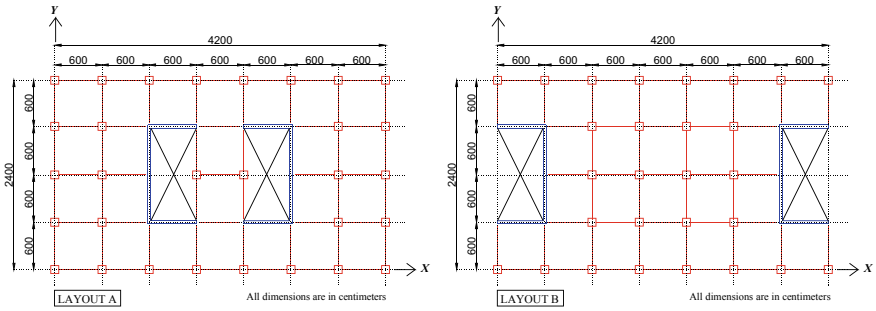

Fig. 1 Buildings plan view: **a** layout A **b** layout B

Table 1 Dimensions of the structural members

Member sizes (cm)						
Story number	Columns			Beams	Slabs	Shear walls
	10 story	20 story	30 story	10, 20, 30 stories	10, 20, 30 stories	10, 20, 30 stories
1–5	60 × 60	90 × 90	110 × 110	75 × 30	16	30
6–10	50 × 50	80 × 80	100 × 100	75 × 30	16	30
11–15	–	70 × 70	90 × 90	75 × 30	16	30
16–20	–	60 × 60	80 × 80	75 × 30	16	30
21–25	–	–	70 × 70	75 × 30	16	30
26–30	–	–	60 × 60	75 × 30	16	30

3 Building Models in SAP2000

Table 2 shows the model names of all 60 buildings used in SAP2000. The building models in Table 2 are categorized for dense (Z1) and medium-dense sands (Z2). A six-letter label is used to describe the models. The first letter in this label denotes to the layout type (layout A or B). The second letter is a number and defines the number of floors. The numbers "1", "2", and "3", which are used next to the letters A and B are for the 10, 20, and 30 story buildings, respectively. The third letter is denoted by "Z" and is used along with a fourth letter, which is another number symbolizing the local site class defined in TEC07. The fifth letter, denoted by "T", is used to define the five different support types. According to these label notation, for example, A3Z2T4 is the name of a building with layout A, 30 stories tall, located in a local site class 2, with support type no. 4.

3.1 Material Properties, Load Cases, and Load Combinations

The concrete class was C25, and its modulus of elasticity and Poisson's ratio were 30,000 MPa and 0.2, respectively. The steel reinforcement had a yield strength of 420 MPa, modulus of elasticity of 2×10^5 MPa, and a Poisson's ratio of 0.2 [14].

In this study, following five load cases were used: (a) dead load, (b) superimposed dead load, (c) live load, (d) statically and dynamically applied lateral earth pressures, and (e) the response spectrum in "x" and "y" directions (see Fig. 1). The unit weight of reinforced concrete was 2.5 t/m^3 and was automatically included by the program. For superimposed dead loads, a 150 kg/m^2 of load was applied to all floors. A constant live load of 350 kg/m^2 was assumed to exist on all floors and was applied to the slabs as uniformly distributed surface loads [15]. The basement walls

Table 2 Model names in SAP2000

Soil type	Layout A(*)			Layout B (*)		
Dense sand	A1Z1T1	A2Z1T1	A3Z1T1	B1Z1T1	B2Z1T1	B3Z1T1
	A1Z1T2	A2Z1T2	A3Z1T2	B1Z1T2	B2Z1T2	B3Z1T2
	A1Z1T3	A2Z1T3	A3Z1T3	B1Z1T3	B2Z1T3	B3Z1T3
	A1Z1T4	A2Z1T4	A3Z1T4	B1Z1T4	B2Z1T4	B3Z1T4
	A1Z1T5	A2Z1T5	A3Z1T5	B1Z1T5	B2Z1T5	B3Z1T5
Medium dense sand	A1Z2T1	A2Z2T1	A3Z2T1	B1Z2T1	B2Z2T1	B3Z2T1
	A1Z2T2	A2Z2T2	A3Z2T2	B1Z2T2	B2Z2T2	B3Z2T2
	A1Z2T3	A2Z2T3	A3Z2T3	B1Z2T3	B2Z2T3	B3Z2T3
	A1Z2T4	A2Z2T4	A3Z2T4	B1Z2T4	B2Z2T4	B3Z2T4
	A1Z2T5	A2Z2T5	A3Z2T5	B1Z2T5	B2Z2T5	B3Z2T5

(*) For the layout details, see Fig. 1

were subjected to two types of lateral earth pressure, static and seismic. The force distribution of static lateral pressure was assumed to be trapezoidal due to the existence of multiple basement floors. The Mononobe-Okabe model was used to apply seismic earth pressure [16, 17].

The buildings in this study were residential located in Izmir, which is prone to the severe earthquakes in Turkey. According to the TEC07, Izmir is located in Seismic Zone 1, which exhibits the highest risk out of four seismic zones [13]. The response spectrum method was selected for the 10, 20, and 30 story buildings. Following seismic parameters had to be determined to apply the response spectrum method: (a) importance factor, (b) seismic zones, (c) local site classes, and (d) ductility. Since the buildings were residential, the importance factor was equal to one. The corresponding earthquake ground motion parameter of Izmir, associated with seismic zone 1, was equal to 0.4. Two separate soil groups (A and B) were used in this study as described in TEC07. The soil group A represents a rock type soil, while soil group B represents dense sand and very stiff clay type of soil.

The static and dynamic loads acting on the buildings were factored by using the load combinations described in TEC 07 and TS500 [13, 14]. In the dynamic analysis, the orthogonal effects of earthquake loads are also included.

3.2 *Response Spectrum Curves*

The framing type for the building models included the joint resistance of frames and solid structural walls. The buildings are assumed to have high ductility levels, and their corresponding seismic load reduction factor was determined to be 7 [12]. The elastic and design acceleration spectrum curves were obtained for both Z1 and Z2 (see Fig. 2).

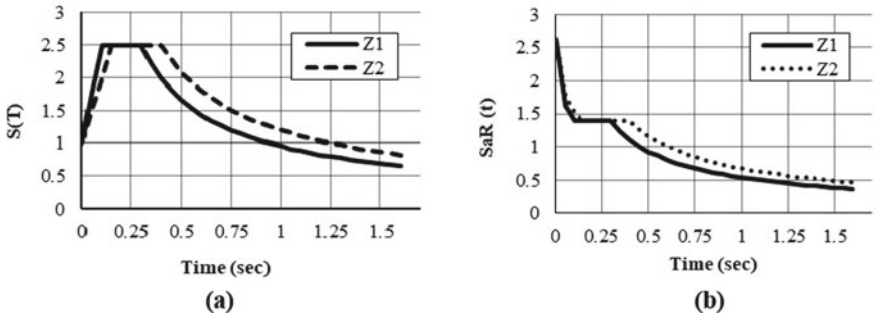

Fig. 2 Response spectrum curves for Z1 and Z2: **a** elastic and **b** design

3.3 Foundation Type

A mat foundation was selected for all buildings. Three different mat thicknesses—60 cm, 120 cm, and 180 cm—were assigned to the 10, 20, and 30 story buildings, respectively. These thicknesses were slightly over conservative in order not to experience any design failures related to the foundation.

3.4 Support Types

Two types of base supports were used in the models: fixed and flexible. In the fixed support case, the bases of the vertical members were assumed to be fixed. In the flexible support case, springs replaced this fixity. The springs were assigned using a parameter called "subgrade reaction modulus, SRM" with two components, horizontal and vertical. The SRM's horizontal component is a function of its vertical component, which is commonly used in the FE analyses of buildings. The numerical values of the vertical SRM is directly linked to the soil class. Based on the soil properties of this study, average values of SRM were determined for the dense (Z1) and medium-dense sand (Z2) soils [18]. Therefore, 80,000 kN/m^3 of SRM was used for the dense sand, and 60,000 kN/m^3 was used for the medium-dense sand.

As illustrated in Fig. 3, a total of five different support types were considered.

Support Type 1. A set of vertical and horizontal area springs were employed to simulate the structural behaviors between (a) footings and soil and (b) basement walls and soil. The area springs were assigned to the footing using the pseudo-coupled method where the springs along the perimeter of a mat are stiffer than those near or at its center [19]. In this method, as illustrated in Fig. 4, the mat was divided into three zones, A, B, and C. The SRM values of these zones were determined for both dense and medium-dense sands based on the SRM values defined above. As described in reference [19], the SRM values of Zones A and B are assumed to be 2 and 1.5 times larger than those of Zone C. Therefore, the values of K_{sA}, K_{sB}, and K_{sC} for dense sand (or Z1) were calculated as 106,666 kN/m^3, 80,000 kN/m^3, and 53,333 kN/m^3, respectively. The same values for the medium-dense sand (or Z2) were 80,000 kN/m^3, 60,000 kN/m^3, and 40,000 kN/m^3, respectively.

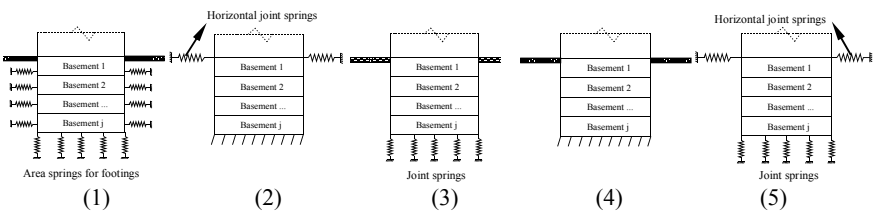

Fig. 3 Support types

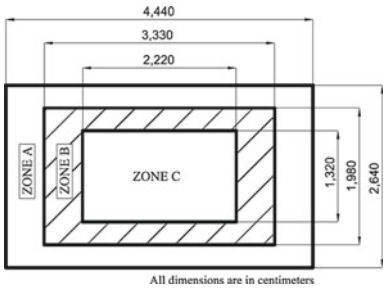

Fig. 4 Zoning of SRM for layouts A and B

Support Type 2. The base was assumed to be fixed. Horizontal springs were utilized only at the ground floor level (i.e., no other springs were assigned to the basement walls). For this purpose, a very large spring constant of 10^{10} kN/m value was used for the horizontal springs since the load transition from the floors above the ground floor level (superstructure) to those below the ground floor level (substructure) were significantly affected.

Support Type 3. In this support type, only vertical joint springs were used. The springs were assigned to each joint using the following 6 by 6 diagonal matrix assuming that the lateral displacements of the springs in the "x" and "y" directions along with its rotational displacements are decoupled (see Eq. 1) [19].

$$\begin{bmatrix} k_x & 0 & 0 & 0 & 0 & 0 \\ 0 & k_y & 0 & 0 & 0 & 0 \\ 0 & 0 & k_z & 0 & 0 & 0 \\ 0 & 0 & 0 & \theta_x & 0 & 0 \\ 0 & 0 & 0 & 0 & \theta_y & 0 \\ 0 & 0 & 0 & 0 & 0 & \theta_z \end{bmatrix}_{6x6} = \begin{bmatrix} \frac{16G}{\pi(2-\upsilon)} & 0 & 0 & 0 & 0 & 0 \\ 0 & \frac{16G}{\pi(2-\upsilon)} & 0 & 0 & 0 & 0 \\ 0 & 0 & \frac{8G}{\pi(1-\upsilon)} & 0 & 0 & 0 \\ 0 & 0 & 0 & \frac{32G}{3\pi(1-\upsilon)} & 0 & 0 \\ 0 & 0 & 0 & 0 & \frac{32G}{3\pi(1-\upsilon)} & 0 \\ 0 & 0 & 0 & 0 & 0 & \frac{8G}{3\pi(1-\upsilon)} \end{bmatrix}_{6x6} \quad (1)$$

In this matrix, G is the shear modulus, and is a function of E and υ, and υ is the Poisson's ratio for the soil. E is the modulus of elasticity, and for the dense sand, the values of E and υ were selected as 81 MPa and 0.4, respectively. For the medium-dense sand, these two values were reduced to 50 MPa and 0.3, respectively.

Support Type 4. In this support type, the bases of the buildings were considered fixed. This support type is the most common support type used in practice.

Support Type 5. The vertical joint springs and the horizontal ones at the ground floor level were utilized. For the details of the vertical joint springs, refer to those used in support type 3; for the horizontal, refer to those used in support type 2.

3.5 Basement Wall—Area Springs

The interaction between the soil and the basement walls were achieved through area springs. The horizontal SRM value was calculated as 6,594 kN/m^3, which was the value suggested for medium-dense sand [20]. The same value was also used for the models with dense sand since the soil behind the walls was assumed to be backfilled with medium-dense sand-type soil during its construction.

4 Results

The results of the 60 models will be examined in four groups: (a) modal mass participation factor (MMPF), (b) fundamental periods, (c) foundation forces, and (d) base shear forces.

4.1 Modal Mass Participation Factor

Table 3 lists the MMPFs of the 60 models. As indicated in the table, for almost all the models, the total MMPFs in the "x" and "y" directions were less than 90%, which is the minimum value prescribed in item 2.8.3.1 of TEC07 [13]. In order to resolve this matter, the number of modes was increased to four digit numbers. However, this attempt failed since the superstructures were more susceptible to ground motion than the substructures. As expected, reinforced concrete buildings with peripheral walls at their basements exhibit a lot more lateral rigidity relative to upper floors.

Based on the results, most of the layouts failed the minimum MMPF requirement of 90% (see the bold values in Table 3). The smallest MMPFs were obtained from the buildings with support type 5. For the 10 and 20 story buildings, support type 1 generated the largest MMPFs only in the "x" direction since the building had the weakest lateral strength in the same direction. None of the models with support types 2, 3, and 5 met the minimum MMPF requirement. As the number of floors above ground floor level increased, the associated MMPFs—except for support type 1—increased. Based on the results, it was concluded that a building with rigid basement walls should be analyzed as one building with its sub and superstructures using a reasonable number of mode shapes. In this article, it was recommended that six times the total number of floors would define the reasonable number of mode shapes.

Table 3 Model mass participation factors, MMPFs

Model name	MMPF in %		Model name	MMPF in %	
	X-Dir	Y-Dir		X-Dir	Y-Dir
A1Z1T1	97	**74**	B1Z1T1	98	**77**
A1Z1T2	**70**	**70**	B1Z1T2	**69**	**70**
A1Z1T3	**66**	**73**	B1Z1T3	**68**	**77**
A1Z1T4	**74**	**80**	B1Z1T4	**74**	**81**
A1Z1T5	**58**	**59**	B1Z1T5	**58**	**59**
A1Z2T1	97	**74**	B1Z2T1	98	**77**
A1Z2T2	**70**	**70**	B1Z2T2	**69**	**70**
A1Z2T3	**68**	**76**	B1Z2T3	**70**	**80**
A1Z2T4	**74**	**80**	B1Z2T4	**74**	**81**
A1Z2T5	**58**	**58**	B1Z2T5	**57**	**58**
A2Z1T1	96	**75**	B2Z1T1	98	**77**
A2Z1T2	**79**	**78**	B2Z1T2	**79**	**77**
A2Z1T3	**82**	**83**	B2Z1T3	**83**	**84**
A2Z1T4	**84**	90	B2Z1T4	**84**	90
A2Z1T5	**67**	**66**	B2Z1T5	**66**	**65**
A2Z2T1	96	**75**	B2Z2T1	98	**77**
A2Z2T2	**79**	**78**	B2Z2T2	**79**	**77**
A2Z2T3	**88**	**87**	B2Z2T3	**88**	**87**
A2Z2T4	**84**	90	B2Z2T4	**84**	90
A2Z2T5	**66**	**65**	B2Z2T5	**64**	**63**
A3Z1T1	**72**	**70**	B3Z1T1	**77**	**69**
A3Z1T2	**78**	**78**	B3Z1T2	**78**	**77**
A3Z1T3	**88**	**87**	B3Z1T3	**87**	**87**
A3Z1T4	92	94	B3Z1T4	91	94
A3Z1T5	**67**	**66**	B3Z1T5	**66**	**65**
A3Z2T1	**73**	**70**	B3Z2T1	**78**	**69**
A3Z2T2	**78**	**78**	B3Z2T2	**78**	**77**
A3Z2T3	93	91	B3Z2T3	92	91
A3Z2T4	92	94	B3Z2T4	91	94
A3Z2T5	**67**	**66**	B3Z2T5	**67**	**66**

4.2 Fundamental Periods

Figure 5 illustrates the variation of the fundamental periods (FP) of all 60 buildings located in Z1 and Z2. Based on the data, the FP—regardless of their layouts—was always in the "x" direction due to weaker lateral strength associated to it. As shown

in Fig. 5a, the fundamental periods from "layout A" were always smaller than their counterparts from "layout B" due to the importance of wall layout resulting from its lateral strength. According to the results, support type 1 generated the largest periods for the 10-story buildings, while support type 3 generated the largest periods for the 20 and 30 story ones. The smallest periods were always extracted from the buildings with support type 2. The support type 4, which was more frequently used in practice, produced the second smallest periods after support type 2.

The FPs were also plotted by normalizing their values (Normalized Periods, NP) for both Z1 and Z2 (see Fig. 5c, d). The data were normalized by dividing the FPs of support types 2, 3, 4, and 5 resulting from each of the 10, 20, and 30 story buildings to those of support type 1 associated with the same building. For both Z1 and Z2, it was observed that the periods of support types 2, 3, 4, and 5 were all less than those of support type 1—except for support type 3 of the 20 and 30 story buildings. As the number of floors increased from 10 to 30, the differences in periods became less significant indicating that for buildings beyond 30 floors, support types had less impact on periods. However, in contrast, support types had a significant effect on periods of buildings with 10 stories.

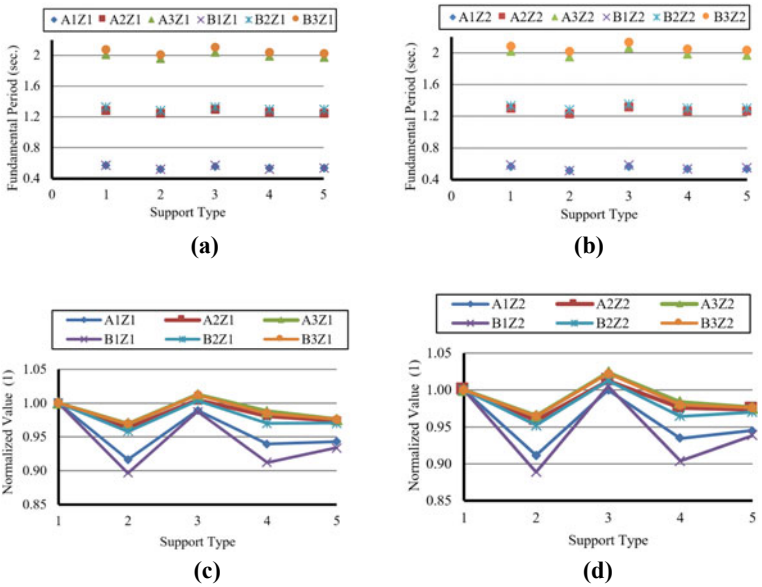

(1) *Normalized Value* $= \dfrac{T(\alpha_i Z_j T_k)}{T(\alpha_i Z_j T_1)}$, *where* α_i *= A, B; i=1,2,3; j=1,2 and k=1,2,3,4,5.*

Fig. 5 FP and NP values: **a** FP with Z1, **b** FP with Z2, **c** NP with Z1, and **d** NP with Z2. (1) Normalized Value $= \dfrac{T(\alpha_i Z_j T_k)}{T(\alpha_i Z_j T_1)}$, where $\alpha_i = A, B$; $i = 1,2,3$; $j = 1, 2$ and $k = 1,2,3,4,5$

4.3 Foundation Forces

The normalized bending moment values of M11 were plotted in Fig. 6 for the mat foundations of all 60 models (M11 is the bending moment about the "y" axis). The bending moments of support types 1 through 5 were all normalized (normalized moments, NM) with respect to the values of support type 1 for the 10-story building with Z1 so that the deviation from support 1, where the SSI is believed to be captured more effectively, could be assessed. M22 results were not included in this study since they were somewhat similar to M11 (M22 is the bending moment about the "x" axis).

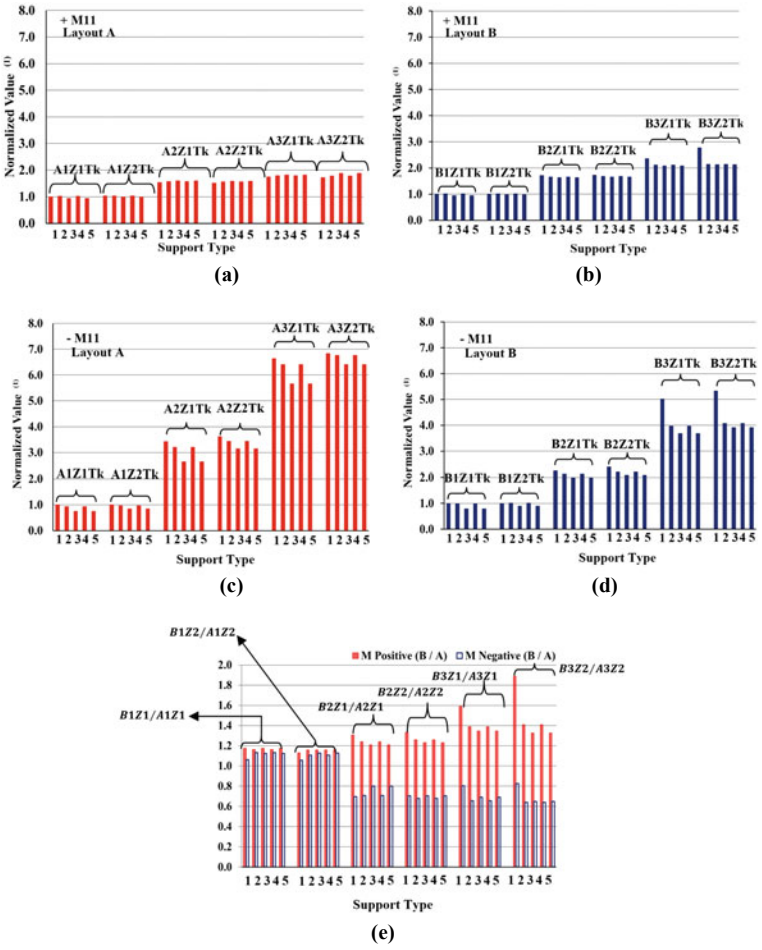

Fig. 6 Mat Foundation: NM values for layouts: **a** A (+M11), **b** B (+M11), **c** A (–M11), **d** B (–M11), and **e** ± M11 ((Layout B)/(Layout)). (1) Normalized Value $= \frac{M11(\propto_i Z_j T_k)}{M11(\propto_i Z_j T_1)}$, where $\alpha_i = A, B$; $i =$ 1,2,3; $j =$ 1,2 and $k =$ 1,2,3,4,5

Figure 6a, b shows the change in normalized positive M11 values for layouts A and B. The positive bending moment determines the bottom reinforcement and is considered more important compared to the top reinforcement resulting from negative bending moments. For layout A, the positive bending moment values increased by an average of 50% as the number of floors increased from 10 to 20 due to the larger gravity forces. The rate of increase in the positive bending moments resulting from the 20 story building to the 30 story one was a lot less (around 12%) due to the joint locations—column face—where the bending moments were extracted. For layout B, the change in the positive bending moments followed a somewhat similar pattern to that of layout A for both the 10 and 20 story buildings. However, in the 30 story building, with the exception of support type 1, the increase from 20 to 30 story building was around 25%, almost doubled when compared to its counterpart for layout A.

Figure 6c, d illustrates the change in the normalized negative M11 values for layouts A and B, respectively. Unlike the trend for the positive bending moment diagrams, the negative bending moment diagrams showed significant changes as the number of floors increased from 10 to 30. For layout A, the moments for the 10-story building in Z1 and Z2 increased by an average ratio of 3.5 and 7 compared to those for the 20 and 30 story buildings, respectively. This increase, however, was slightly less noticeable for layout B since the average numbers for the 20 and 30 story buildings were around 2 and 4. In layout B, as the number of floors increased to 30, the negative M11 values of support type 1 became more prominent. In layout B, for all buildings, the smallest negative M11 values were obtained from support types 3 and 5.

Figure 6e displays the ratios of the bending moments from layouts B to A for both positive and negative values. The data in this figure were obtained by dividing the bending moment values of layout B by those of layout A for each support type resting in Z1 and Z2 of the 10, 20, and 30 story buildings. In the 10-story building, layout B produced an average of 10% more positive bending moments than those of layout A. In the 20 story building, this percentage, for almost all support types, was doubled. When the number of floors increased to 30, the same percentage quadrupled compared to the 10-story building—except for support type 1. Based on these results, one can conclude that specifically for the positive bending moments, the overall increase was somewhat significant due to the change in the wall configuration from layout B to A.

4.4 Base Shear Forces

As illustrated in Fig. 7, the normalized base shear forces were plotted for all 60 models in the "x" and "y" directions. The base shear forces of support types 1 through 5 were all normalized based on the shear force values of the 10-story building's support type 1 in Z1. The largest normalized base shear forces in the "x" direction, for layouts A and B of the buildings with 10 and 20 stories in Z1 and Z2, were all obtained

from support type 1 (see Fig. 7a, b). In the 30 story building case, support type 3 generated the largest base shear forces due to larger MMPFs of support type 3 compared to support type 1. The base shear forces in the "y" direction, however, followed a different pattern. For all buildings, the largest base shear forces were obtained from support type 3—except for the 10 story one in Z1 where the largest base shear forces were obtained from support type 4. The smallest base shear forces were, however, extracted from support type 5 since the associated MMPFs were the smallest.

The base shear forces acting in the "x" direction for all support types of the 10-story building increased by an average of 30% when the results were compared to those from the 20 story one. For the 30 story building—except for support type 1—the results compared to the 20 story building increased by an average of 12%. The larger differences in base shear between support types 1 and 4 of the 10 and 20 story buildings indicated the fact that the fixed supports (support type 4) did not always produce the most critical design forces. Moreover, in this study, for the 10 and 20 story buildings, the fixed support produced as little as 50% less force than those from support type 1. This difference revealed the fact that the springs in the basement walls provided significant lateral strength to the 10 and 20 story buildings and therefore became the cause of the increase in the base shear. This pattern was

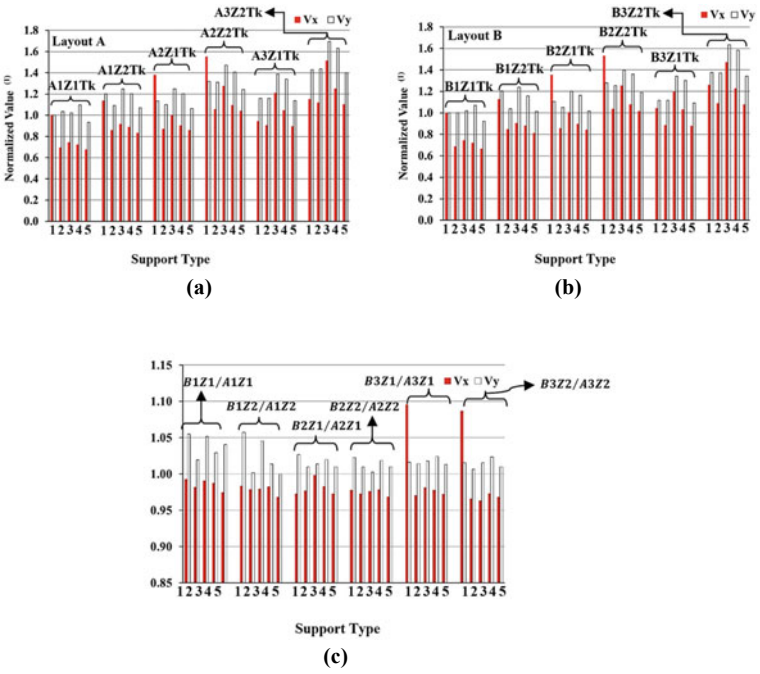

Fig. 7 Base shear forces for layouts: **a** A and **b** B and **c** Vx,y ((Layout B)/(Layout A)). (1) Normalized Value $= \frac{M11(\propto_i Z_j T_k)}{M11(\propto_i Z_j T_1)}$, where $\alpha_i = A, B$; $i = 1,2,3$; $j = 1,2$ and $k = 1,2,3,4,5$

not the same for the 30 story building since the forces from support type 4 increased by 10% when compared to their counterparts from support type 1.

The base shear forces acting in the "x" and "y" directions with medium-dense sand (Z2) were larger than those for the models with dense sand (Z1) for both layouts A and B, since the difference in the design spectrum of Z2 between TA and TB was larger than that of Z1 (the length of horizontal segment at S(T)=2.5, see Fig. 2a). Moreover, it was observed that the normalized base shear forces from support types 2 and 5 generated the least forces when they were compared to those from support types 1, 3, and 4 due to the presence of the horizontal joint springs used only in support types 2 and 5 at the ground floor level.

The ratios of the base shear forces from layouts B to A acting both in the "x" and "y" directions were also compared to each other (see Fig. 7c). Based on the data, it was concluded that the base shear forces in the "x" direction resulting from layout B to layout A—except for support type 1 of the 30 story building—were less than the unit value of one due to the larger period values of layout B. However, in the "y" direction, a different pattern was observed. For all the models, the results from layout B to layout A exceeded the unit value of one due to larger response spectrum accelerations extracted from layout B.

5 Conclusions

Based on the finite element analyses' results, following conclusions can be drawn:

1. For all the models with support types 2, 3, and 5, the total MMPFs in both the "x" and "y" directions were less than the TEC07 specified minimum value of 90%. In order to overcome this problem, the number of modes was increased to four digit numbers. But even then it was observed that the part of the building more susceptible to vibration was its superstructure, not its substructure. Therefore, it was concluded that a building with rigid basement walls should be analyzed as one building with its sub and superstructures based on a reasonable number of mode shapes. In this article, it was recommended that six times the total number of floors would define the reasonable number of mode shapes.
2 The modal analyses' results showed that the FPs of layout A were always smaller than those of layout B. This outcome was the result of the larger lateral strength that existed in the buildings with layout A. In all sixty models, support type 2 produced the smallest periods. The second and third smallest periods were obtained from the models with support types 4 and 5. In some cases, support type 4 produced the second smallest periods, while in others, support type 5 did. The largest periods were obtained from the models with support types 1 and 3. For the 10-story buildings support type 1, and for the 20 and 30 story buildings support type 3, produced the largest periods. These outcomes revealed the fact that buildings with support type 2 exhibited the most rigid behavior, while buildings with support types 1 and 3 exhibited the most flexible behavior.

3. In order to understand the importance of the area and joint springs on the overall dynamic behavior of buildings, the periods of buildings with support type 3 were compared to those with support type 1. The results indicated that the periods generated by the area springs (support type 1) were larger than those generated by the joint springs (support type 3). Support type 5 also had joint springs, but coupled with the horizontal springs located at ground floor level. The periods from support type 5 were always smaller than those from support type 1, revealing the significance of the horizontal springs.
4. This study suggests that as the number of floors increases to 30, the difference in periods resulting from the five support types becomes less prominent.
5. In the mat foundations of all the buildings, the differences between the positive bending moments (for the bottom reinforcement) resulting from the 5 support types were nearly insignificant, except for support type 1 of the 30 story building with layout B. Therefore, it is concluded that in the design stage of a mat foundation, the choice of support type has almost no impact.
6. When the base shear forces of layouts B and A acting in both "x" and "y" directions were compared to each other, it was concluded that the ratio of the forces in the "x" direction resulting from layout B to layout A (except for support type 1 of the 30 story building) was less than one. This result is associated to the larger period values of layout B. However, in the "y" direction, a completely different pattern was observed since the results from layout B to layout A exceeded one. Larger response spectrum accelerations evaluated from layout B are the reason why larger shear forces in the "y" direction (compared to those in the "x" direction) were obtained for layout B.

References

1. Newmark NM, Hall WJ (1969) Seismic design criteria for nuclear reactor facilities. In: Proceedings of the 4th World conference on earthquake engineering, Santiago, Chile, pp 37–50
2. Seed HB, Lysmer J (1978) Soil-structure interaction analyses by finite elements—state of the art. Nucl Eng Des 46(2):349–365
3. Soydemir C, Celebi M (1992) Seismic design of buildings with multi-level basements. In: Proceedings of the tenth world conference on earthquake engineering, Balkema, Rotterdam, The Netherlands
4. Bhattacharya K, Dutta SC, Dasgupta S (2004) Effect of soil-flexibility on dynamic behaviour of building frames on raft foundation. J Sound Vib 274(1–2):111–135
5. Galal K, Naimi M (2008) Effect of soil conditions on the response of reinforced concrete tall structures to near-fault earthquakes. Struct Design Tall Spec Build 17(3):541–562
6. Narayana G, Sharada BH, Manish A (2010) Effect of soil flexibility on dynamic behavior of building frames resting on strip foundation. GeoShanghai International Conference, ASCE, Shanghai, China, pp 92–100
7. Chinmayi HK, Jayalekshmi BR (2013) Soil-structure interaction analysis of RC frame shear wall buildings over raft foundations under seismic loading. Int J Sci Eng Res 4(5):99–102
8. Reza Tabatabaiefar SH, Fatahi B, Samali B (2013) Seismic behavior of building frames considering dynamic soil-structure interaction. Int J Geomech 13(4):409–420

9. Halkude SAA, Kalyanshetti MGB, Barelikar SMB (2014) Seismic response of RC frames with raft footing considering soil structure interaction. Int J Curr Eng Technol 4(3):1424–1431
10. Mohseniana V, Nikkhooa A, Hejazi F (2019) An investigation into the effect of soil-foundation interaction on the seismic performance of tunnel-form buildings. Soil Dyn Earthq Eng 125:105747
11. Khayyat ZKA (2015) Structural analysis and design of buildings with rigid basements and shear walls. MS Thesis, Department of Civil Engineering, Atilim University, Ankara, Turkey
12. SAP2000 (2011) Computer and structures, Inc. Berkeley, California, USA
13. TEC07, Turkish Earthquake Code (2007) The ministry of public works and settlement-government of Republic of Turkey. Ankara, Turkey
14. TS500 (2000) Turkish Standards of Requirements for Design and Construction of Reinforced Concrete Structures, Turkish Standards Institution, Ankara, Turkey
15. TS498 (1997) Turkish standards of design loads for buildings, Turkish Standards Institution, Ankara, Turkey
16. Okabe S (1926)_ General theory of Earth pressure. J Jpn Soc Civil Eng. Tokyo, Japan, 12(1)
17. Mononobe N, Matsuo M (1929) On the determination of earth pressures during earthquakes. Proc World Eng Congress 9:179–187
18. Bowles JE (1997) Foundation analysis and design, 5th edn. McGraw-Hill, New York, USA
19. Coduto DP (2001) Foundation design: principles and practices, 2nd edn. Prentice Hall, New York, USA
20. Langer JA, Mosley E, Thompson C (1984) Laterally loaded deep foundations analysis and performance. American Society for Testing Materials, ASTM Special Technical Publication, 835

Static and Dynamic Responses of Light Gauge Steel-Ultra-High Performance Fibre-Reinforced Concrete Composite Deck

Jun Xia, Jie Li, Guobin Gong, and Pei Song

Abstract This paper investigated the static and dynamic responses of an innovative light gauge steel-ultra-high performance concrete composite deck system, which is aimed to be used as a deck component for prefabricated residential building. The static loading was performed using staged weight loading, while the dynamic responses were examined using human-induced loading. The fix location walking and designated path walking scenario were implemented for walking frequency ranging from 1.5 Hz to 2.6 Hz. Measured RMS values and peak acceleration were compared with the design standard criteria. It was concluded that the RMS value is more reasonable measurement indices for checking against the human-induced vibration. The proposed composite deck exhibits a satisfactory vibration level under human-induced vibration with a walking frequency less than 2.2 Hz. At the same time, more procedure shall be implemented to reduce the acceleration under higher walking frequencies.

Keywords Human-induced loading · Stud connection · Light gauge steel · UHPFRC

J. Xia (✉) · J. Li · G. Gong
Civil Engineering Department, Design School, Xi'an Jiaotong-Liverpool University, Suzhou, Jiangsu, China
e-mail: Jun.xia@xjtlu.edu.cn

J. Xia
Research Institute for Sustainable Material and Environment, Xi'an Jiaotong-Liverpool University, Suzhou, Jiangsu, China

P. Song
Shanghai Jundao Residential Industry Co., Ltd., Shanghai, China

T. Kang (ed.), *Proceedings of 5th International Conference on Civil Engineering and Architecture*, Lecture Notes in Civil Engineering 369,
https://doi.org/10.1007/978-981-99-4049-3_87

1 Introduction

Along with the increasing awareness of the sustainable urbanization, construction approach based on prefabrication has become attractive worldwide [1]. Because components are manufactured off-site, prefabricated construction can reduce the dependency on weather condition and facility requirements. The prefabrication process can help reduce the amount of construction waste [2] and perform better from the environmental protection point of view than the traditional cast-in-place construction approach [3]. In some cases, the overall duration of the construction schedule can be great reduced because different components can be manufactured in different factories simultaneously. Therefore, it helps minimize social impacts due to reducing noise and dust generated on-site during the construction. It is essential to make sure that the prefabricated component performs well during the usage stage. For the prefabricated decks, its responses to the human-induced loading shall be investigated to ensure a satisfactory comfort can be ensured against vibration.

Light gauge steel has been widely used in construction, especially for low rise residential buildings, for their excellent mechanical properties such as high strength, secure processing and reliable connection. Usually, light gauge steel has to work with other insulation materials used in exterior walls or roofing applications because of the high thermal conductivity at around 50 Wm^{-1} K^{-1}. The composite decking system can partially solve the thermal bridge issue related to the building energy consumption [4], by installing a concrete layer on top of the light gauge frames. Additional insulation can be added between the light gauge frame members if necessary.

Ultra-high performance fibre-reinforced concrete (UHPFRC) was developed as a cementitious composite material with superior particle packing, which leads to higher strength and better resistance to external environments than traditional construction materials [5]. By adding fibre to the dense matrix, the tensile strength and ductility can be further improved [6]. Moreover, UHPFRC owns very good resistance to impact, chemical degradation, abrasion and fire [7], enabling its application in various places, especially those with special requirements on strength or self-weight. By utilizing UHPFRC in the composite deck system. The overall thickness of the concrete part can be reduced while still reaching the design strength capacity. The self-weight of the composite deck can be further reduced, which is beneficial for transportation and installation. However, the reduced composite section may reduce stiffness as the modules of elasticity of UHPFRC are not significantly higher than that of conventional concrete. Therefore, the deformation at the service load or any stiffness related concerns, such as vibration under human-induced loading, shall be investigated.

The human-induced loading has been investigated previously, and several numeric models have been developed to simulate the walking process [8, 9]. The floor vibration is a particular concern for structures with small stiffness, such as pedestrian bridges and floor with large span. Although the vibration caused by a human may not lead to structure failure, the people walking on the structure may feel uncomfortable. This service limit state consideration is usually satisfied by limiting the peak or

the root mean square acceleration in the vertical direction. Based on BS ISO 2631-1-1997, the root mean square acceleration shall be less than 0.315 m/s^2 [10], while the Chinese national standard, JGJT 441–2019 [11] requires that the first vertical vibration frequency shall higher than 3 Hz, and the peak acceleration limit of the floor in a residential building shall be less than 0.050 m/s^2.

Although numerical simulation can help understand the dynamic responses of structure component under human-induced loadings, such as those presented by Cai [12], experiments are still a powerful method to investigate structure components' responses. Vibration responses of steel-timber composite floors were investigated by both experimental and numerical analyses [13, 14]. The design criteria from several standards were compared.

This paper aims to investigate the mechanical responses of an innovative light gauge steel-UHPFRC composite deck panel. The material properties and fabrication procedures of the composite deck are explained, followed by the presentation of the testing procedure and results under static and human-induced loading. The tested system has the potential to be used for prefabricated buildings with excellent static and dynamic resistance to human loading.

2 Material and Specimen

2.1 Light Gauge Steel Profile

Two types of light gauge steel profiles with 2 mm thickness were used in this research. Both profiles were manufactured by low yielding strength steel with yielding strength equals 235 MPa. The shape and dimensions of the cross-sections are shown in Fig. 1b. The C section profiles were placed along the span direction and were kept as un-interrupted, while the U section members were used as either the end bracing or the middle bracing. When used as middle bracing, web opening was intruded to allow the C section member to cross through. Additional web welding at the internal joints was introduced to increase the light gauge steel frame's stability. The layout of the light gauge steel members is shown in Fig. 1a.

2.2 UHPFRC

The UHPFRC material used in this study is a home-made material, which makes use of ground granulated blast furnace slag (GGBS). The mix design of the cementitious matrix can be found in Table 1. Steel fibres with a diameter 0.2 mm and 12 mm were added to the matrix at the dosage of 2% volume fraction. The fibres were added after reaching the fluidity during concrete mixing in order to ensure the uniformity of their spatial and orientation distribution.

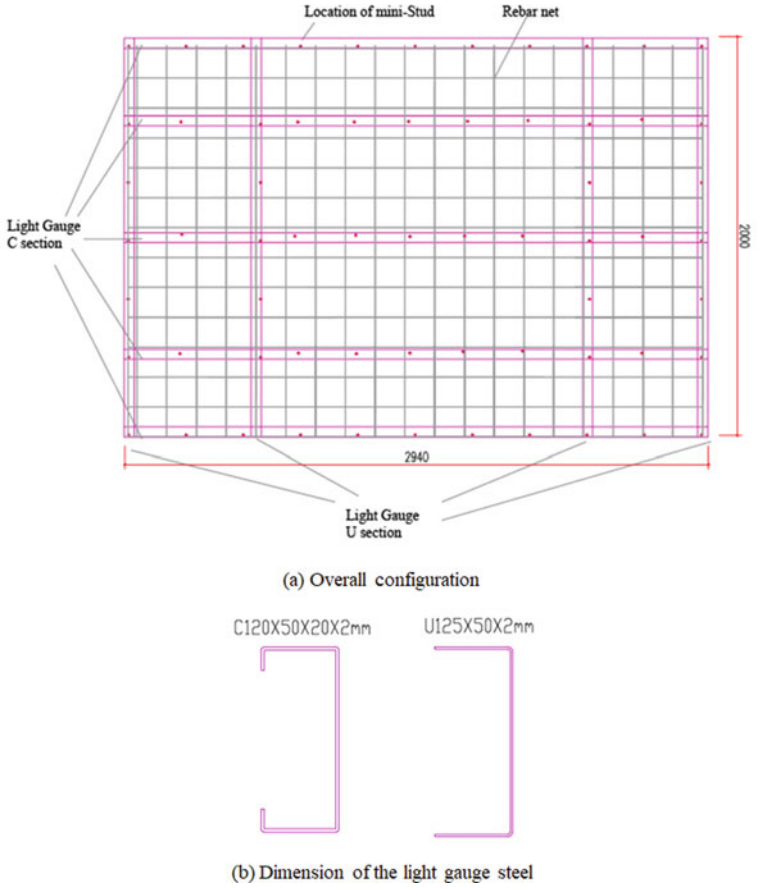

Fig. 1 Dimension of the composite panel and components

Table 1 Mix design of UHPFRC material

Material	kg/m^3
Cement	475
Silica fume	95
Fine sand	1020
Ground Quarte	105
Superplasticizer	40
Ground granulated blast furnace slag (GGBS)	475
Water	190
Total (without fibre)	2400

Six 100 mm by 100 mm cube specimens were prepared along with the composite deck's concrete layer. The cubes specimens were treated in the 90 degree Celsius hot water for 48 h after demoulding. The compressive strength tests were conducted at 7 days of age after the heat treatment. The average compressive strength is 163.6 MPa with a standard deviation of 8.57 MPa. It shall be noted that because it is impossible to enforce the steam curing for the entire composite deck, it is expected that the UHPFRC material has lower compressive than what is tested at the material level.

2.3 UHPFRC Mini-Studs, Reinforcement Net and Fibre Cement Board

Mini-studs were welded to the top flange of the light gauge steel members at spacing around 300 mm. The overall length of the stud is 40 mm, while the diameter is 6 mm. The designed location of the stud can be found in Fig. 1. Reinforce net with smooth rebar at a diameter of 5 mm was welded to the top of the min-stud, as reinforcement for the concrete layer, shown as grey lines in Fig. 1. Fibre cement board with a thickness of 10 mm was used to seal the deck panel's backside. Drill-in rivets were used to secure the back panel to the light gauge steel profiles.

2.4 Specimen Design and Fabrication

The composite deck is designed as simply supported at the two short sides with total length equals 2.94 m and width of 2 m. The main structural component to resist tensile force is the welded light gauge steel frame, while the top 40 mm UHPFRC concrete layer is the major component for compressive force. Mini-studs were used to connect the two parts together. The layout of the light gauge steel frame and mini-studs' locations are shown in Fig. 1a.

The composite deck's major fabrication procedures include cutting and welding of the light gauge steel frame; welding of the mini-studs, placing and welding of reinforcement net; casting the top-layer concrete; drill and installation of the bottom cover panel. A specimen before inserting central member is shown in Fig. 2a, while the final product is shown in Fig. 2b.

3 Static Loading

The panel was first subjected to static loading, as shown in Fig. 3. To simulate the uniformly distributed loading, concrete blocks were placed on the surface of the deck layer by layer to increase the pressure gradually. The additional concrete panel was

(a) Welding of mini-stud to the light gauge steel (b) Finished composite deck (side view)

Fig. 2 Fabrication process and final specimen

added for the final steps. The ultimate pressure added to the deck was 7.28 kPa, which corresponds to 3 mm deflection in the mid-span. The composite deck exhibits linear responses when the pressure is below 4 kPa. While more loading can be added to the deck, the nonlinear response was observed, which may be due to the shear studs' deformation and redistribution of the load transfer. The composite deck panel is still intact under 7.28 kPa, and no sign of failure was observed. The corresponding displacement is only 2.1 mm, which corresponding to approximately 1/1300 of the span.

Because the composite deck's static performance under the simply supported condition is satisfactory, its dynamic responses are of concern. Therefore, the dynamic responses of the composite deck under human walking and jumping are further investigated.

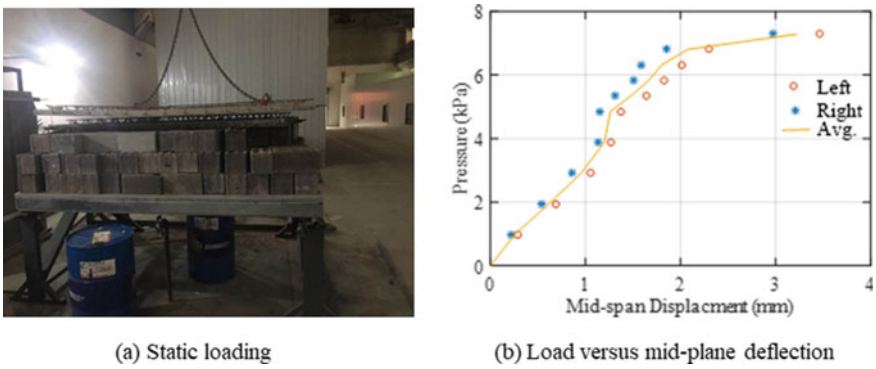

(a) Static loading (b) Load versus mid-plane deflection

Fig. 3 Static loading configuration and results

(a) Fixed location jumping (b) walking along the designated path

Fig. 4 Human-induced loading

4 Dynamic Loading

4.1 Methods

Human walking tests are performed on the simply supported composite deck panel. Two accelerometers were installed at the mid-span on two edges of the panels, as shown in Fig. 4. Two loading cases were performed: fixed point walking, and the other is walking along a designated path. The body weight of the participant in the test is 55 kg. Fig. 4a shows the testing of fixed location walking at the deck panel's central location. The walking frequencies were coordinated by a metronome and ranged from 1.5 Hz to 2.6 Hz with an interval of 0.1 Hz. The testing was repeated three times. Fig. 4 b shows the testing of walking along the centre line of the deck panel. Another two tests with walking paths that are shifted 30 mm and 60 mm from the centre line were also performed, with the same frequency sequence for the fixed location walking.

4.2 Results

Fix Location Walking. Typical dynamic responses of the composite deck under 1.5 Hz walking excitation are obtained. The acceleration recording obtained from the accelerometer on the left edge and RMS is shown in Fig. 5a. Acceleration versus time was plotted in the top plot in Fig. 5a, while the RMS values based on the one-second moving window were shown in the bottom plot, with the x-axis showing the number of sample points in the whole recording period. The bottom plot shows results from sensors installed on the left and right edges of the panel. Same procedures were applied to all three tests for a series of different walking frequencies. Although there are some variations between different tests under the same frequency, the general

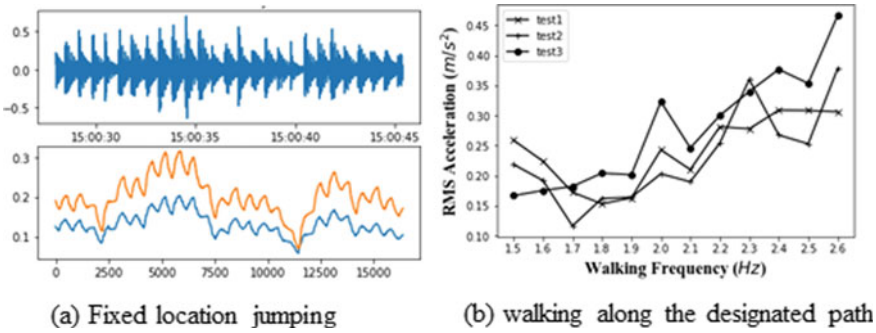

Fig. 5 Response of panel under fixed location jumping

trend is RMS increases with the increase of the walking frequency. RMS reaches the maximum value of 0.384 m/s^2 when walking at a frequency of 2.6 Hz.

Designated Path Walking. The dynamic responses of the composite deck under designated path walking are obtained. Fig. 6 shows the responses at minimal and maximum walking frequencies at 1.5 Hz and 2.6 Hz, for three scenarios: along the centre line, 30 mm, and 60 mm off the centre lines. Acceleration versus time was plotted in the top plot in each subfigure, while the RMS values based on the one-second moving window were shown in the bottom plot, with the x-axis showing the number of sample points in the whole recording period. Each bottom plot shows results from sensors installed on the left and right edges of the panel.

By collecting the peak RMS from each individual walking frequency cases, the overall RMS acceleration versus walking frequency can be found in Fig. 7, for three cases with different walking paths. While for some cases, the RMS value is higher when walking along the centre line, it is in doubt that the centre line is more critical than other walking paths. Along with the increase of walking frequency, the RMS value increases first and then reaches a plateau after reaching a walking frequency of 2.4 Hz. It is most obvious when walking along the central line, while the same trend can also be identified in the other two cases. It is believed that the recording at 2.3 Hz is lower than what it supposes to be as shown in Fig. 7a. Therefore, it can be concluded that when the walking frequency is lower than 2.2 Hz, the composite deck will not cause any comfort concerns. The comparison of peak acceleration is shown in Fig. 7b. However, the record peak acceleration for all walking frequencies is larger than the limiting value at 0.015 m/s^2, according to JGJT 441. It can be attributed to the free vibration due to gravity because the composite deck panel supports are not fully fixed and cannot sustain tensile forces. For this investigation, the criteria based on RMS values are more suitable.

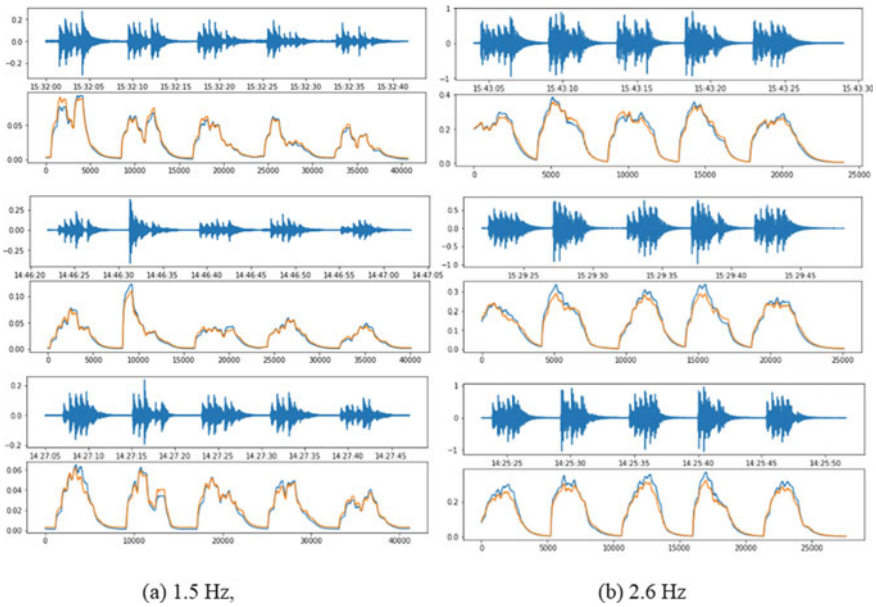

(a) 1.5 Hz, (b) 2.6 Hz

Fig. 6 Dynamic responses under designated path walking: 0, 30 mm, 60 mm off the centre line

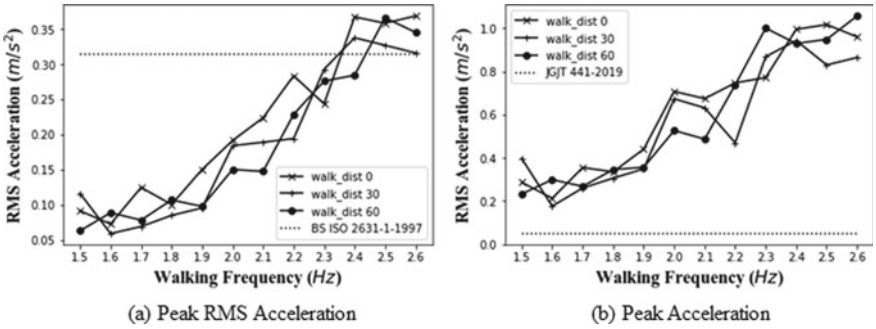

(a) Peak RMS Acceleration (b) Peak Acceleration

Fig. 7 Summarized peak RMS and acceleration

5 Conclusions

A light gauge steel-ultra-high performance fibre-reinforced concrete composite deck was fabricated and tested under static and dynamic loading. Based on the experimental data, the following conclusions can be drawn:

1. The composite deck has a straightforward manufacture process. The mini-studs were easy to install and can provide secure composite action between the light gauge steel and UHPFRC layer.

2. The two-edge simply supported composite deck has a linear response under uniformly distributed load up to 4 kPa. The composite deck has an ultimate load capacity higher than 7.28 kPa.
3. The composite deck exhibits higher RMS value when subject to higher frequency walking excitation. RMS value reaches the maximum of 0.384 m/s^2 when walking at the frequency at 2.6 Hz, while the corresponding RMA value is 0.369 m/s^2 for the path walking cases. The offset distance of the walking path from deck centre line does not change the responses of the composite deck significantly.

The proposed panel structure is suitable for prefabrication and through the static and dynamic testing, and it was approved that the structure has good static and dynamic performance against the human loading. The connections of panel to the supporting member shall be further investigated to ensure the integrity of the structure.

Acknowledgements The support from Xi'an Jiaotong-Liverpool University (Grant No: RDS10120170090) is appreciated.

References

1. Hong J, Shen Q, Li Z et al (2018) Barriers to promoting prefabricated construction in China: a cost–benefit analysis. J Clean Prod 172:649–660. https://doi.org/10.1016/j.jclepro.2017.10.171
2. Li Z, Shen Q, Alshawi M (2014) Measuring the impact of prefabrication on construction waste reduction: an empirical study in China. Resour Conserv Recycling 91:27–39. https://doi.org/10.1016/j/resconrec.2014.07.013
3. Mao C, Shen Q, Shen L, Tang L (2013) Comparative study of greenhouse gas emissions between off-site prefabrication and conventional construction methods: two case studies of residential projects. Energy Build 66:165–176
4. Song J, Lim J, Song S (2016) Evaluation of alternatives for reducing thermal bridges in metal panel curtain wall systems. Energy Build 127:138–158. https://doi.org/10.1016/j.enbuild.2016.05.078
5. Shi C, Mo YL (2008) High-performance construction materials science and applications. World Scientific, Danvers
6. Fehling E, Schmidt M, Walraven J, Leutbecher T, Fröhlich S (2011) Ultra-high performance concrete UHPC: fundamentals, design, examples. Wihelm Ernst and Sohn, Berlin
7. SINTEF Building and Infrastructure (2012) Ultra High Performance Fibre Reinforced Concrete (UHPFRC)—State of the art. COIN Project report
8. Ohlsson SV, Gskola CTH (1982) Floor vibration and human discomfort. Chalmers University of Technology, Division of Steel and Timber Structure
9. Bertram JE, Ruina A (2001) Multiple walking speed-frequency relations are predicted by constrained optimization. J Theor Biol 209(4):445–453
10. ISO 2631–1 (1997) Mechanical vibration and shock—evaluation of human exposure to whole body vibration: part 1: General requirements. International Organization for Standardization
11. JGJT 441–2019 (2019) Technical standard for vibration comfort of building floors. Beijing: Science Press
12. Cai Y, Gong G, Xia J, He J, Hao J (2020) Simulations of human-induced floor vibrations considering walking overlap. SN Appl Sci. 2(1):1–15

13. Chiniforush A, Makki Alamdari M, Dackermann U, Valipour HR, Akbarnezhad A (2019) Vibration behaviour of steel-timber composite floors, part (1): experimental and numerical investigation. J Constr Steel Res [Internet]. 161:244–57
14. Hassanieh A, Chiniforush AA, Valipour HR, Bradford MA (2019) Vibration behaviour of steel-timber composite floors, part (2): evaluation of human-induced vibrations. J Constr Steel Res [Internet] 158:156–170

Strength Analysis of I-Beam under Biaxial Eccentric Load

Wei-Hsun Hsu, Shu-Ti Chung, Wei-Rui Laio, and Wei-Ting Hsu

Abstract Perfect design need make structure stable and wouldn't destroyed, when earthquake or strong wind happened. When an eccentric load on a steel structural member, the force acting on the member is not only the axial load. It would have eccentric behavior for the structural member and also have additional bending moment caused by the eccentric load. In addition, due to the different lengths of the members, the strength of the members needs to be evaluated according to the Flexure-Compression equation of the axial force and the bending moment. In the analysis and calculation, the relationship between the components of the axial force, it is necessary several times during the analysis to deduce the critical value that the component can withstand, to ensure the safe bearing range. In this study, specification formulas of AISC (1989, 1999, 2017) double-symmetrical I-beams are studied and integrated, through the calculation methods-LRFD and ASD. Study expects that through the analysis and integration of the I-beam force behavior suggestions, users can have a reference choice when designing. Through the analysis, it is found the value calculated by ASD will be more conservative than LRFD, and the results calculated by LRFD in 1999 and 2017 are not much different. When calculating the axial force, axial compression is lower in 1999 due to use of different reduction factors (0.9 and 0.85). And the analysis of the three versions of AISC (1989, 1999, 2017), the intensities calculated under the same reference conditions, AISC (2017) value calculated using the LRFD method was the highest.

Keywords Strong axis eccentricity · Weak axis eccentricity · AISC · Biaxial bending moment · Members subject to flexure and compression

W.-H. Hsu
Department of Marketing and Logistics Management, Chaoyang University of Technology, Taichung, Taiwan

S.-T. Chung · W.-R. Laio · W.-T. Hsu (✉)
Department of Construction Engineering at, Chaoyang University of Technology, Taichung, Taiwan
e-mail: wthsu@cyut.edu.tw

T. Kang (ed.), *Proceedings of 5th International Conference on Civil Engineering and Architecture*, Lecture Notes in Civil Engineering 369,
https://doi.org/10.1007/978-981-99-4049-3_88

1 Introduction

I-beam is the most commonly used component in steel structure buildings. Due to the double symmetry shape, it is a very simple and quick object for design and construction. In the study, in order to compare the specification for new one and old, the strength analysis was carried out through the three specifications of AISC (1989, 1999, 2017) [1–3]. According to the specification, the influence of different eccentric shafts on the strength change of the I-beam is analyzed, and the strength comparison is carried out using the respective calculation formulas. The wings is less than the web's length, so the performance of the I-beam as a structural column will be worse than that of a structural beam. According to Stoakes [4], the limit state of a section steel depends on the distribution of axial force, the bending position of the weak axis, the stiffness of the hierarchical torsional support and the magnitude of the rotation in the plane, so the transmission of the force and the positional deviation may be affected. This leads to the unstable condition of the I-beam and even the destruction. Bhowmick et al. [5] showed that AISC uses the same slenderness limit when calculating strong axis and weak axis bending, but the I-shaped strain distribution when bending around the strong axis is significantly different from the strain distribution when bending around the weak axis. Using the same slenderness limit for strong axis and weak axis bending conditions needs to be re-evaluated. When the steel structural members themselves are manufactured in the factory, due to the application and processing of the manufacturing process, there will be residual stress in the steel structural members. Trahair [6] found in his research that the residual stress will increase the change of the steel structure when it is under compression. The residual stress of the bearing capacity that can lead to inelastic buckling is significantly reduced. Bas [7] evaluated the effect of residual stress by analyzing three buckling scenarios of I-type members with different lengths without lateral restraint and found that under different buckling conditions, when the member undergoes torsional buckling, the strength that the load can withstand will decrease about 13%.

2 I-Shaped Section to Flexure and Axial Force

In steel structural members, I-beam sometimes not only has to bear pure axial compression. Affected by eccentricity when the eccentric load, the component will bear the interaction of axial compression and bending moment at the same time. At this time, if want to calculate the load strength that the member can bear. It is not only necessary to calculate by the beam-column formula, but also by substituting the beam-column result into the flexure–compression equation of axial force and bending moment. When the most consistent strength value is found through repeated calculations, the final result is the critical strength value that the I-shaped member can withstand when subjected to eccentric loads. According to the study of Rasmussen et al. [8], if the slenderness ratio of the rod is close to the yield limit,

when the limit is exceeded, the rod will undergo local buckling, and the strength of the short column will be lower than the axial compressive load. In addition, Schafer et al. [9] used ANSI/AISC360-16, the Steel Construction specification. They found that there are some λ_r bending limits in AISC360 that may not be in line with the intended goals, and while all λ_p bending limits ensure that the plastic moment can be achieved. But the torsional case is not achievable.

This research paper adopts the calculation and analysis of the flexure–compression equation of axial force and bending moment of AISC (2017). It is calculated as follows:

When $\frac{P_r}{P_c} \geq 0.2$

$$\frac{P_r}{P_c} + \frac{8}{9}\left(\frac{M_{\mathrm{rx}}}{M_{\mathrm{cx}}} + \frac{M_E}{M_{\mathrm{cy}}}\right) \leq 1.0 \tag{1}$$

When $\frac{P_r}{P_c} < 0.2\,\%$

$$\frac{P_r}{2P_c} + \left(\frac{M_{\mathrm{rx}}}{M_{\mathrm{cx}}} + \frac{M_{\mathrm{ry}}}{M_{\mathrm{cy}}}\right) \leq 1.0 \tag{2}$$

where

P_r = required axial strength, determined in accordance with stability, using LRFD or ASD load combinations, kips (N).

P_c = available axial strength determined in accordance with compression, kips (N).

M_r = required flexural strength, determined in accordance with stability, using LRFD or ASD load combinations, kip-in. (N-mm).

M_c = available flexural strength, determined in accordance with flexure, kip-in. (N-mm).

χ = subscript relating symbol to major axis bending.

y = subscript relating symbol to minor axis bending.

3 Example of Biaxial Eccentricity Strength Calculation

The research angle steel adopts the double-symmetrical I-beam W14 × 82 as the calculation component object (Fig. 1), and the component length is fixed at 8.33ft as the analysis benchmark. The study compared the strength of I-beam members under eccentric loading using AISC specification from three different periods (1989, 1999 and 2017). The analysis calculates the strong and weak axes acting on the I-beam member of eccentric load, compares each other and evaluates intensity changes. Eccentricity is calculated as 1 in. from the center point. In the analysis results below, the research and analysis parameters will be eccentricity from 1 to 4 inches.

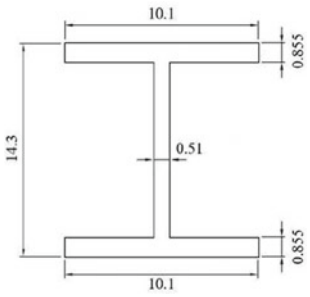

Fig. 1 Double-symmetrical I-beam shape (in.)

According to the study result, Table 1 shows the results of calculated using the AISC (2017)-LRFD and ASD methods. The numerical results are distinguished by the eccentricity acting on the strong axis or acting on the weak axis. It can be found that compared with LRFD, the result intensity value calculated by ASD method is lower than LRFD, whether acting on strong axis or weak axis. Figure 2 shows an intensity value curve from Table 1. AISC (2017)-LRFD was used to calculate and analyze the intensity curve acting on the strong axis, in Fig. 2, the strength curve is called S-LRFD-2017, and the weak axis is called W-LRFD-2017. The calculations in 2017 and 1999 and1989 for both LRFD and ASD were used the name rule. It is possible to get a clearer picture of the strength trend presented by the chart. Intensity differences between two different calculation methods, LRFD and ASD, were used. The horizontal axis is the distance of the eccentric load; the vertical axis is the strength value that the I-shaped member can bear. Since AISC(2017)-LRFD and ASD calculate the axial force and bending moment differently, LRFD multiplies the axial force reduction coefficient (ϕ_c) and bending moment reduction coefficient (ϕ_b) when calculating the axial force and bending moment strength, That is, dividing the axial compressive strength or bending moment strength by the safety factor ($\Omega_c = 1.67$ or $\Omega_b = 1.67$) like ASD, the strength value estimated by ASD will be conservative.

Table 2 shows the numerical results of AISC (1999)-LRFD and AISC (1989)-ASD calculations. According to the analysis results, it can also be found that the strength value calculated by LRFD is also higher than ASD. The difference is that the

Table 1 AISC-LRFD/ASD(2017) strong axis and weak axis of strength value

e(in)	Strong axial		Weak axial	
	LRFD(kips)	ASD(kips)	LRFD(kips)	ASD(kips)
0	958.95	638.02	958.95	638.02
1	840.46	559.04	640.10	424.34
2	748.68	497.94	490.18	324.87
3	675.30	449.10	399.70	264.96
4	615.23	409.12	338.02	224.13

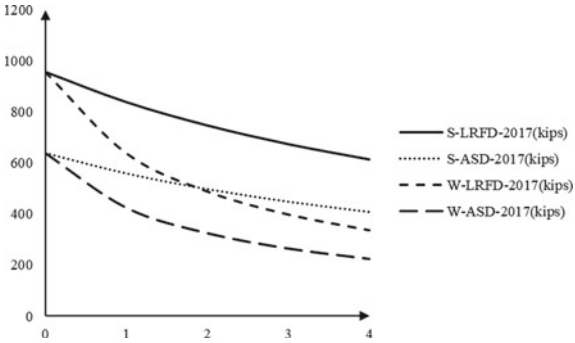

Fig. 2 AISC-LRFD/ ASD(2017) strong axis and weak axis of strength curve

reduction coefficient of axial force (ϕ_c) of LRFD in 1999 is 0.85, and the reduction coefficient of bending moment (ϕ_b) is 0.9. However, the calculation of the axial compressive strength of ASD needs to be calculated using different axial compressive strength formulas according to different applicable conditions. The same is true for the bending moment strength, and there is no need to divide the safety factor. Figure 3 is the strength curve from Table 2. The same as Fig. 2 can be seen in the curve, no matter the eccentric load acts on the strong axis or the weak axis, the strength of the LRFD. The value is also higher than the intensity value of ASD, and the intensity will be lower as the eccentric distance is farther.

Table 2 AISC-LRFD(1999)/ASD(1989) strong axis and weak axis of strength value

e(in)	Strong Axial		Weak Axial	
	LRFD(kips)	ASD(kips)	LRFD(kips)	ASD(kips)
0	905.67	621.46	905.67	621.46
1	799.43	540.78	617.17	370.34
2	716.01	479.16	476.69	271.45
3	648.63	430.50	390.63	215.97
4	593.04	390.93	331.49	179.59

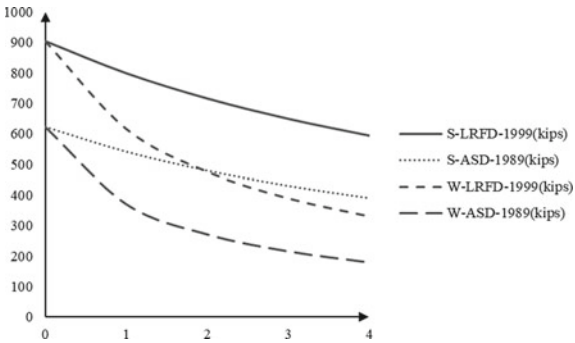

Fig. 3 AISC-LRFD(1999)/ ASD(1989) strong axis and weak axis of strength curve

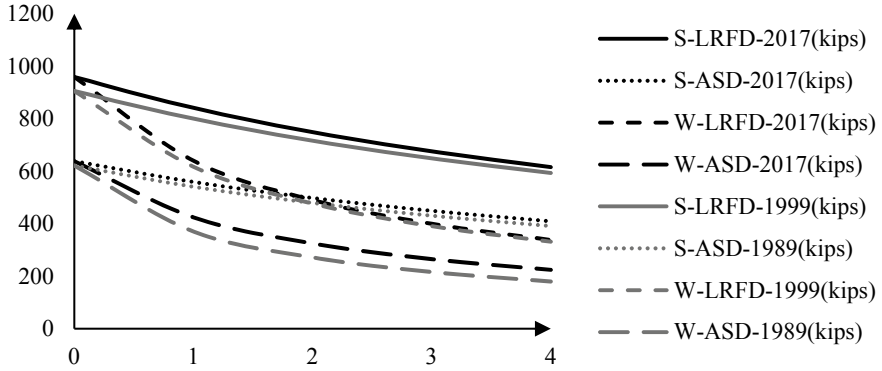

Fig. 4 AISC-LRFD/ASD-(2017), (1999), (1989) strong axis and weak axis of strength curve

Figure 4 shows a comprehensive comparison chart (2017, 1999 and 1989) obtained by Figs. 2 and 3. Taking AISC (2017) as an example, which is calculated using LRFD or ASD. Analysis method for eccentric loading of I-beam, the strength curve in 2017 will be higher than the standard strength in 1999 and 1989. With the same eccentric loading acting on the strong or weak axis, the intensity of LRFD is higher than ASD. In without eccentric strength case, S/W-LRFD-2017 is stronger than S/W-LRFD-1999 about 5.6% strength. But as the eccentric distance is farther, the strength values of the two specifications will be closer. In the same case about without eccentric strength of S/W-ASD-2017 and S/W-ASD-1989 differ by only 2.6%, but the intensity values of ASD will vary different when the distance is farther. When the distance is at 4 inches, S-ASD-2017 and S-ASD-1989 differs about 4.5% strength. And when the distance is at 4 inches, W-ASD-2017 and W-ASD-1989 will differ about 20% strength.

4 Summary

This study sorted out the theoretical specifications of AISC (2017, 1999, 1989) eccentric load calculation for different I-beams. Comparing the data of different specifications, the following results are obtained:

1. The calculation method of I-beam provided by AISC (2017) ASD and LRFD, although the calculation process is the same. But the strength value calculated by LRFD needs to be multiplied by a reduction factor φ, and the strength value calculated by ASD needs to divided by safety factor Ω. It is necessary to multiply different α values (LRFD $= 1$; ASD $= 1.67$) when calculating the amplification factor.

2. Comparing the LRFD methods for 2017 and 1999, the results show that the intensity values in 1999 are lower than those in 2017. Because the reduction factor of the two has been revised, the design axial pressure differs by 5.6%.
3. Comparing the ASD calculation methods of AISC (2017) and AISC (1989). Although the two versions have different lengths and types when judging intervals, they are also similar to the results of LRFD. Intensity values calculated using AISC (2017). Compared with the 1989 value, the difference between the two is only about 4.5% strength without the eccentric strength. But the difference in strength can reach 20% strength with the farther the eccentric distance.
4. According to the characteristics of the I-shaped section, the strength of the strong axis will be higher than that of the weak axis and is seen from Table 1 and Fig. 2. When the farther of distance, the strength decreases more. And when the eccentric distance reaches 4 inches, the difference between the strength values of the strong and weak axes can reach 45% (S/W-LRFD-2017 and S/W-ASD- 2017).

Expect to using the analysis results of this study, the strength behavior of I-beam under eccentric load is compiled a use recommendation, contains the effective length of member and eccentric load. And then provide relevant reference for users in the design and construction.

References

1. Manual of Steel Construction–Allowable Stress Design (1989). 9th Edition, American Institute of Steel Construction, Chicago, Illinois
2. Manual of Steel Construction–Load and Resistance Factor Design (1999) 3rd Edition, American Institute of Steel Construction, Chicago, Illinois
3. Manual of Steel Construction, Specification for Structural Steel Buildings (2017). In: 15th edition, American Institute of Steel Construction, Chicago, Illinois
4. Stoakes CD, Fahnestock LA (2016) Strong-axis stability of wide flange steel columns in the presence of weak-axis flexure. J Struct Eng 142
5. Bhowmick AK, Grondin G (2019) Local buckling of I-shape members bent about their weak axis. Structural stability research council annual stability conference. 1(2019):18–32
6. Trahair NS (2019) Inelastic lateral buckling of continuous steel beams. Eng Struct 190:238–245
7. Bas S (2019) Lateral torsional buckling of steel I-beams: effect of initial geometric imperfection. Steel Compos Struct 30:483–492
8. Rasmussen KJR, Hancock GJ (1992) Plate slenderness limits for high strength steel sections. J Construct Steel Res 23:73–96
9. Ben W. Schafer, Louis F. Geschwindner, Sabol T. and Chia-Mingd Uang: Review of Local Buckling Width-to-Thickness Limits. Engineering Journal. Vol. 59 (2022), p. 65–84